THE UNIVERSITY OF TEXAS AT AUSTIN
CENTER FOR TRANSPORTATION RESEARCH

TECHNICAL REPORT 0-6816-1
TxDOT PROJECT NUMBER 0-6816

Applications of Partial Depth Precast Concrete Deck Panels on Horizontally Curved Steel and Concrete Bridges

Colter Roskos
Paul Biju-Duval
John Kintz
Victoria McCammon
Yang Wang
Sean Donahue
Todd Helwig
Michael Engelhardt
Oguzhan Bayrak
Patricia Clayton
Eric Williamson

April 2018; Published August 2018

http://library.ctr.utexas.edu/ctr-publications/0-6816-1.pdf

Technical Report Documentation Page

1. Report No.	2. Government Accession No.	3. Recipient's Catalog No.
FHWA/TX-18/0-6816-1		

4. Title and Subtitle	5. Report Date
Applications of Partial Depth Precast Concrete Deck Panels on Horizontally Curved Steel and Concrete Bridges	April 2018; Published August 2018
	6. Performing Organization Code
7. Author(s)	8. Performing Organization Report No.
Colter Roskos, Paul Biju-Duval, John Kintz, Victoria McCammon, Yang Wang, Sean Donahue, Todd Helwig, Michael Engelhardt, Oguzhan Bayrak, Patricia Clayton, Eric Williamson	0-6816-1
9. Performing Organization Name and Address	10. Work Unit No. (TRAIS)
Center for Transportation Research The University of Texas at Austin 1616 Guadalupe Street, Suite 4.202 Austin, TX 78701	11. Contract or Grant No. 0-6816
12. Sponsoring Agency Name and Address	13. Type of Report and Period Covered
Texas Department of Transportation Research and Technology Implementation Office P.O. Box 5080 Austin, TX 78763-5080	Technical Report June 2014 – April 2018
	14. Sponsoring Agency Code

15. Supplementary Notes

Project performed in cooperation with the Texas Department of Transportation and the Federal Highway Administration.

16. Abstract

Horizontally curved bridges are commonly used for direct connectors at highway intersections as well as other applications. The majority of curved bridges utilize continuous steel curved I-girder or tub girder systems. In recent years, isolated applications of spliced prestressed concrete U-beams have been successfully used for curved bridge applications in Colorado and are currently being considered for use in Texas bridges. One of the most critical construction stages from a stability perspective is placement of the wet concrete deck at which point the girders must support the full construction load of the system until the deck stiffens and acts compositely. Bridges with a curved geometry experience significant torsional forces and require a substantial amount of bracing to control deformation during construction. Bracing in the form of cross frames for steel I-girder systems, top lateral trusses for steel tub girder systems, and lid slabs for concrete U-beams are provided to improve the girder behavior.

While partial depth precast concrete panels (PCPs) are commonly used as stay-in-place formwork for straight bridges, the panels are not currently permitted on horizontally curved girder systems in Texas. TxDOT would like to extend the use of PCPs to bridges with curved girders. This report focuses on the stability of PCPs that rest on polystyrene bedding strips. The project studied the behavior for PCPs with and without a positive connection to steel girders and also considered the behavior of the current TxDOT reinforcing details for PCPs with concrete U-beam systems. The experimental portion of this study consists of large-scale PCP shear tests and large-scale combined bending and torsion tests on both a twin steel I-girder system and on a single steel tub girder. The PCP shear tests were used to develop a simple and effective connection between the PCPs and the girder, as well as to empirically determine the in-plane stiffness and strength of the PCP/connection system. The large-scale girder tests were used to investigate the performance of PCPs and their connection to a system that simulates the load experienced in a realistic construction situation. Also, parametric finite element modeling of the PCPs and the curved girder systems were performed and validated with the results from the experimental tests. The finite element models were used to develop an understanding of the fundamental behavior of the steel girder systems in combination with the PCP systems. In addition to focusing on connection methods to the PCPs, guidelines were also developed for cases where the panels can be used on horizontally curved girder systems without a positive connection to the girders.

17. Key Words	18. Distribution Statement
Curved Girders, Partial Depth Precast Concrete Panels, Steel I-Girders, Steel Tub Girders, Concrete U-Beams	No restrictions. This document is available to the public through the National Technical Information Service, Springfield, Virginia 22161; www.ntis.gov.

19. Security Classif. (of report)	20. Security Classif. (of this page)	21. No. of pages	22. Price
Unclassified	Unclassified	524	

Form DOT F 1700.7 (8-72) Reproduction of completed page authorized

THE UNIVERSITY OF TEXAS AT AUSTIN
CENTER FOR TRANSPORTATION RESEARCH

Applications of Partial Depth Precast Concrete Deck Panels on Horizontally Curved Steel and Concrete Bridges

Colter Roskos
Paul Biju-Duval
John Kintz
Victoria McCammon
Yang Wang
Sean Donahue
Todd Helwig
Michael Engelhardt
Oguzhan Bayrak
Patricia Clayton
Eric Williamson

CTR Technical Report:	0-6816-1
Report Date:	April 2018; Published August 2018
Project:	0-6816
Project Title:	Partial Depth Precast Concrete Panels on Curved Girders
Sponsoring Agency:	Texas Department of Transportation
Performing Agency:	Center for Transportation Research at The University of Texas at Austin

Project performed in cooperation with the Texas Department of Transportation and the Federal Highway Administration.

Center for Transportation Research
The University of Texas at Austin
3925 W. Braker Lane
Austin, TX 78759

http://ctr.utexas.edu/

Disclaimers

Author's Disclaimer: The contents of this report reflect the views of the authors, who are responsible for the facts and the accuracy of the data presented herein. The contents do not necessarily reflect the official view or policies of the Federal Highway Administration or the Texas Department of Transportation (TxDOT). This report does not constitute a standard, specification, or regulation.

Patent Disclaimer: There was no invention or discovery conceived or first actually reduced to practice in the course of or under this contract, including any art, method, process, machine manufacture, design or composition of matter, or any new useful improvement thereof, or any variety of plant, which is or may be patentable under the patent laws of the United States of America or any foreign country.

Engineering Disclaimer

NOT INTENDED FOR CONSTRUCTION, BIDDING, OR PERMIT PURPOSES.

Project Engineer: Dr. Todd A. Helwig
Professional Engineer License State and Number: Texas No. 94280
P. E. Designation: Research Supervisor

Acknowledgments

The authors are grateful to the Texas Department of Transportation (TxDOT) for providing the funds to conduct this research study. The authors express appreciation to the following TxDOT personnel for their assistance and support on this study: Courtney Holle, Mike Hyzak, Teresa Michalk, Wade Odell, Kevin Pruski, Michelle Romage-Chambers, Todd Speck, Jason Tucker, Greg Turco, and Sara Watts from TxDOT as well as Hector Garcia from FHWA. The authors also express appreciation to David Malaer of Valley Prestress Products, Inc. for generously donating the precast concrete panels for the testing program and appreciation toward all the individuals at Valley Prestress Products. Special thanks are extended towards Steve Crim from Valley Prestress, who cooperated with the research team to meet our needs. A special thanks is also offered to the numerous students and staff members at Ferguson Structural Engineering Laboratory for ensuring the successful completion of the experimental program.

Products

This report contains Product 1, Finite Element Analytical Model of PCPs (Chapter 8) and Product 2, Details and Design Methodology for PCP's in Curved Girders (Chapter 11).

Table of Contents

List of Figures

List of Tables

Chapter 1. Introduction and Background

1.1 Introduction

Horizontally curved girders are frequently used in highway bridge construction. One of the most common applications requiring curved girders are direct connectors in highway interchanges. Although bridges consisting of curved bridge decks supported by straight simply-supported girders (often referred to as chorded bridges) have been utilized in the past, many curved bridges employ continuous steel curved girder systems. The majority of steel girder systems that have historically been constructed consist of either I-shaped girders or trapezoidal box girders (often referred to as tub girders) built up from steel plates with a horizontally curved geometry. The steel girders are shipped to the bridge site in shorter segments and spliced together to create a continuous girder system, and frequently require temporary shoring or holding cranes. Curved steel girders provide an efficient structural system that can be erected relatively quickly. The completed bridge with a composite concrete deck is also a stiff structural system, particularly in the case of tub girders, for resisting the large torque that exists as a result of the curved bridge geometry. More recently, spliced precast post-tensioned curved U-beams (henceforth referred to as spliced curved concrete U-beams) are beginning to see use in states such as Colorado (Reese and Nickas 2010). The state of Texas is currently considering the use of these girders for some horizontally curved girder applications.

Regardless of whether steel or concrete girders are utilized for the bridge system, one of the most critical loading stages from both a strength and stiffness perspective occurs during placement of the wet concrete for the bridge deck. The girders are generally designed to act compositely with the concrete slab in the finished bridge; however, during placement of the concrete deck, the non-composite girders alone must resist the full construction load. Although the cured concrete deck can substantially improve the stiffness of the superstructure in the finished bridge, steel girder systems require a significant amount of bracing to resist the applied loads and to control deformations during construction. The curved precast concrete girders that have been previously constructed also require a lid slab consisting of a precast panel and topping slab to close the box section prior to placement of the full concrete deck slab so as to improve the resistance to the torsional loads. The use of the bracing in steel girders and the lid slab in concrete girders complicates the fabrication and construction process and reduces the economy of these structural systems. To improve the economy and speed of construction for horizontally curved bridges, alternative forms of bracing are of interest. One source of potential bracing is the formwork that is necessary for the concrete bridge deck. However, the bracing potential of the forming systems is sensitive to the connection methods. In addition, there are a variety of potential forming systems available and therefore a brief description of the various forming systems is warranted.

For many years, the formwork that was utilized in bridge systems consisted of plywood forms. Plywood forms are relatively inefficient since the forms are expensive and time consuming to install. In addition, the forms are very difficult to remove after the concrete deck has cured, particularly the ones between interior girders. Improved construction efficiency has been achieved over the past few decades with the innovation of forming systems that remain permanently attached to the bridge. Most steel bridge systems make use of permanent metal deck forms (PMDF), which are also sometimes referred to as metal stay-in-place (SIP) forms. These forming systems consist of corrugated steel sheets that span between the adjacent flanges of the bridge

girders and serve as both a work surface for the construction personnel as well as formwork for the bridge deck. Since the metal forms require support on both edges, they are only used between adjacent girders, with removable plywood forms supported on cantilever brackets used for the bridge overhangs. Concerns about corrosion issues in some coastal regions prevent the use of PMDF, in which case plywood forms are sometimes used throughout the bridge.

Another stay-in-place forming system that is widely used in the bridge industry consists of partial-depth precast concrete deck panels, which are often referred to as precast concrete panels (PCP). The term partial-depth refers to the fact that the panels (usually 4-in. thick) do not serve as the full deck thickness, but instead have fresh concrete cast on top of the panels to obtain the full thickness of the bridge deck. PCP systems typically have an 8-ft cover (along the length of the bridge girders) and span between the adjacent girder flanges. During concrete placement the forms are usually supported at the ends by extruded polystyrene bedding strips positioned so that wet concrete can flow under the ends of the panels providing good vertical support once the concrete cures. The PCPs are relatively quick to install since the weight of the panels keep them in place with no positive connection to the girders required. In the state of Texas, PCP panels are the primary forming system used for straight concrete bridge systems and the forms have also been used for some straight steel girder systems. Current design practice does not allow the use of PCP forms in horizontally curved steel plate or tub girder systems. Because the forms do not have a positive connection with the steel girders, there are concerns about the performance as the girders twist and the flanges deflect from the torsional and bending loads.

Because PCP panels have significant in-plane stiffness and strength, they have excellent potential to serve as braces for both straight and curved girder systems. However, a suitable positive connection between the panels and the girders must be developed that can engage the in-plane stiffness and strength of the panels. The connections must also have adequate strength to resist the demand from the torsional loads in curved girder systems. The potential for eliminating some of the bracing required in straight and curved steel girders or the topping slab in curved concrete U-beams can potentially provide cost savings.

A good understanding of the structural demands on the PCP panels when serving as a bracing element requires a clear understanding of the behavior of curved girder systems as well as the detailing requirements of the forming systems that are used in bridges. Due to significant differences between I-girders, tub girders, and the spliced precast post-tensioned U-beams, the behavior of each of the girder types subjected to torsion is briefly discussed in the following sections. The connection details along with a summary of past investigations on the bracing behavior of PMDF systems are then provided so that the demand on PCP systems can be fully understood.

1.2 Steel I-Girder Systems

A widely used girder type in horizontally curved bridge applications is I-shaped girder sections built-up from steel plates. Because the girders can be fabricated in segments, the pieces can be shipped to the field and spliced together to form a continuous girder system as shown in Figure 1.1. Due to the relatively light weight of the girders, ground splices are often completed on the first segments prior to erection to minimize the necessity of shore towers that complicate right-of-way issues below the bridge. For curved bridge applications, the girders are subjected to combined flexural and torsional stresses from the gravity loads on the structure. A brief overview of the torsional resistance of the girder sections is helpful to understand the necessary bracing to resist the torsional loads and deformations that occur in curved girders.

Figure 1.1: Splicing of Curved I-Girders to Form a Continuous Girder (Photo Courtesy of T. Helwig)

The torsional resistance in thin-walled structures is usually categorized as either Saint-Venant torsional stiffness or warping torsional stiffness. The Saint-Venant stiffness is often referred to as uniform torsion since for a prismatic section the stiffness does not vary along the length and is not sensitive to the support conditions of the girder. The warping torsional resistance, on the other hand, is often referred to as non-uniform torsion since the stiffness is associated with the bending deformation in the plane of the individual plates. The warping stiffness of a section is related to the member's resistance to warping deformation. Two I-shaped sections subjected to a torque at the ends are shown in plan in Figure 1.2 to illustrate warping deformation. Figure 1.2a shows that warping deformation consists of a twist of the flanges relative to each other about a vertical axis through the web. Warping deformation distorts the cross section such that it no longer is a plane section because the two flanges have distorted relative to each other. Twist about the longitudinal axis of the member in Figure 1.2a is prevented at one end, however the warping deformations are not restrained. Since the section is free to warp along the entire length, the flanges remain straight as they twist relative to each other and the member only possesses St. Venant torsional stiffness.

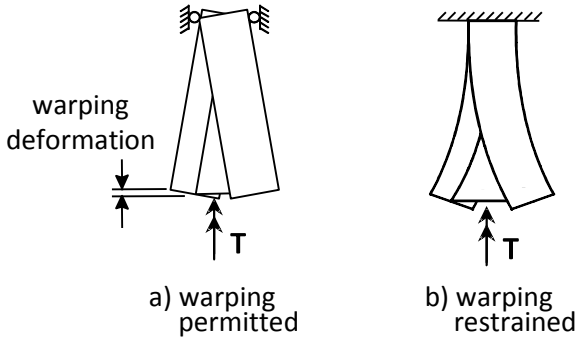

Figure 1.2: Warping Deformations in an I-Section

The wide flange section in Figure 1.2b has both twist and warping deformation prevented at one end. With warping restrained at just one location along the length, the member cannot twist without bending the flanges. Preventing twist at a minimum of two locations along the girder length will engage the warping stiffness of the cross section since the flanges must bend if the member twists and the section therefore possesses warping stiffness. Although warping stiffness is often developed due to continuity of the girders, braces can also be added to restrain the warping deformation and therefore enhance the torsional stiffness. The forming systems that are the focus of this report are a potential source of bracing to restrain the warping deformation of the top flange; however, a suitable connection must be developed that engages the in-plane stiffness of the form to restrain the flange. From a bracing perspective, the PCP panels will primary restrain the warping deformation of the top flange from the in-plane shear stiffness and strength of the panels. The panels will therefore be the most effective in regions where the warping deformations of the top flange are the largest.

From a stability perspective, metal deck forms are routinely relied upon for stability bracing in the building industry; however, conventional connections between the forms in the bridge industry often preclude the use of PMDF as a bracing system. TxDOT has constructed two bridges in Houston relying on PMDF for bracing that utilized connection details developed as part of TxDOT study 0-4145 and outlined in Eglimez et al. (2012). Many of the issues that exist with bracing by PMDF systems are also potential issues with bracing by PCP panels in straight and curved girder applications.

1.3 Steel Tub Girder Systems

Although I-shaped girders have been widely used in curved bridge applications, in the last two decades TxDOT has designed and constructed a number of direct connector bridges utilizing tub girders. Tub girders continue to be used through the state, and therefore improving the economy of these girders has significant benefits to TxDOT. There are a number of advantages to utilizing tub girders for curved bridges including improved aesthetics as well as structural efficiency. From the perspective of structural efficiency, the torsional stiffness of a closed tub girder section is often more than a 1000 times larger than a comparable I-shaped section. The larger torsional stiffness is a result of the relatively large torsional constant, J, associated with the closed shape. Although the torsional stiffness of the tub girder is very large once the concrete deck cures and forms the closed shape, during construction the girder consists of an open section that results in a relatively flexible system. As a result, significant bracing is required during construction to provide adequate stiffness and strength to resist the torsion from the curved geometry.

The primary bracing components that are used in tub girders are shown in Figure 1.3 and consist of internal K-frames, external K-frames or diaphragms, and a top flange lateral truss. The purpose of the internal K-frames is to control distortion of the box girder which results when the torsional stresses are not distributed to the plate elements in proportion to the St. Venant shear flow on the section. The internal K-frames maintain the shape of the box and resist the distortion. Solid plate diaphragms are typically provided at the support, and external K-frames or diaphragms are sometimes provided at intermediate locations along the length of the bridge; however, in many situations, these external braces are not necessary. When intermediate external K-frames are used, the braces are often removed once the concrete deck has cured to avoid potential fatigue problems due to differential girder displacement from truck traffic. In some instances, permanent intermediate external plate diaphragms have been designed to remain on the finished bridge.

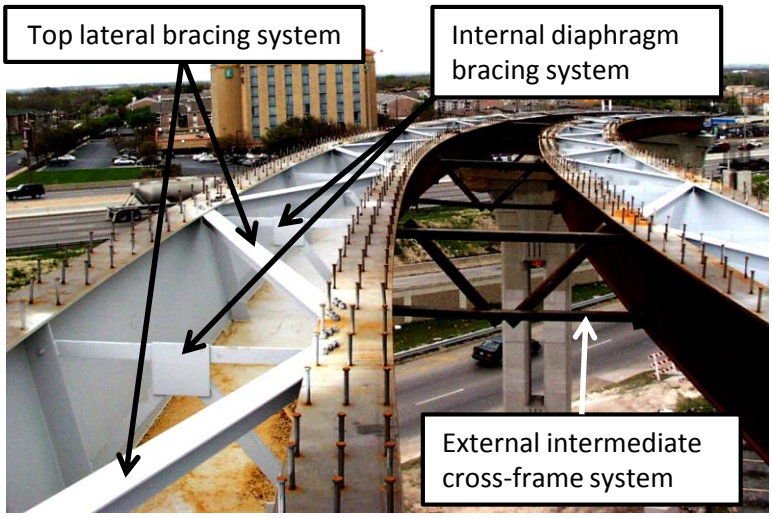

Figure 1.3: Bracing Systems for Steel Tub Girders (Photo Courtesy of T. Helwig)

Because the hardened concrete bridge deck fully closes the tub girder, the top lateral truss is primarily required during the construction stage. A girder with a top lateral truss is often referred to as a quasi-closed box section. There are a number of force components that must be considered in the design of the top lateral truss including components due to both torsional loads and bending induced forces. In cases where a line element (grid) model analysis is carried out, the effect of the top lateral truss on the girder behavior can be modeled using the equivalent plate theory presented in Kollbrunner and Basler (1969). The combined effects of torsion, bending, and distortion induced forces are discussed in TxDOT Report 0-4307 (Helwig et al. 2007). Many of these force components can be directly captured through three-dimensional finite element models. A number of commercial software packages can be used to model the girders; however the program UTrAp (Popp 2004) was developed as part of TxDOT research study 0-1898 for simplified three-dimensional modeling of straight and curved trapezoidal box girder systems with a top lateral truss and internal K-frames.

Due to the high fabrication costs associated with the top lateral truss and the fact that the need for the truss primarily exists during construction, studies have been conducted focused on alternative forms of bracing. The most notable work that focused on tub girders was conducted on TxDOT study 0-1898 (Chen et al. 2005), which considered the bracing contributions of the PMDF forms connected to the top flanges of the tub girders. Various connection methods were studied to engage the large in-plane stiffness of the forms. The connection method that was used in the laboratory studies consisted of the use of powder-actuated fasteners fired through the forms and into the top compression flange. Although the PMDF systems with the fasteners were able to dramatically increase the stiffness of the girders relative to an open section, the primary problem associated with utilizing the PMDF in curved girder applications was associated with inadequate strength to handle the forces induced due to box girder torsion. The use of PCPs for tub girders may permit more substantial connections than the powder actuated fasteners, and, as a result, the potential success of the panels for bracing may be higher than encountered for PMDF systems.

1.4 Spliced Precast Prestressed Concrete U-Beams

Although steel tub girders provide a structurally efficient system for horizontally curved girders, the high fabrication costs of the girders affect the economy of the systems. Therefore, alternative structural systems are currently being considered. One structural system that has been successfully utilized in Colorado relies on horizontally curved prestressed concrete U-beams. The girder segments are post-tensioned, which allows the segments to be spliced together to form a continuous girder. The concrete girders have a shape similar in form to that of the steel trapezoidal box (tub girder), but are instead composed of concrete as shown in Figure 1.4. Figure 1.4a shows the girders during lifting with some temporary bracing installed to maintain the shape of the girders until the topping slab is installed. In Figure 1.4b, a 3-in. thick PCP is used as a lid slab, and a concrete topping slab is cast to close the box girder and improve the torsional stiffness of the girders so that the rest of the concrete bridge deck can be installed. The next phase of the construction consists of adding the PCP between the adjacent girders so that there is a work surface for the construction personnel to install the reinforcing steel for the bridge deck, and the concrete can then be placed. The range of concrete U-beam geometries that have been completed in Colorado have had a wide variety of girder spans and a radius of curvature in the range of 700-800 feet (Reese and Nickas 2010). The maximum span length on many of the bridges was around 225 feet; however, one of the bridges had a maximum span of 275 feet.

a) During Lifting b) With Topping Slab

Figure 1.4: Spliced Precast Prestressed Concrete U Beams During Construction (Reese and Nickas 2010)

While a spliced curved concrete U-beam bridge has yet to be constructed in the state of Texas, TxDOT has begun designing these systems as alternatives to traditional curved steel girder systems. Figure 1.5 shows a typical section of an alternative bridge design for an overpass for US 83 in Hidalgo County, Texas. Figure 1.6 shows the current detail for the closure pour that connects the PCPs to the top of the U-beam to create a closed and torsionally stiff section. After the closure pour has cured, the PCPs spanning between the adjacent girders are placed and the concrete deck

is cast. Therefore, the connection between the PCPs and the U-beam must be able to resist the forces associated with the additional torsion placed on the system by the center PCP and the concrete deck. While similar details have been implemented in bridges outside of Texas, the research team is not aware of any tests on the performance of the detail when subjected to the in-plane shear forces that would develop in a curved girder application.

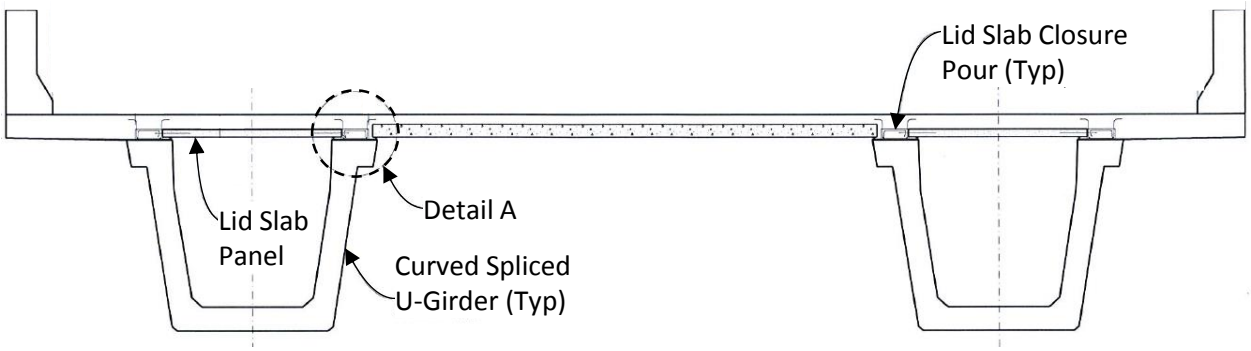

Typical Transverse Section

Figure 1.5: TxDOT Detail for PCP to U-Beam

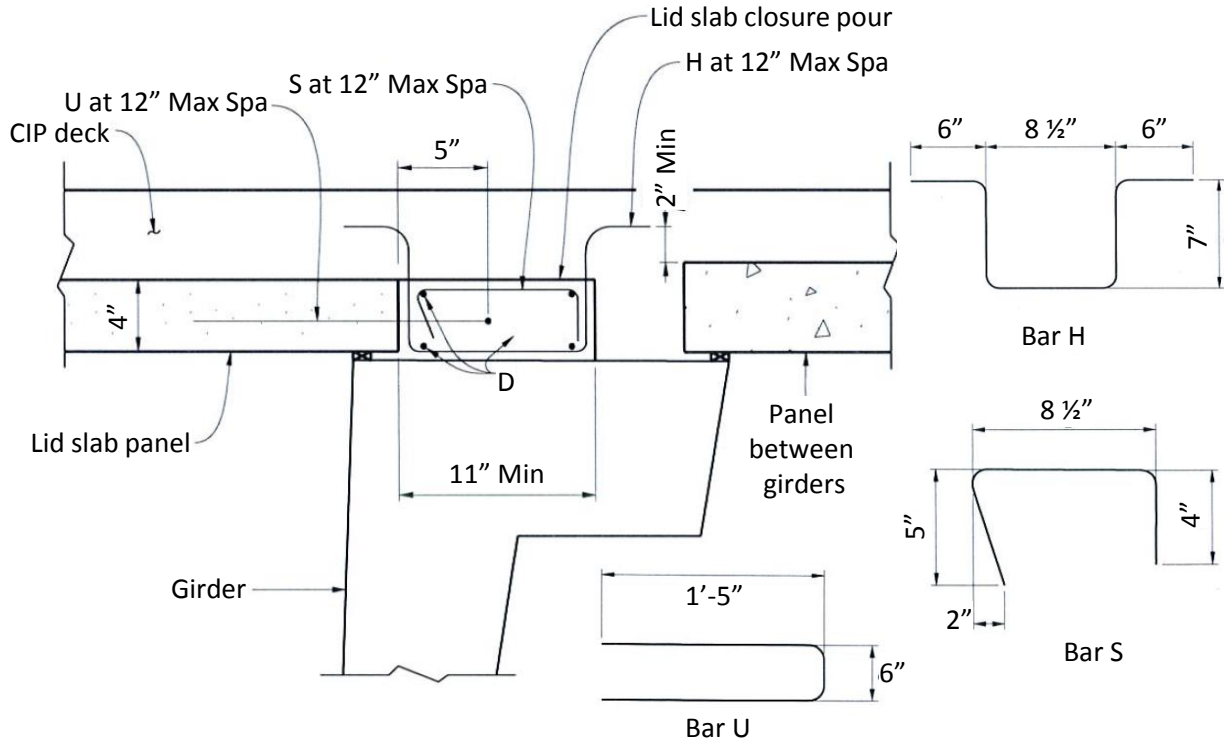

Detail A

Figure 1.6: TxDOT Detail for PCP to U-Beam Connection

1.5 PMDF Systems

Although the focus of the research outlined in this report is on the use of PCP systems for curved steel and concrete girder systems, there have been previous studies on the use of PMDF for bracing of straight steel girders. Understanding some of the detailing requirements and recommended modifications to the details for the PMDF so that the forms can be used for bracing provides a good starting point for the discussion of the factors that are investigated in this research. PMDF systems are commonly used on steel girder system and have also been used on prestressed concrete girder systems for support of the wet concrete deck during construction. As the name implies (permanent metal deck forms) the forms stay on the bridge permanently. The forms consist of profiled sheeting that spans between the adjacent top flanges of the girders. PMDF systems are commonly relied upon for bracing in the design of steel buildings. The forms act as a shear diaphragm to help resist lateral loads from sources such as wind and also provide bracing for the compression flange against lateral torsional buckling. Design methodologies for shear diaphragm bracing from a stability perspective have been developed and presented in the literature (Helwig and Yura, 2008).

Although the forms are routinely relied upon for bracing in the building industry, the forms are not permitted to be relied upon for bracing in the bridge industry due to significant differences in the connection details. In the building industry, the forms are continuous over the beams and are connected directly to the top flange. As a result, the forms have good connections with the members to be braced. In the bridge industry, the forms are supported on a cold-formed angle (L3×2×10gage) that allows the contractor to adjust the form elevation to account for changes in the flange thickness as well as differential camber between adjacent girders. Figure 1.7 depicts the connection detail for the forms in the bridge industry. Depending on the necessary adjustment for camber and variations in the flange thickness, the contractor can orient the support angle leg upwards or downwards providing the ability to adjust the form elevation +/- 2.75 in. The ability to adjust the form elevation is extremely important to achieve a relatively uniform thickness in the deck slab. For example, considering only the variations in flange thickness, the positive moment region may have a flange thickness of 1 in. compared to a 3-in. flange thickness in the negative moment region. If the bridge was to have an 8-in. concrete deck and the form elevation could not be adjusted, the slab in the negative moment region would be 8 in. versus a 10-in. slab in the positive moment region. In addition, the extra concrete results in much larger dead load deflections, thereby increasing the necessary camber. Variations in camber between adjacent girders can also be significant, thereby requiring the ability to make adjustments in the field. Once the girders are erected, the contractor will typically conduct a survey to find the elevations of the flanges at 10-ft intervals along the length of each girder to determine where the form elevation should be set to ensure a uniform deck thickness.

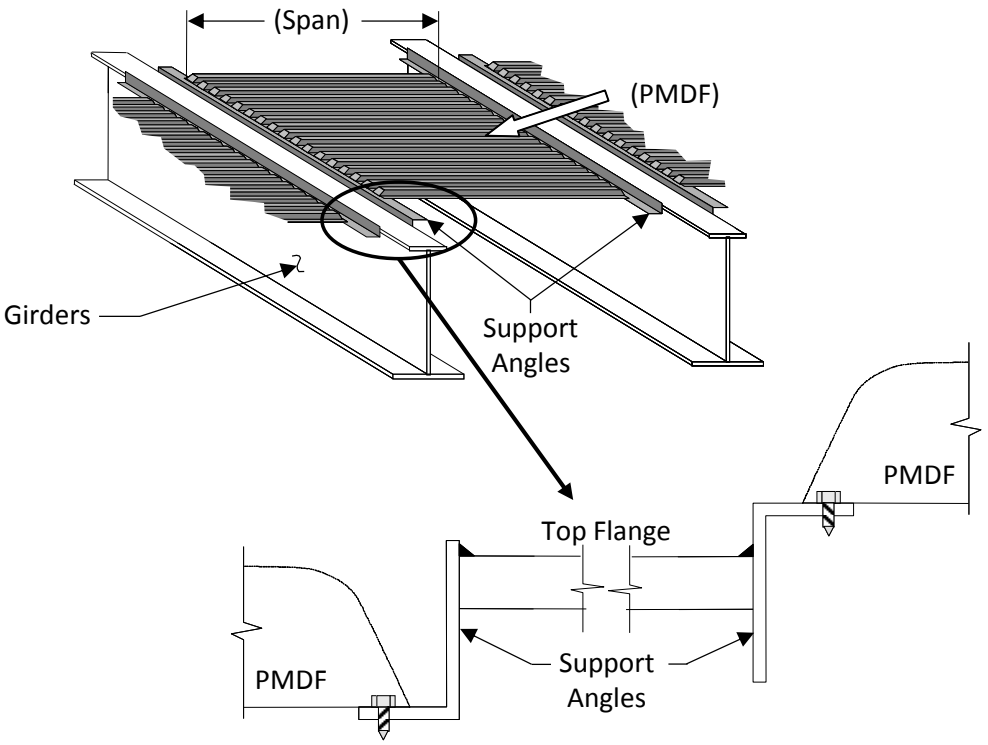

Figure 1.7: Support Angle for Adjusting PMDF Elevation (Egilmez et al.2016)

Although the cold-formed angle provides the ability for the contractor to adjust the form elevation, the angle leads to potentially large eccentricities in the connections. As a result, the connection greatly reduces the stiffness of the PMDF system as a bracing element since the angle just pulls away from the flange as shown in Figure 1.8a. To control the connection flexibility, the stiffening angle shown in Figure 1.8b was incorporated (Egilmez et al, 2012). The modified connection detail was used in the construction of two bridges with a total of five spans on the IH 610 loop in Houston. The 50-ft span bridges were replaced with W18 sections to raise the bridge and eliminate the large number of bridge strikes due to over-height vehicles. The girders had a relatively short span of only 50 ft; however, no intermediate cross frames were necessary, resulting in the elimination of over 300 intermediate cross frames (35 girders required across the width of the IH 610 loop).

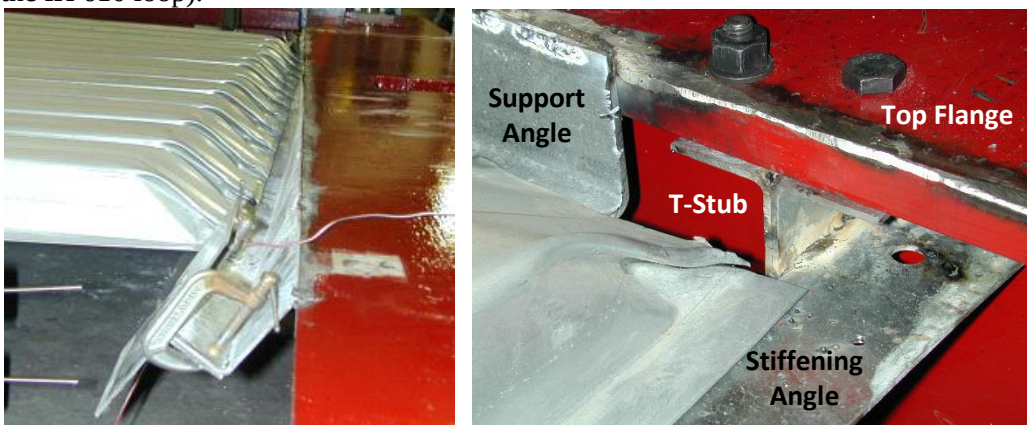

a) Flexible Connection b) Stiffening Angle

Figure 1.8: Stiffening Angle for Controlling Connection Flexibility (Egilmez 2005)

1.6 PCP Systems

PCP systems represent an economical means of creating a work surface and forming system for the concrete bridge deck. The panel thickness on most TxDOT bridges is 4-in.; however, in some instances, thicker or thinner panels have been used. For example, the panels that were used to form a lid slab on some of the curved prestressed U-beam bridges in Colorado had a 3-in. thick PCP. The typical PCP spans necessary in steel girder systems will usually range from 8-10 ft, which can be achieved with conventional Texas PCP panels. Some of the PCP panel spans utilized for the prestressed U-beam curved girders in Colorado were larger, as shown in Figure 1.9.

There have been a number of previous investigations related to PCP panels. Some of the first work that was conducted on PCP panels was carried out by Barker (1975) who considered PCPs, PMDF, and wood forms. For the PCP panels, Barker used different surface finishes as well as some panels with shear reinforcing bars extending into the topping slab. He found that no shear reinforcement was necessary at the panel-to-topping slab interface to achieve good bond.

For many years, the panels were not used near the ends of bridges. Instead a thickened cast-in-place deck was used near the expansion joints. Coselli (2004) conducted research looking at the behavior of systems where the panels were extended to the expansion joint and found good behavior was achieved without the thickened end regions. One concern with extending the panels to the end of the bridge was the long-term fatigue behavior of the deck panels. Agnew (2007) conducted fatigue tests on PCP panels and considered the impact of both positive and negative moment. He found that the panels did not have a problem with fatigue or delamination between the panel and the topping slab under cyclic loads. Although many of the previous studies focused on the use of PCP for bridges with normal supports, Boswell (2008) considered the impact of support skew on the behavior of the panels. He considered the use of trapezoidal shaped panels subjected to both static and cyclic fatigue loads. He found that the panels provided sufficient strength and stiffness to support the current design truck loads.

Following up on some of the work mentioned above by Barker, delamination between the PCP and the topping slab may be a concern with regard to durability of the bridge decks. However Dowell and Smith (2006) carried out tests on panels with a variety of finishes and found no problems with delamination occurring.

Figure 1.9: Longer span PCP's for Colorado Curved U-Beams (Reese and Nickas 2010)

Although the previous work has focused on the behavior of PCPs for typical concrete bridge applications, from a bracing perspective there are a number issues requiring investigation. The following section provides a general summary of research needs necessary in order to use the PCPs in curved girder applications.

1.7 Research Needs

Although there have been a number of previous studies on PCP systems, these past studies have focused on the performance of the panels under the traditional applications with straight concrete girder systems. In these applications the panels are simply supported, relying on gravity with no positive connection to the girder systems. Extending the use of the panels to curved girder applications requires a positive connection between the panels and the steel or concrete girders if they are to be used as bracing elements. From a bracing perspective, the connection details will need to be developed that can engage the large in-plane shear stiffness and strength of the panels. Due to the significant geometrical and structural differences between horizontally curved steel I-girders, steel tub girders, and spliced prestressed concrete U-beams, the behavior of each of these girder systems needs to be evaluated with the PCP systems. One of the fundamental steps paramount to the success of the study is the development of the connection and evaluating the shear stiffness and strength of the panel (PCP) and corresponding connection system.

1.8 Research Purpose

The main objective of this research is to extend the use of partial depth precast concrete deck panels (PCPs) to curved girder systems. Currently, TxDOT does not allow PCPs to be used on curved girder bridges. This study focuses on using PCPs in curved steel I-girder systems, curved steel tub girder systems, and curved spliced prestressed concrete U-beams, which are currently being considered for use in some Texas bridges (although none to date have been constructed in the state).

The research outlined in this report focuses both on using PCPs that are positively connected to the girders and on using PCPs that are not directly connected to the girders. Connection details between the PCPs and the steel girder systems were developed in this study to engage the shear stiffness of the PCPs during the construction phase. Both experiments and finite element models were used to determine if using the PCPs as bracing elements provided significant benefits to the system to potentially allow fewer traditional bracing members (i.e. cross-frames or diaphragms for the I-girder system and top lateral truss members for the steel tub girder system) to be used during construction. Additionally, the stability of PCPs on the bedding strips were investigated to determine if PCPs could be safely used on curved girder systems without falling from the structure during the construction phase. With respect to spliced curved concrete U-beams, this report focuses on gaining a better understanding of the behavior of the closure pour and reinforcing details to connect the PCPs to the U-beams and to determine the load levels experienced by them during construction.

1.9 Research Methods

The methods used in this study were large-scale laboratory testing, finite element modeling, and parametric studies. The laboratory experiments consisted of unconnected stability tests of PCPs on polystyrene bedding strips, shear tests on PCPs (with details to connect the PCPs to both steel I-girders, steel tub girders, and concrete U-beams), and both lateral tests and combined bending and torsion tests on a steel twin I-girder system and a single steel tub girder system.

The laboratory tests were used to study the feasibility using unconnected PCPs on curved girder systems, to investigate the stiffness and strength of PCPs and their connection system, and to demonstrate the effects of using PCPs as bracing elements in steel I-girder and steel tub girder systems. Furthermore, the laboratory results were used to validate the finite element models

created in the three-dimensional finite element program Abaqus/CAE 6.14. The validated models were used to perform parametric studies to investigate the bracing potential and benefits (or lack thereof) of PCPs on a variety of curved girder systems that were more realistic than the systems tested in the laboratory.

For the concrete U-beam system, laboratory tests were used to test the closure pour connecting the PCP to the U-beam in shear to gain an improved understanding of the strength and stiffness of the system. Additionally, parametric finite element models were created to study the behavior of the tub girder with the PCPs attached via the closure pour.

1.10 Report Organization

This report is organized into 12 chapters in total. Following this introductory chapter, a literature review is provided in Chapter 2. This chapter covers a history of the research on PCPs, a summary of state-of-the-art practices for the bracing of curved girder bridges, and a description of several methods that have been used to connect concrete deck panels to girder systems.

In Chapter 3, an experimental program is used to study the stability of unconnected PCPs on bedding strips. This investigation consisted of three different series of laboratory tests. First, the stability of inclined PCPs on bedding strips was tested to determine the performance of PCPs on curved girder systems during the construction phase where system twist is potentially large (i.e. near midspan of the girders). Second, the stability of PCPs on bedding strips was tested where large shear deformations may be present during the construction phase (i.e. near the simply supported end of I-girders). Third, the stability of the PCPs on bedding strips on an actual I-girder system was tested in the laboratory.

Chapter 4 focuses on the experimental evaluation of partial depth precast concrete deck panels subject to shear loading connected to the flanges of steel girder. In particular, the stiffness and strength of the PCP/connection systems were tested to determine their bracing potential. This chapter supplements the work presented in two related research reports by McCammon 2015 and Kintz 2017.

Chapter 5 and Chapter 6 present the experimental study on the twin steel I-girder system and the steel tub girder system. These systems were tested with and without PCPs acting as bracing elements attached to the flanges (to determine the effectiveness of the PCPs as braces). Both systems were tested by applying lateral loads to the girders in a simply supported condition. Furthermore, the I-girders and tub girder were tested in combined bending and torsion in both a simply supported and overhang condition.

Chapter 7 covers the experimental study for the closure pour and reinforcing details to connect the PCPs to the top of the concrete U-beam. The steel shear load frame used in Chapter 4 was modified to simulate the top of a concrete U-beam and a closure pour was used to connect the PCPs to the system. Several load tests were performed to determine the stiffness and strength of the PCP and the connection system with the current TxDOT detail. Additional load tests were performed with modifications made to the reinforcement layout to see if the connection could be improved.

Chapter 8 focuses on the finite element (FE) modeling techniques that were used to develop the models of the PCP/connection system for the experimental shear tests that were conducted in Chapter 4. The goal was to accurately model the stiffness of the PCP/connection system so that the PCPs could be correctly represented for both the validation of the finite element models of the steel I-beam and steel tub girder systems and the parametric studies of these two systems as described in detail in Chapter 9.

Chapter 9 begins with a general discussion of the modeling and analysis techniques used to develop the FE models for the steel I-girder and tub girder systems with and without PCPs used as bracing elements. The models were validated with the experimental results from Chapter 5 and 6 for the steel girder systems to establish confidence in the finite element models that were developed for the parametric studies using the same modeling methods. The parametric study investigated the bracing potential of PCPs on a variety of curved girder systems that were more realistic than the systems tested in the laboratory.

Chapter 10 explains the parametric finite element analysis for the concrete U-beams which was used to investigate the load demands on the PCP panels with the closure pour details. A simplified model was used to represent the stiffness for the PCPs/connection system that was measured in in the experiments discussed in Chapter 7.

Chapter 11 provides recommendations for using unconnected PCPs. The experimental data from Chapter 3 was compared with the results from finite element (FE) models for a number of curved I-girder and tub girder systems with various span lengths and radii of curvature. The goal was to provide an understanding of the limits of using unconnected PCPs in regards to their stability on bedding strips for curved systems during construction.

The final chapter presents the summary and conclusions from this research project with recommendations for future research. Of the work provided in this report, Chapter 3 and Chapter 11 will likely be of the most use to TxDOT. These chapters show that unconnected PCPs are stable on appropriately sized bedding strips as the curved steel I-girders and tub girder systems deform under construction loads. Therefore, the use of PCPs could potentially be expanded to horizontally curved steel plate and tub girders.

Chapter 2. Literature Review

2.1 Introduction

There is no published work (research articles, master's theses, PhD dissertations, or technical papers) available that specifically documenting research on the use of partial depth precast concrete panels (PCPs) in curved girders applications. Therefore, the study documented in this report is the first investigation at using PCPs in curved girders systems. The scope of the investigation, however, follows decades of past research programs on both PCPs (particularly for accelerated bridge construction) and bracing solutions for curved girders, separately. While this project concentrates on investigating the use of PCPs to help brace curved girders in bridges, the present literature review summarizes the research to date on the following related topics:

- A history of the research on the PCPs, which shows the development of technical guidelines to be used by TxDOT or other states based on the fundamental behavior of PCPs. More recent research efforts have focused on the optimization of the PCP design and their ultimate capacity.
- A summary of state-of-the-art practices on the bracing of curved girder bridges, and a description of more innovative solutions to further optimize the location and/or sizing of the different bracing members.
- A description of potential connections between the PCPs and the rest of the bridge superstructure, where priority is given to the feasibility, economy, and bracing capabilities of such connections.

2.2 Partial Depth Precast Concrete Panels (PCPs)

2.2.1 Description, Advantages, and Drawbacks

Partial depth precast concrete panels (PCPs) by definition are precast panels of concrete that span between girders and form part of the depth of the final slab. The PCP contains the bottom layer of reinforcement for the slab; the reinforcement may be prestressed steel, mild reinforcing, or a combination of the two. The PCP is used as the formwork for the upper portion of the slab which is cast on top of the layer of PCPs. The cast-in-place (CIP) topping is thick enough to include a top layer of reinforcing. After the CIP concrete cures, the CIP topping and the PCPs act together (compositely) to carry the live load as well as any additional dead load applied after the topping slab cures.

Precast construction in bridge engineering is a well-known accelerated bridge construction technique. Accelerated bridge construction benefits the public by reducing the time necessary for lane-closures, which in turn reduces the travel delays to the public. Furthermore, active construction adjacent to or above live traffic creates safety risks; reducing the time the construction site is active in turn reduces the accumulated risk to the traveling public. PCPs for bridge applications are quite beneficial since their purpose is twofold: acting as a structural deck element and as formwork for the cast-in-place concrete topping slab.

PCPs were first implemented in the 1950s when an early bridge using PCP was constructed in 1956 on the Illinois Tollway (Goldberg 1987). The first application of PCP in Texas dates back to 1963. As of 2002, approximately 85% of the bridges built in Texas utilized PCPs (Merrill

2002). The main advantages are increased economy and speed of construction, as well as improved safety during construction. However, TxDOT currently prohibits the use of PCPs on curved steel bridges. This is not a limitation based on the geometry (as precasters can fabricate wedge shaped panels), but rather a preference for a monolithic slab due to the complex interaction of the slab and girders on curved bridges (Merrill 2002). Also, the stability of the PCPs on the girders during construction is of concern as there is no positive connection between the elements until the concrete deck stiffens.

Since the PCPs used in the construction of Texas bridges are simply-supported on the top flange of the girders and are only kept in place by their self-weight, they cannot be relied upon for bracing of the girders. Therefore, cross-frames or diaphragms are required at several locations along the length of the bridge to brace the girders so they can adequately support the cast-in-place (CIP) concrete topping during construction. Once the CIP concrete has adequately cured, the top flanges of the girders are continuously braced. In the final configuration, many of the bracing elements are no longer required (especially for straight bridges). The bracing elements in the bridge are often the most costly structural elements per unit weight since they are difficult and time-consuming to fabricate and install.

There are some problems associated with the use of PCPs, including the potential for long-term deck cracking at panel edges. However, these drawbacks are not significant enough to offset the numerous advantages of the PCP system. Merrill (2002) provides a complete description of the use of the PCPs in Texas, the history of their development, how they are constructed, and their advantages and drawbacks.

2.2.2 Past Research Programs

The increased use of PCPs in Texas has been possible thanks to numerous research projects. The earlier projects, starting in the 1960's, are described in Merrill (2002). The primary aspects of the initial research focused on the bond between the PCP and the CIP topping and the load transfer between adjacent panels. The overall behavior, performance, and design recommendations were investigated as the use of PCPs gained traction and was economically feasible. Serviceability was the main objective that was focused on in the development of the design standards. In the recent years, ultimate behavior as well as refined design and crack mitigation recommendations are the trend in research objectives for PCPs.

Fang et al. (1990)

An initial study by Tsui et al. (1986) investigated the stiffness and strength of PCPs loaded out-of-plane. The behavior and load capacity of the PCPs was further examined at the University of Texas at Austin by Fang et al. (1990), with an emphasis on the in-plane membrane forces that develop within the panels under out-of-plane service loads. These membrane forces develop due to the restraint provided by the girders. Prior to cracking, the membrane forces were found to have a negligible effect on the response of the panels. After cracking, however, the membrane forces substantially improved the flexural capacity of the slab. As a result, this "arching action" permits a reduction in the flexural steel required in the slab, which in turn reduces long-term corrosion-related issues.

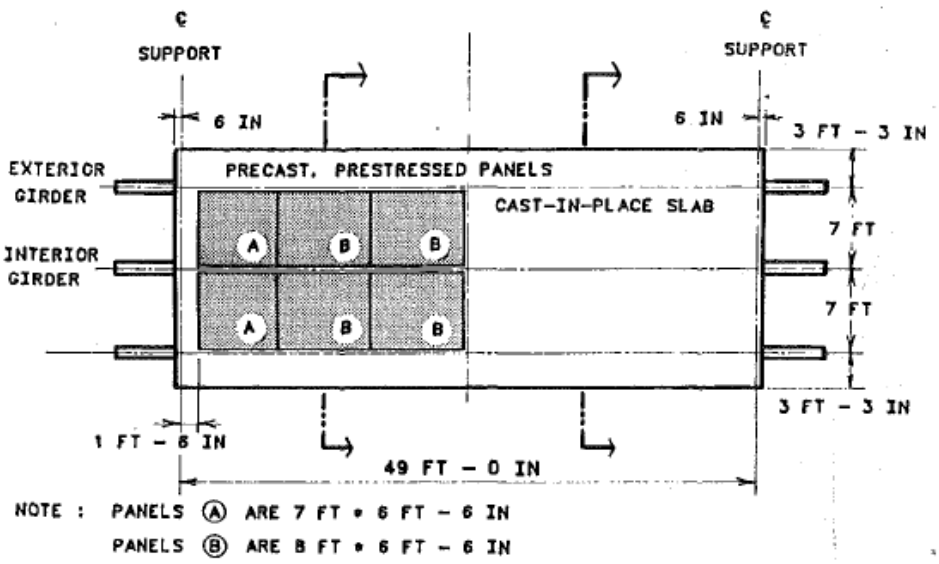

Figure 2.1: Plan View of the Test Specimen (Fang et al. 1990)

Mander et al. (2011)

By subjecting an experimental bridge deck to tandem axles loads, Mander et al. (2011) from Texas A&M University were able to predict a failure load assuming a failure mechanism involving both punching shear in the cast-in-place topping and flexure in the PCP. Yield line theory of a full-depth slab overestimated the failure load as it proved to be insufficient to account for the cast-in-place topping to panel interaction. Punching (two-way) shear assuming a 45 degree failure surface underestimated the experimental failure load. A more refined model was developed to predict the critical load. This model added the capacities of a punching shear failure in the CIP topping and a flexural failure, calculated using yield line theory, in the PCP. Membrane action was recognized to increase the post-cracking behavior of the deck, but was not included in the failure modes analyzed.

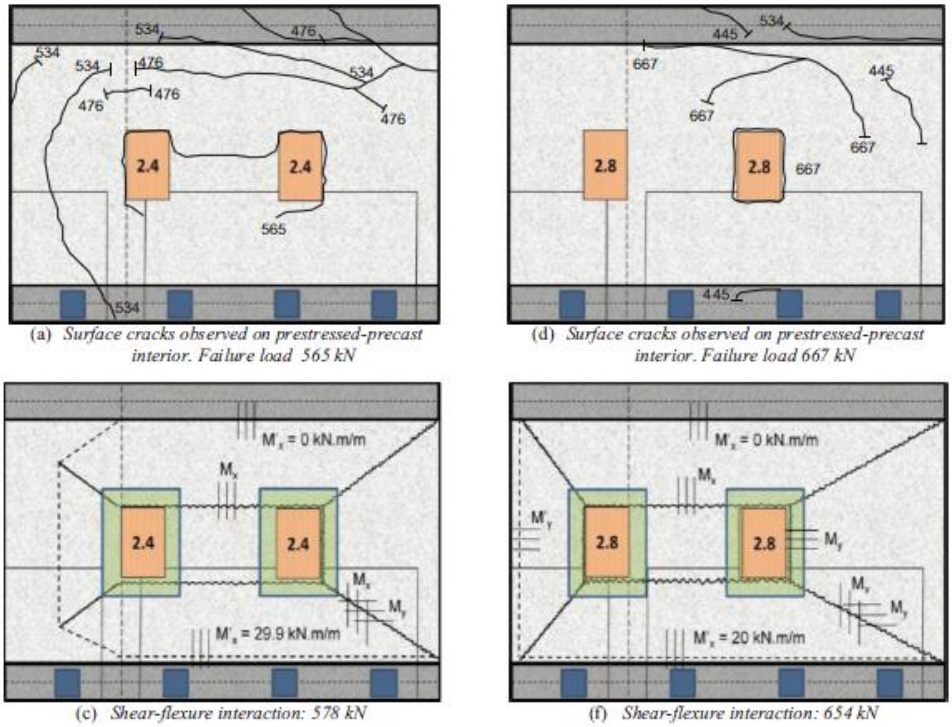

Figure 2.2: Shear-Flexure Failure Mode (Mander et al. 2011)

Kwon (2012)

Kwon (2012) developed provisions to further improve the design of PCP/CIP bridge decks used by TxDOT. The first objective of this dissertation is to reduce the cost of PCP/CIP bridge decks by trying to reduce the reinforcement required in the CIP topping. The current PCP/CIP deck design is shown to be somewhat conservative; by taking advantage of the membrane forces which cause arching action, Kwon suggested reducing the longitudinal bars in the top mat from No. 5 bars spaced at 6 inches to No. 4 bars spaced at 6 inches. TxDOT is in the process of reducing the top longitudinal reinforcing to No. 4 bars spaced at 9 inches, as outlined in TxDOT's Bridge Detailing Guide (TxDOT 2014a).

The second objective of Kwon's dissertation is to reduce the rejection of PCPs due to cracking observed at the construction site. Cracking of the PCPs may occur during handling and transportation. Kwon suggested reducing the initial prestress in the panels, reducing the lump-sum prestress losses from 45 ksi to 25 ksi, and proposed a new equation to calculate losses that takes into account aggregate type and level of initial prestress. TxDOT has reduced the prestress force in the PCP from 16.1 kips per strand to 14.4 kips per strand as outlined in TxDOT's PCP-FAB standard drawing (TxDOT 2014b).

2.2.3 In-Plane Shear Behavior of Concrete Panels

Early research on PCPs started with assessing their behavior under traffic service loads in order to produce technical specifications and standards directly applicable in the bridge industry. More recent research has focused on ultimate limit states, reinforcement optimization, and crack mitigation. Since possible bracing applications for PCPs have not been of main focus of past programs, little has been reported on the in-plane shear behavior of PCPs for bridge applications.

This gap in knowledge for the bridge industry can be somewhat filled by reviewing the existing literature on the in-plane shear behavior of reinforced concrete shear walls. Even though the dimensions and thicknesses of the shear wall elements differ from the PCPs, significant insight on the behavior may be gained by reviewing the literature.

Vecchio (1981, 2000, 2001)

The University of Toronto has significant history related to reinforced concrete shear wall research. In his PhD dissertation, Vecchio (1981) developed an analytical model to predict the shear behavior of reinforced concrete panels subject to combined in-plane shear stress and biaxial normal stresses. The analytical model was validated with various experimental tests and is known as modified compression field theory (MCFT).

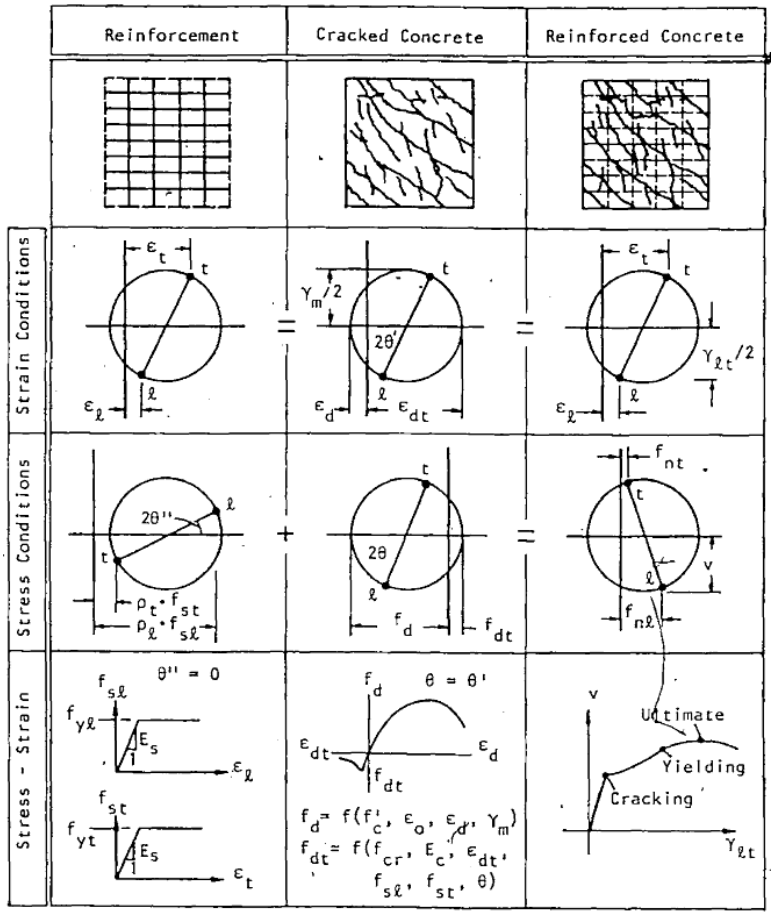

Figure 2.3: Modified Compression Field Theory (Vecchio 1981)

The analytical model was based on compatibility requirements, constitutive relationships, and equilibrium conditions. The compatibility requirements assumes that the average strain in the panel, as represented by Mohr's circle of strain, is the same as the average strain in the reinforcement and the average strain in the concrete. The equilibrium condition assumed that the average stress in the panel, as represented by Mohr's circle of stress, is the summation of the average stress in the reinforcement and the average stress in the concrete. The constitutive

relationship for the reinforcing assumes an elastic perfectly plastic condition, with the maximum stress equal to the material yield strength. The constitutive relationship for the concrete in compression is a function of the cylinder strength (f′c), the strain in the cylinder at f′c , and the shear strain in the concrete. The constitutive relationship for the concrete in tension is a function of the cracking stress, the modulus of elasticity of the concrete, the stress in the transverse and longitudinal reinforcement, and the angle of the crack. This model includes compression softening and cracked concrete with tension stiffening in the compatibility relationship of the concrete. This model also assumes the stress and strain fields for the concrete are coincident. This approach is not valid for members with a shear response governed by a single dominant crack and it is only appropriate to use on members with sufficient reinforcing for crack control.

Vecchio (2000, 2001) further worked on the behavior of reinforced concrete and proposed the Disturbed Stress Field Model (DSFM). This theory modifies his original MCFT and increases the accuracy of the theory in specific situations where the previous theory was known to be inaccurate. The stress and strain fields of the concrete are no longer assumed to be coincident and new compatibility, constitutive, and equilibrium relationships are used. This theory, like the MCFT, is a smeared crack theory; however, unlike the MCFT, the DSFM considers the local conditions at crack locations. The DSFM more closely represents the behavior when shear crack slip is the failure mode, and more closely matches the observed degree of compression softening.

Oliver et al. (2009)

Various researchers have looked for crack propagation models to predict the post-cracking behavior of reinforced concrete. One of the most recent models was developed by Oliver et al. (2007) from Spain, using a composite material model with the "Continuum Strong Discontinuity Approach" (CSDA). Reasonable accuracy was achieved between prediction from analytical models and experimental test results.

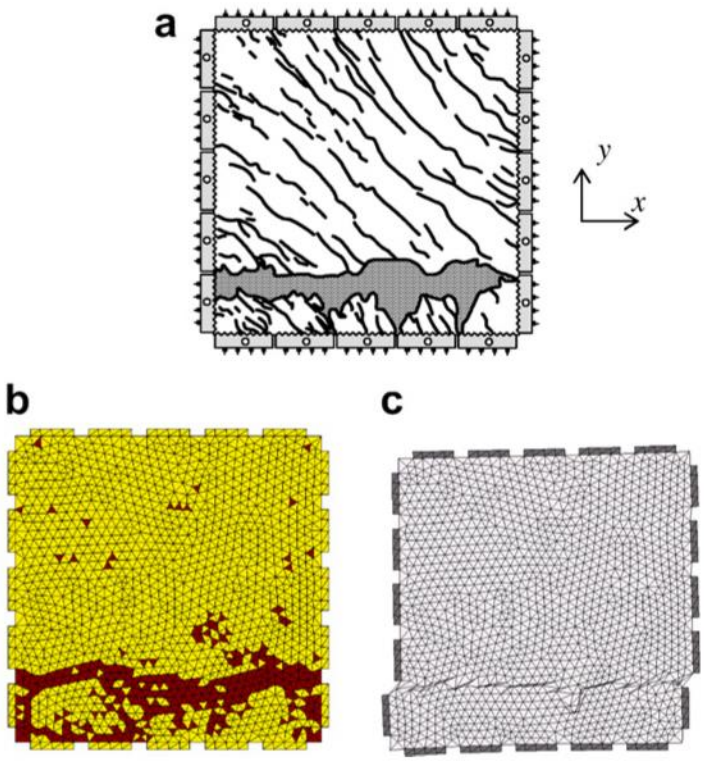

Figure 2.4: (a) Experimental Crack Patterns, (b) Elements in Elastic Loading, (c) Amplified Deformed Shape (Oliver et al., 2009)

The proposed methodology uses mixture theory to create a continuum composite model. The composite element is composed of a matrix representing the concrete and two orthogonal fibers representing the reinforcement. This composite model accounts for "concrete matrix failure, rebar mechanical failure, bond/slip effects, and dowel action". By using this composite model, the finite element model is significantly simpler than modeling these effects directly. This composite model is then used with the CSDA framework to get a fairly realistic response.

The CSDA "aims at modeling discontinuous displacement/velocity fields (strong discontinuities) across a failure (discontinuity) line." The CSDA uses a finite element that has an embedded strong discontinuity (discontinuity interface) that is oriented based on the stress-strain field (continuum constitutive model). This embedded discontinuity allows the cracks to form within an element, making the model less dependent on mesh size. Using a continuum instead of a fixed crack orientation makes the crack propagation in the model independent of the mesh orientation.

The mixture theory assumes the whole volume composed of the mixture can be represented by a continuum of infinitely small elements of the same composition as the mixture. All the components that constitute the composite element experience the same strain field that the composite element experiences. The stress of the composite element is the combination of the stresses of the different components ratio based on the volume of that component to the whole.

The constitutive model of the concrete matrix is a "non-symmetric tensile/compressive strength isotropic damage model." The constitutive model of the fiber is composed of a uniaxial elasto-plastic model for the reinforcing aligned with the fiber, a "uniaxial slip dissipative model"

for the steel to concrete interface, and a "uniaxial shear-strain dissipative model" for the shear of the reinforcing crossing the fiber (dowel action).

2.2.4 Other Precast Concrete Panels Systems

PCPs are just one method to enhance speed of construction. A summary and comparison of the different precast techniques is provided by Roddenberry (2012). Roddenberry investigated the state of practice across the United States for all precast elements and systems, from foundations to parapets, and evaluated them based on whether they would be beneficial if adopted by Florida DOT. The different deck types investigated are full-depth precast concrete deck panels, open grid decks, concrete/steel hybrid decks, fiber reinforced polymer (FRP) deck panels, partial-depth precast deck panels, and timber deck panels.

While not widely used in Texas, full-depth precast concrete panels allow for faster construction than partial-depth precast panels, as no CIP concrete deck is required, saving time in placing and curing of the concrete deck. However, a method for connecting the beams to the panels is necessary. Some full-depth panels use shear pockets which consist of voids in the panel over the beam's top flange where the shear studs are welded; these pockets are grouted to provide a composite connection to the beams. If the full depth panels are the final riding surface, excellent geometric control is vital to ensure good ride quality. To avoid the poor ride quality due to fit up problems, a concrete or asphalt overlay can be placed on top of the panels.

An alternative system is the NUDECK system as described by Badie et al. at the University of Nebraska (1998), which is a full-width partial-depth precast prestressed panel system. The NUDECK panels are the full width of the bridge, including overhangs. The panel lengths vary to accommodate crane capacities and transportation limitations. The panels are 3 to 4 inches thick and are prestressed transversely to the beam lines. There are full length gaps over the beams to accommodate shear studs; these gaps are heavily reinforced with mild steel to resist the prestress force and to stabilize the gaps during transportation and handling. The transverse joint between adjacent panels consists of a full length reinforced shear key and longitudinal reinforcing splices at pockets every 2 feet. The panels are placed and leveled and then the beam line gaps, shear keys, and pockets are grouted before the topping slab concrete is cast. The NUDECK system aims at reducing crack formation. One of the benefits of this system is it eliminates formwork for the overhangs. All materials used in this system are non-proprietary, which helps keep the cost of this system low. There are no ride quality concerns as there is with the full depth panels. This system would likely work well for a singly-sloped roadway, however, the panel would need to be kinked or designed for extra topping concrete on a roadway with a house-top cross-slope profile. The NUDECK system would work best on steel beams, where the geometry control is tighter as the variability in the camber of prestressed beams would complicate the leveling of these full-width panels.

2.3 Curved Girders

2.3.1 Analysis of Curved Bridges

The analysis of curved bridges is complex for various reasons. Those reasons include: combination of bending and torsion, composite action, cross-frame action, and second-order effects.

Zureick (1999)

Zureick (1999), from the Georgia Institute of Technology, conducted a thorough literature review on the different analysis methods available to the engineer to model curved girder bridges, and classified them into two broad groups: 1) approximate methods, and 2) refined methods. Approximate methods require little modelling effort and are generally easier to use for the engineer, whereas refined methods, which generally have better accuracy, are more time-consuming. Approximate methods include:

- The plane grid method, where the structure is modelled with 2D grid elements.
- The space frame method, where the structure is modelled with 3D frame elements.
- The V-load method, where the curved structure is modelled as a series of straight girders, and fictitious vertical shear forces located at the position of the cross-frames make up for the effects of curved geometry.

The plane grid method and the space frame method are relatively user-friendly, but they do not account for the effect of warping. The refined methods include:

- The 3D finite element analysis (FEA) method, where the displacements at the nodes are used to find the strains and stresses within all elements. Accuracy of the method may be enhanced by refining the mesh or adding more degrees of freedom to the nodes. However, modelling full bridges in this manner may prove to be a tedious process.
- The finite strip method, where the structure is modelled with longitudinal curved elements. This method considers warping but is not as user-friendly as the 3D FEA.
- The finite difference method, where the general fourth order differential equation for the displacement field is solved by algebraic methods on small grid elements.
- The solution to governing differential equations, where the general fourth order differential equation is solved analytically. The solution may be a closed-form solution or a Fourier series. Analysis is complex and turns into a mathematical problem.
- The slope-deflection method, where the general differential equations are converted into slope-deflection equations. The solution is a Fourier series.

Inelastic analysis on the whole bridge structure consisting of both material non-linearity and geometrical non-linearity, is also addressed. How relevant it may be for design purposes and how it should be tackled has according to Zureick not been discussed clearly. Fifteen years later, 3D FEA programs have been developed and do provide an insight to such questions, for example by Chang (2006), as it will be shown later in this report.

Chang and White (2008)

Zureick (1999) discussed the lack of an in-depth comparison of existing programs at assessing the accuracy of the different analysis methods presented in his paper. Chang and White, from the Georgia Institute of Technology, discussed results from a full-scale bending experimental

test on a composite curved I-girder bridge, which served as a reference for evaluating various analysis methods (Chang and White 2008). These methods were:

- A 1D line-girder analysis coupled with the V-load method (as outlined by the NSBA).
- A 2D grid analysis
- A 3D grid analysis
- A 3D FEA analysis, with the composite slab and the girder web modelled with shell elements and the girder flanges modelled with traditional beam elements.
- A 3D grid analysis, with the composite slab modelled either with beam or shell elements and the girders modelled using open-section thin-walled beam theory.
- A 3D analysis, with an appropriate width of the composite slab and the girder modelled together as one equivalent element, using open-section thin-walled beam theory.

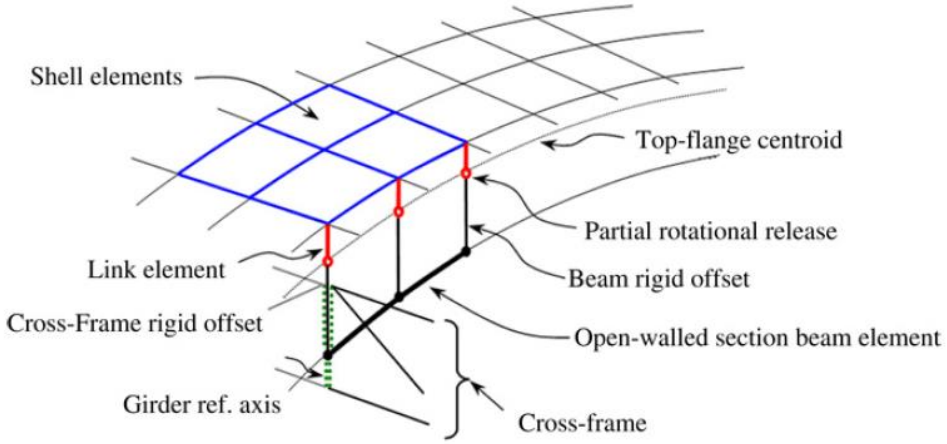

Figure 2.5: 3D Modelling using Open-Section Thin-Walled Beam Theory for Girders

Chang and White (2008) focused on using the last two models, in order to capture web distortion, which is a fundamental feature in the girder's torsional response and is commonly overlooked in both 1D line-girder analysis and 2D grid analysis. Web distortion occurs as the composite deck provides torsional restraint to the girder top flange, but the web is not stiff enough to transfer that restraint down to the bottom flange. Bottom flange lateral bending stress and lateral displacements between cross-frames are consequences of web distortion. The V-load method does not consider the girder torsional flexibility, while grid programs such as MDX and DESCUS assume that some of the nodal displacements or rotations are negligible, whereas a warping degree of freedom must exist at the girder nodes to account for warping. Accounting for web distortion may be done using shell elements for the web or open-section thin-walled beam theory for the girders.

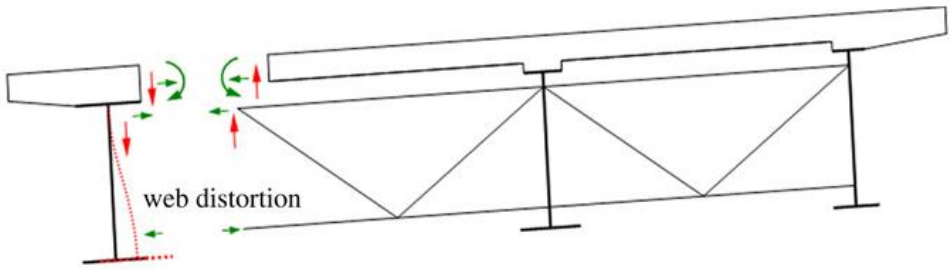

Figure 2.6: Internal Forces in Composite I-Girder Bridge

Other aspects addressed in the paper are cross-frame modelling, load height effects (which induce a tipping effect on the girders), and displacement compatibility between the slab and the girder. Furthermore, common pitfalls to be avoided when using the different analysis methods are presented and analysis results are compared. It is shown that the most accurate analysis method is the 3D FEA, with webs modelled with shell elements. 3D grid models using open-section thin-walled beam theory, namely 7 degrees of freedom per node for girder elements, also prove to be accurate, provided that a rotational release is implemented at the interface between the slab and the girder and therefore breaking rotational compatibility at the joint. Composite equivalent elements are also accurate, provided the slab is neglected when computing the torsional stiffness of the equivalent element.

The use of open-section thin-walled beam theory based prototype finite elements was developed by Chang (2006) and implemented in GT-SABRE, a program developed at the Georgia Institute of Technology.

Chang (2006)

Chang (2006) developed finite element software aimed at predicting the response of horizontally curved I-girder bridges during erection and placing of the composite slab. Chang was motivated to develop a program that could be specifically used to model curved girder bridges since the existing structural analysis software had several issues in modeling these systems, namely:

- 3D FEA software may be used to analyze curved bridges, but modelling is tedious, staged construction is not considered, and recovery of the results does not come in a direct form to the design engineer (results are not presented in a traditional manner, e.g. shear and moment for a particular girder)
- 2D or 3D grid software are based on a reduced set of degrees of freedom (some displacements or rotations are assumed negligible), which makes the capture of the warping response impossible; their use is acceptable for standard bridges, but irrelevant for long-span, highly-skewed or highly-curved horizontal bridges.

Chang's software combines an open-section thin-walled beam element for the steel girders with a grid formulation for the composite slab. The finite element formulation results in an analysis that is quite accurate for horizontally curved bridge applications. Calculations are generally faster than for traditional 3D FEA software. The following is accounted for in the software:

- An accurate description of the geometry of the structure, including cambers (defined by a combination of Bezier and B-spline curves) and cross-frame positions along the depth of the girders
- A second-order analysis of the structure, i.e. the analysis is performed on the deformed shape of the structure
- The potential use of temporary supports such as cranes and shoring towers, and a stress and displacement analysis during lifting of the girders
- The calculation of the forces required to assemble the members together
- The induced forces in the cross-frames and girders due to initial lack-of-fit
- The calculation of potential uplift at the supports, for example at the ones closer to the center of curvature, which are prone to uplift
- The concrete cast sequence and therefore the sequence at which composite action is progressively taking place.
- The calculation of the displacements, stresses, and reactions at all stages of the construction process.

A special beam element with seven degrees of freedom per node (one for warping) is formulated and validated with benchmarking problems. Web distortion is not considered at the kinematics level, but is compensated by releasing the rotation at the slab to girder intersection. Without this release, bottom flange lateral displacements and lateral bending stresses may be highly underestimated. Additional modelling features include:

- Cross-frames are modeled with truss and beam elements; rigid offsets are specified to accurately model their position
- The modelling of the actual height of the bearings, as it impacts the magnitude of the horizontal reactions
- The modelling of the load height, as it may cause tipping of the girders

Chang notes that intermediate stiffeners shall be omitted through the analysis because plastic hinges typically form at their top under strength load combinations, which prevents them from fully transferring the torsional restraint provided by the composite slab. This ensures a conservative design.

Figure 2.7: GT-SABRE Viewer

Chang recognizes the following items for future improvement of his software:

- A formulation of the thin-walled beam element that recognizes cross-sectional distortion
- A modelling of the slab with shell elements, for better capture of long-term creep and shrinkage effects for a staged concrete cast sequence.

Topkaya and Williamson (2003)

Previous studies mainly or exclusively focused on I-girder sections. Limitations for the use of the grid analysis also apply to other cross-sectional shapes, such as the trapezoidal box section. Topkaya and Williamson (2003), at the University of Texas at Austin, developed a software package for bridge engineers that was better able to capture the behavior of horizontally curved trapezoidal box bridges.

UTrap can calculate cross-frame member forces (which are of critical importance for proper cross-frame sizing to prevent buckling) and girder stresses during erection and concrete stages (to prevent lateral-torsional buckling), considering warping within the cross-section. In this program, the number of girders is limited to two and partial composite action at early ages is taken into account. UTrap also performs a staged analysis, considering a multiple stage concrete cast sequence. Shell elements are used for the composite slab and the steel girder. Shear studs are modelled with spring elements.

UTrap was validated against ANSYS results as well as experimental results. Popp (2004) showed using UTrap that the Marcy Bridge collapse in the state of New York was inevitable with the bracing provided, and that marginal additional bracing would have prevented it. The Marcy Bridge was a straight bridge, but failed in a lateral-torsional buckling mode during the casting of the composite deck because of insufficient bracing. The collapse prompted further studies on adequate brace sizing for trapezoidal tub girder bridges.

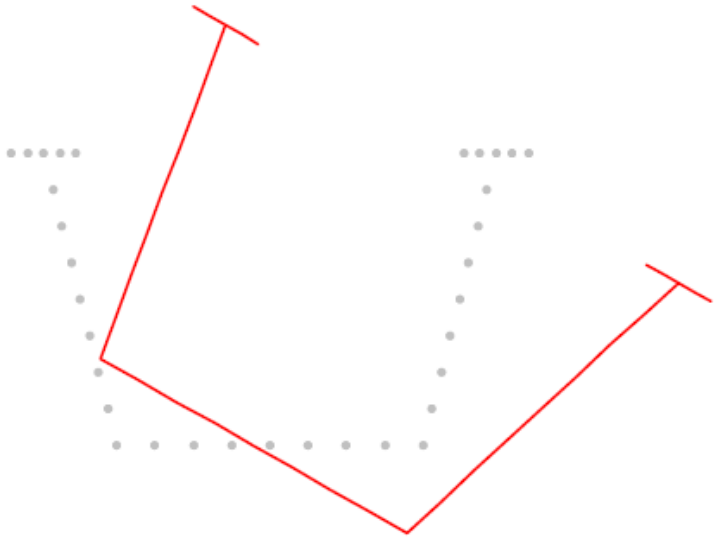

Figure 2.8: UTrap Cross-Section of Collapsed Marcy Bridge (Popp 2004)

Stith et al. (2010)

As part of this study, UT Bridge V2.2 (Biju-Duval, 2017) was developed. While version 2.2 is a totally new program developed from scratch – the fundamental framework of the software is an extension of UT Bridge V1.0, which was developed by Stith, Petruzzi and Kim (Stith 2010). The effort for the software was divided into three steps: 1) preprocessor, 2) processor, and 3) post-processor. Stith mainly focused on the main processor, which included the element formulations and incorporated the solver and eigensolver. Petruzzi and Kim developed the pre-processor and post-processor, respectively. Development of the program was carried out following detailed field and parametric studies on an investigation funded by TxDOT. The study focused on the behavior of curved plate girder bridges during construction. UT Bridge V1.0 produced a three-dimensional shell representation of curved plate girder bridges that was based upon basic input prompted from the user from input screens in the preprocessor. UT Bridge V1.0 was released to a wide audience of engineers and performed generally well. However, as is common with software, a number of modelling issues and limitations were encountered in the years following the initial release. Many of the problems were fixed and released in subsequent versions of the software with the final version culminating in Version 1.6. Limitations in the software modelling decisions made basic modifications to fix and expand some of the modeling capabilities impractical. Some of the modelling limitations and problems included the underestimation of deflections (primarily for tight curvatures), excessive stiffening effects from transverse web stiffeners on the system buckling eigenvalue, and overestimation of horizontal reactions on curved girder systems. The limitations meanwhile included the restrictive mesh refinement options (in particular, through the web depth), the need for the erection sequence to move from one end of the bridge to the other (for example excluding drop-in segments), the need for the placement on skewed systems to be parallel (whereas in reality, the contractor has the choice between a parallel and a skewed placement scheme). The modifications that were carried out on Version 1.5 were carried out by Biju-Duval and released in Version 1.6; however these modifications were primarily carried out to produce a version that minimized modelling errors until a new version (Version 2.0) could be developed.

Version 2.0 was a totally new program with new preprocessor, processor, and postprocessor and is discussed in next sub-section.

Biju-Duval (2017)

As noted in the last section, Biju-Duval developed and produced a new version of UT Bridge that essentially started from scratch. The program was called UT Bridge V2.0. Unlike Chang's program (Chang 2006), UT Bridge V2.0 models all flanges and webs with isoparametric, quadratic, eight-noded shell elements with four integration points and two integration layers, able to capture both membrane stresses and out-of-plane shear stresses. This way, warping of the cross-section is automatically captured. Whereas UT Bridge version 1.0 used line elements for the transverse stiffeners, in Version 2.0, web stiffeners are modeled with shell elements. UT Bridge V2.0 can model different cross-frame types, such as X-frames and K-frames, as well as different load types, from self-weight to point loads, uniform loads, wind loads and temperature loads. The main advantage of UT Bridge V2.0 compared to commercial programs is the ability to quickly model almost any type of curved, complex bridge, including any type of erection plan and cross-frame arrangement. Bridge plans can easily be converted to state-of-the-art finite element models without actual extensive knowledge of the finite element theory. UT Bridge V2.0 is able to conduct a first-order linear elastic analysis as well as geometrically nonlinear analysis. Structural stability can be checked by performing an eigenvalue buckling analysis, and free vibrations modes determined from a frequency analysis. Additionally, a placement analysis can be conducted by using shell elements for the concrete deck and shear link elements for the shear studs. The stiffness associated to those link elements is time-dependent to account for curing of the concrete. The load versus displacement curve implemented is based from the experimental tests conducted by Topkaya (2002). A time-dependent stiffness is also implemented for the deck elements.

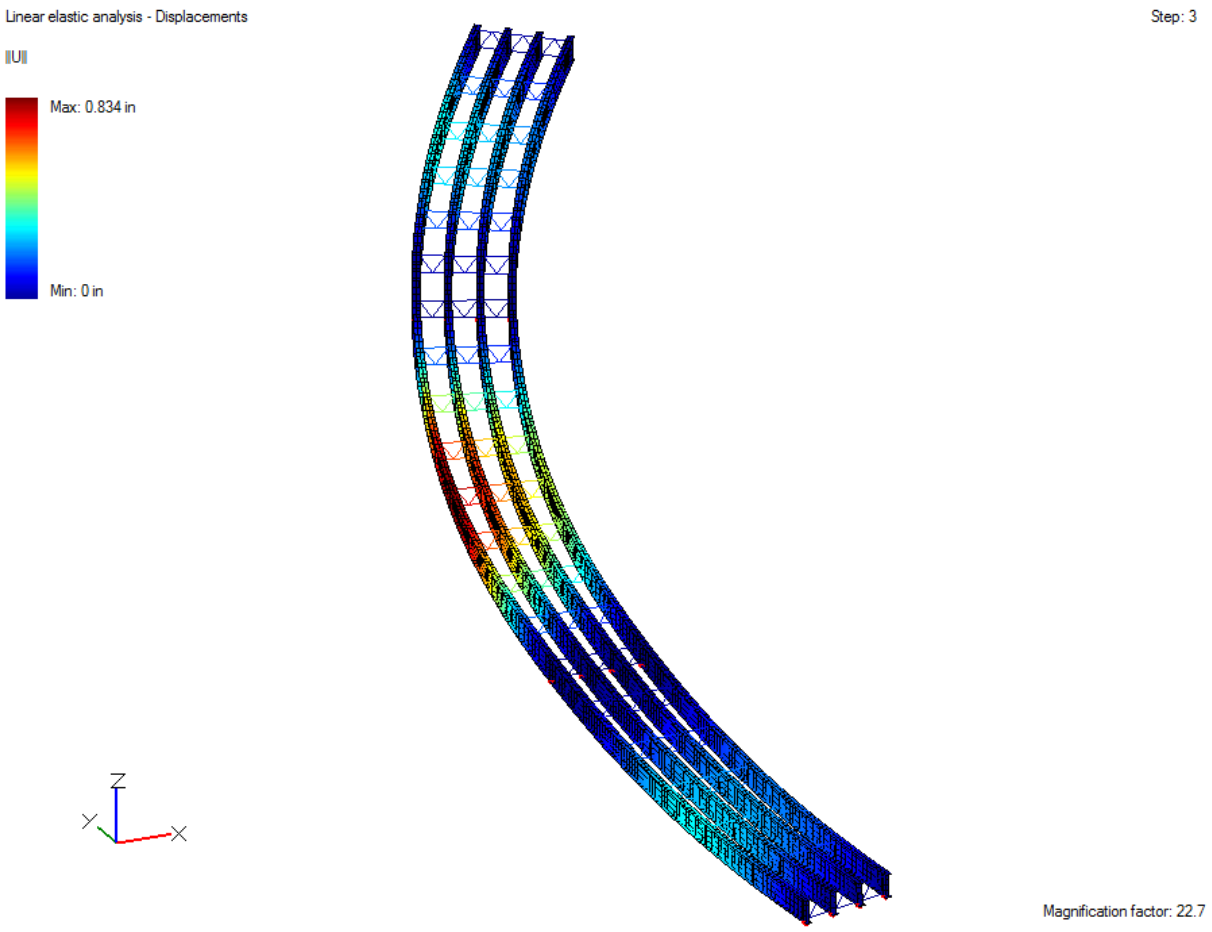

Figure 2.9: Curved I-Girder System in UT Bridge V2.0 (Biju-Duval 2017)

Another feature of UT Bridge V2.0 is that it can automatically draw shear, moment and torsion diagrams, which are important quantities for bridge engineers. Cross-frame forces and support reactions can also be displayed directly on the model for quick evaluation. Displacement charts can be automatically generated, and the same applies for layovers, which are defined as the differential lateral deflection between the top and bottom flanges and give a measurement of the torsional behavior of the structure.

In addition to curved plate girder systems, UT Bridge V2.0 can also model curved tub girder geometries, in a way that is similar to UTrAp, which was a program exclusively developed for those systems (Topkaya 2002). However, unlike Topkaya's program, UT Bridge V2.0 models all steel plates with shell elements, including diaphragms. The graphical interface is also much more developed, and more loads and bracing options are available, including internal K-frames, X-frames, and top struts. Again, an eigenvalue buckling on those systems can quickly evaluate their stability in order to avoid potentially dramatic failures such as the Marcy Bridge collapse (2001).

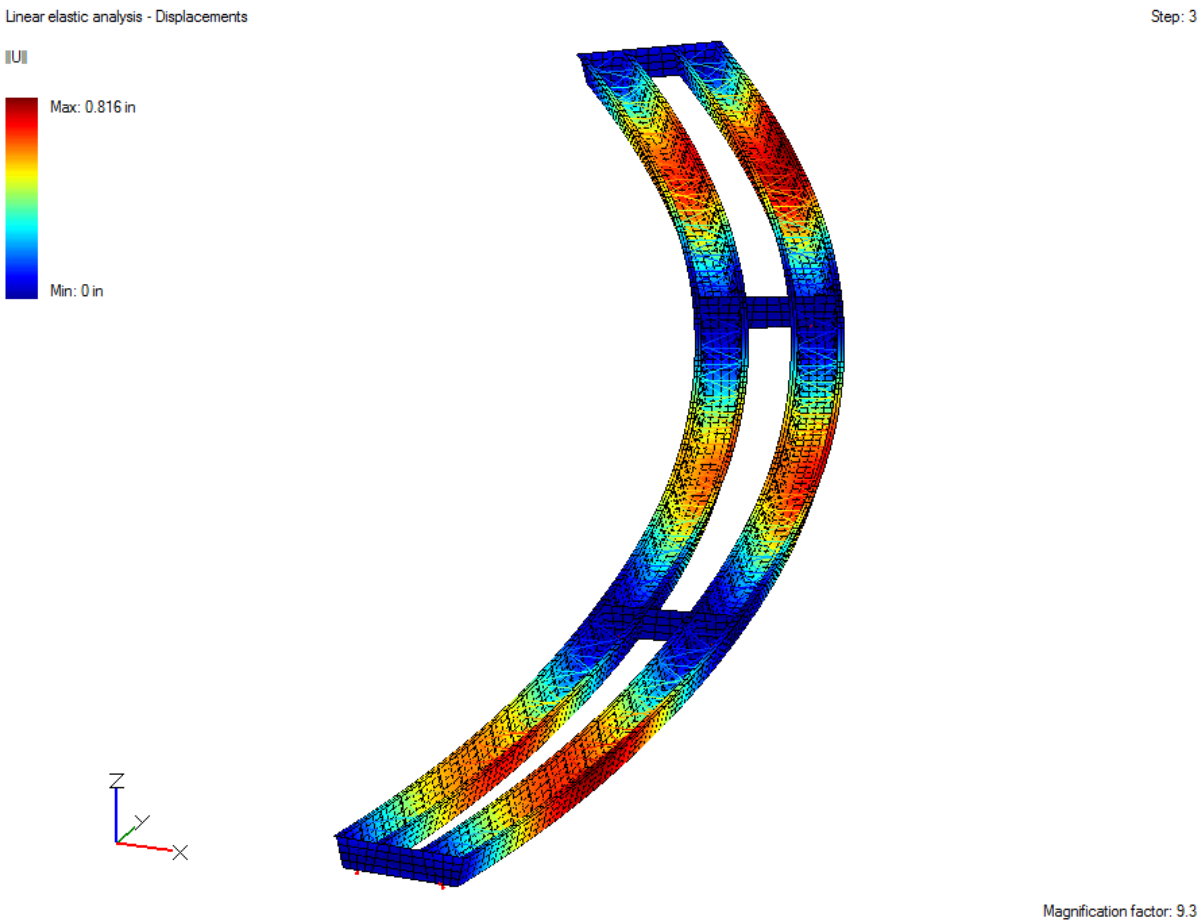

Figure 2.10: Curved Tub Girder System in UT Bridge V2.0 (Biju-Duval 2017)

UT Bridge V1.0-V2.0 has become popular among erectors for a quick analysis of the bridge behavior, but there are also areas of improvement that can still be implemented. For example, the program is currently unable to model general initial imperfections.

2.3.2 Innovative Construction Methods

Amornrattanapong (2006)

Driven by the large span-to-cost ratio of traditional precast prestressed concrete I-girders, Amornrattanapong (2006) conducted a study at the University of Nebraska to promote the use of curved pre-tensioned precast concrete I-girders for bridge applications. This is the first study on pre-tensioned concrete curved bridges, while post-tensioned cast-in-place concrete box girders have already been studied.

Curvature is accomplished by a series of chords – similar to harping in prestressed concrete construction – and does therefore not compare with the pleasant aesthetical appearance of truly curved I-girder bridges. Experimental tests were conducted to show the feasibility of such a bridge construction method. An erection and assemblage sequence was provided for a typical bridge configuration, considering stability issues. A cost analysis was conducted and compared to the cost of a curved steel I-girder bridge.

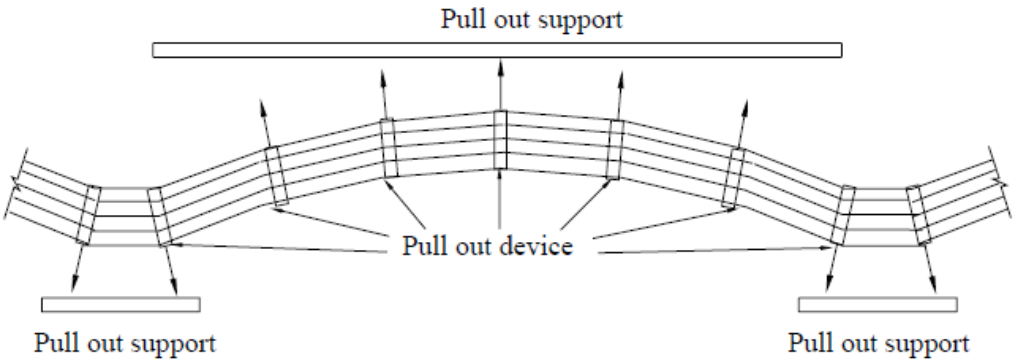

Figure 2.11: Proposed Construction Method for Curved Pre-Tensioned Concrete I-Girder Bridges

Beyond offering an insight of possible concrete I-girder applications for horizontally curved bridges, Amornrattanapong provides an extensive mathematical description of traditional and more state-of-the-art analysis methods for curved bridges, ranging from the AASHTO V-load method to the Vlasov kinematics used by Chang and White (2008) upon formulating the open-section thin-walled beam element within GT-SABRE, therefore echoing in a more mathematical manner the synthesis offered by Zureick (1999). The grid method was validated for the proposed pre-tensioned concrete I-girder bridge. Detailed calculations are provided for a typical curved bridge. However, beyond the limitations of the grid method already pointed out by Zureick (1999) and Chang and White (2008), prestress losses due to horizontal curvature of the prestressing strands were not considered. Prestress losses are of critical importance for durability.

Alawneh (2013)

Driven by the same cost effectiveness purpose and also from the University of Nebraska, Alawneh (2013) proposed a new type of curved precast concrete bridge, using standard small segments kinked together. A maximum segment length of 40 feet is mentioned to approach the truly curved geometrical aspect. The forms may be reused for the whole length of the bridge for economy purposes. The segments are then post-tensioned together at the precast yard. Unlike cast-in-place post-tensioned construction, which is popular in California, no temporary shoring is required, reducing traffic interruption.

Construction feasibility is demonstrated on full-scale specimens, both for an I-girder section (as in Amornrattanapong (2006)), a tub section (as already used in the states of Nebraska and Colorado), and a box section. Box sections prove to be particularly effective for sharp configurations while I-sections are better for longer spans. An erection sequence is also described, as well as a detailed analysis and design methodology. Cracking torsional capacity is tested and compared against FEA results.

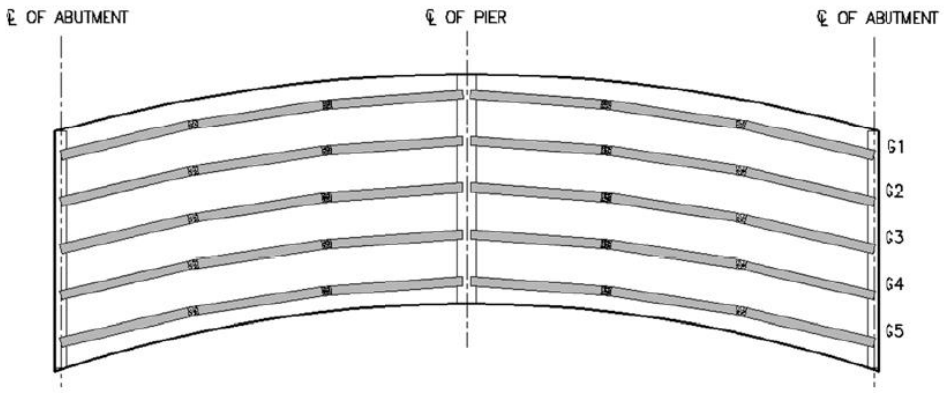

Figure 2.12: Two-Span Bridge with Kink Joints

2.3.3 Bracing of Girders

Lateral-torsional buckling is a critical failure mode that often governs the design of both straight girders and curved girders. Stability is of particular importance for open sections such as I-sections and trapezoidal tub sections since their torsional stiffness is often orders of magnitude less than closed shapes of the same size. For these systems, cross-frames or diaphragms as well as top lateral trusses must be provided to increase the torsional stiffness of the structure and be designed in accordance with AASHTO. Insufficient or improper bracing may result to collapse of the bridge, as shown in the aforementioned Marcy Bridge collapse.

Sharafbayani and Linzell (2014)

Among the most recent studies, Sharafbayani and Linzell (2014) proposed an optimization of the cross-frame positioning along the length of the bridge. The scope of the study is non-skewed horizontally curved I-girder bridges, for which AASHTO recommends the use of cross-frames oriented perpendicular to the girder webs. This distribution results in larger unbraced lengths on the exterior girders that have the larger radius. As those exterior girders usually control the bracing of the bridge, the unbraced lengths for the interior girders are smaller than required, which results in an excessive number of cross-frames, which are per unit weight the most expensive structural components of a bridge.

By using skewed cross-frames instead of radially-orientated cross-frames, a fewer number of cross-frames are required while maintaining acceptable stress and displacements, which are of critical importance respectively for stability and fit-up during erection. 10° to 20° are typical values for the cross-frame skew angle.

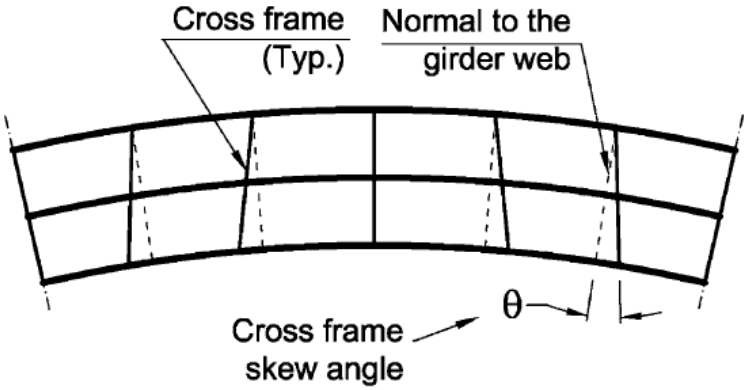

Figure 2.13: Cross-Frame Distribution (Sharafbayani and Linzell 2014)

A 3D sequential FEA reproducing a possible erection sequence was conducted on both single-span and two-span horizontally curved I-girder bridges. Three connection types were tested: the skewed connection stiffener, common for skew angles smaller than 20°, the bent gusset plate, and the split pipe stiffener. The particular bridge studied by the authors showed comparable performance, independently from the type of connection selected. Their stiffness is indeed similar for relatively low skew angles up to 20°.

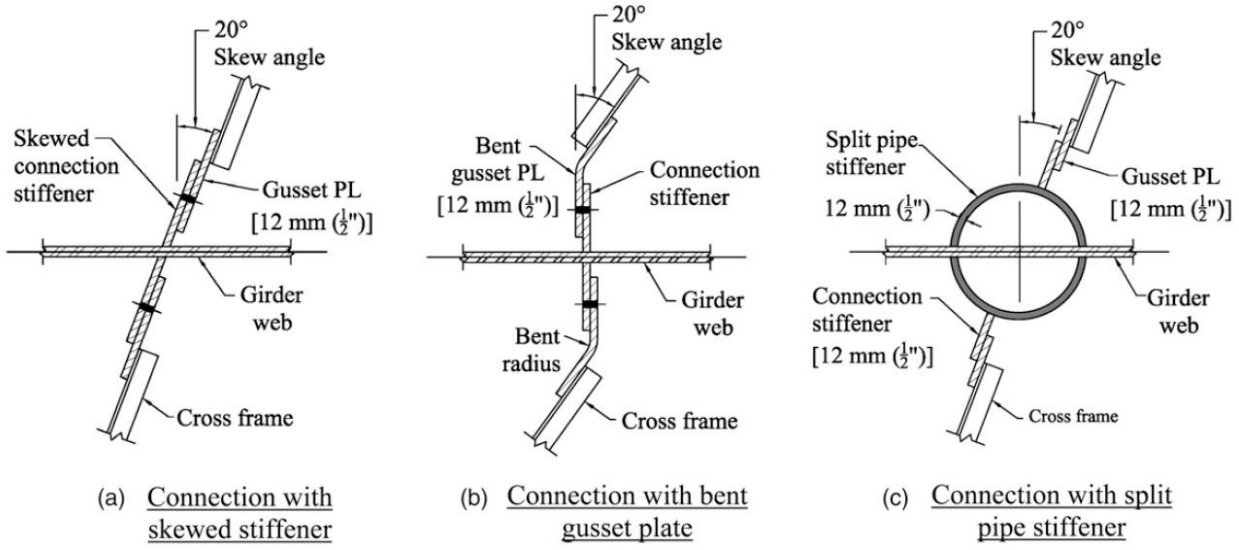

Figure 2.14: Skewed Cross-Frame Connection Details (Sharafbayani and Linzell 2014)

In addition, out-of-plane rotations of the girders were checked. Although no quantitative limit is state by AASHTO, those rotations have to be kept minimal to ensure proper final geometry of the bridge, such as deck elevations and cross-slopes. Implementing a skewed cross-frame distribution again proved to have a favorable impact.

As far as stresses, a more uniform load distribution is achieved between the girders. For larger unbraced lengths, some of them even above the AASHTO limit, a discontinuous skewed distribution was also tested and similar bridge performance was found.

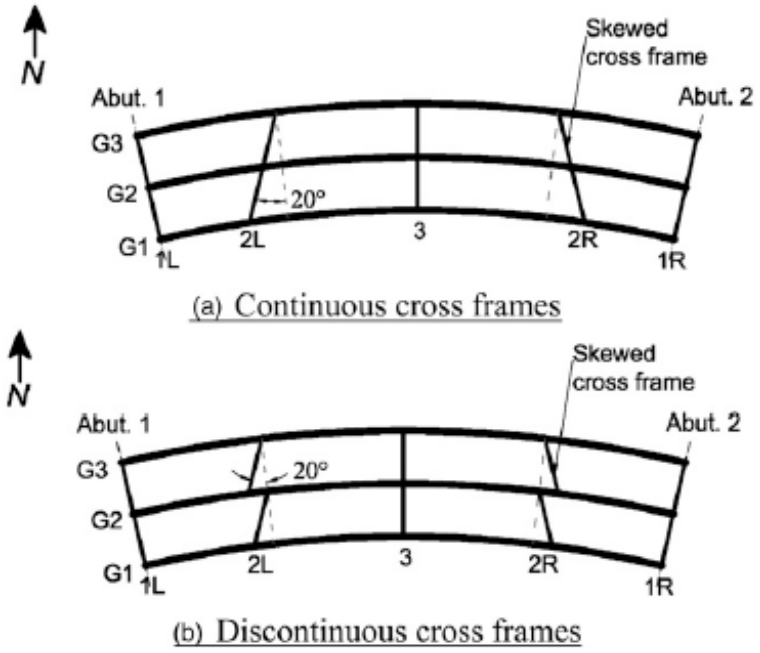

Figure 2.15: Continuous and Discontinuous Skewed Cross-Frame Distribution (Sharafbayani and Linzell 2014)

Helwig and Wang (2003)

Another way of reducing the number of cross-frames required on a bridge is the lean-on concept, as proposed by Helwig and Wang (2003). The original project was followed up with an implementation project that was carried out on three bridges in the Lubbock District. Field instrumentation was carried out and documented by Romage (2008). The work was also documented in a conference paper Herman et al. 2007. The lean-on concept for bridges echoes the braced/unbraced frame distinction made in the building industry, where a braced frame does not require all bays to be braced. Similarly, a bridge may not need bracing elements across its whole width. For example, X-shaped cross-frames consisting of rolled angles may be installed at one bay only (or two or three bays if the bridge section more than 6 girders), while load transfer and lateral displacement compatibility are achieved by only top and bottom struts in the other bays. Lean-on bracing is not only interesting from a cost-savings perspective, but also with regard to structural behavior:

- Fewer cross-frames result in lower erection cost
- Fewer cross-frames result in lower maintenance cost
- For skewed bridges, cross-frames distributions using the lean-on concept result in smaller forces under traffic load.

Several severely-skewed bridges in Texas already were constructed using this concept.

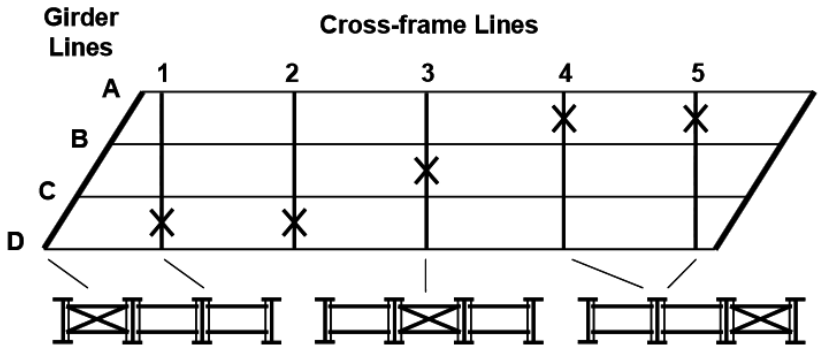

Figure 2.16: Lean-On Concept (Herman et al. 2007)

Park et al. (2005)

Box-sections are popular for horizontally curved bridge applications due their high torsional stiffness inherent to their closed cross-sectional geometry. Park et al. (2005) from Korea University in Seoul conducted parametric studies to produce design charts to optimize the intermediate diaphragm spacing for curved box-girder applications.

A thin-walled curved box-beam finite element having nine degrees of freedom per node, including two distortional degrees of freedom, was developed. The finite element was validated against conventional shell elements. As for the open-section thin-walled finite element mentioned by Chang and White (2008), some simplifying assumptions are made upon formulating the new finite element. One of them is the assumption that some of the displacements are negligible:

- The shear strains due to distortion
- The shear strains due to changes in the bending and warping normal stresses.

The beam element allows for faster analysis. Also, as mentioned by Zureick (1999), modelling with beam elements allows for directly exploitable results by the bridge engineer, such as moment, torsion and shear distributions along the length of the structure, which means a better bridge behavior understanding.

Of particular interest is the consideration of various stress ratio values between the distortional warping normal stress and the bending normal stress as far as determining the spacing between the interior diaphragms required for stability. This ratio differs from country to country. Whereas AASHTO specifies a maximum value of 10%, the code limits it to only 5% in Japan. Inappropriate stress limitations may result in uneconomical designs.

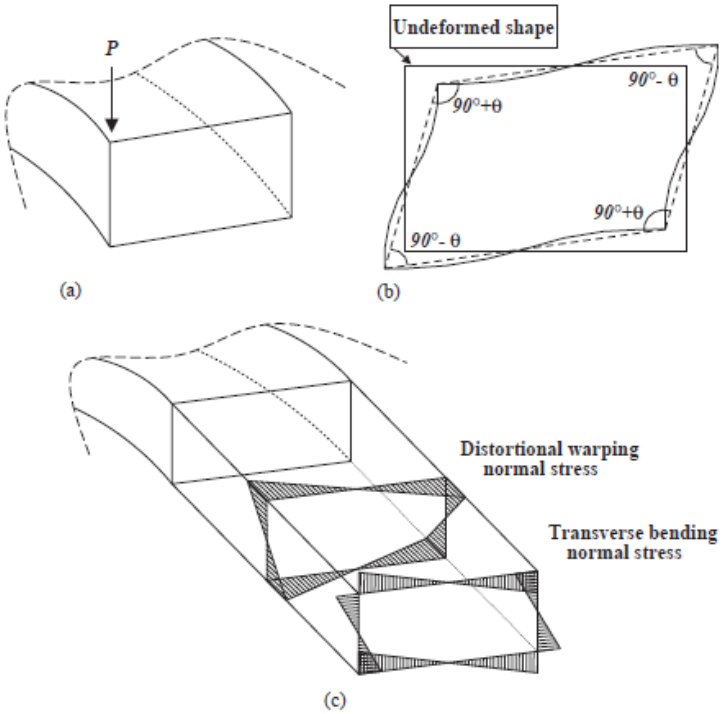

Figure 2.17: Distortional Warping and Bending Normal Stresses (Park et al. 2005)

The design parameters considered in the charts are the following:

- The radius of curvature of the bridge
- The number of spans
- The span length
- The geometric properties of the box-section
- The desired limiting stress ratio between the distortional warping normal stress and the bending normal stress.

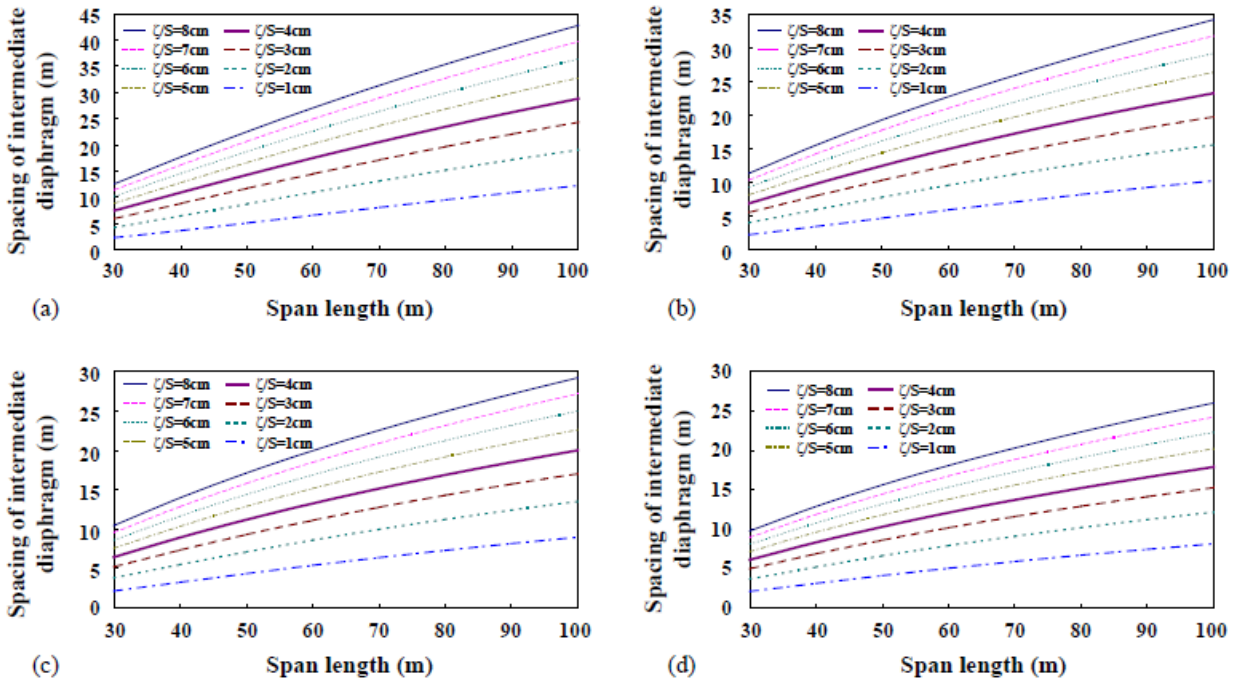

Figure 2.18: Design Charts for Single-Span Curved Box-Girder Bridges (Park et al. 2005)

2.3.4 Shear Diaphragm Bracing of I-Girders

Lateral-torsional buckling of a girder can be opposed by restraining either the lateral deflection of the compression flange or the twist of the cross-section (Yura 2001). When the compression flanges of two neighboring girders are connected by a shear diaphragm, the girders tend to buckle as a unit and the warping deformations of the flanges are resisted by the presence of the diaphragm. Therefore, the bracing provided by the diaphragm increases the buckling capacity of the girders. One of the first practical solutions for shear diaphragm bracing was produced by two independent studies that were published nearly simultaneously (Errera and Apparao 1976; Nethercot and Trahair 1975). However, the solution was focused on diaphragm braced beams subjected to uniform moment. Helwig and Frank (1999) modified this solution to account for more practical loading conditions resulting in the following equation:

$$M_{cr} = C_b^* M_g + mQd \tag{2.1}$$

where,
M_{cr} = buckling capacity of the diaphragm-braced beam
C_b^* = factor for moment gradient that includes effects of load height, if applicable (Helwig et. al 1997; Galambos 1998)
M_g = buckling capacity of the girder without the shear diaphragm
m = factor that depends on the loading type
Q = deck shear rigidity
d = depth of the girder

The deck shear rigidity is expressed as follows:

$$Q = G's_d \tag{2.2}$$

where,
G' = diaphragm effective shear stiffness
s_d = the tributary width of deck bracing a single girder

When a system has n_g girders with a spacing of s_g, the tributary with of the deck bracing a single girder is calculated as:

$$s_d = \frac{n_g - 1}{n_g} s_g \tag{2.3}$$

The effective shear stiffness and ultimate strength of a diaphragm can be determined experimentally using a cantilever shear frame such as the one depicted in Figure 2.19. Since the frame is a mechanism on its own, the diaphragm provides all of the lateral stiffness and strength to the system. The effective shear modulus, G', is derived as follows:

$$G' = \frac{PL}{fw\gamma} \tag{2.4}$$

where,
P = lateral load on test frame
L = length of the test frame
f = center to center spacing of loading beams
w = diaphragm width
γ = diaphragm shear strain

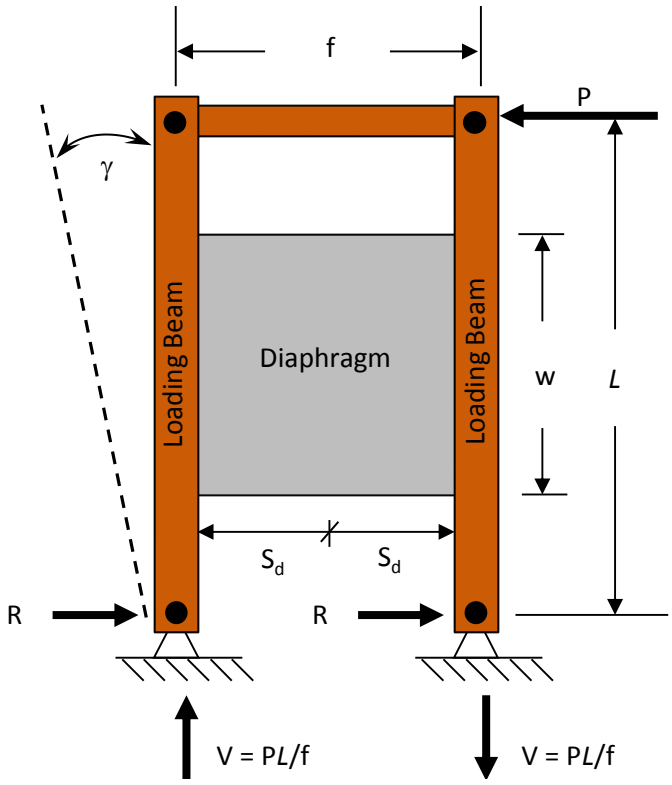

Figure 2.19: Shear Test Frame with Diaphragm

Suitable bracing must possess adequate stiffness and strength (Winter 1960). Traditionally, the ideal stiffness of a brace is defined as the stiffness required for a perfectly straight member to buckle between the brace points. For stability problems, a larger stiffness than the ideal value is required to control deformation and brace forces. Therefore, Equation 2.1 must be modified before it can be used for design. For diaphragm braced beams, Helwig and Yura (2008a) recommended that four times the ideal diaphragm stiffness be used for design. Since diaphragm braced beams are essentially continuously braced, the traditional definition of "buckling between the braced points" was not meaningful. Therefore, the ideal stiffness for diaphragm braced beams was based upon the stiffness required to reach a given load or stress level (Helwig and Yura 2008a). While a given stress limit is somewhat arbitrary, a value such as 50 ksi (or the yield stress of the material under consideration) would be a practical limit. For a given maximum factored moment, M_u, the previous expression can be utilized to obtain the following design equation:

$$M_u = C_b^* M_g + \frac{mG' s_d d}{4} \tag{2.5}$$

In addition to establishing the diaphragm stiffness requirements, Helwig and Yura (2008b) developed the following equation (from parametric study of three different sections at three different span-to-depth ratios) to determine the maximum warping restraining moment per unit length along the longitudinal axis of the girder, M'_{br_max}:

$$M'_{br\_\max} = 0.001\frac{M_u L}{d^2} \tag{2.6}$$

where,
M_u = maximum design moment along the diaphragm braced beam
L = spacing between discrete bracing points that prevent twist
d = beam depth

Equation 2.6 was developed using a large displacement analysis on an imperfect system with the diaphragm stiffness set at four times the ideal value. Notional loads were used to create the imperfection in the top flange while keeping the bottom flange straight which previously studies have shown to represent the critical shape imperfection for beam bracing problems (Wang and Helwig 2005). The maximum twist imperfection at midspan was set to $\theta_o = L/(500d)$ which is conservatively twice the value of the $\theta_o = L/(1000d)$ which is consistent with imperfection limits from the AISC Code of Standard Practice (AISC 2010).

The moment and shear on an unstiffened PMDF diaphragm are calculated as $M_{br} = M'_{br}L_d$ and $V_{br} = 2M_{br}/w_d$, respectively where L_d is the length of the diaphragm segment and w_d is the width of the diaphragm segment (see Figure 2.20). These equations are based on the assumptions that the unstiffened PMDF sheets act independently from one another even though they are connected by intermediate sidelap fasteners. In laboratory tests performed by Egilmez et al. (2005), the unstiffened PMDF sheets were observed to act in this manner.

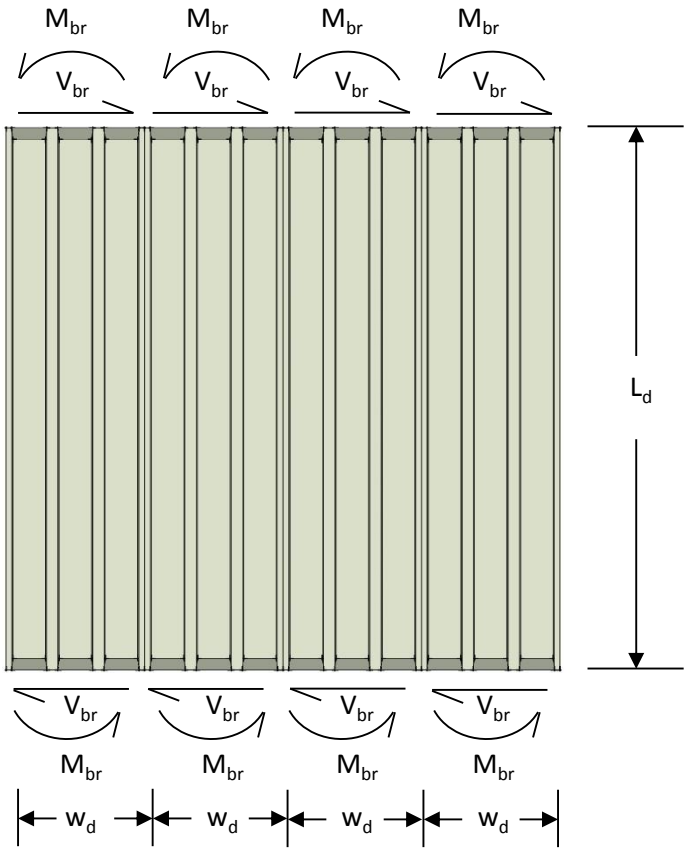

Figure 2.20: Behavior of Unstiffened Diaphragm

In the building industry, PMDFs are often relied upon to laterally brace beams during construction. The large in-plane shear stiffness of PMDFs can effectively restrain the warping deformation of the beams only if an adequate connection is developed between the PMDFs and the girders. Since the top flange of adjacent beams are typically at the same elevation in buildings, PMDFs span continuously across the top of the beams and are connected directly to the flange via mechanical fasteners, puddle welds, or shear studs as shown in Figure 2.21a. In the bridge industry, however, the elevation of the top flange often differs between adjacent girders due to differential camber and along the length of a girder due to a change in the flange thickness (aka a haunch). To maintain a constant deck thickness, angles that support the PMDF are welded to the top flange at different heights to accommodate the elevation difference in the flanges as shown in Figure 2.21b. The support angle eccentricity is defined as the distance from the bottom of the PMDF to the closest face of the top flange. While the support angle connection is quite stiff in the direction parallel to the span of the girder, the angle is flexible and can easily bend when loaded perpendicular to the span of the angle. Currah (1993) showed that the support angle eccentricity substantially decreased the stiffness of the shear diaphragm system.

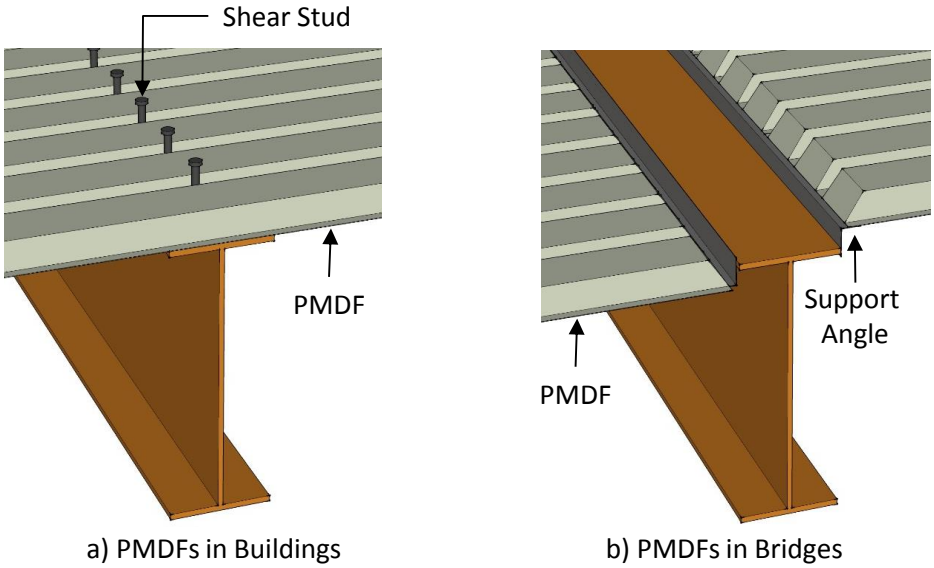

Figure 2.21: Typical PMDF Connections

To increase the connection stiffness perpendicular to the span of the girder, Egilmez (2005) added stiffening angles to the PMDF diaphragm system as shown in Figure 2.22. The stiffening angles spanned between the adjacent girders and were connected to a member attached to the top flange. The angles were placed at the lap splice of two neighboring PMDFs so that one screw would penetrate both PMDFs and fasten them to the stiffening angle. The stiffened PMDF system was successfully implemented on two steel I-girder bridges located on the IH-610 north loop in Houston, TX (Egilmez et al. 2016). Using stiffened PMDFs as bracing elements allowed 680 intermediate diaphragms to be eliminated from the design.

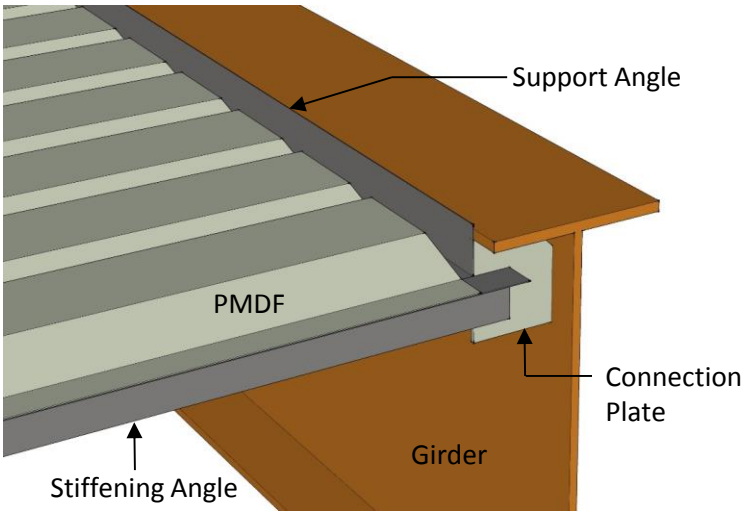

Figure 2.22: PMDF Connection with Stiffening Angles

2.3.5 Detailing

Ozgur (2011)

Horizontally curved bridges exhibit lateral displacements due to the combination of torsion and lateral bending. For I-girder bridges, this may result in fit-up problems during erection that may impact the functional and/or aesthetic aspects of the bridge and lead to legal claims. Resistance to these displacements is provided either partially or entirely by the cross-frames; this is one their main functions along with providing stability to the structure and transferring the load between adjacent girders. Cross-framed are considered primary structural elements for curved bridges.

AASHTO specifies different cross-frame detailing methods. Each method will result in plumb girders for one specific state of stress, which are:

- The no-load condition
- The steel dead load condition
- The total dead load condition.

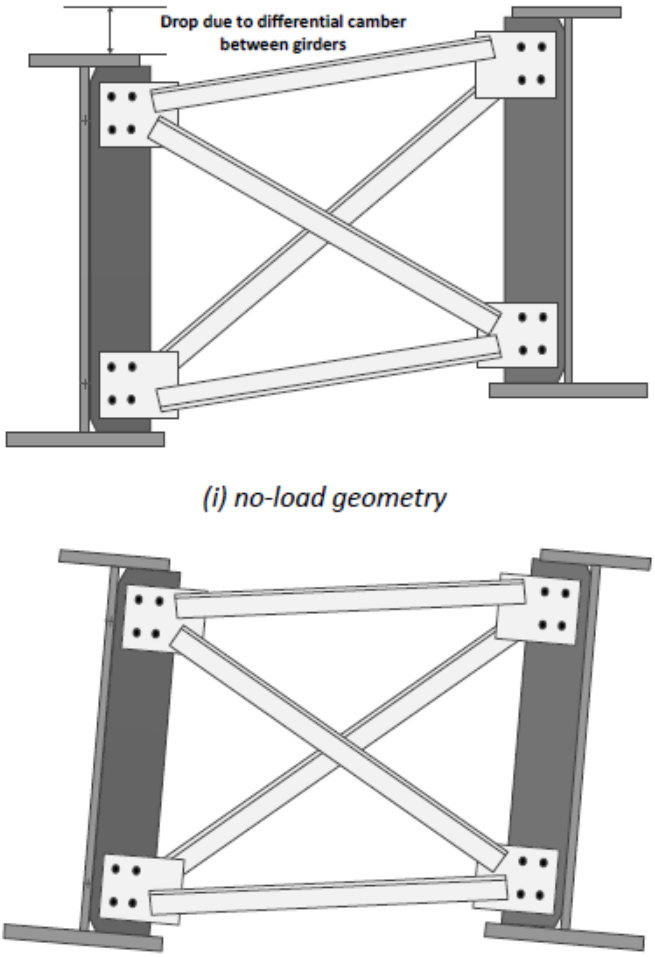

Figure 2.23: No-Load Fit Behavior (Ozgur 2011)

Constructability of the bridge is dependent upon the detailing method selected, as well as behavior. Debates exist among the bridge engineering community to decide which detailing method is the best. Ozgur (2011) addresses this question by conducting extensive numerical studies at the Georgia Institute of Technology, together with experimental tests and field measurements on actual bridges. Curved and/or skewed I-girder bridges are analyzed. Two different cross-frame distributions are considered:

- A radially oriented cross-frame distribution
- A skewed cross-frame distribution.

Practical guidelines are outlined to reduce fit-up difficulties during erection. Detailing methods are selected, depending on the bridge geometry. Procedures are also described to include the lack-of-fit with the analysis.

Sanchez (2011)

While Ozgur (2011) focused on cross-frames detailing methods, Sanchez (2011), also at the Georgia Institute of Technology, investigated the performance of horizontally curved I-girder bridges having skewed supports. The skew amplifies the non-desirable lateral bending and torsion effects of curved bridges, as adjacent girders do not behave equally. Again, those movements may cause fit-up problems, but also bearing misalignment, and inconsistencies as far as the composite deck cross-slopes and elevation. Cross-frames help mitigate those movements.

The interaction between the skew angle and the bracing system is evaluated, with practical guidelines to reduce skew-induced non-desirable effects, for example by using a fanned cross-frame distribution, and also by using the lean-on concept presented by Helwig and Wang (2003). This means bracing the girders at points where they show similar layover.

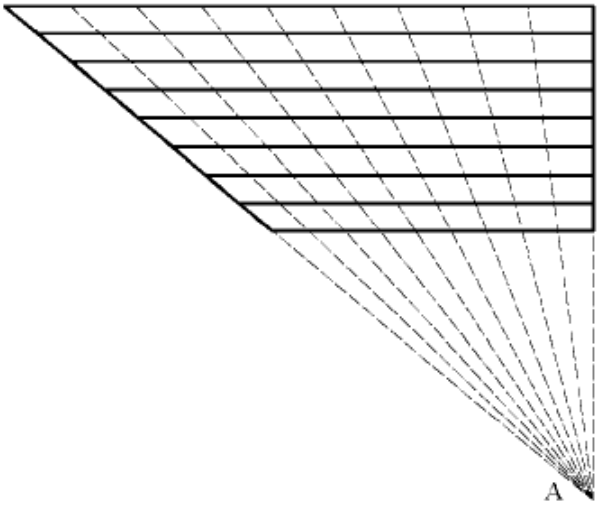

Figure 2.24: Fanned Cross-Frame Distribution

Also, improvements for the imperfect 2D grid analysis are proposed to analyze curved and/or skewed bridges, including:

- The reduction of an X-type brace into an equivalent 2-node finite element, with 6 degrees of freedom per node, by applying the direct stiffness method to the brace; the method may be applied to other brace shapes, for example the V-type or inverted V-type cross-frame
- An equivalent torsional constant to capture flange warping, as torsion for I-girders is dominated by warping rather than St. Venant torsion.

The refined 2D grid analysis, by more accurately capturing the girders torsional stiffness and cross-frame behavior, results in a more precise estimation of the cross-frame forces, which is particularly important for skewed bridges, where cross-frames act not only as brace elements but also as direct load transfer elements.

The brace equivalent 2-node finite element, although it better captures the behavior of the cross-frame, it is not perfect, as some of the displacements are again assumed negligible. It is also recalled that a 2D grid analysis does not capture web flexibility.

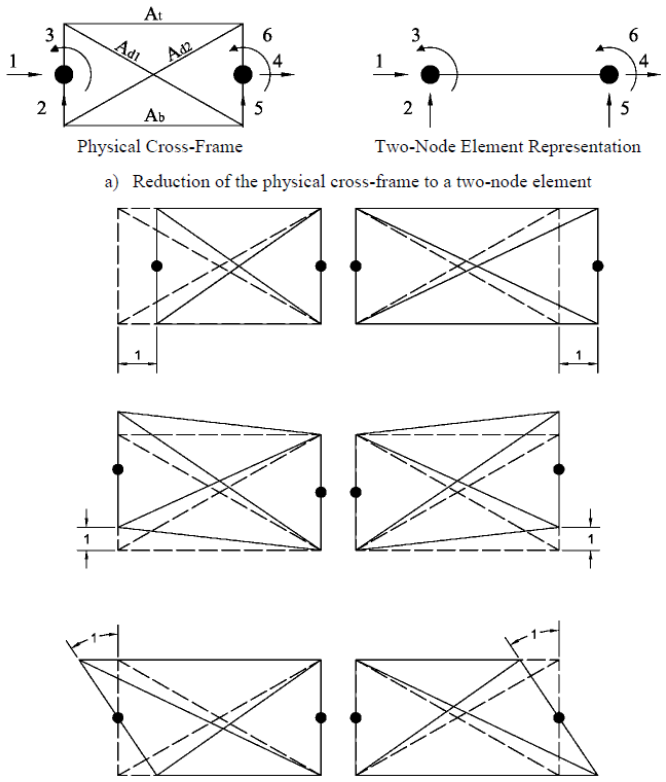

Figure 2.25: Reduction of an X-Type Cross-Frame into an Equivalent 2-Node Finite Element (Sanchez 2011)

2.4 Connection to the Girders

2.4.1 Current TxDOT Connection Detail

In the state of Texas, PCPs are not positively connected to the bridge girders as show in the TXDOT standards. Currently, the specifications show the PCPs resting on extruded polystyrene bedding strips that sit on the edge of the girder's flange (see **Error! Reference source not found.**). The self-weight of the panels (and therefore the associated friction force) keep the panels from moving during the casting of the concrete slab. After the CIP deck has cured, the PCPs are permanently attached to the system and the top flanges of the girders are braced by the cured deck system. As a result of this design methodology, the PCPs are unable to bracing the girders during the construction phase (while the concrete is uncured). Therefore, the unbraced length of the girders during the construction phase is taken as the distance between the cross-frames or the diaphragms.

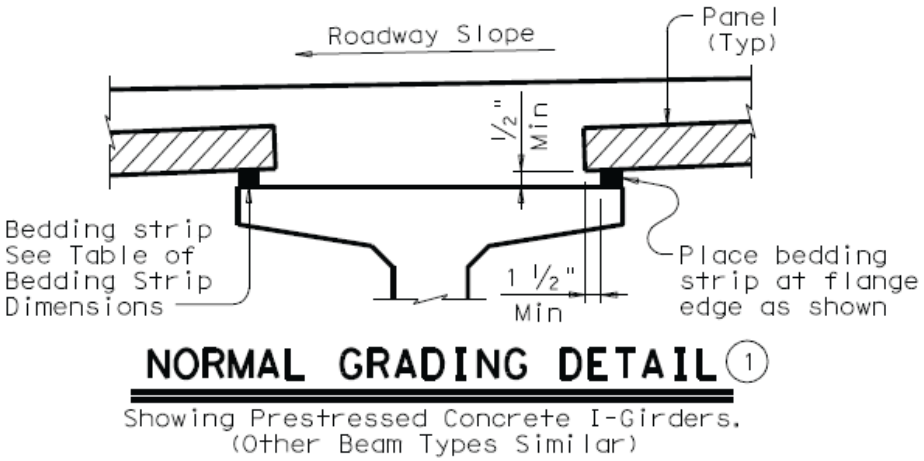

Figure 2.26: PCP to Girder Connection from TxDOT's PCP Standard Drawing (TxDOT 2014a)

A positive connection between the PCPs and the girders is required to allow the PCPs to brace the girders and provide stiffness to the system during construction. With an adequate connection, the PCPs may potentially eliminate some of the bracing systems required in curved steel girder systems and may also eliminate the required topping slab in curved concrete U-beams. The following sections highlight some of the PCP to girder connections that were found in the literature.

2.4.2 Connection by Adherence

For steel-concrete composite bridges, an innovative connection is the connection by adherence, as discussed by Thomann at the Ecole Polytechnique Fédérale de Lausanne (2005), and Thomann et al. (2006). This connection was designed to allow composite action to take place between the full-depth precast slab elements and the steel girders while avoiding issues associated pocked shear stud connections and glued connections. According to Shim and Chang (2003) pocked shear stud connections did not provide satisfactory long-term behavior since cracks form on the upper face of the slab between the shear pockets. Furthermore, pocked shear stud connections can make the post-tension process difficult and are not ideal for rapid construction. The main problem using a glued connection between the panel and the girder flange is the inability to posttension the panels together without loading the girders since the glue often will set before the panels can be posttensioned. The connection by adherence allows the full-depth panels to be placed on the girders, post-tensioned together, and then connected to the girders.

The connection is achieved by welding an embossed steel plate to the top of the girder and casting a notch into the bottom of the precast concrete panel. After prepping a bonding layer on the top flange (epoxy resin roughened with coarse sand), setting the panels on the girders, and post-tensioning the panels together, a cement past is injected into the connection in a manner similar to that of a post-tensioning duct (see Figure 2.27). The concrete-to-cement paste, cement paste-to-embossed steel plate, and the cement paste to bonding layer interfaces resist shear due to their macro-roughness. This system not only allows for short construction time on site, but is also durable and is far less likely to crack the panels than pocketed shear stud connections.

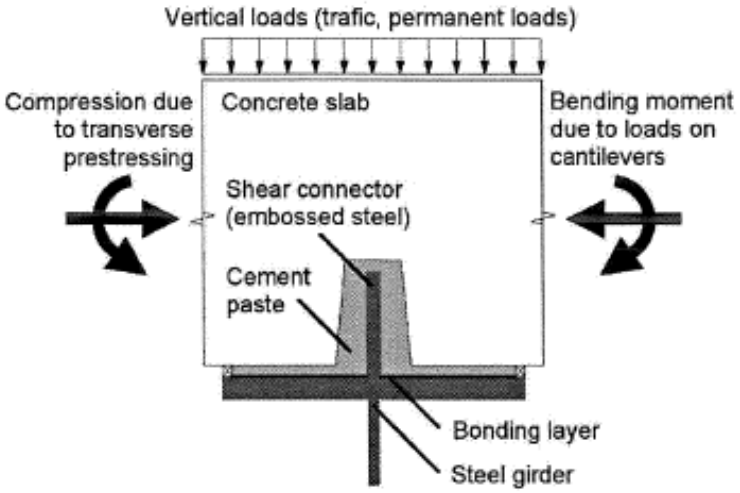

Figure 2.27: Connection by Adherence (Thomann 2005)

The push-out test (see Figure 2.28) was the main test conducted by Thomann et al. (2006) on the connection by adherence method. This test was used to determine the shear capacity, creep resistance, and fatigue resistance of several different types of shear connections. The following configurations were tested in this study: studs (D), Perfobond with bonding layer (PH), Perfobond without bonding layer (P), embossed steel plates with bonding layer (RH), embossed steel plates without bonding layer (R), and steel strip with a bonding layer on both the strip and the top of the flange (HH). The conclusions of the push out test showed that the RH connection was the most promising with high shear strength (up to 2800 kN/m), high stiffness (initial stiffness: about 14,000 kN/mm2), high fatigue resistance, and lower long-term deformations than measured for classical stud connections.

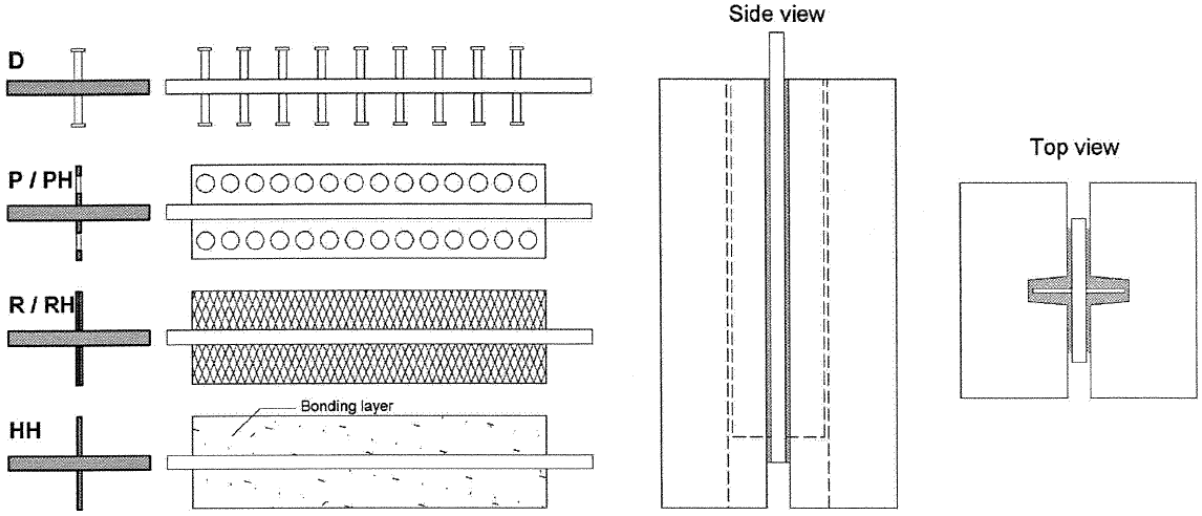

Figure 2.28: Push-Out Tests (Thomann et al. 2006)

The research conducted by Thomann et al. (2006) was limited to testing the shear strength of the connection parallel to the span of the girder. Therefore, further research is needed to rely on such a connection for a bracing application since the direction of the load will not be parallel to

the girder's span. Using this connection for a curved girder application would likely prove difficult as it would require a well-defined curved notch in the concrete panel and a curved steel plate, which might complicated the fabrication process.

2.4.3 Perforated Shear Connectors

The perforated shear connectors resembles the aforementioned connection by adherence and was studied at the Czech Technical University in Prague by Studnicka et al. (2000), who developed design recommendations to be implemented in the Eurocode. Similar to the connection by adherence, perforated shear connecters develop the composite action of the slab without using headed shear stud connectors. The perforated connector is welded along the top flange of the steel girder, while transverse reinforcement passes through the perforation (see Figure 2.29). This particular connection, however, is used in the traditional cast-in-place deck slabs and not in precast panels. The same friction concept as the connection by adherence is used in this system with the addition of the strength that is added depending on the amount of transverse reinforcement that passes though the perforations in the plate.

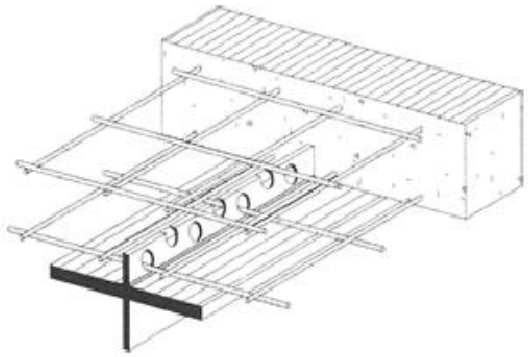

Figure 2.29: Perforated Shear Connector (Studnicka et al. 2000)

Two types of perforated shear connectors were tested by Studnicka et al. (2000) (the first one with 32 mm .diameter openings and the second one with 60 mm diameter openings). In this study, design formulas were proposed that resulted from push tests that determined the capacity of each system. In addition to studying single connector arrangements where the shear connector was located in the center of the flange, Studnicka et al. (2000) investigate a double connector arrangement as shown in Figure 2.30.

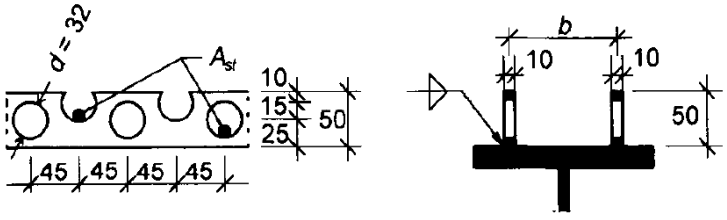

Figure 2.30: Double Perforated Shear Connector Arrangement (Studnicka et al. 2000)

While the perforated shear connector system was only intend to be used for cast-in-place deck systems and these systems were only tested to resist shear parallel to the girder (for composite action), a system similar to this could potentially be used to connect PCPs to steel girders. Using the double connector arrangement above and normal rebar cast to extend out of the PCP, the PCPs could be placed so that the reinforcement extended through the connector perforations. The area above the flange could then be grouted to the elevation of the top of the PCPs. The perforated shear connectors could be design to extend above the elevation of the PCPs to engage the cast in place deck that is placed on top of the PCPs.

2.4.4 Patented Connections

While connections between PCPs and girders are somewhat limited in traditional literature such as journal articles and dissertations, a great number of connection details between the precast panel and the girders for composite bridges were patented. Exploring these patents is useful in not only determining what was previously considered, but they are helpful to look at when trying to create new innovative designs. A few of the patented connections are presented below.

Eskew and Simpson (1991)

Eskew and Simpson (1991) invented a bridge deck panel support system (Figure 2.31) to support precast bridge deck panels on a bridge girder that was more stable than the traditional L-shaped mounting member (Figure 2.32). There are a number of detail references given in Figure 2.31 that will be referred to in the following discussion by the number (#). The support system comprised of a grade bar (28) that was attached to the grade bar support member (24) which in turn was attached to the grade bar support anchor (16). By using a non-shrink grout between the girder and the grade bar, the vertical load is transferred from the grade bar (28), to the grout (32), and finally to the bridge girder (14), which allows for better stability than the traditional system. While this system explicitly allows for elevation adjustment of the PCP, a lot of welding and grouting is required, which implies a reduced speed of construction and would not be desired in negative moment regions (due to fatigue concerns). Note that the PCPs in this invention are not positively connected to the deck panel support system. Therefore, the PCPs in this system cannot be relied on to support the top flange of the girder from a stability perspective.

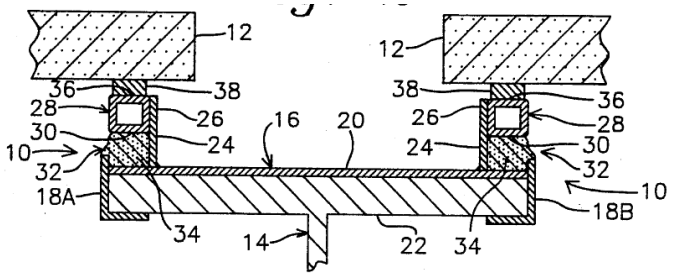

Figure 2.31: Proposed Connection (Eskew and Simpson 1991)

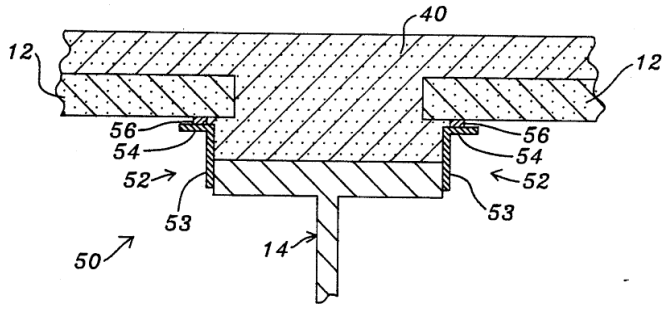

Figure 2.32: L-Shape Mounting System (Eskew and Simpson 1991)

Smith (1997)

Smith (1997) developed a bridge deck panel installation system shown in Figure 2.33-2.35 that contains access holes (14) so that workers can access the girder from the top surface of the panel (see Figure 2.33), thereby reducing the need to work from beneath the panels which is often difficult to access. Following the procedure from the previous section, the (#) refers to the details identified in the figures. Vertical adjustment of the panels is accomplished by turning the leveling bolts (18) and then placing the shimming devices (22) for added capacity (see Figure 2.34). After the panels are in place and at the correct elevation, a plurality of bolts (26) are welded to the girder through the access holes. A hold-down plate (30) is placed over the bolt and tightened against the C-beam pair (12) as shown in Figure 2.35. Finally, access holes are grouted.

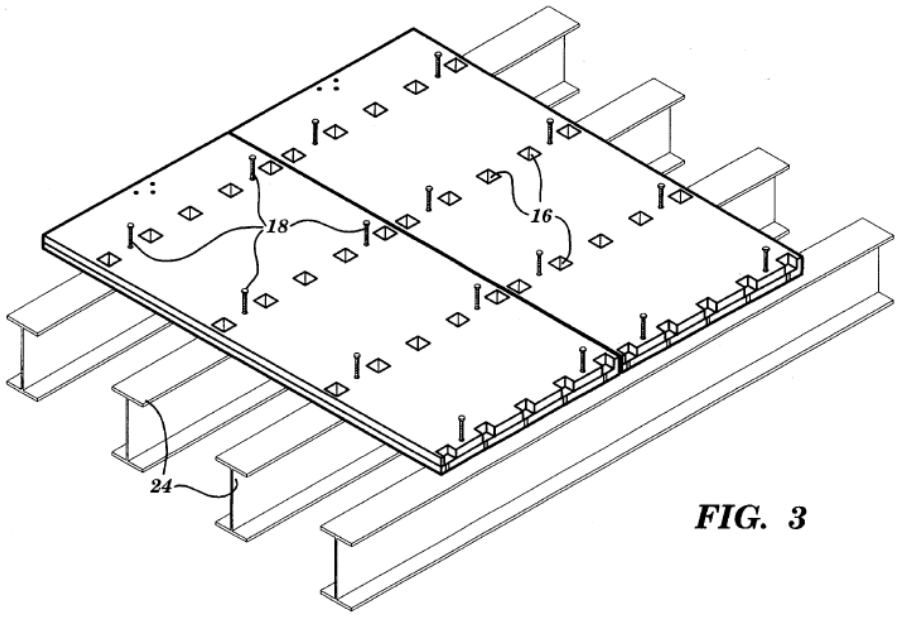

Figure 2.33: Deck Panel Attachment (Smith 1997)

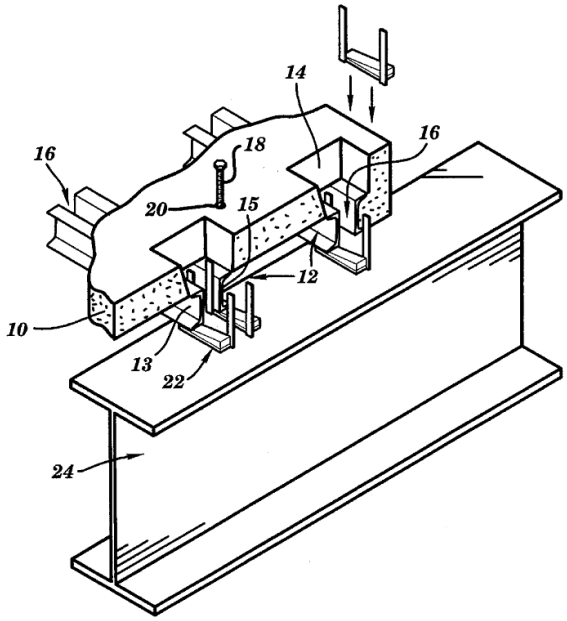

Figure 2.34: Panel Shims and Connection (Smith 1997)

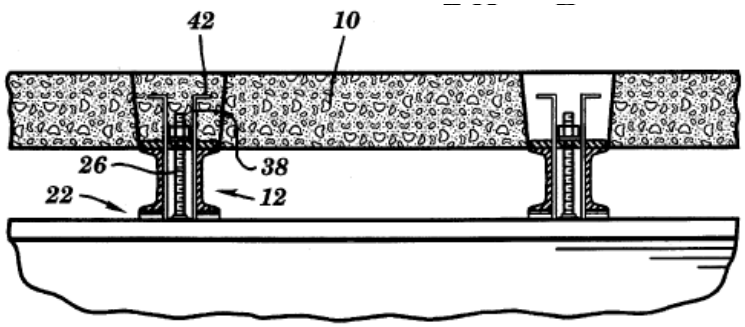

Figure 2.35: Final Installation Cross-Section (Smith 1997)

An advantage of this system over the one by Eskew and Simpson (1991) is that it does not require the use of grout before the bridge can be loaded vertically, therefore enabling for faster construction as grout hardening is not required. Adjusting the elevation of the panels, however, may be time-consuming if leveling a shimming device is required at all locations. The connection method purposed by Smith (1997) provides a positive connection between the girders and the PCPs, allowing the top flange of the girder to be braced to a certain extent by the panels. The stiffness and strength characteristics of this connection need to be tested to determine how much bracing can be realized by this system.

Bumen (2012)

Bumen (2012) developed a connection concept avoiding the use of shear pockets like those presented by Smith (1997). The connection is depicted in Figure 2.36-2.37 with detail reference numbers provided by (#) in the figures. According to Bumen (2012), shear pockets are often a weak zone in the bridge deck where load-induced vibration and freeze-thaw effects in cold climates

may deteriorate the grout and leave the shear pocket exposed. An open shear pocked will lead to corrosion of the steel attachments, lowering the durability of the bridge. The invention created by Bumen (2012) utilizes anchor plates that are cast within the panel with headed shear studs extending up into the concrete. Two runner bars that parallel the girder are clamped to the top flange which keeps the panels from sliding or uplifting. While this system both allows for composite action and effectively braces the top flange of the girder, the connection does not provide any elevation adjustment.

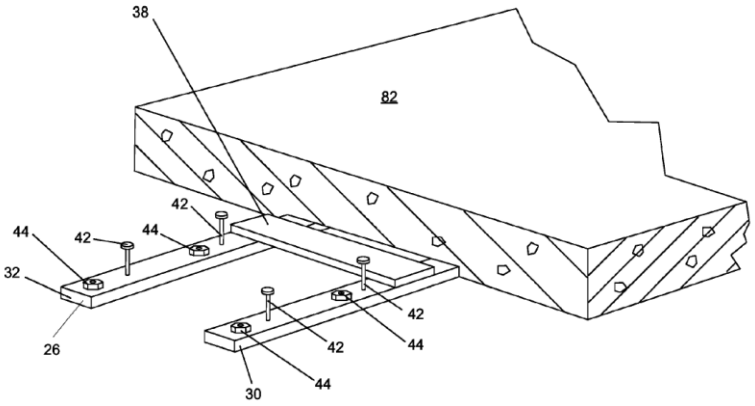

Figure 2.36: Anchor Plates Cast in Panel (Bumen 2012)

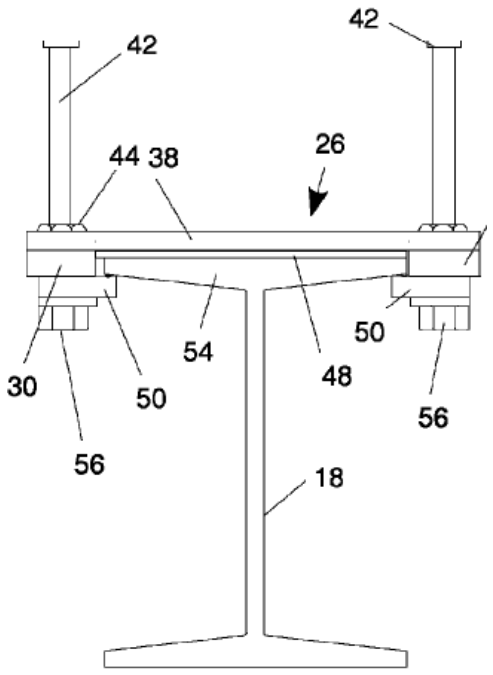

Figure 2.37: Anchor Plate Assembly on Bridge Beam (Bumen 2012)

2.5 Conclusion

Extending the use of PCPs for bracing applications, particularly for curved bridges, is an objective that is to be paralleled with substantial research initiatives in the past decades:

- After focusing on serviceability and durability issues, research on PCPs has been moving on to the study of their ultimate behavior; while in-plane shear behavior has not been studies as such, research on reinforced concrete shear walls in the building industry gives a significant insight on behavior, as well as modelling methods.
- Various finite element formulations have been proposed to capture the specific behavior or horizontally curved I-girder or tub-girder bridges, aimed at representing the torsional response; several techniques have been found and implemented to optimize the bracing distribution along curved bridges, including lean-on bracing and tapped bracing; behavior for curved and/or skewed bridges during erection has become an important matter for bridge engineers.
- Effective connections between the deck slab and the girder top flange on composite bridges have been proposed, some of which are quite innovative, such as the connection by adherence; further innovative details shall be developed to provide the PCPs with bracing capacities.

Chapter 3. Experimental Results of the Stability of PCPs on Bedding Strips

3.1 Introduction

As described in Chapter 1, an objective of this research project was to determine if PCPs could be used to brace curved girders during construction. To serve as braces, the PCPs must be connected to the top flanges of the curved girders. However, an additional objective of this research was to determine if PCPs can be used on curved girders, even if they are not used as bracing elements. In this case, the PCPs do not need to be connected to the top flanges to transfer in-plane forces. Rather, it may be possible to have the PCPs simply sit on top of the beam flanges, with bedding strips used to adjust the elevation of the PCPs, as is the conventional practice when PCPs are used with straight girders. However, greater girders displacements and rotations may occur during construction with curved girders than with straight girders. If these girder deformations are large, there is a concern that the PCPs may fall off of the girders during construction, leading to a serious safety problem. To explore the potential for unconnected PCPs to fall off of curved girders during construction, an experimental program was undertaken to better understand the level of girder deformations that may cause the PCPs to fall off of the girders. This experimental program is described in this chapter.

The experimental program investigating the stability of unconnected PCPs on bedding strips consisted of three different series of laboratory tests. First, the stability of inclined PCPs on bedding strips was tested to determine the performance of PCPs on curved girder systems during the construction phase where system twist is potentially large (i.e. near midspan of the girders). Second, the stability of PCPs on bedding strips was tested where large shear deformations may be present during the construction phase (i.e. near the simply supported end of I-girders). Third, the stability of the PCPs on bedding strips on an actual I-girder system was tested in the laboratory.

The primary purpose of these tests was to generate experimental data that could be compared with the results from finite element (FE) models for a number of realistic curved I-girder and tub girder systems with various spans lengths and radii of curvature. The ultimate goal is to provide guidelines for using unconnected PCPs on curved girder bridges.

3.2 Test Specimens

PCPs with dimensions similar to those commonly used for bridges in the field (8’-0” wide x 8’-3” long x 4” thick) were used for the stability tests of unconnected PCPs on beddings strips. Tests were performed with single PCPs and with two PCPs stacked vertically to simulate the weight of one PCP with 4” concrete placed on top.

The bedding strips that supported the PCPs were cut from 2 inch thick Owens Corning Foamular 400 sheets of extruded polystyrene (conforming to ASTM C578, Type VI - 40 psi compressive strength). A table saw was used to cut the material to produced prismatic sections with clean edges. Loctite PL Premium polyurethane construction adhesive was used to adhere the bedding strips to the steel surface as this particular adhesive is compatible with both materials. Per the manufacturer’s technical data sheet, a minimum cure time of 24 hours was given prior to performing the tests.

According to the TxDOT standards, the minimum and maximum height of a bedding strip is ½ inch and 4 inches, respectively and the height of the bedding strip shall never exceed twice

its width. Figure 3.1 shows the TxDOT detail with a table of standard bedding strip dimensions. Bedding strips with six different cross-sections (1”x1”, 1”x2”, 1.5”x1.5”, 1.5”x3”, 2”x2”, and 2”x4”) were chosen for the inclined tests and the shear test to gain a somewhat comprehensive understanding of the stability of PCPs on bedding strips of various dimensions.

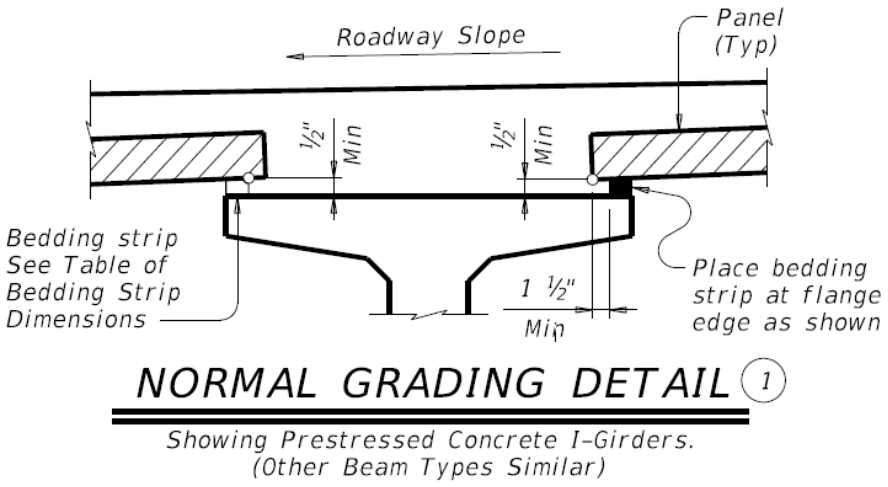

TABLE OF BEDDING STRIP DIMENSIONS

WIDTH	HEIGHT (2)	
	Min	Max
1" (Min)	½"	2"
1 ¼"	½"	2 ½"
1 ½"	½"	3"
1 ¾"	½"	3 ½"
2" (Min)	½"	4"

Figure 3.1: TxDOT Standard for Bedding Strip Dimensions (TxDOT 2014a)

3.3 Inclined Tests of Unconnected PCPs on Bedding Strips

The twist of a curved girder system during the construction phase depends on many factors such as span length, support condition (simply supported or continuous), radius of curvature, concrete deck pouring sequence (continuous or segmented), etc. Stability of the PCPs on the bedding strips throughout the entire construction phase is paramount from a safety perspective.

For a curved I-girder system, the placement of the PCPs may need to accommodate girder drop (shown in Figure 3.2) which depends on the deflected geometry of adjacent girders and the fit condition (no load fit, steel dead load fit, or total load fit) of the cross-frames. Also, the PCPs must be stable on the bedding strips as the system twists throughout the various stages of construction load (during placement of the PCPs, during the concrete deck pour, etc.). Figure 3.3 shows the potential twist of the system as the deck is being poured in one span of a continuous I-girder system. As the I-girder system deforms under construction loads, some separation between the flanges of adjacent girders may occur (see in Figure 3.4) which may impact the stability of the PCPs on the bedding strips. In general, twist and relative movement of steel tub girders is much smaller than steel I-girders during construction do to the large torsional stiffness of the quasi closed tub girder.

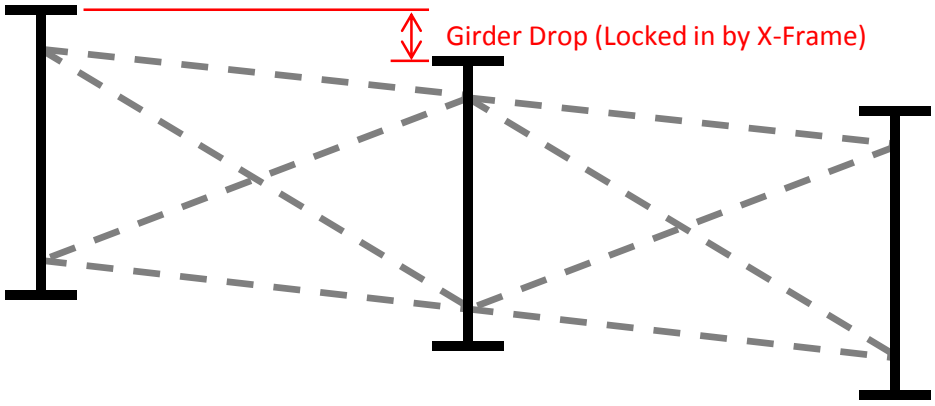

Figure 3.2: Drop between Girders at an Intermediate Cross-Frame

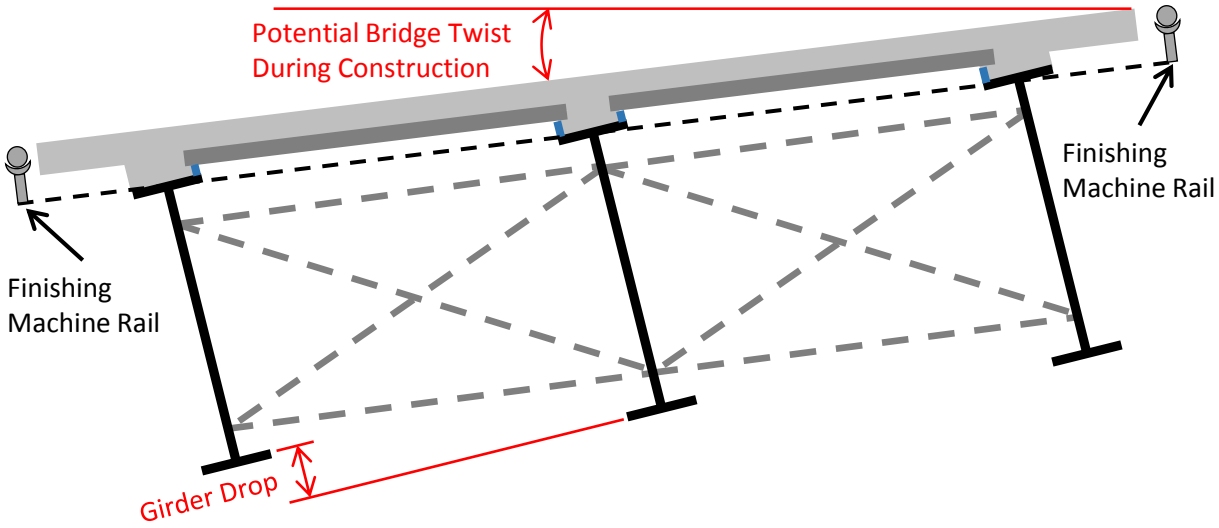

Figure 3.3: Twist of I-Girder System during Construction

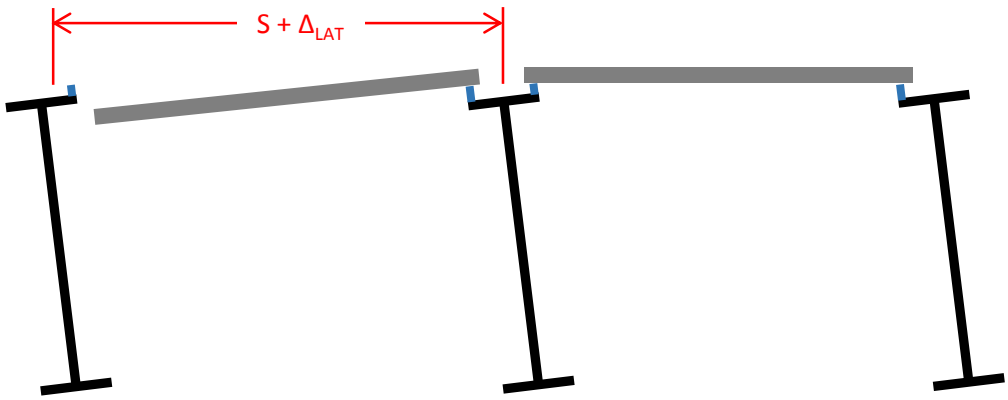

Figure 3.4: Separation of I-Girders during Construction away from Intermediate Cross-Frame

The goal of this testing program was to gather experimental data on the stability of PCPs on bedding strips using a test setup to simulate the aforementioned girder deformations

experienced in curved girder systems. The test setup designed for this experiment is discussed in detail below.

3.3.1 Inclined PCP Test Frame

Figure 3.5 shows an isometric view the of test frame that was constructed to perform inclined PCP bedding strip tests. The frame consisted of several structural shapes connected with slip critical bolts to simulate two adjacent top flanges in either an I-girder or a tub girder system. Without the spacers installed (no girder drop), the plates supporting the bedding strips were both parallel and collinear throughout the tests (simulating PCPs placed on the two flanges of a tub girder). With the four 1 inch spacers installed (girder drop angle of 2.5 degrees), the plates supporting the bedding strips remained parallel throughout the test, but were offset by 4 inches (simulating girder drop which is common in curved I-girder bridges). Photographs of the test frame are shown in Figure 3.6.

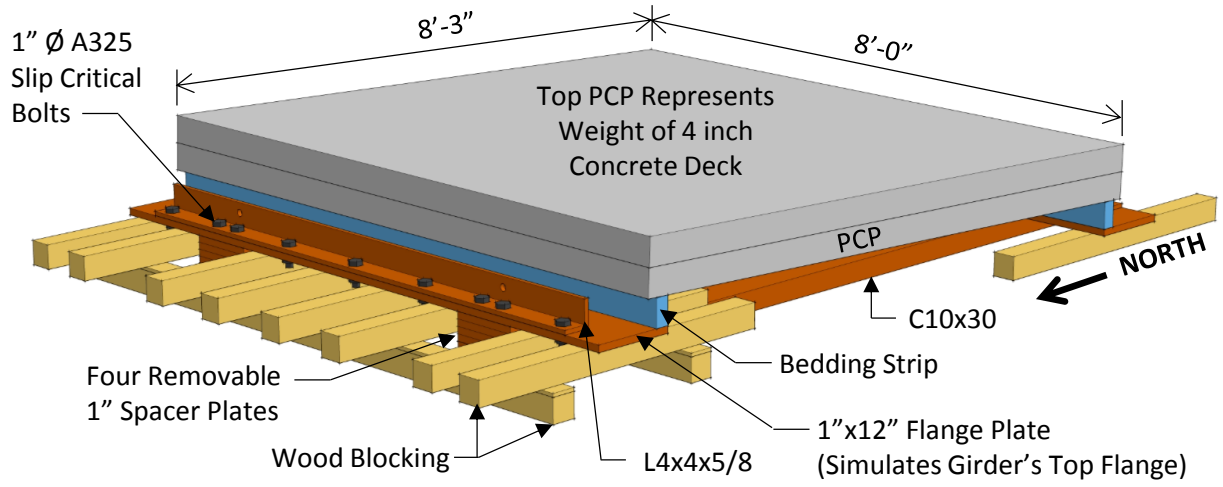

Figure 3.5: Inclined PCP Test Frame – Isometric View

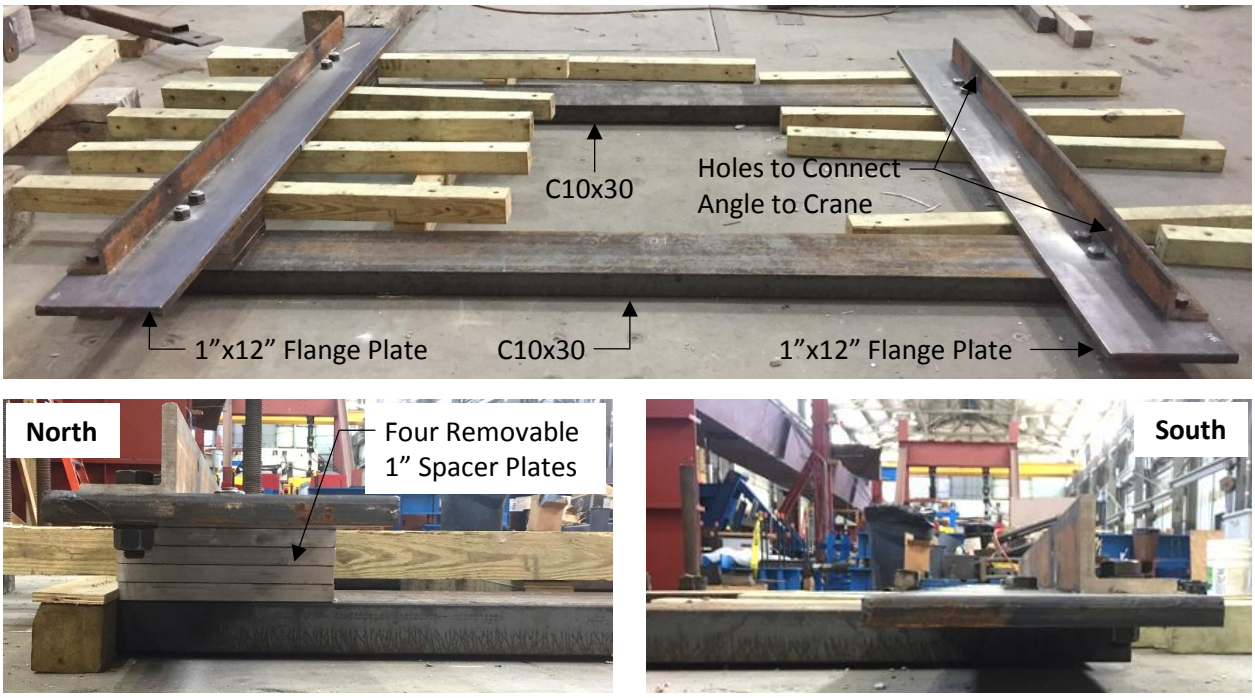

Figure 3.6: Inclined PCP Test Frame – Laboratory Photographs

During the construction phase of a curved girder bridge, relative horizontal separation between the top flanges of adjacent girders (Δ_{LAT} – see Figure 3.4) may occur (especially a at the midpoint between cross-frames in I-girder systems). To account for this separation in the experiments, the south flange plate was unbolted from the two C10x30s and slid a predetermined distance (Δ_{LAT}) to the north. After placing the bedding strips and PCPs, two bolts were turned to slide the flange plate back into position and the assembly was bolted back together (see Figure 3.7). As a result, the bedding strips deformed to account for the relative horizontal separation (Δ_{LAT}) of the flange plates prior to running the inclined PCP test.

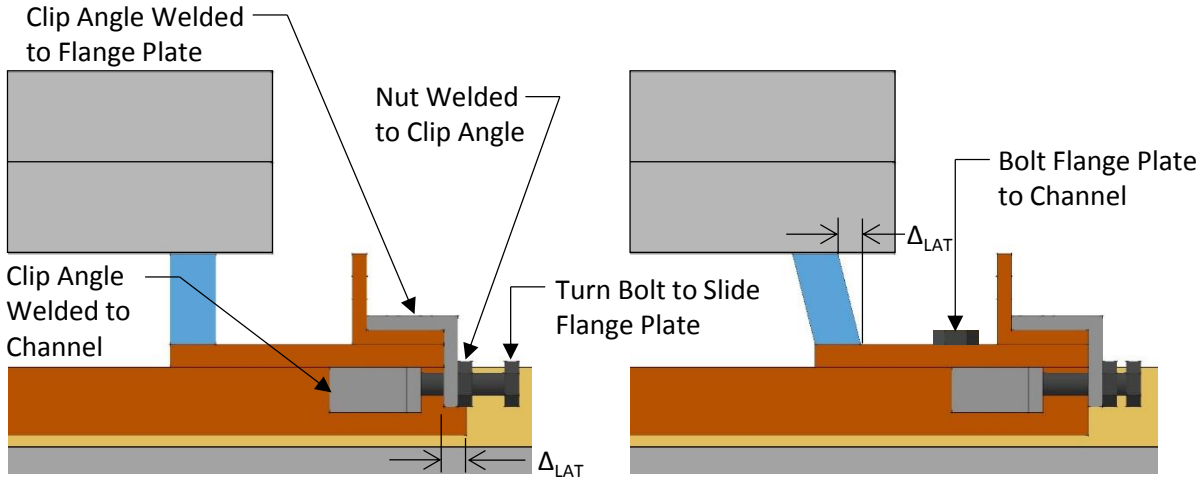

Figure 3.7: Inclined PCP Test Frame – Detail for Flange Plate Separation

3.3.2 Inclined PCP Testing Procedure

The experimental testing procedure varied slightly depending on whether or not the horizontal separation between the top flanges of adjacent girders (Δ_{LAT}) was included. To limit the time required to prepare each test, the majority of the tests were performed without adhering the bedding strips to the flange plates to avoid the 24 hour cure time (a few tests were performed with the bedding strips glued for comparison). The most comprehensive testing procedure is explained in detail below and a schematic of the setup during the test is shown in Figure 3.8.

1. Insert or remove spacer plates to achieve desired girder drop
2. Disconnect the south flange plate and slide north by desired amount (Δ_{LAT}) - use C-clamps to hold flange plates and channels together (if applicable)
3. Place bedding strips on the edge of flange plates (adhering them if applicable)
4. Place first PCP on bedding strips with overhead crane
5. Allow 24 hours minimum for adhesive to cure (if applicable)
6. Place second PCP on top of first PCP with overhead crane
7. Remove C-clamps and turn bolts to slide flange plates apart by a distance of Δ_{LAT} and bolt south flange plate to channels (if applicable)
8. Connect south angle to crane
9. Take initial picture and start recording with video cameras
10. Lift south flange slowly with crane until PCP falls from bedding strip
11. Measure height of south flange plate
12. Take final pictures and stop recording with video cameras.

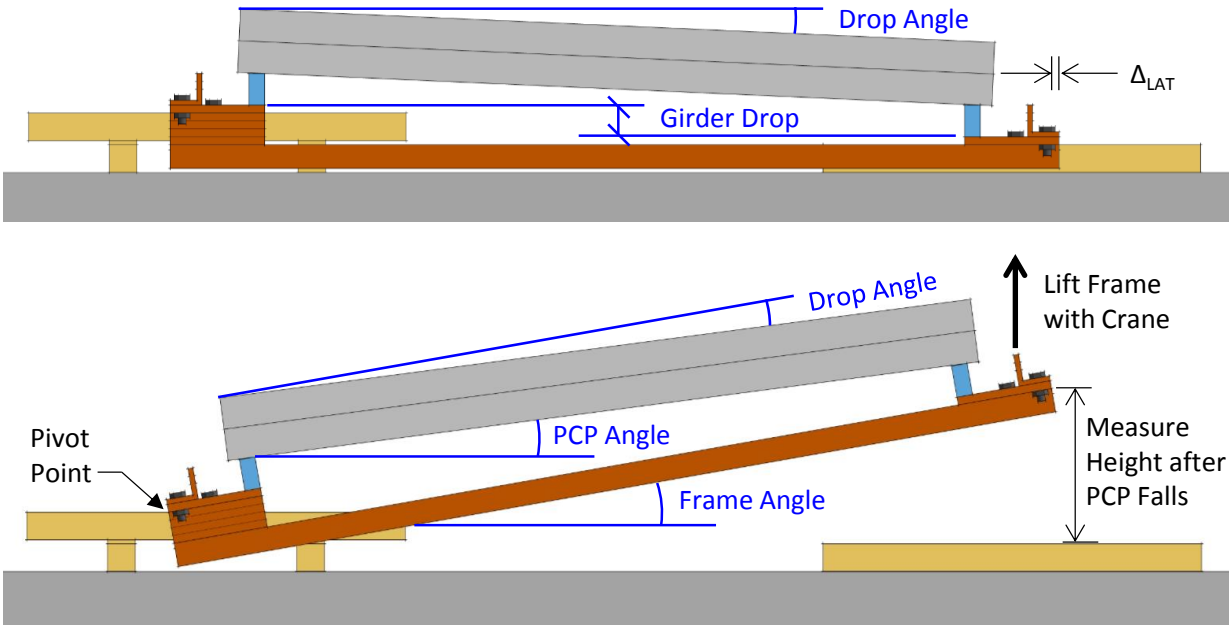

Figure 3.8: Inclined PCP Experimental Tests – Elevation

3.3.3 Inclined PCP Experimental Results

A total of 37 inclined PCP bedding strip tests were performed with the inclined PCP test frame. As mentioned previously, bedding strips with six different cross-sections (1”x1”, 1”x2”, 1.5”x1.5”, 1.5”x3”, 2”x2”, and 2”x4”) were tested and the bedding strips were not adhered to the flange plates for the majority of the tests. The results from the test are given in Table 3.1. In general, reducing the size of the bedding strip reduced the maximum angle that could be achieved by the PCP. Also, adding a second PCP to simulate the weight of the cast-in-place (CIP) concrete deck reduced the maximum angle of the PCP (when bedding strips were not bonded to the flange plates). Furthermore, reducing the aspect ratio (defined as the ratio of the width to the height of the bedding strip) from 1:1 to 1:2 significantly reduced the maximum angle of the PCPs. Bonding the bedding strips to the flange plates increased the maximum PCP angle indicating that the tests with unbonded bedding strips likely produced conservative results.

Table 3.1: Maximum PCP Angle from Inclined PCP Tests (Degrees)

Bedding	Drop Angle = 0°			Drop Angle = 2.5°		
Strip Size	1-PCP	2-PCP	2-PCP*	1-PCP	2-PCP	2-PCP*
1"x1"	26.1	21.4	28.3†	23.5	14.3	28.8†
1.5"x1.5"	26.8	24.0	29.0†	24.2	22.5	29.1†
2"x2"	26.8	25.6	30.6†	24.6	24.6	31.9†
1"x2"	13.3	0.0	0.0	12.0	2.8	0.0
1.5"x3"	16.8	10.6	12.5	15.5	10.6	11.0
2"x4"	18.6	14.3, 19.1†	13.8	16.3	13.7	14.5

*Flange plate horizontal separation (Δ_{LAT} = 0.75")

†Bedding strips bonded to beams with compatible adhesive

Bedding Strips with a 1:1 Aspect Ratio (1”x1”, 1.5”x1.5”, and 2”x2”)

All of the PCPs sitting on bedding strips with a 1:1 aspect ratio were able to undergo large inclinations (relative to the system twist often seen during a bridge’s construction phase) prior to falling off of the flange plates. A minimum inclination of 14.3 degrees was achieved with 1”x1” bedding strips (unbonded) while a maximum inclination of 31.9 degrees was reached with 2”x2” bedding strips bonded to the flange plates (with Δ_{LAT} = 0.75”).

With unbonded bedding strips, failure commenced with the bedding strips sliding relative to the flange plate as observed by slow-motion video footage (see Figure 3.9). Gluing the bedding strip to the top flange would likely have increased the maximum PCP angle for these tests prior to failure. The test with the flange plate separation (Δ_{LAT} = 0.75”) likely outperformed the tests without separation due to the bonding of the bedding strips to the flange plates. The bedding strips for the tests with Δ_{LAT} = 0.75” were glued to the flange plates to keep the bedding strip from sliding relative to the flange plate during the separation of the flange plates (causing the bedding strips to deform and slide with respect to the PCP – Figure 3.10). During the inclined PCP tests, the bedding strip did not slide off of the flange plates, but rather the bedding strip broke at the bonded surface and overturned (see Figure 3.10).

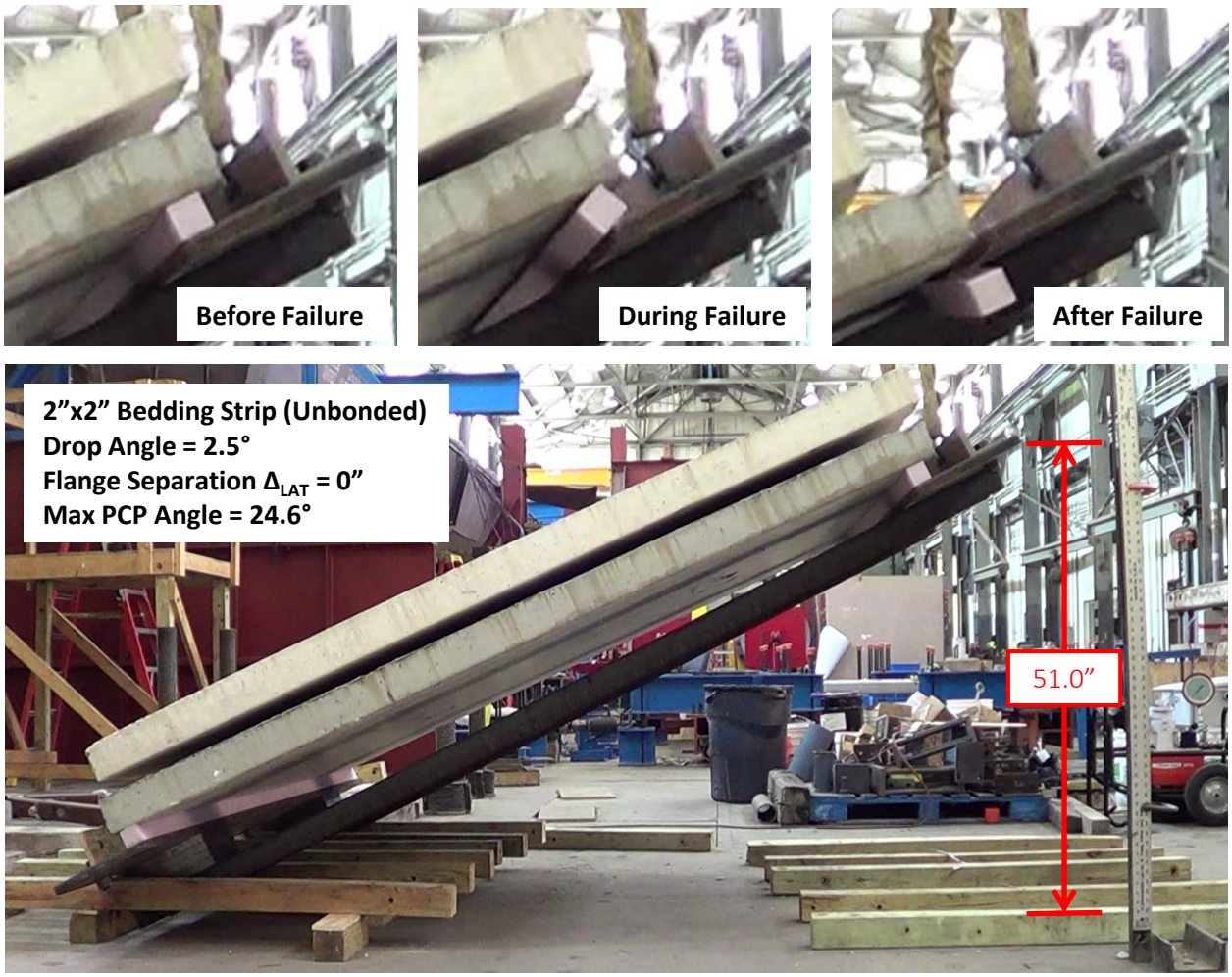

Figure 3.9: Inclined PCP Experimental Tests with 2”x2” Bedding Strips (Unbonded)

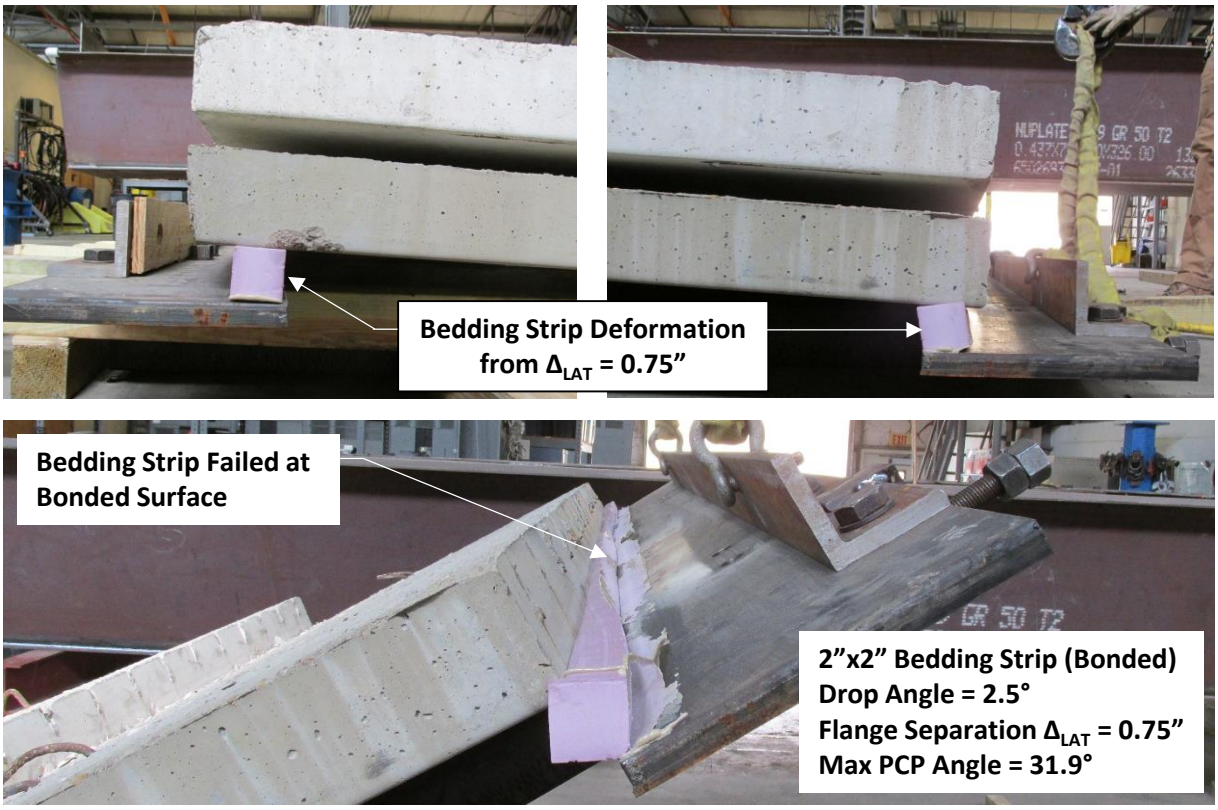

Figure 3.10: Inclined PCP Experimental Tests with 2”x2” Bedding Strips (Bonded)

Bedding Strips with a 1:2 Aspect Ratio (1”x2”, 1.5”x3”, and 2”x4”)

Reducing the aspect ratio of the bedding strips from 1:1 to 1:2 significantly reduced the maximum angle that could be reached with the PCPs. While a maximum PCP angle of 19.1 degrees was achieved with a 2”x4” bedding strips (bonded), one of the tests with 1”x2” bedding strips failed after the second PCP (representing the CIP concrete deck) was placed prior to the test being performed. The pressure from the two PCPs (8’x8’-3”x4”) on the 1 inch wide bedding strips was approximately 34.4 psi which is near the 40 psi bearing capacity of the extruded polystyrene material. With its unfavorable aspect ratio and small width, the 1”x2” bedding strip had a tendency to buckle under the load from the two PCPs. The 1”x2” bedding strips were not able to accommodate the flange separation (Δ_{LAT} = 0.75”) with the bedding strips failing during the flange movement for both tests with and without girder drop.

Figure 3.11 shows the deformation of the 2”x4” unbonded bedding strip after the flange separation (Δ_{LAT} = 0.75”) prior to the test. Including the flange separation (Δ_{LAT} = 0.75”) for the unbonded bedding strips with a 1:2 aspect ratio had varying results. Interestingly, for some of the cases, slightly larger PCP angles were actually achieved with the separation. No conclusive evidence was seen to indicate that a flange separation of Δ_{LAT} = 0.75” significantly reduced the stability of the PCPs on the bedding strips.

Figure 3.11: Flange Separation with 2”x4” Unbonded Bedding Strips

All of the tests with a 1:2 aspect ratio (with the exception of one) were completed without bonding the PCPs to the flange plate. Addition of glue, increased the maximum PCP angle from 14.3 degrees to 19.1 degrees for the 2”x4” bedding strips (see Figure 3.12) and slow motion video footage reveled that failure occurred by overturning of the bedding strip for both cases (rather than the bedding strip sliding relative to the flange plate or the PCP).

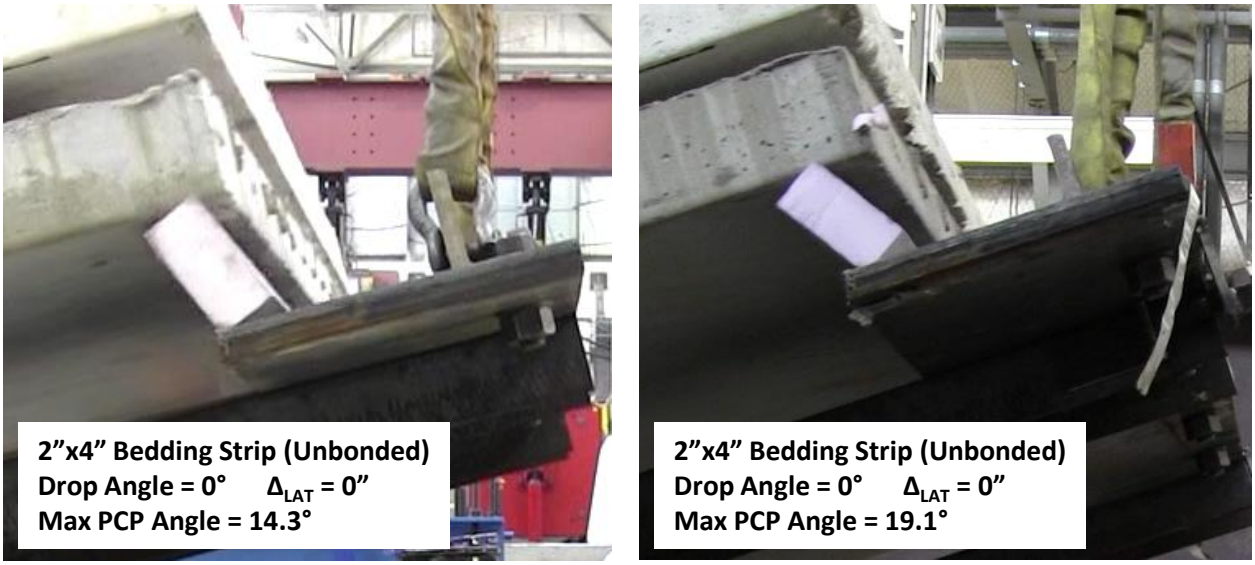

Figure 3.12: Inclined PCP Experimental Tests with 2”x4” Bedding Strips

3.4 Shear Tests of Unconnected PCPs

While system twist is largest near midspan during the construction of a curved girder system, deformations near the support also need to be considered for the stability of PCPs on bedding strips. For curved I-girder systems, warping deformations are largest near the end of the girder at the support where there is a warping permitted boundary condition (see Figure 3.13). As

the girders twist at the warping permitted boundary, the top and bottom flanges do not bend but simply rotate at the end. The top flanges of adjacent girders remain parallel to each other as they rotate about the support by an angle (ϒ) as shown in Figure 3.14. In general, the value of ϒ is relatively small for tub girders as the top lateral truss creates a warping restrained boundary condition for the top flanges.

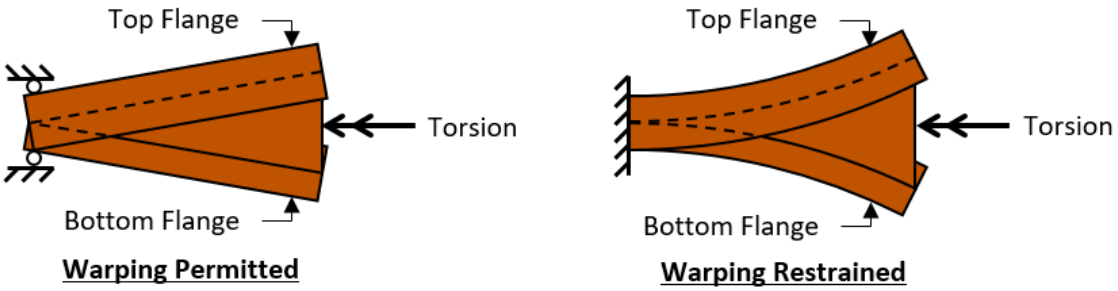

Figure 3.13: Torsion Boundary Conditions of I-Girders

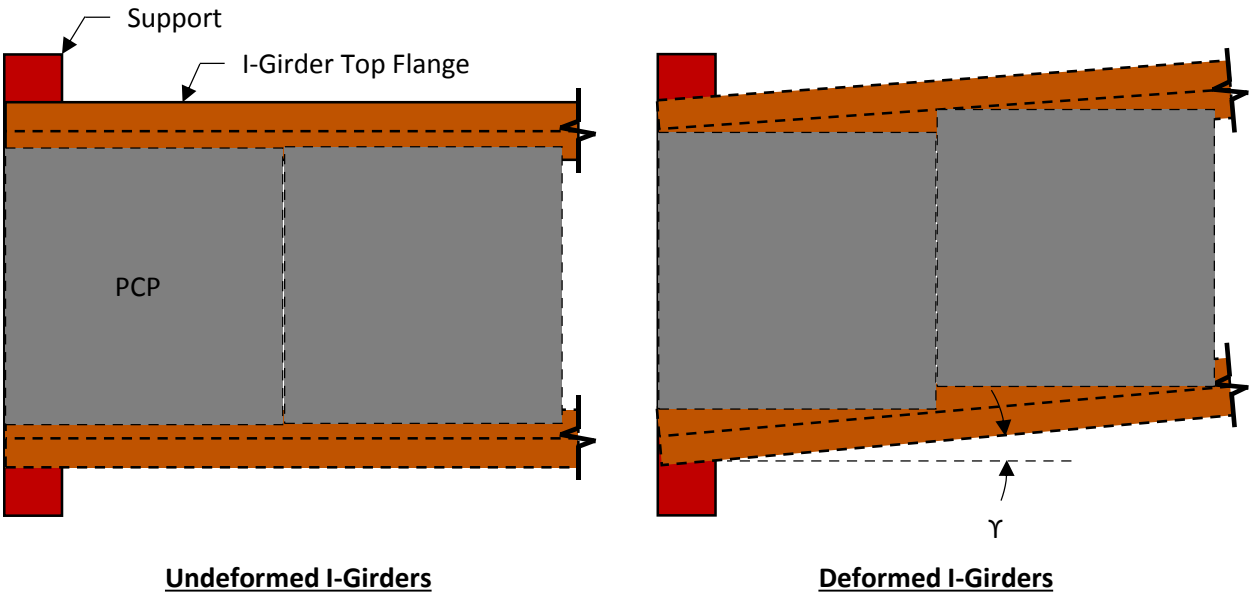

Figure 3.14: I-Girder Deformation near the Supports – Plan View

The goal of this testing program was to gather experimental data on the stability of PCPs on bedding strips using a test setup to simulate the aforementioned girder deformations experienced in curved girder systems. The test setup designed for this experiment is discussed in detail below.

3.4.1 PCP Shear Test Frame

Figure 3.15 shows a plan view of the test frame that was used to perform the unconnected PCP bedding strip shear tests. This same frame was used by Kintz (2017) and McCammon (2015)

to test the shear stiffness and strength of PCPs connected to the frame. The fabrication and function of the shear test frame is discussed in detail by the theses published by the aforementioned authors.

The four pin/needle bearing assemblies allow the shear test frame to behave as a mechanism with minimal resistance to load (only that of friction) when the PCP is unattached to the system. As the hydraulic actuator pushes against the frame, the loading beams remain parallel to each other as the frame sways to the side. The shear strain (ϒ) deformation of the frame simulates the deformation of the top flanges of I-girders near the supports in a curved girder system during the construction phase.

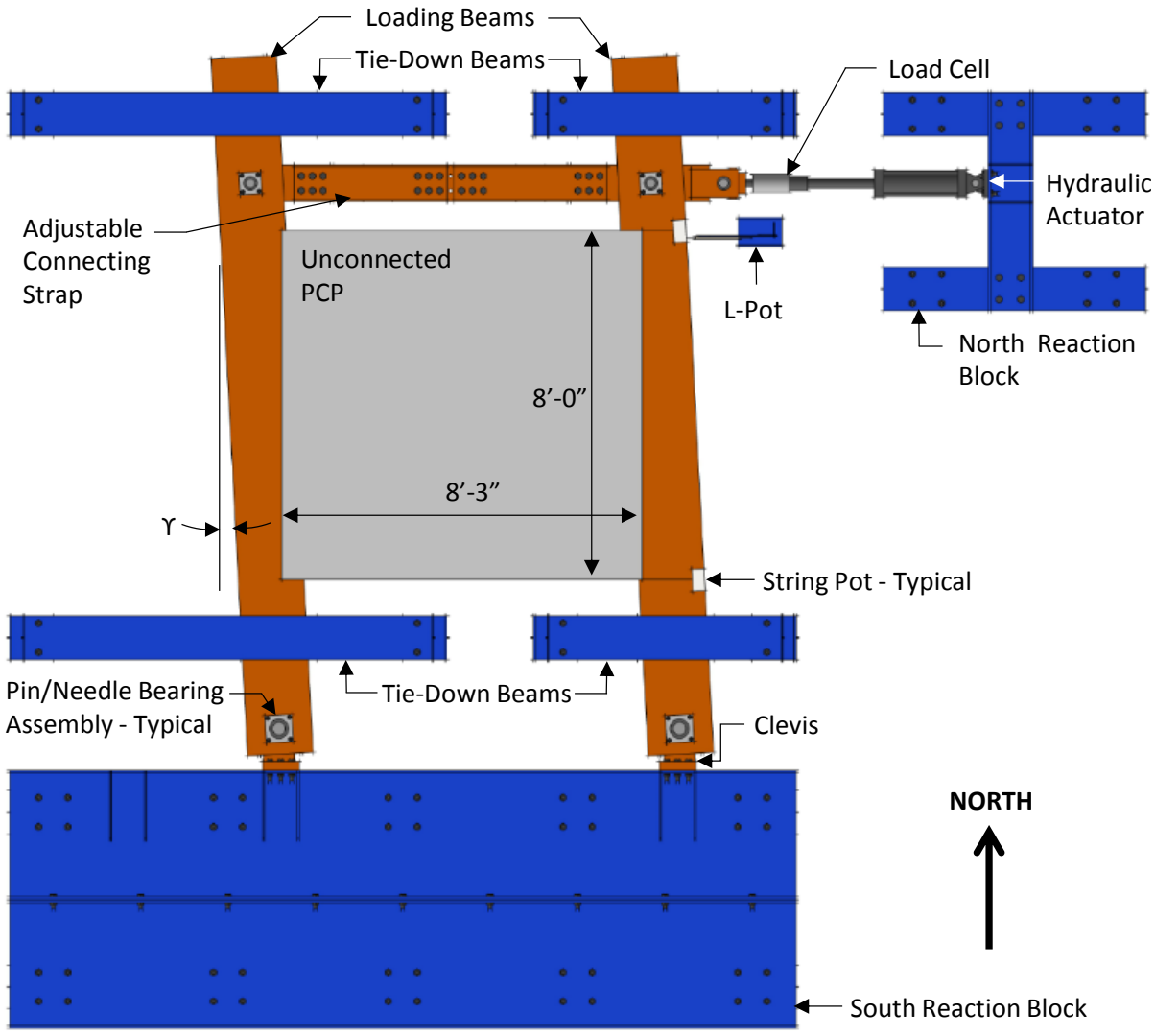

Figure 3.15: PCP Shear Test Frame – Plan View

Linear potentiometers (L-pots) were used to measure the lateral movement of the frame with respect to the strong floor from which the shear strain (ϒ) of the frame could be calculated (see Figure 3.16). String potentiometers (string-pots) were used to measure the movement of the northeast (Δ_{NE}) and southeast (Δ_{SE}) corners of the PCP with respect to the loading beam (positive means the overlap of the PCP on the frame is increasing while negative means the PCP overlap on the frame is decreasing). As the shear strain increased, the overlap of the PCPs on the loading

beams increased at the northeast and southwest corners and decreased at the northwest and the southeast corners (see Figure 3.15).

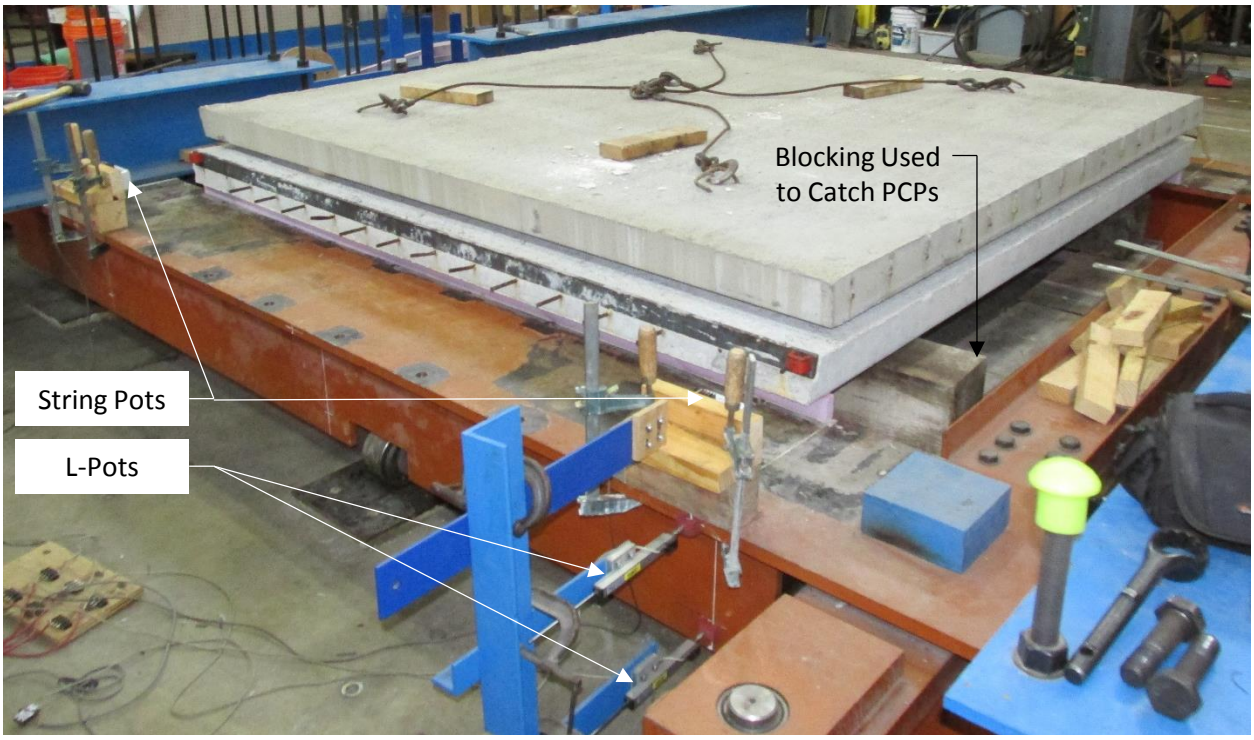

Figure 3.16: PCP Shear Test Frame – Laboratory Photograph

3.4.2 Testing Procedure of Unconnected PCPs in Shear

The testing procedure for the unconnected PCP shear tests is as follows:

1. Adjust test frame so that loading beams are perpendicular to south reaction block
2. Adhere bedding strips to the edge of loading beam flange plates
3. Place first PCP on bedding strips with overhead crane
4. Allow 24 hours minimum for adhesive to cure
5. Place second PCP on top of first PCP with overhead crane (if applicable)
6. Attach string pots to PCP and L-pots to loading beam
7. Take initial pictures and start recording with video cameras
8. Tare instrumentation and begin recording data
9. Apply load to frame with hydraulic actuator to overcome friction and cause frame to sway laterally
10. Stop loading when PCP falls off of the frame or when the sway limits of test frame are reached (Υ_{max} = 4.0 degrees)
11. Stop recording data and video cameras and take final pictures
12. Remove PCP(s) with overhead crane

3.4.3 Unconnected PCP Shear Experimental Results

A total of 9 unconnected PCP bedding strip shear tests were performed in the laboratory with the bedding strips bonded to the flange plates of the loading beams for all tests. Six different cross-sections (1"x1", 1"x2", 1.5"x1.5", 1.5"x3", 2"x2", and 2"x4") were tested for the bedding strips. Table 3.2 shows the results of the 9 tests where Υ_{max} is the maximum shear strain of the test frame and Δ_{NE_MAX} and Δ_{SE_MAX} are the maximum movement of the northeast and southeast corners of the shear PCP with respect to the east loading beam.

Table 3.2: Experimental Results from Unconnected PCPs Shear Tests on Bedding Strips

Bedding	2-PCPs			1-PCP		
Strip Size	Υ_{max} (deg)	Δ_{NE_MAX} (in)	Δ_{SE_MAX} (in)	Υ_{max} (deg)	Δ_{NE_MAX} (in)	Δ_{SE_MAX} (in)
1"x1"	4.0*	-3.4	3.5	-	-	-
1.5"x1.5"	4.0*	-3.8	3.6	-	-	-
2"x2"	4.0*	-3.8	3.2	-	-	-
1"x2"	0.8	-1.1	0.3	1.5	-1.3	1.7
1.5"x3"	1.6	-1.9	1.0	1.7	-1.1	2.2
2"x4"	3.2	-3.7	2.2	3.6	-4.2	2.8

*Test Frame Limit

Bedding Strips with a 1:1 Aspect Ratio (1"x1", 1.5"x1.5", and 2"x2")

For bedding strips with a 1:1 aspect ratio, the limit of the test frame was reached (Υ_{max} = 4.0 degrees) without the PCP falling from the shear frame with 2 PCPs stacked vertically (for this reason, the 1 PCP case was not investigated). As shear strain of the frame increased, the overlap of the PCP on the frame increased at the northeast and southwest corners and decreased at the northwest and southeast corners (see Figure 3.17) causing the bedding strip to twist in opposite directions at each end. Figure 3.18 shows the east edge of the PCP on the loading beam at Υ_{max} = 4.0 degrees for the 1"x1", 1.5"x1.5", and 2"x2" bedding strips. The larger bedding strips were less likely to twist during the test and provided better support to the PCP at larger shear strains.

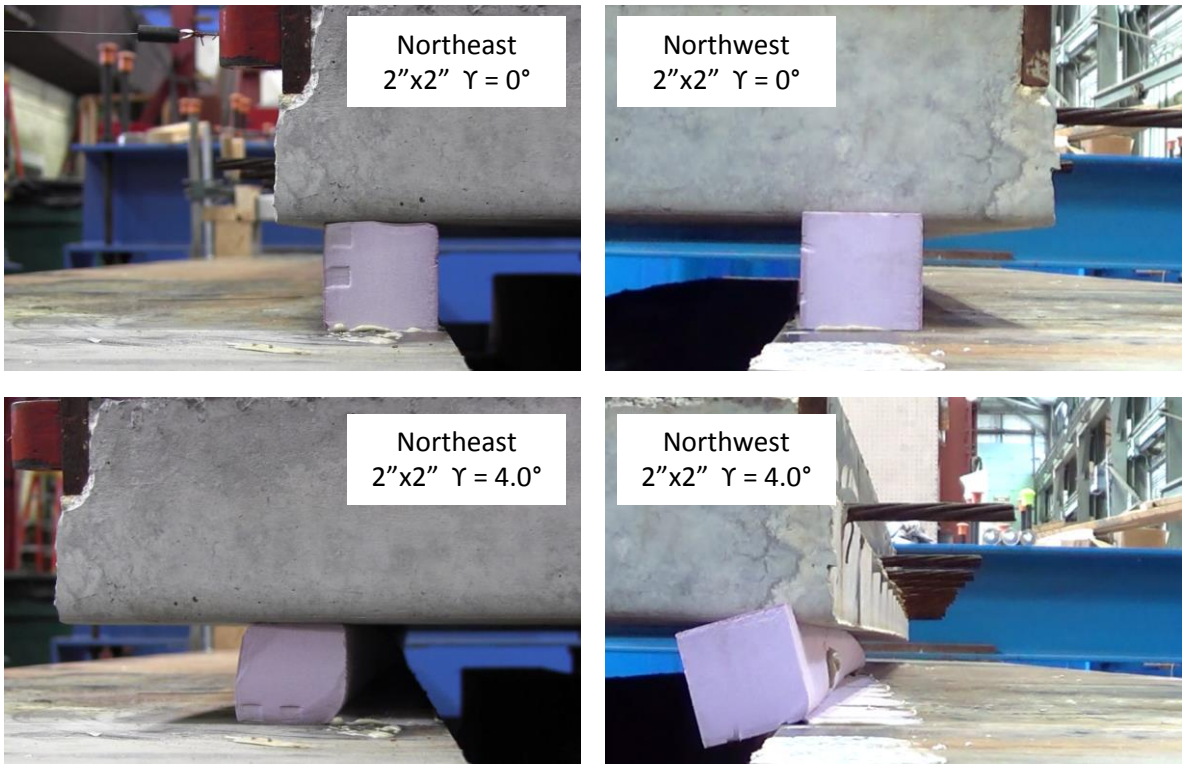

Figure 3.17: 2”x2” Bedding Strip Deformation during Shear Frame Test

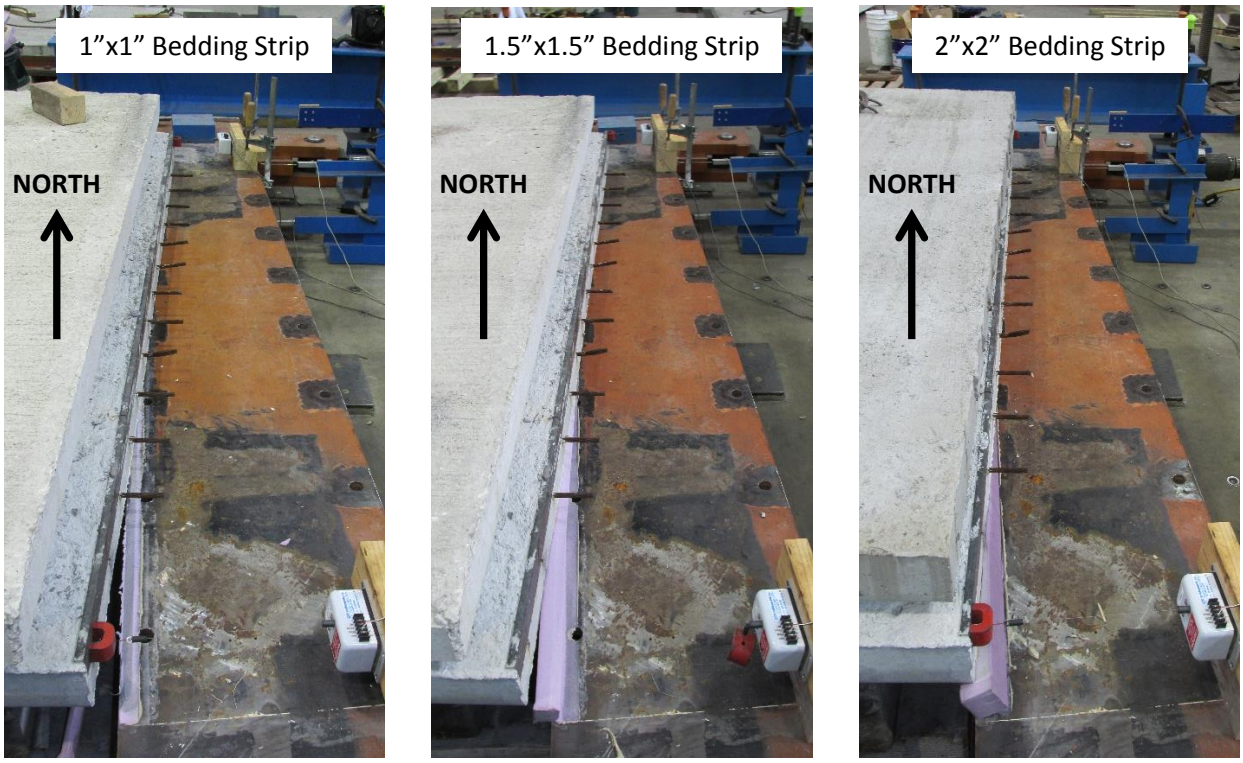

Figure 3.18: PCP Shear Test Frame – Laboratory Photograph

Bedding Strips with a 1:2 Aspect Ratio (1”x2”, 1.5”x3”, and 2”x4”)

Reducing the aspect ratio of the bedding strips from 1:1 to 1:2 significantly reduced the maximum shear strain that could be reached before the PCPs fell from the test frame. Furthermore, reducing the width of the bedding strip significantly reduced the shear strain that could be achieved with the shear frame for bedding strips with a 1:2 aspect ratio. Also, adding a second PCP to simulate the weight of the CIP concrete deck reduced the maximum angle of the shear frame. Figure 3.19 shows the deformation of the bedding strips (1”x2”, 1.5”x3”, and 2”x4”) at the northeast corner of the PCP during several phases of the shear frame test. As the shear strain increased, the bedding strip was twisted to a point where it broke and the PCP fell off of the frame (blocks were placed under the PCP to keep it from crashing to the lab floor).

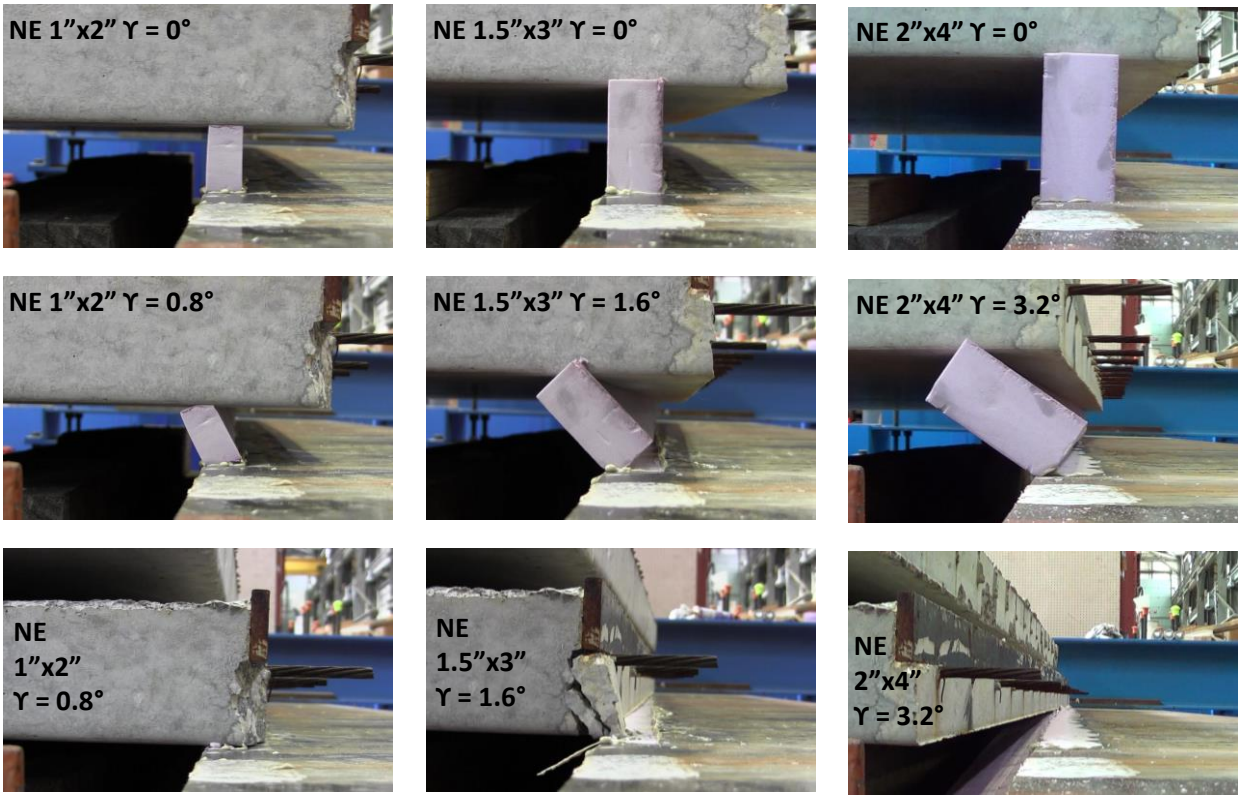

Figure 3.19: Bedding Strip Deformation during Shear Frame Test (1:2 Aspect Ratio)

3.5 Test of Unconnected PCPs on Twin I-Girder System

To further investigate the stability of PCPs on bedding strips on curved girder bridges, PCPs were placed on the ends of a twin I-girder system (near the supports) and load was applied to the system to cause the girders to deform. A semi-warping permitted boundary condition was established at the end of the girders to try and simulated the deformations that are be experienced in a curved I-girder system (see Figure 3.14).

3.5.1 PCP Tests on Twin I-Girder System

Figure 3.20 shows an isometric view of the twin I-girder test frame that was used to perform an unconnected PCP bedding strip test. The components of the setup are explained in detail in

Chapter 5. One PCP was placed at each end of the system on bedding strips and the top flanges of the I-girders were loaded laterally (to the west) with hydraulic actuators located approximately at quarter points of the simply supported span.. The loading condition caused large shearing deformations (ϒ) similar to those from the shear tests frame. The goal of this test was to gain an understanding of the potential of using PCPs near the supports of curved I-girder systems where shearing deformations are large.

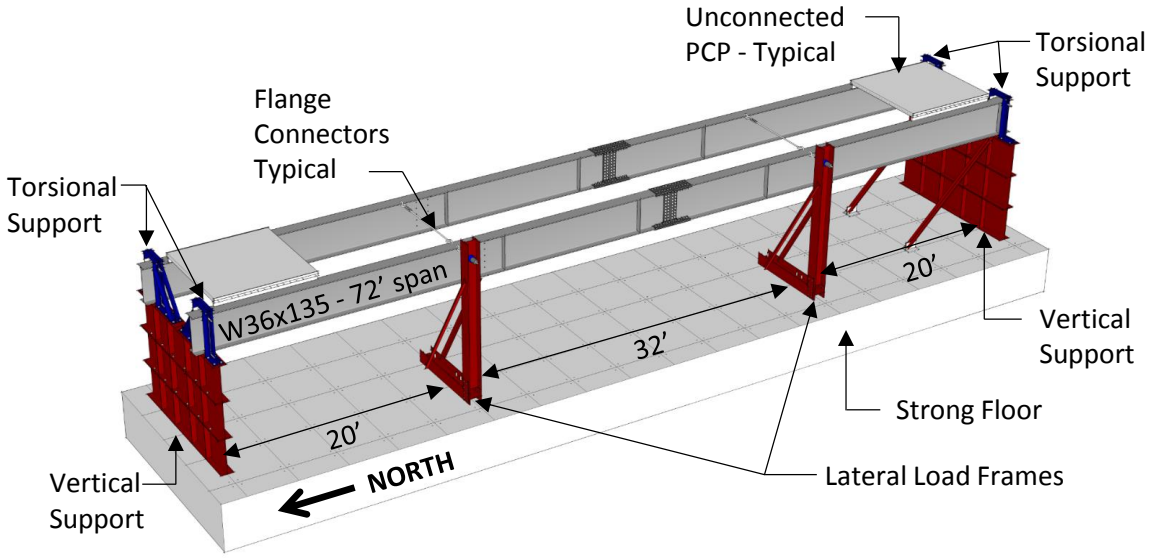

Figure 3.20: Unconnected PCPs on Twin I-Girder System

Figure 3.21 shows the instrumentation plan for the bedding strip tests on the twin I-girder system. Position sensors were placed on the I-girders and two NDI Optotrack Certus HD vision systems were used to measure the deformation of the girders at midspan and the approximate third point (see Chapter 5 for more details on the operation of the vision systems). The load from each hydraulic actuator was monitored with calibrated load cells. String-pots were used to measure the movement of the northeast (Δ_{NE_PCP}) and southeast (Δ_{SE_PCP}) corners of the south PCP with respect to the top flange of the I-girder (positive indicates the overlap of the PCP on the girder is increasing while negative indicates the PCP overlap on the girder is decreasing). A video camera was mounted to the top flange to capture footage of the bedding strip deformation during the test.

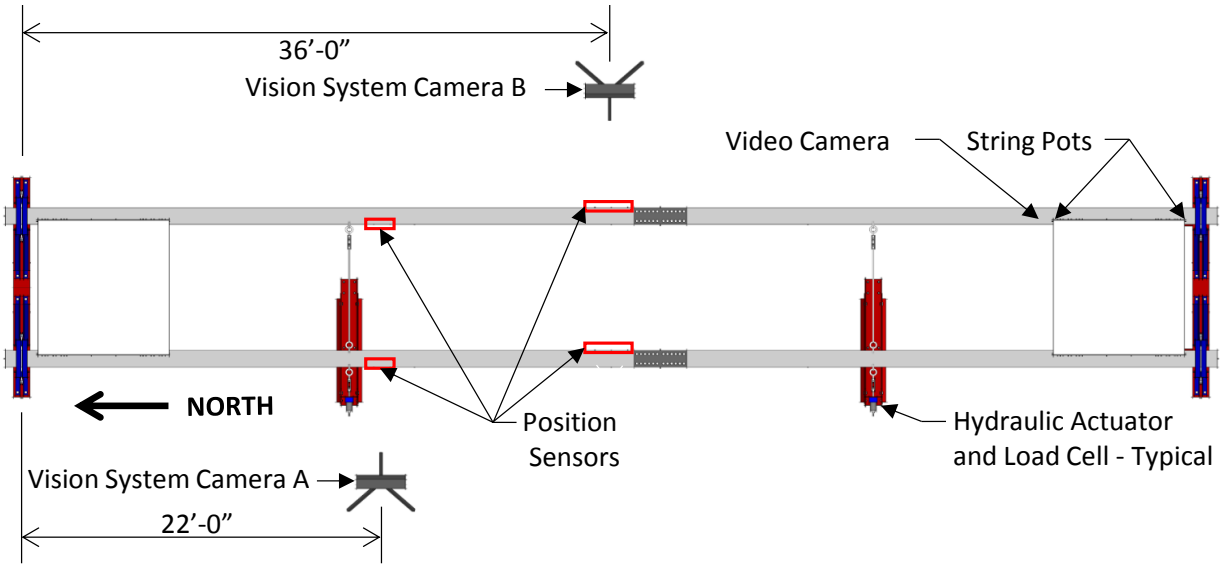

Figure 3.21: Instrumentation Plan Twin I-Girder Tests – Plan View

3.5.2 Unconnected PCP I-Girder Experimental Results

Only one tests was performed in the laboratory using a 2"x4" bedding strip (the bedding strip was not bonded to the I-girder or the PCP). The lateral deflection and twist of the I-girders (at midspan and third points) along with the movement of the PCP at several load steps is given in Table 3.3. At a maximum lateral load of 6.9 kips, the girders experienced large deformations (6.5 inches of deflection and 3.7 degrees of twist at midspan) while the north and south corners of the PCP only moved -1.2 and 1.3 inches, respectively. Figure 3.22 shows the maximum deformation of the bedding strip on the top flange of the I-girders. Upon unloading, the bedding strip rebounded and the PCP moved back to its original position.

Table 3.3: Experimental Results from Unconnected PCPs on Twin I-Girder System

Total	Average Deformation of I-Girders				PCP Movement		
Lateral Load	$\Delta_{TF.M}$	$\Delta_{TF.TP}$	θ_M	θ_{TP}	Δ_{NE_PCP}	Δ_{SE_PCP}	Υ_{PCP}
(kip)	(in)	(in)	(deg)	(deg)	(in)	(in)	(deg)
0.0	0.0	0.0	0.0	0.0	0.0	0.0	0.0
1.0	0.7	0.6	0.4	0.4	-0.1	0.1	0.1
2.0	1.6	1.3	0.9	0.8	-0.3	0.3	0.4
3.0	2.6	2.2	1.5	1.3	-0.5	0.5	0.6
3.9	3.6	3.0	2.1	1.8	-0.7	0.7	0.8
4.9	4.6	3.8	2.6	2.3	-0.9	0.9	1.1
5.9	5.5	4.6	3.1	2.7	-1.0	1.1	1.3
6.9	6.5	5.4	3.7	3.2	-1.2	1.3	1.5
0.0	0.3	0.3	0.2	0.2	-0.1	0.1	0.1

Key: Δ = Lateral Deflection, θ = Twist, ϒ = Shear Deformation, M = Midspan, TF = Top Flange, TP = Third Point, NE = North East, SE = South East

Figure 3.22: Bedding Strip Deformation uring Twin I-Girder Test

3.6 Summary of Bedding Strip Experimental Results

This chapter focused on the experimental tests that were conducted in the laboratory to investigate the stability of unconnected PCPs on bedding strips. Several important results were learned from the experimental program:

- As expected, bedding strips with a larger size (i.e. 2”x2” vs 1”x1” or 2”x4” vs 1”x2”) and a smaller aspect ratio (i.e. 1:1 vs 1:2) provided the most stability to the PCPs to withstand the deformations experienced by curved bridges during the construction phase (i.e. system twist near midspan and shear deformation at the warping permitted supports).
- With respect to system twist, the 2” wide bedding strips (with heights of 1” and 2”) performed well reaching PCP angles of 13.7 degrees at minimum to 31.9 degrees at maximum, before the PCPs fell off of their supports. These tests accounted for a girder drop of 4” between adjacent flanges (drop angle of 2.5 degrees) and a lateral flange separation (Δ_{LAT} = 0.75”).
- With respect to system twist, the 1”x2” bedding strips performed unsatisfactorily. For one of the tests, the bedding strip failed upon placing the second PCP to simulate the load of a 4” CIP concrete deck. Moreover, the bedding strips could not accommodate lateral flange separation (Δ_{LAT} = 0.75”) without failing.
- For the shear frame tests, the 2”x4” bedding strips significantly outperformed the smaller 1”x2” bedding strips with the frame reaching shear strains of 3.6 degrees vs. 1.5 degrees, respectively (for the case of one PCP). The addition of a second PCP (representing the weight of a 4” CIP concrete deck) reduced the maximum shear stain to 0.8 degrees for the 1”x2” bedding strips and to 3.2 degrees for the 2”x4” bedding strips.

- The limit of the shear test frame was reached (γ_{max} = 4.0 degrees) without the PCPs (two stacked vertically) falling from the shear frame when bedding strips with a 1:1 aspect ratio (1”x1”, 1.5”x1.5”, and 2”x2”) were used. The larger bedding strips were less likely to twist during the test and provided better support to the PCP at larger shear strains.
- For the twin I-girder test, large girder deformations (6.5 inches of lateral deflection and 3.7 degrees of twist at midspan) were achieved without failure of the 2”x4” bedding strips. At the maximum I-girder deformation, the east edge of the PCP only rotated 1.5 degrees (Δ_{NE_MAX} = -1.2” and Δ_{SE_MAX} = 1.3”) with respect to the centerline of the girder which was much less than the maximum 4.1 degrees (Δ_{NE_MAX} = -4.2” and Δ_{SE_MAX} = 2.8”) of rotation achieved on the shear frame before the bedding strip failed.

The results documented above are specific to the parameters of the laboratory tests described in this chapter. In particular, only PCPs with a span of 8’-3” were investigated (increasing the width of the PCP will increase the load on the bedding strips which may decrease the stability of the system). Also, all of the tests were performed with Owens Corning Foamular 400 sheets of extruded polystyrene (conforming to ASTM C578, Type VI - 40 psi compressive strength) and the results from these tests may not apply to other types of extruded polystyrene bedding strips. Results from this chapter will be compared to the girder deformations from finite element models for a number of different curved I-girder and tub girder systems (see Chapter 9). Design recommendations for using PCPs on curved girders are given in Chapter 11.

Chapter 4. Experimental Evaluation of Partial Depth Precast Concrete Deck Panels Subject to Shear Loading

4.1 Introduction

The experimental evaluation of partial depth precast concrete deck panels subject to shear loading is covered in detail in two related theses (McCammon 2015 and Kintz 2017). This section is intended to supplement the work presented in the aforementioned reports and summarize the key results and conclusions.

4.2 Shear Frame Test Setup

To investigate the in-plane shear behavior of the PCPs with different connection details, a shear frame was fabricated at the Ferguson Structural Engineering Laboratory at the University of Texas at Austin (Figure 4.1). The shear frame consisted of six main parts, namely: two reaction blocks, two loading beams, one adjustable connecting strap, one hydraulic actuator, and four tie-down beams. The shear frame used for this project resembles the one constructed by Currah (1993) that was used to investigate the in-plane stiffness and strength of PMDFs. The Fabrication of the shear frame test setups is covered in detail by McCammon (2015).

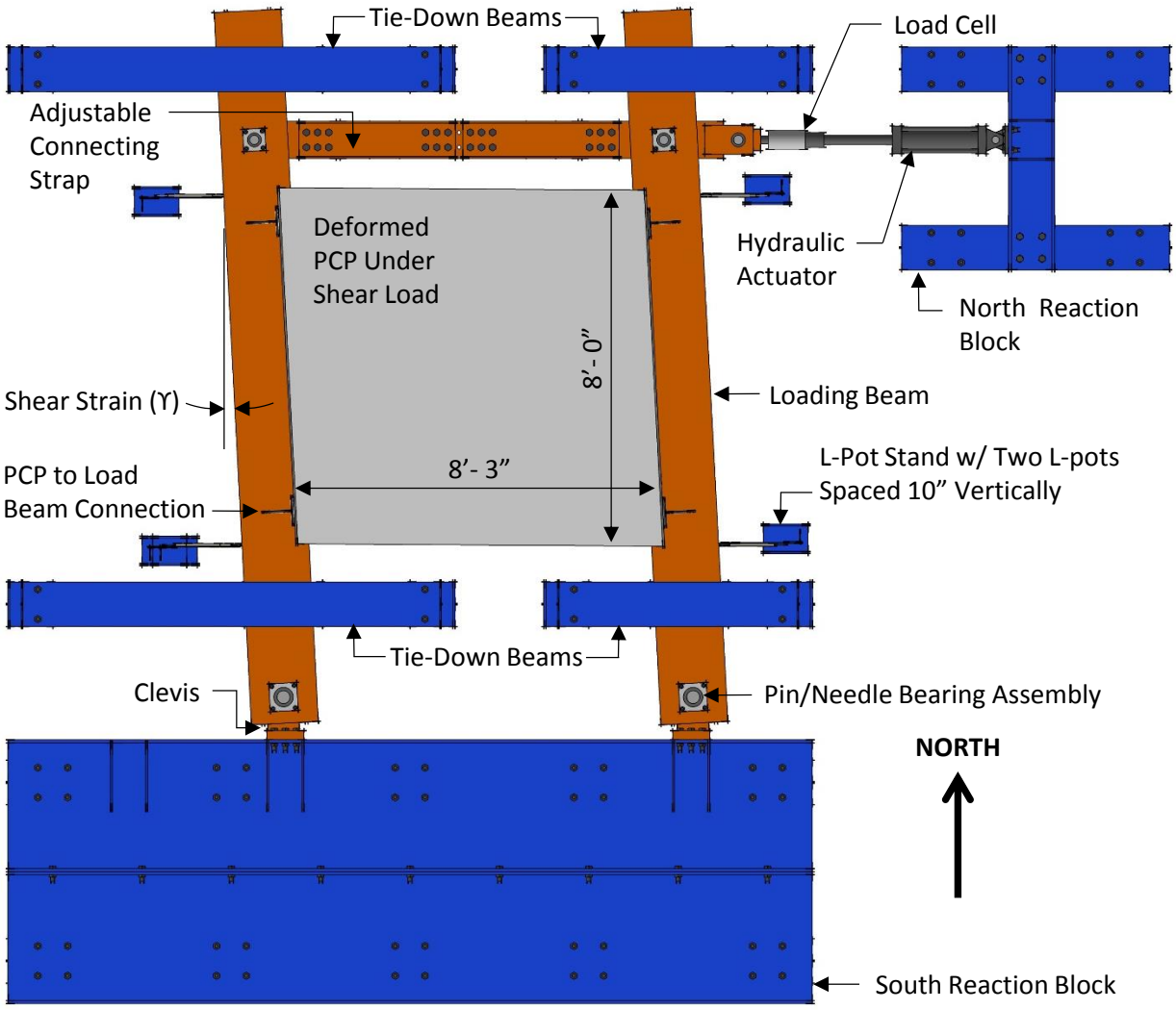

Figure 4.1: Shear Test Frame – Plan View

With no test specimen installed, the needle bearing assemblies allow the frame to deform with a negligible amount of force. Therefore, since the frame is a mechanism on its own, the PCP/connection system provides all of the lateral stiffness and strength to the system. As the load in the actuator increases, the loading beams remain parallel to each other while rotating about the pins at their base, inducing pure shear deformations on the connected PCP. The two "loading beams" simulate the top flanges of two adjacent girders. The shearing deformation simulates the lateral movements of adjacent girders that might be associated with deformations from either girder buckling or torsional deformations in curved girder systems. From statics, the shear force on the PCP is equal to the axial force in the loading beams. Therefore, the relationship of shear force vs. shear strain can easily be determined for the system.

4.3 PCP to Girder Connections

The research team sought the input from a Texas precaster and construction experts to help develop a practical connection between the PCP and the girder without significantly complicating

the construction or precasting process. Several preliminary connection details were tested with normal reinforced (non-prestressed) PCPs which is documented by McCammon (2015). The reinforced panels were used in the initial phase to facilitate the consideration of several different connection details. Once viable connection details were determined from these initial tests, the research team began working with the precaster to have commercially developed PCPs fabricated for additional testing.

4.3.1 Connection Detail

The finalized connection detail between the PCP and the girder is shown Figure 4.2 The PCP is attached to the girders by a steel WT section welded to the girder top flange and to an embed cast into the panel. The embed consists of a 2″ wide flat bar extending the entire width of the PCP that rests above the prestressing strands. To transfer the load from the embed to the concrete, Nelson deformed bar anchors (D2L) were welded to the embed and cast into the PCP as shown in Figure 4.3. Multiple WT sections accompanied by additional embed anchors can be utilized based on the load requirements for the system. A total of eight PCPs (8′-0″ wide x 8′-3″ long) were tested in which the following parameters varied: number of WTs, height of bedding strip/WTs, embed thickness, number of anchors, and anchor size. Table 4.1 shows a summary of the connection information for all eight PCPs. In the labeling nomenclature, MAX and MIN refer to the height of bedding strip that was used. The labels A, B, C, and D represent variations in the number of anchors and the embed size. Additional connection details are presented by Kintz (2017).

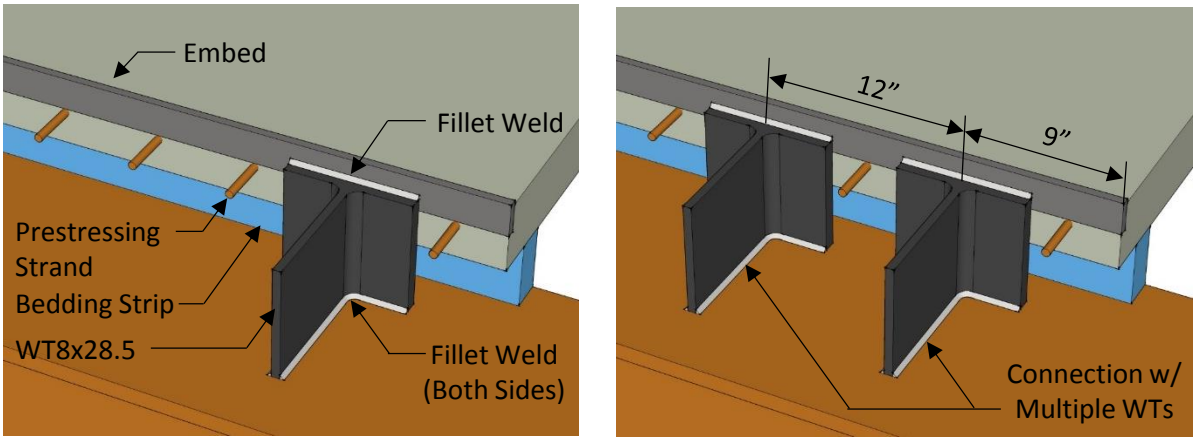

Figure 4.2: Detail of PCP Connection to Top Flange

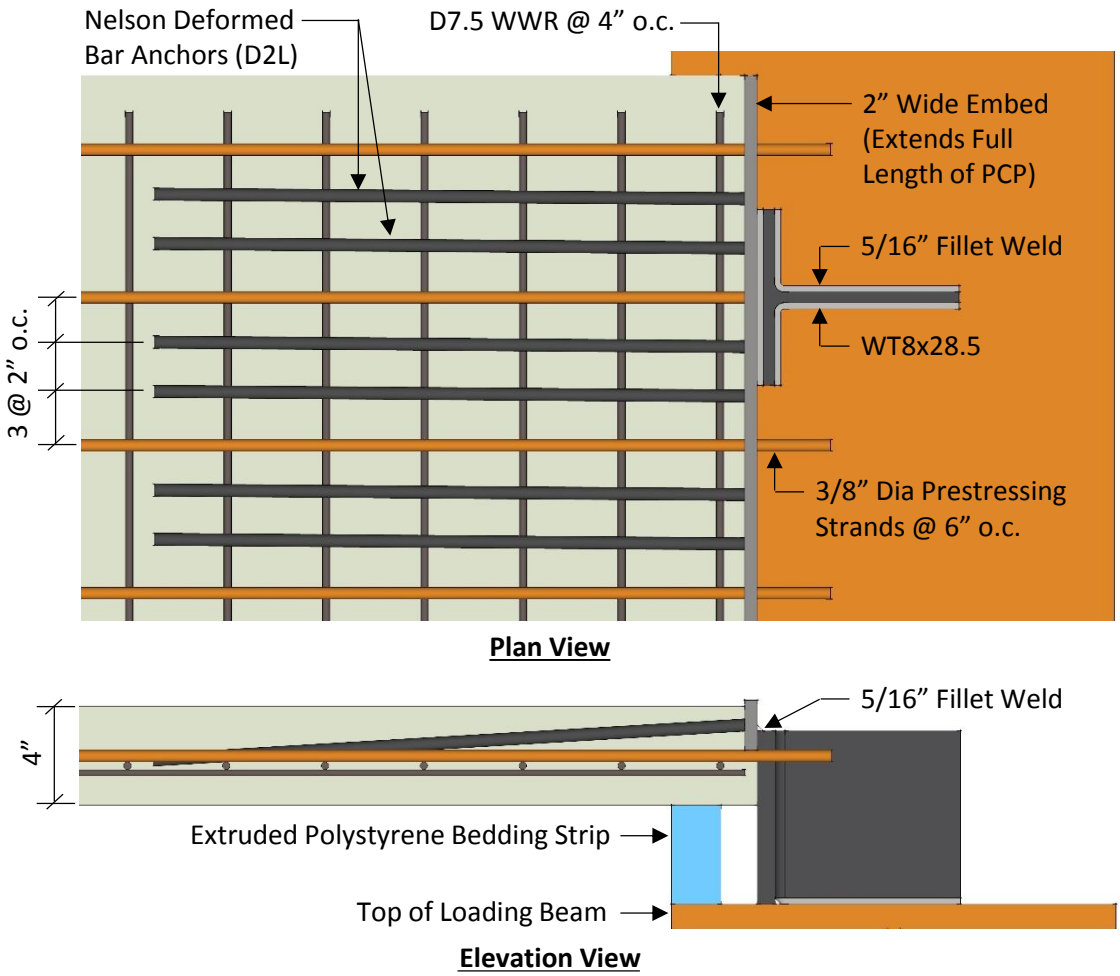

Figure 4.3: Plan and Elevation Views of the Embed-Anchor Detail

Table 4.1: Summary of PCP Details Used in Experiments

Label	Anchors per Corner	Embed Size	WTs per Corner	Bedding Strip Height
A.1.MAX	(6) 1/2" Ø x 2'-0" Long	2"x1/2"	(1) WT8x28.5 x 7"	4"
A.1.MIN	(6) 1/2" Ø x 2'-0" Long	2"x1/2"	(1) WT8x28.5 x 3.5"	1/2"
B.1.MAX	(6) 5/8" Ø x 2'-6" Long	2"x5/8"	(1) WT8x28.5 x 7"	4"
B.1.MIN	(6) 5/8" Ø x 2'-6" Long	2"x5/8"	(1) WT8x28.5 x 3.5"	1/2"
C.2.MAX	(10) 1/2" Ø x 2'-0" Long	2"x5/8"	(2) WT8x28.5 x 7"	4"
C.2.MIN	(10) 1/2" Ø x 2'-0" Long	2"x5/8"	(2) WT8x28.5 x 3.5"	1/2"
D.2.MAX	(8) 5/8" Ø x 2'-6" Long	2"x3/4"	(2) WT8x28.5 x 7"	4"
D.2.MIN	(8) 5/8" Ø x 2'-6" Long	2"x3/4"	(2) WT8x28.5 x 3.5"	1/2"

4.3.2 Industrial Prestressed PCP Fabrication with Embeds

Figure 4.4 shows a photograph during the concrete placement for the eight Prestressed PCPs that were cast near San Antonio, Texas. Based upon discussions with the precaster as well as observations from the research team, the addition of embeds in the PCPs did not significantly

increase the work involved in casting the panels. The embeds cannot be readily fabricated in the field, so the embeds were fabricated at Ferguson Lab and transported to the precasting site for inclusion into the reinforcing steel prior to the concrete placement. Initially, the embeds were only tied to the reinforcing cage via the D2L anchors. However, when the external vibrator was applied to the formwork, the embeds began to separate from the formwork and concrete filled the gap as shown in Figure 4.5. The embeds must be flush with the edge of the PCP so as to achieve a good connection between the WT and the embed in the field. To solve the issue with shifting of the embed during concrete placement, the embeds were tied directly to the formwork through the holes in the formwork for the prestressing strands (see Figure 4.5). After the cast, the precaster indicated that the addition of the embeds was straightforward and did not significantly increase the difficulty of the deck panel fabrication. For consistency, all eight PCPs were cast from the same batch of concrete with f'_c = 8,767 psi, E = 5,020 ksi, and f_t = 630 psi (Kintz 2017).

Figure 4.4: Casting Prestressed PCPs with Embeds

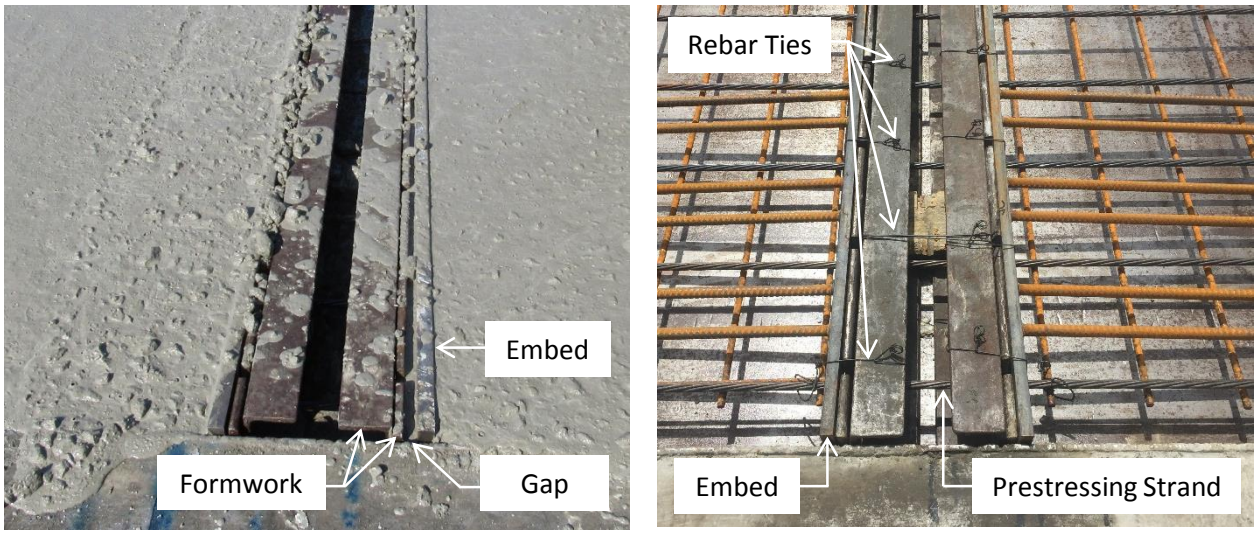

Figure 4.5: Integrating Embeds into PCPs

4.4 Instrumentation and Test Procedure

Both the instrumentation plan and the testing procedure for the PCP shear tests are discussed in detail by Kintz (2017). A calibrated load cell was used to monitor the force applied to the frame by the actuator and eight linear potentiometers (L-pots - two on each stand) were used to measure the deflection of the loading beams near the four corners of the PCP (see Figure 4.1 above). The two L-pots on each stand were spaced vertically at 10″ so that both the lateral deflection and twist of the frame could be measured (see Figure 4.6).

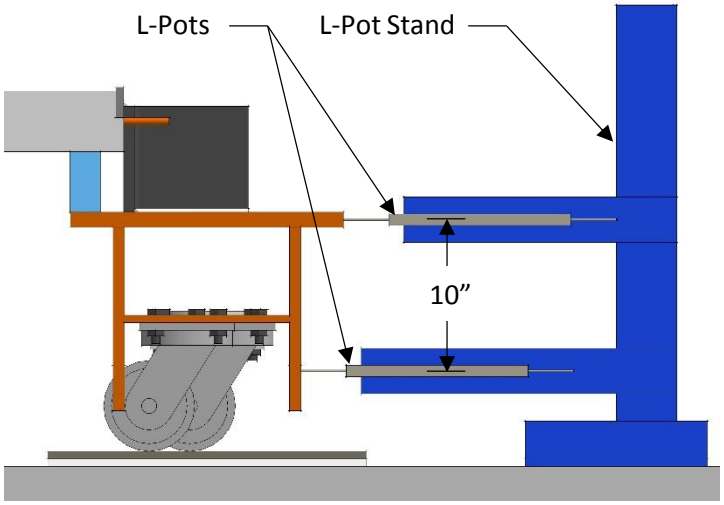

Figure 4.6: L-Pots Used to Measure Deflection of Frame

4.5 Shear Frame Behavior

The L-pot readings that reacted against the testing frame were used to determine the shearing deformation in the panels. The initial assumption was that the testing frame was relatively rigid from both a flexural and torsional stiffness perspective. This assumption was based upon past experience tests on shear diaphragms comprised of light-gage metal sheeting. However, the

relatively large in-plane stiffness of the PCP diaphragm combined with the large eccentricity between the plane of the PCP and the test beam shear center caused the test frame's loading beam to both twist and bend in-plane (Kintz 2017). Thus, the measured stiffness (from L-pots reacting against the frame shown in) was a combination of the stiffness of the PCPs, the stiffness of the connection between the PCPs and the shear frame, and the stiffness of the shear frame itself. Figure 4.7 shows the twist of the shear frame during the test of connection A.1.MAX at the four corners of the PCPs (where the L-pots were located). Note that the beam twist is larger at corners A and C relative to corners B and D which is due to the connections being stiffer in compression (after any initial gap between the PCP and WT closes) than in tension as shown in Figure 4.8 . Therefore, the compression strut that forms between corners A and C is likely stiffer than the tension tie that forms between corners B and D, especially at larger load levels as discussed further by Kintz (2017). Twist of the frame for all eight tests is presented in Appendix A.3 of Kintz (2017).

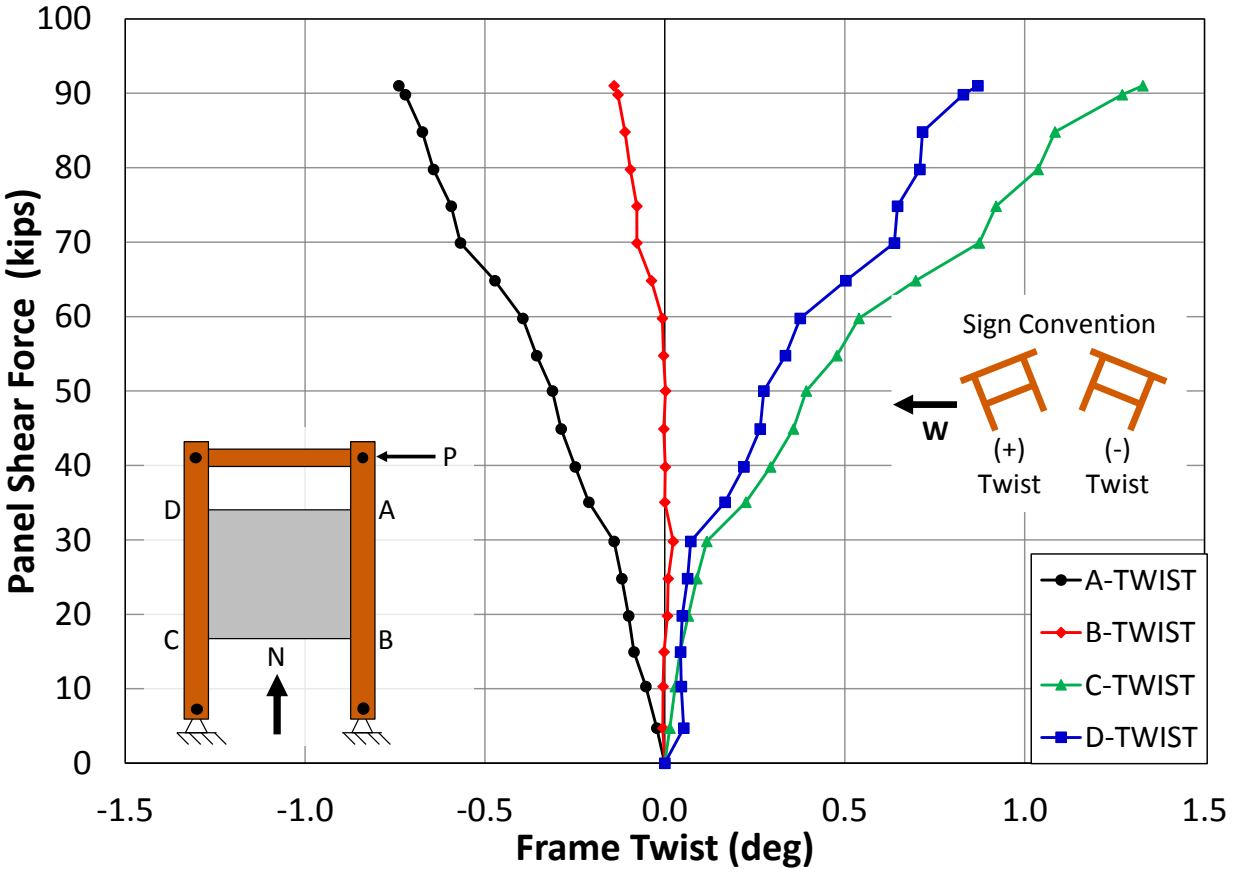

Figure 4.7: Twist Behavior of the Shear Frame for Panel Test A.1.MAX (Kintz 2017)

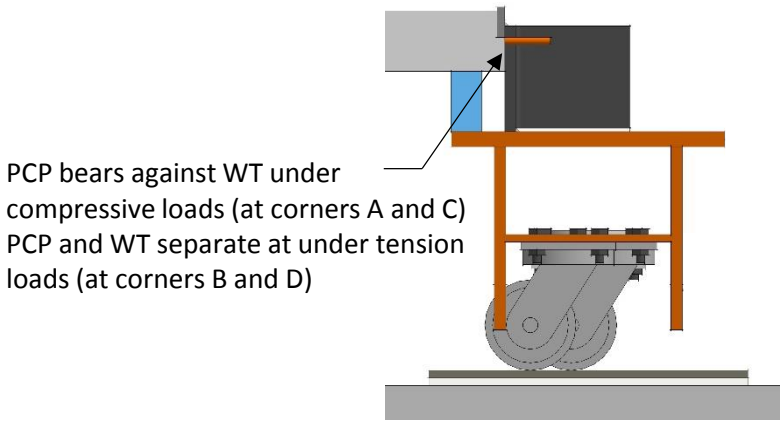

Figure 4.8: PCP and WT Interaction

Figure 4.9 shows the lateral displacements of the shear center of the loading beams at the four corners of the PCP (where the L-pots were located). Frame deflections for all eight tests are presented in Appendix A.3 of Kintz (2017). If the loading beams were rigid, the shear strain would be the same regardless of which frame deflection was used to calculate the value (i.e. $\Upsilon_A = \Upsilon_B = \Upsilon_C = \Upsilon_D = \Upsilon_{AB} = \Upsilon_{DC}$). However, $\Upsilon_A \neq \Upsilon_B \neq \Upsilon_{AB}$ and $\Upsilon_C \neq \Upsilon_D \neq \Upsilon_{DC}$ which indicates that the flexural and torsional deformations of the loading beams during the test were significant (note Υ_{DC} and Υ_{AB} are the likely the most accurate values as they do not measure the bending of the frame south of the PCP) and needed to be considered.

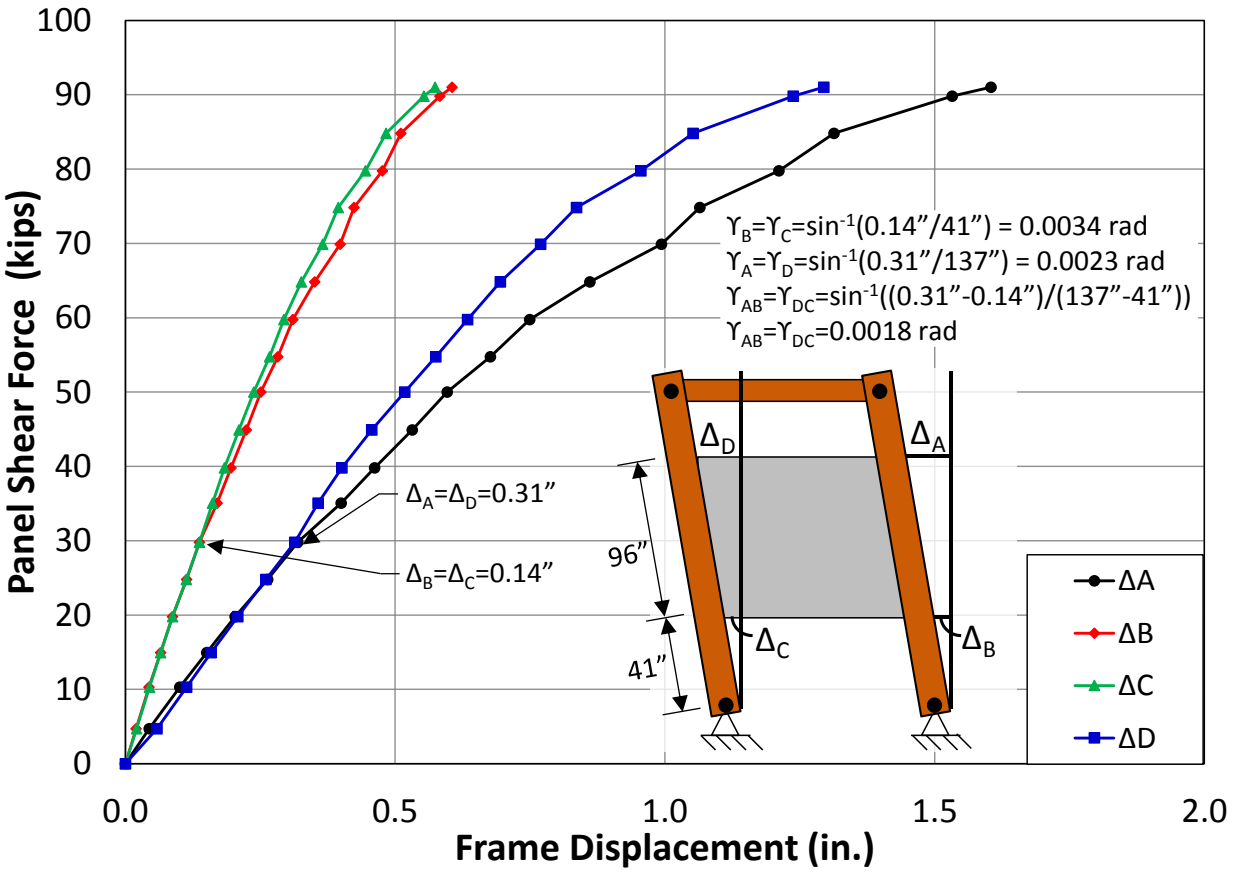

Figure 4.9: Load Beam Shear Center Lateral Displacement for PCP Detail A.1.MAX (Kintz 2017)

4.6 Correction for Shear Frame Deformation

To correct for the flexibility of the shear frame and gain a better understanding of its behavior, several tests were performed with a steel cross-frame providing stiffness to the system (see Figure 4.10). Testing a steel cross-frame was advantageous as the deformation (and force) in each member could be calculated via strain gauges (see Figure 4.11) and the deformation in each connection could be determined via dial gauges (see Figure 4.12). Therefore, the stiffness of the cross-frame and its connections could be measured directly and compared with the stiffness measured from the L-pots on the shear frame (see Figure 4.13) which includes the effects of the frame's flexibility. Additionally, tests were performed with only the compression diagonal connected to the system to see how the frame responded when the stiffness of the compression strut was larger than the stiffness of the tension tie.

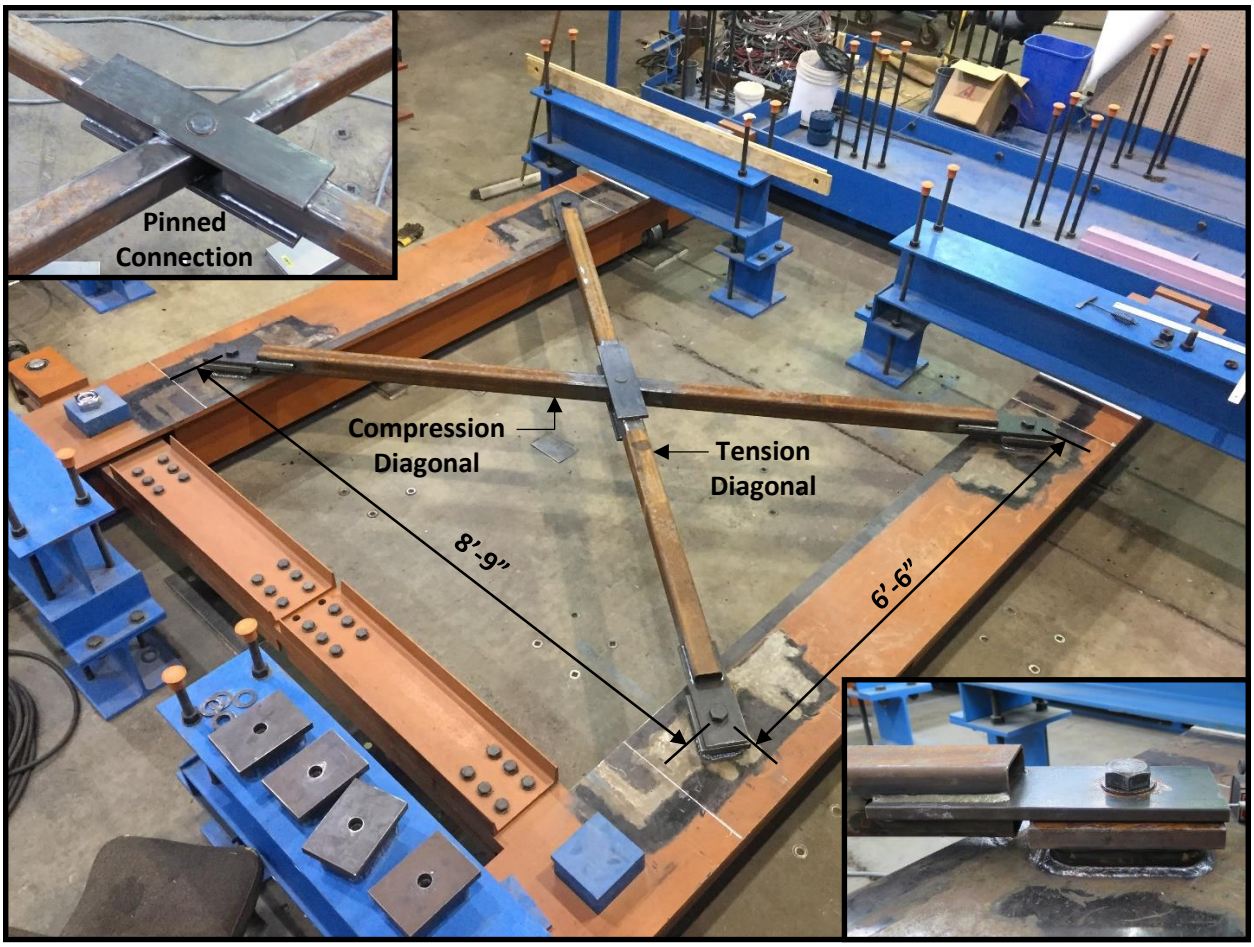

Figure 4.10: Shear Frame Tests of Cross-Frame

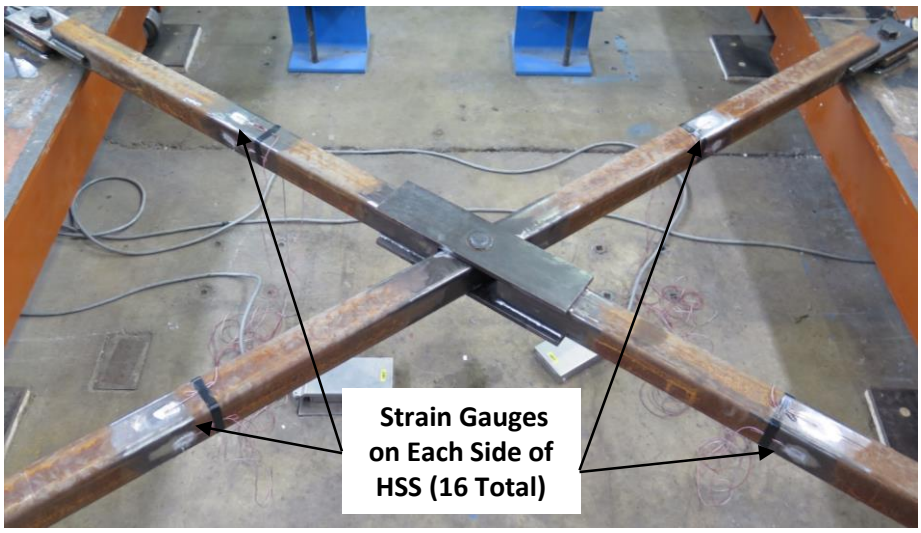

Figure 4.11: Strain Gauge Layout on Cross-Frame

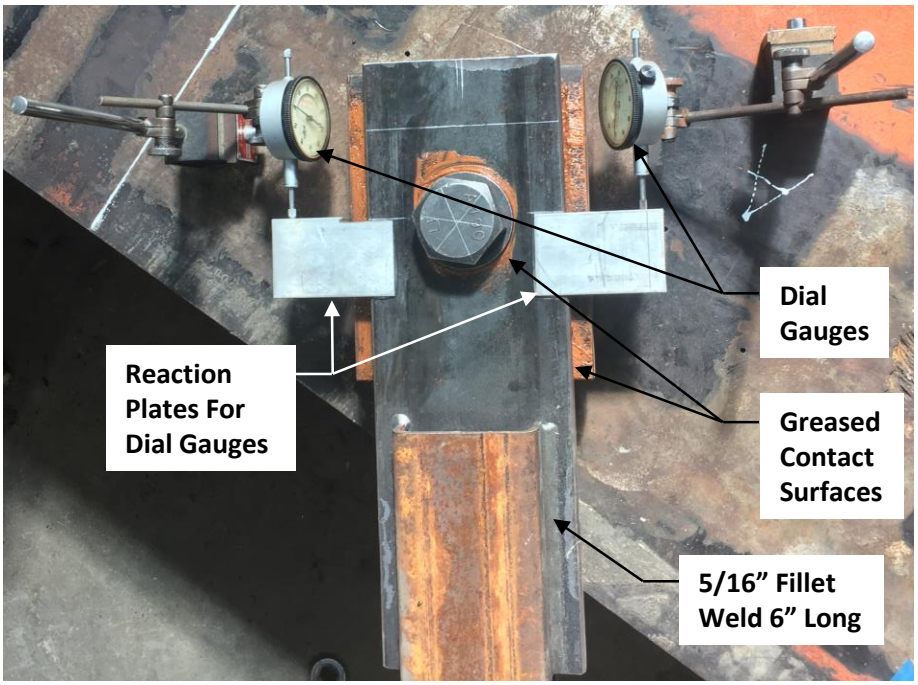

Figure 4.12: Shear Frame Tests of Cross-Frame

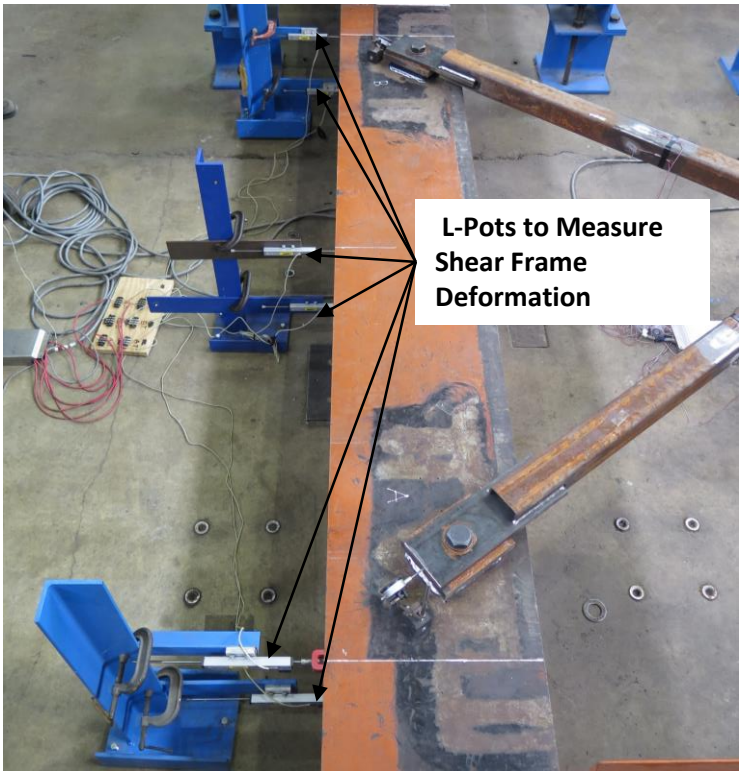

Figure 4.13: Shear Frame L-Pots

4.6.1 Cross-Frame Details

A cross-section of the connection from the cross-frame to the shear frame is shown in Figure 4.14. The connection consisted of a HSS 7x5x1/2 fillet welded to the top plate of the shear frame and to an 8″x6″x1″ plate. A 1-5/16″ diameter hole was drilled through the 8″x6″x1″ plate and a nut was welded to the plate's bottom side. The steel cross-frame was tested at two different eccentricities (2.5″ and 6″) from the top plate of the shear frame to correspond with a 4″ thick PCP sitting on a ½″ bedding strip and a 4″ bedding strip, respectively (allowing the center of the cross-frame to be located at the same elevation as the center of the PCPs). A knife edge and single bolt connection was used to minimize the bending induced on the HSS 3.5x3.5x3/16 member, allowing it to act as a two force truss member, carrying only axial force.

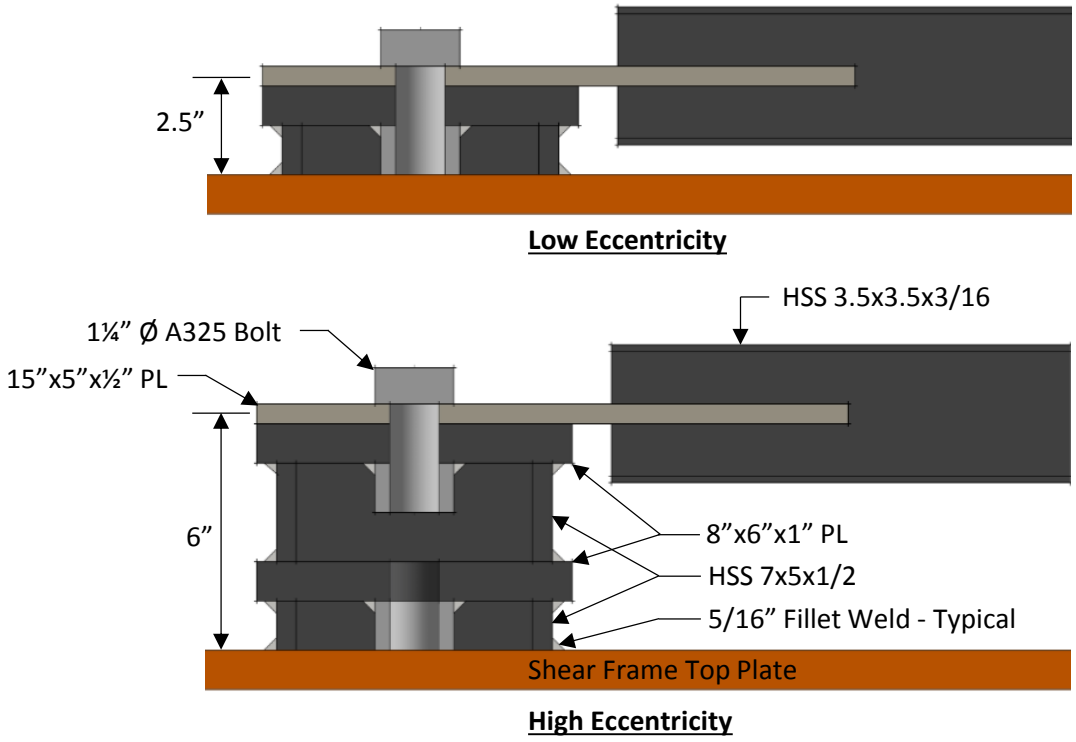

Figure 4.14: Cross-Frame to Shear Frame Connection – Cross-Section

4.6.2 Results from Cross-Frame Tests

Figure 4.15 shows the shear stiffness of the cross-frame measured by the L-pots at the top plate of the shear frame (thus including the flexibility of the frame). As expected, the cross-frame at the higher eccentricity was more flexible than the cross-frame at the lower eccentricity (due to larger torsional loads on the frame and the lower stiffness of the connection to the frame). Figure 4.16 shows the twist of the frame at corners A, B, C, and D for the cross-frame at both the high and low eccentricities.

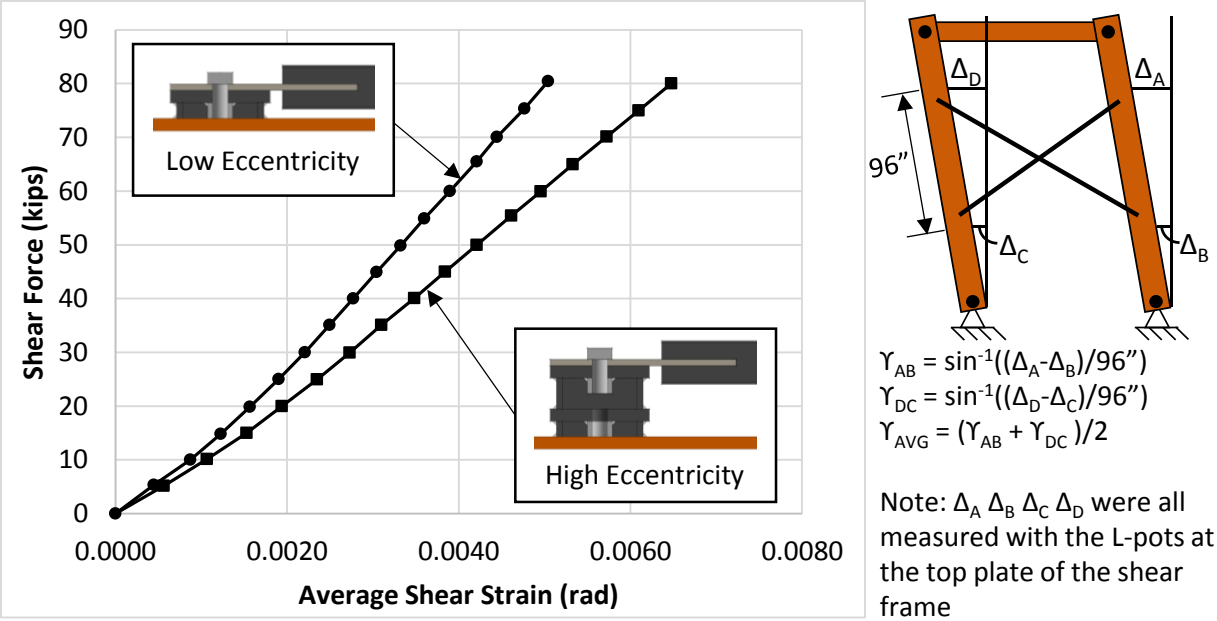

Figure 4.15: Shear Stiffness of Cross-Frame Measured

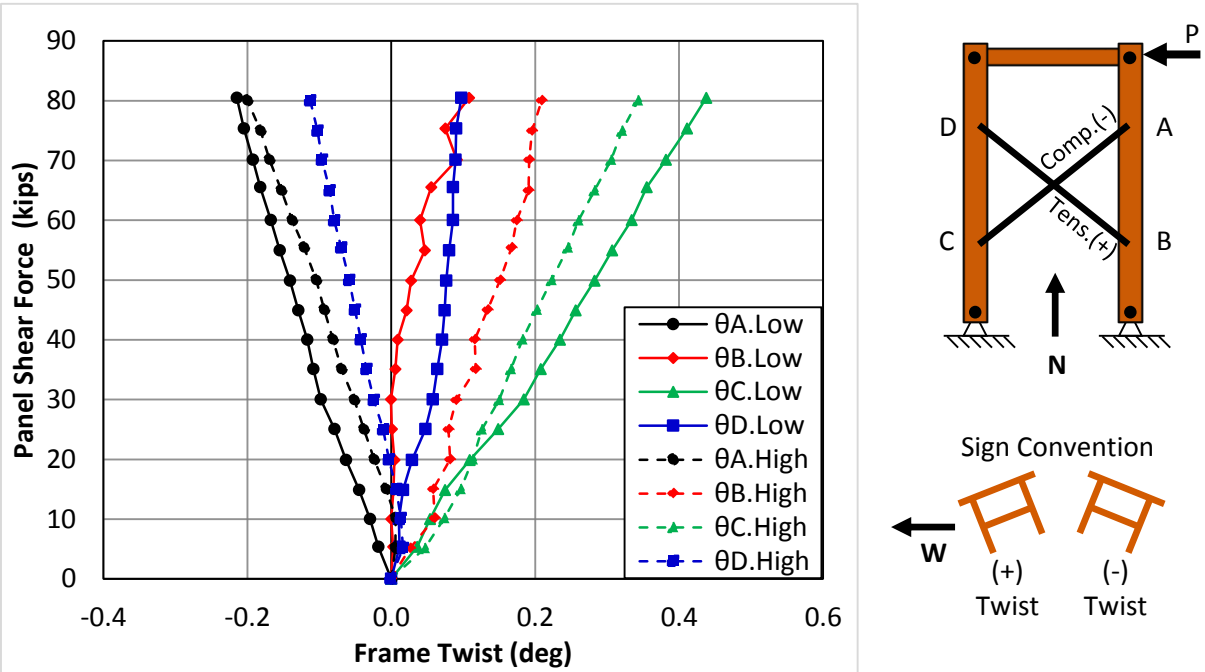

Figure 4.16: Twist Behavior of the Shear Frame for Cross-Frame Tests

Figure 4.17 and Figure 4.18 shows the connection deformation versus the axial force in the cross-frame member for the low and high eccentricity cases, respectively. As expected, the high eccentricity connection was more flexible than the low eccentricity connection. For both connections, an approximately bilinear response was observed for the connection deformation

which is likely attributed to engagement of the bolt as it bears against the connection plates (some localized deformation of the plates at the bolt holes was observed as shown in Figure 4.19).

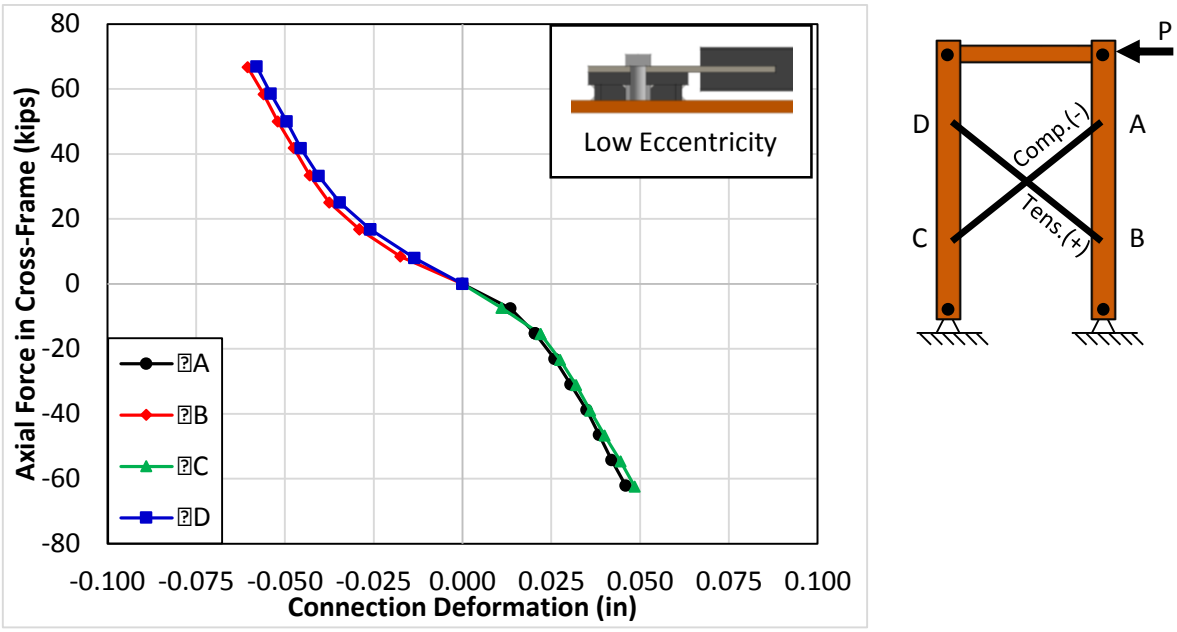

Figure 4.17: Connection Deformation vs Axial Load – Low Eccentricity

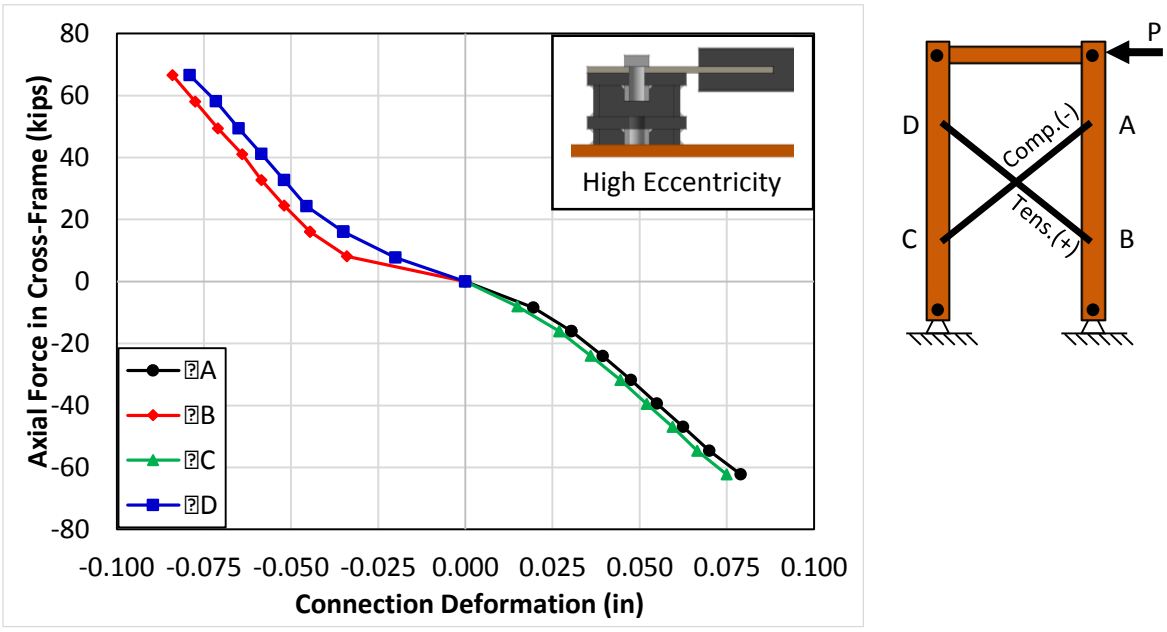

Figure 4.18: Connection Deformation vs Axial Load – High Eccentricity

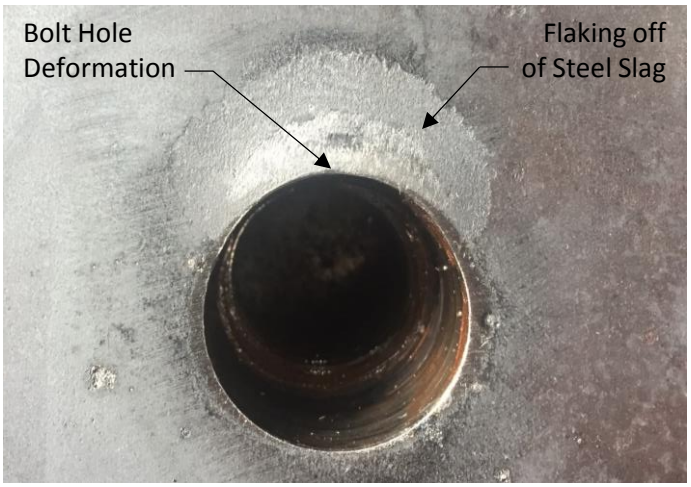

Figure 4.19: Deformation of Plates at Bolt Holes

Since the truss members and their connections behave as springs in series, an equivalent area for the tension and compression truss members can be calculated, accounting for the connection flexibility (see Table 4.2). In Table 4.2, $A_{EQ.AVG.1}$ is the average equivalent area of the truss members the prior to the connections being fully engaged while $A_{EQ.AVG.2}$ is the average equivalent area of the truss members after the connections have been fully engaged. Since an HSS 3.5x3.5x3/6 as an area of 2.24 in^2, the connection flexibility played a significant role in adding flexibility to the system. The stiffness of the high eccentricity case is lower than the stiffness when the cross-frame is at a lower eccentricity since the connection flexibility increased with the eccentricity.

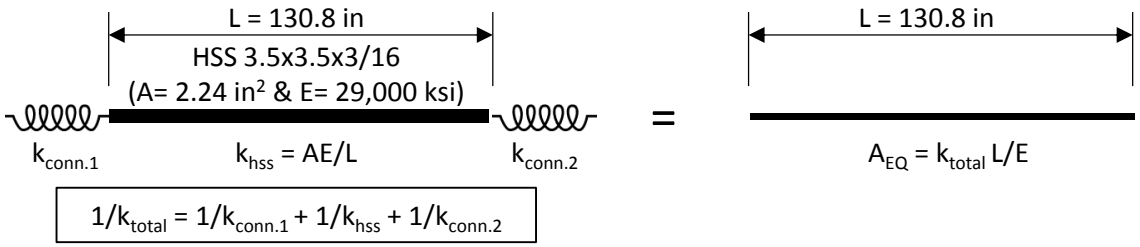

Figure 4.20: Equivalent Area of Member Accounting for Connection Stiffness

Table 4.2: Equivalent Area Accounting for Connection Flexibility

Equivalent Truss Member Area (in^2)	High Eccentricity (2½")	Low Eccentricity (6")
$A_{EQ.T.1}$	0.60	0.71
$A_{EQ.C.1}$	0.79	0.95
$A_{EQ.AVG.1}$	**0.70**	**0.83**
$A_{EQ.T.2}$	1.21	1.33
$A_{EQ.C.2}$	1.09	1.44
$A_{EQ.AVG.2}$	**1.15**	**1.38**

Key: T = Tension, C = Compression, AVG = Average

Figure 4.21 shows the relationship between the shear strain (γ), shear force (V), the diagonal area (A) and its elastic modulus (E), and the geometry of the cross-frame (S, h_b, and L_d). Using this relationship, the shear force versus shear strain was graphed (dashed line) using the equivalent areas mentioned previously for both the low and high eccentricity cases (see Figure 4.22 and Figure 4.23, respectively). The shear strain measured from the L-pots reacting against the top plate was graphed (solid line) in the same figures. After the bolts were fully engaged and the stiffness of the shear frame increased, the accuracy of the measurements from the L-pots on frame decreased significantly, indicating that the accuracy is dependent on the relative stiffness of the cross-frame and the shear frame.

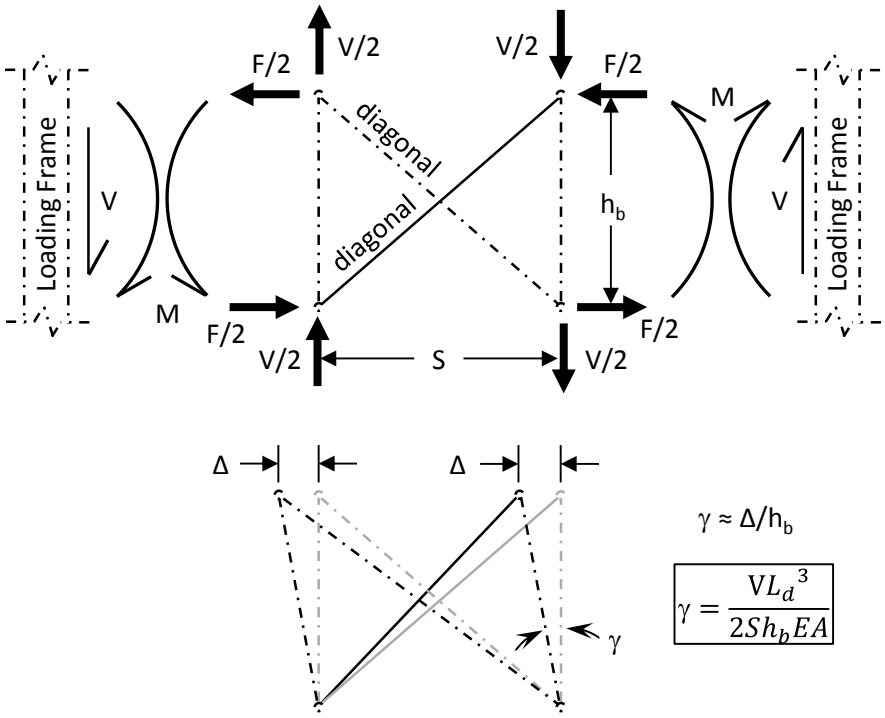

Figure 4.21: Free Body Diagram of Cross-Frame and Shear Frame

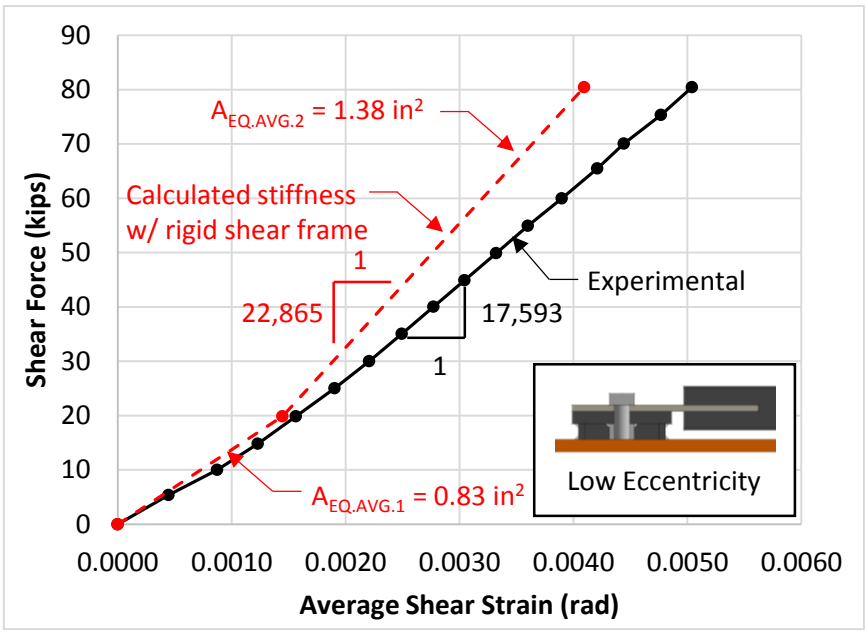

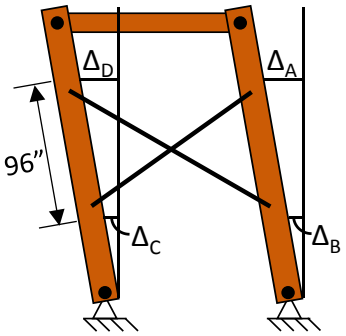

$\Upsilon_{AB} = \sin^{-1}((\Delta_A-\Delta_B)/96")$
$\Upsilon_{DC} = \sin^{-1}((\Delta_D-\Delta_C)/96")$
$\Upsilon_{AVG} = (\Upsilon_{AB} + \Upsilon_{DC})/2$

Note: Δ_A Δ_B Δ_C Δ_D were all measured with the L-pots at the top plate of the shear frame

Figure 4.22: Shear Strain vs. Shear Force – Low Eccentricity

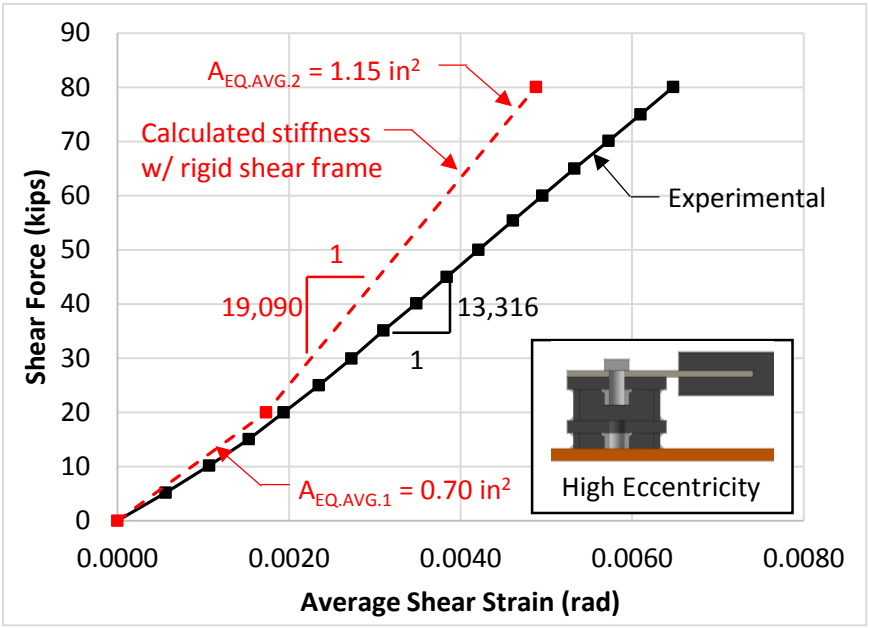

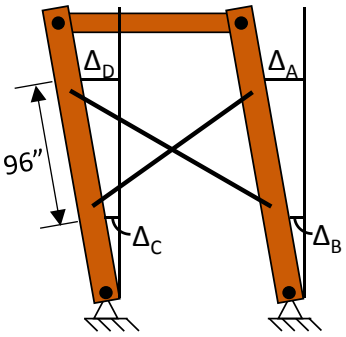

$\Upsilon_{AB} = \sin^{-1}((\Delta_A-\Delta_B)/96")$
$\Upsilon_{DC} = \sin^{-1}((\Delta_D-\Delta_C)/96")$
$\Upsilon_{AVG} = (\Upsilon_{AB} + \Upsilon_{DC})/2$

Note: Δ_A Δ_B Δ_C Δ_D were all measured with the L-pots at the top plate of the shear frame

Figure 4.23: Shear Strain vs. Shear Force –High Eccentricity

For the low eccentricity case (Figure 4.22), the actual stiffness of the cross-frame (dashed line) was 1.30 (22,865/17,593 = 1.30) times larger than the stiffness measured directly from the frame (solid line). For the high eccentricity case (Figure 4.23), the actual stiffness of the cross-frame (dashed line) was 1.43 (19,090/13,316 = 1.43) times larger than the stiffness measured directly from the frame (solid line). As expected, the accuracy of the measurements from the L-pots on the frame decreased as the eccentricity of the cross-frame increase (since larger torsional forces are placed on the frame with increased eccentricity).

Correction factors of 1.30 and 1.43 for the high and low cases, respectively can applied to the shear frame test results to account for the frame's flexibility. These correction factors are specific to the stiffness of the cross-frame used in these tests. Since the stiffness of the PCP/connection was more than the cross-frame, there was concern that the correction factors might be too low so a finite element model of the shear test frame was created and validated with the results from the cross-frame test. This model was used to validate the correction factors of 1.30 and 1.43 for the PCPs which is discussed in further detail in Chapter 8.

4.6.3 Panel Shear Stiffness (Accounting for Shear Frame Flexibility) and Strength

Figure 4.24 shows graphs for the shear strain versus shear force (uncorrected) for the eight tests (4 different details at 2 different bedding strip heights) that were performed in the laboratory (Kintz 2017). **Error! Reference source not found.** summarizes the shear stiffness and strength of t he PCP/connection system as reported by Kintz (2017). The corrected values for the shear stiffness (V/ϒ) accounting for the flexibility of the frame (increasing the stiffness by factors of 1.30 and 1.43 for the 4″ high and ½″ low bedding strips, respectively) are also presented in this table.

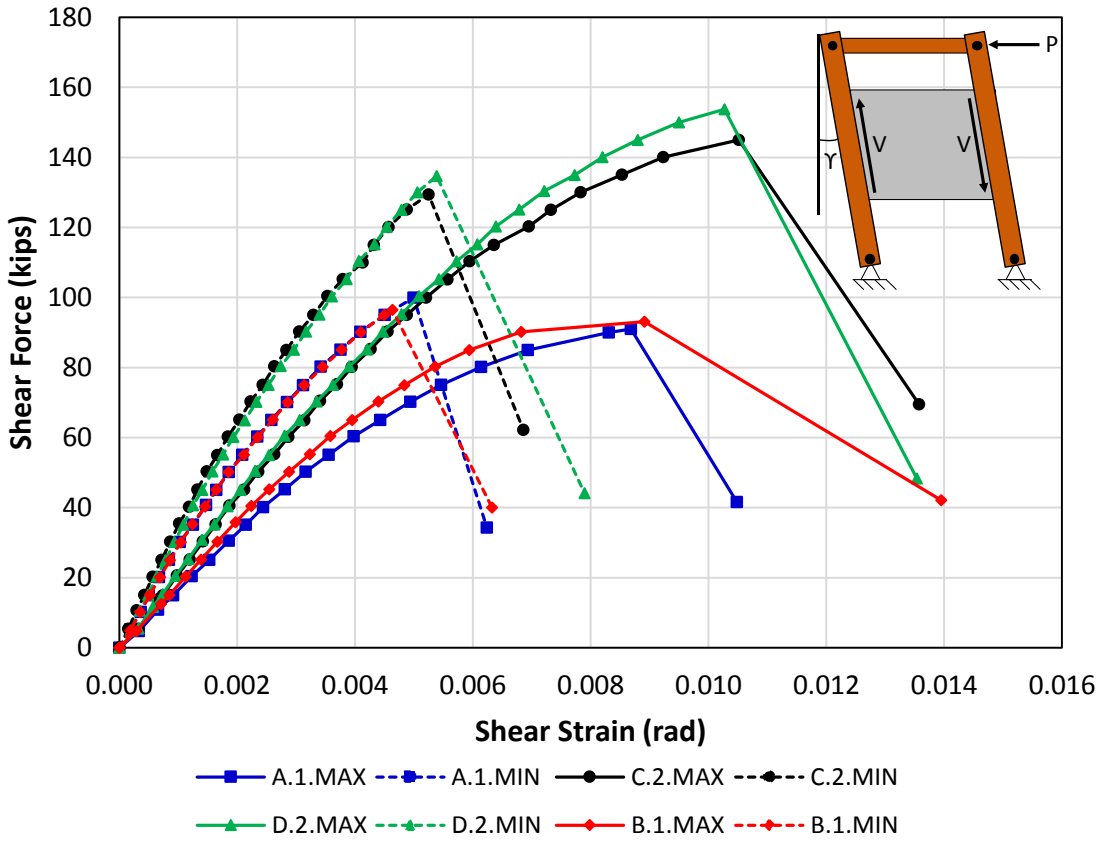

Figure 4.24: Shear Behavior Up to Ultimate Load (Kintz 2017)

Table 4.3: Shear Stiffness and Strength of PCP/Connection Systems

Connection Detail	Bedding Strip Height (in.)	V/ϒ* (L-Pots) (kips/rad)	V/ϒ (Corrected) (kips/rad)	V_{max} (kips)
A.1	4	16,514	23,615	91
	½	28,038	36,449	100
B.1	4	18,341	26,228	93
	½	28,101	36,531	96
C.2	4	21,549	30,815	145
	½	33,797	43,936	129
D.2	4	22,047	31,527	154
	½	32,109	41,742	135

*Values from Kintz (2017)

PCP/Connection Shear Stiffness

Figure 4.25 shows the stiffness behavior (uncorrected) for the A.1.MIN and A.1.MAX details while figures for the rest of the details can be found in Kintz (2017). The shear stiffness of the PCP was calculated as the slope of the shear force vs shear strain curve up to 40% of the ultimate load (representing the elastic stiffness of the PCP/connection prior to damage occurring in the system). As expected, increasing the height of the connection (from ½″ to 4″) reduced the shear stiffness while increasing the number of WTs at each corner from one (for details A.1 and B.2) to two (for details C.2 and D.2) increased the shear stiffness (see **Error! Reference source not found.**).

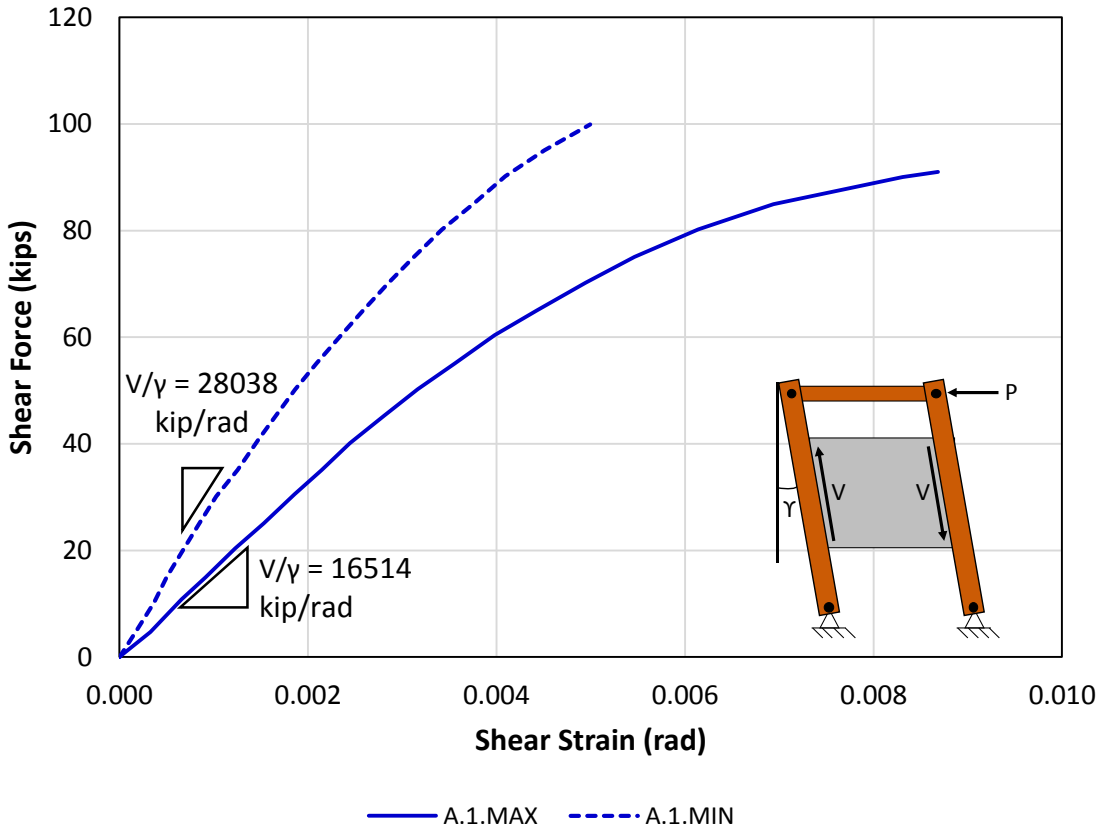

Figure 4.25: Shear Stiffness Behavior for PCP Detail A.1 (Kintz 2017)

PCP/Connection Failure Modes

The eight PCP/connection systems that were tested on the shear frame failed in a relatively brittle manner. The same failure mechanism of concrete breakout parallel to an edge was observed for all of the shear frame tests with the exception of one (detail B.1.MAX which failed via weld rupture between the WT and the loading beam). Figure 4.26 shows the concrete breakout failure mechanism for detail A.1.MAX. This failure mode consisted of a simultaneous break-out of the top face of the two corners on one edge of the PCP, allowing the embed on that edge of the panel to move relative to the PCP (Figure 4.26). Strain gauges on the embed (which extended the full length of the PCP) showed that tensile forces developed in the embed between the corners (indicating that load was transferred from one corner to the other) which is discussed in detail by Kintz (2017).

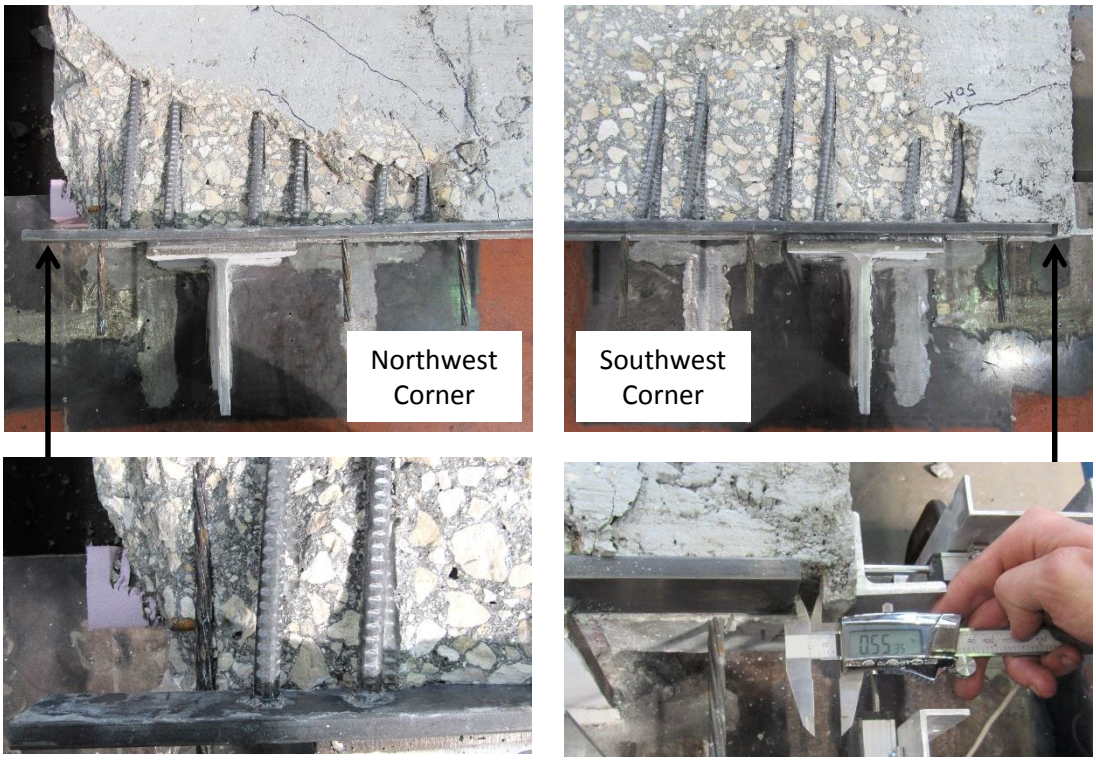

Figure 4.26: Concrete Side Face Breakout Failure for PCP Detail A.1.MAX

Figure 4.27 shows detail B.1.MAX after failure via weld rupture between the WT and the loading beam. While failure occurred at both the northwest and southwest corners, rupture of the weld was first observed in the northwest WT. For this particular test, the weld was mistakenly not wrapped around the corner of the WT extend the full width of the flange as was done in the other seven test which made the weld more vulnerable to unzipping.

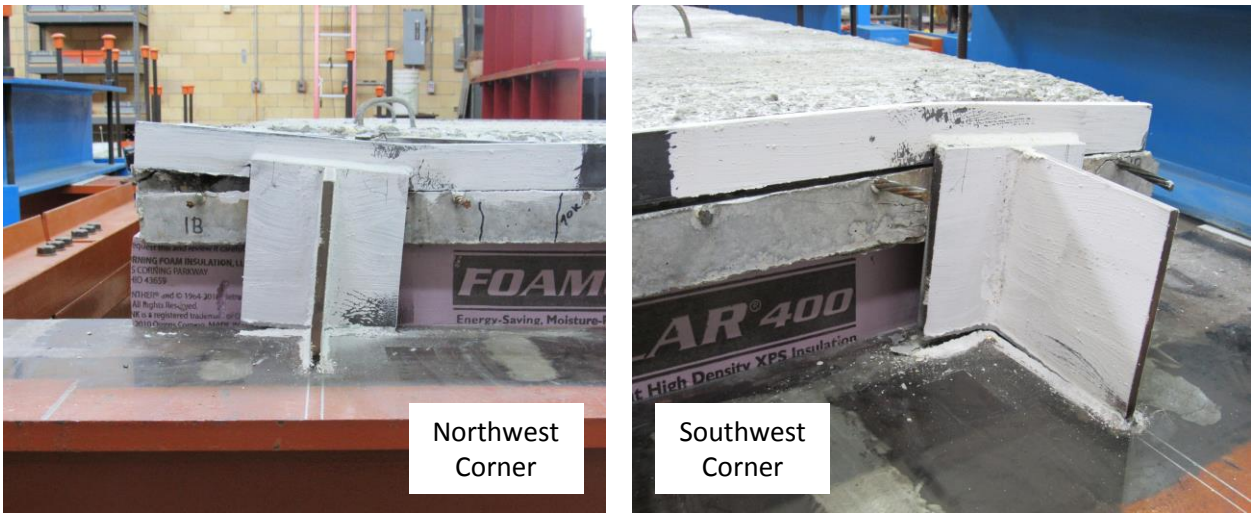

Figure 4.27: WT to Loading Beam Weld Rupture for PCP Detail B.1.MAX (Kintz 2017)

PCP/Connection Strength

Table 4.4 shows the ultimate shear capacity of the panel (V_{max}) along with the LFRD calculated shear capacity of the PCP/connection for the embed (ϕV_{Embed}) and the WT (ϕV_{WT}). Appendix D of the ACI 318-11 code for the anchoring to concrete was used to determine the capacity of the anchors to the PCP while the 14th edition of the AISC steel construction manual was used to determine the capacity of the eccentrically loaded weld groups of the WT to embed and loading beam using the elastic method. The calculations for each connection detail was based on the work by Kintz (2017) are provided in Appendix A.

Table 4.4: Ultimate Load Capacities for PCP Shear Tests (Kintz 2017)

Connection Detail	Bedding Strip Height (in.)	ϕV_{Embed}* (kips)	ϕV_{WT}† (kips)	V_{max} (kips)
A.1.MAX	4	24.3	23.5	91
A.1.MIN	½		43.3	100
B.1.MAX	4	25.5	23.5	93
B.1.MIN	½		43.3	96
C.2.MAX	4	40.0	42.5	145
C.2.MIN	½		78.3	129
D.2.MAX	4	33.7	42.5	154
D.2.MIN	½		78.3	135

†Weld rupture controls (AISC 14th edition - eccentrically loaded weld groups - elastic method)

*Shear breakout parallel to edge controls (ACI 318-11 D.6.2)

The ultimate capacity of the PCPs with a single WT per corner (details A.1 and B.1) ranged from 91 kips to 100 kips and the thicker embed and larger anchors of detail B.1 seemed to have no significant effect on the ultimate capacity of the system. With two WTs per corner and an increased number of embeds at each corner, the ultimate capacities of details C.2 and D.2 (ranging from 129 kips to 154 kips) were larger than those of details A.1 and B.1 as expected. Had the concrete compression strength been f'_c = 5,000 psi (the minimum specified by TxDOT for the PCPs) instead of f'_c = 8,767 psi, the ultimate capacity of the PCPs would have likely been reduced by a factor of 0.76 ($\sqrt{5000}/\sqrt{8600} = 0.76$) for the cases where concrete breakout controlled (all excluding detail B.1.MAX).

Figure 4.28 shows how the forces flow from the WTs into the PCPs via the embeds and D2L anchors (with the assumption that C_{con} and T_{con} are equal and opposite). The overlap of the D2L anchors and the prestressing strands allows the tension force to transfer between the two instead of considering concrete breakout in tension (ACI 318-11 D.5.2.9). Also, the continuous embed allow the assumption to be made that as the anchors on the north begin to breakout in shear, the load gets transferred via the embed to the south anchors that are far away from the edge (so that the entire PCP would have to fail in shear instead of the corner simply breaking out). Concrete breakout parallel to the edge (ACI-318-11 Appendix D.6.2) was calculated to be the controlling limit state for the embed for all four details (A.1, B.1, C.2, and D.2) and as mentioned previously, this failure mechanism occurred in seven of the eight experimental shear tests. The test day compression strength (f'_c = 8,767 psi) was used to calculate the breakout strength shown in Table 4.4. The ratio of the ultimate shear capacity tested in the laboratory verse calculated shear capacity

($V_{max}/\phi V_{Embed}$) ranged from 3.2 to 4.6, indicating that the code is quite conservative for this concrete shear based failure mechanism. Since both the corners with the compression (C_{con}) and tension (T_{con}) forces failed simultaneously, the interaction between tensile and shear forces were not considered in calculating the capacity of the embed (considering this interaction would make the code design equations even more conservative). From a design perspective, the number of ½″ diameter D2L anchors could be increased to a maximum of 30 (two in between each prestressing strand) which would increase ϕV_{Embed} to a maximum 44.6 kips using f'_c = 5,000 psi - the minimum 28-day strength for PCPs specified by TxDOT (2014b).

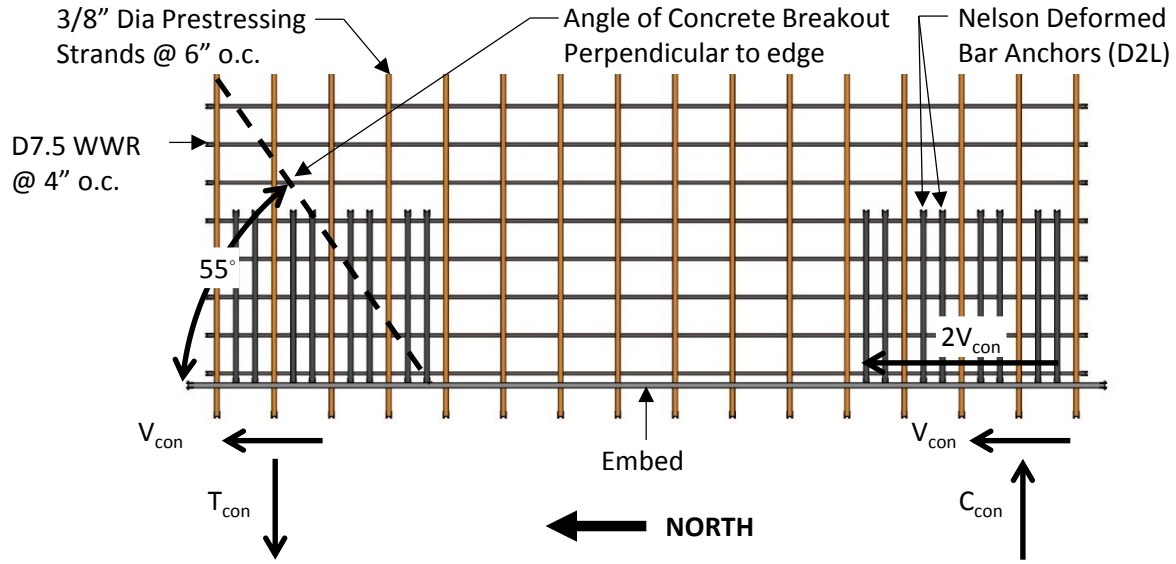

Figure 4.28: PCP Embed Reactions

Figure 4.29 shows the loads on the welds that were used to calculate the capacity of the WT connection. Due to the complexity of the loading condition, the elastic method presented in the AISC 14th edition was used to calculate the capacity of the connection. Note that the elastic method can be somewhat conservative because the ductility of the weld group and the potential load increase according to AISC (2010) is neglected. For the eight cases, V_{max} greatly exceeded ϕV_{WT}. For detail B.1.MAX which failed via weld rupture, $V_{max}/\phi V_{WT}$ = 3.96 indicating that the elastic method is relatively conservative.

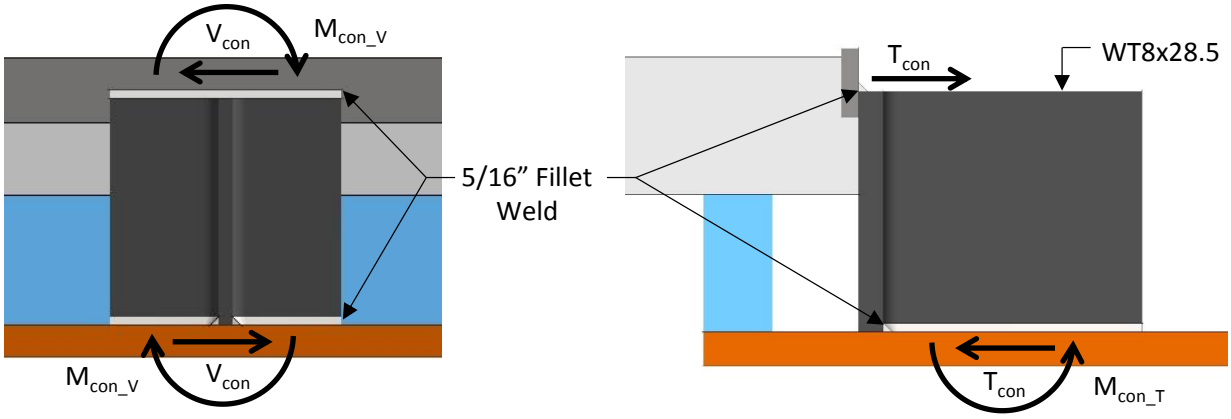

Figure 4.29: Forces on WT Welds

4.7 Conclusions

This section supplements the work presented by McCammon (2015) and Kintz (2017). The work by McCammon (2015) focused on the fabrication of the shear test frame and preliminary connection details considered in the research investigation. Kintz (2017) discusses the shear test results for the 8 tests (4 different details at 2 different bedding strip heights) that were performed in the laboratory and indicated that the flexibility of the shear frame may have influenced the measured stiffness of the PCP/connection system.

- A steel HSS3.5x3.5x3/16 cross-frame was tested in the shear frame and it was shown that the stiffness of the shear frame significantly influenced measured stiffness of the cross-frame (since the L-pots were measuring the displacement of the frame itself). The direct stiffness measurements of the cross-frame were 1.30 and 1.43 times larger than the measurements from frame when the cross-frame was at low (2.5″) and high (6″) eccentricities, respectively. The shear stiffness PCP/connection systems were corrected using the 1.30 and 1.43 factors for the tests when the PCP sat on a ½″ bedding strip and 4″ bedding strip, respectively. The values of the correction factors are validated using finite element models in Chapter 8.
- As the height of the bedding strip decreased (from 4″ to ½″), the stiffness of the PCP/connection system increased for the connections with the same details by factors ranging between 1.32 and 1.54 for the four variations of the connection tested. Also, larger stiffness resulted from increasing the number of WTs at each corner, increasing the embed thickness, and increasing the number of D2L anchors per corner. The maximum shear stiffness (V/ϒ) of the 8 tests was 43,936 kips/rad for detail D.2.MIN while the minimum shear stiffness was 23,615 kips/rad for detail A.1.MAX (these are the values corrected for the flexibility of the shear frame as mentioned previously)
- Seven of the eight PCPs/connection systems fail via concrete breakout parallel to the edge with the top face of the PCP breaking out. Detail B.1.MAX failed via weld rupture between the WT and the loading beam. Detail A.1.MAX was the weakest connection failing at 91 kips in shear while D.2.MAX was the strongest connection failing at a 154 kips in shear.

- The capacity of the embed to PCP connection was calculated using Appendix D of ACI 318-11. The code proved to be quite conservative with the limit state of concrete breakout parallel to the edge controlling and the maximum calculated shear ranging between 24.3 kips to 40.0 kips (LRFD) for the four different embed details. The large conservatism of the code was expected due to the concrete shear based failure mechanism.
- The capacity of the welds connecting the WTs to the embeds and the WTs to the loading beams were calculated using the elastic method of AISC 14th edition. This method proved to be quite conservative with ϕV_{WT} ranging from 23.5 kips for A.1.MAX to 78.3 kips for D.2.MIN. Detail B.1.MAX failed via weld rupture at V_{max} = 93 kips while the capacity for this case was calculated to be ϕV_{WT} = 23.5 kips.
- Increasing the number of ½″ diameter D2L anchors to 30 (to maximized the capacity of the connection to resist concrete breakout parallel to the edge) increases the maximum calculated shear force to 44.6 kips using f′c = 5,000 psi - the minimum 28 day strength for PCPs specified by TxDOT (2014b).

The results mentioned above are specific to the parameters of the laboratory tests described in this chapter. These results will be used to validate finite element models discussed further in Chapter 8. The validated models can then be used to extend the experimental results to a wide array of curved I-gird and tub girder bridges, allowing a better understand of the bracing potential of PCPs on realistic I-girder and tub girder systems to be gained.

Chapter 5. Large-Scale Laboratory Tests on Steel I-Girder System

5.1 Introduction

To investigate the feasibility of using PCPs to brace curved steel I-girder systems, the research team constructed a large-scale twin I-girder system at the Ferguson Structural Engineering Laboratory. The twin I-girder test set-up was designed so that various support, loading, and bracing conditions could be investigated. Two types of loading were applied to the system. One type of loading involved the application of lateral loads to the twin girder system. The other type of loading involved application of vertical loads, to provide combined bending and torsion on the system. Figure 5.1 shows an isometric view of the test setup for the lateral load tests while Figure 5.2 and Figure 5.3 show the test setup for combined bending and torsion load tests in a simply supported and overhanging condition, respectively. Several combinations of bending and torsion were applied to the straight girder system, allowing girders with multiple radii of curvature to be simulated with a single system. The twin I-girders were tested with different numbers of PCPs, with and without the midspan cross-frame and the bottom flange truss. Results from the laboratory tests were used validate the finite element models described in Chapter 9. Photographs of the experimental setup are shown in Figure 5.4.

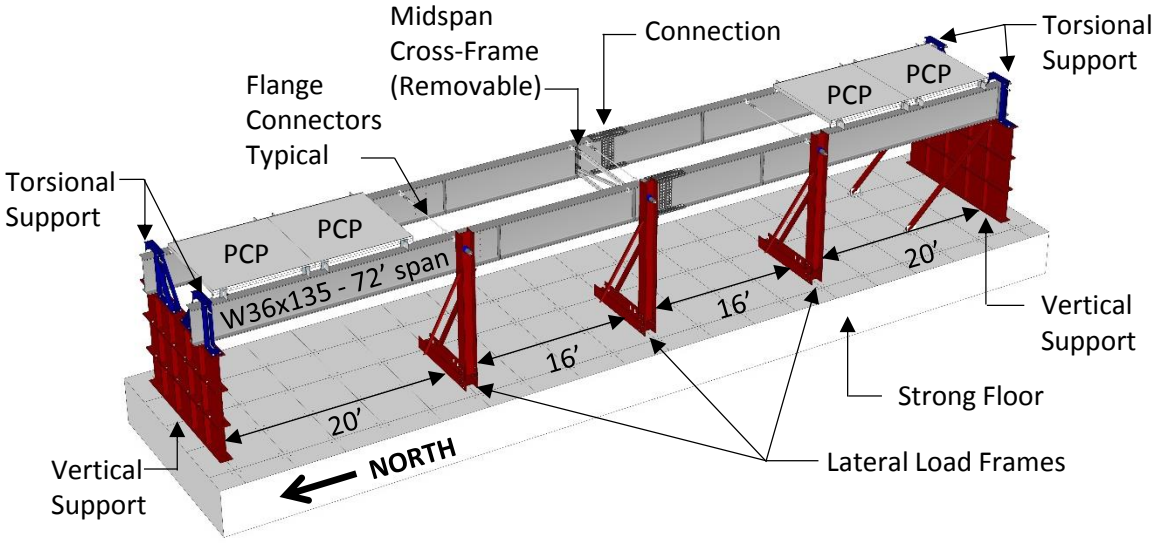

Figure 5.1 Lateral Load Test Setup – Simply Supported

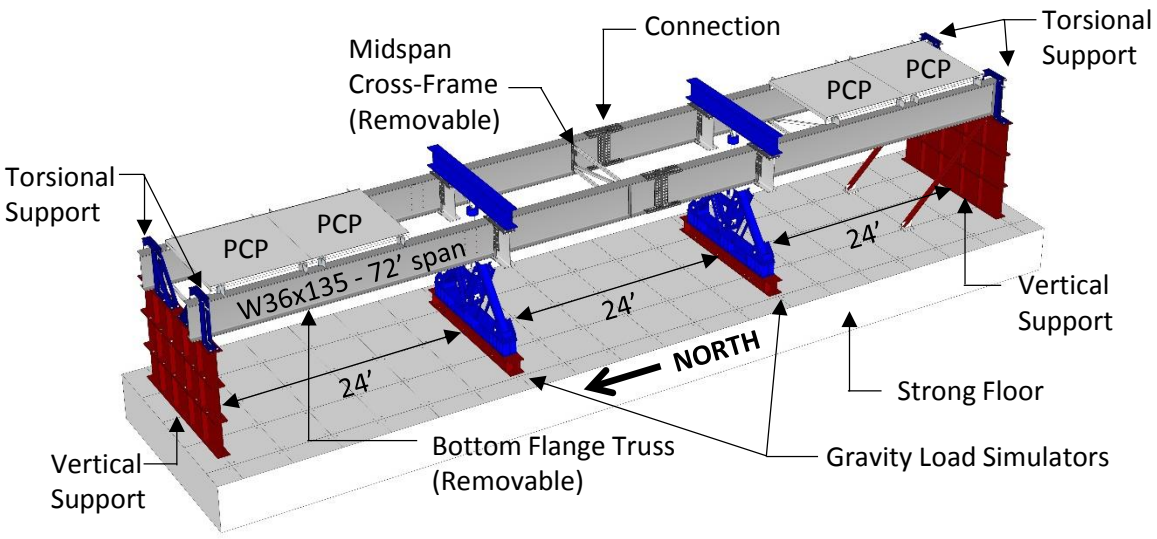

Figure 5.2 Bending & Torsion Test Setup – Simply Supported

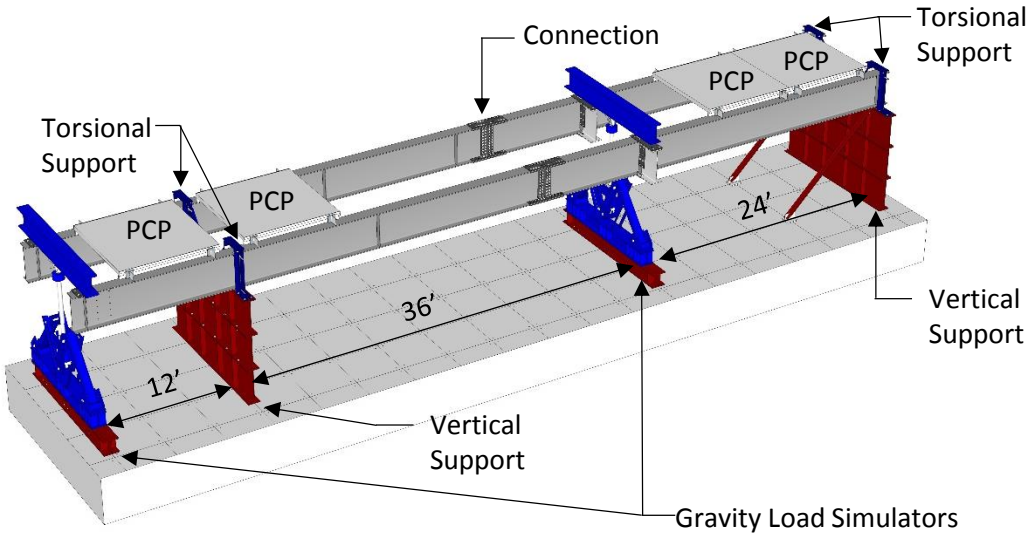

Figure 5.3 Bending & Torsion Test Setup – Overhang

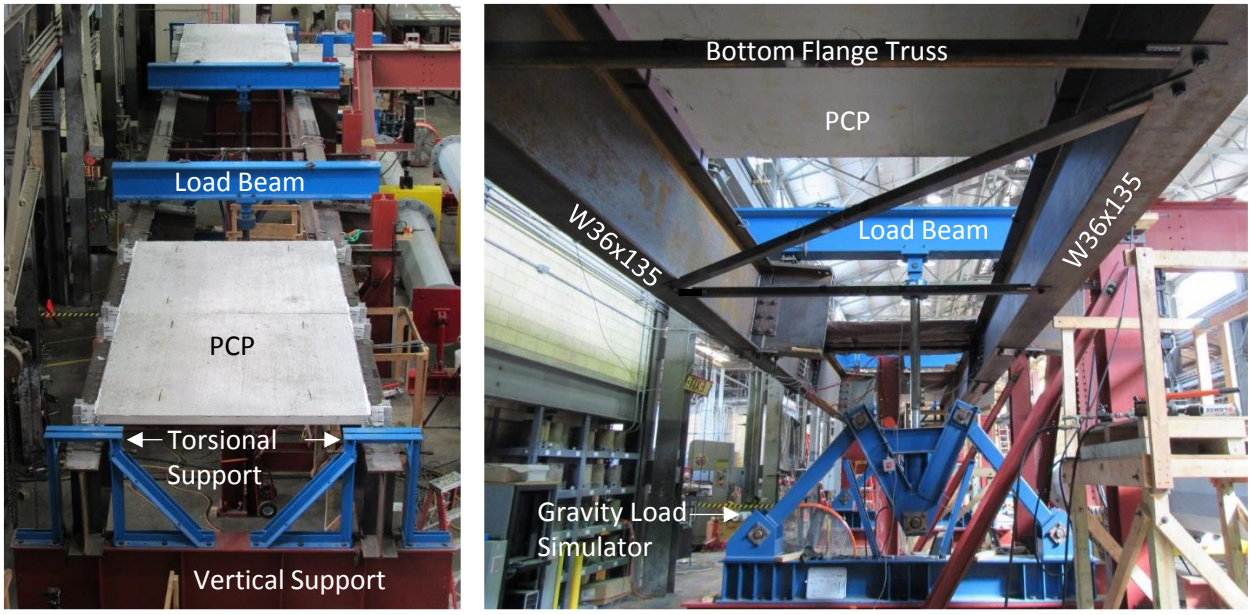

Figure 5.4 Twin I-Girder Experimental Test Setup

5.2 Specimen Fabrication

Two hot-rolled, ASTM 992 W36x135 beams were used for the girders in the setup (results from the tension coupon tests for the W36x135 can be found in Appendix B). The W36x135 cross-section was chosen since it is the lightest and most slender of the standard W36 hot-rolled sections. A clear span of 72 ft was used for the simply supported case (L/D = 24) while a back span of 60′ (L/D = 20) and an overhang of 12′ was used for the overhanging case. The ends of the girders extended 1′-0″ over the top of each support and full depth stiffeners (5/8″ thick by 5″ wide) were welded to the girders at the support locations. The girders were spaced at 8′-8″ on center to accommodate the placement of the 8′-0″ wide PCPs that spanned 8′-3″ between girders (the same dimensions as the PCPs used in Chapter 4). The 12″ wide flange of the W36x135 allowed the PCPs to overlap each flange by 3½″ to accommodate a maximum bedding strip width of 2″ while leaving a 1½″ space for concrete to flow under the panels per the TXDOT standard (see Figure 5.5). Connection detail A.1.MAX (see Chapter 4) was used for the twin I-girder tests since this detail had the lowest stiffness and strength and would therefore provide a lower bound for the results from the other details. To avoid interference with the torsional supports, the edge of the PCP was offset 1′-0″ from the centerline of the vertical supports.

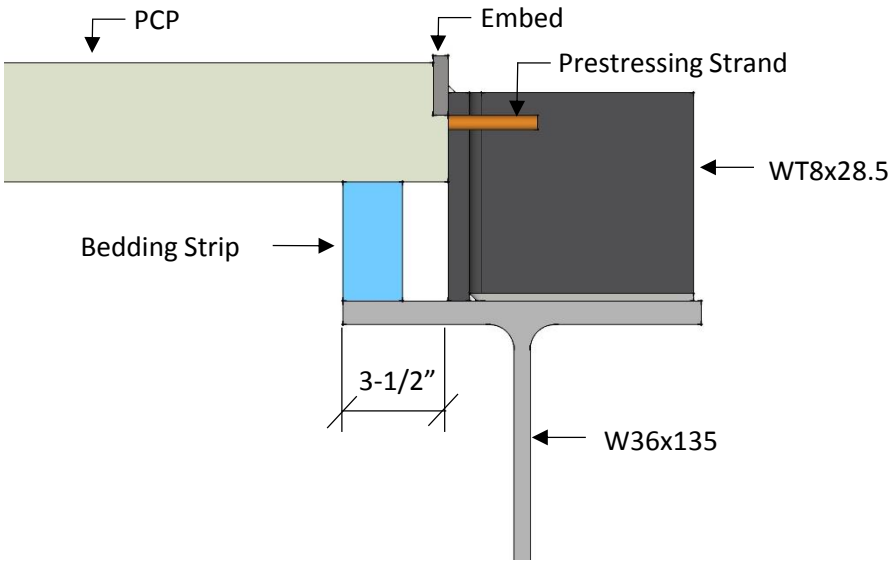

Figure 5.5 PCP to I-Girder Connection

The W36x135 sections were only readily available in lengths of 40′. Therefore, it was required to splice the girders (see Figure 5.6) to obtain the desired span of 72′-0″. To avoid interference with the gravity load simulator (GLS) and the PCPs, the splice was offset 3′-0″ from midspan of the girders in the simply supported configuration. Since the primary purpose of these tests was to simulate the construction condition, all of the tests were conducted in the elastic range of the girders (with the exception of the final test). Therefore, the splice was conservatively designed for 75 percent of the plastic moment capacity of the beam for bending and for 50 percent of the maximum total uniform load for shear. To ensure no relative movement of the girders at the splice, the connection was designed and constructed to be slip critical with a Class A Faying Surface. A490 1″ diameter bolts in double shear were used throughout the connection and were pretensioned using a pneumatic torque wrench. A Skidmore-Wilhelm bolt tension calibrator was used to ensure that the pneumatic torque wrench was capable of achieving the minimum bolt pretension load of 64 kips.

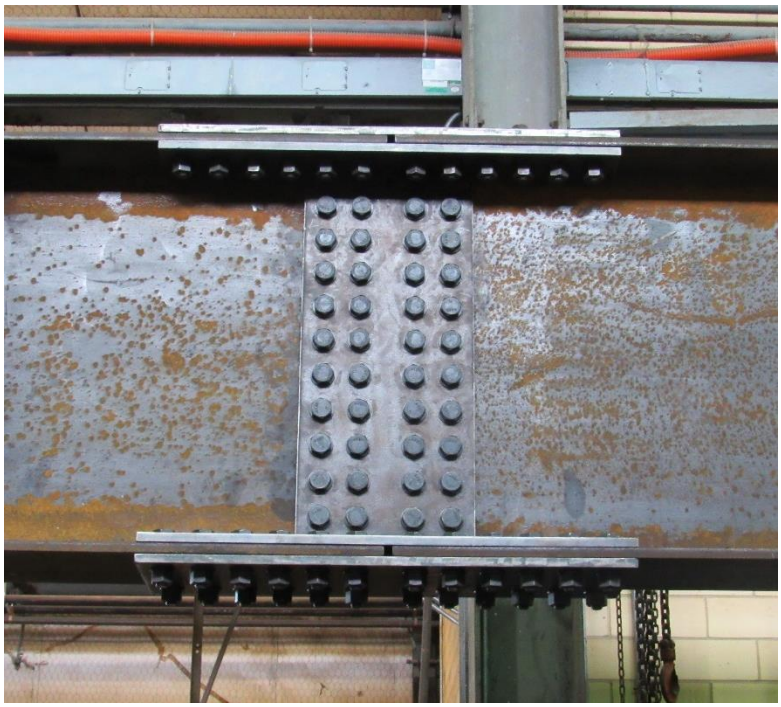

Figure 5.6 I-Girder Splice Connection

A removable single diagonal cross-frame (See Figure 5.7) was fabricated so that the unbraced length of the girders could be halved and the interaction of the PCPs and the cross-frame could be investigated. Also, a removable bottom-flange lateral truss (See Figure 5.8) was fabricated to engage the warping stiffness of the bottom flange. The cross-frame and the bottom flange truss members were constructed of HSS 2½x 2½x¼ sections with the diagonals oriented so that they were always in tension. The HSS section was used to minimize connection eccentricity so that the axial stiffness of the members could be used without reduction in the finite element model validation. A490 1″ diameter slip critical bolts were used to connect both the cross-frame and the bottom-flange truss to the I-girders.

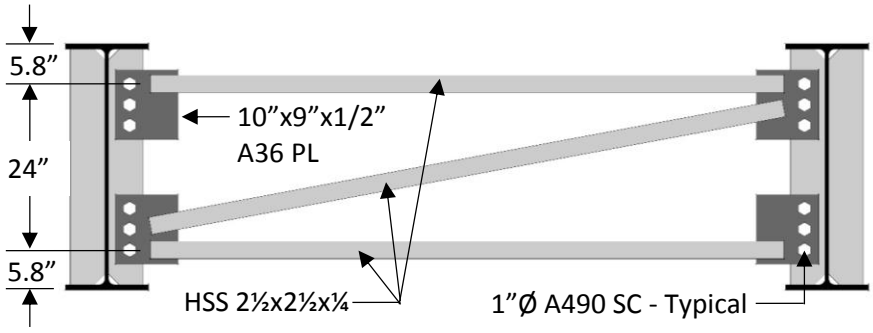

Figure 5.7 Midspan Cross-Frame

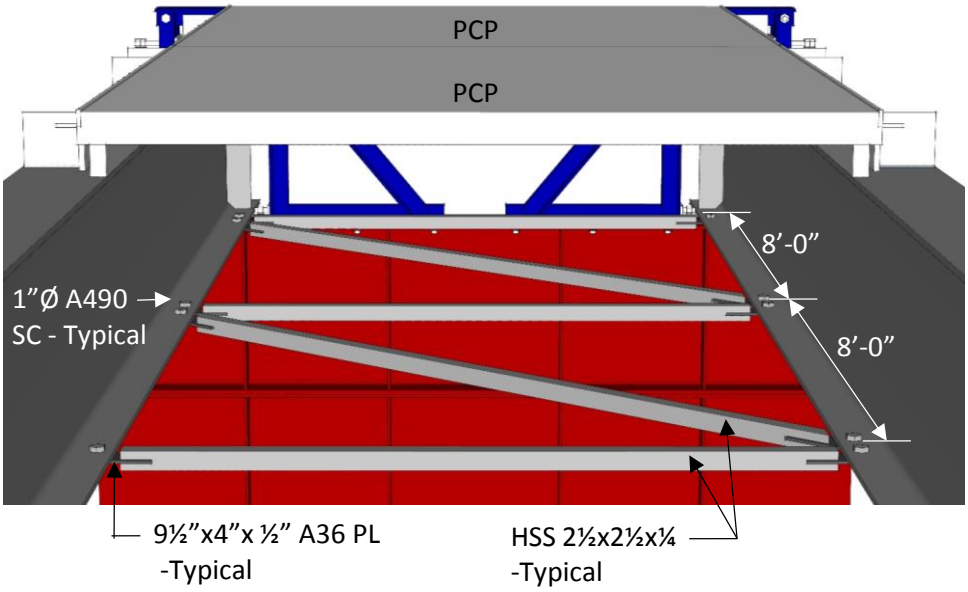

Figure 5.8 Bottom Flange Lateral Truss

The PCPs for the twin I-girder test used the same concrete mix as those tested on the shear frame. Two batches of concrete were used when the 8 PCPs were cast and cylinders from each batch were cast on-site. All cylinders were cured according to the standards outlined in ASTM C31. After curing for 28 days, the compressive strength, modulus of elasticity, and split cylinder tests were performed according to the ASTM C39, ASTM 469, and ASTM 496 guidelines, respectively. The results of the material tests are shown in Table 5.1. The values of the material tests closely matched each other (within 3%) and closely matched those from the shear frame test (within 4%) reported in Chapter 4.

Table 5.1 Results from Concrete Material Tests

Concrete Batch 1		Concrete Batch 2	
f'_c	8850 psi	f'_c	8690 psi
E	5070 ksi	E	5080 ksi
f_t	607 psi	f_t	622 psi

5.3 Boundary Conditions

Figure 5.9 shows an elevation of the twin-girder vertical and torsional support system. The two vertical supports for the twin-girder system each consisted of three W36x135 support beams stacked vertically and bolted to one another. A 9′-0″ tall vertical support was required to elevate the twin I-girders (and tub girder discussed in Chapter 6) so that they would not interfere with the gravity load simulators (discussed in detail below). The bottom of each vertical support was anchored with twelve 1″ diameter B7 threaded rods to the strong floor. To resist web compression buckling from the concentrated loads, full depth stiffeners (5″ wide x ½″ thick) were welded on both sides of the web in all of the support beams below the reaction points of the twin I-girders. This allowed the supports to be conservatively designed as columns cantilevering from the strong

floor with a cruciform cross-section. To ensure global stability of the system, two double-angle braces were connected to the south vertical support wall at a point 8′-0″ high on the support to the strong floor at a 45 degree angle.

Figure 5.9 Twin I-Girder Support System

The system that was created to prevent lateral movement and twist of the girder while minimizing the warping restraint of the girder flanges is shown in Figure 5.10. The top and bottom flanges of the girders were laterally supported on both sides by 1″ diameter threaded rods connected to a truss system that is bolted to the vertical support. Bearing plates were welded to the top and bottom of the flanges at the location of the threaded rods to prevent overturning of the girder if a threaded rod slips off of the edge of the flange. To minimize the warping restraint resulting from friction, thrust bearings were placed between the bottom of the girders and the top of the vertical support. In addition the threaded rods used to prevent twist had the ends rounded to minimize warping restraint.

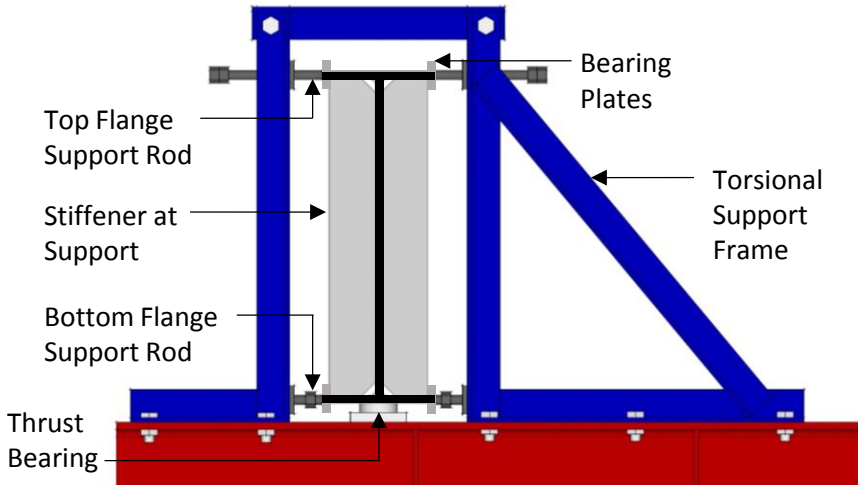

Figure 5.10 Twin I-Girder Torsional Support System

5.4 Load Application

The twin I-girder system was loaded independently with two different systems: lateral load at the top flange and vertical load at the top flange via the gravity load simulators. Both load application systems are described in detail below.

5.4.1 Application of Lateral Loads

To test the system's lateral stiffness, three lateral load frames were assembled on the west side of the structure (see Figure 5.1) and threaded rod assemblies were used to transfer lateral force from the hydraulic actuator to the top flange of the girders (see Figure 5.11). The applied load was measured by calibrated load cells located between the hydraulic actuator and the web of the load frame's column. Forces were applied independently at midspan and approximately at the third points (20 ft from each end) for the simply supported case, creating multiple loading scenarios to validate finite element models. The PCPs were attached to the top flange near the supports at each end and the behavior of the system was observed for the cases without PCPs, with 2 PCPs (one at each end), and with 4 PCPs (two at each end).

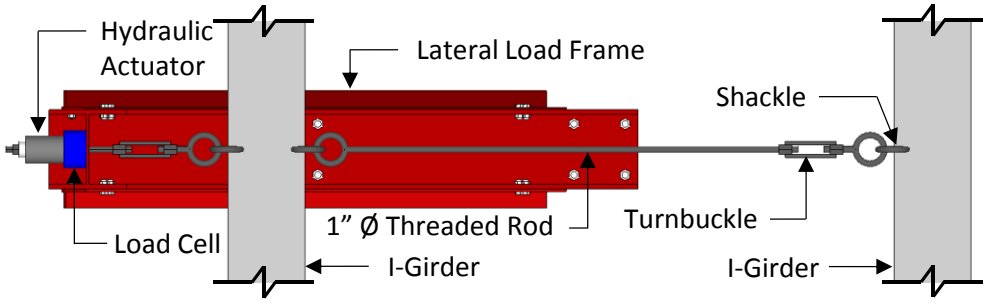

Figure 5.11 Twin I-Girder Lateral Load System - Plan View

5.4.2 Combined Bending and Torsion Loads via Gravity Load Simulator

Two identical gravity load simulators (GLS) designed and constructed by Wongjeeraphat (2011) were used to apply the bending and torsion loads to the twin I-girder system (see Figure 5.12). Gravity load simulators, first proposed by Yarimci et al. (1966), allow the applied load to remain vertical as the test specimens displace laterally and twist. The mechanism of the GLS frame minimizes the lateral restraint at the load point through the use of needle roller bearings, preventing the load point from behaving as a brace point. Each GLS could apply a maximum vertical force of 160 kips to the system while accommodating a maximum lateral displacement of 6 inches. The GLS shown in Figure 5.12 has 5 pins and is unstable when no load is applied via the hydraulic actuator. Thus, two adjustable struts (not shown) are used to support the GLS when no load is applied to the system. Once a minimum load level of approximately 500 lbs was applied to the system with the actuator, the GLS was stable and the adjustable struts could be disengaged.

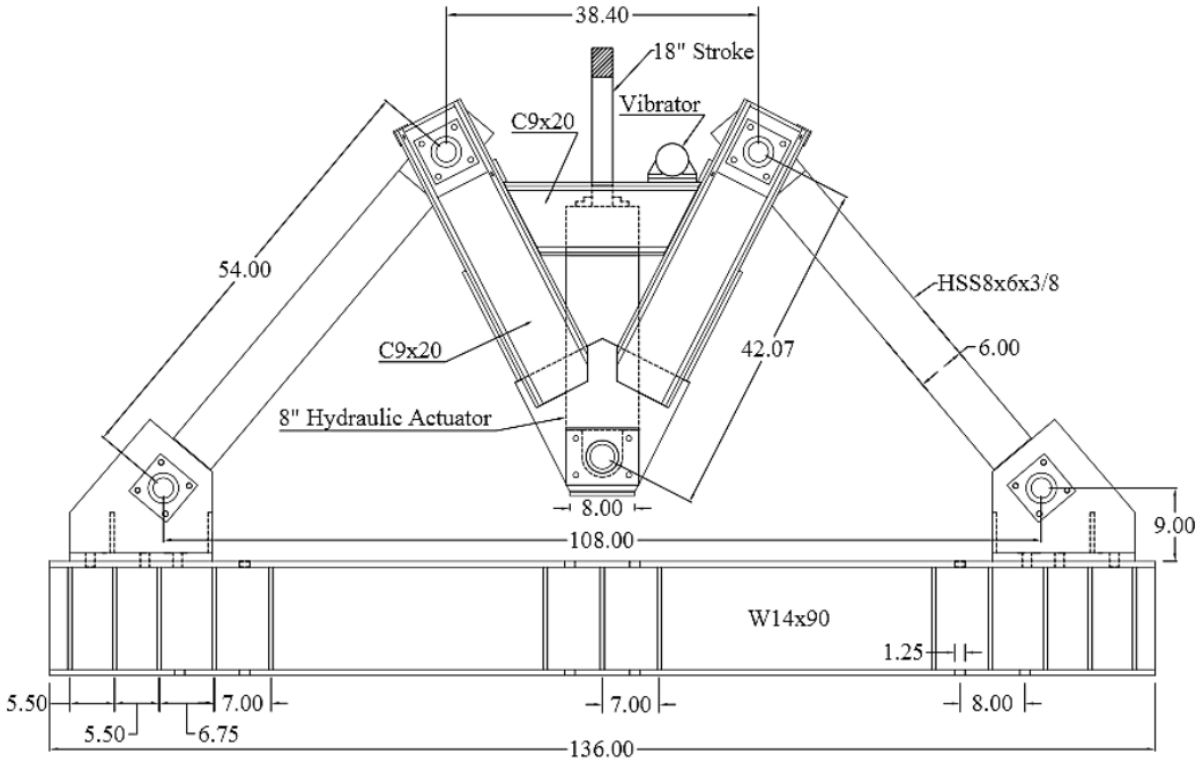

Figure 5.12 Gravity Load Simulator Geometry (Wongjeeraphat 2011)

The test-setup was constructed so that the applied load from the gravity load simulators could be offset from the shear center of the I-girders to vary the ratio of applied torque to bending moment on the system. Offset transfer beams were fabricated so that the gravity load simulators can be moved to accommodate the eccentric loading (see Figure 5.13). Holes were drilled in the top flanges of the offset transfer beams so that the GLS could be moved on and bolted to the beam in 4 inch increments (up to a maximum of 24 inches). Slotted holes 4 inches long were cut in the bottom of the flange of the offset transfer beam so that the beam could be moved on and bolted to

the strong floor at any spacing between 0 and 4 inches. Therefore, the GLS could be positioned eccentrically relative to the girders at any intermediate value between 0 and 24 inches.

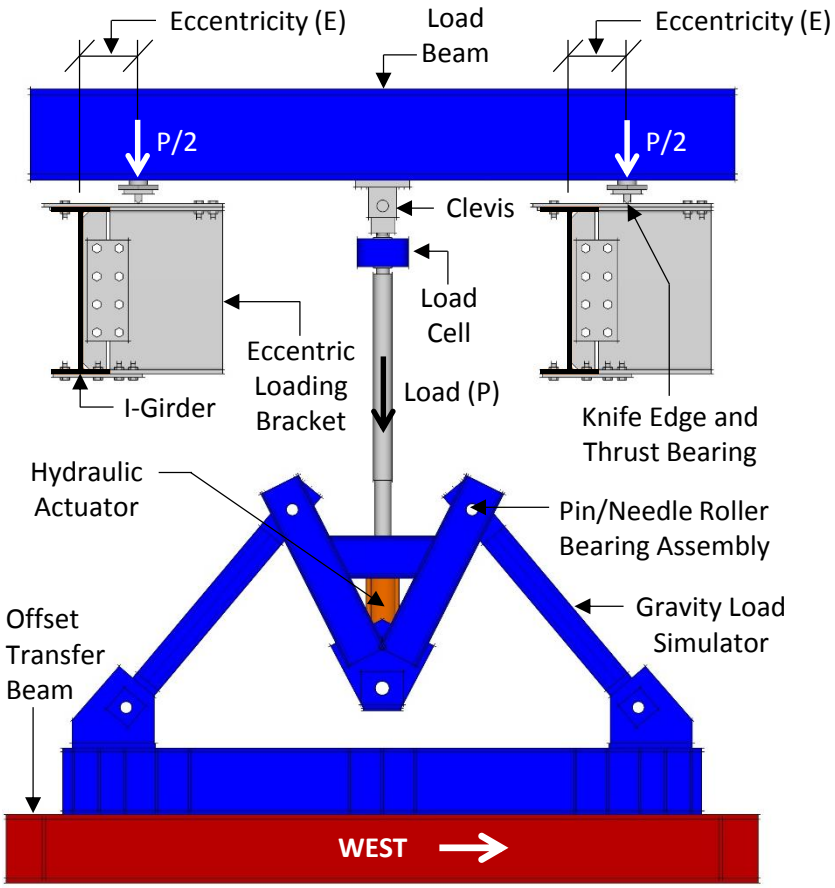

Figure 5.13 Gravity Load Simulator Applying Load to Twin I-Girders

Calibrated load cells with a 200 kip capacity were connected to the actuators in the GLS so that the load applied to the twin I-girder system could be monitored and recorded. Load from the actuator was transferred to the midpoint of the 12′-6″ long W18x143 load beam via a clevis. The load beam in turn transferred equal loads to the eccentric loading brackets via two knife edge and thrust bearing assemblies shown in Figure 5.14. Therefore, the torque applied to each girder by the GLS was equal to half of the load in each hydraulic actuator multiplied by the eccentricity of the knife edge. The knife edges were heat treated to increase the hardness and resist dulling of the edge during loading. The thrust bearings were used to keep the knife edge from constraining the warping deformation of the top flange of the I-girders (the bolts were loosened during the tests). The eccentric loading brackets were constructed by connecting 2′-0″ long sections of a W36x135 to the I-girders as shown in Figure 5.15. A 5″ wide by 5/8″ thick full depth stiffener was welded to the I-girders at the location of the eccentric loading brackets so that the shear force could be transferred from the bracket to the girders. The eccentric loading brackets were conservatively designed to withstand the maximum load applied by the gravity load simulators.

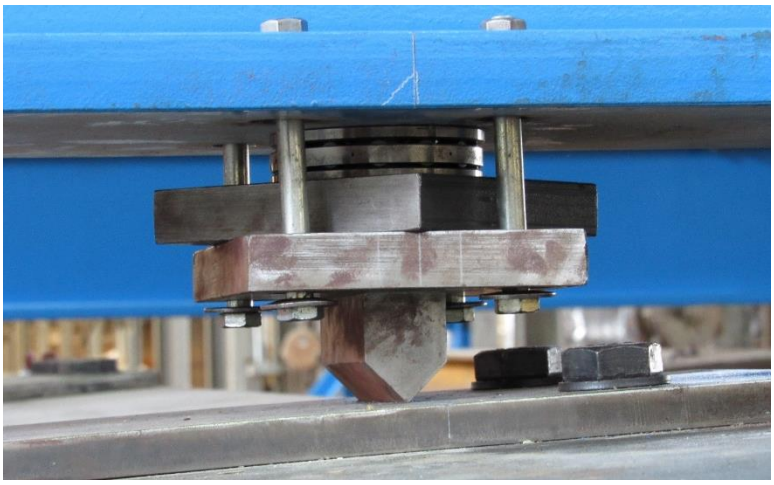

Figure 5.14 Knife Edge and Thrust Bearing Assembly

Figure 5.15 Eccentric Loading Brackets

The deformed shape of the I-girders as the GLS load is applied to the system is shown in Figure 5.16. To accommodate lateral deflection of the top flange of the I-girders (Δ_z) to the right, the left strut of the GLS rotates downward while the right strut of the GLS rotates upward, allowing the hydraulic actuator to always remain vertical. The increased hardness from the heat treatment allowed the knife edge to dig into the softer steel of the eccentric loading bracket, keeping the knife edge from slipping on the loading bracket as the girders twisted (θ). For all experimental tests, west is the positive direction for the lateral deformation and the twist is considered positive when top flange has a larger lateral deformation to the west than the bottom flange (as shown in Figure 5.16).

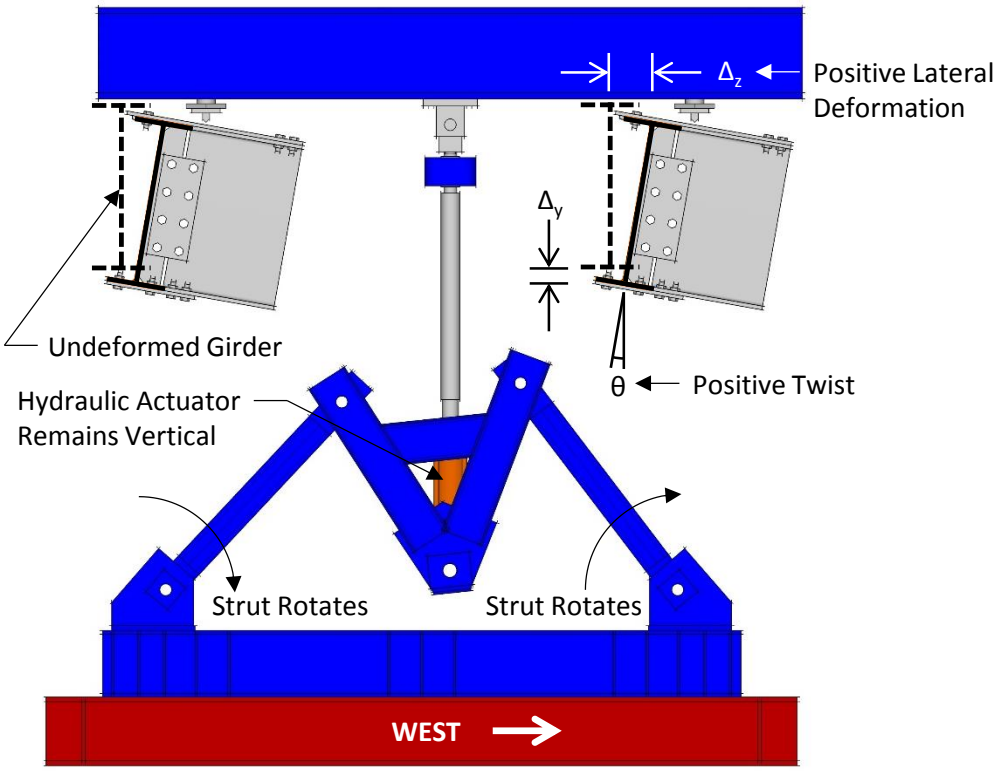

Figure 5.16 Deformation of Twin I-Girders under GLS Load

5.4.3 Bending and Torsion Diagrams for Curved Girders vs Straight Girders

Closed formed equations for moment and torque diagrams have been derived for curved steel box girders with uniform loads by Helwig et al. (2007), but the derivation of these equations assume no cross-sectional distortion and negligible warping torsion. In general, these assumptions are satisfactory for tub girders with adequate bracing (allowing them to act as closed sections), but are invalid for open sections where significant torsional warping occurs. Therefore, Abaqus 6.14 was used to compare the torque and moment diagrams of curved I-girders with uniform load vs straight I-girders loaded eccentrically. The B32OS (3-node quadratic open-section beam in space) finite element was used to model the W36x135 since it specifically includes the warping effects of open, thin-walled sections like I-girders.

Figure 5.17 shows a comparison of the torque and moment diagrams for a 72 ft long simply supported straight W36x135 girder with 12″ eccentric 10 kip point loads at third points versus a 72 ft long simply supported curved W36x135 girder with a radius of curvature of 600 ft and a uniform load of 0.385 kip/ft. While the shape of the torque diagrams slightly differ between the two models, the maximum torque at the ends of the girders and the area under the torque diagram are approximately the same. Also, the moment diagrams closely match. Therefore, the straight girder with eccentric point loads proves to be a reasonable approximation of curved girders with uniform loads. Increasing the radius of curvature from 600 ft to 1200 ft and reducing the eccentricity of the point loads from 12″ to 6″ reduced the magnitude of the torque by a factor of two, but had no effect on the shape of the torque or moment diagrams.

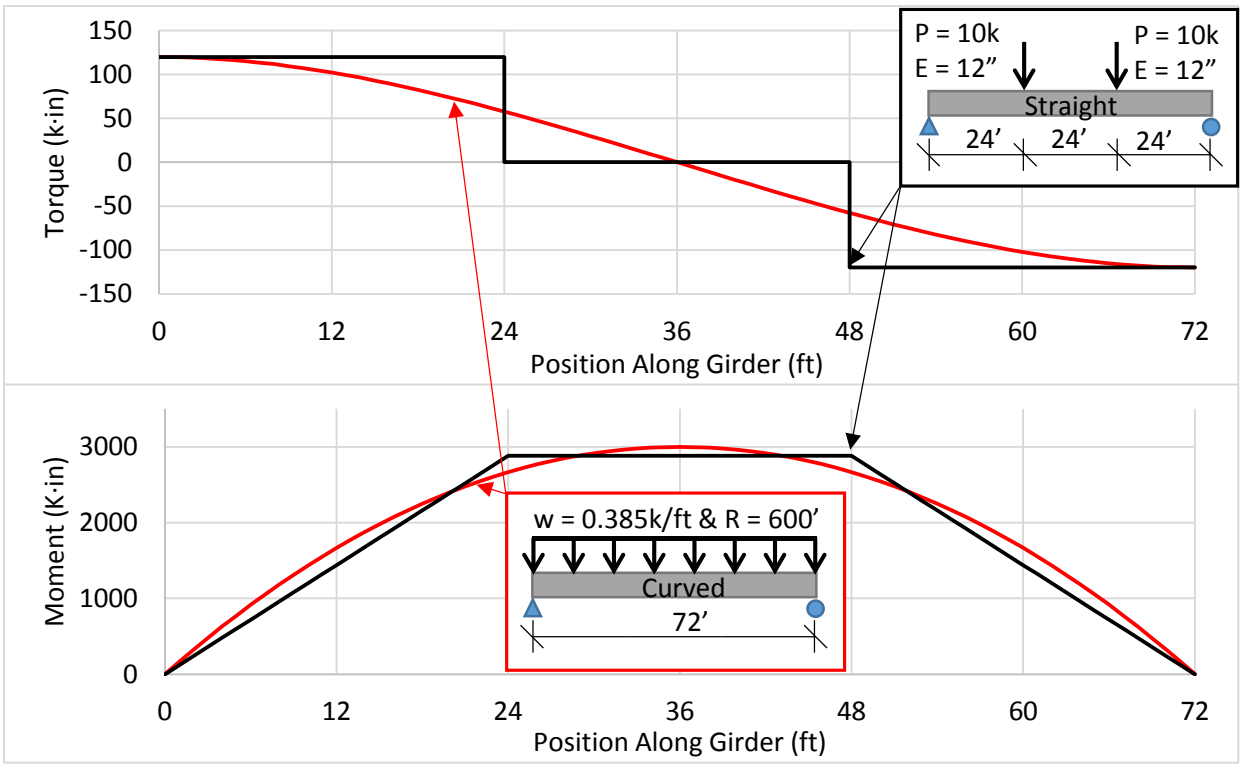

Figure 5.17 Moment & Torque Diagrams for Curved and Straight Simply Supported Girders

While curved I-girders are commonly used in continuous span systems, it was not feasible to test a continuous span system in the laboratory with reasonable span-to-depth ratios due to space limitations. Therefore, the boundary conditions of the simple span system was modified to accommodate an overhanging case so that bracing of PCPs in the negative moment region could be investigated. Figure 5.18 shows a comparison of the torque and moment diagrams from Abaqus 6.14 for a continuous curved I-girder loaded in one span vs an overhanging I-girder with eccentric loads. Similar to the simply supported case, increasing the radius of curvature by a factor of two (from 600 ft to 1200 ft) and decreasing the magnitude of the eccentricity on the straight girder by a factor of two (from -4 in to -2 in and from 8 in to 4 in) decreased the magnitude of the torsion by a factor of two, but did not significantly affect the shape of the torque and moment diagrams.

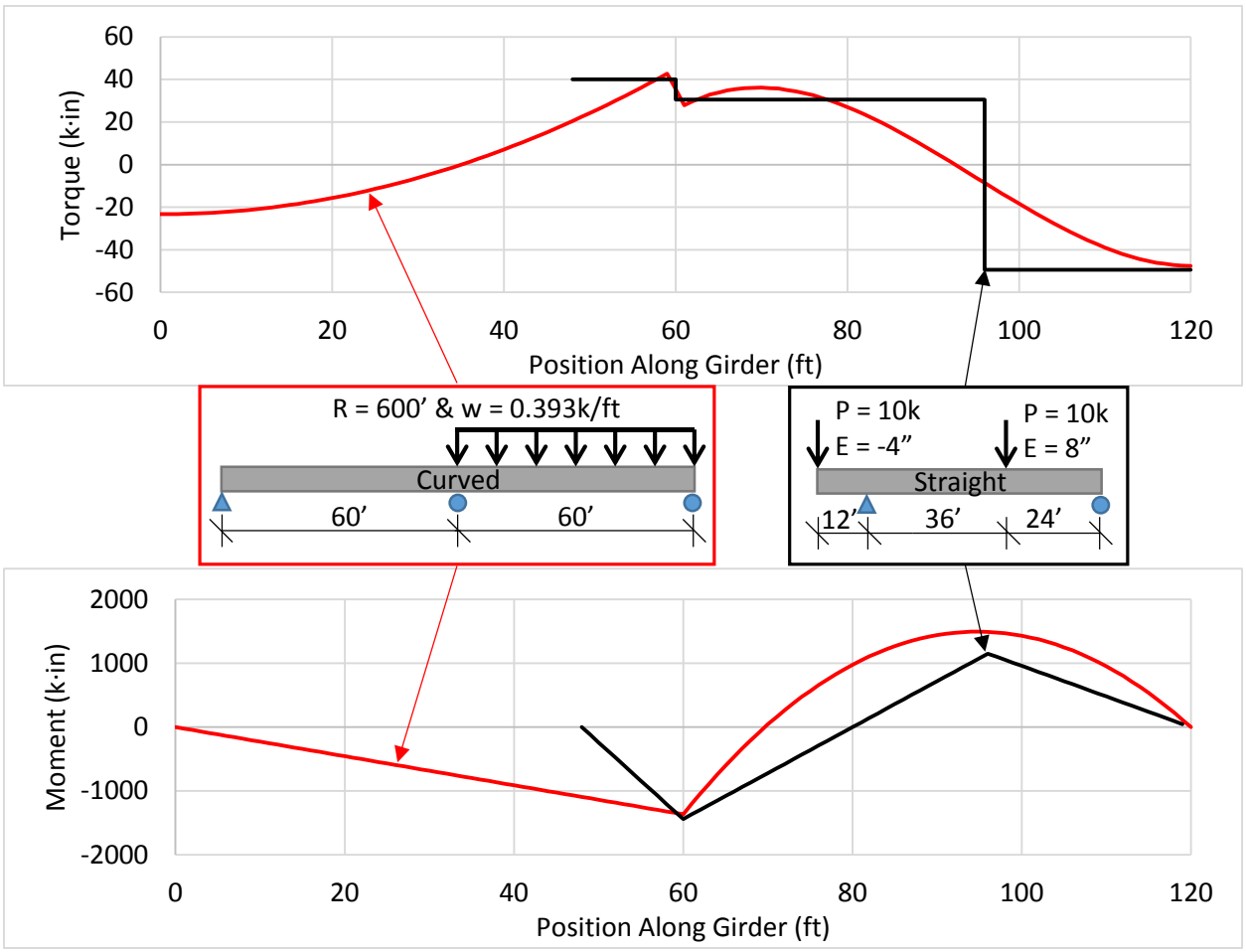

Figure 5.18 Moment & Torque Diagrams for Curved Continuous Girders and a Straight Overhanging Girders

5.5 Instrumentation

Load cells, strain gauges, linear potentiometers (L-pots), and vision systems were all used to gather data during the tests. All load cells and linear potentiometers were calibrated to ensure the accuracy of the measurements. Figure 5.19 shows the instrumentation plan for the simply supported system, while Figure 5.20 shows the instrumentation plan for the overhanging system. The strain gauges on the I-girders were paced at the four flange edges to measure the maximum strain at the given cross-section so that the test could be stopped prior to the girder reaching the inelastic range. Two strain gauges (one on top and one on bottom) were placed at the center of each HSS2x2x¼ member of the midspan cross-frame so that the axial force in each member could be calculated. Two L-pots (spaced 10 in apart vertically) were attached to the indicated lateral load frames with the plungers reacting against a piece of smooth plexiglass glued to the web of the west I-girder (to keep the plungers of the L-pots from bending as the girders deflected vertically), allowing the rotation of the girder to be calculated. The two PCPs on the north end of the setup were instrumented in the same manner as the PCPs in the shear frame setup that Chapter 4 describes.

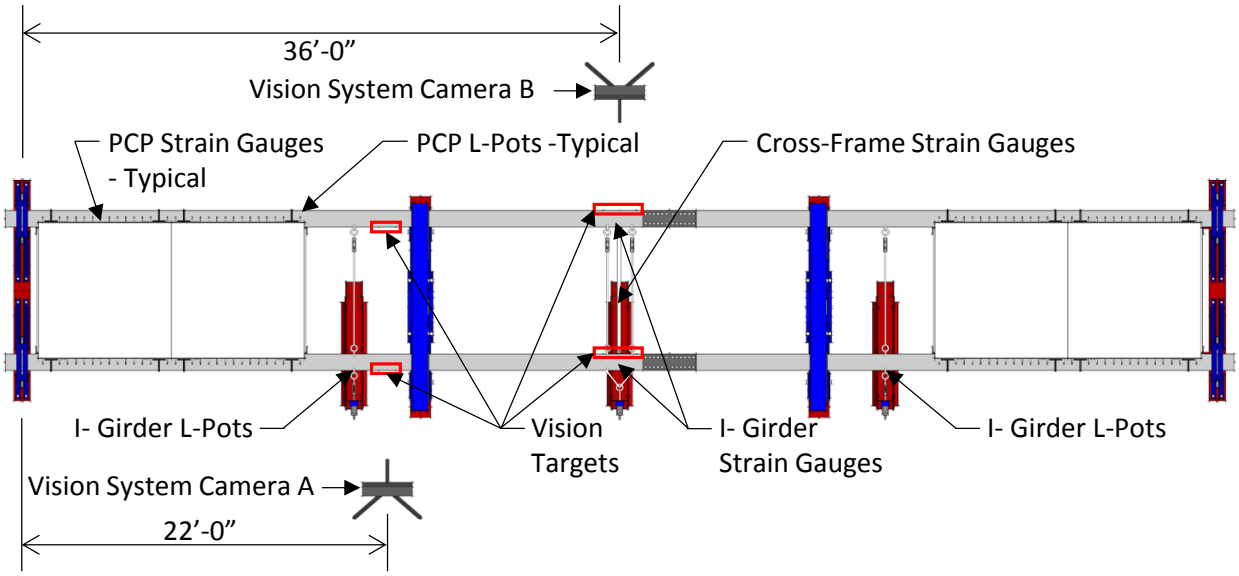

Figure 5.19 Instrumentation Plan for Simply Supported System – Plan View

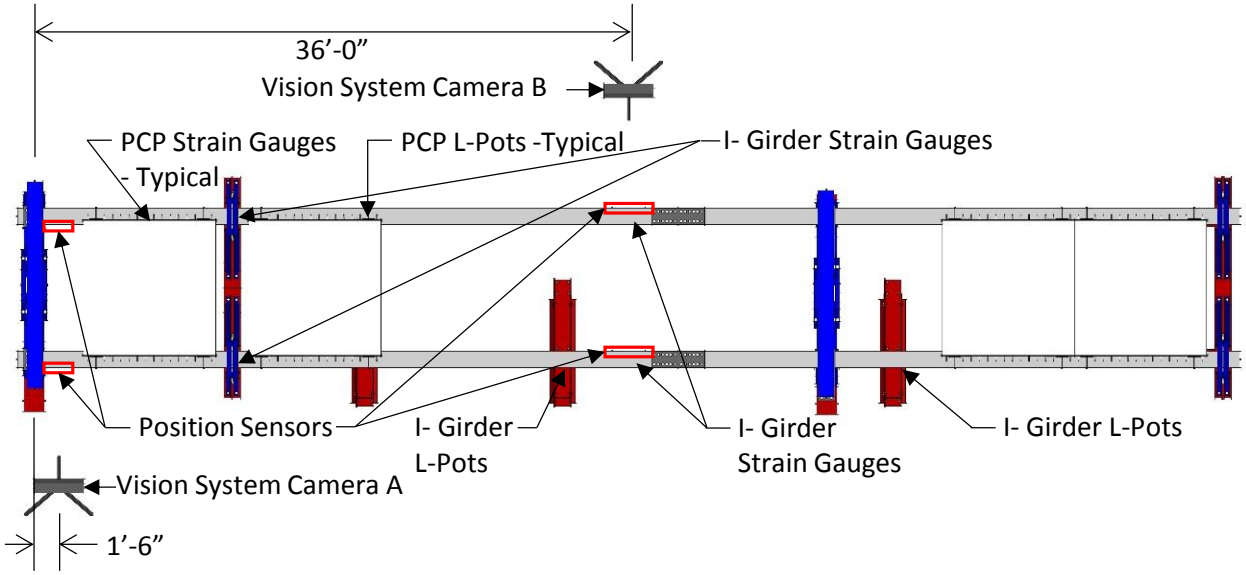

Figure 5.20 Instrumentation Plan for Overhang System – Plan View

5.5.1 Vision System Measurements

Two NDI Optotrack Certus HD vision systems were used to measure the deformation of the girders at the points indicated in Figure 5.19 and Figure 5.20. This system used a camera with three lenses to measure the three dimensional movement of positions sensors attached to the girder. This non-contact tracking method has exceptional accuracy (up to 0.004 in) and was convenient for measuring the displacement of the I-girder as it deflected vertically, horizontally, and twisted. The measurement volume of each camera was large enough to allow position sensors on both girders to be captured with one camera (see Figure 5.21). For redundancy, two columns of position sensors were attached to each girder with a sensor located at the edge of the top and bottom flange

and 5 sensors located on the web in each column. Intense direct sunlight can cause the vision systems to lose track of the markers and so a tarp draped over the top flange was used to shade the position sensors.

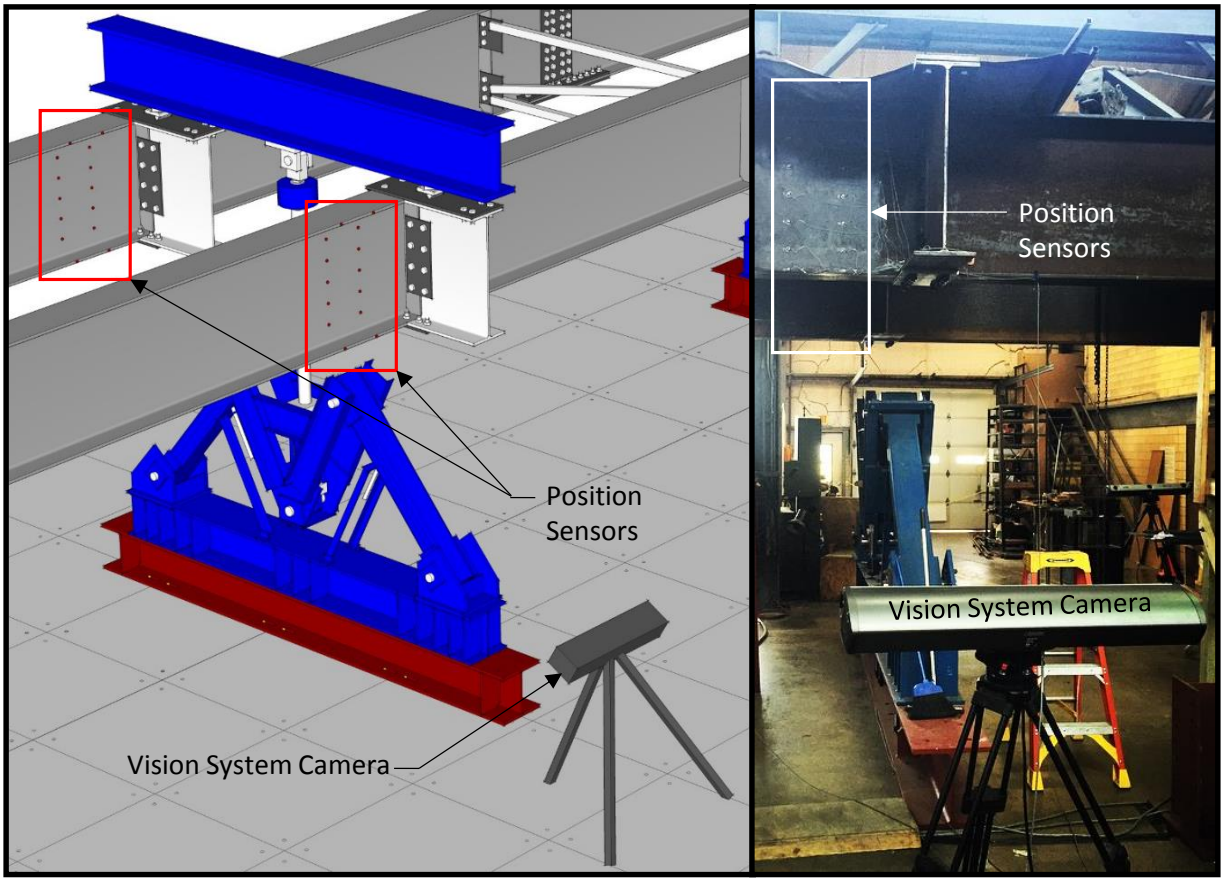

Figure 5.21 NDI Optotrack Certus HD Vision System

To establish a stationary coordinate system for the vision system data, three position sensors were attached to a channel section that was connected a column that cantilevered from the strong floor (see Figure 5.22). A level and a taut piano wire strung parallel to the girders between the vertical supports was used to align the coordinate system with the I-girders. To sync the displacement data from the vision system with the load cell data (as both data collection system are not compatible and have different read rates), a position sensor was attached to an L-pot. At each load step, a string attached to the L-pot was simply pulled.

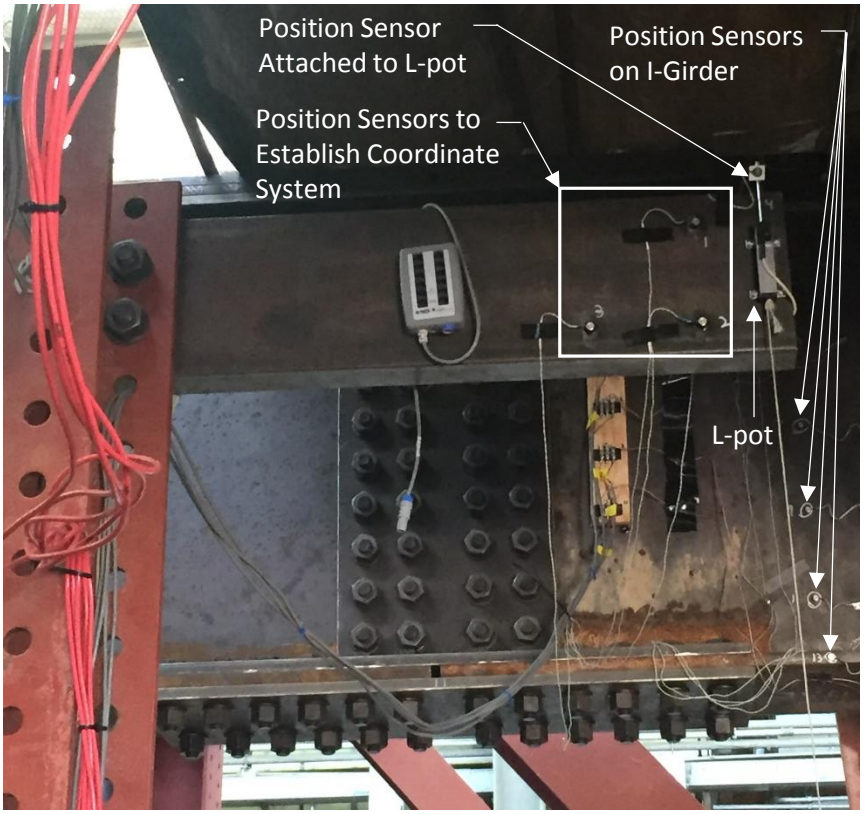

Figure 5.22 Position Sensors to Establish Coordinate System

5.5.2 Initial Imperfection Measurements

The initial imperfections of both girders were measured prior to each load test (even though it was expected that the large eccentric loads would dominate the behavior of the system). A taut piano wire was strung at an equal distance (d_{SUP}) between the edge of the flange at each support. The deviations from the wire at the bottom flange (d_{BF}) were measured directly with calipers while a plumb bob and calipers were used to measure the deviations from the wire at the top flange (d_{TF}). Measurements were conducted at 8 ft increments along the length of the girders. Figure 5.23 shows how the lateral imperfection of the bottom flange (Δ_{BF}), the lateral imperfection of the top flange (Δ_{TF}), and rotation of the girder (θ_G) can be calculated from measurements. Graphs of the initial imperfections for the concentrically load cases can be found in Appendix B (west is the positive direction for the initial imperfections).

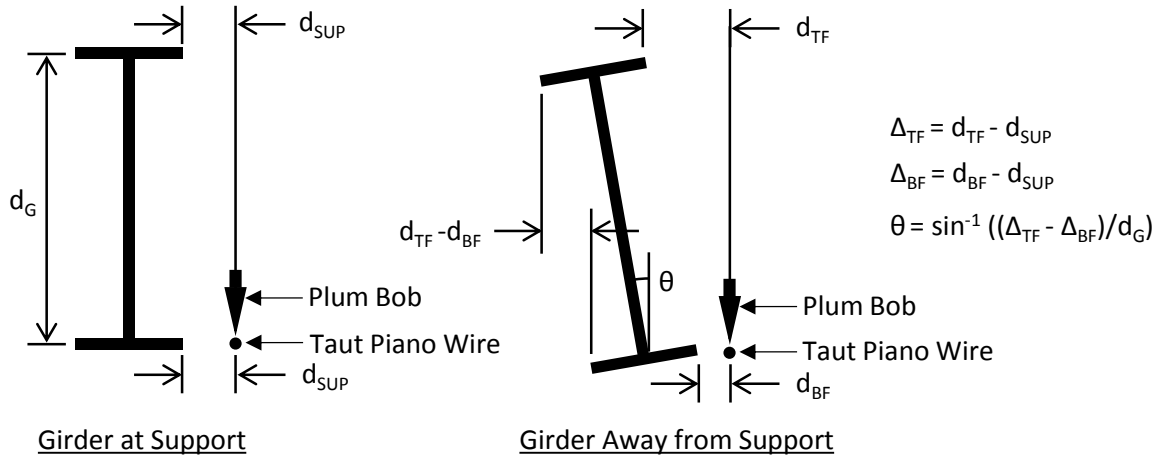

Figure 5.23 Initial Imperfection Measurements and Calculations

5.6 Testing Procedure

While the testing procedure varied slightly between the lateral load test and the GLS tests, the more complicated procedure for the GLS test is explained in detail below. To ensure consistent results, all tests were performed twice and the data was compared.

1. Move GLS to desired eccentricity
2. Measure I-girders' initial imperfections
3. Ensure bolts for knife edges are loose
4. Zero all load cells, L-pots, and strain gauges
5. Begin recording with data acquisition system and the vision systems
6. Apply GLS stabilizing load (500 lbs minimum) with each GLS
7. Disengage GLS adjustable struts so that the system can deflect laterally
8. Apply an incremental load
    a. Sync data recording systems by engaging L-pot with attached position sensor
    b. Mark cracks in PCPs, take applicable pictures, record notes, etc.
9. Repeat Step 8 until maximum load is reached
10. Close hydraulic needle valves then flip the hydraulic pump valve
11. Bleed hydraulic pressure with needle valves until GLS stabilizing load level is reached
12. Engage GLS adjustable struts to stabilize GLS
13. Bleed hydraulic pressure until no load remains on the system and take final readings

5.7 Experimental Results

A total of 12 lateral load tests and 27 gravity load tests were performed on the twin I-girder system at the Ferguson Structural Engineering Laboratory. Results from these test are explained in detail below.

5.7.1 Lateral Load Experimental Results – Simply Supported System

Table 5.2 provides a summary of the 12 lateral load tests that were performed in the laboratory. The nomenclature for the lateral load tests is shown in Figure 5.24. For the lateral tests,

the top flange of the girder was loaded at midspan and at quarter points independently with and without the centerline cross-frame installed. Additionally, the total number of PCPs attached to the girders was varied (0 PCPs, 2 PCPs, and 4 PCPs). A maximum point load of 3.5 kips was applied at each lateral load frame. While graphs for a few of the tests are shown in this section of the report, Appendix B contains graphs showing both the top flange lateral deflection and the twist at third points and midspan for all 12 tests in addition to graphs for the of the cross-frame diagonal forces.

Table 5.2 Summary of Lateral I-Girder Tests

Test Name	Load Location	Cross Frame	Number of PCPS
LAT.1	MS	-	0
LAT.2	MS	-	2
LAT.3	MS	-	4
LAT.4	MS	XF	0
LAT.5	MS	XF	2
LAT.6	MS	XF	4
LAT.7	QP	-	0
LAT.8	QP	-	2
LAT.9	QP	-	4
LAT.10	QP	XF	0
LAT.11	QP	XF	2
LAT.12	QP	XF	4

Key: LAT = Top Flange Lateral Load XF = Cross-Frame
MS = Midspan Load, QP = Quarter Point Load

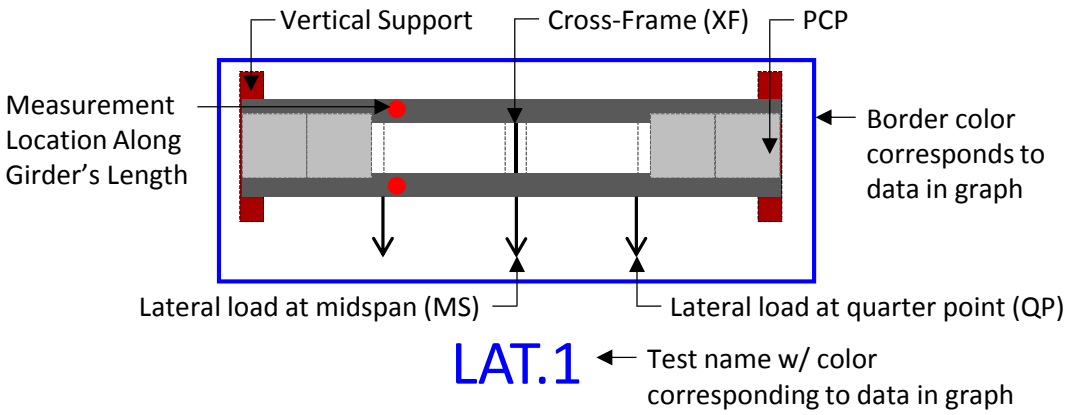

Figure 5.24 Nomenclature for Documentation of Lateral Load I-Girder Tests

The results from the lateral loading test showed that connecting PCPs to the top flange of the I-girders (thereby providing warping restraint to the top flange) significantly reduced the lateral deflection for both cases with and without the cross-frame installed at midspan (see Figure 5.25 and Figure 5.26, respectively). At a total lateral load of 7 kips without the cross-frame installed,

lateral deflection of the girders at the third point reduced from 5.47 in to 0.75 in to 0.24 in for 0 PCPs, 2 PCPs, and 4 PCPs, respectively. Similarly, at a total lateral load of 7 kips with the cross-frame installed, the lateral deflection of the girders at the third point reduced from 4.13 in to 0.69 in to 0.22 in for 0 PCPs, 2 PCPs, and 4 PCPs, respectively. Therefore, addition of 2 PCPs was much more effective at reducing the lateral deformation of the top flange (5.47 in to 0.75 in) than adding a cross-frame at midspan (5.47 in to 4.13 in). Similar results were achieved when the lateral load was applied at midspan and are shown in Appendix B. For completeness, Table 5.3 shows the maximum lateral deflection of the top and bottom flanges for both girders at third points and at midspan for all 12 tests.

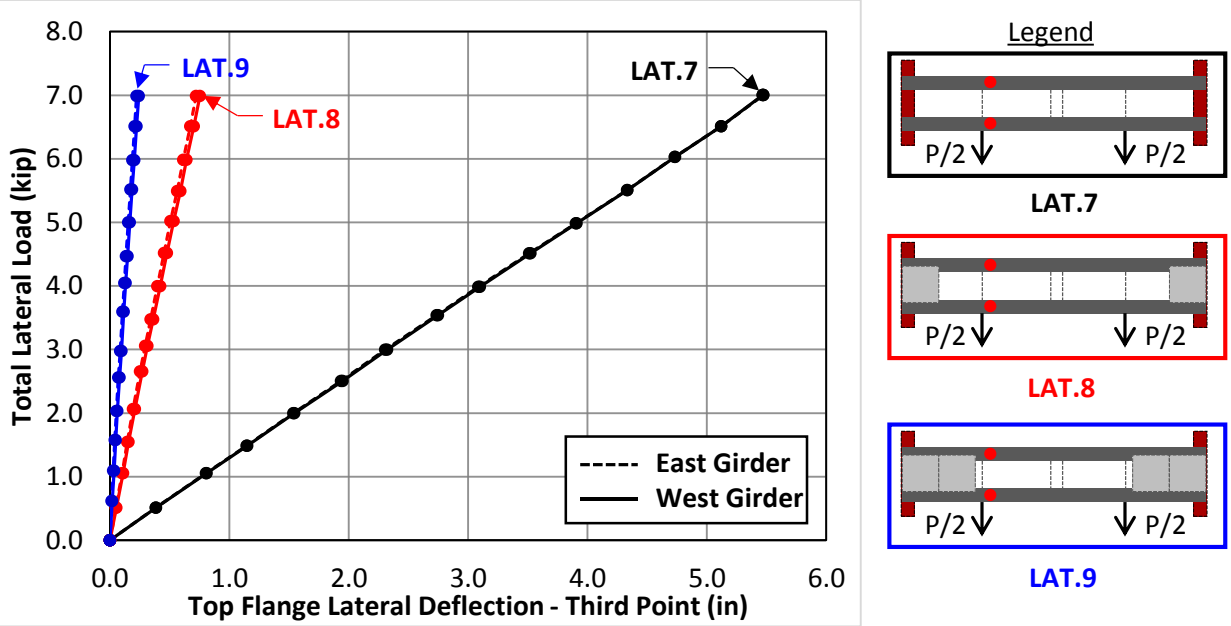

Figure 5.25 Lateral Deflection @ Third Point vs. Lateral Load @ Quarter Points (w/o XF)

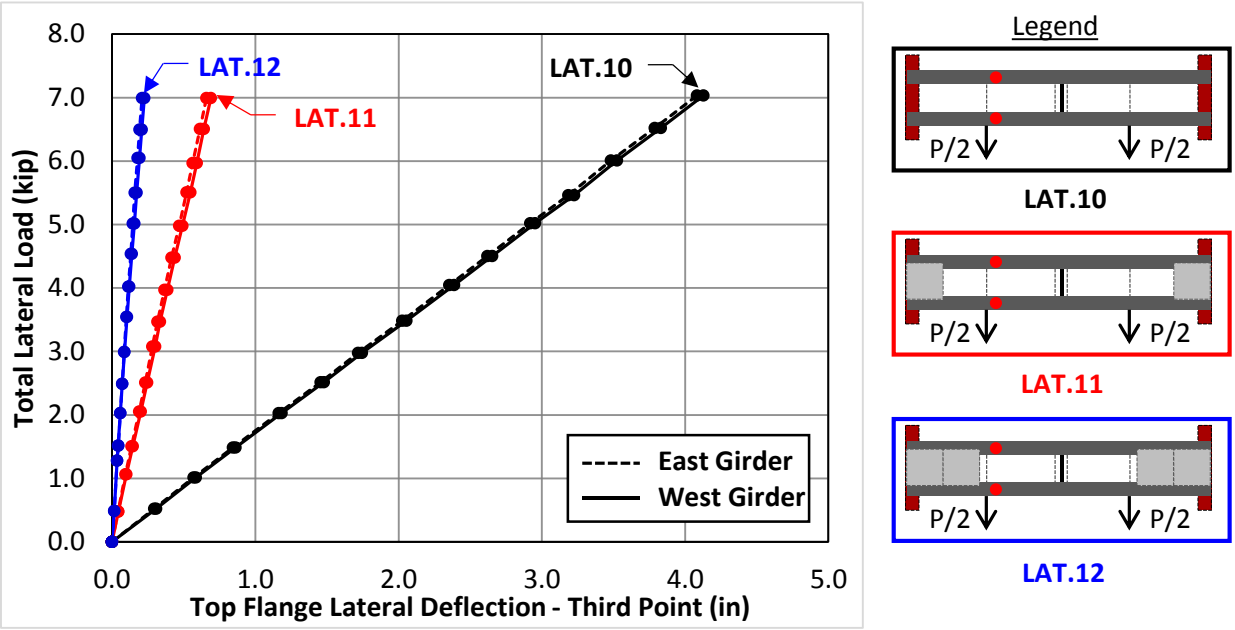

Figure 5.26 Lateral Deflection @ Third Point vs. Lateral Load @ Quarter Points (w/ XF)

Table 5.3 Maximum Lateral Flange Deflections during Lateral Tests

Test Name	Load (kip)	$\Delta_{TF.WG.M}$ (in)	$\Delta_{BF.WG.M}$ (in)	$\Delta_{TF.EG.M}$ (in)	$\Delta_{BF.EG.M}$ (in)	$\Delta_{TF.WG.TP}$ (in)	$\Delta_{BF.WG.TP}$ (in)	$\Delta_{TF.EG.TP}$ (in)	$\Delta_{BF.EG.TP}$ (in)
LAT.1.MS.0PCP	3.5	4.37	2.83	4.31	2.79	3.47	2.28	3.48	2.26
LAT.2.MS.2PCP	3.5	0.91	0.59	0.88	0.55	0.53	0.43	0.53	0.41
LAT.3.MS.4PCP	3.5	0.44	0.29	0.42	0.27	0.18	0.20	0.19	0.20
LAT.4.MS.0PCP.XF	3.4	3.02	2.97	3.02	2.98	2.44	2.36	2.43	2.38
LAT.5.MS.2PCP.XF	3.5	0.80	0.82	0.80	0.82	0.49	0.61	0.49	0.61
LAT.6.MS.4PCP.XF	3.6	0.41	0.43	0.40	0.43	0.18	0.30	0.18	0.31
LAT.7.QP.0PCP	7.0	6.56	4.37	6.61	4.34	5.47	3.58	5.47	3.52
LAT.8.QP.2PCP	7.0	0.97	0.77	0.99	0.68	0.75	0.63	0.72	0.55
LAT.9.QP.4PCP	7.0	0.31	0.36	0.32	0.28	0.24	0.30	0.22	0.24
LAT.10.QP.0PCP.XF	7.0	4.79	4.70	4.79	4.71	4.13	3.80	4.08	3.80
LAT.11.QP.2PCP.XF	7.0	0.90	0.94	0.90	0.93	0.69	0.73	0.66	0.71
LAT.12.QP.4PCP.XF	7.0	0.30	0.34	0.30	0.35	0.22	0.28	0.21	0.28

Key: LAT = Top Flange Lateral Load, CL = Centerline Load, QP = Quarter Point Load, Δ = Lateral Deflection
TF = Top Flange, BF = Bottom Flange, WG = West Girder, EG = East Girder, M = Midspan, TP = Third Point

In addition to reducing the lateral deformation of the system, connecting PCPs to the system also reduced the twist of the I-girders. Table 5.4 shows the maximum twist (at centerline and at third points) of the I-girders during the lateral tests for both the east and west girders. In general, addition of the cross-frames and the PCPs to the system were both effective at reducing the twist of the girders. With the load applied at midspan, the connection of 4 PCPs reduced the midspan rotation from 2.54 deg to 0.25 deg whereas the addition of the cross-frame reduced the midspan rotation from 2.54 deg to 0.08 deg. For several case, the rotation of the girders is negative,

meaning that the bottom flange deflected laterally more than the top flange. Connecting the PCPs to the top flange likely caused the PCP and I-girder system to act as a channel section (where the PCPs acts as the webs and the two I-girders act as the flanges) raising the shear center above the elevation of the PCP and causing I-girders to rotate in the opposite direction (See Figure 5.27). Appendix B contains several graphs of the load vs twist behavior of the girders.

Table 5.4 Maximum Twist of I-Girders during Lateral Tests

Test Name	Load (kip)	$\theta_{WG.M}$ (deg)	$\theta_{EG.M}$ (deg)	$\theta_{WG.TP}$ (deg)	$\theta_{EG.TP}$ (deg)
LAT.1.MS.0PCP	3.5	2.54	2.52	1.95	2.00
LAT.2.MS.2PCP	3.5	0.52	0.55	0.17	0.20
LAT.3.MS.4PCP	3.5	0.25	0.26	-0.03	-0.02
LAT.4.MS.0PCP.XF	3.4	0.08	0.06	0.13	0.09
LAT.5.MS.2PCP.XF	3.5	-0.03	-0.03	-0.19	-0.19
LAT.6.MS.4PCP.XF	3.6	-0.03	-0.05	-0.20	-0.22
LAT.7.QP.0PCP	7.0	3.60	3.75	3.12	3.21
LAT.8.QP.2PCP	7.0	0.33	0.51	0.20	0.29
LAT.9.QP.4PCP	7.0	-0.08	0.05	-0.10	-0.03
LAT.10.QP.0PCP.XF	7.0	0.15	0.14	0.54	0.47
LAT.11.QP.2PCP.XF	7.0	-0.06	-0.05	-0.07	-0.08
LAT.12.QP.4PCP.XF	7.0	-0.08	-0.07	-0.10	-0.11

Key: LAT = Top Flange Lateral Load, MS = Midspan Load, QP = Quarter Point Load
θ = Twist, TF = Top Flange, BF = Bottom Flange, WG = West Girder,
EG = East Girder, M = Midspan, TP = Third Point

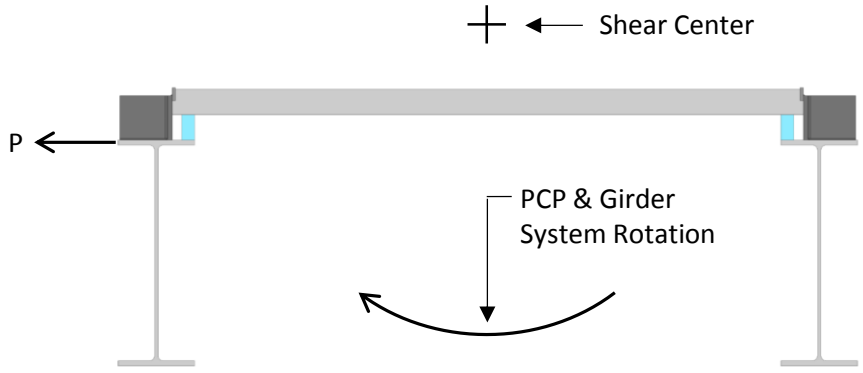

Figure 5.27 Rotation of System with PCPs Attached to I-Girders

5.7.2 Combined Bending and Torsion Simply Supported Test Results

Table 5.5 provides a summary of the 22 bending and torsion load tests that were performed on the simply supported twin I-girder system in the laboratory. The nomenclature for the GLS simply supported load tests is shown in Figure 5.28. Similar to the lateral load test, the total number of PCPs attached to the top flange was varied (0 PCPs, 2 PCPs, and 4 PCPs) and tests were run with and without the cross-frame installed at midspan. The eccentricity of the loads applied with

the GLS were varied between 0 in, 6 in, and 12 in to simulate the moment and torque diagrams of straight girders and girders with radii of curvature of 1200 ft, and 600 ft, respectively. Furthermore, several tests were performed with bottom flange trusses to provide a warping restraint to the I-girders' bottom flange. While graphs for a few of the tests are shown in this section of the report, Appendix B contains graphs showing both the top flange lateral deflection and the twist at third points and midspan for all 22 tests in addition to graphs for the of the cross-frame diagonal forces.

Table 5.5 Summary of Bending and Torsion Simply Supported I-Girder Tests

Test Name	Support Condition	Load Eccentricity	Cross Frame	Bottom Truss	Number of PCPS	Max Total GLS Load
GLS.1	SS	0 & 0	-	-	0	30
GLS.2	SS	0 & 0	-	-	2	100
GLS.3	SS	0 & 0	-	-	4	150
GLS.4	SS	6" & 6"	-	-	0	19
GLS.5	SS	6" & 6"	-	-	2	60
GLS.6	SS	6" & 6"	-	-	4	90
GLS.7	SS	6" & 6"	-	2 BF	4	80
GLS.8	SS	6" & 6"	-	4 BF	4	100
GLS.9	SS	12" & 12"	-	-	0	10
GLS.10	SS	12" & 12"	-	-	2	38
GLS.11	SS	12" & 12"	-	-	4	40
GLS.12	SS	12" & 12"	-	2 BF	4	75
GLS.13	SS	12" & 12"	-	4 BF	4	80
GLS.14	SS	0 & 0	XF	-	0	140
GLS.15	SS	0 & 0	XF	-	2	180
GLS.16	SS	0 & 0	XF	-	4	180
GLS.17	SS	6" & 6"	XF	-	0	90
GLS.18	SS	6" & 6"	XF	-	2	110
GLS.19	SS	6" & 6"	XF	-	4	120
GLS.20	SS	12" & 12"	XF	-	0	60
GLS.21	SS	12" & 12"	XF	-	2	70
GLS.22	SS	12" & 12"	XF	-	4	90

Key: GLS = Gravity Load Simulator Load, SS = Simply Supported
BF = Bottom Flange Truss, XF = Cross-Frame

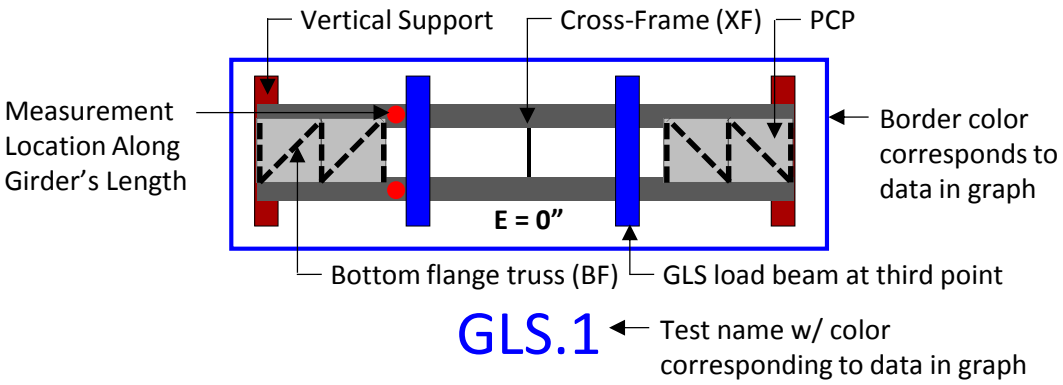

Figure 5.28 Nomenclature for Documentation of GLS Simply Supported I-Girder Tests

Test Result – No Cross-Frame and E=0" (GLS.1, GLS.2, and GLS.3)

Figure 5.29 shows that attaching PCPs to the system significantly increased the load carrying capacity of the concentrically loaded I-girders. To achieve a girder twist of 0.5 degree at the third point, total GLS loads of approximately 16 kips, 59 kips, and 131 kips were applied to the system with 0 PCPs, 2 PCPs, and 4 PCPs, respectively. Therefore, adding 2 PCPs and 4 PCPs to the system increased the load carrying capacity by factors of roughly 3.7 and 8.2, respectively. The buckling behavior of the straight concentrically loaded girders depends largely on the girders initial imperfections which are recorded in Appendix B for the three tests. Appendix B also contains graphs of the girders' twist at midspan and the top flange lateral deflection at midspan and third points.

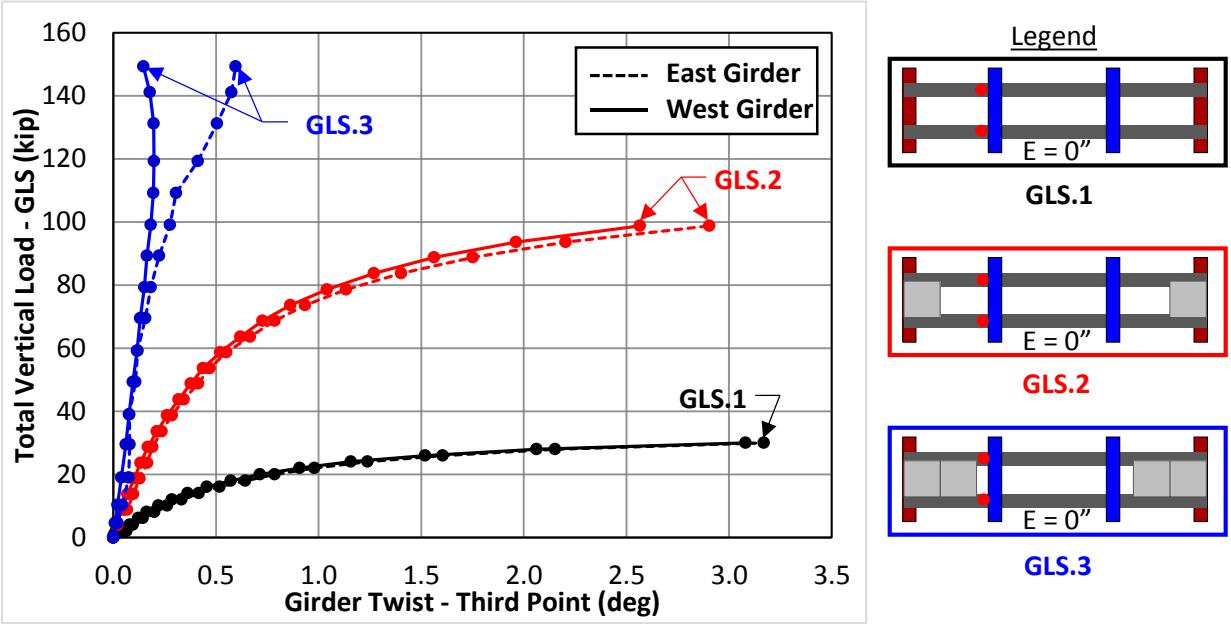

Figure 5.29 Twist @ Third Points vs. GLS Load (E=0" - SS - w/o XF)

Test Result - Cross-Frame and E=0" (GLS.14, GLS.15, and GLS.16)

Addition of the PCPs to the concentrically loaded I-girder system was less beneficial with a cross-frame connected at midspan than without (see Figure 5.30). To achieve a girder twist of 1.0 degree at the third point, total GLS loads of approximately 132 kips, 173 kips, and 175 kips were applied to the system with 0 PCPs, 2 PCPs, and 4 PCPs, respectively. Therefore, adding 2 PCPs and 4 PCPs to the system increased the load carrying capacity by a factor of 1.3 for both cases (increasing the number of PCPs from 2 to 4 did not have a major effect). The girders buckled in an S-shape with the top flanges north of the cross-frame buckling to the west and the top flanges south of the cross-frame buckling to east. Figure 5.31 shows the north and south quarter points of the west girder twisting in opposite directions. Additional graphs of the girder twist at centerline, the top flange lateral deflection at midspan and third points, and the axial force in the diagonal of the cross-frame can be found in Appendix B.

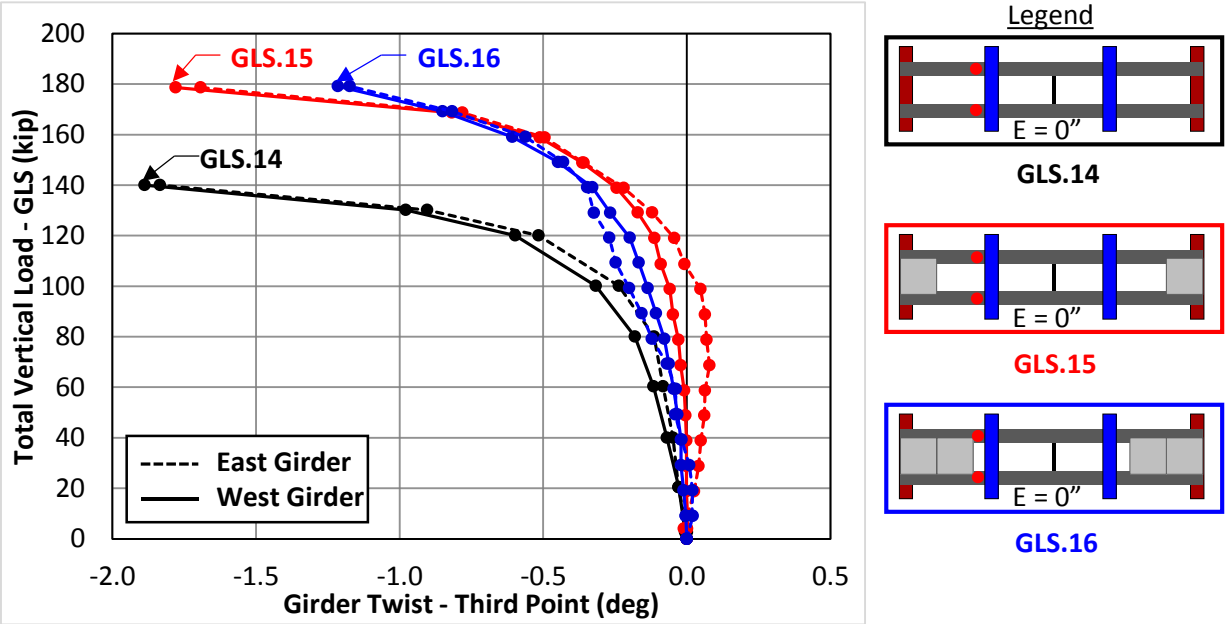

Figure 5.30 Twist @ Third Point vs. GLS Load (E=0" - SS - w/ XF)

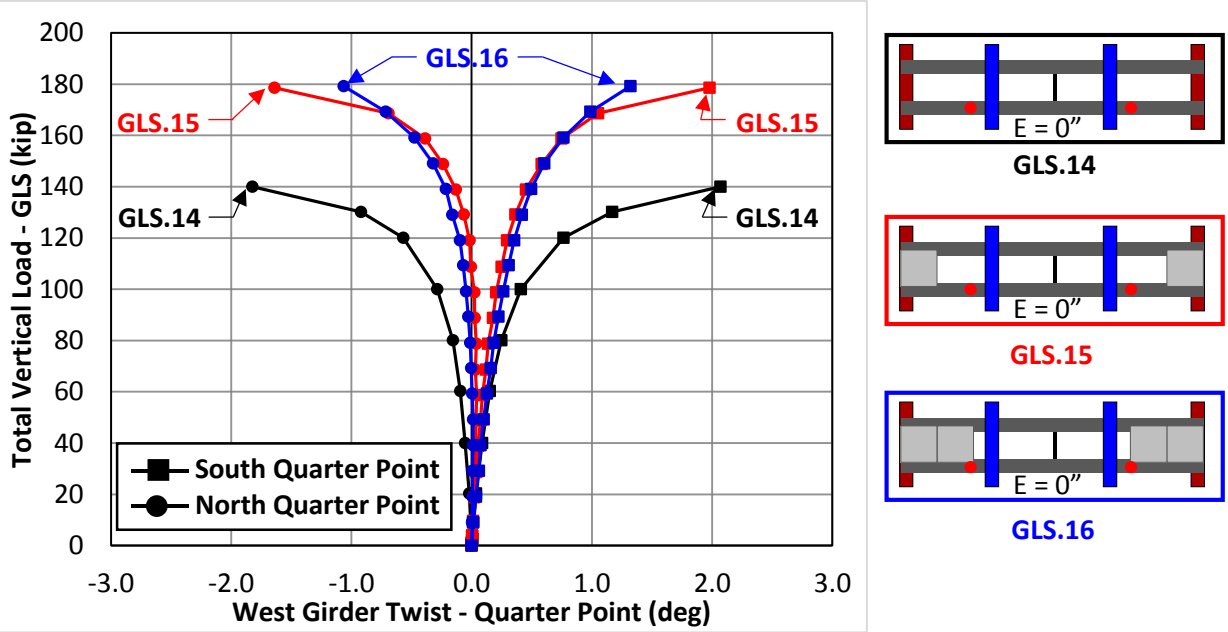

Figure 5.31 Twist @ Quarter Point vs. GLS Load (E=0" - SS - w/ XF)

Test Result - No Cross-Frame and E=6" (GLS.4, GLS.5, GLS.6, GLS.7, and GLS.8)

Adding top flange bracing elements (PCPs) and bottom flange bracing elements (lateral trusses) significantly increased the load carrying capacity of the I-girder system when no midspan cross-frame is installed (See Figure 5.32). To achieve an average girder twist of 1.5 degrees at the third point, total GLS loads of approximately 9 kips, 19 kips, 35 kips, 65 kips, and 90 kips were applied to the system with 0 PCPs, 2 PCPs, 4 PCPs, 4 PCPs and s2 BFs, and 4 PCPs and 4 BFs, respectively. Figure 5.33 shows that the lateral deflection of the top flange significantly reduced as more PCPs were connected to the top flange. For the case with 4 PCPs and no bottom flange truss (shown in blue) the top flange lateral deflection was small (a maximum value of 0.23 in for the west girder and 0.34 in for the east girder) meaning that maximum 3.1 degree twist of the west girder and 4.9 degree twist of the east girder was largely due to lateral deflection of the bottom flange (i.e. the top flange remains stationary and the bottom flange kicks out).

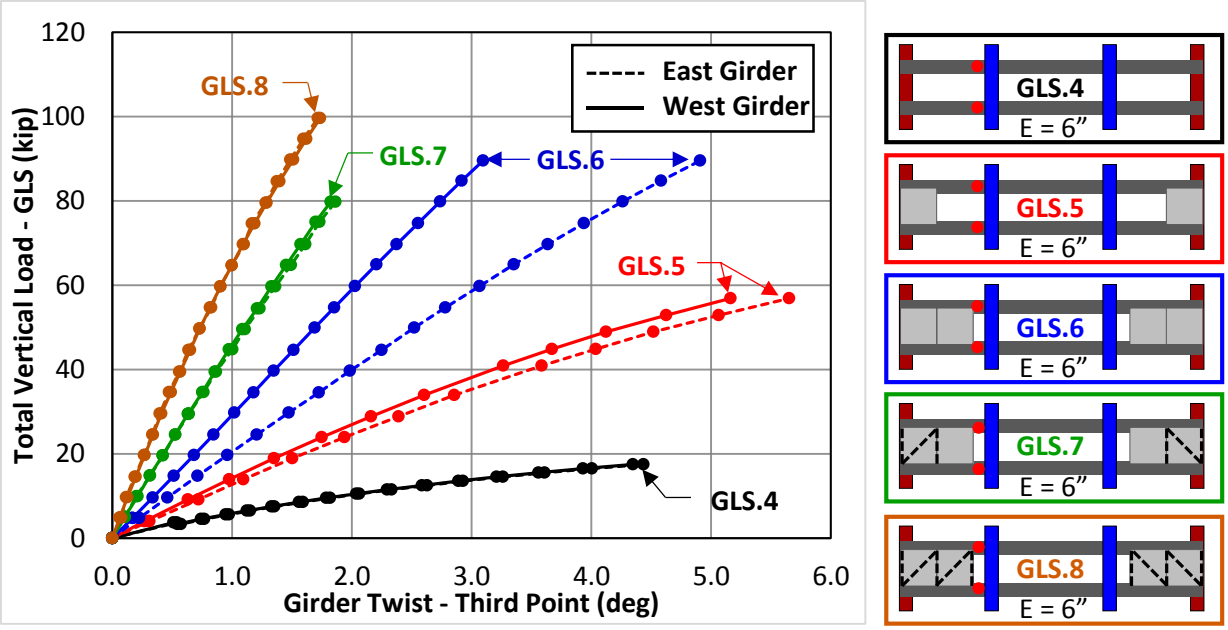

Figure 5.32 Twist @ Third Point vs. GLS Load (E=6"- SS - w/o XF)

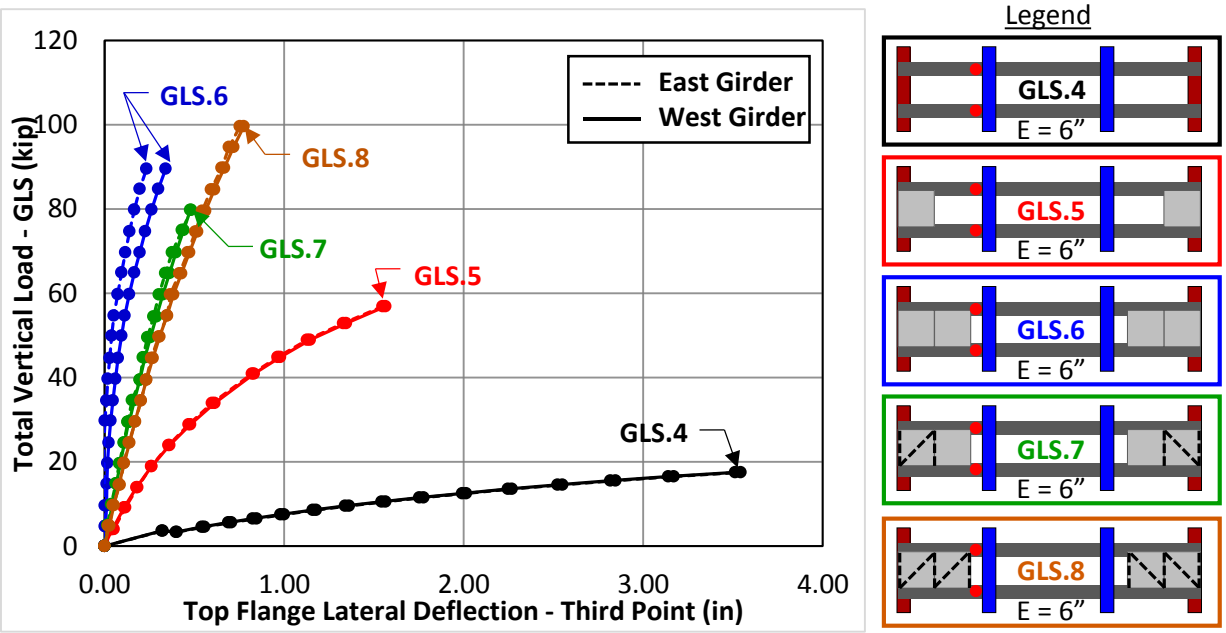

Figure 5.33 Lateral Deflection @ Third Point vs. GLS Load (E=6" - SS - w/o XF)

Figure 5.32 shows that the rotation of the east girder was slightly larger than the rotation of the west girder when only 2 PCPs were attached (GLS.5) and that the rotation of the east girder was significantly larger than the west girder when 4 PCPs were attached (GLS.6). Figure 5.34 showed that when the west girder tried to twist the WT connecting the PCP to the girder bore against the PCP resisting some moment and when the east girder tried to twist the WT pulled away from the PCP. Therefore a twisting restraint was provided to the west girder that was not provided

to the east girder. Since the girders twist more with an increased distance from the support, the case with 4 PCPs provided more twisting restraint to the west girder than the case with 2 PCPs, explaining the larger discrepancy in twist between the two girders for the case with 4 PCPs attached.

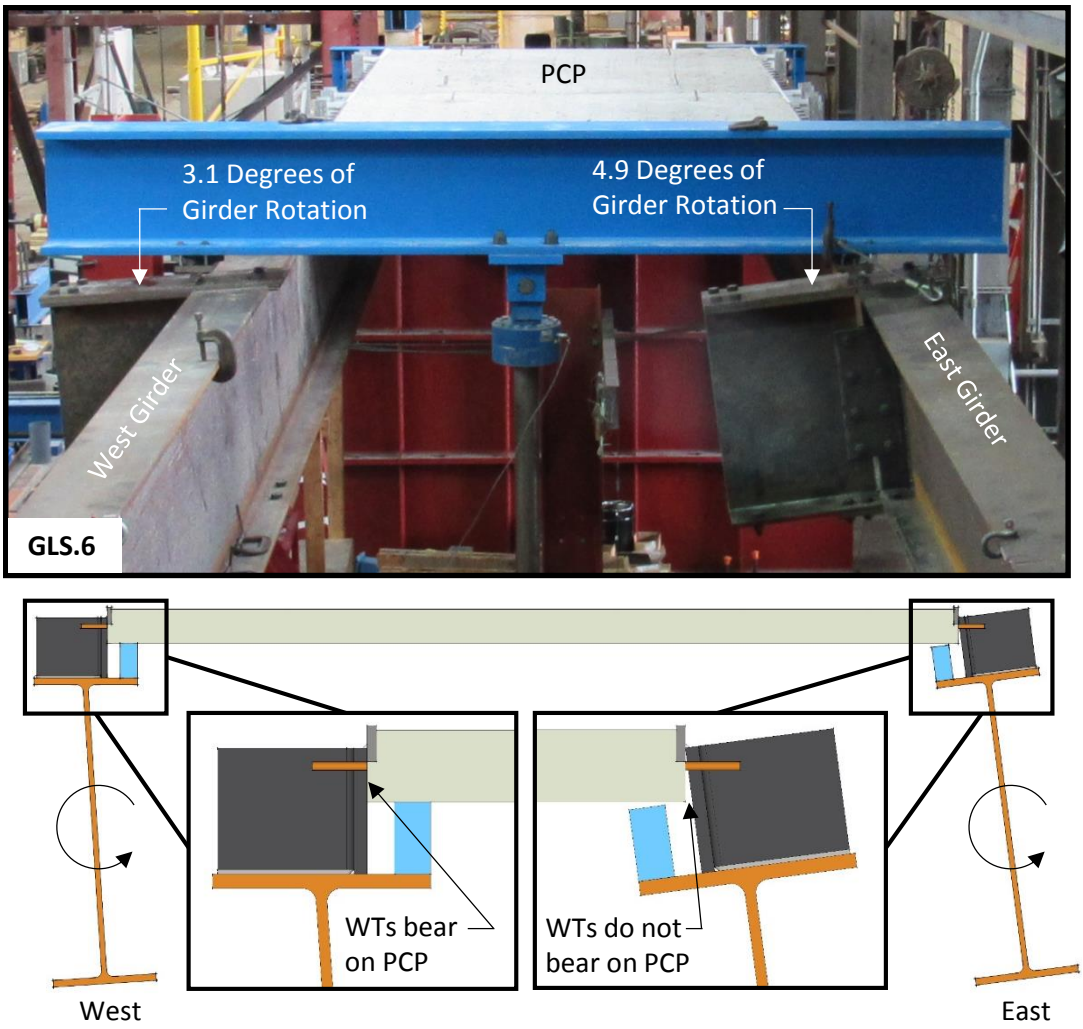

Figure 5.34 Unequal Rotation of West I-Girder and East I-Girder

Additional graphs of the girder twist at midspan and the top flange lateral defection at midspan are shown in Appendix B. Similar system behavior was observed when the load eccentricity was increased from E=6″ (for cases GLS.4, GLS.5, GLS.6 GLS.7, and GLS.8) to E=12″ (for cases GLS.9, GLS.10, GLS.11 GLS.12, and GLS.13) with increased girder twist due to the larger torsional load on the system (see Appendix B).

Test Result - Cross-Frame and E=6″ (GLS.17, GLS.18, and GLS.19)

With a midspan cross-frame in place, the PCPs provided less benefit from the bracing perspective than when no cross-frame was installed. To achieve an average girder twist of 1.0 degree at the third point, total GLS loads of approximately 60 kips, 78 kips, 104 kips, were applied

to the system with 0 PCPs, 2 PCPs, 4 PCPs, respectively (see Figure 5.35). As explained above, the east girder experienced a larger rotation than the west girder when PCPs were attached to the system. Figure 5.36 shows that adding PCPs significantly reduced the top flange lateral deflection meaning that again the girder twist with PCPs attached was dominated by lateral deflection of the bottom flange. Graphs showing the girder twist and top flange lateral defection at midspan and the forces in the cross-frame diagonal are shown in Appendix B. Similar system behavior was observed when the load eccentricity was increased from E=6″ (for cases GLS.17, GLS.18, and GLS.19) to E=12″ (for cases GLS.20, GLS.21, and GLS.22) with increased girder twist due to the larger torsional load on the system (see Appendix B).

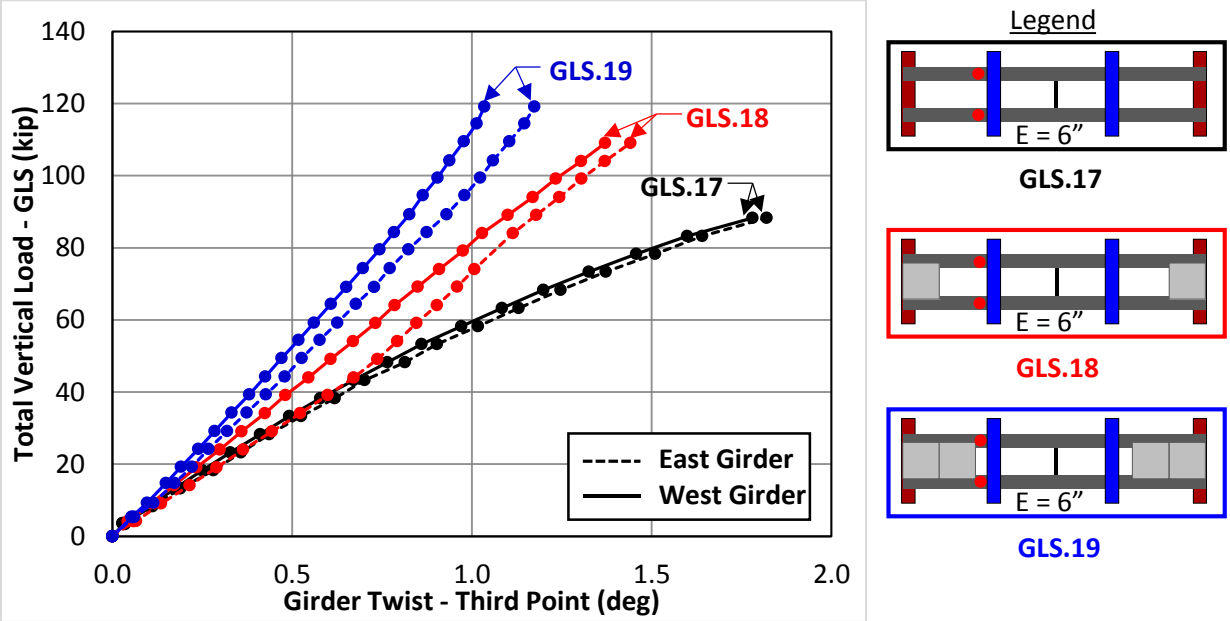

Figure 5.35 Twist @ Third Point vs. GLS Load (E=6″ - SS - w/ XF)

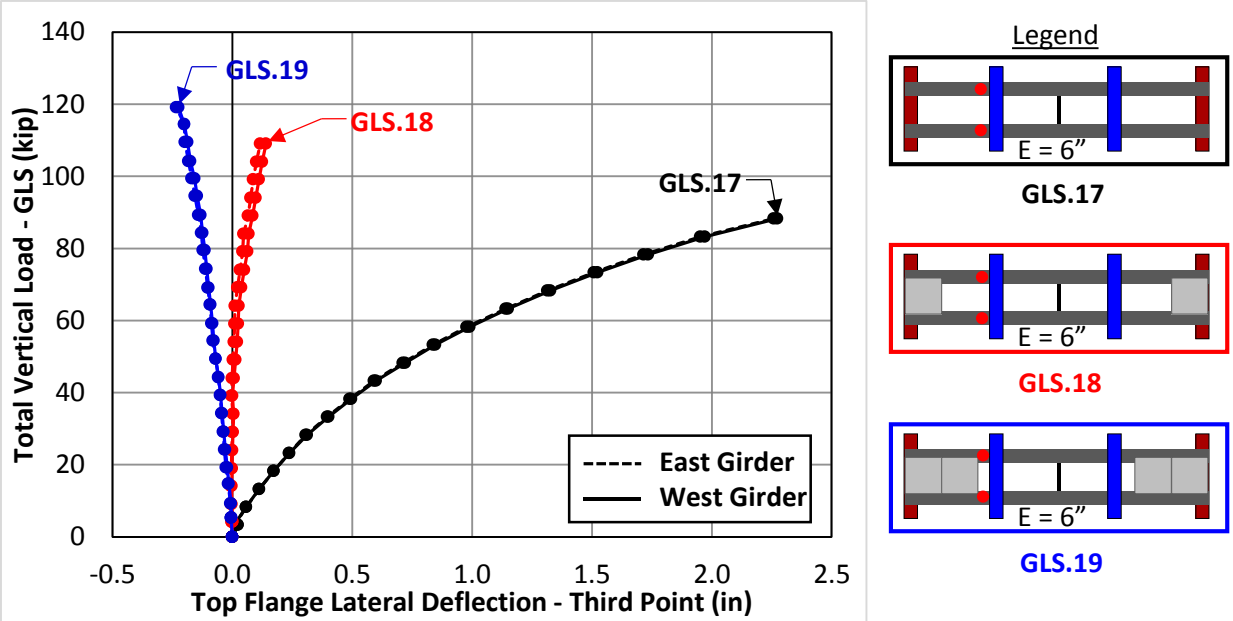

Figure 5.36 Lateral Deflection @ Third Point vs. GLS Load (E=6″ - SS - w/ XF)

5.7.3 PCP Performance during Simply Supported Tests

During the simply supported tests, the PCPs performed well from a serviceability standpoint. Figure 5.37 shows the minor cracks that formed on the top of the PCPs during the tests (permanent markers were used to trace next to the cracks during the test and the marker was traced in the figure to make them visible). The test at which the cracks occurred are labeled in the figure and no crack width exceeded approximately 0.010 inches throughout the tests. Also, no cracking was observed on the bottom of the PCPs (likely due to the embeds being located in the upper portion of the PCP).

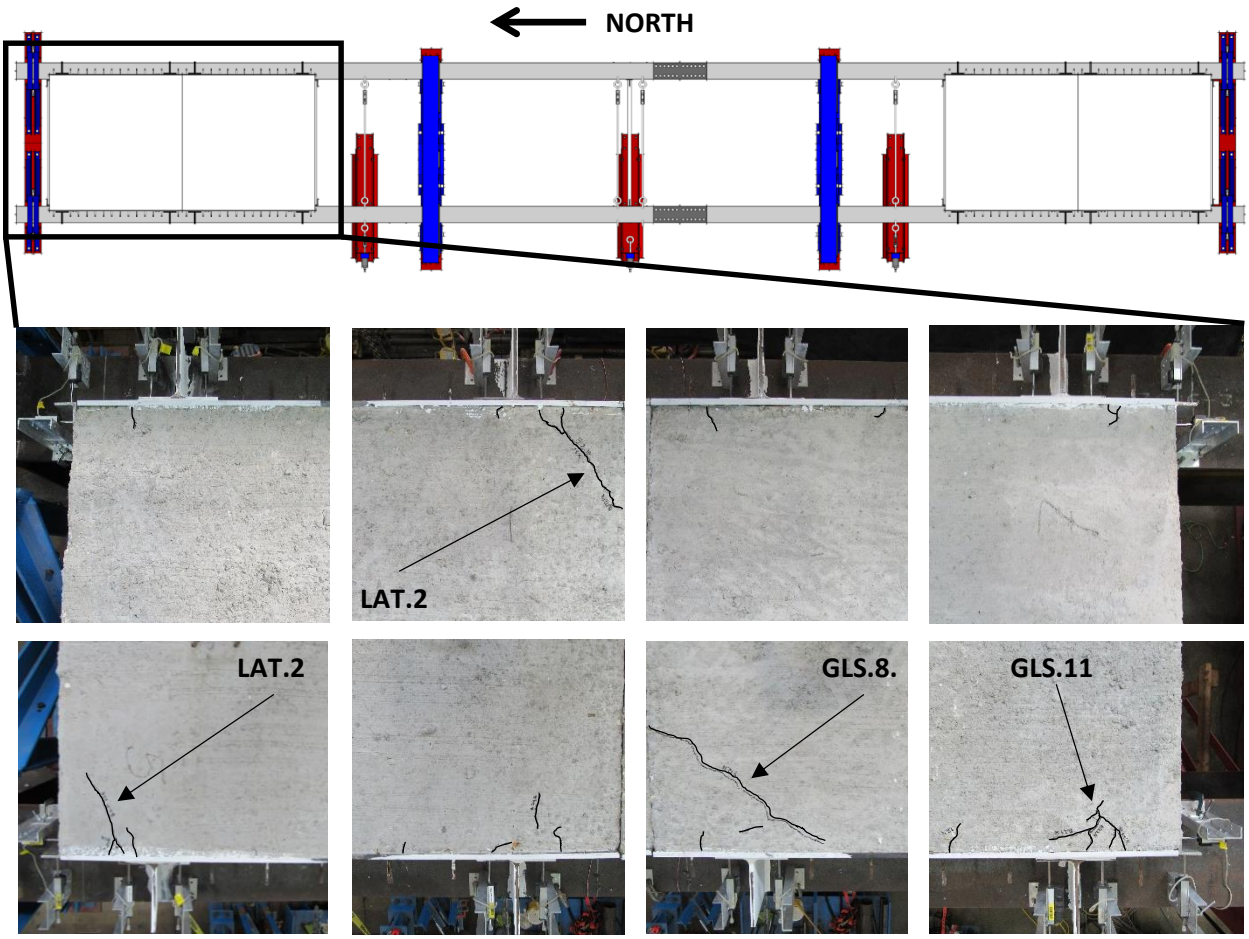

Figure 5.37 Crack Patterns of PCPs during Simply Supported Tests

5.7.4 Combined Bending and Torsion Overhang Test Results

Table 5.6 provides a summary of the 5 bending and torsion load tests that were performed on the overhang twin I-girder system in the laboratory. The nomenclature for the GLS overhang load tests is shown in Figure 5.38. For all overhang tests, 4 PCPs were attached to the top flange of the system with the eccentricity of the load form the north and south GLS being the only variable between tests. A positive eccentricity indicates that the load was offset to the west, while a negative eccentricity indicates that the load was offset to the east. While graphs for a few of the tests are shown in this section of the report, Appendix B contains graphs showing both the top flange lateral deflection and the twist at third points and midspan for all 5 tests.

Table 5.6 Summary of Bending and Torsion Overhang I-Girder Tests

Test Name	Support Condition	GLS North Eccentricity	GLS North Eccentricity	Number of PCPS	Max Total GLS Load
GLS.23	OH	-2"	4"	4	140
GLS.24	OH	-4"	8"	4	100
GLS.25	OH	2"	4"	4	170
GLS.26	OH	4"	8"	4	120
GLS.27	OH	-4"	0"	4	300

Key: GLS = Gravity Load Simulator Load, OH = Overhang

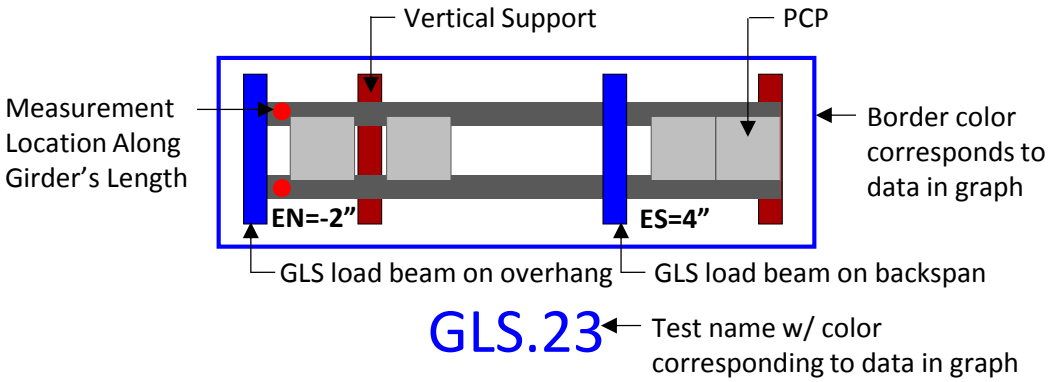

Figure 5.38 Nomenclature for Documentation of GLS Overhang I-Girder Tests

Test Result - GLS Offset in Opposite Directions (GLS.23 and GLS.24)

Figure 5.39 shows the twist of the girders measured with the vision system at the overhang and at the backspan (36 ft along the length) for the cases where the north GLS is offset to the east (negative eccentricity) and the south GLS is offset to the west (positive eccentricity). Offsetting the GLS in opposite directions maximized demand on the PCPs in the negative moment region as it causes more warping deformation of the top flange than when the GLS are offset in the same direction. As expected, a larger girder rotation was seen as the magnitude of the eccentricity increased and the east girder experienced more rotation than the west girder due to the twisting restraint of the connection (explained previously in Figure 5.34). Figure 5.40 shows that the top flange lateral deflections were relatively small at the backspan and at the overhang. The large twist of the girders results from bottom flange lateral deflections (i.e. the bottom flange kicks out).

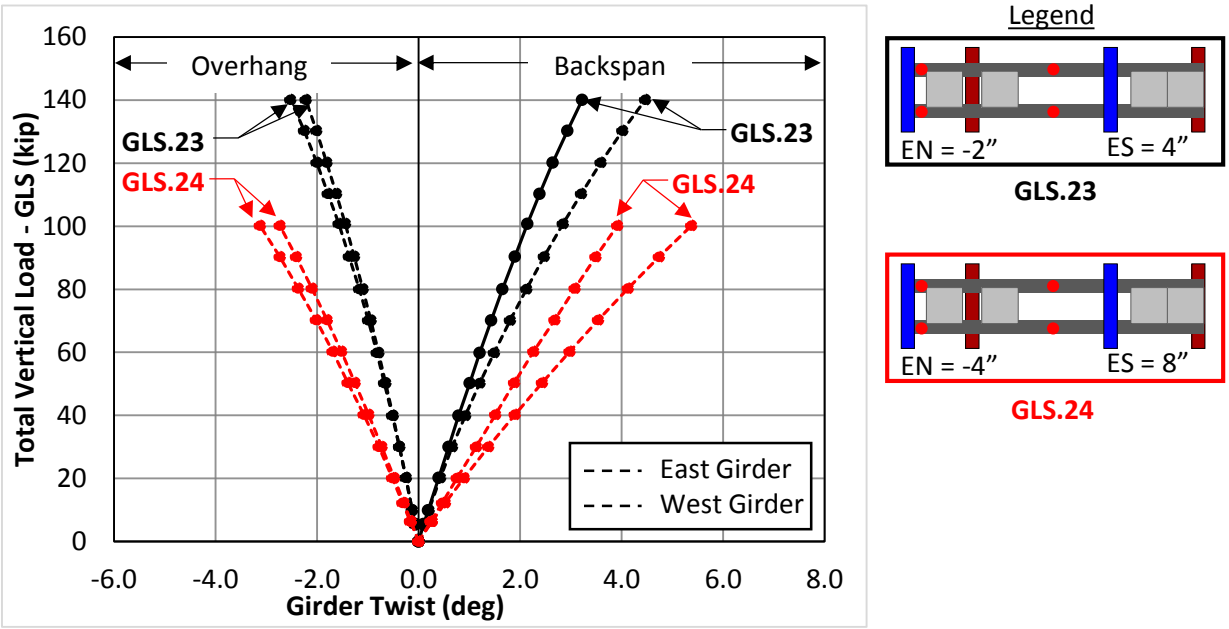

Figure 5.39 Twist @ Overhang and Backspan vs. GLS Load (Opposite Eccentricity Direction)

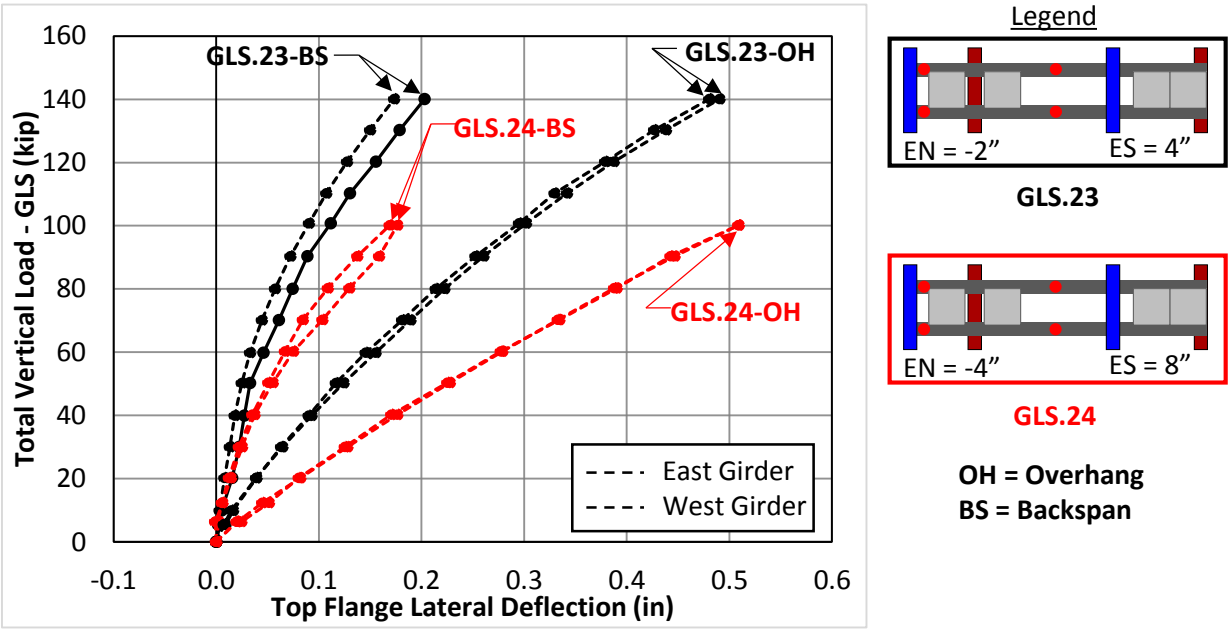

Figure 5.40 Lateral Deflection @ Overhang and Backspan vs. GLS Load (Opposite Eccentricity Direction)

PCP Performance during Overhanging Tests (Excluding GLS.27)

The two PCPs on the north end of the test frame were replaced when the test frame was reconfigured from the simply supported condition. This allowed new cracks from the overhanging test to be easily identified. Even though the PCPs were located in the negative moment region, they performed well from a serviceability standpoint. Figure 5.41 shows the minor cracks that

formed on the top of the PCPs during the tests (permanent markers were used to trace next to the cracks during the test and the marker was traced in the figure to make them visible). The test at which the cracks occurred are labeled in the figure and no crack width exceeded 0.010 inches throughout the tests. Also, no cracking was observed on the bottom of the PCPs.

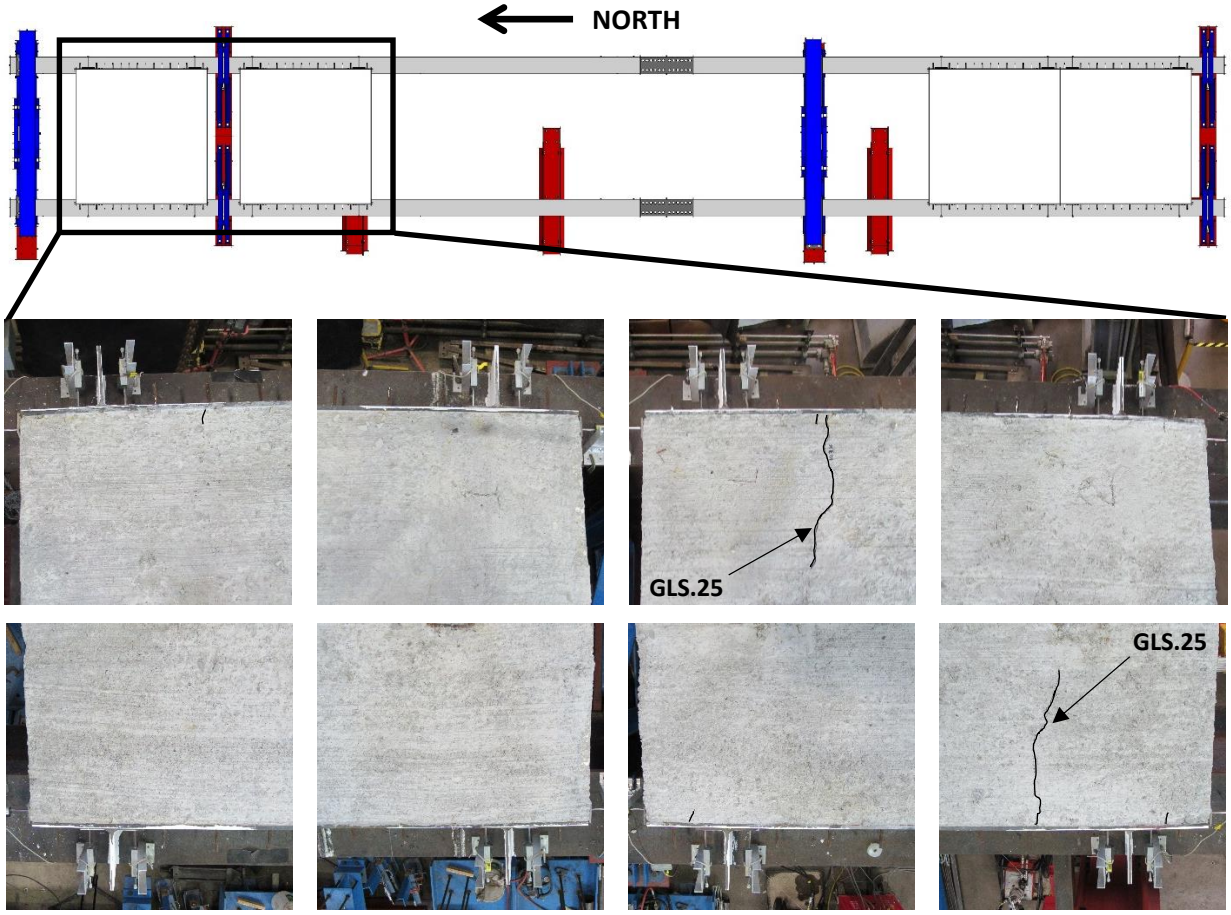

Figure 5.41 Crack Patterns of PCPs during Overhang Tests

Test Result – Maximum Load Overhanging Test (GLS.27)

For the final test conducted with the twin I-girder system, a maximum load of 150 kips was applied with each GLS (for a total GLS load of 300 kips) since each GLS was designed to withstand the aforementioned maximum load of 160 kips. For this particular test only the overhang was loaded eccentrically by 4 inches. Figure 5.42 shows the strain in the edge of the flange for both girders at the northern support. The yield strain of 0.00172 for grade 50 material was only slightly exceeded at the bottom west edge of both girders. Figure 5.43 shows an approximately linear load twist response of the girders until a total vertical GLS load of about 250 kips is reached. At this load level, the PCPs began to show significant cracking and yield lines began to form on the WT on the northeast east corner of the overhang. Figure 5.44 shows the cracking and the yield lines on the WT at the maximum total load of 300 kips, while Figure 5.45 shows the deformation of the system at the maximum load.

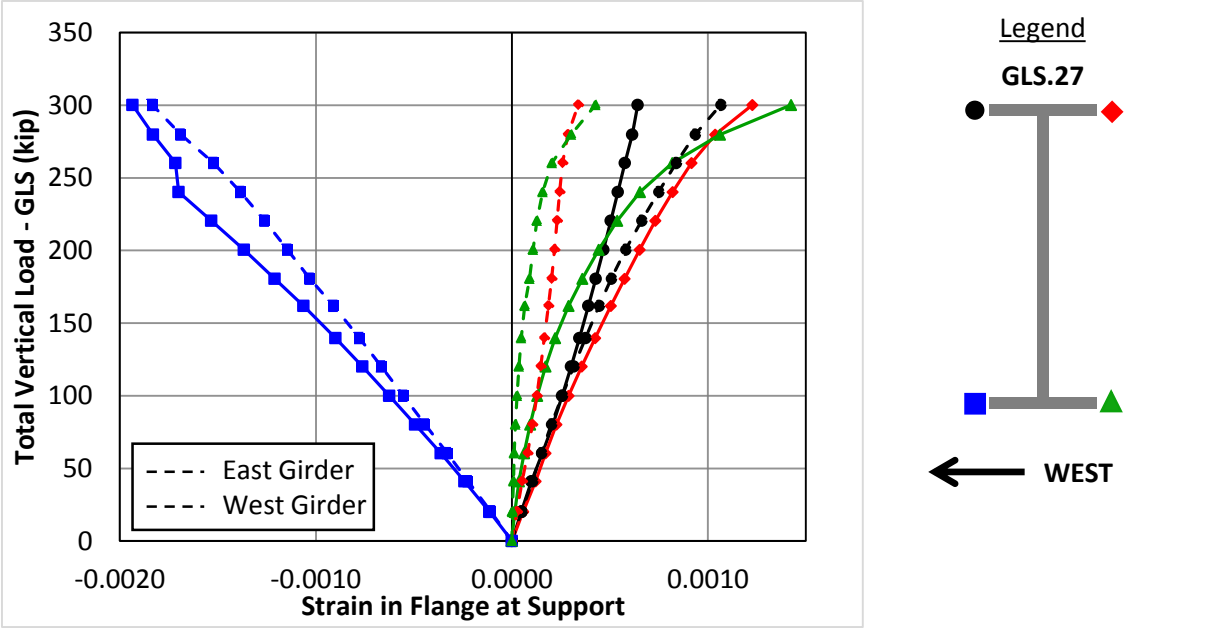

Figure 5.42 Flange Tip Strain during Maximum Load Overhang Tests

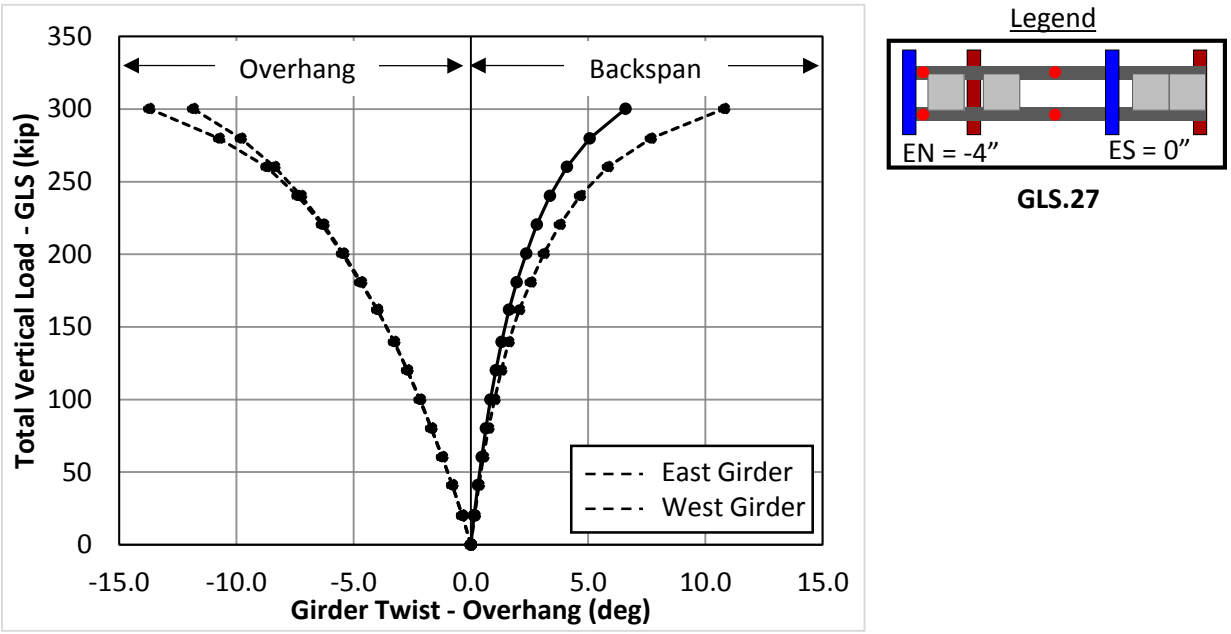

Figure 5.43 Twist @ Overhang and Backspan vs. GLS Load (Maximum Load Test)

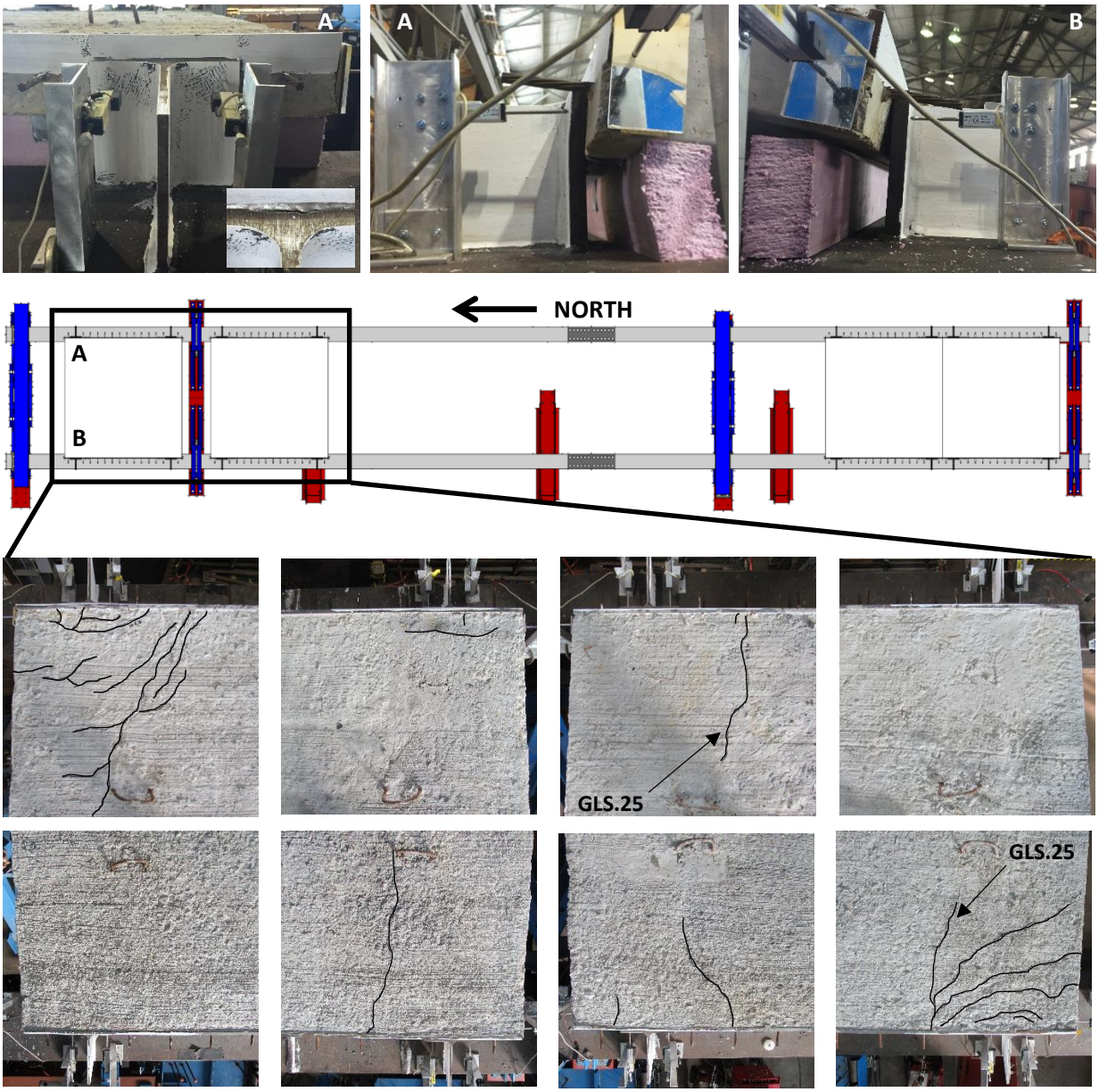

Figure 5.44 Crack Patterns of PCPs and Yield Lines on WTs during Maximum Load Test

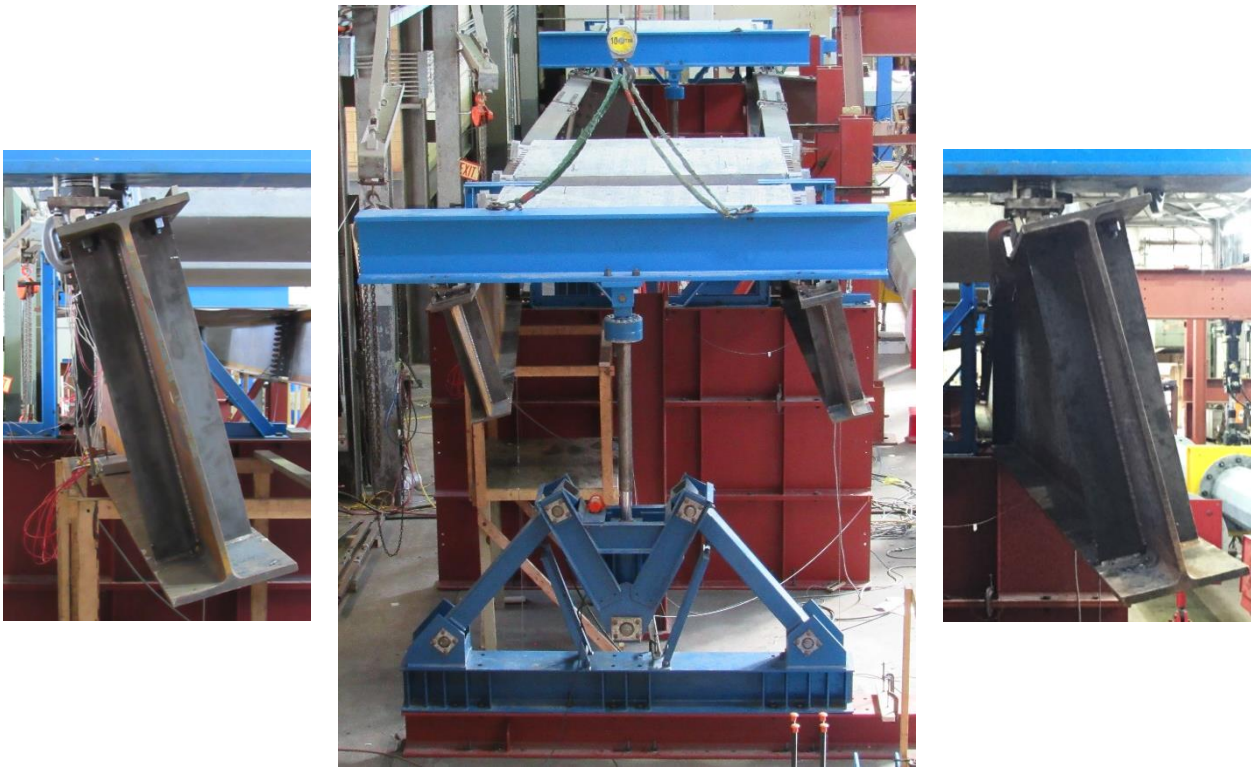

Figure 5.45 System Deformation at Maximum Load (Total Load of 300 kips)

5.8 Summary of Twin I-Girder Experimental Results

This chapter focused on the experimental tests that were conducted in the laboratory on the twin I-girder system. Several conclusions can be drawn from the experimental program:

- Connecting PCPs to the top flanges of the I-girders considerably reduced the lateral deflection of the girders during the lateral load tests both with and without the cross-frame connected at midspan. Furthermore, adding the PCPs to the system significantly reduced the twist of the I-girders when no cross-frame was installed and significantly reduced the twist of the I-girders away from the cross-frame when it was installed.
- Adding PCPs to the top flange of the simply supported concentrically loaded straight twin I-girder system significantly increased the buckling capacity of the system (see Figure 5.29). Therefore, the use of PCP as diaphragm bracing elements could potentially eliminate intermediate diaphragms or cross-frames on simply supported straight girder system. As discussed in Chapter 2, using stiffened permanent medal deck forms (PMDF) as bracing elements allowed 680 intermediate diaphragms to be eliminated from the design of I-girder bridges located on the IH-610 north loop in Houston, TX (Egilmez et al. 2016). The PCP/connection systems tested in Chapter 4 had substantially larger stiffness and strength properties than the stiffened PMDF systems used by Egilmez.
- When no cross-frame was connected at midspan, adding PCPs and bottom flange truss members increased the vertical (GLS) load carrying capacity of the system and

reduced twist of the I-girders (by engaging the warping deformation of the flanges and reducing the unbraced length of the girders). Adding only PCPs to the top flange reduced the top flange lateral deflection which caused the I-girder's twist to be dominated by the lateral deformation of the bottom flange.

- When the cross-frame was connected at midspan, adding PCPs considerably reduced the twist of the I-girders away from the cross-frame and slightly reduced the twist of the I-girders near the cross-frame during the GLS tests. Adding the PCPs also reduced the lateral deflection of the top flange, causing the girder twist away from the cross-frame to be dominated by lateral deflection of the bottom flange. The addition of the PCPs to the system also caused the forces in the diagonal of the cross-frame to be reduced.
- During the simply supported test, minor cracks formed in the PCPs (the largest observed crack width was approximately 0.010 inches. Larger cracks were observed in the PCPs in the negative moment region during the final overhanging test (GLS.27) and yield lines began for form in some of the WT connectors.

The results described above are specific to the parameters of the laboratory tests described in this chapter. These results will be used to validate finite element models discussed further in Chapter 9. The validated models can then be used to extend the experimental results to a wide array of curved I-girder bridge systems, allowing a better understanding of the bracing potential of PCPs on more realistic curved I-girder systems to be gained.

Chapter 6. Large-Scale Laboratory Tests on Steel Tub Girder

6.1 Introduction

To investigate the bracing potential of PCPs on curved steel tub girders, the research team constructed a large-scale experimental test setup at the Ferguson Structural Engineering Laboratory. Similar to the twin I-girder experimental setup, the tub girder setup was designed so that various support, loading, and bracing conditions could be investigated. Various components from the twin I-girder setup were reused for the tub girder setup (thus, a more detailed description of several of the components can be found in Chapter 5). Figure 6.1 shows an isometric view of the test setup for the lateral load tests while Figure 6.2 and Figure 6.3 show the test setup for combined bending and torsion load tests in a simply supported and overhanging condition, respectively. Several combinations of bending and torsion were applied to the straight girder, allowing girders with multiple radii of curvature to be simulated. In addition to being tested with PCPs as bracing elements, the tub girder was also tested with diagonals attached to the top flange so that a side-by-side comparison of the two bracing systems could be observed. Results from the laboratory tests were used validate the finite element models in Chapter 9. Photographs of the experimental setup are shown in Figure 6.4.

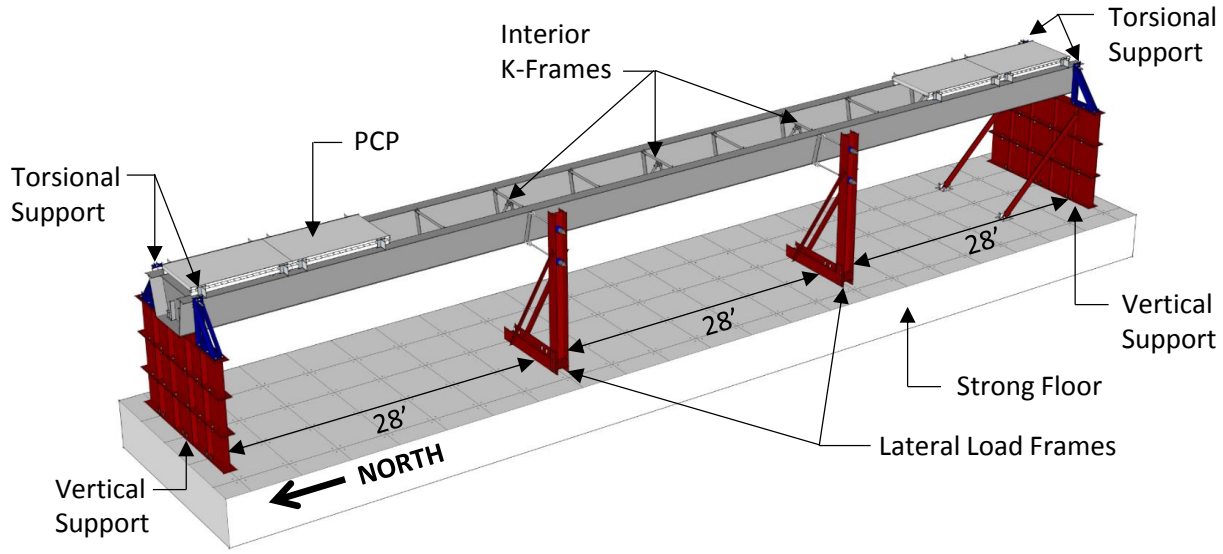

Figure 6.1 Lateral Load Test Setup – Simply Supported

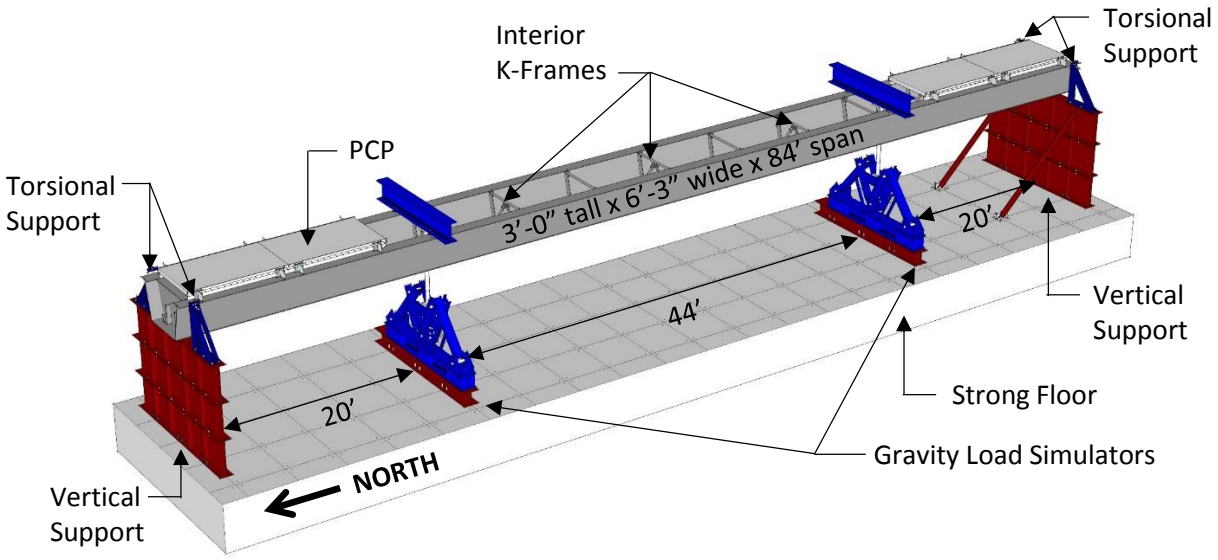

Figure 6.2 Bending & Torsion Test Setup – Simply Supported

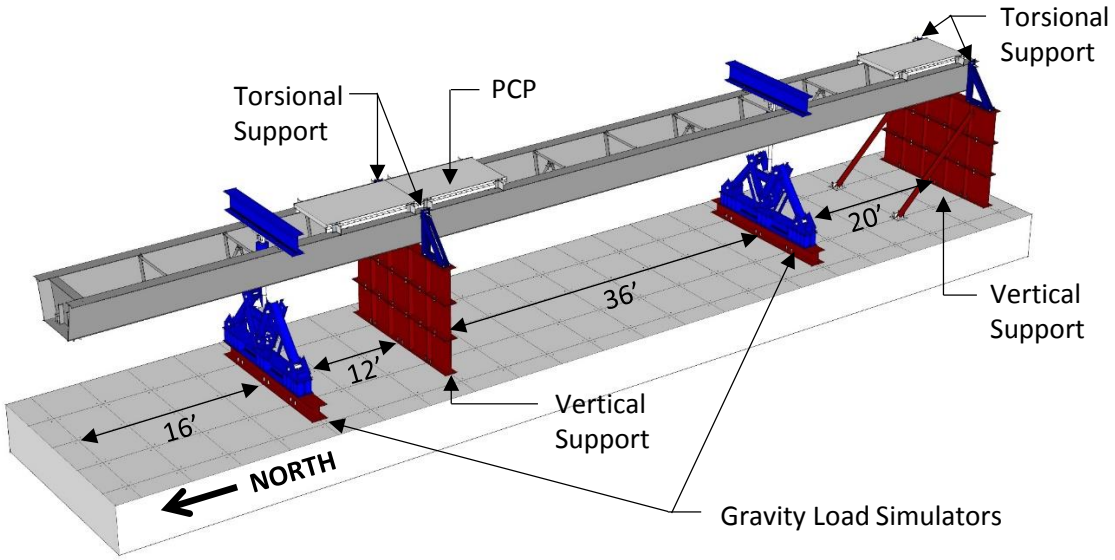

Figure 6.3 Bending & Torsion Test Setup – Overhang

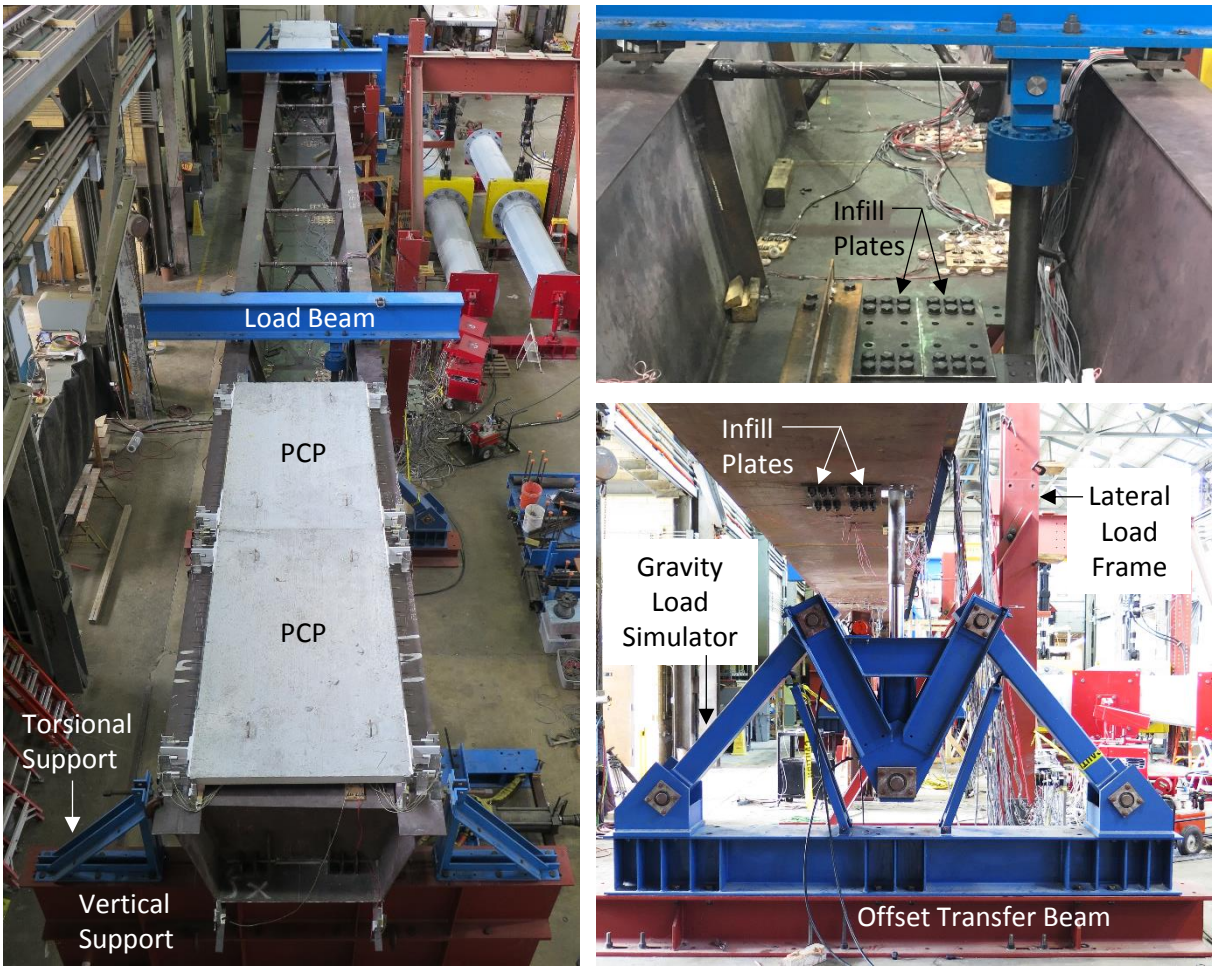

Figure 6.4 Tub Girder Experimental Test Setup - Simply Supported

6.2 Specimen Fabrication

The steel tub girder was constructed of hot-rolled 7/16″ thick, ASTM A709-50 steel plate and fabricated by Hirschfeld Industries in San Angelo, Texas. Tension coupon tests for the tub girder will be presented in the report for TxDOT Project 15-122 (Improved Tub Girder Details) since laboratory experiments are currently underway using the same tub girder for that project. Figure 6.5 shows a cross section of the tub girder. The girder was 86′ long with a clear span of 84′ for a maximum span-to-depth ratio of 28 for the simply supported case. For the overhang case, a backspan of 56′ was used with the load point on the overhanging being 12′ from the support. Interior K-frames built up of 2″ diameter ASTM A53 grade B extra strong pipe were bolted to interior stiffeners at 14′-0″ on center along the length of the girder (see Figure 6.6). The pipe section was used to minimize connection eccentricity so that the axial stiffness of the members could be used without reduction in the finite element model validation. A325 1″ diameter slip critical bolts were used to connect both the K-frames the stiffeners in the tub girder.

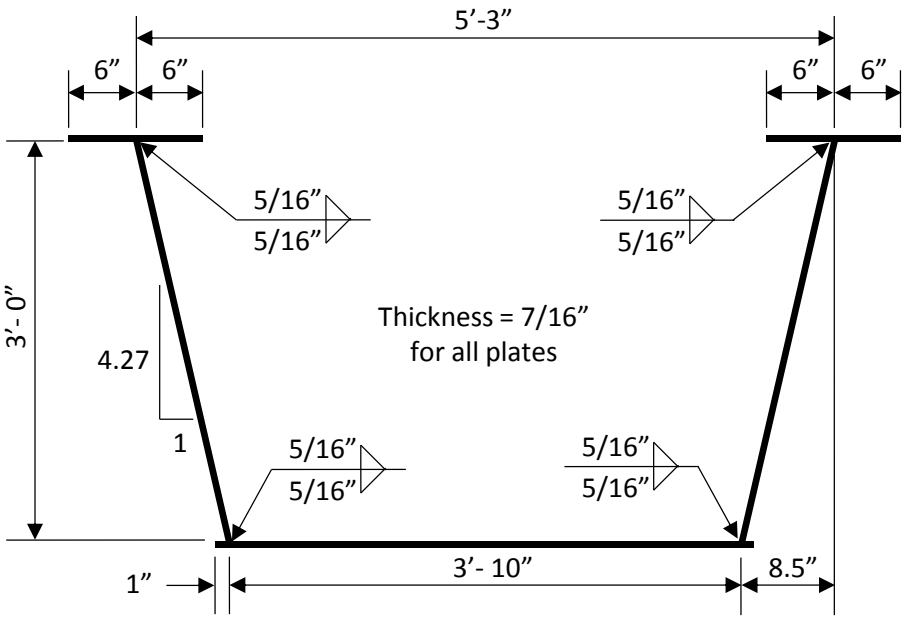

Figure 6.5 Tub Girder Cross-Section

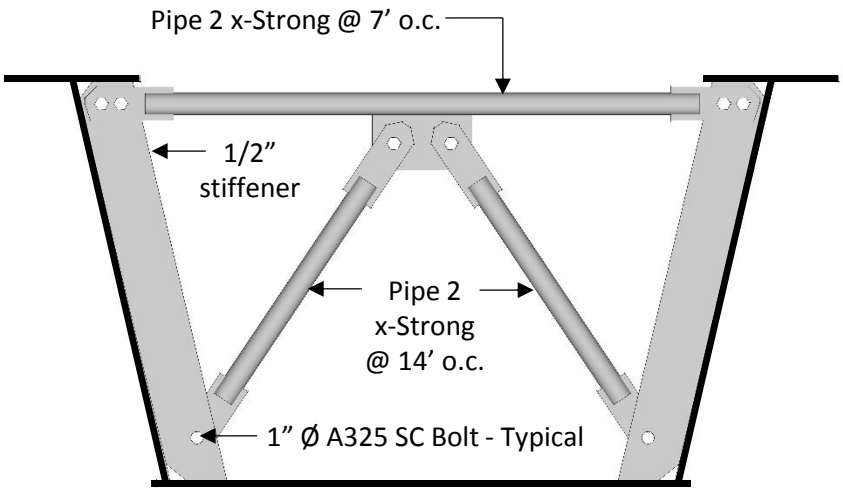

Figure 6.6 Tub Girder Internal K-Frames

Interior diaphragms (½ inch thick) were located at the ends of the tub to resist the concentrated forces from the large support reaction when the girder was loaded in its simply supported configuration. Stiffeners were welded to the diaphragm to resist local buckling from the concentrated load. For the overhang case, a diaphragm was fabricated from a section of W30x90 that was bolted to each stiffener with eight 1″ diameter A490 slip critical bolts (see Figure 6.7).

Figure 6.7 Diaphragm at North Support for Overhang Tests

As previously mentioned, several tests were performed with diagonals attached to the top flange. Figure 6.8 shows the end of the tub girder in plan view with two diagonals bolted directly underneath the top flange with three 7/8″ diameter A325 slip critical bolts at each end. Figure 6.9 shows the end of the tub girder in plan view with the two PCPs connected to the end. As there was no interference between the torsional supports and the PCPs, the edge of the PCPs were aligned with the centerline of the vertical supports. The width of the PCPs was 8 ft. while the spacing of the struts was 7 ft. Therefore, the PCPs provided bracing to the top flange a few inches farther from the vertical support than the diagonals.

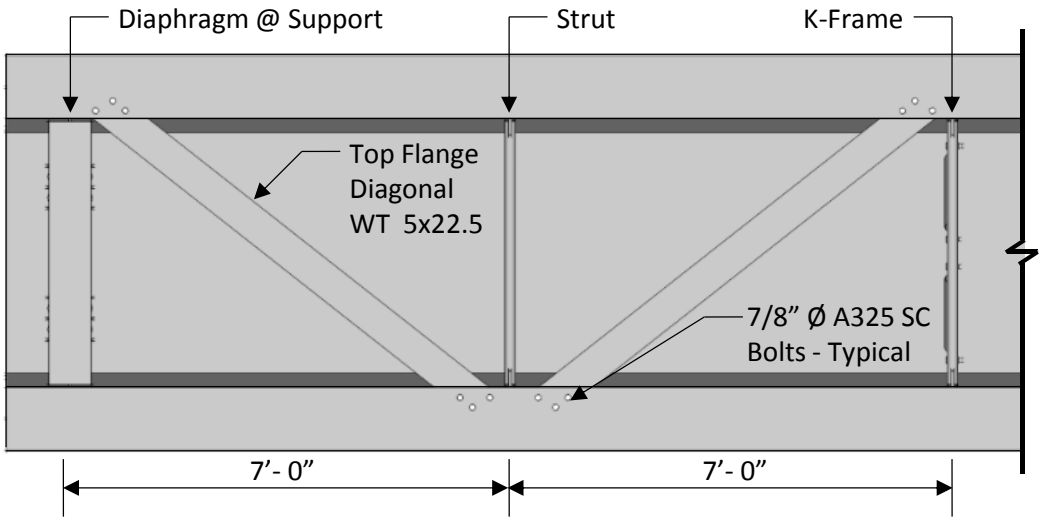

Figure 6.8 Tub Girder with Diagonals - Plan View

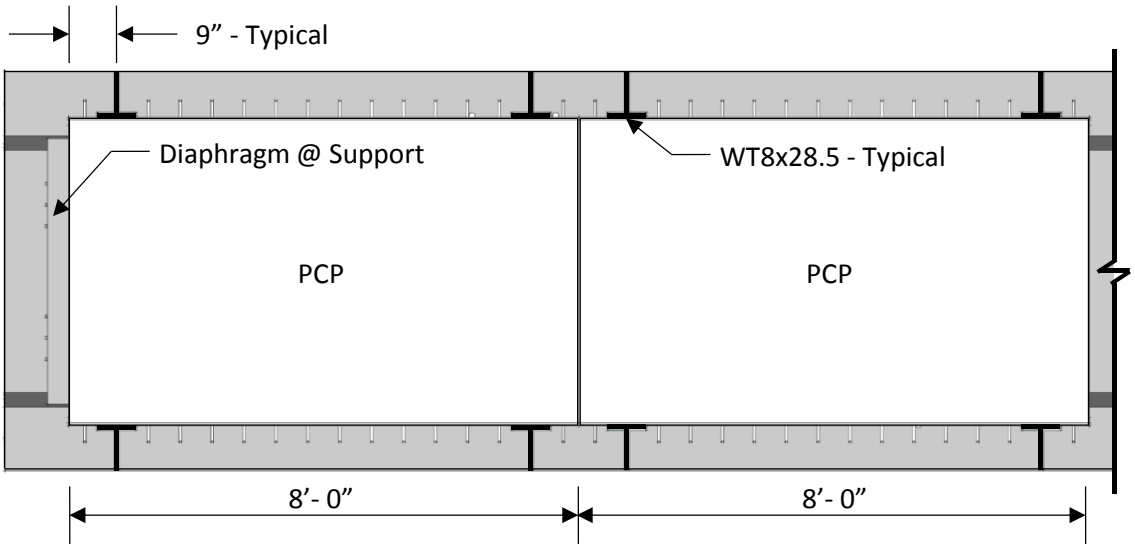

Figure 6.9 Tub Girder with PCPs - Plan View

The 12″ wide flanges of the steel tub girder allowed the PCPs to overlap each flange by 3½″ to accommodate a maximum bedding strip width of 2″ while leaving a 1½″ space for concrete to flow under the panels per the TXDOT standard (see Figure 6.10). Connection detail A.1.MAX (see Chapter 4) was used for the tub girder tests since this detail had the lowest stiffness and strength and would therefore provide a lower bound for the results from the other details. To accommodate the geometry of the tub girder, smaller PCPs were cast (8′-0″ wide x 4′-10″ long) than those used in the shear frame and twin I-girder tests.

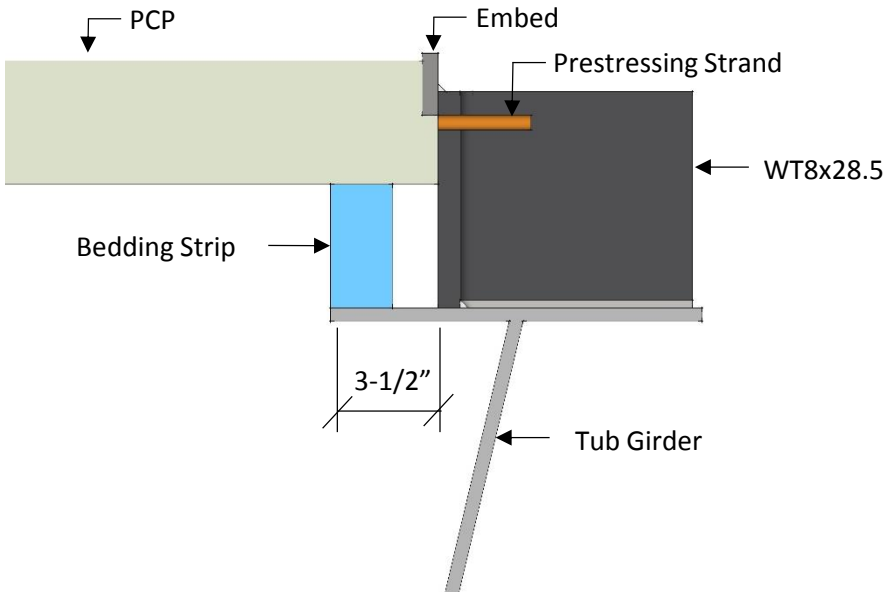

Figure 6.10 PCP to Tub Girder Connection

The PCPs for the tub girder tests used the same concrete mix as those tested on the shear frame and the twin I-girders. One batch of concrete was used when the 10 PCPs were cast and

cylinders from each batch were cast on-site. All cylinders were cured according to the standards outlined in ASTM C31. After curing for 28 days, the compressive strength, modulus of elasticity, and split cylinder tests were performed according to the ASTM C39, ASTM 469, and ASTM 496 guidelines, respectively. The results of the material tests are shown in Table 6.1. The values of the material tests for the tub girder PCPs were slightly lower than those material tests for the shear frame test and the twin I-girder tests Chapter 4 and Chapter 5, respectively.

Table 6.1: Results from Concrete Material Tests

Concrete Batch 1	
f'_c	8665 psi
E	4727 ksi
f_t	481 psi

6.3 Boundary Conditions

The same W36x135 vertical support system used for the twin I-girder system (see Chapter 5) was reused for the tub girder test setup. Figure 6.11 shows the system that was created to prevent lateral movement and twist of the girder. At each support, the bottom flange of the tub girder sat on an 18″ long x 9″ wide x 1¾″ thick bearing pad to distribute the vertical load and simulate the support condition typically used in the field. Some warping restraint will undoubtedly be provided to the bottom flange by the bearing pad while the top flanges are relatively free to warp. The top flanges are supported laterally by 1″ diameter threaded rods connected to a truss system that is bolted to the vertical support. Bearing plates were welded to the top and bottom of the flanges at the location of the threaded rods prevent overturning of the girder if a threaded rod slips off of the edge of the flange. During the lateral load tests, the top flange support rod on the west side was engaged while the east side was disengaged and the WT was bolted to the support. Therefore, lateral support was provided to the top and bottom flanges on the west side of the girder. For the GLS load cases, the WT was bolted to the support was removed.

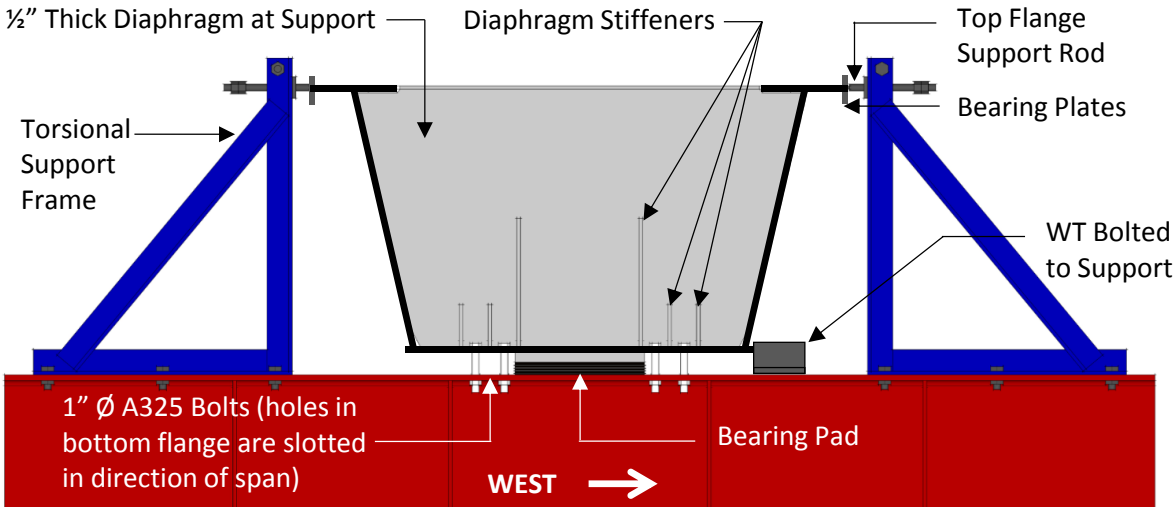

Figure 6.11 Tub Girder Torsional Support System

6.4 Load Application

The tub girder system was loaded independently with two different systems: lateral load via load frames and vertical load via the gravity load simulators. Both load application systems for the tub girder system are similar to the systems used to apply load to the twin I-girder setup and are described in detail below.

6.4.1 Application of Lateral Loads

To test the system's lateral stiffness, two lateral load frames were assembled on the west side of the tub girder (see Figure 6.1) and threaded rod assemblies were used to transfer lateral force from the hydraulic actuators to an external stiffener welded to the girder (see Figure 6.12). The applied load was measured by calibrated load cells located between the hydraulic actuator and the web of the load frame's column. Forces were applied independently at the third points (28 ft from each end) for the simply supported case. The PCPs were attached to the top flange near the supports at each end and the behavior of the system was observed for the cases without PCPs, with 2 PCPs, 4 PCPs, 2 DIAGs, and 4 DIAGs.

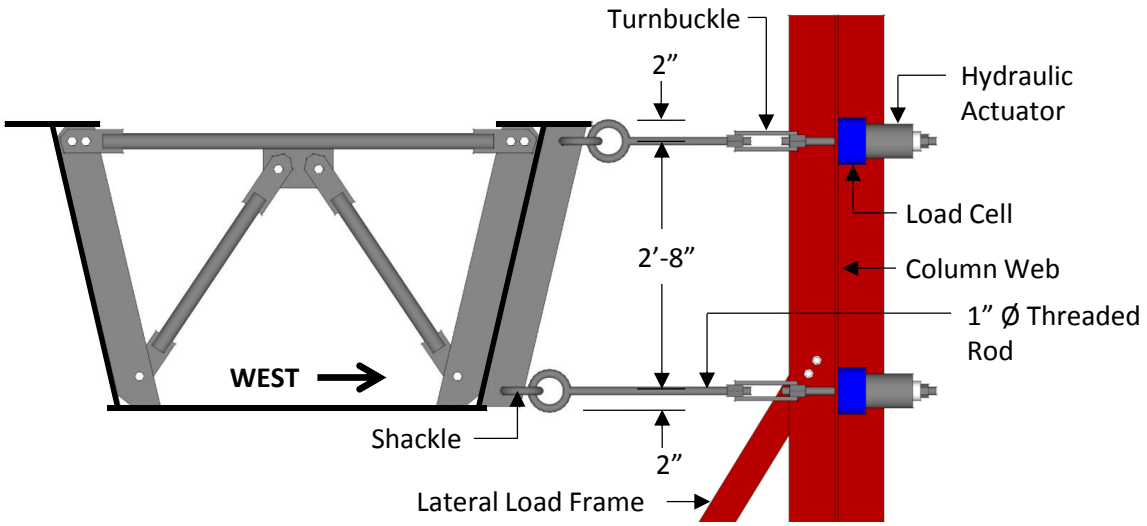

Figure 6.12 Tub Girder Lateral Load System – Cross-Section View

6.4.2 Combined Bending and Torsion Loads via Gravity Load Simulator

The two gravity load simulators used to apply vertical loads to the system are described in detail in Chapter 5. Furthermore, the same load beams, load cells, offset transfer beams, knife edge and trust bearing assemblies, etc. from the twin I-girder setup were reused for the tub girder tests. Unlike the twin I-girder system, torque was applied to the tub girder by offsetting the GLS relative to the load beam and the tub girder by and eccentricity (E) and bolting the clevis to the load beam as shown in Figure 6.13. This figure also shows how the load (P) from the actuator can be resolved into the components causing bending and torsion. Holes (8″x20″) thermally cut into the tub girder's bottom flange allowed the extension rod to pass through the bottom of the tub girder. Two sets of ½″ thick infill plates (see Figure 6.4) were bolted above and below the hole with 12 A490 1″ diameter slip critical bolts to provide continuity across the opening.

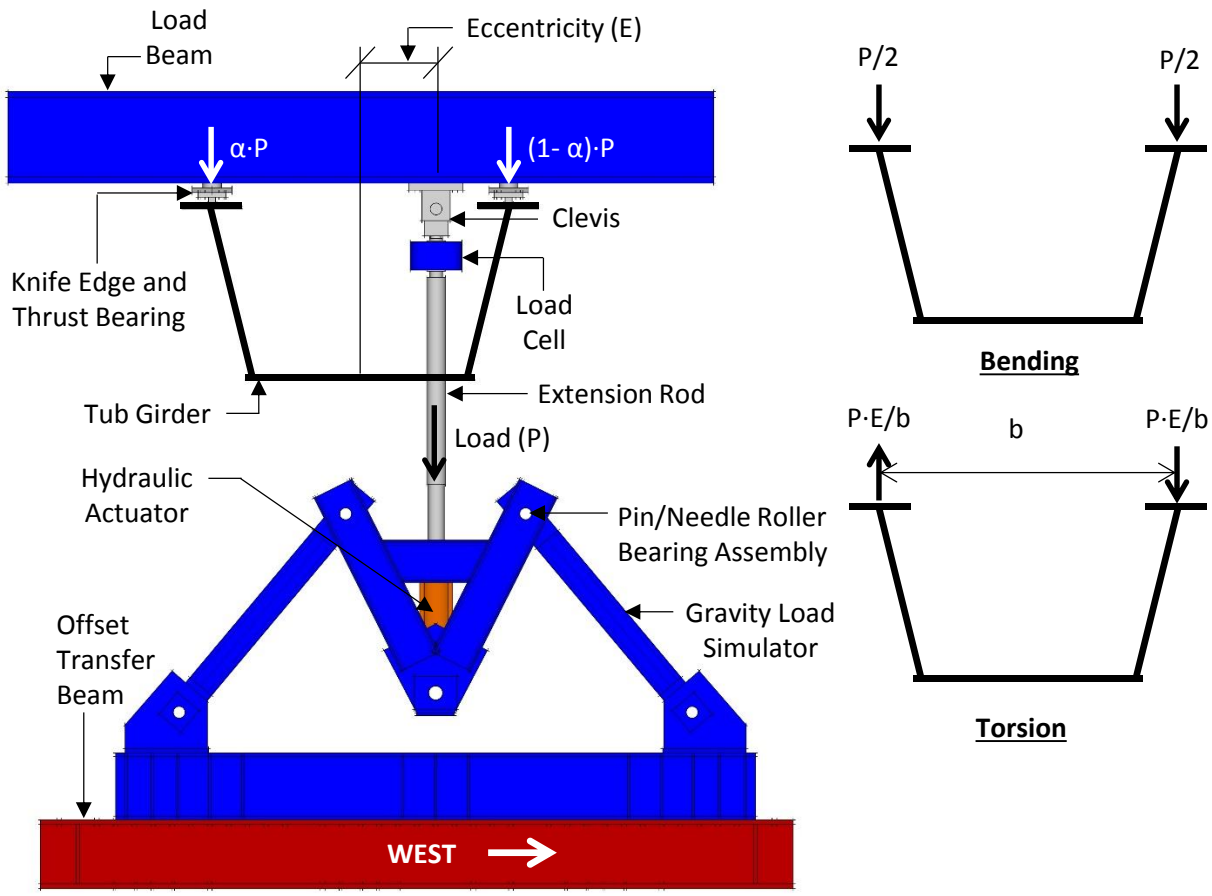

Figure 6.13 Gravity Load Simulator Applying Load to the Tub Girder

The deformed shape of the tub girder as the GLS load was applied to the system is shown in Figure 6.14. To accommodate lateral deflection of the top flanges of the tub girder (Δ_z) to the right, the left strut of the GLS rotates downward while the right strut of the GLS rotates upward, allowing the hydraulic actuator to always remain vertical. The increased hardness from the heat treatment allowed the knife edge to dig into the softer steel of the top flange, keeping the knife edge from slipping on the loading bracket as the girder twisted (θ). Unlike the twin I-girder tests, the load beam did not remain level, but twisted with the tub girder. Therefore, the thrust bearing assemblies were closely monitored throughout the tests to ensure that they did not move relative to the load beams. For all experimental test, west was selected as the positive direction for the lateral deformation and the twist was considered positive when top flange had a larger lateral deformation to the west than the bottom flange (as shown in Figure 6.14).

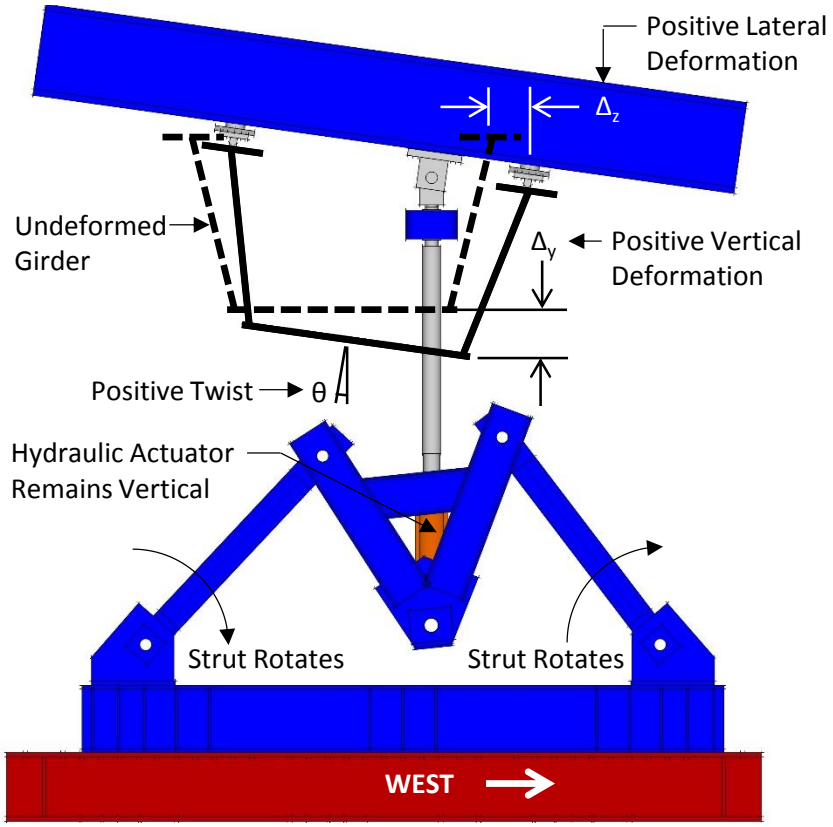

Figure 6.14 Deformation of Tub Girders under GLS Load

6.4.3 Bending and Torsion Diagrams for Curved Tub Girders vs Straight Tub Girders

Closed formed equations for moment and torque diagrams have been derived for curved steel box girders with uniform loads (Helwig et al. 2007). The derivation of these equations assume no cross-sectional distortion and negligible warping torsion. These assumptions are satisfactory for tub girders with adequate bracing (allowing them to act as closed sections), but are invalid for open sections where significant torsional warping occurs. Since the effects of torsion on the moment diagram are relatively small, the moment can be approximated as a straight girder as follows:

$$M(x) = \frac{wx}{2}(L - x) \tag{6.1}$$

where,
M = moment (kip•ft)
L = span length (ft)
x = distance along girder (ft)
w = uniform load (kip/ft)

The approximate girder torque is calculated as follows:

$$T(x) = \frac{wL^2}{24R}\left(4\frac{x^3}{L^2} - 6\frac{x^2}{L} + L\right) \tag{6.2}$$

where,
T = torque (kip•ft)
L = span length (ft)
R = radius of curvature (ft)
x = distance along girder (ft)
w = uniform load (kip/ft)

Due to the geometric constraints in the laboratory, the simply-supported tub girder spanning 84 ft was loaded 20 ft from each support with the gravity load simulator. With eccentric point loads at this location (5·L/24 from the end), both the maximum torque at the end of the girder and the area under the torque diagram could not be simultaneously equated to a curved tub girder with uniform load. Figure 6.15 shows graphs of the torque and moment diagrams for the two systems when the area under torque and moment diagrams for the system are equated. The figure also shows the relationship between the uniform load (w) and the point loads (P) in addition to the relationship between the radius of curvature (R) and the load eccentricity (E) that were derived. For the case specific to the setup in the laboratory with a span of 84 ft. and a load eccentricity of 16 in, the equivalent radius of curvature is 630 ft. Reducing the load eccentricity by a factor of two (from 16 in. to 8 in.) doubles the equivalent radius of curvature (from 630 ft. to 1260 ft.).

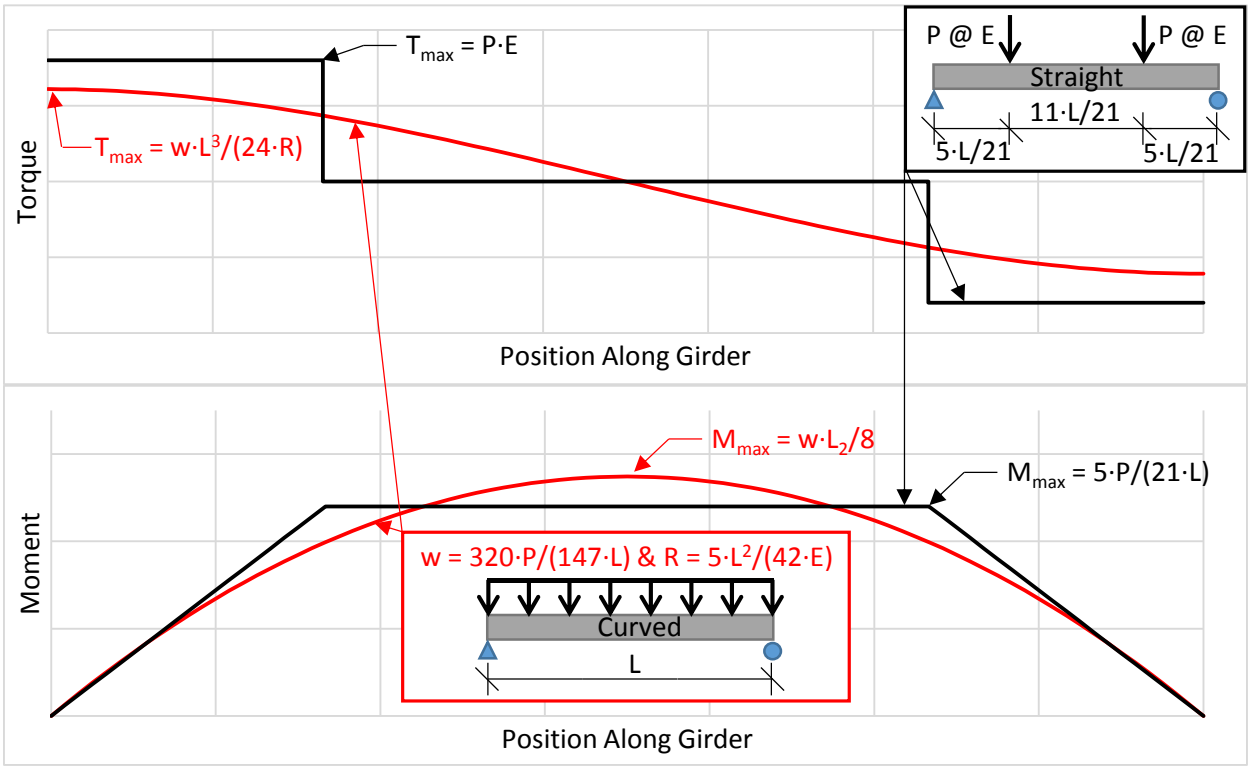

Figure 6.15 Moment & Torque Diagrams for Curved & Straight Simply Supported Tub Girders

6.5 Instrumentation

Load cells, strain gauges, string potentiometers (string-pots), and vision systems were all used to gather data during the tests. All load cells and string-posts were calibrated to ensure the

accuracy of the measurements. Figure 6.16 shows the instrumentation plan for the simply supported system, while Figure 6.17 shows the instrumentation plan for the overhanging system. Figure 6.18 shows the location of the strain gauges, string-pots, and position sensors on a cross-section of the tub girder. The strain gauges on the tub girder were primarily used to monitor the strain in the girder so that the test could be stopped prior to the girder reaching the inelastic range. Four strain gauges were placed at the center of each pipe member of the K-frames so that the axial force in each member could be calculated. Also, seven strain gauges were used at the centerline of each WT bracing members so that the axial force in the braces could be calculated. Four string-pots were mounted to each lateral loading frame (two connected vertically to the bottom flange and two connected horizontally to the web) so that deflections and twist of the girder could be captured at these locations. The two PCPs on the north end of the setup were instrumented in the same manner as the PCPs in the shear frame setup described in Chapter 4.

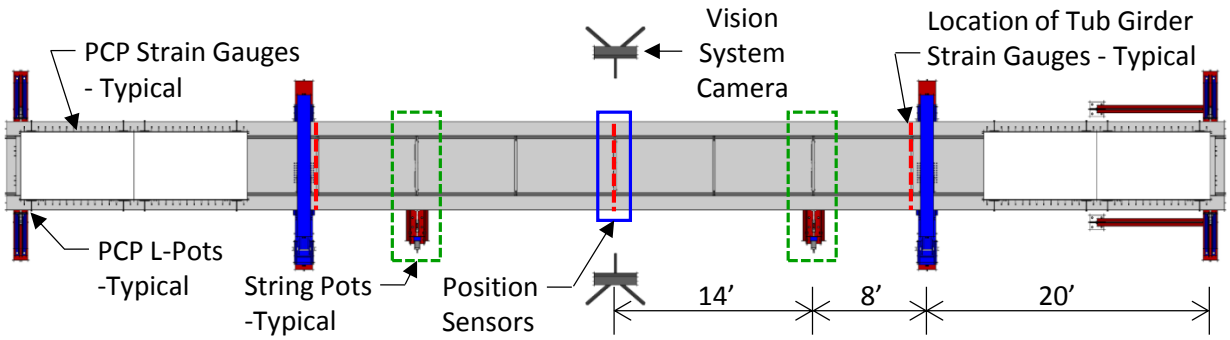

Figure 6.16 Instrumentation Layout for Simply Supported System – Plan View

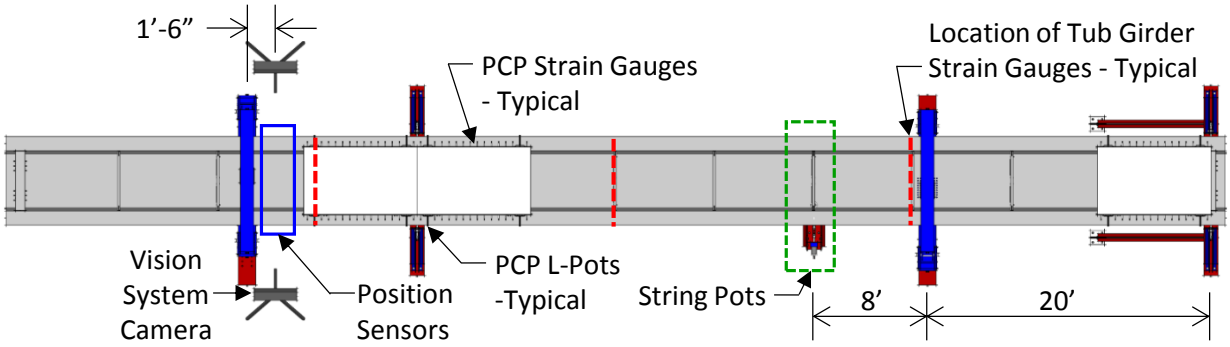

Figure 6.17 Instrumentation Layout for Overhang System – Plan View

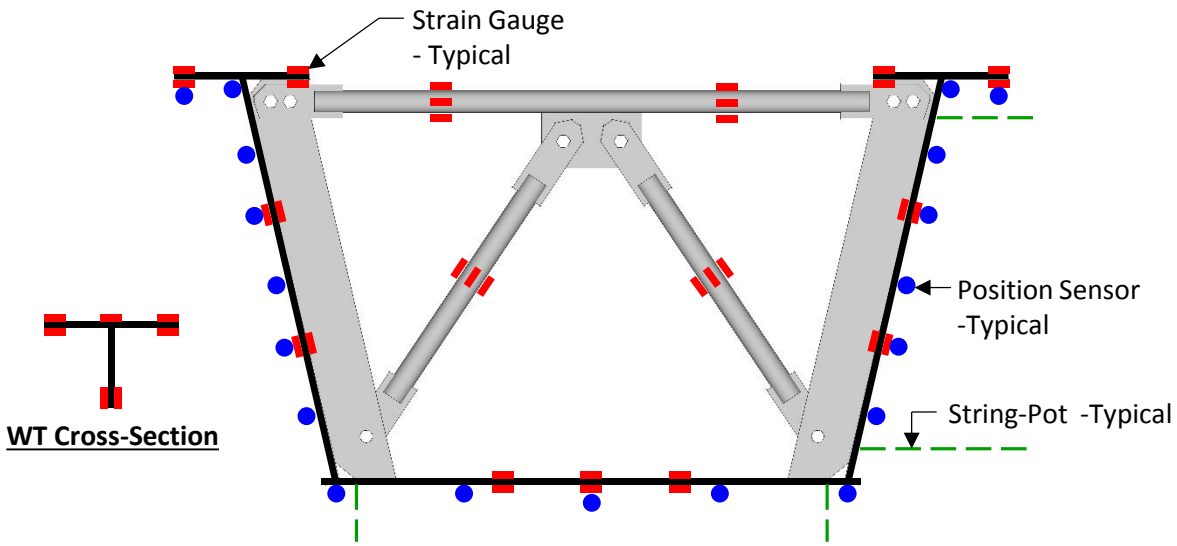

Figure 6.18 Instrumentation Layout on Tub Girder Cross-Section

6.5.1 Vision System Measurements

The two NDI Optotrack Certus HD vision system cameras used for the I-girder tests were used in tandem to measure the deformation of the girders at the points indicated in Figure 6.16 and Figure 6.17. The same method used establish the coordinate system and sync the data for the twin I-girder tests (Chapter 5) were used for the tub girder tests. Figure 6.19 shows the two cameras in use for the overhanging tub girder test.

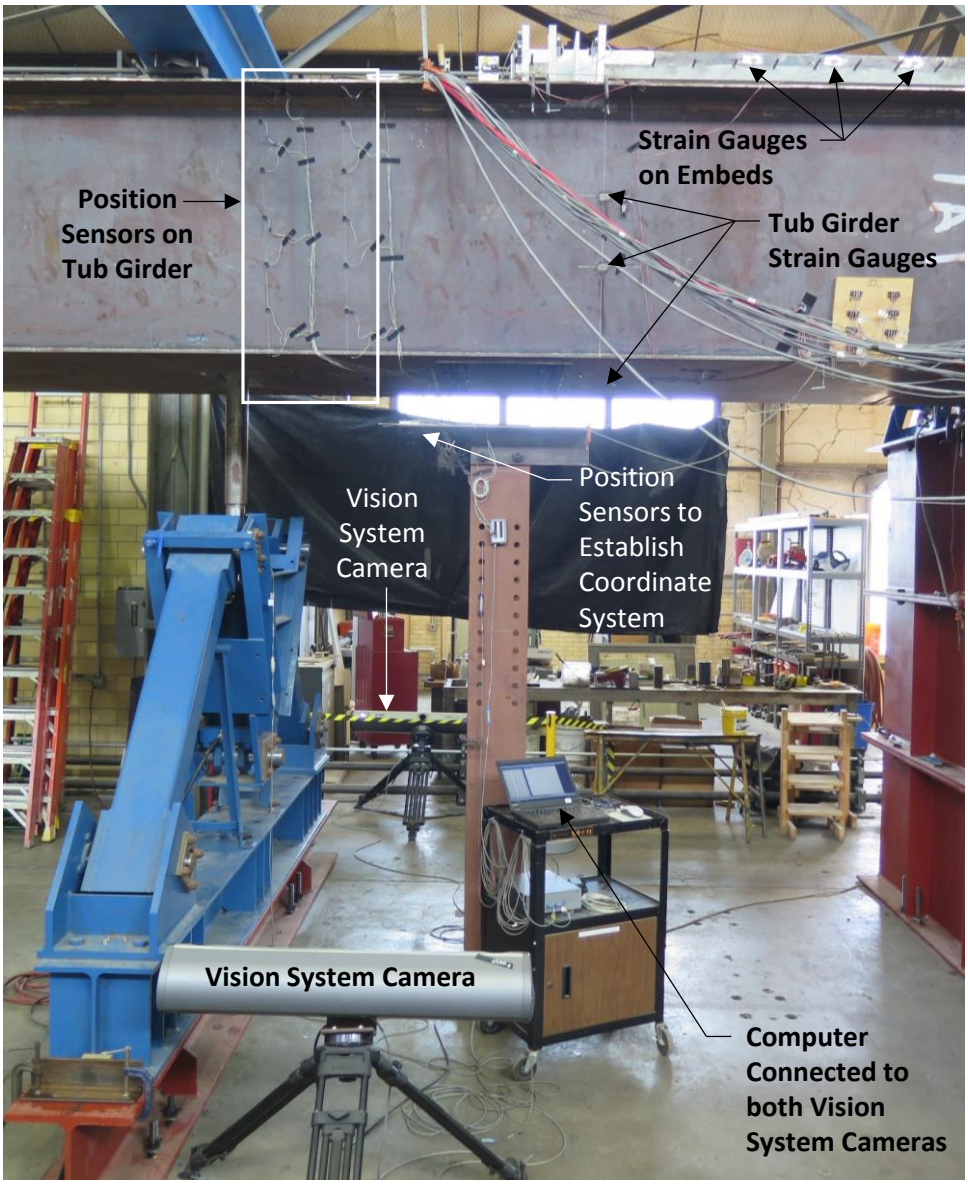

Figure 6.19 NDI Optotrack Certus HD Vision System – Tub Girder

6.5.2 Initial Imperfection Measurements

The initial imperfections of the tub girder were measured prior to the load test. A taut piano wire was strung the same distance from the bottom flange (d_{SUP_BF}) and the same distance from the top flange (d_{SUP_TF}) at each support. The deviations from the wire at the bottom flange (d_{BF}) were measured directly with calipers while a plumb bob and calipers were used to measure the deviations from the wire at the top flange (d_{TF}). Figure 6.20 shows the how the lateral imperfection of the bottom flange (Δ_{BF}), the lateral imperfection of the top flange (Δ_{TF}), and rotation of the girder (θ) can be calculated from the horizontal measurements. Data for the imperfections was collected at 7 ft increments along the length of the girders on both sides of the girders (the average values are presented in this report). Graphs of the initial imperfections are reported in Appendix C (note: west was selected as the positive direction for the initial imperfections).

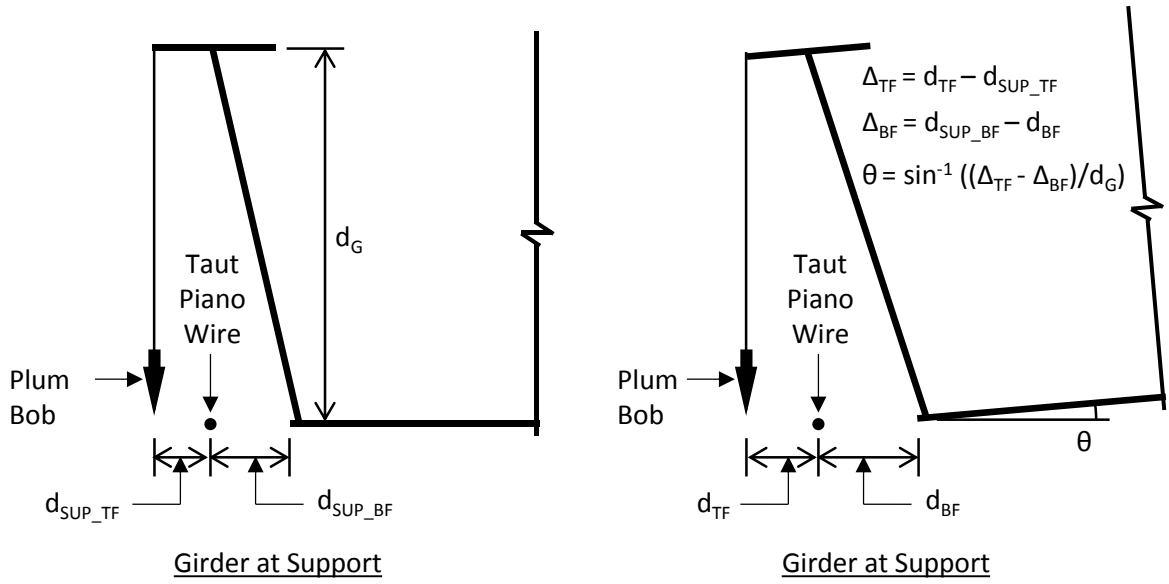

Figure 6.20 Tub Girder Initial Imperfection Measurements and Calculations

6.6 Testing Procedure

The same testing procedure for the twin I-girder tests was used for the tub girder tests. For convenience, the procedure is repeated below. To ensure consistent results, all tests were performed twice and the data was compared.

1. Move GLS to desired eccentricity
2. Measure tub girder's initial imperfections
3. Ensure bolts for knife edges are loose
4. Zero all load cells, L-pots, and strain gauges
5. Begin recording with data acquisition system and the vision systems
6. Apply GLS stabilizing load (500 lbs minimum) with each GLS
7. Disengage GLS adjustable struts so that the system can deflect laterally
8. Apply an incremental load
    a. Sync data recording systems by engaging L-pot with attached position sensor
    b. Mark cracks in PCPs, take applicable pictures, record notes, etc.
9. Repeat Step 8 until maximum load is reached
10. Close hydraulic needle valves then flip the hydraulic pump valve
11. Bleed hydraulic pressure with needle valves until GLS stabilizing load level is reached
12. Engage GLS adjustable struts to stabilize GLS
13. Bleed hydraulic pressure until no load remains on the system and take final readings

6.7 Experimental Results for Tub Girder Tests

A total of 5 lateral load tests and 24 gravity load tests were performed on the tub girder system at the Ferguson Structural Engineering Laboratory. Results from these test as explained in detail below.

6.7.1 Lateral Load Experimental Results – Simply Supported Tub

Table 6.2 provides a summary of the 5 lateral load tests that were performed in the laboratory. The nomenclature for the lateral load tests is shown in Figure 6.21. For these tests, the girder was loaded at third points (28 ft. from each end) near the top and bottom flanges (see Figure 6.12) with equal loads from all four hydraulic actuators (a maximum lateral load of 20 kips was placed on the system). Both PCPs and steel WT5x22.5 diagonals (DIAG) were used independently as bracing elements, with the total number of bracing elements varying (0, 2 PCPs, 4 PCPs, 2 DIAG, 4 DIAG) to determine their effect on the stiffness of the system. While graphs for the deflection and twist at midspan are shown in this section of the report, Appendix C containing the deflection and twist at the third point.

Table 6.2: Summary of Lateral Tub Girder Tests

Test Name	Load Loacation	K-Frame Location	Number of Braces
LAT.1	TP	2-Panel	0
LAT.2	TP	2-Panel	2 PCP
LAT.3	TP	2-Panel	4 PCP
LAT.4	TP	2-Panel	2 DIAG
LAT.5	TP	2-Panel	4 DIAG

Key: LAT = Top & Bottom Flange Lateral Load
TP = Third Point Loading, DIA = Diagonal

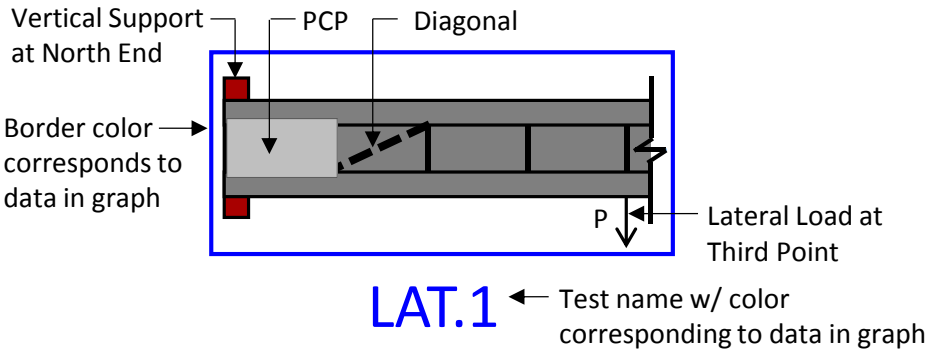

Figure 6.21 Nomenclature for Lateral Load Tub Girder Tests

The results from the lateral load tests showed that connecting PCPs to the top flange of the I-girders (thereby forming a torsionally stiff closed section at the end of the girder) significantly reduced the twist and top flange lateral deflection (see Figure 6.22 and Figure 6.23, respectively). Furthermore, each PCP provided approximately the same amount of stiffness to the system as each diagonal considering the girder deformation with 2 PCPs and 2 DIAGs and the girder deformation

with 4 PCPs and 4 DIAGs coincided with one another. Adding 2 PCPs or 2 DAIGs reduced the maximum measured twist at midspan from 4.2 degrees to 1.6 degrees and reduced the top flange lateral deflection at midspan from 4.2 in to 1.9 in. With 4 PCPs or DIAGs installed, the midspan twist and top flange lateral deflection was further reduced to approximately 0.65 degrees and 0.95 in, respectively. Therefore, the incremental increase in stiffness was larger going from no bracing to two than from two bracing elements to four. The PCPs were inspected during the lateral load tests and no cracking or damage to the PCPs was observed during the tests. Additional graphs for these tests are provided in Appendix C.

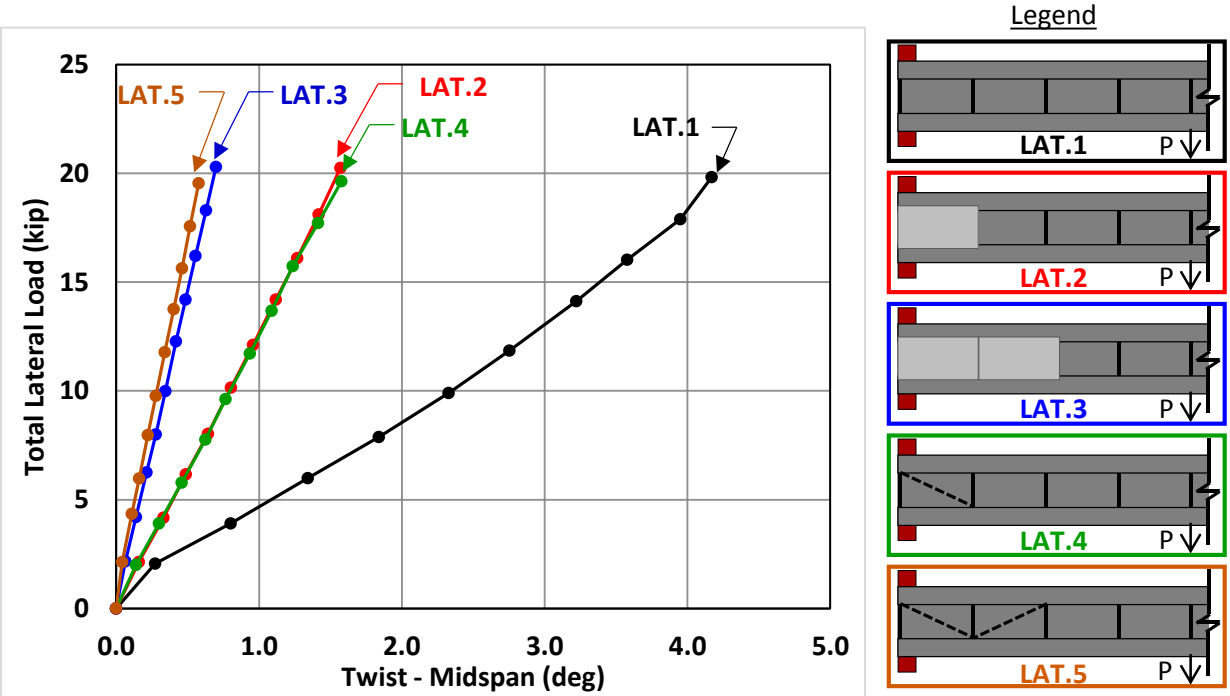

Figure 6.22 Twist @ Midspan vs. Lateral Load @ Third Point

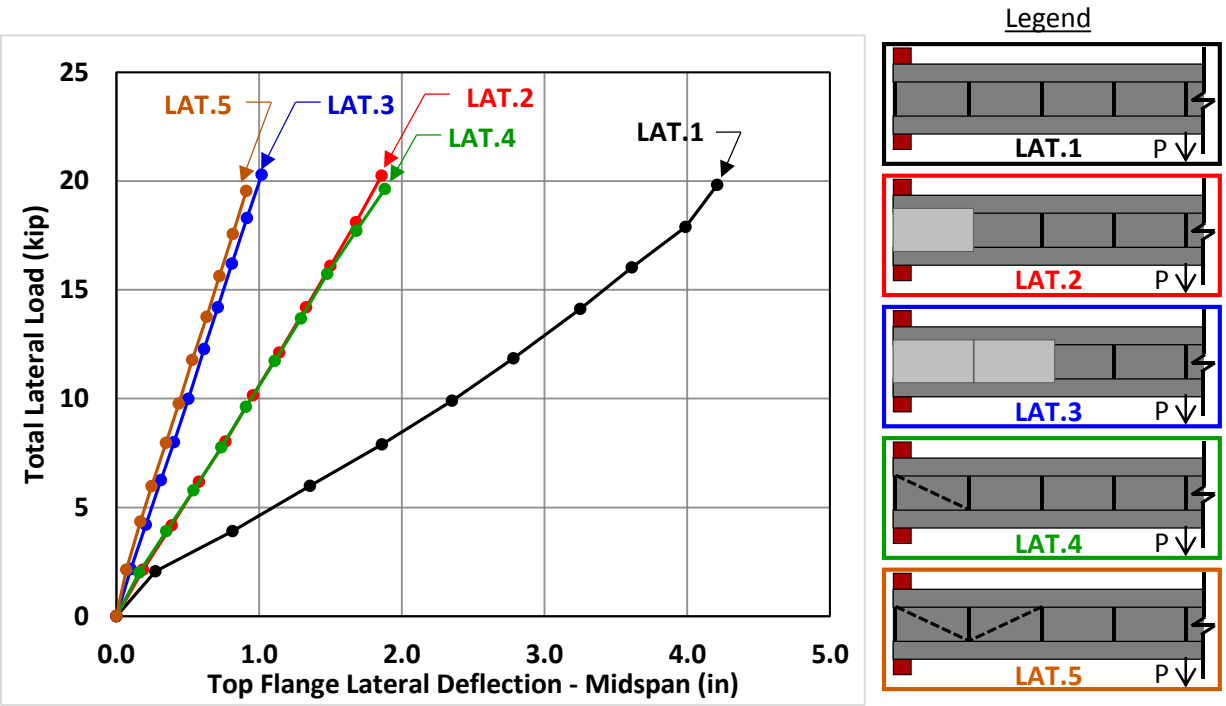

Figure 6.23 Lateral Deflection @ Midspan vs. Lateral Load @ Third Point

6.7.2 Combined Bending and Torsion Experimental Results - Simply Supported Tub

Table 6.3 provides a summary of the 15 bending and torsion load tests that were performed on the simply supported tub girder in the laboratory. The nomenclature for the GLS simply supported load tests is shown in Figure 6.24. Similar to the lateral load test, the total number of top flange bracing elements was varied (0 PCPs, 2 PCPs, 4 PCPs, 2 DIAG, and 4 DIAG). The eccentricity of the loads applied with the GLS were varied between 0 in., 8 in., and 16 in. to simulate the moment and torque diagrams of straight girders and girders with radii of curvature of infinity (straight), 1260 ft., and 630 ft., respectively. While graphs for a few of the tests are discussed in detail for this section of the report, a comprehensive collection of the graphs for the experimental results is provided in Appendix C.

Table 6.3: Summary of Bending and Torsion Simply Supported Tub Girder Tests

Test Name	Support Condition	Load Eccentricity	K-Frame Location	Number of Braces	Max Total GLS Load
GLS.1	SS	0 & 0	2-Panel	0	84
GLS.2	SS	0 & 0	2-Panel	2 PCP	100
GLS.3	SS	0 & 0	2-Panel	4 PCP	100
GLS.4	SS	0 & 0	2-Panel	2 DIAG	72
GLS.5	SS	0 & 0	2-Panel	4 DIAG	76
GLS.6	SS	8" & 8"	2-Panel	0	52
GLS.7	SS	8" & 8"	2-Panel	2 PCP	100
GLS.8	SS	8" & 8"	2-Panel	4 PCP	100
GLS.9	SS	8" & 8"	2-Panel	2 DIAG	80
GLS.10	SS	8" & 8"	2-Panel	4 DIAG	84
GLS.11	SS	16" & 16"	2-Panel	0	32
GLS.12	SS	16" & 16"	2-Panel	2 PCP	60
GLS.13	SS	16" & 16"	2-Panel	4 PCP	100
GLS.14	SS	16" & 16"	2-Panel	2 DAIG	52
GLS.15	SS	16" & 16"	2-Panel	4 DIAG	80

Key: GLS = Gravity Load Simulator Load, SS = Simply Supported
PCP = Partial Depth Precast Concrete Deck Panel, DIA = Diagonal

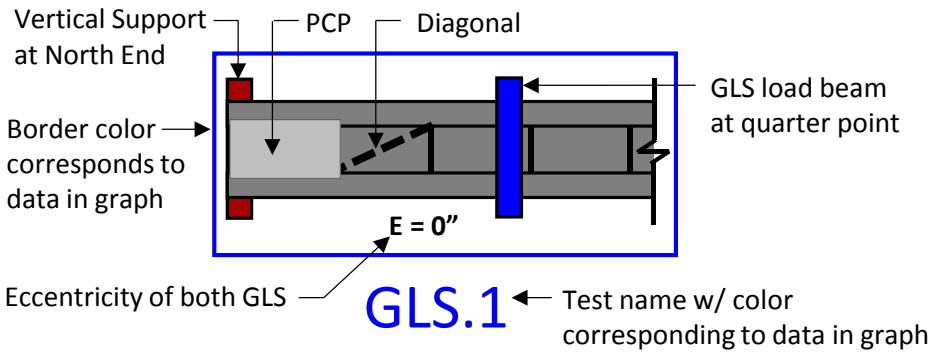

Figure 6.24 Nomenclature for GLS Simply Supported Tub Girder Tests

Concentrically Loaded (E=0") Simply Supported Tests (GLS.1 through GLS.5)

The midspan twist and top flange lateral deflection of the tub girder at midspan are shown in Figure 6.25 and Figure 6.26, respectively for the concentrically loaded girder. The addition of just one bracing element to each end of the tub girder (2 PCPs or 2 DIAGs) significantly increased the stiffness of the girder with respect to the resistance of both twist and lateral deflection. At a total GLS load of approximately 70 kips, the measured girder twist was reduced from -1.96 degrees to -0.29 degrees with the addition of 2 DIAGs and to -0.17 with the addition of 2 PCPs. The girder stiffness was further increased when one more bracing element was added to each end reducing the measured twist to -0.09 degrees for 4 DIAGs and to -0.02 for 4 PCPs under the same load level. Therefore, the PCPs added slightly more stiffness to the system than the WT diagonals for the GLS

tests with concentric loads. Additional graphs of the girders twist and lateral deflection at third points are given in Appendix C.

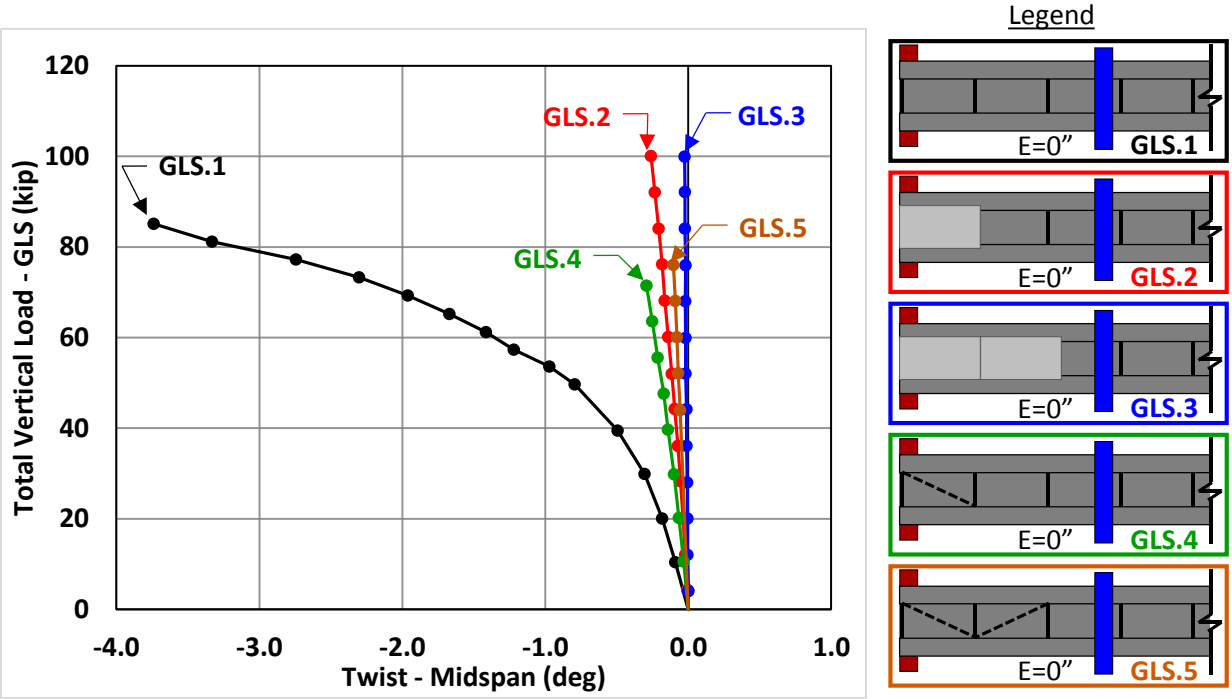

Figure 6.25 Twist @ Midspan vs. GLS Load (E=0")

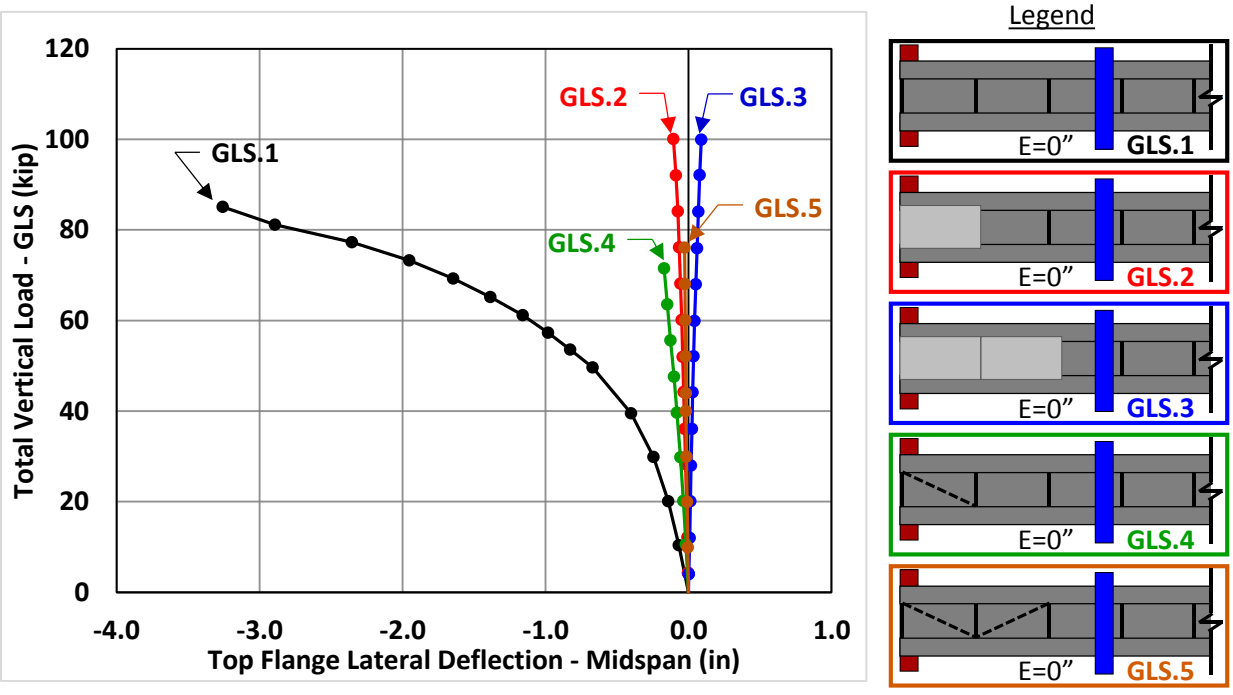

Figure 6.26 Lateral Deflection @ Midspan vs. GLS Load (E=0")

A linear regression method similar to the one used by Fan (1999) was used to calculate the axial force in the WT diagonals from the 7 strain gauges that were located at each cross-sections midspan. Figure 6.27 shows the forces in the diagonals as the total GLS load was increased for the concentric load cases. The addition of a diagonal reduced the average force in the first diagonal by a factor of 1.65 (from -4.1 kips to -2.5 kips in compression) when a total load of 70 kips was placed on the system by the two GLS.

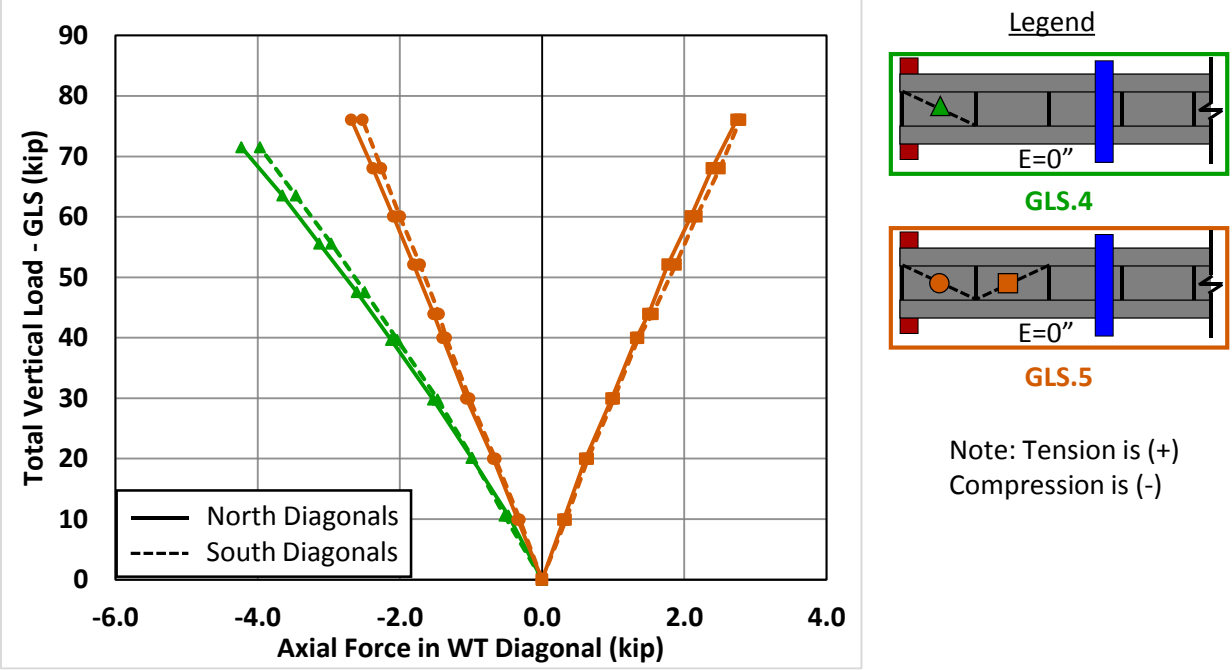

Figure 6.27 Diagonal Forces vs. GLS Load (E=0")

Eccentrically Loaded (E=16") Simply Supported Tests (GLS.11 through GLS.15)

The midspan twist and top flange lateral deflection of the tub girder at midspan are shown in Figure 6.28 and Figure 6.29, respectively for the tub girder loaded with a 16 in. eccentric load. Similar to the concentric case, the addition of just one bracing element to each end of the tub girder (2 PCPs or 2 DIAGs) significantly increased the stiffness of the girder with respect to both twist and lateral deflection. At a total GLS load of approximately 32 kips, the measured girder twist was reduced from 4.65 degrees to 0.92 degrees with the addition of 2 DIAGs and to 0.83 with the addition of 2 PCPs. The girder stiffness was further increased when one more bracing element was added to each end reducing the twist to 0.27 degrees for 4 PCPs and to 0.21 for 4 DIAGs. Therefore, the 4 PCPs added slightly more stiffness to the system than the 4 DIAGs, but the 2 DIAGs added slightly more stiffness than the 2 PCPs. Additional graphs of the girders twist and lateral deflection at third points are given in Appendix C. The girders twisted in opposite directions for the eccentric load cases (positive twist) and the concentric load cases (negative). The direction of twist was dominated by the initial imperfections of the tub girder for the concentric case and dominated by the direction offset load for the eccentric case.

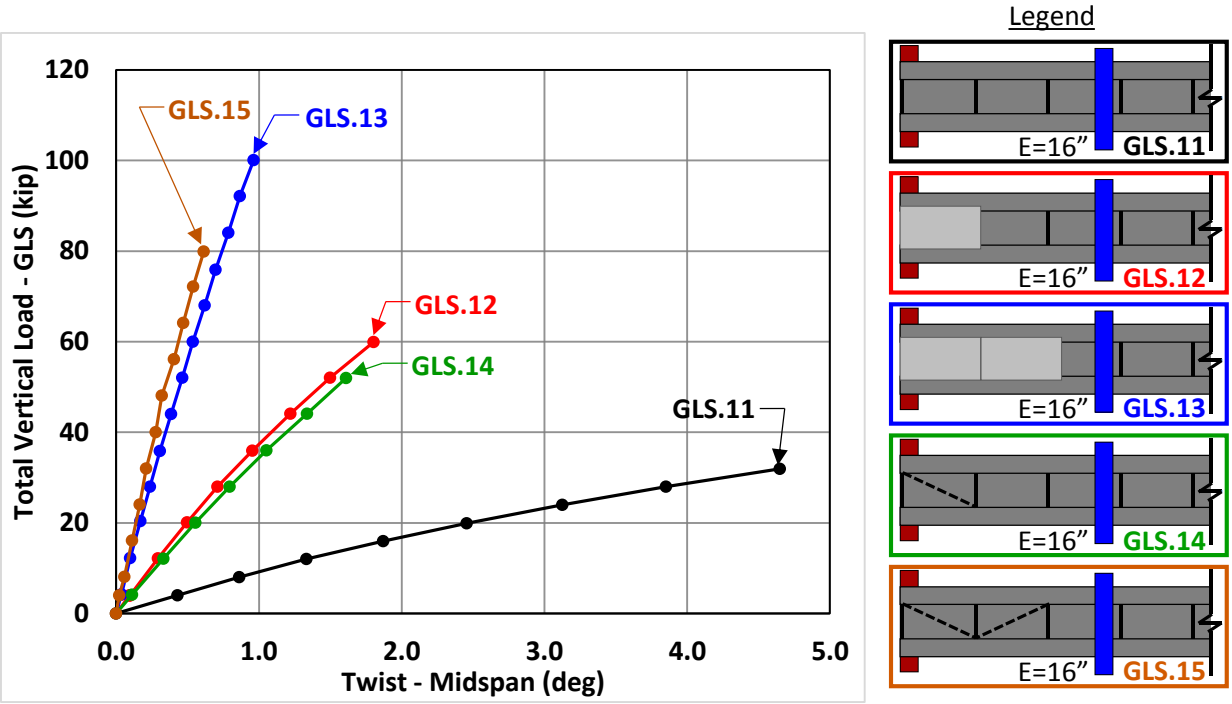

Figure 6.28 Twist @ Midspan vs. GLS Load (E=16")

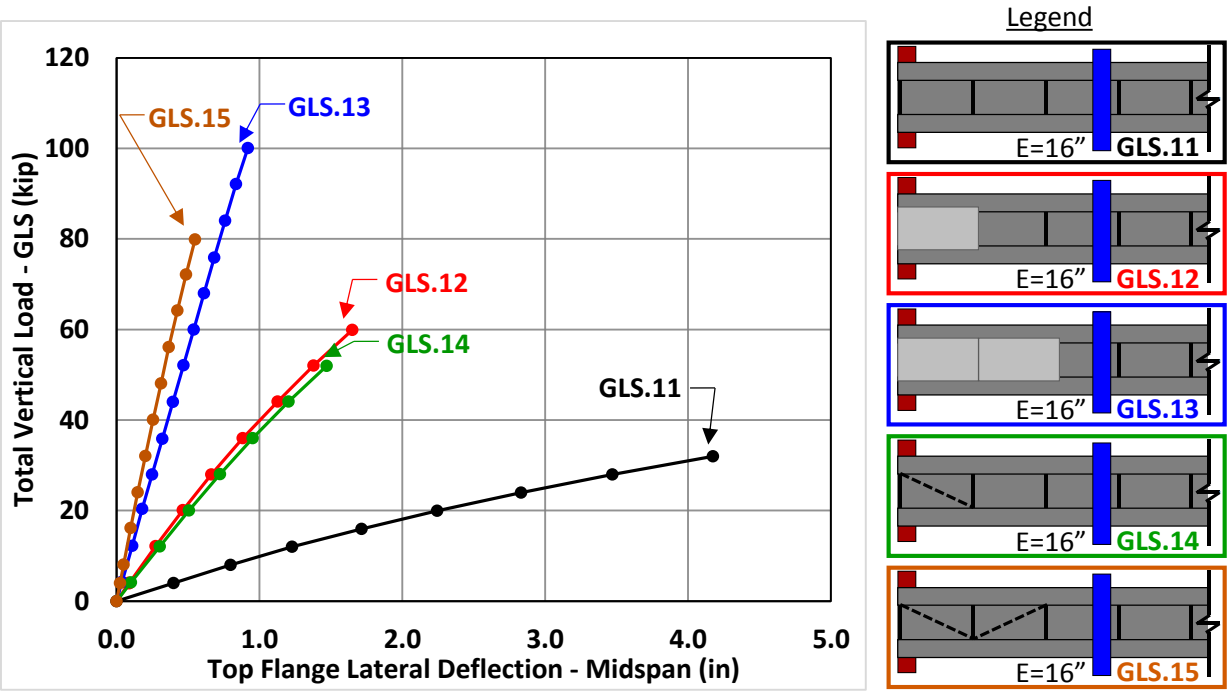

Figure 6.29 Lateral Deflection @ Midspan vs. GLS Load (E=16")

Similar to the concentric GLS load case, the addition of a diagonal elements significantly reduced the force in the first diagonal element for the eccentric load cases. At a total GLS load of 52 kips and an eccentricity of 16 inches, the average force in the first brace reduced by a factor of 1.9 (from 23.6 kips to 12.4 kips in tension) when a second brace was added to each end of the girder (see Figure 6.30). Of the six tests conducted with diagonals for the simply supported case, a maximum brace force of -24.2 kips (compression) was recorded during GLS.15.

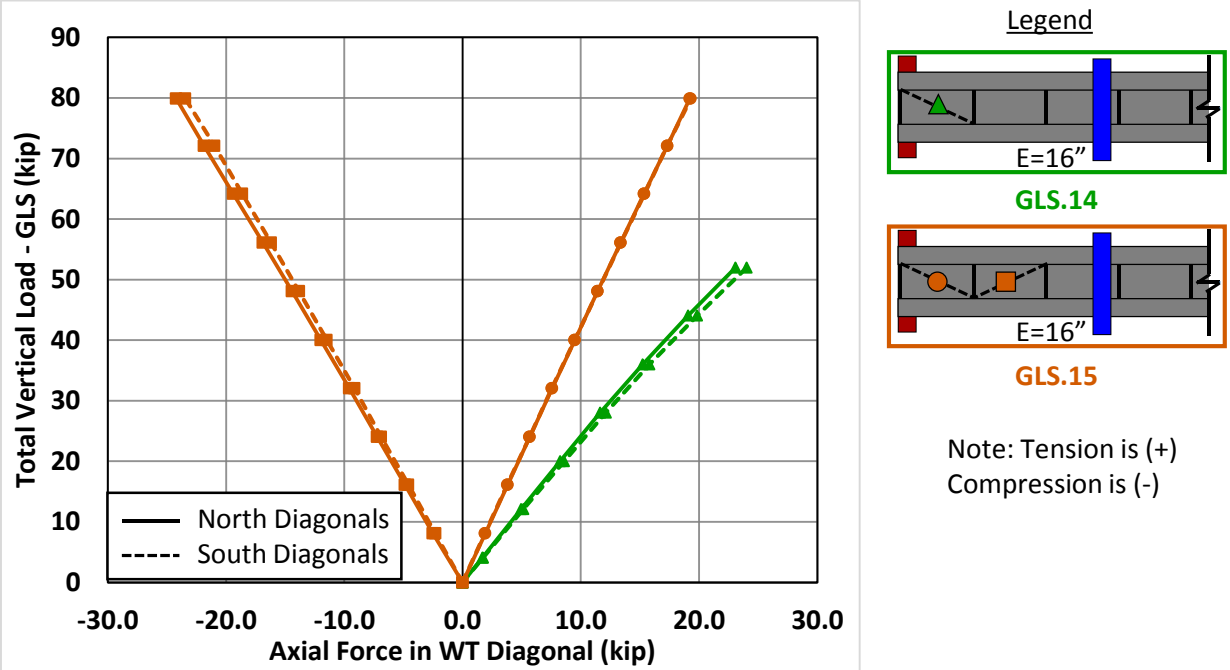

Figure 6.30 Diagonal Forces vs. GLS Load (E=16″)

The relative behavior of the tub girder with and without PCPs and DIAGs was similar when the load eccentricity was decreased from E=16″ (for cases GLS.11 through GLS.15) to E=8″ (for cases GLS.6, through GLS.10) with the magnitude of the twist, lateral deflection, and diagonal forces decreasing due to the smaller torsional load on the system. Experimental results for cases GLS.6 through GLS.10 can be found in Appendix C.

PCP Performance during Simply Supported GLS Tests

During the simply supported GLS tests, the PCPs performed well from a serviceability standpoint. Figure 6.31 shows the minor cracks that formed on the top of the PCPs during the tests (permanent markers were used to trace next to the cracks during the test and the marker was traced in the figure below to make them visible). The majority of the cracks occurred during GLS.12 where only one PCP was connected at each end of the girder and the GLS were placed at the maximum of 16 inches. No crack width exceeded approximately 0.010 inches throughout the tests for the simply supported girder. Also, no cracking was observed on the bottom of the PCPs (likely due to positioning of the embeds in the upper portion of the PCP).

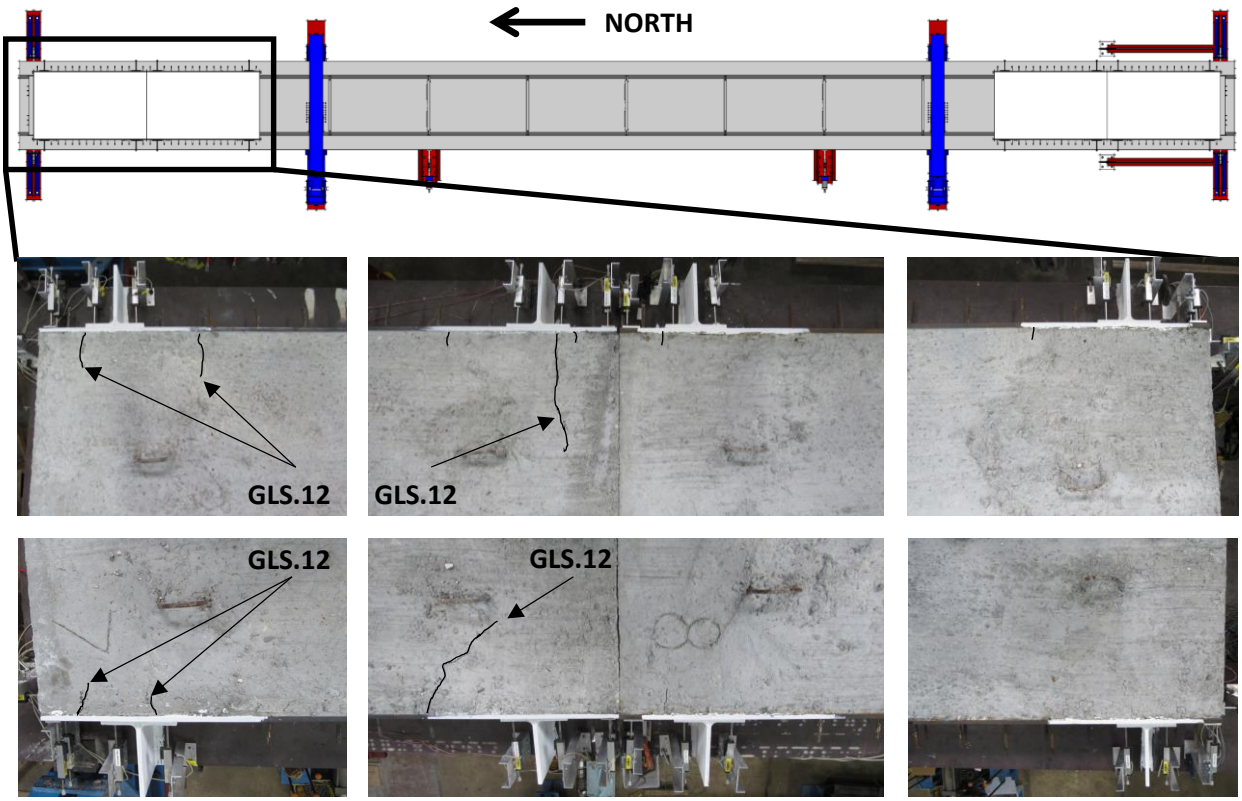

Figure 6.31 Crack Patterns of PCPs during Simply Supported Tests

6.7.3 Combined Bending and Torsion Experimental Results - Overhang Tub

Table 6.4 provides a summary of the 9 bending and torsion load tests that were performed on the overhang tub girder system in the laboratory. The nomenclature for the GLS overhang load tests is shown in Figure 6.32. The overhang tests were performed with the GLS at three different load eccentricities with the north GLS offset east (negative eccentricity) of the center of the tub and the south GLS offset west (positive eccentricity) of the center of the tub. The tub was tested without any bracing at the top flange, with three diagonals at the top flange (3 DIAG – see Figure 6.33), and with three PCPs connected to the top flange (3 PCPs – see Figure 6.34). While graphs for a few of the tests are discussed in detail for this section of the report, a comprehensive collection of the graphs with the experimental results are provided in Appendix C.

Table 6.4: Summary of Bending and Torsion Overhang Tub Girder Tests

Test Name	Support Condition	GLS North Eccentricity	GLS South Eccentricity	K-Frame Location	Max Total GLS Load	Max Total GLS Load
GLS.16	OH	-2"	4"	2-Panel	0	200
GLS.17	OH	-2"	4"	2-Panel	3 PCP	200
GLS.18	OH	-2"	4"	2-Panel	3 DIAG	200
GLS.19	OH	-4"	8"	2-Panel	0	200
GLS.20	OH	-4"	8"	2-Panel	3 PCP	200
GLS.21	OH	-4"	8"	2-Panel	3 DIAG	200
GLS.22	OH	-6"	12"	2-Panel	0	200
GLS.23	OH	-6"	12"	2-Panel	3 PCP	300
GLS.24	OH	-6"	12"	2-Panel	3 DIAG	200

Key: GLS = Gravity Load Simulator Load, OH = Overhang Support
PCP = Partial Depth Precast Concrete Deck Panel, DIA = Diagonal

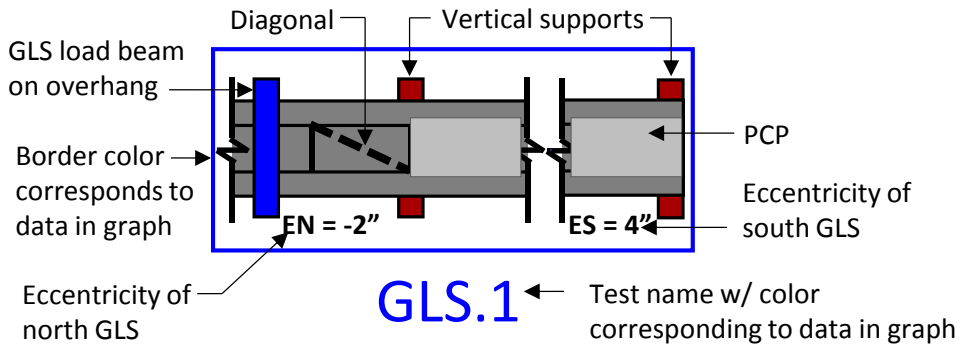

Figure 6.32 Nomenclature for GLS Overhang Tub Girder Tests

Figure 6.33 Tub Girder Experimental Test Setup – Overhang – 3 DIAGs

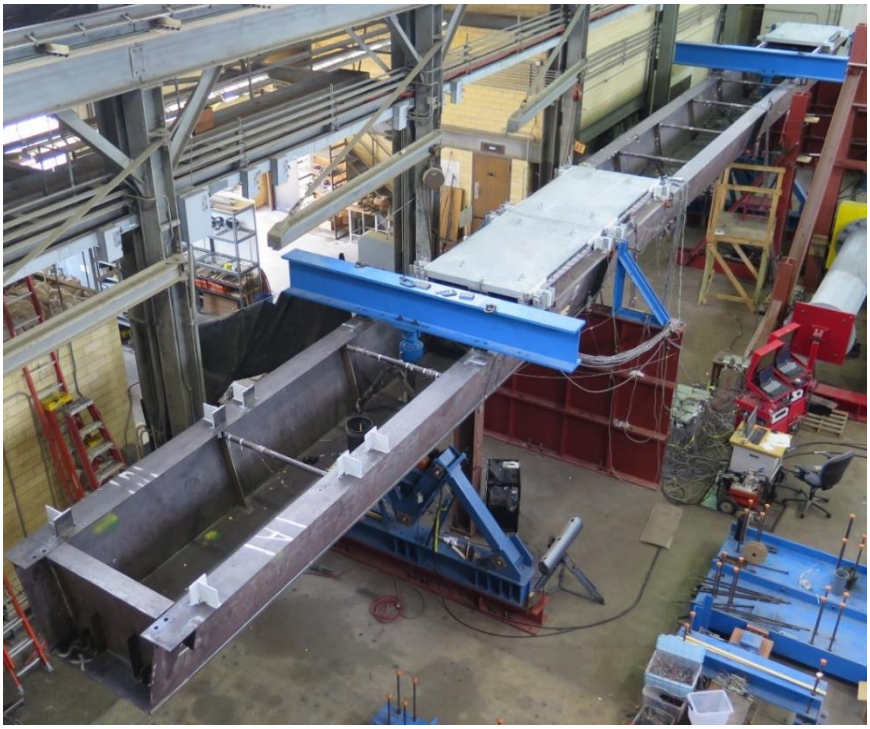

Figure 6.34 Tub Girder Experimental Test Setup – Overhang – 3 PCPs

GLS Overhang w/ Minimum Eccentricity Tests (GLS.16, GLS.17, and GLS.18)

Figure 6.35 shows the twist of the tub girder measured with the vision system at the overhang (10.5 ft. from the support) and the twist of the girder at the centerline of the backspan using string-pots. Similarly, Figure 6.36 shows the top flange lateral deflection of the tub girder at the same locations. The GLS on overhang was offset to the east of the center of the girder by 2″ (negative eccentricity) while the GLS on the backspan was offset to the west of the center of the girder by 4″ (positive eccentricity). Offsetting the GLS in opposite directions maximized demand on the PCPs in the negative moment region as it causes more warping deformation of the top flange than when the GLS are offset in the same direction. Similar to the simply supported case, adding bracing components to the top flange significantly decreased both the twist of the girder and the lateral defection of the top flange. Adding PCPs and DIAGs reduced the maximum measured twist of the girder at the overhang by more than a factor of 5 (from -1.27 degrees to -0.24 degrees for both PCPs and DIAGs) and reduced the maximum twist of the at the back span by more than a factor of 4 (from 1.58 degrees to 0.38 degrees and 0.22 degrees for the DIAGs and PCPs, respectively). In regards to both twist and top flange lateral deflection, the tests with PCPs and DIAGs produced similar results with the PCPs providing slightly more stiffness to the system at the backspan.

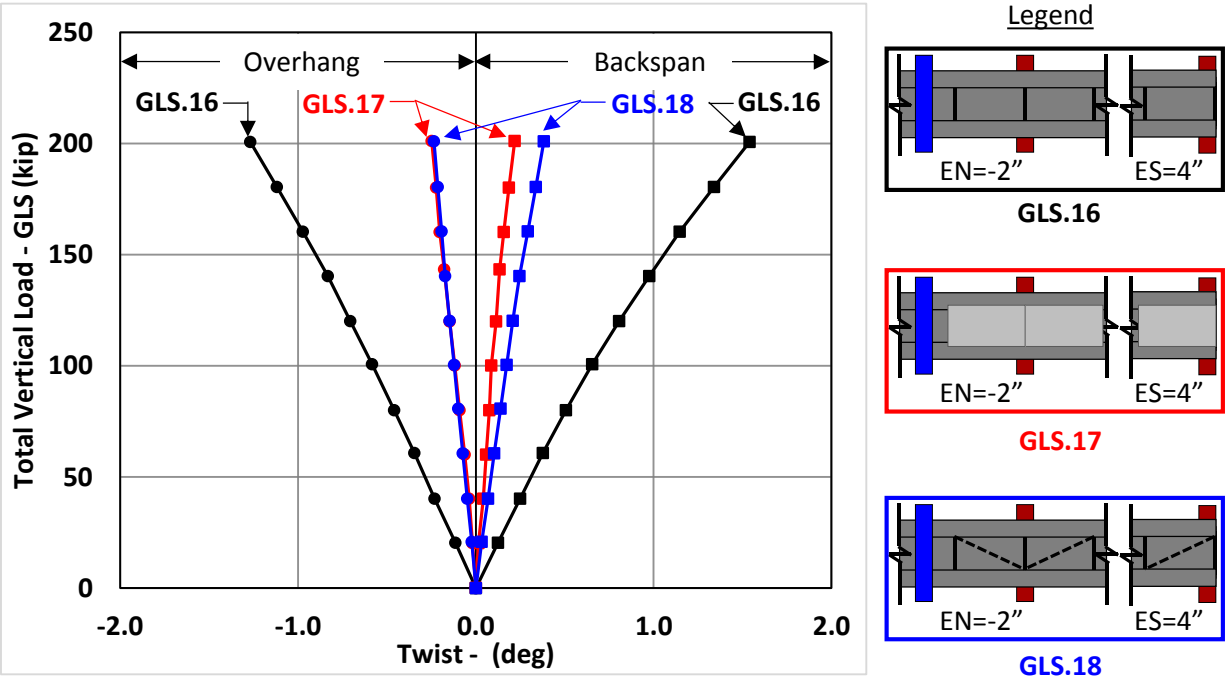

Figure 6.35 Twist vs. GLS Load (EN=-2" & ES=4")

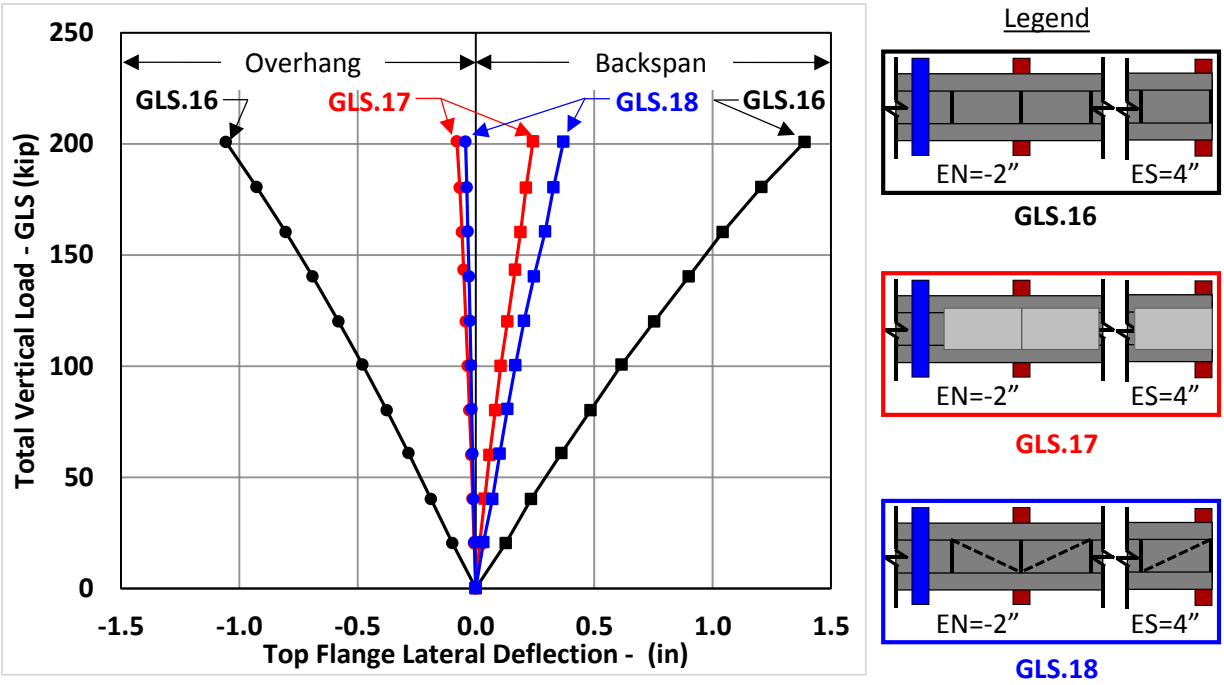

Figure 6.36 Lateral Deflection vs. GLS Load (EN=-2" & ES=4")

GLS Overhang w/ Maximum Eccentricity Tests (GLS.22, GLS.23, and GLS.24)

Figure 6.37 and Figure 6.38 shows the twist and the top flange lateral defection at the overhang and the back span when the overhanging tub girder was loaded at the maximum eccentricity (6 inch eccentricity to the east at the overhang and 12 inches to the west at the backspan). Adding PCPs and DIAGs reduced the measured twist of the girder at the overhang by more than a factor of 6 (from -3.73 degrees to -0.57 degrees for both PCPs and DIAGs) and reduced the measured twist at the back span by more than a factor of 4 (from 5.36 degrees to 1.16 degrees and 0.92 degrees for the DIAGs and PCPs, respectively) when a total vertical load of 200 kips was placed on the system with the GLS. Figure 6.29 shows the deformation of the girder under a total vertical load of 200 kips with and without the PCPs installed. In regards to both twist and top flange lateral deflection, the tests with PCPs and DIAGs produced similar results with the PCPs providing slightly more stiffness to the system at the backspan. For the final test conducted on the tub girder system (GLS.23), a maximum load of 150 kips was placed on the tub girder with each GLS (for a total vertical load of 300 kips) which is just below the 160 kip capacity of each GLS. Above a total load of 250 kips, some non-linear behavior was observed in the backspan of the girder.

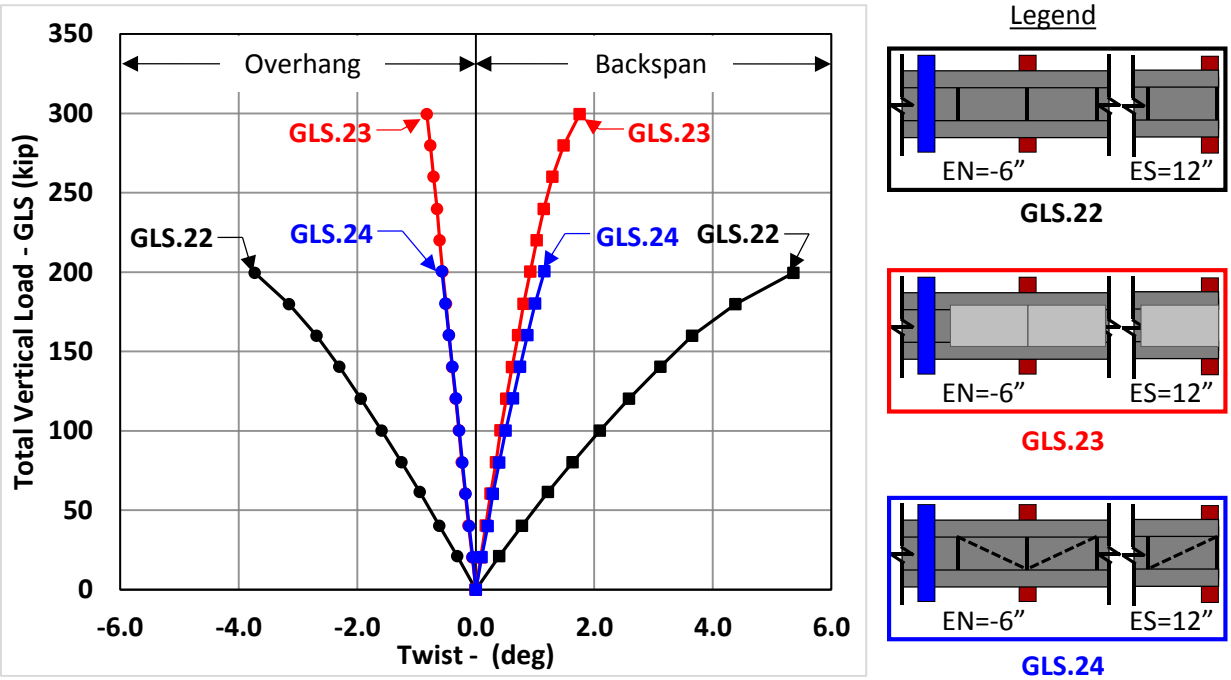

Figure 6.37 Twist vs. GLS Load (EN=-6" & ES=12")

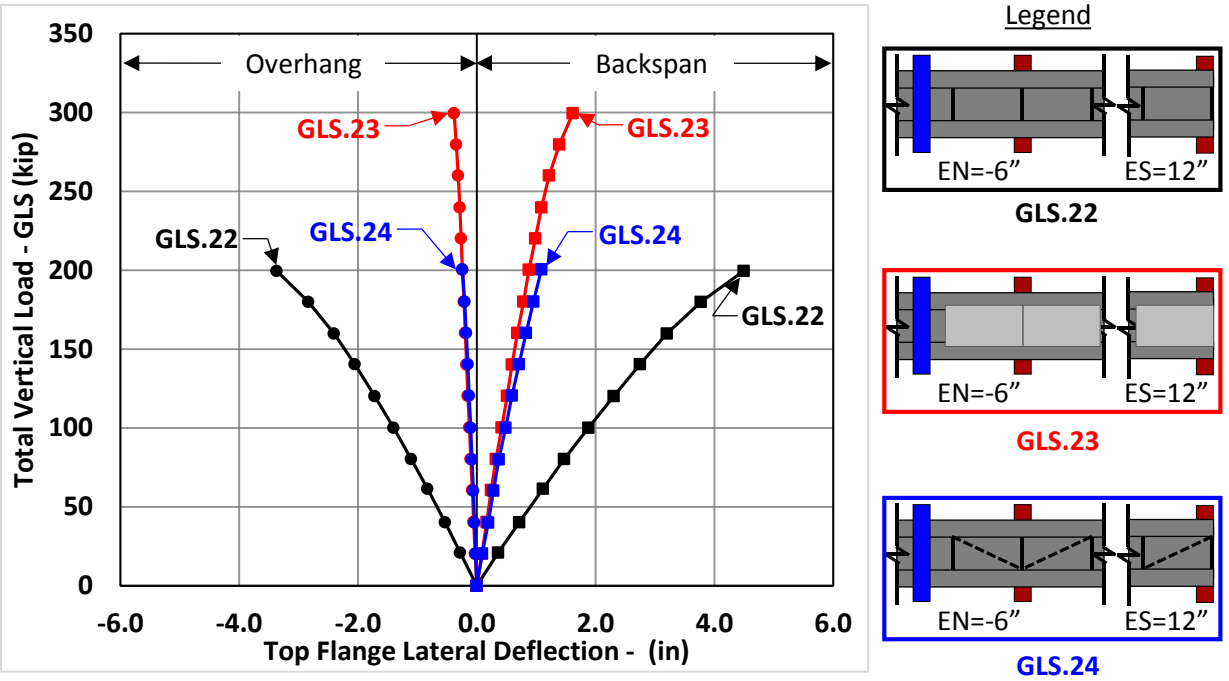

Figure 6.38 Lateral Deflection vs. GLS Load (EN=-6" & ES=12")

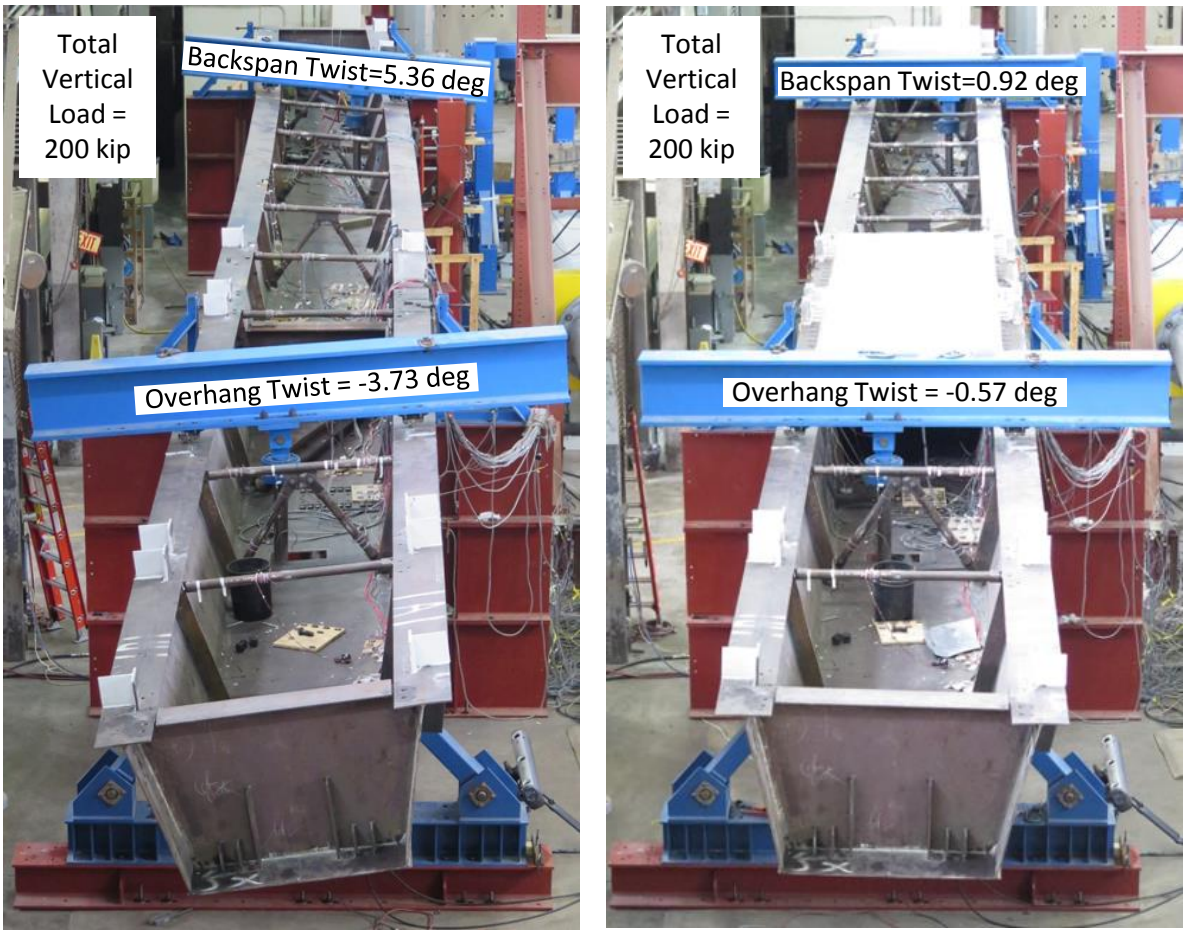

Figure 6.39 Photo of Girder Deformation with and without PCPs

Diagonal Forces during Overhang GLS Tests (GLS.16 through GLS.24)

Figure 6.40 shows the axial forces in all three diagonals during the overhang tests at the three different levels of load eccentricity. As expected, the force in each diagonal increased with increased eccentricity on the tub girder. The diagonals were orientated in a manner that resulted in compression in the north diagonal in the backspan and while the other two diagonals experienced tensile stresses.

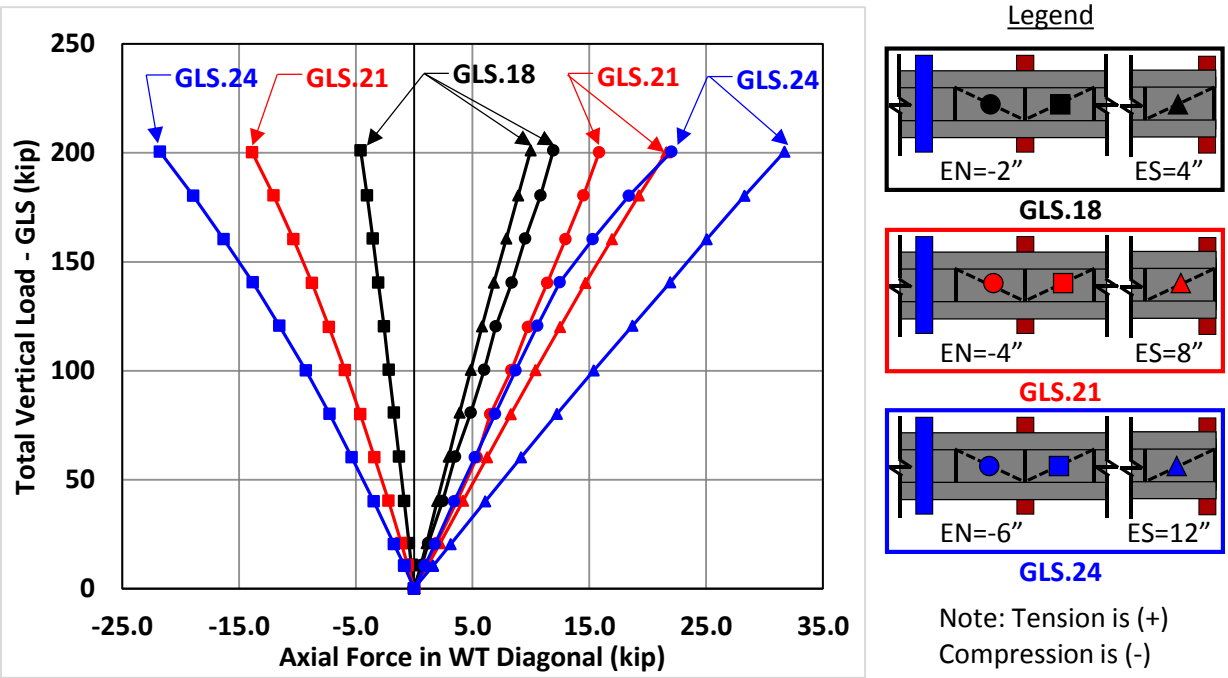

Figure 6.40 Diagonal Forces vs. GLS Load – Overhang

PCP Performance during Overhang GLS Tests

Figure 6.41 shows the crack patterns of the PCPs during the overhang tests (permanent markers were used to trace next to the cracks during the test and the marker was traced in the figure below to make them visible). The color of the traced crack corresponds to the test in which the crack occurred. Note the PCPs from the simply supported tests had very little damage and were reused for the overhang test (cracks from the simply supported test are traced in black in the figure). Much larger crack widths were observed for the overhanging tests than for the simply supported tests with the largest crack width of 0.040 inches occurring at the maximum load during GLS.23 (see Figure 6.41). No cracking was observed on the bottom of the PCPs. The crack pattern indicated that a compression strut was forming in each PCP.

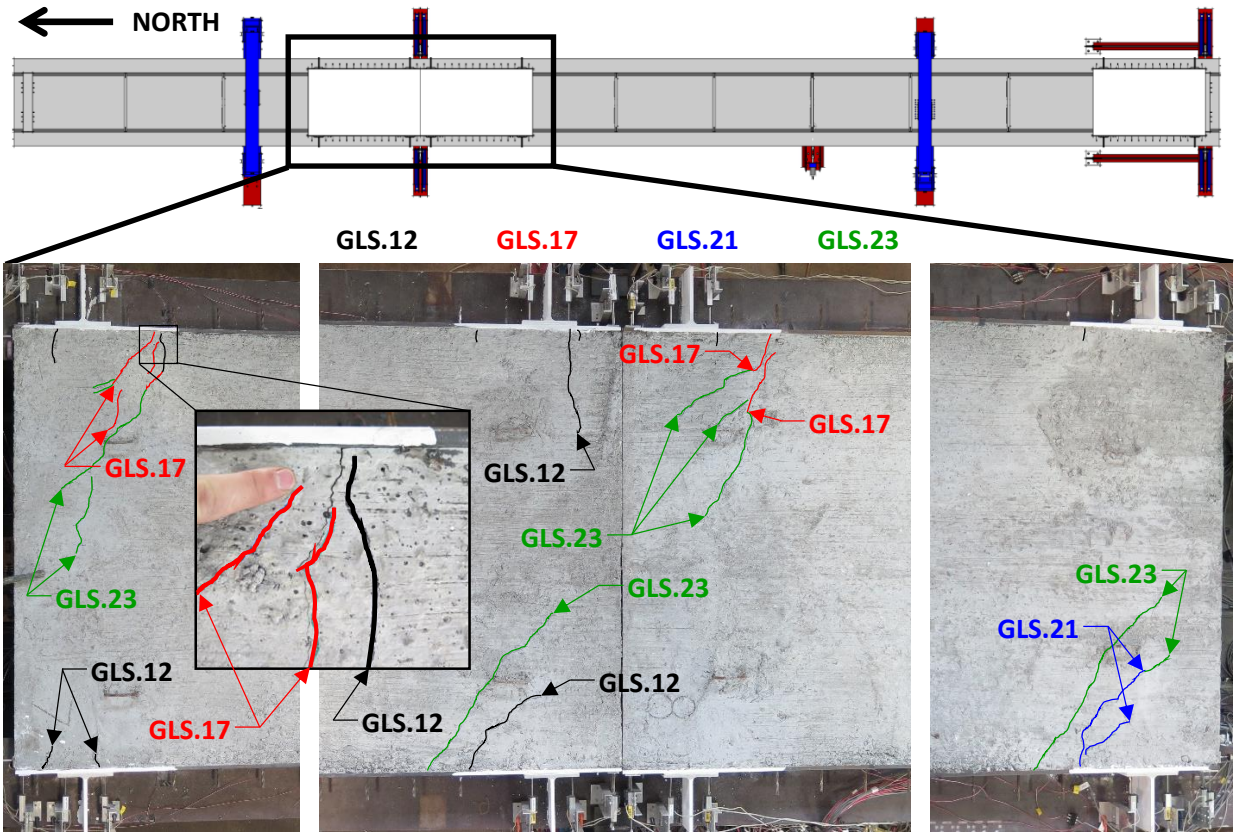

Figure 6.41 Crack Patterns of PCPs during Overhang Tests

6.8 Summary of Tub Girder Experimental Results

This chapter focused on the experimental test that were conducted in the laboratory on the tub girder system. Several conclusion can be drawn from the experimental program:

- Connecting PCPs or DIAGs to the tub girder system significantly reduced the lateral deflection of the girder during the lateral load tests. Similar results were observed when the same number of PCPs and DIAGs were attached to the top flange.
- Connecting PCPs or DIAGs to the tub girder system significantly reduced both the girder twist and the top flange lateral deflection for both the simply supported system and the overhang system. In general, adding the same number of PCPs to the system as DIAGs produced similar results (with the PCPs providing slightly more stiffness in some cases).
- During the simply-supported test, minor cracks formed in the PCPs (the largest observed crack width was approximately 0.010 inches. Larger cracks were observed in the PCPs in the negative moment region during the overhanging case with a maximum observed crack width of approximately 0.040 inches. Throughout the tests, no yield lines or visible forms of damage were observed on the WT connectors. Also, no cracks were visible in the welds of the connection to the WTs to the top flanges of the girder or the embeds.

- The brace forces in the WT diagonals were monitored throughout the tub girder experimental program. A maximum axial diagonal force of 24.2 kips was observed during the simply-supported case while a maximum axial diagonal force of 31.7 kips was observed during the overhang case.
- The lateral bracing elements were more effective when placed near the supports of the simply supported system (where shear deformations of the girders were maximum). Addition of one bracing element (PCP or DIAG) at each end significantly increased the stiffness of the system. The inclusion of additional bracing elements resulted in a smaller incremental increase in the system stiffness. Therefore, adding bracing elements at the end of the girder proved to be more effective than adding them towards midspan.

The results mentioned above are specific to the parameters of the laboratory tests described in this chapter. Comparisons of these results and FEA models are shown in Chapter 9 for the purposes of validation of the finite element models. The validated models were used to extend the experimental results to a wide array of curved tub girder bridges, allowing a better understanding of the bracing potential of PCPs on more realistic tub girder systems.

Chapter 7. Full-Scale Shear Tests on PCP to U-Beam Connections

As described in Chapter 1, horizontally curved prestressed concrete U-beams can potentially be an economical alternative to steel I-girders or steel tub girders for horizontally curved bridges. Bridges with curved concrete U-beams have been successfully utilized in Colorado. In these applications, horizontally curved prestressed concrete U-beams are spliced together with post-tensioning to form a continuous girder. While a spliced curved concrete U-beam bridge has yet to be constructed in the state of Texas, TxDOT has begun designing these systems as alternatives to traditional curved steel girder systems.

In constructing bridges with spliced curved concrete U-beams, after the U-beams are erected, the approach used in Colorado and envisioned in Texas calls for the placement of partial-depth precast concrete panels (PCPs) as lid slabs on top of the U-Beam. The PCP lid slabs are attached to the top flanges of the U-beam through a closure pour. After completion of the closure pour, the U-beam is closed and can provide high torsional stiffness as the deck construction is completed. The next step in construction is to place PCPs between adjacent U-beams. Finally, deck is completed by pacing the cast-in-place (CIP) topping.

The connection between the PCP lid slab and the top flanges of the U-beams must be able to resist the forces associated with the additional torsion placed on the system by the PCPs spanning between U-beams and by the placement of the CIP topping and the concrete deck. While TxDOT has developed a detail for the closure pour that connects the PCP lid slab to the U-beam, there have not been any tests on the performance of this detail when subjected to the in-plane shear forces that would develop during the construction of this bridge system. Further, little data is available on the actual forces that will be developed at this connection detail during the various construction phases for the deck.

A series of experiments were undertaken to evaluate the strength and stiffness of the proposed connection detail between the PCP lid slab and the U-beam, and to examine possible changes to this detail for improved structural performance and constructability. By modifying the shear frame developed by the research team (see Chapter 4), the shear strength and stiffness of the closure pour connection detail using a variety of reinforcement details and connection geometries was evaluated. These tests are described in this chapter. The results of these tests were then used in parametric finite element studies (discussed in Chapter 10) to determine the effectiveness of using connected PCPs to brace curved concrete U-beams during deck construction.

7.1 Existing Closure Pour Detail

Although TxDOT has yet to utilize concrete U-beams for curved girder applications, the concrete deck construction will likely follow the procedure that has been used in other applications such as the method employed in the state of Colorado (Reese and Nickas 2010). In these previous applications, the deck was cast in two separate stages. The first stage will typically consist of a closure pour intended to connect a precast concrete panel lid slab to a prestressed concrete U-beam (See Figure 7.1), forming a closed section, and providing the capacity to resist the torsion created during the remaining stages of the deck construction. The second stage will then consist of placing an additional unconnected PCP between the girders, and casting a topping slab to complete the full thickness of the bridge deck (See Figure 7.2). The detail that is to be evaluated in this program focuses on the first stage, with the closure pour that will engage the PCP lid slab and concrete

girder. The reinforcing shown in Figure 1.1 is the current TxDOT recommended detail for the reinforcing detail for the closure pour; however the performance of this detail has not been previously tested or used in the state of Texas. In the recommended detail, PCP's are cast with #4 U-bars installed collinear with the existing pretensioned strands. (See Figure 7.3). These U-bars, along with the R-bars already in the U-girder (not shown in the TxDOT detail) provide a connection between the closure pour, the PCP lid slab, and the U-beam. A rebar cage is then installed in the closure pour to allow the strip to transmit forces between these two components. However, although the detail has been implemented in bridges elsewhere, the research team is not aware of any tests on the performance of the detail when subjected to the shears that would develop in a curved girder application. Additionally, the limited size of the existing detail results in a congested reinforcement layout (See Figure 7.4), potentially affecting the constructability and performance of closure pours in practice.

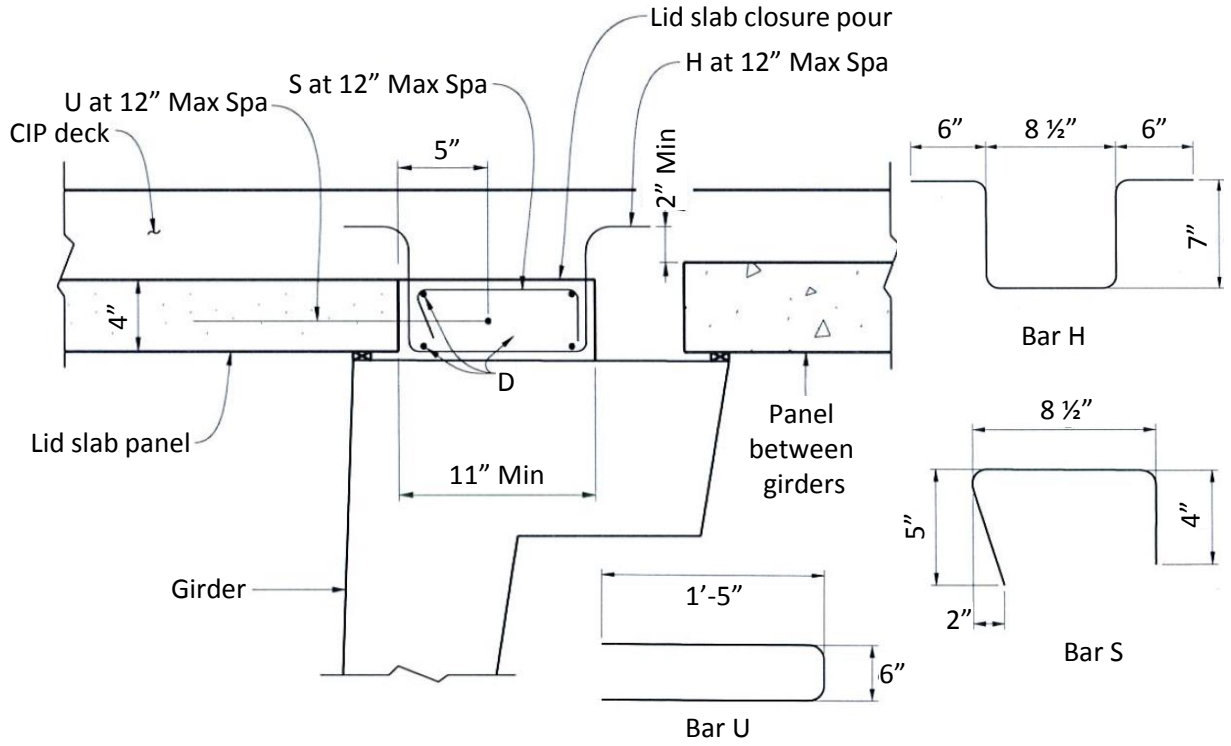

Figure 7.1 TxDOT Detail for Connection between Concrete U-Beam and PCP Lid Slab

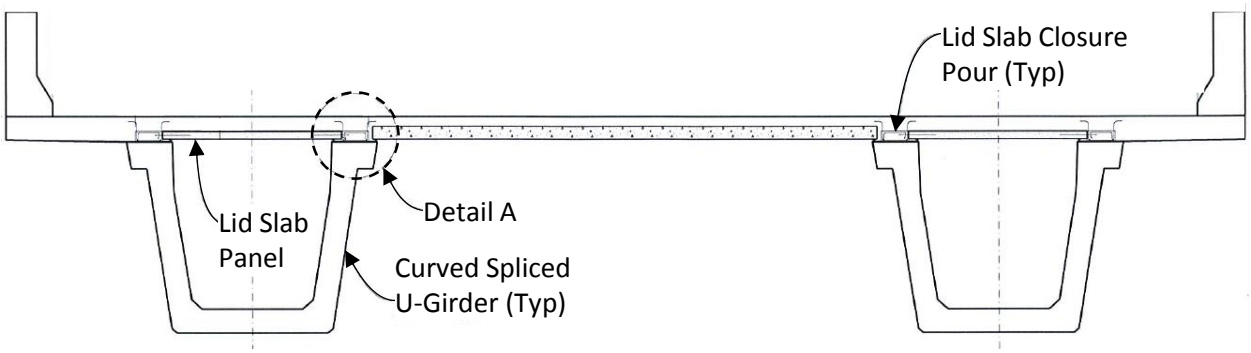

Typical Transverse Section

Figure 7.2 TxDOT Detail for Deck Pour after Lid Slab is Connected

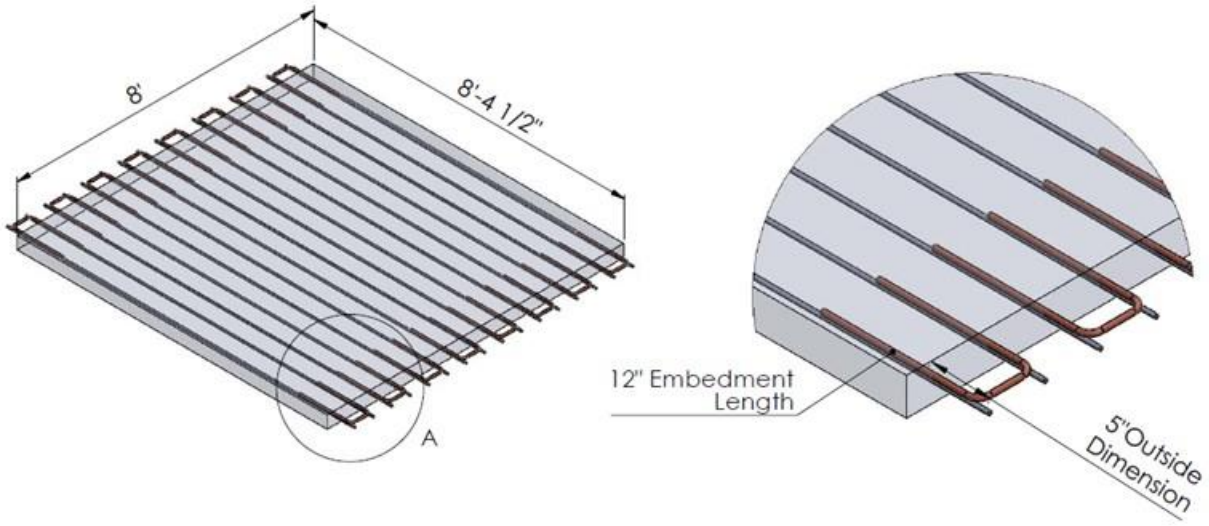

Figure 7.3 Precast Panel Dimension and U-bar Detail

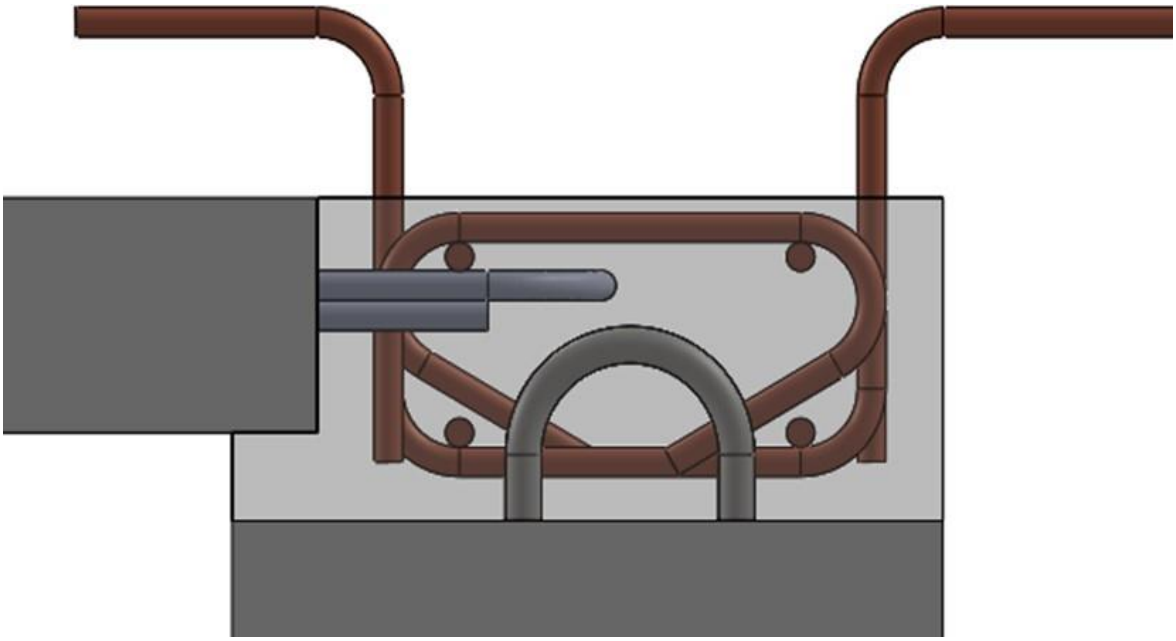

Figure 7.4 Congestion of Reinforcement in Closure Pour

7.2 Modification of Shear Frame Test Set-Up

Full scale testing of the closure pour connection was conducted in the existing shear frame setup used to test the panel-to-steel-girder connections (See Figure 7.5). As the existing setup was designed to simulate the top flange of a steel girder, modifications were necessary to allow the shear frame to simulate the top flanges of a concrete U-beam. While the design of the closure pour assumes load is transferred to the U-beam solely through the R-bars in the girder, there also exists the potential for significant load transfer due to the bond between the concrete of the closure pour and the U-beam (Birkeland and Birkeland 1966). Thus, the test setup needed to include both the fully developed R-bars and a concrete surface to accurately simulate the connection between the closure pour and U-beam flange.

Steel plates (1″ thick x 18″ wide x 96″ long) were used as the base plate for the simulated concrete girder flange. To simulate the R-bars, custom #4 deformed bar stud anchors were used, one 2-1/2″ long, one 6-1/2″ tall with a 180° hook. These were welded to the steel base plates at a 6″ spacing, and then spliced together with a double flaring groove weld to provide a full capacity connection to both legs of the top 180° hook (See Figure 7.6 and Figure 7.7). Two rows of 2″ long 3/4″ diameter shear studs were also welded to the base plate at 6″ spacing to provide a secure connection between the base plate and concrete. 2 mats of 6x6x2.9 welded wire reinforcement (providing approximately 3% reinforcement in each direction) were added, and then a 3″ layer of concrete was cast on the plates. (See Figure 7.8). For fabrication simplicity, this concrete was typically cast concurrent with the casting of one of the closure pour specimens, and thus was made with the same concrete mix, rather than a mix representative of a concrete U-girder. While minor cracking was observed in this concrete during some tests, no significant damage or failure occurred in this portion of the assembly, and this potential inaccuracy was deemed not to be significant. This assembly could then be bolted to the loading beams of the existing shear test setup with 2 rows of fully tensioned 1″ A490 bolts at 12″ spacing to provide a fixed connection between the assembly and the loading beams of the existing test setup.

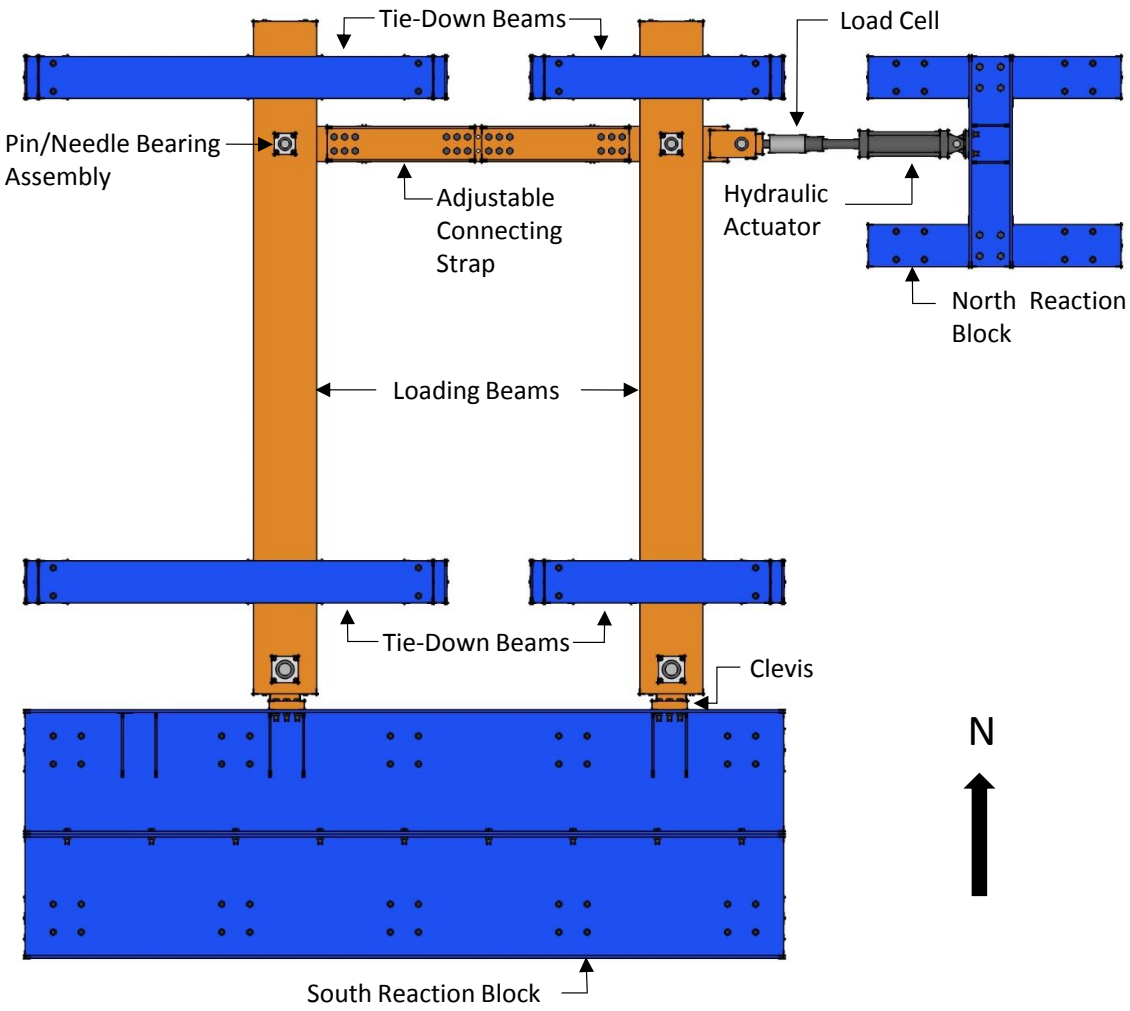

Figure 7.5 Existing Shear Frame Test Set-up

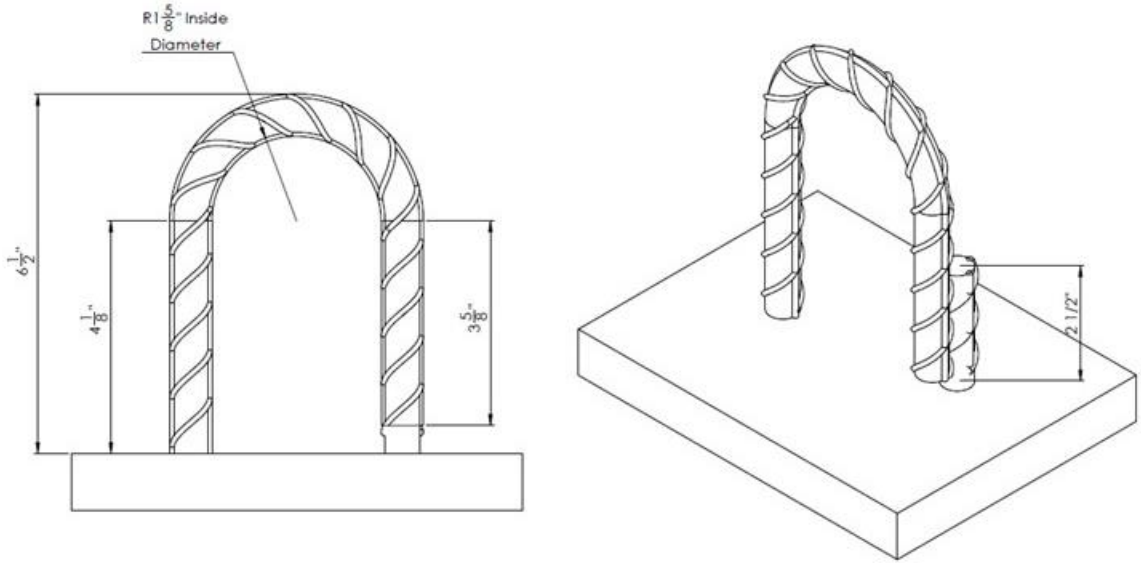

Figure 7.6 R-bar Dimensions

Figure 7.7 Rebar and Studs Welded to Base Plate

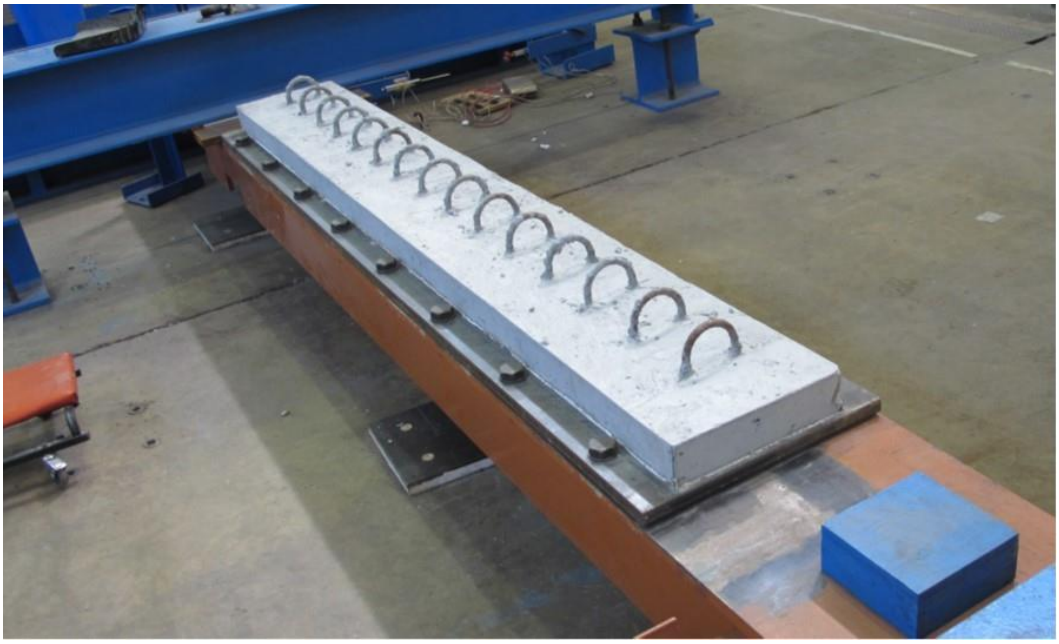

Figure 7.8 Simulated Girder Flange Assembly Installed

7.3 Precast Panel Fabrication

Fabrication of the precast panels was conducted in accordance to TxDOT standards for prestressed deck panels, and was largely identical to the production of precast panels used in the previous shear tests (described in Kintz 2017). As the closure pour detail requires a 1-1/2″ overlap between the panel and girder, the panel width had to be increased to 8′ 4-1/2″ to fit in the existing test setup. Additionally, 8 #4 U-bars (with legs spaced 6″ on center) were installed on each side of the panels collinear with the prestressing tendons. These bars had 12″ of development length in the panels and extended 5″ from the face (See Figure 7.3). Due to the long lead time in fabricating panels, all panels were cast prior to testing. Thus, although alternative designs for the panel embeds were considered, without any test results to base new designs off of, the decision was made to fabricate all test panels with the same U-bar design specified by the existing TxDOT detail.

7.4 Closure Pour Details

7.4.1 Closure Pour 1

The first test specimen (referred to as "Original Detail") was constructed according to the detail provided by TxDOT (Figure 7.1). The precast panel was set on a 2″ wide by 1-1/2″ tall bedding strip (the minimum height needed to avoid conflict between the panel U-bars and girder R-bars), with the panel overhanging the bedding strip and girder 1-1/2″ per the TxDOT requirement (See Figure 7.9). Next, #4 hat bars and ties were added as shear reinforcement at a spacing of 12″ on center, with four #4 bars installed as longitudinal reinforcement (Figure 7.10). Due to the close proximity between the U-bar and the end of the closure pour, there was insufficient room to place shear reinforcement at the very end of the closure pour. As the geometry of the hat bars did not allow placement of shear reinforcement inside the U-bar, no shear reinforcement could be placed until approximately 10″ from the end of the closure pour, resulting in a lack of confinement at the corners of the closure pour (See Figure 7.11).

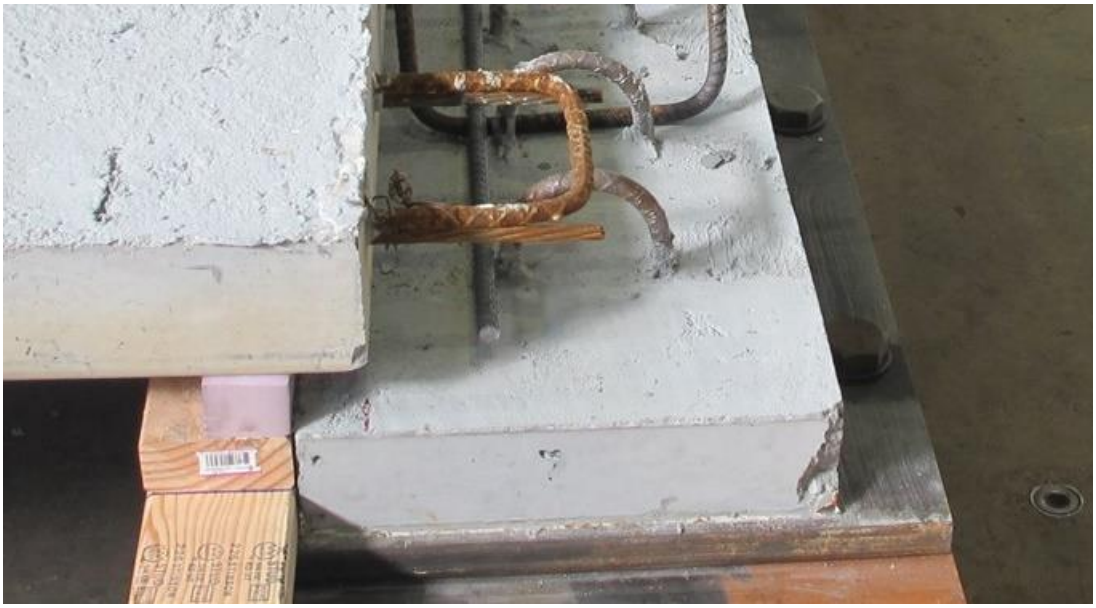

Figure 7.9 Installation of Precast Panel

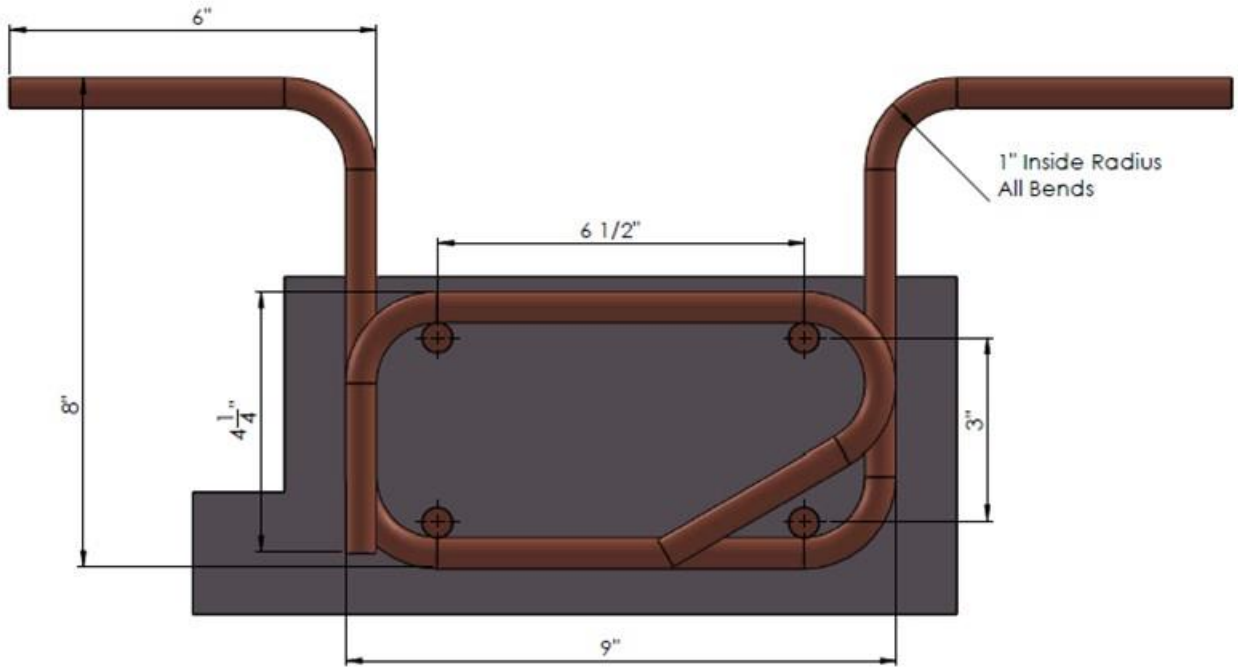

Figure 7.10 Closure Pour Rebar Dimensions

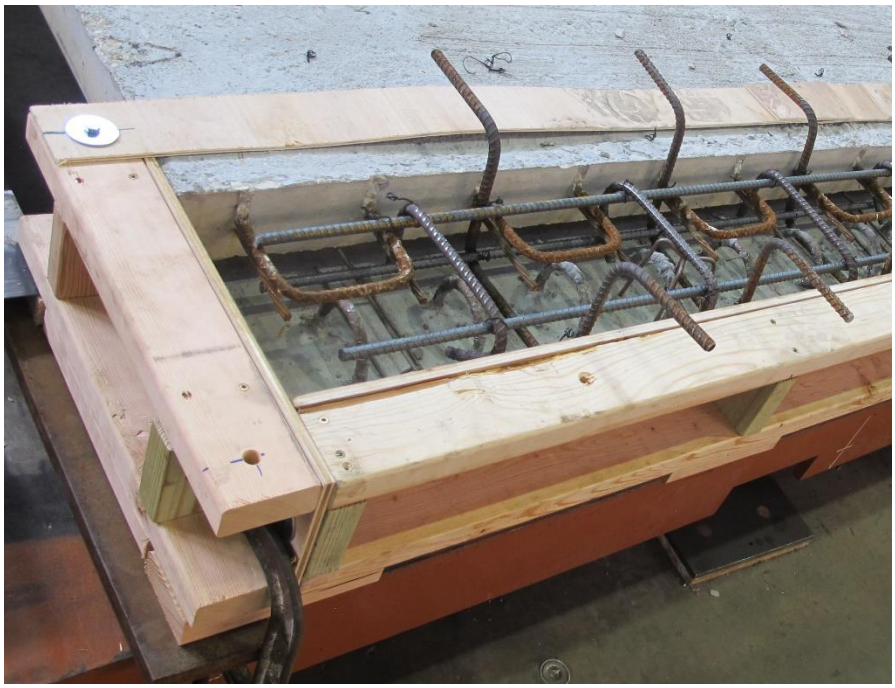

Figure 7.11 Lack of Confinement at Corner of Precast Panel

7.4.2 Closure Pour 2

While the lack of corner confinement in the test setup does match a condition that will be present in a full scale application near the ends of the girders, this condition will not be present in most panels. A typical application of this detail in a full bridge will involve a large number of

panels placed in series, with the closure pour for all of them cast as one continuous detail. In such a configuration, there will be room to place shear reinforcement between the U-bars of neighboring panels at the edges, and the longitudinal rebar will be continuous across the joint (See Figure 7.12). This continuity at the joint may result in an increase in the ability of the panel to resist the tension developed at the corners, and improve the shear capacity of the panel. Unfortunately, the test setup does not allow the testing of multiple precast panels in series. However, by providing a cap plate to the closure pour, the continuity that would be seen in a full scale application can be simulated.

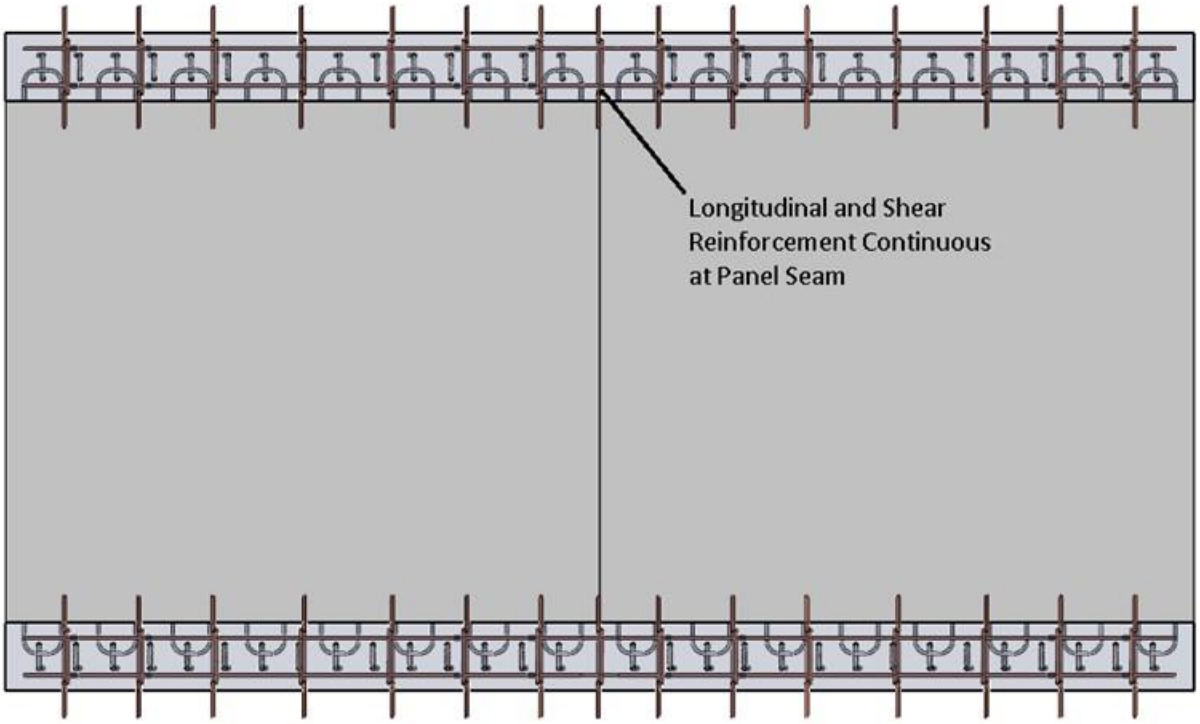

Figure 7.12 Continuity of Reinforcement at PCP Seam

Specimen 2 (referred to as "Cap Plate") included this cap plate to mimic the boundary conditions that would be present in an interior panel, as well as serve as a potential detail that could be installed in exterior panels to improve behavior. The cap plate is an 8″ x 5″ plate, 3/8″ thick, with 4 #4 bars, 24″ long stud welded to the plate (See Figure 7.13). These cap plates are then cast into the closure pour so that the outside face is coincident with the end surfaces of the pours. The reinforcing bars are welded so they sit immediately inside the location of the longitudinal bars already present in the specimen (See Figure 7.14). By creating a lap splice between the bars, the addition of the cap plate can effectively provide continuous longitudinal reinforcement that is fully anchored at each end of the specimen. The attachment of the bars to the cap plate also prevents relative lateral movement of the bars, simulating the confinement that would be provided by the hat bar and tie that would be placed at the interface between precast panels.

Figure 7.13 Fabricated Cap Plate

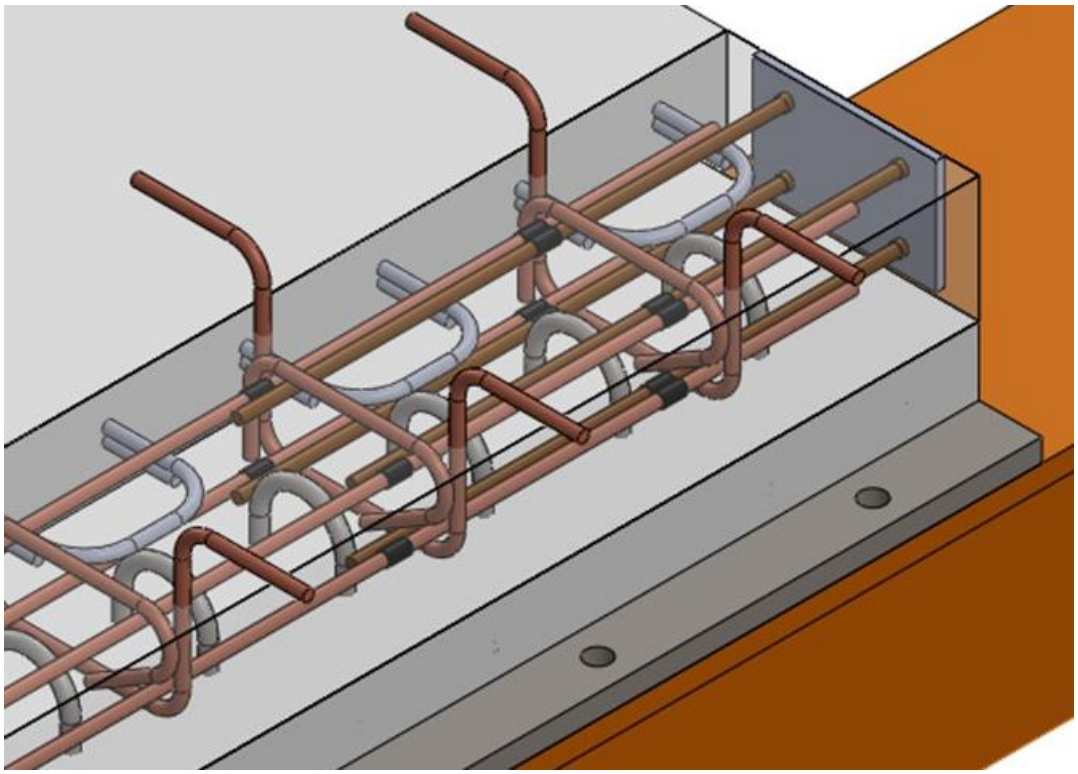

Figure 7.14 Isometric of Cap Plate Installed in Closure Pour

7.4.3 Closure Pour 3

While the cap plate provided some enhancement to the performance of the second closure pour specimen, the specimen's capacity was still limited by the lack of confinement provided at the corners of the closure pour. Thus, specimen 3 (referred to as "Corner Confinement") included additional shear reinforcement placed at the corners of the pour. Due to the congestion of the U-bars and R-bars, the normal shear reinforcement could not be installed near the specimen's corners. Confinement for the bottom longitudinal reinforcement was provided by U-bars with a 9″ outside dimension, 4-1/2″ tall (essentially hat bars with the two top horizontal legs removed) (See Figure 7.15). Confinement for the top longitudinal reinforcement was provided by the ties used throughout the specimen. Both bars were installed immediately inside the U-bar closest to the corner. An additional pair of reinforcing bars was installed immediately outside the U-bar (Figure 7.16). However, as these provided confinement to the cap plate's longitudinal reinforcement, rather than the full length reinforcement, these bars were one inch narrower than the previous pair to account for the different reinforcement location.

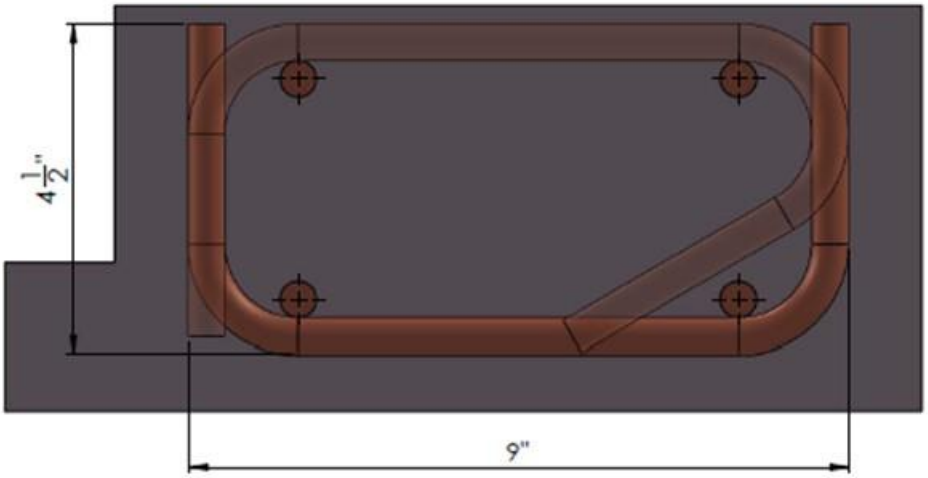

Figure 7.15 Dimensions of Modified Shear Reinforcement

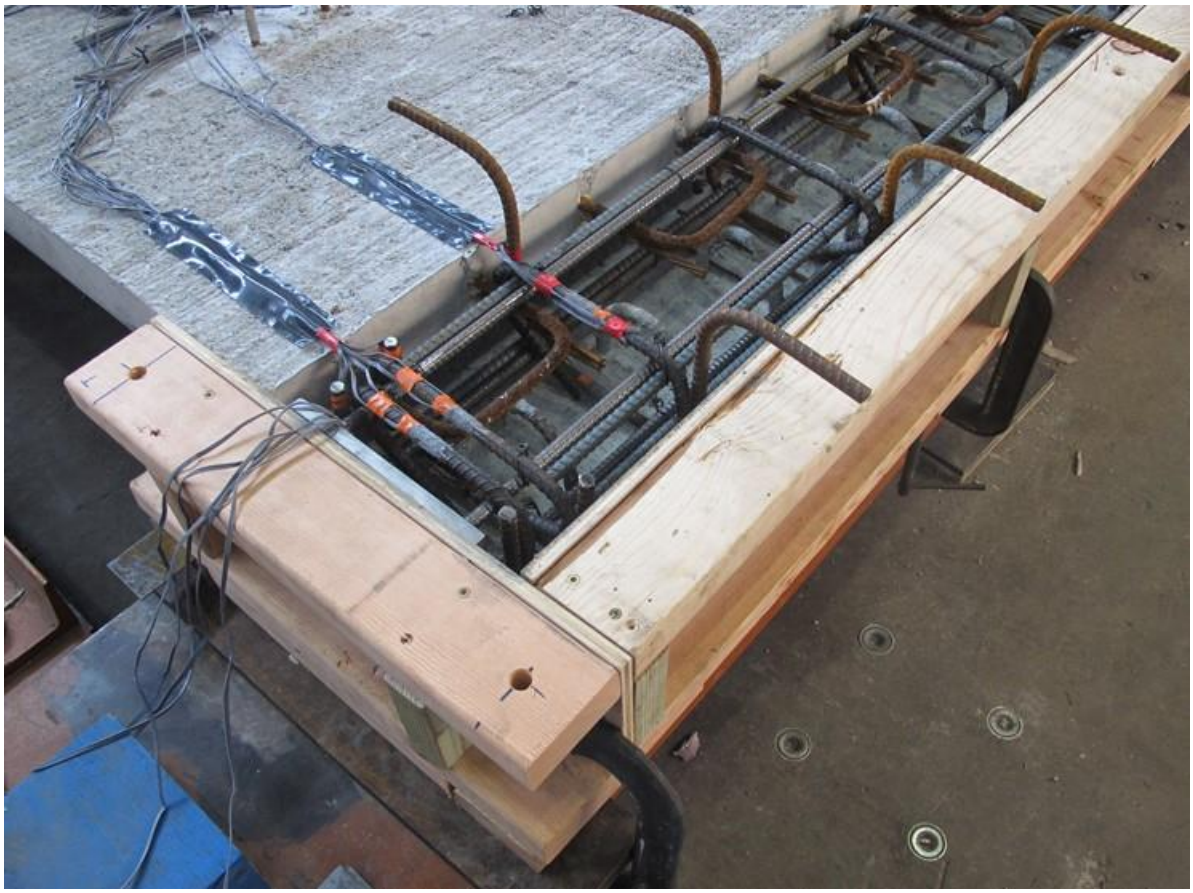

Figure 7.16 Closure Pour with Additional Shear Reinforcement at Corner

7.4.4 Closure Pour 4

The inclusion of additional reinforcement at the ends of the closure pour resulted in a significant enhancement in capacity, and altered the mechanism of failure. However, observations during the test (discussed in greater detail later in the chapter) suggested that the heavy reinforcing at the corner may have led to large point loads on the surrounding elements, and thus a premature system failure. In an effort to better distribute the strength of the connection, the next specimen (referred to as "6″ Reinf Spacing") included shear reinforcement throughout the closure pour at a 6″ spacing, rather than the 12″ spacing specified by the detail (See Figure 7.17). As this resulted in half the shear reinforcement being placed inside the panel U-bars, the modified reinforcement from the previous specimen (with U-bars instead of hat bars confining the bottom reinforcement) were used for the additional shear reinforcement.

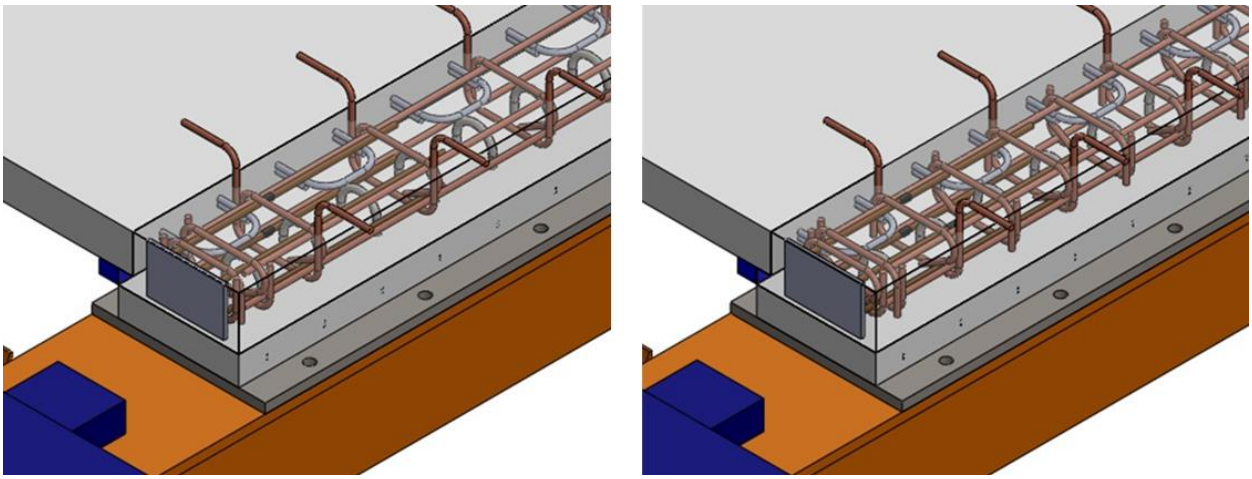

(a) (b)

Figure 7.17 Reinforcement Detail at (a) 12″ Spacing and (b) 6″ Spacing

7.4.5 Closure Pour 5

The 6″ reinforcement spacing specimen failed primarily due to the vertical force caused by the eccentricity between the panel U-bars and R-bars, and the lack of vertical capacity provided by the closure pour detail, as the existing shear reinforcement can only effectively provide lateral confinement (See Figure 7.18). This limit state is of particular concern, as the previous specimens were all constructed with the shortest possible bedding strip. A higher bedding strip (which may be needed to account for errors in initial beam camber) would result in a much higher eccentricity between the U-bars and R-bars, and therefore a much higher vertical demand on the closure pour (See Figure 7.19). For the final specimen (referred to as "High Eccentricity") the precast panel was constructed on a 4″ bedding strip (the maximum allowed by TxDOT erection standards) rather than the 1-1/2″ bedding strip used in the previous specimens.

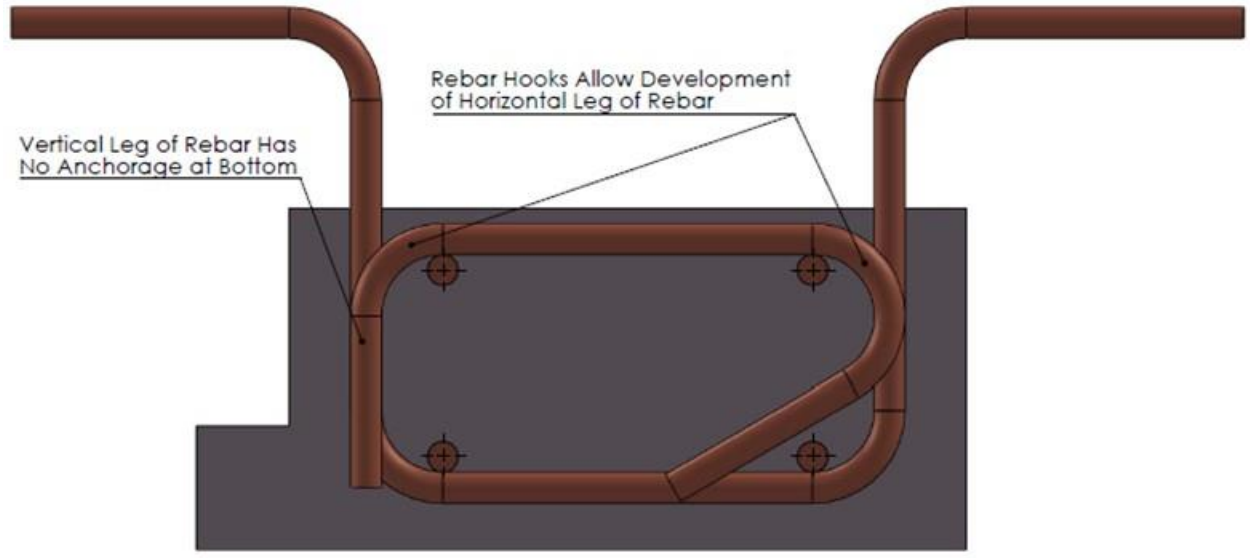

Figure 7.18 Effectiveness of Shear Reinforcement for Lateral/Vertical Load

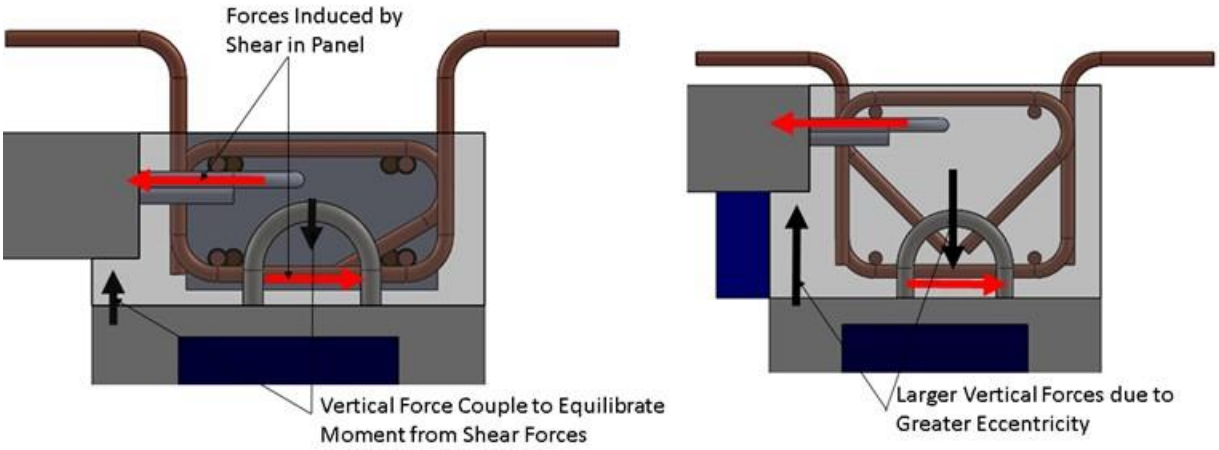

Figure 7.19 Greater Uplift Forces on Panel due to Higher Bedding Strip

Unfortunately, providing vertical capacity to the closure pour is difficult. Due to the limited height of the detail, and congestion of the existing reinforcement, adding vertical ties is difficult from a standpoint of constructability. Additionally, the minimal top cover provided by the detail would inhibit the ability of a rebar hook to provide sufficient anchorage (See Figure 7.20). Vertical capacity was instead provided through a modification of the existing cap plate detail. The cap plate was extended so that it spanned the full depth of the closure pour and the 3″ concrete layer used to simulate the top flange of the U-beam, resting on the steel base plate that attached to the test frame. It was then fully fillet welded to the base plate prior to casting of the U-beam flange concrete (see Figure 7.21). Thus, the longitudinal reinforcement stud welded to the cap plate would be fixed against vertical movement, and could resist the uplift in the closure pour. Due to the geometry of the various elements, the top inside rebar could not be stud welded to the cap plate prior to installation of the precast panel, as it would conflict with the panel's U-bars, and access issues prevented stud welding after panel installation. Thus, a 5/8″ hole was drilled in the cap plate at the desired location of the rebar. Then, after installation of the PCP, a #4 bar, 2 ft. long was inserted through the hole into the specimen, and plug welded to develop its full capacity (See Figure 7.22).

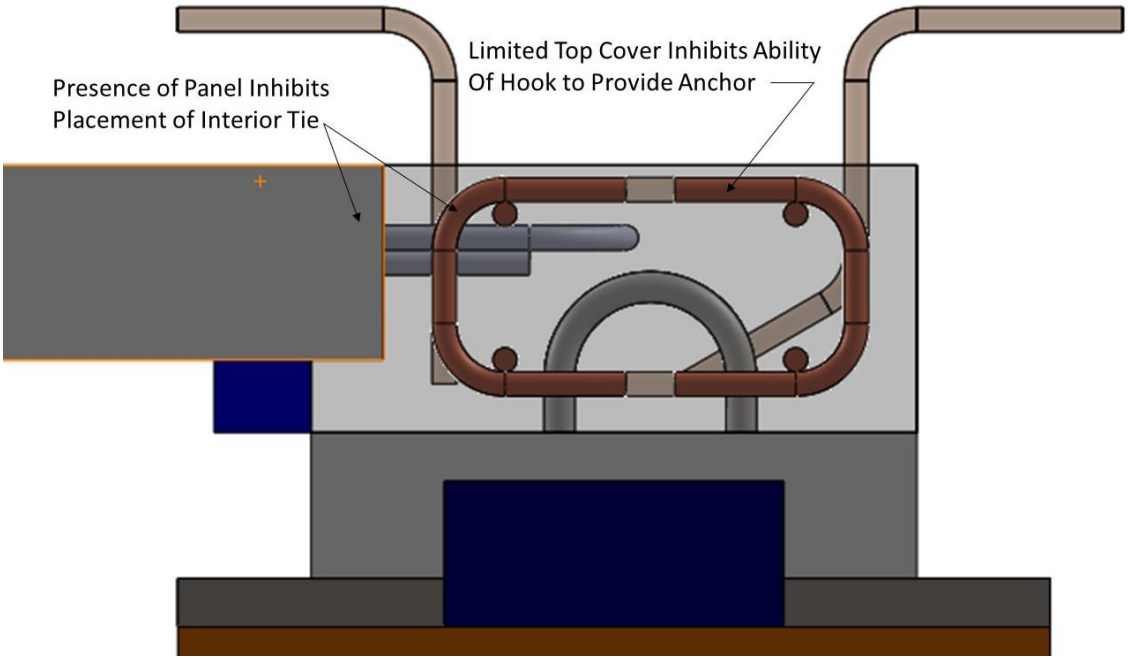

Figure 7.20 Difficulty in Providing Vertical Reinforcement to Closure Pour

Figure 7.21 Cap Plate Welded to Steel Base Plate

Figure 7.22 Top Inside Rebar Plug Welded to Cap Plate

While this detail proved effective at providing vertical capacity to the system, it would be difficult to implement in a full scale application. Attaching the cap plate will be difficult in a real bridge, as a bridge U-girder will not have a base plate to weld to. Additionally, fabrication of the detail requires multiple steps and tight tolerances that are achievable in a laboratory setting, but could prove difficult and costly in a field setting. The detail was selected as the best way to determine an upper bound of the system's capacity that could be achieved given the tight time frame of the test program, but further refinements to the constructability of the detail are likely necessary before full implementation.

In addition to improving the vertical capacity of the closure pour, additional alterations were made to improve the anchorage between the closure pour and girder. For all previous tests, the girder R-bars (which are at a 6″ spacing), start 6″ from the end of the closure pour (See Figure 7.23), which was selected as a conservative "worst case" scenario for the panel, as the location of the panels relative to the R-bars will typically vary along the length of the girder. This meant the first 9″ of the closure pour (where the demand is highest) has only one R-bar to react against. To simulate a more likely configuration for the end PCP (which will typically be the PCP with the highest demand), an additional R-bar was welded to the base plate 3″ from the end of the closure pour (See Figure 7.23). Additionally, a 2ft long #4 bar was tied to the inside of the R-bars at the ends of the specimen prior to casting of the closure pour, to provide the concrete with more reinforcement to react against when loaded (See Figure 7.24 and Figure 7.25). This increase in reinforcement allowed more of the concrete to be engaged in resisting potential uplift forces, better

distributing the load demand, and preventing a local failure of the concrete from causing a premature failure of the system.

(a) (b)

Figure 7.23 (a) Original R-Bar Layout and (b) Modified Corner R-Bar Layout

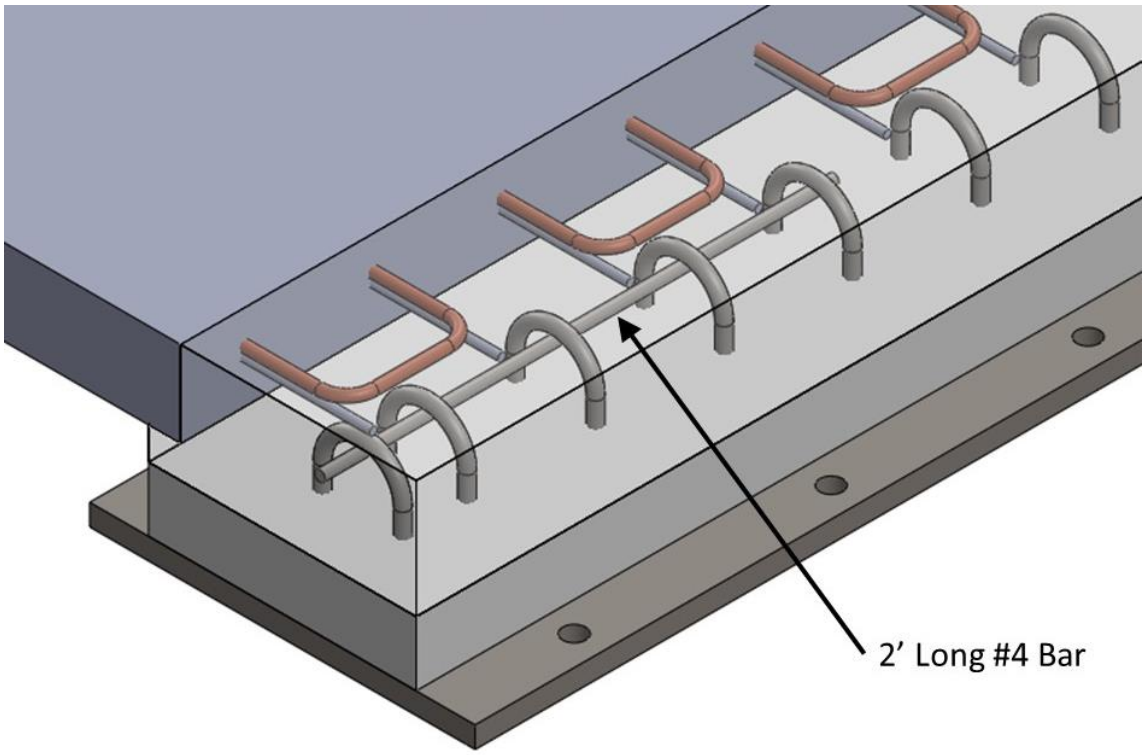

Figure 7.24 Additional Reinforcement to Improve Engagement of R-Bars (Model)

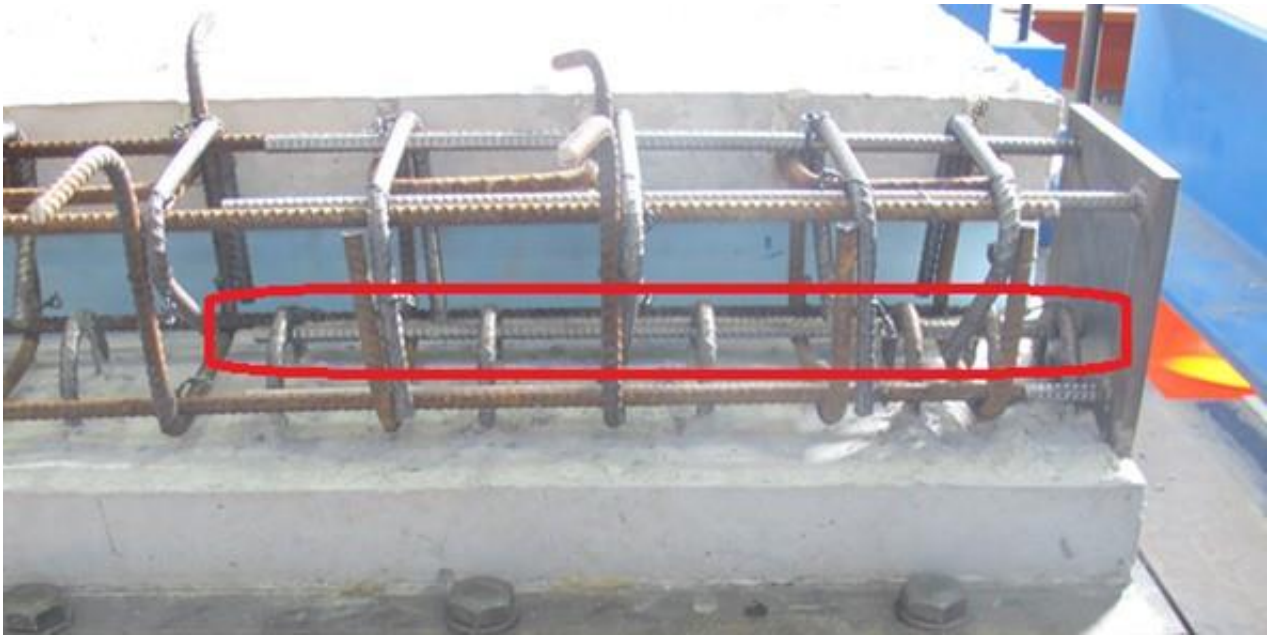

Figure 7.25 Additional Reinforcement to Improve Engagement of R-Bars (Photo)

7.4.6 Instrumentation

Shear in the panel was monitored in a manner identical to that used in the previous panel tests (see Chapter 4). A load cell installed on the hydraulic actuator captured the load applied to the test specimen. This load was multiplied by the ratio of the actuator moment arm (150″) to the distance between centroids of the loading beams (110″) (See Figure 7.26). Shear strain was also monitored in a manner similar to the previous panel tests. 6″ linear potentiometers were placed near all four corners of the specimen to monitor shear displacements (See Figure 7.27). The shear angle of a loading beam was taken as the difference in displacement at the north and south corners, divided by the total distance between L-pots. The angle of each loading beam was then averaged to provide the reported shear angle of the panel (See Figure 7.28). Note that unlike the previous tests, the loading beams do not simulate the top flange of the bridge girder. The top flange of the U-beam is simulated by the 3″ layer of concrete bolted to the loading beams. In order to determine the shear displacement at that location, two L-pots were attached to the loading beam at each corner, at a 10″ vertical spacing. The displacement at the level of the closure pour-to-girder connection could then be found by extrapolating from the two recorded L-pot values. While L-pots were also attached to the concrete to monitor the shear displacement more directly, damage at the concrete surface limited the accuracy of this measured value, and the extrapolated values were used to calculate shear angle. L-pots were also placed at various locations at the interface between connected elements. However, due to the frequent change in failure mode between specimens, none of these L-pots captured behavior at the controlling limit state, and no meaningful conclusions were drawn from the data. Thus, these values are not discussed in the report. Uniaxial strain gages were also installed on the longitudinal rebar and on many of the shear ties (See Figure 7.29).

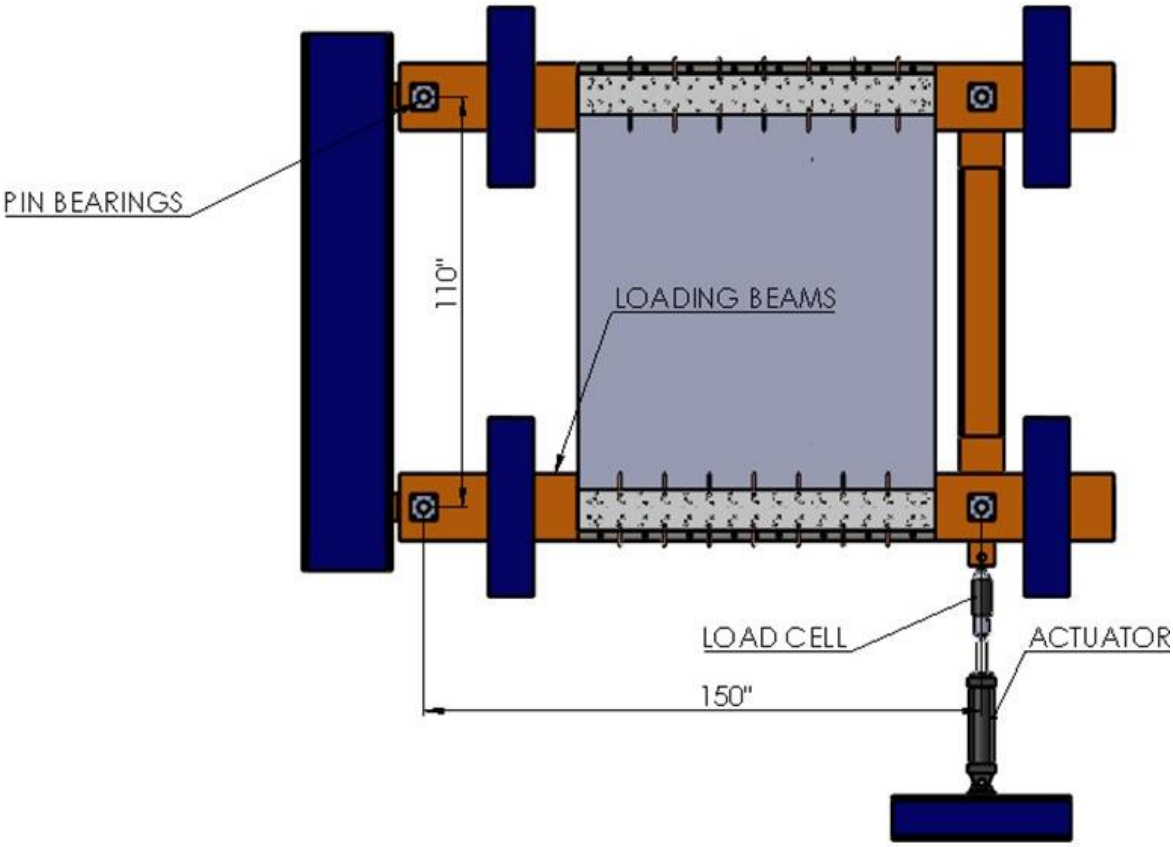

Figure 7.26 Actuator and Loading Beam Dimension

Figure 7.27 Shear Displacement L-Pots

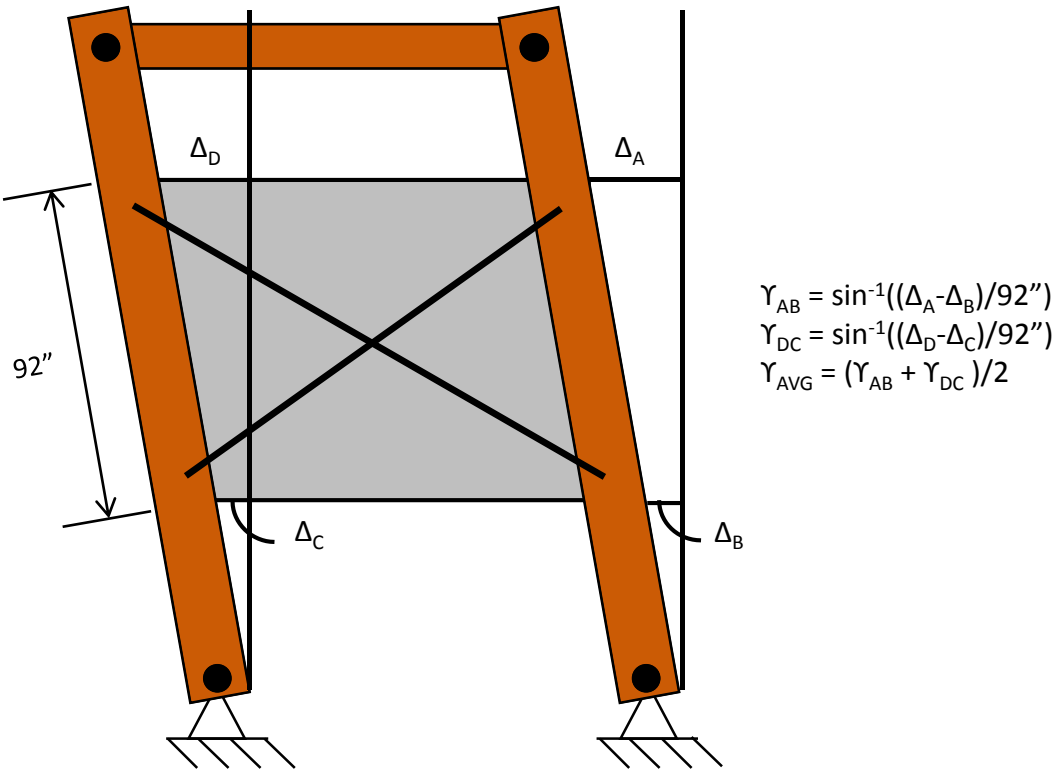

Figure 7.28 Calculation of Panel Shear Strain

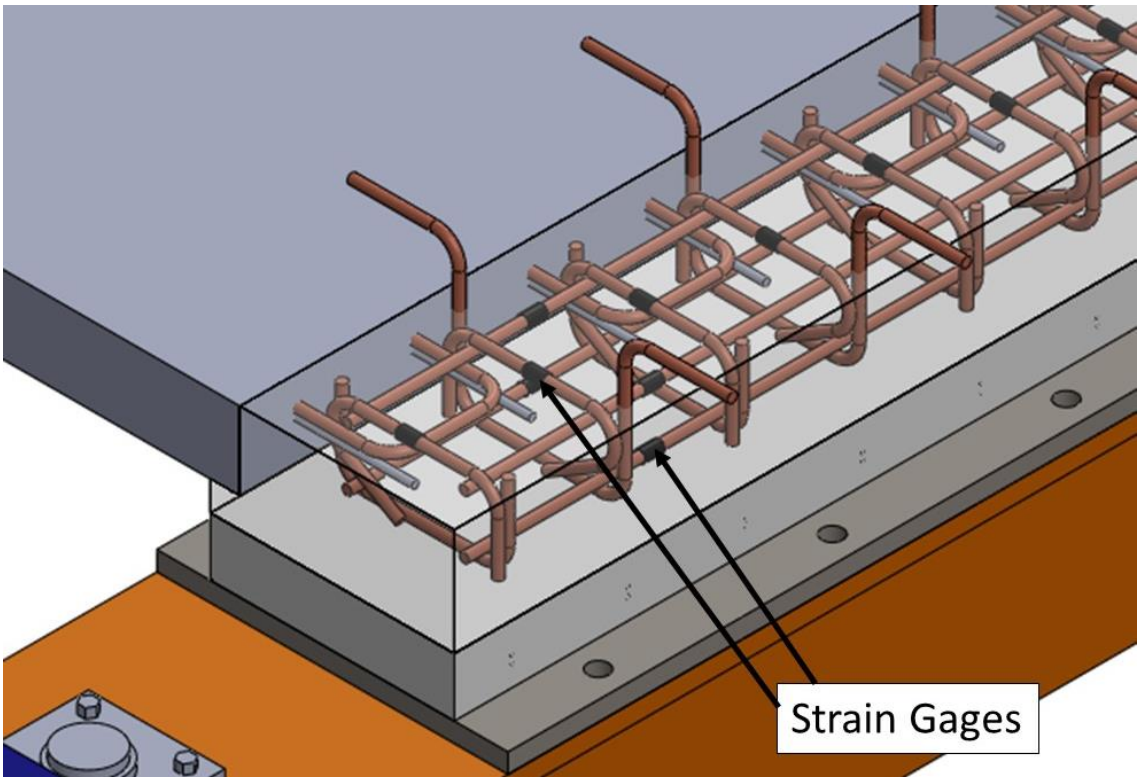

Figure 7.29 Reinforcement Strain Gages

7.4.7 Material Properties

Although all closure pours and base plates were cast with an identical mix design, minor variations in strength occurred between specimens due to differences in batching between casts and time between cast and testing. Additionally, the precast panels were cast in two batches, and thus had minor variations between specimens. Compressive cylinder tests for all three concretes, as well as flexural modulus of rupture tests for the closure pour, (done according to ASTM C39 and ASTM C78 test procedures, respectively) were run immediately after testing each specimen. Table 7.1 summarizes the measured properties.

Table 7.1: Summary of Material Properties

Closure Pour 1 (Original Detail)	
Closure Pour Compressive Strength (ksi)	6.63
Closure Pour Modulus of Rupture (ksi)	0.611
Base Plate Compressive Strength	6.12
Precast Panel Compressive Strength (ksi)	9.11

Closure Pour 2 (Cap Plate)	
Closure Pour Compressive Strength (ksi)	6.03
Closure Pour Modulus of Rupture (ksi)	0.59
Base Plate Compressive Strength	6.2
Precast Panel Compressive Strength (ksi)	9.63

Closure Pour 3 (Corner Confinement)	
Closure Pour Compressive Strength (ksi)	7.98
Closure Pour Modulus of Rupture (ksi)	0.669
Base Plate Compressive Strength	7.92
Precast Panel Compressive Strength (ksi)	10.13

Closure Pour 4 (6" Reinf Spacing)	
Closure Pour Compressive Strength (ksi)	6.63
Closure Pour Modulus of Rupture (ksi)	0.585
Base Plate Compressive Strength	9.26
Precast Panel Compressive Strength (ksi)	10.1

Closure Pour 5 (High Eccentricity)	
Closure Pour Compressive Strength (ksi)	7.92
Closure Pour Modulus of Rupture (ksi)	0.737
Base Plate Compressive Strength	5.88
Precast Panel Compressive Strength (ksi)	9.42

7.5 Results

Figure 7.30 shows the shear in the closure pour versus the shear strain of the precast panel. For better comparison between specimens, the curves below show only the instantaneous strength of the specimens measured at the sampling loads, with the temporary losses in capacity due to creep and hydraulic bleed omitted. Full shear curves (with all real time data included), as well as observations of the individual specimens are included in the sections below.

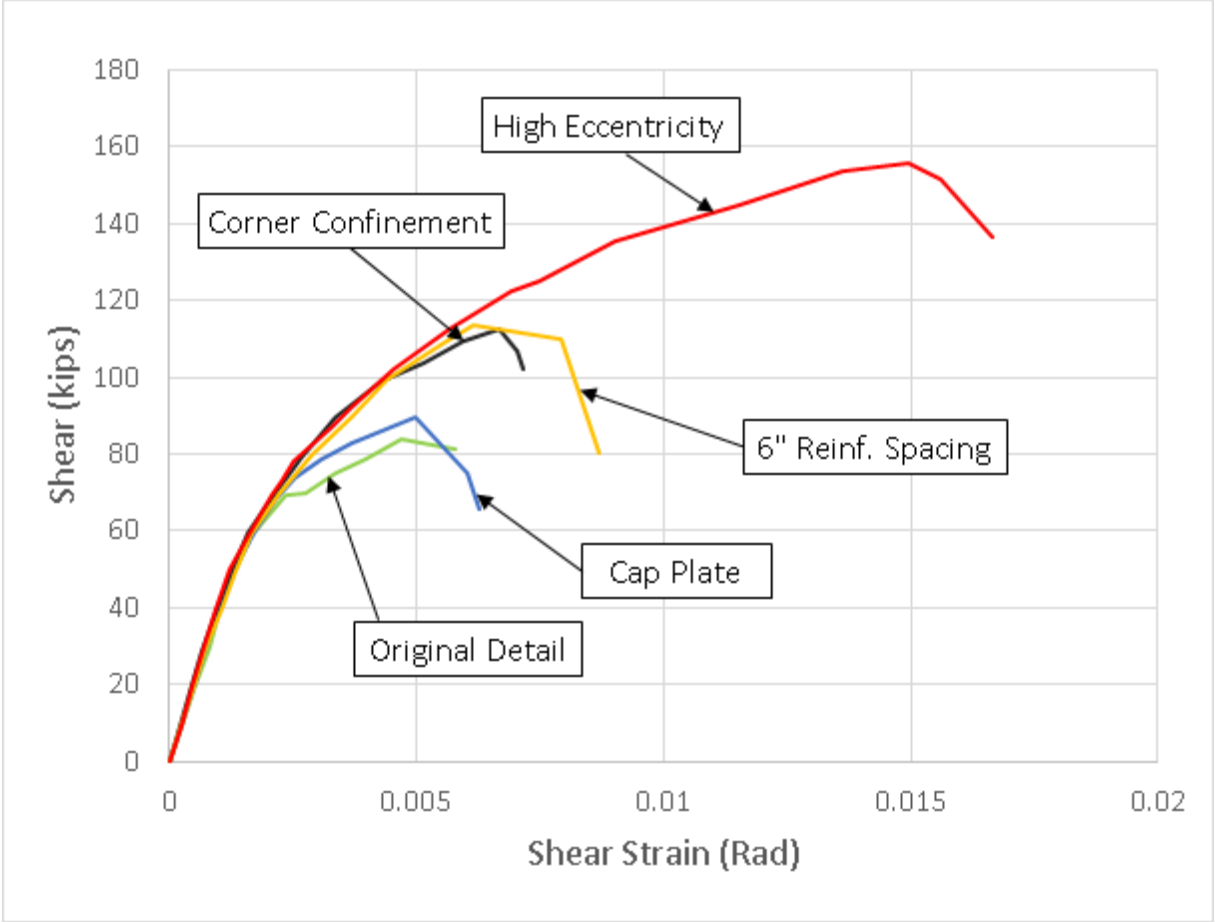

Figure 7.30 Panel Shear vs Shear Strain

7.5.1 Closure Pour 1 (Original Detail) Observations

As discussed previously in Chapter 4, the overall geometry of the panel system does not result in the panel experiencing pure shear. Two edges of the precast panel are effectively "free edges," both in our test specimen and in a full scale application. Thus, there is an additional moment that develops at the ends of the panel to achieve system equilibrium (See Figure 7.31). This moment creates an additional tensile force at the interface between the precast panel and the closure pour at two of the corners. As mentioned in the previous section, the existing TxDOT detail includes limited shear reinforcement at the ends of the closure pour. This lack of confinement at the corners, combined with the tensile forces induced by the moment at the end of the panel led to splitting of the concrete of the closure pour. Cracking initiated at the middle of the closure pour (approximately above the outermost portion of the panel U-bars) at 71 kips, growing rapidly in size and length until reaching the maximum capacity of the system at 84 kips. (See Figure 7.32 and Figure 7.33).

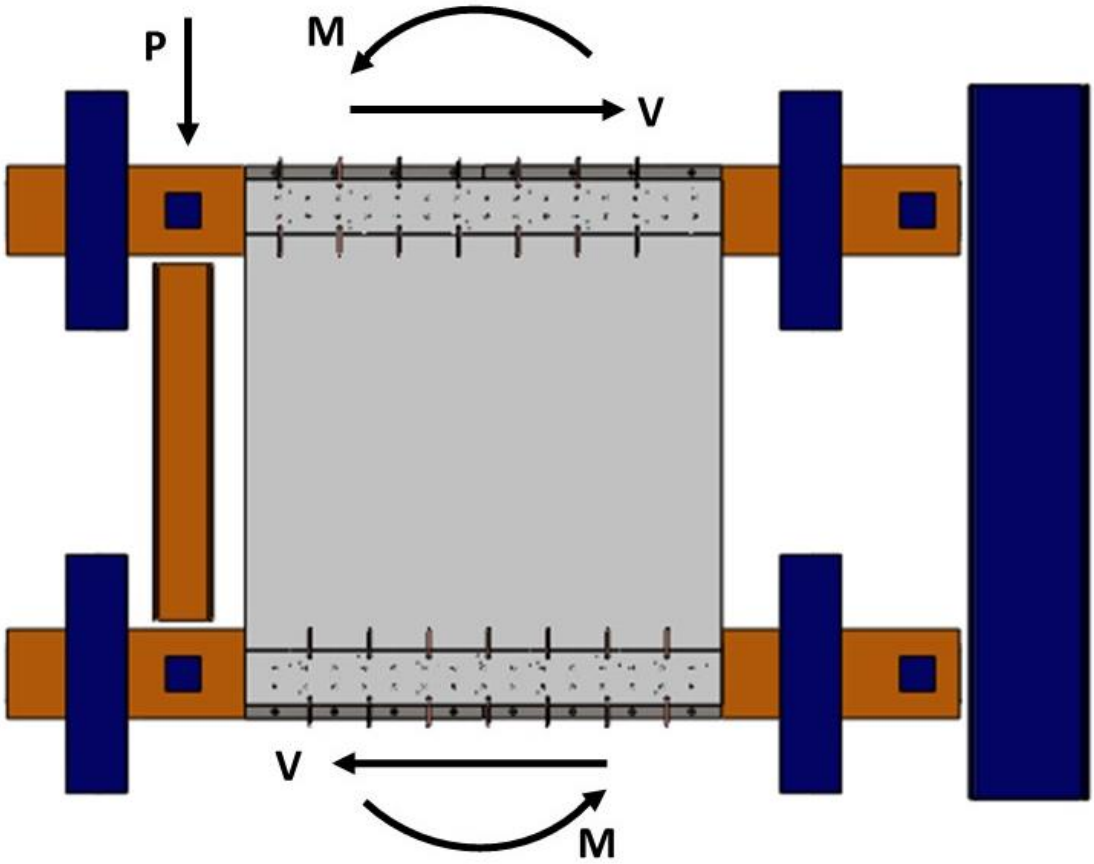

Figure 7.31 Load Distribution in Precast Panel

Figure 7.32 Cracking in Closure Pour (Original Detail) at 84 kips

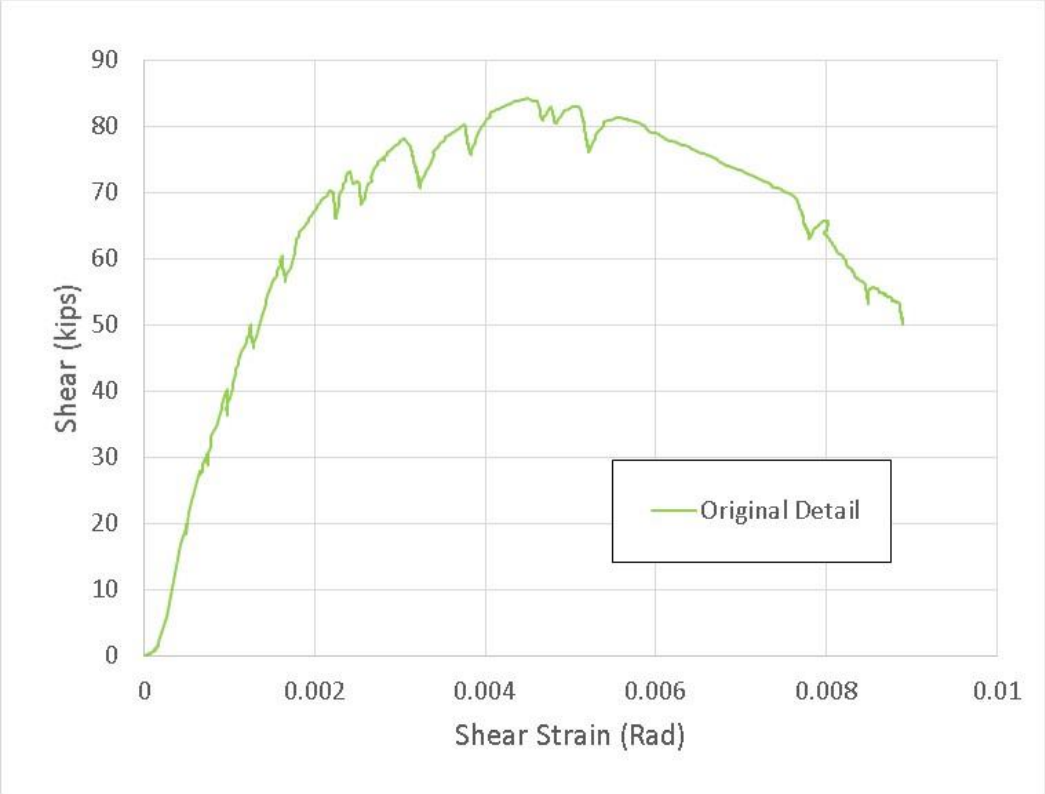

Figure 7.33 Shear Force vs Shear Strain for Original Detail Specimen

7.5.2 Closure Pour 2 (Cap Plate) Results

The presence of the cap plate did improve the overall capacity of the closure pour to shear loading, however, this enhancement was relatively minor, increasing the maximum capacity from approximately 84 kips to 90 kips. (See Figure 7.34). The damage trends in the cap plate specimen were also similar to the previous specimen, with minor cracks developing at the interface between the closure pour and precast panel, as well as small cracks collinear with the longitudinal rebar, followed by a large crack developing along the approximate middle of the closure pour at two corners, which grew rapidly, resulting in a loss of capacity shortly thereafter (See Figure 7.35).

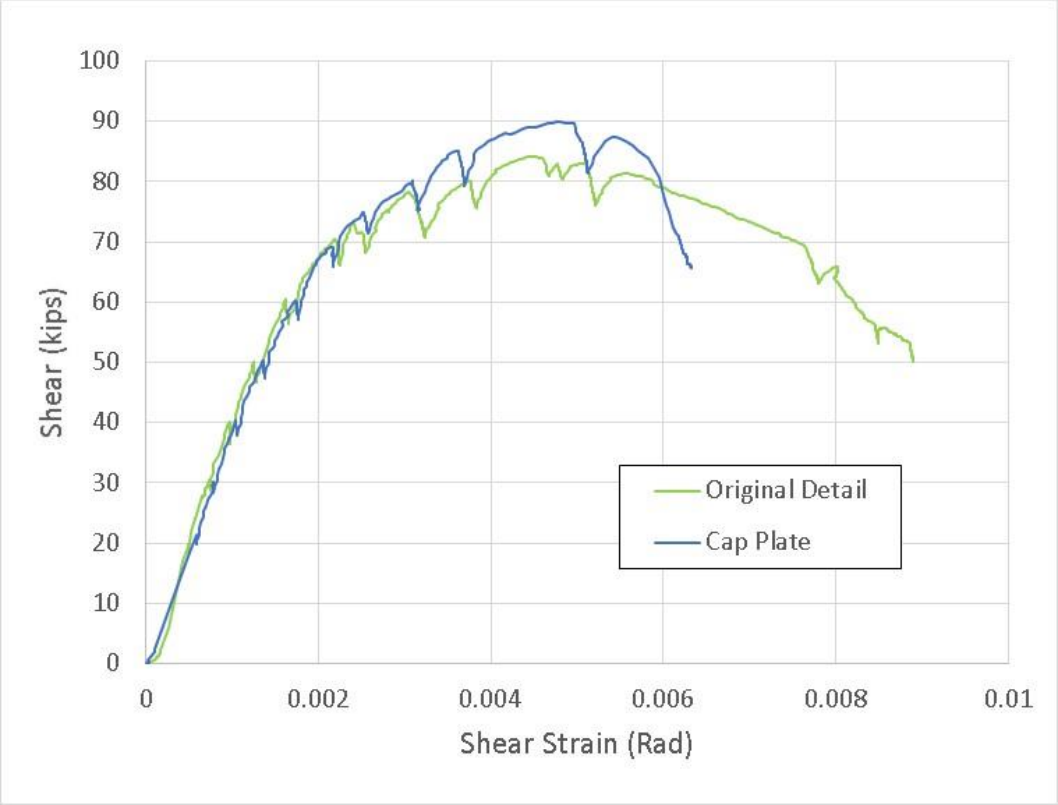

Figure 7.34 Shear Force vs Shear Strain for Cap Plate Specimen

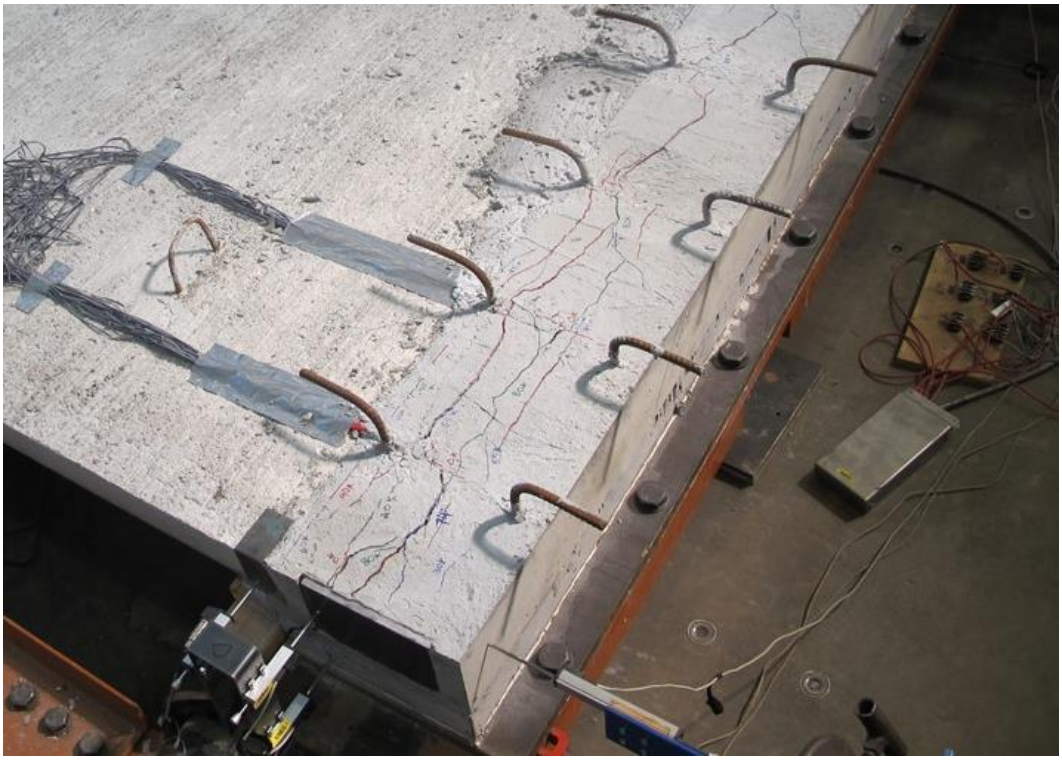

Figure 7.35 Cracking of Cap Plate Specimen at Failure

There are likely two main reasons for the limited enhancement provided by the cap plate. First, the longitudinal reinforcement in the closure pour seems to play a limited role in the response of the system. The response of the strain gages placed on the longitudinal rebar (See Figure 7.36) suggests that only the top inside rebar (See Figure 7.37) sees any significant force during loading of the specimen. This is consistent with the assumption that the load transfer mechanism between the panel and girder is primarily between the panel's U-bars and girder R-bars. As the longitudinal reinforcement is not located near the interface between those elements, it does not see significant engagement during shear loading of the system. The top inside rebar is located close enough to the U-bar that is carries some load from the U-bar into the closure pour, but the overall contribution of the longitudinal reinforcement to the system is limited. Thus, the cap plate's providing of fully anchored longitudinal bars did not significantly improve the performance of the closure pour.

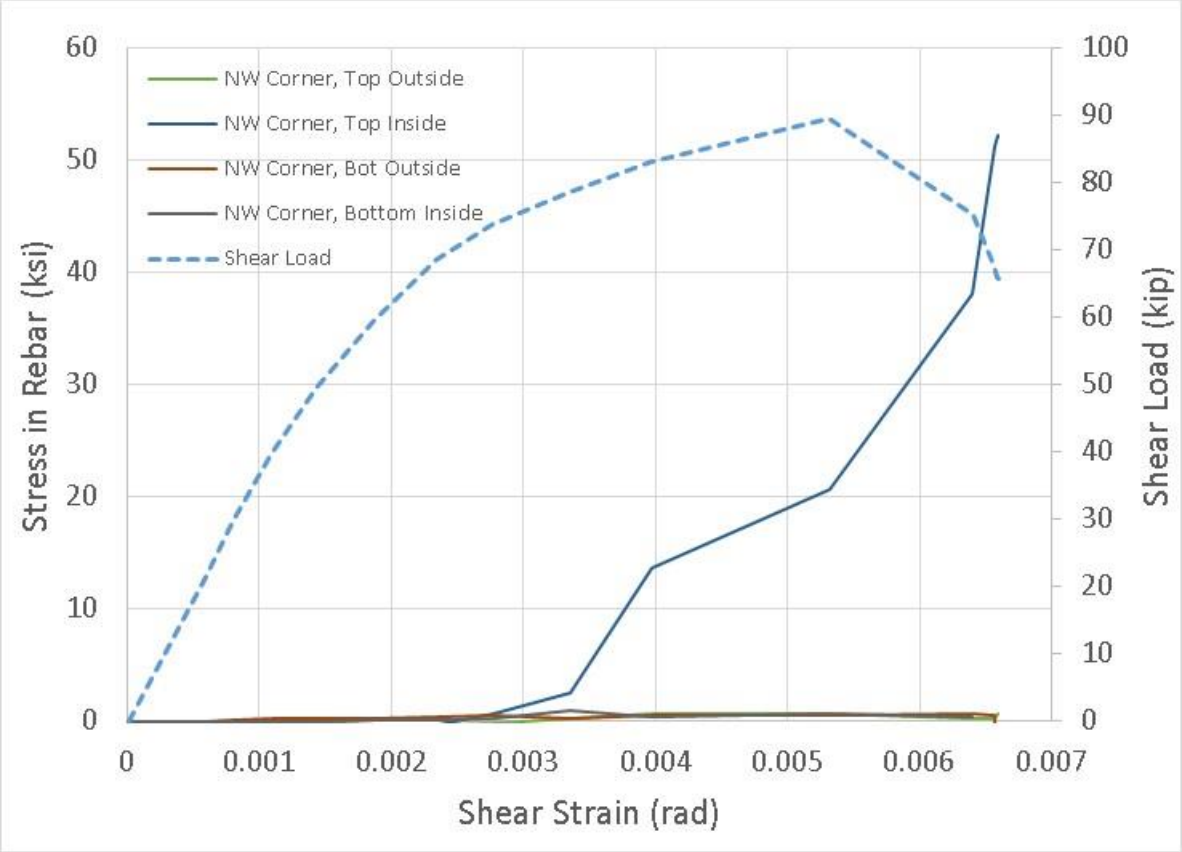

Figure 7.36 Long. Reinforcement Stress vs Shear Strain for Cap Plate Rebar

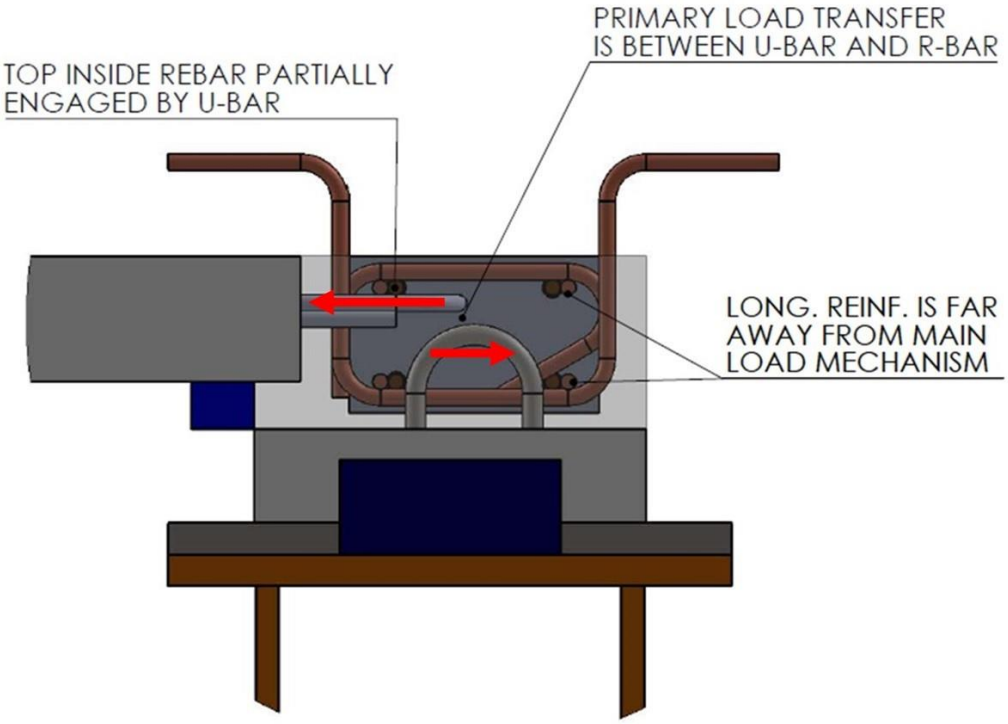

Figure 7.37 Limited Engagement of Long. Reinforcement

Additionally, while the cap plate was also meant to provide a simulation of shear reinforcement to the system by fixing the cap plate's longitudinal reinforcement against lateral movement, the low flexural stiffness of the rebar meant this was of limited effectiveness. Examination of the failed specimen revealed significant bending of the cap plate rebar (See Figure 7.38). Thus, while the rebar was fixed at the cap plate, most of the rebar's length (and therefore most of what the closure pour concrete was reacting against) was relatively free to translate, meaning it could not provide effective confinement, and the closure pour failed in a manner consistent with the previous specimen.

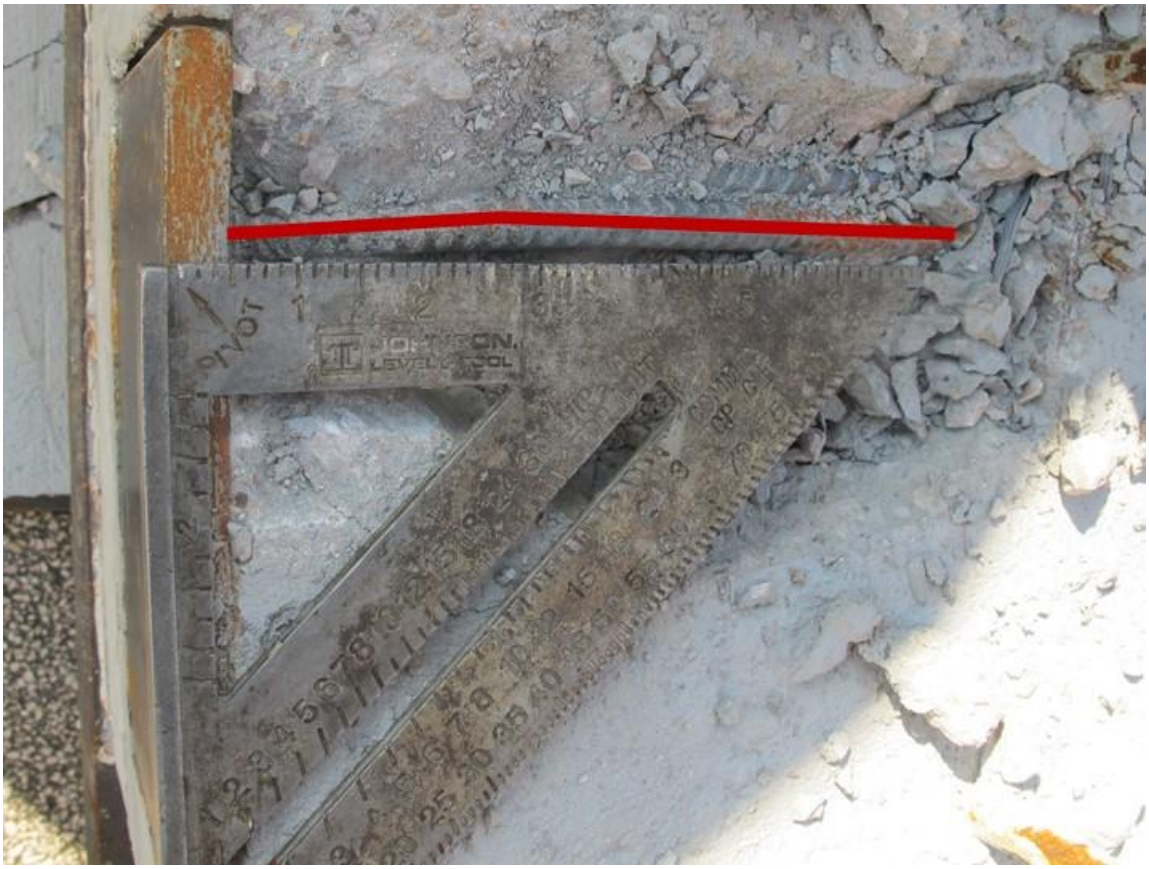

Figure 7.38 Bending of Cap Plate Long. Reinforcement

7.5.3 Closure Pour 3 (Corner Confinement) Observations

The placement of additional shear reinforcement at the ends of the closure pour allowed the pour to resist the tensile forces induced by the panel end moments, greatly reducing the splitting cracks seen in previous tests (See Figure 7.39). The additional confining reinforcement shifted the failure mode out of the closure pour and into the precast panel (See Figure 7.40) and the interface between the closure pour and the concrete in the base plate (simulating the top flange of the U-girder) (See Figure 7.41). This resulted in a significant enhancement in total shear capacity, with the specimen failing at 113 kips of shear, rather than the 84 kip capacity of the Original Detail specimen (See Figure 7.42).

Figure 7.39 Reduced Splitting in Closure Pour at 113 Kips of Shear

Figure 7.40 Cracking in Precast Panel at 113 Kips of Shear

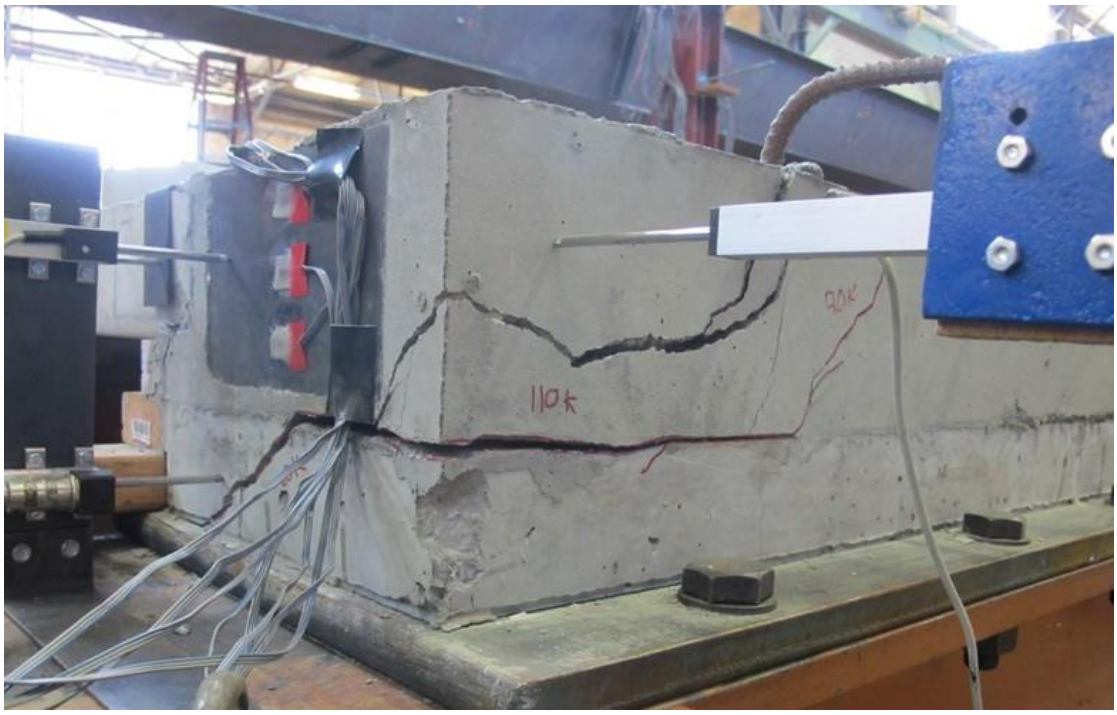

Figure 7.41 Failure at Interface between Closure Pour and Simulated Girder Flange at 113 Kips

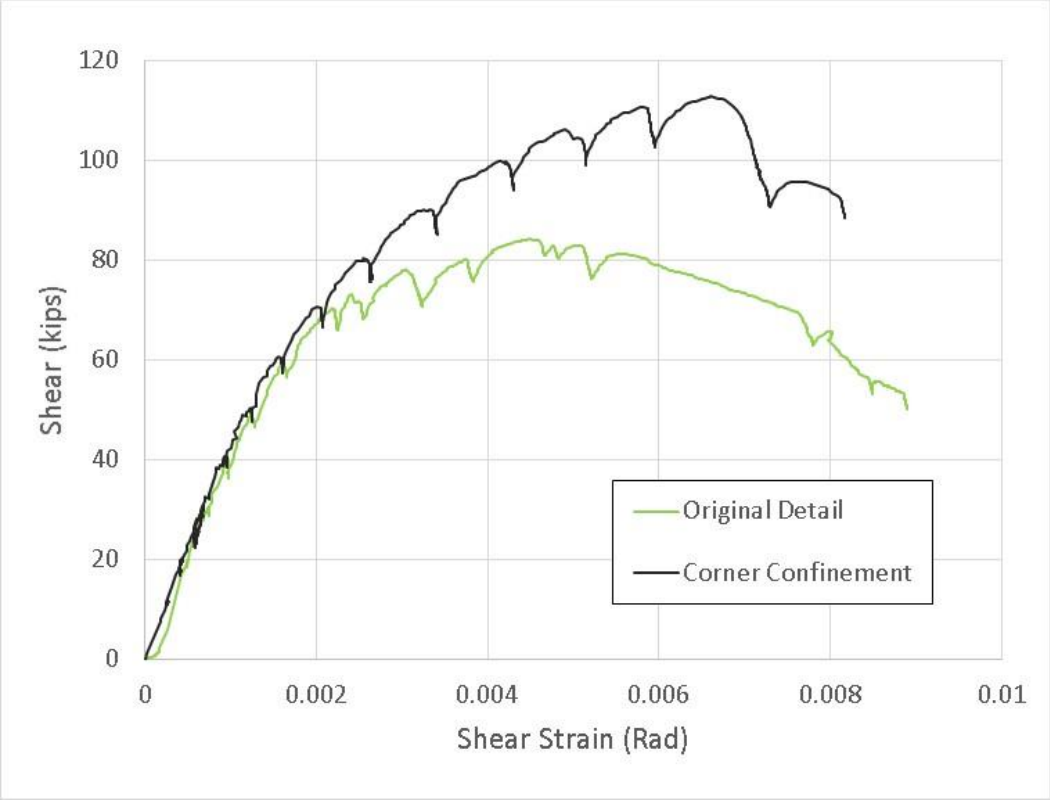

Figure 7.42 Shear Force vs Shear Strain for Corner Confinement Specimen

Note that one of the controlling limit states in this specimen (uplift at the closure pour/girder interface) is likely due in part to the setup simulating only a single panel. In a girder with a continuous closure pour, the twist acting at the end of a precast panel will be reduced somewhat by an opposite twist occurring at the neighboring panel (See Figure 7.43). Thus the total demand on the R-bars anchoring the closure pour to the girder will likely be reduced at the joint between panels. As the exterior panel, which often sees the greatest load demand (See Chapter 10), will not have this continuity benefit, it is still important to control this failure mode. However, it should be noted these results may be conservative when examining the behavior of a system of precast panels in series.

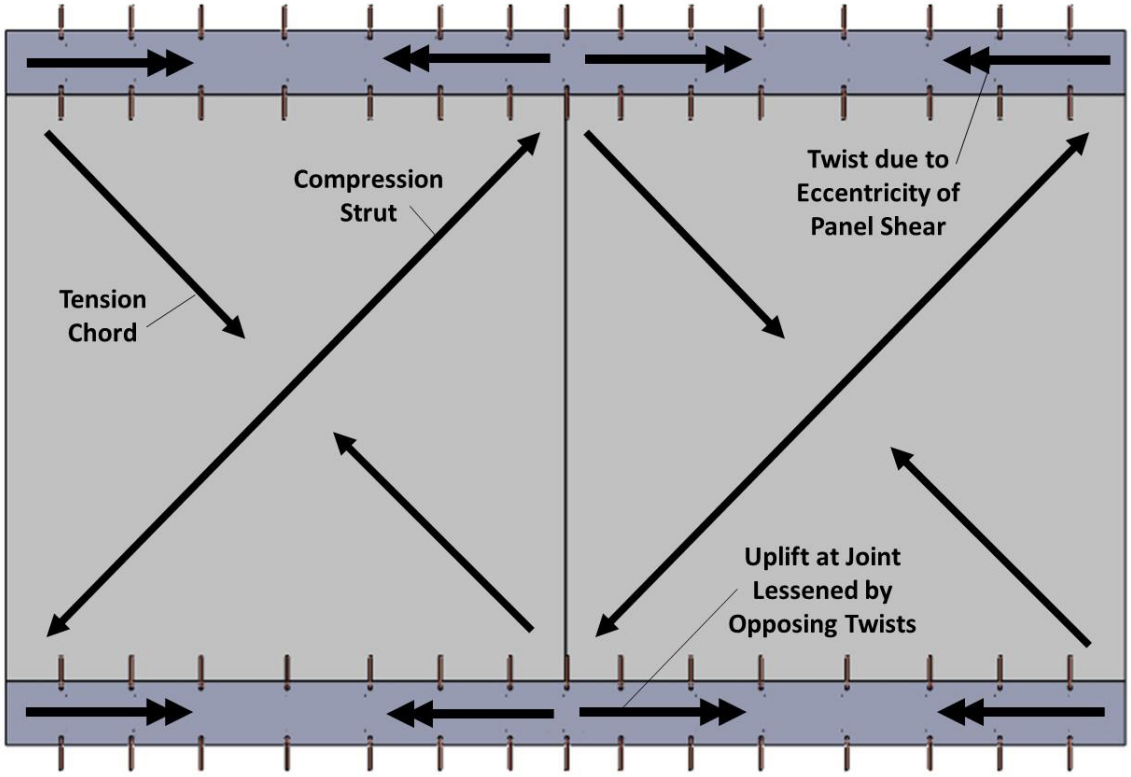

Figure 7.43 Reduced Uplift in Closure Pour at Panel Joint

While failure did not occur in the closure pour, the damage pattern seen in the specimen indicated that the closure pour may still be limiting the capacity of the panel. Cracking in the closure pour was more severe approximately 1 ft away from the end, in the less densely reinforced section, rather than at the end, where the total stress was greatest (See Figure 7.39). Additionally, the damage that ultimately led to failure (the cracking in the PCP and separation between the closure pour and base plate concrete) was concentrated in a small area near the end of the closure pour (See Figure 7.40 and Figure 7.41). This suggests that during loading, the lightly reinforced areas of the closure pour broke down at a low level of load, and ceased contributing meaningfully to the system strength. The heavily reinforced areas then attracted all the system's load, concentrating the demand on the connected elements, leading to a premature overload of those components (See Figure 7.44).

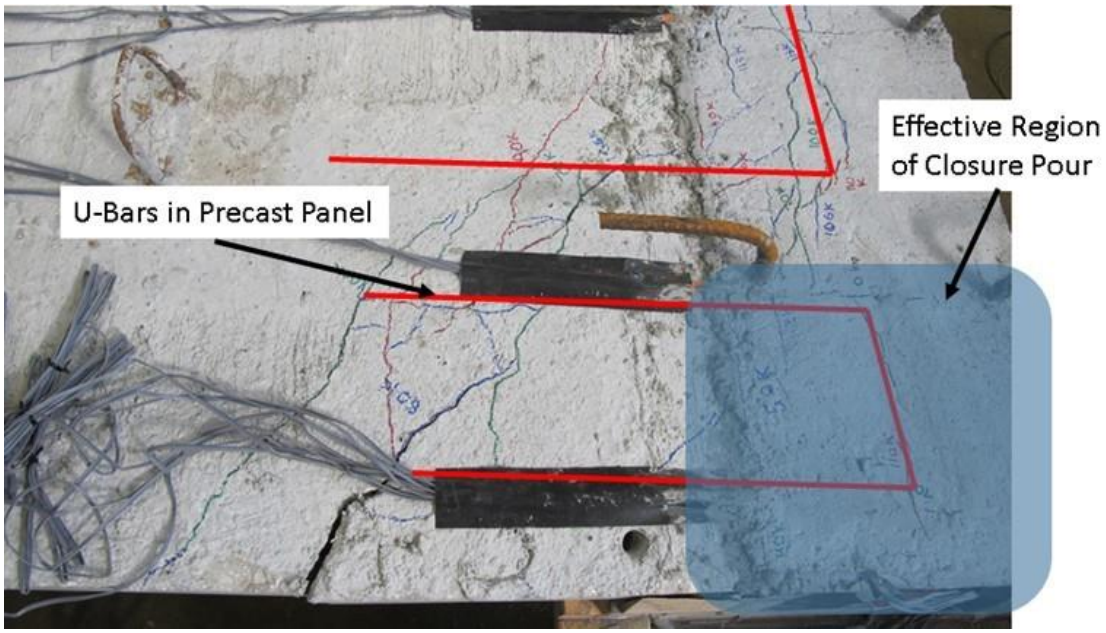

Figure 7.44 Concentration of Strength in Closure Pour Leading to Overload of U-bar and Premature Failure of Precast Panel

7.5.4 Closure Pour 4 (6″ Reinf. Spacing) Detail

Placement of additional reinforcement throughout the closure pour did seem to reduce the concentration of strength in the system. Cracking at the top face of the closure pour occurred more evenly throughout its length (See Figure 7.45). Additionally, cracking at the corners of the precast panel occurred over a much larger total area, which more evenly distributed the stress on the element, significantly reducing the size of the cracks: the largest PCP crack in the Corner Confinement specimen was 75 mils at 110 kips of shear, while the largest PCP crack in the 6″Reinf. Spacing specimen was only 15 mils at the same load level (See Figure 7.46). However, the overall capacity of the system was unchanged by the additional reinforcement, failing at the interface between the closure pour and girder flange at 114 kips, as in the previous specimen (See Figure 7.47 and Figure 7.48). Strain gages placed on the shear ties suggest that the reinforcement does see significant engagement far from the end of the closure pour, with similar stresses observed in the reinforcement over the first two feet of the closure pour (with stresses beginning to drop off at approximately three feet from the end) (See Figure 7.49). This would suggest that additional reinforcement throughout the pour would enhance the strength. However, the controlling failure mode (concrete breakout at the R-bar anchors) is brittle. Note that cracking initiated at this interface at 110 kips, and progressed very rapidly to complete failure at 114 kips (See Figure 7.47). This likely meant the system did not have the ductility to redistribute load to the interior ties as damage accumulated, limiting their effectiveness. Improved detailing at the girder-to-closure pour connection could improve the strength and ductility of this mechanism, giving the system sufficient ductility for the increased shear reinforcement to provide greater capacity. However, further testing is needed to determine the effectiveness of this detail.

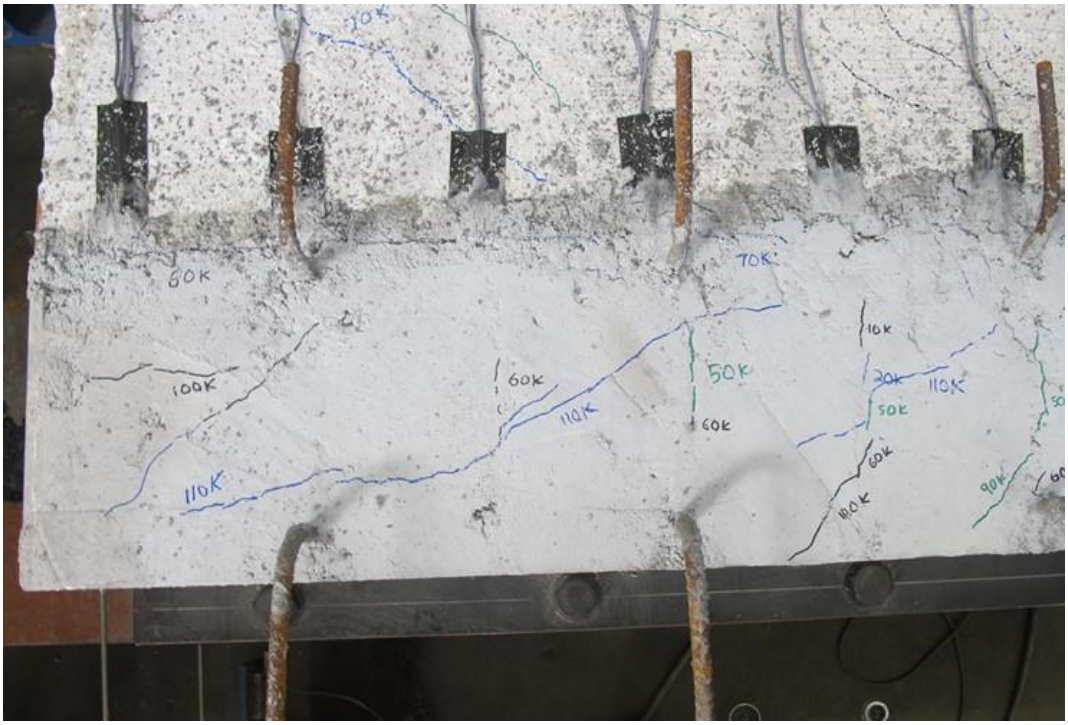

Figure 7.45 Even Distribution of Cracking in Closure Pour of 6" Reinforcement Spacing Detail at 110 kips

Figure 7.46 Even Distribution of Cracking in Precast Panel of 6" Reinforcement Spacing Detail at 110 kips

Figure 7.47 Initiation of Closure Pour to Girder Interface Crack at 110 kips and Failure at 114 kips (6" Reinforcement Spacing Specimen)

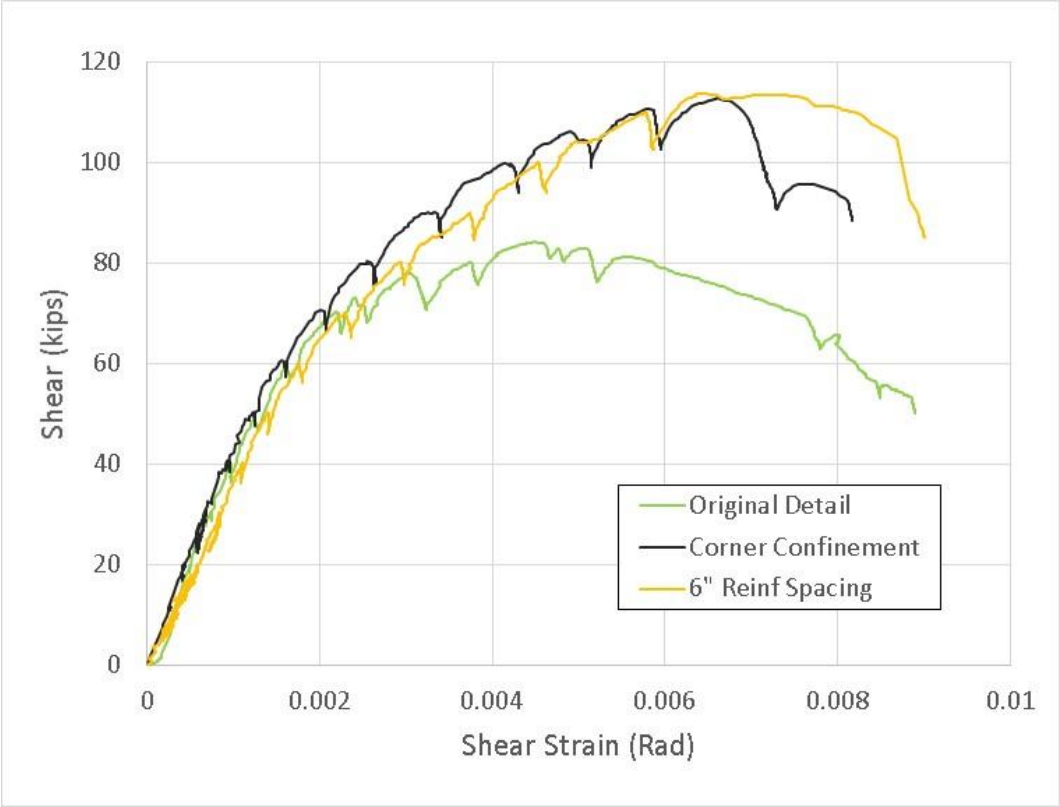

Figure 7.48 Shear Force vs Shear Strain of 6" Reinforcement Spacing Specimen

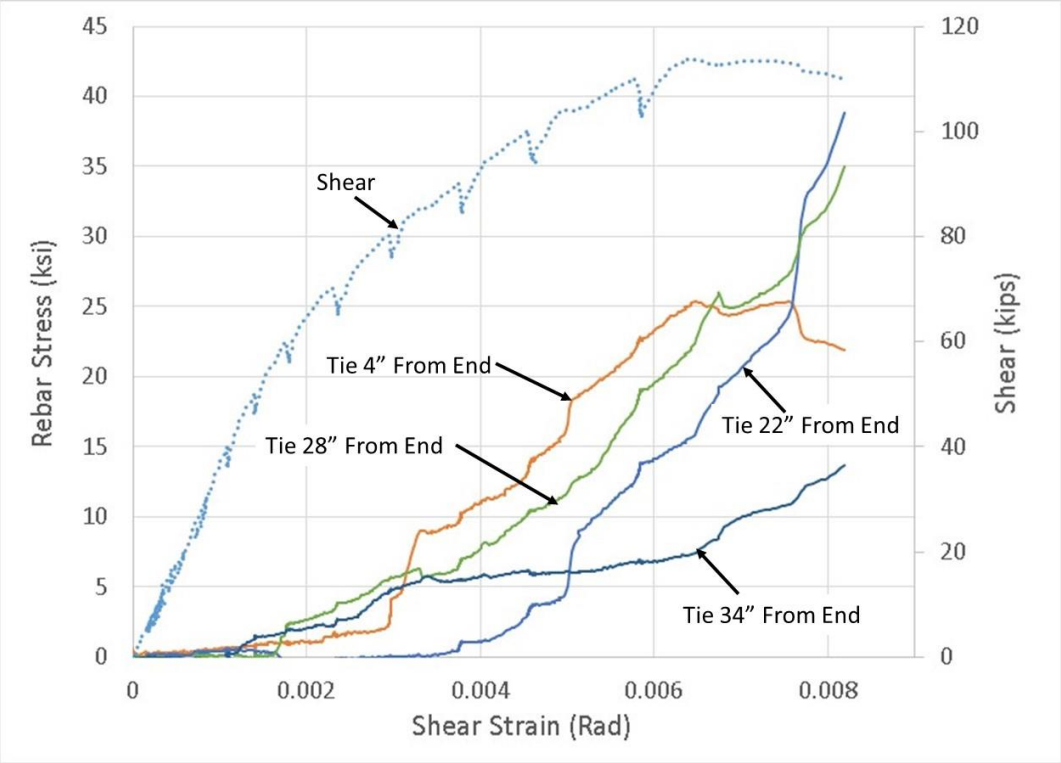

Figure 7.49 Stress in Shear Ties at SE Corner, 6" Reinforcement Spacing Specimen

7.5.5 Closure Pour 5 (High Eccentricity) Detail

The damage pattern in the high eccentricity specimen closure pour was significantly different than that of previous specimens. Cracking in previous specimens was dominated by "splitting" cracks that occurred on the top face of the closure pour due to tensile forces created by the moment at the end of the panel. While these did occur in the high eccentricity case, they were very limited. Instead damage to the closure pour was primarily in the form of diagonal cracks that occurred along the entire length of the pour (See Figure 7.50). Note that these cracks are perpendicular to the orientation of cracks that would occur due to shear in the panel (i.e. the cracks are opening in the direction of principal compression stress seen in the "cross frame" assumption for the panel (discussed in Chapter 8)). The cracks are likely due to torsion created in the system by the eccentricity of the panel. The tension in the northwest and southeast corners, and the compression in the northeast and southwest corners both act at a height several inches above the girder they react against, creating a significant twist in the system. Fortunately, the orientation of these cracks means they are resisted by both the shear and longitudinal reinforcement, keeping their width small (less than 10 mils) throughout the test, minimizing the damage to the closure pour.

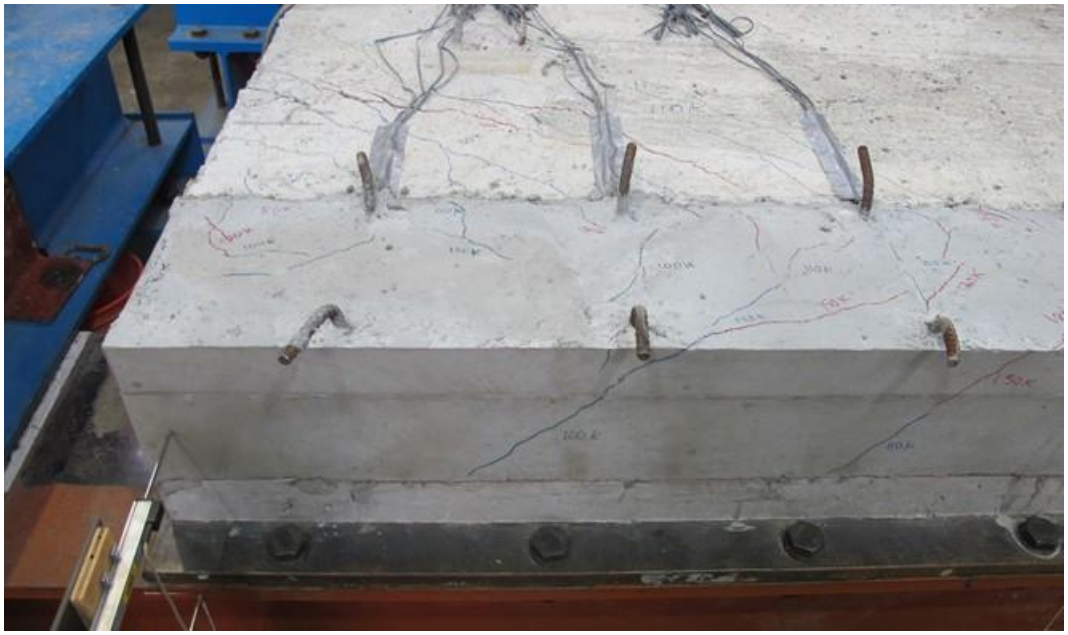

Figure 7.50 Cracking in Closure Pour of High Eccentricity Specimen

Behavior at the interface between the closure pour and simulated girder flange was significantly improved in the High Eccentricity specimen, with no observed cracking at the interface throughout the test. This improvement in behavior is very significant, as the increased eccentricity of the detail would have imposed a greater total uplift force on the closure pour-to-girder connection than in previous tests. The lack of failure in this case suggests a large increase in uplift capacity at the connection. It is difficult to determine which of the alterations to the detail are responsible for the increase in capacity. However, moderate cracking was observed in the concrete in the girder flange, unlike in previous specimens (See Figure 7.51). This suggests that there was an increase in load demand on that component, due to greater stress being placed on the R-bars. Were the enhancement to have come solely from the fixity of the cap plate, little stress would have occurred in the girder concrete, as the load would travel directly through the weld to base plate. This, along with the limited lateral confinement provided by the cap plate in previous specimens leads the researchers to believe that the improved R-bar connection detail is the primary reason for the enhancement in uplift capacity. However, more testing is needed to conclusively determine the relative contribution of the two detail alterations.

Note that the anchorage failure mode in previous specimens (concrete breakout in tension) is typically assumed to occur as an approximately 35^0 cone (ACI 2011). This means that the original 6″ spacing of the R-bars, along with their 3″ height, is likely sufficient to engage the full area of the concrete between them. The tensile capacity of the R-bars themselves also significantly exceeds the expected uplift capacity of the concrete. The additional R-bar at the ends of the closure pour is meant primarily to create a smaller distance to the first R-bar, rather than providing a greater number of total R-bars. Thus, the researchers do not feel it is necessary to provide a closer R-bar spacing at the ends of the panels, but care should be taken to ensure that the initial R-bar is located near the end of the closure pour for the end panels.

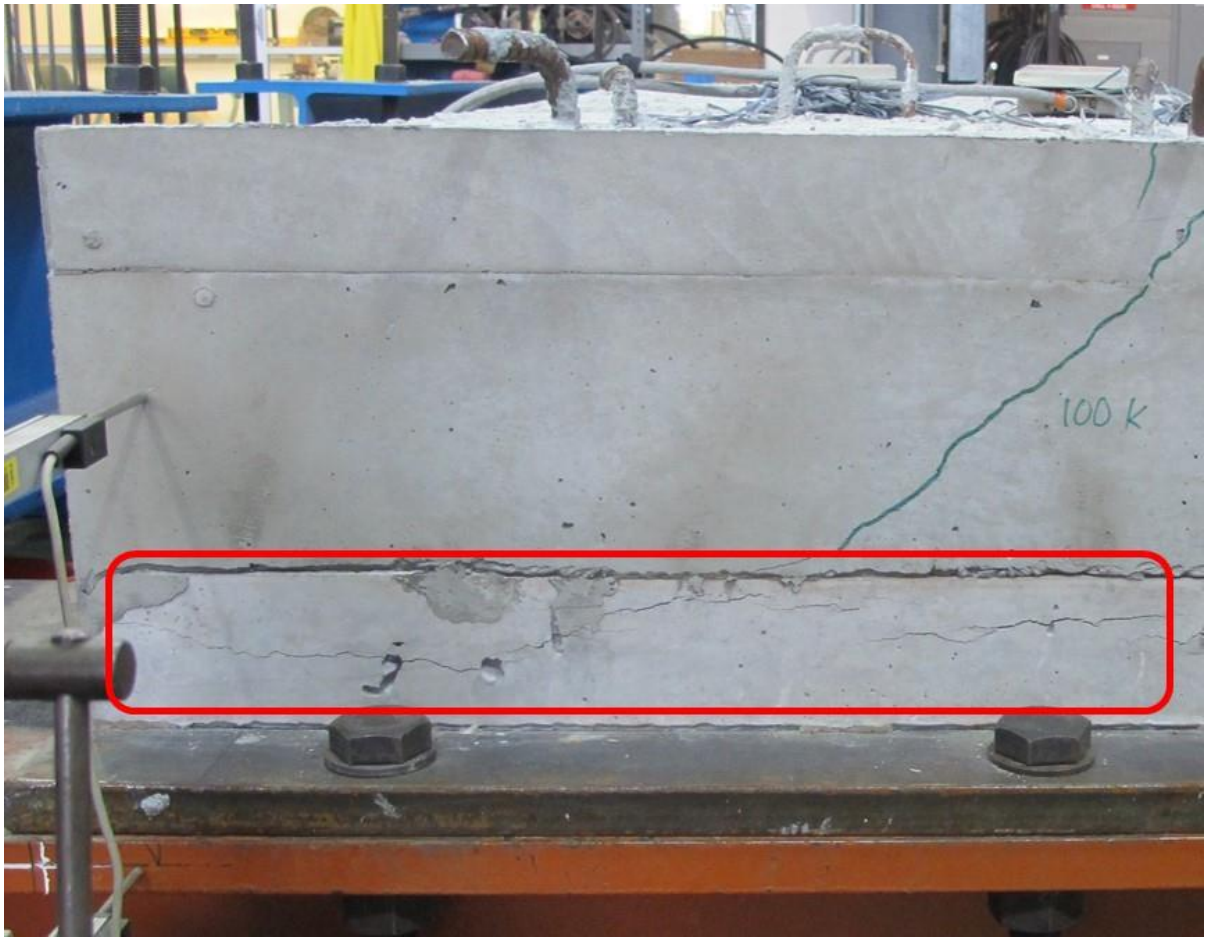

Figure 7.51 Cracking in "Girder" Concrete of High Eccentricity Specimen

Cracking in the precast panel was more severe than in any of the previous specimens. In addition to the diagonal cracking at the "tension" corners of the precast panel, moderate cracking was observed at the compression corners as well (See Figure 7.52), though this is likely due to the previously mentioned twist between the closure pour and panel rather than crushing of the concrete at these locations. Additionally, several much longer cracks appeared, running nearly the entire length of the specimen from one compression corner to the other (See Figure 7.53). Due to the large pre-stressing force in the tendons, these cracks remained small, and are not believed to have significantly contributed to the failure of the system. At approximately 155 kips, the large number of diagonal cracks at the NW corner merged, forming one relatively continuous crack along the side of the panel, at approximately the location of the end of the panel U-bars (See Figure 7.54). This crack, combined with the cracking at the SW corner due to twist of the closure pour, spanned nearly the entire section of the PCP, resulting in a shear slip of the panel at that location. This led to spalling off of concrete at the NW corner of the specimen, as well as the beginnings of concrete blowout at the SC corner, as the prestressing tendon was loaded laterally while trying to maintain compatibility with the displaced sections of concrete (See Figure 7.55). This led to a significant drop in shear capacity, and the failure of the system (See Figure 7.56). This failure load of 155 kips is similar to the largest loads seen in the precast panels connected to steel girders. That, along with the failure mode (shear failure across the full section of the precast panel) suggests that the

capacity seen in this closure pour detail is an upper bound of the capacity that could be reasonably achieved by a lid slab.

Figure 7.52 Cracking at SW Corner of Precast Panel

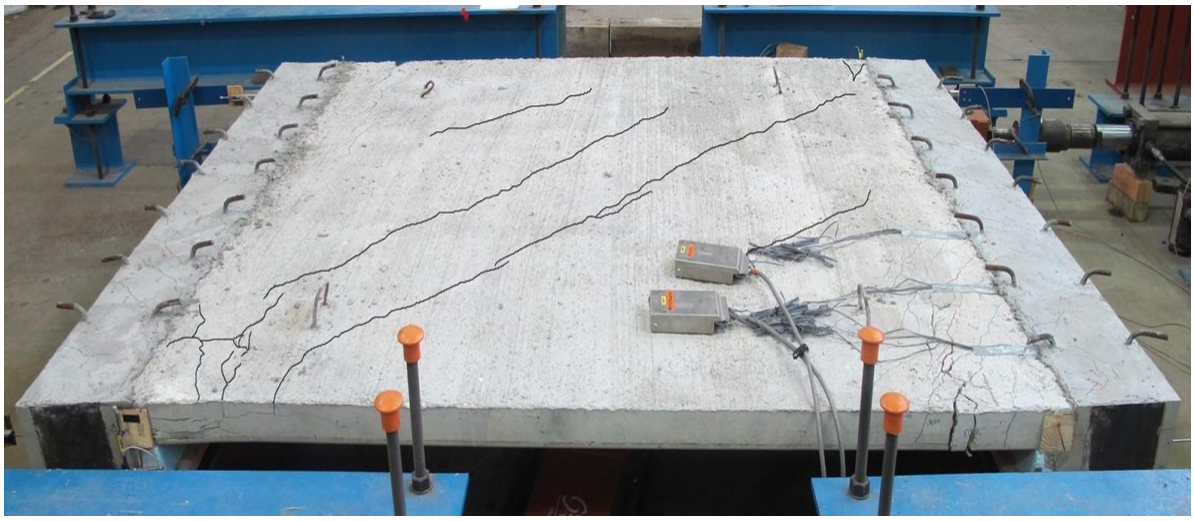

Figure 7.53 Full-Length Diagonal PCP Cracks

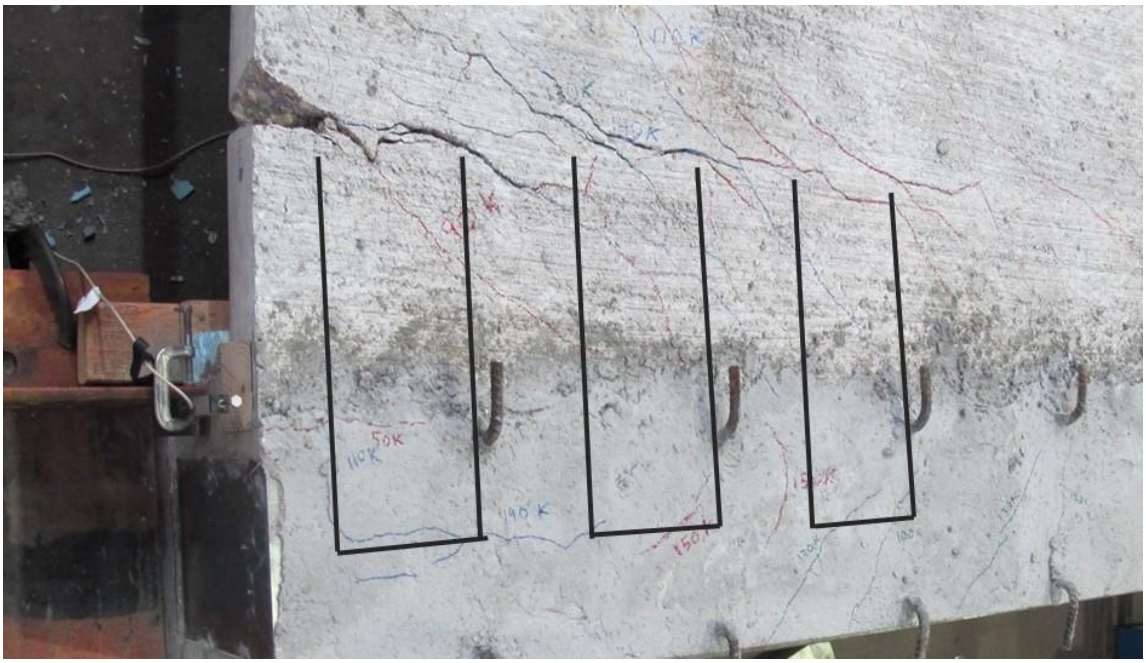

Figure 7.54 Merging of NW PCP Corner Cracks (U-bars Drawn in for Reference)

Figure 7.55 Beginnings of Side Face Blowout at South-most Tendon due to Shear Slip of Precast Panel

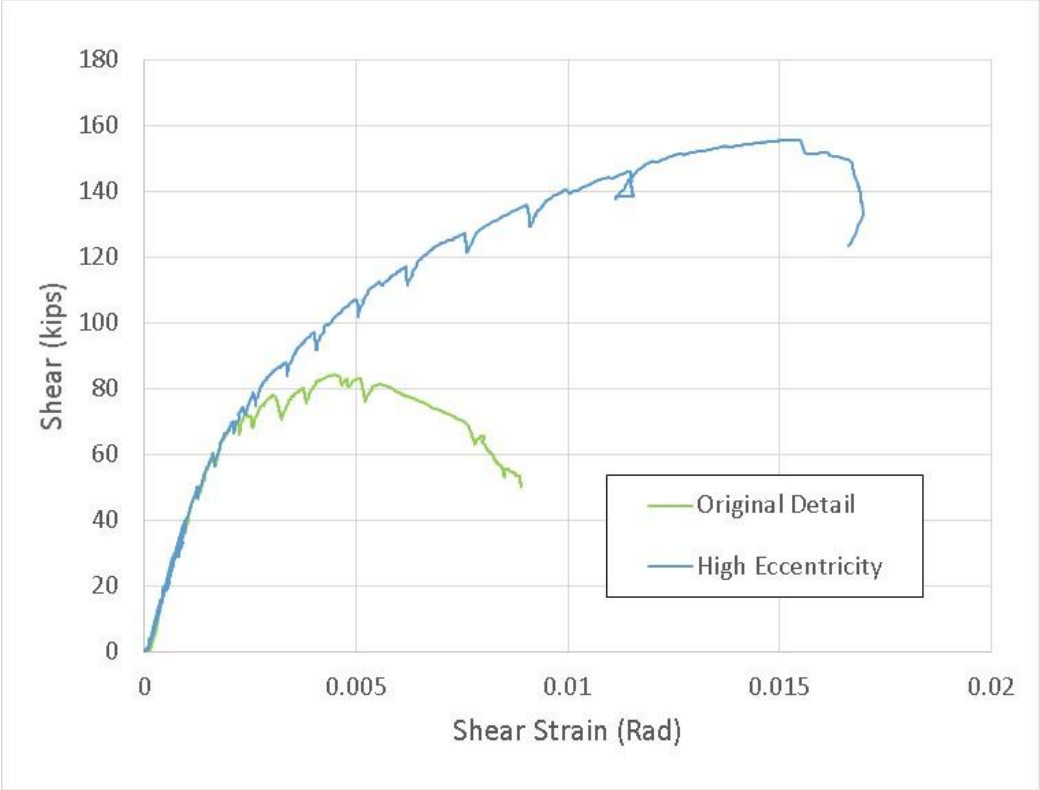

Figure 7.56 Shear Force vs Shear Strain of High Eccentricity Specimen

7.6 Summary and Design Recommendations

Testing in this research program has demonstrated that closure pours can be used to connect precast panel lid slabs to a concrete U-girder to form a torsionally stiff member. The existing TxDOT detail results in a stiff top diaphragm on the U-girder, enabling it to function as a closed shape. However, this detail fails at low shear loads, and may not have the capacity to withstand the torsion present in a highly curved U-girder. Thus, the existing detail is likely only appropriate for straight, or minimally curved U-girders. If a closure pour is to be used on a U-girder with a tight radius of curvature, modifications to the detail are likely necessary to improve capacity. Further estimates of shear demand on the closure pours for a variety of bridge geometries are presented in Chapter 10.

Due to the limited number of tests performed in this program, further research is needed before a definitive "improved" detail could be developed. However, recommendations can be made based on the results of the test program. Additional shear reinforcement should be placed at the closure pour near the ends of each panel, with ties and hat bars at approximately 4″ spacing over the first foot of the closure pour. Note that this will likely require coping of the hat bar at some locations to allow installation inside the panel U-bars. Decreasing the shear reinforcement spacing to 6″ along the entire closure pour may also improve behavior, but further research is needed to determine the enhancement provided by this change. Additionally, the researchers recommend a #4 bar be tied to the inside of the R-bars of the girder (See Figure 7.24). This additional bar is most critical at the end of the exterior panel, as the continuity between panels will alleviate the anchor demands at other locations. However, due to the relative ease of installation of this bar, and the undesirably brittle nature of anchorage failure, the researchers recommend this

bar be continuous along the specimen, to achieve maximum improvement in anchorage of the closure pour.

The specimens all exhibited reasonable ductility, with large ratios between the yield strain and failure strain. Additionally, the systems failed gradually, softening rather than experiencing an abrupt drop in load. However, the specimens also frequently experienced significant cracking in either the closure pour or precast panel at loads significantly below their failure load. Due to the construction sequence of this system, this may not be a significant concern, as the cracked elements should not be exposed to the environment in the finished girder (See Figure 7.2). However, if the designer wishes to limit cracking under service load, the forces on the closure pour should be kept well below their ultimate capacity.

The tests reported in this chapter will be supplemented by the analytical work done in Chapter 10 to examine expected demands on concrete U-girders for different girder spans and curvature radii. Based on the results of that work, further observations will be provided on what closure pour detail could be appropriate for different bridge geometries.

Chapter 8. Development of Finite Element Model for Precast Concrete Panels

8.1 Introduction

This chapter focuses on the finite element (FE) modeling techniques that were used to develop the models of the PCP/connection system for the experimental shear tests that were conducted in Chapter 4. The goal was to accurately model the stiffness of the PCP/connection system so that the PCPs could be correctly represented for both the validation of the finite element models of the steel I-beam and steel tub girder systems and the parametric studies of these two systems as described in detail in Chapter 9. The three-dimensional finite element program Abaqus/CAE 6.14 was used for all finite element modeling throughout the entirety of this report.

8.2 Simple Truss Model

A number of different preliminary modeling techniques were used to represent the PCP/connection system. In one model, shell elements were used to represent the PCP and the WTs which significantly overestimated the stiffness of the PCP/connection systems tested in the laboratory. The larger stiffness of the FE model was likely due to the lack of accurately modelling of the connection between the WT and the PCP. In reality, load is transferred from the PCP to the deformed anchors (D2Ls) to the embeds to the WTs and into the loading beams. However, in the FE model the nodes between the PCP and the WTs and between the WTs and the loading beams were directly connected. As a result, the flexibly of many of the components were not accounted for in the FE model. While more detailed models could be used to explicitly represent the PCPs, the embeds, the D2L anchors, WTs, and the welds with brick elements, it was deemed unreasonable to use solid-element models for the parametric study due to the large number of elements and degrees of freedom required for these models. Therefore, a more simplified approach was taken using truss members to represent the in-plane stiffness of the PCP/connection system similar to the work done by Helwig and Yura (2008a).

8.2.1 Truss Models for Permanent Metal Deck Forms (PMDFs)

Helwig and Yura (2008a) used two-node truss elements to model shear diaphragms of light gauge metal deck forms in twin I-girder finite element analysis models (see Figure 8.1). For this system, the in-plane stiffness of a single truss panel was given by (Yura 2001)

$$\beta_b = \frac{AEs^2h_b^2}{2L_c^3 + S^3} \tag{8.1}$$

where,
β_b = stiffness of the truss panel (kip·in/rad)
A = area of the struts and the diagonal of the truss panel (equal areas were employed)
E = modulus of elasticity
S = girder spacing
h_b = distance between struts of truss panel
L_c = length of the diagonal member

The stiffness of the truss panel was changed by modifying the value for the cross-sectional area of the truss members.

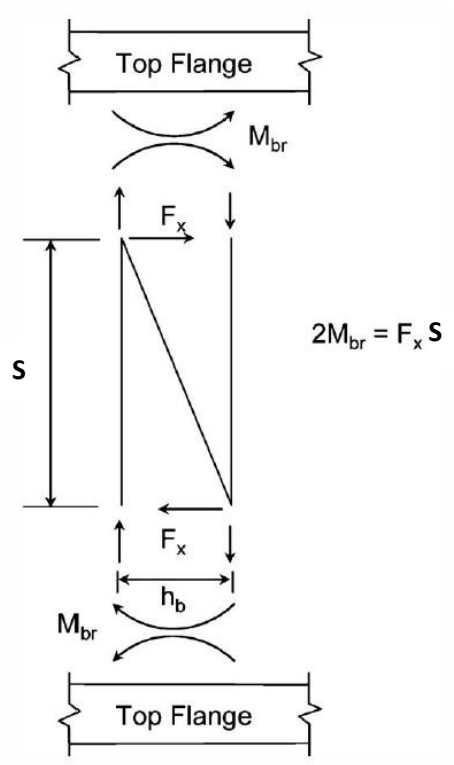

Figure 8.1: Truss Panel Model for FEA Studies (Helwig and Yura 2008a)

8.2.2 Truss Models for the PCP/Connection System

In a similar manner to Helwig and Yura (2008a), two-node truss elements were used as a simple model for the PCP/connection system. A two diagonal X-frame configuration was used as shown in Figure 8.2. For this system, the in-plane stiffness of a single truss panel was given by (Yura 2001)

$$\beta_b = \frac{A_{truss} E S^2 h_b^2}{L_d^3} \tag{8.2}$$

where,
β_b = stiffness of truss panel (kip·in/rad)
A_{truss} = area of the diagonal member
E = elastic modulus
h_b = strut spacing
S = girder spacing (centerline to centerline)
L_d = diagonal length

The equation for the cross-sectional area of the truss members was derived to be:

$$A_{truss} = \frac{V}{\gamma} \cdot \frac{L_d^3}{2ESh_b^2} \quad (8.3)$$

where,
V = the shear force on the panel (kip)
γ = the shear strain on the panel (rad)

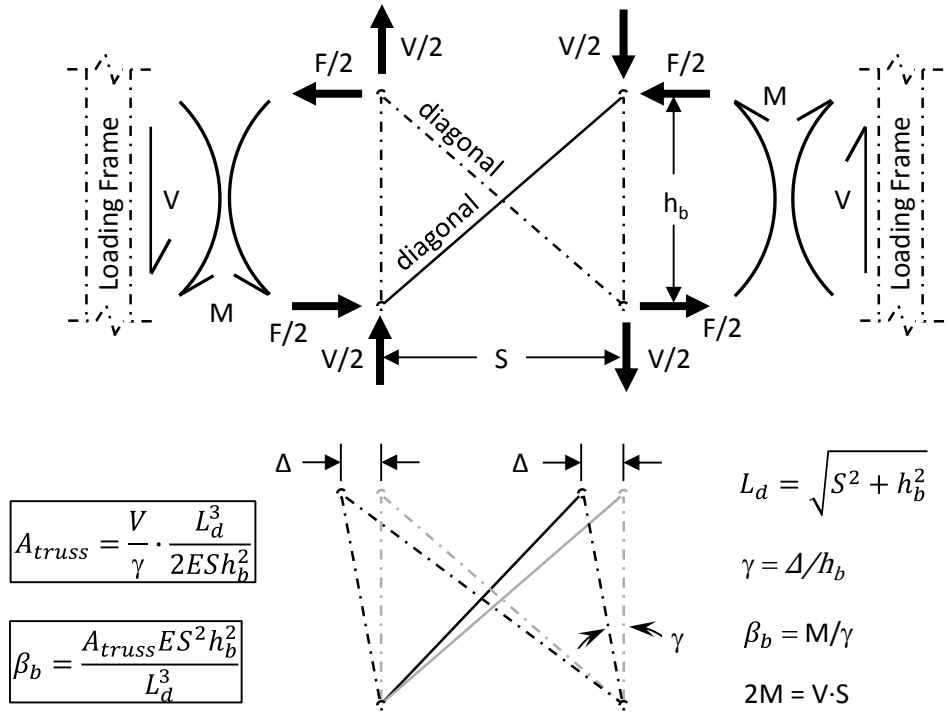

Figure 8.2: Truss Panel Lateral Stiffness

Figure 8.3 shows the dimensions of the truss panel that were used to model the stiffness of the PCP/connection system that was tested in the laboratory. The ends of the truss members terminated at approximately the center of the WT connections with S = 105″ and h_b = 78″ (note that these are the same dimension as the steel cross-frame that was tested on the shear frame). Setting the elastic modulus of equal to the value for steel (E = 29,000 ksi), the area of the truss members were calculated in Table 8.1 for the 8 tests conducted in the laboratory (see Chapter 4). Note that these values were corrected to account for the flexibility of the shear frame as discussed in Chapter 4. The stiffness of the brace (β_b) is also presented in Table 8.1.

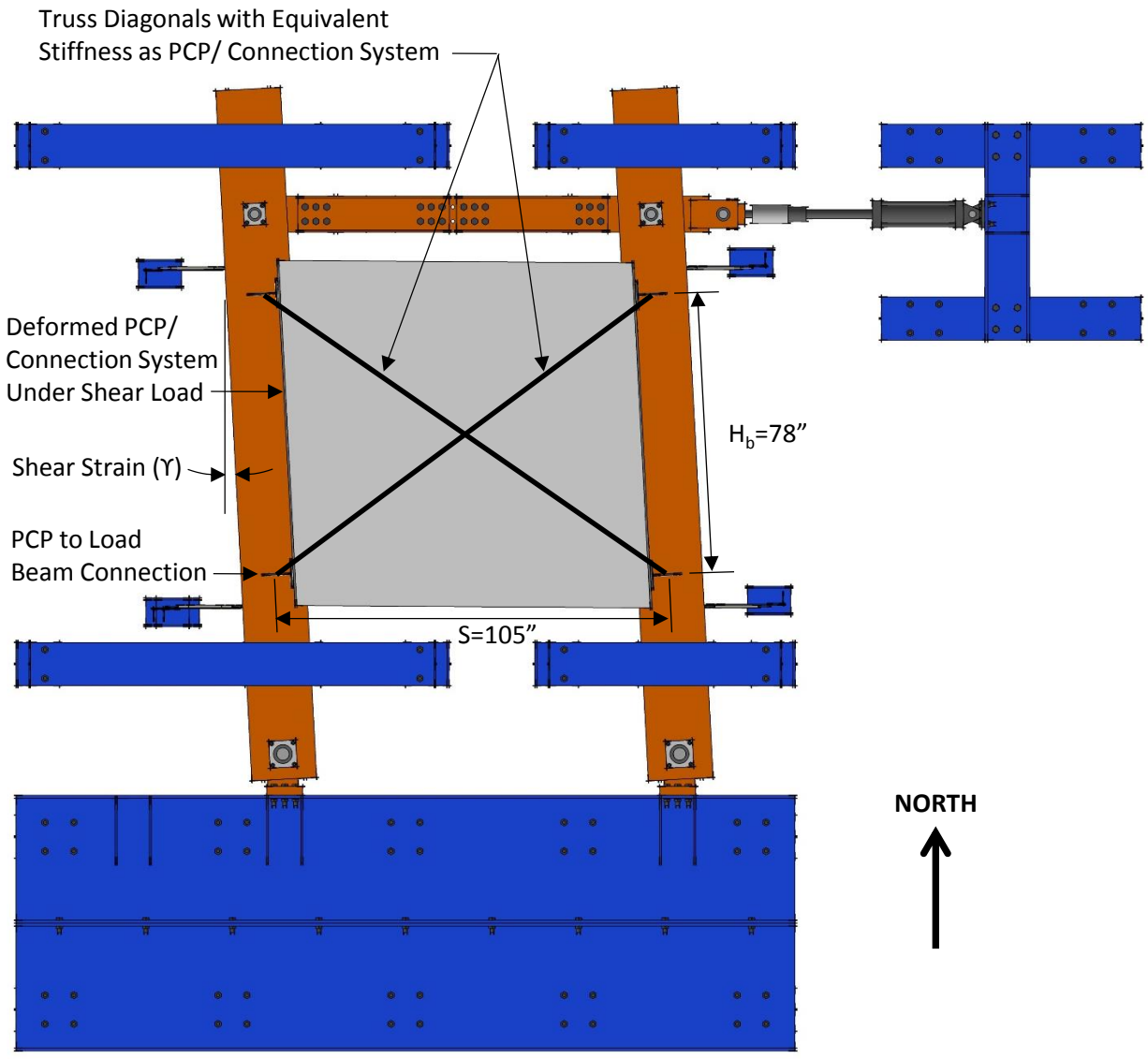

Figure 8.3: Truss Panel with Equivalent Stiffness as PCP/Connection System

Table 8.1: Area of Truss Panels for Equivalent Stiffness from Experimental Tests

Connection Detail	Bedding Strip Height (in.)	V/ϒ (Corrected) (kips/rad)	β_b* (kip·in/rad)	A_{truss}* (in^2)
A.1.MAX	4	23,615	1,239,789	1.43
A.1.MIN	½	36,449	1,913,594	2.20
B.1.MAX	4	26,228	1,376,951	1.58
B.1.MIN	½	36,531	1,917,893	2.21
C.2.MAX	4	30,815	1,617,791	1.86
C.2.MIN	½	43,936	2,306,645	2.65
D.2.MAX	4	31,527	1,655,179	1.90
D.2.MIN	½	41,742	2,191,439	2.52

*Calculated Using E = 29,000 ksi, S = 105", h_b = 78", L_d = 130.8"

8.2.3 Accounting for Change in PCP Stiffness

In the state of Texas, PCPs are typically 8′-0″ wide (parallel to the girder span) and have a variable span to accommodate the spacing of the girders in a bridge (TxDOT 2014b). Figure 8.4 shows a PCP rigidly connected to the shear test frame. The loading condition on the PCP mimics that of a shear wall that is fixed at the top and bottom where the lateral deflection for an uncracked fixed-fixed shear wall was derived as:

$$\Delta_{PCP} = \frac{V}{Et}\left[\left(\frac{S_{pcp}}{h_{pcp}}\right)^3 + 2.3\left(\frac{S_{pcp}}{h_{pcp}}\right)\right] \tag{8.4}$$

where,
V = shear force
E = elastic modulus of concrete
t = thickness
S_{pcp} = shear wall height
h_{pcp} = shear wall width/PCP length

Equation 8.4 accounts for deflections from both shear and bending and the 2.3 constant is the ratio of the elastic modulus of concrete to the shear modulus of concrete (assuming a Poisson's ratio of 0.15 for uncracked concrete). From Equation 8.4 the in-plane stiffness of the PCP (β_{PCP}) was calculated as:

$$\beta_{PCP} = \frac{S_{pcp}^2 Et}{2\left[\left(\frac{S_{pcp}}{h_{pcp}}\right)^3 + 2.3\left(\frac{S_{pcp}}{h_{pcp}}\right)\right]} \tag{8.5}$$

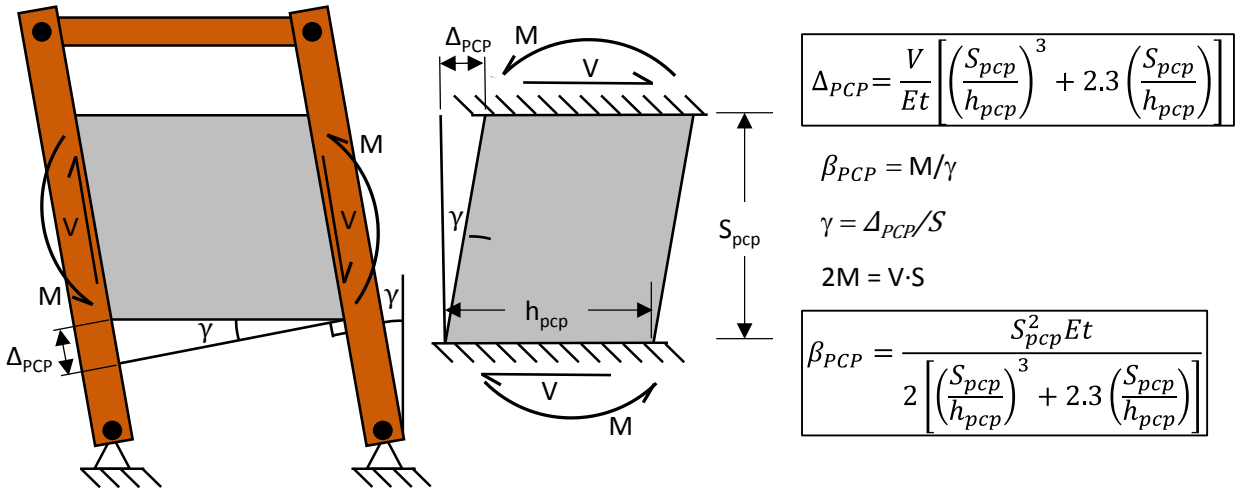

Figure 8.4: Deformation of PCP Rigidly Connected to Shear Frame

For an 8′-3″ x 8′-0″ x 4″ thick PCP with E = 5,020 ksi, the in-plane stiffness of the PCP is calculated as $\beta_{PCP} = 28{,}369{,}503$ kip·in/rad (from Equation 8.5) whereas the experimental stiffness of the PCP/connection system was measured as $\beta_b = 1{,}296{,}445$ kip·in/rad for connection A.1.MAX (see Table 8.1). The stiffness of the PCP is more than an order of magnitude larger than the stiffness of the PCP/connection system measured in the experiment, indicating that the majority of the flexibility of the systems comes from the low stiffness of the connection (β_{con}). Since the PCP and the connections behave as springs in series, the effective in-plane stiffness of the brace β_b is defined as the follows:

$$\frac{1}{\beta_b} = \frac{1}{\beta_{PCP}} + \frac{1}{\beta_{con}} \qquad (8.6)$$

Table 8.2 shows the stiffness of the connections derived from the equation above for the eight PCPs tested in Chapter 4. For all eight cases, $\beta_b \approx \beta_{con}$ signifying that the stiffness of the PCP played a small role in the stiffness of the system. Equation 8.6 can be used to determine the effective stiffness of the brace β_b for PCPs of various sizes and with different modulus of elasticities using Equation 8.5 to derive β_{PCP} and taking β_{con} from Table 8.2.

Table 8.2: Calculated Connection Stiffness from Experimental Tests

Connection Detail	Bedding Strip Height (in.)	β_b (kip·in/rad)	β_{PCP}* (kip·in/rad)	β_{con} (kip·in/rad)
A.1.MAX	4	1,239,789	28,369,503	1,296,445
A.1.MIN	½	1,913,594	28,369,503	2,052,006
B.1.MAX	4	1,376,951	28,369,503	1,447,192
B.1.MIN	½	1,917,893	28,369,503	2,056,951
C.2.MAX	4	1,617,791	28,369,503	1,715,626
C.2.MIN	½	2,306,645	28,369,503	2,510,791
D.2.MAX	4	1,655,179	28,369,503	1,757,731
D.2.MIN	½	2,191,439	28,369,503	2,374,891

*Calculated Using E = 5,020 ksi, S_{pcp} = 99", h_{pcp} = 96", t = 4"

8.2.4 PCP Connection Stiffness

The stiffness of the PCP connection does not remain constant as the dimensions of the PCP change. Figure 8.5 shows that as the girder spacing doubles, the shear force on the PCP also doubles when the moment remains constant. Therefore, the force on the connections of the PCP (and the resulting deformation of the connections) is a function of the girder spacing.

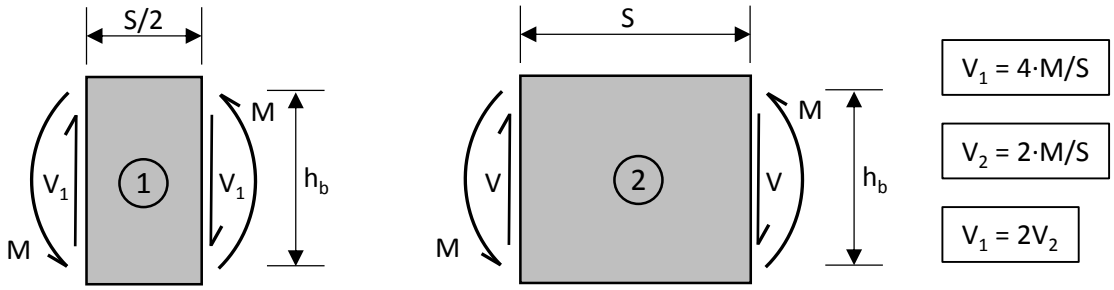

Figure 8.5: Forces on PCPs as Girder Spacing Changes

The PCP connection system can be represented as springs in two directions at each connection point (Figure 8.6). Figure 8.7 shows the rotation of the frame (γ_x) only considering the flexibility of the horizontal springs (i.e. when $k_y = \infty$) while Figure 8.8 shows the rotation of the frame (γ_y) only considering the flexibility of the vertical springs (i.e. when $k_x = \infty$). Summing the effects from the vertical and horizontal springs leads to the following equation for the total connection deformation:

$$\gamma_{con} = \gamma_x + \gamma_y = \frac{V \cdot S}{h_b^2 \cdot k_x} + \frac{V}{S \cdot k_y} \qquad (8.7)$$

L-Pot data from the shear frame tests indicates that the stiffness of the springs is approximately the same in both directions ($k_x \approx k_y$). Note: the exact relative stiffness of k_x and k_y could have been back calculated had PCP of two different dimensions been tested. Setting $k_{con} = k_x = k_y$ the connection stiffness can be derived as follows:

$$\beta_{con} = \frac{M}{\gamma_{con}} = \frac{V \cdot S}{2\gamma_{con}} = \frac{k_{con}}{2\left(\frac{1}{h_b^2} + \frac{1}{S^2}\right)} \tag{8.8}$$

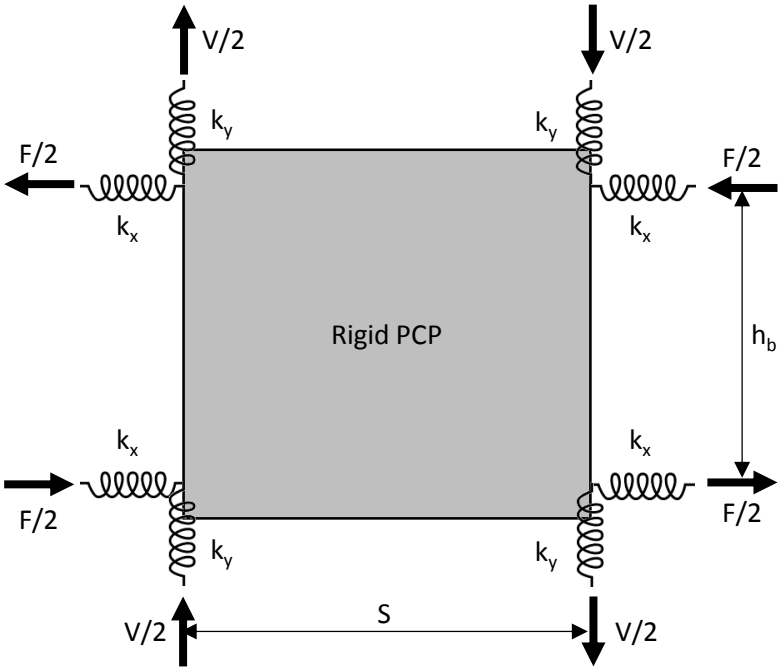

$$\Delta_x = \frac{F}{2} \cdot \frac{1}{k_x}$$

$$F = \frac{V \cdot S}{h_b}$$

$$\Delta_y = \frac{V}{2} \cdot \frac{1}{k_y}$$

Figure 8.6: Model of PCP Connection Stiffness

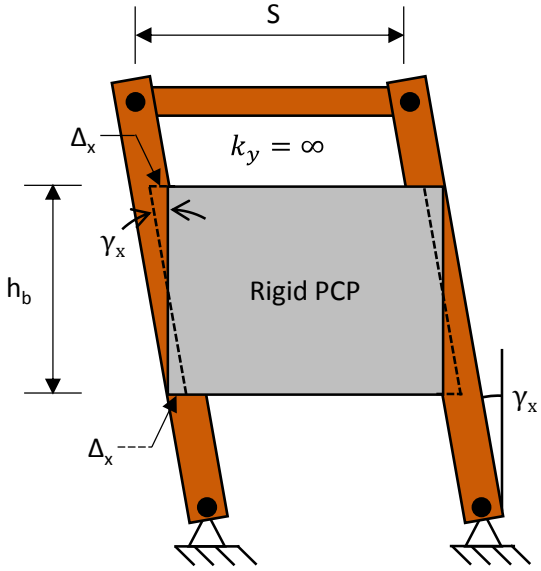

$$\gamma_x = \frac{2\Delta_x}{h_b}$$

$$\Delta_x = \frac{F}{2} \cdot \frac{1}{k_x}$$

$$F = \frac{V \cdot S}{h_b}$$

$$\gamma_x = \frac{2}{h_b} \cdot \frac{F}{2} \cdot \frac{1}{k_x} = \frac{2}{h_b} \cdot \frac{V \cdot S}{2h_b} \cdot \frac{1}{k_x}$$

$$\boxed{\gamma_x = \frac{V \cdot S}{h_b^2 \cdot k_x}}$$

Figure 8.7: Connection Deformation for $k_y = \infty$

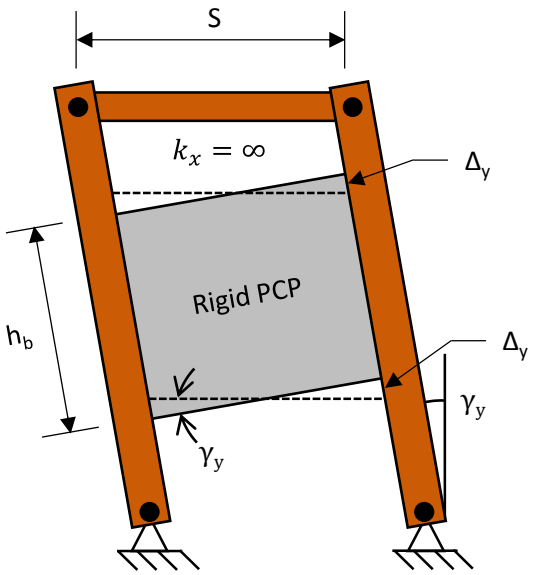

$$\gamma_y = \frac{2\Delta_y}{S}$$

$$\Delta_y = \frac{V}{2} \cdot \frac{1}{k_y}$$

$$\gamma_y = \frac{2}{S} \cdot \frac{V}{2} \cdot \frac{1}{k_y}$$

$$\boxed{\gamma_y = \frac{V}{S \cdot k_y}}$$

Figure 8.8: Connection Deformation for $k_x = \infty$

Using Equation 8.8 and the values for the connection stiffness (β_{con}) from Table 8.2, the spring stiffness (k_{con}) can be calculated at shown in Table 8.3. The spring stiffness is independent of the dimensions of the PCPs.

Table 8.3: Stiffness of Springs Representing Connections

Connection Detail	Bedding Strip Height (in.)	β_{con} (kip·in/rad)	$k_{con} = k_x = k_y$ (kip·in/rad)
A.1.MAX	4	1,296,445	640
A.1.MIN	½	2,052,006	1,014
B.1.MAX	4	1,447,192	715
B.1.MIN	½	2,056,951	1,016
C.2.MAX	4	1,715,626	848
C.2.MIN	½	2,510,791	1,240
D.2.MAX	4	1,757,731	868
D.2.MIN	½	2,374,891	1,173

*Calculated Using S_{pcp} = 110", h_b = 78", t = 4"

8.3 Validating Correction Factors

As discussed thoroughly in Chapter 4, it was discovered that the shear frame members experienced measurable torsional and flexural deformations that impacted the measurements of deformations in the experimental PCP shear tests. A steel cross-frame constructed of HSS members was connected to the frame tested to determine the how the deformation of the shear frame influenced the accuracy of the reading from the experiments. After the bolted connections were fully engaged, the direct stiffness measurements of the cross-frame were 1.30 and 1.43 times larger than the measurements from frame when the cross-frame was at low (2.5″) and high (6″)

eccentricities, respectively. The shear stiffness PCP/connection systems were corrected using the 1.30 and 1.43 factors for the tests when the PCP sat on a ½″ bedding strip and 4″ bedding strip, respectively.

The following procedure was used to validate that the 1.30 and 1.43 correction factors used for the steel cross-frame were applicable to the experimental data for the PCP/connection system. First, Abaqus/CAE 6.14 was used to construct a three dimensional finite element model of the shear frame, taking special care to correctly model the complex boundary conditions of the shear frame. Next, the Abaqus model was validated with the experimental data from the steel cross-frame tests to ensure that the model produced reasonable results and that the boundary conditions were modeled correctly. Finally, the stiffness of the cross-frame in the FE model was changed to match the corrected values (see Table 8.1) and the results were compared with the experimental PCP tests to validate that the 1.30 and 1.43 correction factors were correct.

8.3.1 Finite Element Model of Shear Frame

Figure 8.9 shows the three dimensional FE model of the shear frame used for the experimental tests in the laboratory (Figure 8.10). The loading beams, tie down beams, connections, and casters were all modeled using C3D20R (20-node quadratic brick with reduced integration) brick elements. Also, the stitched fillet welds between the W-shape and the top plate of the loading beam were explicitly modeled using brick elements and the surfaces of the fillet welds were tied to both members. In the model, frictionless contact interactions were used between the casters and the strong floor and between the loading beams and the tie-down beams (simulating the low-friction needle bearings in the test setup). This allowed the members to separate freely and also caused normal forces to occur when contact was made similar to the conditions in the laboratory. Vertical springs with the stiffness equal to the threaded rods connected to the strong floor were used at each corner of the tie-down beams to accurately model the stiffness of the system. The rigid material properties were used for the connections to the HSS truss members (for both the low and high eccentricity cases) as the connection flexibility was accounted for in the reduced area of the members representing the HSS. Both T3D2 truss elements (2-node linear 3-dimensional) and linear spring elements were used to model the HSS/connection members which produced virtually identical results.

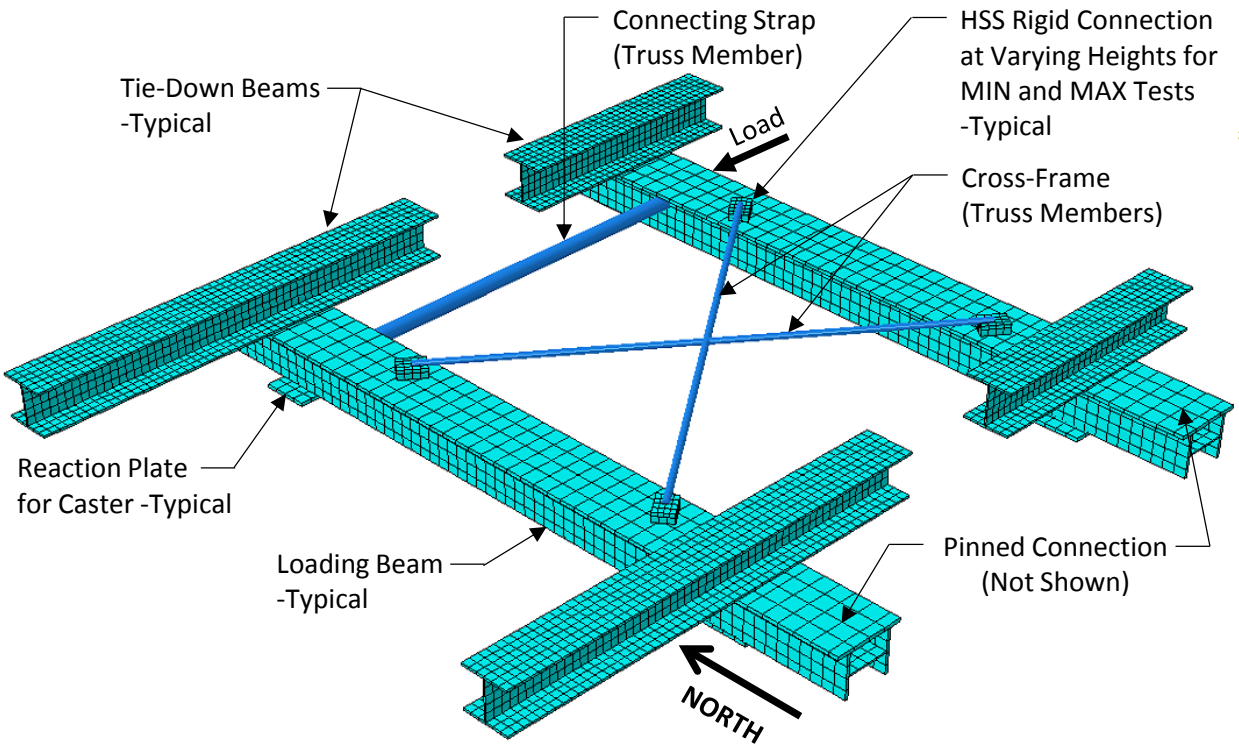

Figure 8.9: Finite Element Model of Shear Frame

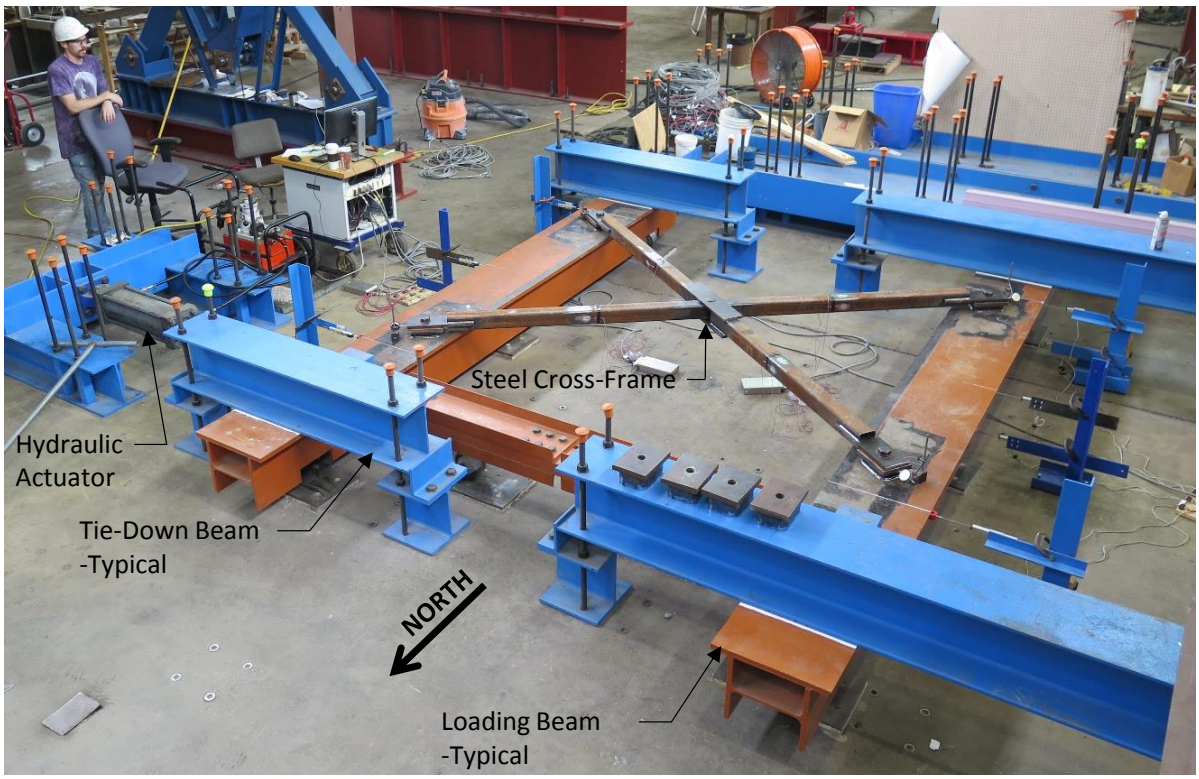

Figure 8.10: Experimental Tests on Steel Cross-Frame

8.3.2 Validating Finite Element Model of Shear Frame

Table 8.4 shows the equivalent area of the steel cross-frame members (copied directly from Chapter 4) for the high and low eccentricity cases (2.5″ and 6″, respectively) that were derived from the flexibility both the HSS member and the connections measured in the laboratory. These equivalent areas were used for the truss members in the finite element models with both the low and high eccentricities.

Table 8.4: Equivalent Area Accounting for Connection Flexibility

Equivalent Truss Member Area (in^2)	High Eccentricity (2½")	Low Eccentricity (6")
$A_{EQ.T.1}$	0.60	0.71
$A_{EQ.C.1}$	0.79	0.95
$A_{EQ.AVG.1}$	**0.70**	**0.83**
$A_{EQ.T.2}$	1.21	1.33
$A_{EQ.C.2}$	1.09	1.44
$A_{EQ.AVG.2}$	**1.15**	**1.38**

Key: T = Tension, C = Compression, AVG = Average

Figure 8.11 and Figure 8.12 show comparisons of the experimental stiffness measured via L-pots on the shear frame and the stiffness of the finite element models for the high and low eccentric cases, respectively. The data shown with the dashed line is from the measured stiffness of the steel cross-frame and connections which is not influenced by the stiffness of the shear frame as explained in Chapter 4 (i.e. these would be the results if the shear frame was perfectly rigid). For both cases, the finite element model was slightly stiffer than the experimental results (by factors of 1.13 and 1.17 for the high and low eccentricity cases, respectively).

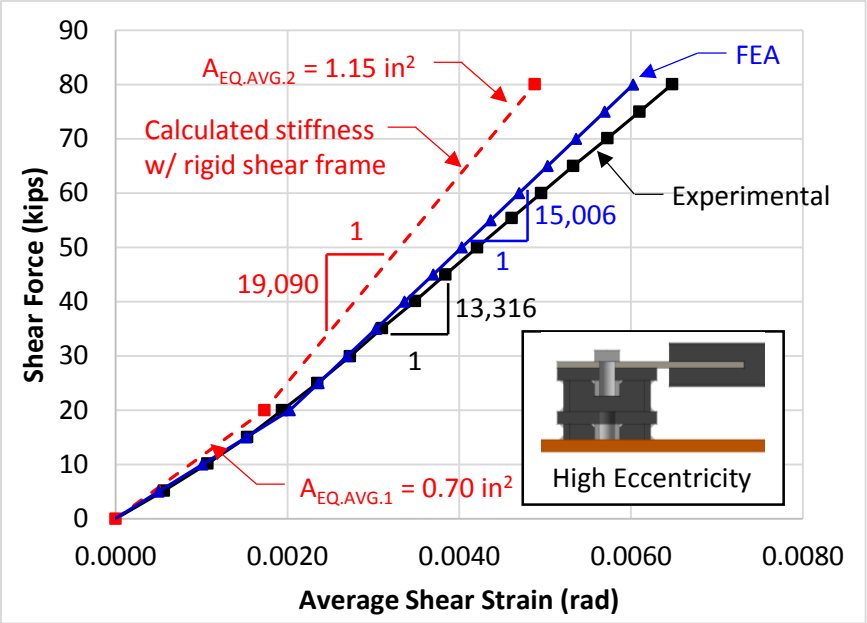

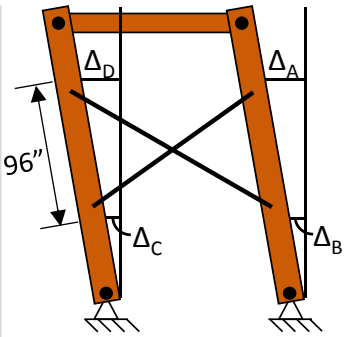

$\Upsilon_{AB} = \sin^{-1}((\Delta_A-\Delta_B)/96”)$
$\Upsilon_{DC} = \sin^{-1}((\Delta_D-\Delta_C)/96”)$
$\Upsilon_{AVG} = (\Upsilon_{AB} + \Upsilon_{DC})/2$

Note: Δ_A Δ_B Δ_C Δ_D were all measured with the L-pots at the top plate of the shear frame and at the same location in the FE model

Figure 8.11: Shear Strain vs. Shear Force – High Eccentricity

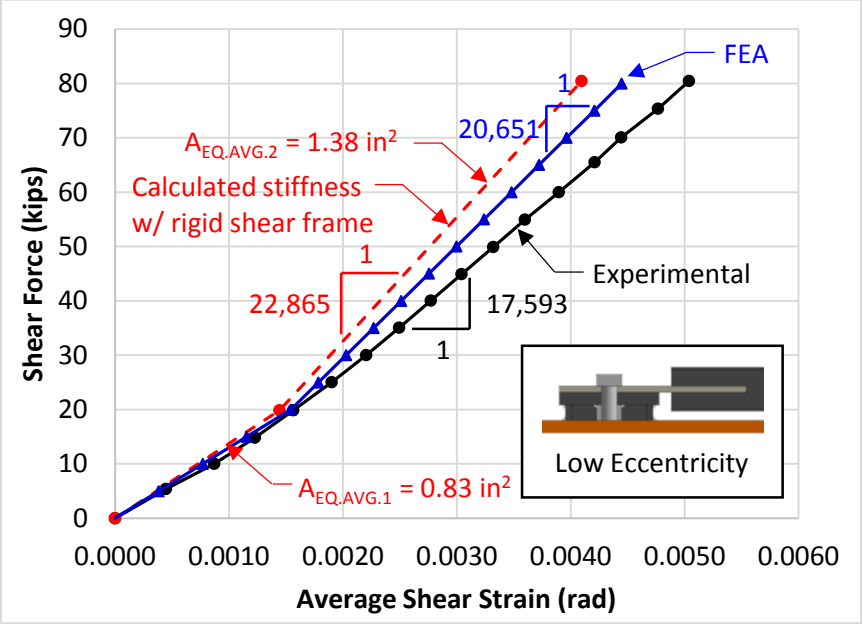

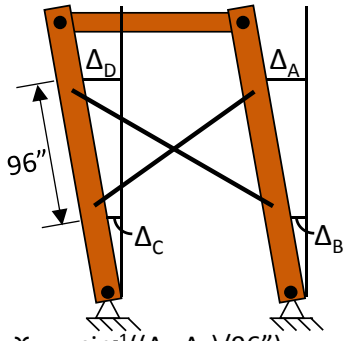

$\Upsilon_{AB} = \sin^{-1}((\Delta_A-\Delta_B)/96”)$
$\Upsilon_{DC} = \sin^{-1}((\Delta_D-\Delta_C)/96”)$
$\Upsilon_{AVG} = (\Upsilon_{AB} + \Upsilon_{DC})/2$

Note: Δ_A Δ_B Δ_C Δ_D were all measured with the L-pots at the top plate of the shear frame and at the same location in the FE model

Figure 8.12: Shear Strain vs. Shear Force – Low Eccentricity

8.3.3 Validating Correction Factors for PCP Shear Tests

To validate the 1.30 and 1.43 correction factors used to correct the experimental data for the PCP/connection system, the finite element model shown in Figure 8.9 was analyzed using the eight different stiffness for the corrected cross-frame areas from Table 8.1. The X-frame in the FE model was connected at the same elevation as the center of the PCP in the experiment so that the same torque would be applied to the loading beams. The results from the finite element models

were compared with the experimental tests data for the eight PCP shear tests in Chapter 4 shown in Figure 8.13 through Figure 8.16. For all eight cases, the stiffness of the FE models closely matched the stiffness of the PCP/connection system indicating that the correction factors were reasonable and likely a little low since the FE model overestimated the stiffness for the steel cross-frame tests above.

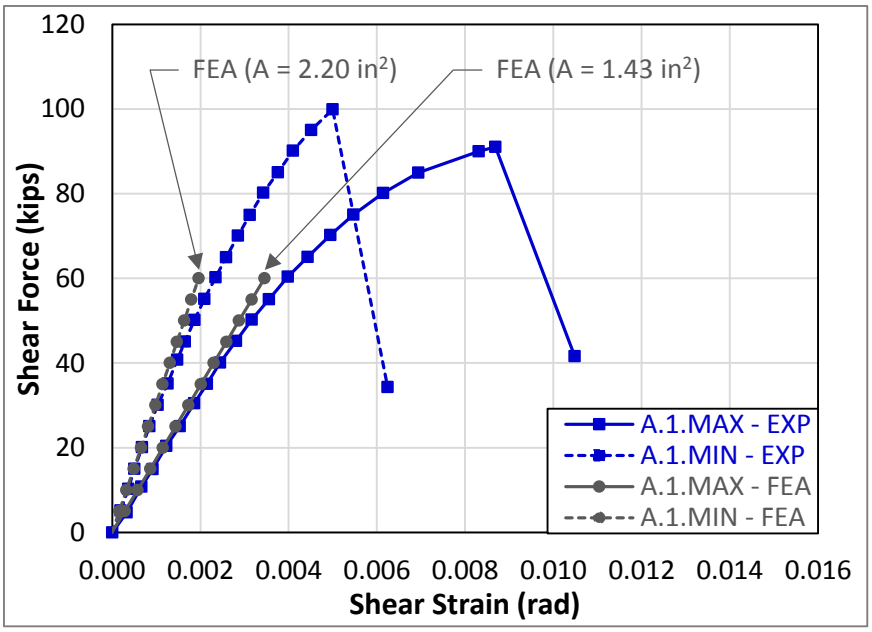

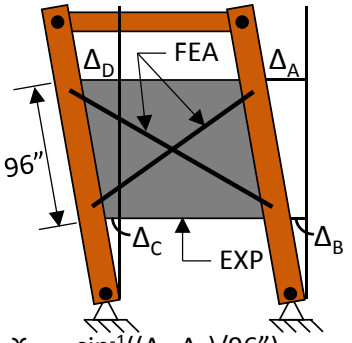

$\Upsilon_{AB} = \sin^{-1}((\Delta_A-\Delta_B)/96")$
$\Upsilon_{DC} = \sin^{-1}((\Delta_D-\Delta_C)/96")$
$\Upsilon_{AVG} = (\Upsilon_{AB} + \Upsilon_{DC})/2$

Note: Δ_A Δ_B Δ_C Δ_D were all measured with the L-pots at the top plate of the shear frame and at the same location in the FE model

Figure 8.13: Experimental Stiffness vs. Finite Element Model Stiffness – Detail A.1

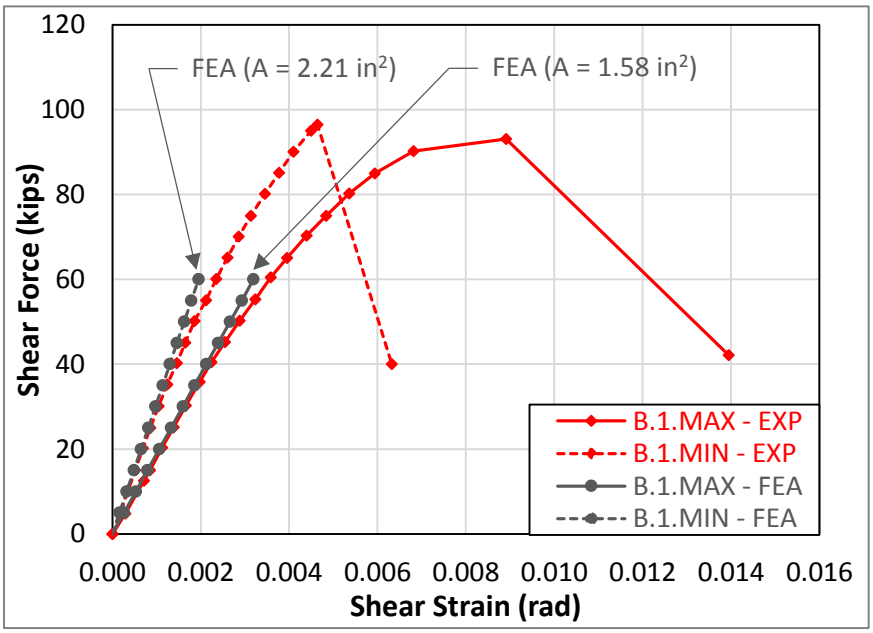

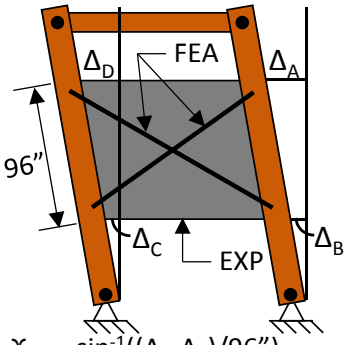

$\Upsilon_{AB} = \sin^{-1}((\Delta_A-\Delta_B)/96")$
$\Upsilon_{DC} = \sin^{-1}((\Delta_D-\Delta_C)/96")$
$\Upsilon_{AVG} = (\Upsilon_{AB} + \Upsilon_{DC})/2$

Note: Δ_A Δ_B Δ_C Δ_D were all measured with the L-pots at the top plate of the shear frame and at the same location in the FE model

Figure 8.14: Experimental Stiffness vs. Finite Element Model Stiffness – Detail B.1

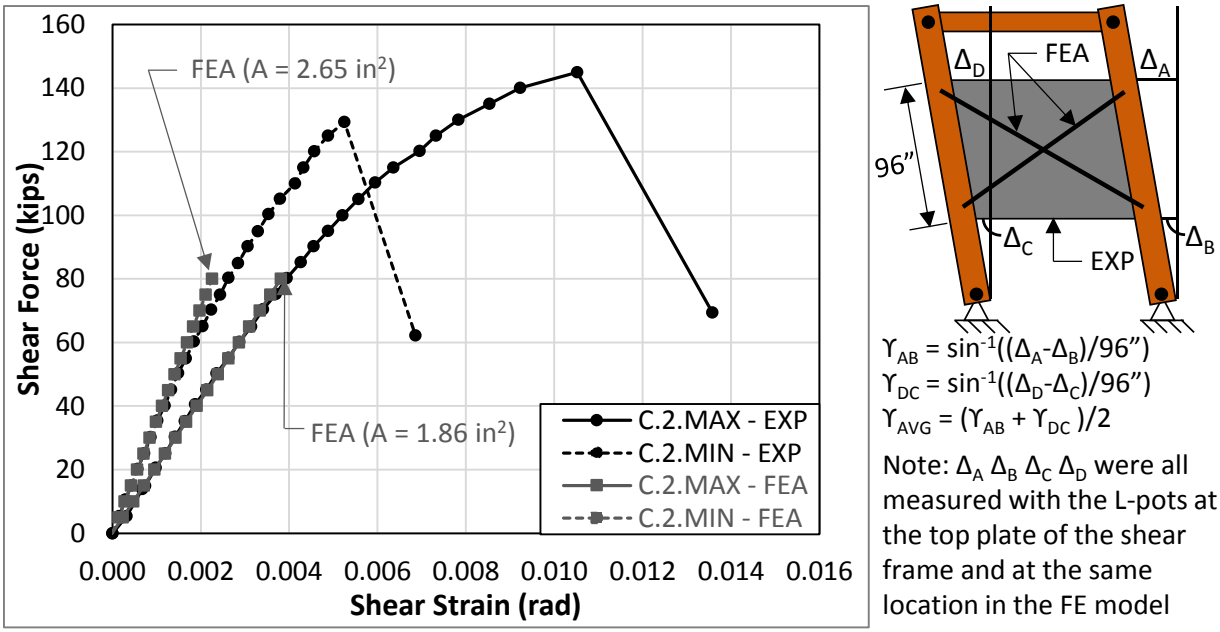

Figure 8.15: Experimental Stiffness vs. Finite Element Model Stiffness – Detail C.1

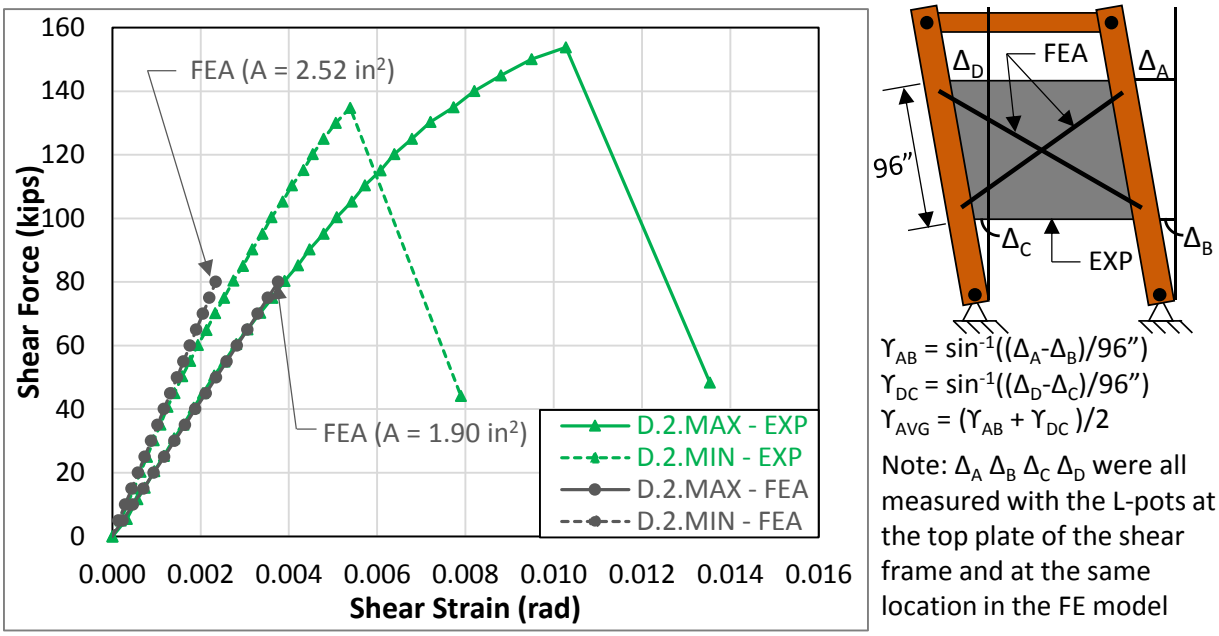

Figure 8.16: Experimental Stiffness vs. Finite Element Model Stiffness – Detail D.1

8.4 Conclusions

This section focused on the finite element modeling techniques that were used to develop the models of the PCP/connection system for the experimental shear tests that were conducted in Chapter 4. A simplified model using truss members was used to represent the in-plane stiffness of

the PCP/connection system similar to the model that was used by Helwig and Yura (2008a) to represent the in-plane stiffness of PMDFs and their connections.

- The in-plane stiffness of the 8′-0″ by 8′-3″ PCPs and their connection was accurately represented by a 6′-6″ by 8′-6″ wide X-frame (the dimensions of the X-frame were chosen to attach to the frame at the center of the outer WT connections for the PCPs). Using the elastic modulus of steel (E = 29,000 ksi), the area of the each X-frame member ranged from 1.43 in^2 to 2.65 in^2 for PCP details A.1.MAX and C.2.MIN, respectively.
- An equation was derived to calculate the stiffness of a PCP rigidly connected to the shear frame. The calculated stiffness of the PCP was more than an order of magnitude larger than the stiffness of the PCP/connection system from the experiments. Since the PCP and the connections function as springs in series, it was determined that the flexibility of the system was predominantly controlled by the flexibility of the connection. Therefore, changing the width of the PCPs (i.e. distance between adjacent girders) or the modulus of elasticity will not significantly influence the stiffness of the system as a whole.
- An equation was derived to represent the stiffness of the PCP connections. The equation accounted for deformation of the connection parallel and perpendicular to the girder span using springs in both directions. From the experimental shear tests, the stiffness of the connection springs was determined.
- A three dimension finite element model of the shear frame from Chapter 4 was created to further explore the flexibility of the frame during the shear tests. The FE model was validated with the experimental results from the steel cross-frame tests with high and low eccentricities. The results from the FE model slightly overestimated the stiffness of the system by factors of 1.13 to 1.17.
- In Chapter 4, the stiffness for the eight PCP/connection system experiments were increased to account for the flexibility of the shear frame by factors of 1.30 and 1.43 for the PCPs on the low (½″) and high (4″) bedding strips, respectively. To validate the correction factors, the finite element model using X-frames with the eight different corrected stiffness were compared to the experimental results from the eight PCP shear tests. The stiffness from the FE models closely matched the stiffness from the experimental tests, indicating that the correction factors were reasonable and likely a low since the FE model overestimated the stiffness of the steel cross-frame.

The simplified X-frame model for the PCP/connection system described in this chapter will be used to represent the in-plane stiffness of the panels in the FE models for the steel I-girder and steel tub girder systems. The FE models of the steel girder systems with the PCPs will be validated with the results from the experiments in Chapters 5 and 6.

Chapter 9. Parametric Finite Element Modeling of Steel I-Girder and Steel Tub Girder Systems

9.1 Introduction

This chapter describes the finite element (FE) modeling techniques and associated parametric studies for the steel twin I-girder system and the steel tub girder system with PCPs attached to the top flanges. One goal of this work is to validate the modeling techniques used for the laboratory systems to establish confidence in the finite element models. An additional goal of this work is to conduct parametric studies using the validated finite element modeling techniques to investigate the bracing potential of PCPs on a variety of curved girder systems that are more realistic than the systems tested in the laboratory. The three-dimensional finite element program Abaqus/CAE 6.14 was used for all finite element modeling in this chapter.

This chapter begins with a general discussion of the modeling and analysis techniques used to develop the FE models. The specific components of the FE models (e.g. girders, PCP, cross-frames, stiffeners, boundary conditions, etc.) are discussed in detail. Next, the analytical solutions are compared with the experimental results (additional validation results are found in Appendix D and Appendix E for the twin I-girder system and the tub girder system, respectively). Finally, the parametric study for the steel I-girder and steel tub girder system is explained in detail focusing on the effects of attaching PCPs to the top flanges of the systems.

9.2 Modeling and Analysis Techniques for FE Model Validation

A second-order elastic analysis (non-linear geometric analysis) was the primary analysis method used to validate the FE models with the experimental data. Since the vast majority of the laboratory tests were performed in the elastic rang of the I-girders and tub girder (as monitored by strain gauges at key location of the girders), an elastic analysis was deemed sufficient. Similarly, steel girders typically are designed to remain elastic during the construction phase so an elastic material model was considered sufficient for the parametric study. The FE model was required to capture second-order geometry effects as significant torsional loads were place on the straight girders (to represent a curved girder system) and to capture the second-order effects of the curved girders for the parametric study.

9.2.1 Modeling of Steel Girders

The steel I-girders and tub girders were modeled using S8R5 shell elements (8-node doubly curved thin shell, reduced integration, using five degrees of freedom per node) at the mid thickness of the various steel component (flanges, webs, web stiffeners, diaphragms etc.). As a curved element, the S8R5 is suitable for modeling curved geometries (which was required to accurately model the girders for the parametric studies) and the element can accurately model thin shells which is the case for the components of the steel girders.

The flanges, webs, stiffeners, and eccentric loading brackets of the I-girder were all created in the same part in the FE model while the flanges, webs, stiffeners, and diaphragms for the tub girder were all created in the same part in the FE model. After specifying the appropriate material properties for the steel ($E = 29{,}000$ ksi, $\nu = 0.30$, and $\rho = 490$ lb/ft^3) and thicknesses of the various components, the entire part was meshed and the element type was specified. This method was

advantageous as it does not require constraint equations to be specified between the various components of the girders modeled with shell elements.

Two different mesh densities were investigated for both the I-girder and tub girder systems. The coarse mesh density for the I-girder system consisted of 6 elements through the depth of the girder and 2 elements across the width of the flange while the fine mesh cut the element size in half (see Figure 9.1). Similarly, for the tub girder system the coarse mesh density consisted of 6 elements through the depth, 2 elements across the width of the top flanges, and 8 elements across the width of the bottom flange while the fine mesh density cut the element size in half (see Figure 9.2).

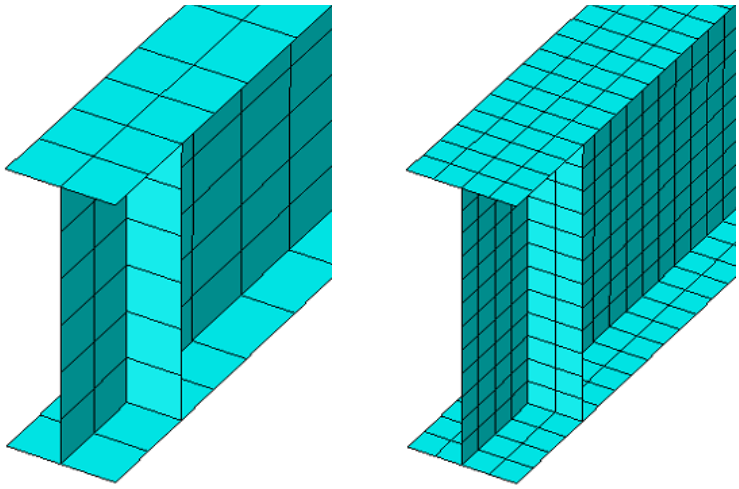

Figure 9.1 I-Girder Mesh Density

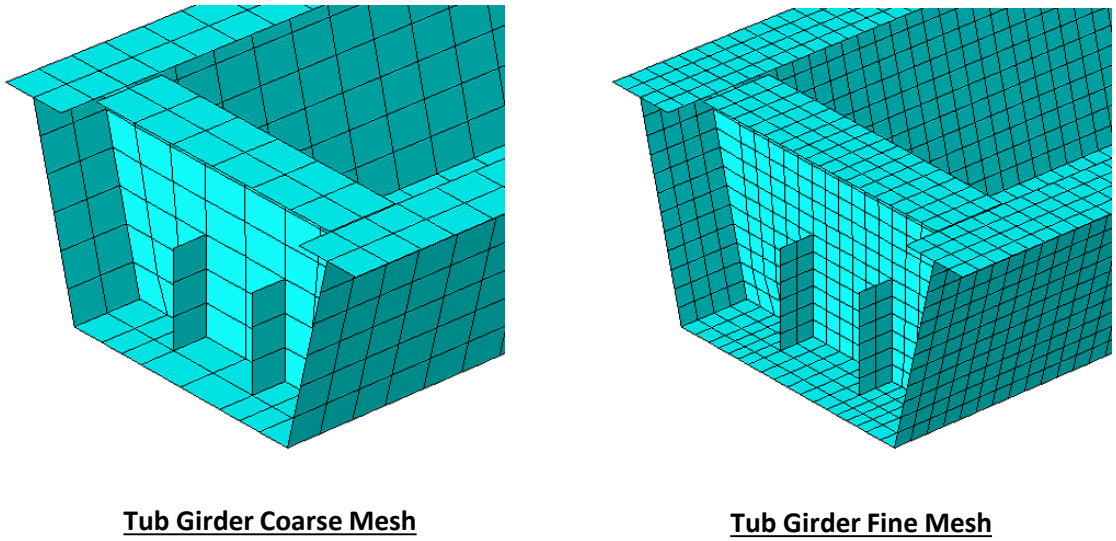

Figure 9.2 Tub Girder Mesh Density

The validation models were analyzed with both coarse and fine mesh densities for the I-girder and tub girder systems. There was no significant difference between the analytical results either in predicted displacements or stresses, indicating that the course mesh density was suitable to produce accurate results for both systems. Table 9.1 shows the average and worst aspect ratios of the shell elements used in the FE models.

Table 9.1 Mesh Aspect Ratios

Mesh Density	Average Aspect Ratio	Worst Aspect Ratio
I-Girder Coarse	1.31	1.55
I-Girder Fine	1.01	1.03
Tub Girder Coarse	1.22	2.12
Tub Girder Fine	1.09	2.14

9.2.2 Modeling of Bracing Components

The K-frames and struts in the steel tub girder FE models were modeled using B32 beam elements (a 3-node quadratic beam in space). The properties of the beam element were set equal to those of a 2″ diameter ASTM A53 grade B extra strong pipe. Since the gusset plates were welded at the centerline of the pipes, the connection eccentricity was small and so the stiffness reduction due to the connections was not accounted for in the model. The top flange diagonals (WT5x22.5) for the tub girders were modeled with S8R5 shell elements and a surface to surface constraint was used to tie the flange of the WT to the flanges of the tub girder. The midspan cross-frame for the twin I-girder system was modeled with both T3D2 truss elements (2-node linear 3-dimensional) and linear spring elements. Since the strains in the cross-frame were small, comparable results were obtained using both elements. The loading beams tied the lateral movement of the adjacent girders together (since the knife edge/ bearing assemblies did not move relative to the girders or the loading beams). The loading beams were modeled with T3D2 truss elements and linear spring elements tied between the locations of the load application on the top flanges girders (i.e. where the knife edges were located) with the results not being affected by the type of element used. Furthermore, the flange connectors for the lateral load tests on the I-girder system were modeled with T3D2 tension only truss elements (as the connectors were not capable of transferring load in compression). Figure 9.3 and Figure 9.4 show isometric views of the I-girder and tub girder models, respectively for the simply supported load conditions.

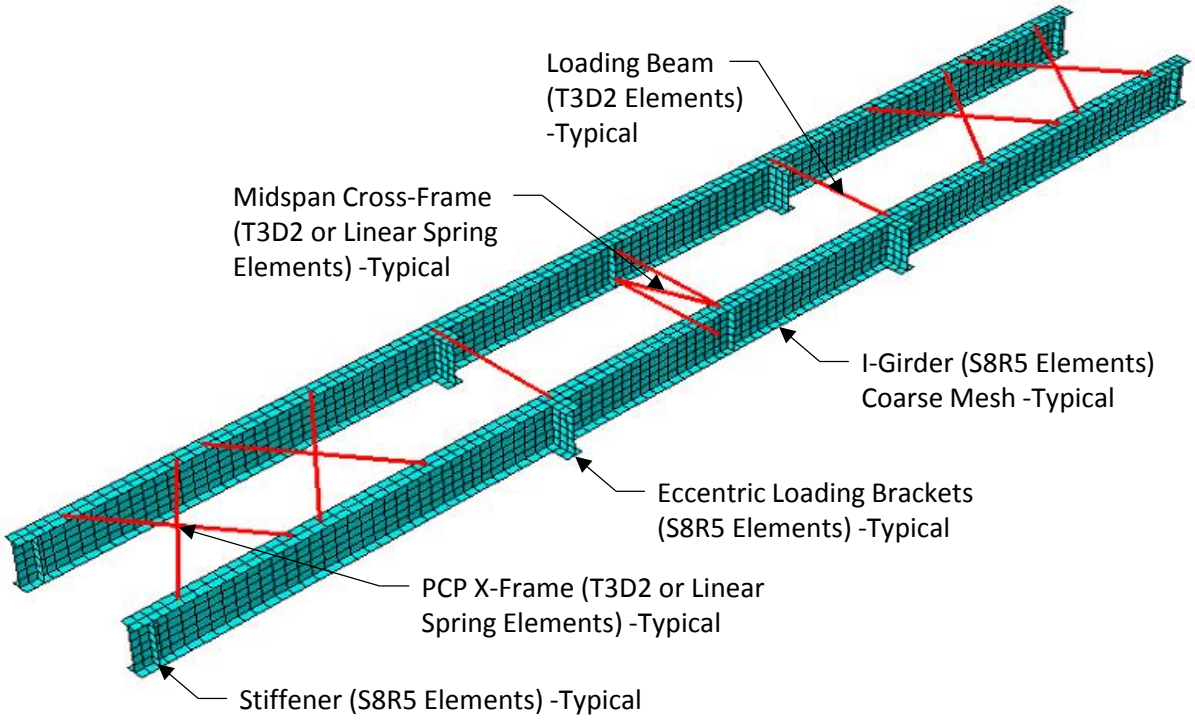

Figure 9.3 Finite Element Model of the Twin I-Girder System – Simply Supported

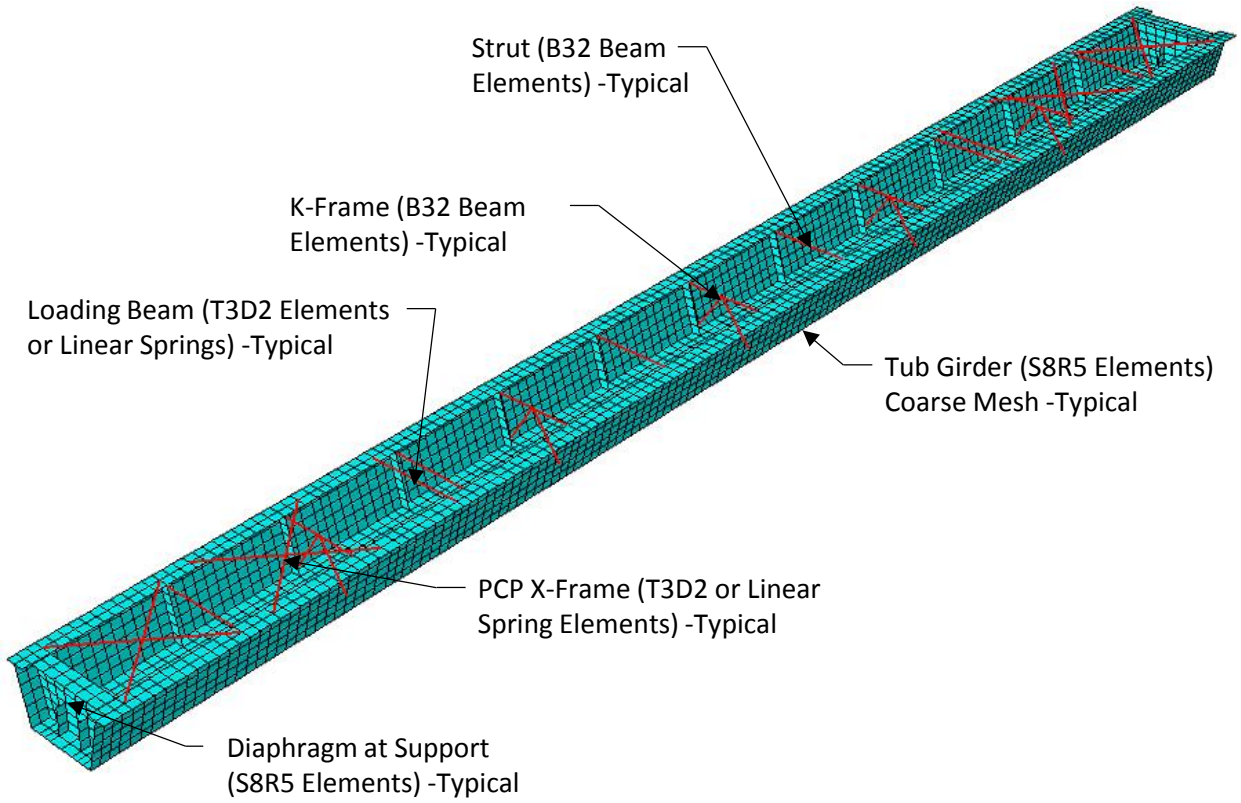

Figure 9.4 Finite Element Model of the Tub Girder System – Simply Supported

9.2.3 Modeling of PCPs

The simplified X-frame truss model discussed in Chapter 8 was used to represent the in-plane stiffness of the PCP/connection system in the FE model for the I-girder and tub girder systems. Connection detail A.1.MAX tested on the shear frame (see Chapter 4) was used to attach the PCPs to both the I-girder and tub girder experimental systems. The I-girders for the experimental setup were spaced at 104″ on center while the top flanges of the tub girder were spaced at 63″ on center (see Figure 9.5). The average elastic modulus (E) for the PCPs of the I-girder system and tub girder system was measured to be 5,075 ksi and 4,727 ksi, respectively.

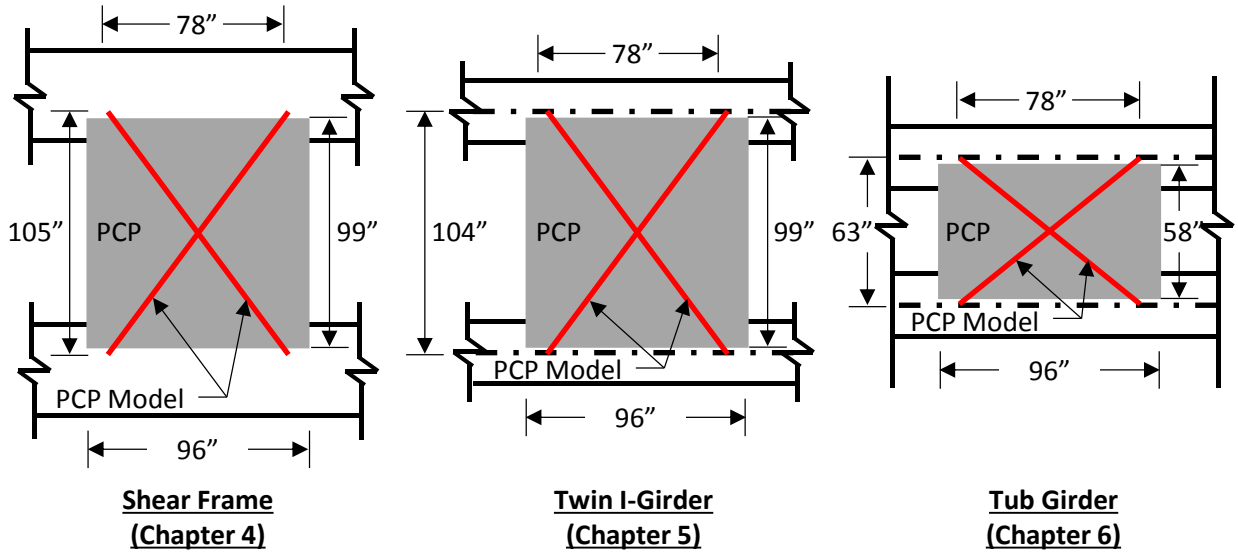

Figure 9.5 PCP Model on Various Systems

Table 9.2 shows the calculated stiffness of the PCPs (β_{PCP}), the stiffness of the connections (β_{con}), and the overall stiffness of the brace (β_b). From the brace stiffness, the area of the truss members (A_{truss}) were calculated (assuming E_s =29,000 ksi) and the axial stiffness of the members were determined ($k_{truss} = A_{truss} \cdot E_s / L_d$). For both girder systems, the X-frame members were connected to nodes at the intersection of the top flange and the web. Since the stiffness of the connection was already accounted for in the calculation of the X-frame members, connecting the X-frame at the elevation of the top flange was a reasonable assumption. Both T3D2 truss elements (2-node linear 3-dimensional) and linear spring elements were used to model the X-frame for the PCPs. Since the strains in the X-frame were small, similar results were obtained using both elements types.

Table 9.2 Area of Truss Panel Members for Equivalent Stiffness of PCPs

Test Setup	E of PCP* (ksi)	PCP Size (in)	β_{PCP} (kip·in/rad)	Model Size (in)	$k_{con} = k_x = k_y$ (kip/in)	β_{con} (kip·in/rad)	β_b (kip·in/rad)	A_{truss}† (in^2)	k_{truss} (kip/in)
Shear Frame	5020	99x96	28,369,503	105x78	661	1,296,445	1,239,789	1.43	316
Twin I-Girder	5075	99x96	28,680,325	104x78	661	1,287,598	1,232,275	1.42	316
Tub Girder	4727	58x96	19,752,169	63x78	661	794,302	763,595	1.10	318

*Measured †Calculated Using E=29,000 ksi

The stiffness of springs ($k_{con\_A.1.MAX}$) representing the connection was calculated as follows:

$$\left(\frac{V}{\gamma}\right)_{A.1.MAX} = 23{,}615\,\frac{kip}{rad}$$

$$\beta_{b\_A.1.MAX} = \frac{V}{\gamma}\cdot\frac{S}{2} = 23{,}615\,\frac{kip}{rad}\cdot\frac{105in}{2} = 1{,}239{,}789\,\frac{kip\cdot in}{rad}$$

$$\beta_{PCP\_A.1.MAX} = \frac{S_{pcp}^2 Et}{2\left[\left(\frac{S_{pcp}}{h_{pcp}}\right)^3 + 2.3\left(\frac{S_{pcp}}{h_{pcp}}\right)\right]} = \frac{(99in)^2\cdot 5020ksi\cdot 4in}{2\left[\left(\frac{99in}{96in}\right)^3 + 2.3\left(\frac{99in}{96in}\right)\right]} = 28{,}369{,}503\,\frac{kip\cdot in}{rad}$$

$$\frac{1}{\beta_{con\_A.1.MAX}} = \frac{1}{\beta_{b\_A.1.MAX}} - \frac{1}{\beta_{PCP_A.1.MAX}}$$

$$\frac{1}{\beta_{con\_A.1.MAX}} = \frac{1}{1{,}239{,}789\cdot kip\cdot in/rad} - \frac{1}{28{,}369{,}503\cdot kip\cdot in/rad}$$

$$\beta_{con_A.1.MAX} = 1{,}296{,}445\,\frac{kip\cdot in}{rad}$$

$$\beta_{con\_A.1.MAX} = \frac{k_{con\_A.1.MAX}}{2\left(\frac{1}{h_b^2}+\frac{1}{S^2}\right)} \rightarrow 1{,}296{,}445\,\frac{kip\cdot in}{rad} = \frac{k_{con\_A.1.MAX}}{2\left(\frac{1}{(78in)^2}+\frac{1}{(105in)^2}\right)}$$

$$\boxed{k_{con\_A.1.MAX} = 661\,\frac{kip}{in}}$$

The bracing stiffness (β_{b_tub}) of the PCP connection system on the tub girder was calculated as follows:

$$\beta_{PCP\_tub} = \frac{S_{pcp}^2 Et}{2\left[\left(\frac{S_{pcp}}{h_{pcp}}\right)^3 + 2.3\left(\frac{S_{pcp}}{h_{pcp}}\right)\right]} = \frac{(58in)^2\cdot 4727ksi\cdot 4in}{2\left[\left(\frac{58in}{96in}\right)^3 + 2.3\left(\frac{58in}{96in}\right)\right]} = 19{,}752{,}169\,\frac{kip\cdot in}{rad}$$

$$\beta_{con\_tub} = \frac{k_{con\_A.1.MAX}}{2\left(\frac{1}{h_{b\_tub}^2}+\frac{1}{S_{tub}^2}\right)} = \frac{661kip/in}{2\left(\frac{1}{(78in)^2}+\frac{1}{(63in)^2}\right)} = 794{,}302\,\frac{kip\cdot in}{rad}$$

$$\frac{1}{\beta_{b\_tub}} = \frac{1}{\beta_{con\_tub}} + \frac{1}{\beta_{PCP\_tub}} = \frac{1}{794{,}302\cdot kip\cdot in/rad} + \frac{1}{19{,}752{,}169\cdot kip\cdot in/rad}$$

$$\boxed{\beta_{b\_tub} = 763{,}595\,\frac{kip \cdot in}{rad}}$$

The truss member stiffness (k_{truss_tub}) for the diagonals of the simplified X-frame truss model of the PCPs/connection system on the tub girder was calculated as follows:

$$A_{truss\_tub} = \frac{\beta_{b\_tub} L_d^3}{ES^2 h_b^2} = \frac{(763{,}595kip \cdot in/rad)(100.3in)^3}{(29{,}000ksi)(63in)^2(78in)^2} = 1.10in^2$$

$$k_{truss\_tub} = \frac{EA_{truss\_tub}}{L_d} = \frac{(29{,}000ksi)(1.10in^2)}{100.3in}$$

$$\boxed{k_{truss\_tub} = 318\,\frac{kip}{in}}$$

Using the method above, the stiffness of the truss members in Table 9.2 have been calibrated to accurately represent the in-plane bracing stiffness of the PCP/connection system. The torsional loads on the FE models of the girder systems will cause one diagonal of the brace to be loaded in tension (positive value) and the other diagonal of the brace to be loaded in compression (negative value) as shown in Figure 9.6. The shear force on the PCP (V_{PCP}) can be calculated as follows:

$$V_{PCP} = (T - C)\frac{h_b}{L_d} \tag{9.1}$$

where,
T = tension in brace from FE model
C = compression in braced from FE model
h_b = height of brace
L_d = length of diagonal

Note that the simplified X-frame model for the PCPs may not accurately represent the stiffness of the PCP/connection system to resist loads induced from bending moments on the girders (i.e. where the PCPs act somewhat compositely with the girders). Therefore, forces in the PCPs from girder bending cannot be accurately captured with this simplified model.

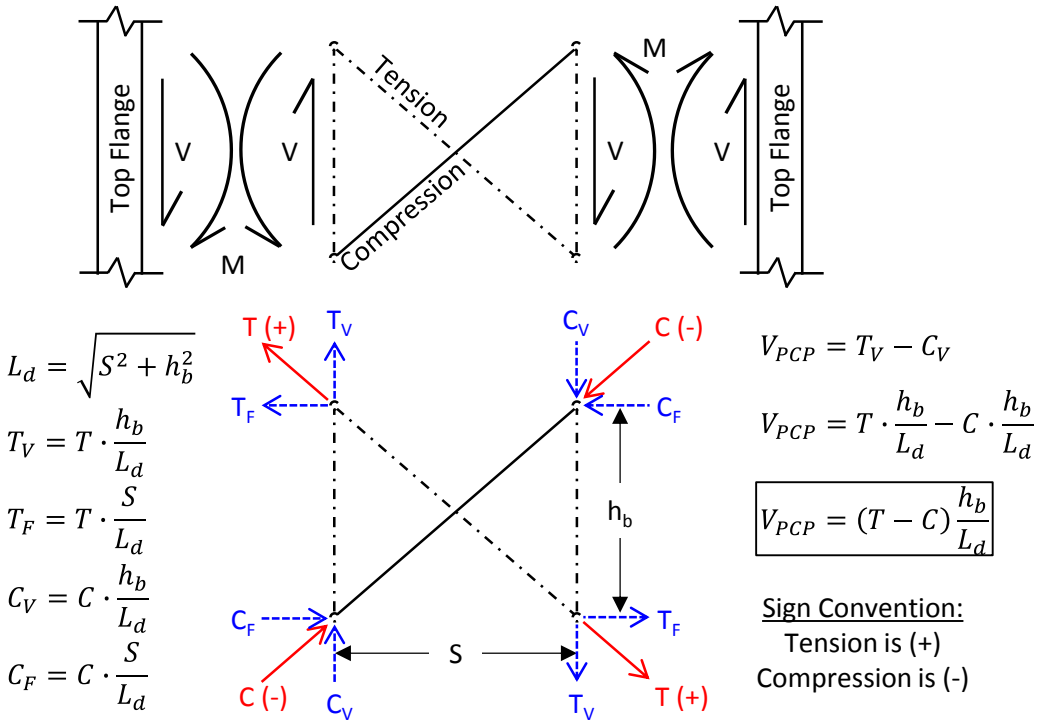

Figure 9.6 PCP Shear Force Calculated from Diagonal Forces

9.2.4 Load Application

The density of the steel (ρ = 490 lb/ft^3) was included as one of the material properties for the S8R5 shell elements, the B32 beam elements, and the T3D2 truss elements in the FE model (excluding the elements used to represent the PCPs). A gravitational acceleration was used to apply the self-weight for the elements in the model. The self-weight of each PCP was applied using four point loads on the top flange at the location where the X-frames representing the PCPs connect to the girders (assuming ρ = 150 lb/ft^3 for concrete). In the first analysis step, the entire self-weight of the system was applied in Abaqus. The subsequent step was used to apply the load from either lateral load frames or the gravity load simulators. The same load increments were used as in the experimental tests to achieve a direct comparison between the output from the FEA and the measurements from the experimental data.

9.2.5 Initial Imperfections

The initial imperfection of the I-girder and tub girders were measured as described in Chapters 5 and 6, respectively. The following procedure was used to include the imperfections into the FE model.

1. Create a FE model of the girder system.
2. Make a copy of the FE model and rename it "Imperfection Model."
3. In the Imperfection Model, apply the lateral displacements measured in the laboratory to the top and bottom flanges at the appropriate location along the girder's length. Run analysis to generate the initial imperfection geometry (neglecting the effects of the self-weigh of the system).

4. Make a copy of the FE model and rename it "Large Displacement Model."
5. Import the deformed geometry with an initial reduction factor of 0.90 from the Imperfection Model into the Large Displacement Model (using the *Imperfection command in Abaqus). The deformed geometry was imported in a load step prior to the load step for the self-weight. Run the analysis to generate the deformed shape with the effects of self-weight included.
6. Compare the deformed shape from Step 5 with the lateral displacements measured in the laboratory. If the results are satisfactory, proceed to Step 7. If not, adjusted the reduction factor accordingly and repeat Step 5.
7. Add a load step to the Large Displacement Model after the step for the self-weight and apply the load from the gravity load simulators. Run the analysis to generate the response of the system with the initial imperfections included.

The initial imperfections were only included when the girders were concentrically loaded by the gravity load simulators. Several cases were investigated with and without the initial imperfections for the eccentrically loaded girders. The large load eccentricity drove the response of the girders, rendering the girders imperfections negligible.

9.2.6 Boundary Conditions

To accurately model the laboratory experiments with a finite element model, the effects of boundary conditions had to be considered. For both the I-girder and tub girder systems, some warping restraint was provided at the supports, which was difficult to both measure and quantify. The support rods that prevent twisting of the I-girders (see Figure 9.7) were expected to provide some warping restraint to the top and bottom flanges. Likewise, the bearing pads in the tub girder system (see Figure 9.8) provided some warping restraint to the bottom flange of the tub. This section describes how the boundary conditions were applied in the FE models of both systems to account for warping restraint at the supports.

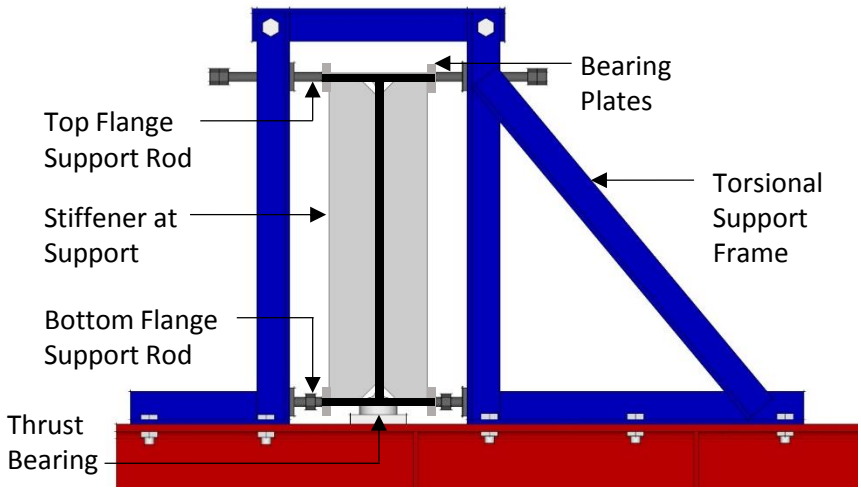

Figure 9.7 I-Girder Experimental Boundary Conditions (Chapter 5)

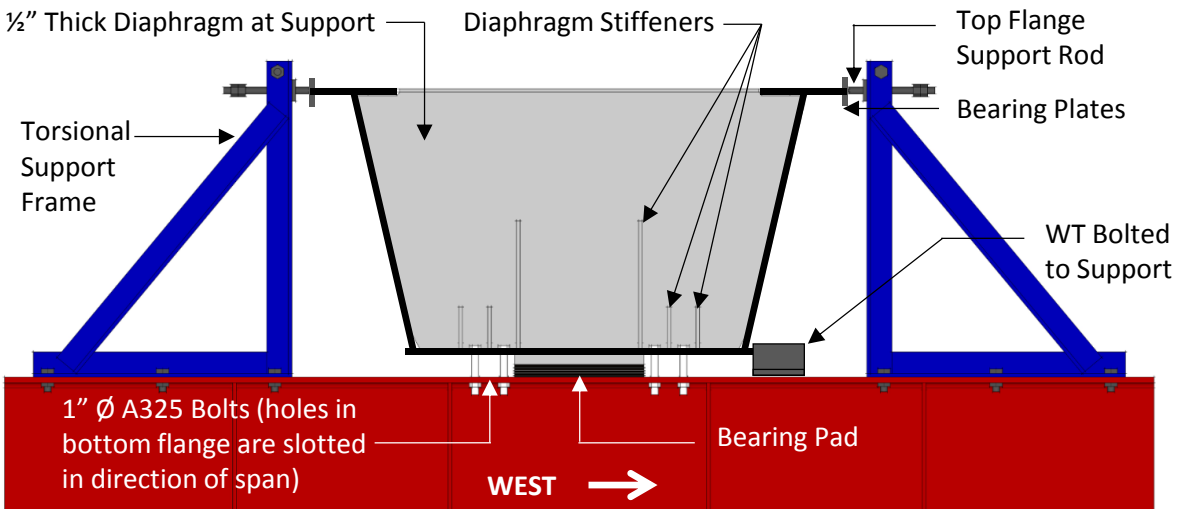

Figure 9.8 Tub Girder Experimental Boundary Conditions (Chapter 6)

I-Girder Analytical Validation

Prior to comparing the results from the FE models with the experimental data, the FE model for the I-girders were validated with an analytical solution. The elastic buckling strength of a doubly-symmetric I-girder section, modified to account for the moment gradient (AISC 2010), is given as follows:

$$M_{cr} = C_b \frac{\pi}{L_b} \sqrt{EI_y GJ + \left(\frac{\pi E}{L_b}\right)^2 I_y C_w} \tag{9.2}$$

where,
C_b = moment gradient and load height factor
L_b = unbraced length
E = elastic modulus
I_y = weak axis moment of inertia
J = torsional constant
G = shear modulus
C_w = warping constant

A W36×135 (the same section used for the experimental tests) was used to compare the FE model with the analytical solution for the case of mid-height uniform loading (C_b = 1.12). The standard pin-roller boundary conditions shown in Figure 9.9 were used in the FE model and an eigenvalue buckling analysis was performed. Table 9.3 shows the comparison of the analytical solution with the results from the FE models. The results closely matched (within 1%) with and without the inclusion of the fillets at the web-flange junction. In the FE model, the fillets were accounted for using B32 beam elements with a specified torsional constant (J = 0.275 in^4) tied to the shells of the I-girder at the intersection of the web and the top and bottom flanges. For a W36x135, the torsional constant J = 7.00 in^4 according to AISC 2010 while the calculated value for the plates without fillets is J = 6.45 in^4. Including the effects of the fillets changed the results of the FE model solutions by less than 5%. For accuracy, the fillets were included in the validation

of the FE models with the experimental results. In addition to a buckling analysis, the girder was independently loaded at midspan at the center of the web in the vertical and lateral directions, and a small-displacement analysis was performed. The vertical and lateral midspan deflections from the FE model were within 2% of the analytical solution ($\Delta = PL^3/48EI$).

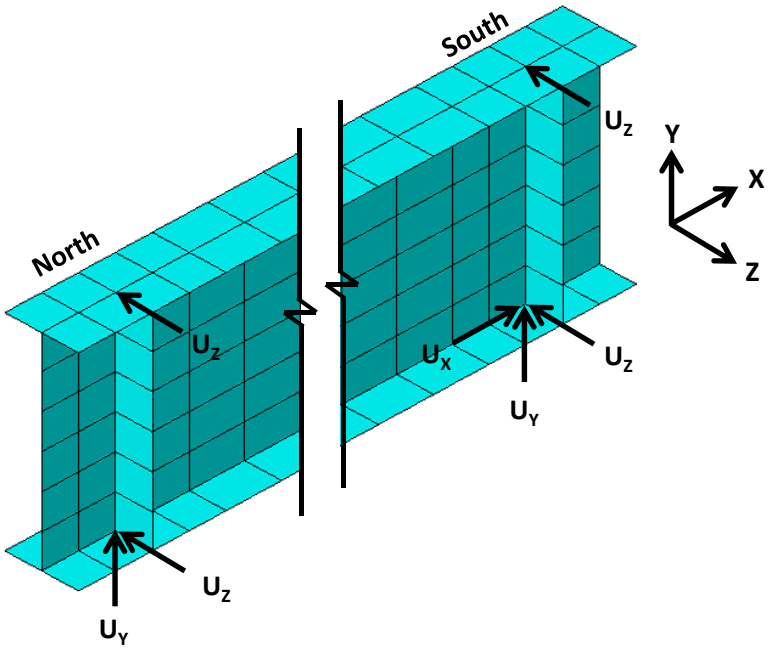

Figure 9.9 I-Girder FE Model Boundary Conditions

Table 9.3 FE Model Validation with Analytical Solution

Section Properties	$M_{cr(analytic)}$	$M_{cr(FEM)}$	$M_{cr(FEM)}/M_{cr(analytic)}$
Without Fillets	3287	3347	1.018
With Fillets	3387	3446	1.017

I-Girder Boundary Conditions

After validating the FE model of the I-girder with the analytical solution, the FEA results were compared with the experimental results for the case where the girders were loaded laterally at quarter points along the top flange with no intermediate brace (test LAT.7 in Chapter 5). This case was chosen for comparison because the largest lateral load is placed on the most flexible system, which maximizes the influence of warping restraint at the flanges. Figure 9.10 shows a comparison of the experimental results with the FEA results using the simple boundary conditions (B.C.) shown in Figure 9.9. To add warping stiffness to the ends of the girders, the thickness of the stiffeners at the supports were simply increased (to a value of 4″) until the adjusted twist from the FE model (in blue) matched the twist from the experimental results (in black) – similar results can be achieved by using springs at the support to increase the warping restraint. This support condition lies between the lower and upper bound of warping free and warping fixed boundary conditions.

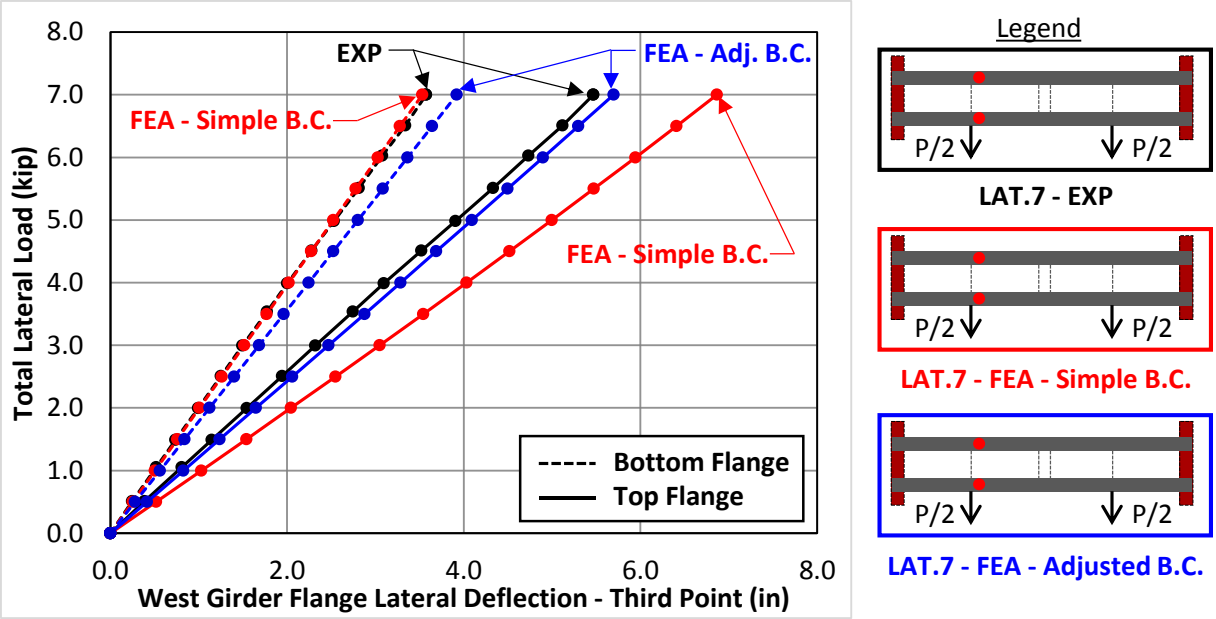

Figure 9.10 Lateral Deflection vs. Lateral Load (w/o XF) – FE Model vs. EXP

To validate that the appropriate stiffness was added at the supports in the FE model to account for the boundary conditions in the laboratory, the experimental data for the GLS tests without PCPs was compared with the FE models with the adjusted boundary conditions. Figure 9.11 and Figure 9.12 show comparisons of the girder's twist and top flange lateral deflection, respectively for the experimental (EXP) and FE model results for the following I-girder cases: GLS.1, GLS.4, and GLS.9. The results from the FE model closely match the experimental results, indicating that the adjustment to the boundary conditions from the lateral tests was reasonable as it produced good results for entirely different loading scenarios. These results are limited to the comparisons in this particular study and may not apply in general; further research would be helpful to better understand the behavior at the boundary conditions for the I-girder system.

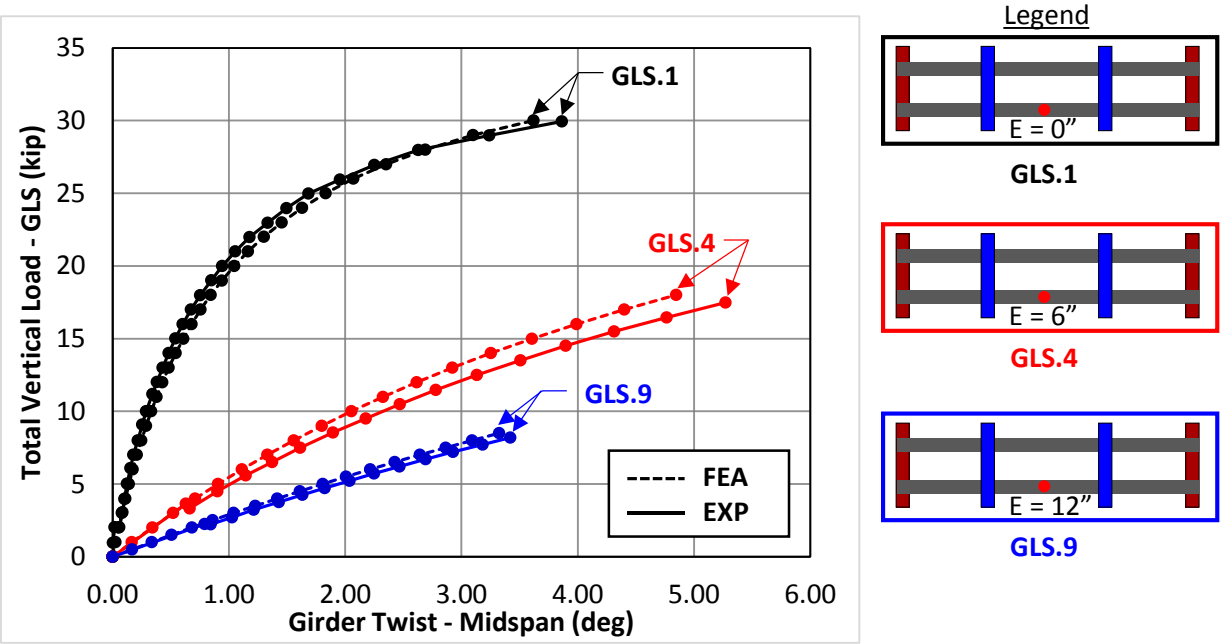

Figure 9.11 Twist @ Midspan vs. GLS Load (SS - w/o XF) – FE Model vs EXP

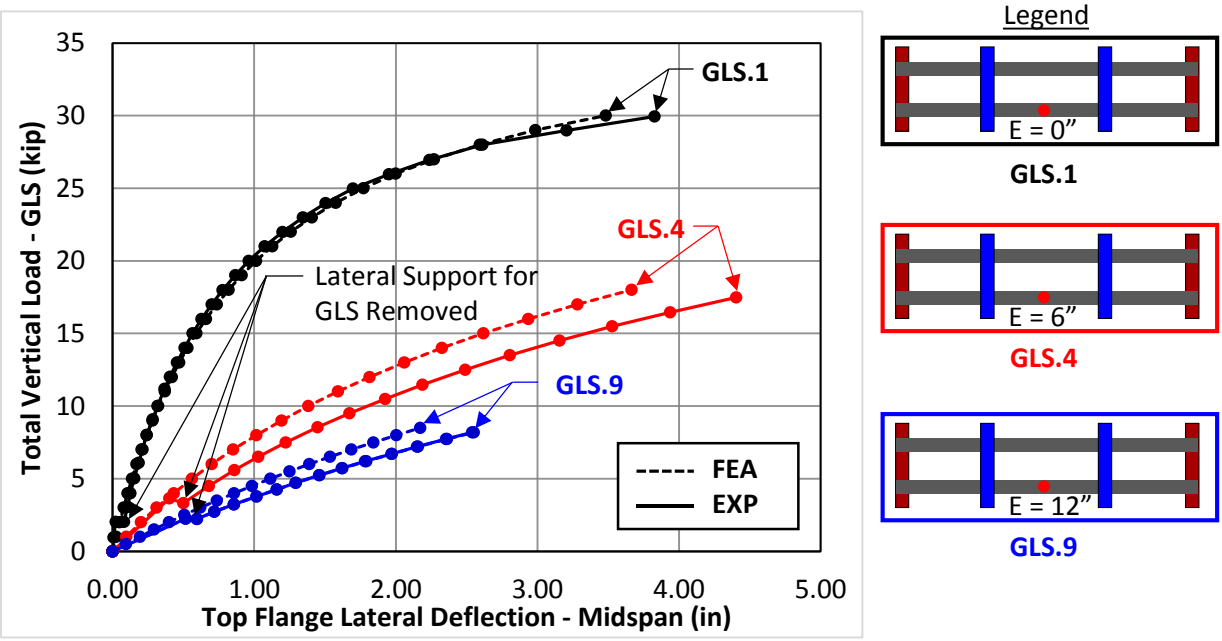

Figure 9.12 Lateral Deflection @ Midspan vs. GLS Load (SS - w/o XF) – FE Model vs EXP

Tub Girder Boundary Conditions

Figure 9.13 shows the boundary conditions used for the tub girder in the finite element model. The liner springs (K_X) at the supports were used to account for the warping restraint on the girder bottom flange provided by the bearing pad. The two springs at each support were tied to

one another in the X-direction (and not tied to the ground in the model) to provide warping restraint without providing support to facilitate catenary action from vertical bending of the girder.

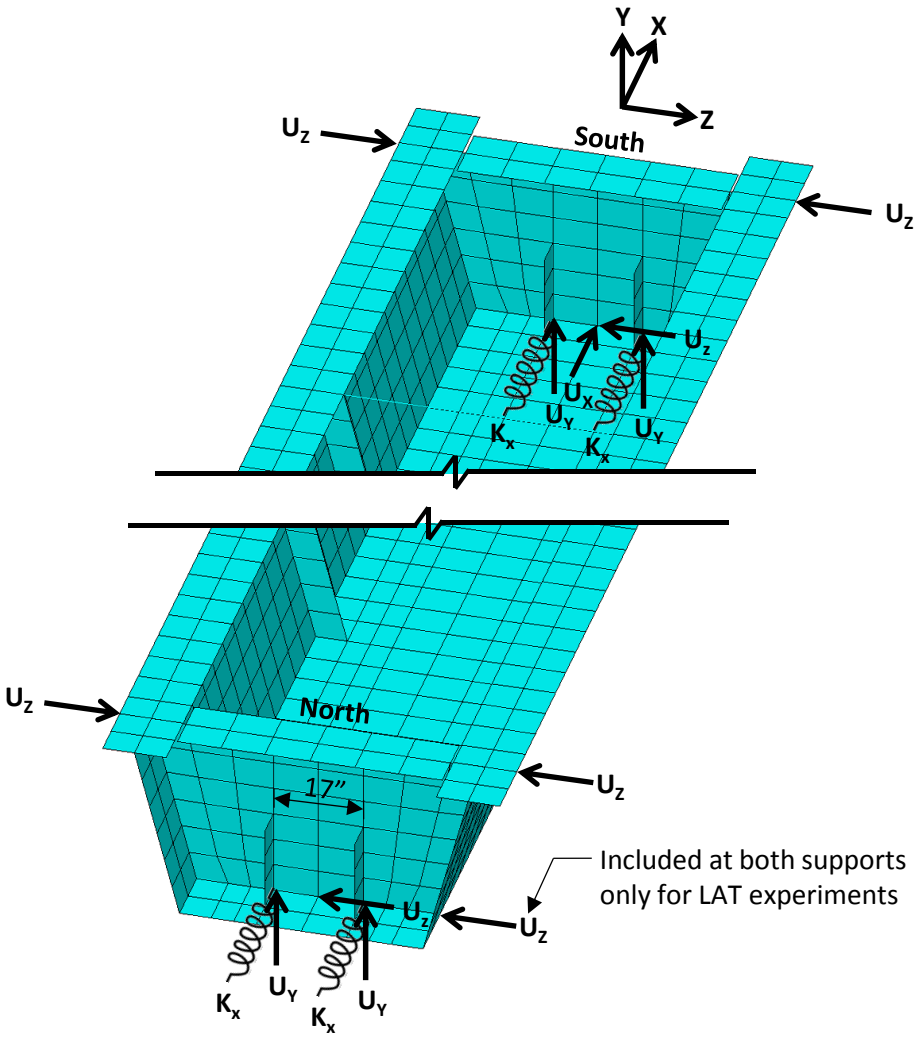

Figure 9.13 Tub Girder FE Model Boundary Conditions

The stiffness of the springs were increased (to a value of K_X = 4000 kip/in) until the girder twist in the FEA matched the experimental results (for LAT.1). Figure 9.14 shows the lateral deflection of the top and bottom flanges of the tub for the experimental results and the FE model with and without the warping restraint for the bottom flange. This support condition lies between the lower and upper bounds of warping free and warping fixed boundary conditions.

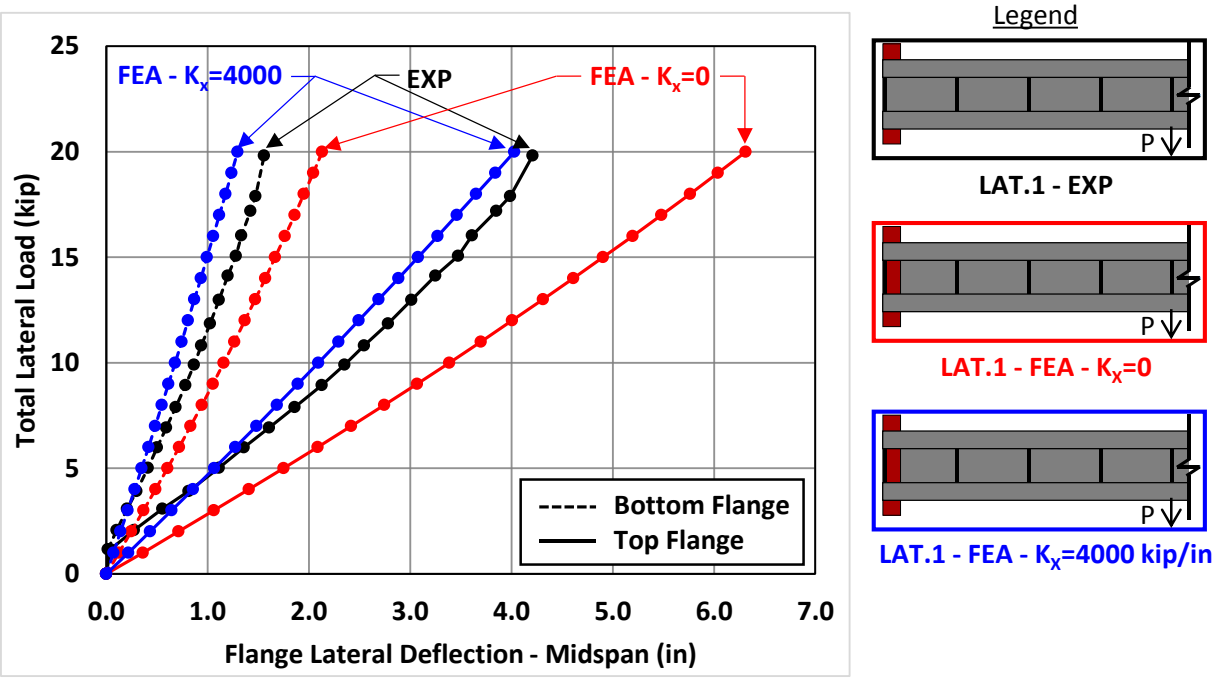

Figure 9.14 Twist @ Midspan vs. Lateral Load @ Third Point – EXP vs. FE Model

To validate that the appropriate stiffness was added at the supports in the FE model to account for the warping restraint associated with the boundary conditions in the laboratory, the experimental data for the GLS tests without PCPs or DIAGs was compared with the FE analyses with the adjusted boundary conditions. Figure 9.15 and Figure 9.16 show comparisons of the girder's twist and top flange lateral deflection, respectively, for the experimental and FE model results for the following tub girder cases: GLS.1, GLS.6, and GLS.11. The results from the FEA closely match the experimental results, indicating that the adjustment to the boundary conditions from the lateral tests were reasonable as they produced good results for entirely different loading scenarios. These results are limited to the comparisons in this particular study and may not apply in general; further research would be helpful to better understand the behavior at the boundary conditions for the tub girder system.

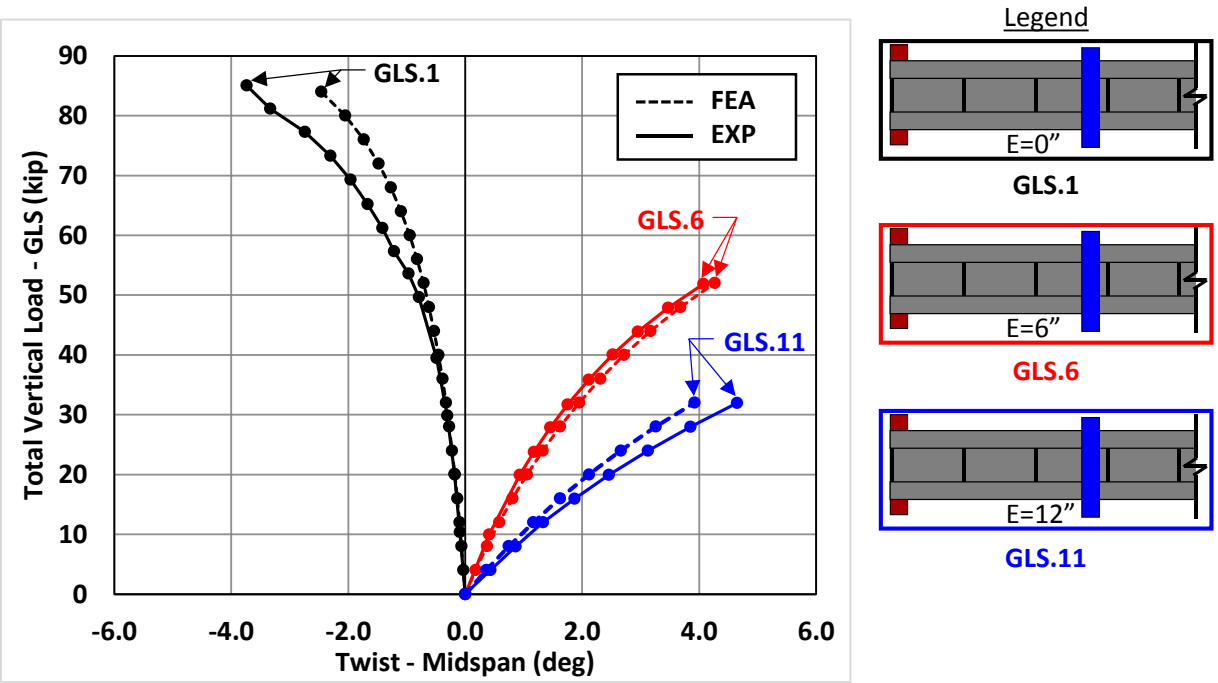

Figure 9.15 Twist @ Midspan vs. GLS Load – FE Model vs. EXP

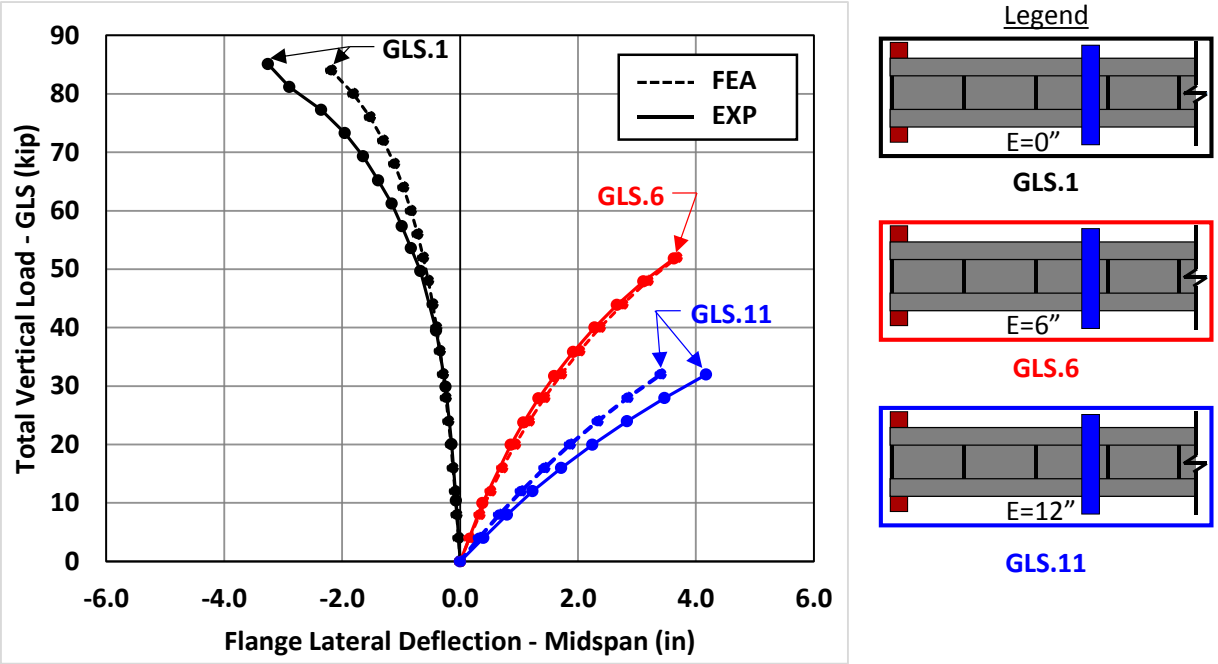

Figure 9.16 Lateral Deflection @ Midspan vs. GLS Load – FE Model vs. EXP

9.3 Steel I-Girder FE Model Validation

The FE model for the I-girder system described above was validated with the 12 lateral load tests and 27 gravity load tests that were performed at the Ferguson Structural Engineering Laboratory. Appendix D contains graphs comparing the FE model with laboratory test data for all 39 tests. The FEA results for the east and west girders were similar for most cases and therefore only the results for the west girder are reported for the majority of the tests.

9.3.1 I-Girder Lateral Load FE Model Validation

Table 9.4 shows a summary of the 12 lateral load experimental tests that were performed on the I-girder system which were used to validate the FE model. Figure 9.17 and Figure 9.18 show a comparison between the FE model and the experimental results for the girder twist and top flange lateral deflection, respectively for three cases. Graphs for the other 9 cases are shown in Appendix D. In general, the FE model accurately represented the top flange lateral deflection of the girder. The model had a tendency to underestimate the twist of the girder for the cases when the PCPs were attached to the top flange of the girder. This was expected since the simplified X-frame truss model for the PCPs does not provide the twisting restraint to the girders that was observed in the laboratory (see Chapter 5).

Table 9.4 Summary of Lateral I-Girder Test

Test Name	Load Location	Cross Frame	Number of PCPS
LAT.1	MS	-	0
LAT.2	MS	-	2
LAT.3	MS	-	4
LAT.4	MS	XF	0
LAT.5	MS	XF	2
LAT.6	MS	XF	4
LAT.7	QP	-	0
LAT.8	QP	-	2
LAT.9	QP	-	4
LAT.10	QP	XF	0
LAT.11	QP	XF	2
LAT.12	QP	XF	4

Key: LAT = Top Flange Lateral Load XF = Cross-Frame
MS = Midspan Load, QP = Quarter Point Load

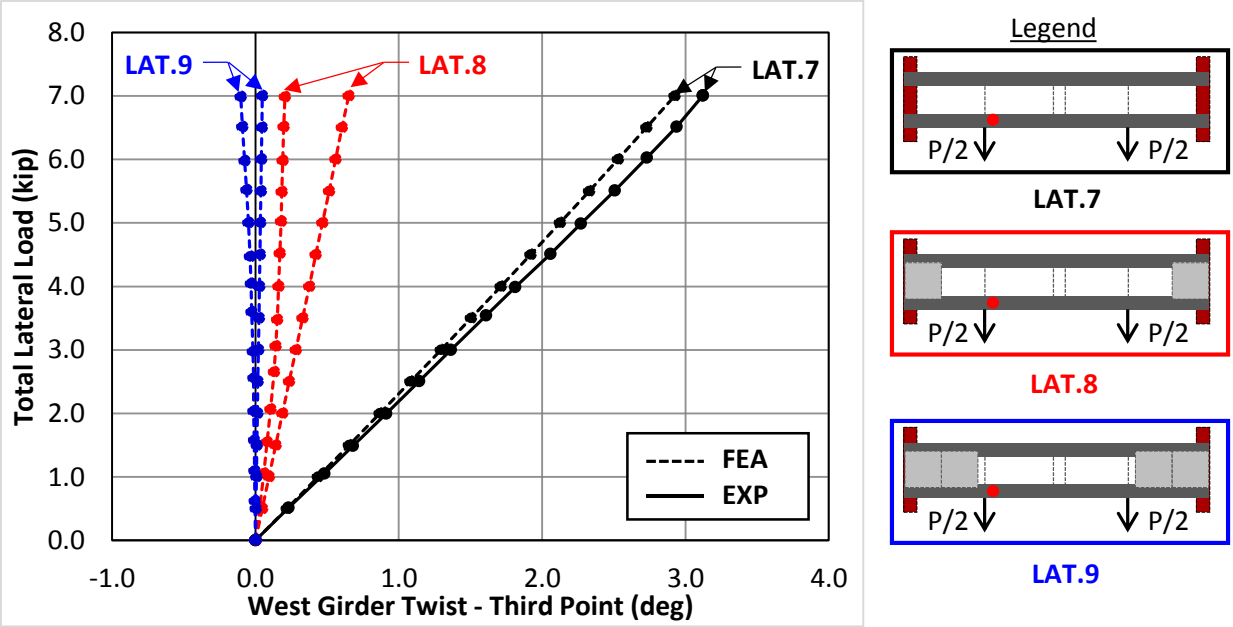

Figure 9.17 Twist @ Third Point vs. Lateral Load @ Quarter Points (w/o XF) - West

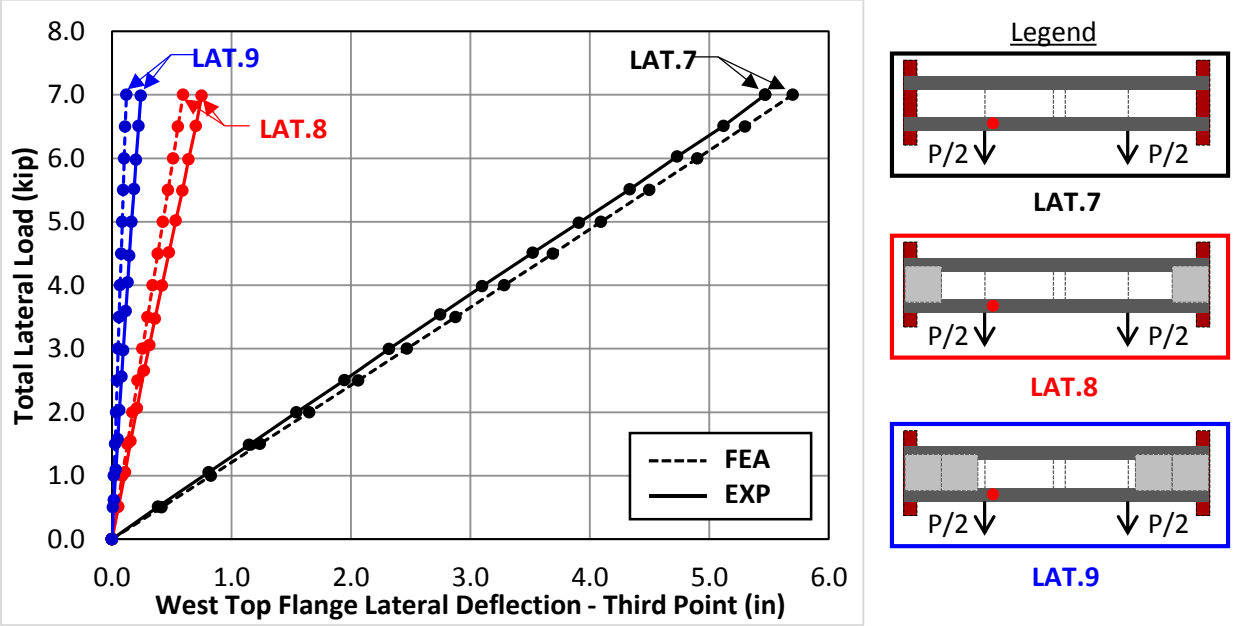

Figure 9.18 Lateral Deflection @ Third Point vs. Lateral Load @ Quarter Points (w/o XF) - West

9.3.2 I-Girder Combined Bending and Torsion Simply Supported FE Model Validation

Table 9.5 shows a summary of the 22 gravity load experimental tests that were performed on the simply supported I-girder system all of which were used to validate the FE model. Figure 9.19 and Figure 9.20 show a comparison between the FE model and the experimental results for the twist of the east and west girder, respectively for five different cases while Figure 9.21 shows

the top flange lateral deflection for the west girder. Graphs for the other 17 cases are shown in Appendix D. The FE model was the most accurate when the number of PCPs matched the number of bottom flange trusses (i.e. for GLS.8) and was more flexible torsionally when fewer bottom flange trusses were used than PCPs (i.e. for GLS.6). For GLS.8, a pseudo box-section was formed at the ends of the girders and the twisting restraint of the PCPs was engaged to a lesser degree since the lateral deflection of the bottom flanges are restrained by the bottom flange truss. Since the simplified X-frame truss model for the PCPs does not provide the twisting restraint to the girders, the model proves to be quite accurate for GLS.8. For GLS.6 the twisting restraint of the PCPs are engaged to the highest degree out of the 5 cases (with the PCP providing more restraint to the west girder than the east girder) which likely explains the discrepancy between the FEA and the experimental results.

Table 9.5 Summary of Bending and Torsion Simply Supported I-Girder Test

Test Name	Support Condition	Load Eccentricity	Cross Frame	Bottom Truss	Number of PCPS	Max Total GLS Load
GLS.1	SS	0 & 0	-	-	0	30
GLS.2	SS	0 & 0	-	-	2	100
GLS.3	SS	0 & 0	-	-	4	150
GLS.4	SS	6" & 6"	-	-	0	19
GLS.5	SS	6" & 6"	-	-	2	60
GLS.6	SS	6" & 6"	-	-	4	90
GLS.7	SS	6" & 6"	-	2 BF	4	80
GLS.8	SS	6" & 6"	-	4 BF	4	100
GLS.9	SS	12" & 12"	-	-	0	10
GLS.10	SS	12" & 12"	-	-	2	38
GLS.11	SS	12" & 12"	-	-	4	40
GLS.12	SS	12" & 12"	-	2 BF	4	75
GLS.13	SS	12" & 12"	-	4 BF	4	80
GLS.14	SS	0 & 0	XF	-	0	140
GLS.15	SS	0 & 0	XF	-	2	180
GLS.16	SS	0 & 0	XF	-	4	180
GLS.17	SS	6" & 6"	XF	-	0	90
GLS.18	SS	6" & 6"	XF	-	2	110
GLS.19	SS	6" & 6"	XF	-	4	120
GLS.20	SS	12" & 12"	XF	-	0	60
GLS.21	SS	12" & 12"	XF	-	2	70
GLS.22	SS	12" & 12"	XF	-	4	90

Key: GLS = Gravity Load Simulator Load, SS = Simply Supported
BF = Bottom Flange Truss, XF = Cross-Frame

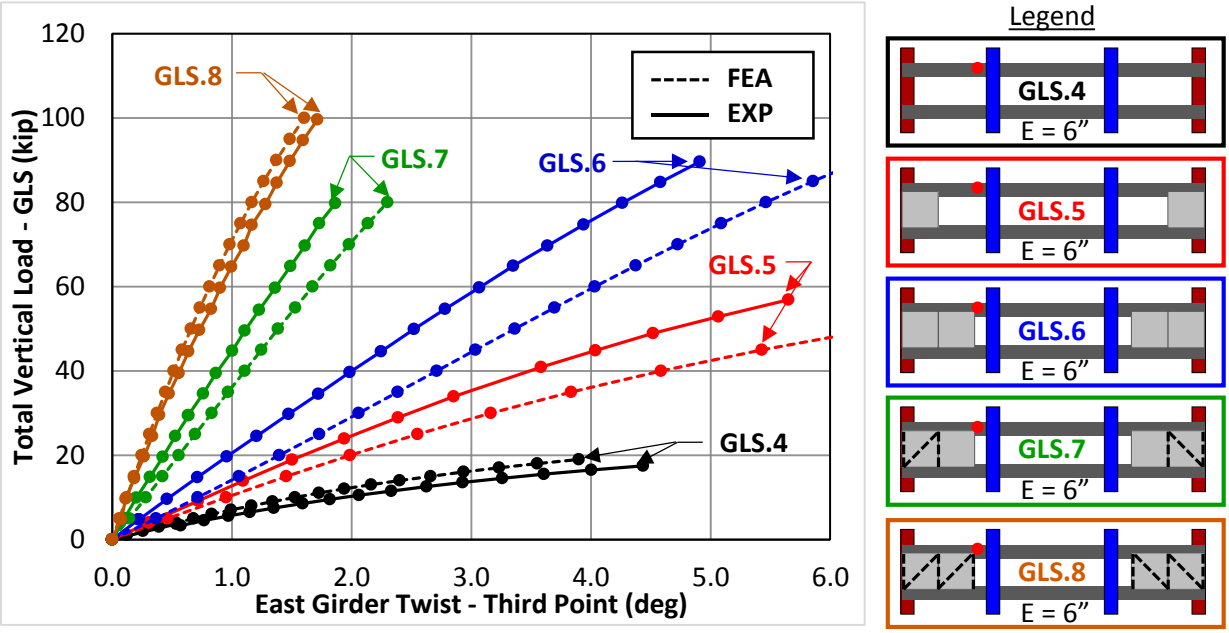

Figure 9.19 Twist @ Third Point vs. GLS Load (E=6" - SS - w/o XF) - East

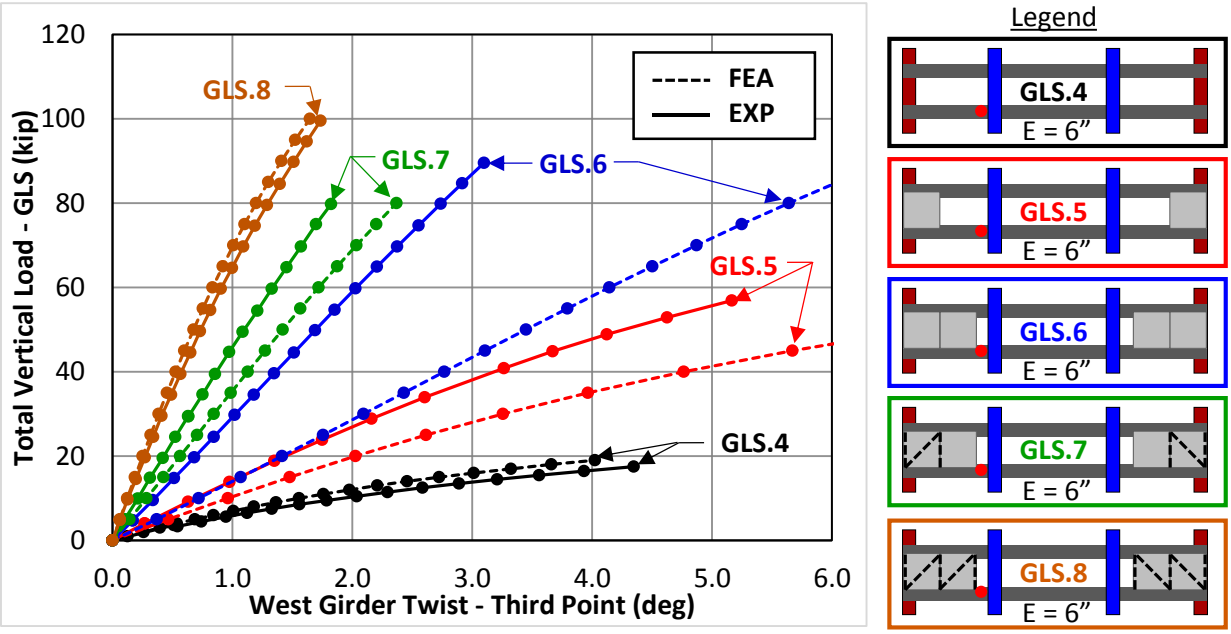

Figure 9.20 Twist @ Third Point vs. GLS Load (E=6" - SS - w/o XF) - West

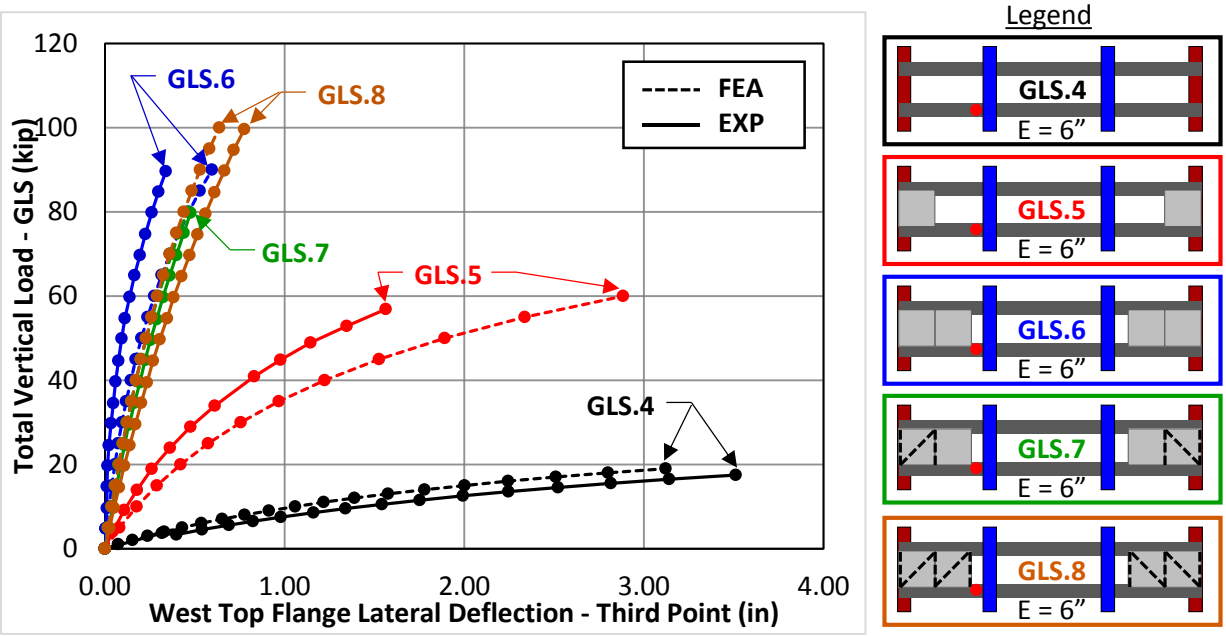

Figure 9.21 Lateral Deflection @ Third Point vs. GLS Load (E=6" - SS - w/o XF) - West

9.3.3 I-Girder Combined Bending and Torsion Overhanging FE Model Validation

Table 9.6 shows a summary of the five gravity load experimental tests that were performed on the overhanging I-girder system each of which was used to validate the FE model. Figure 9.22 and Figure 9.23 show a comparison between the FE model and the experimental results for the girder twist and top flange lateral deflection, respectively for two cases. Graphs for the other three cases are shown in Appendix D. For GLS.23 and GLS.24 the FE model reasonably represented the twist of the girders at the backspan and the overhang (with the FE model being slightly more flexible) while the top flange lateral deflection is somewhat underestimated by the FE model at the back span for both cases.

Table 9.6 Summary of Bending and Torsion Overhang I-Girder Tests

Test Name	Support Condition	GLS North Eccentricity	GLS North Eccentricity	Number of PCPS	Max Total GLS Load
GLS.23	OH	-2"	4"	4	140
GLS.24	OH	-4"	8"	4	100
GLS.25	OH	2"	4"	4	170
GLS.26	OH	4"	8"	4	120
GLS.27	OH	-4"	0"	4	300

Key: GLS = Gravity Load Simulator Load, OH = Overhang

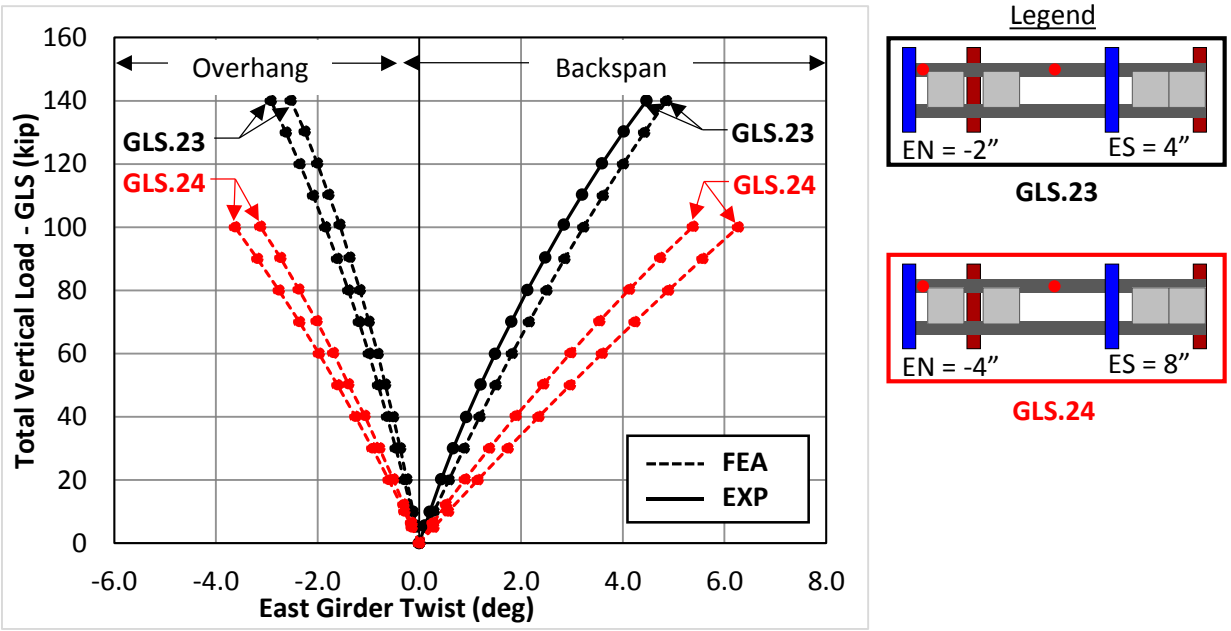

Figure 9.22 Twist @ Overhang and Backspan vs. GLS Load (Opposite Eccentricity) - East

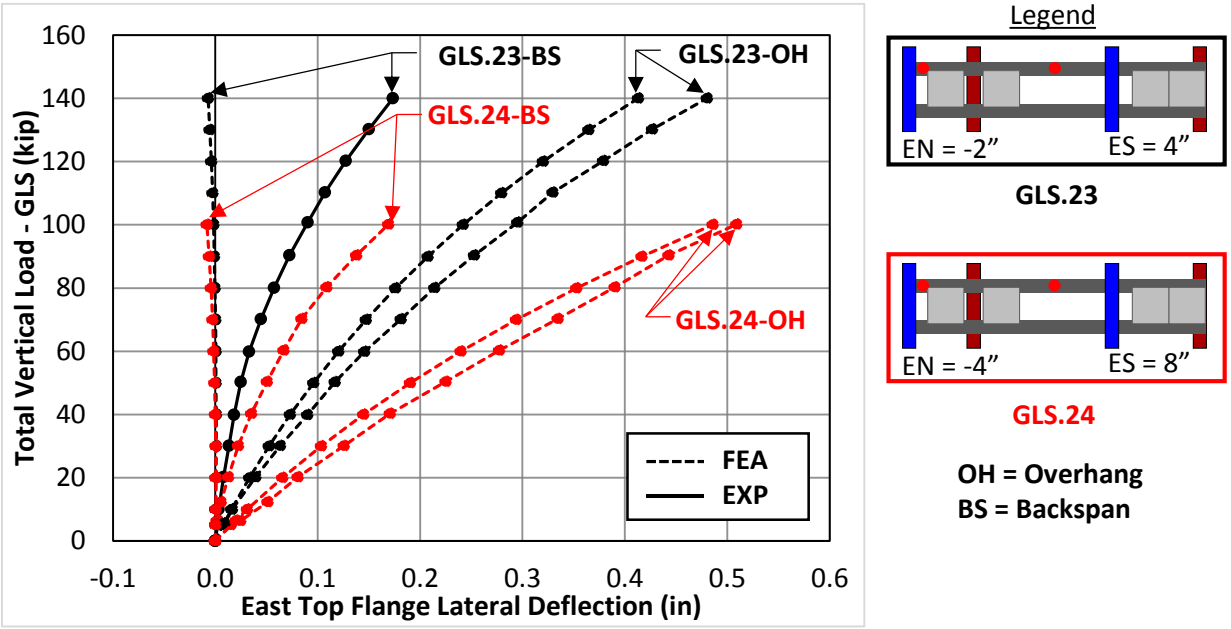

Figure 9.23 Lateral Deflection @ Overhang and Backspan vs. GLS Load (Opposite Eccentricity) - East

9.4 Steel Tub Girder FE Model Validation

The FE model for the tub girder system described above was validated with the 5 lateral load tests and 24 gravity load tests that were performed at the Ferguson Structural Engineering

Laboratory. Appendix E contains graphs comparing the FE model with laboratory test data for all 29 tests.

9.4.1 Tub Girder Lateral Load FE Model Validation

Table 9.7 shows a summary of the five lateral load experimental tests that were performed on the tub girder system all of which were used to validate the FE model. Figure 9.24 and Figure 9.25 show a comparison between the FE model and the experimental results for the girder twist and top flange lateral deflection, respectively for three cases. Graphs for the other two cases (where WT diagonals are used as bracing elements instead of PCPs) are shown in Appendix E. In general, the results from the FEM model and experimental test closely matched each other for both twist and top flange lateral deflection.

Table 9.7 Summary of Lateral Tub Girder Tests

Test Name	Load Loacation	K-Frame Location	Number of Braces
LAT.1	TP	2-Panel	0
LAT.2	TP	2-Panel	2 PCP
LAT.3	TP	2-Panel	4 PCP
LAT.4	TP	2-Panel	2 DIAG
LAT.5	TP	2-Panel	4 DIAG

Key: LAT = Top & Bottom Flange Lateral Load
TP = Third Point Loading, DIA = Diagonal

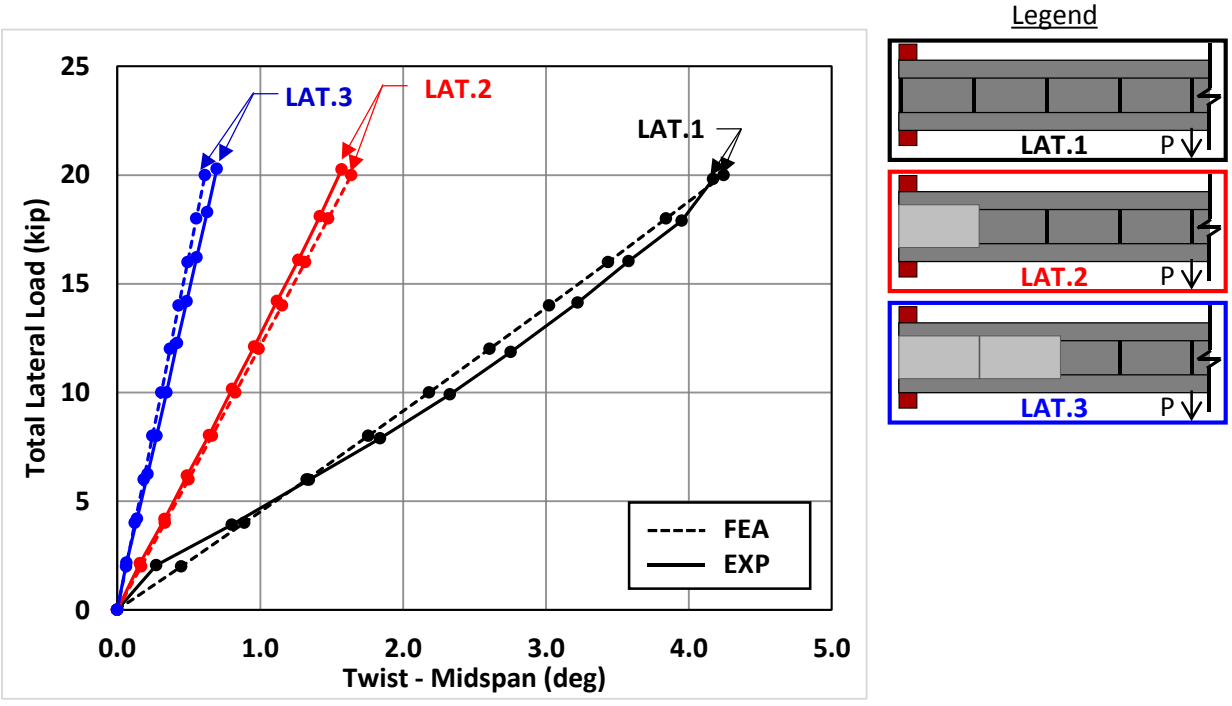

Figure 9.24 Twist @ Midspan vs. Lateral Load @ Third Point - PCP

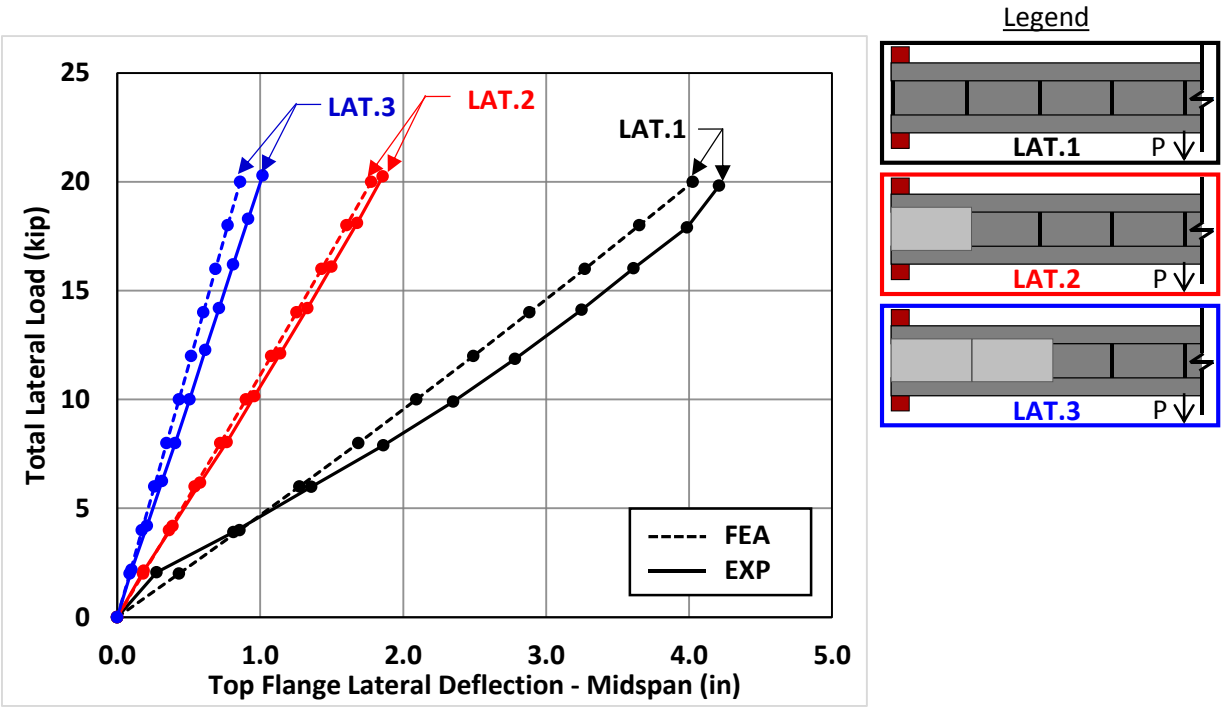

Figure 9.25 Lateral Deflection @ Midspan vs. Lateral Load @ Third Point - PCP

9.4.2 Tub Girder Combined Bending and Torsion Simply Supported FE Model Validation

Table 9.8 shows a summary of the 15 gravity load experimental tests that were performed on the simply supported tub girder system all of which were used to validate the FE model. Figure 9.26 and Figure 9.27 show a comparison between the FE model and the experimental results for the girder twist and top flange lateral deflection, respectively for three cases. Graphs for the other 12 cases are shown in Appendix E. In general, the results from the FE model and experimental test closely matched each other for both twist and top flange lateral deflection. Also, the FE model was not significantly more accurate when modeling the cases with the WT diagonals versus modeling the cases with the simplified X-frame truss model for the PCPs. Figure 9.28 and Figure 9.29 show a comparison between the FE model and the experimental results for the girder twist and top flange lateral deflection when the WT diagonals were used as bracing elements instead of PCPs.

Table 9.8 Summary of Bending and Torsion Simply Supported Tub Girder Tests

Test Name	Support Condition	Load Eccentricity	K-Frame Location	Number of Braces	Max Total GLS Load
GLS.1	SS	0 & 0	2-Panel	0	84
GLS.2	SS	0 & 0	2-Panel	2 PCP	100
GLS.3	SS	0 & 0	2-Panel	4 PCP	100
GLS.4	SS	0 & 0	2-Panel	2 DIAG	72
GLS.5	SS	0 & 0	2-Panel	4 DIAG	76
GLS.6	SS	8" & 8"	2-Panel	0	52
GLS.7	SS	8" & 8"	2-Panel	2 PCP	100
GLS.8	SS	8" & 8"	2-Panel	4 PCP	100
GLS.9	SS	8" & 8"	2-Panel	2 DIAG	80
GLS.10	SS	8" & 8"	2-Panel	4 DIAG	84
GLS.11	SS	16" & 16"	2-Panel	0	32
GLS.12	SS	16" & 16"	2-Panel	2 PCP	60
GLS.13	SS	16" & 16"	2-Panel	4 PCP	100
GLS.14	SS	16" & 16"	2-Panel	2 DAIG	52
GLS.15	SS	16" & 16"	2-Panel	4 DIAG	80

Key: GLS = Gravity Load Simulator Load, SS = Simply Supported
PCP = Partial Depth Precast Concrete Deck Panel, DIA = Diagonal

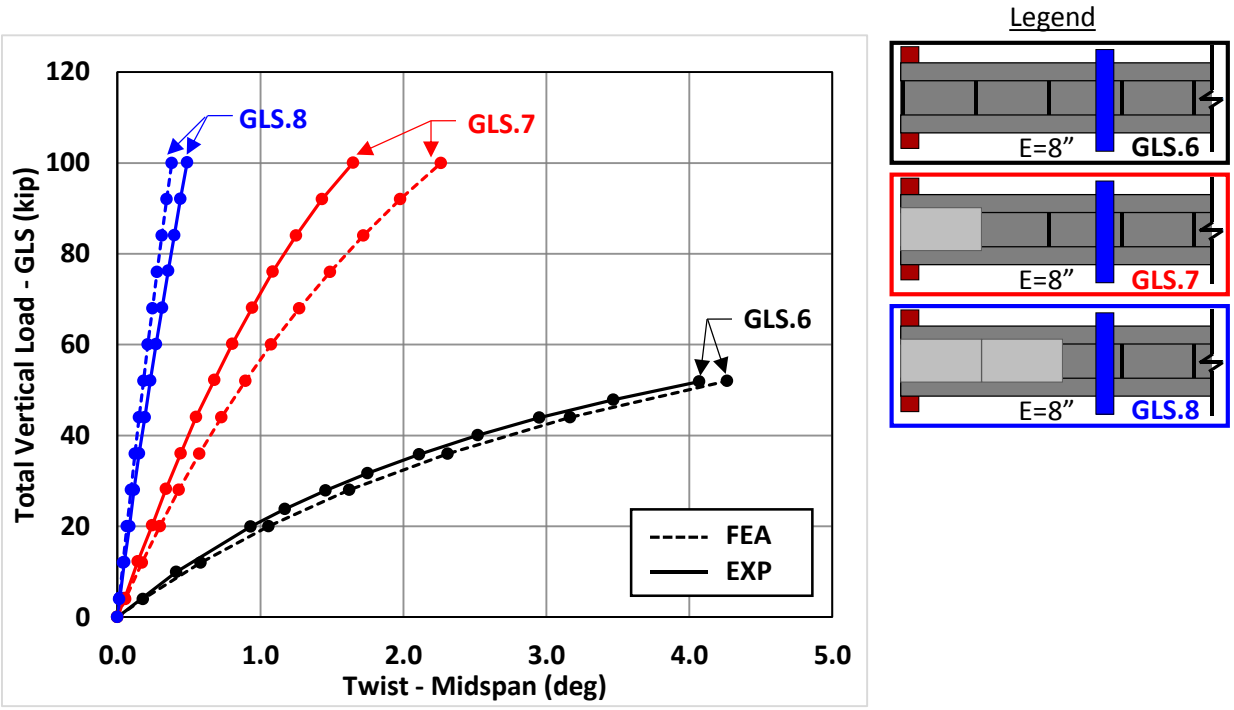

Figure 9.26 Twist @ Midspan vs. Lateral Load @ Third Point - PCP

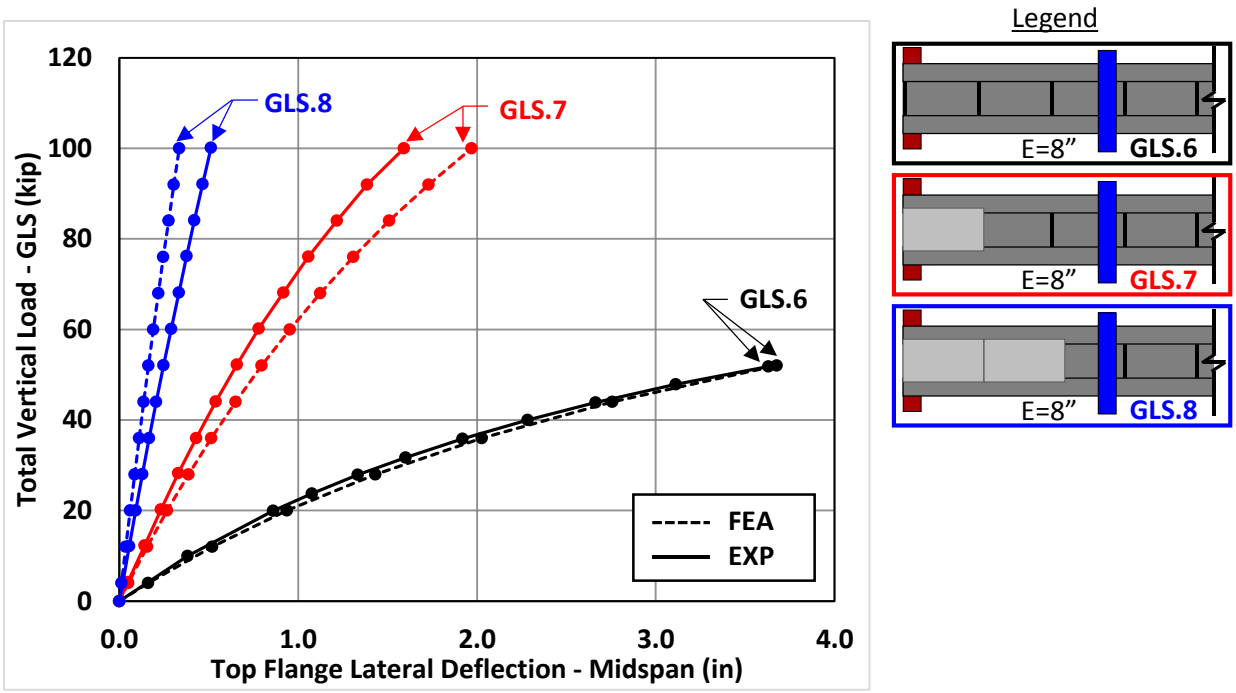

Figure 9.27 Lateral Deflection @ Midspan vs. Lateral Load @ Third Point - PCP

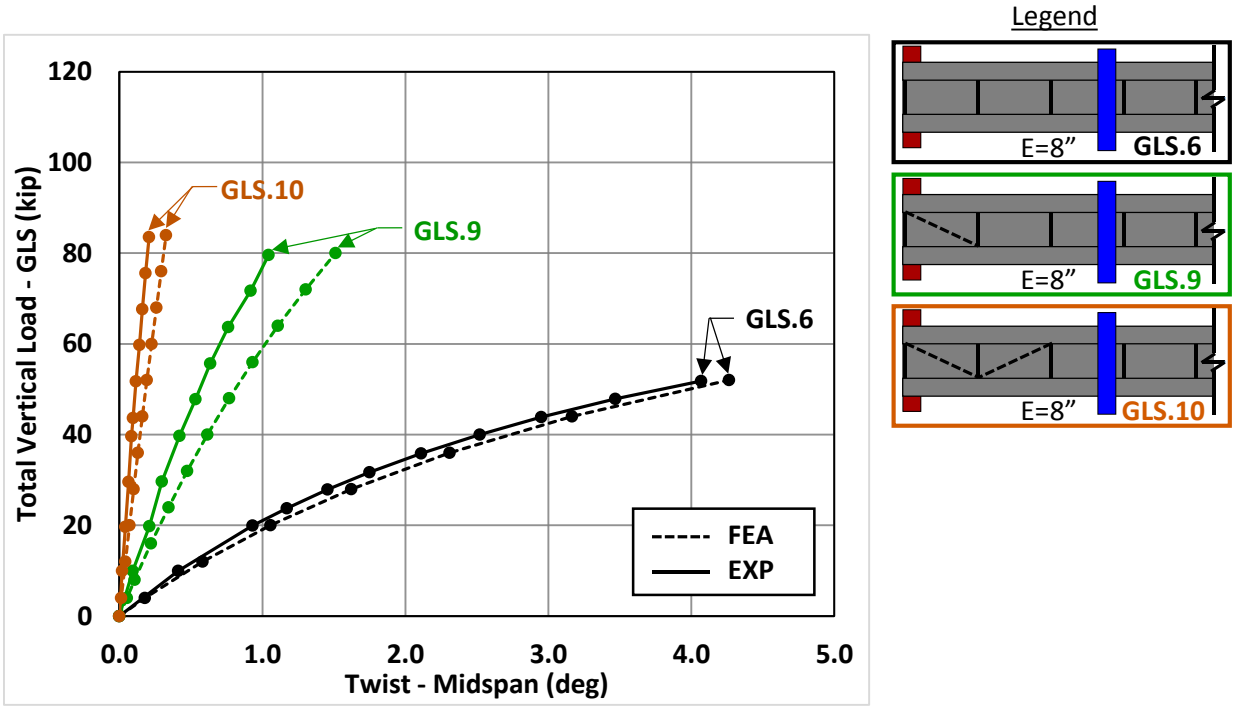

Figure 9.28 Twist @ Midspan vs. Lateral Load @ Third Point - DIAG

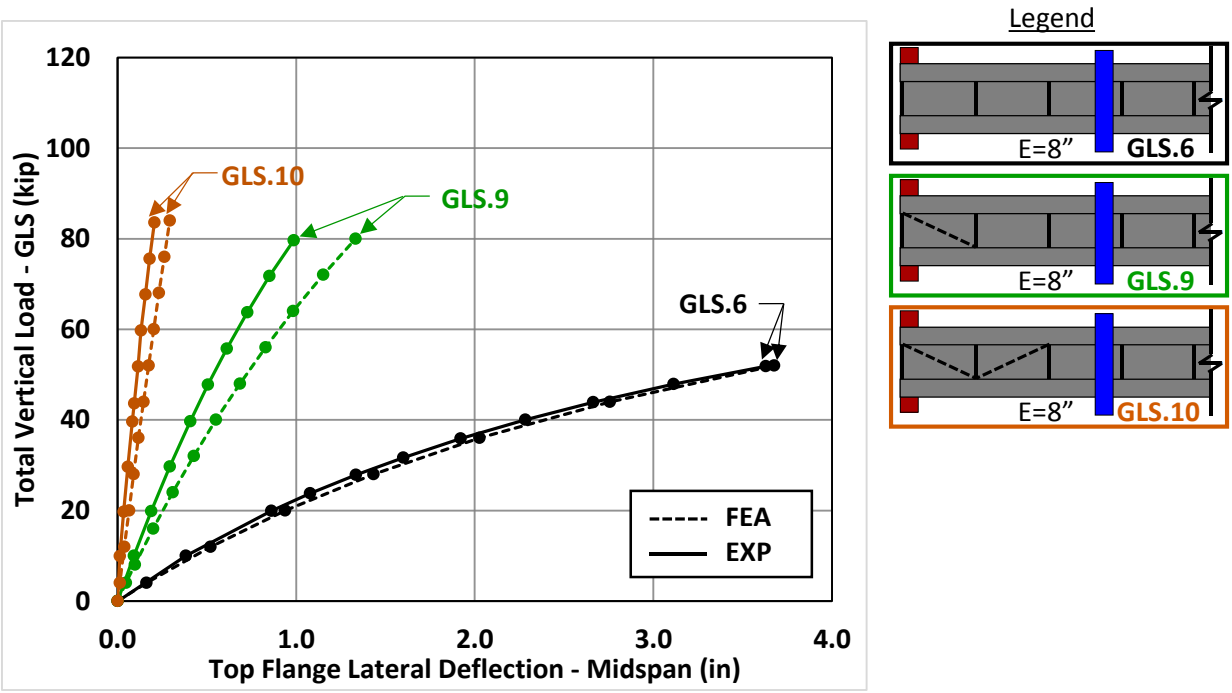

Figure 9.29 Lateral Deflection @ Midspan vs. Lateral Load @ Third Point - DIAG

9.4.3 Tub Girder Combined Bending and Torsion Overhanging FE Model Validation

Table 9.9 shows a summary of the 9 gravity load experimental tests that were performed on the overhanging tub girder system each of which was used to validate the FE model. Figure 9.30 and Figure 9.31 show a comparison between the FE model and the experimental results for the girder twist and top flange lateral deflection, respectively for two cases. Graphs for the other seven cases are shown in Appendix E. For GLS.23 and GLS.24 the FE model accurately represented the twist of the girders and the top flange lateral deflection at the backspan and the overhang for both cases.

Table 9.9 Summary of Bending and Torsion Overhang Tub Girder Tests

Test Name	Support Condition	GLS North Eccentricity	GLS South Eccentricity	K-Frame Location	Max Total GLS Load	Max Total GLS Load
GLS.16	OH	-2"	4"	2-Panel	0	200
GLS.17	OH	-2"	4"	2-Panel	3 PCP	200
GLS.18	OH	-2"	4"	2-Panel	3 DIAG	200
GLS.19	OH	-4"	8"	2-Panel	0	200
GLS.20	OH	-4"	8"	2-Panel	3 PCP	200
GLS.21	OH	-4"	8"	2-Panel	3 DIAG	200
GLS.22	OH	-6"	12"	2-Panel	0	200
GLS.23	OH	-6"	12"	2-Panel	3 PCP	300
GLS.24	OH	-6"	12"	2-Panel	3 DIAG	200

Key: GLS = Gravity Load Simulator Load, OH = Overhang Support
PCP = Partial Depth Precast Concrete Deck Panel, DIA = Diagonal

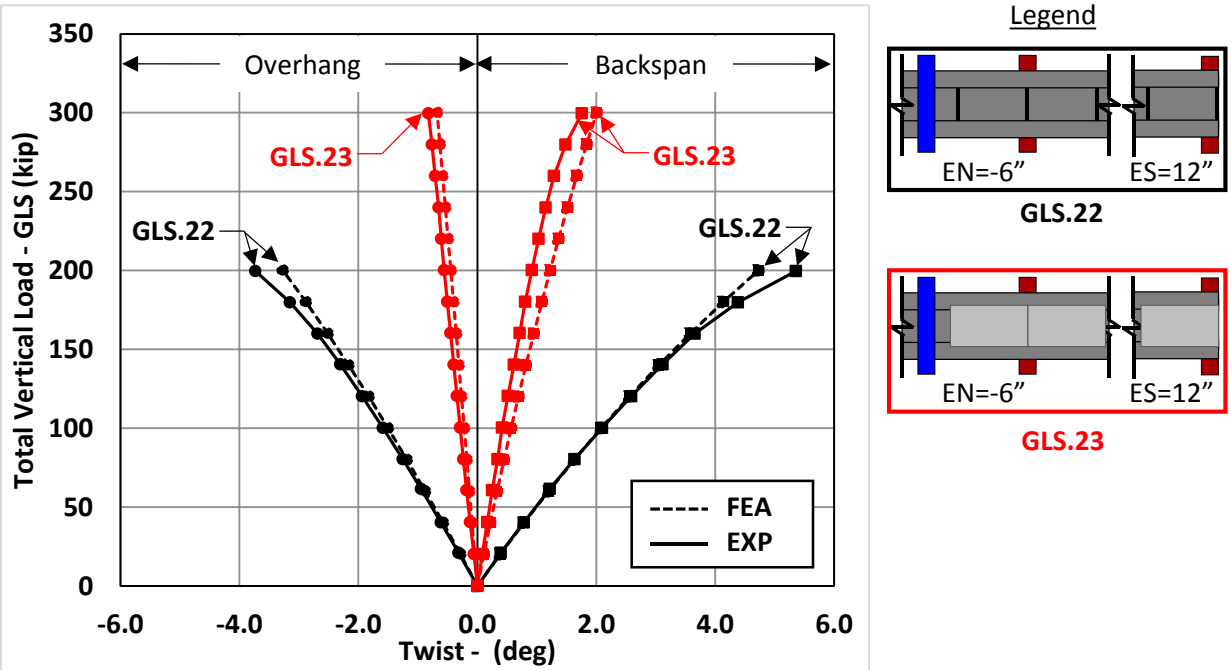

Figure 9.30 Twist vs. GLS Load (EN=-2" & ES=4") - PCP

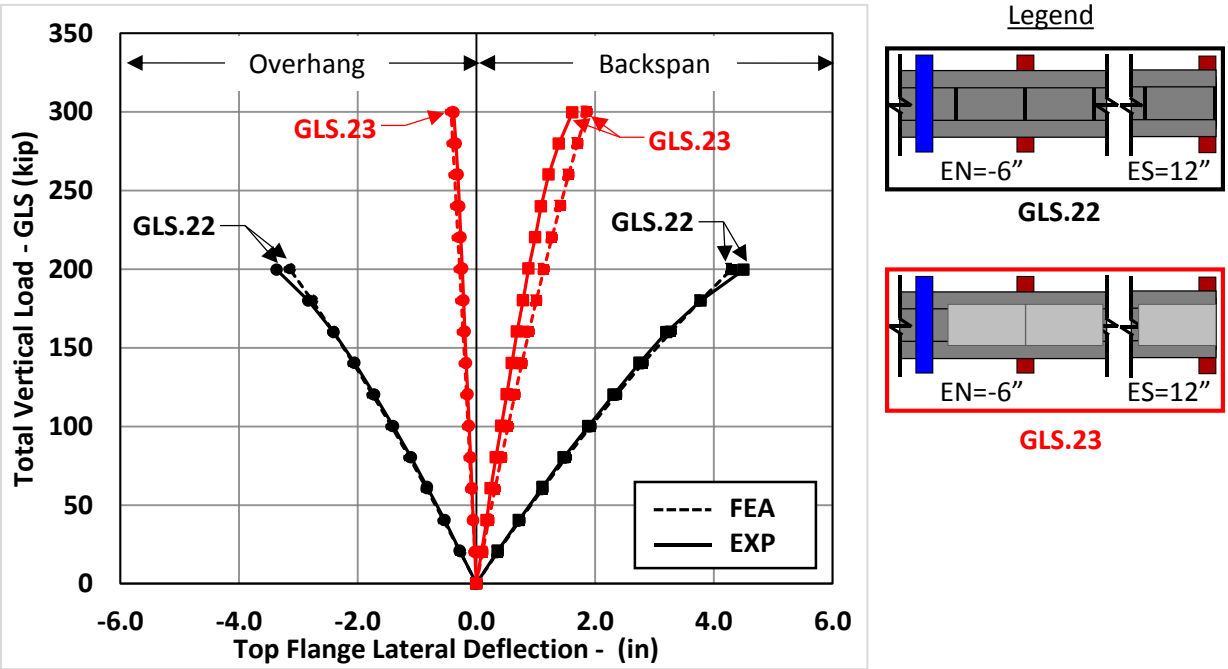

Figure 9.31 Lateral Deflection vs. GLS Load (EN=-2″ & ES=4″) – PCP

9.5 Estimated PCP Force in Laboratory Experiments

The PCP shear force can be estimated from the simplified X-frame model for the PCPs in the FE models for the I-girder and tub girder systems. The forces in the diagonals were output from the FE model and the shear force was calculated using Equation 9.1.

9.5.1 Estimated PCP Shear Force from I-Girder FE Models

Figure 9.32 shows the estimated PCP shear force vs the total vertical load placed on the simply supported girder with the GLS (at E = 12″). Doubling the number of PCPs attached to the system (from one at each end to two) did not significantly reduce the maximum shear force in the PCPs. When four PCPs were attached to the system (and no bottom flange truss members were connected), the estimated shear force in the PCPs near the supports was relatively small (less than 1 kip). Adding bottom flange truss members (see Figure 9.33) significantly stiffened the system and allowed engagement of the PCPs near the supports. Appendix D shows the graphs of the PCP shear force for all of the combined bending and torsion I-girder tests with PCPs attached to the top flanges.

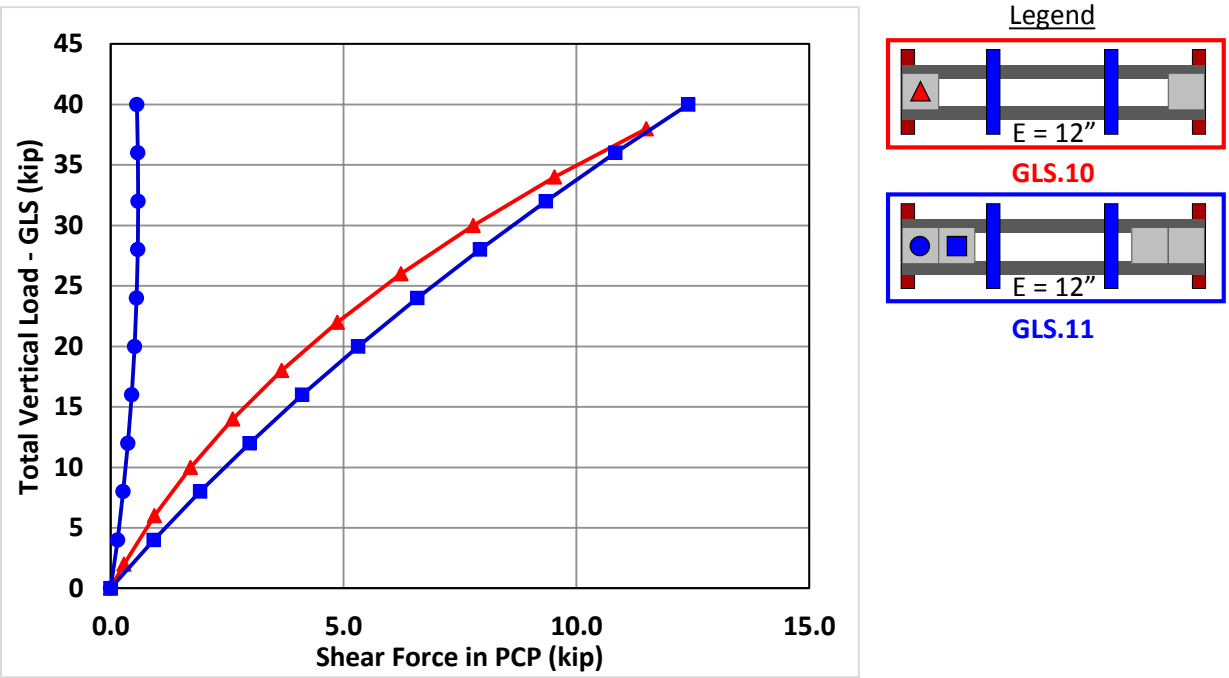

Figure 9.32 Estimated Shear in PCP vs. GLS Load (E=12")

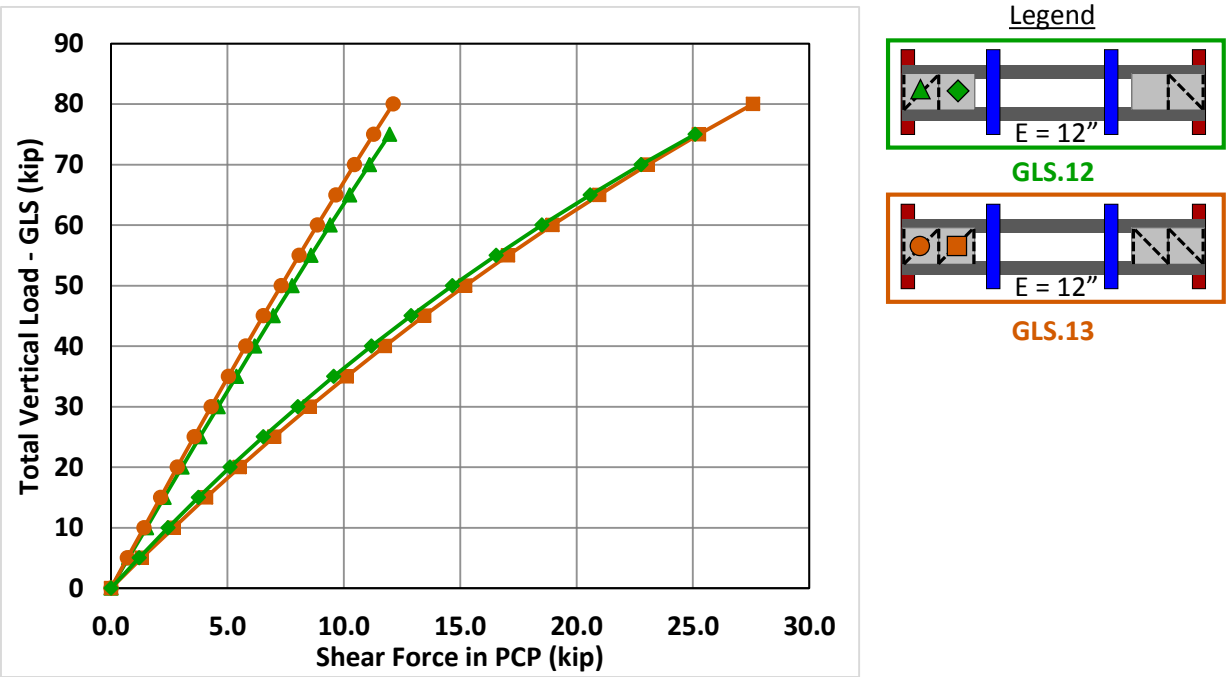

Figure 9.33 Estimated Shear in PCP vs. GLS Load (E=12") – Bottom Flange Truss

9.5.2 Estimated PCP Shear Force from Tub Girder FE Models

Figure 9.34 shows the estimated PCP shear force vs the total vertical load placed on the simply supported girder with the GLS (at E = 16″). Doubling the number of PCPs attached to the system (from one at each end to two) allowed the GLS load to be significantly increased (from 60 kips to 100 kips) before the same shear force was achieved in the PCPs (a force of approximately 24 kips). Figure 9.35 shows the PCP shear force vs the total vertical load placed on the overhang supported girder with the GLS placed at various load eccentricities. As expected, the forces in the PCPs doubled and tripled as the load eccentricity (i.e. torsion) increased by factors of two and three, respectively. Appendix E shows the graphs of the PCP shear force for all of the combined bending and torsion tub girder tests with PCPs attached to the top flanges. The largest shear force on the PCPs during the tub girder tests was calculated to be 40.2 kips from the FE models which is less than the PCP failure load (V_{max} = 91 kips) for connection A.1.MAX (see Chapter 4).

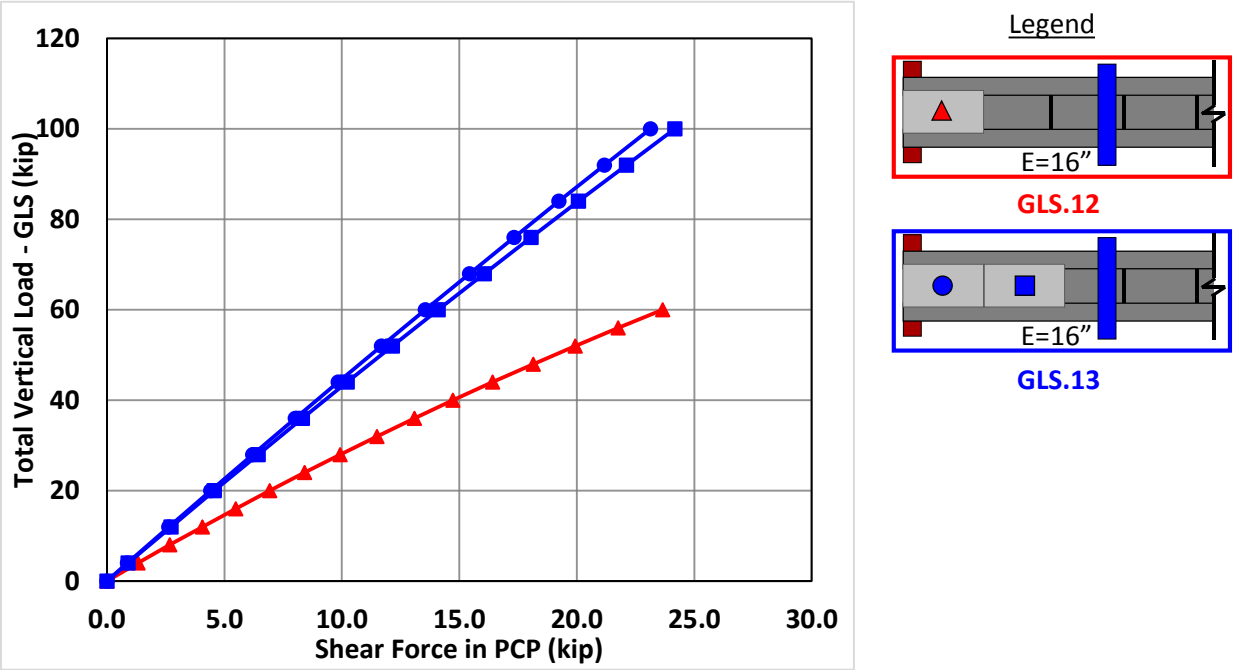

Figure 9.34 Estimated Shear Force in PCPs vs. GLS Load (E=16″)

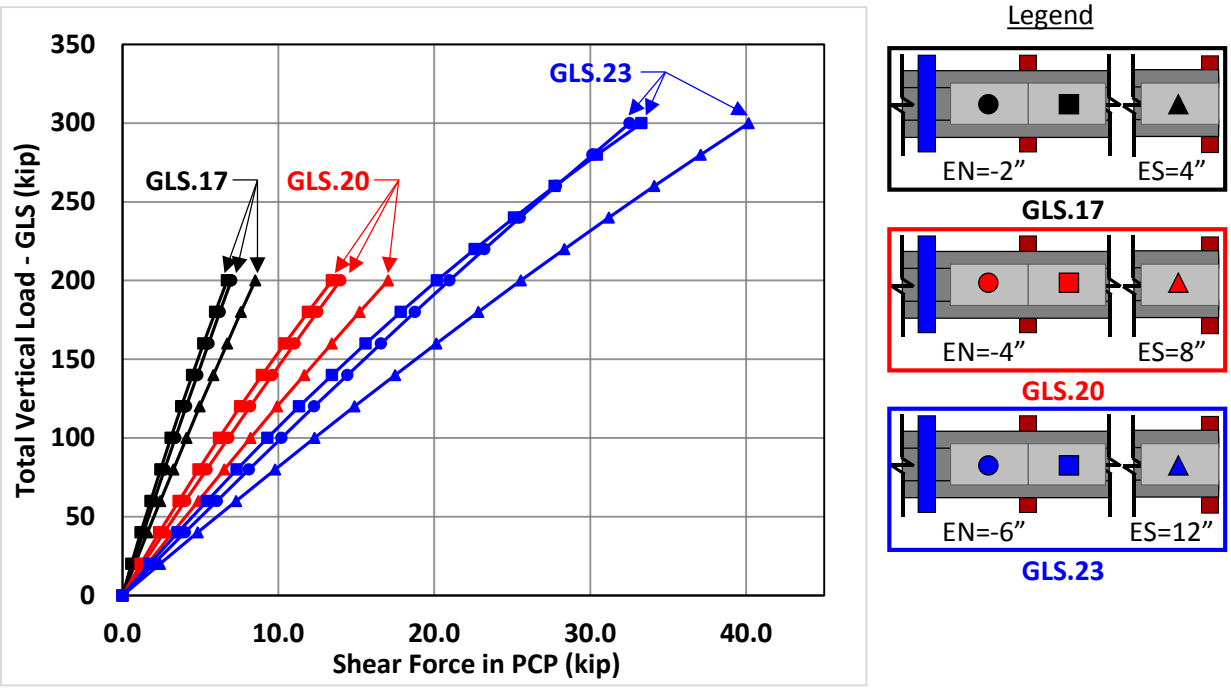

Figure 9.35 Estimated Shear Force in PCPs vs. GLS Load – Overhang

9.6 Parametric FE Model of Steel I-Girder System

The finite element modeling techniques for the validated twin I-girder system (described above) were used to perform parametric studies to investigate the potential benefit of using PCPs as bracing elements on curved steel I-girder bridges. The experiments in the laboratory (and the FE model validation) showed that connecting PCPs to the I-girders, had a tendency to reduce the girder deformation as well as lessen the forces in the cross-frame when it was connected at midspan. These experiments were limited to a twin I-girder system with a maximum of one intermediate cross-frame for the simply supported system. The parametric study was used to investigate the potential benefit of using PCPs on larger and more realistic curved I-girder systems where multiple cross-frames are used in each span and more than two I-girders are present. Plan sets for numerous bridges constructed for TxDOT and the current TxDOT guidelines (Texas Steel Quality Council 2015) were referenced so that realistic girder-sections and bridge geometries would be used in this study. The following parameters were varied:

1. Radius of curvature (600 ft, 1200 ft, and 1800 ft)
2. Girder cross-section (D4, D6, and D8 – shown in detail below)
3. Girder spans (equal span with L/D = 30 & unequal span with L/D = 20 and L/D = 30)
4. Number of PCPs attached at the end of each span (0, 1, and 2)
5. Cross-frame spacing (20 ft on center and 40 ft on center)

9.6.1 I-Girder Layout

Figure 9.36 shows the plan view of the three I-girder, two span system that was used for the parametric study. The radius of curvature was measured to the center of the three girders with

the on-center spacing of the girders set at a constant of 9 feet. A total of 18 different models were created and the geometry of each model is given in Figure 9.36.

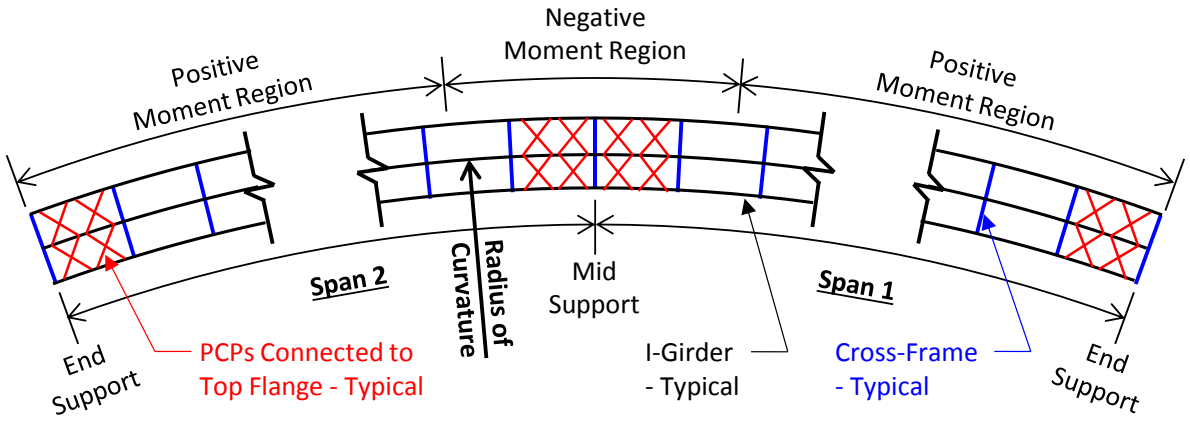

Figure 9.36 I-Girder Layout for Parametric Study – Plan View

Table 9.10 FE Models for I-Girder Parametric Study

Model Name	Girder Depth (ft)	Radius of Curvature (ft)	Span 1 Length (ft)	Span 2 Length (ft)
EQ.D4.R600	4	600	120	120
EQ.D4.R1200	4	1200	120	120
EQ.D4.R1800	4	1800	120	120
EQ.D6.R600	6	600	180	180
EQ.D6.R1200	6	1200	180	180
EQ.D6.R1800	6	1800	180	180
EQ.D8.R600	8	600	240	240
EQ.D8.R1200	8	1200	240	240
EQ.D8.R1800	8	1800	240	240
UEQ.D4.R600	4	600	80	120
UEQ.D4.R1200	4	1200	80	120
UEQ.D4.R1800	4	1800	80	120
UEQ.D6.R600	6	600	120	180
UEQ.D6.R1200	6	1200	120	180
UEQ.D6.R1800	6	1800	120	180
UEQ.D8.R600	8	600	160	240
UEQ.D8.R1200	8	1200	160	240
UEQ.D8.R1800	8	1800	160	240

Figure 9.37 shows the layout of the PCPs attached to the top flange of the I-girders (the simplified X-frame truss model discussed in Chapter 8 was used to represent the in-plane stiffness of the PCP/connection system for the parametric study). The PCPs were attached near the end supports (where warping deformation is large) and near the interior support. When both the

geometry and loading conditions are symmetric about the mid support, there is no warping deformation of the flanges at the mid support. Warping deformation does occur, however, when the two span lengths are unequal and/or the loading is unequal in the two spans.

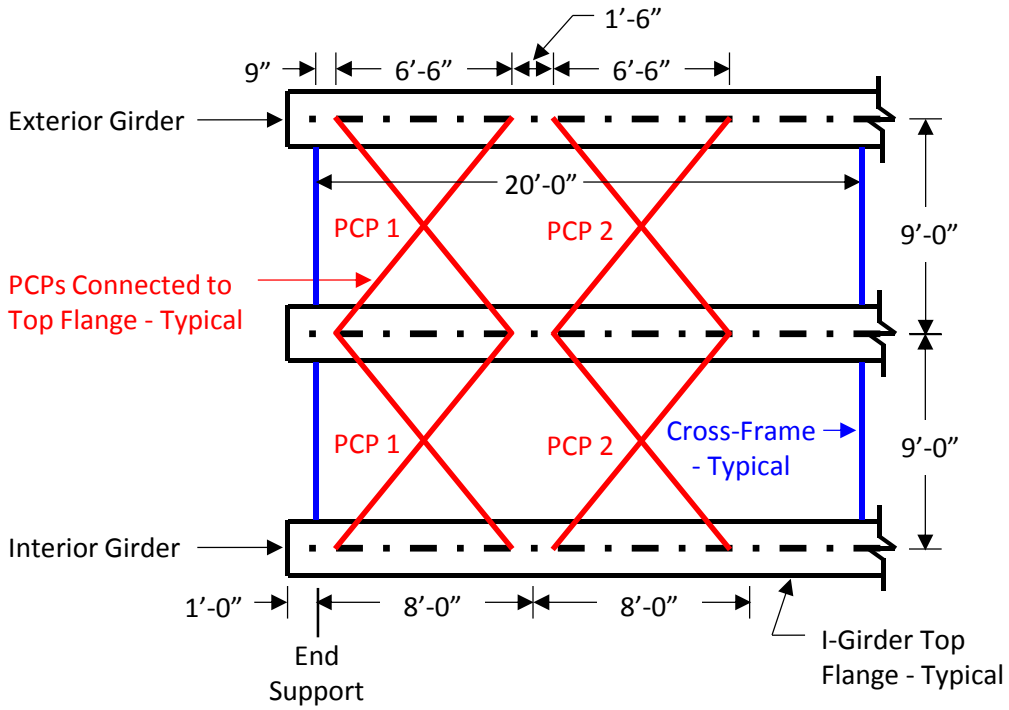

Figure 9.37 PCP Layout for on I-Girders – Plan View

Two different values for the stiffness of the simplified X-frame truss model representing the PCPs were used for the parametric study. The two extreme values for the stiffness of the PCP/connection system was varied using the values for the minimum and maximum stiffness from the shear panel tests (connections A.1.MAX and C.2.MIN described in Chapter 4 and Chapter 8). Table 9.11 shows the stiffness of the members which were calculated using the stiffness of concrete with a 28 day strength of f'_c = 5000 psi.

Table 9.11 Truss Member Stiffness Representing PCPs for I-Girder Parametric Study

Connection Detail	E of PCP† (ksi)	PCP Size (in)	Model Size (in)	β_{PCP} (kip·in/rad)	$k_{con} = k_x = k_y$ (kip/in)	β_{con} (kip·in/rad)	β_b (kip·in/rad)	A_{truss}* (in^2)	k_{truss} (kip/in)
A.1.MAX	4031	≈98x96	108x78	22,694,498	661	1,322,203	1,249,411	1.44	312
C.2.MIN	4031	≈98x96	108x78	22,694,498	1281	2,560,676	2,301,044	2.64	575

*Calculated Using E=29,000 ksi † E = 57(5000)^(1/2)

9.6.2 I-Girder Cross-Sections

Three representative cross-sections (Figure 9.38) were used for the parametric study of the I-girder system summarized in this chapter. These cross-sections were based on current TxDOT guidelines (Texas Steel Quality Council 2015). Per the guidelines, the flange width (b_t) was taken

as the maximum of the girder depth divided by 4 or 15 inches and the minimum recommended thicknesses for the flanges and webs were followed. The flange width and web thickness remained constant through the entirety of the bridge while the thickness of the flanges doubled in the negative moment region (specified as 25% of the girder's span length). Stiffeners (½″ thick) were provided at the location of the cross-frames having the same width as the flanges to simplify meshing of the FE model.

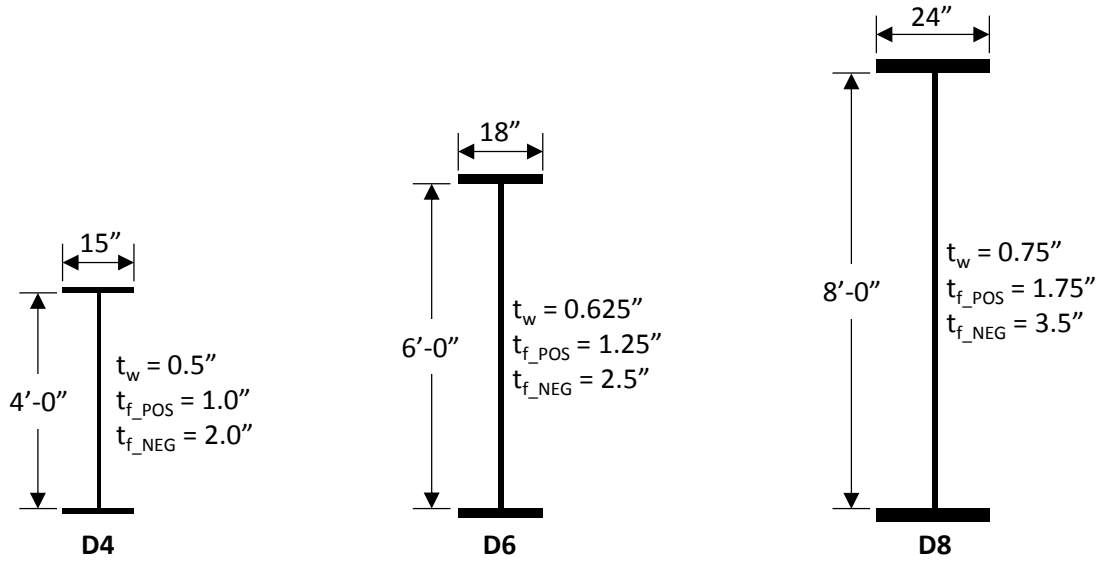

Figure 9.38 Cross-Sections Used for the I-Girder Parametric Study

9.6.3 I-Girder Cross-Frames

Current TxDOT guidelines state that L3.5x3.5x3/8, L4x4x3/8, and L5x5x1/2 angles are a common angle size used for cross-frames in I-girder bridges (Texas Steel Quality Council 2015). For this study, L4x4x3/8 angles were used for all cross-frame members (chords and diagonals) and the stiffness of these members were reduced to account for the connection eccentricity of the single angle members. The following stiffness reduction factor was used that was specifically developed for members of an X-type cross frames (Battistini et al. 2013):

$$R_{est-SX} = 1.063 - 0.087\frac{S}{h_b} - 0.159\bar{y} - 0.403t \tag{9.3}$$

where,
S = girder spacing
h_b = height of the brace
$\bar{y}$ = distance from connection pate to angle center of gravity
t = thickness of the angle

The cross-frames were spaced at 20 ft on center since TxDOT prefers that cross-frames be placed at 15 to 20 feet maximum for curved girders (Texas Steel Quality Council 2015). The FE models were also analyzed with every other cross-frame removed (i.e. cross-frame spacing at 40 ft on center) to see if attaching PCPs could significantly reduce the cross-frames needed along the length

of the girders. The cross-frame members were modeled using liner spring elements with the stiffness equal to the axial stiffness of the angle multiplied by the stiffness reduction factor (Equation 9.3).

9.6.4 Load Application on I-Girders and Connection of Bracing Members

A cross-section of the curved I-girder system is shown in Figure 9.39. The loads from the wet concrete deck and the PCPs were applied to the nodes at the web-to-flange intersection (at 5 feet on center). The torsional effects from the bridge overhang bracket to support the wet concrete deck on the fascia girders were not considered. The weight of the I-girders was applied using gravitational acceleration of the shell elements. No load factors were used for the analysis.

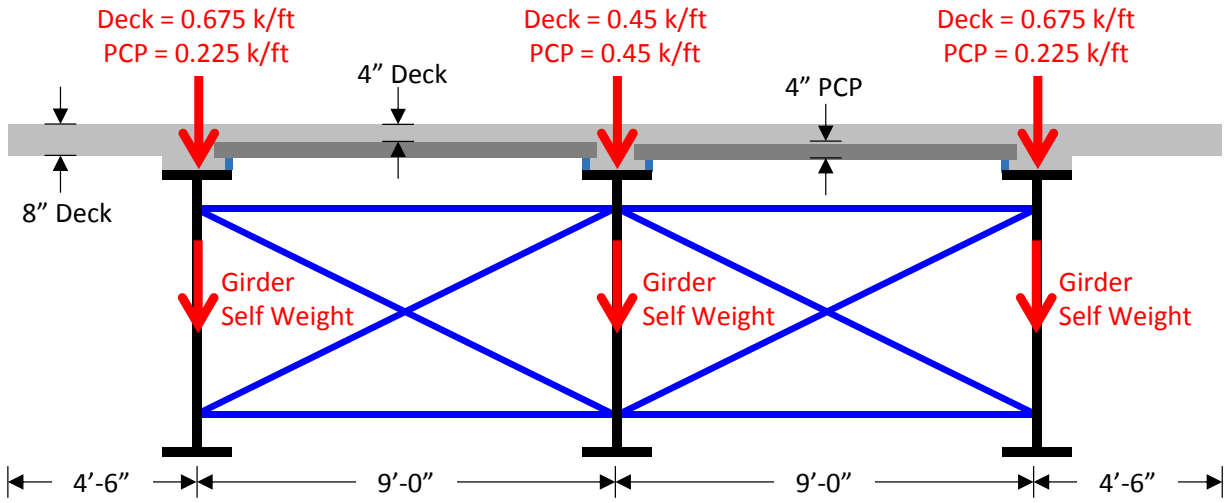

Figure 9.39 Loads on Curved I-Girder System

9.6.5 Finite Element Model – I-Girder Parametric Study

A cross-section of the FE model for the curved I-girder parametric study is shown in Figure 9.40. S8R5 shell elements were used for the flanges, webs, and the stiffeners in the curved I-girder system (8 elements through the depth of the girder and two elements across the width of the flanges). The cross-frames were connected at the intersection of the flange and stiffener at 1/8th the girder depth from the flange-to-web intersection. Linear spring elements were used to model the cross-frames and the simplified X-frame truss for PCPs. At the end supports, the nodes at the intersection of the web, bottom flange, and stiffener were fixed from translation in the vertical and radial directions. At the mid support, the nodes at the intersection of the web, bottom flange, and stiffener were fixed from translation in the vertical, radial, and tangential directions.

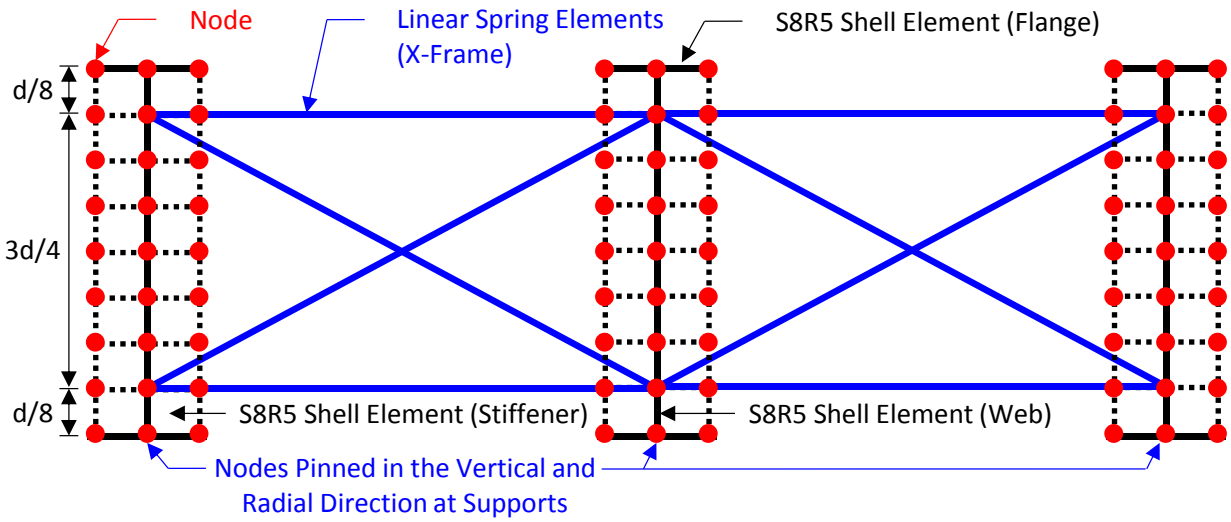

Figure 9.40 Cross-Sections of FE Model for the I-Girder Parametric Study

The model of the curved I-girder system was created with the cross-frames installed prior to the application of the steel load (i.e. a no load fit condition was used for the cross-frames). In the FE model, the top flanges of all girders were at the same elevation prior to the application of any load on the system. Two placement sequences where investigated a non-continuous PCP placement (Option A) and a continuous PCP placement (Option B). A non-continuous PCP placement (Option A) would involve setting and connecting the PCPs at the end of the span prior to placing the unconnected PCPs at the center of the span (note that this potentially cause fit-up issues for the last PCP in each span). For this case, the PCPs would act as bracing elements during both the placement of the majority of the PCPs and during the placement of the wet concrete deck. A continuous PCP placement (Option B) would involve first setting all of the PCPs on the system and then connecting the PCPs towards the end of the span. For this case, the PCPs would only act as bracing elements during the application the placement of the wet concrete deck. Option A would potentially increase the effectiveness of the PCPs as bracing elements while Option B would likely be easier to construct. A continuous deck placement was used in the model and the stiffening effects of the concrete as it cured was not considered. The following sequence was used for the FE model:

1. Create model of curved I-girder system with cross-frames installed and boundary conditions applied
2. Apply steel dead load to entire model (Load Step 1)
3. Connect PCPs at the end of the girders span (option A)
4. Apply PCP load to Span 1 (Load Step 2)
5. Apply PCP load to Span 2 (Load Step 3)
6. Connect PCPs at the end of the girders span (option B)
7. Apply deck load to Span 1 (Load Step 4)
8. Apply deck load to Span 2 (Load Step 5)

9.6.6 Results from Parametric FEA of I-Girder System

This section summarizes the results of the parametric FEA for the I-girder system. The goal was to investigate the potential of using PCPs as bracing elements in curved girder systems as a means to add stability to the system during construction and potentially reduce the number of intermediate cross-frames. TxDOT currently suggests that cross-frames or diaphragms be place at a maximum spacing of 20 ft in curved girder bridges to help limit flange lateral bending stresses and forces in the cross-frame/diaphragm members (Texas Steel Quality Council 2015).

Cross-Frame Forces during Construction

Figure 9.41 shows the interaction between a cross-frame and two I-girders in a curved girder-system. The diagonal forces in the cross-frame were output from the FE models and were used to compute the shear force on the cross-frame (V_{XF}) using the following equation:

$$V_{XF} = (T - C)\frac{h_b}{L_d} \tag{9.4}$$

where,
T = tension in brace from FE model
C = compression in braced from FE model
h_b = height of brace
L_d = length of diagonal

The cross-frame shear force (V_{XF}) was then compared between systems with and without PCPs as bracing elements.

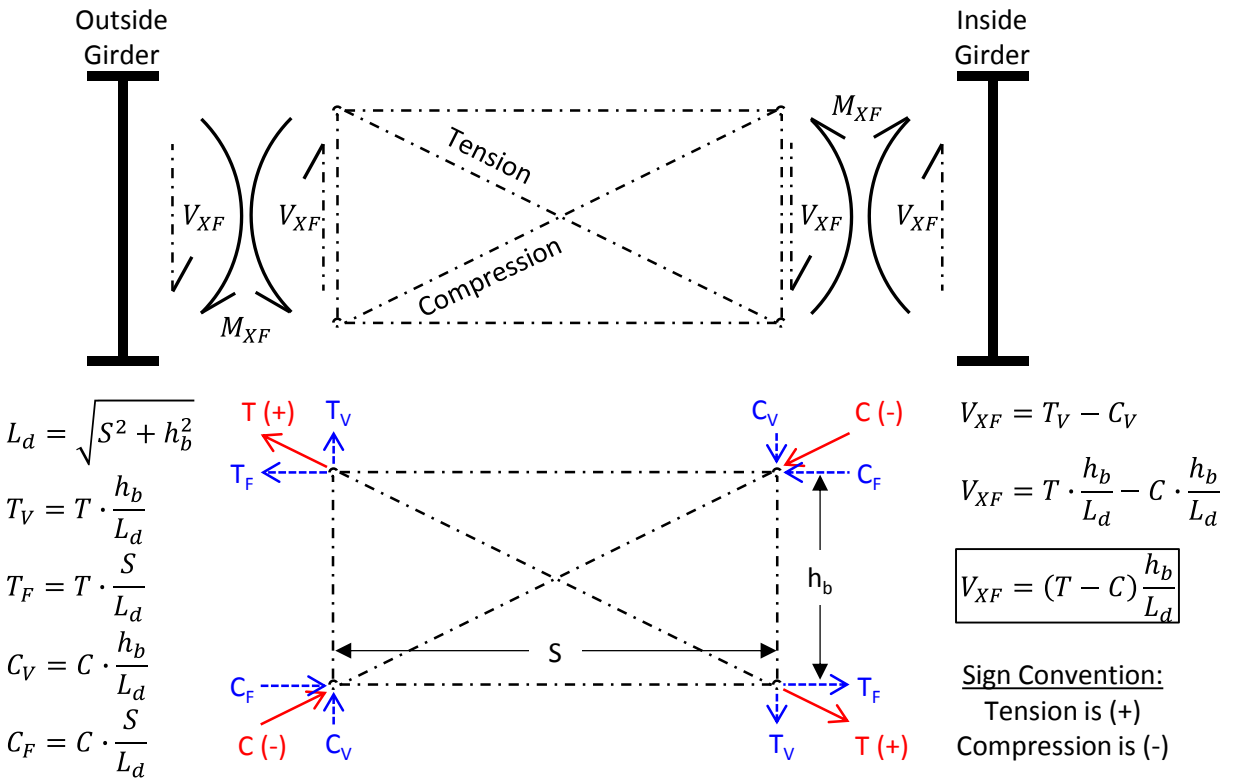

Figure 9.41 Cross-Frame Shear Force Calculated from Diagonal Forces

Figure 9.42 shows the cross-frame shear force (V_{XF}) for the cases with and without the two PCPs (with stiffness C.2.MIN) attached (after Load Step 1) at the ends of each span after Load Step 4 and Load Step 5. The cross-frames were spaced at 20 ft on center in these FE models. These graphs indicate that connecting the two PCPs do not significantly reduce the forces in the cross frames. Table 9.12 and Table 9.13 show the maximum cross-frame shear force for all 18 models after the 5 construction load steps with and without connected PCPs, respectively. For all 18 models, the addition of the PCPs did not significantly reduce the maximum load in the cross-frames. Therefore, when cross-frame spacing is governed by the forces in the cross-frame, using PCPs as bracing elements will not allow the spacing to be increased.

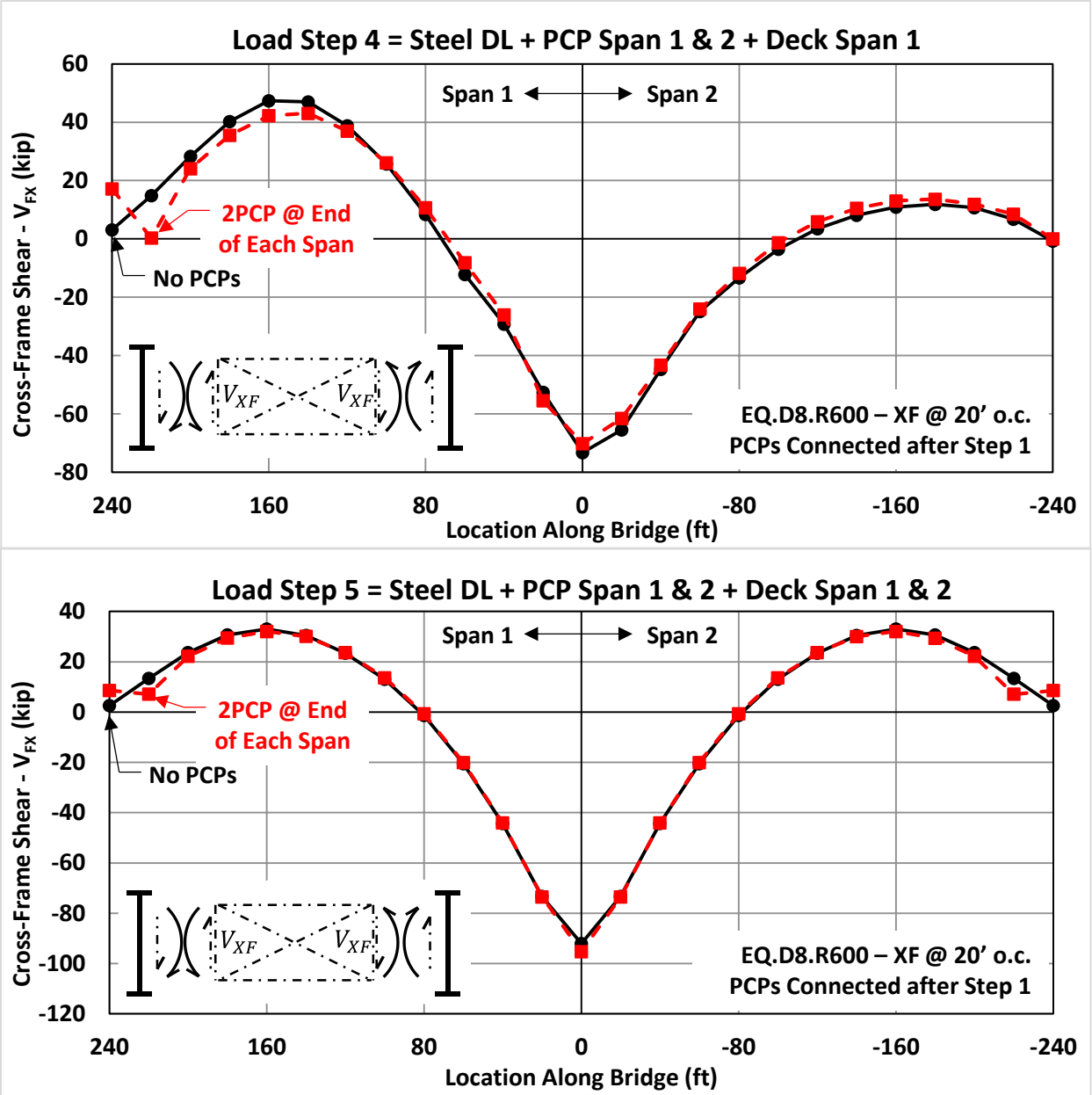

Figure 9.42 Cross-Frame Shear Force (V_{FX}) along the Bridge – EQ.D8.R600-XF@20ft

Table 9.12 Maximum Cross-Frame Shear without PCPs – XF@20ft

I-Girder System	Max V_{XF} (kip) Load Step 1 (Steel DL)	Max V_{XF} (kip) Load Step 2 (+ PCP Span 1)	Max V_{XF} (kip) Load Step 3 (+ PCP Span 2)	Max V_{XF} (kip) Load Step 4 (+ Deck Span 1)	Max V_{XF} (kip) Load Step 5 (+ Deck Span 2)	Max V_{XF} All Load Steps (kip)
EQ.D4.R1800	0.3 , -0.7	2.8 , -1.2	2.6 , -1.7	2.5 , -2.7	2.0 , -3.8	**2.8 , -3.8**
EQ.D4.R1200	0.5 , -1.0	3.3 , -1.8	3.0 , -2.6	3.8 , -4.0	3.0 , -5.6	**3.8 , -5.6**
EQ.D4.R600	1.0 , -2.1	4.9 , -3.7	4.3 , -5.2	7.5 , -8.3	5.9 , -11.6	**7.5 , -11.6**
EQ.D6.R1800	1.3 , -2.9	5.1 , -4.2	4.4 , -5.6	8.1 , -7.5	5.6 , -10.5	**8.1 , -10.5**
EQ.D6.R1200	2.0 , -4.4	6.7 , -6.3	5.7 , -8.2	12.0 , -11.5	8.3 , -15.9	**12.0 , -15.9**
EQ.D6.R600	3.8 , -9.6	11.3 , -13.8	9.3 , -18.1	22.8 , -26.1	16.0 , -35.2	**22.8 , -35.2**
EQ.D8.R1800	4.4 , -9.9	10.2 , -12.2	8.8 , -14.9	18.4 , -18.6	12.8 , -24.4	**18.4 , -24.4**
EQ.D8.R1200	6.4 , -15.6	14.1 , -19.4	12.0 , -23.4	26.7 , -30.3	18.6 , -39.0	**26.7 , -39.0**
EQ.D8.R600	11.8 , -36.0	24.5 , -45.2	20.2 , -54.5	47.3 , -73.2	33.1 , -92.0	**47.3 , -92.0**
UEQ.D4.R1800	0.4 , -0.5	1.9 , -1.2	2.7 , -1.4	2.6 , -1.7	2.4 , -2.8	**2.7 , -2.8**
UEQ.D4.R1200	0.6 , -0.8	2.0 , -1.1	3.2 , -2.0	3.0 , -2.4	3.6 , -4.2	**3.6 , -4.2**
UEQ.D4.R600	1.2 , -1.8	2.6 , -2.2	4.7 , -4.4	4.3 , -5.4	7.2 , -9.6	**7.2 , -9.6**
UEQ.D6.R1800	1.6 , -2.2	2.8 , -2.7	5.0 , -4.2	4.6 , -5.1	7.6 , -7.5	**7.6 , -7.5**
UEQ.D6.R1200	2.4 , -3.4	3.3 , -4.0	6.6 , -6.2	5.9 , -7.5	11.2 , -11.7	**11.2 , -11.7**
UEQ.D6.R600	4.6 , -7.6	4.7 , -8.6	10.9 , -14.2	9.8 , -16.4	21.0 , -27.3	**21.0 , -27.3**
UEQ.D8.R1800	5.4 , -7.5	4.9 , -8.4	10.6 , -11.2	9.6 , -13.0	18.2 , -17.7	**18.2 , -17.7**
UEQ.D8.R1200	7.9 , -12.2	7.3 , -13.2	14.6 , -18.1	13.2 , -20.4	25.9 , -29.5	**25.9 , -29.5**
UEQ.D8.R600	14.0 , -30.0	13.3 , -31.5	24.2 , -45.4	22.4 , -48.6	43.1 , -76.9	**43.1 , -76.9**

Note: No PCPs attached to top flange

Table 9.13 Maximum Cross-Frame Shear w/ PCPs attached at Ends of Span – XF@20ft

I-Girder System	Max V_{XF} (kip) Load Step 1 (Steel DL)	Max V_{XF} (kip) Load Step 2 (+ PCP Span 1)	Max V_{XF} (kip) Load Step 3 (+ PCP Span 2)	Max V_{XF} (kip) Load Step 4 (+ Deck Span 1)	Max V_{XF} (kip) Load Step 5 (+ Deck Span 2)	Max V_{XF} All Load Steps (kip)
EQ.D4.R1800	0.3 , -0.7	2.7 , -1.4	2.5 , -2.1	2.4 , -3.5	2.0 , -5.1	**2.7 , -5.1**
EQ.D4.R1200	0.5 , -1.0	3.2 , -2.0	2.9 , -3.0	3.6 , -4.9	2.9 , -7.0	**3.6 , -7.0**
EQ.D4.R600	1.0 , -2.1	4.8 , -3.8	4.2 , -5.7	7.1 , -9.1	5.8 , -13.0	**7.1 , -13.0**
EQ.D6.R1800	1.3 , -2.9	4.9 , -4.3	4.4 , -6.1	6.9 , -9.0	5.3 , -13.0	**6.9 , -13.0**
EQ.D6.R1200	2.0 , -4.4	6.5 , -6.5	5.6 , -9.0	10.3 , -13.1	7.9 , -18.8	**10.3 , -18.8**
EQ.D6.R600	3.8 , -9.6	10.9 , -13.8	9.2 , -18.7	20.2 , -26.6	15.2 , -38.1	**20.2 , -38.1**
EQ.D8.R1800	4.4 , -9.9	9.8 , -12.4	8.7 , -15.6	15.6 , -20.3	12.0 , -27.8	**15.6 , -27.8**
EQ.D8.R1200	6.4 , -15.6	13.6 , -19.4	11.9 , -24.2	23.0 , -31.1	17.7 , -42.4	**23.0 , -42.4**
EQ.D8.R600	11.8 , -36.0	23.8 , -44.4	20.0 , -55.1	43.0 , -70.2	32.0 , -95.3	**43.0 , -95.3**
UEQ.D4.R1800	0.4 , -0.5	1.7 , -1.0	2.6 , -1.6	2.5 , -2.0	2.3 , -3.8	**2.6 , -3.8**
UEQ.D4.R1200	0.6 , -0.8	1.9 , -1.1	3.2 , -2.3	2.9 , -2.8	3.5 , -5.3	**3.5 , -5.3**
UEQ.D4.R600	1.2 , -1.6	2.4 , -2.1	4.7 , -4.4	4.2 , -5.4	6.9 , -9.9	**6.9 , -9.9**
UEQ.D6.R1800	1.6 , -2.2	2.7 , -2.6	4.9 , -4.5	4.5 , -5.7	6.7 , -9.6	**6.7 , -9.6**
UEQ.D6.R1200	2.4 , -3.4	3.2 , -4.0	6.4 , -6.8	5.9 , -8.3	10.0 , -13.9	**10.0 , -13.9**
UEQ.D6.R600	4.6 , -7.6	4.7 , -8.7	10.7 , -14.6	9.7 , -17.1	19.0 , -29.0	**19.0 , -29.0**
UEQ.D8.R1800	5.4 , -7.5	5.0 , -8.4	10.4 , -11.7	9.5 , -13.8	16.0 , -20.2	**16.0 , -20.2**
UEQ.D8.R1200	7.9 , -12.2	7.3 , -13.4	14.3 , -18.6	13.0 , -21.3	23.3 , -31.6	**23.3 , -31.6**
UEQ.D8.R600	14.0 , -30.0	13.3 , -31.6	23.8 , -45.5	22.1 , -49.1	40.1 , -77.2	**40.1 , -77.2**

Note: 2 PCPs (C.2.MIN) connected between Load Step 1 and Load Step 2 at the end of each span

The FE models were also analyzed with the cross-frames spaced at 40 ft on center to see if the PCPs had a more predominate influence on the forces in the cross-frames when they had a larger spacing. Figure 9.43 shows the cross-frame shear force (V_{XF}) for the cases with and without the two PCPs (with stiffness C.2.MIN) attached (after Load Step 1) at the ends of each span after Load Step 4 and Load Step 5. These graphs indicate that connecting the two PCPs do not significantly reduce the forces in the cross-frames even when a larger spacing was used. Table 9.14 and Table 9.15 show the maximum cross-frame shear force for all 18 models after the 5 construction load steps with and without connected PCPs, respectively. For all 18 models, the addition of the PCPs did not significantly reduce the maximum load in the cross-frames. Therefore, when cross-frame spacing is governed by the forces in the cross-frame, using PCPs as bracing elements will not allow the spacing to be increased. Doubling the spacing of the cross-frames (from 20 ft to 40 ft) approximately doubled the maximum forces in the cross frames.

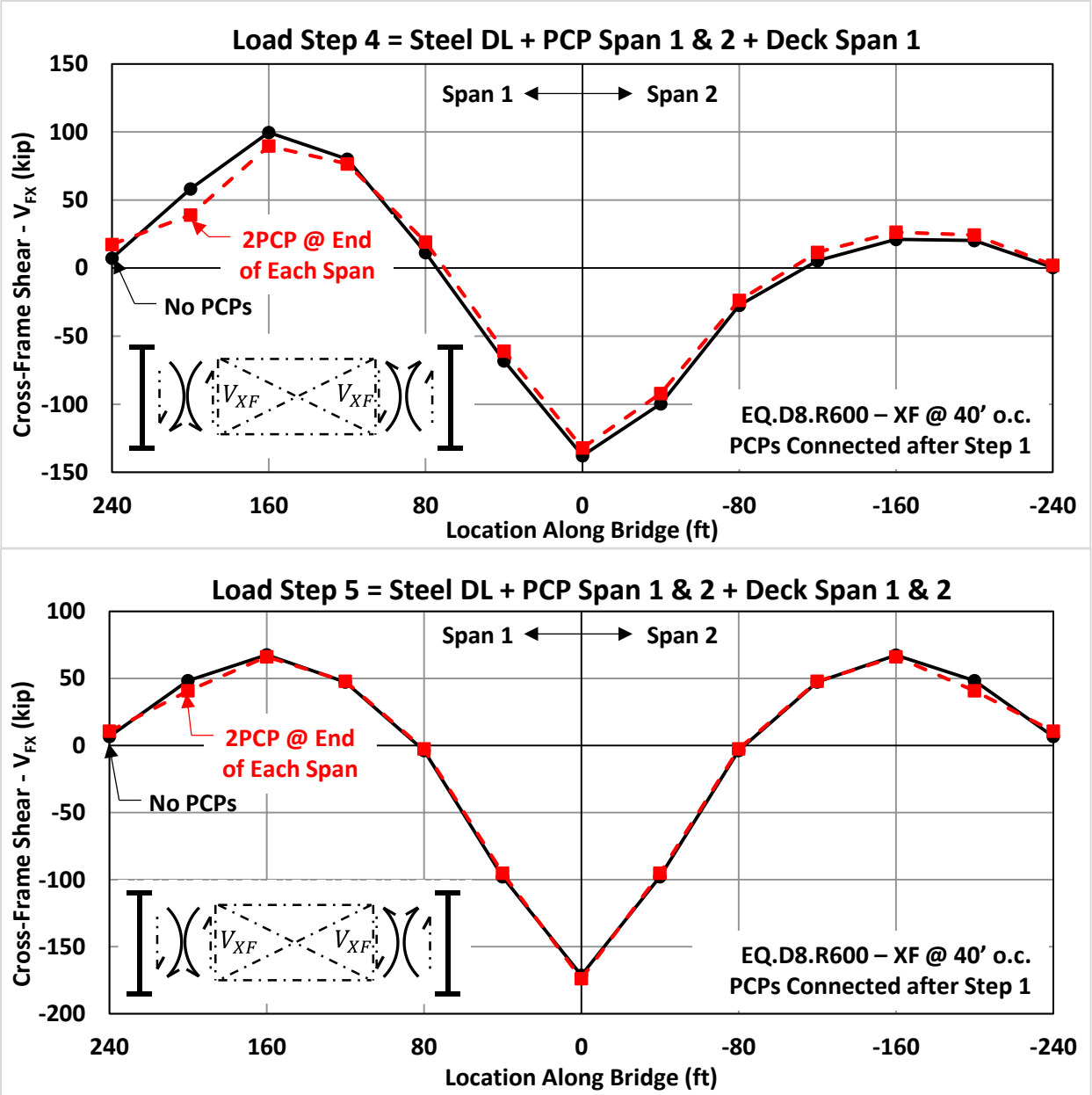

Figure 9.43 Cross-Frame Shear Force (V_{FX}) along the Bridge – EQ.D8.R600-XF@40ft

Table 9.14 Maximum Cross-Frame Shear without PCPs – XF@40ft

I-Girder System	Max V_{XF} (kip) Load Step 1 (Steel DL)	Max V_{XF} (kip) Load Step 2 (+ PCP Span 1)	Max V_{XF} (kip) Load Step 3 (+ PCP Span 2)	Max V_{XF} (kip) Load Step 4 (+ Deck Span 1)	Max V_{XF} (kip) Load Step 5 (+ Deck Span 2)	Max V_{XF} All Load Steps (kip)
EQ.D4.R1800	0.7 , -1.1	5.5 , -2.0	5.0 , -2.9	5.6 , -4.6	4.2 , -6.3	**5.6 , -6.3**
EQ.D4.R1200	1.0 , -1.7	6.6 , -3.0	5.9 , -4.3	8.4 , -7.0	6.3 , -9.6	**8.4 , -9.6**
EQ.D4.R600	2.0 , -3.6	10.0 , -6.4	8.5 , -9.1	16.7 , -15.4	12.3 , -20.3	**16.7 , -20.3**
EQ.D6.R1800	2.4 , -5.1	8.8 , -7.4	7.8 , -9.8	14.4 , -13.7	10.2 , -18.9	**14.4 , -18.9**
EQ.D6.R1200	3.6 , -7.9	11.6 , -11.4	10.2 , -15.0	21.7 , -21.5	15.3 , -29.4	**21.7 , -29.4**
EQ.D6.R600	6.9 , -17.4	20.1 , -25.3	16.9 , -33.1	43.8 , -51.1	29.4 , -65.7	**43.8 , -65.7**
EQ.D8.R1800	8.8 , -18.1	20.5 , -22.4	17.8 , -27.1	36.9 , -34.6	25.9 , -45.2	**36.9 , -45.2**
EQ.D8.R1200	12.9 , -28.5	28.5 , -35.6	24.3 , -43.0	54.1 , -56.2	37.8 , -72.1	**54.1 , -72.1**
EQ.D8.R600	23.5 , -66.0	49.9 , -83.4	40.9 , -100.3	99.7 , -137.8	67.5 , -171.4	**99.7 , -171.4**
UEQ.D4.R1800	0.8 , -0.8	3.1 , -1.9	5.3 , -2.2	5.1 , -2.6	5.3 , -4.6	**5.3 , -4.6**
UEQ.D4.R1200	1.2 , -1.3	3.4 , -1.6	6.4 , -3.2	6.0 , -3.8	7.9 , -7.1	**7.9 , -7.1**
UEQ.D4.R600	2.4 , -2.7	4.4 , -3.2	9.6 , -6.8	8.7 , -8.0	15.5 , -15.6	**15.5 , -15.6**
UEQ.D6.R1800	2.8 , -3.9	5.4 , -4.6	8.7 , -7.4	8.1 , -8.8	13.4 , -13.7	**13.4 , -13.7**
UEQ.D6.R1200	4.2 , -6.1	6.5 , -6.9	11.5 , -11.4	10.6 , -13.4	20.1 , -21.8	**20.1 , -21.8**
UEQ.D6.R600	8.1 , -13.8	9.4 , -15.3	19.5 , -26.3	17.7 , -29.5	38.6 , -53.1	**38.6 , -53.1**
UEQ.D8.R1800	10.6 , -13.8	9.9 , -15.1	21.2 , -20.5	19.4 , -23.5	36.4 , -33.0	**36.4 , -33.0**
UEQ.D8.R1200	15.5 , -22.3	14.5 , -24.1	29.2 , -33.4	26.7 , -37.5	52.5 , -55.0	**52.5 , -55.0**
UEQ.D8.R600	27.9 , -55.3	26.4 , -57.8	49.0 , -84.1	45.4 , -89.5	89.1 , -144.9	**89.1 , -144.9**

Note: No PCPs attached to top flange

Table 9.15 Maximum Cross-Frame Shear w/ PCPs attached at Ends of Span – XF@40ft

I-Girder System	Max V_{XF} (kip) Load Step 1 (Steel DL)	Max V_{XF} (kip) Load Step 2 (+ PCP Span 1)	Max V_{XF} (kip) Load Step 3 (+ PCP Span 2)	Max V_{XF} (kip) Load Step 4 (+ Deck Span 1)	Max V_{XF} (kip) Load Step 5 (+ Deck Span 2)	Max V_{XF} All Load Steps (kip)
EQ.D4.R1800	0.7 , -1.1	5.3 , -2.2	4.8 , -3.4	4.7 , -5.6	3.7 , -7.8	**5.3 , -7.8**
EQ.D4.R1200	1.0 , -1.7	6.4 , -3.3	5.7 , -4.9	7.0 , -8.1	5.6 , -11.2	**7.0 , -11.2**
EQ.D4.R600	2.0 , -3.6	9.5 , -6.7	8.2 , -9.7	13.9 , -16.2	11.0 , -22.0	**13.9 , -22.0**
EQ.D6.R1800	2.4 , -5.1	8.3 , -7.8	7.6 , -10.6	12.0 , -15.8	8.9 , -21.9	**12.0 , -21.9**
EQ.D6.R1200	3.6 , -7.9	10.9 , -11.8	9.8 , -16.0	18.2 , -23.6	13.2 , -32.5	**18.2 , -32.5**
EQ.D6.R600	6.9 , -17.4	18.7 , -25.3	16.2 , -33.8	37.0 , -49.8	25.5 , -67.8	**37.0 , -67.8**
EQ.D8.R1800	8.8 , -18.1	19.9 , -22.9	17.6 , -28.3	31.1 , -37.7	24.7 , -49.7	**31.1 , -49.7**
EQ.D8.R1200	12.9 , -28.5	27.6 , -35.9	24.1 , -44.1	46.3 , -58.3	36.4 , -76.6	**46.3 , -76.6**
EQ.D8.R600	23.5 , -66.0	48.8 , -82.3	40.9 , -100.8	89.7 , -132.1	66.3 , -173.8	**89.7 , -173.8**
UEQ.D4.R1800	0.8 , -0.8	2.8 , -1.7	5.1 , -2.5	4.9 , -3.1	4.6 , -5.9	**5.1 , -5.9**
UEQ.D4.R1200	1.2 , -1.3	3.1 , -1.7	6.1 , -3.7	5.7 , -4.4	6.8 , -8.5	**6.8 , -8.5**
UEQ.D4.R600	2.4 , -2.7	4.0 , -3.4	9.1 , -7.3	8.3 , -8.7	13.3 , -16.9	**13.3 , -16.9**
UEQ.D6.R1800	2.8 , -3.9	5.3 , -4.7	8.3 , -8.0	7.8 , -9.7	11.7 , -16.5	**11.7 , -16.5**
UEQ.D6.R1200	4.2 , -6.1	6.3 , -7.2	10.9 , -12.2	10.1 , -14.5	17.6 , -24.6	**17.6 , -24.6**
UEQ.D6.R600	8.1 , -13.8	9.2 , -15.6	18.4 , -26.8	16.9 , -30.6	34.1 , -53.8	**34.1 , -53.8**
UEQ.D8.R1800	10.6 , -13.8	9.9 , -15.3	20.7 , -21.4	19.2 , -24.8	31.9 , -37.1	**31.9 , -37.1**
UEQ.D8.R1200	15.5 , -22.3	14.6 , -24.4	28.6 , -34.2	26.5 , -38.7	46.8 , -58.5	**46.8 , -58.5**
UEQ.D8.R600	27.9 , -55.3	26.4 , -58.1	48.6 , -84.0	45.2 , -90.2	84.3 , -143.7	**84.3 , -143.7**

Note: 2 PCPs (C.2.MIN) connected between Load Step 1 and Load Step 2 at the end of each span

Influence of PCPs on System Twist during Construction

In the FE model, the top flanges of all girder were at the same elevation prior to the application of any load on the system (note that the actual girder profiles under no load are based on the roadway profile plus the total vertical cambers, which are the negative of the total dead load deflection of the system). The girders in the FE model twist as a system during the application of the construction loads (see Figure 9.44) since the girders are attached with cross-frames. The system twist was compared for the cases with and without the PCPs attached at the ends of the spans to investigate the influence of the PCPs on the torsional stiffness of the system as a whole.

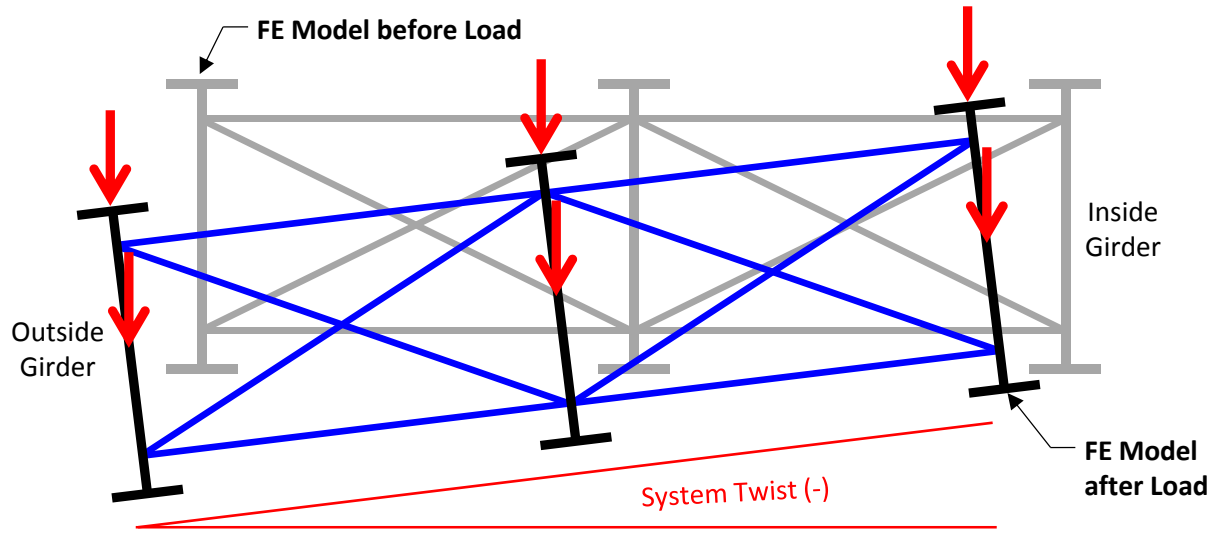

Figure 9.44 Bridge Twist during Construction

Figure 9.45 shows the system twist for the cases with and without the two PCPs (with stiffness C.2.MIN) attached (after Load Step 1) at the ends of each span after Load Step 4 and Load Step 5. The cross-frames were spaced at 20 ft on center in the FE models. These graphs indicate that connecting the two PCPs slightly reduced the twist of the I-girder system. Table 9.16 and Table 9.17 show the maximum system twist for all 18 models after the 5 construction load steps with and without connected PCPs, respectively. For all 18 models, the connecting the PCPs after Load Step 1 slightly reduced the maximum twist of the I-girder system (ranging from 5% at worst to 33% at best). When the PCPs were connected after Load Step 3, there was even less of a reduction in system twist. In the end, adding the PCPs did not have a major impact on the torsional stiffness of the system as a whole.

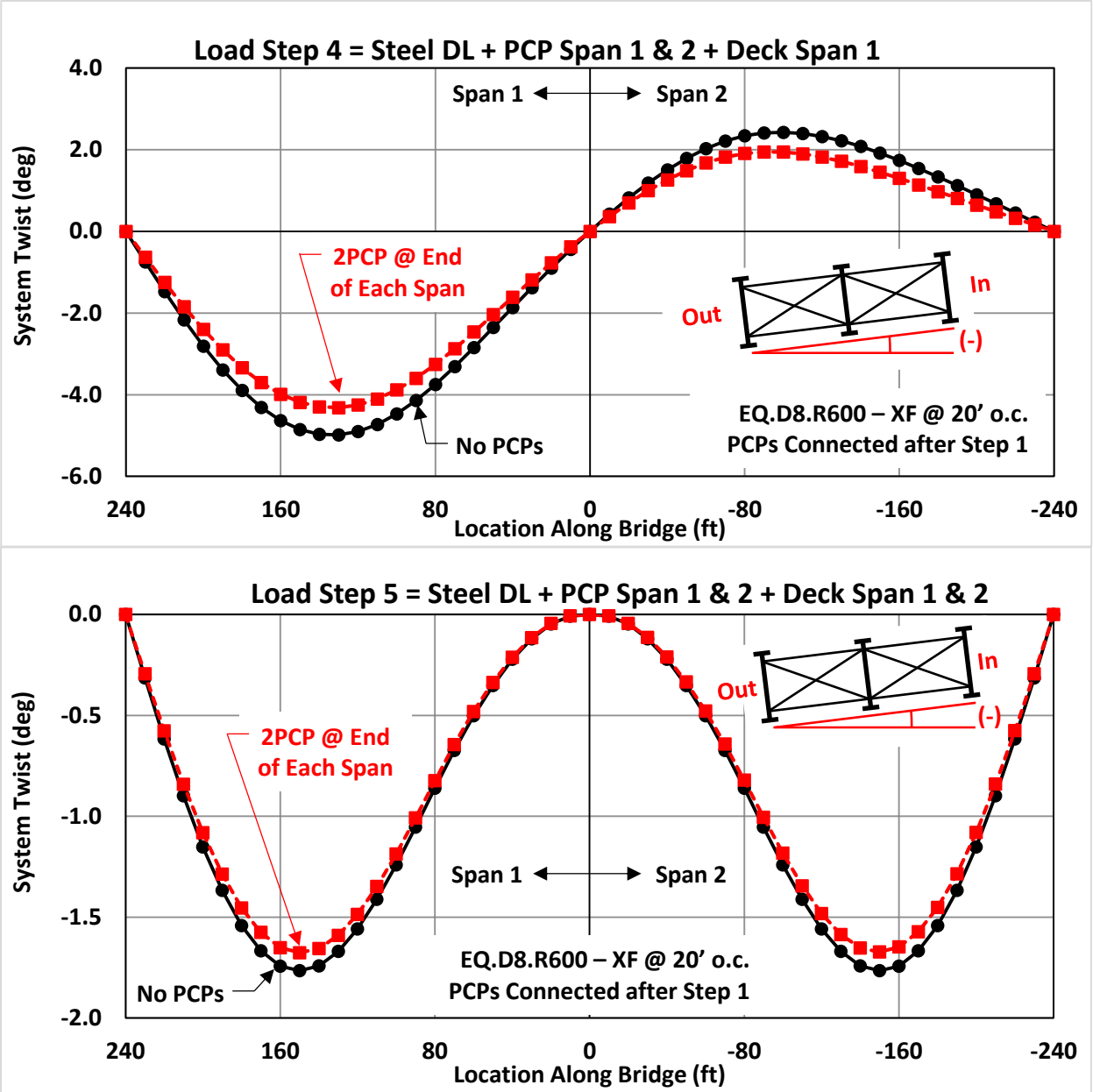

Figure 9.45 System Twist – EQ.D8.R600-XF@20ft

Table 9.16 Max System Twist without PCPs – XF@20ft

I-Girder System	Max Twist Load Step 1 (Steel DL)	Max Twist Load Step 2 (+ PCP Span 1)	Max Twist Load Step 3 (+ PCP Span 2)	Max Twist Load Step 4 (+ Deck Span 1)	Max Twist Load Step 5 (+ Deck Span 2)	Max Twist All Load Steps (deg)
EQ.D4.R1800	0.0 , 0.0	0.1 , -0.1	0.0 , 0.0	0.1 , -0.3	0.0 , -0.1	**0.1 , -0.3**
EQ.D4.R1200	0.0 , 0.0	0.1 , -0.2	0.0 , -0.1	0.2 , -0.4	0.0 , -0.2	**0.2 , -0.4**
EQ.D4.R600	0.0 , -0.1	0.2 , -0.4	0.0 , -0.1	0.4 , -0.8	0.0 , -0.3	**0.4 , -0.8**
EQ.D6.R1800	0.0 , -0.1	0.2 , -0.4	0.0 , -0.2	0.4 , -1.0	0.0 , -0.4	**0.4 , -1.0**
EQ.D6.R1200	0.0 , -0.1	0.2 , -0.6	0.0 , -0.3	0.6 , -1.4	0.0 , -0.5	**0.6 , -1.4**
EQ.D6.R600	0.0 , -0.3	0.5 , -1.2	0.0 , -0.5	1.3 , -2.8	0.0 , -1.0	**1.3 , -2.8**
EQ.D8.R1800	0.0 , -0.3	0.2 , -0.8	0.0 , -0.4	0.7 , -1.8	0.0 , -0.7	**0.7 , -1.8**
EQ.D8.R1200	0.0 , -0.4	0.4 , -1.2	0.0 , -0.6	1.0 , -2.6	0.0 , -1.0	**1.0 , -2.6**
EQ.D8.R600	0.0 , -0.7	0.9 , -2.3	0.0 , -1.0	2.4 , -5.0	0.0 , -1.8	**2.4 , -5.0**
UEQ.D4.R1800	0.0 , 0.0	0.0 , 0.0	0.0 , -0.1	0.0 , -0.1	0.1 , -0.2	**0.1 , -0.2**
UEQ.D4.R1200	0.0 , -0.1	0.0 , 0.0	0.0 , -0.1	0.0 , -0.1	0.1 , -0.3	**0.1 , -0.3**
UEQ.D4.R600	0.0 , -0.1	0.0 , -0.1	0.1 , -0.3	0.0 , -0.2	0.2 , -0.7	**0.2 , -0.7**
UEQ.D6.R1800	0.1 , -0.2	0.0 , -0.1	0.1 , -0.4	0.0 , -0.3	0.2 , -0.8	**0.2 , -0.8**
UEQ.D6.R1200	0.1 , -0.3	0.0 , -0.2	0.1 , -0.6	0.0 , -0.4	0.3 , -1.2	**0.3 , -1.2**
UEQ.D6.R600	0.2 , -0.6	0.0 , -0.4	0.3 , -1.1	0.1 , -0.7	0.6 , -2.3	**0.6 , -2.3**
UEQ.D8.R1800	0.2 , -0.6	0.1 , -0.5	0.2 , -0.9	0.1 , -0.7	0.5 , -1.7	**0.5 , -1.7**
UEQ.D8.R1200	0.2 , -0.8	0.1 , -0.7	0.4 , -1.3	0.2 , -1.0	0.7 , -2.4	**0.7 , -2.4**
UEQ.D8.R600	0.5 , -1.4	0.3 , -1.2	0.7 , -2.2	0.3 , -1.7	1.3 , -4.0	**1.3 , -4.0**

Note: No PCPs attached to top flange

Table 9.17 Max System Twist with PCPs – XF@20ft

I-Girder System	Max Twist Load Step 1 (Steel DL)	Max Twist Load Step 2 (+ PCP Span 1)	Max Twist Load Step 3 (+ PCP Span 2)	Max Twist Load Step 4 (+ Deck Span 1)	Max Twist Load Step 5 (+ Deck Span 2)	Max Twist All Load Steps (deg)
EQ.D4.R1800	0.0 , 0.0	0.1 , -0.1	0.0 , 0.0	0.1 , -0.3	0.0 , -0.1	**0.1 , -0.3**
EQ.D4.R1200	0.0 , 0.0	0.1 , -0.2	0.0 , -0.1	0.2 , -0.4	0.0 , -0.2	**0.2 , -0.4**
EQ.D4.R600	0.0 , -0.1	0.2 , -0.4	0.0 , -0.1	0.3 , -0.8	0.0 , -0.3	**0.3 , -0.8**
EQ.D6.R1800	0.0 , -0.1	0.1 , -0.4	0.0 , -0.2	0.3 , -0.8	0.0 , -0.3	**0.3 , -0.8**
EQ.D6.R1200	0.0 , -0.1	0.2 , -0.6	0.0 , -0.3	0.5 , -1.2	0.0 , -0.5	**0.5 , -1.2**
EQ.D6.R600	0.0 , -0.3	0.5 , -1.2	0.0 , -0.5	1.1 , -2.4	0.0 , -1.0	**1.1 , -2.4**
EQ.D8.R1800	0.0 , -0.3	0.2 , -0.7	0.0 , -0.4	0.5 , -1.5	0.0 , -0.7	**0.5 , -1.5**
EQ.D8.R1200	0.0 , -0.4	0.3 , -1.1	0.0 , -0.6	0.8 , -2.2	0.0 , -1.0	**0.8 , -2.2**
EQ.D8.R600	0.0 , -0.7	0.8 , -2.2	0.0 , -1.0	2.0 , -4.3	0.0 , -1.7	**2.0 , -4.3**
UEQ.D4.R1800	0.0 , 0.0	0.0 , 0.0	0.0 , -0.1	0.0 , -0.1	0.1 , -0.2	**0.1 , -0.2**
UEQ.D4.R1200	0.0 , -0.1	0.0 , 0.0	0.0 , -0.1	0.0 , -0.1	0.1 , -0.3	**0.1 , -0.3**
UEQ.D4.R600	0.0 , -0.1	0.0 , -0.1	0.1 , -0.3	0.0 , -0.2	0.2 , -0.6	**0.2 , -0.6**
UEQ.D6.R1800	0.1 , -0.2	0.0 , -0.1	0.1 , -0.4	0.0 , -0.2	0.2 , -0.7	**0.2 , -0.7**
UEQ.D6.R1200	0.1 , -0.3	0.0 , -0.2	0.1 , -0.5	0.0 , -0.4	0.3 , -1.1	**0.3 , -1.1**
UEQ.D6.R600	0.2 , -0.6	0.0 , -0.4	0.3 , -1.0	0.1 , -0.7	0.6 , -2.1	**0.6 , -2.1**
UEQ.D8.R1800	0.2 , -0.6	0.1 , -0.5	0.2 , -0.8	0.1 , -0.7	0.4 , -1.5	**0.4 , -1.5**
UEQ.D8.R1200	0.2 , -0.8	0.1 , -0.7	0.3 , -1.2	0.2 , -1.0	0.6 , -2.1	**0.6 , -2.1**
UEQ.D8.R600	0.5 , -1.4	0.3 , -1.2	0.7 , -2.2	0.3 , -1.7	1.2 , -3.7	**1.2 , -3.7**

Note: 2 PCPs (C.2.MIN) connected between Load Step 1 and Load Step 2 at the end of each span

Influence of PCPs on Radial Deflection during Construction

In addition to twisting during construction, the girders in the FE model deflect laterally in the radial direction as shown in Figure 9.46. The lateral deflection was compared for the cases with and without the PCPs attached at the ends of the spans to investigate the influence of the PCPs on the lateral stiffness of the system as a whole.

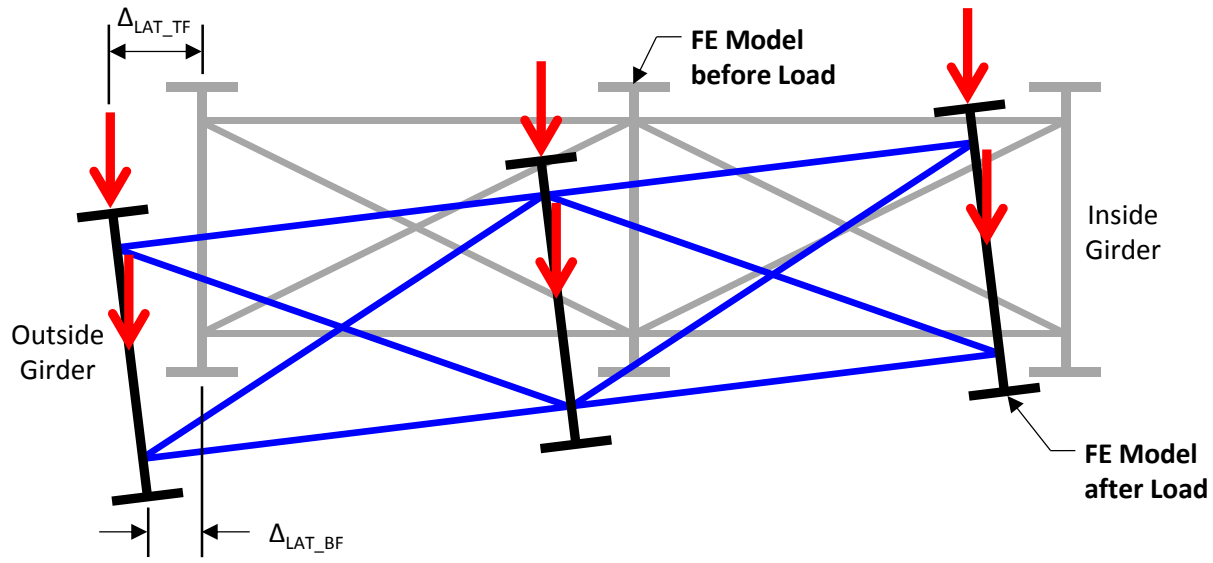

Figure 9.46 Bridge Lateral Deflection (Δ_{LAT}) during Construction

Figure 9.47 shows the radial deflection for the cases with and without the two PCPs (with stiffness C.2.MIN) attached (after Load Step 1) at the ends of each span after Load Step 4 and Load Step 5. The cross-frames were spaced at 20 ft on center in the FE models. These graphs indicate that connecting the two PCPs significantly reduced the lateral deflection of the I-girder system in the radial direction. Table 9.18 and Table 9.19 show the maximum lateral deflection for all 18 models after the 5 construction load steps with and without connected PCPs, respectively. For all 18 models, the addition of the PCPs significantly reduced the maximum lateral deflection of the I-girder system. Therefore, while adding the PCPs does not have a major impact on the torsional stiffness of the system as a whole, they do significantly reduce the lateral deflection of the system during construction.

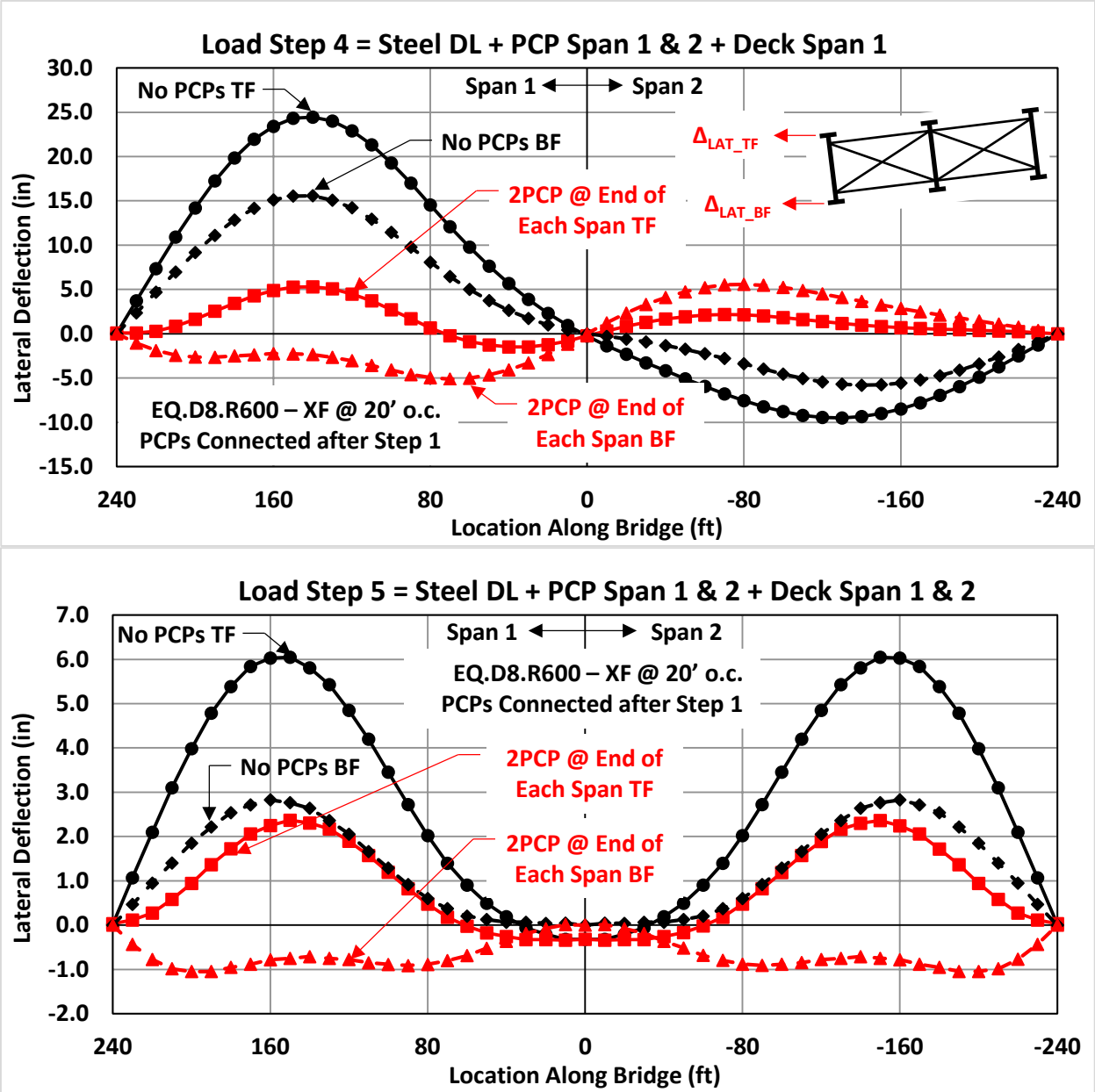

Figure 9.47 System Lateral Deflection – EQ.D8.R600-XF@20ft

Table 9.18 Max Lateral Deflection without PCPs – XF@20ft

I-Girder System	Max Δ_{LAT_TF} Load Step 1 (Steel DL)	Max Δ_{LAT_TF} Load Step 2 (+ PCP Span 1)	Max Δ_{LAT_TF} Load Step 3 (+ PCP Span 2)	Max Δ_{LAT_TF} Load Step 4 (+ Deck Span 1)	Max Δ_{LAT_TF} Load Step 5 (+ Deck Span 2)	Max Δ_{LAT_TF} All Load Steps (in)
EQ.D4.R1800	0.0 , 0.0	0.2 , -0.1	0.0 , 0.0	0.7 , -0.3	0.2 , 0.0	**0.7 , -0.3**
EQ.D4.R1200	0.0 , 0.0	0.2 , -0.1	0.1 , 0.0	1.0 , -0.4	0.3 , -0.1	**1.0 , -0.4**
EQ.D4.R600	0.0 , 0.0	0.5 , -0.2	0.1 , -0.1	2.1 , -0.8	0.6 , -0.1	**2.1 , -0.8**
EQ.D6.R1800	0.1 , 0.0	1.2 , -0.5	0.4 , 0.0	5.1 , -2.1	1.3 , 0.0	**5.1 , -2.1**
EQ.D6.R1200	0.2 , 0.0	1.8 , -0.7	0.5 , 0.0	7.5 , -3.1	1.8 , -0.1	**7.5 , -3.1**
EQ.D6.R600	0.4 , -0.1	3.6 , -1.5	1.0 , -0.1	14.1 , -5.6	3.4 , -0.2	**14.1 , -5.6**
EQ.D8.R1800	0.5 , 0.0	3.0 , -1.1	1.0 , 0.0	10.5 , -4.2	2.8 , -0.1	**10.5 , -4.2**
EQ.D8.R1200	0.7 , -0.1	4.4 , -1.6	1.5 , -0.1	14.9 , -5.9	4.0 , -0.1	**14.9 , -5.9**
EQ.D8.R600	1.2 , -0.1	7.7 , -2.9	2.4 , -0.2	24.5 , -9.5	6.1 , -0.3	**24.5 , -9.5**
UEQ.D4.R1800	0.0 , 0.0	0.0 , 0.0	0.1 , 0.0	0.1 , 0.0	0.5 , -0.1	**0.5 , -0.1**
UEQ.D4.R1200	0.1 , 0.0	0.0 , 0.0	0.2 , -0.1	0.1 , 0.0	0.8 , -0.2	**0.8 , -0.2**
UEQ.D4.R600	0.1 , 0.0	0.1 , 0.0	0.4 , -0.1	0.2 , -0.1	1.6 , -0.4	**1.6 , -0.4**
UEQ.D6.R1800	0.3 , -0.1	0.2 , 0.0	1.1 , -0.2	0.6 , -0.1	4.1 , -0.8	**4.1 , -0.8**
UEQ.D6.R1200	0.5 , -0.1	0.3 , -0.1	1.6 , -0.3	1.0 , -0.2	6.0 , -1.2	**6.0 , -1.2**
UEQ.D6.R600	1.0 , -0.2	0.6 , -0.1	2.9 , -0.6	1.8 , -0.3	10.7 , -2.0	**10.7 , -2.0**
UEQ.D8.R1800	1.5 , -0.3	1.2 , -0.3	3.2 , -0.7	2.3 , -0.5	9.4 , -1.9	**9.4 , -1.9**
UEQ.D8.R1200	2.1 , -0.5	1.7 , -0.4	4.5 , -0.9	3.2 , -0.6	12.9 , -2.5	**12.9 , -2.5**
UEQ.D8.R600	3.3 , -0.7	2.7 , -0.6	6.7 , -1.3	5.1 , -1.0	18.0 , -2.8	**18.0 , -2.8**

Note: No PCPs attached to top flange

Table 9.19 Max Lateral Deflection with PCPs – XF@20ft

I-Girder System	Max Δ_{LAT_TF} Load Step 1 (Steel DL)	Max Δ_{LAT_TF} Load Step 2 (+ PCP Span 1)	Max Δ_{LAT_TF} Load Step 3 (+ PCP Span 2)	Max Δ_{LAT_TF} Load Step 4 (+ Deck Span 1)	Max Δ_{LAT_TF} Load Step 5 (+ Deck Span 2)	Max Δ_{LAT_TF} All Load Steps (in)
EQ.D4.R1800	0.0 , 0.0	0.0 , 0.0	0.0 , 0.0	0.1 , -0.1	0.0 , -0.1	**0.1 , -0.1**
EQ.D4.R1200	0.0 , 0.0	0.1 , -0.1	0.0 , 0.0	0.1 , -0.1	0.1 , -0.1	**0.1 , -0.1**
EQ.D4.R600	0.0 , 0.0	0.1 , -0.1	0.1 , -0.1	0.2 , -0.2	0.1 , -0.1	**0.2 , -0.2**
EQ.D6.R1800	0.1 , 0.0	0.2 , -0.1	0.2 , 0.0	0.8 , -0.2	0.4 , -0.1	**0.8 , -0.2**
EQ.D6.R1200	0.2 , 0.0	0.4 , -0.2	0.2 , 0.0	1.3 , -0.3	0.5 , -0.1	**1.3 , -0.3**
EQ.D6.R600	0.4 , -0.1	0.7 , -0.4	0.5 , -0.1	2.5 , -0.7	1.0 , -0.2	**2.5 , -0.7**
EQ.D8.R1800	0.5 , 0.0	0.8 , -0.2	0.6 , -0.1	2.1 , -0.4	1.1 , -0.1	**2.1 , -0.4**
EQ.D8.R1200	0.7 , -0.1	1.2 , -0.3	0.9 , -0.1	3.1 , -0.6	1.6 , -0.2	**3.1 , -0.6**
EQ.D8.R600	1.2 , -0.1	2.0 , -0.7	1.5 , -0.2	5.3 , -1.5	2.4 , -0.3	**5.3 , -1.5**
UEQ.D4.R1800	0.0 , 0.0	0.0 , 0.0	0.0 , 0.0	0.0 , 0.0	0.1 , -0.1	**0.1 , -0.1**
UEQ.D4.R1200	0.1 , 0.0	0.1 , 0.0	0.1 , 0.0	0.0 , 0.0	0.1 , -0.1	**0.1 , -0.1**
UEQ.D4.R600	0.1 , 0.0	0.1 , 0.0	0.1 , 0.0	0.1 , -0.1	0.3 , -0.1	**0.3 , -0.1**
UEQ.D6.R1800	0.3 , -0.1	0.3 , -0.1	0.4 , -0.1	0.4 , -0.1	1.0 , -0.1	**1.0 , -0.1**
UEQ.D6.R1200	0.5 , -0.1	0.5 , -0.2	0.7 , -0.1	0.6 , -0.1	1.5 , -0.1	**1.5 , -0.2**
UEQ.D6.R600	1.0 , -0.2	0.9 , -0.3	1.2 , -0.2	1.1 , -0.3	2.7 , -0.3	**2.7 , -0.3**
UEQ.D8.R1800	1.5 , -0.3	1.4 , -0.4	1.8 , -0.3	1.7 , -0.4	3.1 , -0.2	**3.1 , -0.4**
UEQ.D8.R1200	2.1 , -0.5	2.1 , -0.5	2.6 , -0.4	2.4 , -0.5	4.4 , -0.3	**4.4 , -0.5**
UEQ.D8.R600	3.3 , -0.7	3.3 , -0.9	3.9 , -0.6	3.7 , -0.9	6.6 , -0.5	**6.6 , -0.9**

Note: 2 PCPs (C.2.MIN) connected between Load Step 1 and Load Step 2 at the end of each span

Summary of I-girder Parametric Study

Results from this parametric study on the curved I-girder systems indicate that connecting PCPs to the top flange near the supports does not significantly affect the forces in the cross-frames throughout the bridge. The largest change in cross-frame forces occurred in the cross-frames closest to the connected PCPs. Therefore, if the spacing of the cross-frames is governed by the forces in the cross-frames, adding PCPs to the system will not allow a significant number of cross-frames to be removed from the system. Also, connecting the PCPs to the I-girders near the support only slightly reduced the twist of the I-girder system as a whole. The presence of the PCPs did, however, significantly reduce the lateral deflection of the I-girders during the construction loads.

9.7 Parametric FE Model of Tub Girder System

The finite element modeling techniques for the validated twin tub girder system (described above) were used to perform parametric studies to investigate the potential benefit of using PCPs as bracing elements on curved steel tub girder bridges. The experiments in the laboratory (and the FE model validation) showed that connecting PCPs to the tub girder, had a tendency to reduce the girder deformation and were as effective as the traditional diagonals used for the top lateral truss. These experiments were limited to a single tub girder of a specific size. The parametric study was used to investigate the potential benefit of using PCPs on larger and more realistic curved tub girder systems where multiple tub girders are present. Plan sets for numerous bridges constructed for TxDOT and current TxDOT guidelines (Texas Steel Quality Council 2015) were referenced

so that realistic girder-sections and bridge geometries would be used in this study. The following parameters were varied:

1. Radius of curvature (600 ft, 1200 ft, and 1800 ft)
2. Girder cross-section (T4, T6, and T8 – shown in detail below)
3. Stiffness of PCP/connection system (A.1.MAX and C.2.MIN)

9.7.1 Tub Girder Layout

Figure 9.48 shows the plan view of the double tub girder, two span system that was used for the parametric study. The radius of curvature was measured to the center of the two tub girders and a total of 9 different models were created. The geometry of each model is given in Table 9.20. For curved tub girders, current TxDOT guidelines recommend that internal cross-frames or diaphragms be located at every other later bracing point which should result in a spacing of 14 to 18 feet (Texas Steel Quality Council 2015). Therefore, the internal K-frames were located at every other panel point as indicated in Figure 9.48, resulting in a spacing of 16 feet on center. Struts were located at the brace points where the K-frames were not present.

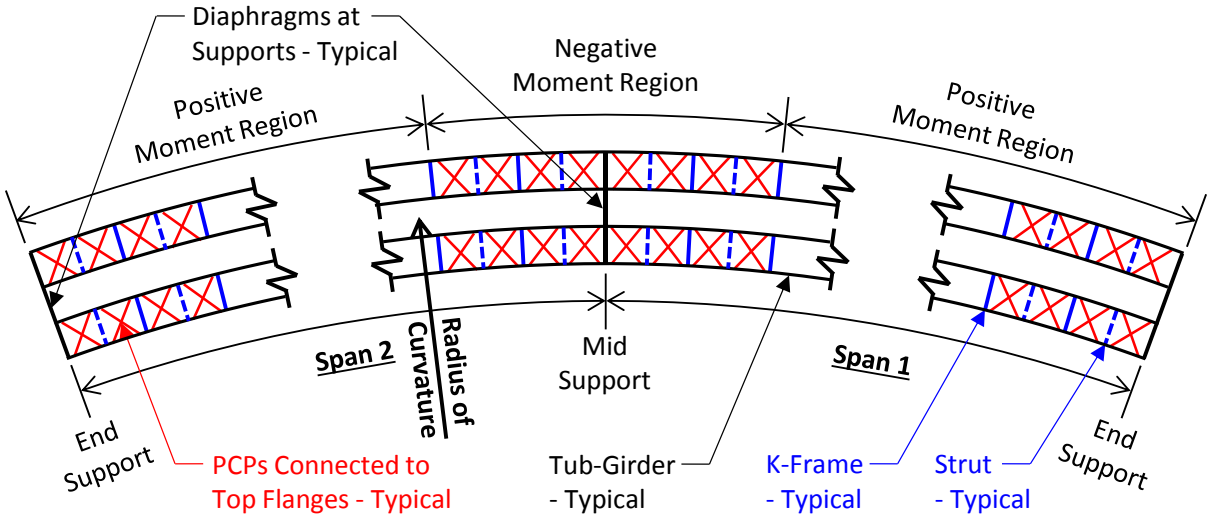

Figure 9.48 Tub Girder Layout for Parametric Study – Plan View

Table 9.20 FE Models for Tub Girder Parametric Study

Model Name	Girder Depth (ft)	Radius of Curvature (ft)	Span 1 Length (ft)	Span 2 Length (ft)
EQ.T4.R600	4	600	128	128
EQ.T4.R1200	4	1200	128	128
EQ.T4.R1800	4	1800	128	128
EQ.T6.R600	6	600	192	192
EQ.T6.R1200	6	1200	192	192
EQ.T6.R1800	6	1800	192	192
EQ.T8.R600	8	600	256	256
EQ.T8.R1200	8	1200	256	256
EQ.T8.R1800	8	1800	256	256

Figure 9.49 shows the PCPs attached to the top flange at each panel of the tub girders (the simplified X-frame truss model discussed in Chapter 8 was used to represent the in-plane stiffness of the PCP/connection system for the parametric study). The PCPs were attached near the end supports and the interior support (in the regions where the torsional load is large) to create a quasi-closed shape that is torsionally stiff. The PCPs were only connected on 25% of the span length at each end. Research by (Yura and Widianto 2005) indicated that bracing of the end panels is much more effective than bracing near midspan for a straight simply supported girder system. Furthermore, it was found that bracing more that 20% of the span length at each end did not have a large impact on the global lateral-torsional buckling strength of the system.

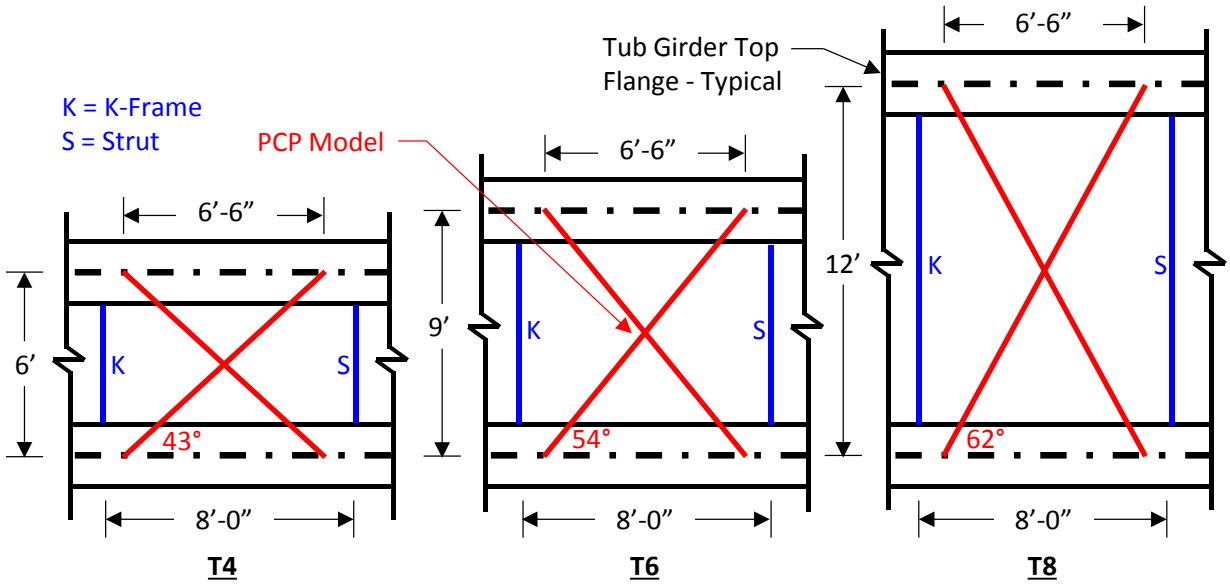

Figure 9.49 PCP Layout on tub Girders – Plan View

Two different values for the stiffness of the simplified X-frame truss model representing the PCPs were used for the parametric study. The two extreme values for the stiffness of the PCP/connection system was varied using the values for the minimum and maximum stiffness from the shear panel tests (connections A.1.MAX and C.2.MIN described in Chapter 4 and Chapter 8).

Table 9.21 shows the stiffness of the members that were calculated using the stiffness of concrete with a 28 day strength of f'_c = 5000 psi.

Table 9.21 Truss Member Stiffness Representing PCPs for Tub Girder Parametric Study

Tub	Connection Detail	E of PCP† (ksi)	PCP Size (in)	Model Size (in)	β_{PCP} (kip·in/rad)	$k_{con} = k_x = k_y$ (kip/in)	β_{con} (kip·in/rad)	β_b (kip·in/rad)	A_{truss}* (in^2)	k_{truss} (kip/in)
T4	A.1.MAX	4031	≈64x96	72x78	18,046,235	661	925,589	880,432	1.15	315
T4	C.2.MIN	4031	≈64x96	72x78	18,046,235	1,281	1,792,564	1,630,594	2.13	583
T6	A.1.MAX	4031	≈97x96	108x78	22,603,284	661	1,322,203	1,249,134	1.44	312
T6	C.2.MIN	4031	≈97x96	108x78	22,603,284	1,281	2,560,676	2,300,102	2.64	575
T8	A.1.MAX	4031	≈124x96	144x78	24,180,597	661	1,555,487	1,461,473	1.75	311
T8	C.2.MIN	4031	≈124x96	144x78	24,180,597	1,281	3,012,470	2,678,746	3.22	569

*Calculation Uses E=29,000 ksi † E = 57(5000)^(1/2)

The top flange lateral truss can be converted to an equivalent plate thickness, (t_{eq}) which is a function of the area of the diagonals, top flange areas, and the area of the web (see Figure 9.50). The formula for t_{eq} was derived by Kollbrunner and Basler (1969). The diagonals must be large enough to minimize torsional deformations and so that warping normal stresses can be neglected. For curved tub girders, AASHTO (2017) suggests that $A_d \geq 0.03w$ (all units in inches) which is based on the recommendation by Heins (1978) that $t_{eq} \geq 0.05$ inches to limit the warping normal stresses to less than ten percent of the maximum bending stresses. Table 9.22 shows the equivalent thickness for the PCP/connection system with the stiffest (C.2.MIN) and the softest (A.1.MAX) connections for the three tub girder sections used in the parametric study. The stiffest PCP/connection system (C.2.MIN) is close to meeting the $t_{eq} \geq 0.05$ inches thickness requirement.

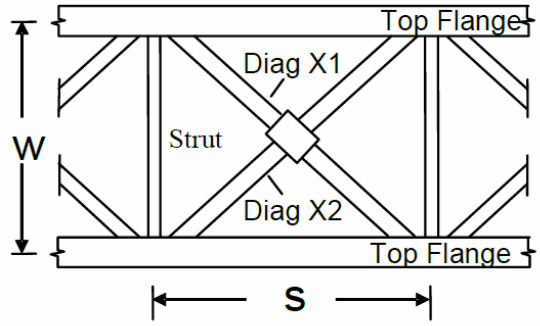

$$t_{eq} = \frac{2.60sw}{\left[\frac{L_d^3}{2A_d} + \frac{S^3}{12}\left(\frac{2}{A_t}\right)\right]}$$

t_{eq} = equivalent plate thickness
s = spacing between struts
w = width between flanges
L_d = diagonal length = $\sqrt{s^2 + w^2}$
A_d = area of diagonal
A_f = area of one top flange
A_w = area of one web
$A_t = A_f + 1/4\ A_w$
A_s = area of strut

Figure 9.50 Geometric Layout and Equivalent Plate Thickness of Top Lateral System (Helwig and Yura 2012)

Table 9.22 Equivalent Plate Thickness (in inches) for PCP/Connection Details

Tub	Connection Detail	
	A.1.MAX	C.2.MIN
T4	0.024	0.044
T6	0.026	0.047
T8	0.024	0.045

9.7.2 Tub Girder Cross-Sections

Three representative cross-sections (Figure 9.51) were used for the parametric study of the tub girder system summarized in this chapter. These cross-sections were based on current TxDOT guidelines (Texas Steel Quality Council 2015). Per the guidelines, the top flange width (b_t) was taken as the maximum of the girder depth divided by 4 or 15 inches and the minimum recommended thicknesses for the flanges and webs were followed. The flange width increased by 33.3% while the thickness of the top and bottom flanges doubled in the negative moment region (specified as 25% of the girder's span length). The bottom flange width and web thickness remained constant through the entirety of the bridge. Interior stiffeners (½″ thick) were provided at the location of the K-frames and struts and were one-half the width of the top flange (in the positive moment region) to simplify meshing of the FE model.

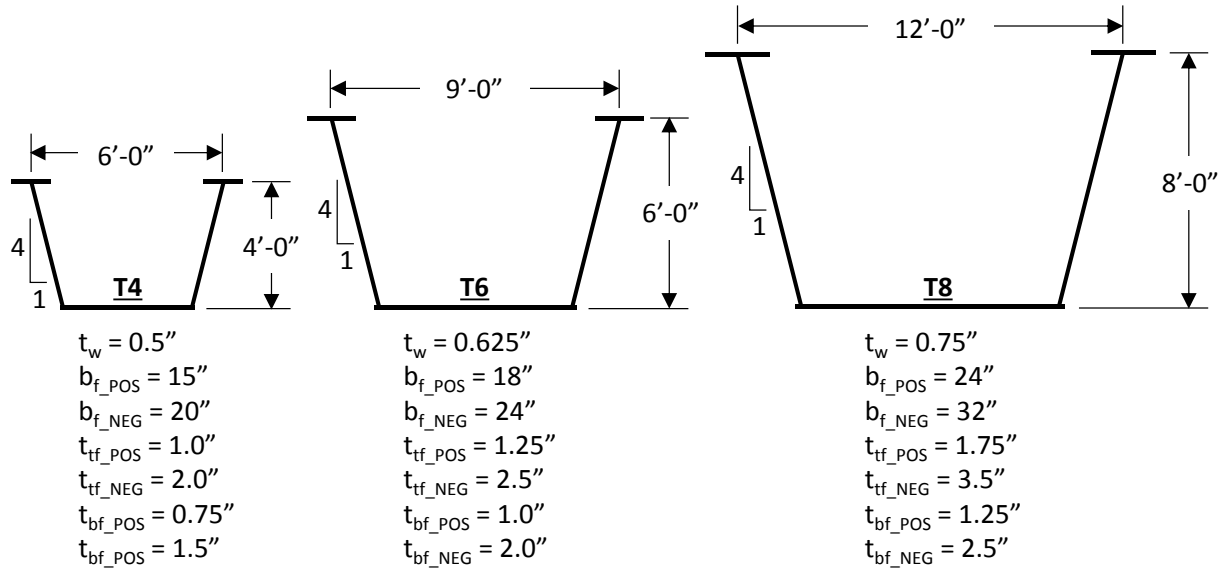

Figure 9.51 Cross-Sections Used for the I-Girder Parametric Study

9.7.3 Tub Girder K-Frames

For this study, L4x4x3/8 angles were used for the K-frame members (chords and diagonals) and the stiffness of these members were reduced to account for the connection eccentricity of the single angle members. The following stiffness reduction factor was used that was specifically developed for members of a K-type cross frames (Battistini et al. 2013):

$$R_{reg-SK} = 0.943 - 0.042\frac{S}{h_b} - 0.048\bar{y} - 0.420t \quad (9.5)$$

where,
S = girder spacing
h_b = height of the brace
$\bar{y}$ = distance from connection pate to angle center of gravity
t = thickness of the angle

The cross-frames were located at every other panel point (at 16 feet on center) with struts located at the panel points without K-frames. The K-frame members and struts were modeled using liner spring elements with the stiffness equal to the axial stiffness of the angle multiplied by the stiffness reduction factor (Equation 9.5).

9.7.4 Load Application on Tub Girders and Connection of Bracing Members

A cross-section of the curved tub girder system is shown in Figure 9.52. The loads from the wet concrete deck and the PCPs were applied to the nodes at the web-to-top flange intersection (at 8 feet on center). The torsional effects from the bridge overhang bracket to support the wet concrete deck on the exterior girders were not considered. The weight of the tub girders was applied using gravitational acceleration of the shell elements. No load factors were used for the analysis.

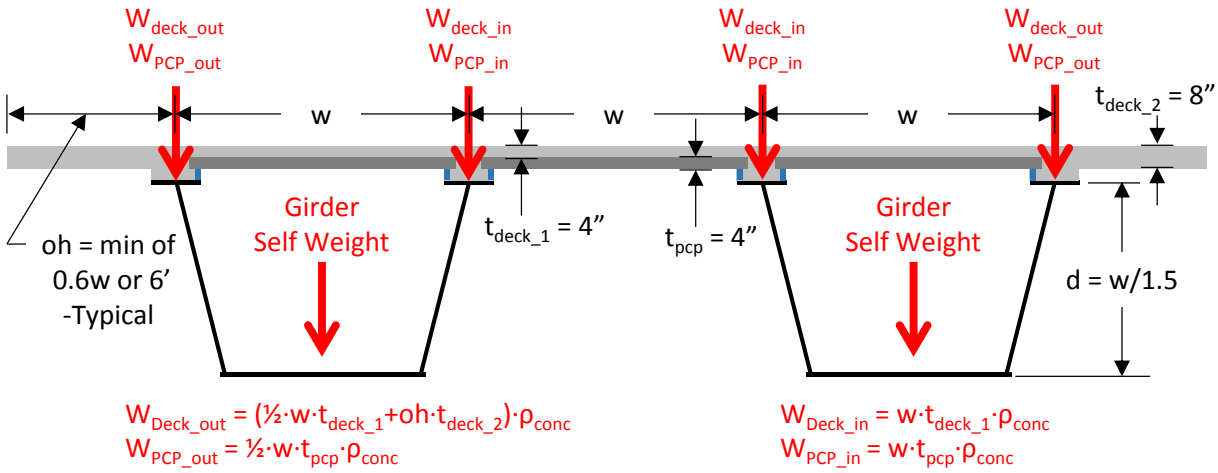

Figure 9.52 Loads on Curved I-Girder System

9.7.5 Finite Element Model – Tub Girder Parametric Study

A cross-section of the FE model for the curved tub girder parametric study is shown in Figure 9.53. S8R5 shell elements were used for the flanges, webs, and the stiffeners in the curved tub girder system (8 elements through the depth of the girder and two elements across the width of the flanges). The K-frames were connected to the edge of the top flange and to the stiffener at 1/8th the girder depth above the bottom flange. B32 beam elements were used to model the K-frame and linear spring elements were used to model the PCPs. At the end supports, the center

nodes at the intersection of the web, bottom flange, and support diaphragm were fixed from translation in the vertical and radial directions. At the mid support, the center nodes at the intersection of the web, bottom flange, and stiffener were fixed from translation in the vertical, radial, and tangential directions. The warping stiffness of the bottom flange was not adjusted to account for any restraint from a bearing stiffener. Figure 9.54 shows the meshed tub girder and the diaphragms (internal and external) at the support.

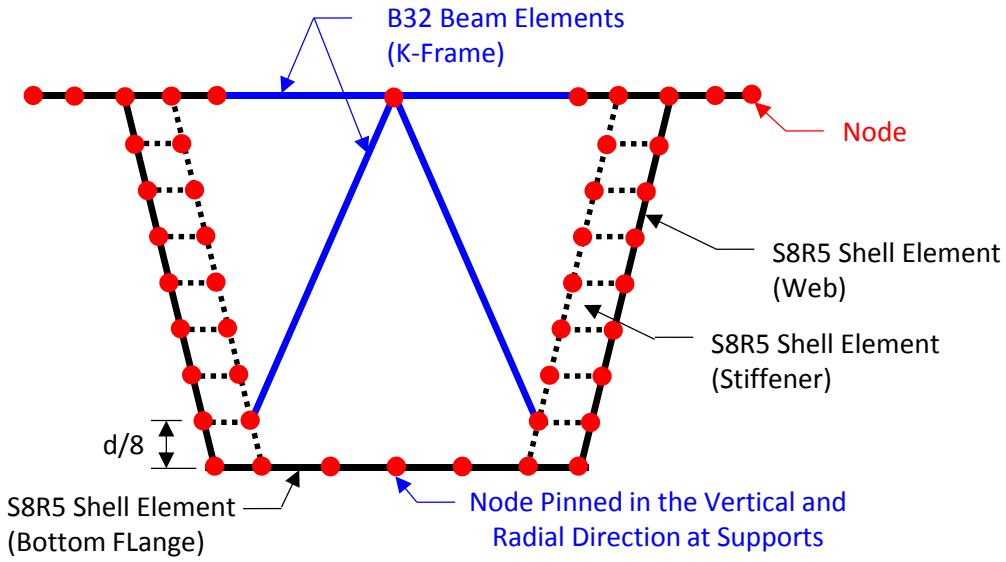

Figure 9.53 Cross-Sections of FE Model for the Tub Girder Parametric Study

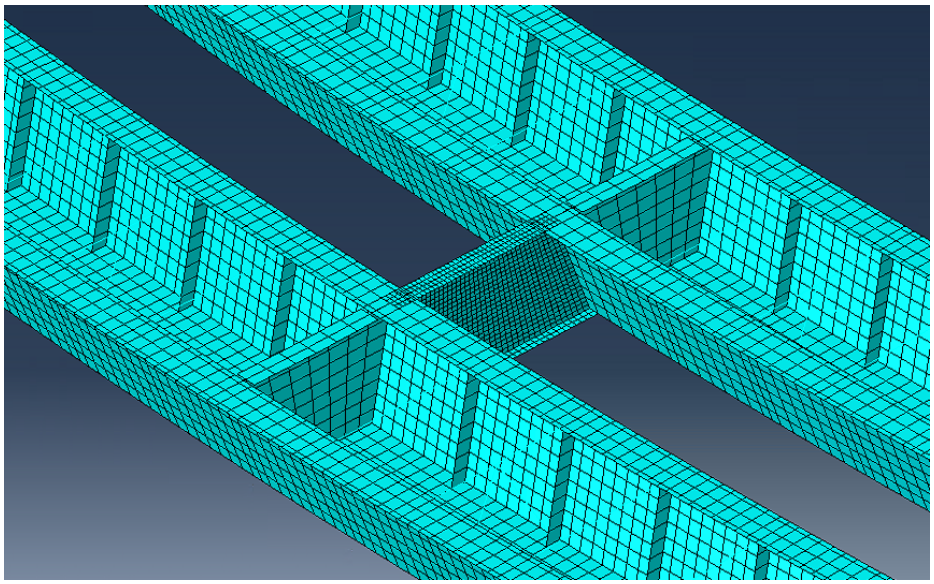

Figure 9.54 Tub Girder Internal and External Diaphragms at Support

The model of the curved tub girder system was created with the K-frames installed prior to the application of the steel load (it is typical for the K-frames to be installed in the fabrication

shop). In the FE model, the top flanges of all girder were at the same elevation prior to the application of any load on the system. Two placement sequences where investigated a non-continuous PCP placement (Option A) and a continuous PCP placement (Option B). A non-continuous PCP placement (Option A) would involve setting and connecting the PCPs at the end of the span prior to placing the unconnected PCPs at the center of the span (note that this potentially cause fit-up issues for the last PCP in each span). For this case, the PCPs would act as bracing elements during both the placement of the majority of the PCPs and during the placement of the wet concrete deck. A continuous PCP placement (Option B) would involve first setting all of the PCPs on the system and then connecting the PCPs towards the end of the span. For this case, the PCPs would only act as bracing elements during the application the placement of the wet concrete deck. Option A would potentially increase the effectiveness of the PCPs as bracing elements while Option B would likely be easier to construct. A continuous deck placement was used in the model and the stiffening effects of the concrete as it cured was not considered. The following sequence was used for the model:

1. Create model of curved tub girder system with K-frames installed and boundary conditions applied
2. Apply steel dead load to entire model (Load Step 1)
3. Connect PCPs at the end of the girders span (Option A)
4. Apply PCP load to Span 1 (Load Step 2)
5. Apply PCP load to Span 2 (Load Step 3)
6. Connect PCPs at the end of the girders span (Option B)
7. Apply deck load to Span 1 (Load Step 4)
8. Apply deck load to Span 2 (Load Step 5)

9.7.6 Results from Parametric FEA of Tub Girder System

This section summarizes the results of the parametric FEA for the tub girder system. The goal was to investigate the potential of using PCPs as bracing elements in curved girder systems as a replacement for the traditional top lateral truss (which is commonly made of WT diagonal members).

Tub Girder Deformation during Construction

Table 9.23 shows the maximum twist of the two tub girders at the 5 different loading stages during construction. A traditional X-type top lateral truss was used with the members sized so that an equivalent plate thickness of 0.05 in was achieved for all 9 FE models. The top lateral truss was assumed to be installed prior to application of steel dead load (as it is common for the top lateral truss to be installed in the fabrication shop). In general, the maximum twist of the tub girders increased as the depth (and corresponding span) of the girder increased and as the radius of curvature of the girder decreased. A maximum twist of 0.93 degrees was observed which occurred in the largest tub girder (T8) at the tightest radius of curvature (R600) when the two span system was unevenly loaded by the placement of the concrete deck (Load Step 4).

Table 9.23 Max Tub Twist at Various Load Steps (X-Type Brace - t_{eq} = 0.05 in – 100%)

Tub Girder System	Max Twist (deg) Load Step 1 (Steel DL)	Max Twist (deg) Load Step 2 (+ PCP Span 1)	Max Twist (deg) Load Step 3 (+ PCP Span 2)	Max Twist (deg) Load Step 4 (+ Deck Span 1)	Max Twist (deg) Load Step 5 (+ Deck Span 2)	Max Twist All Load Steps (deg)
T4-R1800	0.01	0.09	0.07	0.10	0.07	**0.10**
T4-R1200	0.02	0.11	0.08	0.14	0.10	**0.14**
T4-R600	0.04	0.17	0.12	0.27	0.18	**0.27**
T6-R1800	0.03	0.16	0.13	0.21	0.15	**0.21**
T6-R1200	0.05	0.21	0.16	0.31	0.21	**0.31**
T6-R600	0.10	0.35	0.24	0.59	0.38	**0.59**
T8-R1800	0.07	0.26	0.20	0.31	0.21	**0.31**
T8-R1200	0.11	0.34	0.25	0.47	0.32	**0.47**
T8-R600	0.21	0.58	0.39	0.93	0.61	**0.93**

Note: Top lateral brace attached prior Load Step 1 on 100% of span

The preferred sequence of construction would likely be to attach the PCPs to the top flange after all of the PCPs have been place on the system. As mentioned previously, a non-continuous PCP placement and connection plan (i.e. placing and connecting the PCPs at the end of the span and then infilling with PCPs between the connected PCPs) could potentially cause fit-up issues for placement of the last PCP in each span. Table 9.24 shows the maximum twist of the two tub girders at the 5 different loading stages during construction. The PCPs with connection C.2.MIN were connected to the system between Load Step 3 and Load Step 4. Excessive twist were observed for all 9 FE models indicating that the tub girders do not have enough torsional stiffness without a top lateral truss to support both the weight of the girders and the weight of the unattached PCPs.

Table 9.24 Max Tub Twist at Various Load Steps (PCP with C.2.MIN – 50%)

Tub Girder System	Max Twist (deg) Load Step 1 (Steel DL)	Max Twist (deg) Load Step 2 (+ PCP Span 1)	Max Twist (deg) Load Step 3 (+ PCP Span 2)	Max Twist (deg) Load Step 4 (+ Deck Span 1)	Max Twist (deg) Load Step 5 (+ Deck Span 2)	Max Twist All Load Steps (deg)
T4-R1800	0.48	5.72	2.65	2.75	2.64	**5.72**
T4-R1200	0.67	6.52	2.84	3.03	2.88	**6.52**
T4-R600	1.01	8.08	2.98	3.40	3.15	**8.08**
T6-R1800	1.24	1.76	1.59	2.27	1.90	**2.27**
T6-R1200	1.57	2.19	1.93	3.00	2.45	**3.00**
T6-R600	1.98	13.04	4.39	5.35	4.76	**13.04**
T8-R1800	2.02	12.49	5.47	6.16	5.78	**12.49**
T8-R1200	2.38	13.17	5.34	6.24	5.73	**13.17**
T8-R600	2.80	14.94	4.93	6.58	5.50	**14.94**

Note: PCP with C.2.MAX attached between Load Step 3 and Load Step 4 on the end 25% of each span

Table 9.25 shows the maximum twist of the two tub girders at the 5 different loading stages during construction when the PCPs with connection C.2.MIN were attached to the top flange between Load Step 1 and Load Step 2. This FE modeling sequence approximates the case where the PCPs are attached as they are placed (starting near the support and working towards the center of the spans) which would be less convenient than first placing all of the PCPs and then creating

the connection. Comparing the girder twist from Table 9.23 with Table 9.25 it is observed that the girders deformation is much larger using the PCPs connected at the ends than using traditional bracing method along the entire span. In fact, the twist of girders under their own self weight (Load Step 1 - steel DL) increased by more than an order of magnitude when no top lateral truss was present (from 0.01 to 0.48 degrees for T4-R1800 and from 0.21 to 2.80 degrees for T8-R600).

Table 9.25 Max Tub Twist at Various Load Steps (PCP with C.2.MIN – 50%)

Tub Girder System	Max Twist (deg) Load Step 1 (Steel DL)	Max Twist (deg) Load Step 2 (+ PCP Span 1)	Max Twist (deg) Load Step 3 (+ PCP Span 2)	Max Twist (deg) Load Step 4 (+ Deck Span 1)	Max Twist (deg) Load Step 5 (+ Deck Span 2)	Max Twist All Load Steps (deg)
T4-R1800	0.48	0.70	0.65	0.82	0.71	**0.82**
T4-R1200	0.67	0.93	0.84	1.15	0.98	**1.15**
T4-R600	1.01	1.34	1.19	1.88	1.53	**1.88**
T6-R1800	1.24	1.63	1.50	2.05	1.76	**2.05**
T6-R1200	1.57	2.03	1.84	2.70	2.27	**2.70**
T6-R600	1.98	2.53	2.18	3.88	3.03	**3.88**
T8-R1800	2.02	2.53	2.32	3.11	2.68	**3.11**
T8-R1200	2.38	2.95	2.65	3.89	3.26	**3.89**
T8-R600	2.80	3.56	3.08	5.30	4.08	**5.30**

Note: PCP with C.2.MAX attached between Load Step 1 and Load Step 2

Without a top lateral truss, the stiffness of the tub girder system was shown to decrease considerably under the steel dead load. The FE models used in this study assumed that the entire steel superstructure was erected prior to application of the steel dead load. In reality, the curved steel tub girder will be loaded with its own self weight as it is lifted into place. It is expected that the increased flexibility of the curved tub girder system without a top lateral truss will prohibit the lifting of the tub girders. Research at the University of Texas on "Improved Tub Girder Details" TxDOT project 0-6862 is currently investigating lifting of tub girders with only a partial top lateral truss installed. Furthermore, this research is investigating the possibility removing the top flange lateral truss near midspan where the torsional forces are low (Armijos et al. 2018). Figure 9.55 shows the girder twist when the top lateral truss members (with t_{eq} = 0.05 in) are connected (prior to Load Step 1) along the entire span versus when they are only connected at the end 25% of each span for a highly curved system (R = 600 ft). The girder twist at midspan is considerably larger for the case where top flange truss is only connected near the supports. Table 9.26 shows the maximum girder twist when the top lateral truss members were connected at the end 25% of the each span for all 9 FE models. The maximum girder twist is considerably larger (by approximately four times) than in Table 9.23 where the truss members are connected across the entire span. Therefore, it is expected that panels near midspan can only be eliminated for straight or mildly curved girder systems.

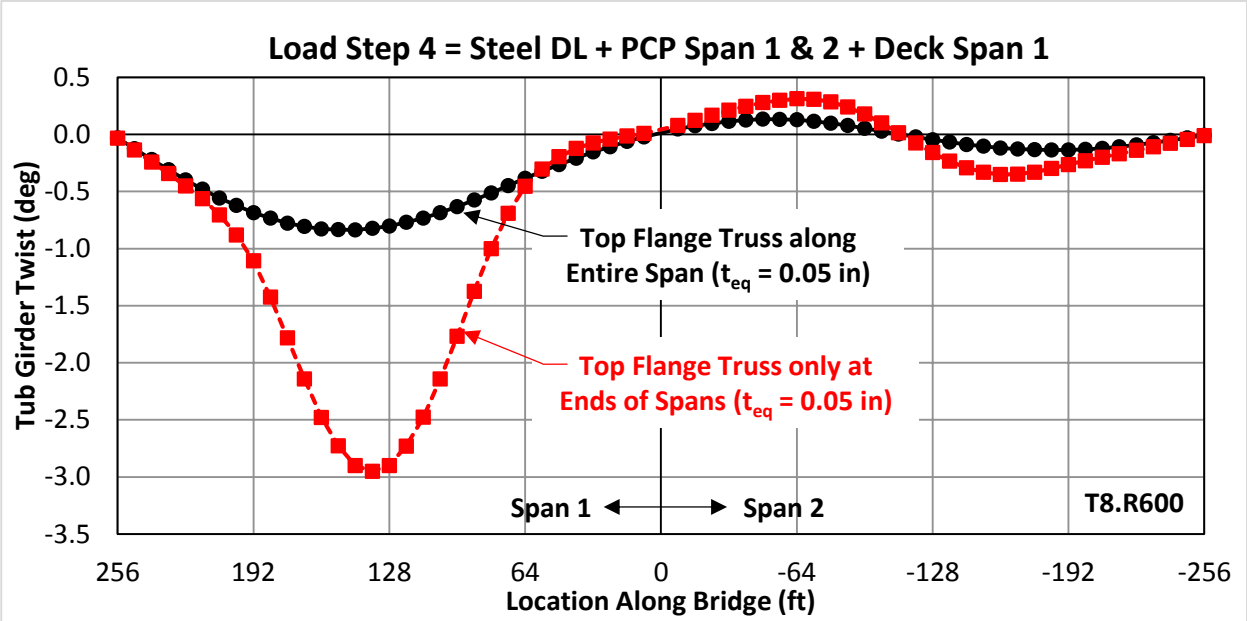

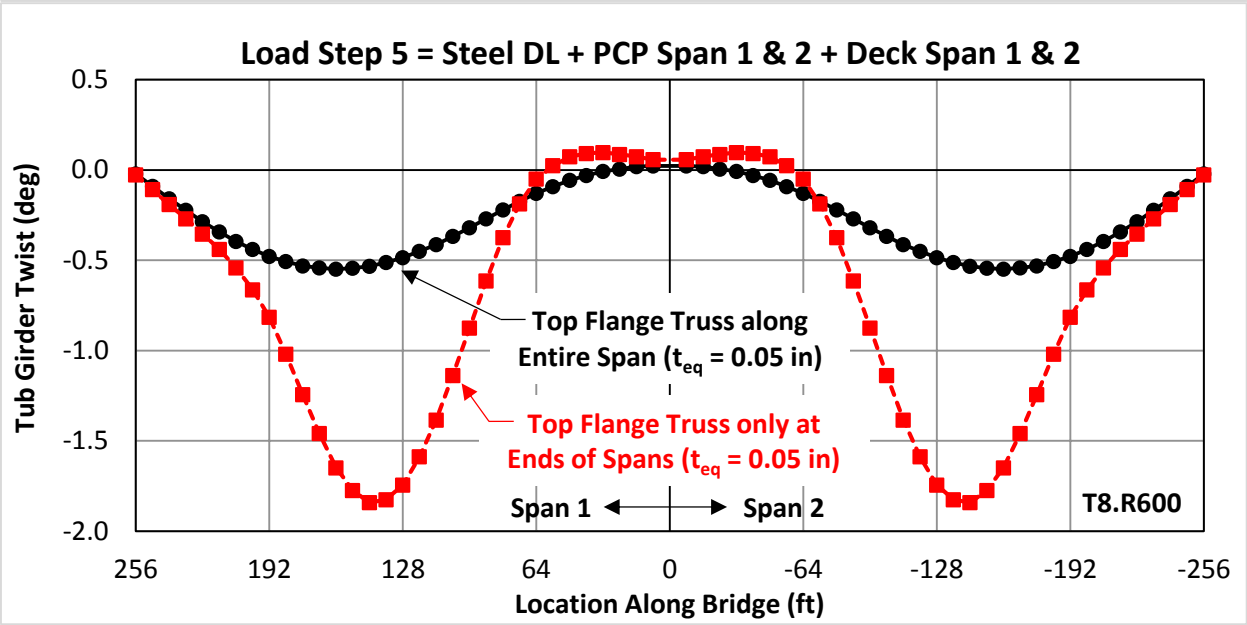

Figure 9.55 Tub Girder Twist with and without Top Flange Truss along Entire Span – T8.R600

Table 9.26 Max Tub Twist at Various Load Steps (X-Type Brace - t_{eq} = 0.05 in – 50%)

Tub Girder System	Max Twist (deg) Load Step 1 (Steel DL)	Max Twist (deg) Load Step 2 (+ PCP Span 1)	Max Twist (deg) Load Step 3 (+ PCP Span 2)	Max Twist (deg) Load Step 4 (+ Deck Span 1)	Max Twist (deg) Load Step 5 (+ Deck Span 2)	Max Twist All Load Steps (deg)
T4-R1800	0.05	0.32	0.26	0.41	0.28	**0.41**
T4-R1200	0.08	0.39	0.30	0.58	0.39	**0.58**
T4-R600	0.15	0.61	0.43	1.08	0.71	**1.08**
T6-R1800	0.14	0.62	0.48	0.93	0.64	**0.93**
T6-R1200	0.21	0.79	0.59	1.34	0.90	**1.34**
T6-R600	0.39	1.27	0.87	2.50	1.57	**2.50**
T8-R1800	0.26	0.89	0.68	1.26	0.85	**1.26**
T8-R1200	0.39	1.17	0.86	1.87	1.23	**1.87**
T8-R600	0.69	1.87	1.22	3.53	2.12	**3.53**

Note: Top lateral brace attached prior Load Step 1 on end 25% of each span

Summary of Tub Girder Parametric Study

Results from this parametric study on the curved tub girder systems indicate that curved tub girders without a top lateral truss are likely too flexible to carry their own self-weight. Additionally, the 9 systems studied certainly do not have the stiffness required to carry the steel dead load and the weight of the PCPs without excessive deformation without a top lateral truss. Thus, a top lateral truss must be present to add stability to the girders during the construction of the steel superstructure and especially during the placement of the PCPs. The PCPs could be used as supplemental bracing elements to the top lateral truss to add stiffness and strength to the system during the placement of the concrete deck, however, it would likely be more cost effective to use a larger top lateral truss and leave the PCPs unconnected. Chapter 11 provides guidelines for using unconnected PCPs on curved tub girder bridges.

9.8 Summary of FEA of Steel Girders

This chapter focused on the finite element analysis techniques that were used to model the I-girder and tub girder systems with PCPs as bracing elements. The simplified truss model (explained in detail in Chapter 8) was used to represent the in-plane stiffness of the PCP/connection system while shell elements were used to model both the I-girders and tub girders. The FE models for both girder systems were validated with the experimental data from the laboratory tests conducted in Chapter 5 and Chapter 6, respectively. After validating the FE models, a series of parametric FEA studies were conducted to investigate the influence of PCPs on larger and more realistic curved girder systems (that were too large to be tested in the Ferguson Structural Engineering Laboratory). Several conclusion were drawn from the I-girder and tub girder finite element analysis:

- The FE model for the twin I-girder system with and without attached PCPs was validated with the 12 lateral load tests and the 27 gravity load tests performed at the Ferguson Structural Engineering Laboratory. In the FE model, the boundary conditions at the support were modified to account for the fact that the idealized warping free boundary condition could not be achieved in the laboratory. In general, the analytical results from the FE model corresponded well with the experimental results. For several cases with the PCPs connected to the top flange, the FE model

underestimated the stiffness of the system which was attributed to the fact that the idealized two diagonal X-frame model for the PCPs only represented the in-plane stiffness of the PCP/connection system. In reality, the connected PCPs provide a twisting restraint (discussed in Chapter 5) that was not accounted for in the FE model. While a shell element model for the PCP and WTs could more effectively capture the twisting restraint observed in the laboratory, the shell element model significantly overestimated the in-plane stiffness of the PCP/connection systems (likely due to the fact that the shell elements do not capture the deformation of the anchors in the concrete) as discussed in Chapter 8. Therefore, it was decided use the idealized two diagonal X-frame model to correctly represent the in-plane stiffness of the PCP/connection system and neglect the twisting restraint.

- The experiments in the laboratory (and the FE model validation) showed that connecting PCPs to the I-girders, reduced the forces in the cross-frame when it was connected at midspan. For larger more realistic I-girder systems (with multiple girders and multiple cross-frames in each span), the parametric study shows that connecting the PCPs at the ends of the spans does not significantly reduce the forces in the cross-frames throughout the bridge. Therefore, if the spacing of the cross-frames is governed by the forces in the cross-frames, adding PCPs to the system will not allow a significant number of cross-frames to be removed from the system.
- The experiments in the laboratory (and the FE model validation) also showed that connecting PCPs to the I-girders, reduced the twist of the I-girders under combined torsion and bending loads (especially when no cross-frame was connected at midspan and away from the midspan cross-frame when it was connected). The parametric study investigated the influence that the PCPs had on the torsional stiffness of a multi I-girder system with multiple cross-frames connected along the span. Results from the parametric study showed that connecting PCPs near the support had only a minimal effect on reducing the twist of the system as a whole. Therefore, while the addition of PCPs can significantly reduce the twist of the individual I-girders between the cross-frames, it does not significantly reduce the twist of the entire bridge system as a whole. Addition of the PCPs did, however, significantly reduce the lateral deflection of the girders during construction.
- The FE model for the tub girder system with and without the PCPs and DIAGs installed was validated with the 5 lateral load tests and the 24 gravity load tests performed at the Ferguson Structural Engineering Laboratory. In the FE model, the boundary conditions at the support were modified to account for the warping restraint provided to the bottom flange of the girder by the bearing pad. In general, the analytical result from the FE model corresponded well with the experimental results. The FE model was not significantly more accurate for the cases with the DIAGs than it was for the cases with the PCPs.
- The experiments in the laboratory (and the FE model validation) showed that connecting PCPs to the tub girder, reduced the twist of the girder under combined torsion and bending loads. The parametric study investigated the influence that the PCPs had on the torsional stiffness of the larger curved girder systems during the construction phase. The construction sequence is such that the PCPs will be placed

after the erection of the steel superstructure. Therefore, to replace the top lateral truss with PCPs, the tub girders must be capable to supporting their own self-weight without a top lateral truss until the PCPs can be attached to the top flanges. Result from the parametric FEA showed that the twist of the curved tub girders under its own self weight increase by more than an order of magnitude when no top flange truss was present. Therefore, it is likely not practical to erect the steel superstructure with no top lateral truss. The PCPs could be used as supplemental bracing elements to the top lateral truss to add stiffness and strength to the system during the placement of the concrete deck, however, it would likely be more cost effective to use a larger top lateral truss and leave the PCPs unconnected.

The results mentioned above are specific to the parameters of the FEA analyses described in this chapter. The parametric studies revealed that there are likely no major benefits to using PCPs as bracing elements on curved steel I-girder systems. Also, the typical construction sequence for curved tub girder systems will likely not make it possible to used PCPs as a replacement for the top lateral truss. Using unconnected PCPs on curved steel I-girder and tub girder bridges, however, may provide significant benefits by accelerating construction of the bridge and allowing the PCPs and deck to be placed in a manner to reduce demands on the bridge during construction. Chapter 11 provides guidelines for using unconnected PCPs on curved steel I-girder and tub girder systems.

Chapter 10. Parametric Finite Element Analyses of Straight and Horizontally Curved Precast Concrete U-Beam Systems

10.1 Introduction

Parametric finite element analyses (FEAs) were performed for straight and horizontally curved pre-cast concrete U-beams to develop a comprehensive understanding of the fundamental behavior of the prestressed concrete girders in combination with the partial-depth precast concrete panel (PCP) system. The main goal of the analysis was investigated the strength demand on the PCP panel and the proposed closure pour details. The parameters that were considered included the girder span length, horizontal radius of curvature and the concrete strength/stiffness. This study only focused on the behavior during critical stage during construction. Therefore, service and ultimate conditions in the finished bridge were not evaluated. Using the FE model of PCP panels developed in Chapter 8, the parametric finite element studies considered the interaction of PCP panels and connection stiffness with straight and horizontally curved precast concrete box girder systems**.** Based upon information collected from the pre-stressed concrete industry, some simplified analyses were also performed to study the behavior of the girder systems during lifting and erection. This chapter documents the development and the analysis assumptions of FEA models, the parameters considered and the results of the parametric study.

10.2 TxDOT Standard U-Beam Cross Sections

Over the time period from the mid-1980s to early-1990s, TxDOT developed several standard precast concrete U-beam sections, such as the U40 and U54 sections, to create alternatives to the commonly used precast concrete I-sections. The goal was not to replace the precast concrete I-beam but to provide an alternative with the potential to improve aesthetics and ease of construction. Since the first concrete U-beam was constructed in Houston in 1993, research has been conducted to provide better understanding of the basic behavior of the U-beams and contribute to the development of standard U-beam sections. In general, the standard concrete U-beam is trapezoidal in cross section and is open at the top with two flanged stems as depicted in Figure 10.1. The standard sections for U-beams are often referred to as ‘U123’ with the letter U indicating its shape and the number showing its depth in inches. While U40 and U54 sections are more commonly used for straight and short span bridge girder, the recently adopted U72, U84 and U96 are more suitable for spliced long span and horizontally curved application. In this study, U54 and U96 sections were selected to represent typical straight and horizontally curved U-beam system respectively.

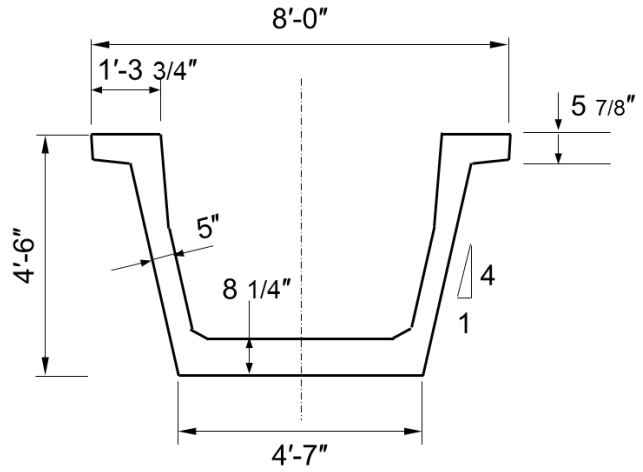

Figure 10.1 TxDOT Standard U-Beam Section U54

The nomenclature of the TxDOT U-shaped beams is U##, in which the number (##) indicates the nominal depth of the beam. In as such, TxDOT U54 section has a depth of 54 in. As shown in Figure 10.1, the U54 in has a total width at the top of the stems of 96 in., a thickness of 5 in. per web, and the bottom flange thickness can accommodate three rows of strands, varying between 6.25 in. (U54A) and 8.25 in (U54B). Figure 10.1 shows the configuration and dimensions of the U54B beam cross-section. For normal concrete strengths and 0.5 in. diameter strands, the recommended economical span length limit is 130 ft. with a girder spacing of 9.75 ft. for the U54 beam in TxDOT Bridge Design Manual.

The TxDOT U96-10 section has a depth of 96 in. with a total width at the top of the stems of 135 in., a thickness of 10 in. per web, and a minimum bottom flange thickness of 9 in. Figure 10.2 shows the configuration and dimensions of the U96 beam cross-section. Since U96 was mainly developed for spliced concrete girder applications, the span length can be in the range of 265 ft.~280 ft. with a girder spacing of approximately 20 ft., resulting in fewer girder lines. The construction of spliced concrete U-beams will typically require shoring frames and additional construction steps until cast-in-place closure pours are completed and continuity prestressing is installed.

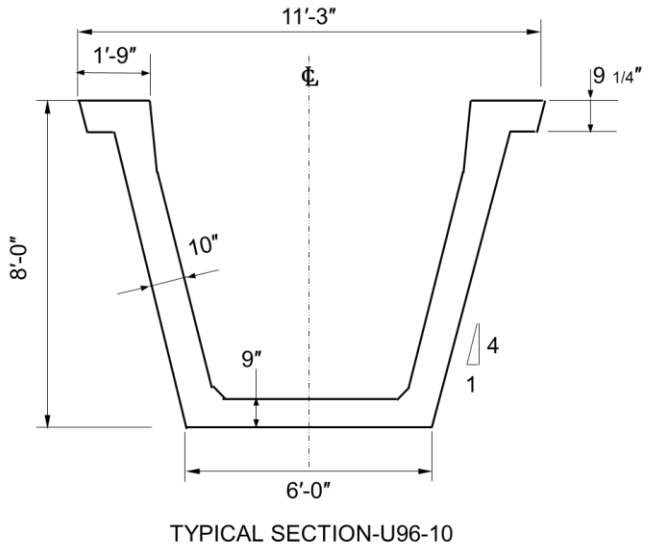

Figure 10.2 TxDOT Standard U-Beam Section U96-10

10.3 Assumptions and Consideration in FEA Models

10.3.1 Modeling of U-Beam Geometry

The goals of the analysis were to determine range of magnitudes in the brace forces of the concrete girders during construction. As a result, the main objective was to capture the stiffness of the open girder section and interaction with PCP panel and cast-in-place closure pour details. The research team relied up the extensive FEA studies that have been carried out on steel tub girders. Instead of using solid elements to comprise the girders, shell element models similar to the steel tub girder models were utilized that provided a good measure of the stiffness of the girder sections. To simplify the modeling of concrete U-beam sections, the original concrete section with solid walls was transformed into an equivalent steel section composed of thin shells (original thickness divided by the modular ratio of Es / Ec=6 with Es=29000 ksi and Ec=4833 ksi respectively). Shell elements are generally used to model features that are relatively thin. Although different literatures have specified different criteria to justify the rationality of using shell elements, a general rule of thumb is that the thickness of the body is at least 20 times less than the length. For U96 beam (depth of beam = 96 inches), the maximum thickness of the concrete wall is 9.25 inches. If assuming a span-to-depth ratio of 25, the ratio of span length to maximum wall thickness is around 260, therefore, satisfying the criterion. See Figure 10.3.

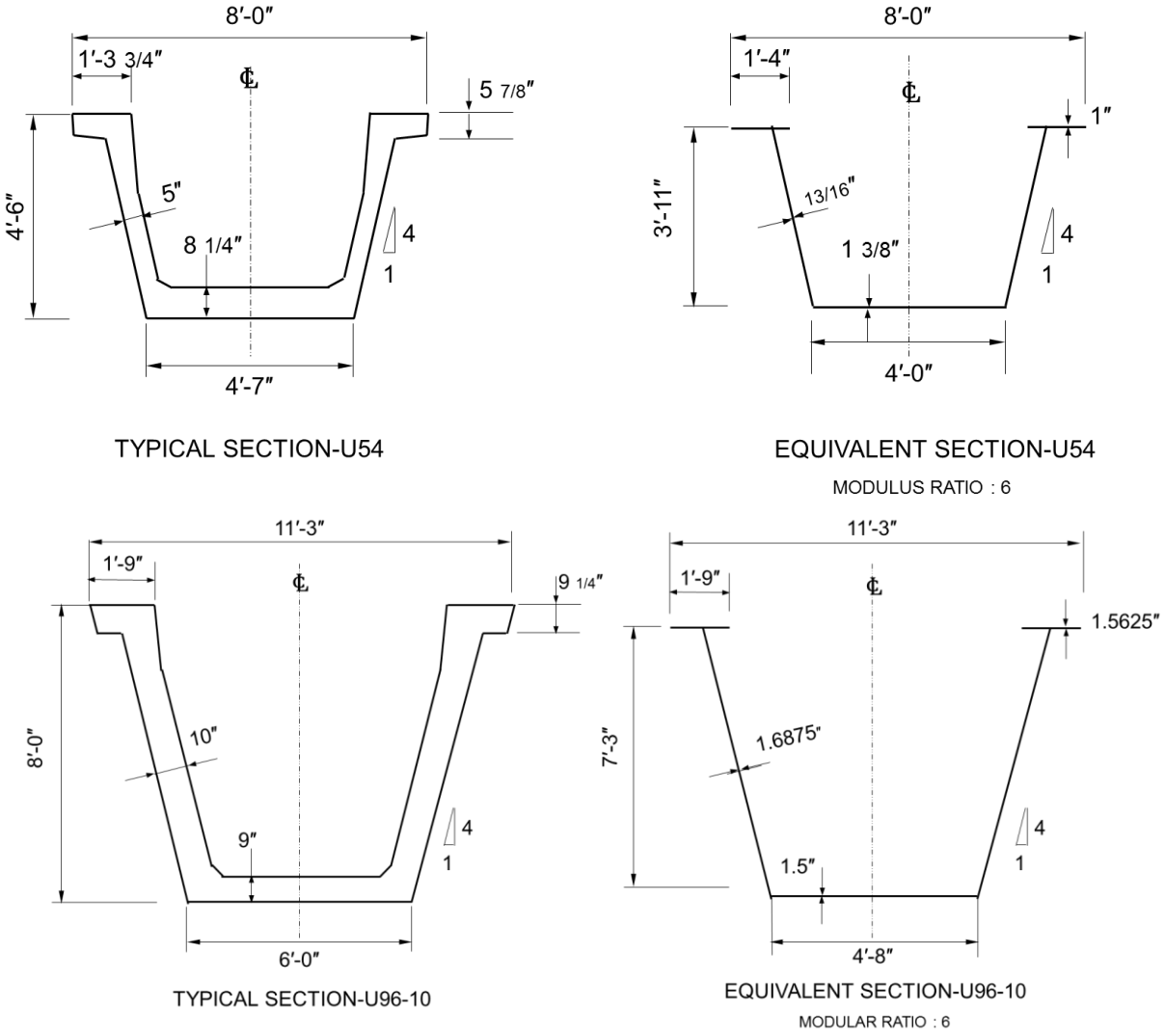

Figure 10.3 U96 and U54 Beam and Equivalent Steel Section dimensions

Also, since the focus of this study is based upon the force demand rather than the stress analyses on the concrete sections, this simplification is suitable for the study. The modelling decisions at the outset were directed at properly capturing the cross-sectional stiffness. Table 10.1 and Table 10.2 provide comparisons of the section properties for U96/U54 and the corresponding equivalent sections. The axial stiffness EA and bending stiffness EI are almost identical. Moreover, since PCPs were included in the model, the cross section of the U-beam sections were quasi-closed and the enclosed area by the middle surface of each wall was greater than that of the equivalent section with PCP modeled as a pair of spring elements connected at the level of top flange stems. Compared with solid element models, the models comprised of shell elements are easier to mesh and less prone to negative Jacobian errors. Therefore, the simplified modeling of the U-beams comprised of shell elements provided a reliable option for this study.

Table 10.1: Section Property Comparison Summary for U96-10

Modulus Ratio n=6					
Concrete U-Beam **U96-10** Section Properties			Equivalent Steel Tub Section Properties		
Elastic Modulus Ec	4833	ksi	Elastic Modulus Es	29,000	ksi
Poisson's Ratio ν	0.15		Poisson's Ratio ν	0.30	
Weight	2,791	plf	Weight	1522	plf
Area	2,680	$in.^2$	Area	447	$in.^2$
Axial Stiffness					
E_cA_c	12,952,440	kips	E_sA_s	12,963,000 (Error: +0.1%)	kips
I_x	2,806,535	$in.^4$	I_x	476,710	$in.^4$
Strong Axis Bending					
$E_c I_x$	$1.36x10^{10}$	$kips{\cdot}in^2$	E_sI_x	$1.38 x10^{10}$ (Error: +1.5%)	$kips{\cdot}in^2$

Table 10.2: Section Property Comparison Summary for U54B

Modulus Ratio n=6					
Concrete U-Beam **U54B** Section Properties			Equivalent Steel Tub Section Properties		
Elastic Modulus Ec	4833	ksi	Elastic Modulus Es	29,000	ksi
Poisson's Ratio ν	0.15		Poisson's Ratio ν	0.30	
Weight	1167	plf	Weight	633	plf
Area	1,120	$in.^2$	Area	187	$in.^2$
Axial Stiffness					
E_cA_c	5,412,960	kips	EsAs	5,426,060 (Error: +0.2%)	kips
I_x	403,020	$in.^4$	I_x	70,327	$in.^4$
Strong Axis Bending					
$E_c I_x$	$1.95x10^9$	$kips{\cdot}in^2$	E_sI_x	$2.03 x10^9$ (Error: +4.0%)	$kips{\cdot}in^2$

Three-dimensional FEA models of two typical three-span continuous curved U-beams were created to study the shear load demand of U-beams interacting with partial-depth concrete panels with the proposed closure pour detail. The performed analyses consider the construction loads and sequences during the concrete deck casting. Under the loading conditions in the laboratory shear frame test, the shear load was applied to specimen by a force couple in the plane of the panel. The torsional loading for most applications however is caused by eccentric gravity loading as a result of the horizontally curved geometry. Therefore, the three-span continuous curved girders shown in Figure 10.4 were developed for the parametric studies. The radius of curvature of the girder that was considered consisted of 1800, 1200 and 800 ft., which are a reasonable representation of geometries that would be used in practice. The models were created

as prismatic sections with constant depth, which are also reasonable with respect to what would be found in practice. The models were comprised of shell elements (Abaqus - S4R element) to model the U-beam section.

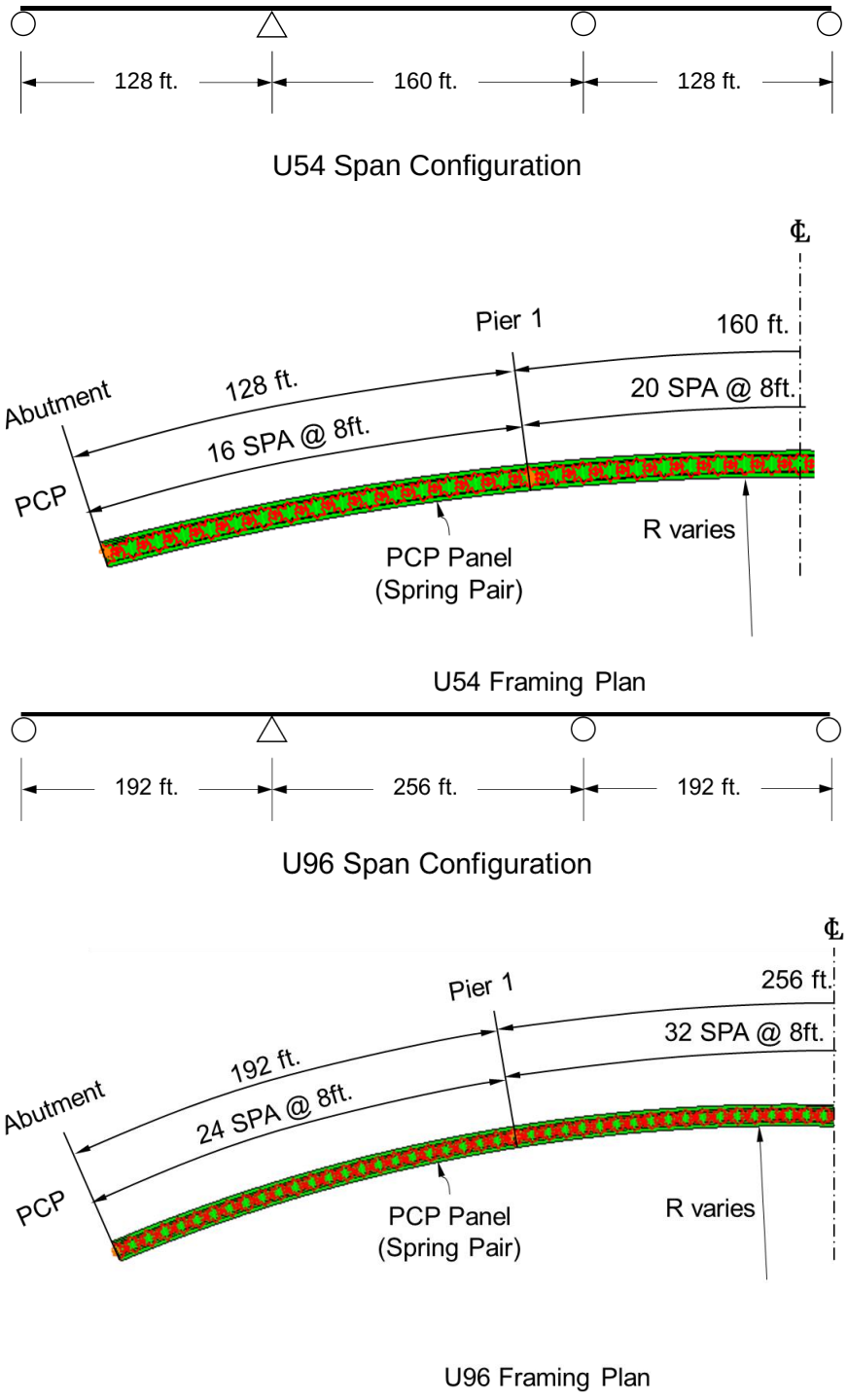

Figure 10.4 Framing Plans of U96 and U54 FE Models for Three-span Continuous Curved System

10.3.2 Modeling of Partial-Depth Precast Concrete (PCP) Panels

A pair of linear spring elements were used to represent the PCP panels in the FEAs as in Figure 10.5. The stiffness of the linear spring was defined in the line of action aligned with the pair of diagonal panel points. The general idea is to use a pair of spring elements to reflect the stiffness data of PCP panels with closure pour details. A more detailed discussion of this simplification can be found in Chapter 8. This simplification reflects the interaction between the PCP panel and closure pour details and would be beneficial for the construction sequence simulations discussed later in this document. The stiffness of the PCP interacting with the closure pour details was determined from the experimental panel shear deflection curves as shown in Figure 10.6 and summarized in Table 10.3.

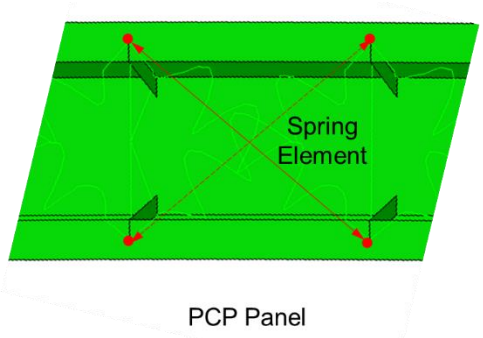

Figure 10.5 FEA Representation of PCP Panels using Spring Elements

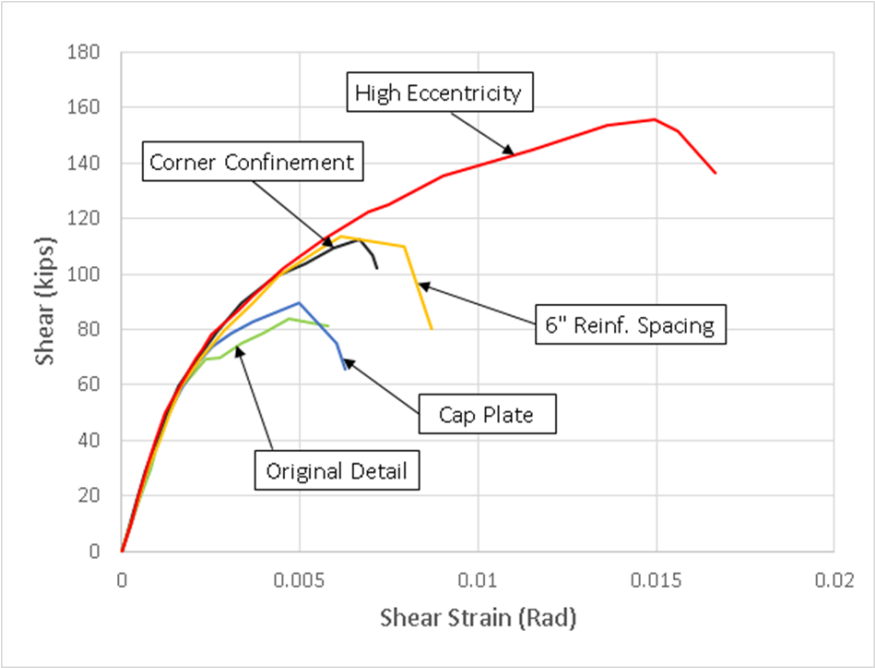

Figure 10.6 Experimental Panel Shear vs. Shear Deflection Curves

Table 10.3: Lab Test PCP Stiffness Summary

Elastic Modulus	29000	ksi.
Diagonal length L	136	in.
Panel length f	96	in.
Panel width w	99	in.
Closure Pour Detail	**Slope**	
Average Value	350	kip/in
Closure Pour Detail	**Shear Capacity**	
Original Detail	83	kip
Cap Plate Detail	90	kip
Corner Confinement	112	kip
6″ Reinf. Spacing	114	kip
High Eccentricity	156	kip

10.3.3 Modeling of Loading and Boundary Conditions

Figure 10.7 shows the support conditions applied on the FEA models. The girder expansion was fixed only at the first intermediate support with other translational components of displacement. Simple support conditions were applied at the mid-point of the bottom flange at girder ends and pier restraining the vertical movement. Two lateral supports were provided to prevent sectional twist and represent the diaphragm connection the twin girders. The simulated load stage is the concrete deck placement stage after all the PCP panels are placed in position as illustrated in Figure 10.8. The twin-girder system was simplified as a single girder. The interior girder was modeled because of the larger radius of curvature.

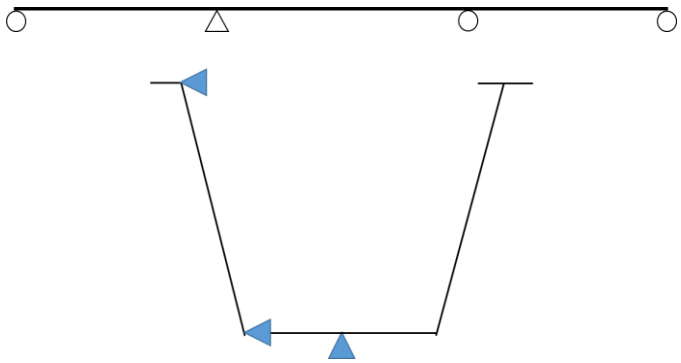

Figure 10.7 FE Model Support Conditions

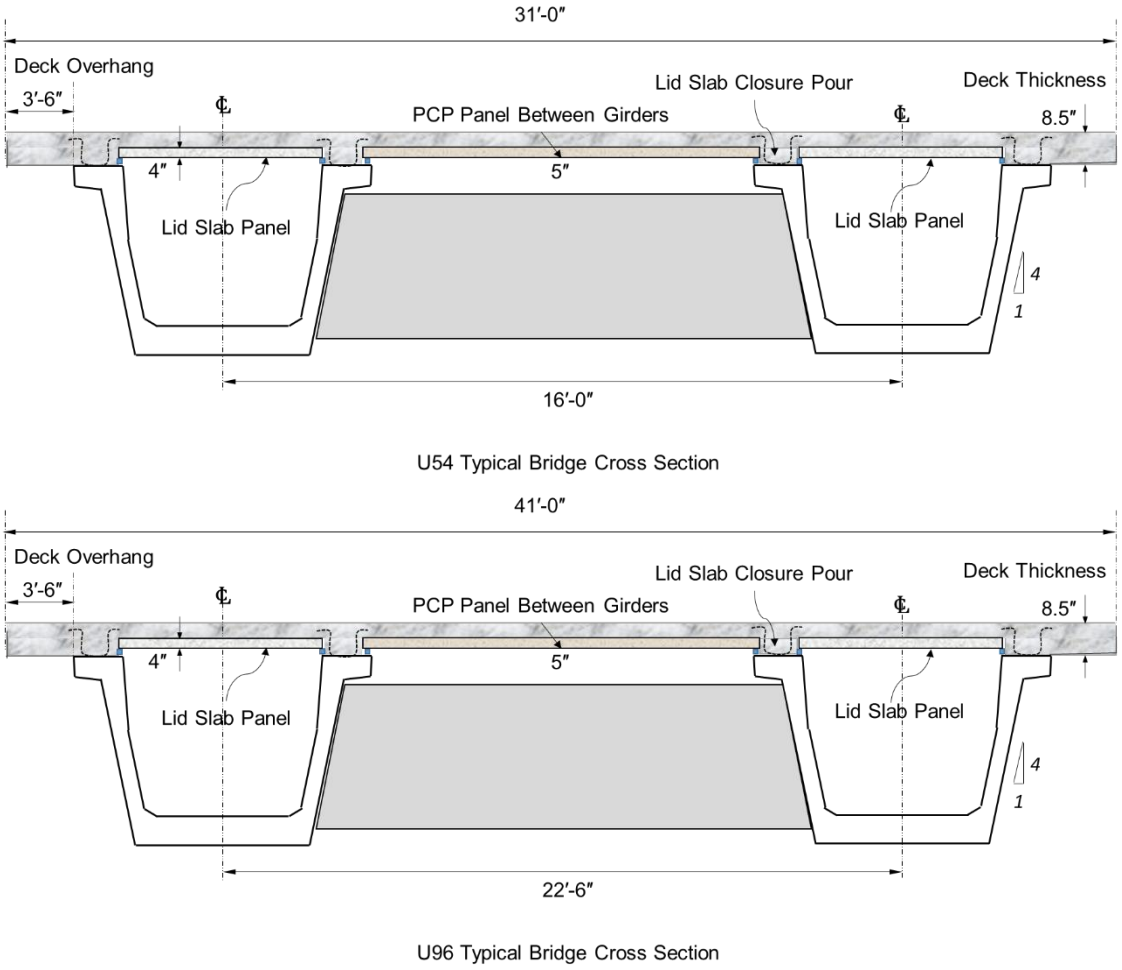

Figure 10.8 Typical Bridge Cross Section for U96 and U54

10.3.4 Construction Stages and Computational Simulation

The construction of spliced pre-cast concrete U-beams generally utilizes complex staged construction that requires temporary falsework. Shoring falseworks are necessary during construction because concrete U-beams have a relatively large self-weight. The weight per unit length for spliced U-beams typically range from 2000 plf to 3000 plf. Girder segments can weigh up to 200 tons. Therefore, stability is a major concern during shipping, handling and erection of the girder segments. Carefully planned field and erection engineering are required to ensure safe and rapid construction. Staged construction is performed, and the construction phases need to be carefully planned considering the the required additional steps for temporary falsework setup, lid slab casting and additional post tensioning.

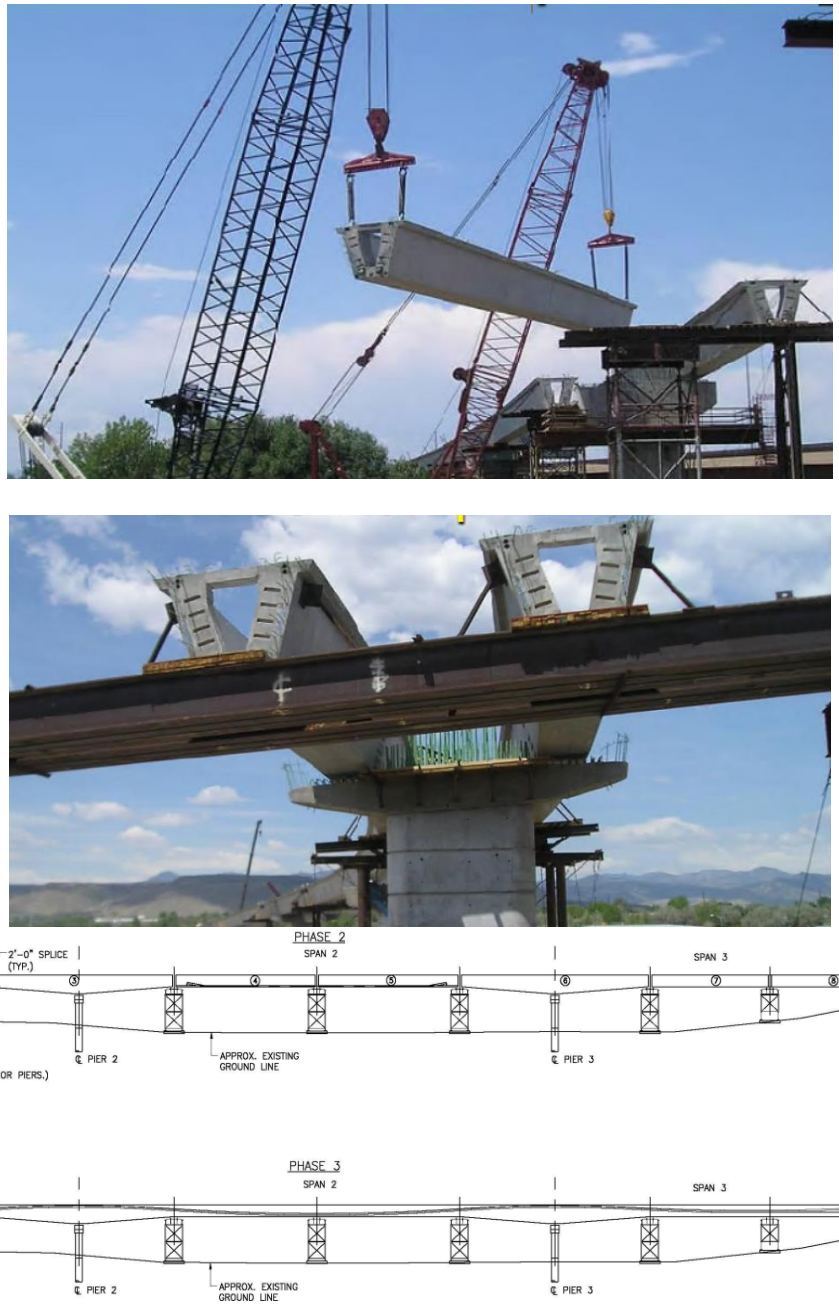

Figure 10.9 Stage-1-a Erection of U-Beam and U-Beam Stabilized on Shoring Towers and Piers And Shoring Tower Plan – Falsework provided at Beam Segment Ends (Reese and Nickas 2010)

Figure 10.10 Stage-1-b Cast of Splice, Pier Diaphragm, and Expansion Diaphragm (Reese and Nickas 2010)

Figure 10.11 Stage-1-c PCP between Webs Placed and Lid Slab with Closure Pour Cast in Place and Cured prior to Post-tensioning (Reese and Nickas 2010)

Figure 10.12 Stage-2-a PCP Panels between Girders Placed and Shoring Tower Removed (Reese and Nickas 2010)

Figure 10.13 Stage-2-b Deck Placed or Cast in Unshored Conditions (Reese and Nickas 2010)

The photos in Figure 10.9 through Figure 10.13 depict the complete construction sequences of a spliced concrete U-beam bridge project in Colorado. In general, the construction is performed in the two-primary staged-shored and unshored stage. The construction staging typically begins with the erection of the U-beam segments with cranes and spreader bars. Then, the beam segments are stabilized on the piers and temporary supports. Falsework shoring towers are usually provided at the ends of the U girder segments in the main span. After that, expansion diaphragms and splices are cast in place. Pre-cast concrete panels between the webs of the girder are placed and set on the girder flange stems. Temporary formworks are then placed, and the lid slab closure pours are cast in place. The lid slabs close the cross section and greatly increase the torsional strength and stiffness of the girders. PCP panels between the girders are placed after which the shoring towers can often be removed. The concrete topping slab can be place to complete the deck which is usually carried out in an unshored condition.

A common construction sequence would consist of the following deck placement in the following sequence to account for the constructability limits, as illustrated in Figure 10.14 1) the concrete is first cast from the left abutment to the dead load inflection point in the north span; 2) the concrete between dead load inflection point and the right abutment in the south span is cast second: 3) the concrete between the dead load inflection points in the center span would be cast third; 4) finally, the concrete between the points of dead load contra-flexure over the two piers is cast. For simplicity in the analysis, earlier concrete casts were not made composite for each subsequent cast. The deck load, the weight of deck overhang and all other construction loads were considered in the analyses. The eccentric loading and subsequent lateral force on the flanges from the overhang were also considered.

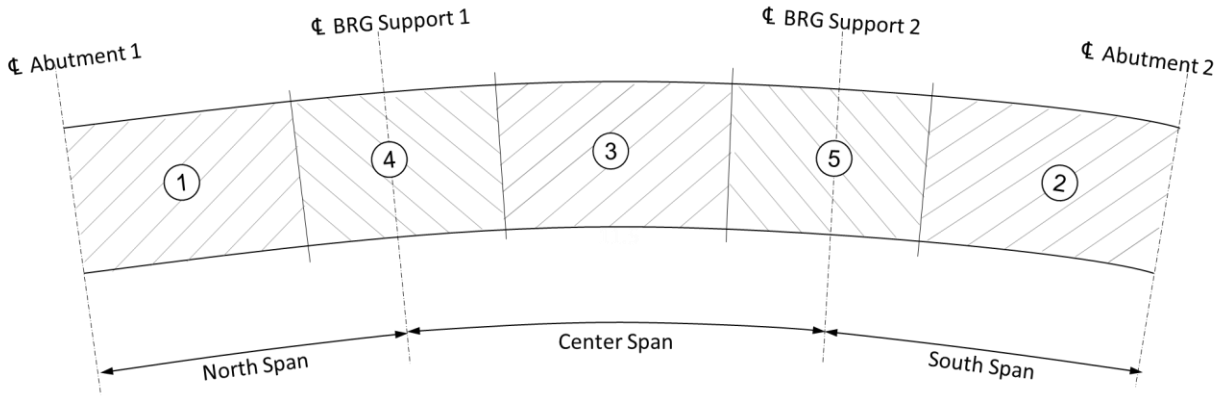

Figure 10.14 Three-span Continuous System deck placement sequence

To simulate the construction sequence, multiple steps were performed in the FEA analyses. Table 10.4 shows a summary of all the analyzed steps and a brief description of each step. The first step considered the first stage of the spliced U-beam construction in shored conditions. Only the gravity load of the girder and PCP panels were applied on the models. The FE models were stabilized and supported on the falsework and piers. In the second analysis step, linear spring element pairs were added into the FE models with no initial deformation to represent the gradual engagement of the PCP panels between webs and cured closure pour to form the lid slabs. The gravity load of the PCP panels between the girders were applied in this step. The following steps from 3 to 7 represent the deck placement sequences. The first two steps are depicted in Figure 10.15 and Figure 10.16.

Table 10.4: FEA Construction Sequence Definition

STEP NO.	STEP NAME	DESCRIPTION	Notes
1	GRAVITY	GIRDER SELFWEIGHT PCP BETWEEN WEBS TEMP SUPPORT LID SLAB NO ENGAGED	Shored
2	GRAVITY-1	LID SLAB ENGAGED TEMP SUPPORT REMOVED PCP BETWEEN GIRDERS	Unshored
3	CSTRN-NS POS M	NORTH SPAN POS M REGION	Unshored
4	CSTRN-SS POS M	SOUTH SPAN POS M REGION	Unshored
5	CSTRN-CS POS M	CENTER SPAN POS M REGION	Unshored
6	CSTRN-NS NEG M	NORTH NEG M	Unshored
7	CSTRN-SS NEG M	SOUTH NEG M	Unshored

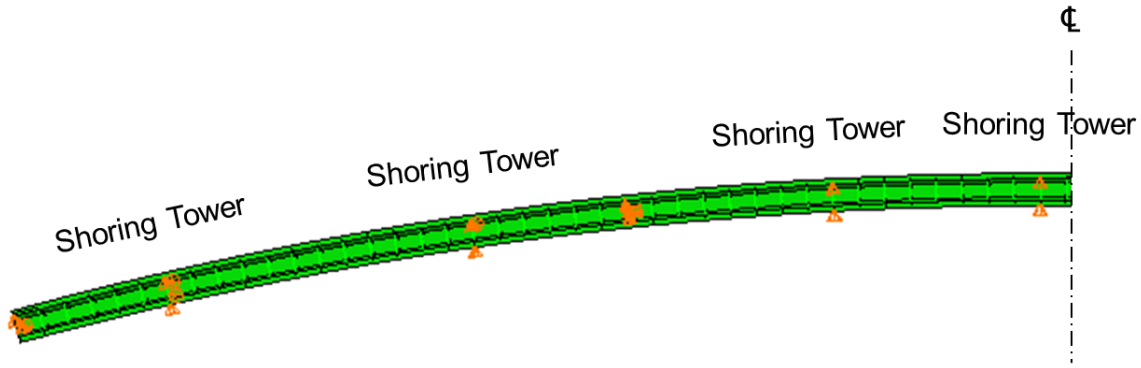

Figure 10.15 Step 1 FE Model in Shored Conditions

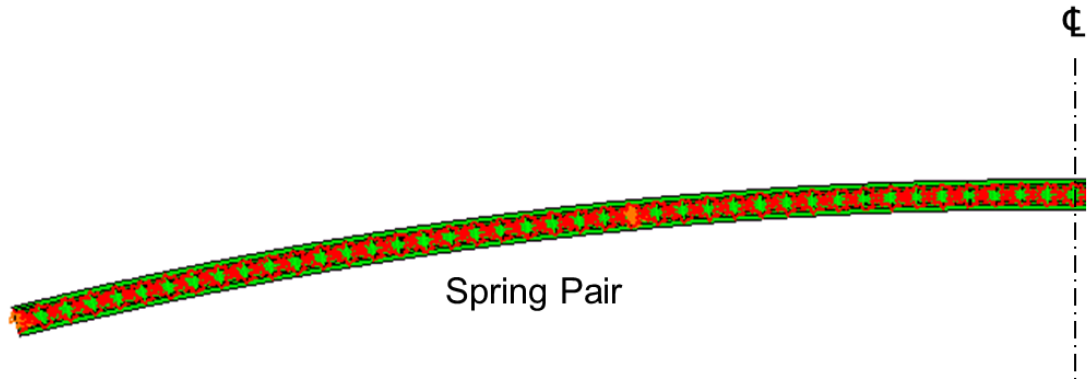

Figure 10.16 Step 2 FE Model with PCP Springs in Unshored Conditions

10.4 Design Parameters

The selected variables for the overall parametric study are shown in Table 10.5. Table 10.6 shows additional design variables considered in this parametric study.

Table 10.5: Design Parameters

Variable	Description / Selected Values
Specification & Codes	AASHTO LRFD Specifications 2014 TxDOT Bridge Design Manual 2015
Concrete Strength (psi)	Min 5000, Max: 8500 per TxDOT Bridge design manual
Girder Sections	TxDOT U54 and U96
Girder Spacing (ft.)	10′ for U54 and 22′ -6″ for U96
Span Length (ft.)	Max 128 for U54 and Max 240 for U96
Horizontal Radii of Curvature (ft.)	Infinity for U54 and {1800,1200, 800} for U96

The TxDOT Bridge Design Manual (2015) specifies that a standard concrete deck thickness of 8.5 in. Thinner concrete decks are not permitted. The Manual also states that the maximum overhang is 3.33 ft. beyond the design section for negative moment specified in

AASHTO LRFD Article 4.6.2.1.6, but not more than 1.3 times the girder depth. The minimum overhang is 0.5 ft. from the top beam or flange edge except for spread slab and box beams, which are permitted to have no overhang. See Figure 10.17.

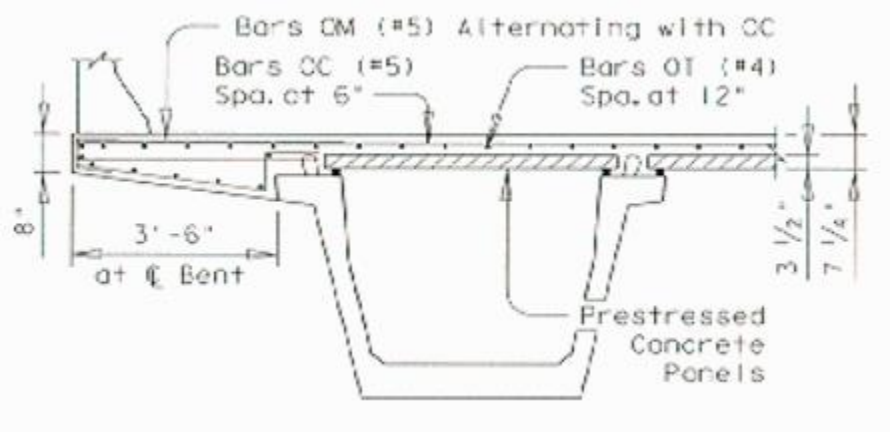

Figure 10.17 Typical Cross Section of Southbound Louettea Road Superstructure showing the Deck Overhang

Table 10.6: Additional Parameters

Material	Variable	Selected Values
Concrete Precast	Unit Weight (wc)	150 pcf
	Modulus of Ealsticity Ec	$57\sqrt{f'_c}$ (f'_c precast)
Concrete- CIP Slab	Unit Weight (wc)	150 pcf
	Modulus of Ealsticity	$57\sqrt{f'_c}$ (f'_c CIP)
	Deck Width	
	Deck Thickness (in.)	8.5
	Deck Overhang (ft.)	3′-6″
Concrete PCP	Unit Weight (wc)	150 pcf
Steel	Modulus of Ealsticity Es (ksi)	29000
Steel / Concrete	Modulus Ratio n	Es / Ec

10.5 Results and Discussion

10.5.1 Case Study of the Stability of the U96 Girder in Unshored Conditions during Construction

Pre-cast concrete U-beam sections generally have relatively large self-weights and are relatively weak torsionally during girder erection. The construction sequence, temporary construction bracing, and supports are crucial to ensure a safe and rapid construction. Before the casting of lid slab and the deck, falsework shoring towers are usually necessary, and the closure pour cast of lid slab has to be completed to enhance the torsional stiffness of the cross section

before the falsework towers can be removed. Otherwise, instability of the U-girder may occur. To study the stability behavior of the concrete U-beams during construction, a typical three-span continuous curved U96 system with the spans of 192 ft.-240 ft.-192 ft was modelled.

Three finite element models were built with the span arrangement. The selected parameter of interest is the horizontal radii of curvature. The chosen values for the radii were 1800 ft, 1200 ft, and 800 ft, which likely to occur in practice. Radii beyond 800 ft would require significant reductions in the permissible speed limits for safety. Large displacement analyses were performed on models considering only the girder self-weight. Support conditions were the same as considered for a typical three-span continuous system described in the previous chapter. From the lateral deflection and cross-sectional twist angle plot in Figure 10.18 and Figure 10.19, it can be concluded that in unshored conditions, U-beams are likely to experience global lateral torsional buckling (LTB) under self-weight. The instability behavior was observed in all three cases analyzed with significant amount of lateral deflection and cross section twist. The only difference in the analysis was that the most critical span shifted from center span to end span as the radius of curvature was varied. As a result, shored conditions would be recommended during most cases of construction of the lid slab.

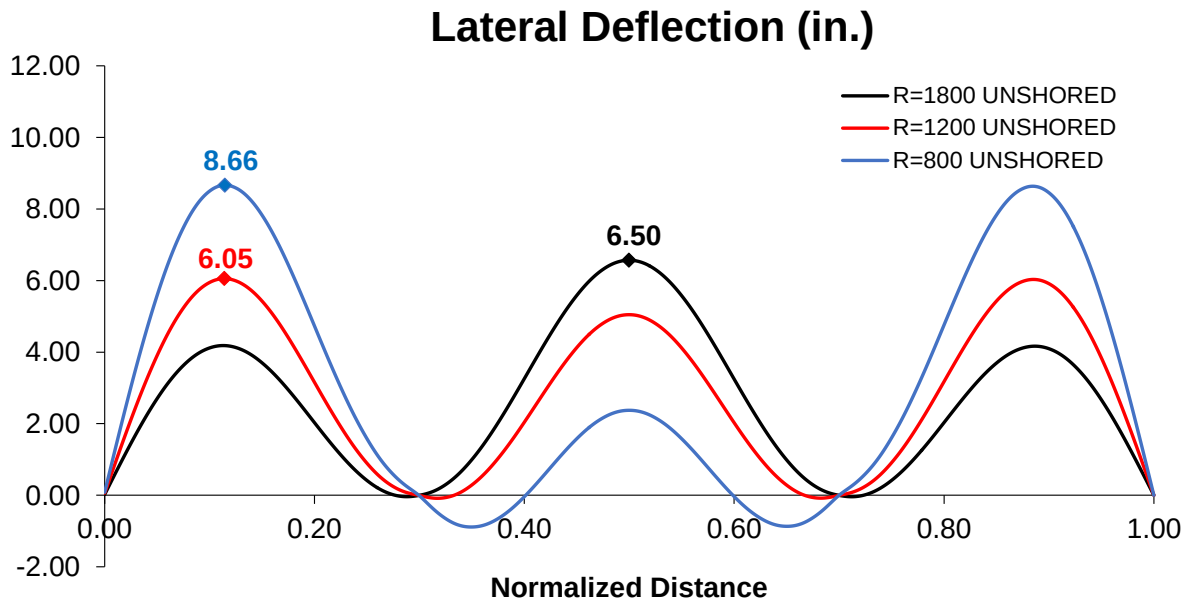

Figure 10.18 Lateral Deflection Distribution of the Girder with Different Radii of Curvature (Unshored)

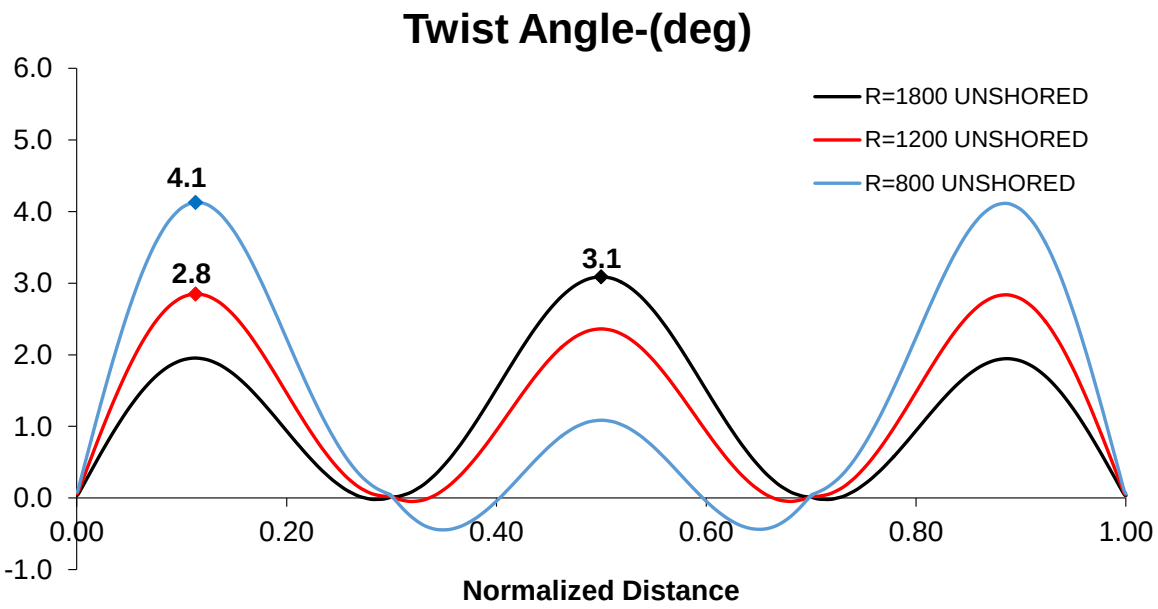

Figure 10.19 Sectional Twist Distribution of the Girder with Different Radii of Curvature (Unshored)

10.5.2 Estimation of Load Demands on PCP panels with Closure Pour during Construction

One of the primary goals to perform parametric finite element analyses on pre-cast concrete U-beams is to provide a reasonable estimation of the load demands on PCP panels with the proposed closure pour details during concrete deck placement. The estimated load demands could then be compared to the experimental loads tested in the laboratory and the feasibility of the proposed closure pour details would therefore be examined. Since PCP panels in this study were simplified and modelled as two linear spring elements with an equivalent stiffness calculated based on the shear frame test data, the forces on each pair of tension and compression spring must be decomposed into longitudinal components to obtain the resultant shear force. The general procedure of load demand estimation is summarized as follows: a pair of spring elements were created to represent the PCP panels with the proposed closure pour detail and the stiffness of the springs were determined from the shear force and deflection curves collected from the laboratory tests in Chapter 7; for each different case of U96/U54 beam models with different horizontal radius of curvatures, FE analyses were performed with the assumed concrete deck placement sequence; the critical panel with max spring forces was then identified at the critical construction stage and the criteria to determine the critical panels was to ensure that the absolute difference value of tension (with positive sign) and compression (with negative sign) forces on the panel to obtain maximum shear forces; the forces on tension and compression springs were then decomposed into the longitudinal direction of the beam to obtain the resultant shear forces on PCP panels; the load demands were then compared with the experimental load deflection curve to examine the shear deflection and whether the shear demand would exceed the test shear strength based on the lab data.

Case Study-1 Three-span Continuous Horizontally Curved U96 Beam with Different Radii of Horizontal Curvatures

A case study was performed to understand the shear demands on PCP panels with the proposed closure pour details during construction. Three-span continuous horizontally curved U96 girder FE models were studied with different radii of curvature. To reduce the computational cost, the commonly used twin U-beam system was simplified as a single U-beam with lateral restraint provided at the supports to simulate the restraining effect of the end diaphragm between the twin beams. The analyses were performed on U96 sections with a horizontal radius of 1800 ft., 1200 ft. and 800 ft., respectively. Based on the stiffness obtained from experimental shear force deflection curves, the equivalent linear spring stiffness was varied from 350 ~ 400 kip/in. In this study, the stiffness of the spring element was set at the minimum value of 350 kip/in which corresponds to the closure pour detail with extra shear reinforcement.

For each different radius of horizontal curvature, Figure 10.20 through Figure 10.22 present first the force distribution in the spring element pair at the critical construction stage and then the resultant shear forces on the critical panel were illustrated on a PCP panel sketch. From the figure, the load demands on the PCP panels increases with the horizontal radii of curvature while the critical panels remain the same. The maximum shear force occurred when R=800 ft. Figure 10.23 provides a summary of the results.

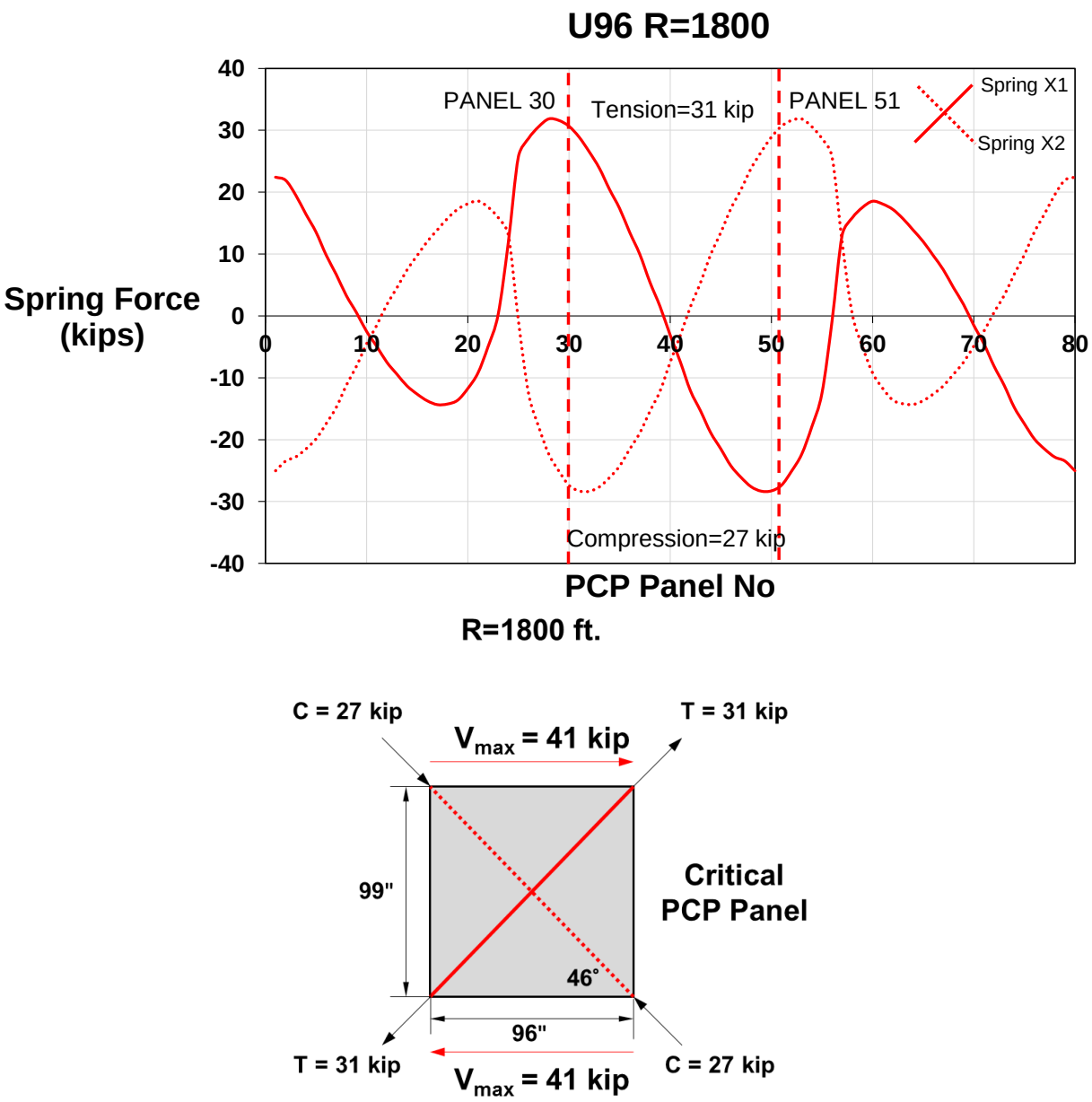

Figure 10.20 Panel Force Distribution & Critical Panel Force Sketch – R=1800 ft.

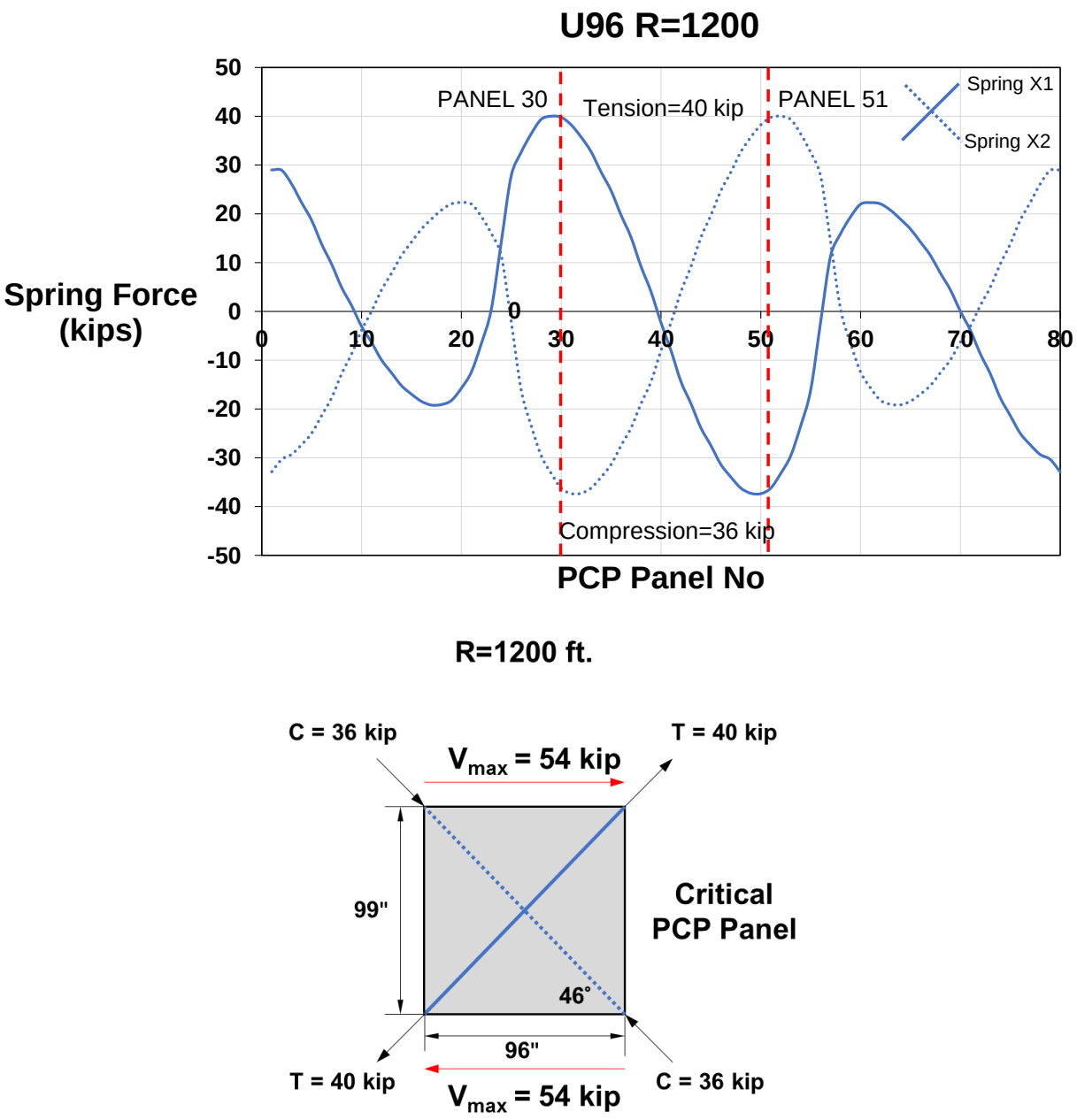

Figure 10.21 Panel Force Distribution & Critical Panel Force Sketch – R=1200 ft.

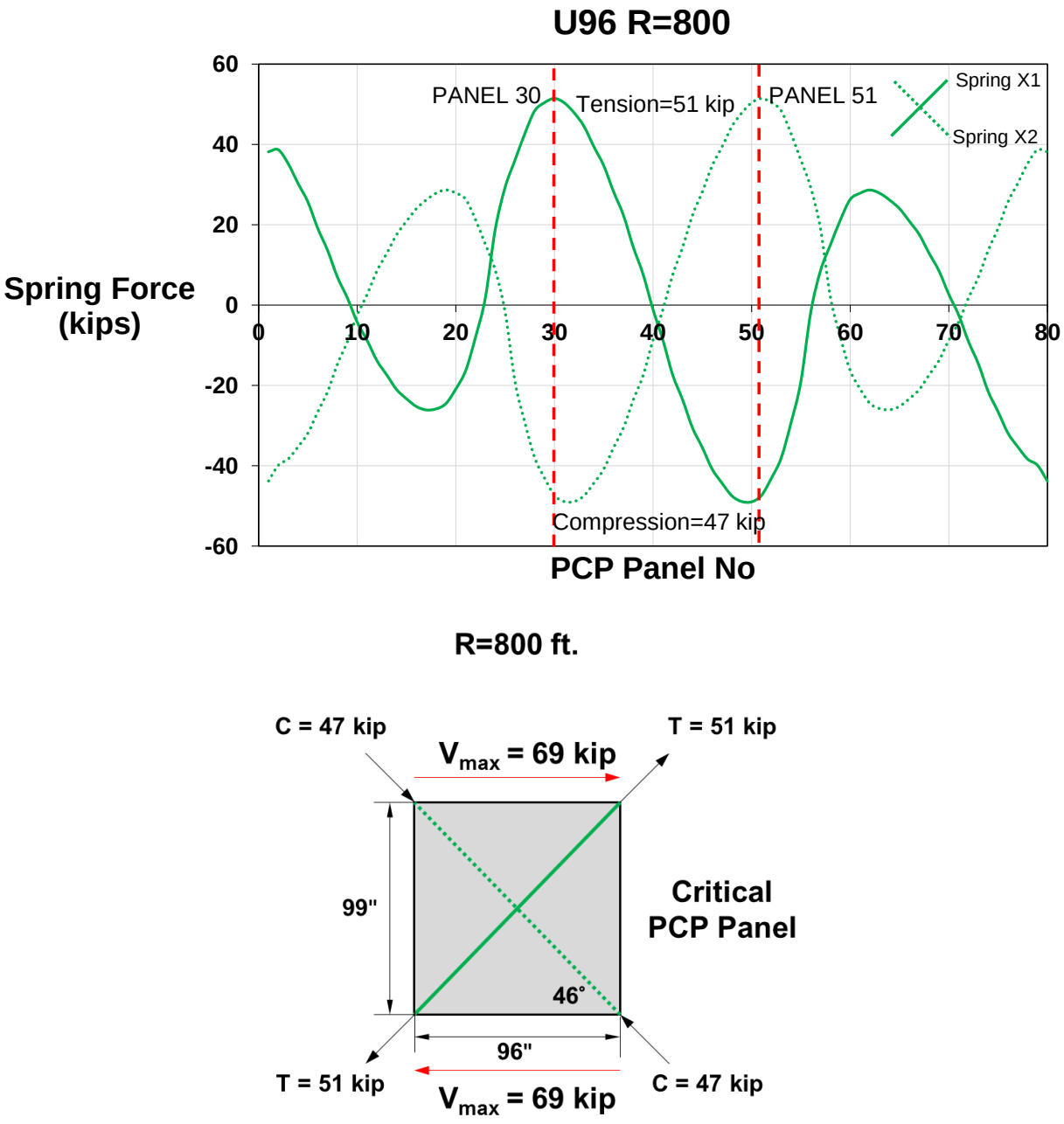

Figure 10.22 Panel Force Distribution & Critical Panel Force Sketch – R=800 ft.

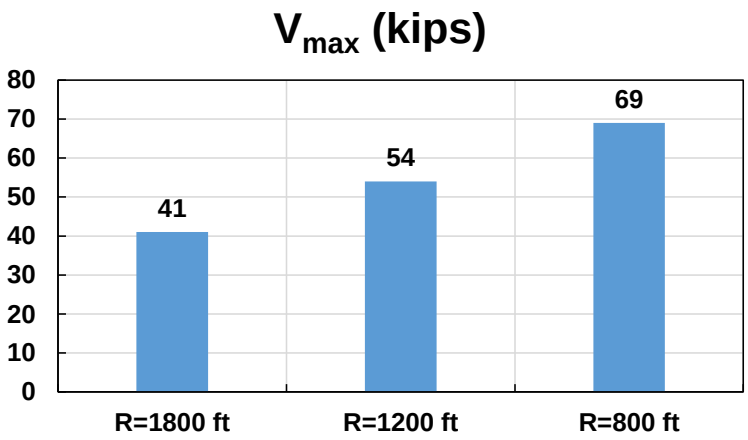

Figure 10.23 Comparison of Shear Load Demand on PCP for U96 Beam

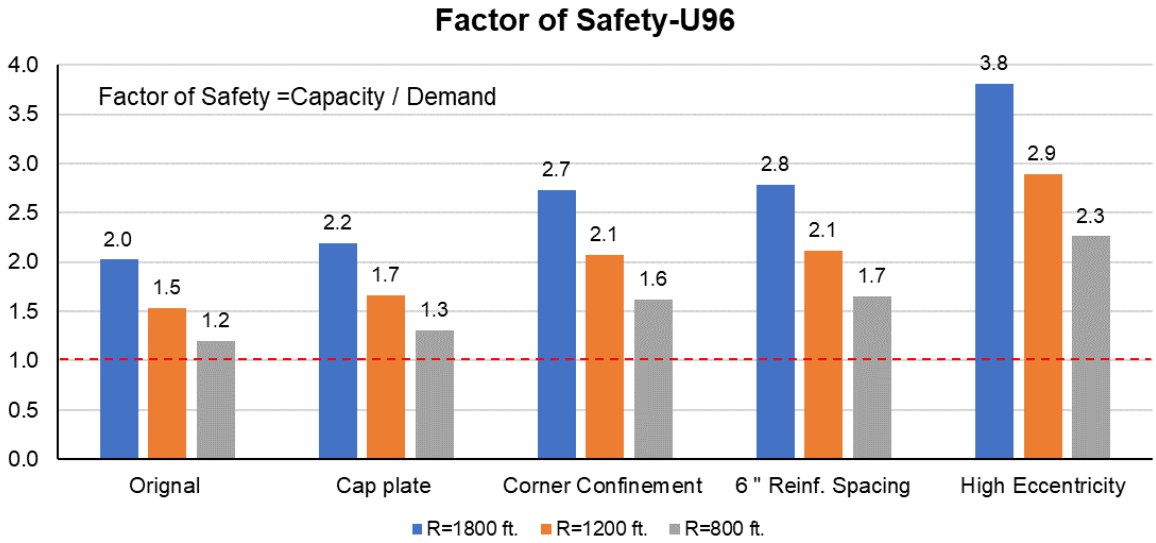

Figure 10.24 Factor of Safety Chart for Different Closure Pour Details

After obtaining the max shear load demands, the values were used to calculate the design safety factor, i.e., the ratio of shear load capacity of PCP panel with each proposed closure pour detail based on the experimental shear deflection repose to shear demand on the PCP panel from FE analyses. As indicated in Figure 10.24, for all the closure pour details, the capacity of PCP panel with closure pour seems to be adequate to satisfy shear load demand while the safety reserve for some of the details were relatively low. As horizontal radius of curvature increases, the safety margin for different proposed details decreases. For R=1800 ft., all the proposed closure pour details could satisfy the load demand with a minimum factor of safety of 2.0. For R=1200 ft., the factors of safety for original detail and the detail with cap plates were below 2.0. For R=800 ft., only the detail with high eccentricity has a factor of safety greater than 2.0.

Case Study-2 Three-span Continuous Straight and Curved U54 Beam with Different Horizontal Radii

The analysis was first performed on a straight U54 beam model. As presented in the PCP panel sketch in Figure 10.25, the panel size for U54 needs to be adjusted to account the geometry change. For straight concrete U-beams, the force in the PCP panels were caused by the net torque applied on the cross section due to the eccentricity of construction load. The shear demand was relatively low. The maximum expected shear load was only 15.5 kips. The critical panel was near the two intermediate supports. The criteria to determine the critical PCP panel is the same as before, i.e., selecting panels with the absolute difference value of the tension and compression spring force.

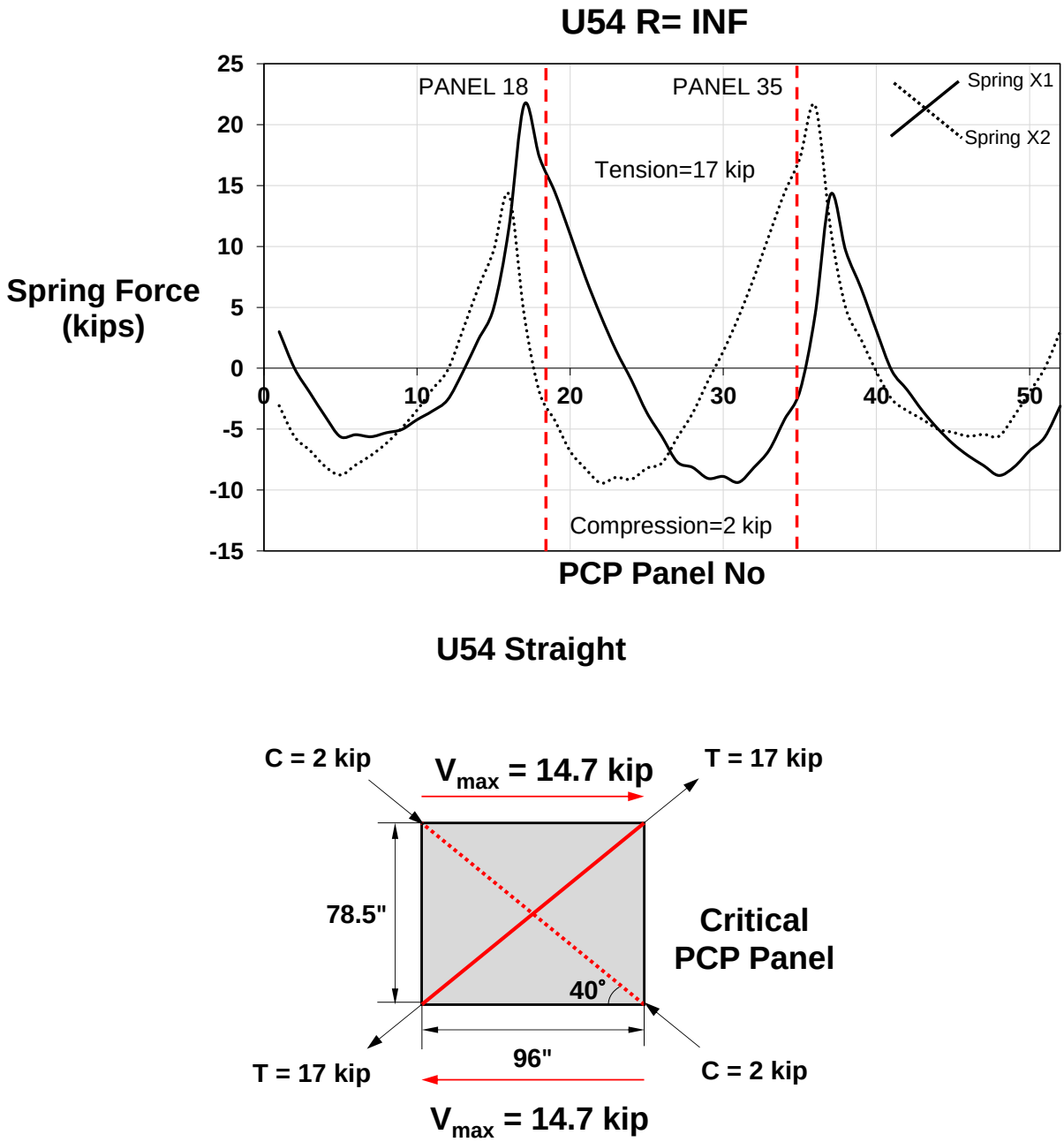

Figure 10.25 Panel Force Distribution & Critical Panel Force Sketch – R=INF

The analysis was performed on curved U54 beam models with different radii of curvature. As shown in Figure 10.26, the max shear demand on U54 beams is 24 kips when R=800 ft. Compared to those values for U96 section, the force demands on PCP panels were substantially lower as expected. The factors of safety for U54 were significantly higher. All the closure pour details could provide enough shear strength for the assumed construction sequence.

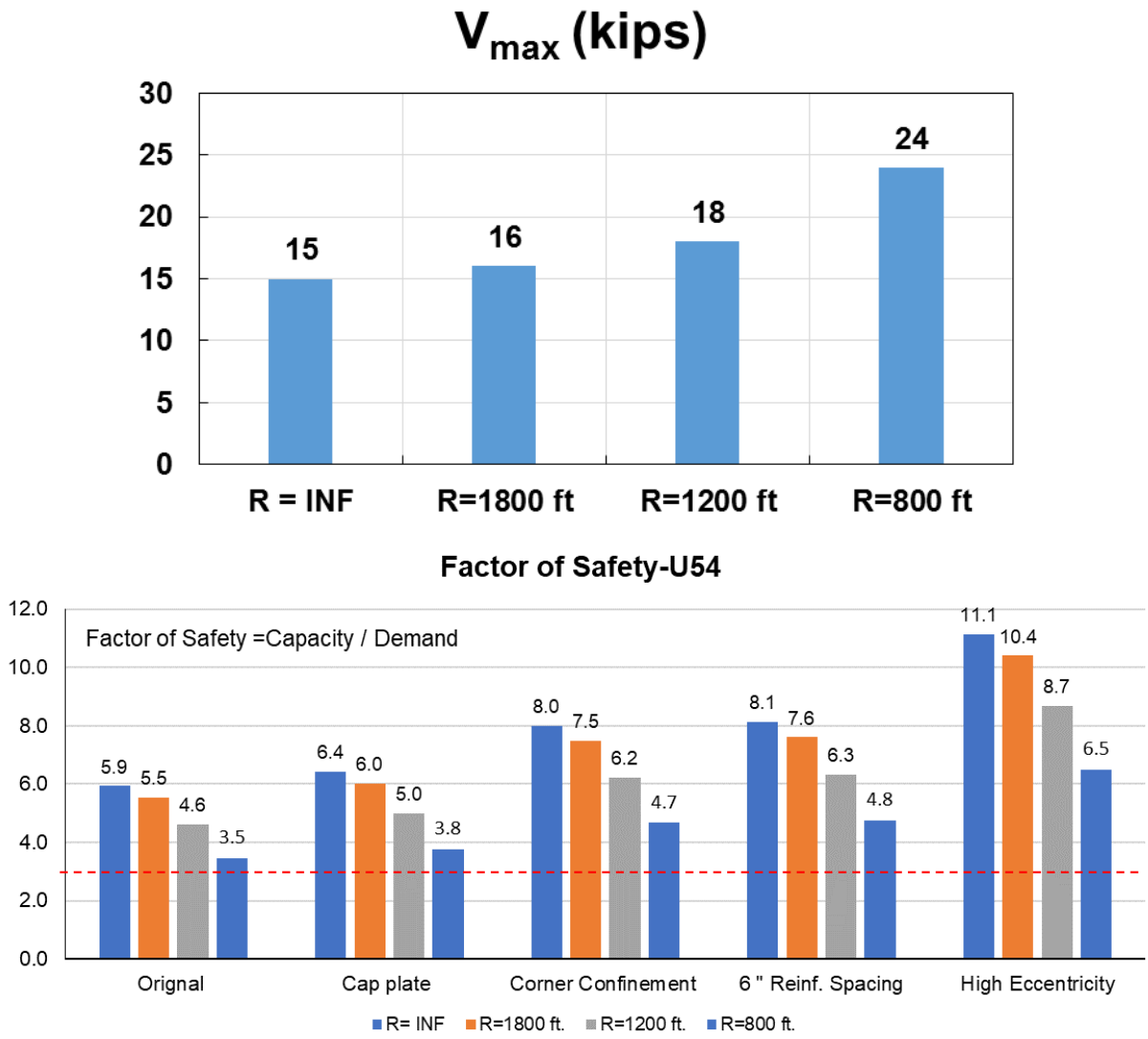

Figure 10.26 Comparison of Shear Load Demand on PCP for U54 Beam with Different R and Factor of Safety for Different Closure Pour Detail

Case study-3 Effect of Concrete Strength on the Shear Load Demand

For precast U-beams the TxDoT Bridge Design Manual specifies that the allowable concrete strength is class H concrete with a minimum f'_c=5ksi and a maximum f'_c=8.5 ksi. To examine the effect of different concrete strength on the shear load demand on PCP panels, FE analyses have been performed on three-span continuous curved U96 and U54 system with a horizontal radius of curvature R of 800 ft. The variation of concrete strength leads to different values of the modular ratio, which results in different equivalent girder cross section dimensions with a modulus ratio of 6 when f'_c=4.8 ksi and a modulus ratio of 3.4 when f'_c=8.5 ksi. Higher concrete strength result in an equivalent steel section with larger values of the flange and web thickness.

As indicated in the graph in Figure 10.27, for both U96 and U54 with R=800 ft., the use of high strength concrete leads to notable increases in the shear load demand on the PCP panels. For

U96 beam, the maximum shear forces with f'_c= 5 ksi is 17% higher than that if f'_c=8.5 ksi. For U54 beam, the change is more significant with 37.5% increase while remaining relative low compared to the shear demand for U96 beam.

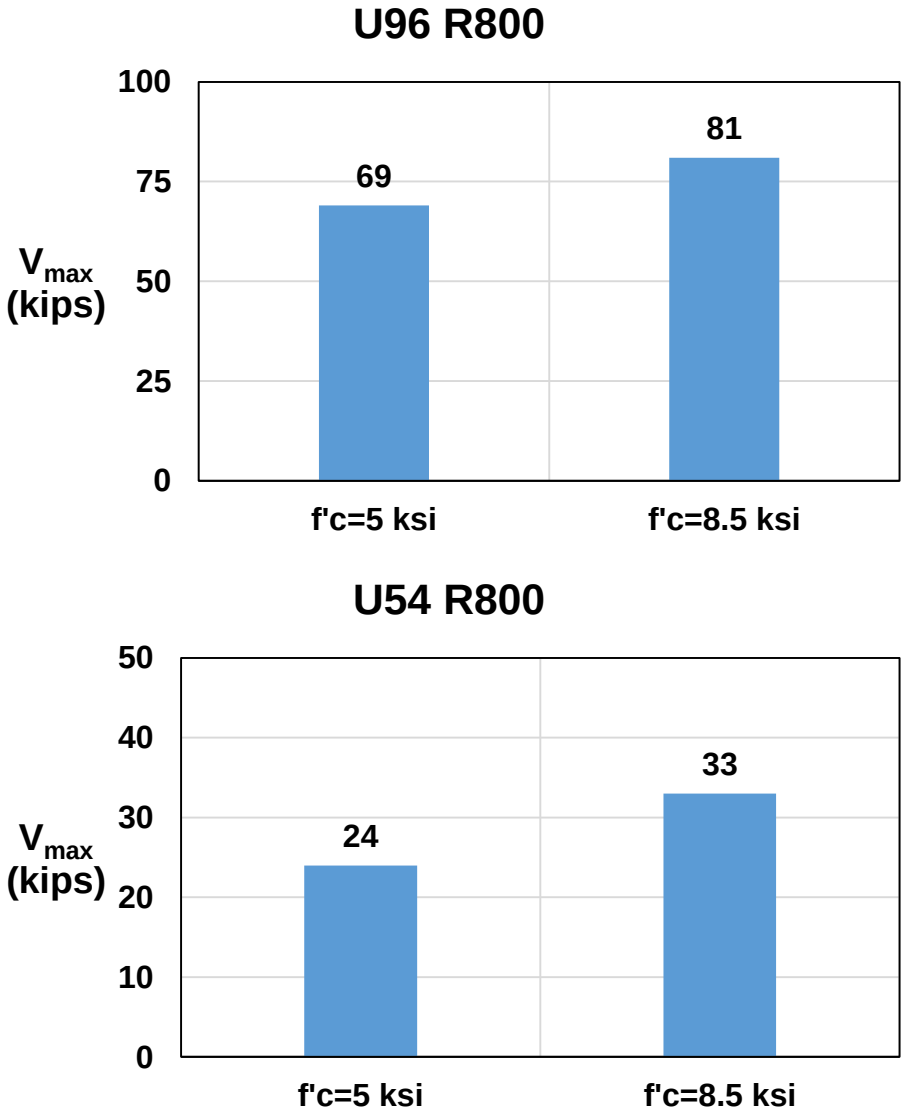

Figure 10.27 Comparison of Shear Load Demand on PCP for U54 Beam with Different f'c

10.5.3 Lifting Analyses of U96 Beam with Various Radii of Curvature

Large displacement analyses were performed to study the behavior of U-beams during girder segment lifting. Typical transportation limits on the length of the beam segment usually ranges from 120~ 130 ft. To account for the limits from transportation and crane capacity, the span length of the segment was chosen as 128 ft. which corresponds to one of the segments analyzed before in the three-span curved system. Only gravity load was applied during the analyses. Vertical supports were provided at the lifting points located 3 ft. away from the segment ends. In line with the resultant of the two lifting forces, longitudinal and transverse restraints were applied on the mid bottom to prevent instability problem during the analyses. See Figure 10.28.

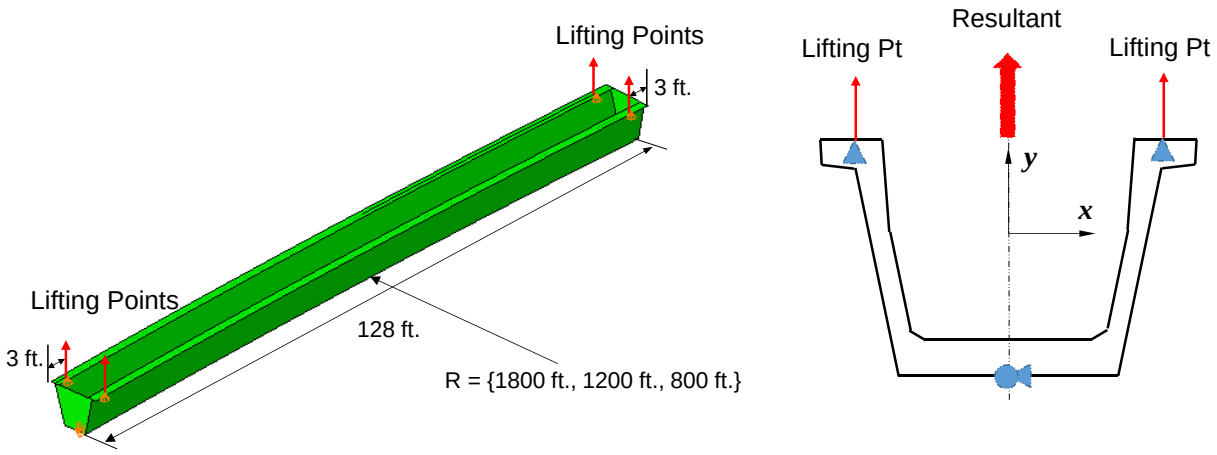

Figure 10.28 Lifting Analyses Schemes

U-beam segments with three different radii of curvature were studied and compared, i.e., 800 ft., 1200 ft. and 1800 ft. Two charts in Figure 10.29 and Figure 10.30 summarize the comparison of lateral deflection and Von Mises stress distributions for each different radius of curvature. For Von Mises stress values, the original results on the steel equivalent sections were divided by the modular ratio to obtain the stress in the concrete sections. During the lifting of U-beam segments, the primary concern is the potential excessive deformation and stress. As the beam segments become more curved, the segments deflect more laterally, and the Von Mises stresses increase while still staying below f'c.

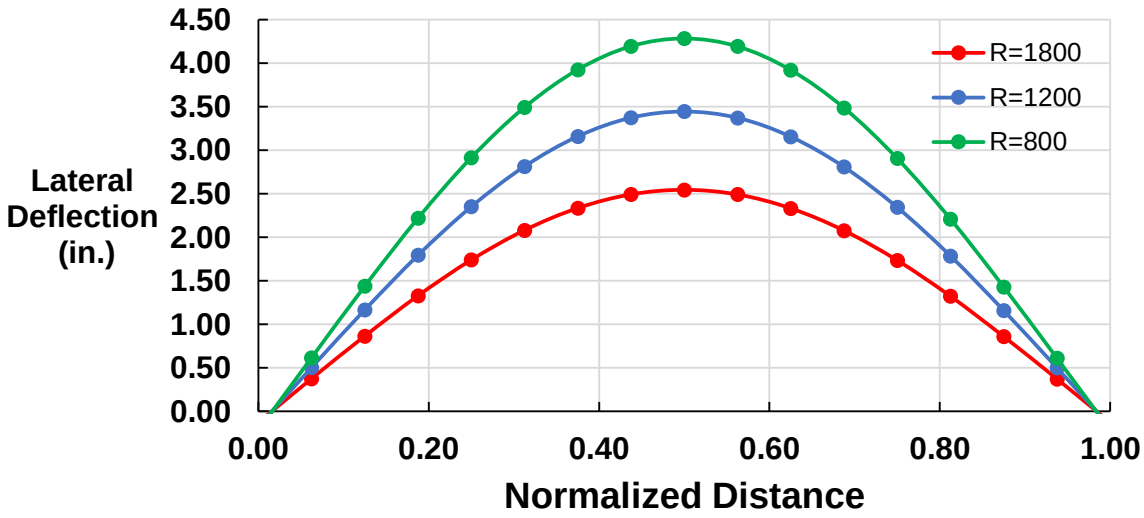

Figure 10.29 Lateral Deflection Distribution

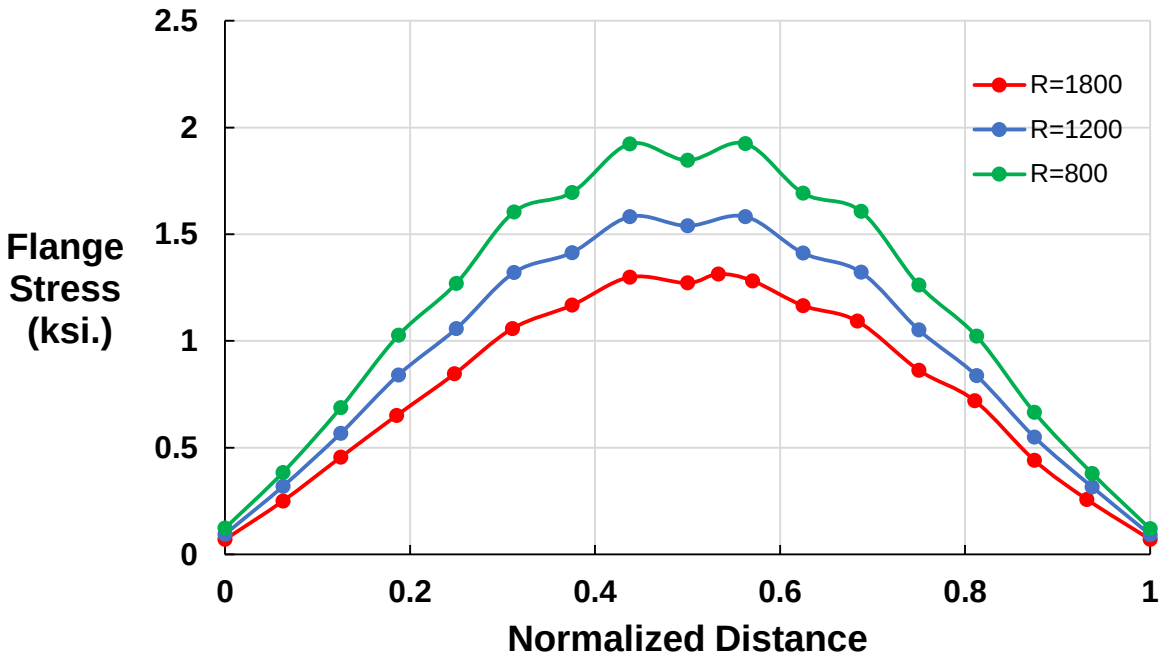

Figure 10.30 Flange Stem von Mises Stress Distribution

10.6 Conclusion and Future Work

In this chapter, parametric finite element analyses were performed on straight and horizontally curved U-beam system to provide an understanding of the fundamental behavior of U-beam and its interaction with PCP panels. Girder segment lifting, and staged construction sequence were simulated to identify the potential critical conditions during construction. The critical conditions were then used to investigate the maximum shear load demand on the PCP panels with proposed closure pour details. According to the analysis results, during girder lifting, curved U-beam segments may experience notable lateral deflection and flange stress with increased horizontal radius of curvature. Caution should be taken to select proper lengths and limits on the radius of curvature of the segment. For U-beam segments that have relatively long lengths and tighter curvatures, multiple pick-up locations with tandem operating crane groups will likely be necessary to control excessive stress and deformation and prevent the girder segments from rolling over. Moreover, the results indicated that lateral-torsional buckling could occur if U-beams were placed on the supports in unshored conditions. Temporary shoring falsework may be required to prevent section twist before the completion of the cast-in-place lid slab. Shoring frames may be necessary at the ends of girder segments for each span. The maximum shear forces occur at the support end regions with the maximum shear deformation during the asymmetric stage of deck casting or placement. Based on the analysis results in this study, the proposed closure pour details could provide sufficient shear stiffness and strength for straight and mildly-curved bridge application ($R \leq 1200$ ft.). However, when it comes to increased bridge curvature, discretion needs to be taken on the selection of proper closure-pour details because potential shear failure might occur. The utilization of high-strength concrete on concrete U-beam could significantly increase the load demand on the PCP panels. The conclusions in this chapter were based on simplified three-dimensional FEA analyses. The interpretation of the results depends on the assumptions and simplifications adopted in the analyses. Only construction limit states were evaluated in this study

without considering any post-tensioning. Future work could focus on refined analysis to evaluate both construction and serviceability limit states.

TxDOT has existing details for the reinforcing between the PCPs and the U-beams for the closure pour of U-Beams. Comparisons between experimental results and the predicted demand for horizontally curved girders systems with a radius of curvature between 1800 and 800 feet showed that the existing detail was inadequate and requires modifications. Several modifications were tested that had beneficial effects on improving the behavior and strength of the connections. There may be additional considerations on the performance of the connections that need to be discussed with TxDOT as well as the precast industry. Additional testing and analysis is likely necessary to arrive at the most efficient detail.

Chapter 11. Recommendations for using Unconnected PCPs on Curved Steel I-Girders and Tub Girders

11.1 Introduction

TxDOT currently does not permit partial depth precast concrete deck panels (PCPs) to be used on curved steel I-girder or tub girder systems. One concern is the stability of the unattached PCPs on the bedding strips supported by the girders during the construction phase (before the concrete deck stiffens and locks the PCPs into place) as shown in Figure 11.1. A number of experimental tests were performed in Chapter 3 to investigate the stability of the unconnected PCPs on the bedding strips as the girders deflect during the construction phase. This chapter compares girder deflections from the finite element (FE) models developed for the parametric study of the curved steel I-girder and tub girder systems (Chapter 9) with the experimental results from Chapter 3. Recommendations for using PCPs on curved steel I-girders and tub girder are developed.

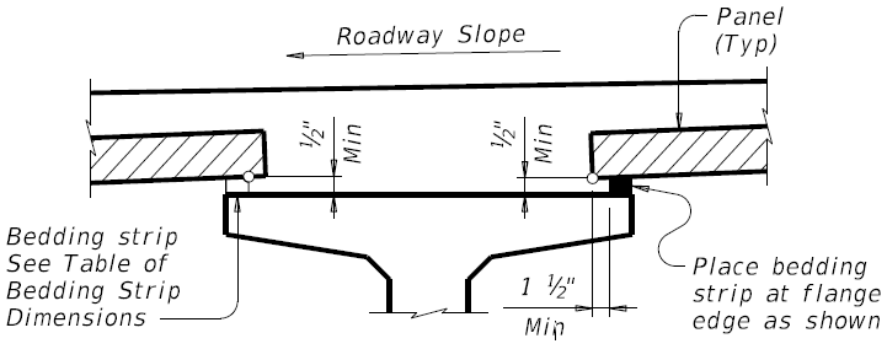

TABLE OF BEDDING STRIP DIMENSIONS

WIDTH	HEIGHT (2)	
	Min	Max
1" (Min)	½"	2"
1 ¼"	½"	2 ½"
1 ½"	½"	3"
1 ¾"	½"	3 ½"
2" (Min)	½"	4"

Figure 11.1 TxDOT Standard for Bedding Strip Dimensions (TxDOT 2014a)

11.2 Unconnected PCPs on Curved I-Girders

In addition to investigating the potential benefits of providing a positive connection between PCPs and the I-girders, the behavior of PCPs on curved girder systems with no positive connection to the girders was investigated. This application is essentially the same as the current use in straight girder systems. A major difference between the straight and curved girder systems is the relative vertical and lateral deformation that will occur in curved systems as the adjacent girders with different radii of curvature torsionally deform during placement of the PCPs and the concrete deck. The stability of the unconnected PCPs on the bedding strips is of concern due to the differential deformations that may occur at the supported ends of the panels. The effects can be intensified due to potential inclinations due to differences in elevations between adjacent girders (i.e. girder drop). Furthermore, the adjacent girders will experience varying levels of inclination (especially for continuous girders) during placement of the PCPs and the concrete deck as the

bridge twists under the dead loads. In addition to bridge twist, stability of the PCPs on the bridge system can be influenced by the separation between the top flanges of the adjacent girders (between the intermediate cross-frames) and by the warping deformation of the I-girders during construction.

11.2.1 Steel I-Girder Construction Details

Curved I-girder bridges experience system twist during construction due to the torsional load from the horizontal curvature of the system. The internal torsion in horizontally-curved I-girder bridges is resisted by interconnecting the girders with cross-frames or diaphragms which apply vertical loads (referred to as "V-loads") to the I-girders as they resist torsion. The V-loads act downward on the outside girder and upward on the inside girder. Therefore, the outside girder is more heavily loaded than the inside girder, causing the entire system to twist. To achieve the desired roadway profile, the I-girders are cambered so that the girders have the correct elevation after all of the dead loads are applied and the bridge is complete. Typically, the outside girders will have more camber than the inside girders since the outside girders carry more vertical load (due to the V-loads) and are slightly more flexible due to their slightly longer span. Also, the outside girders are typically set at a higher elevation at the supports to achieve the desired superelevation for the Roadway Cross-Slope (RCS).

To construct the steel superstructure of a curved I-girder system, the detailer selects a "fit condition" for the bridge which is defined as the dead load condition where it is desired for the webs of the I-girders to be plumb. No-Load Fit (NLF) gives plumb girder webs when no load is on the system (i.e. on the shop floor when the girders are continuously supported), Steel Dead Load Fit (SDLF) gives plumb girder webs when the steel dead load is present (i.e. when the steel superstructure is constructed), and Total Dead Load Fit (TDLF) gives plumb girder webs when all of the dead load is present (i.e. when the construction of the bridge is completed). Figure 11.2, Figure 11.3, and Figure 11.4 show the girders in the NLF, SDLF, and TDLF conditions, respectively. To achieve the desired fit condition, the detailer sets the girder "drops" for the fabrication of the cross-frames. As shown in Figure 11.2, Figure 11.3, and Figure 11.4, the "drops" are the difference in vertical elevation between the top of the webs of adjacent girders in the desired dead load condition (no load, steel dead load, or total dead load). The fully-cambered girder geometry in the No-Load (NL) position is equal to the negative of the Total Dead Load (TDL) deflections from the analysis. According to the National Steel Bridge Alliance (2016), the detailer typically determines the girder geometry in the target fit condition by subtracting the vertical Steel Dead Loads (SDL) or the TDL from the fully-cambered NL geometry and the girders are assumed to be plumb in all three NL, SDL, and TDL conditions (i.e. only the vertical deflections are considered). More detailed information on behavior of curved steel I-girder bridges and cross-frame fit conditions is provided by the National Steel Bridge Alliance (2016).

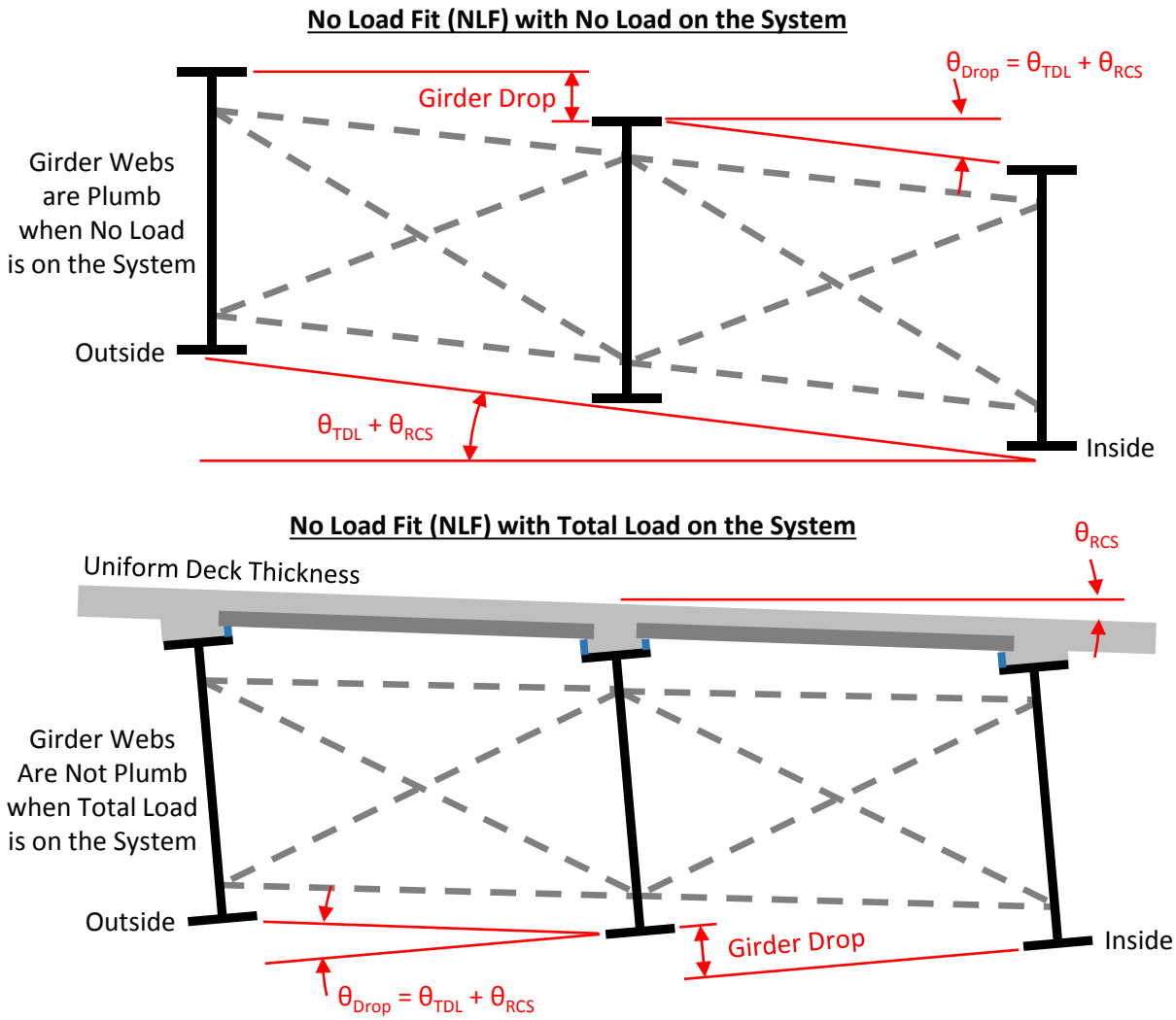

Figure 11.2 No Load Fit (NLF) of Cross-Frames for I-Girders

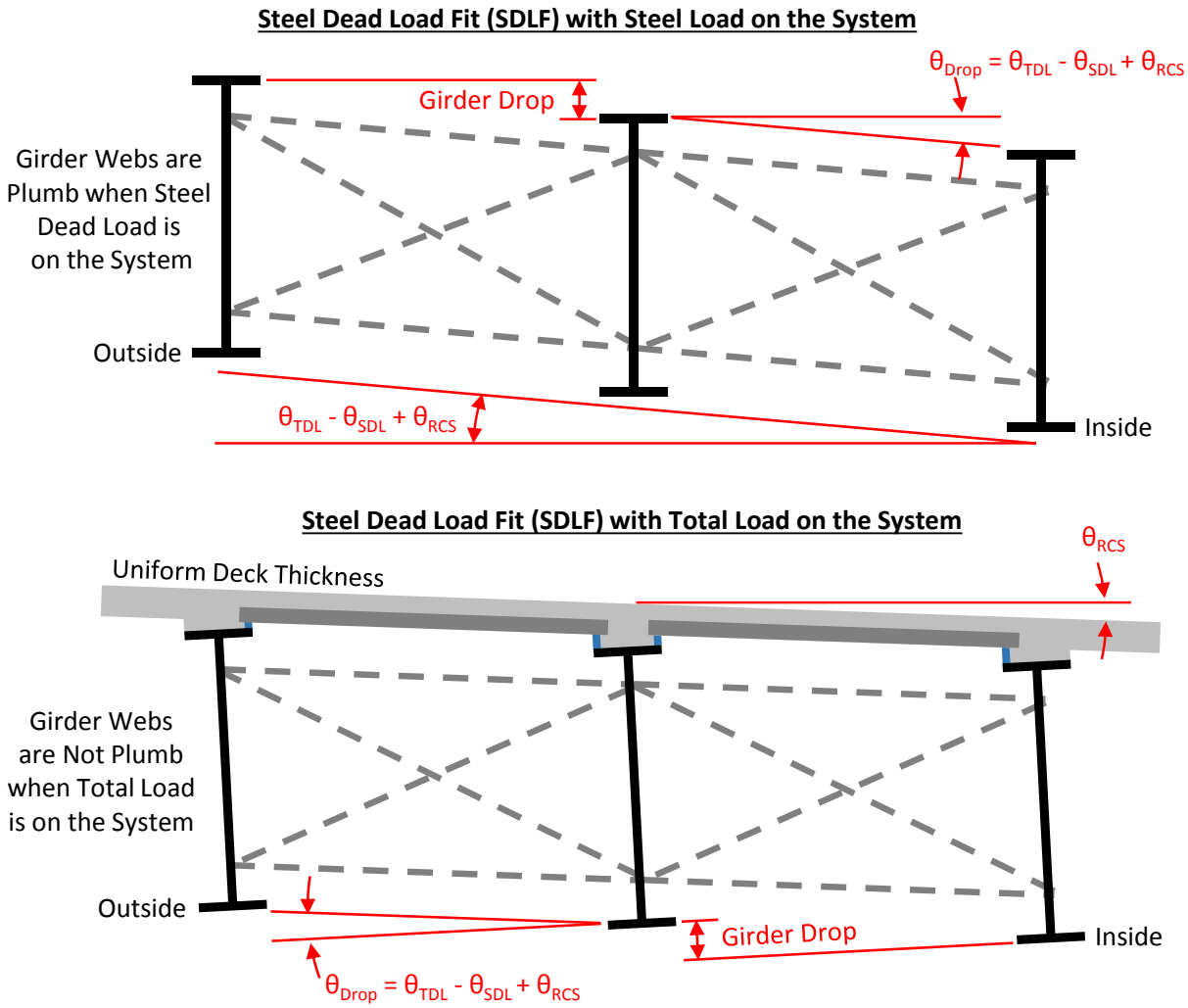

Figure 11.3 Steel Dead Load Fit (SDLF) of Cross-Frames for I-Girders

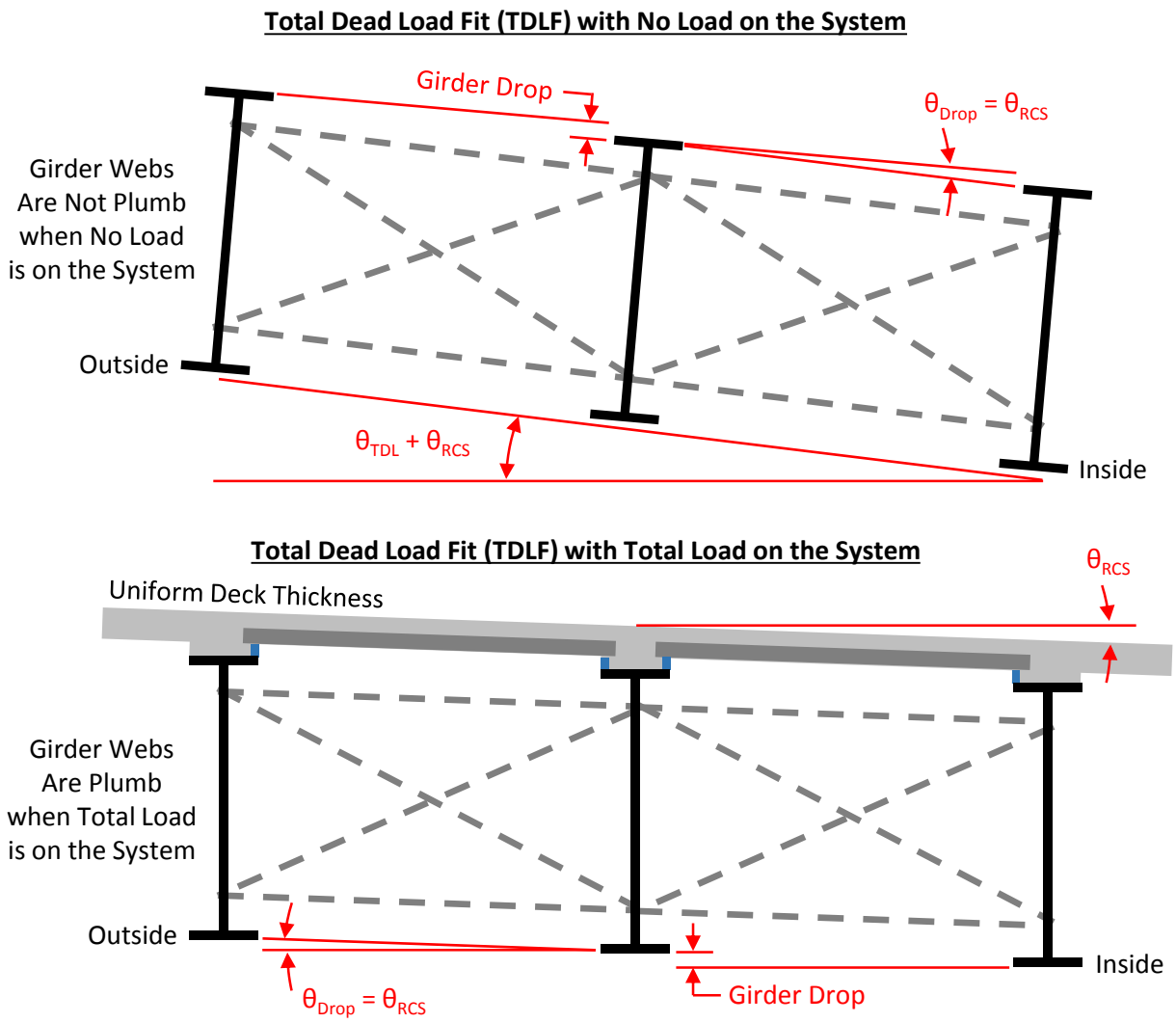

Figure 11.4 Total Dead Load Fit (TDLF) of Cross-Frames for I-Girders

The angle of the PCP relative to the top flange of the I-girders equals the drop angle (θ_{Drop}) as shown in Figure 11.2, Figure 11.3, and Figure 11.4. The NLF condition results in the largest girder drop angle while the TDLF condition results in the smallest girder drop angle (the drops are only present to account for the roadway cross-slope). According to the National Steel Bridge Alliance (2016), SDLF is the most commonly used fit up condition for horizontally curved steel I-girder bridges and the TDLF condition is typically avoided as it can potentially render the bridge unconstructible.

11.2.2 Flange Separation of Adjacent I-Girders between Cross-Frames

As the I-girder system deforms under construction loads, some separation between the flanges of adjacent girders may occur (see in Figure 11.5) which can impact the stability of the PCPs on the bedding strips. The top flange separation (Δ_{LAT}) tends to be maximum at the midpoint between cross-frames. Overhang brackets are typically attached to the exterior girders, and tend to drive the separation between top flanges of the interior and exterior girders due to the torsional

load on the external girder. Figure 11.6 shows the loads on the overhang bracket and how the loads are resolved into the exterior girder.

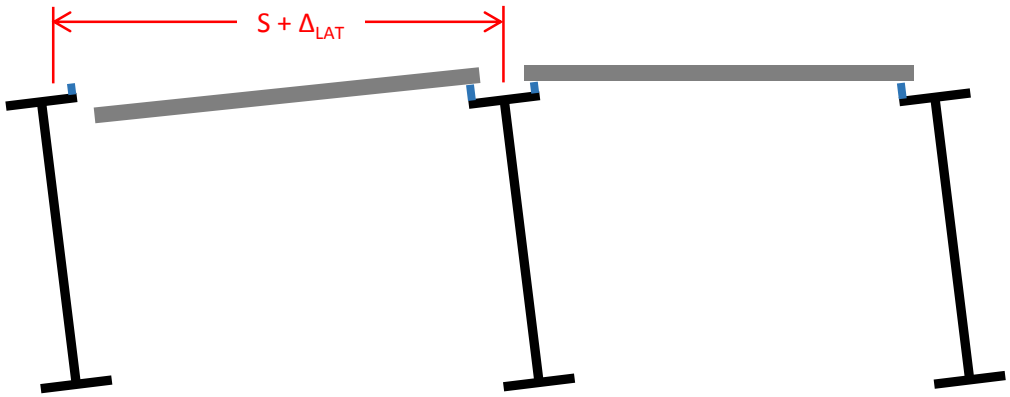

Figure 11.5 Separation of I-Girders During Construction away from Cross-Frame

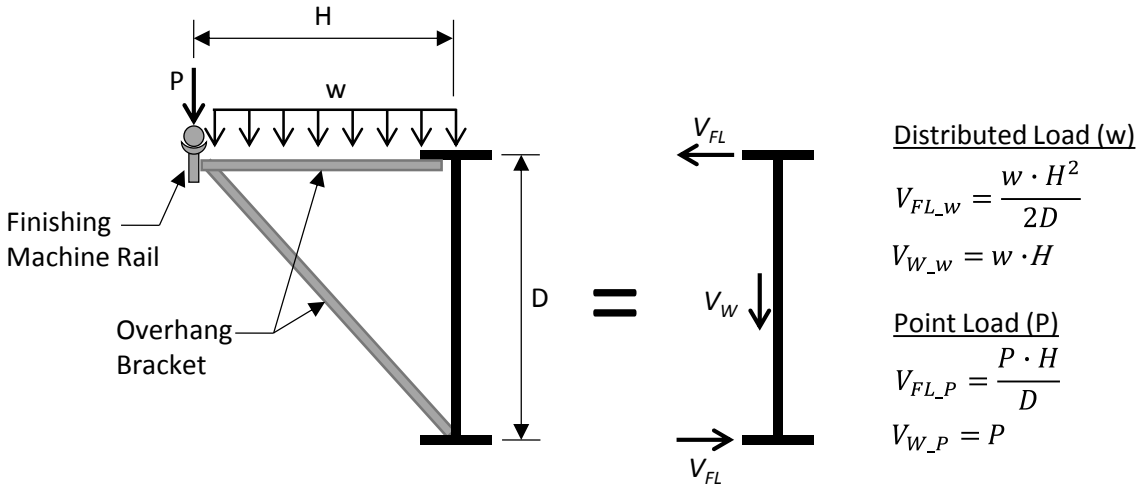

Figure 11.6 Loads and Free Body Diagram of Overhang Bracket System

The three I-girder sections used for the parametric study in Chapter 9 (shown in Figure 11.7) were used to determine some realistic values for the maximum top flange separation ($\Delta_{LAT\_MAX\_1}$) due to the overhang bracket. A finite element model of each I-girder section (using the values for the positive moment region - POS) was created between the cross-frames (assuming a cross-frame spacing of 20 ft) as shown in Figure 11.8. In reality, the beam is continuous which will increase the torsional stiffness to resist the load from the overhang bracket (i.e. the FE model will produce larger deflections than expected in reality). The width of the overhang (H) was assumed to be 4.5 ft and the depth of the concrete was taken as 8 inches (ρ = 150 lb/ft^3 was used for concrete). The weight of the finished machine was assumed to be 10 kips acting on the end of the overhang bracket (4.5 ft from the web of the exterior girder). Results from the FEA (Figure 11.8) showed that Δ_{LAT_MAX} was 0.48, 0.16, and 0.04 inches for section D4, D6, and D8, respectively.

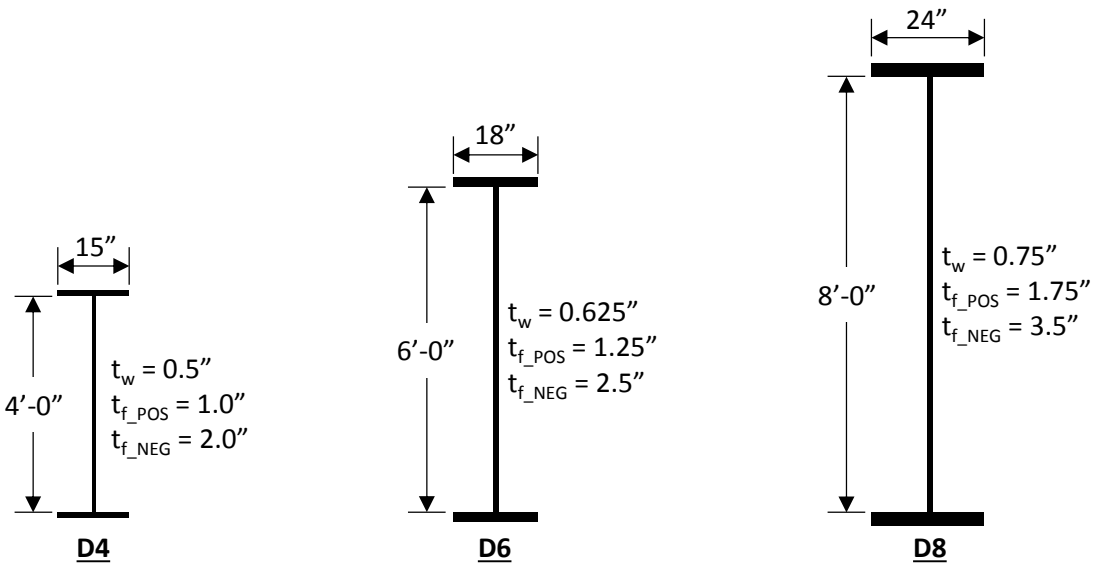

Figure 11.7 Cross-Sections Used for the I-Girder Parametric Study

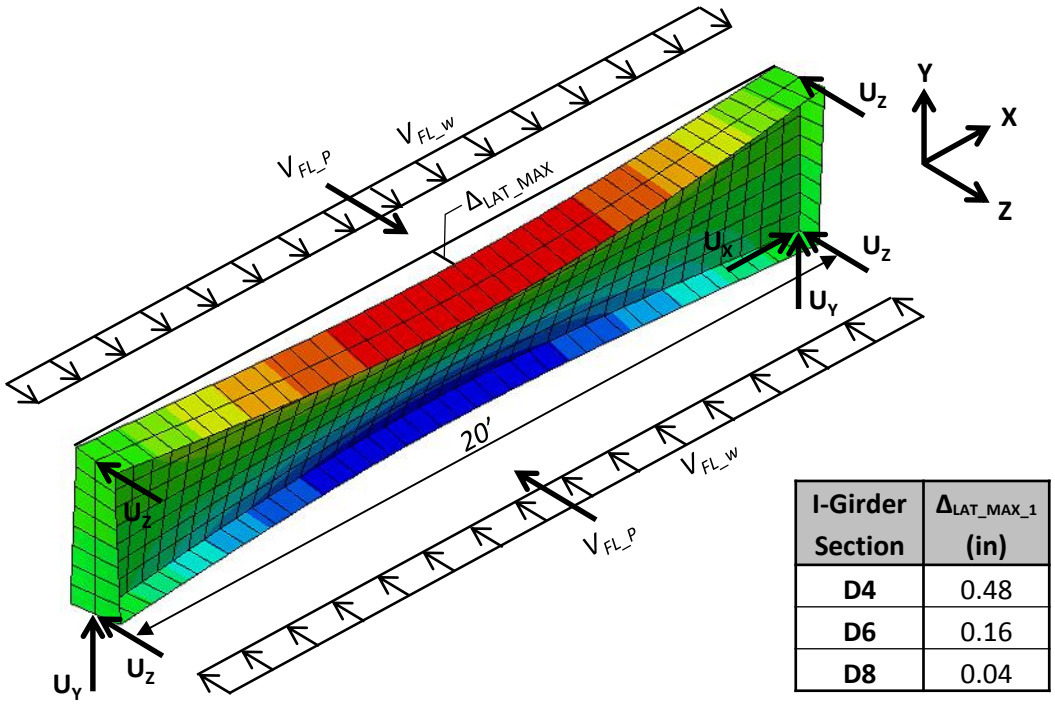

I-Girder Section	$\Delta_{LAT\_MAX\_1}$ (in)
D4	0.48
D6	0.16
D8	0.04

Figure 11.8 I-Girder Deflection from Overhang Bracket Loads

The maximum top flange separation ($\Delta_{LAT\_MAX\_2}$) was output from the 18 models (Table 11.1) from the parametric study for the I-girders (Chapter 9). These models did not include the torque on the exterior girders from the overhang brackets. Therefore, the maximum total top flange separation ($\Delta_{LAT\_MAX\_TOTAL}$) is approximately the summation of the components from both FE

models ($\Delta_{LAT\_MAX\_TOTAL} = \Delta_{LAT\_MAX\_1} + \Delta_{LAT\_MAX\_2}$). Table 11.2 shows the maximum total top flange separation ($\Delta_{LAT\_MAX\_TOTAL}$) for all 18 FE models. Of the 18 systems studied in this report, 0.54 inches was the absolute largest top flange separation which is less than the value of Δ_{LAT} = 0.75 inches that was used for the inclined PCP tests in Chapter 3.

Table 11.1 Top Flange Separation without Effects from Overhang Brackets

I-Girder System	$\Delta_{LAT\_MAX\_2}$ (in)	I-Girder System	$\Delta_{LAT\_MAX\_2}$ (in)
EQ.D4.R1800	0.01	UEQ.D4.R1800	0.01
EQ.D4.R1200	0.02	UEQ.D4.R1200	0.02
EQ.D4.R600	0.06	UEQ.D4.R600	0.05
EQ.D6.R1800	0.02	UEQ.D6.R1800	0.02
EQ.D6.R1200	0.05	UEQ.D6.R1200	0.04
EQ.D6.R600	0.15	UEQ.D6.R600	0.13
EQ.D8.R1800	0.04	UEQ.D8.R1800	0.04
EQ.D8.R1200	0.08	UEQ.D8.R1200	0.08
EQ.D8.R600	0.26	UEQ.D8.R600	0.21

Table 11.2 Total Top Flange Separation

I-Girder System	$\Delta_{LAT\_MAX\_TOTAL}$ (in)	I-Girder System	$\Delta_{LAT\_MAX\_TOTAL}$ (in)
EQ.D4.R1800	0.49	UEQ.D4.R1800	0.49
EQ.D4.R1200	0.50	UEQ.D4.R1200	0.50
EQ.D4.R600	0.54	UEQ.D4.R600	0.53
EQ.D6.R1800	0.18	UEQ.D6.R1800	0.18
EQ.D6.R1200	0.21	UEQ.D6.R1200	0.20
EQ.D6.R600	0.31	UEQ.D6.R600	0.29
EQ.D8.R1800	0.08	UEQ.D8.R1800	0.08
EQ.D8.R1200	0.12	UEQ.D8.R1200	0.12
EQ.D8.R600	0.30	UEQ.D8.R600	0.25

11.2.3 Steel I-Girder System Twist during Construction

The twist of the bridge system should be considered at each loading stage during construction to ensure that the unconnected PCPs are stable on the bedding strips. The 18 models (Table 11.3) from the parametric study for the I-girders (Chapter 9) were used to determine the maximum twist of the I-girder system (which is approximately equal to the angle of inclination of the PCPs in each span during the construction). In the FE models, the top flanges of all girders were at the same elevation prior to the application of any load on the system. The fully-cambered girder geometry in the NL position was taken as the negative of the TDL deflections considering only the vertical deflections. Figure 11.9 shows the plan view of the three I-girder, two span system that was used for the parametric study (Chapter 9 contains a detailed description of the models).

The EQ.D8.R600 model was also analyzed with 5 girders across the width to see how increasing the number of girders affected the torsional stiffness of the system. Figure 11.10 through Figure 11.15 show the twist of the system at Section A-A for the no load case and for the five load steps during construction (the load on the system is identified in each figure) assuming a SDLF was used. As described in detail in Chapter 9, a continuous PCP placement and a continuous deck placement were used for construction (i.e. the PCPs were first placed in span 1, then span 2 and next the deck was placed in span 1 and then in span 2).

Table 11.3 FE Models for I-Girder Parametric Study

Model Name	Girder Depth (ft)	Radius of Curvature (ft)	Span 1 Length (ft)	Span 2 Length (ft)
EQ.D4.R600	4	600	120	120
EQ.D4.R1200	4	1200	120	120
EQ.D4.R1800	4	1800	120	120
EQ.D6.R600	6	600	180	180
EQ.D6.R1200	6	1200	180	180
EQ.D6.R1800	6	1800	180	180
EQ.D8.R600	8	600	240	240
EQ.D8.R1200	8	1200	240	240
EQ.D8.R1800	8	1800	240	240
UEQ.D4.R600	4	600	80	120
UEQ.D4.R1200	4	1200	80	120
UEQ.D4.R1800	4	1800	80	120
UEQ.D6.R600	6	600	120	180
UEQ.D6.R1200	6	1200	120	180
UEQ.D6.R1800	6	1800	120	180
UEQ.D8.R600	8	600	160	240
UEQ.D8.R1200	8	1200	160	240
UEQ.D8.R1800	8	1800	160	240

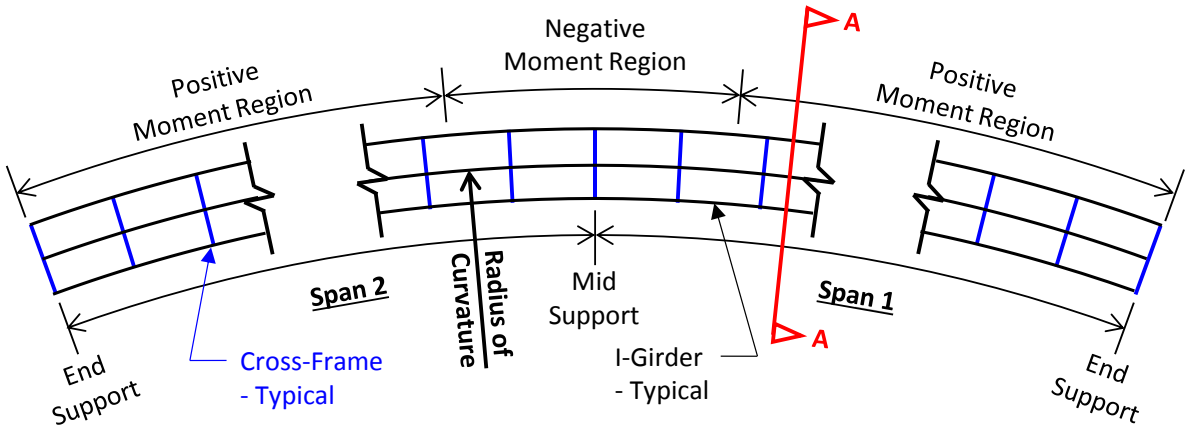

Figure 11.9 I-Girder Layout for Parametric Study – Plan View

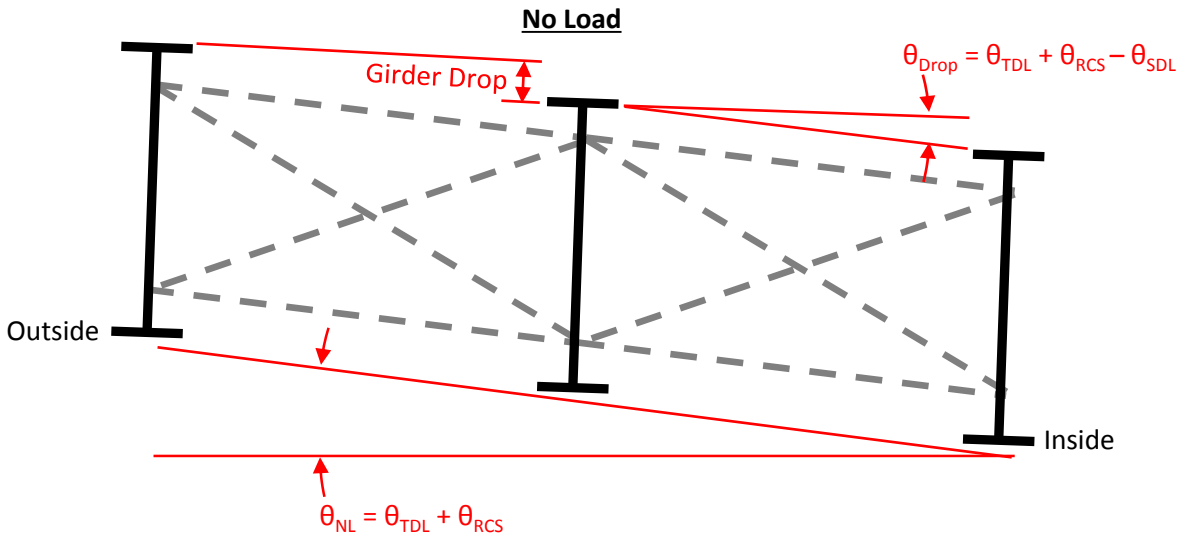

Figure 11.10 No Load – Steel I-Girder System Twist SDLF – Section A-A

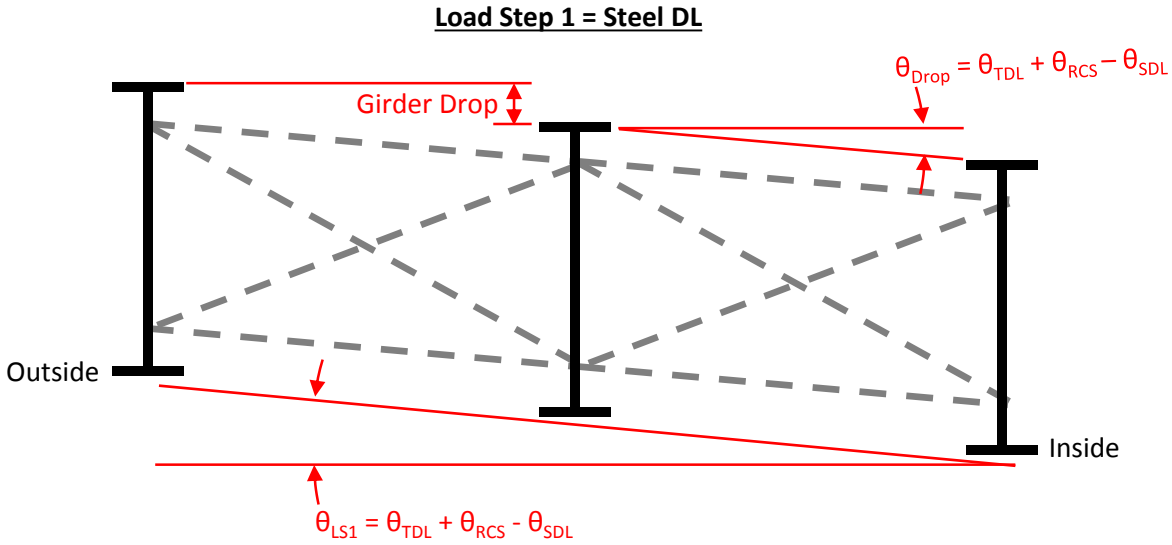

Figure 11.11 Load Step 1– Steel I-Girder System Twist SDLF – Section A-A

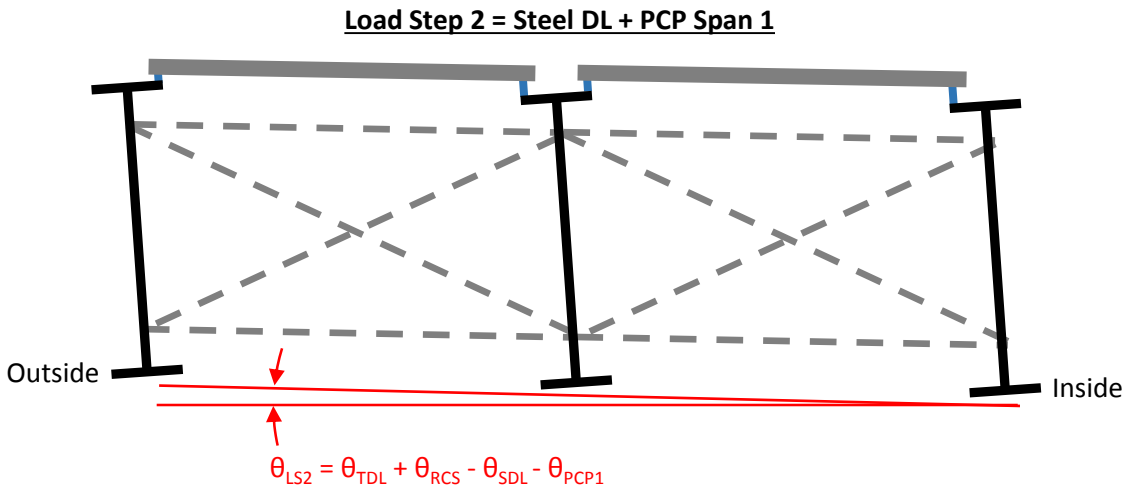

Figure 11.12 Load Step 2– Steel I-Girder System Twist SDLF – Section A-A

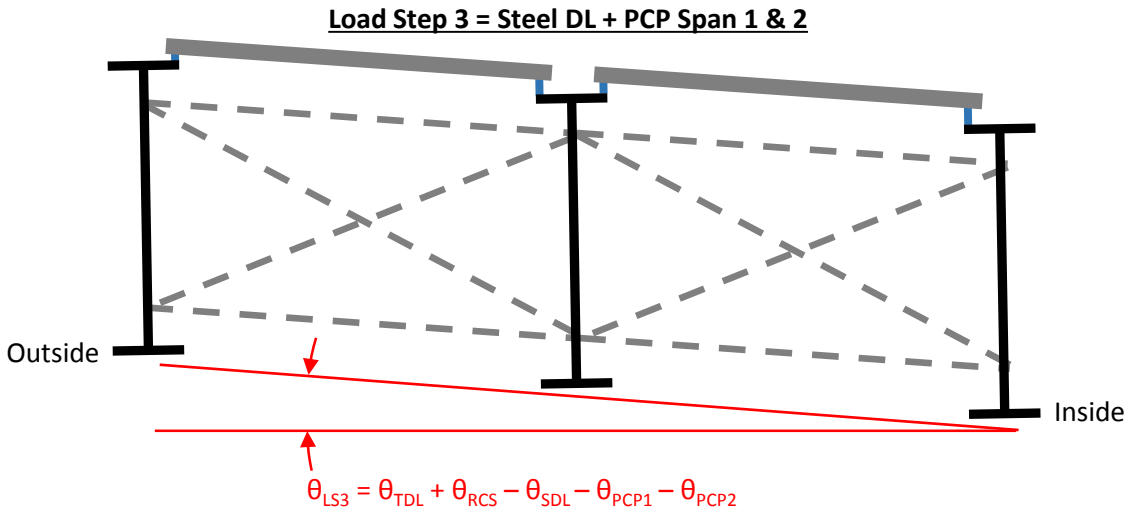

Figure 11.13 Load Step 3– Steel I-Girder System Twist SDLF – Section A-A

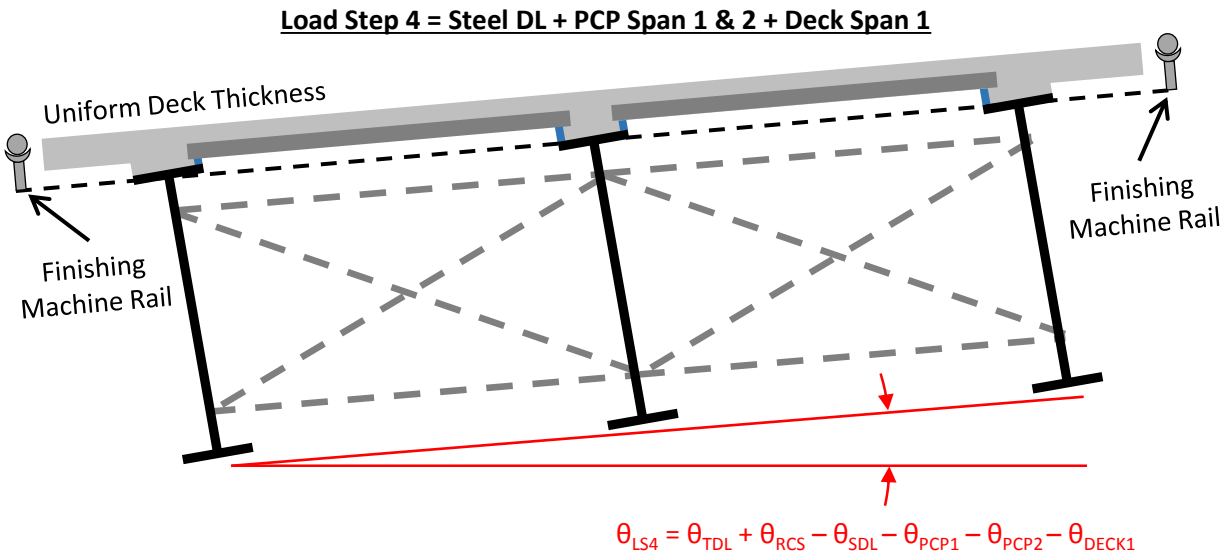

Figure 11.14 Load Step 4– Steel I-Girder System Twist SDLF – Section A-A

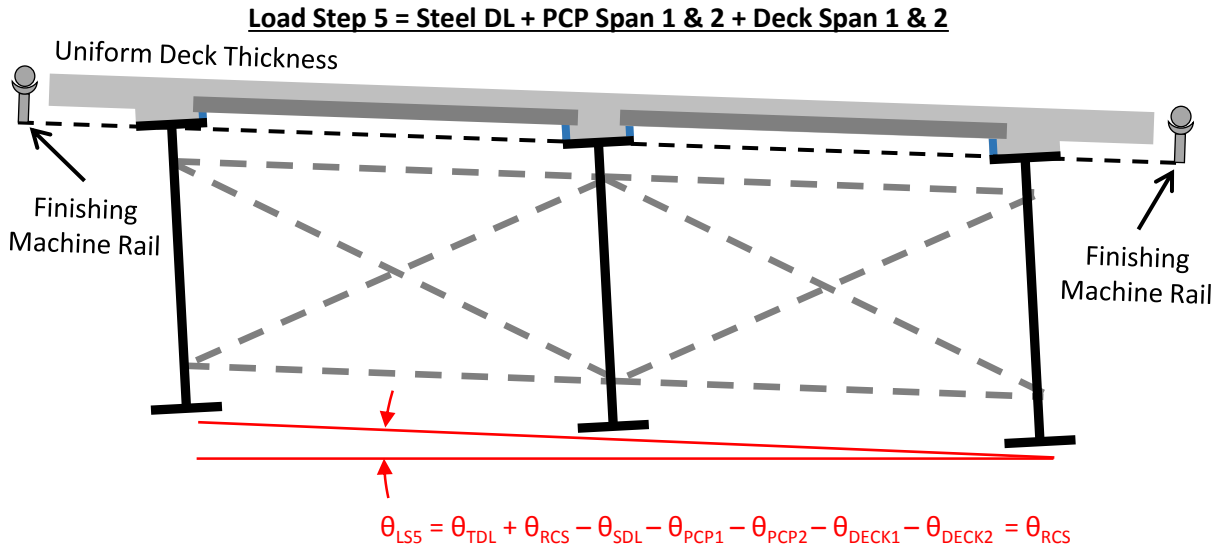

Figure 11.15 Load Step 5– Steel I-Girder System Twist SDLF – Section A-A

The maximum I-girder drop angle (θ_{Drop}) for all 18 FE models for all three fit conditions (NLF, SDLF, and TDLF) are given in Table 11.4. This table assumes there is no roadway cross-slop (i.e. $\theta_{RCS} = 0$). The desired roadway cross-slope will be a positive value that can be added to the values in the table (a positive angle indicates that the outer girder is at a higher elevation than the inner girder). The drop angles increased as the radius of curvature decreased and as the girder depth (and correspond span length) increased. Also, the NLF produced highest drop angles while the TDLF produced the lowest drop angles. The maximum drop angle for the SDLF (the most common fit-up condition) was 2.6 degrees plus the angle of the roadway cross-slope (θ_{RCS}).

Table 11.4 Girder Maximum Drop Angle from I-Girder Parametric Study

I-Girder System	θ_{Drop} (deg) NLF		θ_{Drop} (deg) SDLF		θ_{Drop} (deg) TDLF	
	Span1	Span2	Span1	Span2	Span1	Span2
EQ.D4.R1800	0.1	0.1	0.0	0.0	0.0	0.0
EQ.D4.R1200	0.2	0.2	0.1	0.1	0.0	0.0
EQ.D4.R600	0.3	0.3	0.3	0.3	0.0	0.0
EQ.D6.R1800	0.4	0.4	0.3	0.3	0.0	0.0
EQ.D6.R1200	0.5	0.5	0.4	0.4	0.0	0.0
EQ.D6.R600	1.0	1.0	0.8	0.8	0.0	0.0
EQ.D8.R1800	0.7	0.7	0.5	0.5	0.0	0.0
EQ.D8.R1200	1.0	1.0	0.7	0.7	0.0	0.0
EQ.D8.R600	1.8	1.8	1.1	1.1	0.0	0.0
EQ.D8.R600*	0.8	0.8	0.5	0.5	0.0	0.0
UEQ.D4.R1800	-0.1	0.2	0.0	0.2	0.0	0.0
UEQ.D4.R1200	-0.1	0.3	-0.1	0.3	0.0	0.0
UEQ.D4.R600	-0.2	0.7	-0.1	0.6	0.0	0.0
UEQ.D6.R1800	-0.2	0.8	-0.2	0.6	0.0	0.0
UEQ.D6.R1200	-0.3	1.2	-0.2	0.9	0.0	0.0
UEQ.D6.R600	-0.6	2.3	-0.5	1.8	0.0	0.0
UEQ.D8.R1800	-0.5	1.7	-0.3	1.2	0.0	0.0
UEQ.D8.R1200	-0.7	2.4	-0.4	1.6	0.0	0.0
UEQ.D8.R600	-1.3	4.1	-0.8	2.6	0.0	0.0

Note: The roadway cross-slope (θ_{RCS}) is not included in table.

Positive (+) for outside girder higher than inside girder.

*Five girder system used instead of three girder system

The maximum I-girder system twist for all 18 FE models are given in Table 11.5. The values in the table were calculated assuming there was no roadway cross-slope (i.e. $\theta_{RCS} = 0$) which is a positive value that can be simply added to the values in the table. A positive angle indicates that the outer girder is at a higher elevation than the inner girder and vice versa for a negative angle. For the 9 equal span systems, the maximum system twist (negative in Span 1 and positive in Span 2) occurred during Load Step 4 (when the concrete deck was present in Span 1 but not in Span 2). For the 9 unequal span systems, the maximum positive system twist occurred in Span 2 during Load Step 1 and the maximum negative system twist occurred in Span 1 during Load Step 4. The magnitude of the system twist increased as the radius of curvature decreased and as the girder depth (and correspond span length) increased. Of the 18 cases investigated, EQ.D8.600 had the largest positive and negative twists (-3.4 degrees and 3.9 degrees) during the five loading stages for the typical 3 I-girder system (a system that is this flexible in torsion would likely not be practical for design). Increasing the total number of girders from 3 to 5 significantly stiffened the system and the largest positive and negative twists during the five load stages dropped to -1.0 degrees and 1.2 degrees.

Table 11.5 I-Girder Maximum System Twist from Parametric Study

I-Girder System	θ_{NL} (deg) No Load (Full Camber)		θ_{LS1} (deg) Load Step 1 (Steel DL)		θ_{LS2} (deg) Load Step 2 (+PCP Span1)		θ_{LS3} (deg) Load Step 3 (+PCP Span2)		θ_{LS4} (deg) Load Step 4 (+Deck Span1)		θ_{LS5} (deg) Load Step 5 (+Deck Span2)		θ_{MAX} (deg) Load Steps 1 Through 5	
	Span1	Span2	Span1	Span2	Span1	Span2	Span1	Span2	Span1	Span2	Span1	Span2	Span1	Span2
EQ.D4.R1800	0.1	0.1	0.0	0.0	0.0	0.2	0.0	0.0	-0.2	0.2	0.0	0.0	**-0.2**	**0.2**
EQ.D4.R1200	0.2	0.2	0.1	0.1	-0.1	0.2	0.0	0.0	-0.2	0.3	0.0	0.0	**-0.2**	**0.3**
EQ.D4.R600	0.3	0.3	0.3	0.3	-0.1	0.5	0.2	0.2	-0.5	0.7	0.0	0.0	**-0.5**	**0.7**
EQ.D6.R1800	0.4	0.4	0.3	0.3	-0.1	0.5	0.2	0.2	-0.6	0.7	0.0	0.0	**-0.6**	**0.7**
EQ.D6.R1200	0.5	0.5	0.4	0.4	-0.2	0.7	0.3	0.3	-0.9	1.1	0.0	0.0	**-0.9**	**1.1**
EQ.D6.R600	1.0	1.0	0.8	0.8	-0.4	1.5	0.5	0.5	-1.9	2.2	0.0	0.0	**-1.9**	**2.2**
EQ.D8.R1800	0.7	0.7	0.5	0.5	-0.2	0.9	0.3	0.3	-1.1	1.3	0.0	0.0	**-1.1**	**1.3**
EQ.D8.R1200	1.0	1.0	0.7	0.7	-0.3	1.3	0.5	0.5	-1.7	1.9	0.0	0.0	**-1.7**	**1.9**
EQ.D8.R600	1.8	1.8	1.1	1.1	-0.8	2.4	0.8	0.8	-3.4	3.9	0.0	0.0	**-3.4**	**3.9**
EQ.D8.R600*	0.8	0.8	0.5	0.5	-0.4	1.0	0.3	0.3	-1.0	1.2	0.0	0.0	**-1.0**	**1.2**
UEQ.D4.R1800	-0.1	0.2	0.0	0.2	-0.1	0.2	0.0	0.1	-0.1	0.2	0.0	0.0	**-0.1**	**0.2**
UEQ.D4.R1200	-0.1	0.3	-0.1	0.3	-0.1	0.3	0.0	0.2	-0.1	0.2	0.0	0.0	**-0.1**	**0.3**
UEQ.D4.R600	-0.2	0.7	-0.1	0.6	-0.2	0.6	-0.1	0.4	-0.2	0.5	0.0	0.0	**-0.2**	**0.6**
UEQ.D6.R1800	-0.2	0.8	-0.2	0.6	-0.2	0.7	-0.1	0.5	-0.2	0.6	0.0	0.0	**-0.2**	**0.7**
UEQ.D6.R1200	-0.3	1.2	-0.2	0.9	-0.3	1.0	-0.2	0.7	-0.3	0.9	0.0	0.0	**-0.3**	**1.0**
UEQ.D6.R600	-0.6	2.3	-0.5	1.8	-0.6	1.9	-0.3	1.3	-0.6	1.6	0.0	0.0	**-0.6**	**1.9**
UEQ.D8.R1800	-0.5	1.7	-0.3	1.2	-0.4	1.2	-0.2	0.8	-0.4	1.0	0.0	0.0	**-0.4**	**1.2**
UEQ.D8.R1200	-0.7	2.4	-0.4	1.6	-0.5	1.8	-0.3	1.2	-0.5	1.5	0.0	0.0	**-0.5**	**1.8**
UEQ.D8.R600	-1.3	4.1	-0.8	2.6	-1.0	2.9	-0.6	1.8	-1.0	2.4	0.0	0.0	**-1.0**	**2.9**

Note: The roadway cross-slope (θ_{RCS}) is not included in table. Positive (+) for outside girder higher than inside girder.

*Five girder system used instead of three girder system

11.2.4 Inclined PCP Experimental Results and Recommendations

The results from the 37 inclined PCP bedding strip tests (explained in detail in Chapter 3) are repeated in Table 11.6 for convenience. According to the sign convention in this chapter (a positive angle means that the outside girder is at a higher elevation than the inside girder), the tests in Chapter 3 were performed where the drop angle was positive and the maximum PCP angle from the inclined PCP tests (Table 11.6) were negative (it was not suspected that testing the PCPs in the opposite direction would significantly change the test results). Table 11.6 shows that increasing the drop angle from 0 degrees to 2.5 degrees reduced the maximum angle by less than 10% on average. It is not expected that further increasing the drop angle (to say 5 degrees) will significantly reduce the maximum angle that can be achieved, but more laboratory experiments should be conducted to validate this hypothesis. The testing procedure of the unconnected PCPs on the bedding strips is covered in detail in Chapter 3.

Table 11.6 Maximum PCP Angle from Inclined PCP Tests (Degrees)

Bedding	Drop Angle = 0°			Drop Angle = 2.5°		
Strip Size	1-PCP	2-PCP	2-PCP*	1-PCP	2-PCP	2-PCP*
1"x1"	26.1	21.4	28.3†	23.5	14.3	28.8†
1.5"x1.5"	26.8	24.0	29.0†	24.2	22.5	29.1†
2"x2"	26.8	25.6	30.6†	24.6	24.6	31.9†
1"x2"	13.3	0.0	0.0	12.0	2.8	0.0
1.5"x3"	16.8	10.6	12.5	15.5	10.6	11.0
2"x4"	18.6	14.3, 19.1†	13.8	16.3	13.7	14.5

*Flange plate horizontal separation (Δ_{LAT} = 0.75")

†Bedding strips bonded to beams with compatible adhesive

Since a PCP falling from the superstructure could prove to be catastrophic, the research team recommends that a relatively large factor of safety (FS) of 3.0 be used for design. Table 11.7 shows the maximum recommended PCP angle that should be used for each bedding strip size. The recommendation is based on the minimum values from the tests with test with drop angles of 0° and 2.5° (using 2 PCPs with Δ_{LAT} = 0.75″ and FS = 3.0). Linear interpolation was used to populate the table between the bedding strip sized that were tested (extrapolation was not used to increase the angle for the bedding strips with the aspect ratios less than 1:1). The bedding strips should be bonded to the steel flanges with compatible adhesive and allowed to cure prior to placement of the PCPs. Bonding of the bedding strip was shown to help prevent the sliding of the bedding strips on the flanges and increase the maximum angle of the PCPs (which was especially true for bedding strips with a 1:1 aspect ratio). Placing the PCPs on the bedding strips prior to curing of the adhesive should be avoided as the uncured adhesive will effectively act as a lubricant which will likely reduce the maximum angle of the unconnected PCP. Also, the maximum top flange separation (Δ_{LAT}) should not exceed 0.75 inches (since tests were not conducted past this limitation).

Table 11.7 Maximum PCP Inclination Angle (deg.) for Design (FS = 3.0)

Bedding Strip	Height														
Width	½"	¾"	1"	1 ¼"	1 ½"	1 ¾"	2"	2 ¼"	2 ½"	2 ¾"	3"	3 ¼"	3 ½"	3 ¾"	4"
1"	9.4	9.4	9.4*	7.1	4.7	2.4	0*	-	-	-	-	-	-	-	-
1 ¼"	9.6	9.6	9.6	9.6	8.0	6.5	4.9	3.4	1.9	-	-	-	-	-	-
1 ½"	9.7	9.7	9.7	9.7	9.7*	8.7	7.7	6.7	5.7	4.7	3.7*	-	-	-	-
1 ¾"	10.0	10.0	10.0	10.0	10.0	10.0	9.1	8.3	7.5	6.6	5.8	5.0	4.2	-	-
2"	10.2	10.2	10.2	10.2	10.2	10.2	10.2*	9.5	8.8	8.1	7.4	6.7	6.0	5.3	4.6*

*Minimum values from labortory test with drop angle = 0° and 2.5° & Δ_{LAT} = 0.75" divided by FS = 3.0

The three I-girder EQ.D8.R600 system with an assumed roadway cross-slope of 4 degrees (θ_{RCS} = 4°) will be used as an example assuming a SDLF condition for the cross-frames. The value for the roadway cross-slope is added to the maximum positive and negative system twist from the analysis (-3.4° and 3.9° from Table 11.5). Therefore, the PCPs will experience inclinations between approximately 0.6° and 7.9° during the five loading stages. Referencing Table 11.7, any bedding strip with a 1:1 aspect ratio (1″x1″ through 2″x2″) can be used (since 7.9° < 9.4° and 10.2°). For this case, however, the maximum bedding strip height is limited to 2 ¾″ when a 2″

wide bedding strip is used. The maximum flange separation for this case (Δ_{LAT} = 0.30″) was less than the limiting value of 0.75″. For the five I-girder EQ.D8.R600 system, the system twist ranged from -1.0° to 1.2° degrees (from Table 11.5) which was significantly less than the three I-girder system. Again with an assumed roadway cross-slope of 4 degrees (θ_{RCS} = 4°) the PCPs will experience inclinations between approximately 3.0° and 5.2° during the five construction stages. Therefore, a 2″ wide bedding strip up to 3 ¾″ tall can be used for this system (since 5.2° < 5.3°).

11.2.5 Steel I-Girder Warping Deformations during Construction

While system twist is largest near midspan during the construction of a curved girder system, deformations near the support also need to be considered for the stability of PCPs on bedding strips. For curved I-girder systems, warping deformations are largest near the end of the girder at the support where there is a warping permitted boundary condition (see Figure 11.16). As the girders twist at the warping permitted bounty, the top and bottom flanges do not bend but simply rotate at the end. The top flanges of adjacent girder remain parallel to each other as they rotate about the support by an angle (ϒ) as shown in Figure 11.17.

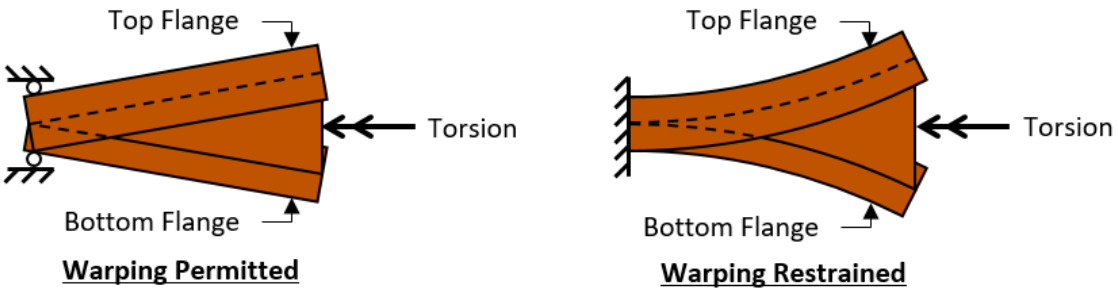

Figure 11.16 Torsion Boundary Conditions of I-Girders

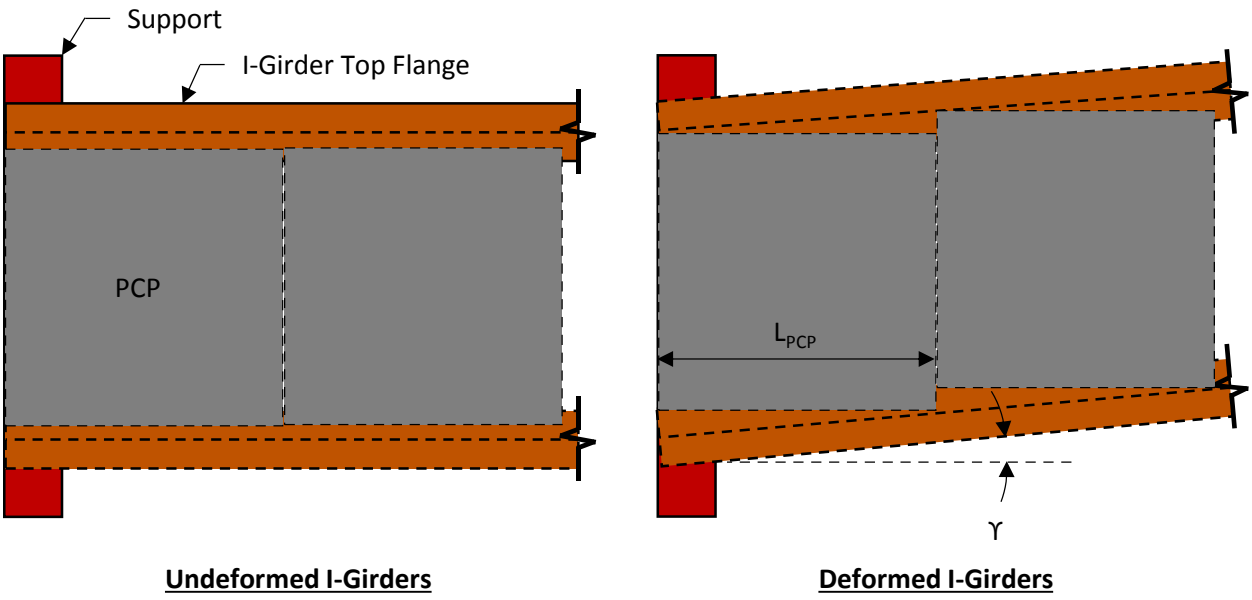

Figure 11.17 I-Girder Deformation near the Supports – Plan View

The warping deformations of the I-girders near the supports should be considered at each loading stage during construction to ensure that the unconnected PCPs are stable on the bedding strips. The 18 models (Table 11.3) from the parametric study for the I-girders (Chapter 9) were used to determine the maximum warping deformation of the various I-girder systems during the five construction loading stages. Table 11.8 shows the maximum warping deformation in each span which was measured near the supports of the system. For the 9 equal span systems, the maximum warping deformation was near the end support in Span 1 during Load Step 4 (when the concrete deck was present in Span 1 but not in Span 2). For the 9 unequal span systems, the maximum warping deformation occurred in Span 2 near the end support during Load Step 5. Of the 18 cases investigated, EQ.D8.600 had the largest warping deformation (2.0 degrees) during the five loading stages (for the typical 3 I-girder system). Increasing the total number of girders from 3 to 5 significantly stiffened the system and the largest warping deformation during the five load stages dropped to 0.8 degrees.

Table 11.8 I-Girder Maximum Warping Deformation from Parametric Study

I-Girder System	Υ_{LS1} (deg) Load Step 1 (Steel DL)		Υ_{LS2} (deg) Load Step 2 (+PCP Span1)		Υ_{LS3} (deg) Load Step 3 (+PCP Span2)		Υ_{LS4} (deg) Load Step 4 (+Deck Span1)		Υ_{LS5} (deg) Load Step 5 (+Deck Span2)		Υ_{MAX} (deg) Load Steps 1 Through 5	
	Span1	Span2	Span1	Span2	Span1	Span2	Span1	Span2	Span1	Span2	Span1	Span2
EQ.D4.R1800	0.0	0.0	0.0	0.0	0.0	0.0	0.1	0.1	0.0	0.0	**0.1**	**0.1**
EQ.D4.R1200	0.0	0.0	0.0	0.0	0.0	0.0	0.2	0.1	0.1	0.1	**0.2**	**0.1**
EQ.D4.R600	0.0	0.0	0.1	0.1	0.0	0.0	0.3	0.2	0.1	0.1	**0.3**	**0.2**
EQ.D6.R1800	0.0	0.0	0.1	0.1	0.1	0.1	0.5	0.2	0.2	0.2	**0.5**	**0.2**
EQ.D6.R1200	0.0	0.0	0.2	0.1	0.1	0.1	0.7	0.4	0.2	0.2	**0.7**	**0.4**
EQ.D6.R600	0.1	0.1	0.4	0.2	0.1	0.1	1.4	0.7	0.4	0.4	**1.4**	**0.7**
EQ.D8.R1800	0.1	0.1	0.2	0.1	0.1	0.1	0.8	0.4	0.3	0.3	**0.8**	**0.4**
EQ.D8.R1200	0.1	0.1	0.4	0.2	0.2	0.2	1.1	0.5	0.4	0.4	**1.1**	**0.5**
EQ.D8.R600	0.1	0.1	0.6	0.3	0.3	0.3	2.0	0.8	0.6	0.6	**2.0**	**0.8**
EQ.D8.R600*	0.1	0.1	0.3	0.2	0.1	0.1	0.8	0.4	0.3	0.3	**0.8**	**0.4**
UEQ.D4.R1800	0.0	0.0	0.0	0.0	0.0	0.0	0.0	0.0	0.0	0.1	**0.0**	**0.1**
UEQ.D4.R1200	0.0	0.0	0.0	0.0	0.0	0.0	0.0	0.0	0.1	0.1	**0.1**	**0.1**
UEQ.D4.R600	0.0	0.0	0.0	0.0	0.0	0.1	0.0	0.0	0.1	0.3	**0.1**	**0.3**
UEQ.D6.R1800	0.0	0.0	0.0	0.0	0.1	0.1	0.0	0.1	0.2	0.4	**0.2**	**0.4**
UEQ.D6.R1200	0.0	0.1	0.0	0.0	0.1	0.2	0.0	0.1	0.2	0.6	**0.2**	**0.6**
UEQ.D6.R600	0.1	0.1	0.0	0.1	0.1	0.3	0.1	0.2	0.4	1.1	**0.4**	**1.1**
UEQ.D8.R1800	0.1	0.1	0.1	0.1	0.1	0.3	0.1	0.2	0.3	0.7	**0.3**	**0.7**
UEQ.D8.R1200	0.1	0.2	0.1	0.1	0.2	0.4	0.1	0.3	0.4	1.0	**0.4**	**1.0**
UEQ.D8.R600	0.2	0.3	0.1	0.2	0.3	0.6	0.2	0.5	0.5	1.5	**0.5**	**1.5**

*Five girder system used instead of three girder system

11.2.6 Inclined PCP Experimental Results and Recommendations

The result from the 9 unconnected PCP bedding strip warping tests (explained in detail in Chapter 3) are repeated in Table 11.9 for convenience. The test frame was limited to a maximum of 4.0 degrees of deformation which was reached prior to the PCP falling from the bedding strips with a 1:1 aspect ratio (1″x1″, 1.5″x1.5″, and 2″x2″). Figure 11.18 shows the edge of the PCP on the loading beam at Υ_{max} = 4.0 degrees for the 1″x1″, 1.5″x1.5″, and 2″x2″ bedding strips. While the PCPs did not fall from the frame, one corner of the PCP had moved to where there was no overlap between the PCP and the top flange which is undesirable from a constructability standpoint (the overlap had increased at the other corner of the PCP). TxDOT (2014a) requires that the PCP

extend past the bedding strip towards the web of the girder a minimum of 1½″ so that concrete can flow under and support the PCP (see Figure 11.1).

Table 11.9 Experimental Results from Unconnected PCPs Shear Tests on Bedding Strips

Bedding Strip Size	2-PCPs			1-PCP		
	Υ_{max} (deg)	Δ_{NE_MAX} (in)	Δ_{SE_MAX} (in)	Υ_{max} (deg)	Δ_{NE_MAX} (in)	Δ_{SE_MAX} (in)
1"x1"	4.0*	-3.4	3.5	-	-	-
1.5"x1.5"	4.0*	-3.8	3.6	-	-	-
2"x2"	4.0*	-3.8	3.2	-	-	-
1"x2"	0.8	-1.1	0.3	1.5	-1.3	1.7
1.5"x3"	1.6	-1.9	1.0	1.7	-1.1	2.2
2"x4"	3.2	-3.7	2.2	3.6	-4.2	2.8

*Test Frame Limit

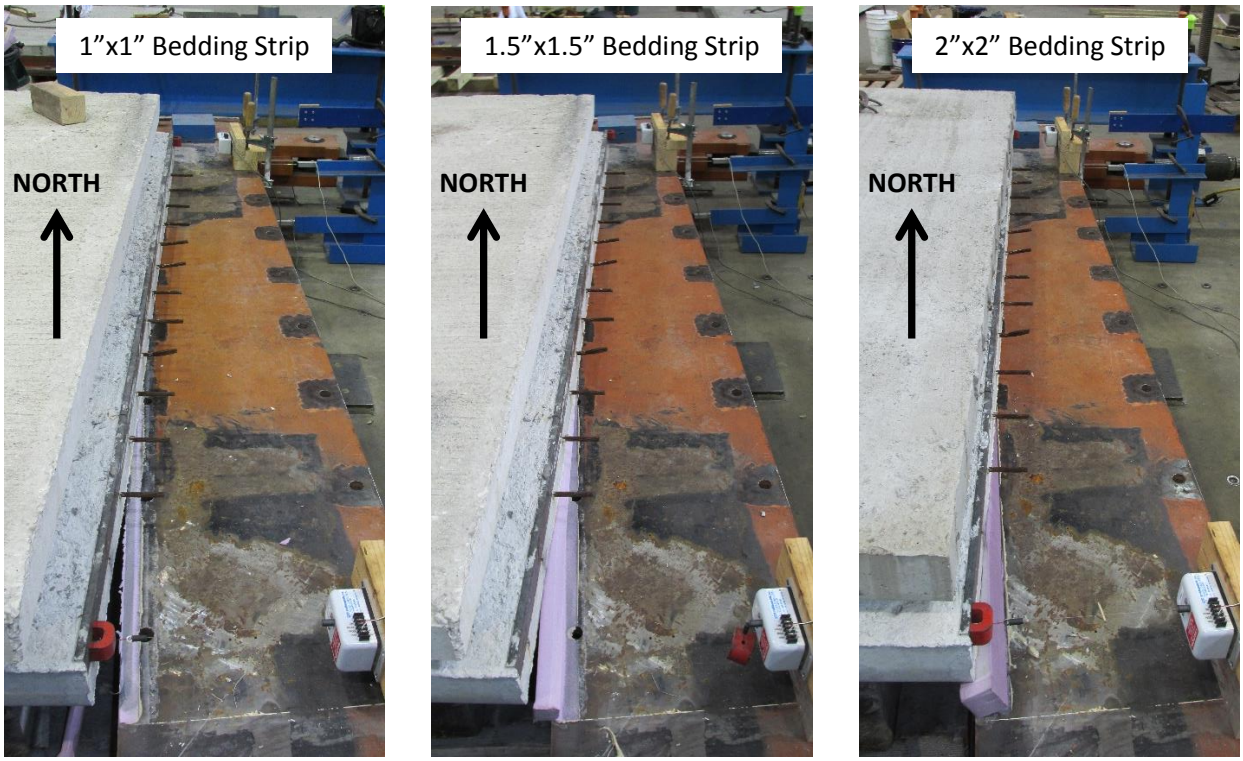

Figure 11.18 PCP Shear Test Frame – Laboratory Photograph

When using PCPs on curved girder systems where warping deformations are significant, the dimension that the PCP extends past the bedding strip (X_{con} in Figure 11.19) should be calculated as follows:

$$X_{con} = 0.5 \cdot L_{pcp} \cdot \tan(\gamma_{max}) + 1.5" \tag{11.1}$$

where,

L_{pcp} = PCP length
γ_{max} = maximum warping deformation of PCPs

This will allow the PCP to be supported by a minimum of 1.5 inches of concrete, accounting for the warping deformation of the girders. As a side note, increasing the overlap of the PCPs on the top flange will require the outer shear studs to be moved closer to the center of the flange.

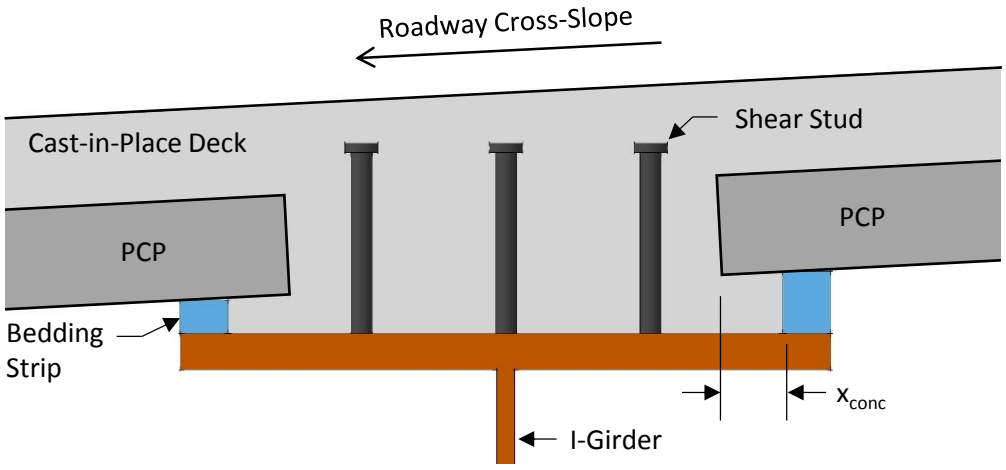

Figure 11.19 PCP Shear Test Frame – Laboratory Photograph

Once again, the research team recommends that a factor of safety of 3.0 be used for design. One of the reasons for the large factor of safety is that the tests were performed with the level PCPs (i.e. the two simulated top flanges on the testing frame were at the same elevation). In a real bridge system, the warping deformation will occur with the PCPs at an incline (near the support the incline will approximately equal the roadway cross-slope). Table 11.10 shows the maximum recommended shear deformation that should be used for each bedding strip size. The recommendation is based on the laboratory tests that were performed using 2 PCPs (to represent the weight of the deck and the PCP). Linear interpolation was used to populate the table between the bedding strip sizes that were tested (extrapolation was not used to increase the angle for the bedding strips with the aspect ratios less than 1:1). The bedding strips should be bonded to the steel flange with compatible adhesive and allowed to cure prior to placement of the PCPs. Placing the PCPs on the bedding strips prior to curing of the adhesive should be avoided as the uncured adhesive will effectively act as a lubricant which will likely reduce the maximum values in Table 11.10.

Table 11.10 Maximum Warping Angle (deg.) for Bedding Strip Size for Design (FS = 3.0)

Bedding Strip	Height														
Width	½"	¾"	1"	1 ¼"	1 ½"	1 ¾"	2"	2 ¼"	2 ½"	2 ¾"	3"	3 ¼"	3 ½"	3 ¾"	4"
1"	1.33	1.33	1.33*	1.07	0.80	0.53	0.27*	-	-	-	-	-	-	-	-
1 ¼"	1.33	1.33	1.33	1.33	1.15	0.96	0.77	0.59	0.40	-	-	-	-	-	-
1 ½"	1.33	1.33	1.33	1.33	1.33*	1.20	1.07	0.93	0.80	0.67	0.53*	-	-	-	-
1 ¾"	1.33	1.33	1.33	1.33	1.33	1.33	1.26	1.18	1.10	1.03	0.95	0.88	0.80	-	-
2"	1.33	1.33	1.33	1.33	1.33	1.33	1.33*	1.30	1.27	1.23	1.20	1.17	1.13	1.10	1.07*

*Minimum values from labortory test divided by FS = 3.0

Again, the three I-girder EQ.D8.R600 system will be used as an example. From Table 11.8 the maximum warping deformation (Υ_{max}) was 2.0 degrees. This value exceeds the maximum value in Table 11.10 and therefore PCPs should not be used on a system with such a large amount of warping deformation and a more traditional formwork system should be considered (such as permanent metal deck forms). For the five I-girder EQ.D8.R600 system, the maximum warping deformation (Υ_{max}) was 0.8 degrees. Referencing Table 11.10, a 2 inch wide bedding strip could be used up to a height of 4″ (since 0.8° < 1.1°). Assuming the length of the standard PCP is 8′-0″, the PCP should extend past the bedding strip 2 ¼ inches ($X_{con} = 0.5 \cdot 96'' \cdot \tan(0.8) + 1.5'' = 2.17'' \approx 2\ ¼''$). Therefore, the total overlap of the PCP and the flange will be 4 ¼ inches (2 ¼″ plus 2″ for the bedding strip).

11.2.7 Details to Minimize Bedding Strip Height

The experimental tests from Chapter 3 showed that increasing the height of the bedding strip had a tendency to reduce the stability of the unconnected PCPs on the superstructure. In Texas, steel I-girders are typically fabricated with a constant web depth and a varying overall depth due to changes in the flange thickness (see Figure 11.20). Therefore, the height of the bedding strip will increase in portions of bridge to maintain a constant deck thickness along the length of the bridge. To reduce the height of the bedding strips (and the associated instability of the PCPs on the bedding strips), the girders can be fabricated with a constant depth along the length (see Figure 11.21). The change in the flange thickness can occur at a bolted splice location and will likely not be a fabrication issue. Constant depth girders with similar details to Figure 11.21 were used with success in the approach spans for the Tappan Zee Bridge in New York (LaViolette 2014).

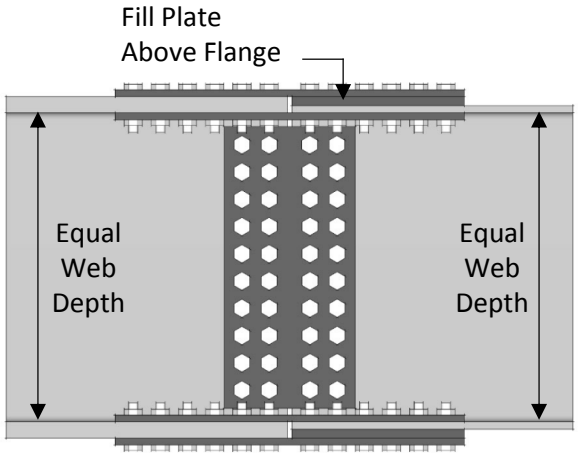

Figure 11.20 Standard Girder Connection Elevation

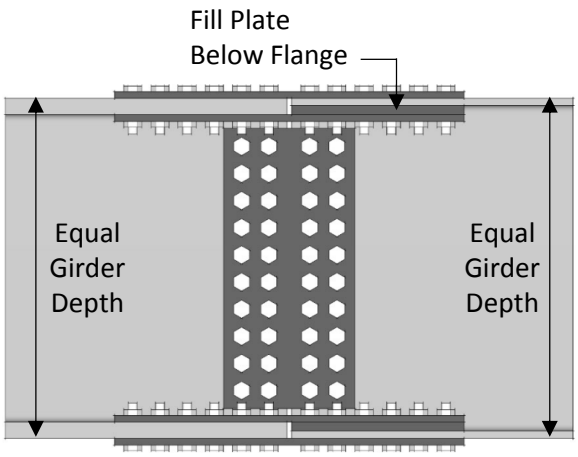

Figure 11.21 Proposed Girder Connection Elevation

11.3 Unconnected PCPS on Curved Steel Tub Girders

In addition to investigating the potential benefits of providing a positive connection between PCPs and tub girders, the stability of PCPs on curved tub girder systems with no positive connection to the girders was investigated (assuming that a traditional top lateral truss was used and the PCPs were acting only as stay-in-place formwork). This application is essentially the same as the current use in straight girder systems. A major difference between the straight and curved girder systems is the relative vertical and lateral deformation that will occur as the adjacent tub girders torsionally deform during placement of the PCPs and the concrete deck (especially if no intermediate external cross-frames are used between adjacent tub-girders). The stability of the unconnected PCPs on the bedding strips is of concern due to the differential deformations that may occur at the supported ends of the panels. In addition to looking at the stability of unconnected the PCPs between tub girders, the stability of the PCPs placed on the tub girders (above the top lateral truss) was considered.

11.3.1 Steel Tub Girder Construction Details

Steel tub girders with an adequate top lateral truss will effectively act as a torsionally stiff quasi-closed section. In curved girder systems, the individual girders will twist and deflect independent of each other when no intermediate external cross-frames are used to tie the girders together. A preliminary analytical procedure for simply supported curved tub girders was developed by Helwig et al. (2007) to approximate the relative deformation of the two tub girders to determine if intermediate external cross-frames are needed to control twist. Figure 11.22 shows both the undeformed and deformed section of the girders during construction where ϕ_{ext} and ϕ_{int} are the twist of the exterior and interior tub girders, respectively. Since the finishing machine rails are supported on the overhanging brackets, the exterior and interior rails will move with their corresponding tub girders. Therefore, the finished concrete deck will be parallel to the line that passes through the points A and D at a slope of ϕ^*. The relative deviation from a uniform deck thickness is given by the following expression:

$$\Delta_{max} = |\Delta_B^*| + |\Delta_C^*| \quad (11.2)$$

where,
$\Delta^*_B = (\phi_{ext} - \phi^*)(C_A + C_B)$
$\Delta^*_C = (\phi_{int} - \phi^*)(C_C + C_D)$

This derivation assumes that the top flanges of the tub girders are collinear prior to the application of the load. Helwig et al. (2007) indicated that 0.5 inches is a reasonable limit for Δ_{max}.

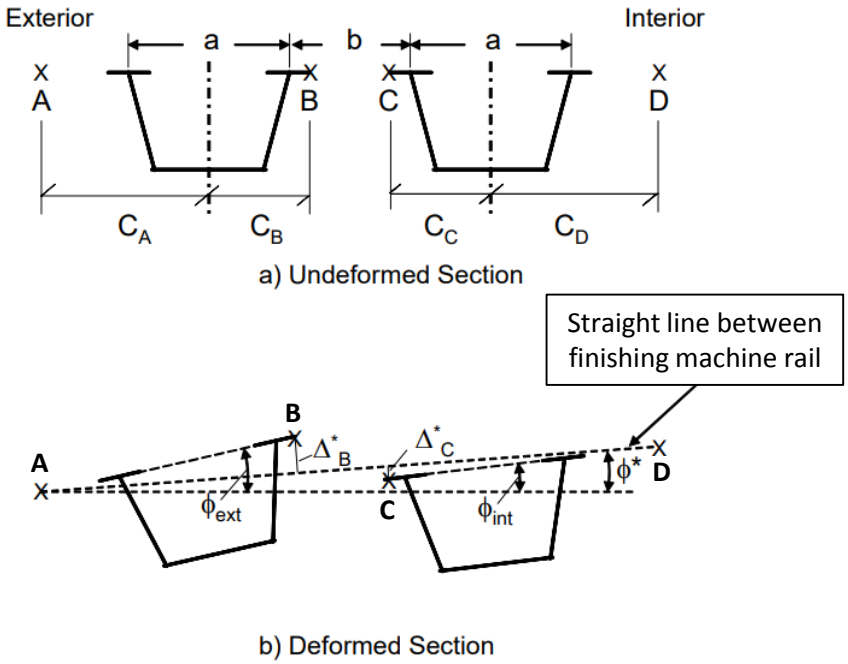

Figure 11.22 Critical Locations Affecting Deck Thickness (Helwig et al. 2007)

When intermediate external cross-frames are used for tub girders, they are typically detailed to fit the girders in the NL or SDL condition (depending on the erection sequence) as the large torsional stiffness of the girders makes them difficult to twist to accommodate fit-up of the external cross-frames. According to the National Steel Bridge Alliance (2016), steel tub girders are typically designed and detailed to be normal to the roadway cross-slope with all of the webs having equal depth. Additionally, tub girders with large twists may need to be detailed and fabricated with different cambers in each web to create a built-in "reverse" twist to counteract the girder twist under dead load so that the girders are perpendicular to the roadway cross-slope in the completed structure (National Steel Bridge Alliance 2016).

11.3.2 Steel Tub Girder Twist during Construction

The 9 models (Table 11.11) from the parametric study for the tub girders (Chapter 9) were used to determine the deflections of the tub girders at each of the 5 loading stages during construction. The results from the analysis can be used to determine the maximum twist of the girders (to determine the inclination of the PCPs on the girder above the top lateral truss) and to

determine the inclination of the PCPs that span between the adjacent girders. Also, the maximum top flange separation (Δ_{LAT}) was examined to ensure that the values used for the experiments were not exceeded. In the FE models, the top flanges of all girders were at the same elevation prior to the application of any load on the system. The fully-cambered girder geometry in the NL position was taken as the negative of the TDL deflections considering only the vertical deflections and all four of the girder webs were cambered the same amount (i.e. the four top flanges were collinear prior to the application of load). Figure 11.23 shows the plan view of the two tub girder, two span system that was used for the parametric study (Chapter 9 contains a detailed description of the FE models). Figure 11.24 through Figure 11.29 shows the twist of the system at Section A-A for the no load case and for the five load steps during construction (the load on the system is identified in each figure). As described in detail in Chapter 9, a continuous PCP placement and a continuous deck placement were used for construction (i.e. the PCPs were first placed in span 1, then span 2 and next the deck was placed in span 1 and then in span 2). Also, the stiffening of the concrete deck was not considered in this analysis. A top lateral truss with a stiffness of t_{eq} = 0.05 inches was used in each of the FE models.

Table 11.11 FE Models for Tub Girder Parametric Study

Model Name	Girder Depth (ft)	Radius of Curvature (ft)	Span 1 Length (ft)	Span 2 Length (ft)
EQ.T4.R600	4	600	128	128
EQ.T4.R1200	4	1200	128	128
EQ.T4.R1800	4	1800	128	128
EQ.T6.R600	6	600	192	192
EQ.T6.R1200	6	1200	192	192
EQ.T6.R1800	6	1800	192	192
EQ.T8.R600	8	600	256	256
EQ.T8.R1200	8	1200	256	256
EQ.T8.R1800	8	1800	256	256

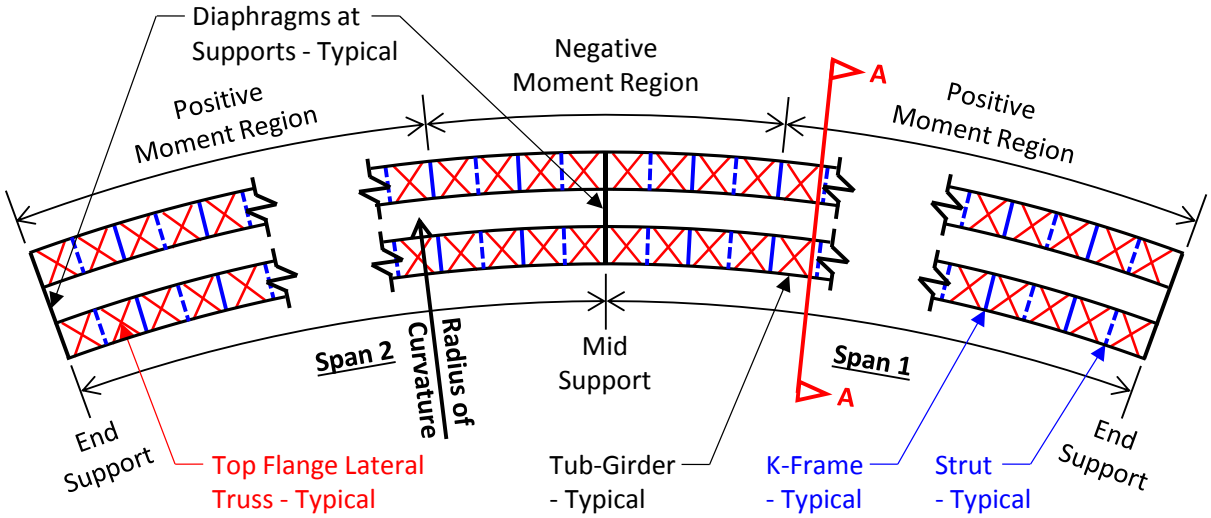

Figure 11.23 Tub Girder Layout for Parametric Study – Plan View

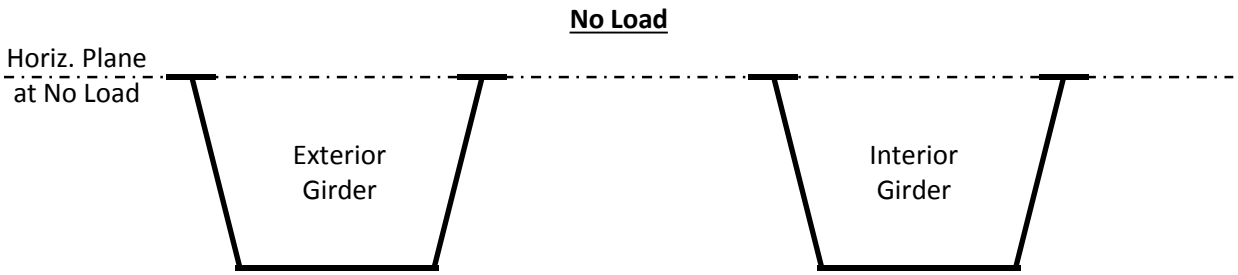

Figure 11.24 No Load – Unconnected Steel Tub Girder Twist – Section A-A

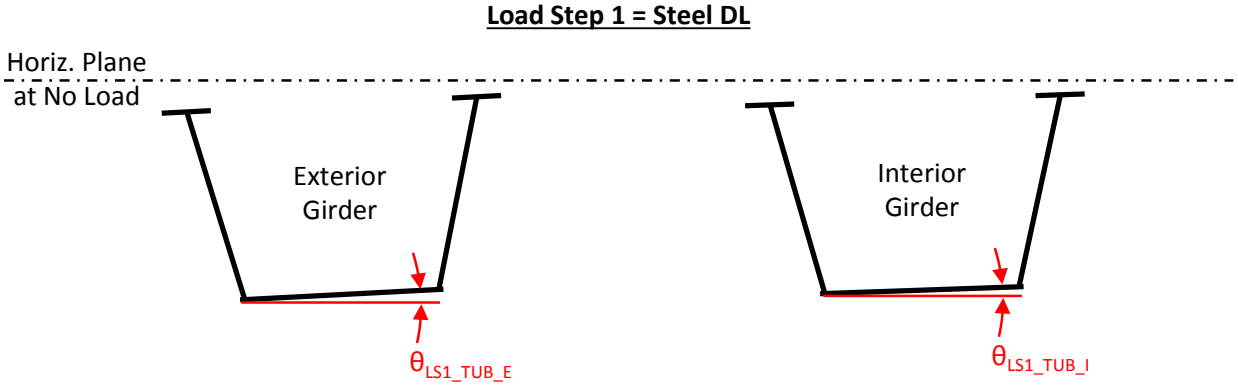

Figure 11.25 Load Step 1 – Unconnected Steel Tub Girder Twist – Section A-A

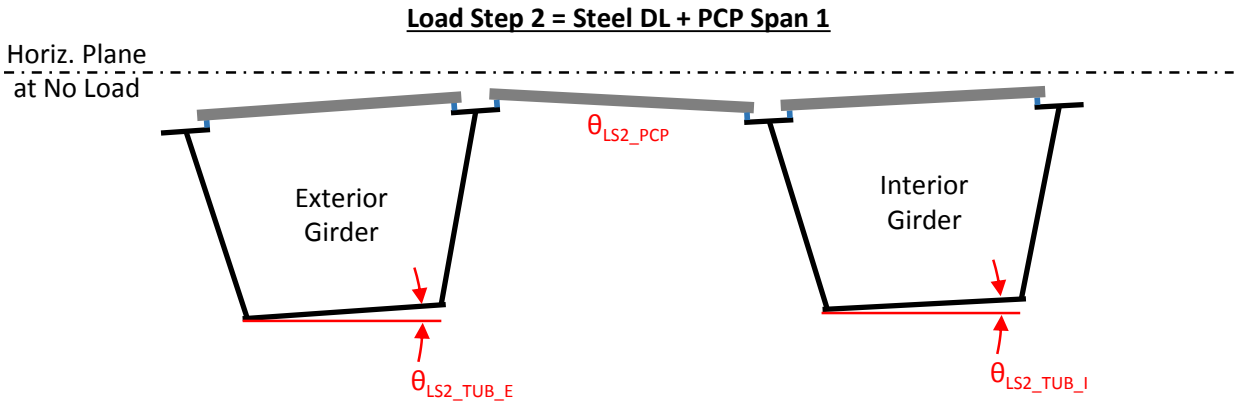

Figure 11.26 Load Step 2 – Unconnected Steel Tub Girder Twist – Section A-A

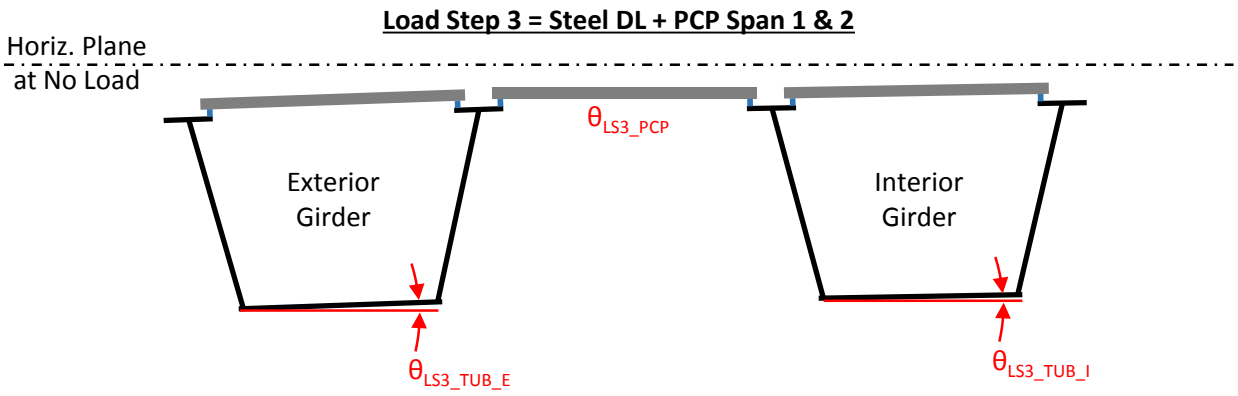

Figure 11.27 Load Step 3 – Unconnected Steel Tub Girder Twist – Section A-A

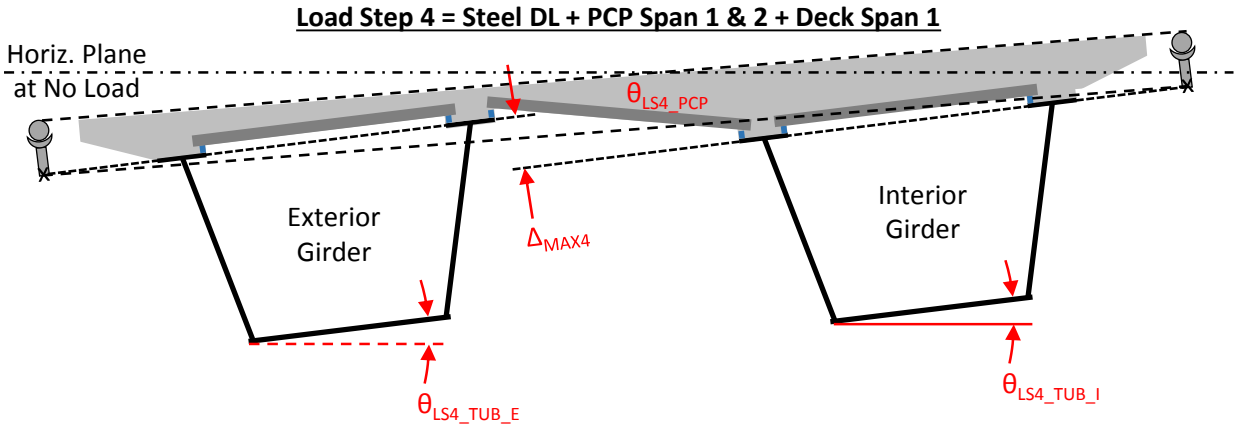

Figure 11.28 Load Step 4 – Unconnected Steel Tub Girder Twist – Section A-A

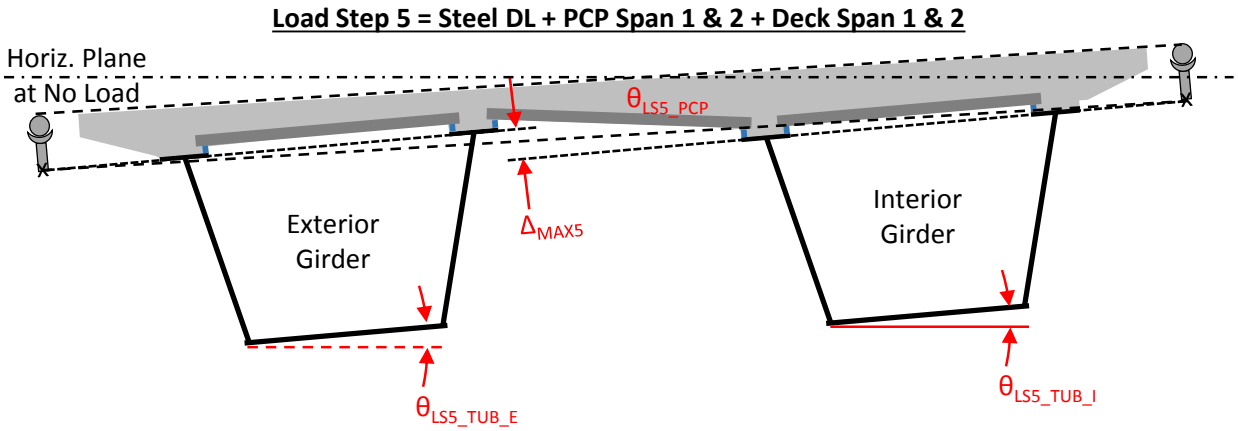

Figure 11.29 Load Step 5 – Unconnected Steel Tub Girder Twist – Section A-A

The maximum of the exterior tub girder twist (θ_{TUB_E}) and the interior tub girder twist (θ_{TUB_I}) at all 5 load steps is given in Table 11.12 which corresponds to the tilt angle of the PCP that sits above the top lateral truss. Also, the maximum angle of the center PCPs (θ_{PCP}) at all 5 load steps is given in Table 11.13 for all 9 FE models. Again, the four top flanges were assumed to be collinear prior to the application of load and the values in the tables were calculated assuming there was no roadway cross-slope (i.e. $\theta_{RCS} = 0$) which is a positive value that can be simply added to the values in the table. A positive angle indicates that the outer flange of the tub girder is at a higher elevation than the inner flange and vice versa for a negative angle.

Table 11.12 Max Tub Twist at Various Load Steps (X-Type Brace - t_{eq} = 0.05 in)

Tub Girder System	Max Tub Twist Load Step 1 (Steel DL)		Max Tub Twist Load Step 2 (+ PCP Span 1)		Max Tub Twist Load Step 3 (+ PCP Span 2)		Max Tub Twist Load Step 4 (+ Deck Span 1)		Max Tub Twist Load Step 5 (+ Deck Span 2)		Max Tub Twist Load Steps 1 Through 5	
	Span1	Span2	Span1	Span2	Span1	Span2	Span1	Span2	Span1	Span2	Span1	Span2
T4-R1800	-0.01	-0.01	-0.09	0.01	-0.07	-0.07	-0.10	0.05	-0.07	-0.07	**-0.10**	**0.05**
T4-R1200	-0.02	-0.02	-0.11	0.02	-0.08	-0.08	-0.14	0.06	-0.10	-0.10	**-0.14**	**0.06**
T4-R600	-0.04	-0.04	-0.17	0.03	-0.12	-0.12	-0.27	0.09	-0.18	-0.18	**-0.27**	**0.09**
T6-R1800	-0.03	-0.03	-0.16	0.02	-0.13	-0.13	-0.21	0.09	-0.15	-0.15	**-0.21**	**0.09**
T6-R1200	-0.05	-0.05	-0.21	0.03	-0.16	-0.16	-0.31	0.10	-0.21	-0.21	**-0.31**	**0.10**
T6-R600	-0.10	-0.10	-0.35	0.07	-0.24	-0.24	-0.59	0.17	-0.38	-0.38	**-0.59**	**0.17**
T8-R1800	-0.07	-0.07	-0.26	0.03	-0.20	-0.20	-0.31	0.11	-0.21	-0.21	**-0.31**	**0.11**
T8-R1200	-0.11	-0.11	-0.34	0.05	-0.25	-0.25	-0.47	0.14	-0.32	-0.32	**-0.47**	**0.14**
T8-R600	-0.21	-0.21	-0.58	0.12	-0.39	-0.39	-0.93	0.25	-0.61	-0.61	**-0.93**	**0.25**

Note: Top lateral brace attached prior Load Step 1 on 100% of span with teq = 0.05 in

Table 11.13 Max PCP Angle between Tubs at Various Load Steps (X-Type Brace - t_{eq} = 0.05 in)

Tub Girder System	Max PCP Angle Load Step 1 (Steel DL)		Max PCP Angle Load Step 2 (+ PCP Span 1)		Max PCP Angle Load Step 3 (+ PCP Span 2)		Max PCP Angle Load Step 4 (+ Deck Span 1)		Max PCP Angle Load Step 5 (+ Deck Span 2)		Max PCP Angle Load Steps 1 Through 5	
	Span1	Span2	Span1	Span2	Span1	Span2	Span1	Span2	Span1	Span2	Span1	Span2
T4-R1800	0.00	0.00	0.02	-0.01	0.01	0.01	0.02	0.00	0.01	0.01	**0.02**	**-0.01**
T4-R1200	0.00	0.00	0.03	-0.02	0.01	0.01	0.02	-0.01	0.02	0.02	**0.03**	**-0.02**
T4-R600	0.00	0.00	0.06	-0.04	0.03	0.03	0.04	-0.01	0.03	0.03	**0.06**	**-0.04**
T6-R1800	0.01	0.01	0.05	-0.03	0.03	0.03	0.04	-0.01	0.03	0.03	**0.05**	**-0.03**
T6-R1200	0.01	0.01	0.08	-0.04	0.04	0.04	0.06	-0.02	0.05	0.05	**0.08**	**-0.04**
T6-R600	0.01	0.01	0.14	-0.09	0.07	0.07	0.11	-0.03	0.08	0.08	**0.14**	**-0.09**
T8-R1800	0.02	0.02	0.09	-0.04	0.05	0.05	0.07	-0.02	0.05	0.05	**0.09**	**-0.04**
T8-R1200	0.03	0.03	0.14	-0.06	0.07	0.07	0.12	-0.03	0.08	0.08	**0.14**	**-0.06**
T8-R600	0.04	0.04	0.26	-0.14	0.12	0.12	0.21	-0.07	0.15	0.15	**0.26**	**-0.14**

Note: Top lateral brace attached prior Load Step 1 on 100% of span with teq = 0.05 in

The 9 equal span tub girder systems with adequately sized top lateral trusses proved to be torsionally stiff. The largest tub girder twists occurred in the T8-R600 system (see Table 11.12) ranging from -0.93 to 0.25 degrees (which corresponds to the maximum angles of the PCP sitting on top of the tub girders). The largest angles of the PCPs spanning between the adjacent girders

ranged from -0.14 to 0.26 degrees (for the T8-R600 system). With an assumed roadway cross-slope of 4 degrees (θ_{RCS} = 4°), the PCPs would experience inclinations between approximately 3.07° and 4.26° during the five loading stages (which is not much different than simply using the value for the roadway cross-slope). Referencing Table 11.7, a number of different bedding strip sizes could safely be used for all of the tub girder systems. Also, since the tubs are torsionally stiff, neglecting the twist of the girders and selecting the bedding strip sized based on the angle of the roadway cross-slope would not significantly change results.

11.3.3 Flange Separation of Adjacent Tub Girders

As the twin tub girder system deforms under construction loads, some separation between the flanges of the adjacent girders may occur (see in Figure 11.30) which can impact the stability of the PCPs that span between the two girders on their bedding strips. The top flange separation (Δ_{LAT}) tends to be maximum near midspan of the girders. The maximum top flange separation (Δ_{LAT_MAX}) was output from the 9 FE models (Table 11.14) from the parametric study for the tub girders (Chapter 9). Of the 9 systems studied in this report, 0.43 inches was the absolute largest top flange separation which is less than the value of Δ_{LAT} = 0.75 inches that was used for the inclined PCP tests in Chapter 3. Therefore, the separation of the two tub girders was relatively small even when no intermediate exterior cross-frames were used, the spans were large (256 feet), and with tight radius of curvatures (R=600 feet).

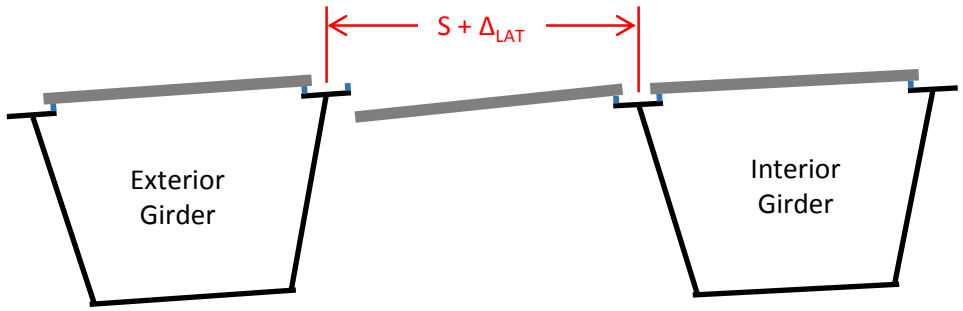

Figure 11.30 Separation of Tub Girders During Construction without Intermediate External Cross-Frames

Table 11.14 Top Flange Separation Tub Girder

Tub Girder System	Δ_{LAT_MAX} (in)
T4-R1800	0.13
T4-R1200	0.13
T4-R600	0.14
T6-R1800	0.30
T6-R1200	0.30
T6-R600	0.31
T8-R1800	0.38
T8-R1200	0.39
T8-R600	0.43

11.3.4 Deviation from Uniform Deck Thickness

In addition to the tub girder twist and top flange separation of adjacent girders, the maximum relative deviation from the uniform deck thickness (Δ_{max} shown in Figure 11.28 and Figure 11.29) was calculated for all 9 of the FE models (based on the vertical deflection of the four top flanges). Table 11.15 summarized Δ_{max} during placement of the concrete deck in Span 1 (Δ_{max4} for Load Step 4) and in Span 2 (Δ_{max5} for Load Step 5). In the calculation of Δ_{max}, the finishing machine rails were assumed to be located at $1.875 \cdot d$ away from the centerline of the tub girders (d = tub girder depth). Of the 9 systems studied, only the T4-R1800 and T4-R1200 tub girder systems do not exceed the 0.50 inch limit suggested by Helwig et al. (2007). Therefore, intermediate external diaphragms would likely be used for the 7 other tub girder systems to allow a more uniform deck thickness to be achieved. Using intermediate external diaphragms will further increase the stiffness of the system and will increase the stability of the PCPs that span between the adjacent girders.

Table 11.15 Deviation from Uniform Deck Thickness

Tub Girder System	Δ_{MAX4} (in)	Δ_{MAX5} (in)
T4-R1800	0.22	0.15
T4-R1200	0.33	0.22
T4-R600	0.66	0.44
T6-R1800	0.51	0.34
T6-R1200	0.76	0.51
T6-R600	1.49	0.98
T8-R1800	0.59	0.41
T8-R1200	0.92	0.64
T8-R600	1.76	1.19

11.3.5 Steel Tub Girder Warping Deformations during Construction

As shown above, warping deformation for I-girder systems can be significant during construction (due to the warping permitted boundary condition) which may impact the stability of the PCPs on the bedding strips near the supports. The top lateral truss of the tub girder system (see Figure 11.31) connects the two top flanges of the girder, creating a torsionally stiff quasi-closed shape. Therefore, the warping deformations for these systems are typically small and are not expected to significantly impact the stability of the PCPs on the bedding strips during construction.

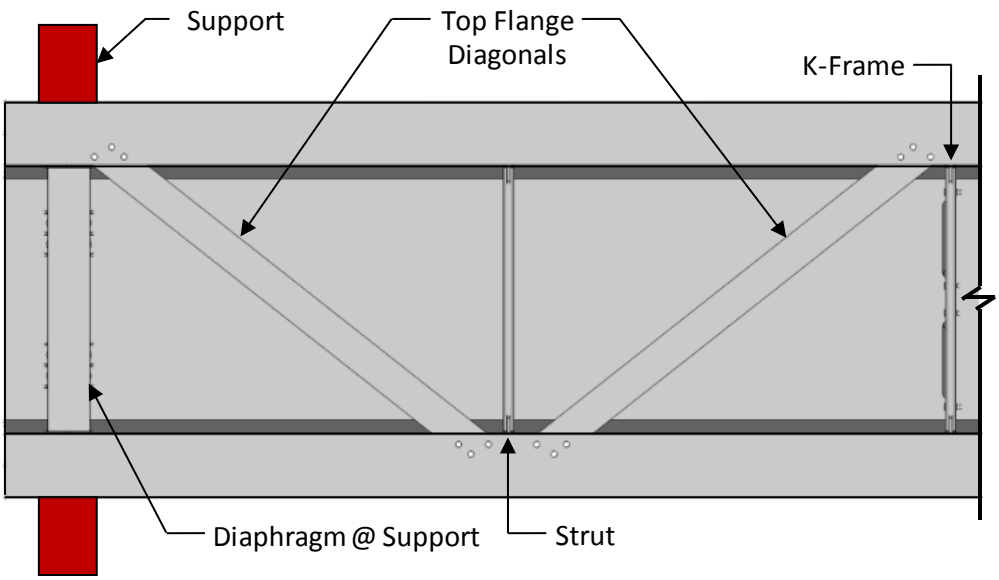

Figure 11.31 Tub Girder Deformation near the Supports – Plan View

11.4 Summary of Unconnected PCPs on Curved I-Girder and Tub Girders

This chapter focused on using unconnected PCPs on curved steel I-girder and tub girder systems by examining the stability of the unattached PCPs on the bedding strips supported by the girders during construction. Limitations on bedding strip sizes versus girder deformations were established based on the experimental results from Chapter 3 and were compared with the deformations from the finite element (FE) models from the parametric studies for the I-girder system and the tub girders in Chapter 9. Below is a summary of this chapter:

- The stability of the unconnected PCPs on the bedding strips is affected by the girder deformation during construction and can be significantly impacted by twist of the girder system, warping deformation of the girders, and separation of adjacent flanges supporting PCPs during construction.
- Limitations on the bedding strip sizes versus the girder twist were established (see Table 11.7) based on the experiments from Chapter 3 using a factor of safety of 3.0. Table 11.7 is based on tests that had a maximum drop angle of 2.5° and a maximum top flange separation (Δ_{LAT}) of 0.75 inches. Note, increasing the drop angle from 0 degrees to 2.5 degrees reduced the maximum angle by less than 10% on average. Therefore, it is not expected that further increasing the drop angle will significantly reduce the maximum angle that can be achieved (more laboratory experiments should be conducted to validate this hypothesis).
- Limitations on the bedding strip sizes versus the I-girder warping deformations were also established (see Table 11.10) based on the experiments from Chapter 3 using a factor of safety of 3.0. When the warping deformations are significant, Equation 11.1 should be used to determine how far the PCP should extend past the bedding strip so that the PCP is supported by a minimum of 1.5″ of concrete.

- The maximum top flange separation was examined for the 18 FE models in the I-girder parametric study with cross-frames at 20 feet on center. Since the effects from the overhang bracket were not explicitly accounted for in the FE model, a model of the I-girder segment between cross-frames was used to account for the twist of the exterior girders between cross-frames. The maximum top flange separation of 0.54 inches was observed for the I-girder system with the longest span and the smallest radius of curvature (i.e. D8.R600) which is less than the value of 0.75 inches that was used for several experiments in Chapter 3. Therefore, it is not suspected that flange separation would have a significant effect on the stability of the PCPs for the I-girder systems with a maximum cross-frame spacing of 20 feet on center.
- The maximum system twist (Table 11.5) and warping deformations (Table 11.8) were presented in this chapter for the 18 FE models in the I-girder parametric study. The girder deformations were investigated at each loading step during construction and the maximum values were compared with the limitations on the bedding strip sizes in Table 11.7 and Table 11.10.
- The maximum flange separation of the adjacent girders for the 9 FE models in the tub girder parametric study (without intermediate exterior cross-frames) was examined. For all 9 systems, the maximum separation of 0.43 inches was observed which occurred in the system with the largest span and the smallest radius of curvature (T8-R600). This values was less than $\Delta_{LAT} = 0.75$ inches that was used for several experiments in Chapter 3. Results from the FE models also showed that intermediate external diaphragm would likely be needed for the majority of the systems to allow a uniform deck thickness to be achieved. Using intermediate exterior cross-frames will further reduce the separation of the adjacent girder and increase the stability of the PCPs. Therefore, flange separation would likely not have a significant effect on the stability of the PCPs for the tub girder systems studied in this chapter.
- The maximum tub girder twist and inclination of the PCPs spanning between adjacent tub girders is given in Table 11.12 and Table 11.13, respectively. The inherent large torsional stiffness of the quasi-closed girders resulted in relatively small twist during the construction phase for the 9 FE models investigated in this chapter (less than 1 degree maximum). Therefore, the angle at which the PCPs sit will be dominated by the inclination of the roadway cross-slope. The use of intermediate external diaphragms will further increase the stability of the PCPs on the tub girder system.
- The bedding strips should be bonded to the steel flange with compatible adhesive and allowed to cure prior to placement of the PCPs. Placing the PCPs on the bedding strips prior to curing of the adhesive should be avoided as the uncured adhesive will effectively act as a lubricant which will reduce the maximum values in Table 11.7 and Table 11.10.

The results mentioned above are specific to the parameters of the FEA described in this chapter and the laboratory experiments performed in Chapter 3. Table 11.7 and Table 11.10 can be used by the designer to limit the size of the bedding strips based on girder deformation during construction. The deformations of the girder systems should be studied on a case-by-case basis during all construction loading phases (as was shown in this chapter) to ensure that the PCPs are

stable during construction. While Abaqus/CAE 6.14 was used in this report to determine girder deformations, this program is often impractical to use for design as it requires extensive knowledge and training to be used efficiently. Biju-Duval (2017) developed a program to analyze curved steel I-girder and tub bridges during erection and construction, named UT Bridge V2.0. The main advantage of UT Bridge V2.0 compared to commercial programs is the ability to quickly model almost any type of curved, complex bridge, including any type of erection plan, cross-frame arrangement, deck placement scenario, etc. With UT Bridge, the designer can easily determine the deformations of the girders during construction to determine if the bedding strip sizes need to be limited to provide stability during construction.

Chapter 12. Conclusions and Recommendations

12.1 Introduction

TxDOT does not currently allow precast concrete deck panels (PCPs) to be used on horizontally curved girder systems. The objective of this research was to investigate extending the use of PCPs to curved girder systems. The focus of the study included steel I-girder systems, steel tub girder systems, and spliced prestressed concrete U-beams, which are currently being considered for use in some Texas bridges.

This report focused both on using PCPs that were positively connected to the girders (before placement of the concrete deck) as well as using PCPs that were not directly connected to the girders during construction. Connection details between the PCPs and the steel girder systems were developed in this study to engage the shear stiffness of the PCPs during the construction phase. The tests on PCPs that were not positively connected are also beneficial since a methodology that demonstrates the panels can be used without a positive connection provides the contractor with an alternative on horizontally curved girder systems. Both experiments and finite element (FE) models were used to study the bracing behavior of PCPs since such an application could reduce the number of traditional bracing members (i.e. cross-frames or diaphragms for the I-girder system and top lateral truss members for the steel tub girder system) that were required during construction. Additionally, the behavior of PCPs on the bedding strips without a positive connection to the girders were investigated to determine if PCPs could be safely used on curved girders. With respect to spliced curved concrete U-beams, this research worked to gain a better understanding of the behavior of the closure pour and reinforcing details to connect the PCPs to the U-beams. Also, FEA parametrical studies were carried out to determine the load levels experienced by the PCPs and the closure pour connection during construction.

12.2 Unconnected PCPs on Curved Girder Systems

Chapter 3 focused on the experimental tests that were conducted in the laboratory to investigate the behavior of PCPs on the bedding strips that are unconnected throughout the construction phase (until the concrete deck stiffens). The behavior of the PCPs with various girder twists (including the girder "drops" associated with cross frame fit-up), separation of adjacent flanges, and warping deformations of the girders were all considered for six different bedding strip sizes (1″x1″, 1″x2″ 1.5″x1.5″, 1.5″x3″, 2″x2″, and 2″x4″). In general, the PCPs were more stable on wider bedding strips with larger aspect ratios (i.e. the 2″x2″ bedding strip was the most stable while the 1″x2″ bedding strip was the least stable). The PCPs withstood extremely large inclinations (31.9 degrees) on 2″x2″ bedding strips, but the 1″x2″ bedding strips failed under the load of one PCPs and a 4″ thick concrete deck prior to the onset of the experimental test. In regards to warping deformations, the 2″x2″ bedding strips withstood 4.0 degrees of deformation while the 1″x2″ bedding strips failed at 0.8 degrees. Therefore, the stability of the PCPs on the bedding strips is highly dependent on the size of the bedding strip. For this study, only PCPs 8′-0″ wide with a span of 8′-3″ were tested in the laboratory and it is expected that the increased load from larger PCPs will decrease the stability of the system.

In Chapter 11, limitations on bedding strip sizes versus girder twist (Table 11.7) and warping deformations (Table 11.10) were established based on the laboratory experiments using a factor of safety of 3.0. The results from the FE models for the I-girder and tub girder parametric studies (Chapter 9) were used to investigate girder deformations under construction loads of numerous systems with different girder sizes, spans, and radii of curvature. The results were

compared with the limitations in Table 11.7 and Table 11.10. For all of the I-girder systems (with cross-frames at 20 feet on center) and tub girder systems (without intermediate external cross frames), the separation of the flanges did not exceed 0.75 inches (the value used in the laboratory experiments in Chapter 3). Therefore, it is not expected that flange separation will have a significant effect on the stability of PCPs on curved girder systems. For the I-girder bridges, the system twist and the warping deformation significantly increased as the span increased, the number of girders decreased, and the radius of curvature decreased. Thus, I-girder systems should be analyzed on a case-by-case basis at their various construction stages and the angle of the roadway cross-slope should be considered to determine what sized of bedding strips will allow the PCPs to be stable during construction. UT Bridge V2.0 (Biju-Duval 2017) can be used to quickly and accurately analyze curved steel I-girder and tub bridges during erection and construction. The inherent large torsional stiffness of the quasi-closed tub girders resulted in relatively small twist during the construction phase (less than 1 degree maximum for the 9 tub girder systems studied in Chapter 9). Therefore, the inclination of the PCPs will likely be dominated by the angle of the roadway cross-slope; Table 11.7 in Chapter 11 can be used to define the bedding strip sizes used during construction. The warping deformations for tub girder systems are typically small and not expected to significantly impact the stability of the PCPs on the bedding strips during construction.

12.3 Shear Stiffness and Strength of PCPs

Chapter 4 supplements the work presented by Kintz (2017) on the 8 PCP/connection systems (4 different details at 2 different bedding strip heights – ½″ and 4″) that were tested in the laboratory to characterize their stiffness and strength. Kintz (2017) indicated that the flexibility of the shear frame likely influenced the measured stiffness of the PCP/connection system. In Chapter 4, the flexibility of the frame was accounted for and the stiffness results were adjusted. For the 8 tests, the shear stiffness (V/ϒ) ranged from 43,936 kips/rad maximum to 23,615 kips/rad minimum (these values were corrected for the flexibility of the shear frame as mentioned previously) and the shear capacity ranged from 154 kips maximum to 91 kips minimum. Seven of the PCPs/connection systems fail via concrete breakout parallel to the edge with the top face of the PCP breaking out while one system failed via weld rupture between the WT and the loading beam.

In Chapter 8, the in-plane stiffness of the PCP/connection system was represented with a simplified model using truss members similar to the model that was used by Helwig and Yura (2008a) to represent the in-plane stiffness of PMDFs and their connections. An equation was derived to calculate the stiffness of a PCP rigidly connected to the shear frame. The calculated stiffness of the PCP was more than an order of magnitude larger than the stiffness of the PCP/connection system from the experiments in Chapter 4. Since the PCP and the connections function as springs in series, it was determined that the flexibility of the system was predominantly controlled by the flexibility of the connection and an equation was derived to represent the stiffness of the PCP connections. The equation accounted for deformation of the connection parallel and perpendicular to the girder span using springs in both directions. The stiffness of the connection springs was determined from the experimental shear tests. Therefore, the stiffness of the members in the simplified truss model could be calculated for a PCP with any span (i.e. distance between adjacent girder flanges) using any of the connections tested in Chapter 4.

12.4 PCPs on Curved I-Girder Systems

Chapter 5 documents the results of the laboratory experiments for the straight twin I-girder system which was designed so that various support, loading, and bracing conditions could be

investigated. The system was loaded laterally in the simply-supported conditions and was also loaded with various combinations of bending and torsion in both a simply-supported and overhanging configuration (this allowed girders with multiple radii of curvature to be simulated with a single straight system). Various bracing conditions were investigated with and without PCPs connected to the top flanges, truss elements connected to the bottom flanges, and one cross-frame connected at midspan (for the simply supported condition). Connecting PCPs to the top flanges of the I-girders considerably reduced the lateral deflection of the girders during the lateral load tests both with and without the cross-frame connected at midspan. In general, adding PCPs and bottom flange truss members increased the load carrying capacity of the system and reduced twist of the I-girders between brace points (by engaging the warping deformation of the flanges and reducing the unbraced length of the girders). When the PCPs were attached to the top flange without the bottom flange truss members, the twist of the girders were dominated by the lateral deflection of the bottom flange (i.e. the bottom flange would kick out). The addition of the PCPs to the system also reduced the forces in the diagonal of the single cross-frame at midspan.

Chapter 9 provides a description of the FE model that was created for the I-girder system with and without the PCPs, bottom flange truss elements, and midspan cross-frame. In the FE model of the I-girder system, the simplified truss model from Chapter 8 was used to represent the in-plane stiffness of the PCP/connection system, but did not account for the tipping restraint that the PCPs provided to the system as observed to occur in the laboratory experiments. The FE model was validated with the 12 lateral load tests and the 27 gravity load tests performed in the laboratory. In the FE model, the boundary conditions at the support were modified to account for the fact that the idealized warping free boundary condition could not be achieved in the laboratory. In general, the analytical results from the FE model corresponded well with the experimental results. For several cases with the PCPs connected to the top flange, however, the FE model underestimated the stiffness of the system which was attributed to the fact that the idealized model for the PCPs only represented the in-plane stiffness of the PCP/connection system and did not account for the tipping restraint.

After validating the FE model for the I-girder system with the experimental results in Chapter 9, a parametric study was conducted which investigated the influence that attaching PCPs had on the torsional stiffness and cross-frame forces on 18 curved I-girder two span systems (with both equal and unequal spans) during the construction phase. Three different girder sections were considered at three different radii of curvature. The systems studied were larger than what could be tested in the laboratory and were representative of those commonly used in Texas with multiple I-girders along the width of the bridge and multiple cross-frames connected along the length. Results from the parametric study showed that connecting PCPs near the support had only a minimal effect on reducing the twist of the bridge system as a whole. Therefore, while the addition of PCPs can significantly reduce the twist of the individual I-girders between the cross-frames, they did not significantly reduce the twist of the entire bridge system for the cases studied in this report. While the laboratory experiments showed that connecting PCPs to the I-girders reduced the forces in the single midspan cross-frame, the parametric study showed that connecting the PCPs at the ends of the spans does not significantly reduce the forces in the cross-frames throughout the bridge. Therefore, if the spacing of the cross-frames is governed by the forces in the cross-frames, adding PCPs to the system will not allow a significant number of cross-frames to be removed from the system.

12.5 PCPs on Curved Tub Girder Systems

Chapter 6 documents the results of the laboratory experiments for the straight tub girder system which was designed so that various support, loading, and bracing conditions could be investigated. Similar to the I-girder system, the tub girder was load laterally in the simply supported conditions and was also loaded with various combinations of bending and torsion in both a simply supported and overhanging configuration (this allowed girders with multiple radii of curvature to be simulated with a single straight system). The tub girder was tested without any top flange bracing elements, with the tradition bracing system (using steel WT diagonals), and with PCPs acting as the bracing elements. Connecting either PCPs or diagonals to the tub girder system significantly increases the torsional and lateral stiffness of the girder for both the simply supported system and the overhanging system. In general, adding the same number of PCPs to the system as WT diagonals produced similar results in regards to stiffness.

Chapter 9 provides a description of the FE model that was created for the tub girder system with and without the PCPs and the diagonal truss members connected to the top flange of the girders. In the FE model of the tub girder system, the simplified truss model from Chapter 8 was used to represent the in-plane stiffness of the PCP/connection system. The FE model was validated with the 5 lateral load tests and the 24 gravity load tests performed in the laboratory. In the FE model, the boundary conditions at the support were modified to account for the warping restraint provided to the bottom flange of the girder by the bearing pad. Over all, the analytical results from the FE model corresponded well with the experimental results and the FE model was not significantly more accurate for the cases with the WT diagonals than it was for the cases with the PCPs.

After validating the FE model for the tub girder with the experimental results, a parametric study was conducted that investigated the influence that the PCPs had on the torsional stiffness of 9 curved twin tub girder two span systems during the construction phase. Three different girder sections were considered at three different radii of curvature. The systems studied were larger than what could be tested in the laboratory and were representative of those commonly used in Texas. The construction sequence is such that the PCPs will be placed after the erection of the steel superstructure. Therefore, to replace the top lateral truss with PCPs, the tub girders must be capable to supporting their own self-weight without a top lateral truss until the PCPs can be attached to the top flanges. Results from the parametric FEA showed that the twist of the curved tub girders under their own self weight increased by more than an order of magnitude when no top flange truss was present. Therefore, the research team does not feel it is practical or safe to erect the steel superstructure with no top lateral truss panels.

The cost of the top flange truss is driven by fabrication cost and changing the member size by a few pounds per foot should not have a large impact on the economics of the design. The PCPs could be used as supplemental bracing elements to the top lateral truss to add stiffness and strength to the system during the placement of the concrete deck, however, it would likely be more cost effective to use a larger top lateral truss and leave the PCPs unconnected.

12.6 Shear Tests on PCP to U-Beam Connections

A research program was conducted to determine the viability of connecting precast panel lid slabs to concrete U-girders to provide torsional stiffness and strength. The proposed TxDOT detail of casting a reinforced closure pour along the interface between the lid slab and girder does result in the formation of a stiff top diaphragm. However, the layout of the system means the lid slab does not function as fully closed box due to the free edges between PCPs in series. Instead

the system behaves more like a system with series of top flange x-braces, similar to quasi-closed tub girders. This results in large concentrated forces at the corners of the panels, which can lead to failure of the connection under low shear loads. Thus, the existing proposed TxDOT detail may not have the capacity to withstand the torsion present in a highly curved U-girder and is likely only appropriate for straight, or minimally curved U-girders. If a closure pour is to be used on a U-girder with a tight radius of curvature, modifications to the detail are likely necessary to improve capacity.

Unfortunately, due to the limited number of tests performed in this program, the behavior of these closure pours is not fully understood, and further research is needed before a definitive "improved" detail can be developed. However, recommendations can be made based on the results of the test program. To prevent splitting failures at the corners of the closure pour, additional shear reinforcement should be placed at the closure pour near the ends of each panel, with ties and hat bars at approximately 4″ spacing over the first foot of pour, rather than the 12″ spacing currently called for. Note that this will likely require coping of the hat bar at some locations to allow installation inside the panel U-bars. Further enhancement in capacity could be possible through decreasing the shear reinforcement spacing along the entire closure pour, but more tests would be needed to determine the resultant increase in strength, if any. To prevent anchorage failures in the closure pour, the researchers recommend a #4 bar be tied to the inside of the R-bars of the girder. While this is most critical over the few feet at the ends of each panel, the researchers recommend this bar be continuous along the specimen (with lap splices as needed), to better take advantage of the continuity between panels in series.

Due to the limited number of tests in the program, an appropriate safety factor for the capacity of the closure pour cannot be determined at this point. The specimens all exhibited reasonable ductility, with large ratios between the yield strain and failure strain. Additionally, the systems failed gradually, softening rather than experiencing an abrupt drop in load. The observed behavior suggests that a limited safety factor can be applied. However, the specimens also frequently experienced significant cracking in either the closure pour or precast panel at loads significantly below their failure load. Due to the construction sequence of this system, this may not be a significant concern, as the cracked elements would not be exposed to the environment in the finished girder. However, if the designer wishes to limit cracking under service load, a significant safety factor will be needed to ensure adequate performance of the system. More research is needed before a conclusion on the appropriate safety factor for the system can be determined.

12.7 Parametric Finite Element Analyses of Straight and Horizontally Curved Precast Concrete U-Beam Systems

In this report, parametric finite element analyses were performed on straight and horizontally curved U-beam system to provide an understanding of the fundamental behavior of U-beam and its interaction with PCP panels. Girder segment lifting, and staged construction sequence were simulated to identify the potential critical conditions during construction. The critical conditions were then used to investigate the maximum shear load demand on the PCP panels with proposed closure pour details. According to the analysis results, during girder lifting, curved U-beam segments may experience notable lateral deflection and flange stress with increased horizontal radius of curvature. Caution should be taken to select proper lengths and limits on the radius of curvature of the segment. For U-beam segments that have relatively long lengths and tighter curvatures, multiple pick-up locations with tandem operating crane groups will likely

be necessary to control excessive stress and deformation and prevent the girder segments from rolling over. Moreover, the results indicated that lateral-torsional buckling could occur if U beams were placed on the supports in unshored conditions. Temporary shoring falsework may be required to prevent section twist before the completion of the cast-in-place lid slab. Shoring frames may be necessary at the ends of girder segments for each span. The maximum shear forces occur at the support end regions with the maximum shear deformation during the asymmetric stage of deck casting or placement. Based on the analysis results in this study, the proposed closure pour details could provide sufficient shear stiffness and strength for straight and mildly-curved bridge application (R≤1200 ft.). However, when it comes to increased bridge curvature, discretion needs to be taken on the selection of proper closure-pour details because potential shear failure might occur. The utilization of high-strength concrete on concrete U beam could significantly increase the load demand on the PCP panels. The conclusions in Chapter 10 were based on simplified three-dimensional FEA analyses. The interpretation of the results depends on the assumptions and simplifications adopted in the analyses. Only construction limit states were evaluated in this study without considering any post-tensioning. Future work could focus on refined analysis to evaluate both construction and serviceability limit states.

TxDOT has existing details for the reinforcing between the PCPs and the U-beams for the closure pour of U-Beams. Comparisons between experimental results and the predicted demand for horizontally curved girders systems with a radius of curvature between 1800 and 800 feet showed that the existing detail was inadequate and requires modifications. Several tested modifications had beneficial effects on the behavior and strength of the connections. Additional considerations on the performance of the connections may need to be discussed with TxDOT as well as the precast industry. Additional testing is likely necessary to achieve the greatest efficiency.

12.8 Recommendation for Future Work

This research report focused on using PCPs with and without a positive connection to the curved girder systems. The study focused on the behavior during the construction condition, which would be the critical time for the PCPs. While this report provides guidelines for the stability of PCPs on bedding strips during construction, additional work is still needed to fully understand the interaction between the PCPs, the concrete deck, and the curved girders after construction has been completed and the bridge is subject to both dead load and live load. Currently, TxDOT prefers to have a monolithic deck on bridges with curved steel girders due to the complicated interaction between the deck and the girders.

While this research has primarily focused on using PCPs on curved girder systems, several laboratory experiments were conducted on the straight steel I-girder and tub girder systems with concentric vertical loads (i.e. the girders experienced bending moments with no torsion applied to the system). Connecting PCPs to straight steel girder systems significantly increased the elastic buckling capacity of the girders, indicating that the PCPs would likely produce suitable diaphragm bracing elements for the compression flanges of straight steel girder systems.

The main area for which additional work is necessary is on the behavior of curved concrete U-beams during construction. As noted, significant testing was carried out to look at the behavior of the existing TxDOT reinforcing details and modifications to the detailing requirements were tested. Additional testing on the reinforcing that focuses on improved limits to the cracking is recommended.

References

ACI (2011). Building Code Requirements for Structural Concrete (ACI 318-11) and Commentary (ACI 318R-11). American Concrete Institute. Farmington Hills, MI

Agnew, L. S. (2007). Evaluatoin of the Fatigue Behavior of Bridge Decks with Precast Panels at Expansion Joints, M.S. Thesis, University of Texas, Austin.

AISC (2010). Code of standard practice for steel buildings and bridges, 14th Ed., Chicago.

American Association of State Highway Transportation Officials (AASHTO) (2017), *LRFD Bridge Design Specifications*, 8th Edition, Washington, D.C.

Amornrattanapong (2006). *Horizontally Curved Concrete I-Girder Bridges*, PhD Dissertation, University of Nebraska, Lincoln, Nebraska

Armijos, S.M., Wang, Y., Helwig, T.A., Engelhardt, M., Clayton, P., and Williamson, E., (2018) "Experimental Study on the Interaction of Partial Top Lateral and K-Frame Bracing on Tub Girders." Structural Stability Research Council Proceedings, Annual Stability Conference, Baltimore, Maryland, April 10-13

ASTM C39-12: Compressive Strength of Cylindrical Concrete Specimens. West Conshohocken: ASTM International, 2012.

ASTM C78-16: Standard Test Method for Flexural Strength of Concrete (Using Simple beam with Third-Point Loading). West Conshohocken: ASTM International, 2016.

Badie, Baishya and Tadros (1998). NUDECK – A New Prestressed Stay-in-Place Concrete Panel for Bridge Decks, Proceedings from the 1998 Transportation Conference Proceedings, pp. 45-50

Barker, J. M. (1975). Research, Application, and Experience with Precast Prestressed Bridge Deck Panels. PCI Journal, Vol. 20, No. 6.

Battistini, A., Wang, W., Donahue, S., Helwig, T., Engelhardt, M., and Frank, K., (2013). "Improved Cross Frame Details for Steel Bridges." Report 0-6564-1, Center for Transportation Research, University of Texas at Austin, October

Biju-Duval, P., (2017). Development of Three-Dimensional Finite Element Software for Curved Plate Girder and Tub Girder Bridges during Construction. PhD Dissertation, University of Texas at Austin, Austin, TX

Birkeland, P.W., and Birkeland, H.W (1966). Connections in precast concrete construction, American Concrete Institute, Journal of the American Concrete Institute, Vol. 63, No. 3, pp. 345-368

Boswell, C. A., (2008), Simple Design Details Using Precast Concrete Panels at Skewed Expansion Joints, M.S. Thesis, University of Texas, Austin.

Bumen (2012). Bridge Decking Panel with Fastening Systems, US Patent 8,166,595, filed October, 3, 2011 and issued May, 1, 2012

Chang, C. J., (2006). *Construction Simulation of Curved Steel I-Girder Bridges,* PhD Dissertation, Georgia Institute of Technology, Atlanta, GA

Chang and White (2008). "An Assessment of Modelling Strategies for Composite Curved Steel I-Girder Bridges", *Engineering Structures*, Vol. 30, No. 11, pp. 2991-3002

Chen, B., Yura, J., Williamson, E. and Frank, K. (2005). "Top-Lateral Bracing System for Trapezoidal Steel Box-Girder Bridges", Report 0-1898-4, Center for Transportation Research, University of Texas at Austin, August

Coselli, C. J. (2004). *Behavior of Bridge Decks with Precast Panels at Expansion Joints*, M.S. Thesis, University of Texas, Austin.

Currah, R. M. (1993). Shear strength and shear stiffness of permanent steel bridge deck forms. M.S. Thesis, University of Texas, Austin

Dowell, R. K., and Smith, J. W. (2006). Structural Tests of Precast, Prestressed Concrete Deck Panels for California Freeway Bridges. PCI Journal, March-April, 2-13.

Egilmez, O. O. (2005). *Lateral bracing of steel bridge girders by permanent metal deck forms*. PhD. Dissertation, Univ. of Houston, Houston.

Egilmez, O., Helwig, T. A., and Herman, R. S. (2005). "Strength of metal deck forms used for stability bracing of steel bridge girders." *Proc., Structural Stability Research Council/North American Steel Construction Conf.*, Montreal, 257–276.

Egilmez, Ozgur; Helwig, Todd; and Herman, Reagan (2012). "Buckling Behavior of Steel Bridge I-Girders Braced by Permanent Metal Deck Forms," *ASCE Journal of Bridge Engineering*, Vol. 17, No. 4, pp. 624-633 July/August 2012.

Egilmez, O.O., Helwig, T.A. and Herman, R. (2016). "Using Metal Deck Forms for Construction Bracing in Steel Bridges", *Journal of Bridge Engineering*, Vol. 21, No. 5, May

Errera, S., and Apparao, T. (1976). "Design of I-shaped beams with diaphragm bracing." *Journal of the Structural Division*, 102(4), 769–781.

Eskew and Simpson (1991). Bridge Deck Panel Support System and Method, US Patent 5,025,522, filed January, 25, 1990 and issued June, 25, 1991

Fang, Worley, Burns & Klingner (1990). "Behavior of Isotropic R/C Bridge Decks on Steel Bridge Decks", *Journal of Structural Engineering*, Vol. 116, No. 3, pp. 659-678

Galambos, T. V., ed. (1998). *Guide to stability design criteria for metal structures*, 5th Ed., Wiley, New York.

Goldberg, D. (1987). “Precast prestressed concrete bridge deck panels.” PCI J., 32(2), 26–45.

Heins, C. (1978). “Box Girder Design – State of the Art”, *Engineering Journal, AISC*, Vol. 15, No.4, pp.126-142.

Helwig, T. A., and Frank., K. H., (1999). “Stiffness requirements for diaphragm bracing of beams.” *Journal of Structural Engineering*, 125(11) 1249–1256.

Helwig, T. A., Frank., K. H., and Yura, J. A. (1997). “Lateral-torsional buckling of singly-symmetric I-beams.” *Journal of Structural Engineering*, 123(9) 1172–1179.

Helwig, T. A., and Yura, J. A. (2012). “Steel Bridge Design Handbook: Bracing System Design.” U.S.Department of Transportation Federal Highway Administration, FHWA-IF-12-052 - Vol. 13

Helwig, T. A., and Yura, J. A. (2008a). “Shear diaphragm bracing of beams. I: Stiffness and sterngth.” *Journal of Structural Engineering*, 134(3) 348–356.

Helwig, T. A., and Yura, J. A. (2008b). “Shear diaphragm bracing of beams. II: Design requirements.” *Journal of Structural Engineering*, 134(3) 357–363.

Helwig, T. A.; Yura, J. A.; Herman, Reagan S.; and Williamson, E. (2007). “Design Guidelines for Steel Trapezoidal Box Girder Systems” Research Report 0-4307-1, Center for Transportation Research, University of Texas at Austin, April 2007.

Helwig, T. A.; Yura, J. A.; Herman, Reagan S.; and Williamson, E. (2007). “Design Guidelines for Steel Trapezoidal Box Girder Systems” Research Report 0-4307-1, Center for Transportation Research, University of Texas at Austin, April 2007.

Helwig, T.A., and Wang, L. (2003). “Cross-Frame and Diaphragm Behavior for Steel Bridges with Skewed Supports,” Research Report No. 1772-1, Project No. 0-1772, Department of Civil and Environmental Engineering, University of Houston, Houston, TX.

Herman, Helwig and Zhou (2007). Use of Lean-On Cross-Frame Bracing in Steel Girder Bridges, Proceedings from the 2007 Structures Congress: New Horizons and Better Practices, pp. 1-6

Fan, Z. (1999). Field and Computational Studies of Steel Trapezoidal Box Girder Bridges. PhD Dissertation, University of Houston, Houston, TX

Kintz, J. R. (2017). Experimental Evaluation of Partial Depth Precast Concrete Deck Panels Subjected to Shear Loading. M.S. Thesis, University of Texas, Austin

Kollbrunner, C. and Basler, K. (1969). Torsion in Structures – An Engineering Approach, Springer-Verlag, New York.

Kwon (2012). *Design Recommendations for CIP-PCP Bridge Decks*, PhD Dissertation, University of Texas at Austin, Austin, Texas

LaViolette, M.D., (2014). "Tappan Zee Hudson River Crossing" *STRUCTURE Magazine*, October. http://www.structuremag.org/wp-content/uploads/2014/09/SF-Tappenzee-Oct141.pdf (Accessed March 13, 2018)

Mander, Mander & Head (2011). "Compound Shear Flexural Capacity of Reinforced Concrete Topped-Precast Prestressed Bridge Decks", *Journal of Bridge Engineering*, Vol. 16, No. 1, pp. 4-11

McCammon, V. E. (2015). *In-Plane Shear Strength and Stiffness of Precast Concrete Panels*. M.S. Thesis, University of Texas, Austin

Merrill (2002). Texas' Use of Precast Concrete Stay-in-Place Forms for Concrete Bridge Decks, Publication of the Texas Department of Transportation from the 2002 Bridge Conference

National Steel Bridge Alliance (2016). "Skewed and Curved Steel I-Girder Bridge Fit." American Institute of Steel Construction. August. https://www.aisc.org/globalassets/nsba/technical-documents/skewed-curved-steel-bridges-august-2016-summary-final.pdf (Accessed March 13, 2018)

Nethercot, D., and Trahair, N. (1975). "Design of diaphragm-braced I-beams." *Journal of the Structural Division*, 101(10) 2045–2061.

Oliver, Linero, Huespe & Manzoli (2009). "Two-Dimensional Modeling of Material Failure in Reinforced Concrete by Means of a Continuum Strong Discontinuity Approach", Computer Methods in Applied Mechanics and Engineering, Vol. 197, pp. 332-348

Ozgur, C. (2011). *Influence of Cross-Frame Detailing on Curved and Skewed Steel I-Girder Bridges*, PhD Dissertation, Georgia Institute of Technology, Atlanta, Georgia

Park, Choi, and Kang (2005). "Spacing of Intermediate Diaphragms in Horizontally Curved Steel Box Girder Bridges", Finite Elements in Analysis and Design, Vol. 41, No. 9-10, pp. 925-943

Popp, D.R. (2004). *UTrAp 2.0: Linearized Buckling Analysis of Steel Trapezoidal Girders.* Master's Thesis, University of Texas at Austin, Austin, Texas

Reese, G. and Nickas, W. (2010). "Development of Spliced Precast U Beam Bridge Construction." Powerpoint Presentation. November 2010. <http://www.fdot.gov/structures/Innovation/U-Beam/Images/UBeamDevelopment.pdf>

Roddenberry (2012). Prefabricated/Precast Bridge Elements and Systems (PBES) for Off-System Bridges, Publication of the Florida Department of Transportation, Contract number BDK83 977-13

Romage, M. L. (2008), Field Measurements on Lean-On-Bracing for Steel Girder Bridges with Skewed Supports, Master's Thesis, University of Texas at Austin, Austin, TX

Sanchez, T.A. (2011). Influence of Bracing Systems on the Behavior of Curved and Skewed Steel I-Girder Bridges during Construction, PhD Dissertation, Georgia Institute of Technology, Atlanta, Georgia

Sharafbayani & Linzell (2014). "Optimizing Horizontally Curved, Steel Bridge, Cross-Frame Arrangements to Enhance Construction Performance." *Journal of Bridge Engineering*, Vol. 19, No. 7

Shim & Chang (2003). "Design of Shear Connection in Composite Steel and Concrete Bridges with Precast Decks." *Journal of Constructional Steel Research*, Vol. 59, No. 2, pp. 201-214

Smith (1997). Bridge Deck Panel Installation System and Method, US Patent 5,617,599, filed May, 19, 1995 and issued April 8, 1997

Stith, J.C. (2010). *Predicting the Behavior of Horizontally Curved I-Girders during Construction*, Ph.D. Dissertation, The University of Texas at Austin, Austin, TX

Studnicka, Machacek & Krpata (2000). "Perforated Shear Connector for Composite Steel and Concrete Beams", Proceedings of the 4th Composite Construction in Steel and Concrete Conference, pp. 367-378

Texas Steel Quality Council (2015). "Preferred Practices for Steel Bridge Design, Fabrication, and Erection." Texas Department of Transportation. February 2015. http://ftp.dot.state.tx.us/pub/txdot-info/library/pubs/bus/bridge/steel_bridge.pdf (Accessed March 12, 2018)

Thomann (2005). *Connexions par Adhérence pour les Ponts Mixtes Acier-Béton*, PhD Dissertation, Ecole Polytechnique Fédérale de Lausanne, Lausanne, Switzerland

Thomann, Lebet & Dauner (2006). "Experimental and Theoretical Research on a New Partial Adherence Shear Connection." *Proceedings of the 5th International Conference on Composite Construction in Steel and Concrete*, pp. 553-563

Topkaya, C. (2002). *Behavior of Curved Steel Trapezoidal Box Girders During Construction*, Ph.D. Dissertation, The University of Texas at Austin, Austin, TX

Topkaya, C. and Williamson, E.B. (2003). "Development of Computational Software for Analysis of Curved Girders Under Construction Loads." *Computers & Structures*, Vol. 81, No. 21, September, pp. 2087-2098

Tsui, Burns & Klingner (1986). "Behavior of Ontario-Type Bridge Deck on Steel Girders: Negative Moment Region and Load Capacity," Research Report No. 350-3, Center for Transportation Research, Austin, Texas

TxDOT (2013). Bridge Design Manual – LRFD, Texas Department of Transportation, March 2013

TxDOT (2014a). Prestressed Concrete Panels Deck Details (PCP), Texas Department of Transportation, 2006, Rev. November 2014

TxDOT (2014b). Prestressed Concrete Panel Fabrication Details (PCP-FAB), Texas Department of Transportation, 2010, Rev. November 2014

Vecchio (1981). *The Response of Reinforced Concrete to In-Plane Shear and Normal Stresses*, PhD Dissertation, University of Toronto, Toronto, Canada

Vecchio (2000). "Disturbed Stress Field Model for Reinforced Concrete: Formulation." *Journal of Structural Engineering*, Vol. 126, No. 9, pp. 1070-1077

Vecchio (2001). "Disturbed Stress Field Model for Reinforced Concrete: Formulation." *Journal of Structural Engineering*, Vol. 127, No. 1, pp. 12-20

Wang, L., and Helwig, T. A. (2005). "Critical imperfections for beam bracing systems." *Journal of Structural Engineering*, 131(6) 933–940.

Winter, G. (1960). "Lateral bracing of columns and beams." *Transactions of the American Society of Civil Engineering*, 125, 809–825.

Wongjeeraphat, R. (2011). *Stability Bracing Behavior for Truss Systems.* PhD Dissertation, University of Texas at Austin, Austin, TX

Yarimci, E., Yura, J.A., and Lu, L. (1966). Techniques for Testing Structures Permitted to Sway. Lehigh University, Bethlehem, PA, 1966.

Yura, J.A. (2001). "Fundamentals of Beam Bracing." *Engineering Journal, American Institute of Steel Construction*, Vol. 38, No. 1

Yura, J.A. and Widianto (2005). "Lateral Buckling and Bracing of Beams – A Re-evaluation after the Marcy Bridge Collapse" Structural Stability Research Council Proceedings, Annual Stability Conference, Montreal, QC, Canada, April 6-9

Zureick, A. and Naqib, R. (1999). "Horizontally Curved Steel I-Girders State-of-the-Art Analysis Methods." *Journal of Bridge Engineering*, Vol. 4, No. 1, February

Appendix A. PCP Connection Calculations

A.1 PCP Embed Design Capacity Calculations – Detail A.1

PCP REINFORCEMENT

PCP Information

Shear Frame: Geometry

$P_{ram} := 17.8kip$ (Load in Actuator) $w := 78in$ (Connection Spacing)

$L := 150in$ (Loading Beam Length) $h := 99in$ (PCP Span Length)

$f := 110in$ (Loading Beam Spacing)

Embeds Members: **2"x1/2" Plates**

$F_{y\_em} := 36ksi$ (Embed Yield) $d_{em} := 2in$ (Embed Depth)

$F_{u\_em} := 50ksi$ (Embed Fracture) $t_{em} := 0.5in$ (Embed Thickness)

$A_{em} := d_{em} \cdot t_{em} = 1.0 \cdot in^2$

Concrete Anchors: **1/2" Diameter D2L 24" Long**

$d_{d2l} := 0.5in$ (Anchor Diameter) $N_{d2l\_T} := 4$ (Tension Anchors per Corner)

$f_{uta\_d2l} := 61ksi$ (Anchor Tensile Strengt $N_{d2l\_V} := 6$ (Shear Anchors per Corner)

Concrete Anchor Tension Reinforcement: **3/8" Diameter Prestressing Strands**

$d_{ps} := 0.375in$ (Strand Diameter) $A_{ps} := 0.085in^2$ (Strand Area)

$f_{ps} := 270ksi$ (Strand Strength) $N_{ps} := 3$ (Number of Strands)

Phi & Omega Safety Factors

$\phi_1 := 0.75$ $\phi_2 := 0.90$ $\phi_3 := 1$ $\phi_4 := 0.65$

Shear Frame and PCP Dimensions

$V_{pcp} := \frac{P_{ram} \cdot L}{f} = 24.3 \cdot kip$ $T_{con} := \frac{P_{ram} \cdot L \cdot h}{2f \cdot w} = 15.4 \cdot kip$

$M_{pcp} := V_{pcp} \cdot h = 200.2 \cdot kip \cdot ft$ $V_{con} := \frac{P_{ram} \cdot L}{2f} = 12.1 \cdot kip$

Developement Length of D2L & Prestressing Strands

Developement Length of Deformed Bars - D2L (ACI 318-11 12.2)

$f_c := 5000 \cdot psi^2$ $\lambda := 1.0$ $\psi_t := 1.0$ $\psi_e := 1.0$ $\psi_s := 1.0$ $l_d := \left(\frac{f_{uta\_d2l} \cdot \psi_t \cdot \psi_e \cdot \psi_s}{25 \cdot \lambda \cdot \sqrt{f_c}} \right) \cdot d_{d2l} = 17.3 \cdot in$

Developement Length of Prestressing Strands (ACI 318-11 12.2)

Prestressing strands are loaded to 14.4 kips per strand (TxDOT 2015)

$f_{se} := \frac{14.4kip}{A_{ps}} = 169.4 \cdot ksi$ $f_{ps} := 177ksi$ $l_d := \frac{f_{se}}{3000psi} \cdot d_{ps} + \frac{(f_{ps} - f_{se})}{1000psi} \cdot d_{ps} = 24.0 \cdot in$

Strength of Embeds and Anchors

Embed Tension Yield (AISC 14th J4.1)

$V_1 := F_{y\_em} \cdot A_{em} \cdot \phi_2$

$V_1 = 32.4 \cdot kip$

D2L Anchor Tension Rupture (ACI 318-11 D.5.1)

$A_{d21} := \pi \cdot (0.5 \cdot d_{d21})^2 = 0.20 \cdot in^2$

$T_1 := N_{d21\_T} \cdot f_{uta\_d21} \cdot A_{d21} \cdot \phi_1$

$T_1 = 35.9 \cdot kip$

Anchor Tension Reinforcement Instead of Concrete Breakout (ACI 318-11 D.5.2.9)

$T_2 := N_{ps} \cdot A_{ps} \cdot f_{ps} \cdot \phi_1$

$T_2 = 33.9 \cdot kip$

D2L Anchor Shear Rupture (ACI 318-11 D.6.1)

$V_2 := N_{d21\_V} \cdot f_{uta\_d21} \cdot A_{d21} \cdot \phi_4$

$V_2 = 46.7 \cdot kip$

D2L Anchor Pullout (ACI 318-11 D.5.3)

Anchor pullout (ACI D.5.3) is for cast-in-place headed studs, headed bolts, J-bolts, and L-bolts. The code equations rely only the bearing component, neglecting any frictional component of the anchor. D2L anchors are deformed similar to rebar (and have no bearing component) so development length provisions should be satisfied instead of anchor pullout.

D2L Concrete Pryout Strength of Anchor in Shear (ACI 318-11 D.6.3)

Stocky studs, those defined with h_{ef}/d less than 4.5, oftentimes failed in a concrete pryout failure mode in normal weight concrete while cast-in headed studs with h_{ef}/d greater than or equal to about 4.5 often fail in a steel stud shearing mode in normal weight concrete according to research by Anderson and Meinheit (2005). The h_{fe}/d for this case is 48 and therefore the pryout failure mechanism does not control by inspection.

Concrete Breakout Parallel to an Edge - Shear (ACI 318-11 D.6.2)

$c_{a1} := 1.5in$ $c_{a2} := 14in + 2 \cdot 1.5 \cdot c_{a1} = 18.5 \cdot in$ $f_c := 8767 \cdot psi^2$ $l_e := 8 \cdot d_{d21} = 4.0 \cdot in$

$\phi_{ec\_V} := 1.0$ $\phi_p := 2.0$ $\phi_{ed\_V} := 1$ $\phi_{c\_V} := 1.0$ $\phi_{h\_V} := 1.0$

$A_{vc} := c_{a2} \cdot 1.5 \cdot c_{a1} = 41.6 \cdot in^2$

$A_{vco} := 4.5 \cdot (c_{a1})^2 = 10.1 \cdot in^2$

$$V_b := \min\left[\left[8 \cdot \left(\frac{l_e}{d_{d21}}\right)^{0.2} \cdot \sqrt{d_{d21}}\right] \cdot 1 \cdot \sqrt{f_c} \cdot (c_{a1})^{1.5}, 9 \cdot 1 \cdot \sqrt{f_c} \cdot (c_{a1})^{1.5} \cdot in^{0.5}\right] = 1.5 \cdot kip$$

$V_3 := \frac{A_{vc}}{A_{vco}} \cdot \phi_{ec\_V} \cdot \phi_{ed\_V} \cdot \phi_{c\_V} \cdot \phi_{h\_V} \cdot V_b \cdot \phi_p = 12.1 \cdot kip$ (Capacity per Corner)

$V_4 := 2 \cdot V_3 = 24.3 \cdot kip$ (Capacity per Embed)

Unity Check Shear and Tension Separately (ACI D.5 & D.6 Unity < 1.0)

$\frac{T_{con}}{T_1} = 0.429$	$\frac{T_{con}}{T_2} = 0.455$	$\frac{V_{con}}{V_1} = 0.375$	$\frac{V_{pcp}}{V_2} = 0.52$	$\frac{V_{pcp}}{V_4} = 1.00$

A.2 PCP Embed Design Capacity Calculations – Detail B.1

PCP REINFORCEMENT

PCP Information

Shear Frame: Geometry

$P_{ram} := 18.6kip$ (Load in Actuator) $w := 78in$ (Connection Spacing)

$L := 150in$ (Loading Beam Length) $h := 99in$ (PCP Span Length)

$f := 110in$ (Loading Beam Spacing)

Embeds Members: 2"x5/8" Plates

$F_{y\_em} := 36ksi$ (Embed Yield) $d_{em} := 2in$ (Embed Depth)

$F_{u\_em} := 50ksi$ (Embed Fracture) $t_{em} := 0.625in$ (Embed Thickness)

$A_{em} := d_{em} \cdot t_{em} = 1.3 \cdot in^2$

Concrete Anchors: 5/8" Diameter D2L 30" Long

$d_{d2l} := 0.625in$ (Anchor Diameter) $N_{d2l\_T} := 4$ (Tension Anchors per Corner)

$f_{uta\_d2l} := 61ksi$ (Anchor Tensile Streng $N_{d2l\_V} := 6$ (Shear Anchors per Corner)

Concrete Anchor Tension Reinforcement: 3/8" Diameter Prestressing Strands

$d_{ps} := 0.375in$ (Strand Diameter) $A_{ps} := 0.085in^2$ (Strand Area)

$f_{ps} := 270ksi$ (Strand Strength) $N_{ps} := 3$ (Number of Strands)

Phi & Omega Safety Factors

$\phi_1 := 0.75$ $\phi_2 := 0.90$ $\phi_3 := 1$ $\phi_4 := 0.65$

Shear Frame and PCP Dimensions

$V_{pcp} := \frac{P_{ram} \cdot L}{f} = 25.4 \cdot kip$ $T_{con} := \frac{P_{ram} \cdot L \cdot h}{2f \cdot w} = 16.1 \cdot kip$

$M_{pcp} := V_{pcp} \cdot h = 209.2 \cdot kip \cdot ft$ $V_{con} := \frac{P_{ram} \cdot L}{2f} = 12.7 \cdot kip$

Developement Length of D2L & Prestressing Strands

Developement Length of Deformed Bars - D2L (ACI 318-11 12.2)

$f_c := 5000 \cdot psi^2$ $\lambda := 1.0$ $\psi_t := 1.0$ $\psi_e := 1.0$ $\psi_s := 1.0$ $l_d := \left(\frac{f_{uta\_d2l} \cdot \psi_t \cdot \psi_e \cdot \psi_s}{25 \cdot \lambda \cdot \sqrt{f_c}} \right) \cdot d_{d2l} = 21.6 \cdot in$

Developement Length of Prestressing Strands (ACI 318-11 12.2)

Prestressing strands are loaded to 14.4 kips per strand (TxDOT 2015)

$f_{se} := \frac{14.4kip}{A_{ps}} = 169.4 \cdot ksi$ $f_{ps} := 193ksi$ $l_d := \frac{f_{se}}{3000psi} \cdot d_{ps} + \frac{(f_{ps} - f_{se})}{1000psi} \cdot d_{ps} = 30.0 \cdot in$

Strength of Embeds and Anchors

Embed Tension Yield (AISC 14th J4.1)

$V_1 := F_{y\_em} \cdot A_{em} \cdot \phi_2$

$V_1 = 40.5 \cdot kip$

D2L Anchor Tension Rupture (ACI 318-11 D.5.1)

$A_{d2l} := \pi \cdot (0.5 \cdot d_{d2l})^2 = 0.31 \cdot in^2$

$T_1 := N_{d2l\_T} \cdot f_{uta\_d2l} \cdot A_{d2l} \cdot \phi_1$

$T_1 = 56.1 \cdot kip$

Anchor Tension Reinforcement Instead of Concrete Breakout (ACI 318-11 D.5.2.9)

$T_2 := N_{ps} \cdot A_{ps} \cdot f_{ps} \cdot \phi_1$

$T_2 = 36.9 \cdot kip$

D2L Anchor Shear Rupture (ACI 318-11 D.6.1)

$V_2 := N_{d2l\_V} \cdot f_{uta\_d2l} \cdot A_{d2l} \cdot \phi_4$

$V_2 = 73 \cdot kip$

D2L Anchor Pullout (ACI 318-11 D.5.3)

Anchor pullout (ACI D.5.3) is for cast-in-place headed studs, headed bolts, J-bolts, and L-bolts. The code equations rely only the bearing component, neglecting any frictional component of the anchor. D2L anchors are deformed similar to rebar (and have no bearing component) so development length provisions should be satisfied instead of anchor pullout.

D2L Concrete Pryout Strength of Anchor in Shear (ACI 318-11 D.6.3)

Stocky studs, those defined with h_{ef}/d less than 4.5, oftentimes failed in a concrete pryout failure mode in normal weight concrete while cast-in headed studs with h_{ef}/d greater than or equal to about 4.5 often fail in a steel stud shearing mode in normal weight concrete according to research by Anderson and Meinheit (2005). The h_{fe}/d for this case is 48 and therefore the pryout failure mechanism does not control by inspection.

Concrete Breakout Parallel to an Edge - Shear(ACI D.6.2)

$c_{a1} := 1.5in$ $c_{a2} := 14in + 2 \cdot 1.5 \cdot c_{a1} = 18.5 \cdot in$ $f'_c := 8767 \cdot psi^2$ $l_e := 8 \cdot d_{d2l} = 5.0 \cdot in$

$\phi_{ec\_V} := 1.0$ $\phi_p := 2.0$ $\phi_{ed\_V} := 1$ $\phi_{c\_V} := 1.0$ $\phi_{h\_V} := 1.0$

$A_{vc} := c_{a2} \cdot 1.5 \cdot c_{a1} = 41.6 \cdot in^2$

$A_{vco} := 4.5 \cdot (c_{a1})^2 = 10.1 \cdot in^2$

$$V_b := \min\left[\left[8 \cdot \left(\frac{l_e}{d_{d2l}}\right)^{0.2} \cdot \sqrt{d_{d2l}}\right] \cdot 1 \cdot \sqrt{f'_c} \cdot (c_{a1})^{1.5}, 9 \cdot 1 \cdot \sqrt{f'_c} \cdot (c_{a1})^{1.5} \cdot in^{0.5}\right] = 1.5 \cdot kip$$

$$V_3 := \frac{A_{vc}}{A_{vco}} \cdot \phi_{ec\_V} \cdot \phi_{ed\_V} \cdot \phi_{c\_V} \cdot \phi_{h\_V} \cdot V_b \cdot \phi_p = 12.7 \cdot kip \quad \text{(Capacity per Corner)}$$

$V_4 := 2 \cdot V_3 = 25.5 \cdot kip$ (Capacity per Embed)

Unity Check Shear and Tension Separately (ACI D.5 & D.6 Unity < 1.0)

$\frac{T_{con}}{T_1} = 0.287$	$\frac{T_{con}}{T_2} = 0.436$	$\frac{V_{con}}{V_1} = 0.313$	$\frac{V_{pcp}}{V_2} = 0.35$	$\frac{V_{pcp}}{V_4} = 1.00$

A.3 PCP Embed Design Capacity Calculations – Detail C.2

PCP REINFORCEMENT

PCP Information

Shear Frame: Geometry

$P_{ram} := 29.3kip$ (Load in Actuator) $w_o := 78in$ (Outer Connection Spacing)

$L := 150in$ (Loading Beam Length) $w_i := 54in$ (Inner Connection Spacing)

$f := 110in$ (Loading Beam Spacing) $h := 99in$ (PCP Span Length)

Embeds Members: 2"x5/8" Plates

$F_{y\_em} := 36ksi$ (Embed Yield) $d_{em} := 2in$ (Embed Depth)

$F_{u\_em} := 50ksi$ (Embed Fracture) $t_{em} := 0.625in$ (Embed Thickness)

$A_{em} := d_{em} \cdot t_{em} = 1.3 \cdot in^2$

Concrete Anchors: 1/2" Diameter D2L 24" Long

$d_{d2l} := 0.5in$ (Anchor Diameter) $N_{d2l\_T} := 4$ (Tension Anchors per Connection)

$f_{uta\_d2l} := 61ksi$ (Anchor Tensile Strength) $N_{d2l\_V} := 10$ (Shear Anchors per Corner)

Concrete Anchor Tension Reinforcement: 3/8" Diameter Prestressing Strands

$d_{ps} := 0.375in$ (Strand Diameter) $A_{ps} := 0.085in^2$ (Strand Area)

$f_{ps} := 270ksi$ (Strand Strength) $N_{ps} := 2.5$ (Strands per Connection)

Phi & Omega Safety Factors

$\phi_1 := 0.75$ $\phi_2 := 0.90$ $\phi_3 := 1$ $\phi_4 := 0.65$

Shear Frame and PCP Dimensions

$$V_{pcp} := \frac{P_{ram} \cdot L}{f} = 40.0 \cdot kip$$

$$M_{pcp} := V_{pcp} \cdot h = 3955.5 \cdot kip \cdot in$$

$$T_{con\_o} := \frac{M_{pcp}}{2\left(w_o + \frac{w_i^2}{w_o}\right)} = 17.1 \cdot kip$$

$$T_{con\_i} := \frac{T_{con\_o} \cdot w_i}{w_o} = 11.9 \cdot kip$$

$$V_{con} := \frac{P_{ram} \cdot L}{2f} = 20.0 \cdot kip$$

Developement Length of D2L & Prestressing Strands

Developement Length of Deformed Bars - D2L (ACI 318-11 12.2)

$f_c := 5000 \cdot psi^2$ $\lambda := 1.0$ $\psi_t := 1.0$ $\psi_e := 1.0$ $\psi_s := 1.0$

$$l_d := \left(\frac{f_{uta\_d2l} \cdot \psi_t \cdot \psi_e \cdot \psi_s}{25 \cdot \lambda \cdot \sqrt{f_c}}\right) \cdot d_{d2l} = 17.3 \cdot in$$

Developement Length of Prestressing Strands (ACI 318-11 12.2)

Prestressing strands are loaded to 14.4 kips per strand (TxDOT 2015)

$$f_{se} := \frac{14.4kip}{A_{ps}} = 169.4 \cdot ksi \quad f_{ps} := 177ksi$$

$$l_d := \frac{f_{se}}{3000psi} \cdot d_{ps} + \frac{(f_{ps} - f_{se})}{1000psi} \cdot d_{ps} = 24.0 \cdot in$$

Strength of Embeds and Anchors

Embed Tension Yield (AISC 14th J4.1)

$V_1 := F_{y\_em} \cdot A_{em} \cdot \phi_2$

$V_1 = 40.5 \cdot kip$

D2L Anchor Tension Rupture (ACI 318-11 D.5.1)

$A_{d2l} := \pi \cdot (0.5 \cdot d_{d2l})^2 = 0.20 \cdot in^2$

$T_1 := N_{d2l\_T} \cdot f_{uta\_d2l} \cdot A_{d2l} \cdot \phi_1$

$T_1 = 35.9 \cdot kip$

Anchor Tension Reinforcement Instead of Concrete Breakout (ACI 318-11 D.5.2.9)

$T_2 := N_{ps} \cdot A_{ps} \cdot f_{ps} \cdot \phi_1$

$T_2 = 28.2 \cdot kip$

D2L Anchor Shear Rupture (ACI 318-11 D.6.1)

$V_2 := N_{d2l\_V} \cdot f_{uta\_d2l} \cdot A_{d2l} \cdot \phi_4$

$V_2 = 77.9 \cdot kip$

D2L Anchor Pullout (ACI 318-11 D.5.3)

Anchor pullout (ACI D.5.3) is for cast-in-place headed studs, headed bolts, J-bolts, and L-bolts. The code equations rely only the bearing component, neglecting any frictional component of the anchor. D2L anchors are deformed similar to rebar (and have no bearing component) so development length provisions should be satisfied instead of anchor pullout.

D2L Concrete Pryout Strength of Anchor in Shear (ACI 318-11 D.6.3)

Stocky studs, those defined with h_{ef}/d less than 4.5, oftentimes failed in a concrete pryout failure mode in normal weight concrete while cast-in headed studs with h_{ef}/d greater than or equal to about 4.5 often fail in a steel stud shearing mode in normal weight concrete according to research by Anderson and Meinheit (2005). The h_{fe}/d for this case is 48 and therefore the pryout failure mechanism does not control by inspection.

Concrete Breakout Parallel to an Edge - Shear (ACI 318-11 D.6.2)

$c_{a1} := 1.5in$ $c_{a2} := 26in + 2 \cdot 1.5 \cdot c_{a1} = 30.5 \cdot in$ $f_c := 8767 \cdot psi^2$ $l_e := 8 \cdot d_{d2l} = 4.0 \cdot in$

$\phi_{ec\_V} := 1.0$ $\phi_p := 2.0$ $\phi_{ed\_V} := 1$ $\phi_{c\_V} := 1.0$ $\phi_{h\_V} := 1.0$

$A_{vc} := c_{a2} \cdot 1.5 \cdot c_{a1} = 68.6 \cdot in^2$

$A_{vco} := 4.5 \cdot (c_{a1})^2 = 10.1 \cdot in^2$

$$V_b := \min\left[\left[8 \cdot \left(\frac{l_e}{d_{d2l}}\right)^{0.2} \cdot \sqrt{d_{d2l}}\right] \cdot 1 \cdot \sqrt{f_c} \cdot (c_{a1})^{1.5}, 9 \cdot 1 \cdot \sqrt{f_c} \cdot (c_{a1})^{1.5} \cdot in^{0.5}\right] = 1.5 \cdot kip$$

$V_3 := \frac{A_{vc}}{A_{vco}} \cdot \phi_{ec\_V} \cdot \phi_{ed\_V} \cdot \phi_{c\_V} \cdot \phi_{h\_V} \cdot V_b \cdot \phi_p = 20.0 \cdot kip$ (Capacity per Corner)

$V_4 := 2 \cdot V_3 = 40.0 \cdot kip$ (Capacity per Embed)

Unity Check Shear and Tension Seperately (ACI 318-11 D.5 & D.6 Unity < 1.0)

$\frac{T_{con\_o}}{T_1} = 0.477$	$\frac{T_{con\_o}}{T_2} = 0.608$	$\frac{V_{con}}{V_1} = 0.493$	$\frac{V_{pcp}}{V_2} = 0.51$	$\frac{V_{pcp}}{V_4} = 1.00$

A.4 PCP Embed Design Capacity Calculations – Detail D.2

PCP REINFORCEMENT

PCP Information

Shear Frame: Geometry

$P_{ram} := 24.8kip$ (Load in Actuator) $w_o := 78in$ (Outer Connection Spacing)

$L := 150in$ (Loading Beam Length) $w_i := 54in$ (Inner Connection Spacing)

$f := 110in$ (Loading Beam Spacing) $h := 99in$ (PCP Span Length)

Embeds Members: 2"x3/4" Plates

$F_{y\_em} := 36ksi$ (Embed Yield) $d_{em} := 2in$ (Embed Depth)

$F_{u\_em} := 50ksi$ (Embed Fracture) $t_{em} := 0.75in$ (Embed Thickness)

$A_{em} := d_{em} \cdot t_{em} = 1.5 \cdot in^2$

Concrete Anchors: 5/8" Diameter D2L 30" Long

$d_{d2l} := 0.625in$ (Anchor Diameter) $N_{d2l\_T} := 4$ (Tension Anchors per Connection)

$f_{uta\_d2l} := 61ksi$ (Anchor Tensile Strength) $N_{d2l\_V} := 8$ (Shear Anchors per Corner)

Concrete Anchor Tension Reinforcement: 3/8" Diameter Prestressing Strands

$d_{ps} := 0.375in$ (Strand Diameter) $A_{ps} := 0.085in^2$ (Strand Area)

$f_{ps} := 270ksi$ (Strand Strength) $N_{ps} := 2.5$ (Strands per Connection)

Phi & Omega Safety Factors

$\phi_1 := 0.75$ $\phi_2 := 0.90$ $\phi_3 := 1$ $\phi_4 := 0.65$

Shear Frame and PCP Dimensions

$$V_{pcp} := \frac{P_{ram} \cdot L}{f} = 33.8 \cdot kip$$

$M_{pcp} := V_{pcp} \cdot h = 3348.0 \cdot kip \cdot in$

$$T_{con\_o} := \frac{M_{pcp}}{2\left(w_o + \frac{w_i^2}{w_o}\right)} = 14.5 \cdot kip$$

$$T_{con\_i} := \frac{T_{con\_o} \cdot w_i}{w_o} = 10.0 \cdot kip$$

$$V_{con} := \frac{P_{ram} \cdot L}{2f} = 16.9 \cdot kip$$

Developement Length of D2L & Prestressing Strands

Developement Length of Deformed Bars - D2L (ACI 318-11 12.2)

$f_c := 5000 \cdot psi^2$ $\lambda := 1.0$ $\psi_t := 1.0$ $\psi_e := 1.0$ $\psi_s := 1.0$

$$l_d := \left(\frac{f_{uta\_d2l} \cdot \psi_t \cdot \psi_e \cdot \psi_s}{25 \cdot \lambda \cdot \sqrt{f_c}}\right) \cdot d_{d2l} = 21.6 \cdot in$$

Developement Length of Prestressing Strands (ACI 318-11 12.2)

Prestressing strands are loaded to 14.4 kips per strand (TxDOT 2015)

$$f_{se} := \frac{14.4kip}{A_{ps}} = 169.4 \cdot ksi \quad f_{ps} := 193ksi$$

$$l_d := \frac{f_{se}}{3000psi} \cdot d_{ps} + \frac{(f_{ps} - f_{se})}{1000psi} \cdot d_{ps} = 30.0 \cdot in$$

Strength of Embeds and Anchors

Embed Tension Yield (AISC 14th J4.1)

$V_1 := F_{y\_em} \cdot A_{em} \cdot \phi_2$

$V_1 = 48.6 \cdot kip$

D2L Anchor Tension Rupture (ACI 318-11 D.5.1)

$A_{d21} := \pi \cdot (0.5 \cdot d_{d21})^2 = 0.31 \cdot in^2$

$T_1 := N_{d21\_T} \cdot f_{uta\_d21} \cdot A_{d21} \cdot \phi_1$

$T_1 = 56.1 \cdot kip$

Anchor Tension Reinforcement Instead of Concrete Breakout (ACI 318-11 D.5.2.9)

$T_2 := N_{ps} \cdot A_{ps} \cdot f_{ps} \cdot \phi_1$

$T_2 = 30.8 \cdot kip$

D2L Anchor Shear Rupture (ACI 318-11 D.6.1)

$V_2 := N_{d21\_V} \cdot f_{uta\_d21} \cdot A_{d21} \cdot \phi_4$

$V_2 = 97.3 \cdot kip$

D2L Anchor Pullout (ACI 318-11 D.5.3)

Anchor pullout (ACI D.5.3) is for cast-in-place headed studs, headed bolts, J-bolts, and L-bolts. The code equations rely only the bearing component, neglecting any frictional component of the anchor. D2L anchors are deformed similar to rebar (and have no bearing component) so development length provisions should be satisfied instead of anchor pullout.

D2L Concrete Pryout Strength of Anchor in Shear (ACI 318-11 D.6.3)

Stocky studs, those defined with h_{ef}/d less than 4.5, oftentimes failed in a concrete pryout failure mode in normal weight concrete while cast-in headed studs with h_{ef}/d greater than or equal to about 4.5 often fail in a steel stud shearing mode in normal weight concrete according to research by Anderson and Meinheit (2005). The h_{fe}/d for this case is 48 and therefore the pryout failure mechanism does not control by inspection.

Concrete Breakout Parallel to an Edge - Shear (ACI 318-11 D.6.2)

$c_{a1} := 1.5in$ $c_{a2} := 20in + 2 \cdot 1.5 \cdot c_{a1} = 24.5 \cdot in$ $f_c := 8767 \cdot psi^2$ $l_e := 8 \cdot d_{d21} = 5.0 \cdot in$

$\phi_{ec\_V} := 1.0$ $\phi_p := 2.0$ $\phi_{ed\_V} := 1$ $\phi_{c\_V} := 1.0$ $\phi_{h\_V} := 1.0$

$A_{vc} := c_{a2} \cdot 1.5 \cdot c_{a1} = 55.1 \cdot in^2$

$A_{vco} := 4.5 \cdot (c_{a1})^2 = 10.1 \cdot in^2$

$$V_b := \min\left[\left[8 \cdot \left(\frac{l_e}{d_{d21}}\right)^{0.2} \cdot \sqrt{d_{d21}}\right] \cdot 1 \cdot \sqrt{f_c} \cdot (c_{a1})^{1.5}, 9 \cdot 1 \cdot \sqrt{f_c} \cdot (c_{a1})^{1.5} \cdot in^{0.5}\right] = 1.5 \cdot kip$$

$V_3 := \frac{A_{vc}}{A_{vco}} \cdot \phi_{ec\_V} \cdot \phi_{ed\_V} \cdot \phi_{c\_V} \cdot \phi_{h\_V} V_b \cdot \phi_p = 16.9 \cdot kip$ (Capacity per Corner)

$V_4 := 2 \cdot V_3 = 33.7 \cdot kip$ (Capacity per Embed)

Unity Check Shear and Tension Separately (ACI 318-11 D.5 & D.6 Unity < 1.0)

$\frac{T_{con\_o}}{T_1} = 0.258$	$\frac{T_{con\_o}}{T_2} = 0.472$	$\frac{V_{con}}{V_1} = 0.348$	$\frac{V_{pcp}}{V_2} = 0.35$	$\frac{V_{pcp}}{V_4} = 1.00$

A.5 PCP Weld Design Capacity Calculations – Detail 1.MAX

Frame Load, Frame Geometry, and Connection Geometry

P =	17.2	kip	
V =	23.5	kip	
L =	150	in	
f =	110	in	
w =	78	in	
h =	99	in	
b_f =	7.12	in	WT8x28.5
t_f =	0.715	in	
d =	8.22	in	
t_w =	0.43	in	
h_w =	3	in	
h_{bs} =	4	in	

Loads at Corners of Connections

T_{con} =	14.9	kip
V_{con} =	11.7	kip

Fillet Weld and Base Metal Parameters

D =	5	Size
F_{exx} =	70.0	ksi
Φ =	0.75	
F_y =	50.0	ksi
F_u =	65.0	ksi

Weld Strength

ΦR_n =	7.0	kip/in

Base Metal Check

t_{f_min} =	0.24	in
t_{w_min} =	0.48	in

Flange Unity = 0.33

Web Unity = 1.11

WT to PCP Connection in the Plane of the Faying Surface

L =	7.12	in	
I_x =	0.00	in^4/in	
I_y =	30.08	in^4/in	
I_p =	30.08	in^4/in	
e =	3.50	in	
c_x =	3.56	in	
c_y =	0.00	in	
R_{px} =	1.65	kip/in	
R_{py} =	0.00	kip/in	
R_{mx} =	0.00	kip/in	
R_{my} =	4.87	kip/in	
R_{xy} =	5.14	kip/in	

WT to Girder Connection in the Plane of the Faying Surface

L =	21.7	in	
$\bar{y}$ =	2.60	in	
I_x =	135.61	in^4/in	
I_y =	30.77	in^4/in	
I_p =	166.39	in^4/in	
e =	2.60	in	
c_x =	3.56	in	CG to A
c_y =	2.60	in	CG to A
R_{px} =	0.54	kip/in	
R_{py} =	0.69	kip/in	
R_{mx} =	0.48	kip/in	
R_{my} =	0.65	kip/in	
R_{xy} =	1.68	kip/in	

WT to Girder Connection in the Plane of the Faying Surface

c_x =	0.22	in	CG to B
c_y =	4.91	in	CG to B
R_{px} =	0.54	kip/in	
R_{py} =	0.69	kip/in	
R_{mx} =	0.90	kip/in	
R_{my} =	0.04	kip/in	
R_{xy} =	1.61	kip/in	

WT to Girder Connection Normal to Plane of the Faying Surface

R_{pz} =	2.1	kip/in	
R_{mz} =	0.0	kip/in	
R_z =	2.1	kip/in	

WT to Girder Connection Normal to Plane of the Faying Surface

R_{mz} =	4.8	kip/in	CG to A
R_{mz} =	2.0	kip/in	CG to A
R_z =	6.8	kip/in	

WT to Girder Connection Normal to Plane of Faying Surface

R_{mz} =	0.3	kip/in	CG to B
R_{mz} =	3.8	kip/in	CG to B
R_z =	4.1	kip/in	

WT to PCP Connection Max Load on Weld

R_{max} = 5.5 kip/in

Unity = 0.80

WT to Girder Connection Max Load on Weld

R_{max} = 7.0 kip/in

Unity = 1.00

WT to Girder Connection Max Load on Weld

R_{max} = 4.4 kip/in

Unity* = 0.70

*Increased by factor of 1.11 since weld is stronger than web base metal

A.6 PCP Weld Design Capacity Calculations – Detail 1.MIN

Frame Load, Frame Geometry, and Connection Geometry

P =	31.8	kip	
V =	43.3	kip	
L =	150	in	
f =	110	in	
w =	78	in	
h =	99	in	
b_f =	7.12	in	WT8x28.5
t_f =	0.715	in	
d =	8.22	in	
t_w =	0.43	in	
h_w =	3	in	
h_{bs} =	0.5	in	

Loads at Corners of Connections

T_{con} =	27.5	kip
V_{con} =	21.7	kip

Fillet Weld and Base Metal Parameters

D =	5	Size
F_{exx} =	70.0	ksi
Φ =	0.75	
F_y =	50.0	ksi
F_u =	65.0	ksi

Weld Strength

ΦR_n =	7.0	kip/in

Base Metal Check

t_{f_min} =	0.24	in
t_{w_min} =	0.48	in

Flange Unity = 0.33

Web Unity = 1.11

WT to PCP Connection in the Plane of the Faying Surface

L =	7.12	in
I_x =	0.00	in^4/in
I_y =	30.08	in^4/in
I_p =	30.08	in^4/in
e =	1.75	in
c_x =	3.56	in
c_y =	0.00	in
R_{px} =	3.04	kip/in
R_{py} =	0.00	kip/in
R_{mx} =	0.00	kip/in
R_{my} =	4.49	kip/in
R_{xy} =	5.42	kip/in

WT to Girder Connection in the Plane of the Faying Surface

L =	21.7	in
$\bar{y}$ =	2.60	in
I_x =	135.61	in^4/in
I_y =	30.77	in^4/in
I_p =	166.39	in^4/in
e =	2.60	in
c_x =	3.56	in CG to A
c_y =	2.60	in CG to A
R_{px} =	1.00	kip/in
R_{py} =	1.27	kip/in
R_{mx} =	0.88	kip/in
R_{my} =	1.20	kip/in
R_{xy} =	3.10	kip/in

WT to Girder Connection in the Plane of the Faying Surface

c_x =	0.22	in CG to B
c_y =	4.91	in CG to B
R_{px} =	1.00	kip/in
R_{py} =	1.27	kip/in
R_{mx} =	1.66	kip/in
R_{my} =	0.07	kip/in
R_{xy} =	2.98	kip/in

WT to Girder Connection Normal to Plane of the Faying Surface

R_{pz} =	3.9	kip/in
R_{mz} =	0.0	kip/in
R_z =	3.9	kip/in

WT to Girder Connection Normal to Plane of the Faying Surface

R_{mz} =	4.4	kip/in CG to A
R_{mz} =	1.8	kip/in CG to A
R_z =	6.2	kip/in

WT to Girder Connection Normal to Plane of Faying Surface

R_{mz} =	0.3	kip/in CG to B
R_{mz} =	3.5	kip/in CG to B
R_z =	3.8	kip/in

WT to PCP Connection Max Load on Weld

R_{max} =	6.7	kip/in

Unity = 0.96

WT to Girder Connection Max Load on Weld

R_{max} =	7.0	kip/in

Unity = 1.00

WT to Girder Connection Max Load on Weld

R_{max} =	4.8	kip/in

Unity* = 0.76

*Increased by factor of 1.11 since weld is stronger than web base metal

A.7 PCP Weld Design Capacity Calculations – Detail 2.MAX

Frame Load, Frame Geometry, and Connection Geometry

P =	31.2	kip	
V =	42.5	kip	
M =	4210.2957	kip*in	
L =	150	in	
f =	110	in	
w_o =	78	in	
w_i =	54	in	
h =	99	in	
b_f =	7.12	in	WT8x28.5
t_f =	0.715	in	
d =	8.22	in	
t_w =	0.43	in	
h_w =	3	in	
h_{bs} =	4	in	

Loads at Corners of Connections

T_{con_o} =	18.2	kip
V_{con_o} =	10.6	kip
T_{con_i} =	12.6	kip
V_{con_i} =	10.6	kip

Fillet Weld and Base Metal Parameters

D =	5	Size
F_{exx} =	70.0	ksi
Φ =	0.75	
F_y =	50.0	ksi
F_u =	65.0	ksi

Weld Strength

$ΦR_n$ = 6.96 kip/in

Base Metal Check

t_{f_min} =	0.24	in
t_{w_min} =	0.48	in

Flange Unity = 0.33

Web Unity = 1.11

WT to PCP Connection in the Plane of the Faying Surface

L =	7.12	in	
I_x =	0.00	in^4/in	
I_y =	30.08	in^4/in	
I_p =	30.08	in^4/in	
e =	3.50	in	
c_x =	3.56	in	
c_y =	0.00	in	
R_{px} =	1.49	kip/in	
R_{py} =	0.00	kip/in	
R_{mx} =	0.00	kip/in	
R_{my} =	4.40	kip/in	
R_{xy} =	4.65	kip/in	

WT to Girder Connection in the Plane of the Faying Surface

L =	21.7	in	
$\bar{y}$ =	2.60	in	
I_x =	135.61	in^4/in	
I_y =	30.77	in^4/in	
I_p =	166.39	in^4/in	
e =	2.60	in	
c_x =	3.56	in	CG to A
c_y =	2.60	in	CG to A
R_{px} =	0.49	kip/in	
R_{py} =	0.84	kip/in	
R_{mx} =	0.43	kip/in	
R_{my} =	0.59	kip/in	
R_{xy} =	1.70	kip/in	

WT to Girder Connection in the Plane of the Faying Surface

c_x =	0.22	in	CG to B
c_y =	4.91	in	CG to B
R_{px} =	0.49	kip/in	
R_{py} =	0.84	kip/in	
R_{mx} =	0.81	kip/in	
R_{my} =	0.04	kip/in	
R_{xy} =	1.57	kip/in	

WT to Girder Connection Normal to Plane of the Faying Surface

R_{pz} =	2.6	kip/in	
R_{mz} =	0.0	kip/in	
R_z =	2.6	kip/in	

WT to Girder Connection Normal to Plane of the Faying Surface

R_{mz} =	4.3	kip/in	CG to A
R_{mz} =	2.4	kip/in	CG to A
R_z =	6.7	kip/in	

WT to Girder Connection Normal to Plane of Faying Surface

R_{mz} =	0.3	kip/in	CG to B
R_{mz} =	4.6	kip/in	CG to B
R_z =	4.9	kip/in	

WT to PCP Connection Max Load on Weld

R_{max} = 5.3 kip/in

Unity = 0.76

WT to Girder Connection Max Load on Weld

R_{max} = 7.0 kip/in

Unity = 1.00

WT to Girder Connection Max Load on Weld

R_{max} = 5.1 kip/in

Unity* = 0.82

*Increased by factor of 1.11 since weld is stronger than web base metal

A.8 PCP Weld Design Capacity Calculations – Detail 2.MIN

Frame Load, Frame Geometry, and Connection Geometry

P =	57.4	kip	
V =	78.3	kip	
M =	7754.0862	kip*in	
L =	150	in	
f =	110	in	
w_o =	78	in	
w_i =	54	in	
h =	99	in	
b_f =	7.12	in	WT8x28.5
t_f =	0.715	in	
d =	8.22	in	
t_w =	0.43	in	
h_w =	3	in	
h_{bs} =	0.5	in	

Loads at Corners of Connections

T_{con_o} =	33.6	kip
V_{con_o} =	19.6	kip
T_{con_i} =	23.3	kip
V_{con_i} =	19.6	kip

Fillet Weld and Base Metal Parameters

D =	5	Size
F_{exx} =	70.0	ksi
Φ =	0.75	
F_y =	50.0	ksi
F_u =	65.0	ksi

Weld Strength

ΦR_n = 7.0 kip/in

Base Metal Check

t_{f_min} =	0.24	in
t_{w_min} =	0.48	in

Flange Unity = 0.33

Web Unity = 1.11

WT to PCP Connection in the Plane of the Faying Surface

L =	7.12	in
I_x =	0.00	in^4/in
I_y =	30.08	in^4/in
I_p =	30.08	in^4/in
e =	1.75	in
c_x =	3.56	in
c_y =	0.00	in
R_{px} =	2.75	kip/in
R_{py} =	0.00	kip/in
R_{mx} =	0.00	kip/in
R_{my} =	4.06	kip/in
R_{xy} =	4.90	kip/in

WT to Girder Connection in the Plane of the Faying Surface

L =	21.7	in
$\bar{y}$ =	2.60	in
I_x =	135.61	in^4/in
I_y =	30.77	in^4/in
I_p =	166.39	in^4/in
e =	2.60	in
c_x =	3.56	in CG to A
c_y =	2.60	in CG to A
R_{px} =	0.90	kip/in
R_{py} =	1.55	kip/in
R_{mx} =	0.79	kip/in
R_{my} =	1.09	kip/in
R_{xy} =	3.13	kip/in

WT to Girder Connection in the Plane of the Faying Surface

c_x =	0.22	in CG to B
c_y =	4.91	in CG to B
R_{px} =	0.90	kip/in
R_{py} =	1.55	kip/in
R_{mx} =	1.50	kip/in
R_{my} =	0.07	kip/in
R_{xy} =	2.89	kip/in

WT to Girder Connection Normal to Plane of the Faying Surface

R_{pz} =	4.7	kip/in
R_{mz} =	0.0	kip/in
R_z =	4.7	kip/in

WT to Girder Connection Normal to Plane of the Faying Surface

R_{mz} =	4.0	kip/in CG to A
R_{mz} =	2.3	kip/in CG to A
R_z =	6.2	kip/in

WT to Girder Connection Normal to Plane of Faying Surface

R_{mz} =	0.2	kip/in CG to B
R_{mz} =	4.3	kip/in CG to B
R_z =	4.5	kip/in

WT to PCP Connection Max Load on Weld

R_{max} = 6.8 kip/in

Unity = 0.98

WT to Girder Connection Max Load on Weld

R_{max} = 7.0 kip/in

Unity = 1.00

WT to Girder Connection Max Load on Weld

R_{max} = 5.3 kip/in

Unity* = 0.85

*Increased by factor of 1.11 since weld is stronger than web base metal

Appendix B. Twin I-Girder Experimental Results

B.1 Initial Imperfections of Concentric Twin I-Girder Tests

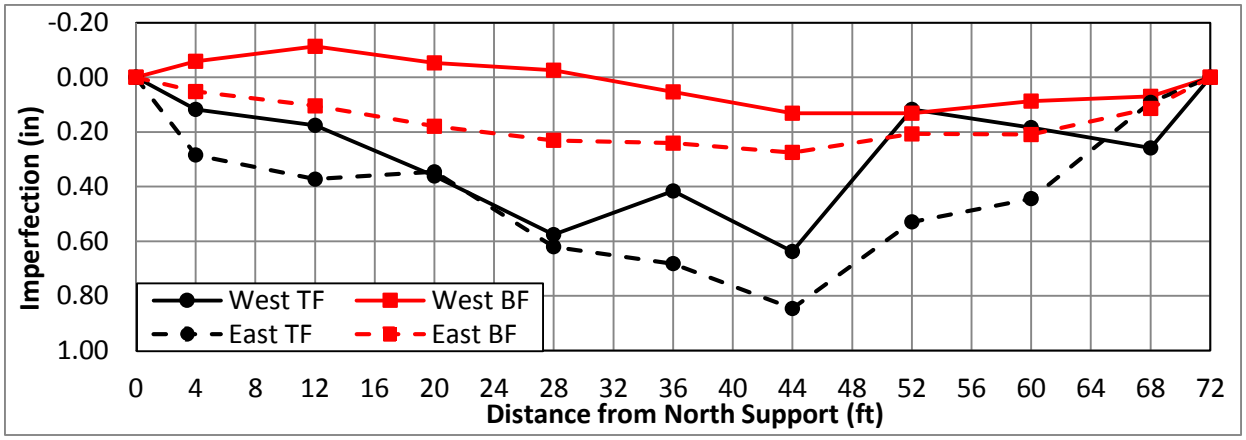

Figure B.1: Initial Imperfections - GLS.1

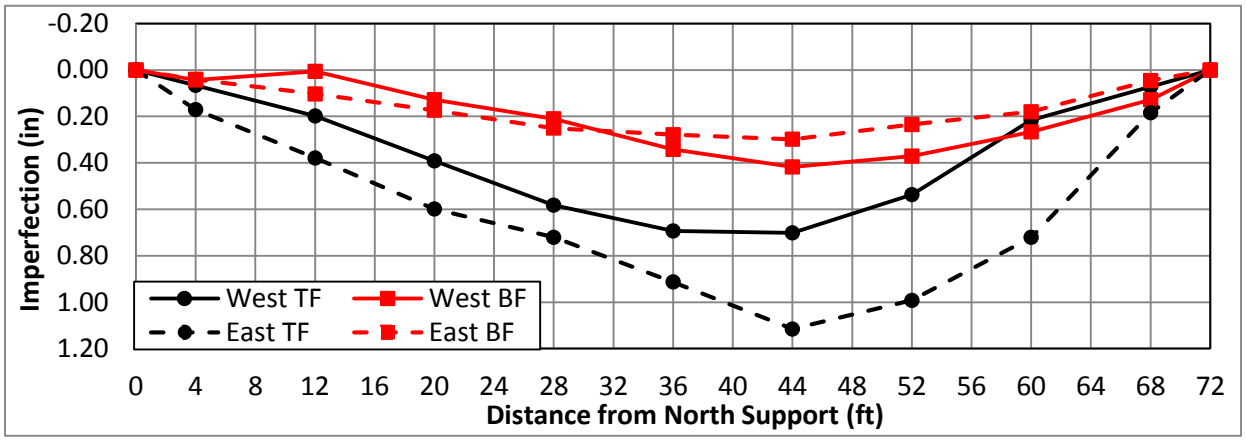

Figure B.2: Initial Imperfections - GLS.2

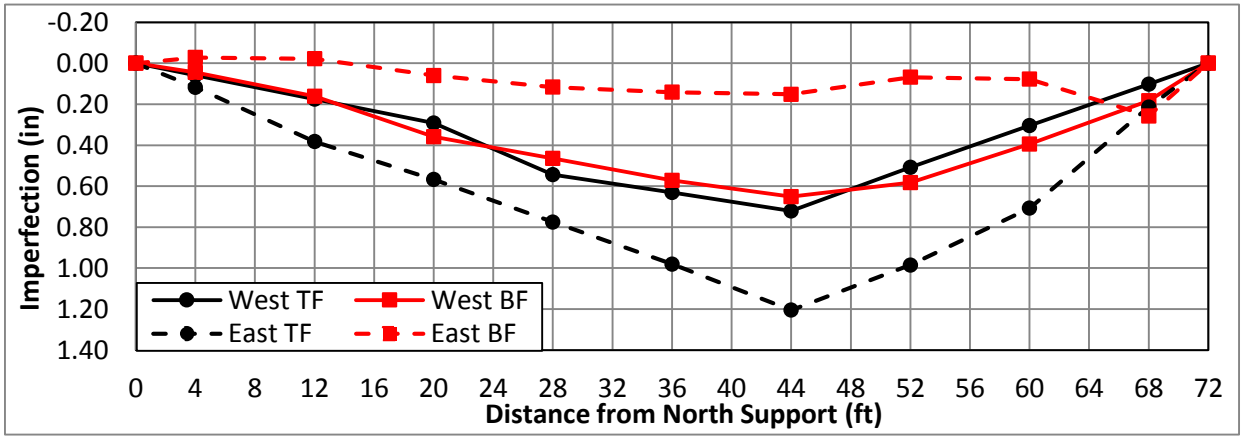

Figure B.3: Initial Imperfections - GLS.3

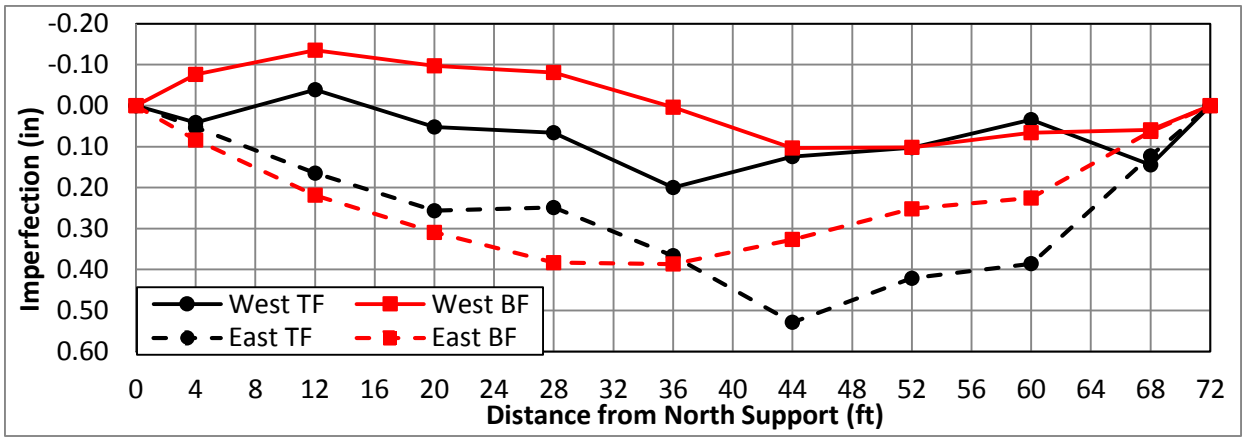

Figure B.4: Initial Imperfections - GLS.14

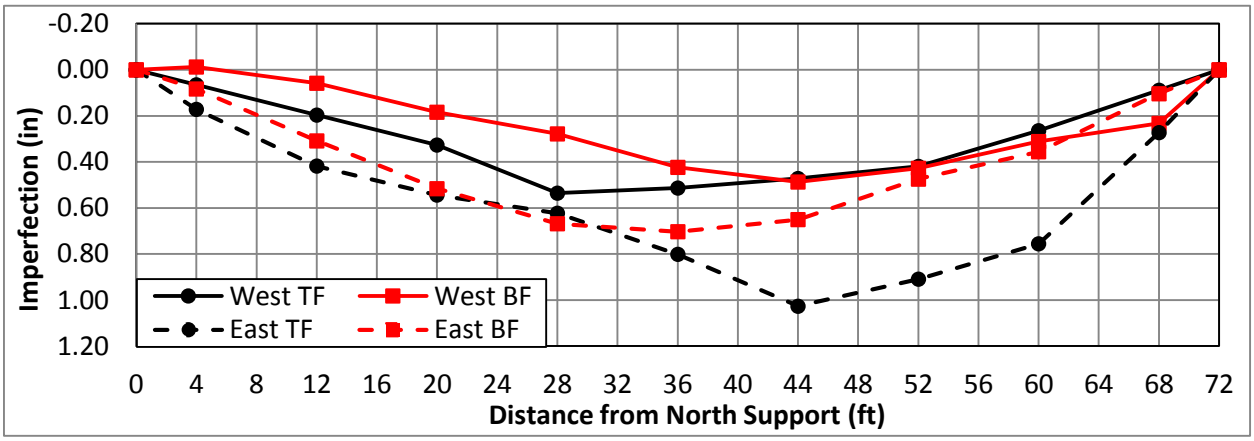

Figure B.5: Initial Imperfections - GLS.15

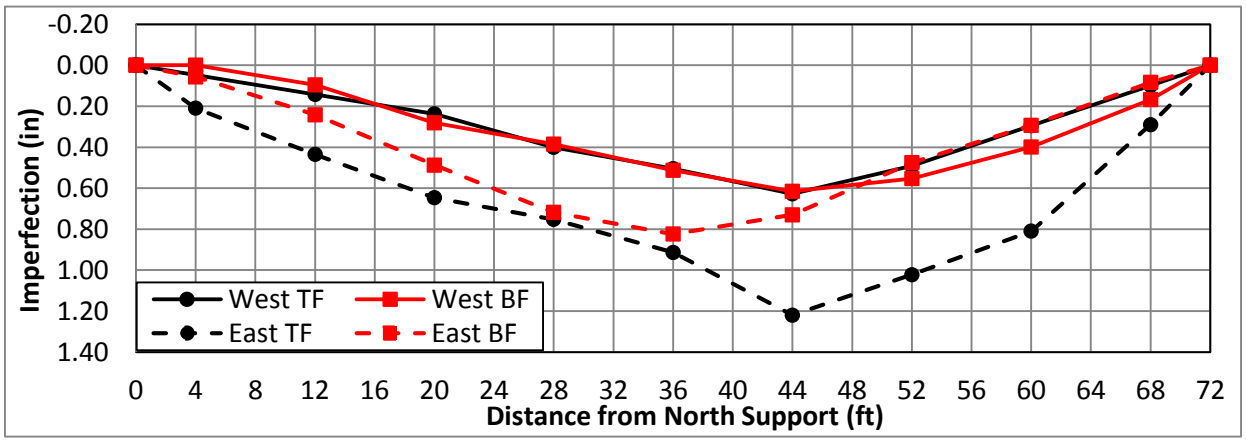

Figure B.6: Initial Imperfections - GLS.16

B.2 Experimental Results for Lateral Load I-Girder Tests

Table B.1: Summary of Lateral I-Girder Tests

Test Name	Load Location	Cross Frame	Number of PCPS
LAT.1	MS	-	0
LAT.2	MS	-	2
LAT.3	MS	-	4
LAT.4	MS	XF	0
LAT.5	MS	XF	2
LAT.6	MS	XF	4
LAT.7	QP	-	0
LAT.8	QP	-	2
LAT.9	QP	-	4
LAT.10	QP	XF	0
LAT.11	QP	XF	2
LAT.12	QP	XF	4

Key: LAT = Top Flange Lateral Load XF = Cross-Frame
MS = Midspan Load, QP = Quarter Point Load

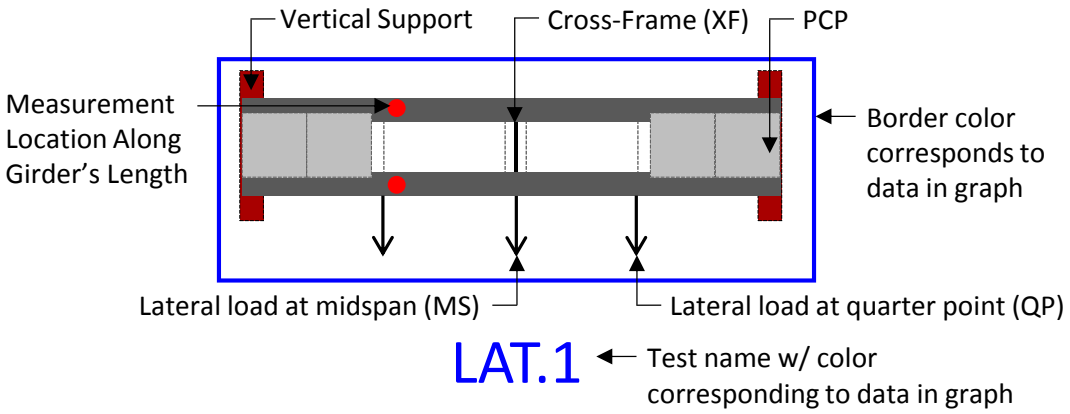

Figure B.7: Nomenclature for Documentation of Lateral Load I-Girder Tests

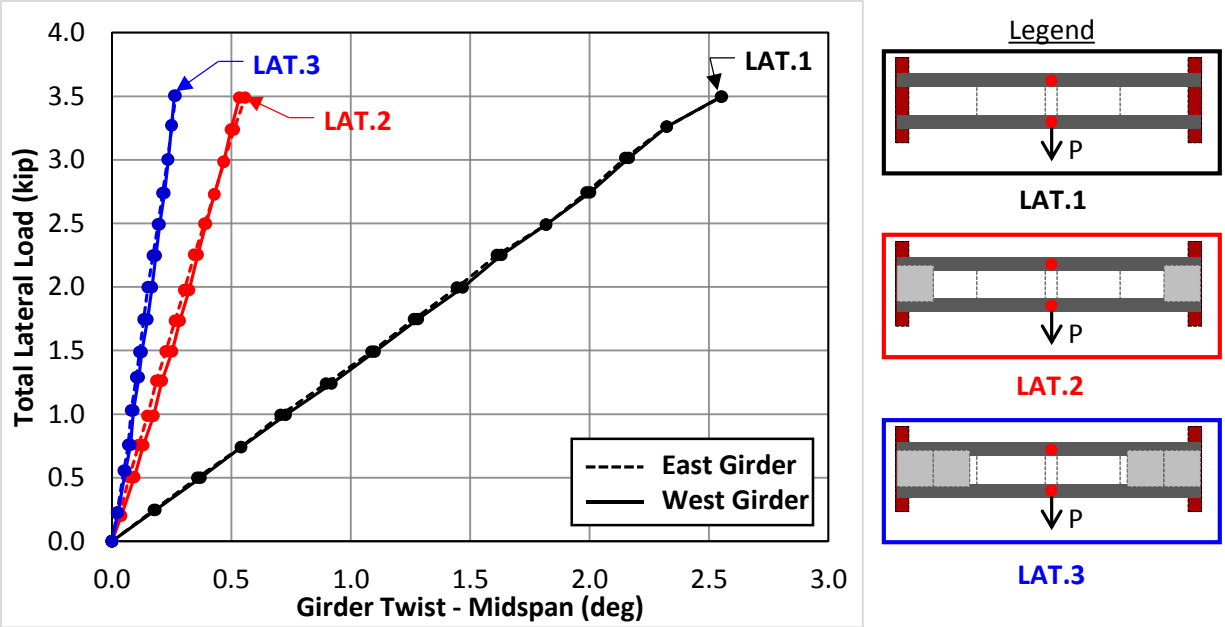

Figure B.8: Twist @ Midspan vs. Lateral Load @ Midspan (w/o XF)

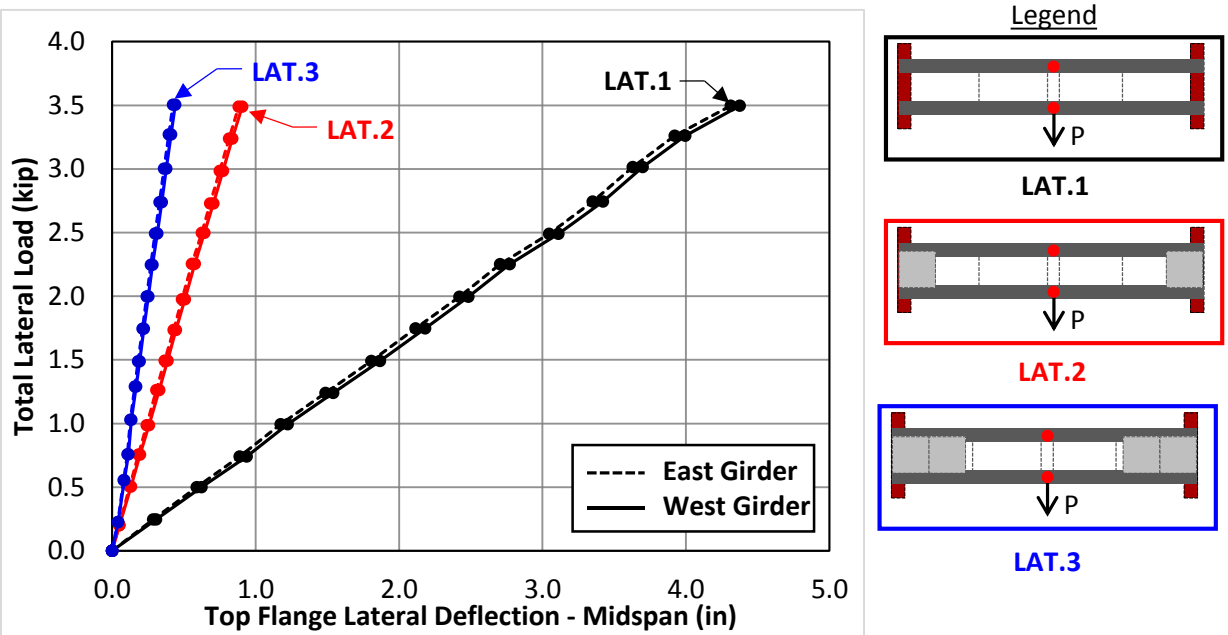

Figure B.9: Lateral Deflection @ Midspan vs. Lateral Load @ Midspan (w/o XF)

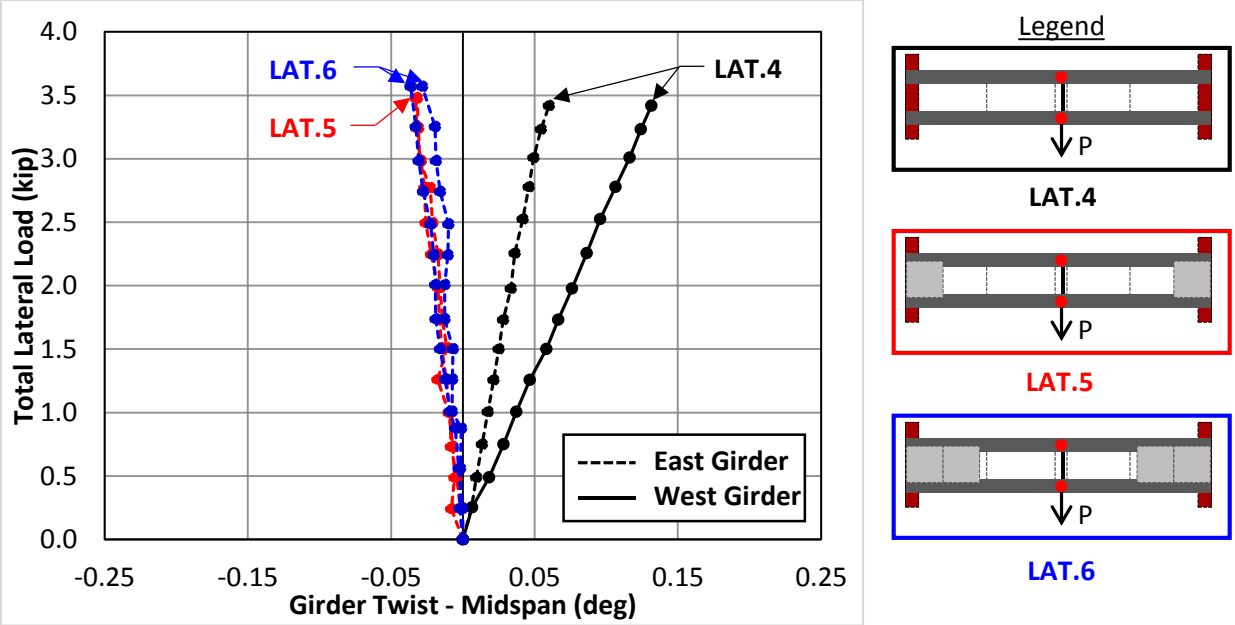

Figure A.10: Twist @ Midspan vs. Lateral Load @ Midspan (w/ XF)

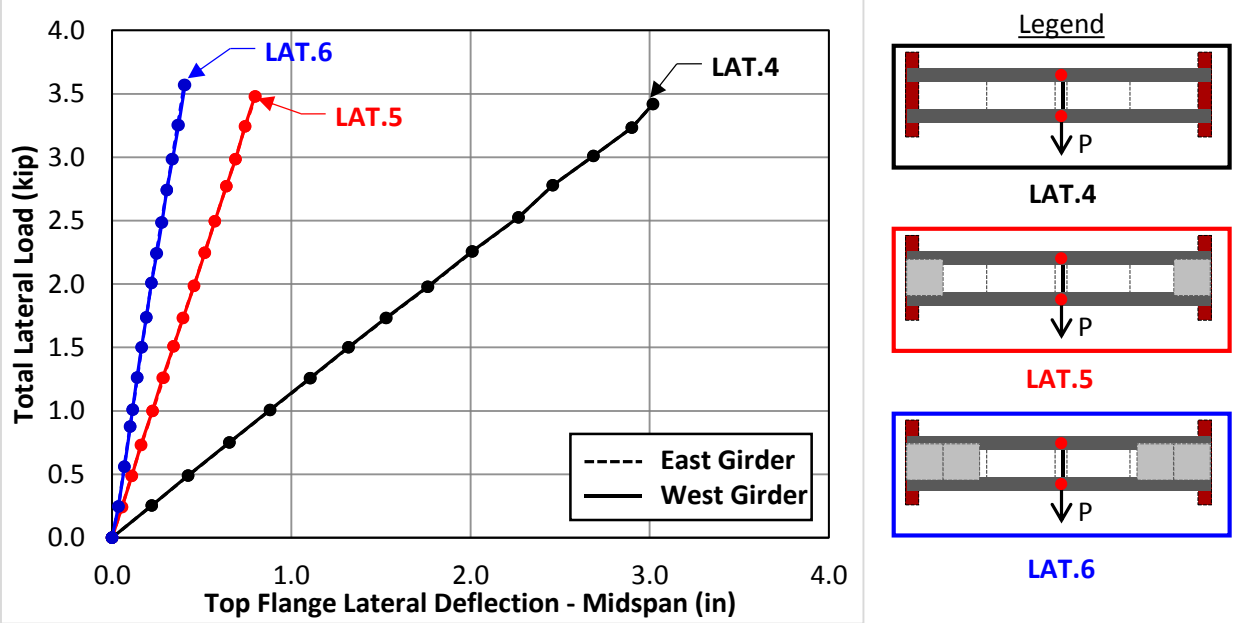

Figure B.11: Lateral Deflection @ Midspan vs. Lateral Load @ Midspan (w/ XF)

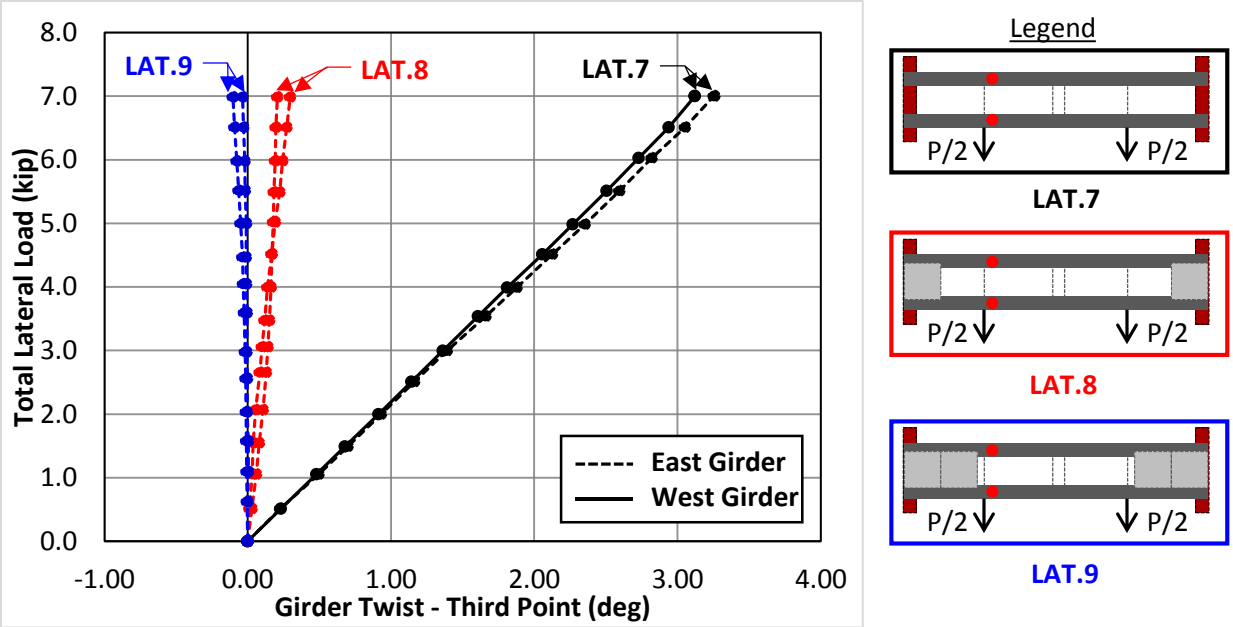

Figure B.12: Twist @ Third Point vs. Lateral Load @ Quarter Points (w/o XF)

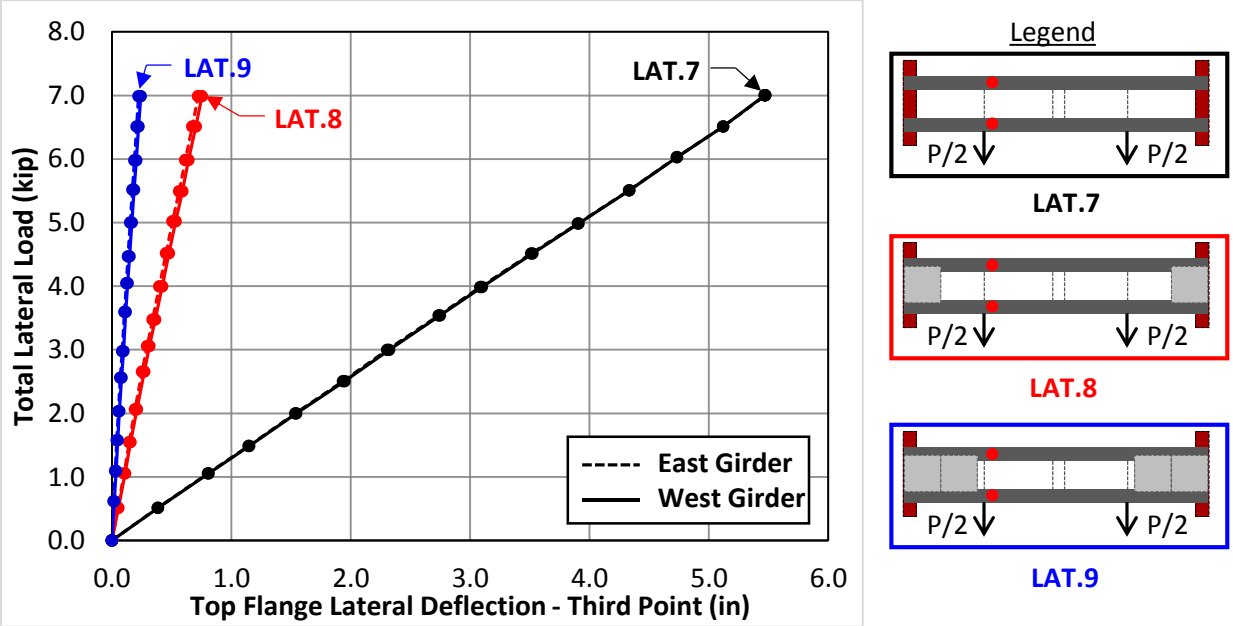

Figure B.13: Lateral Deflection @ Third Point vs. Lateral Load @ Quarter Points (w/o XF)

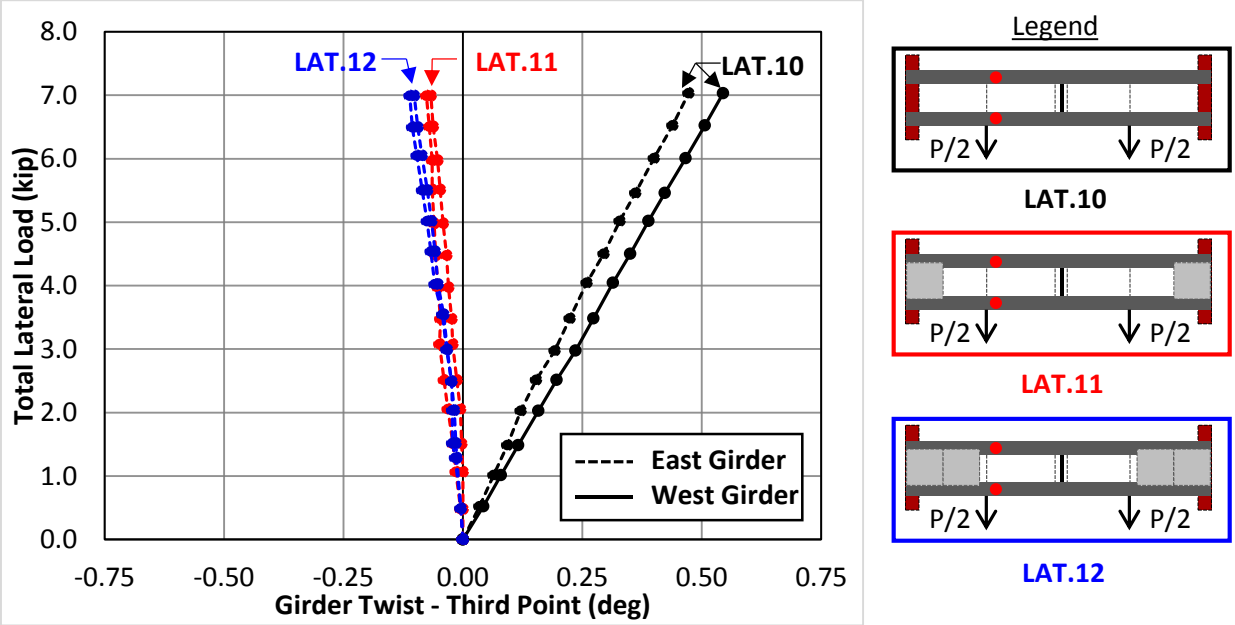

Figure B.14: Twist @ Third Point vs. Lateral Load @ Quarter Points (w/ XF)

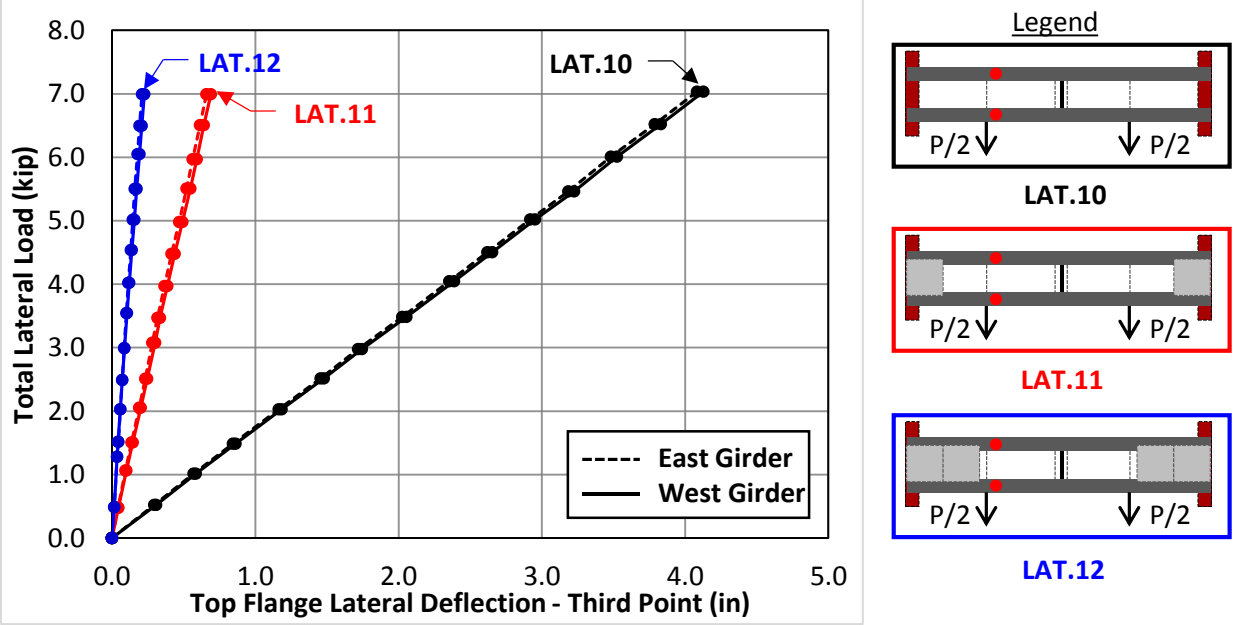

Figure B.15: Lateral Deflection @ Third Point vs. Lateral Load @ Quarter Points (w/ XF)

B.3 Experimental Results for Combined Bending and Torsion Simply Supported I-Girder Test

Table B.2: Summary of Bending and Torsion Simply Supported I-Girder Tests

Test Name	Support Condition	Load Eccentricity	Cross Frame	Bottom Truss	Number of PCPS	Max Total GLS Load
GLS.1	SS	0 & 0	-	-	0	30
GLS.2	SS	0 & 0	-	-	2	100
GLS.3	SS	0 & 0	-	-	4	150
GLS.4	SS	6" & 6"	-	-	0	19
GLS.5	SS	6" & 6"	-	-	2	60
GLS.6	SS	6" & 6"	-	-	4	90
GLS.7	SS	6" & 6"	-	2 BF	4	80
GLS.8	SS	6" & 6"	-	4 BF	4	100
GLS.9	SS	12" & 12"	-	-	0	10
GLS.10	SS	12" & 12"	-	-	2	38
GLS.11	SS	12" & 12"	-	-	4	40
GLS.12	SS	12" & 12"	-	2 BF	4	75
GLS.13	SS	12" & 12"	-	4 BF	4	80
GLS.14	SS	0 & 0	XF	-	0	140
GLS.15	SS	0 & 0	XF	-	2	180
GLS.16	SS	0 & 0	XF	-	4	180
GLS.17	SS	6" & 6"	XF	-	0	90
GLS.18	SS	6" & 6"	XF	-	2	110
GLS.19	SS	6" & 6"	XF	-	4	120
GLS.20	SS	12" & 12"	XF	-	0	60
GLS.21	SS	12" & 12"	XF	-	2	70
GLS.22	SS	12" & 12"	XF	-	4	90

Key: GLS = Gravity Load Simulator Load, SS = Simply Supported
BF = Bottom Flange Truss, XF = Cross-Frame

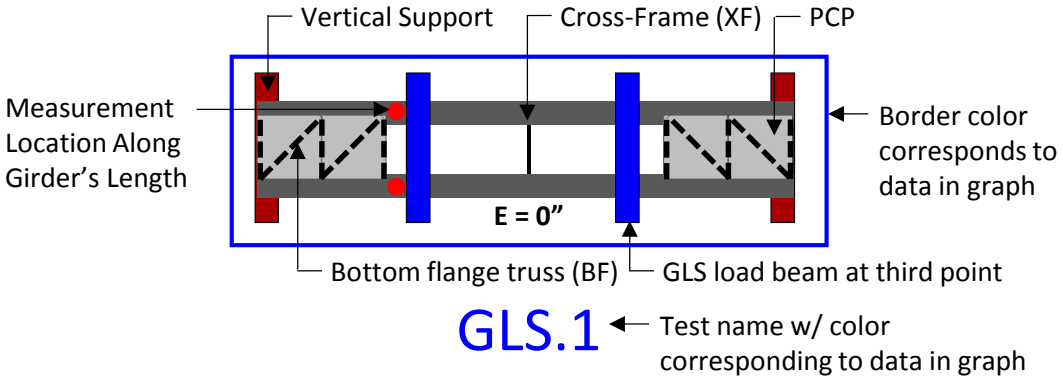

Figure B.16: Nomenclature for Documentation of GLS Simply Supported I-Girder Tests

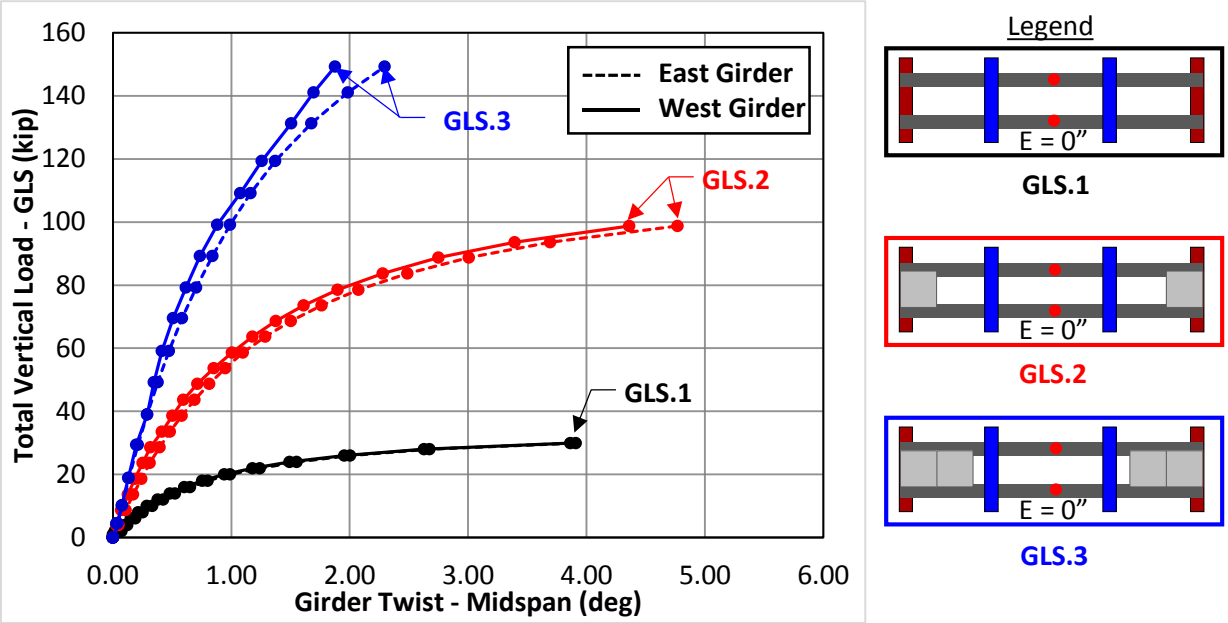

Figure B.17: Twist @ Midspan vs. GLS Load (E=0" - SS - w/o XF)

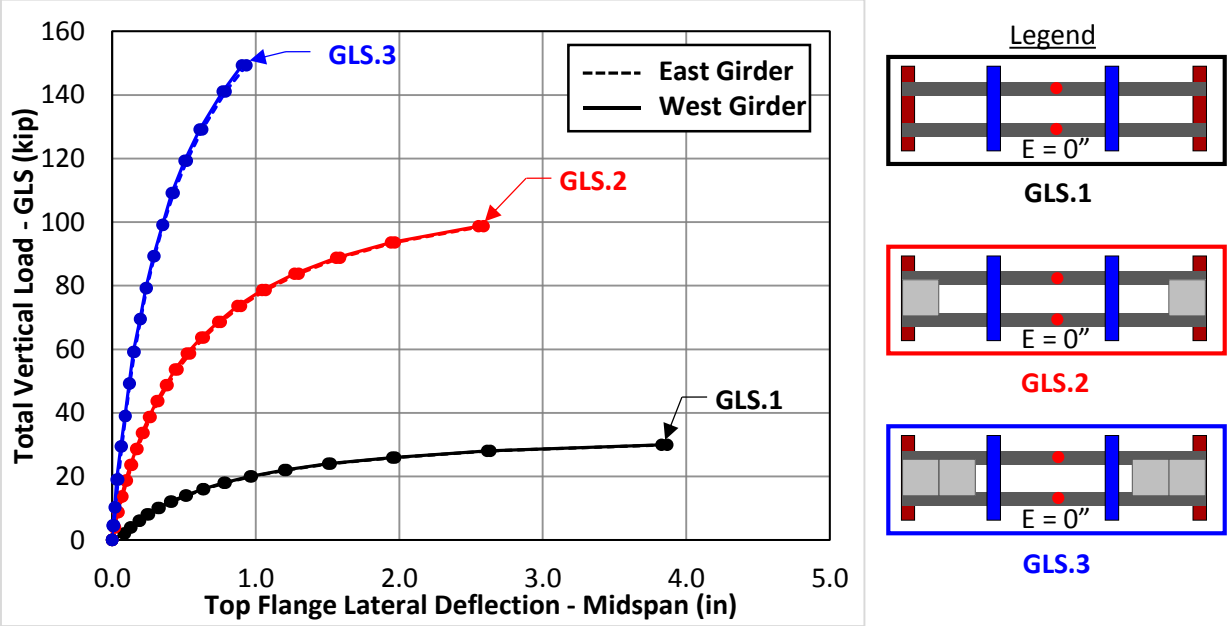

Figure B.18: Lateral Deflection @ Midspan vs. GLS Load (E=0" - SS - w/o XF)

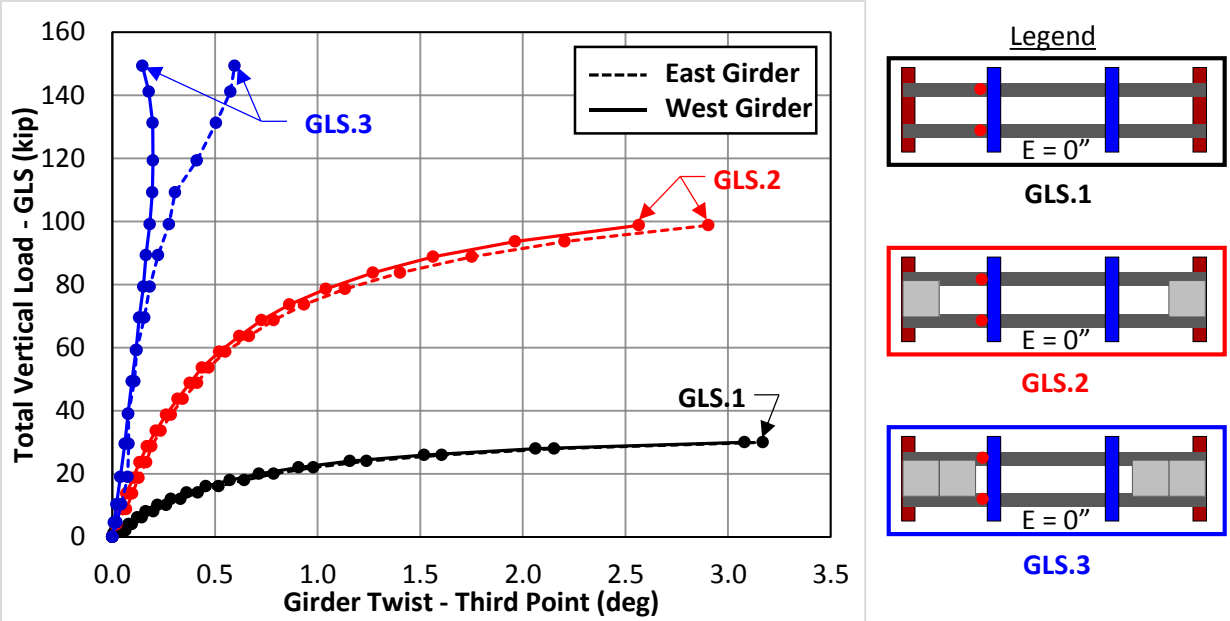

Figure B.19: Twist @ Third Points vs. GLS Load (E=0" - SS - w/o XF)

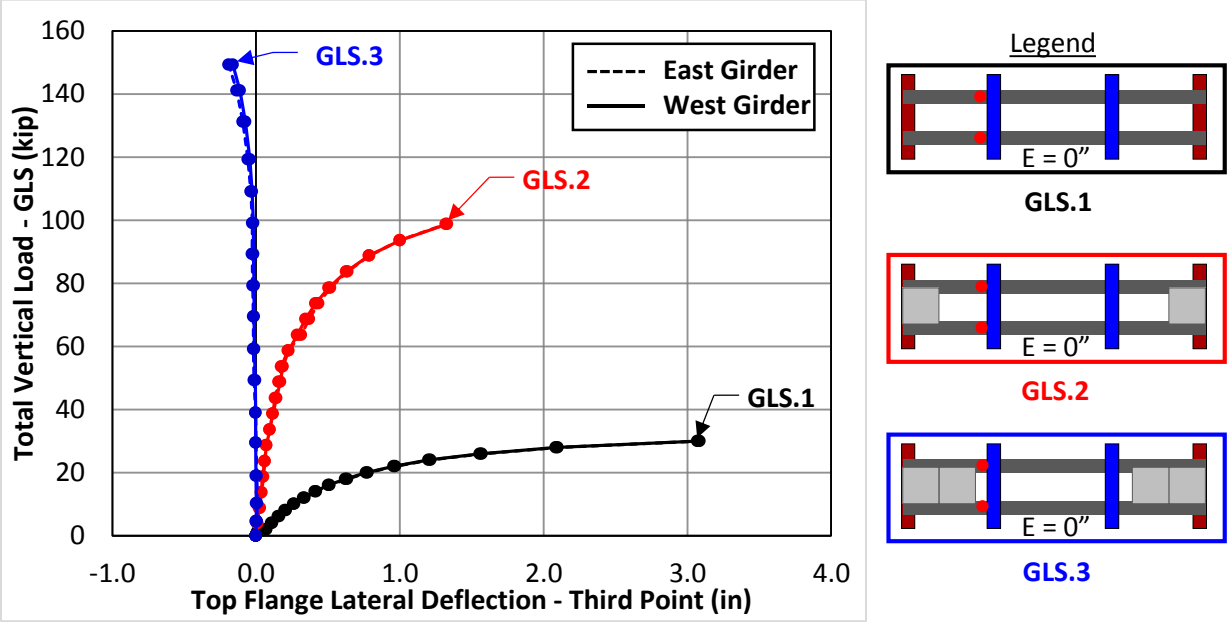

Figure B.20: Lateral Deflection @ Third Points vs. GLS Load (E=0" - SS - w/o XF)

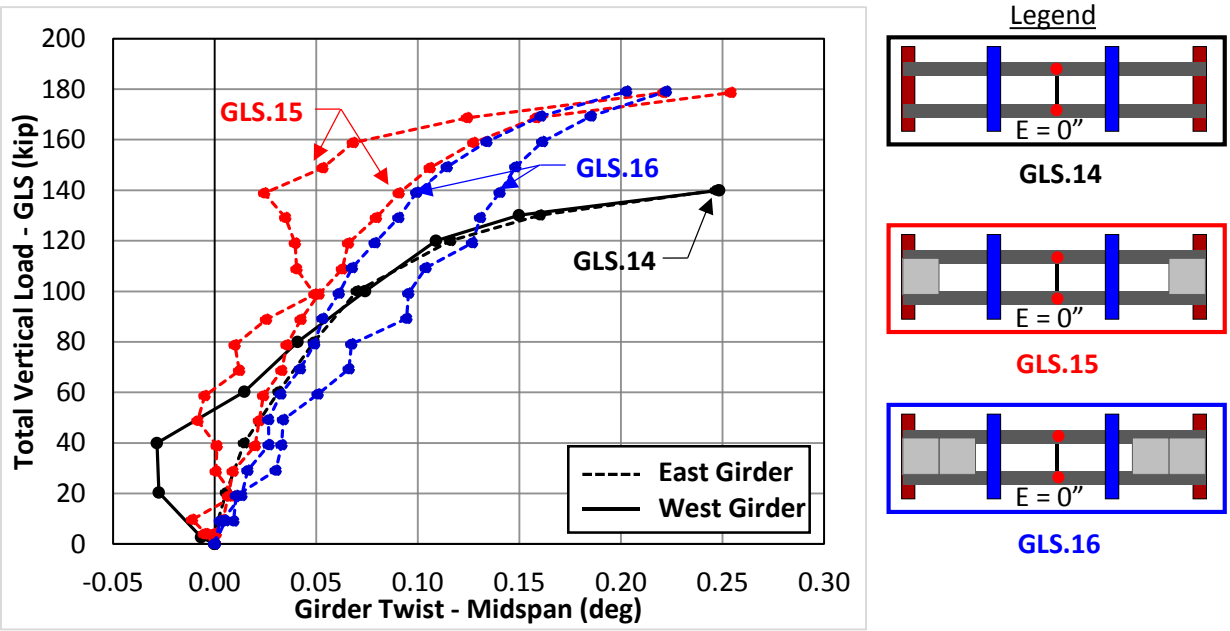

Figure B.21: Twist @ Midspan vs. GLS Load (E=0" - SS - w/ XF)

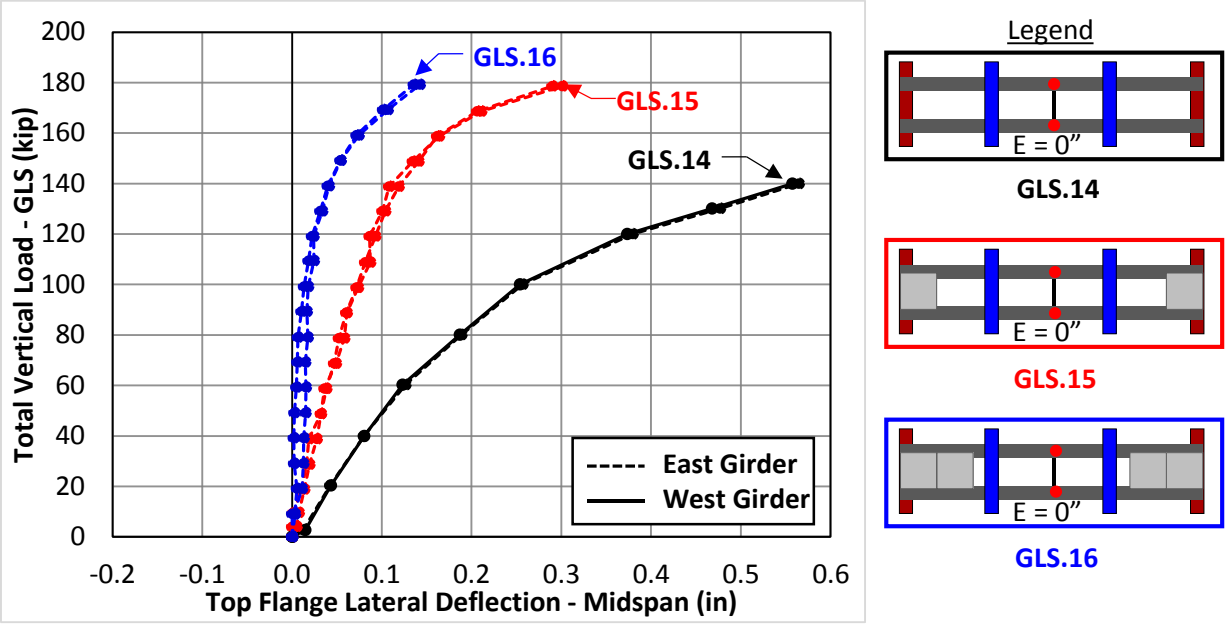

Figure B.22: Lateral Deflection @ Midspan vs. GLS Load (E=0" - SS - w/ XF)

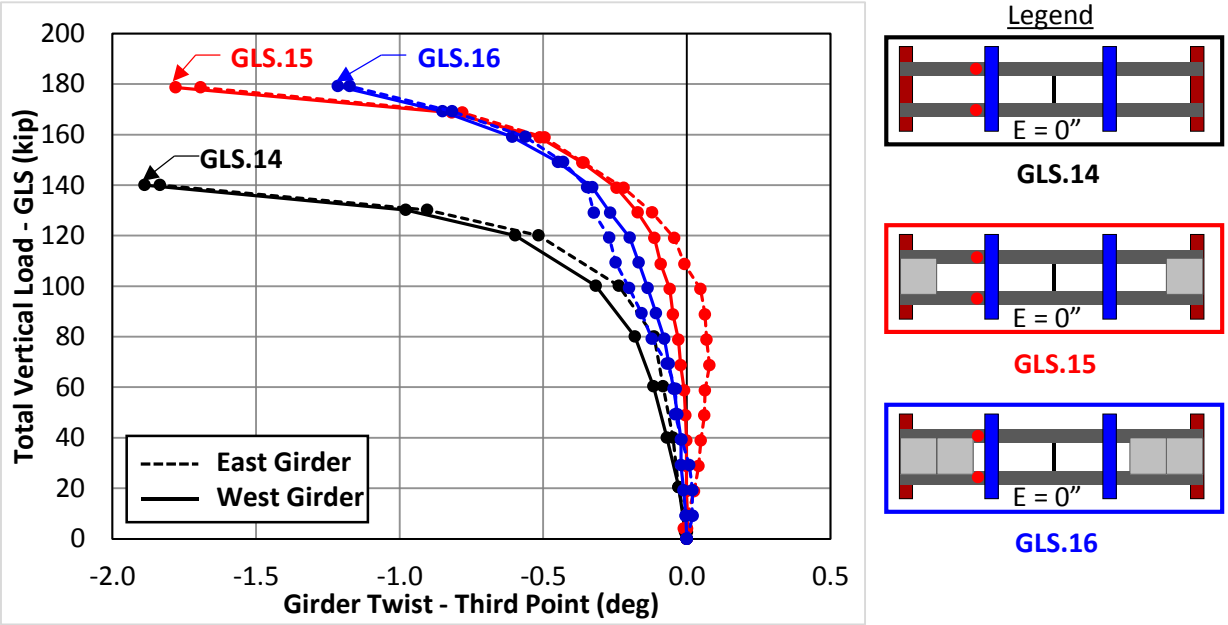

Figure B.23: Twist @ Third Point vs. GLS Load (E=0" - SS - w/ XF)

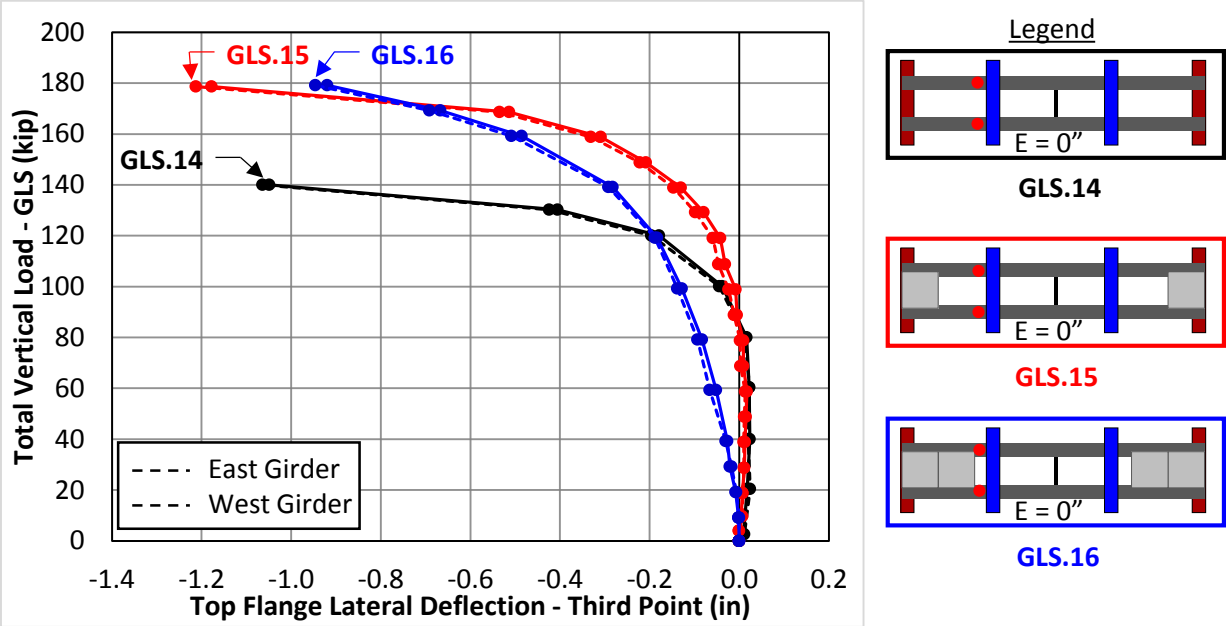

Figure B.24: Lateral Deflection @ Third Point vs. GLS Load (E=0" - SS - w/ XF)

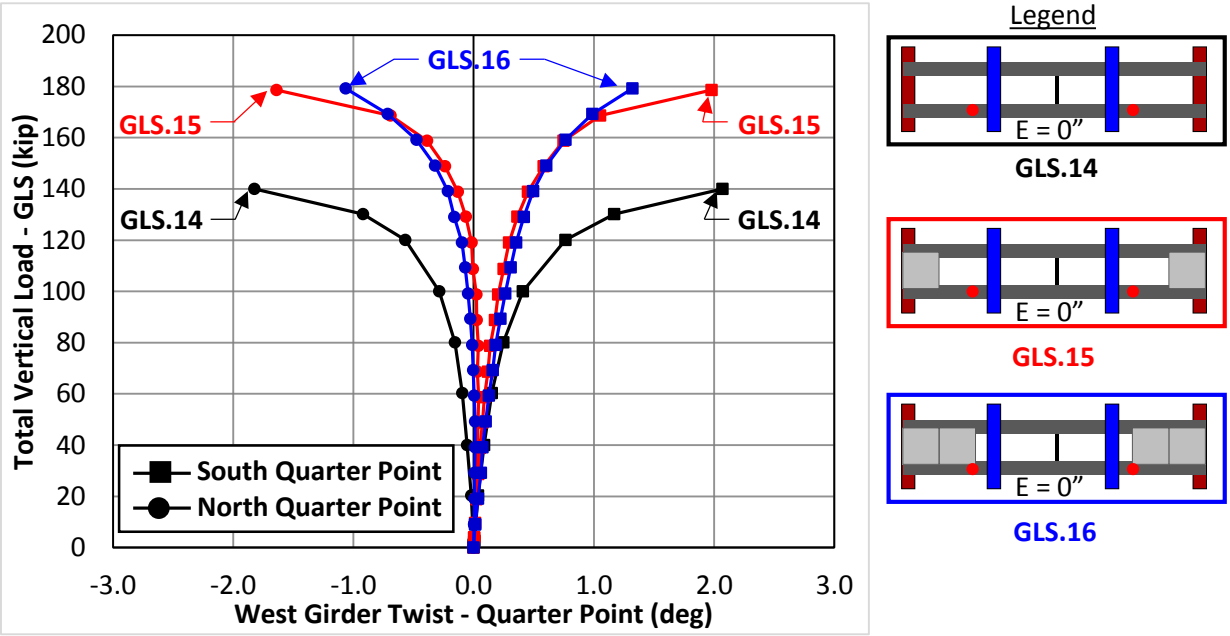

Figure B.25: Twist @ Quarter Point vs. GLS Load (E=0" - SS - w/ XF)

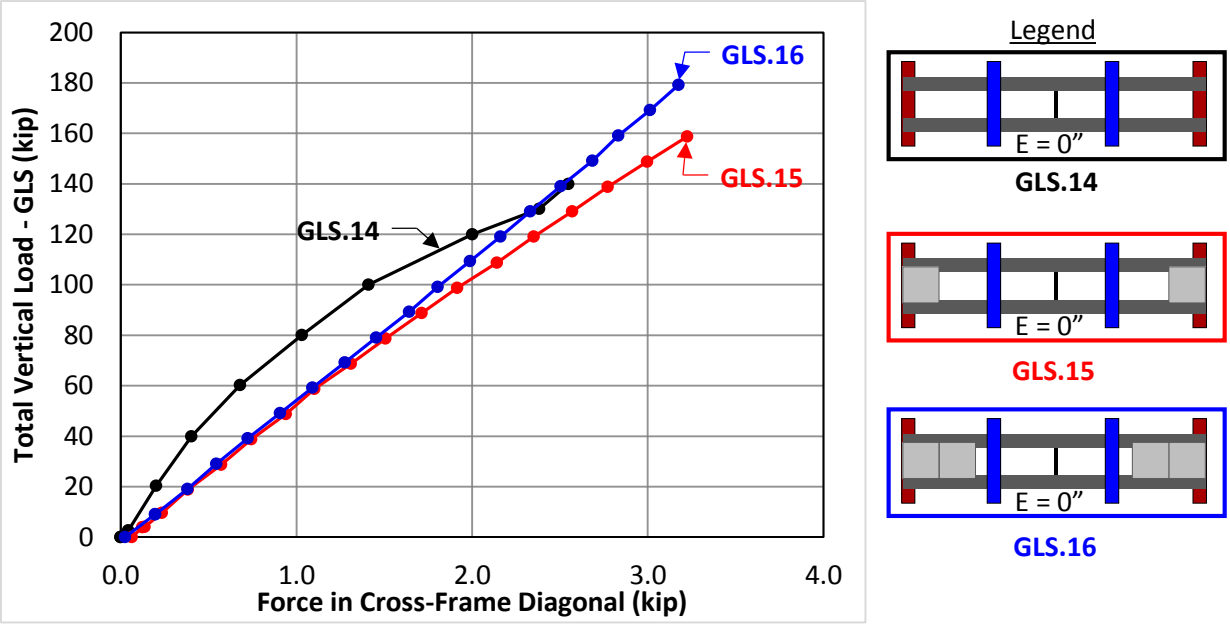

Figure B.26: Cross-Frame Diagonal Force vs. GLS Load (E=0" - SS)

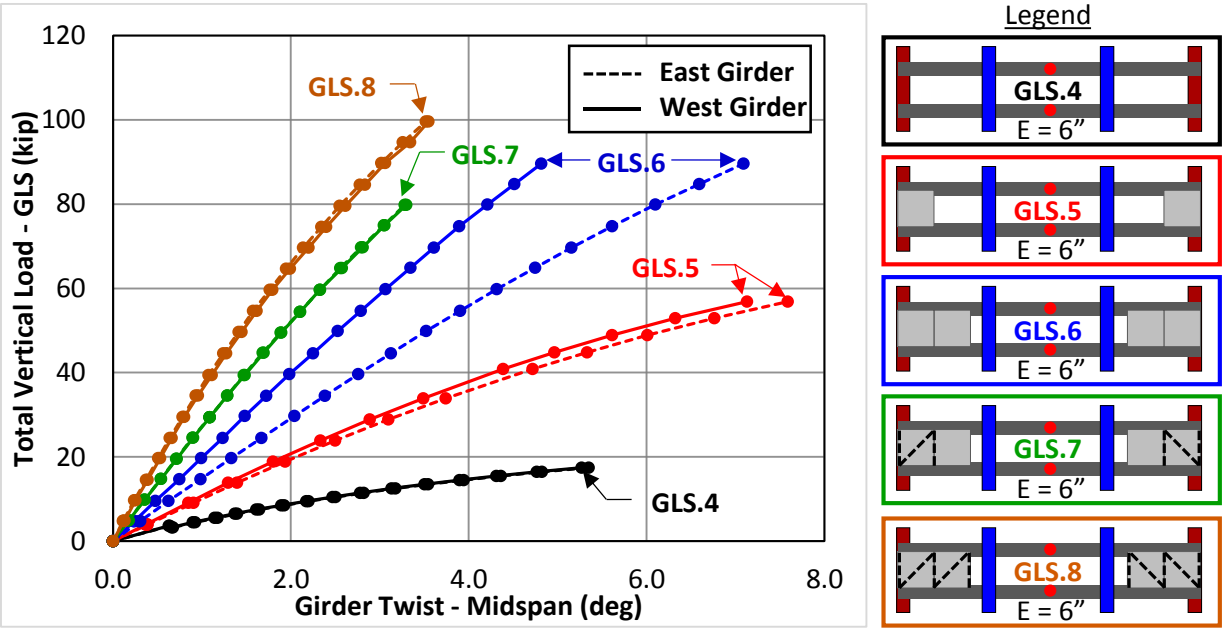

Figure B.27: Twist @ Midspan vs. GLS Load (E=6" - SS - w/o XF)

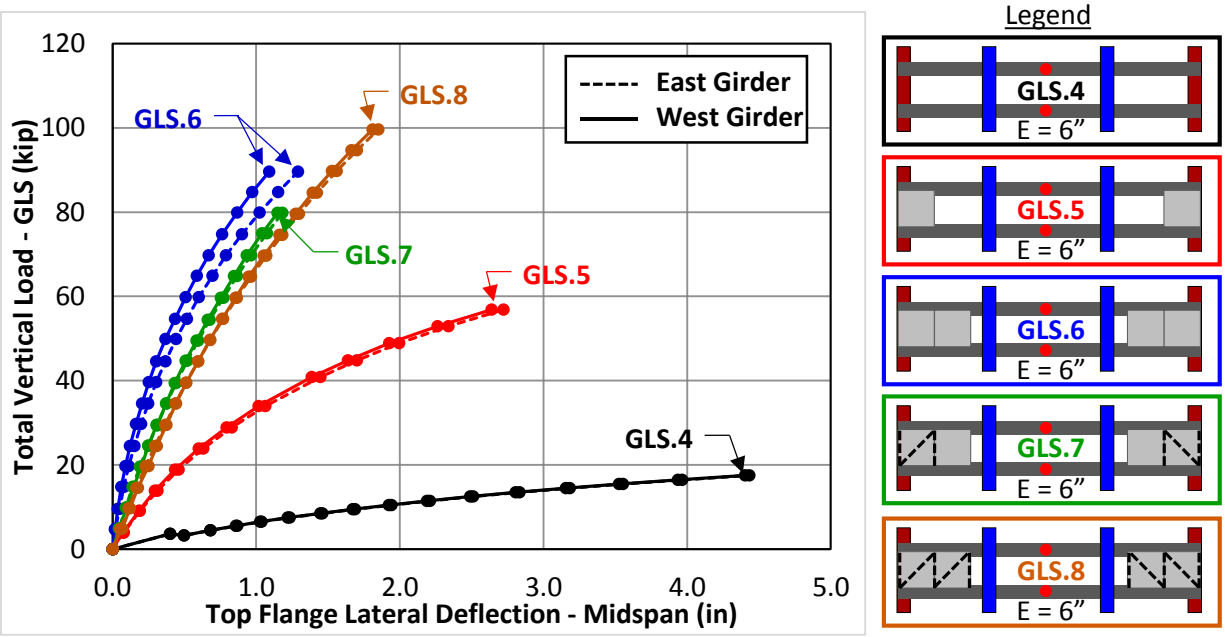

Figure B.28: Lateral Deflection @ Midspan vs. GLS Load (E=6" - SS - w/o XF)

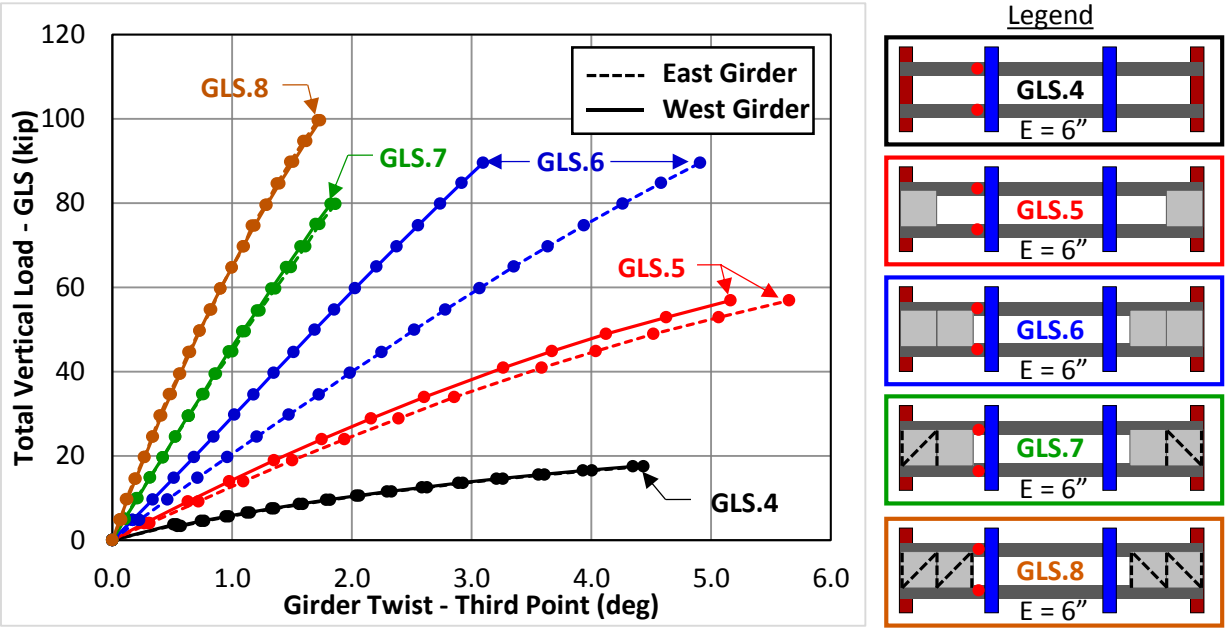

Figure B.29: Twist @ Third Point vs. GLS Load (E=6" - SS - w/o XF)

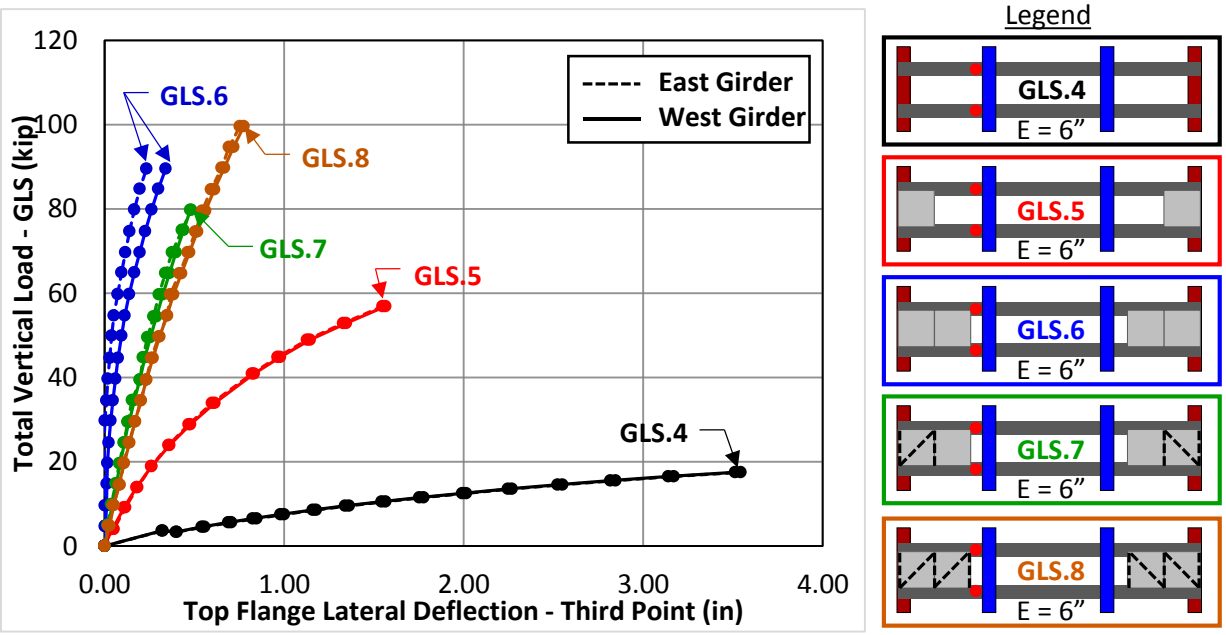

Figure B.30: Lateral Deflection @ Third Point vs. GLS Load (E=6" - SS - w/o XF)

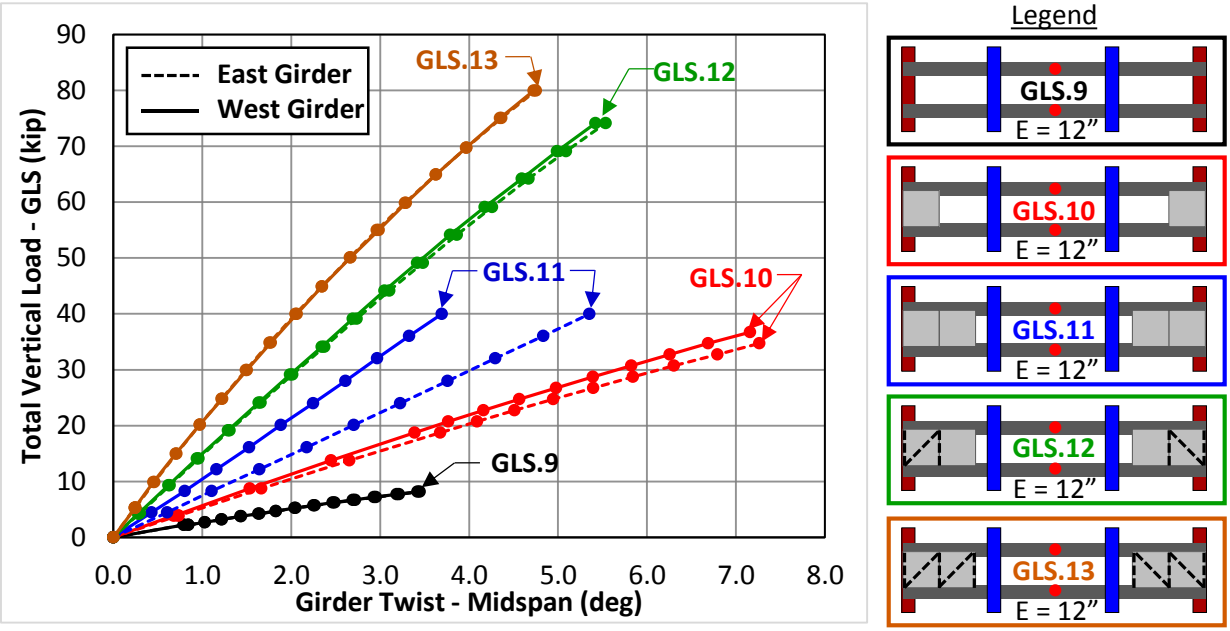

Figure B.31: Twist @ Midspan vs. GLS Load (E=12" - SS - w/o XF)

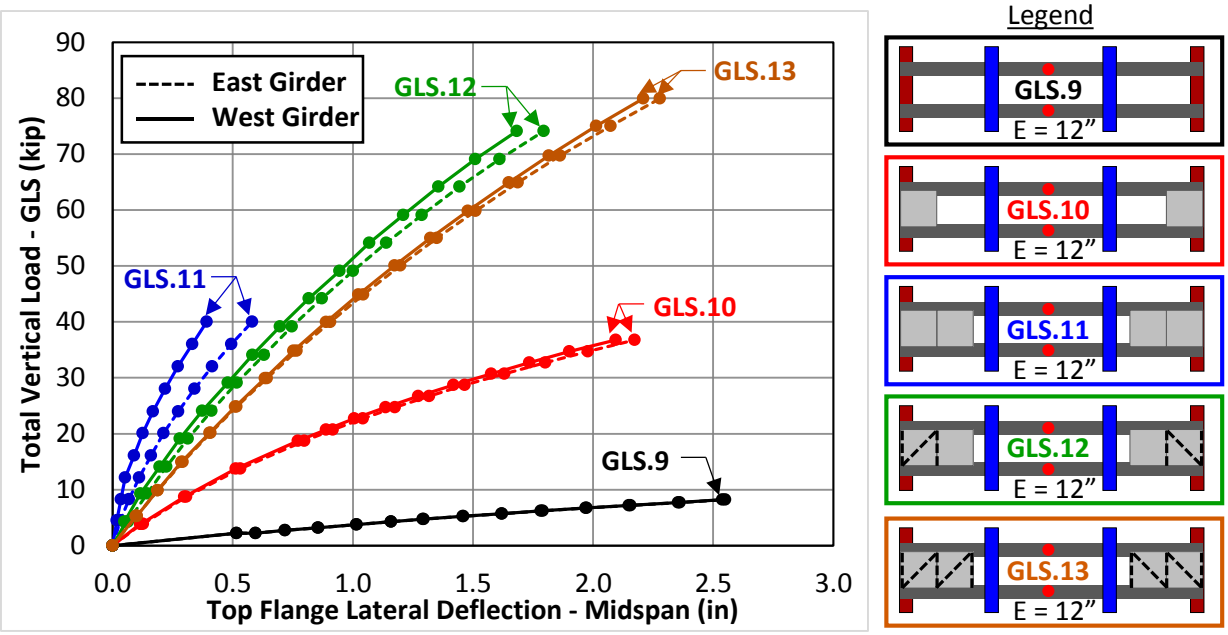

Figure B.32: Lateral Deflection @ Midspan vs. GLS Load (E=12" - SS - w/o XF)

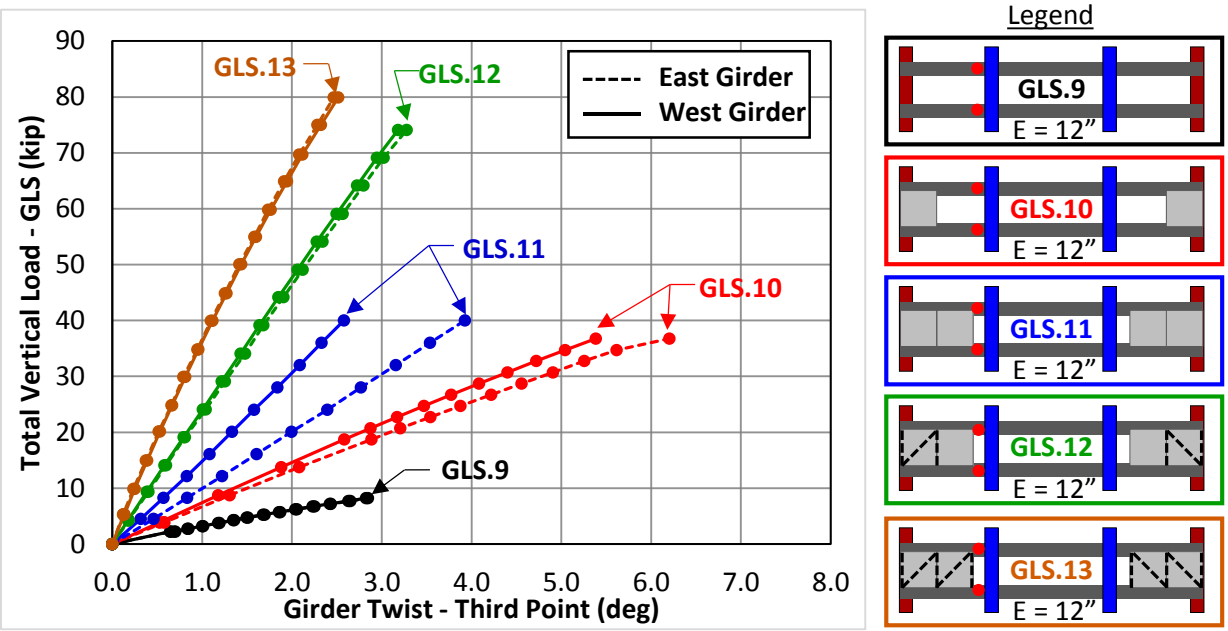

Figure B.33: Twist @ Third Point vs. GLS Load (E=12" - SS - w/o XF)

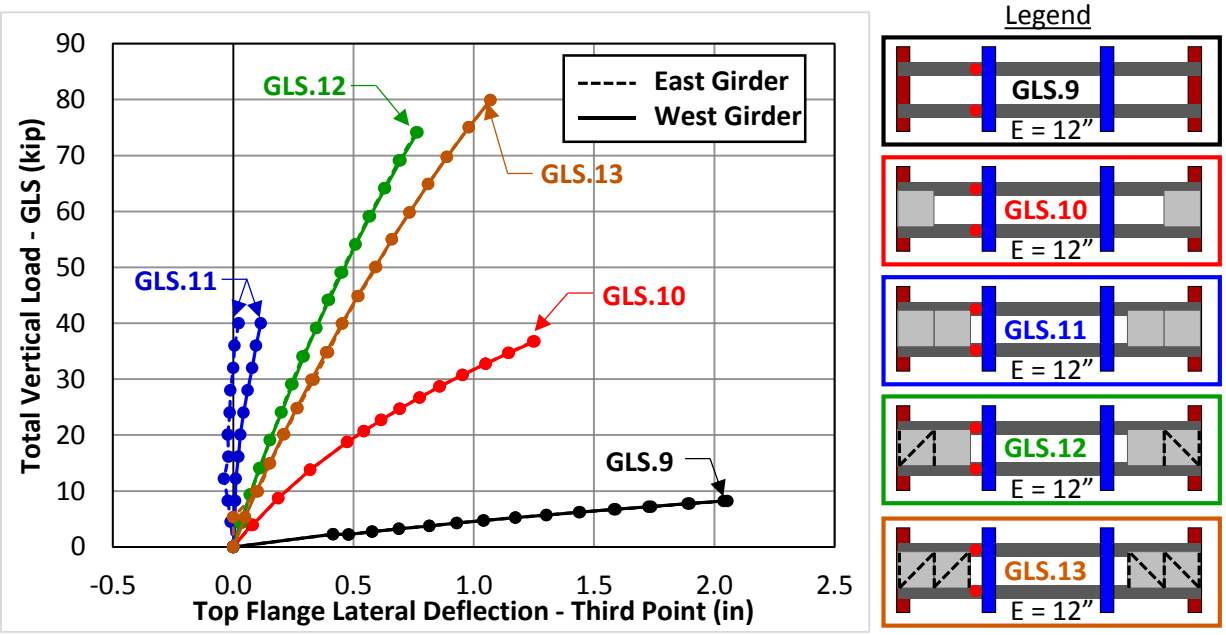

Figure B.34: Lateral Deflection @ Third Point vs. GLS Load (E=12" - SS - w/o XF)

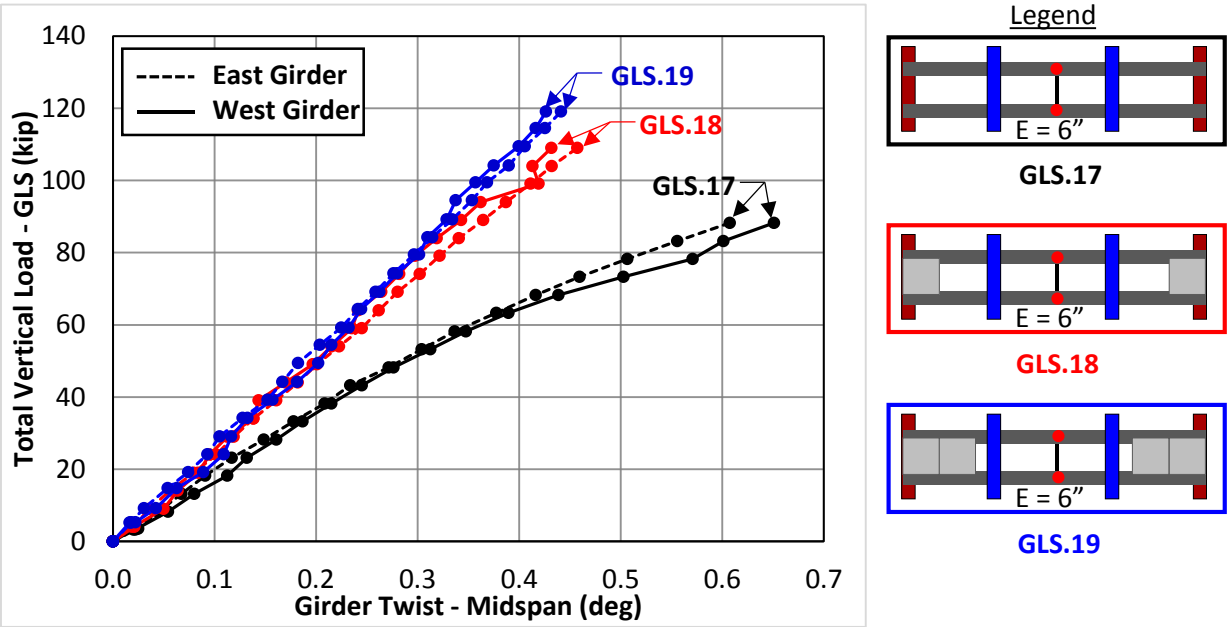

Figure B.35: Twist @ Midspan vs. GLS Load (E=6" - SS - w/ XF)

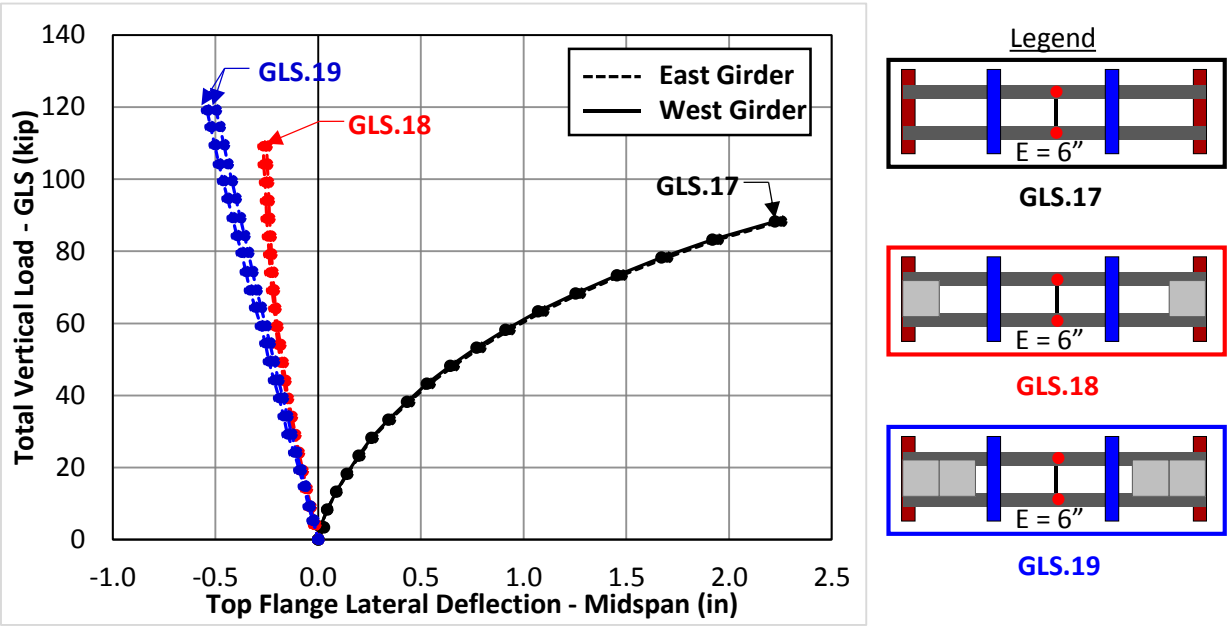

Figure B.36: Lateral Deflection @ Midspan vs. GLS Load (E=6" - SS - w/ XF)

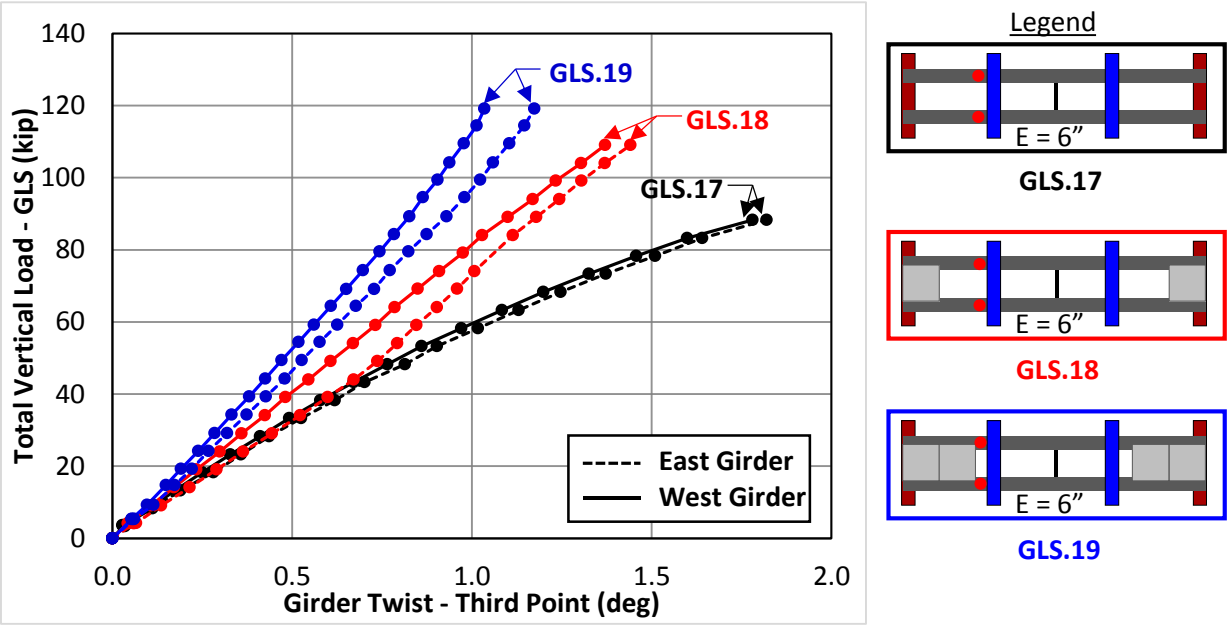

Figure B.37: Twist @ Third Point vs. GLS Load (E=6" - SS - w/ XF)

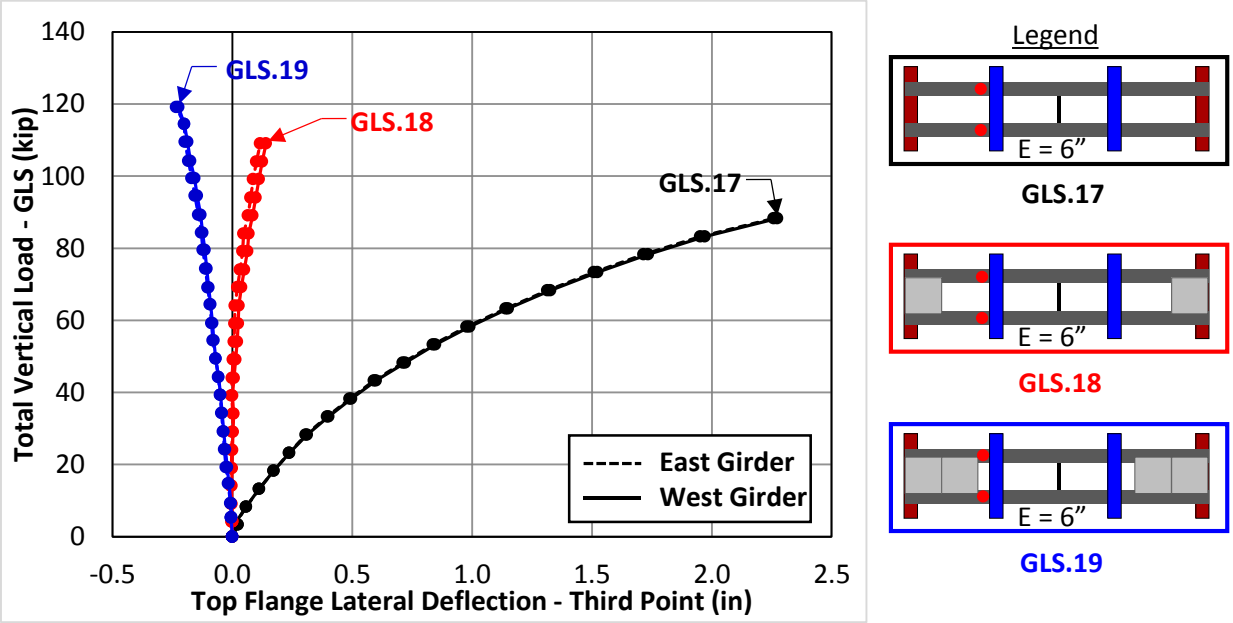

Figure B.38: Lateral Deflection @ Third Point vs. GLS Load (E=6" - SS - w/ XF)

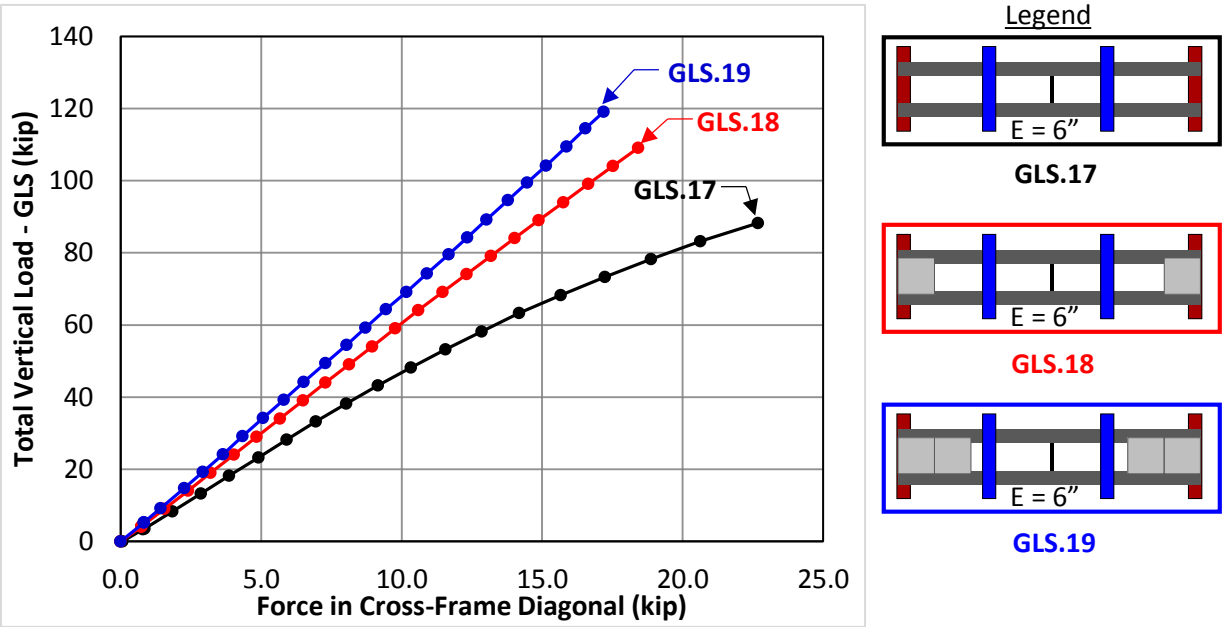

Figure B.39: Cross-Frame Diagonal Force vs. GLS Load (E=6" - SS)

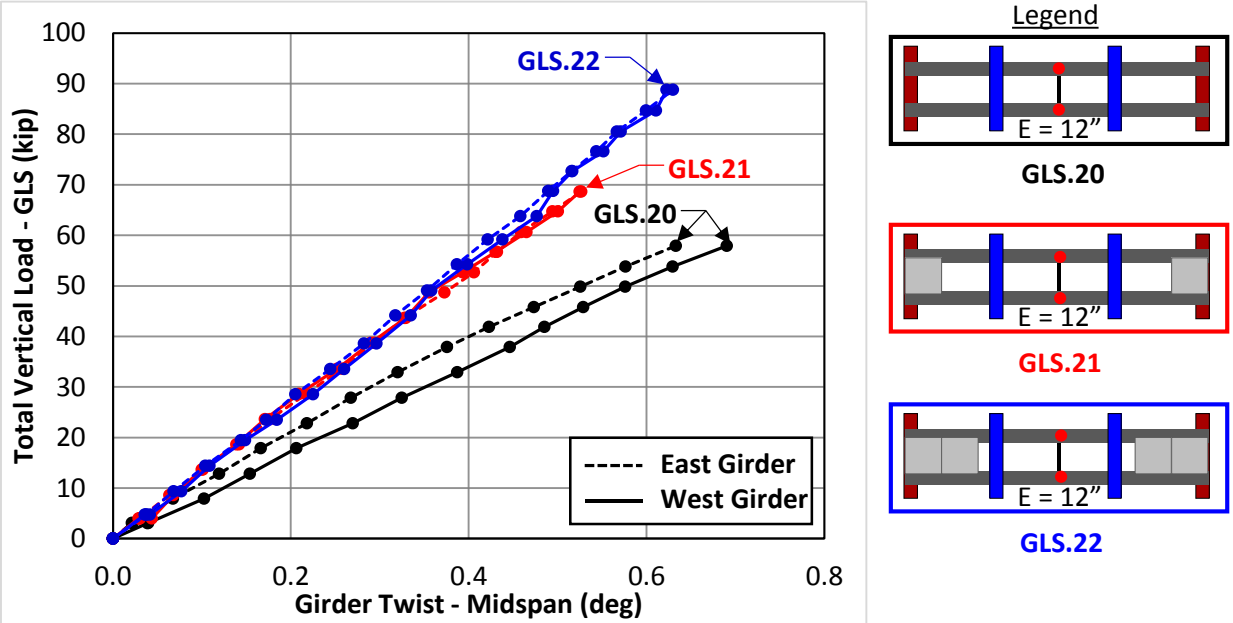

Figure B.40: Twist @ Midspan vs. GLS Load (E=12" - SS - w/ XF)

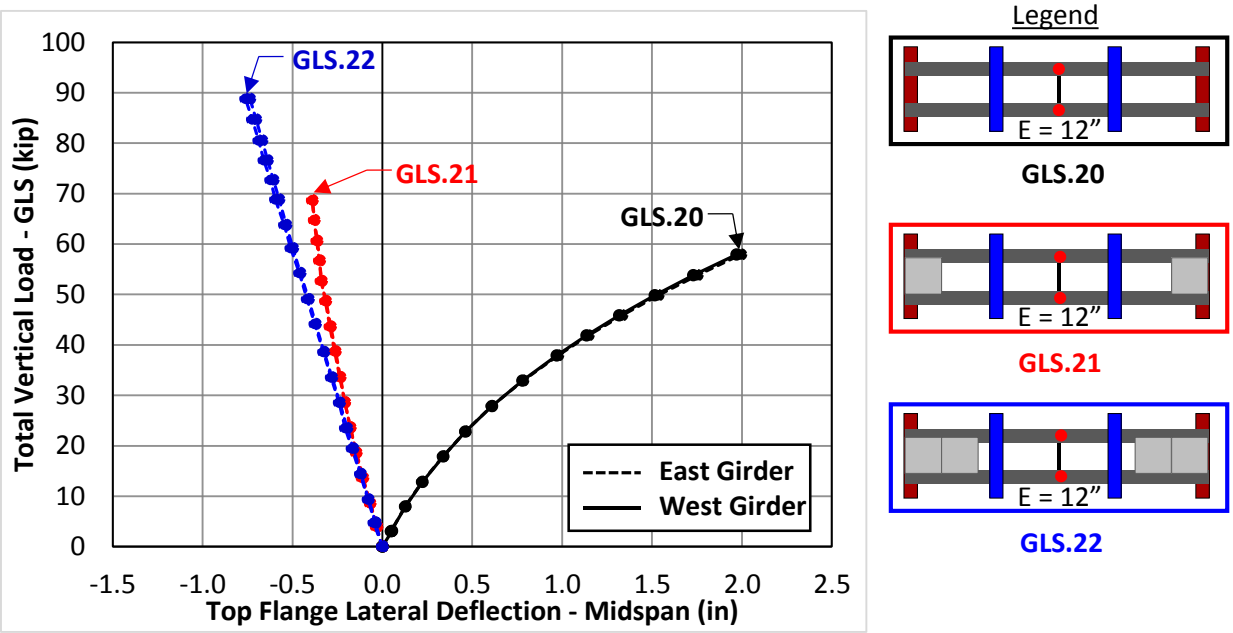

Figure B.41: Lateral Deflection @ Midspan vs. GLS Load (E=12" - SS - w/ XF)

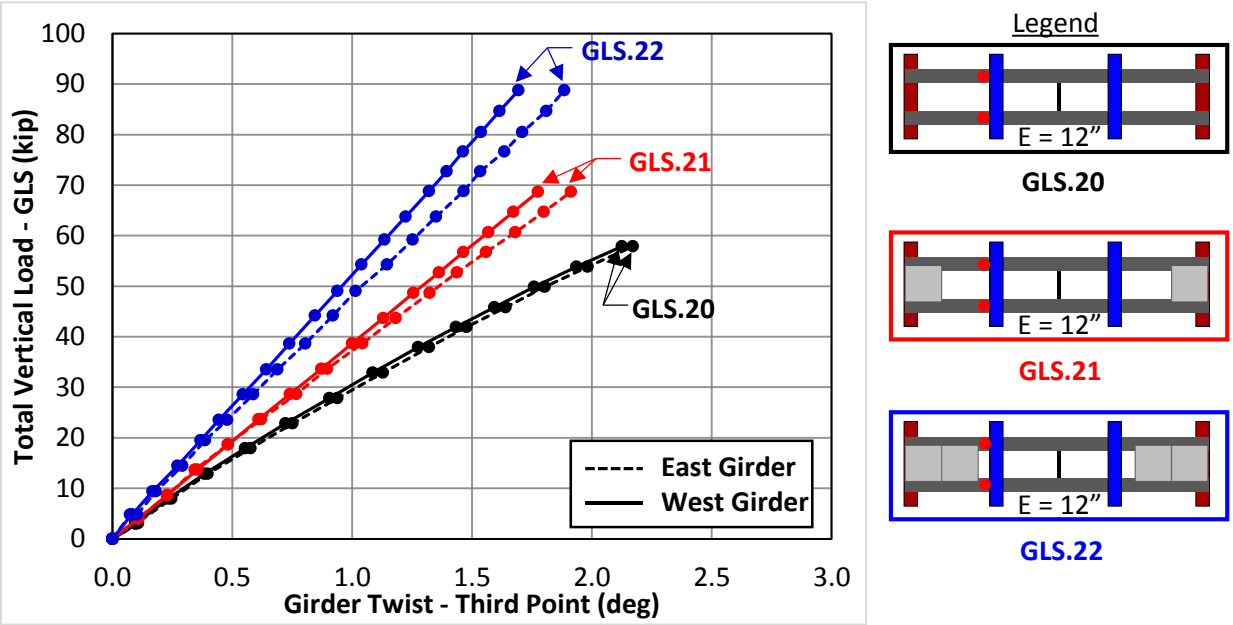

Figure B.42: Twist @ Third Point vs. GLS Load (E=12" - SS - w/ XF)

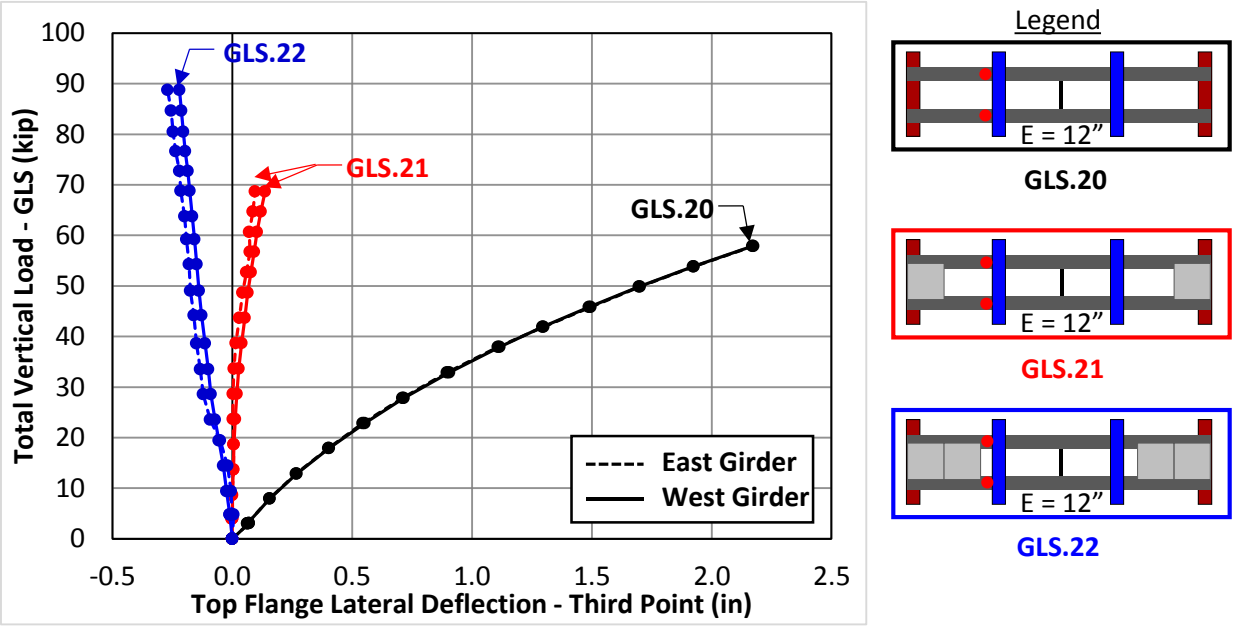

Figure B.43: Lateral Deflection @ Third Point vs. GLS Load (E=12" - SS- w/ XF)

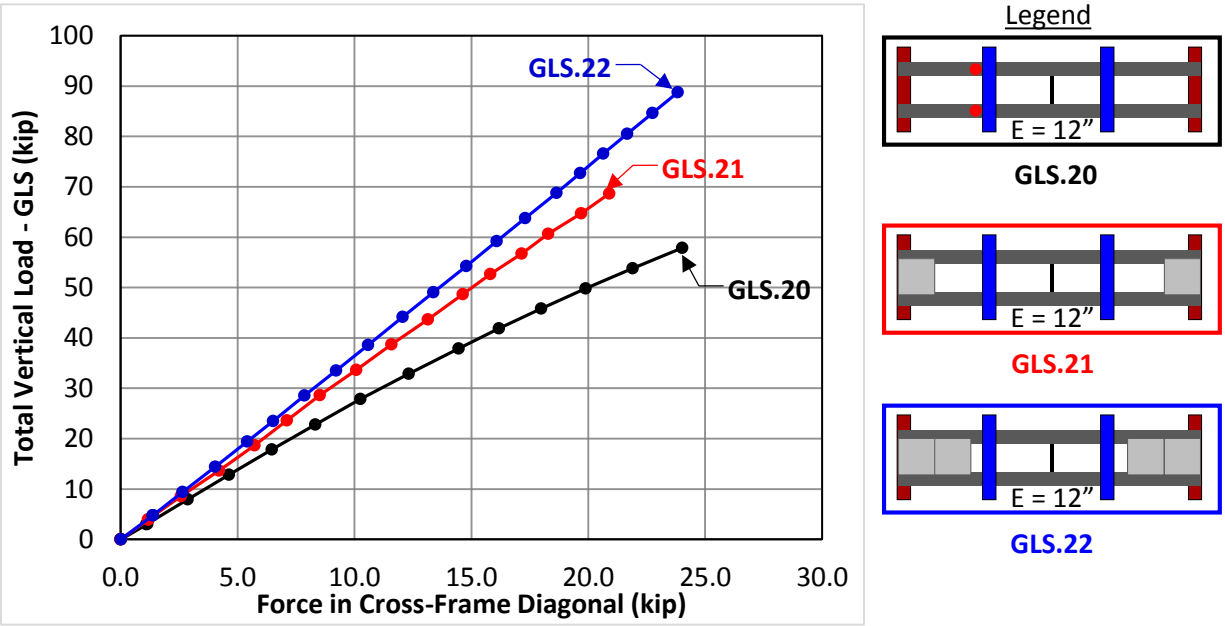

Figure B.44: Cross-Frame Diagonal Force vs. GLS Load (E=12" - SS)

B.4 Experimental Results for Combined Bending and Torsion Overhang I-Girder Tests

Table B.3: Summary of Bending and Torsion Overhang I-Girder Tests

Test Name	Support Condition	GLS North Eccentricity	GLS North Eccentricity	Number of PCPS	Max Total GLS Load
GLS.23	OH	-2"	4"	4	140
GLS.24	OH	-4"	8"	4	100
GLS.25	OH	2"	4"	4	170
GLS.26	OH	4"	8"	4	120
GLS.27	OH	-4"	0"	4	300

Key: GLS = Gravity Load Simulator Load, OH = Overhang

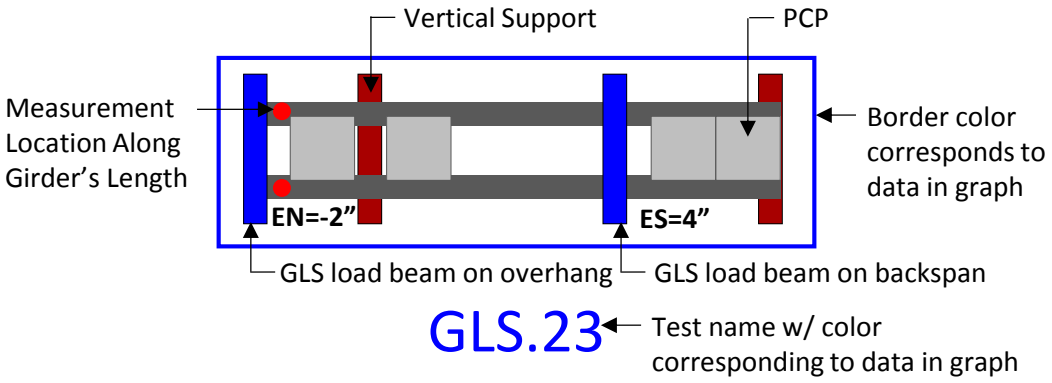

Figure B.45: Nomenclature for Documentation of GLS Overhang I-Girder Tests

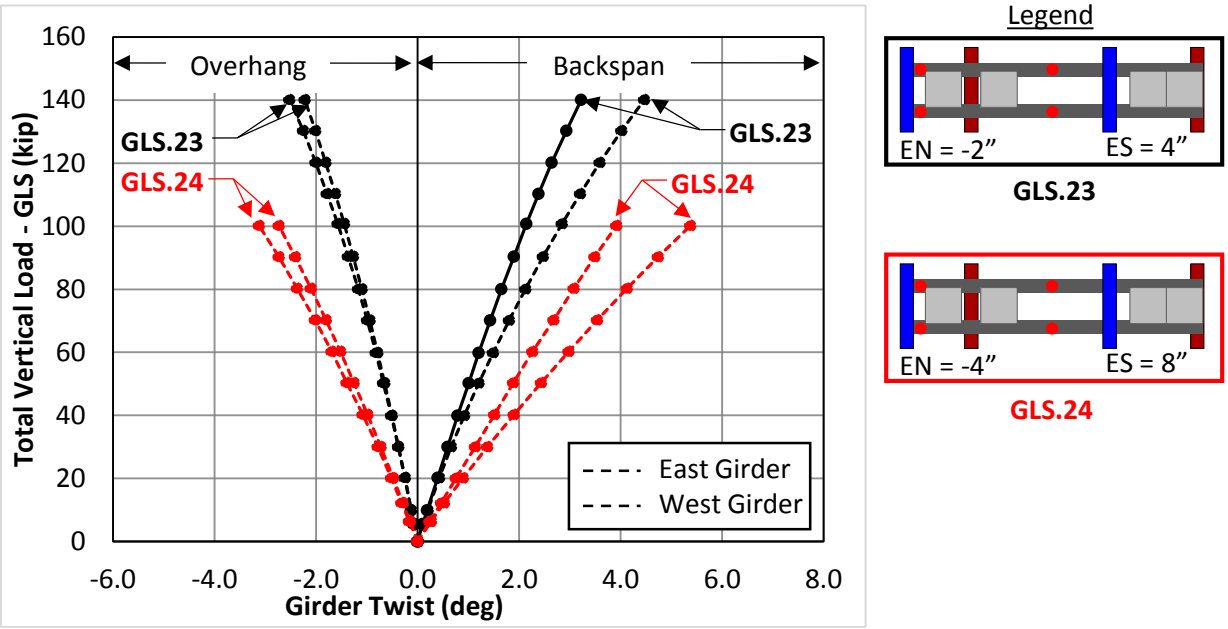

Figure B.46: Twist @ Overhang and Backspan vs. GLS Load (Opposite Eccentricity)

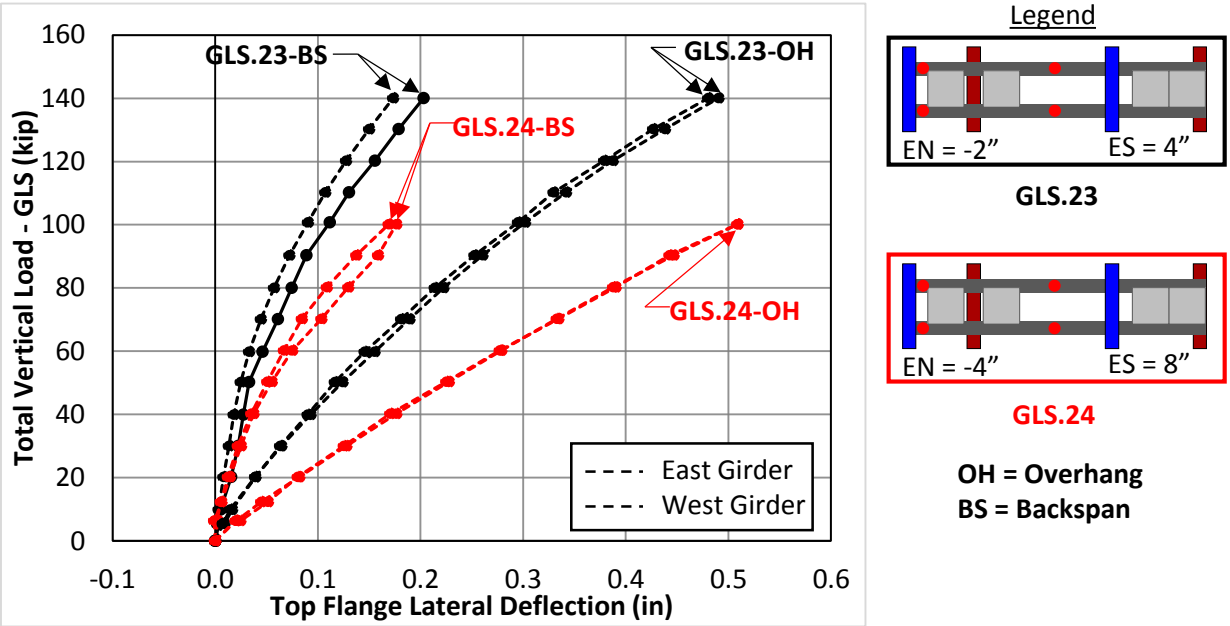

Figure B.47: Lateral Deflection @ Overhang and Backspan vs. GLS Load (Opposite Eccentricity)

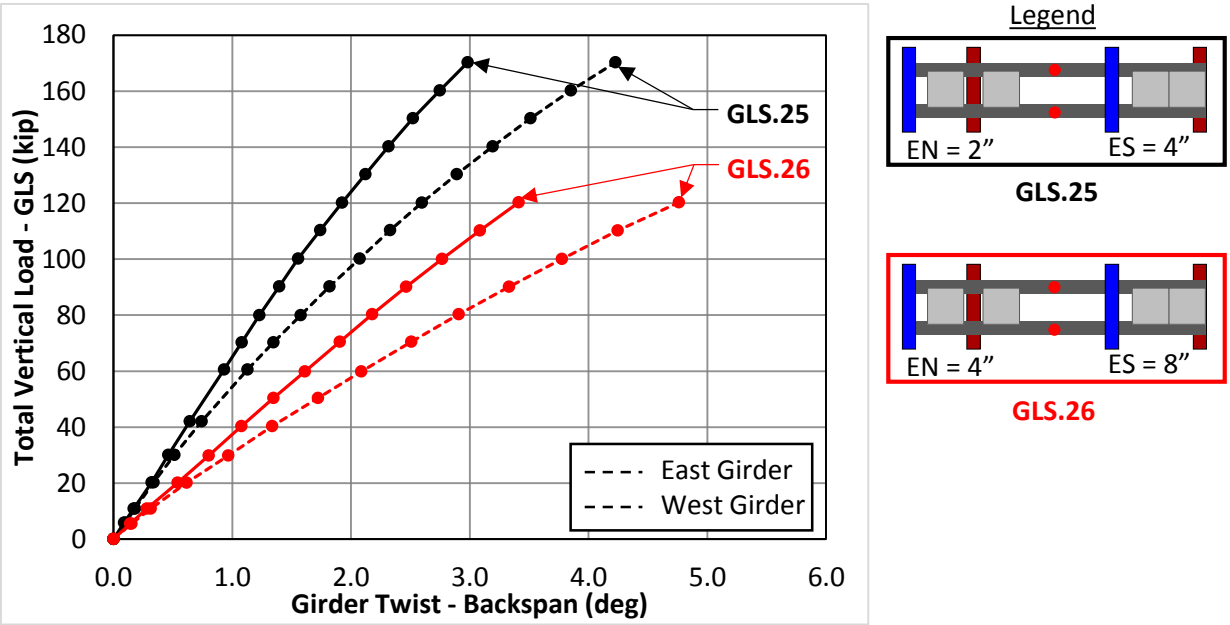

Figure B.48: Twist @ Backspan vs. GLS Load (Same Eccentricity Direction)

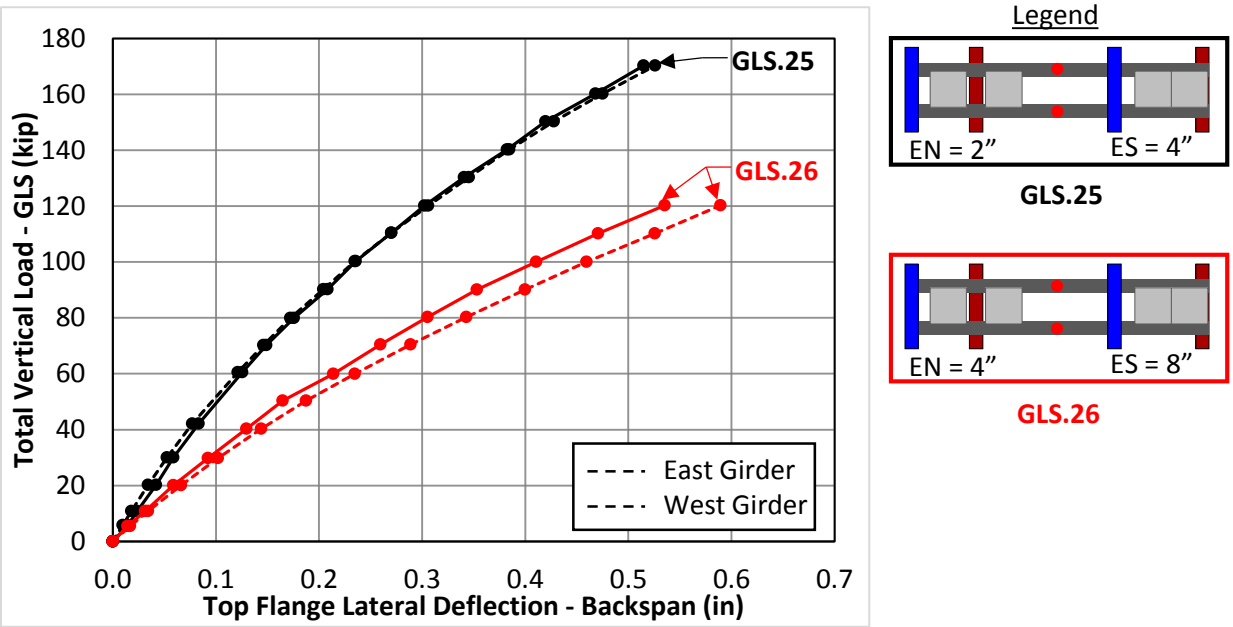

Figure B.49: Lateral Deflection @ Backspan vs. GLS Load (Same Eccentricity Direction)

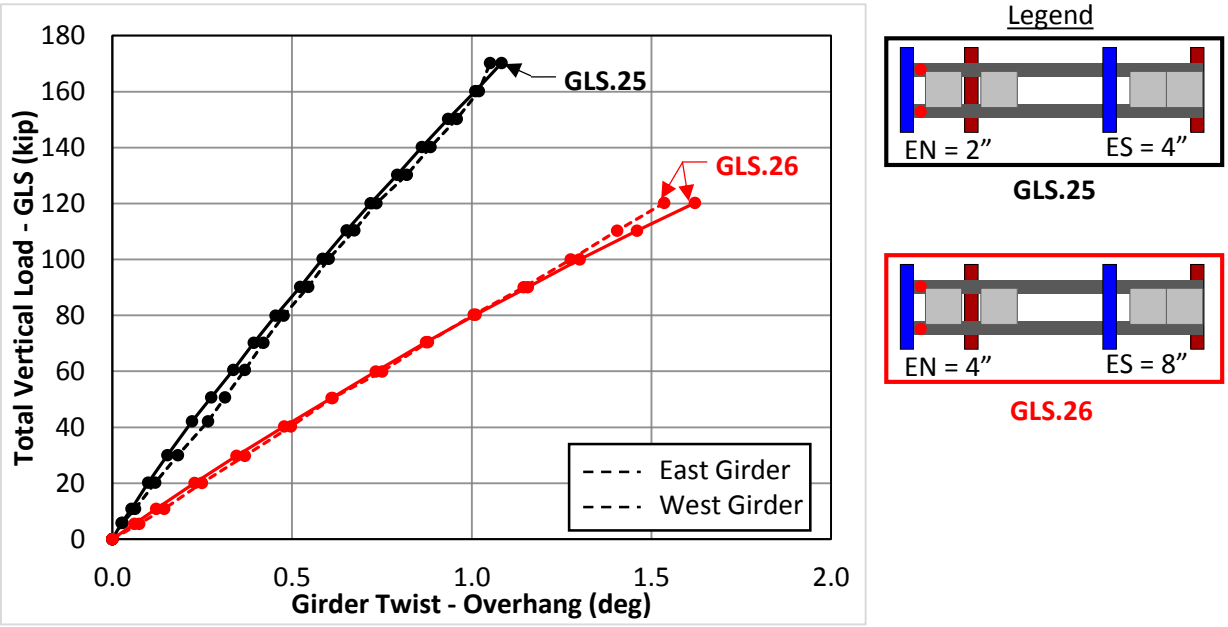

Figure B.50: Twist @ Overhang vs. GLS Load (Same Eccentricity Direction)

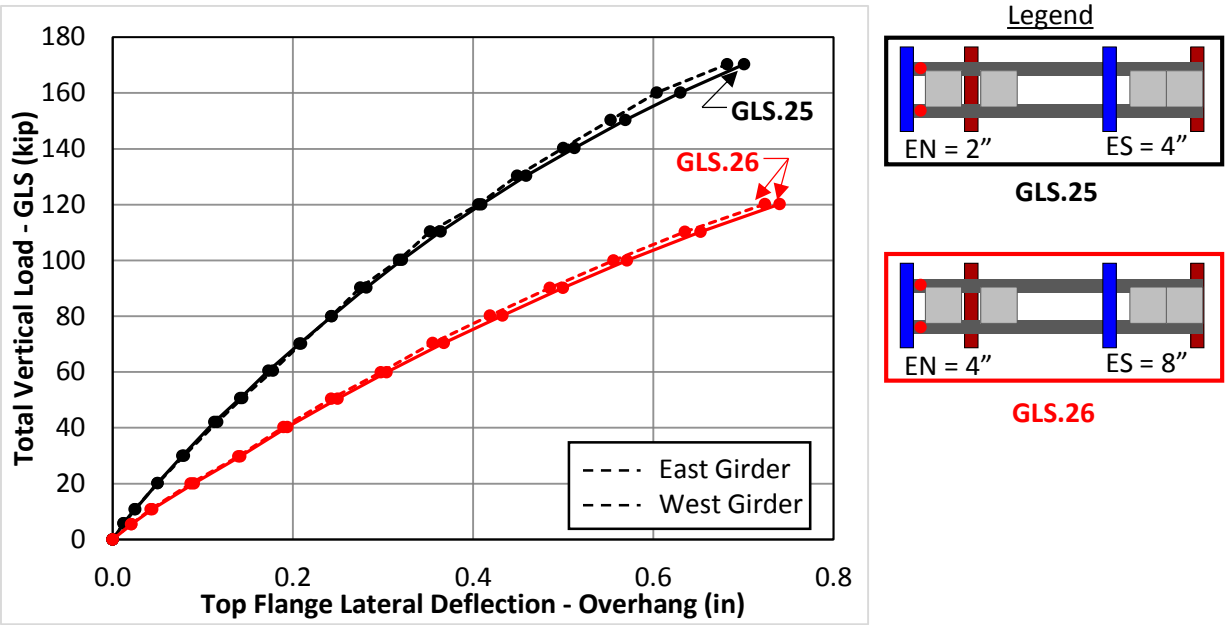

Figure B.51: Lateral Deflection @ Overhang vs. GLS Load (Same Eccentricity Direction)

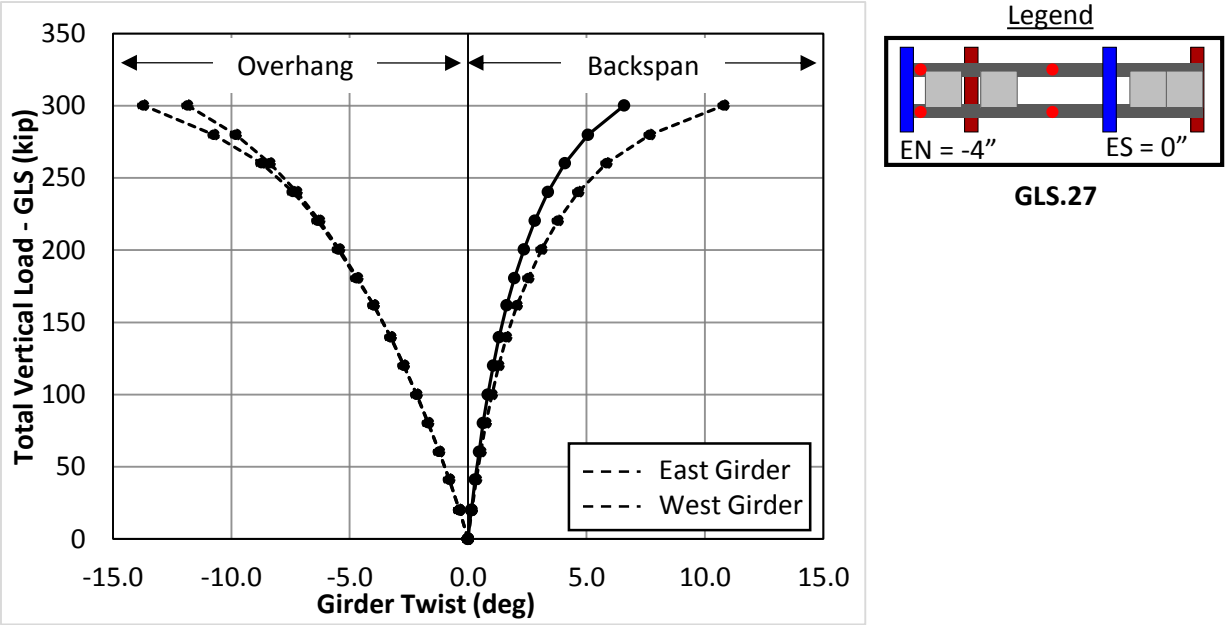

Figure B.52: Twist @ Overhang and Backspan vs. GLS Load (Maximum Load Test)

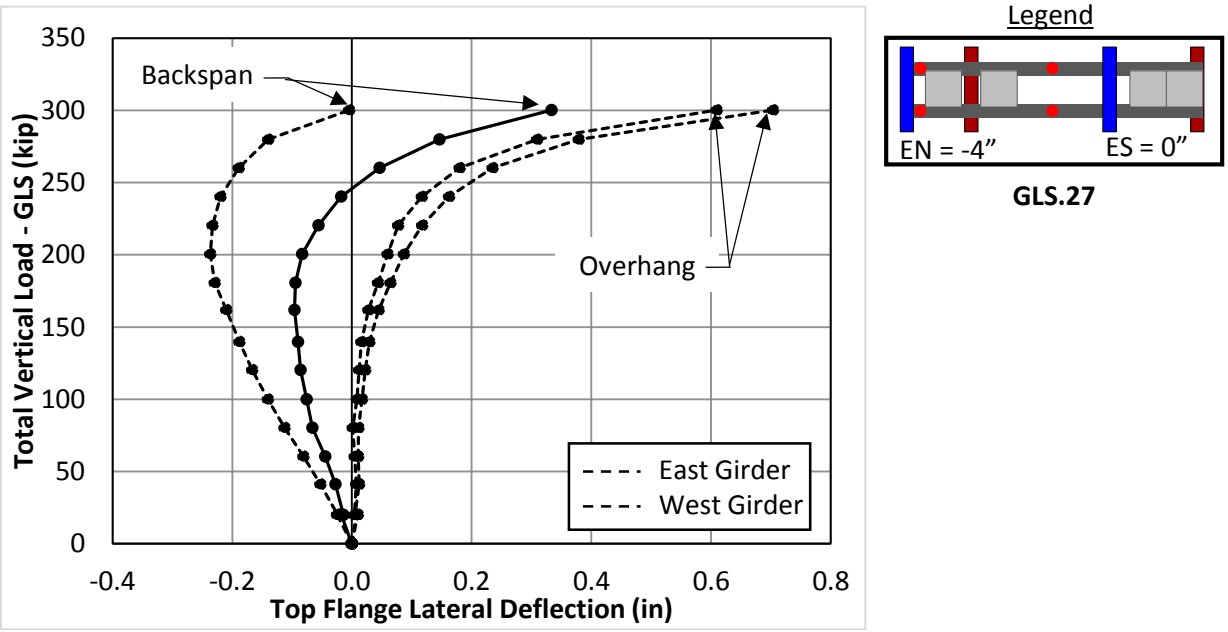

Figure B.53: Lateral Deflection @ Overhang and Backspan vs. GLS Load (Maximum Load Test)

B.5 I-Girder Material Tests

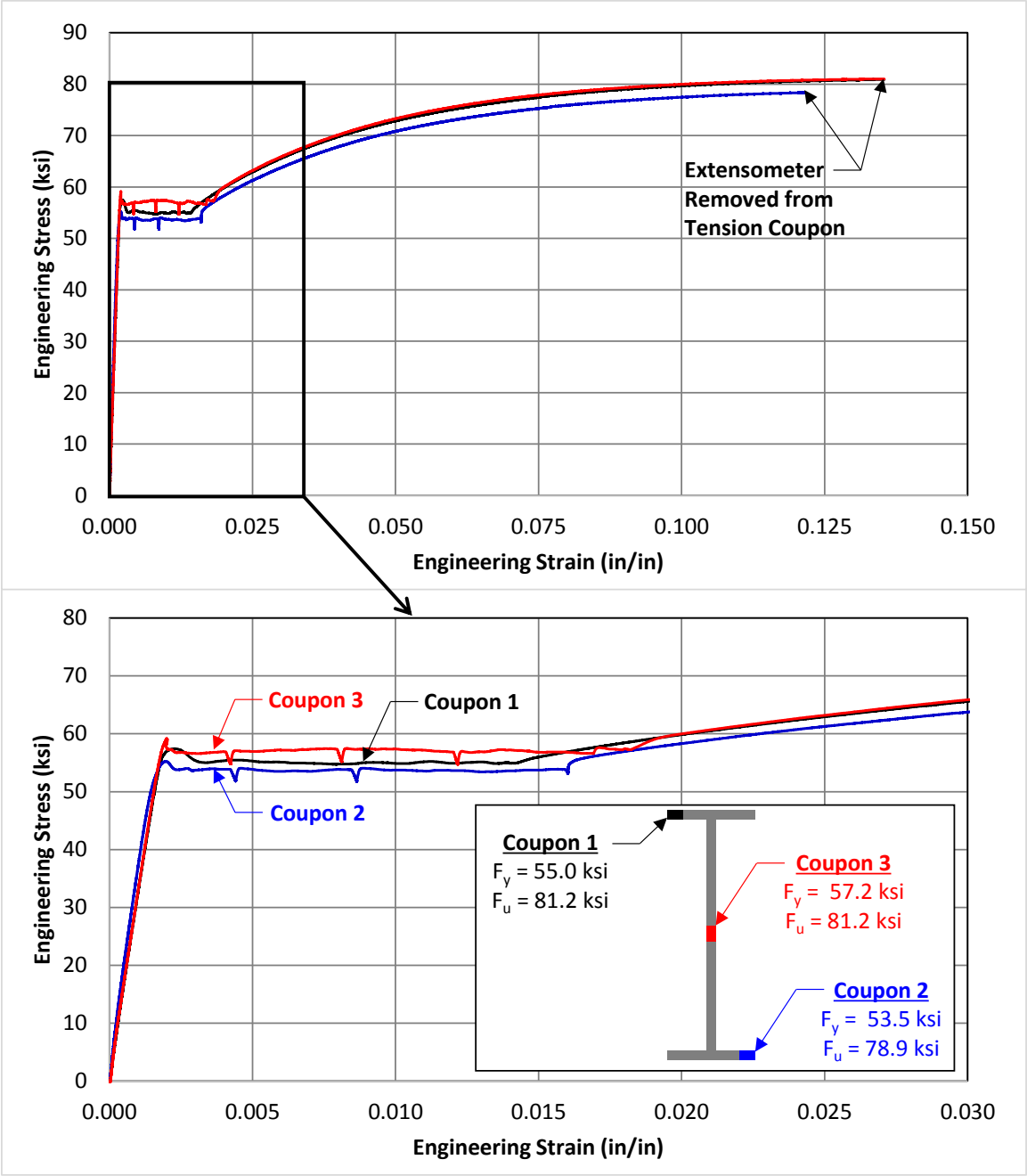

Figure B.54: Tension Coupon Tests from I-Girder Cross-Section

Appendix C. Tub Girder Experimental Results

C.1 Initial Imperfections of Concentric Tub Girder Tests

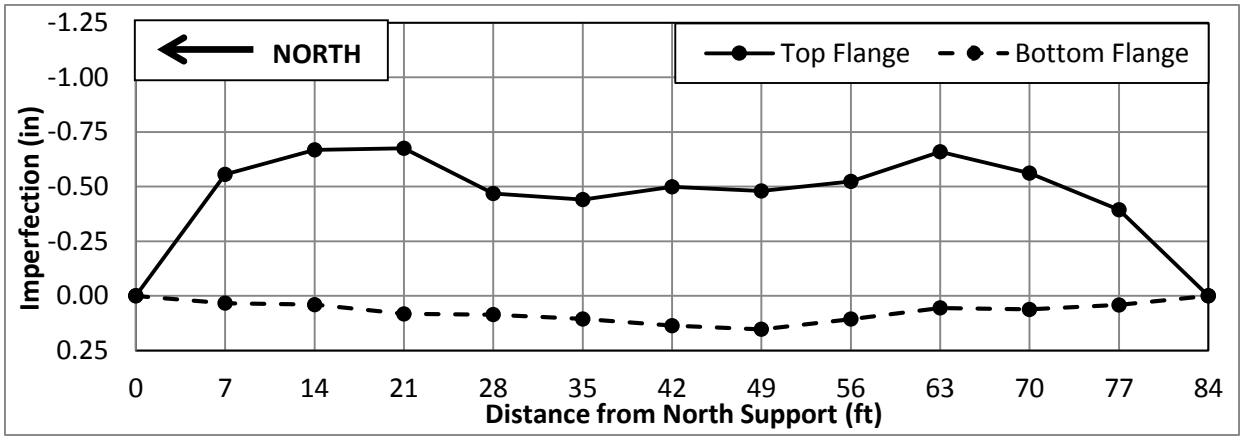

Figure C.1: Initial Imperfections – No Top Lateral Truss

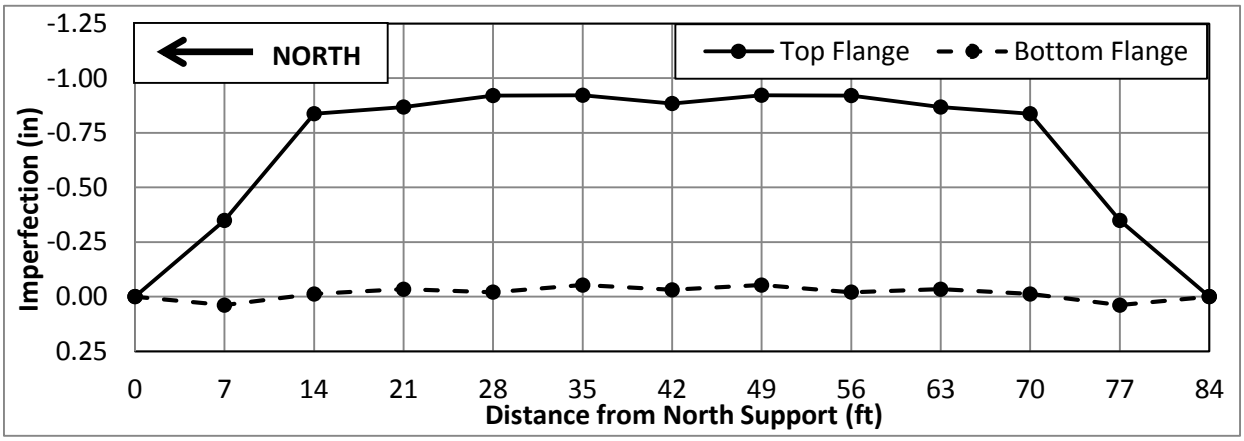

Figure C.2: Initial Imperfections – One WT Diagonal per End

C.2 Experimental Results for Lateral Load Tub Girder Tests

Table C.1: Summary of Lateral Tub Girder Tests

Test Name	Load Loacation	K-Frame Location	Number of Braces
LAT.1	TP	2-Panel	0
LAT.2	TP	2-Panel	2 PCP
LAT.3	TP	2-Panel	4 PCP
LAT.4	TP	2-Panel	2 DIAG
LAT.5	TP	2-Panel	4 DIAG

Key: LAT = Top & Bottom Flange Lateral Load
TP = Third Point Loading, DIA = Diagonal

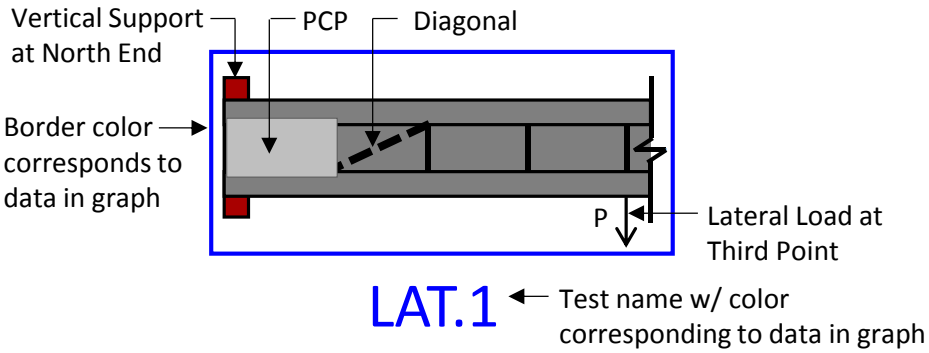

Figure C.3: Nomenclature for Lateral Load Tub Girder Tests

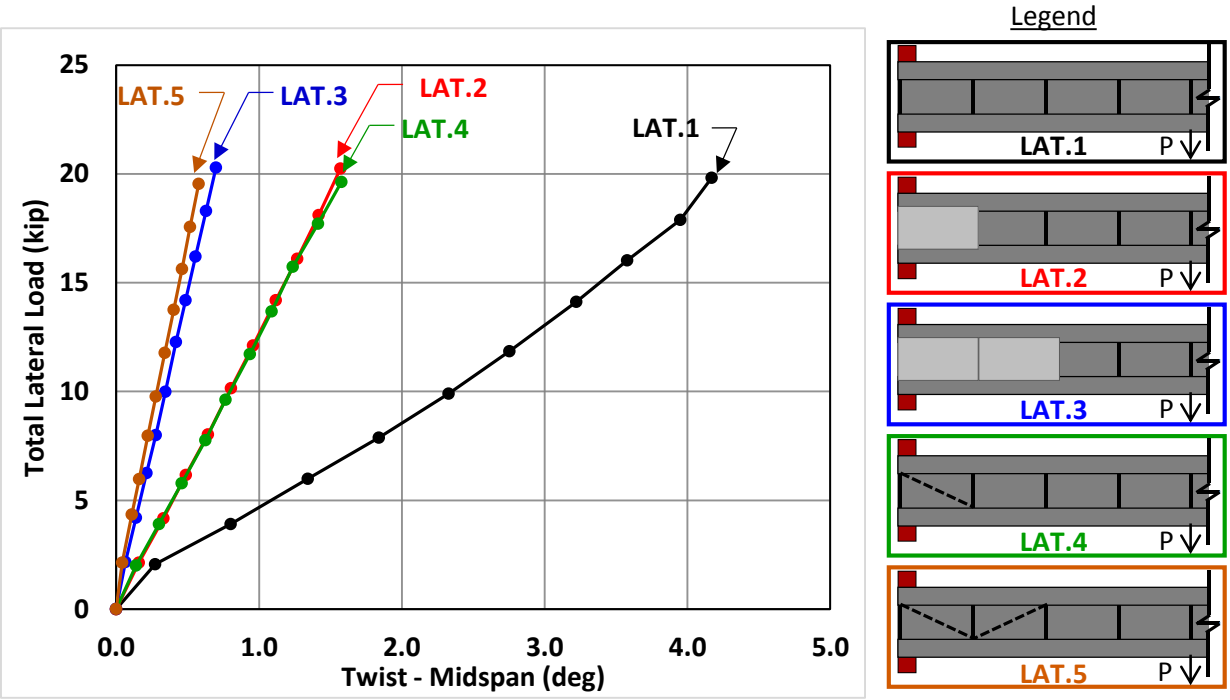

Figure C.4: Twist @ Midspan vs. Lateral Load @ Third Point

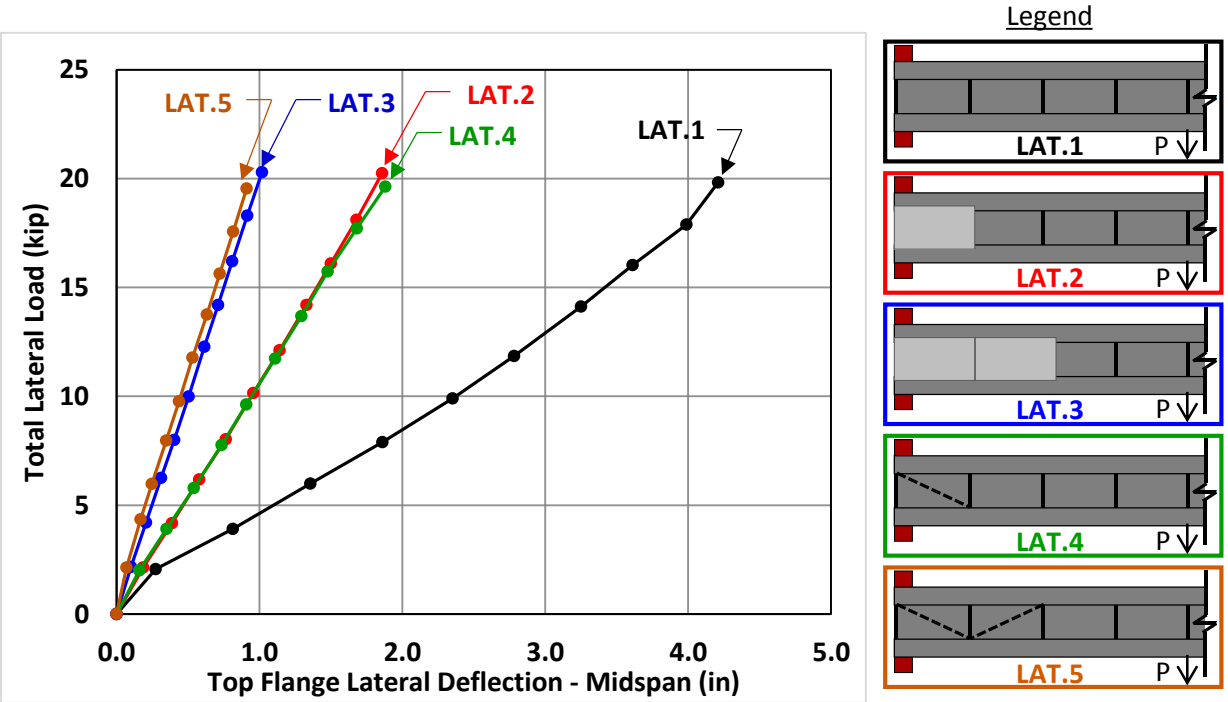

Figure C.5: Lateral Deflection @ Midspan vs. Lateral Load @ Third Point

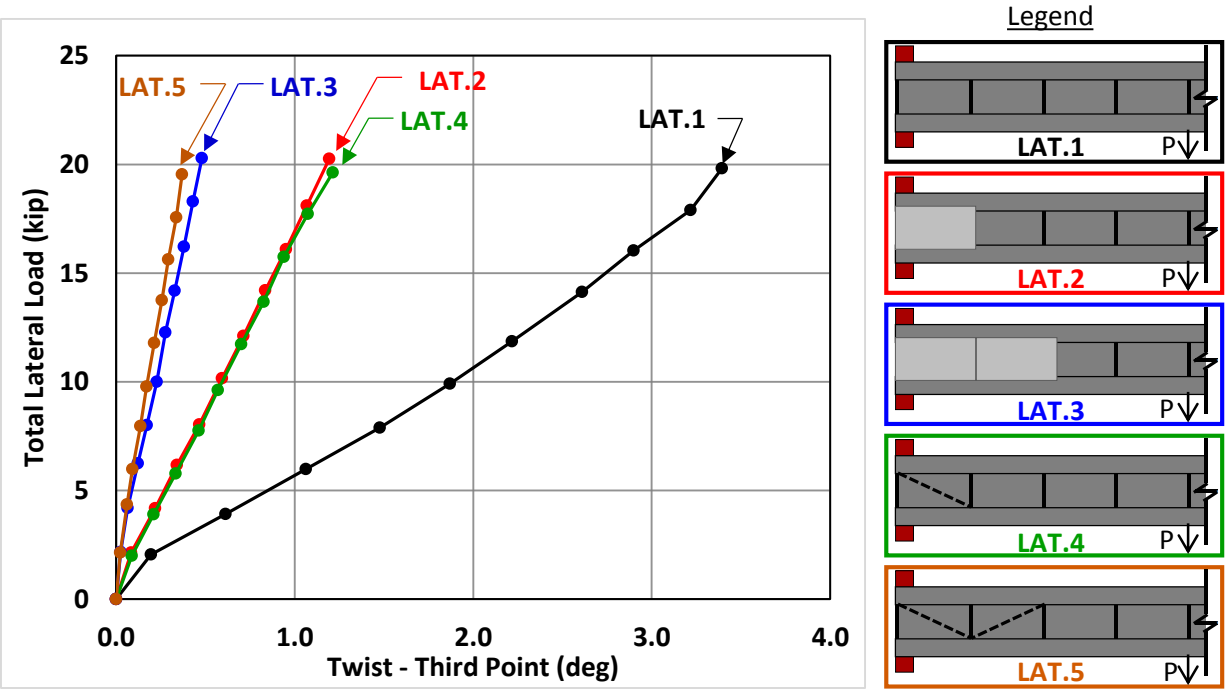

Figure C.6: Twist @ Third Point vs. Lateral Load @ Third Point

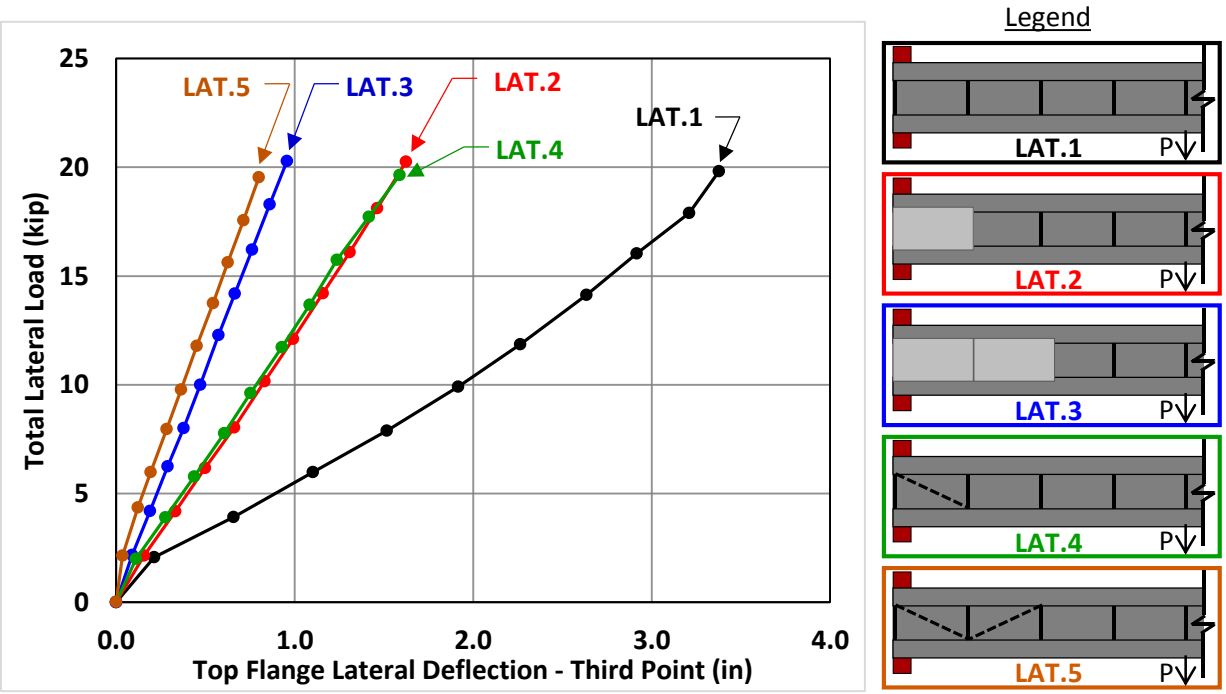

Figure C.7: Lateral Deflection @ Third Point vs. Lateral Load @ Third Point

C.3 Experimental Results for Combined Bending and Torsion Simply Supported Tub Girder Test

Table C.2: Summary of Bending and Torsion Simply Supported Tub Girder Tests

Test Name	Support Condition	Load Eccentricity	K-Frame Location	Number of Braces	Max Total GLS Load
GLS.1	SS	0 & 0	2-Panel	0	84
GLS.2	SS	0 & 0	2-Panel	2 PCP	100
GLS.3	SS	0 & 0	2-Panel	4 PCP	100
GLS.4	SS	0 & 0	2-Panel	2 DIAG	72
GLS.5	SS	0 & 0	2-Panel	4 DIAG	76
GLS.6	SS	8" & 8"	2-Panel	0	52
GLS.7	SS	8" & 8"	2-Panel	2 PCP	100
GLS.8	SS	8" & 8"	2-Panel	4 PCP	100
GLS.9	SS	8" & 8"	2-Panel	2 DIAG	80
GLS.10	SS	8" & 8"	2-Panel	4 DIAG	84
GLS.11	SS	16" & 16"	2-Panel	0	32
GLS.12	SS	16" & 16"	2-Panel	2 PCP	60
GLS.13	SS	16" & 16"	2-Panel	4 PCP	100
GLS.14	SS	16" & 16"	2-Panel	2 DAIG	52
GLS.15	SS	16" & 16"	2-Panel	4 DIAG	80

Key: GLS = Gravity Load Simulator Load, SS = Simply Supported
PCP = Partial Depth Precast Concrete Deck Panel, DIA = Diagonal

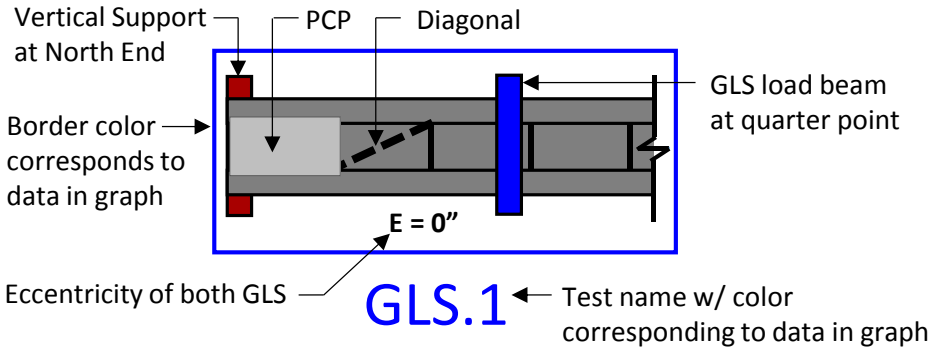

Figure C.8: Nomenclature for GLS Simply Supported Tub Girder Tests

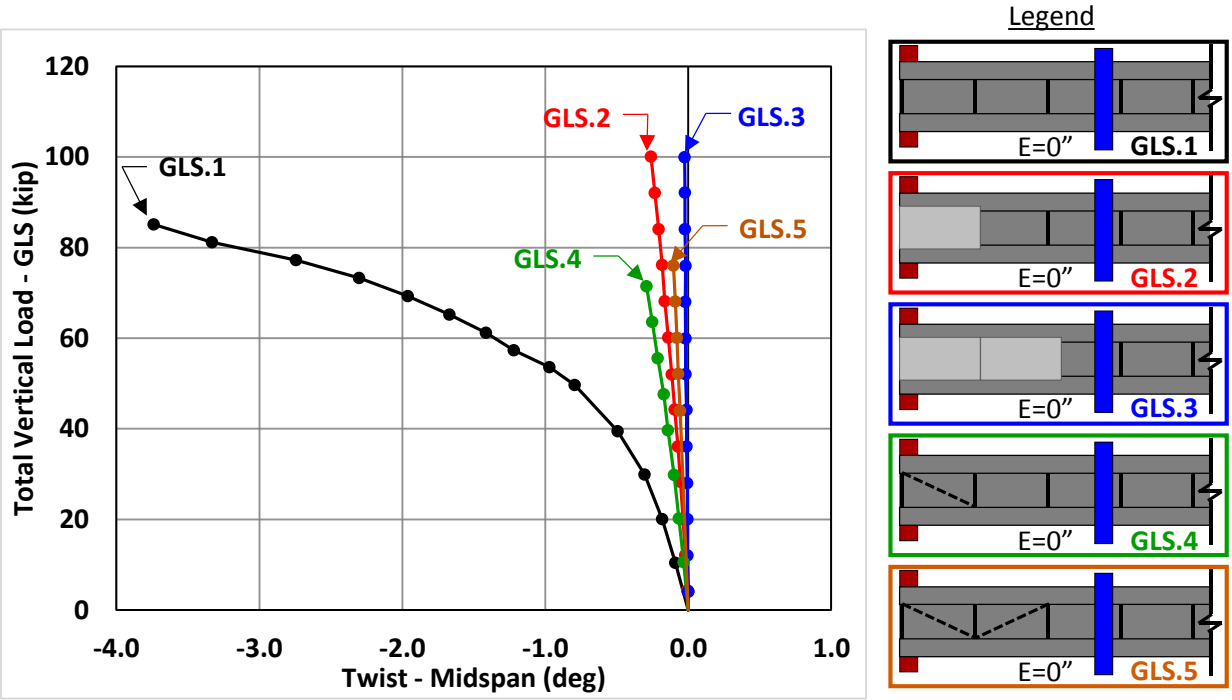

Figure C.9: Twist @ Midspan vs. GLS Load (E=0")

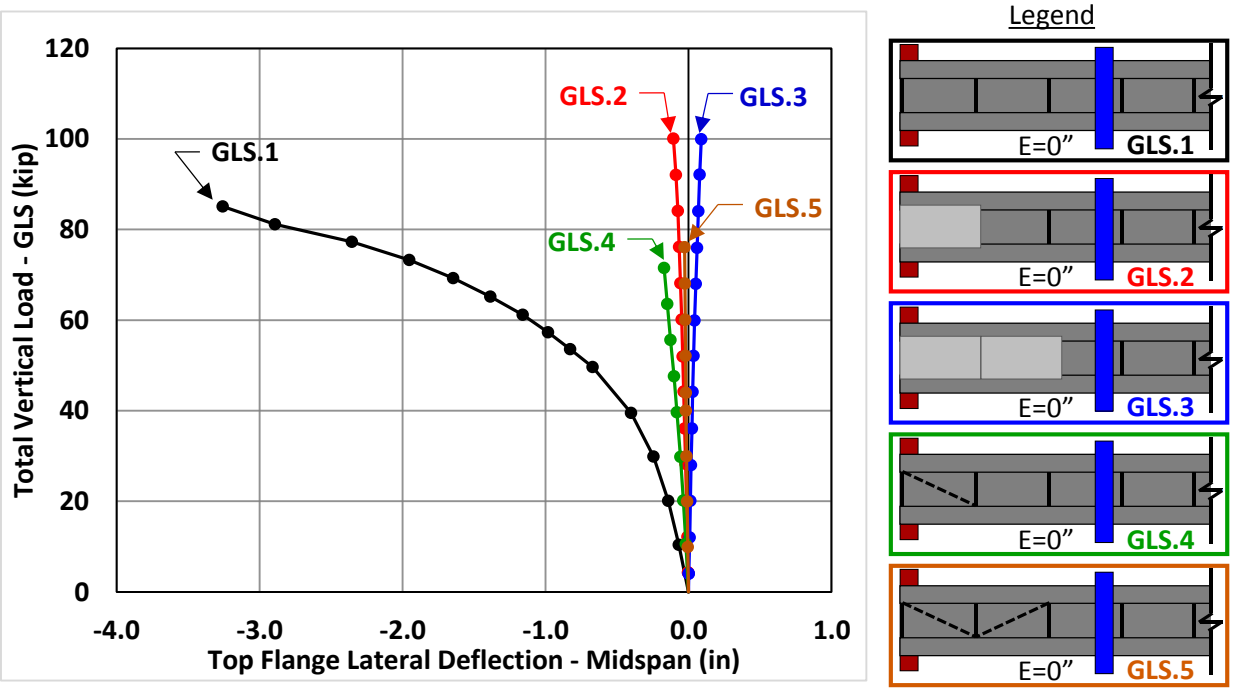

Figure C.10: Lateral Deflection @ Midspan vs. GLS Load (E=0")

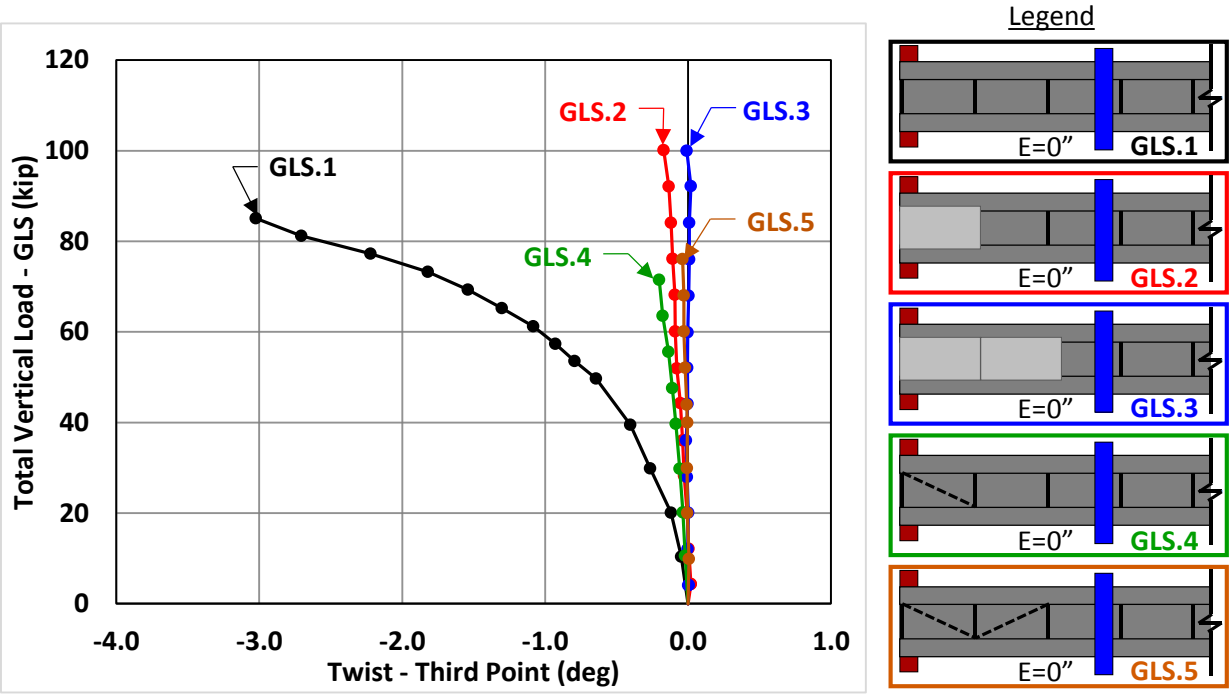

Figure C.11: Twist @ Third Point vs. GLS Load (E=0")

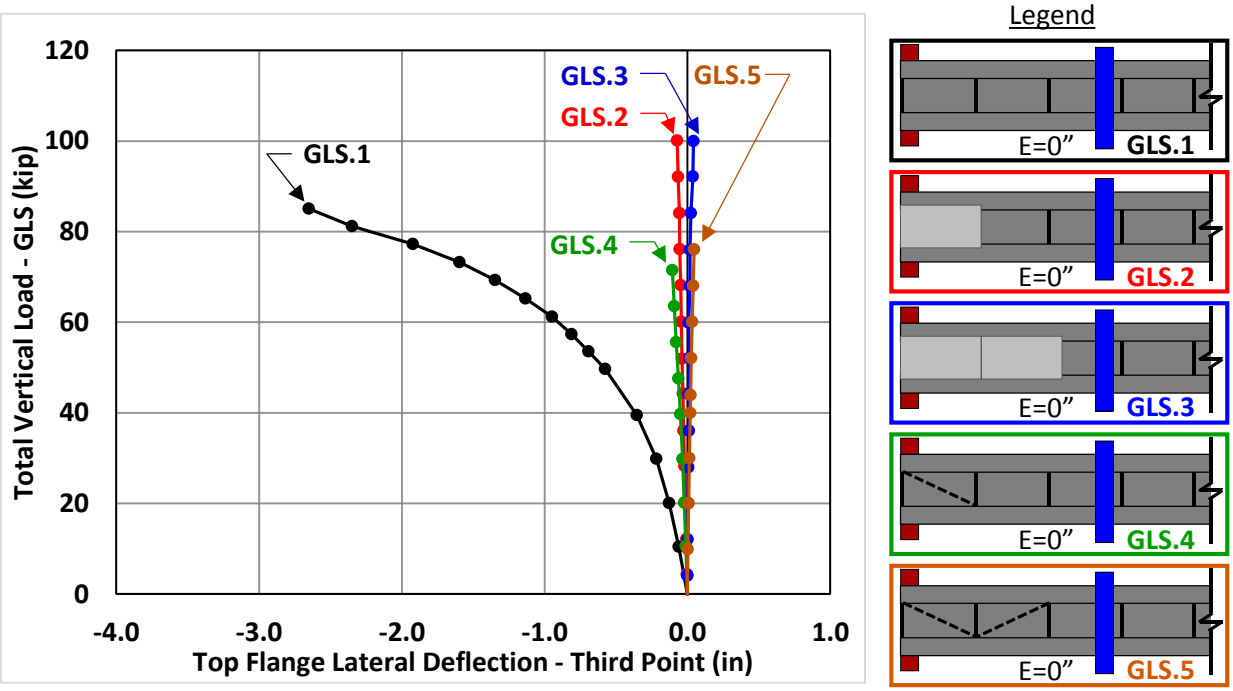

Figure C.12: Lateral Deflection @ Third Point vs. GLS Load (E=0")

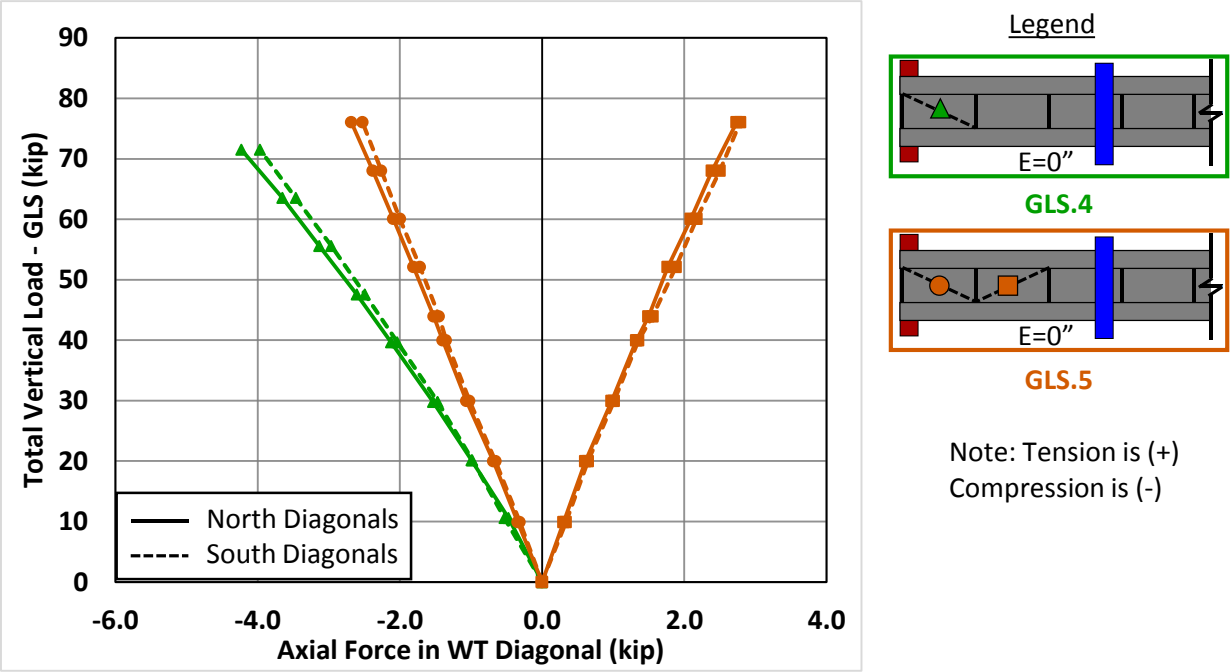

Figure C.13: Diagonal Forces vs. GLS Load (E=0")

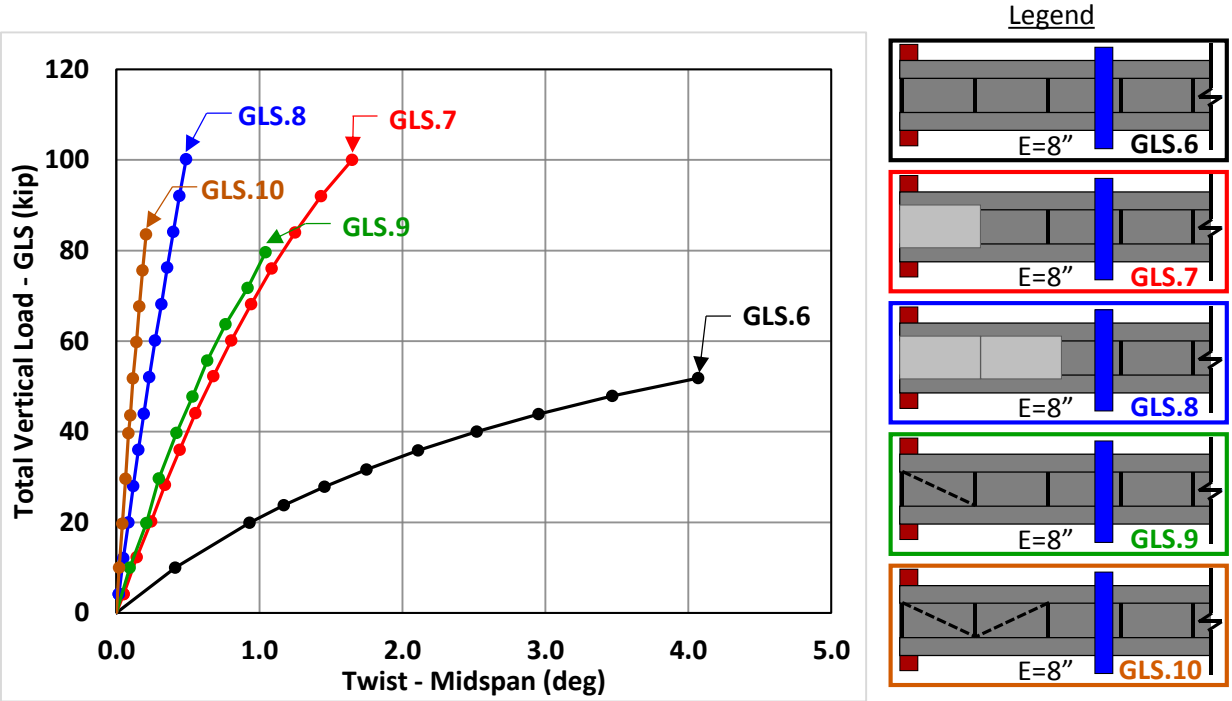

Figure C.14: Twist @ Midspan vs. GLS Load (E=8")

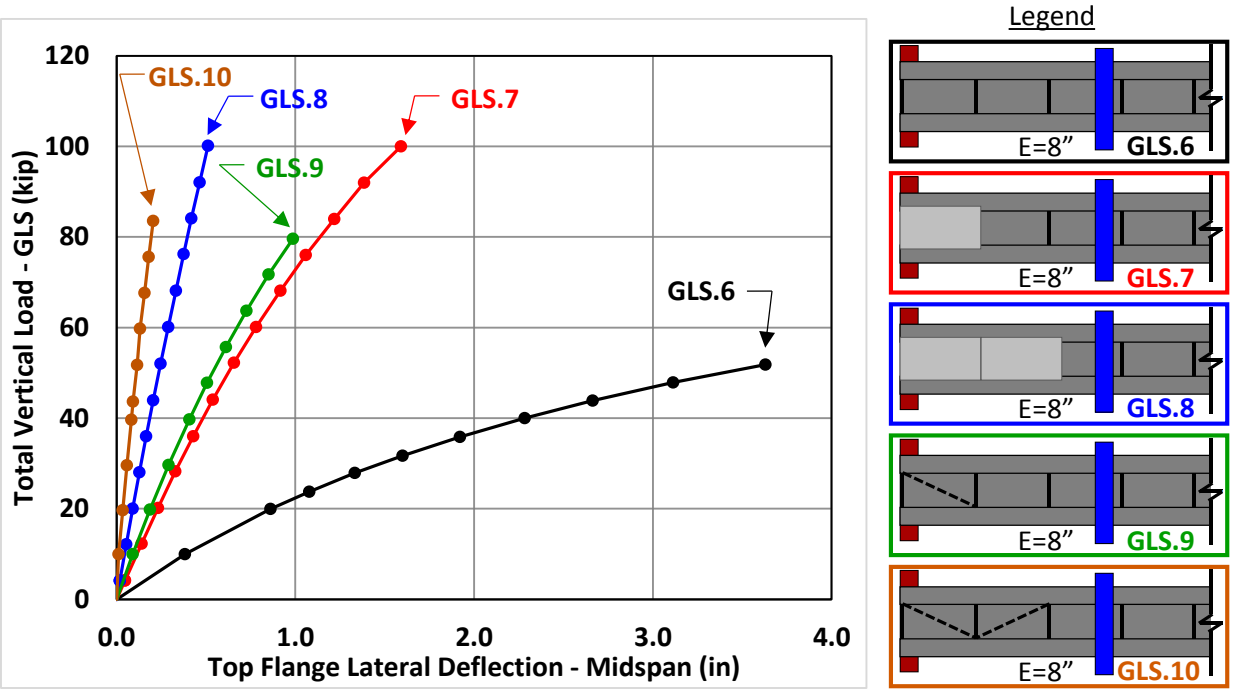

Figure C.15: Lateral Deflection @ Midspan vs. GLS Load (E=8")

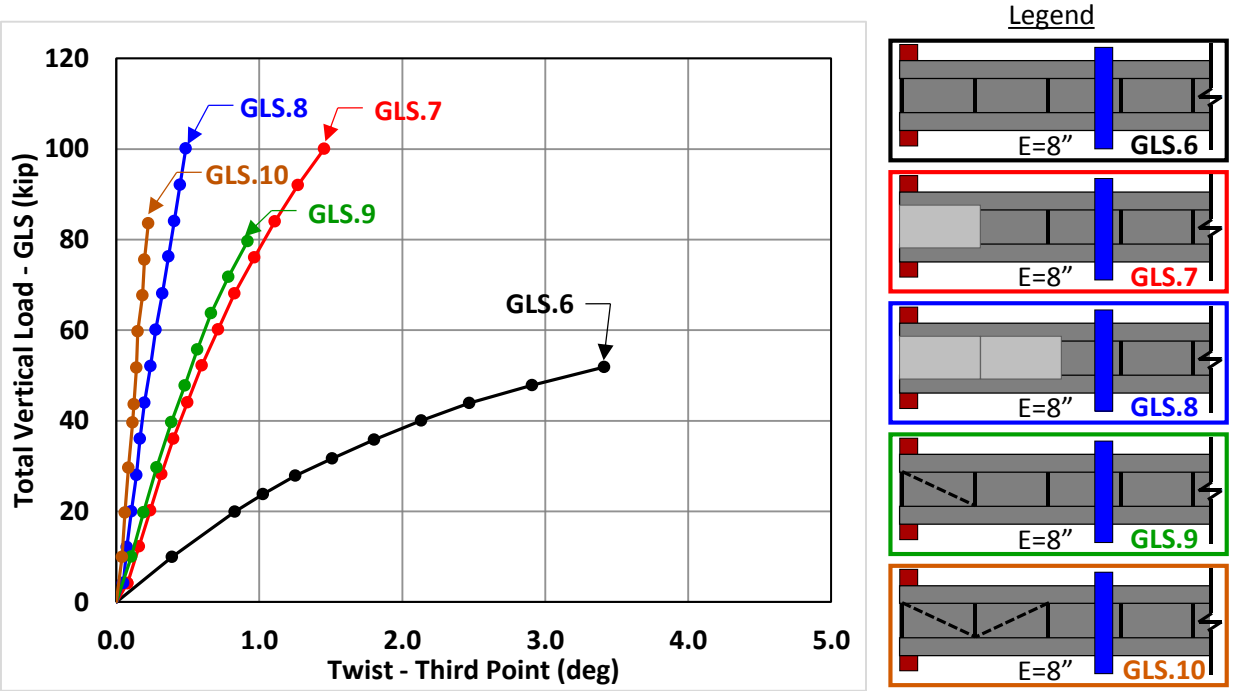

Figure C.16: Twist @ Third Point vs. GLS Load (E=8")

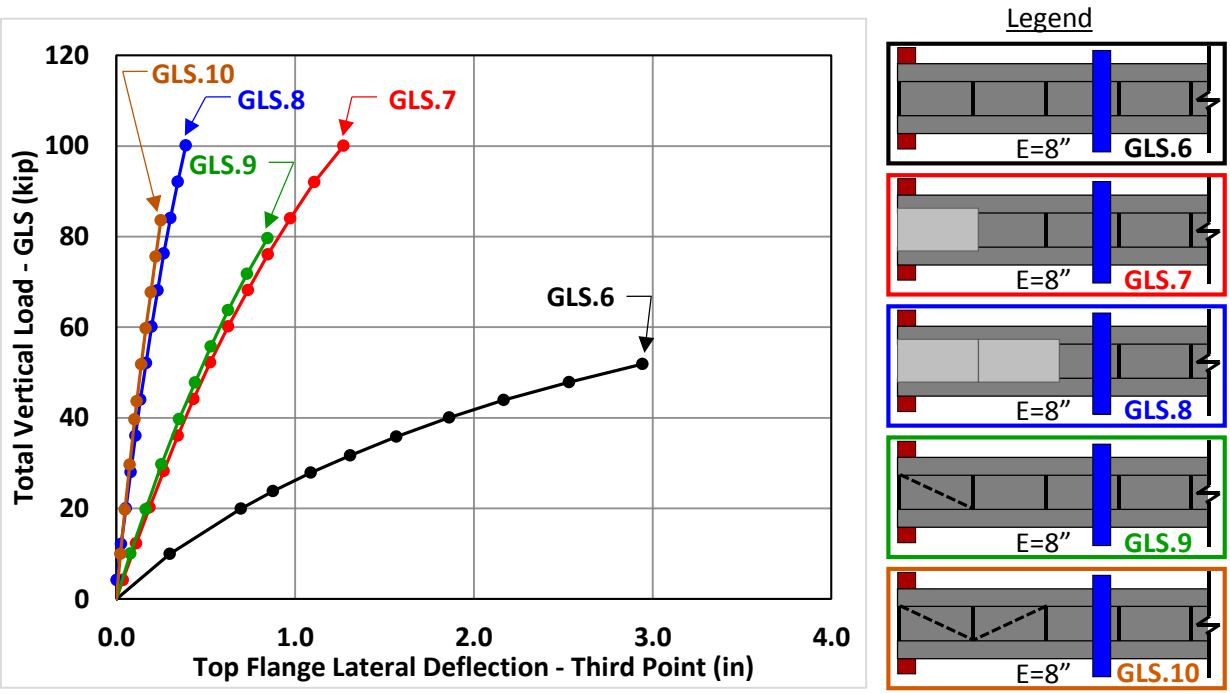

Figure C.17: Lateral Deflection @ Third Point vs. GLS Load (E=8")

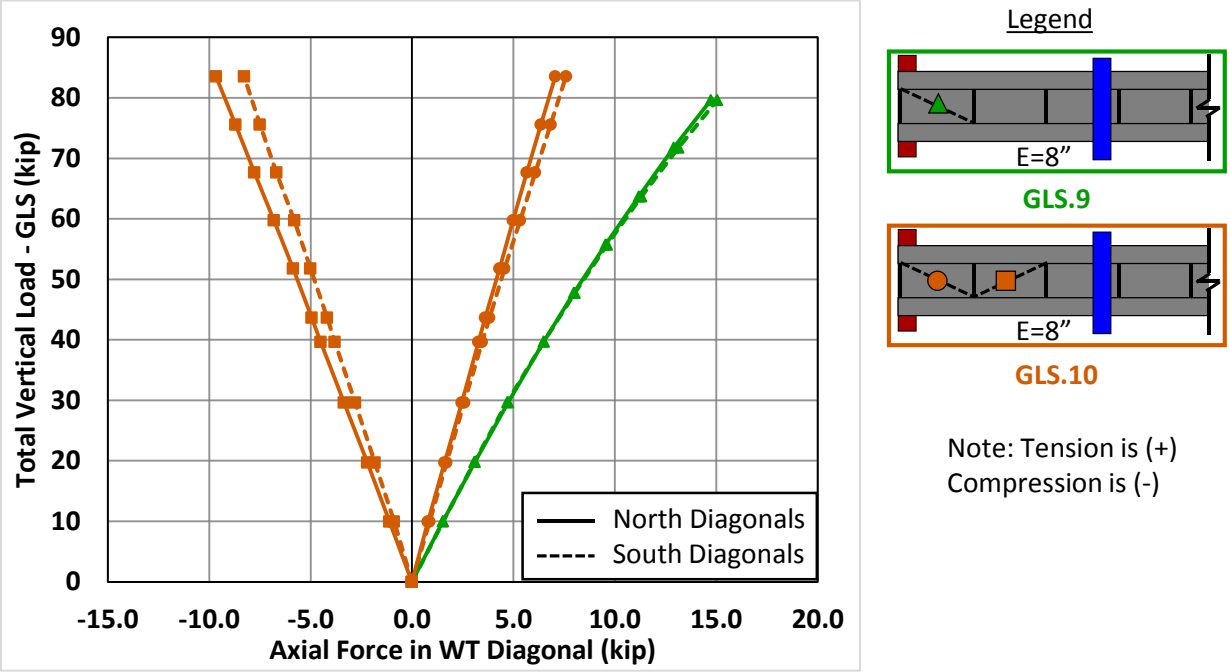

Figure C.18: Diagonal Forces vs. GLS Load (E=8")

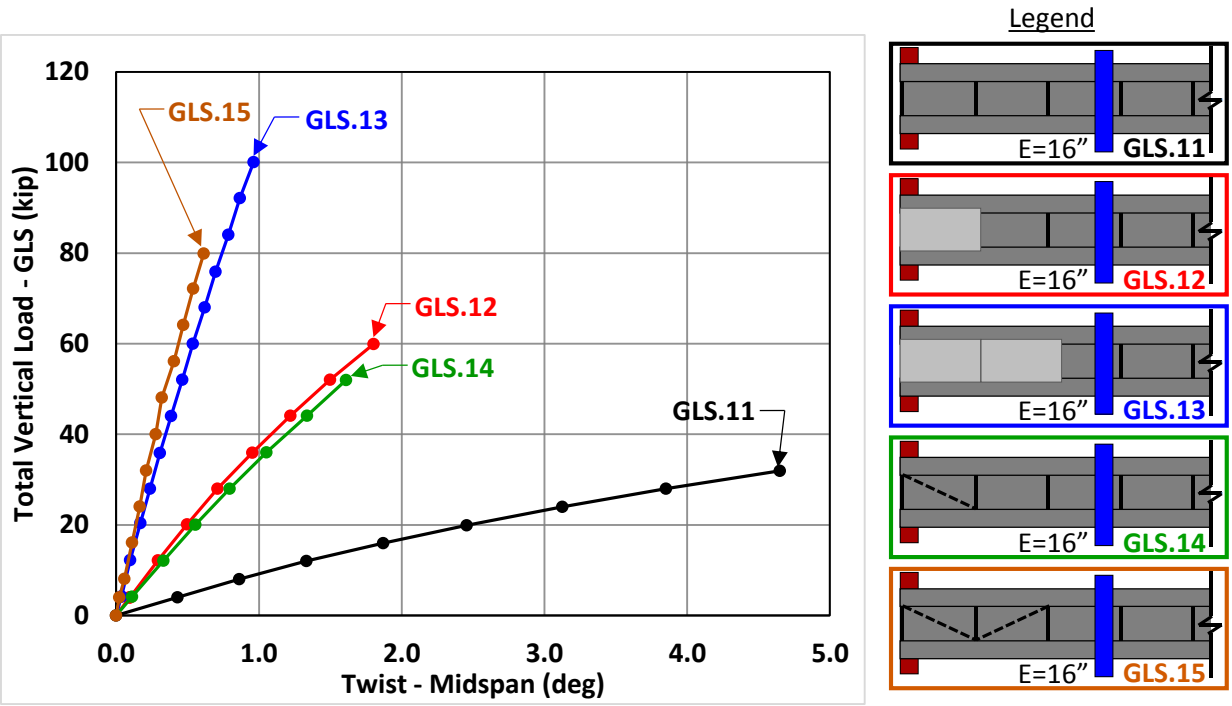

Figure C.19: Twist @ Midspan vs. GLS Load (E=16")

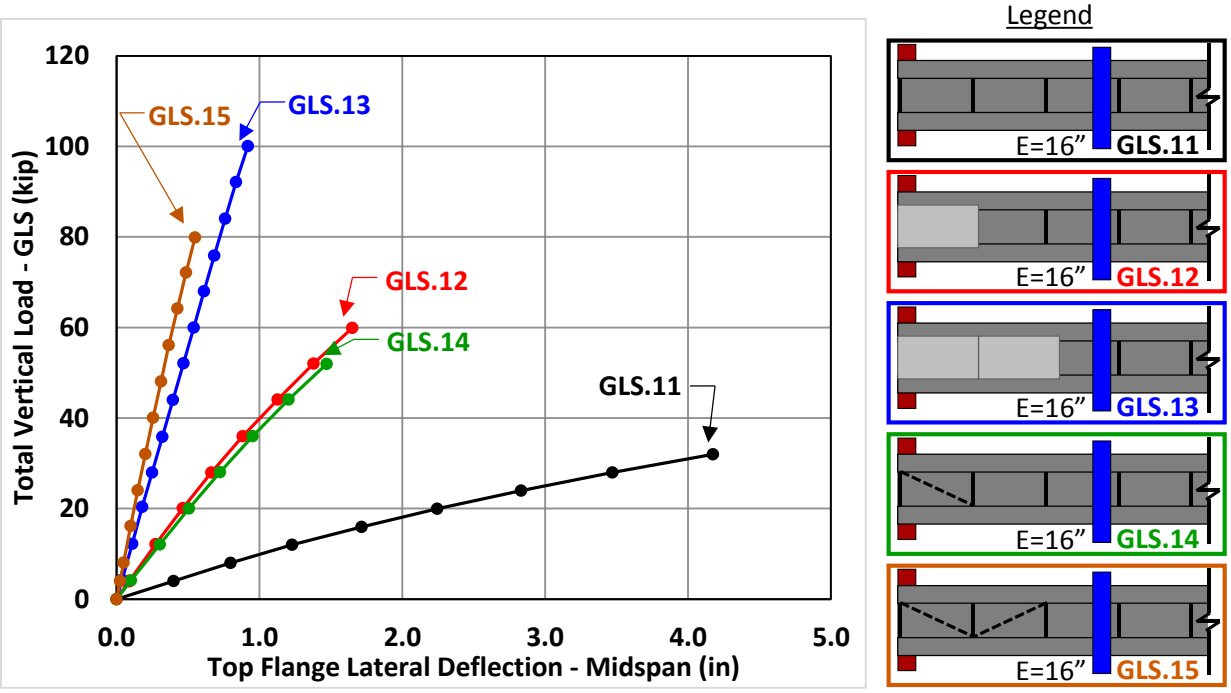

Figure C.20: Lateral Deflection @ Midspan vs. GLS Load (E=16")

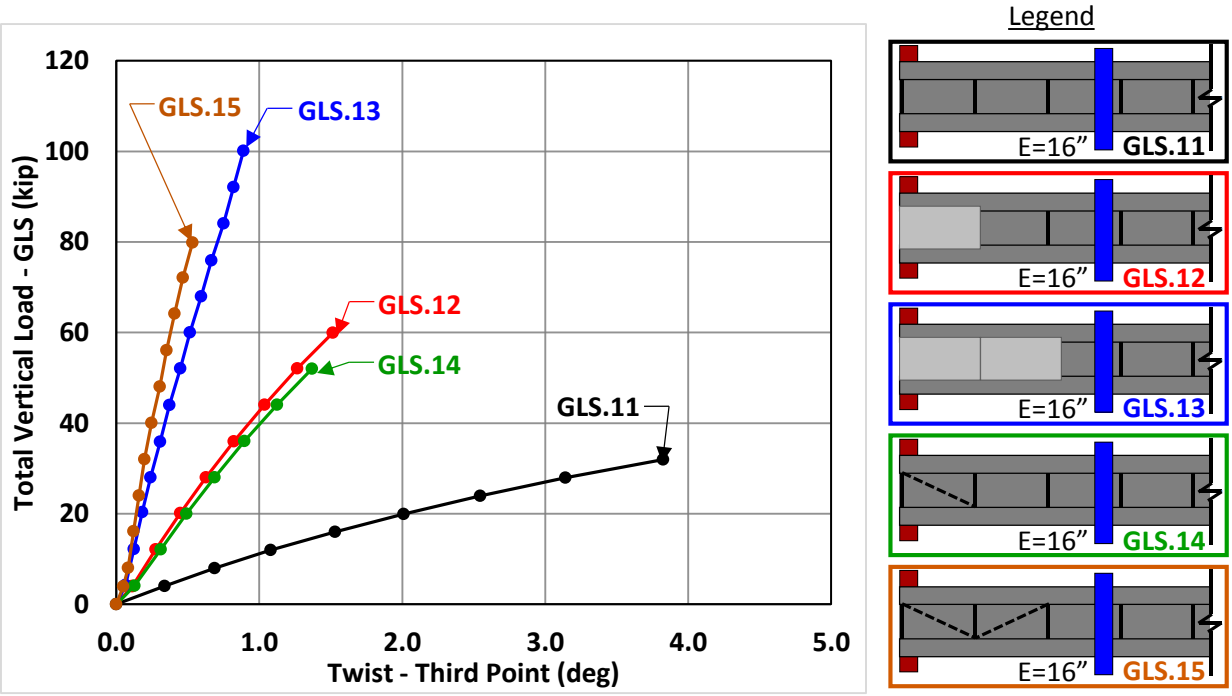

Figure C.21: Twist @ Third Point vs. GLS Load (E=16")

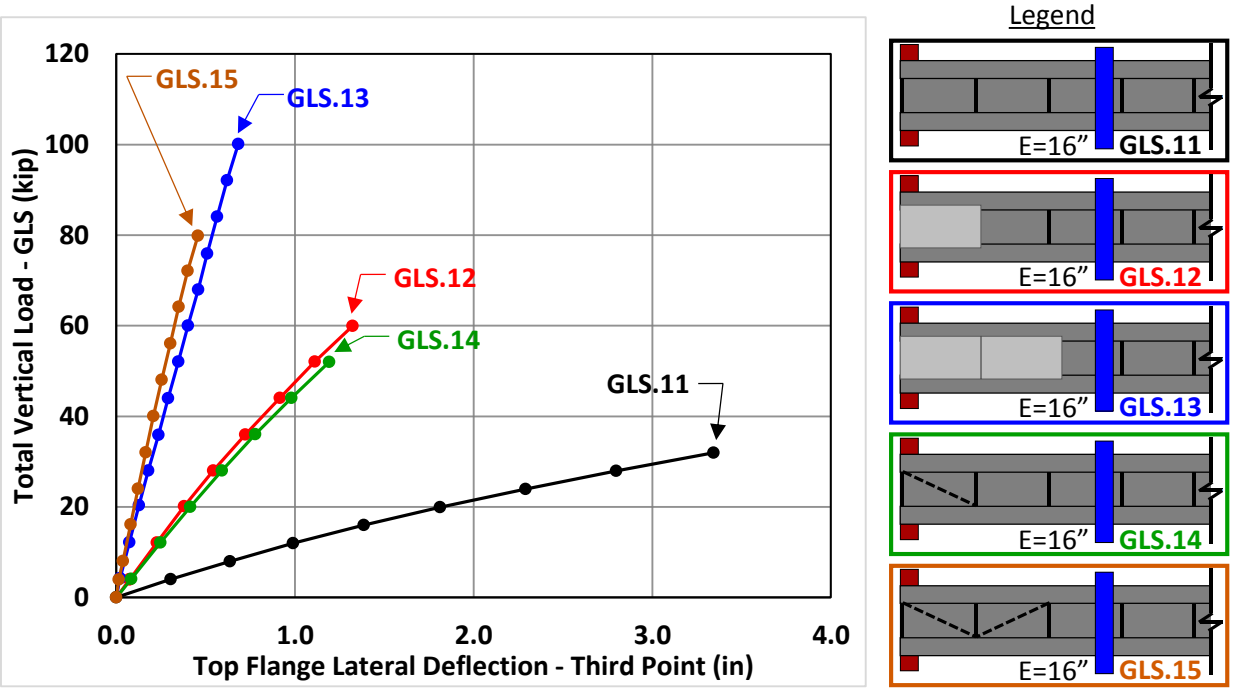

Figure C.22: Lateral Deflection @ Third Point vs. GLS Load (E=16")

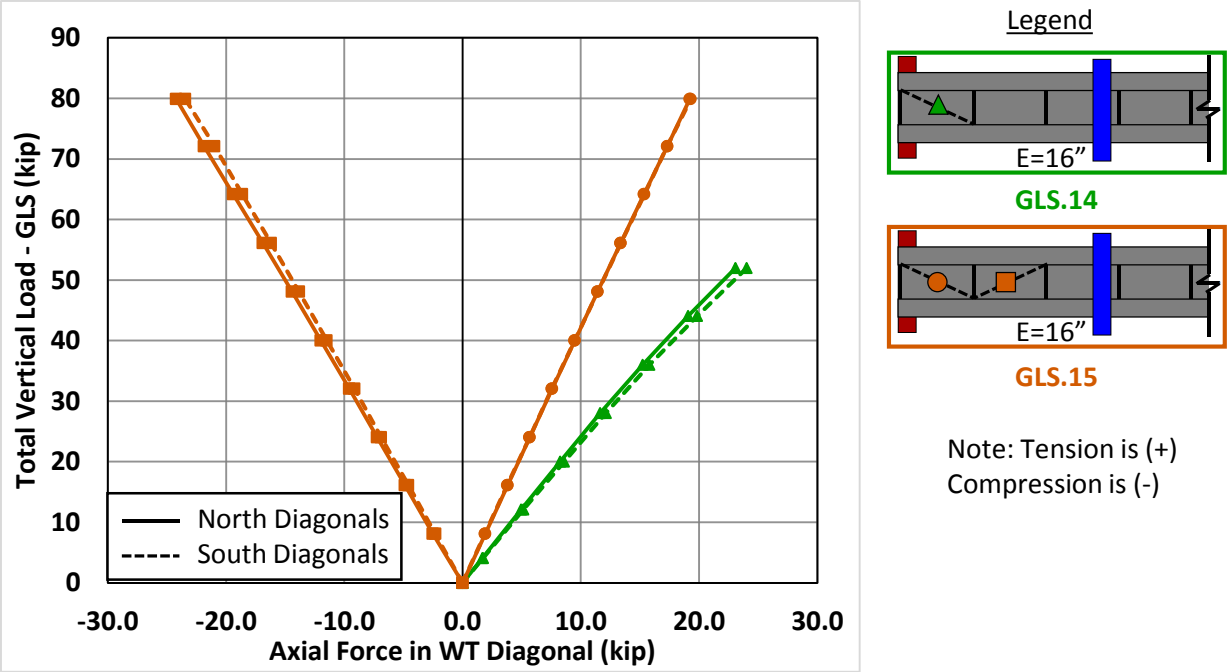

Figure C.23: Diagonal Forces vs. GLS Load (E=16")

C.4 Experimental Results for Combined Bending and Torsion Overhang Tub Girder Tests

Table C.3: Summary of Bending and Torsion Overhang Tub Girder Tests

Test Name	Support Condition	GLS North Eccentricity	GLS South Eccentricity	K-Frame Location	Max Total GLS Load	Max Total GLS Load
GLS.16	OH	-2"	4"	2-Panel	0	200
GLS.17	OH	-2"	4"	2-Panel	3 PCP	200
GLS.18	OH	-2"	4"	2-Panel	3 DIAG	200
GLS.19	OH	-4"	8"	2-Panel	0	200
GLS.20	OH	-4"	8"	2-Panel	3 PCP	200
GLS.21	OH	-4"	8"	2-Panel	3 DIAG	200
GLS.22	OH	-6"	12"	2-Panel	0	200
GLS.23	OH	-6"	12"	2-Panel	3 PCP	300
GLS.24	OH	-6"	12"	2-Panel	3 DIAG	200

Key: GLS = Gravity Load Simulator Load, OH = Overhang Support
PCP = Partial Depth Precast Concrete Deck Panel, DIA = Diagonal

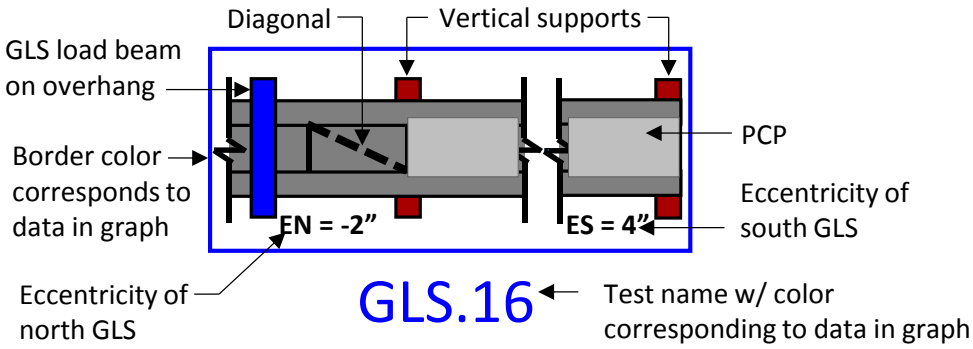

Figure C.24: Nomenclature for GLS Overhang Tub Girder Tests

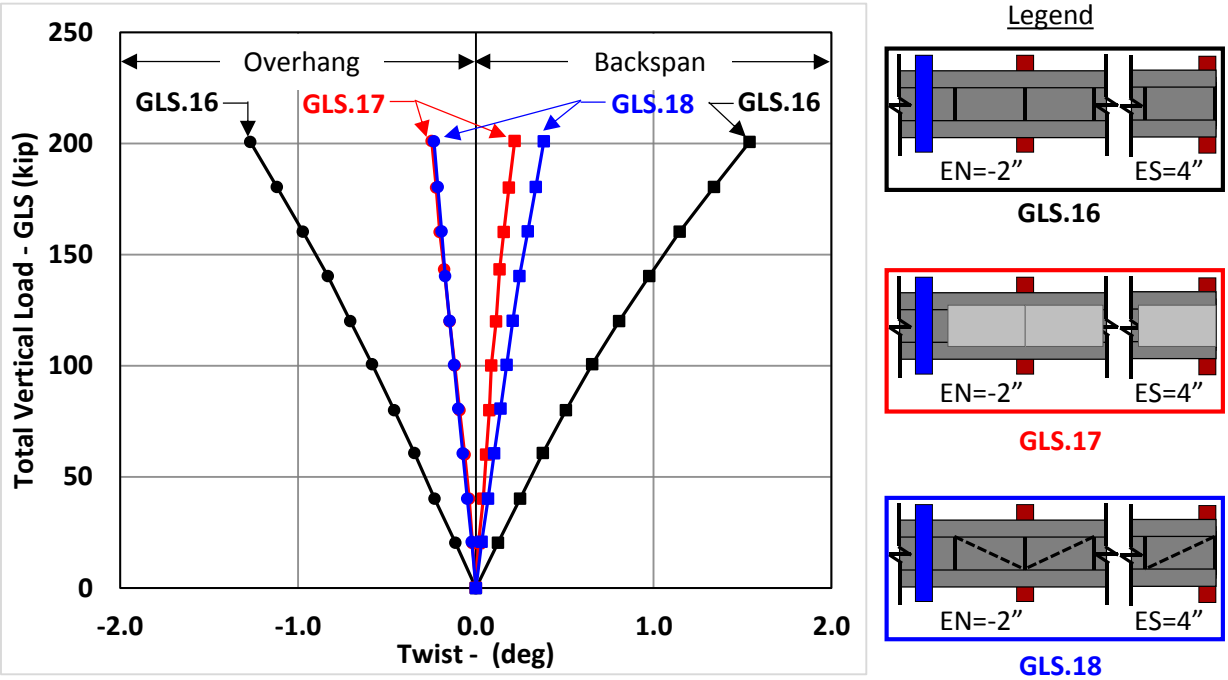

Figure C.25: Twist vs. GLS Load (EN=-2" & ES=4")

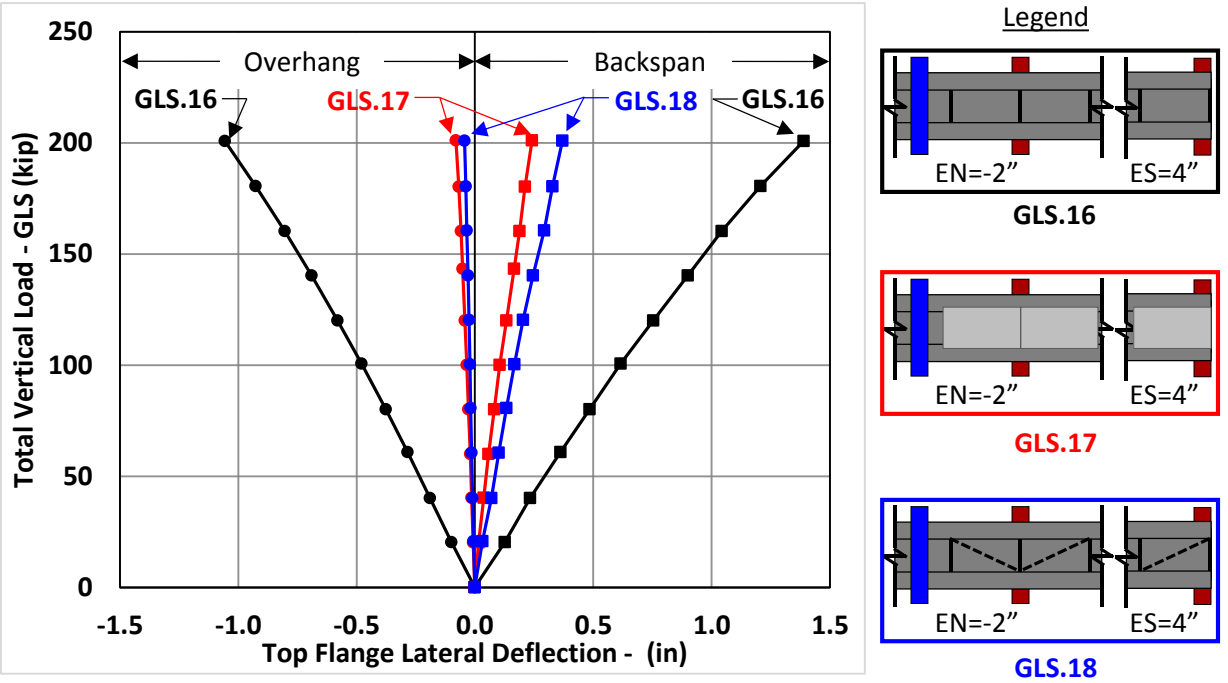

Figure C.26: Lateral Deflection vs. GLS Load (EN=-2" & ES=4")

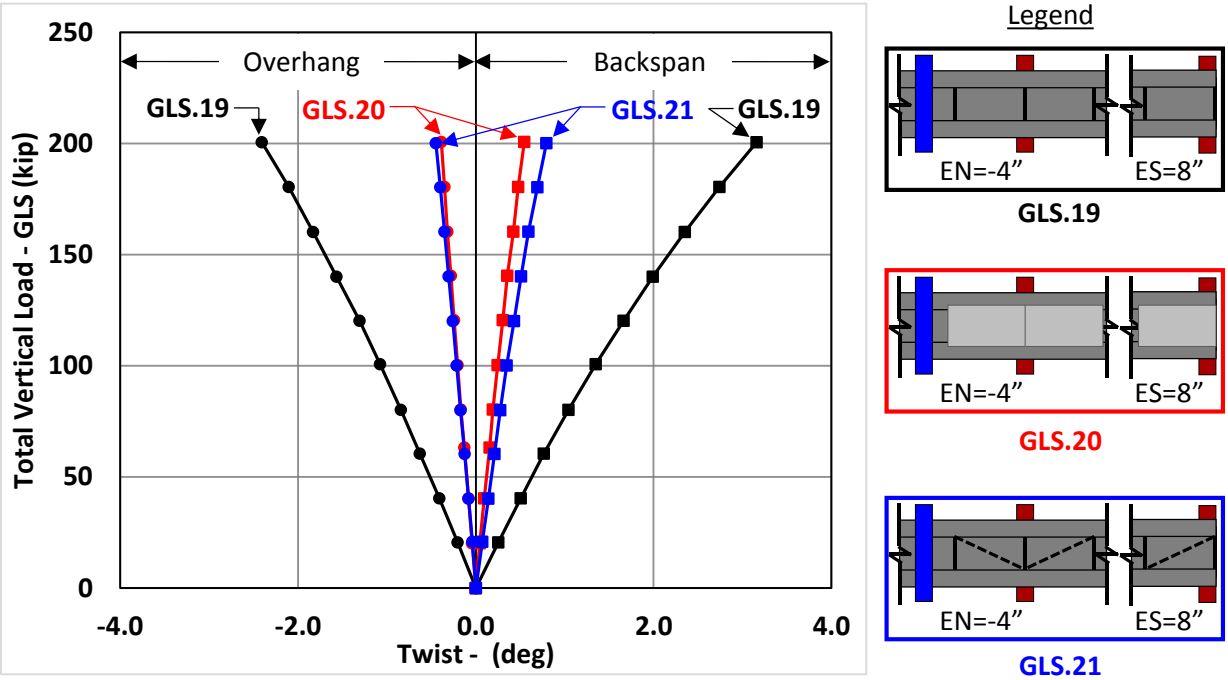

Figure C.27: Twist vs. GLS Load (EN=-4" & ES=8")

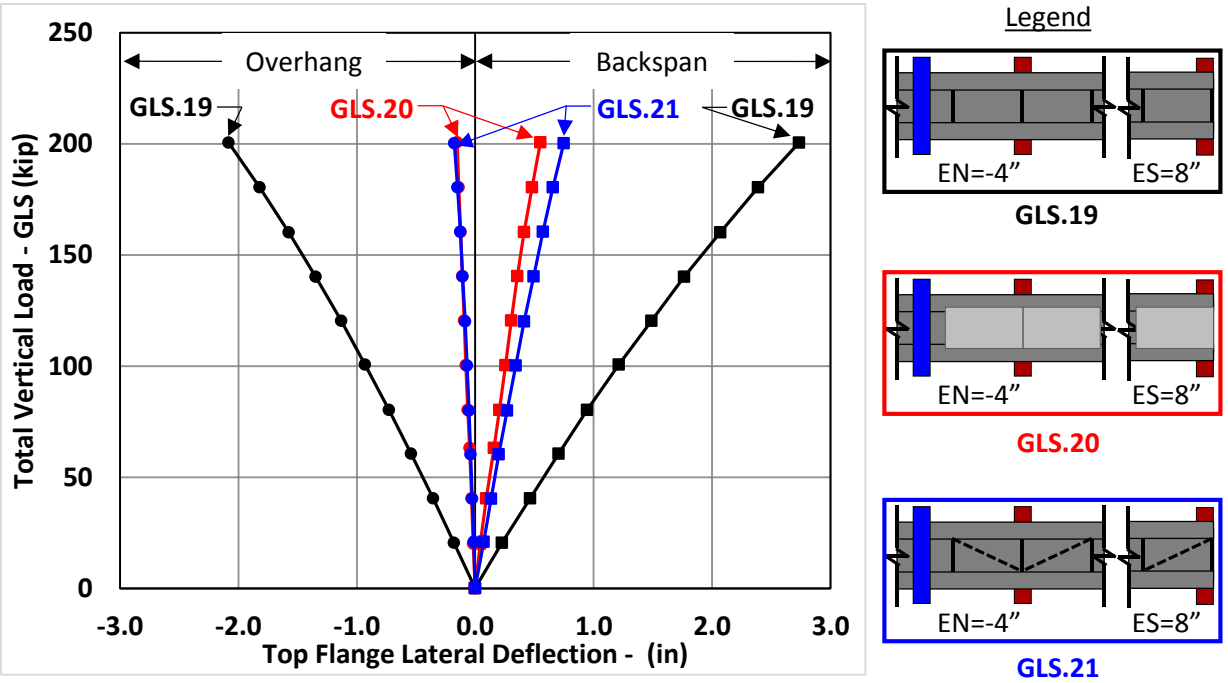

Figure C.28: Lateral Deflection vs. GLS Load (EN=-4" & ES=8")

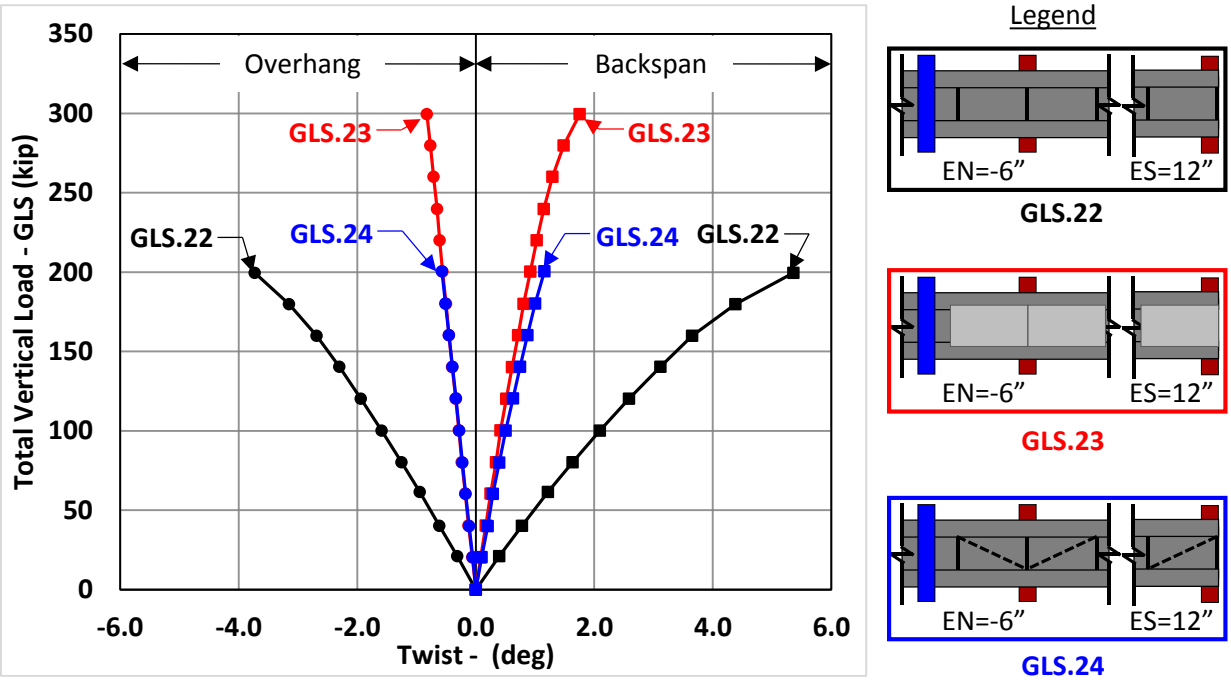

Figure C.29: Twist vs. GLS Load (EN=-6" & ES=12")

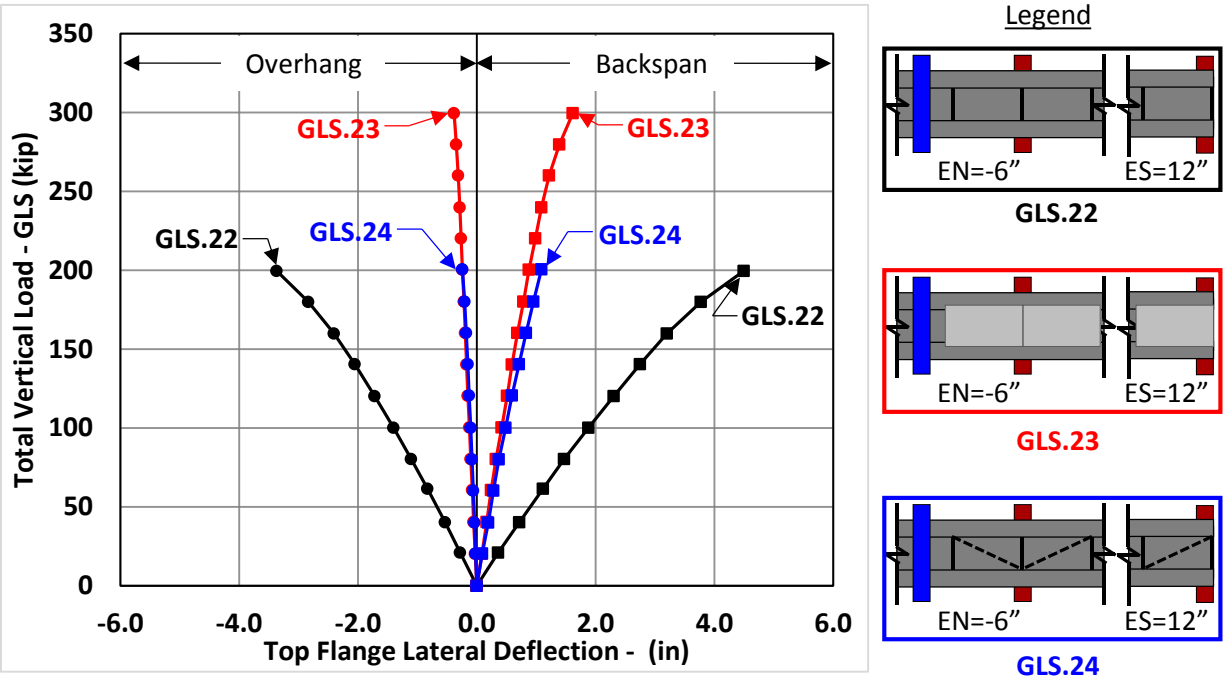

Figure C.30: Lateral Deflection vs. GLS Load (EN=-6" & ES=12")

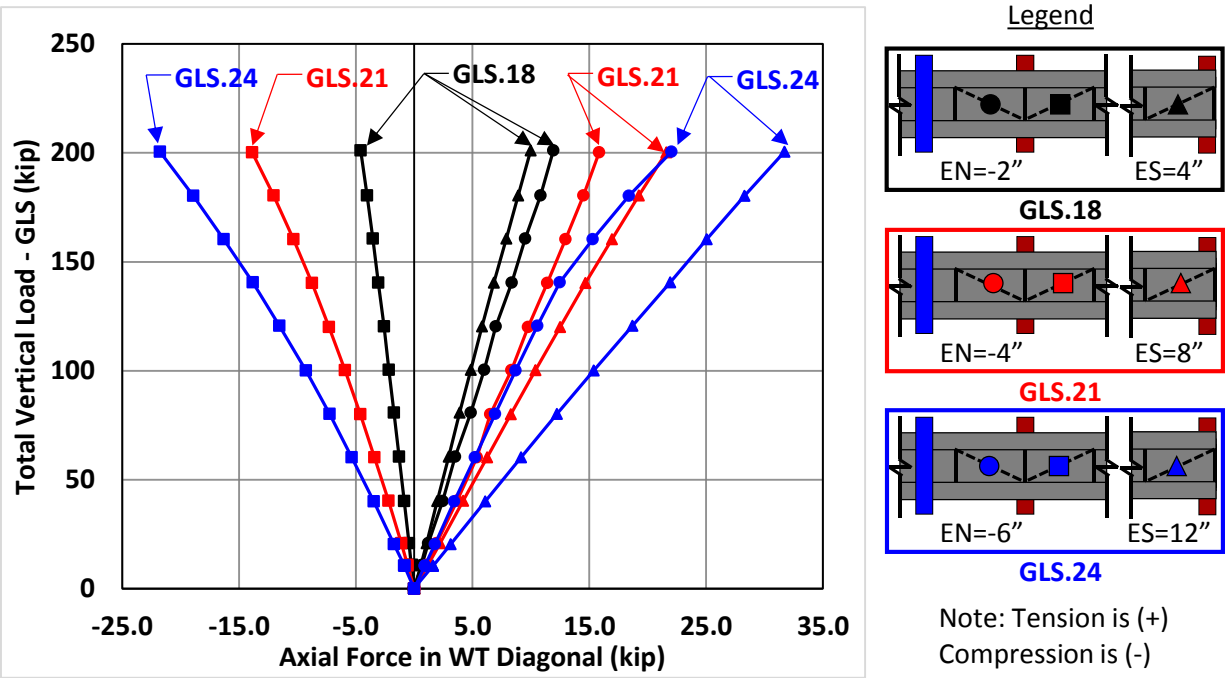

Figure C.31: Diagonal Forces vs. GLS Load – Overhang

Appendix D: Twin I-Girder FEA Validation with Experimental Results

D.1 FEA Validation with Experimental Results for Lateral Load I-Girder Tests

Table D.1: Summary of Lateral I-Girder Tests

Test Name	Load Location	Cross Frame	Number of PCPS
LAT.1	MS	-	0
LAT.2	MS	-	2
LAT.3	MS	-	4
LAT.4	MS	XF	0
LAT.5	MS	XF	2
LAT.6	MS	XF	4
LAT.7	QP	-	0
LAT.8	QP	-	2
LAT.9	QP	-	4
LAT.10	QP	XF	0
LAT.11	QP	XF	2
LAT.12	QP	XF	4

Key: LAT = Top Flange Lateral Load XF = Cross-Frame
MS = Midspan Load, QP = Quarter Point Load

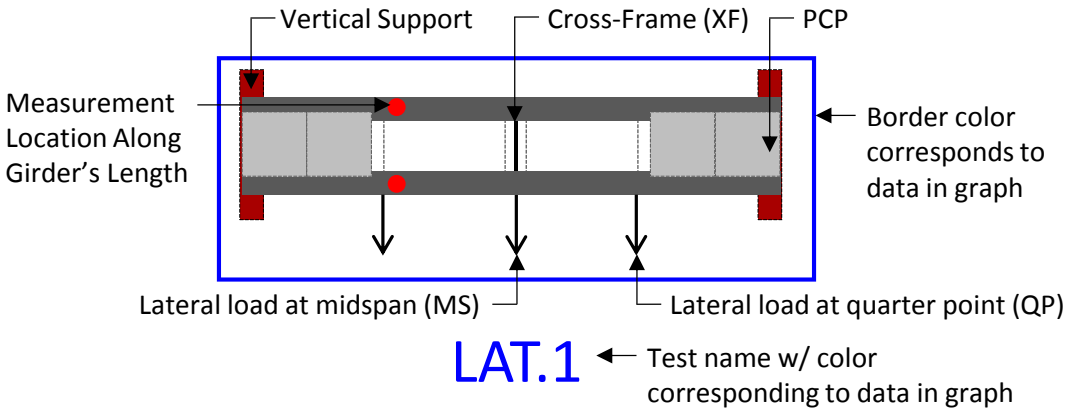

Figure D.1: Nomenclature for Documentation of Lateral Load I-Girder Tests

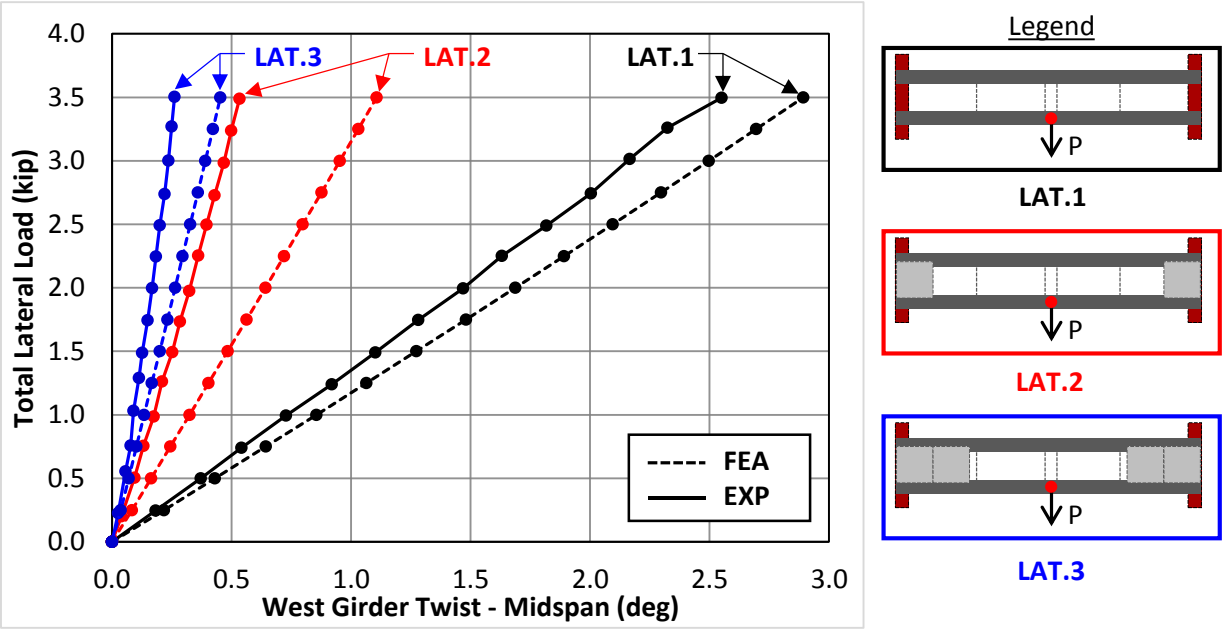

Figure D.2: Twist @ Midspan vs. Lateral Load @ Midspan (w/o XF) - West

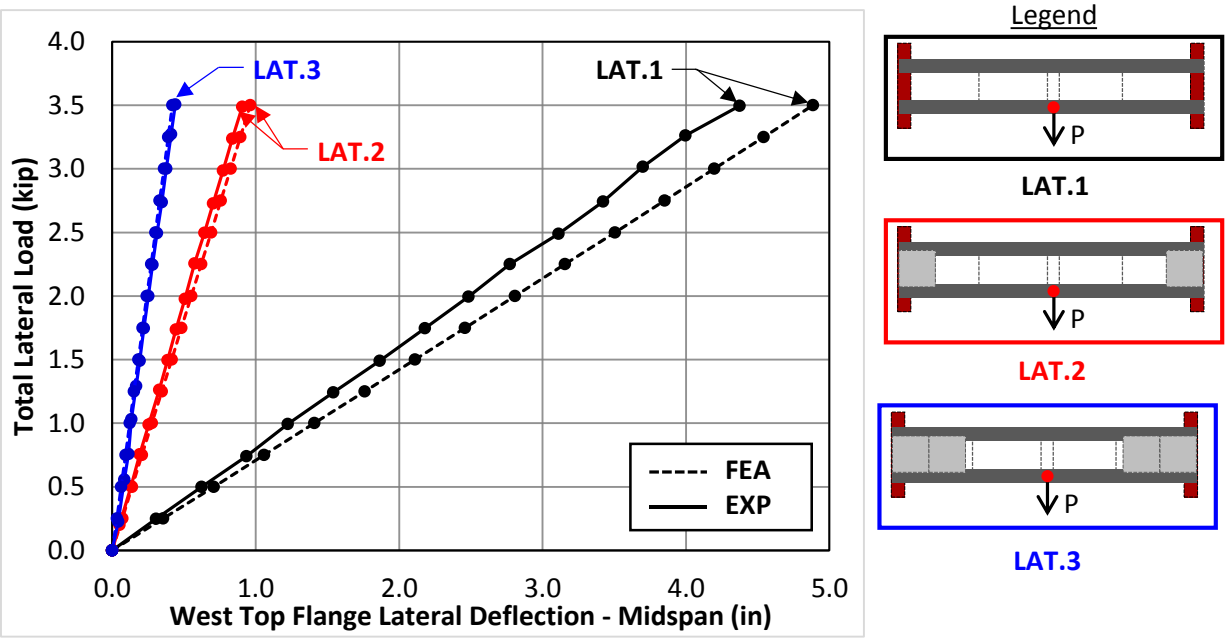

Figure D.3: Lateral Deflection @ Midspan vs. Lateral Load @ Midspan (w/o XF) - West

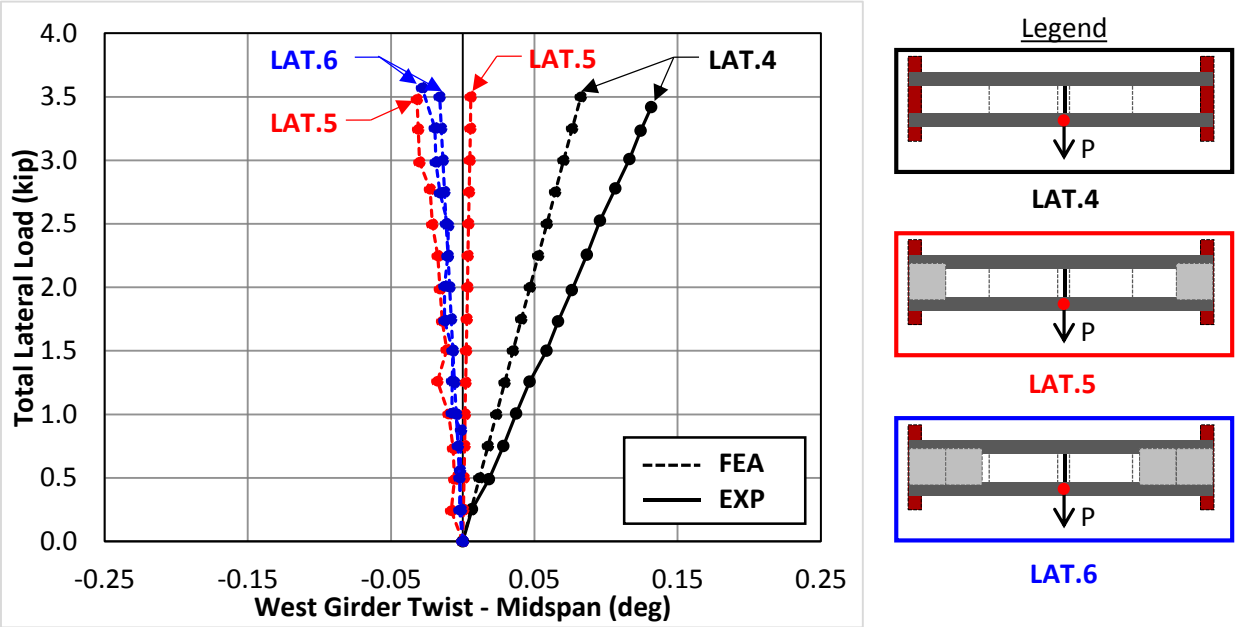

Figure D.4: Twist @ Midspan vs. Lateral Load @ Midspan (w/ XF) - West

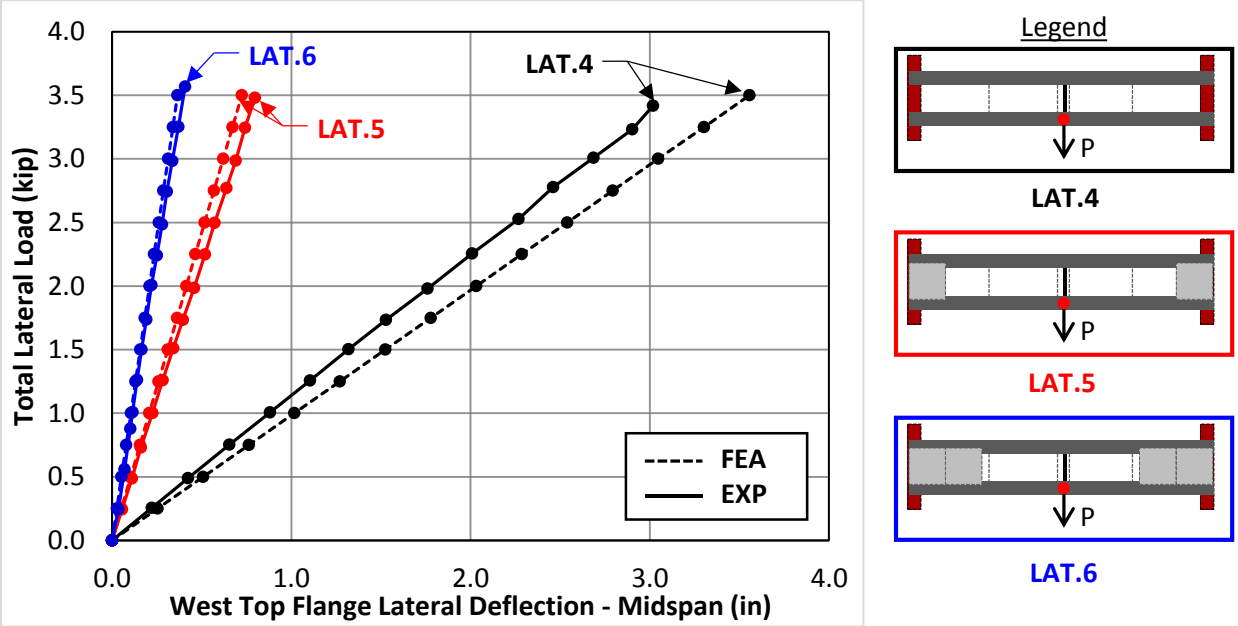

Figure D.5: Lateral Deflection @ Midspan vs. Lateral Load @ Midspan (w/ XF) - West

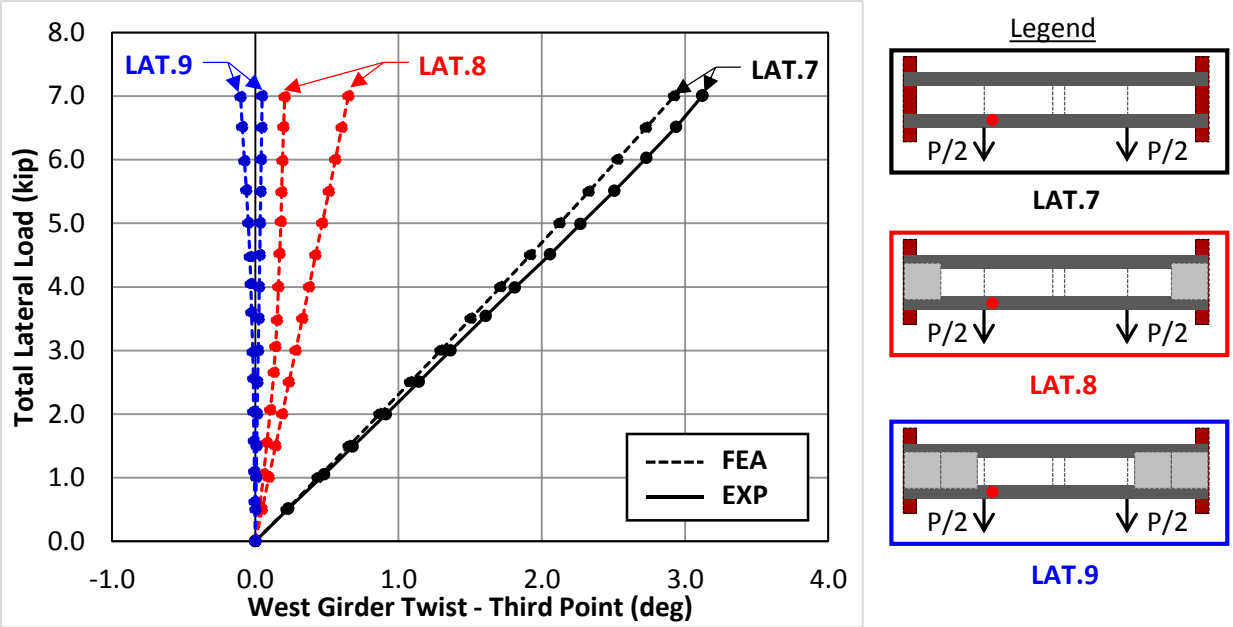

Figure D.6: Twist @ Third Point vs. Lateral Load @ Quarter Points (w/o XF) - West

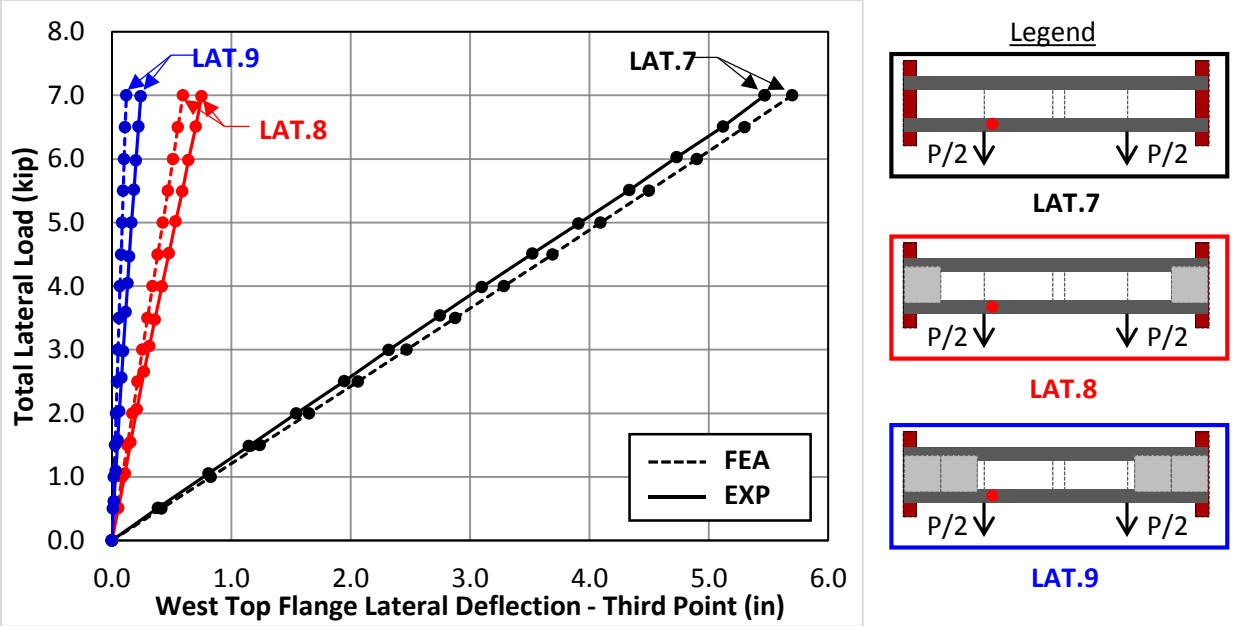

Figure D.7: Lateral Deflection @ Third Point vs. Lateral Load @ Quarter Points (w/o XF) - West

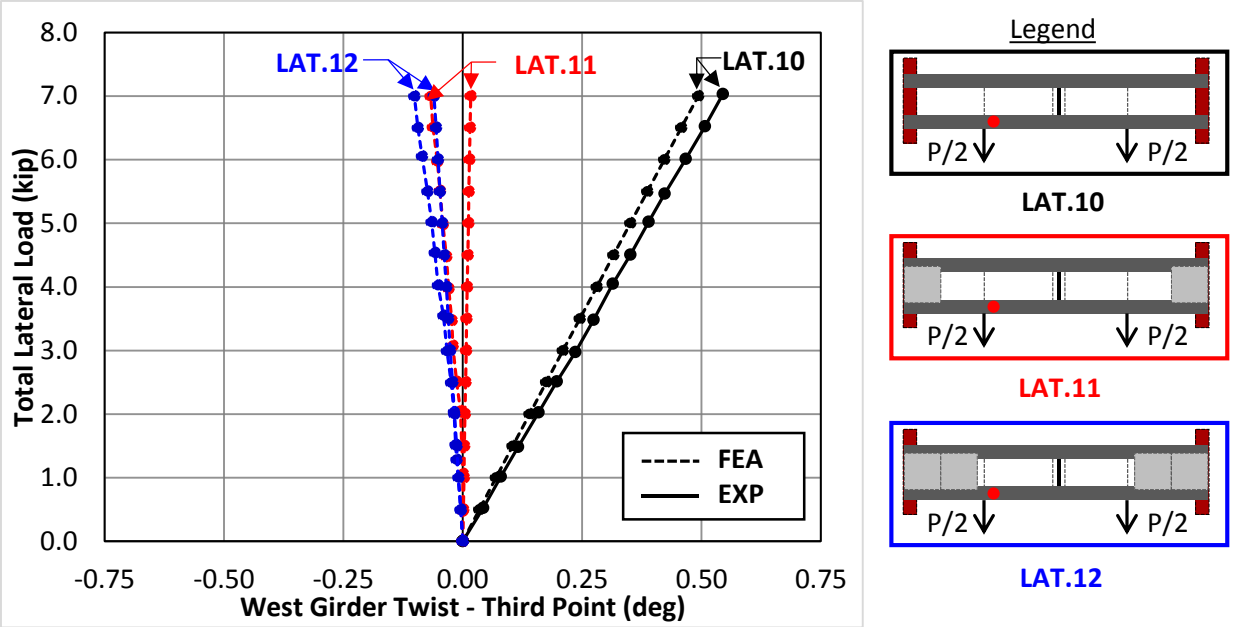

Figure D.8: Twist @ Third Point vs. Lateral Load @ Quarter Points (w/ XF) - West

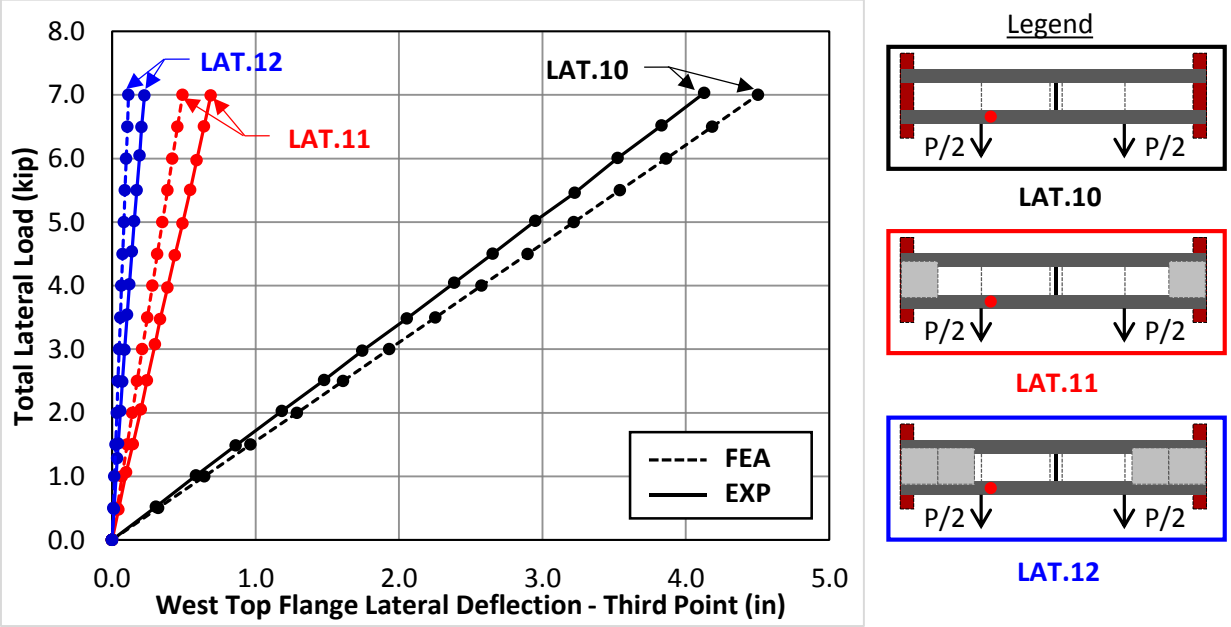

Figure D.9: Lateral Deflection @ Third Point vs. Lateral Load @ Quarter Points (w/ XF) - West

D.2 FEA Validation with Experimental Results for Combined Bending and Torsion Simply Supported I-Girder Tests

Table D.2: Summary of Bending and Torsion Simply Supported I-Girder Tests

Test Name	Support Condition	Load Eccentricity	Cross Frame	Bottom Truss	Number of PCPS	Max Total GLS Load
GLS.1	SS	0 & 0	-	-	0	30
GLS.2	SS	0 & 0	-	-	2	100
GLS.3	SS	0 & 0	-	-	4	150
GLS.4	SS	6" & 6"	-	-	0	19
GLS.5	SS	6" & 6"	-	-	2	60
GLS.6	SS	6" & 6"	-	-	4	90
GLS.7	SS	6" & 6"	-	2 BF	4	80
GLS.8	SS	6" & 6"	-	4 BF	4	100
GLS.9	SS	12" & 12"	-	-	0	10
GLS.10	SS	12" & 12"	-	-	2	38
GLS.11	SS	12" & 12"	-	-	4	40
GLS.12	SS	12" & 12"	-	2 BF	4	75
GLS.13	SS	12" & 12"	-	4 BF	4	80
GLS.14	SS	0 & 0	XF	-	0	140
GLS.15	SS	0 & 0	XF	-	2	180
GLS.16	SS	0 & 0	XF	-	4	180
GLS.17	SS	6" & 6"	XF	-	0	90
GLS.18	SS	6" & 6"	XF	-	2	110
GLS.19	SS	6" & 6"	XF	-	4	120
GLS.20	SS	12" & 12"	XF	-	0	60
GLS.21	SS	12" & 12"	XF	-	2	70
GLS.22	SS	12" & 12"	XF	-	4	90

Key: GLS = Gravity Load Simulator Load, SS = Simply Supported
BF = Bottom Flange Truss, XF = Cross-Frame

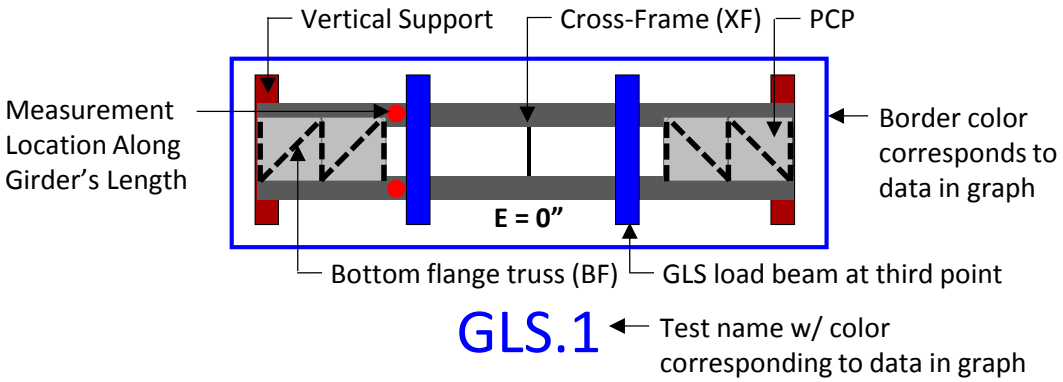

Figure D.10: Nomenclature for Documentation of GLS Simply Supported I-Girder Tests

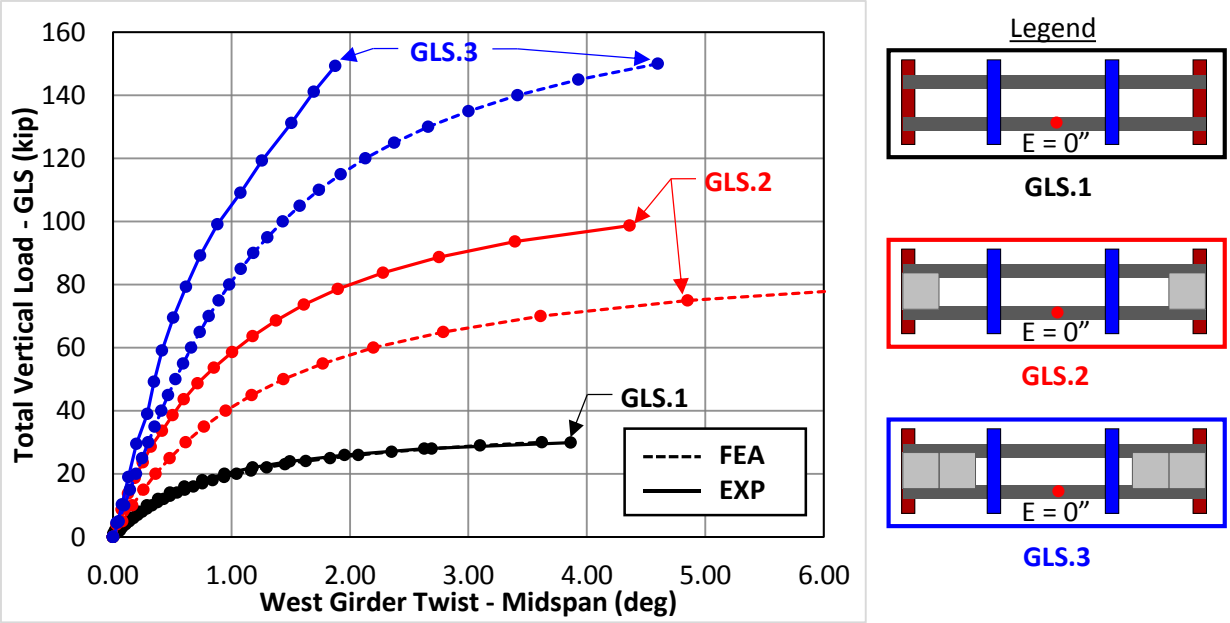

Figure D.11: Twist @ Midspan vs. GLS Load (E=0" - SS - w/o XF) - West

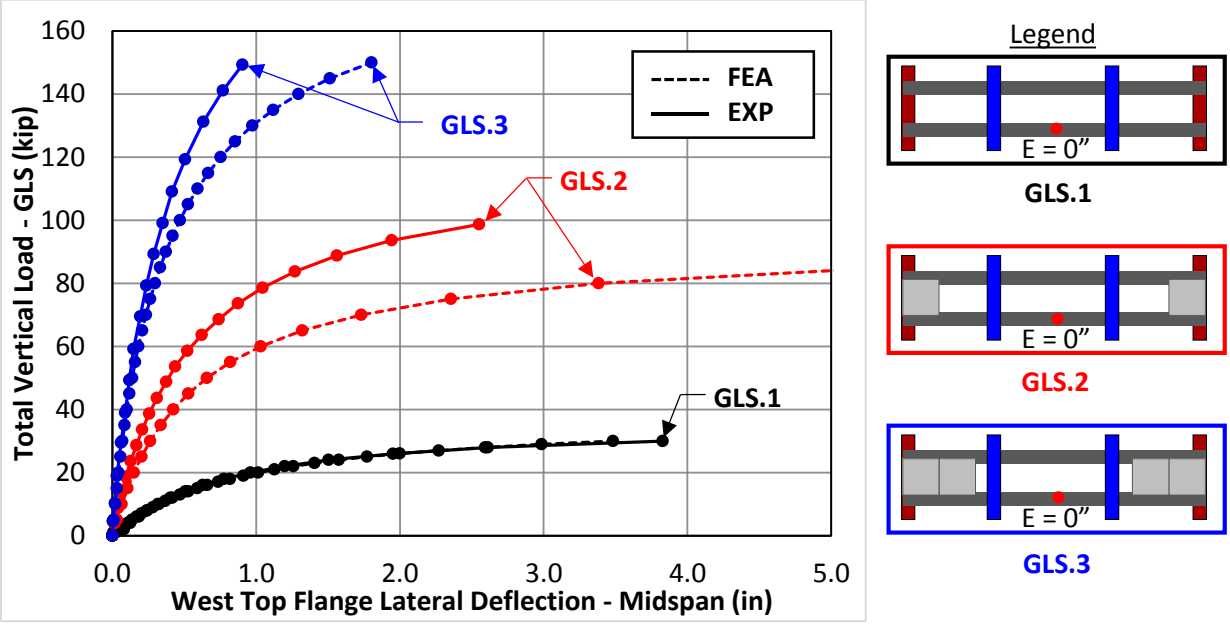

Figure D.12: Lateral Deflection @ Midspan vs. GLS Load (E=0" - SS - w/o XF) - West

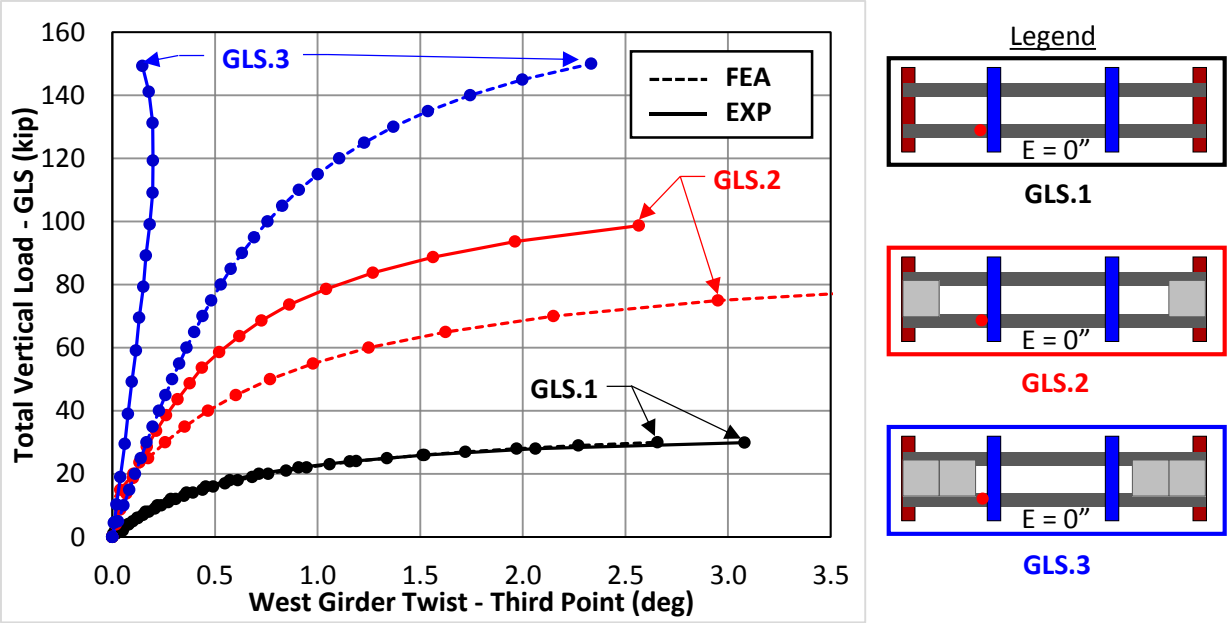

Figure D.13: Twist @ Third Points vs. GLS Load (E=0" - SS - w/o XF) - West

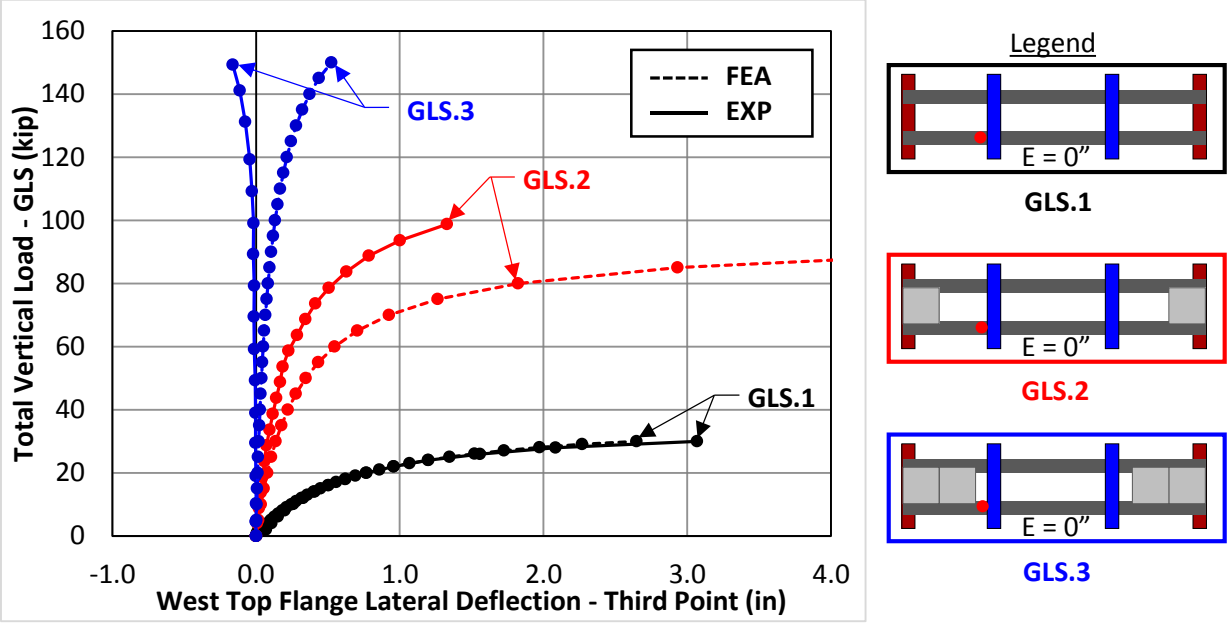

Figure D.14: Lateral Deflection @ Third Points vs. GLS Load (E=0" - SS - w/o XF) - West

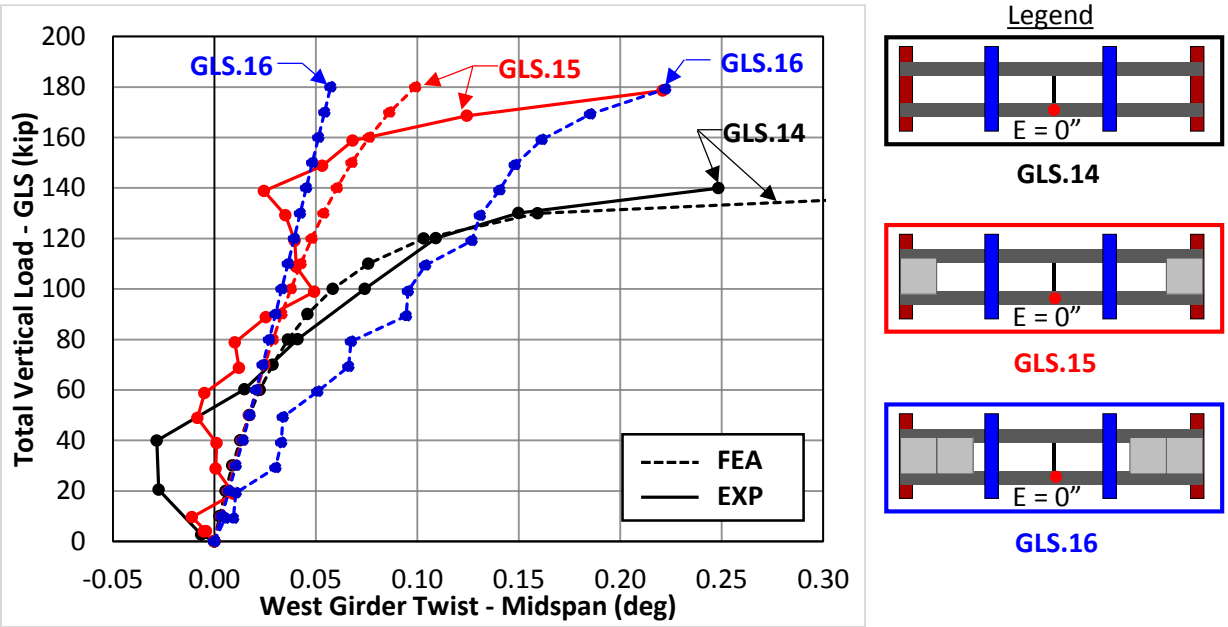

Figure D.15: Twist @ Midspan vs. GLS Load (E=0" - SS - w/ XF) - West

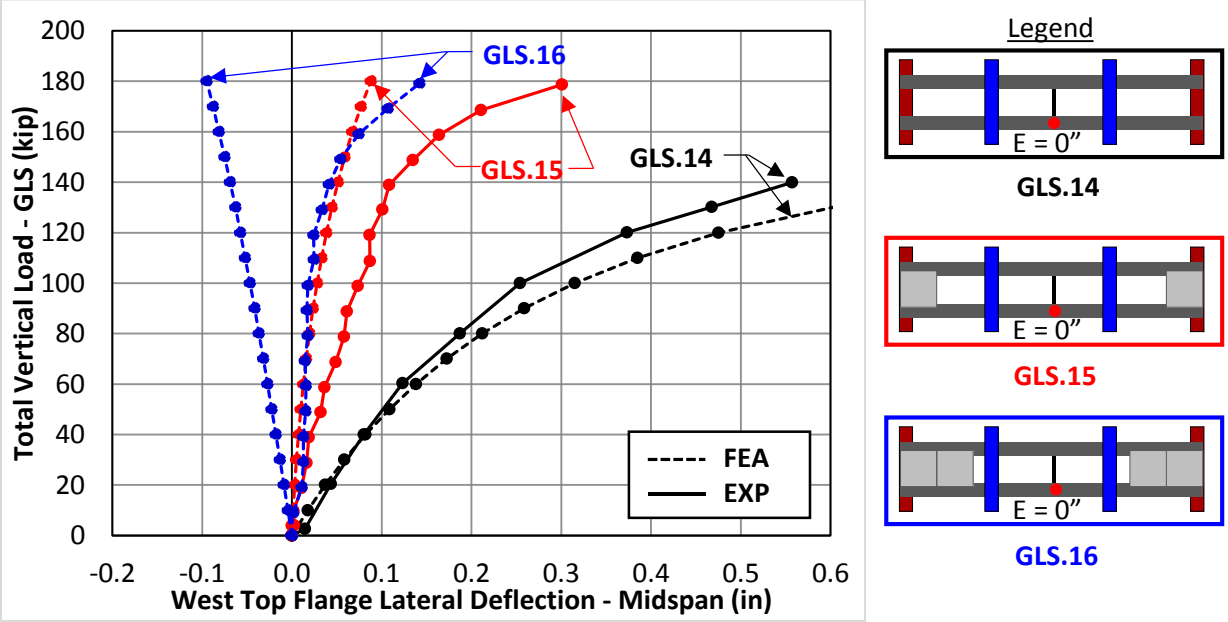

Figure D.16: Lateral Deflection @ Midspan vs. GLS Load (E=0" - SS - w/ XF) - West

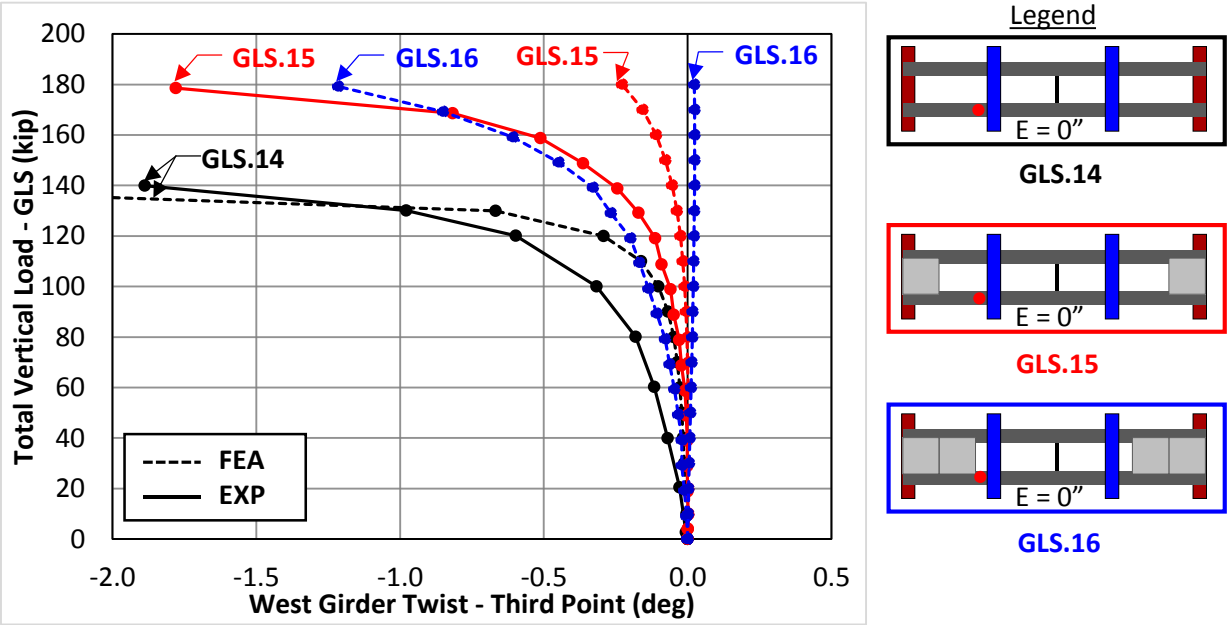

Figure D.17: Twist @ Third Point vs. GLS Load (E=0" - SS - w/ XF) - West

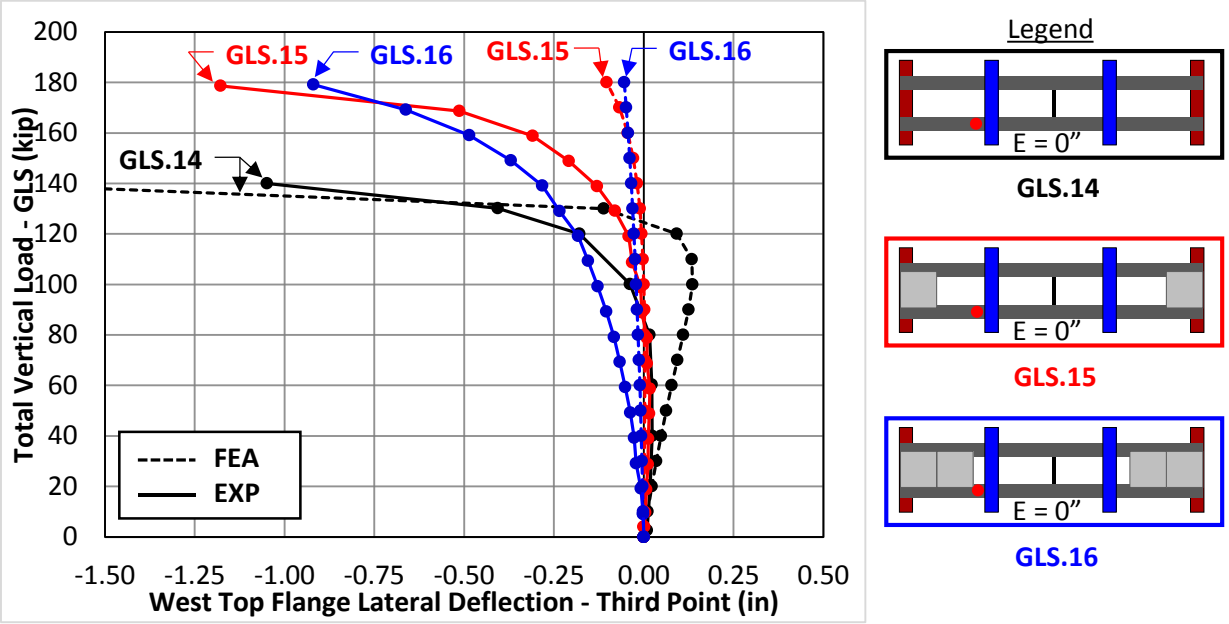

Figure D.18: Lateral Deflection @ Third Point vs. GLS Load (E=0" - SS - w/ XF) - West

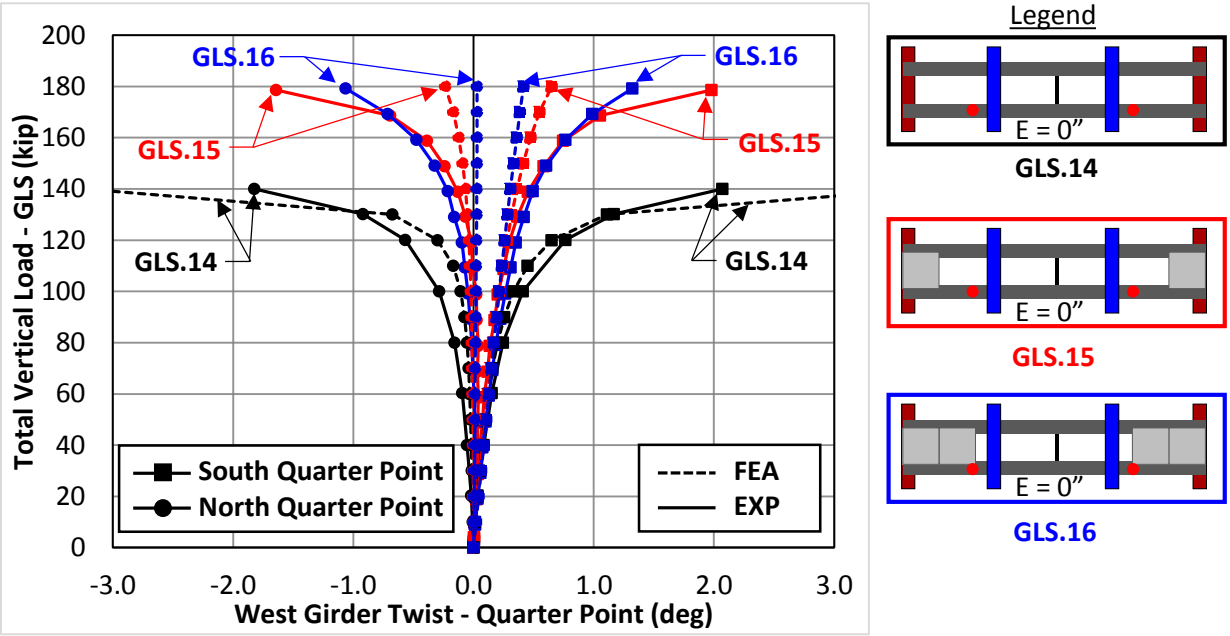

Figure D.19: Twist @ Quarter Point vs. GLS Load (E=0" - SS - w/ XF)

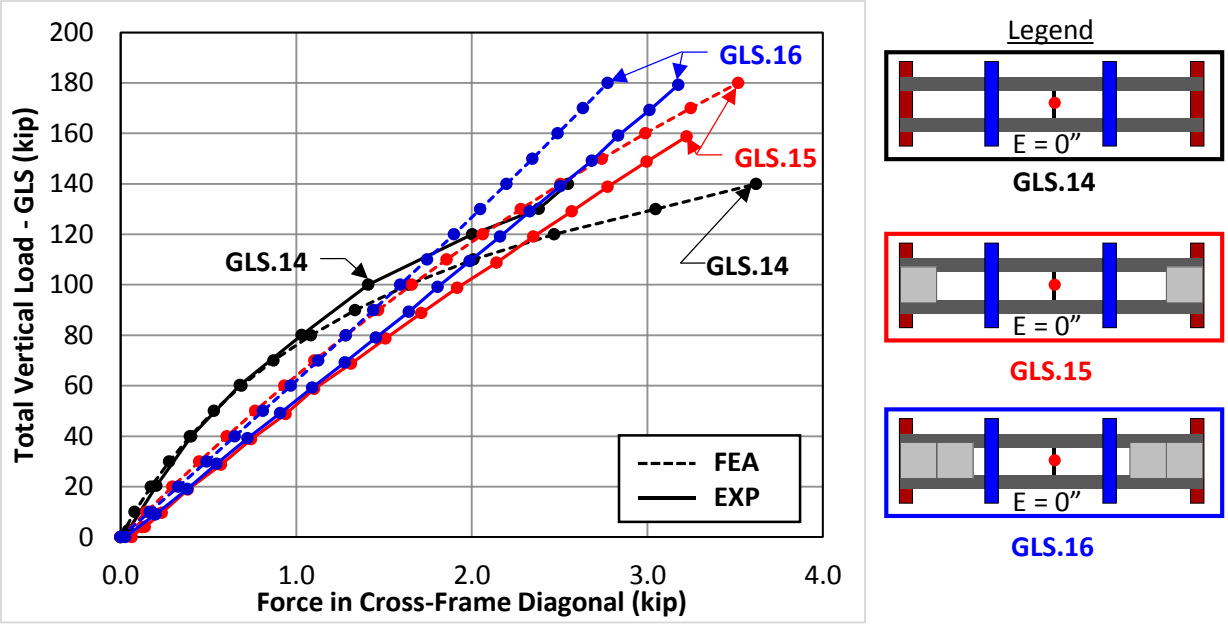

Figure D.20: Cross-Frame Diagonal Force vs. GLS Load (E=0" - SS)

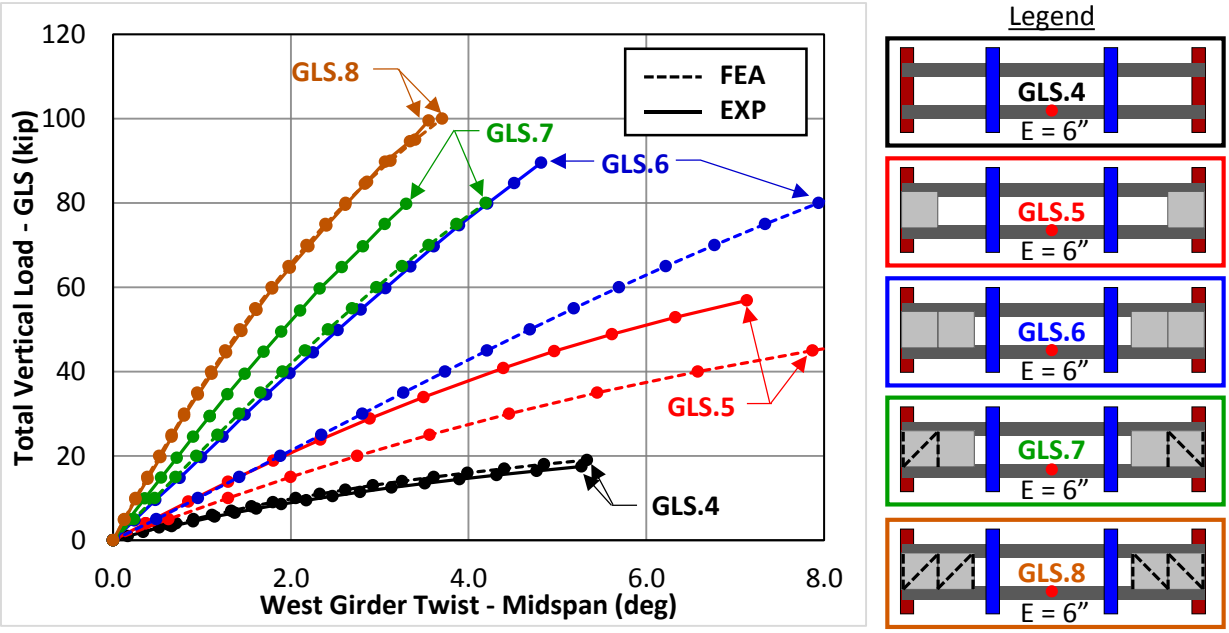

Figure D.21: Twist @ Midspan vs. GLS Load (E=6" - SS - w/o XF) - West

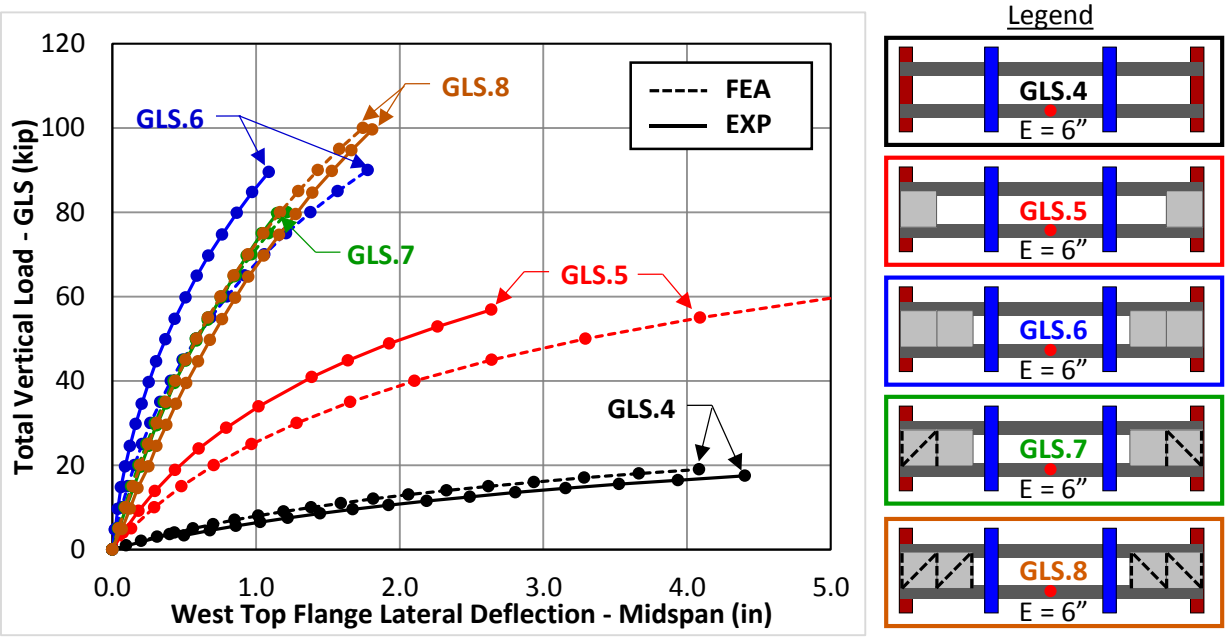

Figure D.22: Lateral Deflection @ Midspan vs. GLS Load (E=6" - SS - w/o XF) - West

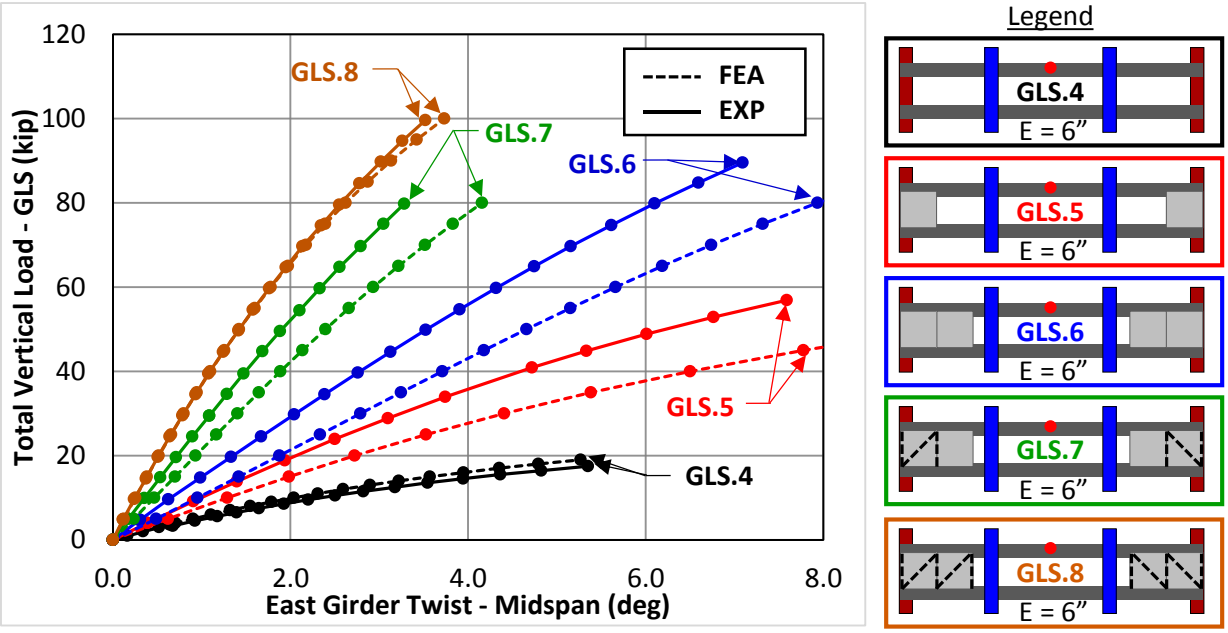

Figure D.23: Twist @ Midspan vs. GLS Load (E=6" - SS - w/o XF) - East

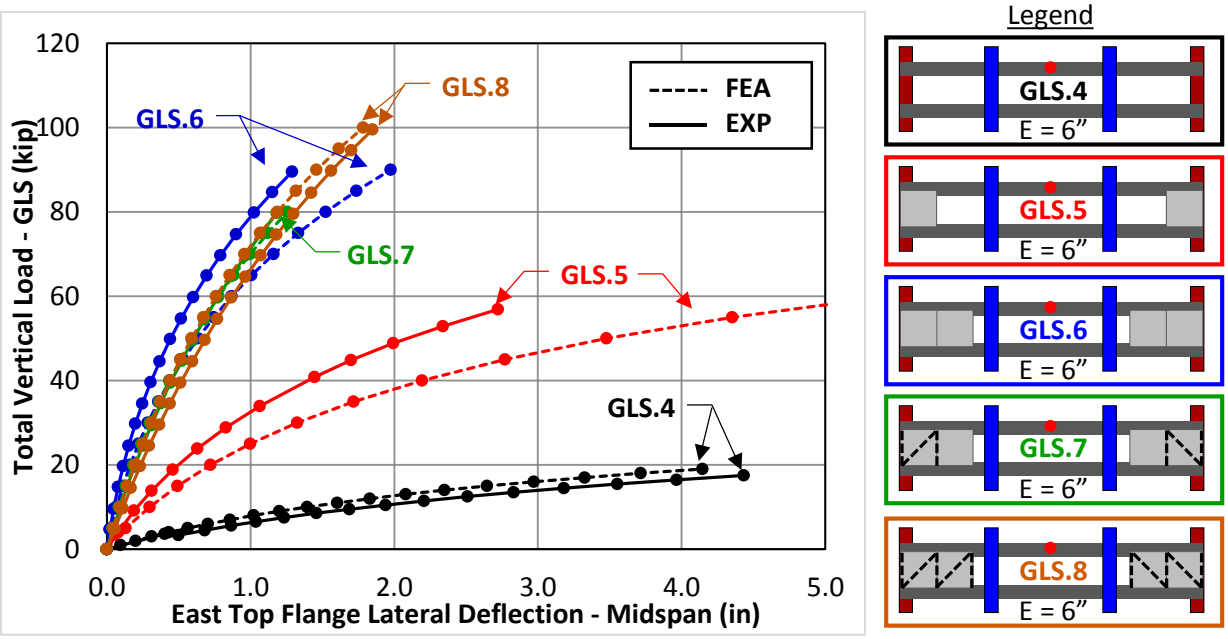

Figure D.24: Lateral Deflection @ Midspan vs. GLS Load (E=6" - SS - w/o XF) - East

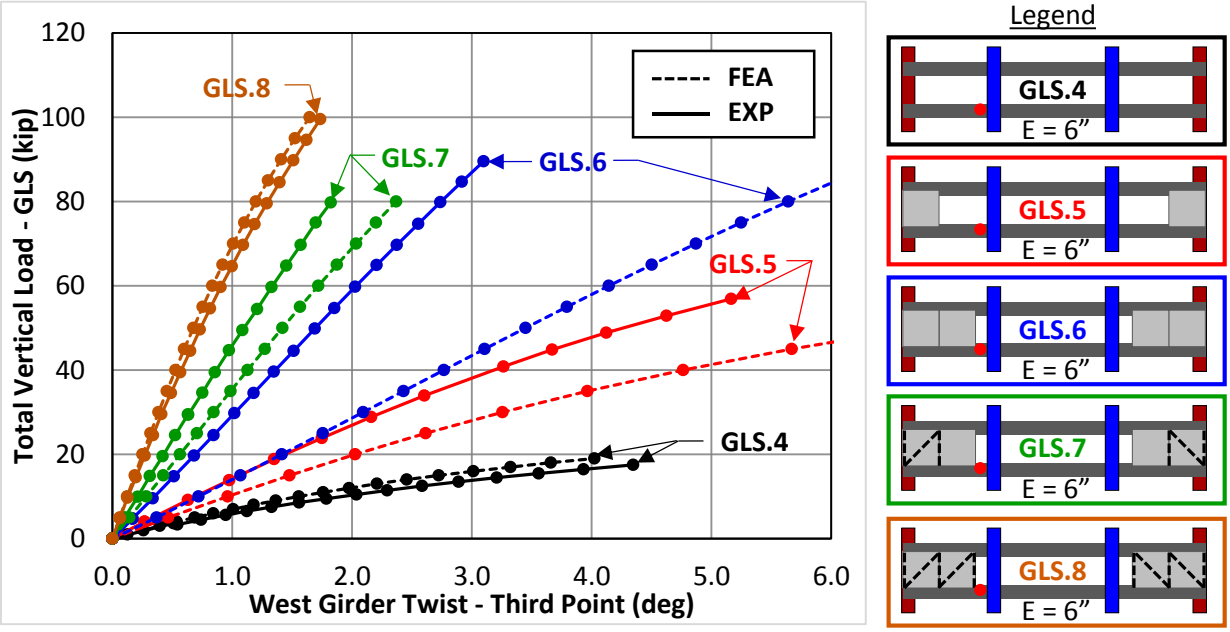

Figure D.25: Twist @ Third Point vs. GLS Load (E=6" - SS - w/o XF) - West

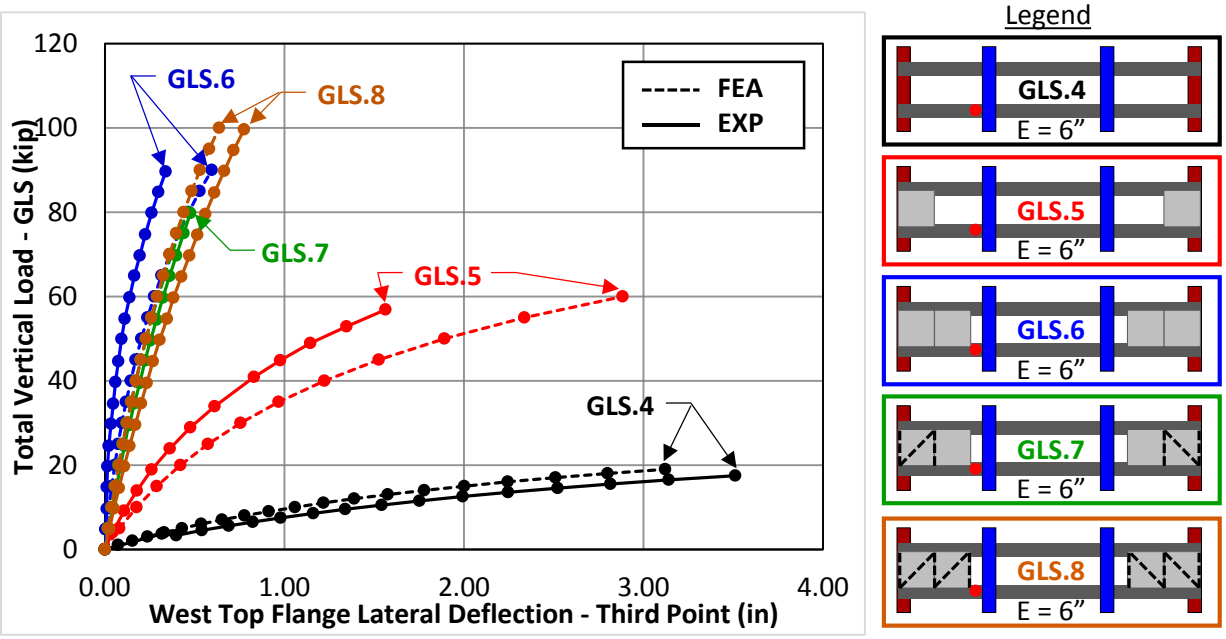

Figure D.26: Lateral Deflection @ Third Point vs. GLS Load (E=6" - SS - w/o XF) - West

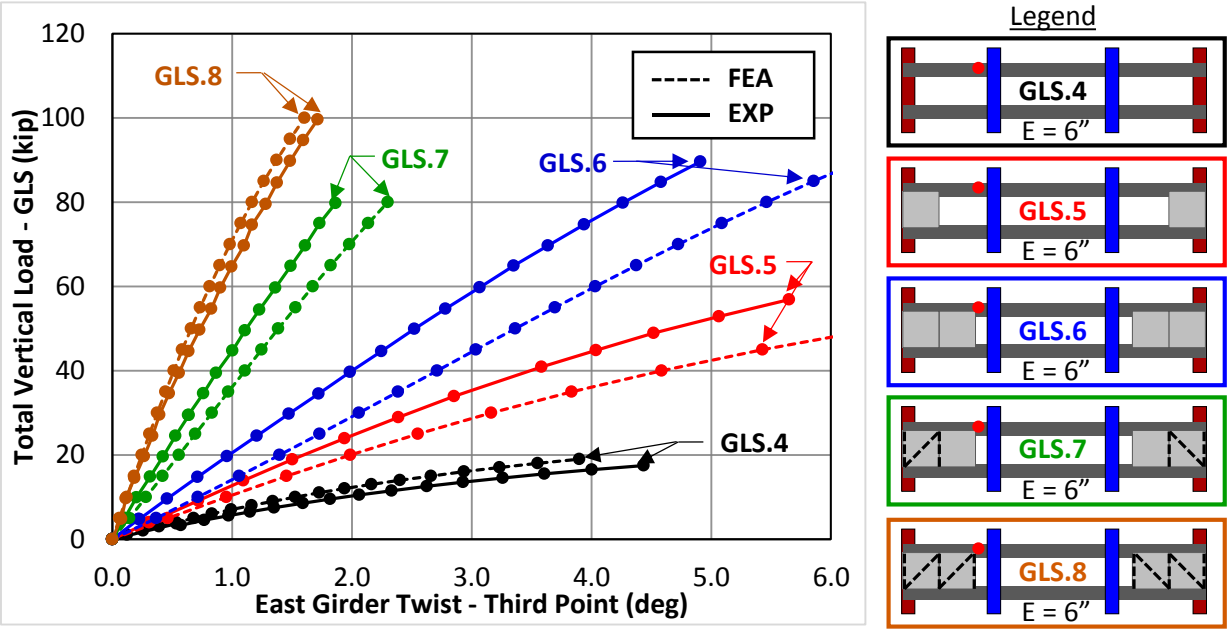

Figure D.27: Twist @ Third Point vs. GLS Load (E=6" - SS - w/o XF) - East

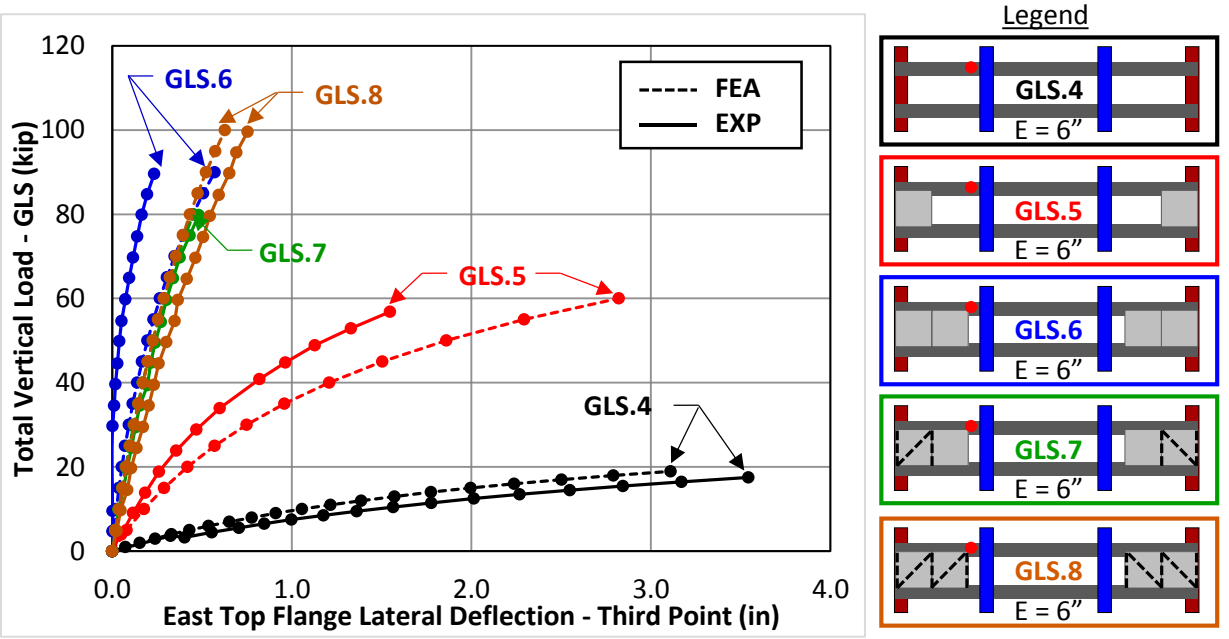

Figure D.28: Lateral Deflection @ Third Point vs. GLS Load (E=6" - SS - w/o XF) - East

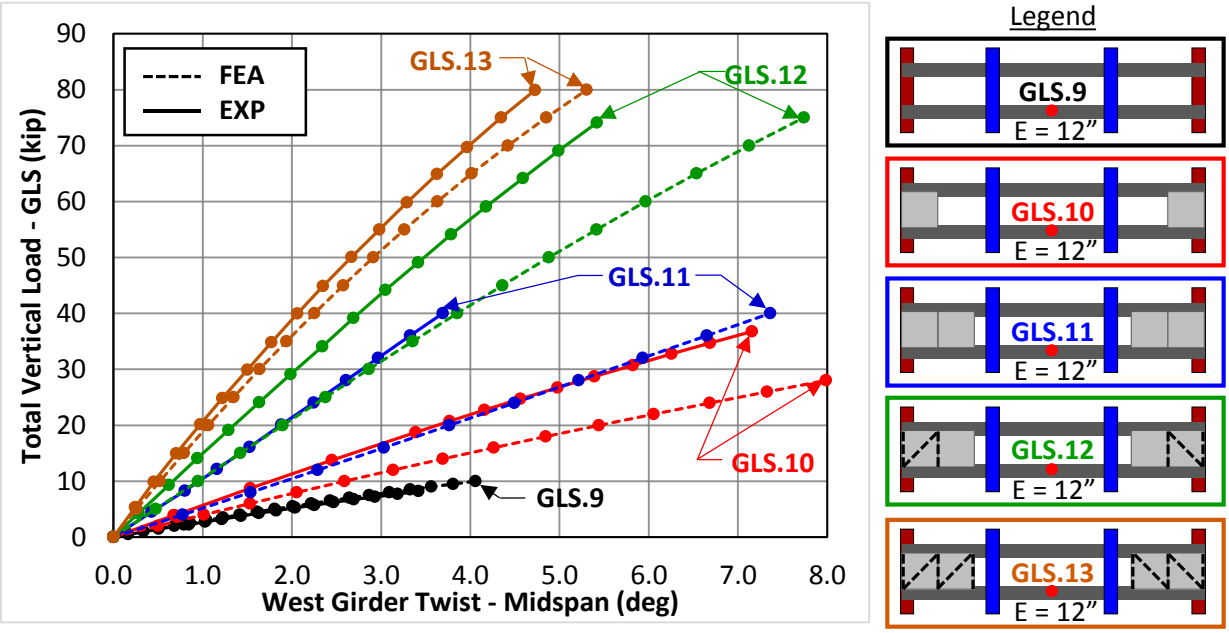

Figure D.29: Twist @ Midspan vs. GLS Load (E=12" - SS - w/o XF) - West

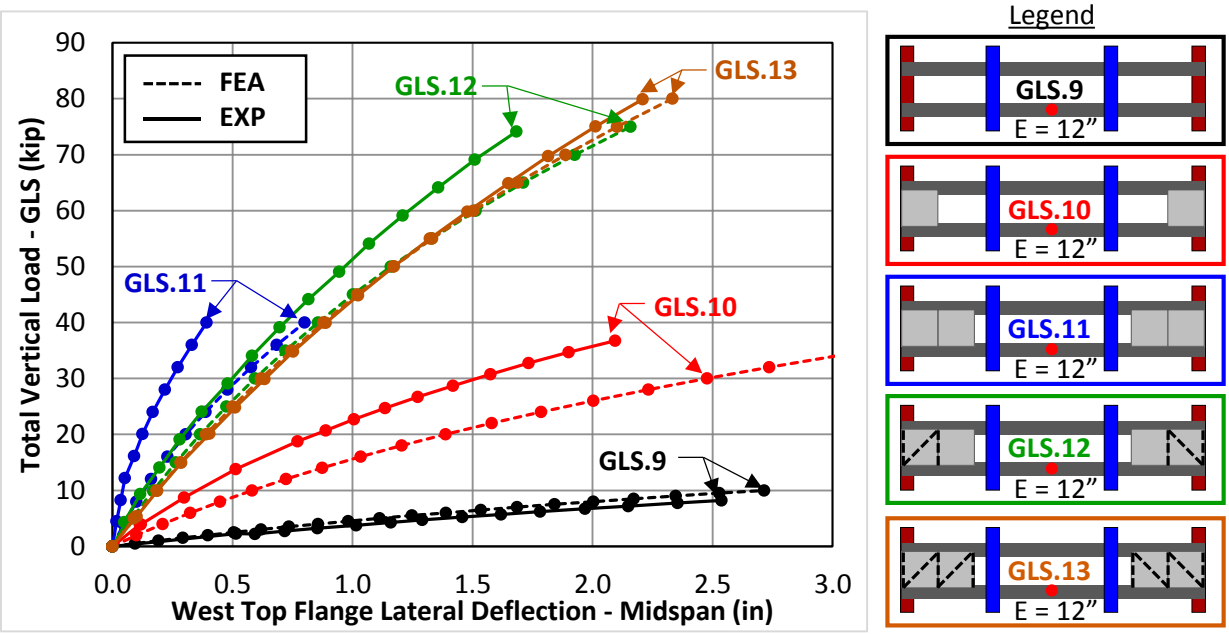

Figure D.30: Lateral Deflection @ Midspan vs. GLS Load (E=12" - SS - w/o XF) - West

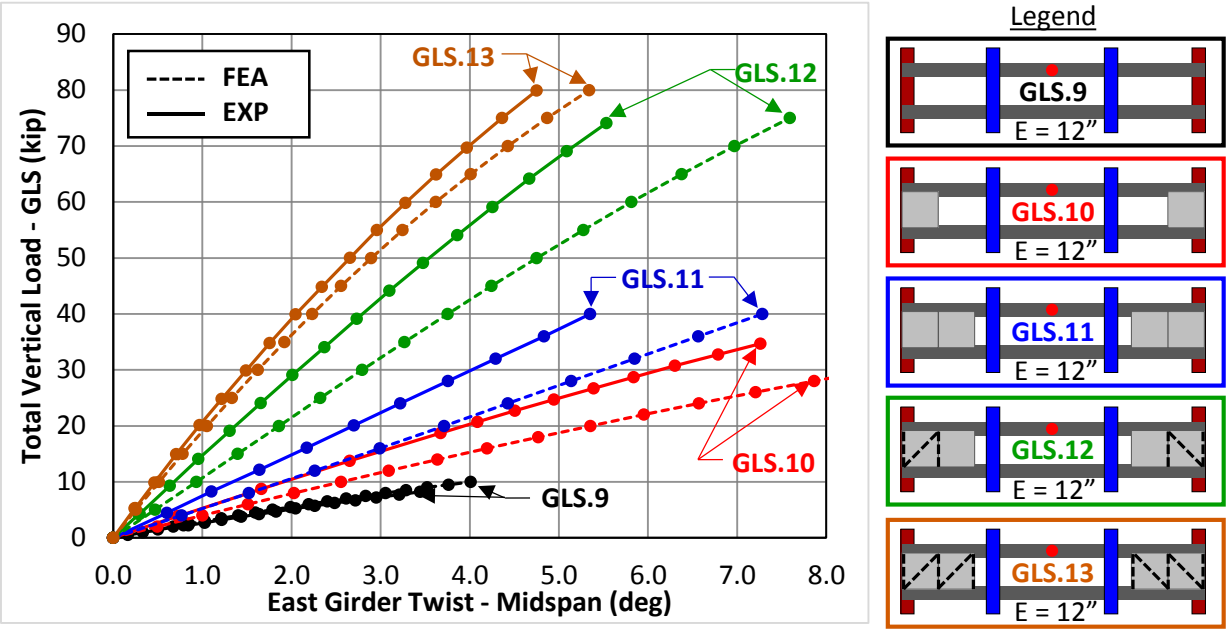

Figure D.31: Twist @ Midspan vs. GLS Load (E=12" - SS - w/o XF) - East

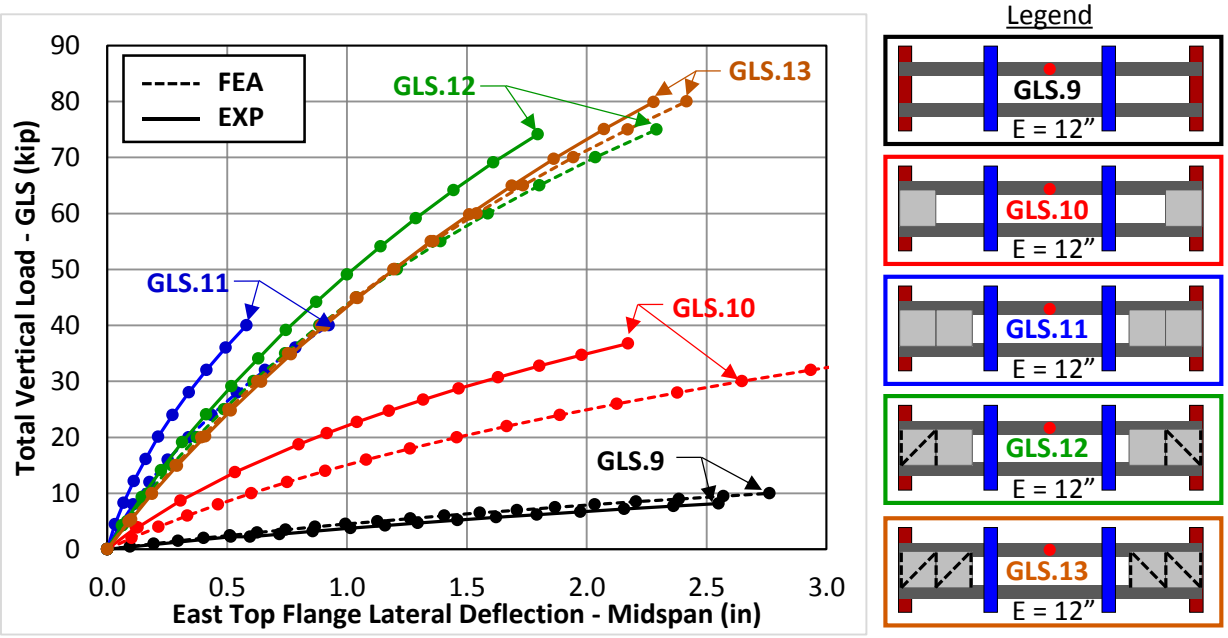

Figure D.32: Lateral Deflection @ Midspan vs. GLS Load (E=12" - SS - w/o XF) - East

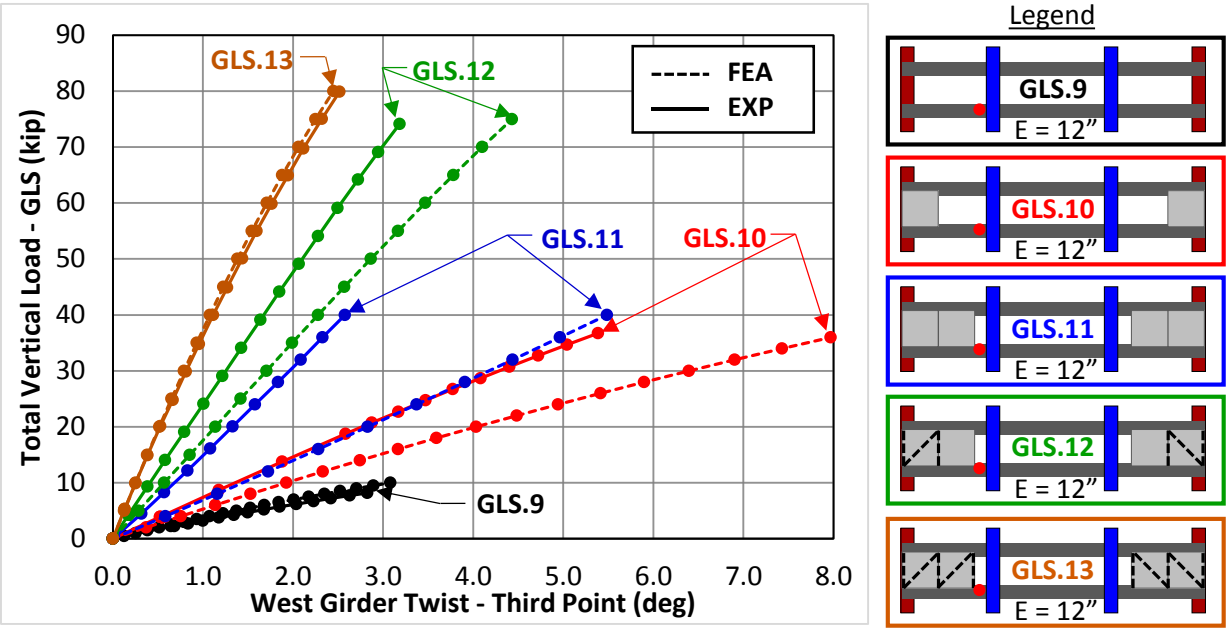

Figure D.33: Twist @ Third Point vs. GLS Load (E=12" - SS - w/o XF) - West

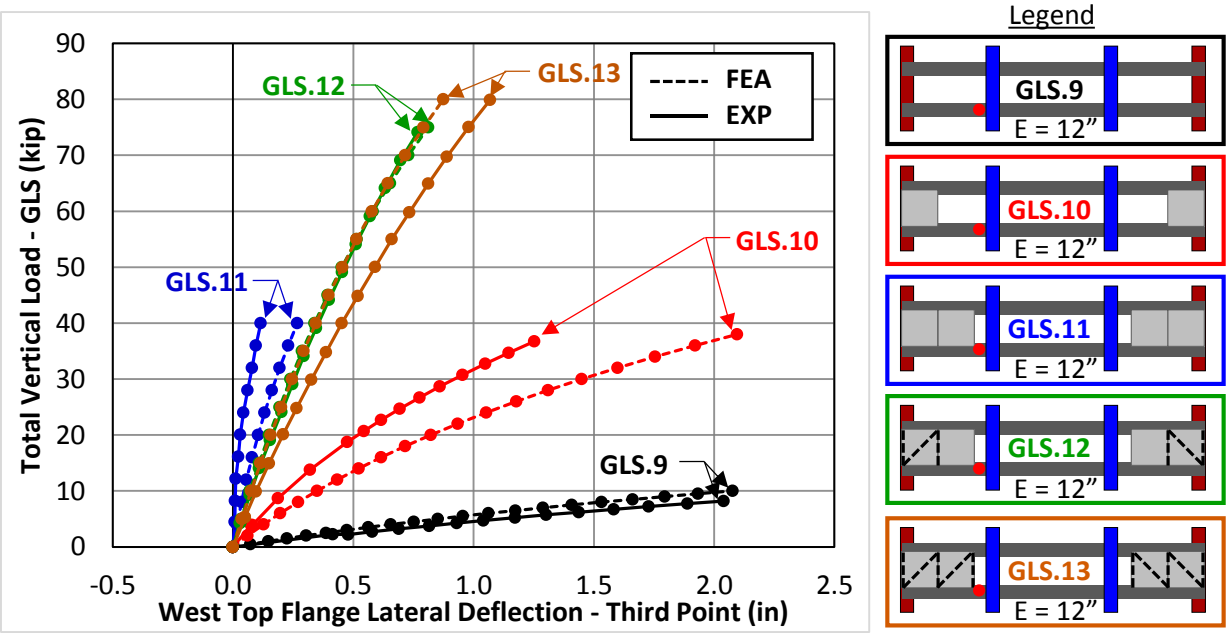

Figure D.34: Lateral Deflection @ Third Point vs. GLS Load (E=12" - SS - w/o XF) - West

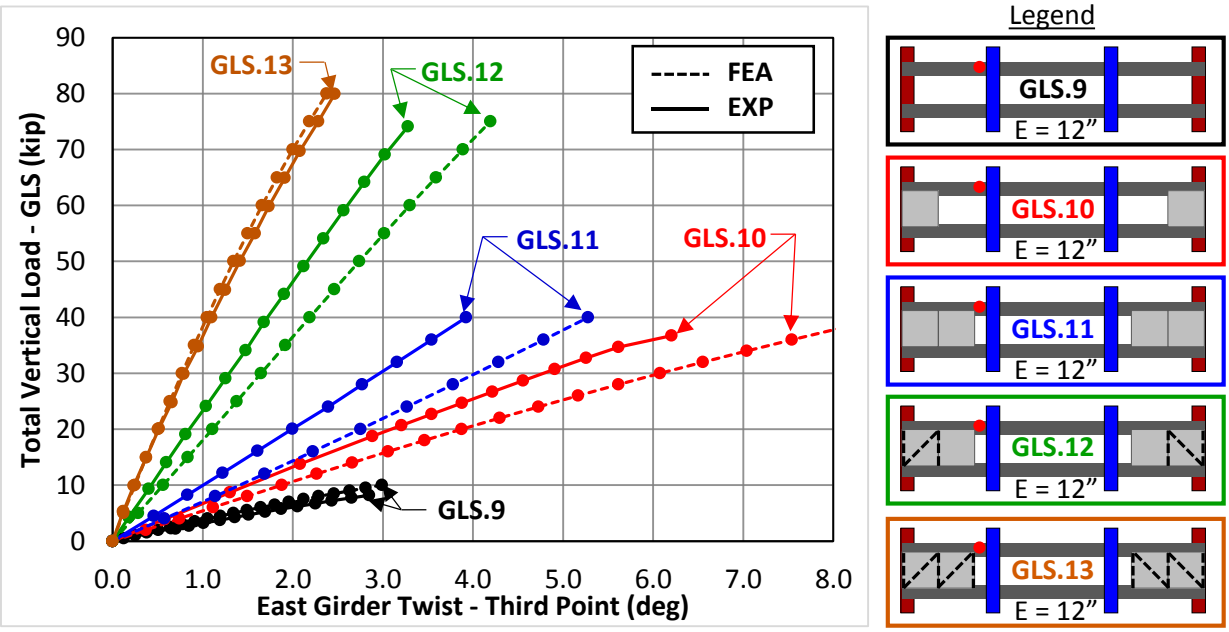

Figure D.35: Twist @ Third Point vs. GLS Load (E=12" - SS - w/o XF) - East

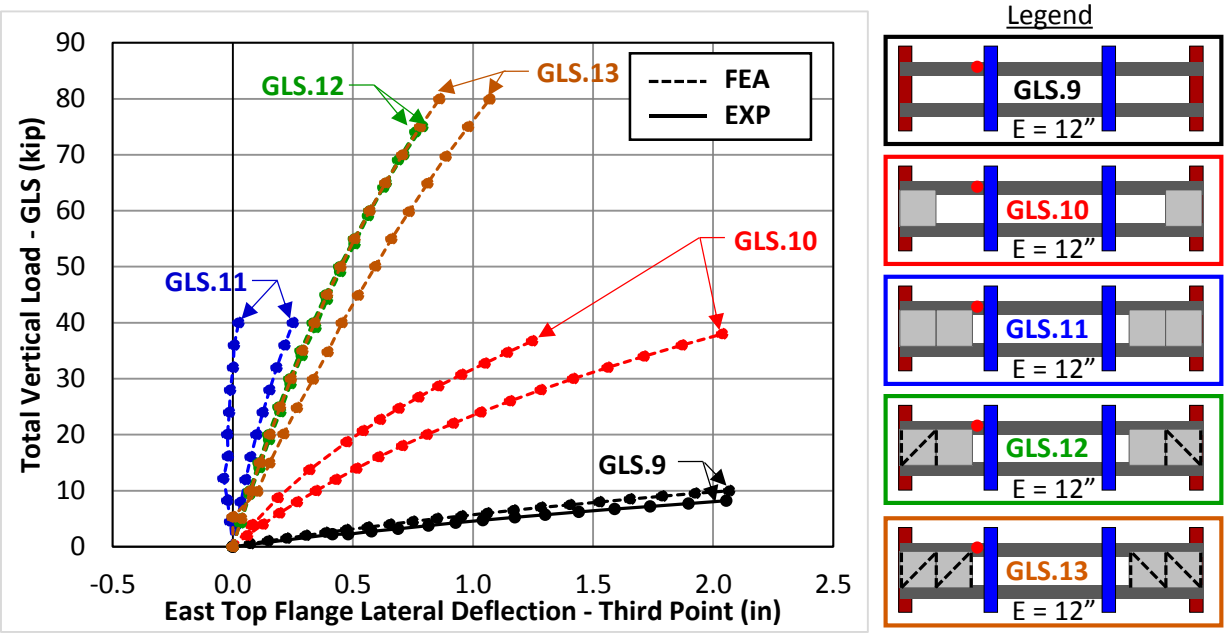

Figure D.36: Lateral Deflection @ Third Point vs. GLS Load (E=12" - SS - w/o XF) - East

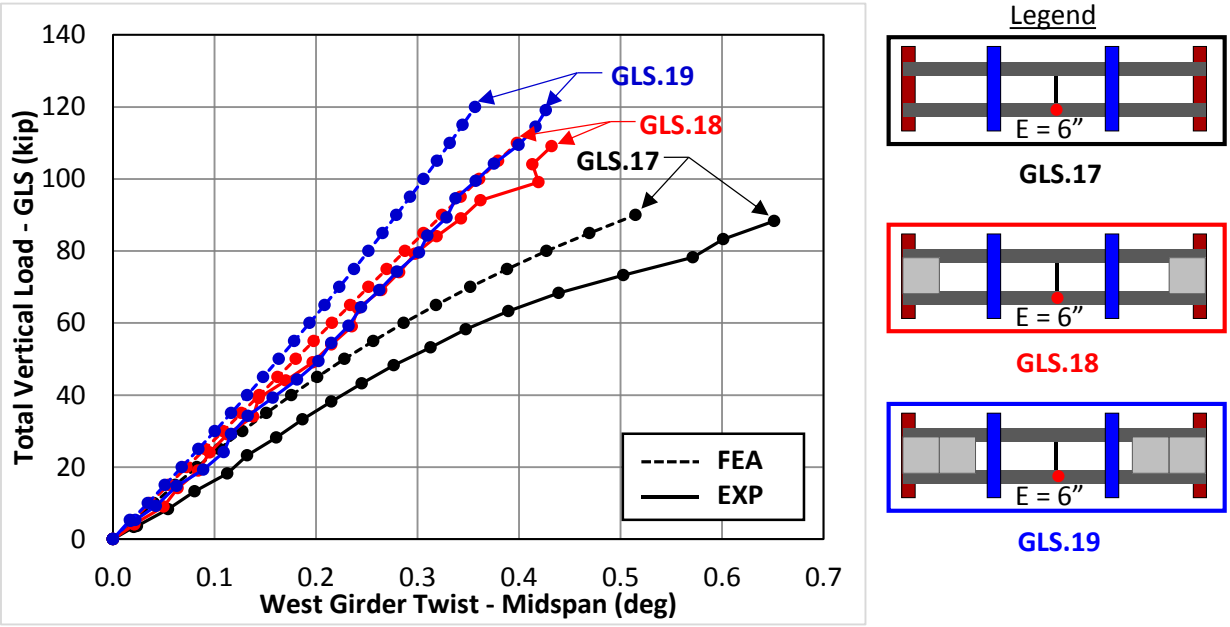

Figure D.37: Twist @ Midspan vs. GLS Load (E=6″ - SS - w/ XF) - West

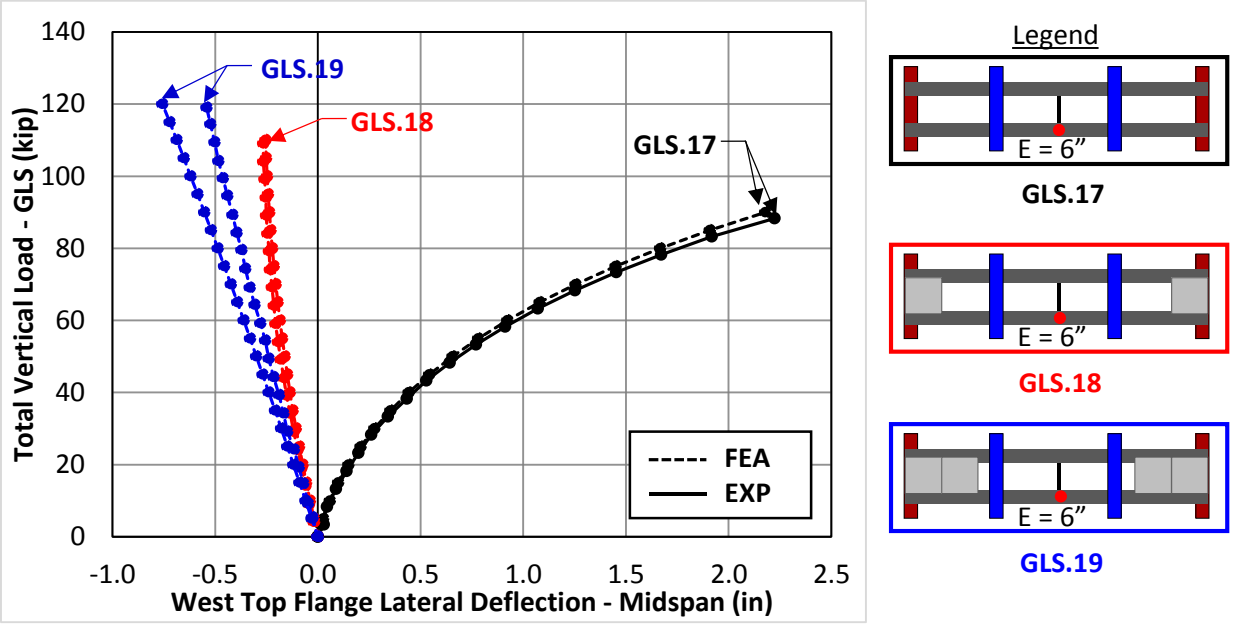

Figure D.38: Lateral Deflection @ Midspan vs. GLS Load (E=6″ - SS - w/ XF) - West

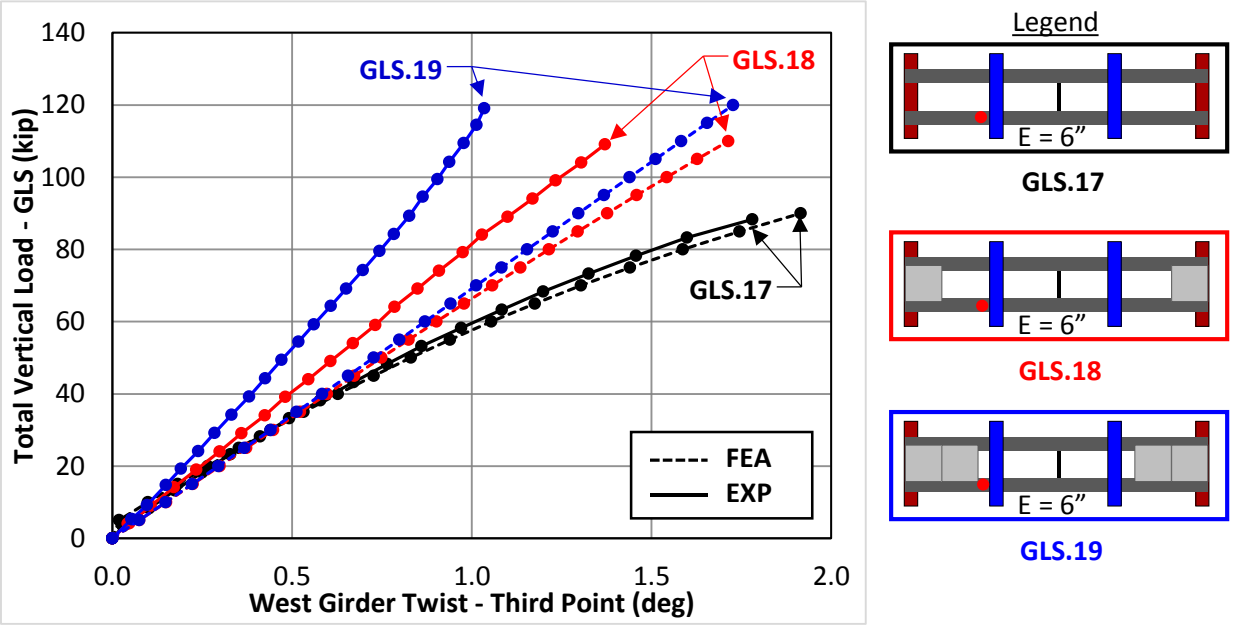

Figure D.39: Twist @ Third Point vs. GLS Load (E=6" - SS - w/ XF) - West

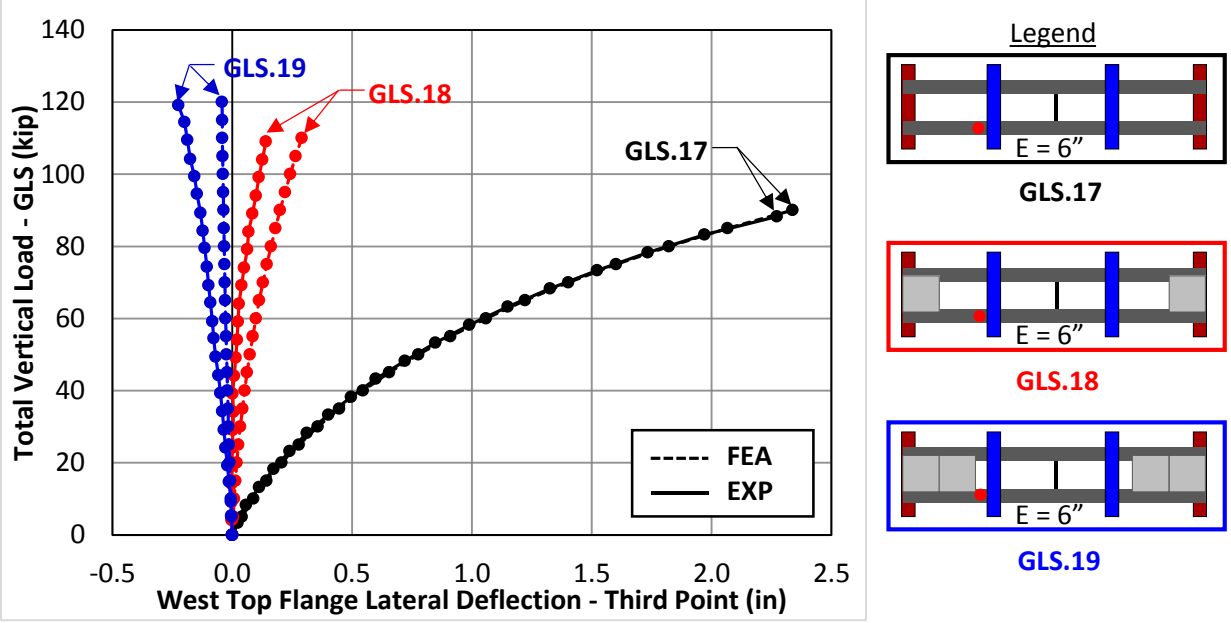

Figure D.40: Lateral Deflection @ Third Point vs. GLS Load (E=6" - SS - w/ XF) - West

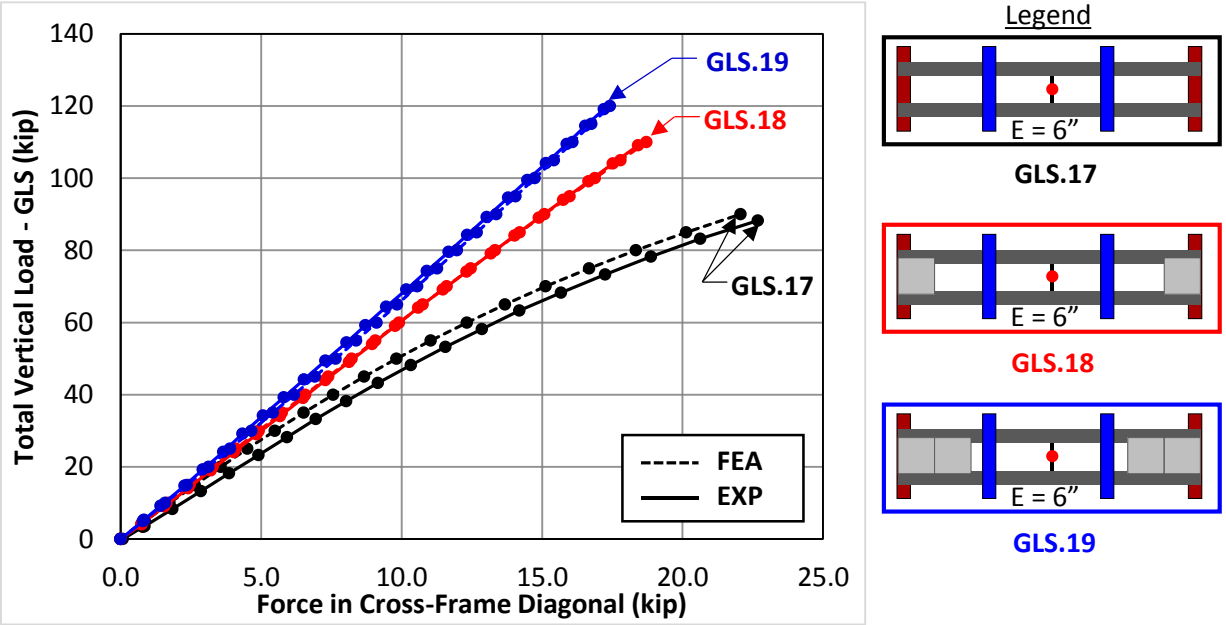

Figure D.41: Cross-Frame Diagonal Force vs. GLS Load (E=6" - SS)

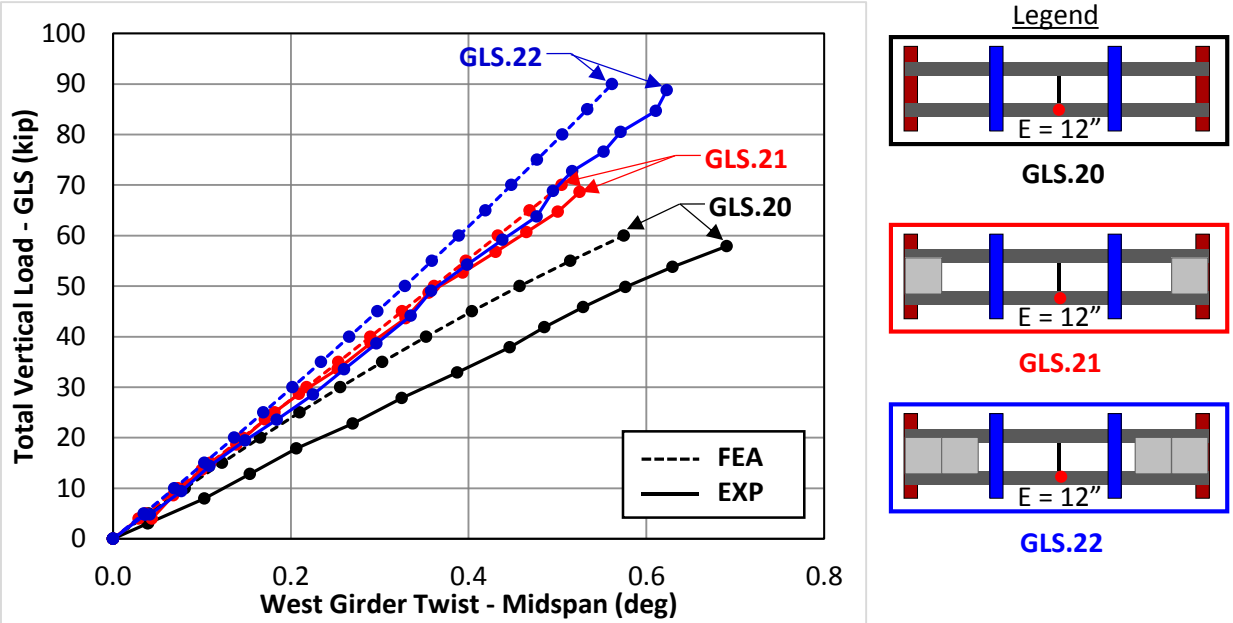

Figure D.42: Twist @ Midspan vs. GLS Load (E=12" - SS - w/ XF) - West

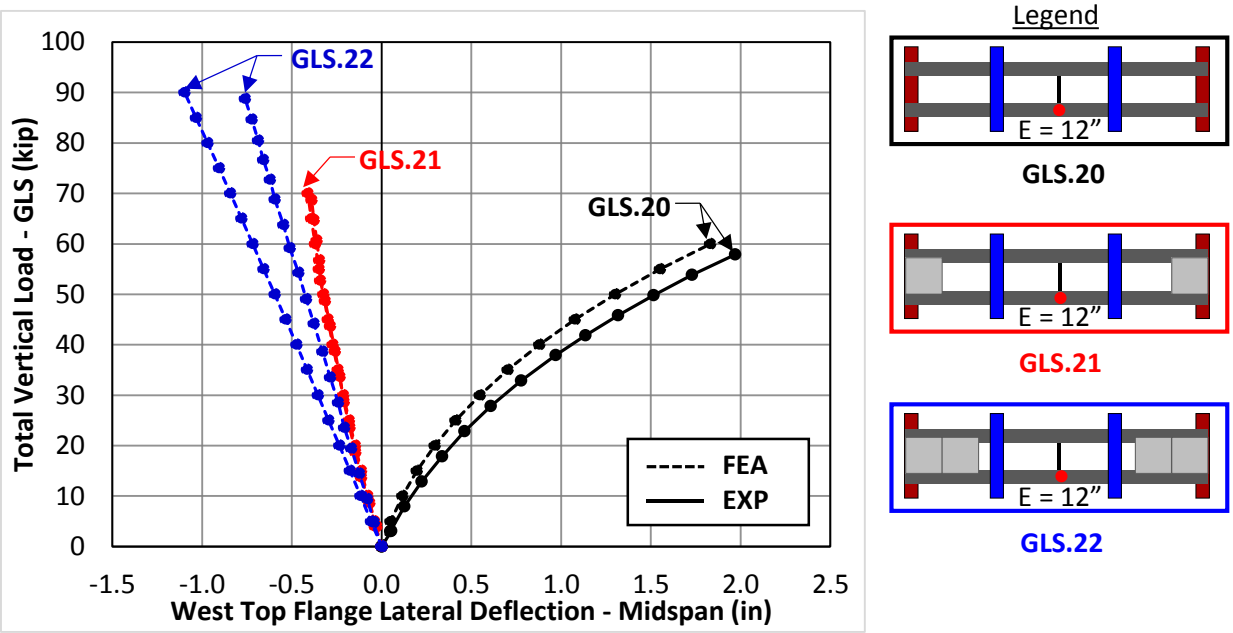

Figure D.43: Lateral Deflection @ Midspan vs. GLS Load (E=12" - SS - w/ XF) - West

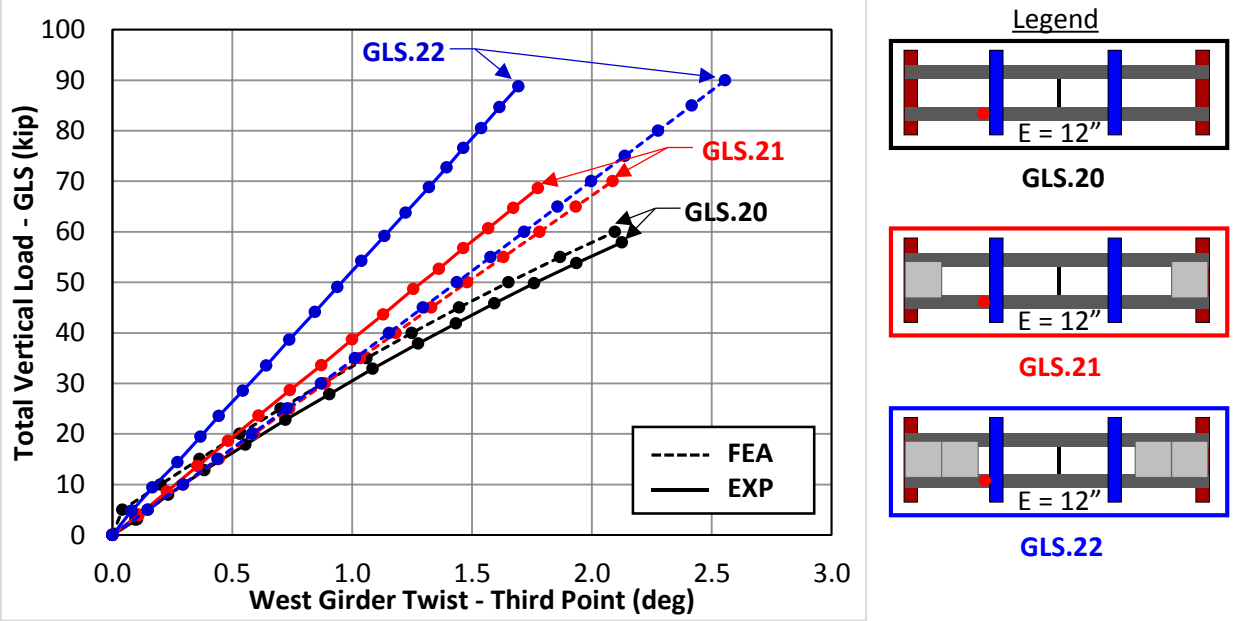

Figure D.44: Twist @ Third Point vs. GLS Load (E=12" - SS - w/ XF) - West

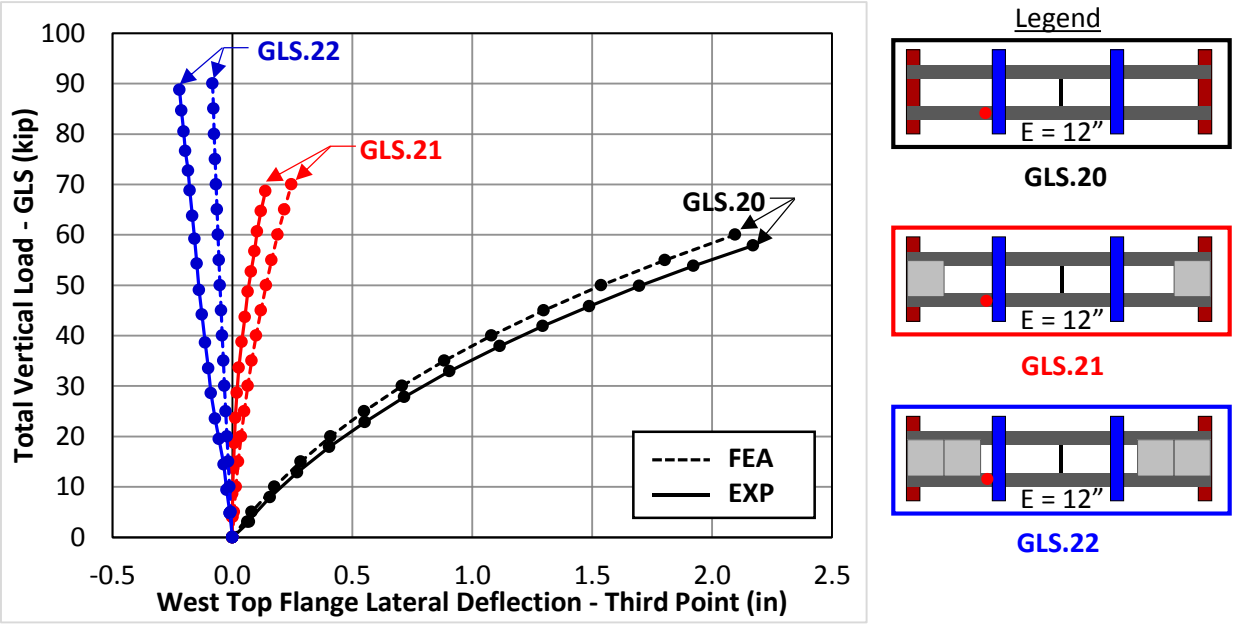

Figure D.45: Lateral Deflection @ Third Point vs. GLS Load (E=12" - SS- w/ XF) - West

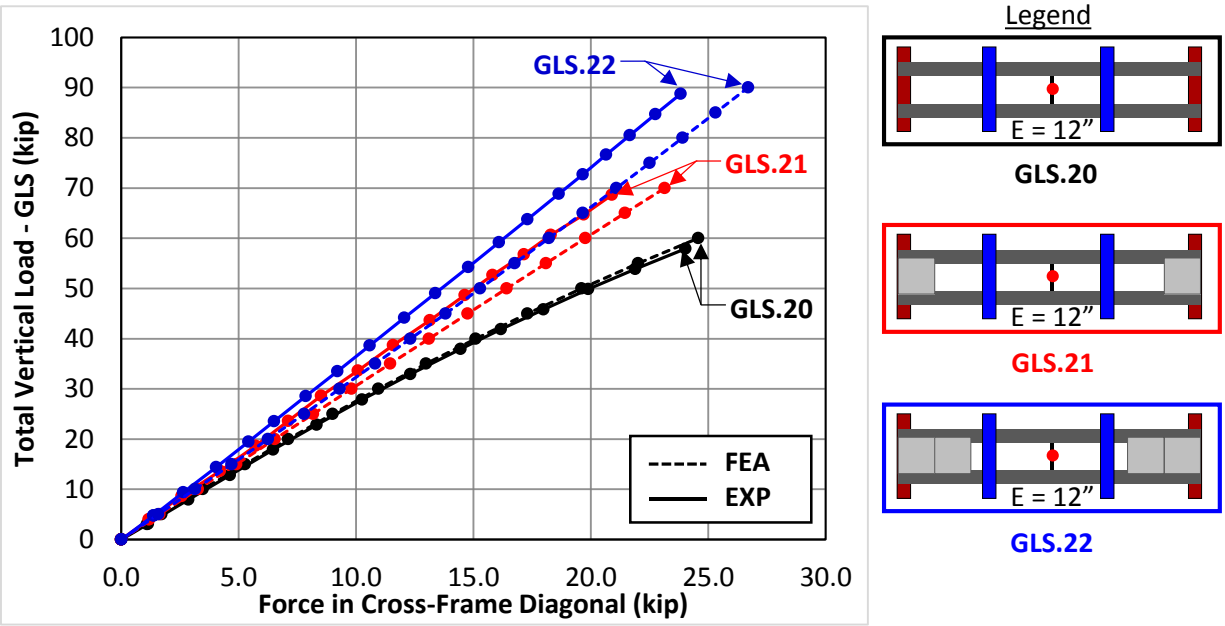

Figure D.46: Cross-Frame Diagonal Force vs. GLS Load (E=12" - SS) - West

D.3 FEA Validation with Experimental Results for Combined Bending and Torsion Overhang I-Girder Tests

Table D.3: Summary of Bending and Torsion Overhang I-Girder Tests

Test Name	Support Condition	GLS North Eccentricity	GLS North Eccentricity	Number of PCPS	Max Total GLS Load
GLS.23	OH	-2"	4"	4	140
GLS.24	OH	-4"	8"	4	100
GLS.25	OH	2"	4"	4	170
GLS.26	OH	4"	8"	4	120
GLS.27	OH	-4"	0"	4	300

Key: GLS = Gravity Load Simulator Load, OH = Overhang

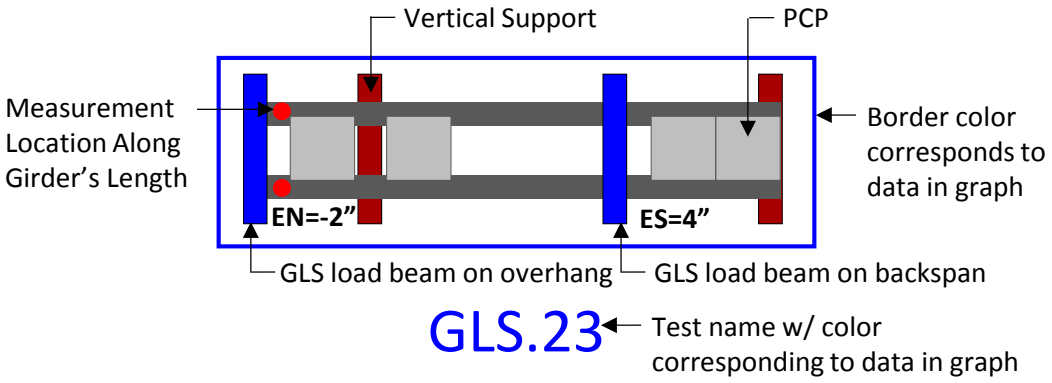

Figure D.47: Nomenclature for Documentation of GLS Overhang I-Girder Tests

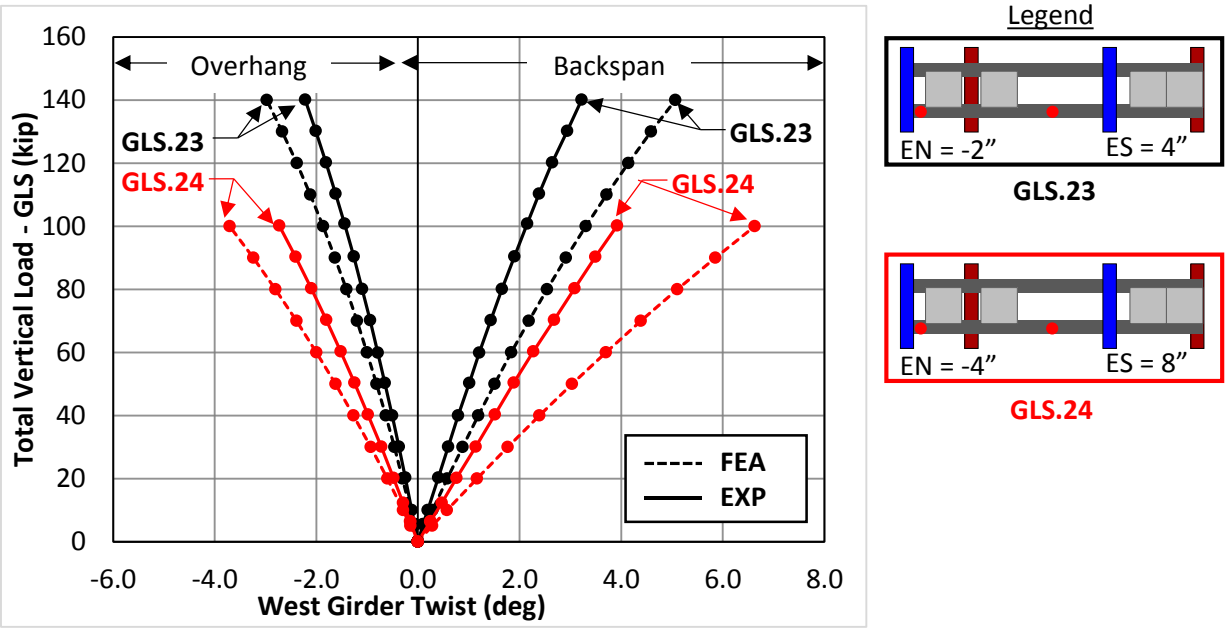

Figure D.48: Twist @ Overhang and Backspan vs. GLS Load (Opposite Eccentricity) - West

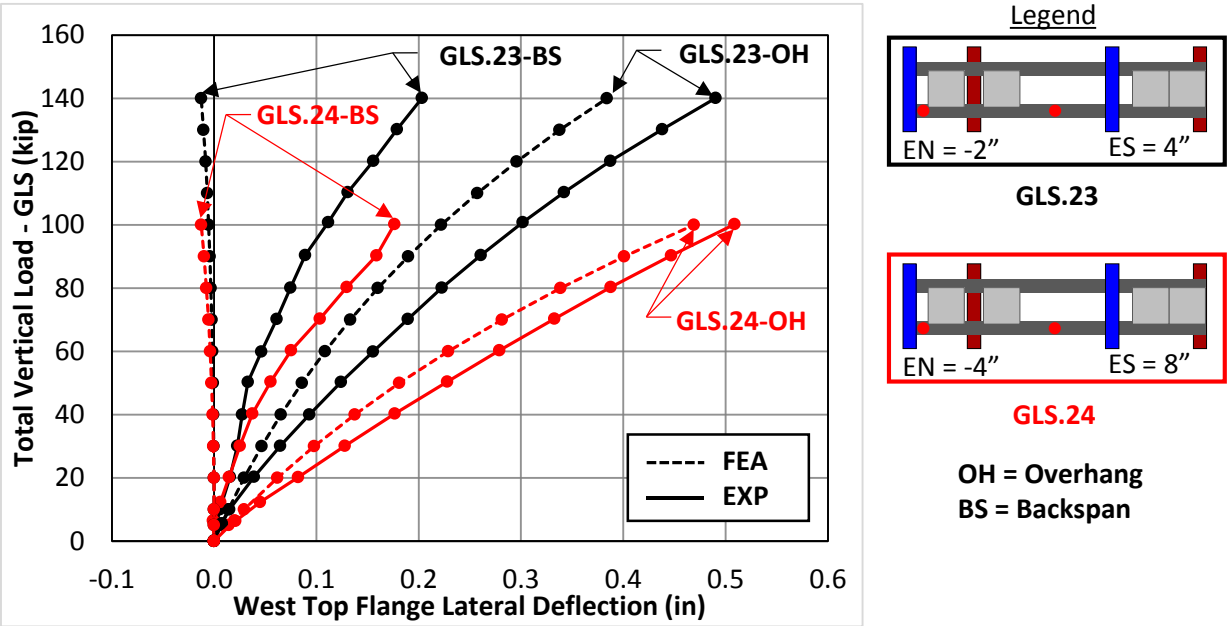

Figure D.49: Lateral Deflection @ Overhang and Backspan vs. GLS Load (Opposite Eccentricity) - West

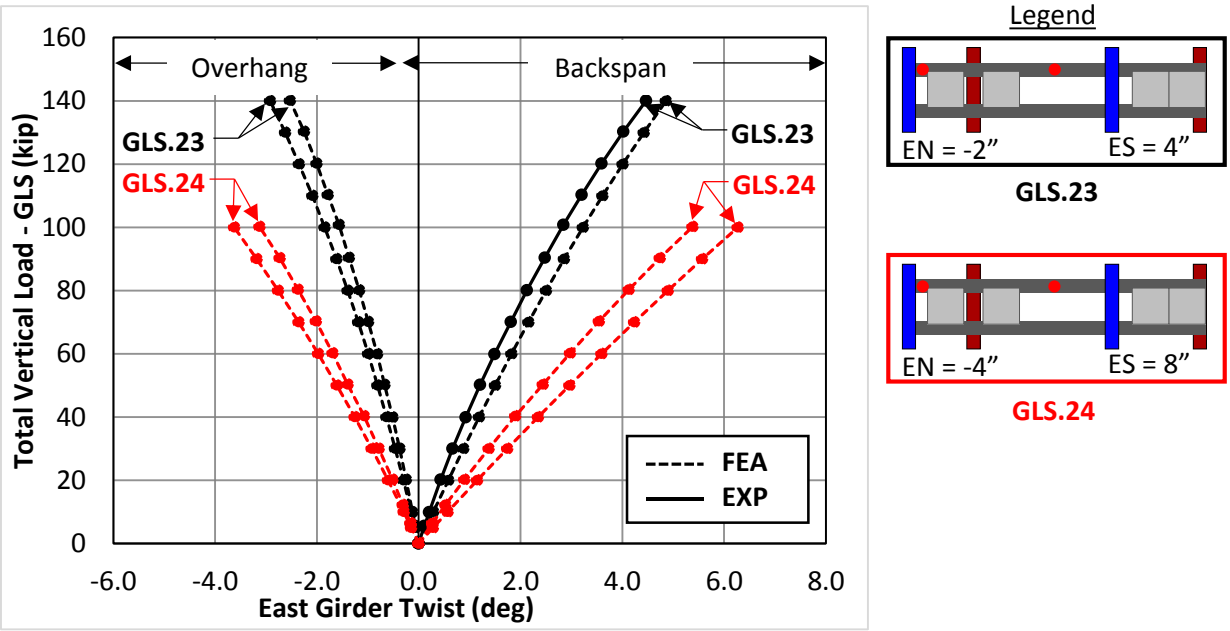

Figure D.50: Twist @ Overhang and Backspan vs. GLS Load (Opposite Eccentricity) - East

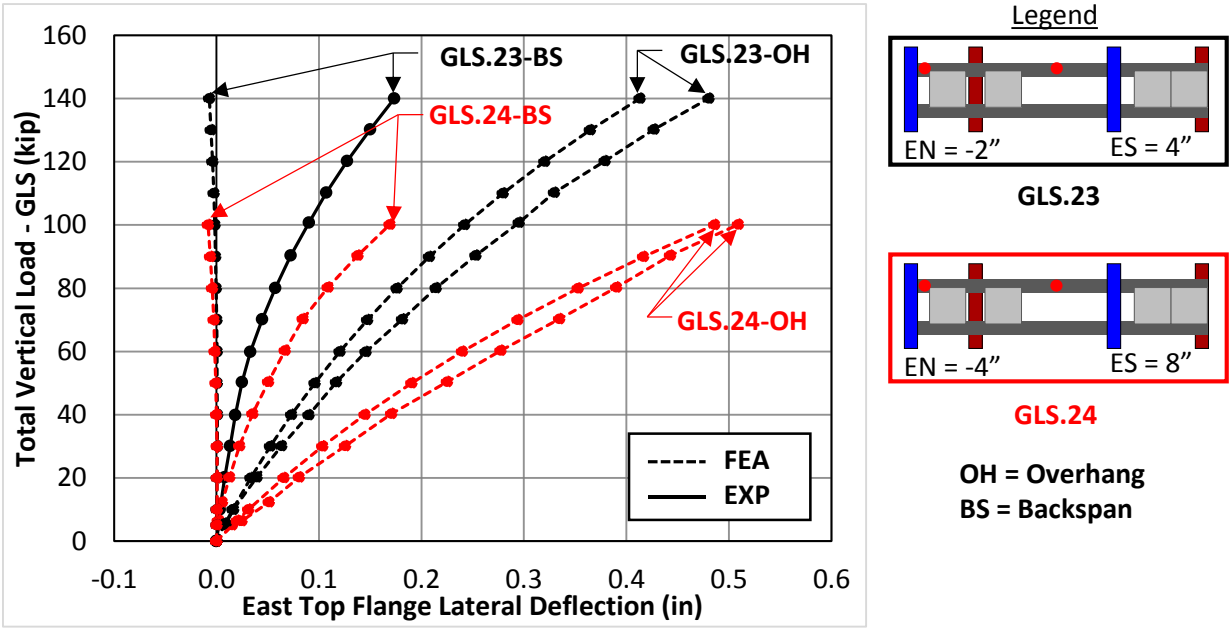

Figure D.51: Lateral Deflection @ Overhang and Backspan vs. GLS Load (Opposite Eccentricity) - East

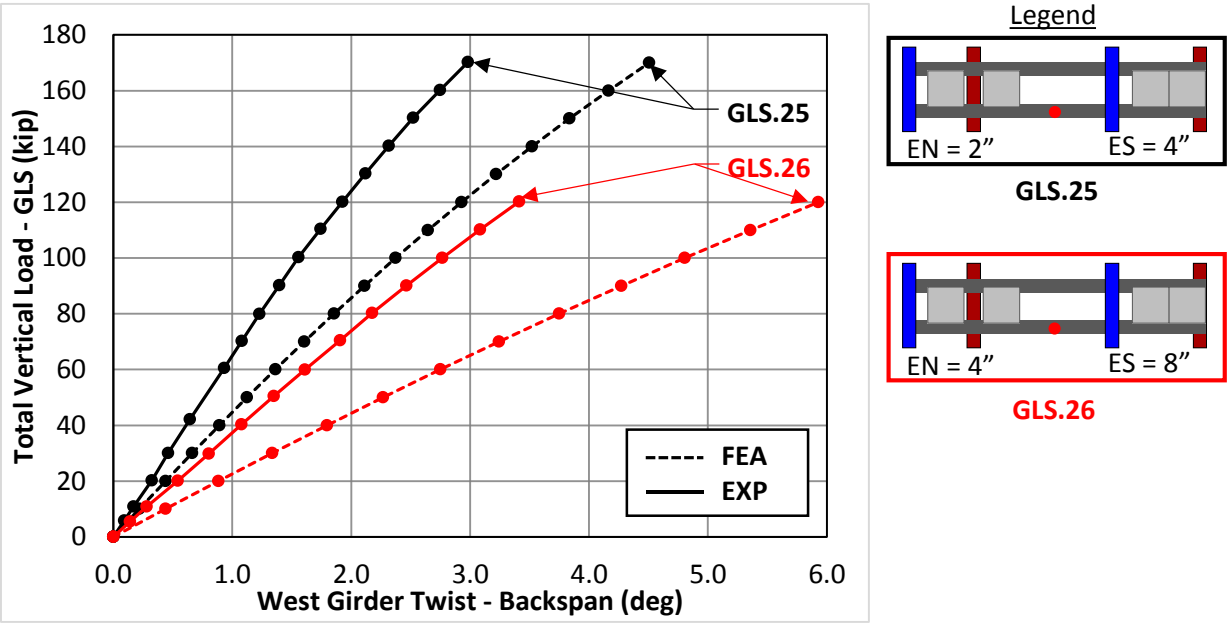

Figure D.52: Twist @ Backspan vs. GLS Load (Same Eccentricity Direction) - West

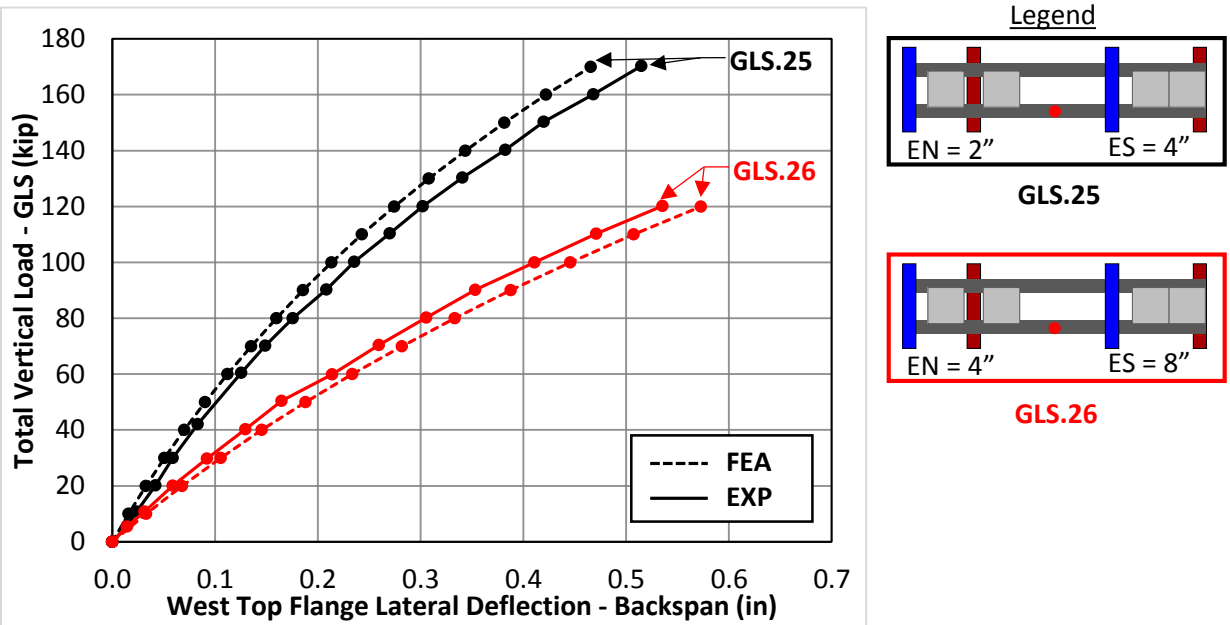

Figure D.53: Lateral Deflection @ Backspan vs. GLS Load (Same Eccentricity Direction) - West

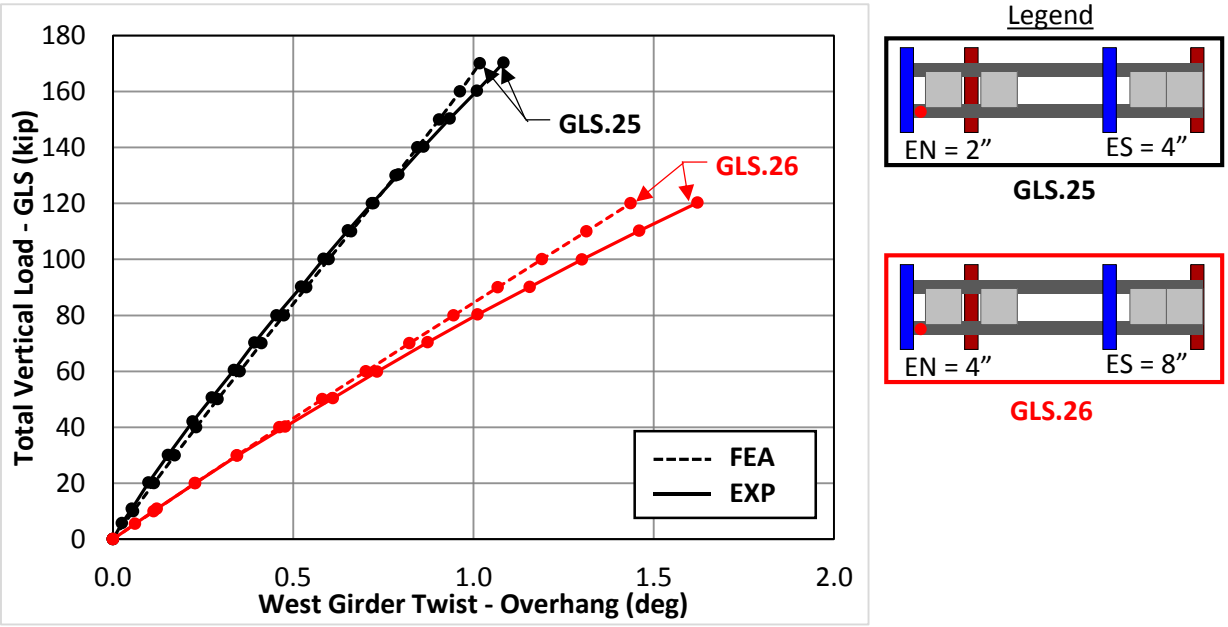

Figure D.54: Twist @ Backspan vs. GLS Load (Same Eccentricity Direction) - West

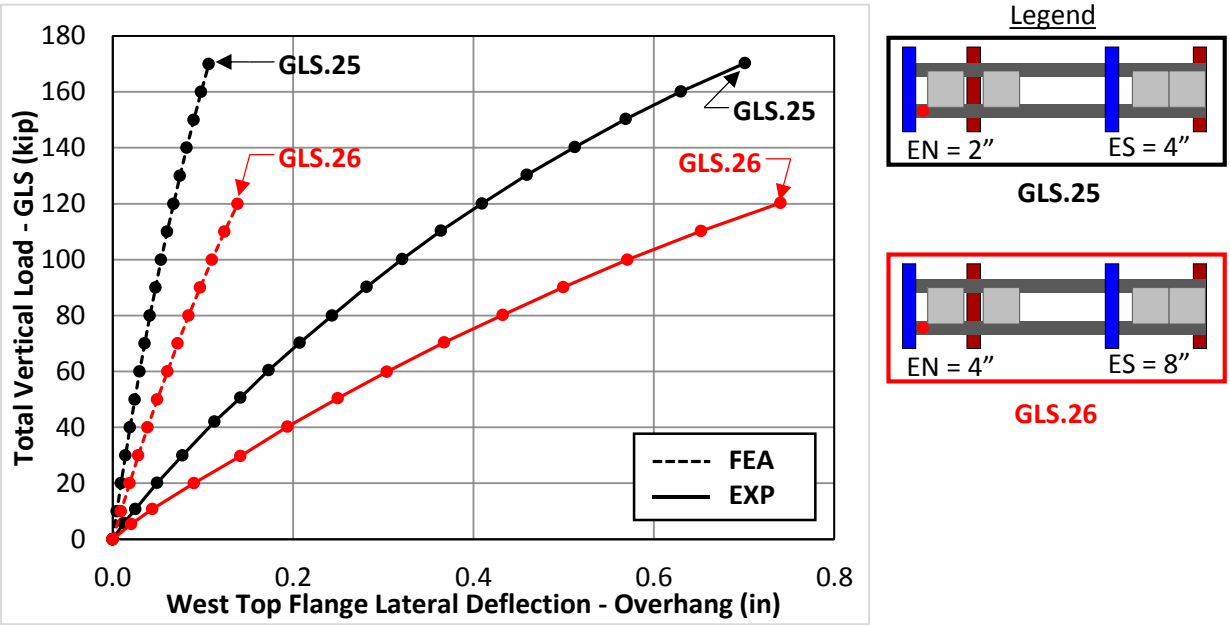

Figure D.55: Lateral Deflection @ Backspan vs. GLS Load (Same Eccentricity Direction) - West

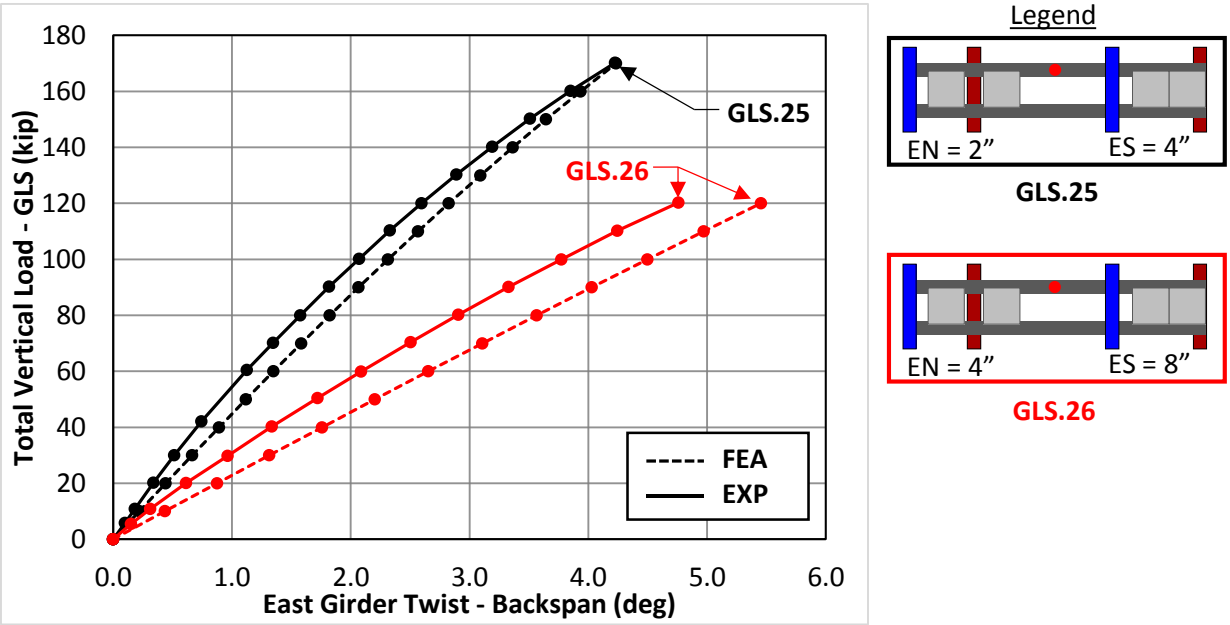

Figure D.56: Twist @ Overhang vs. GLS Load (Same Eccentricity Direction) - East

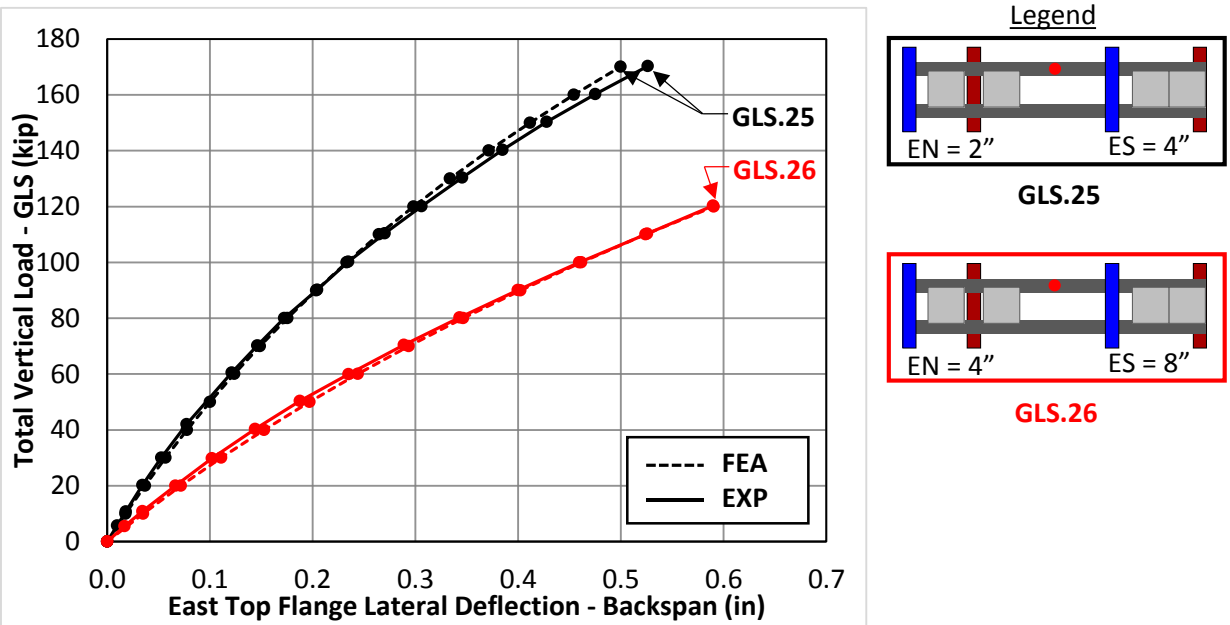

Figure D.57: Lateral Deflection @ Overhang vs. GLS Load (Same Eccentricity Direction) - East

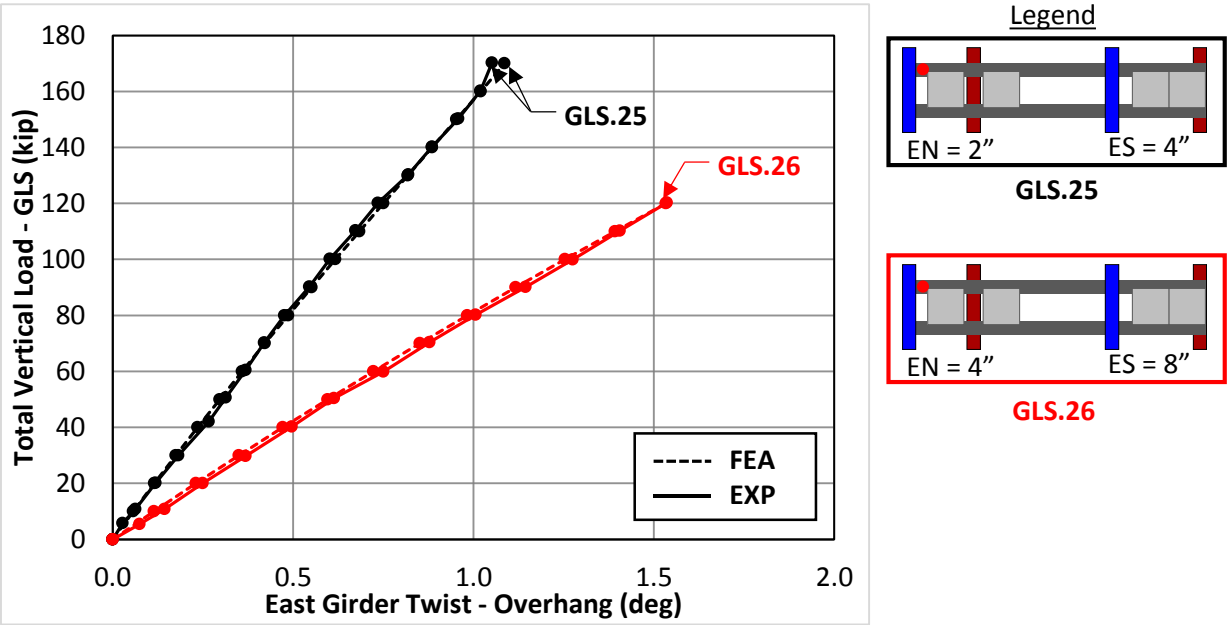

Figure D.58: Twist @ Overhang vs. GLS Load (Same Eccentricity Direction) - East

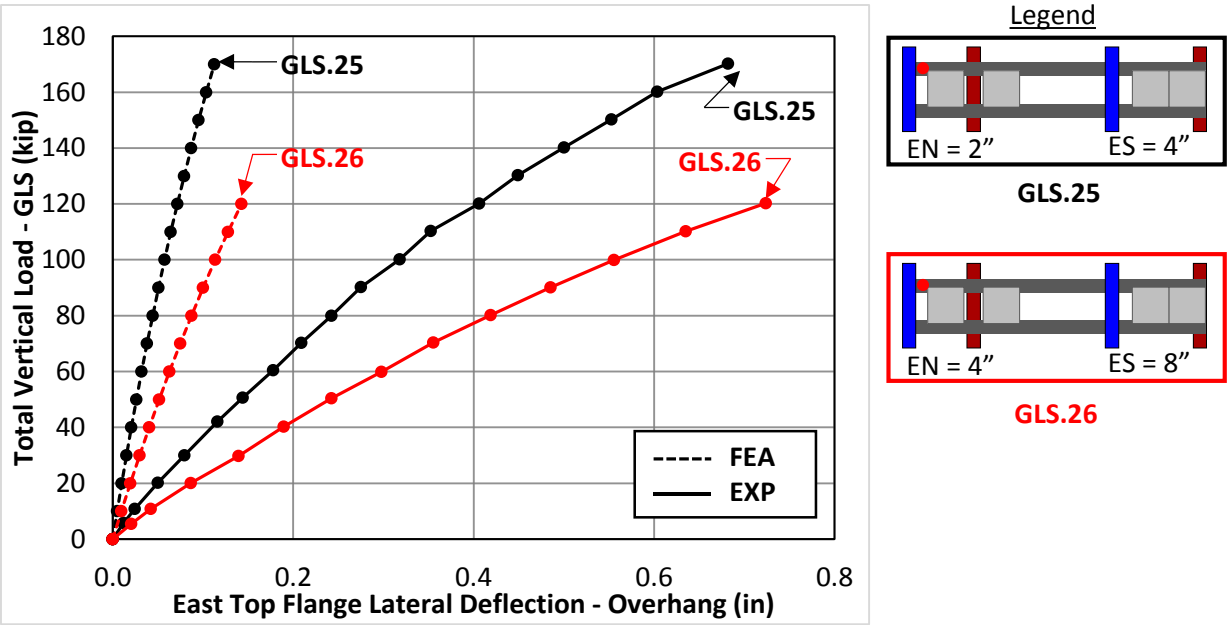

Figure D.59: Lateral Deflection @ Overhang vs. GLS Load (Same Eccentricity Direction) - East

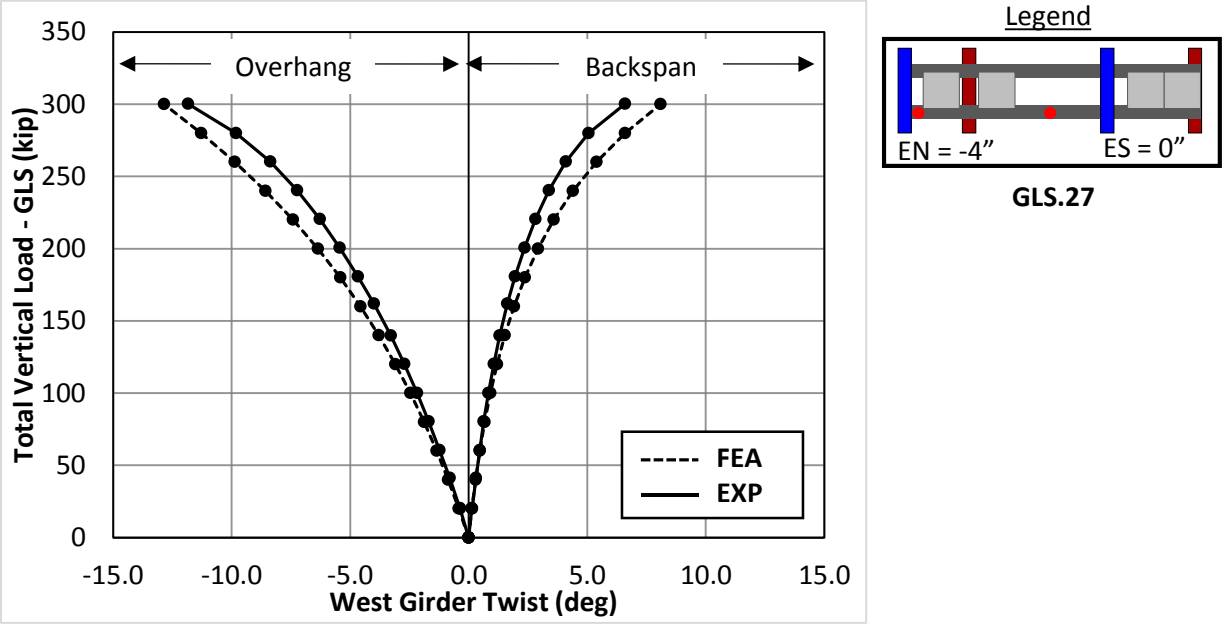

Figure D.60: Twist @ Overhang and Backspan vs. GLS Load (Maximum Load Test) - West

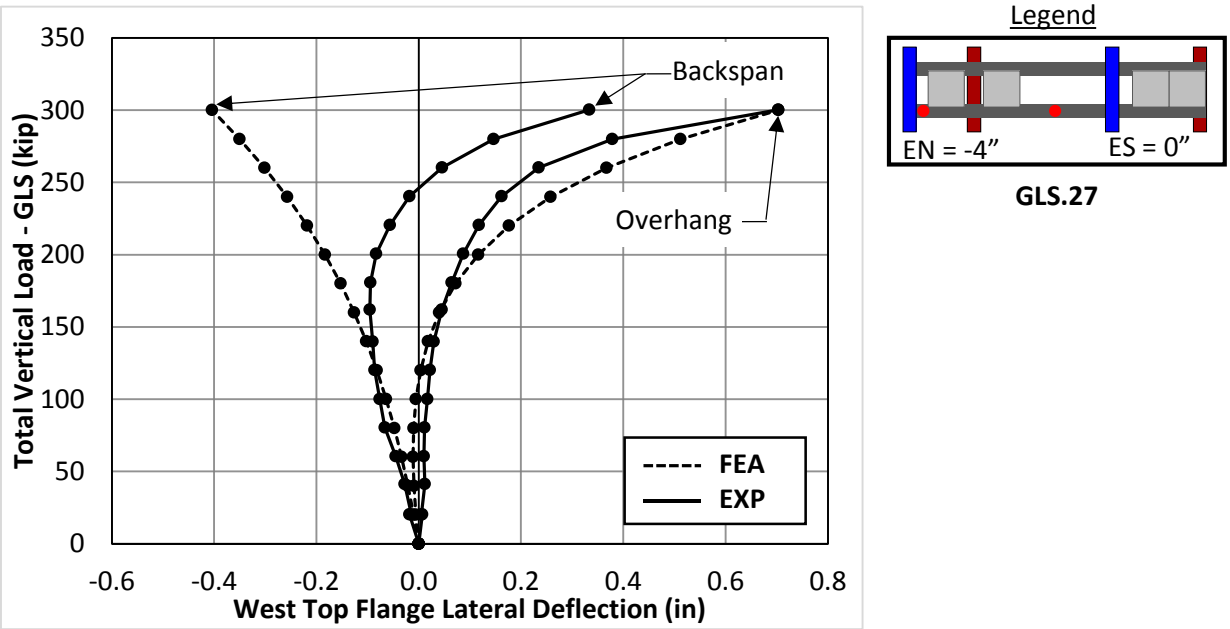

Figure D.61: Lateral Deflection @ Overhang and Backspan vs. GLS Load (Maximum Load Test) - West

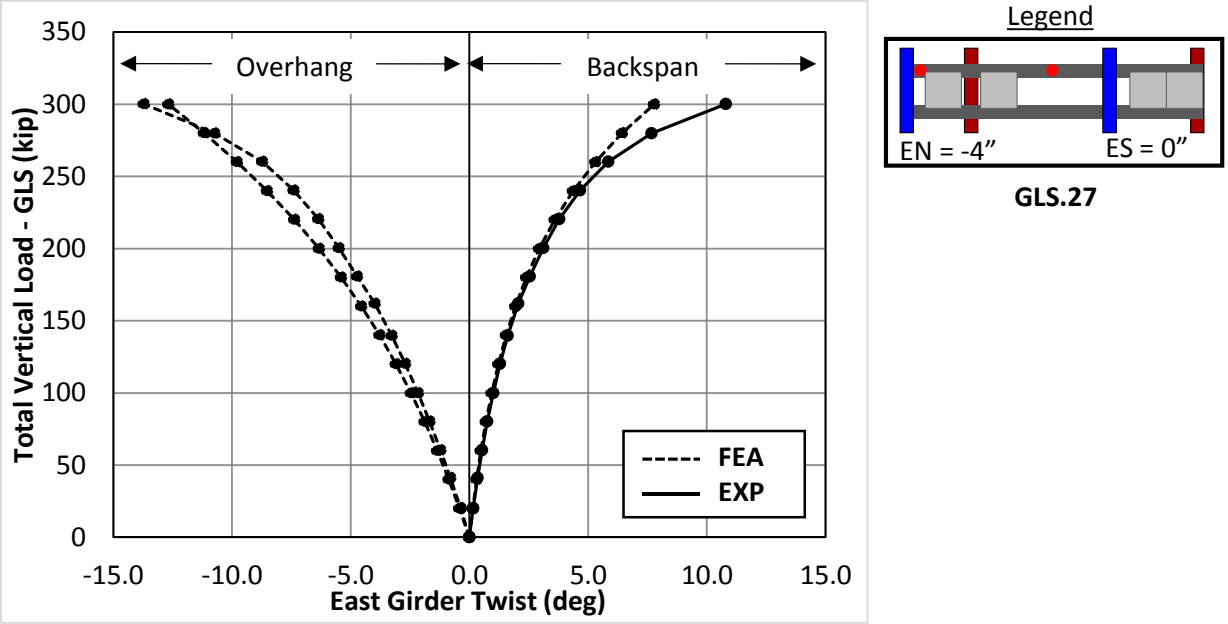

Figure D.62: Twist @ Overhang and Backspan vs. GLS Load (Maximum Load Test) - East

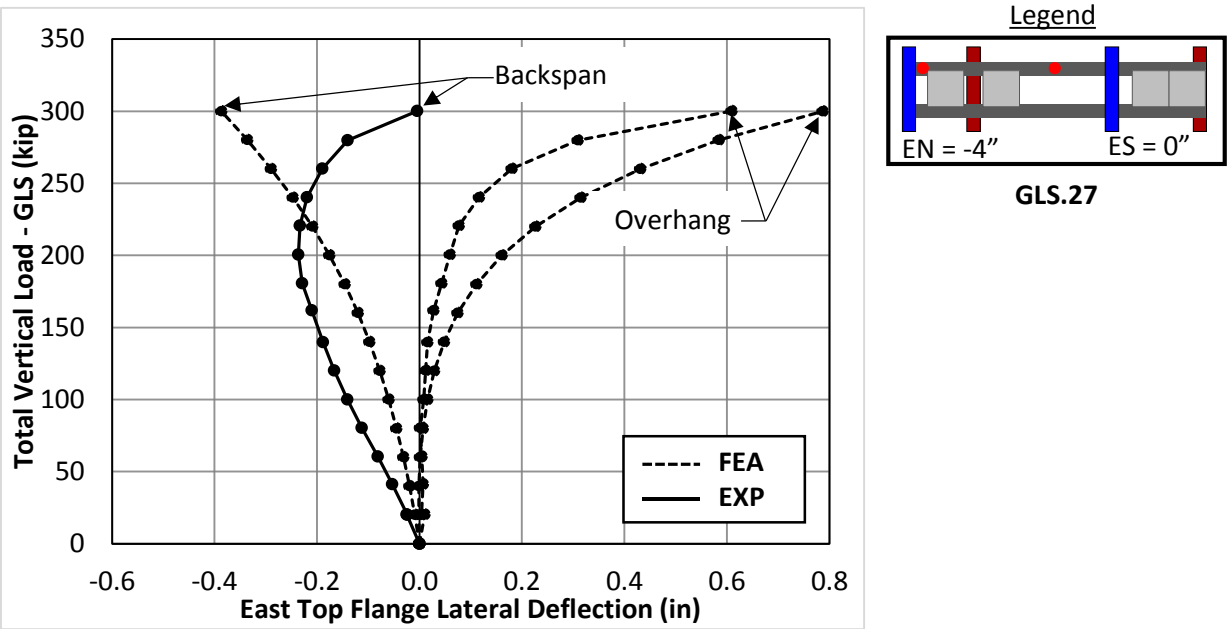

Figure D.63: Lateral Deflection @ Overhang and Backspan vs. GLS Load (Maximum Load Test) - East

D.4 Estimated PCP Shear Force from I-Girder FE Models

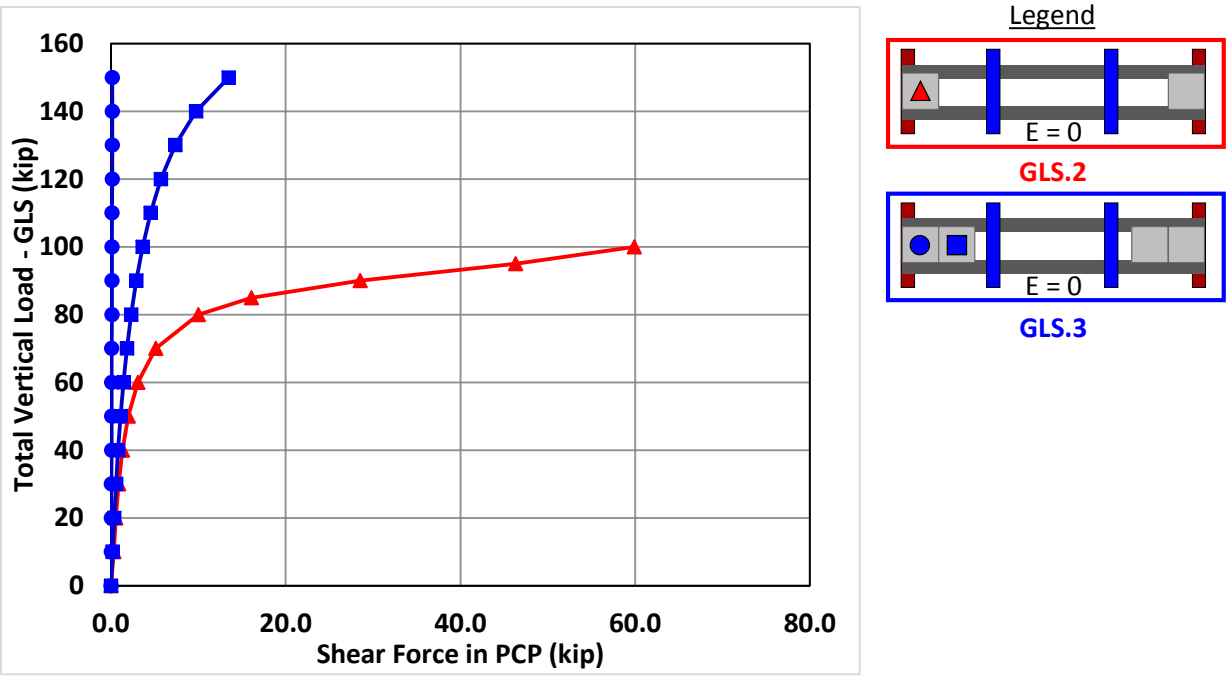

Figure D.64: Estimated Shear in PCP vs. GLS Load (E=0")

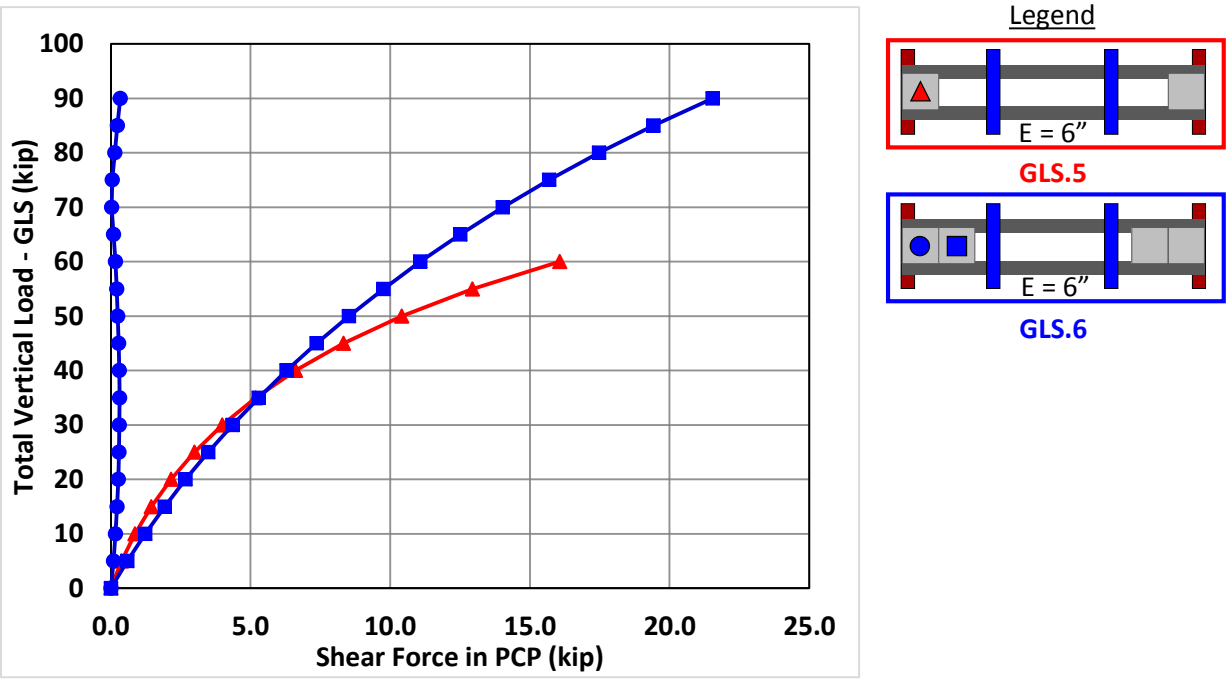

Figure D.65: Estimated Shear in PCP vs. GLS Load (E=6")

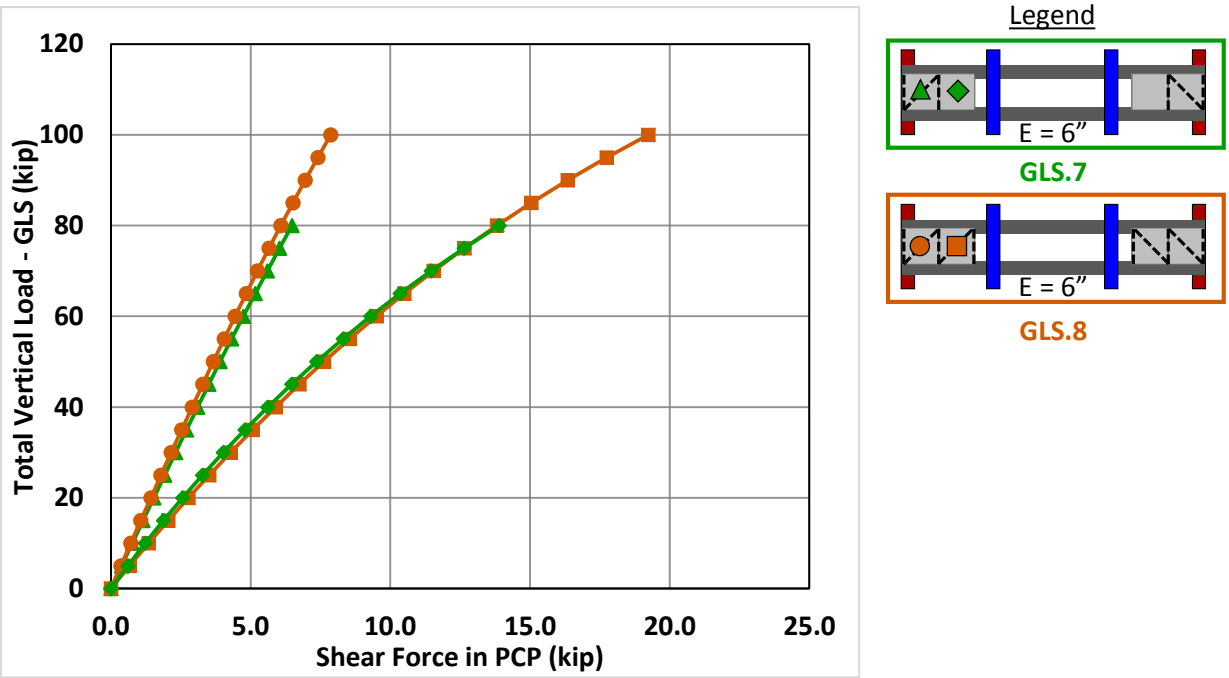

Figure D.66: Estimated Shear in PCP vs. GLS Load (E=6") – Bottom Flange Truss

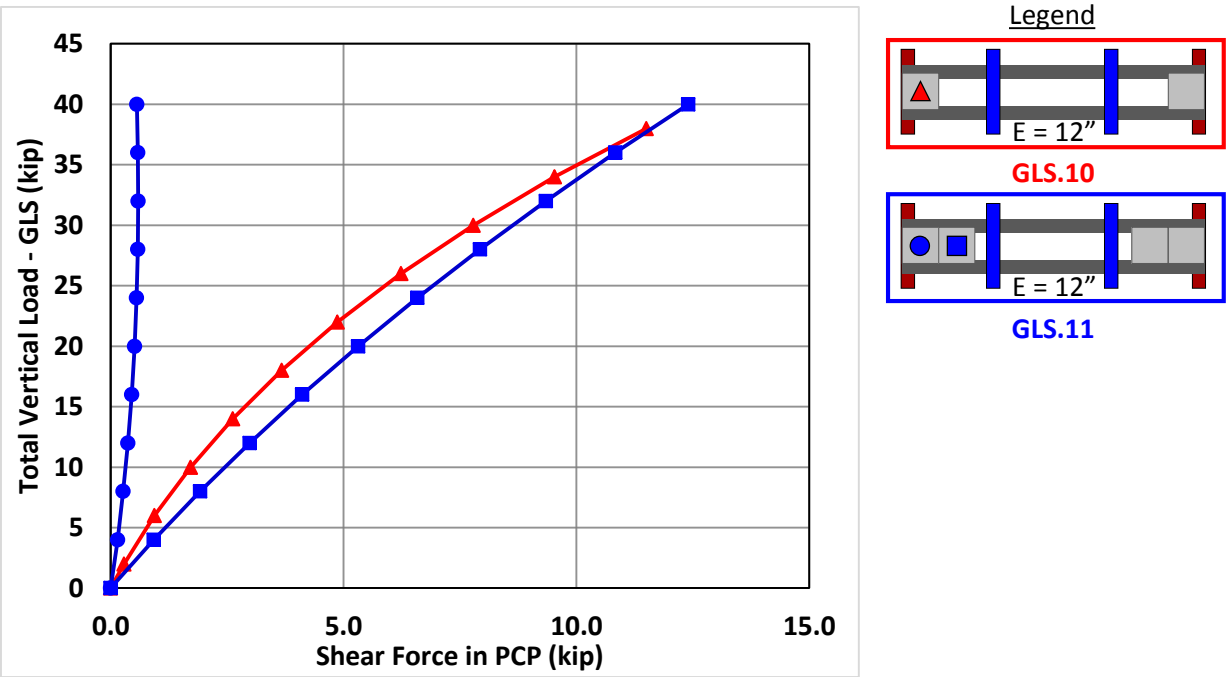

Figure D.67: Estimated Shear in PCP vs. GLS Load (E=12")

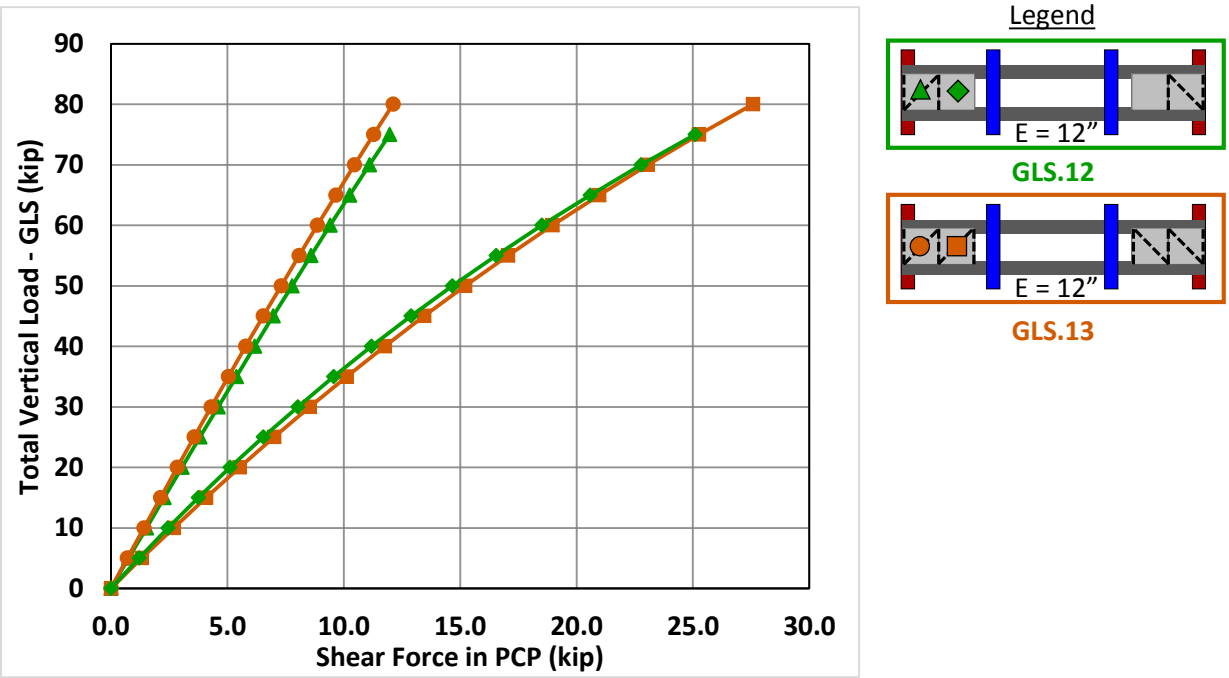

Figure D.68: Estimated Shear in PCP vs. GLS Load (E=12") – Bottom Flange Truss

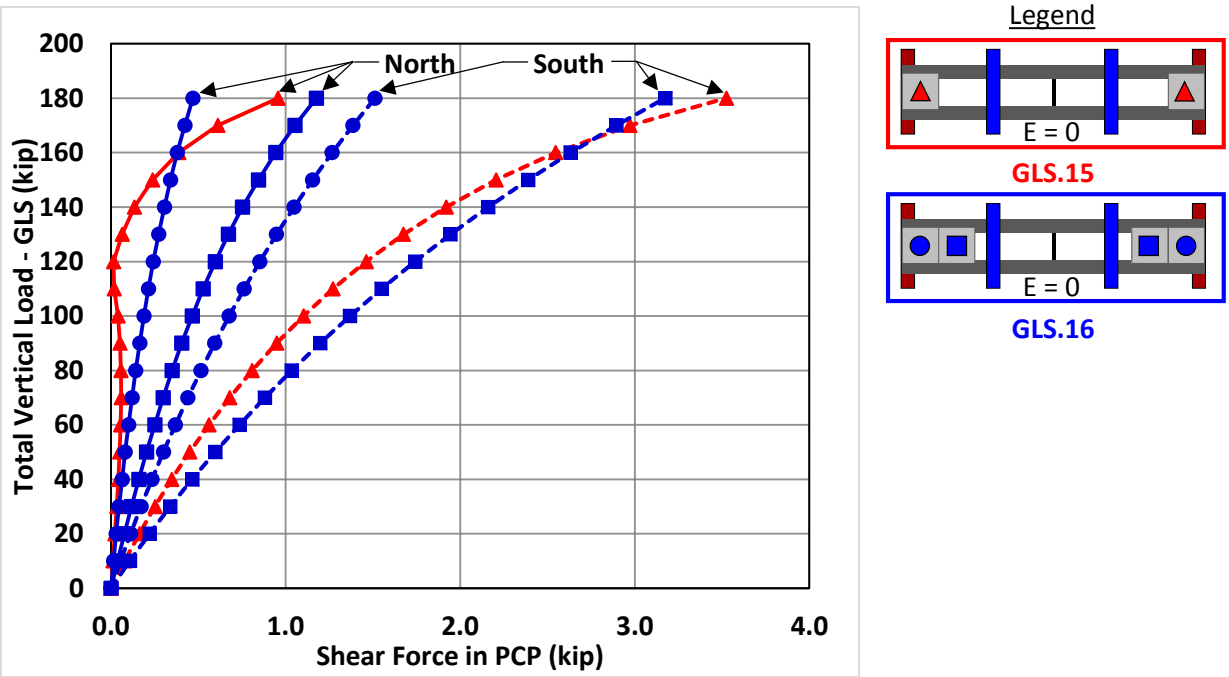

Figure D.69: Estimated Shear in PCP vs. GLS Load (E=0") – with XF

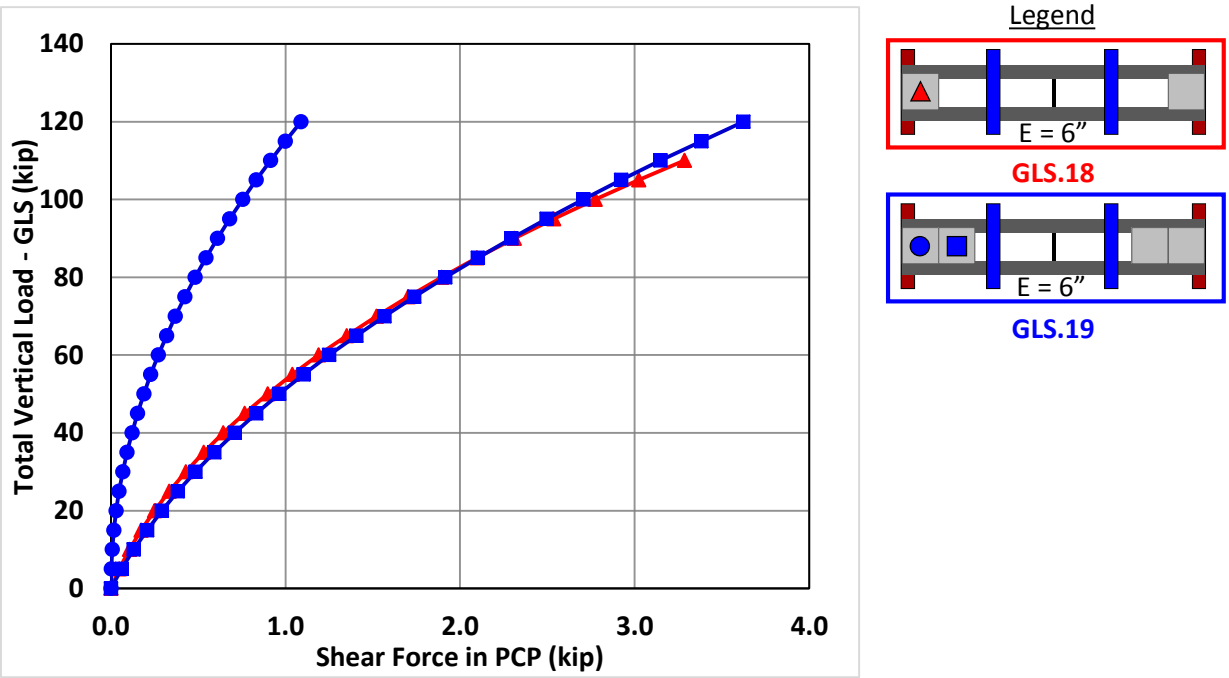

Figure D.70: Estimated Shear in PCP vs. GLS Load (E=6") – with XF

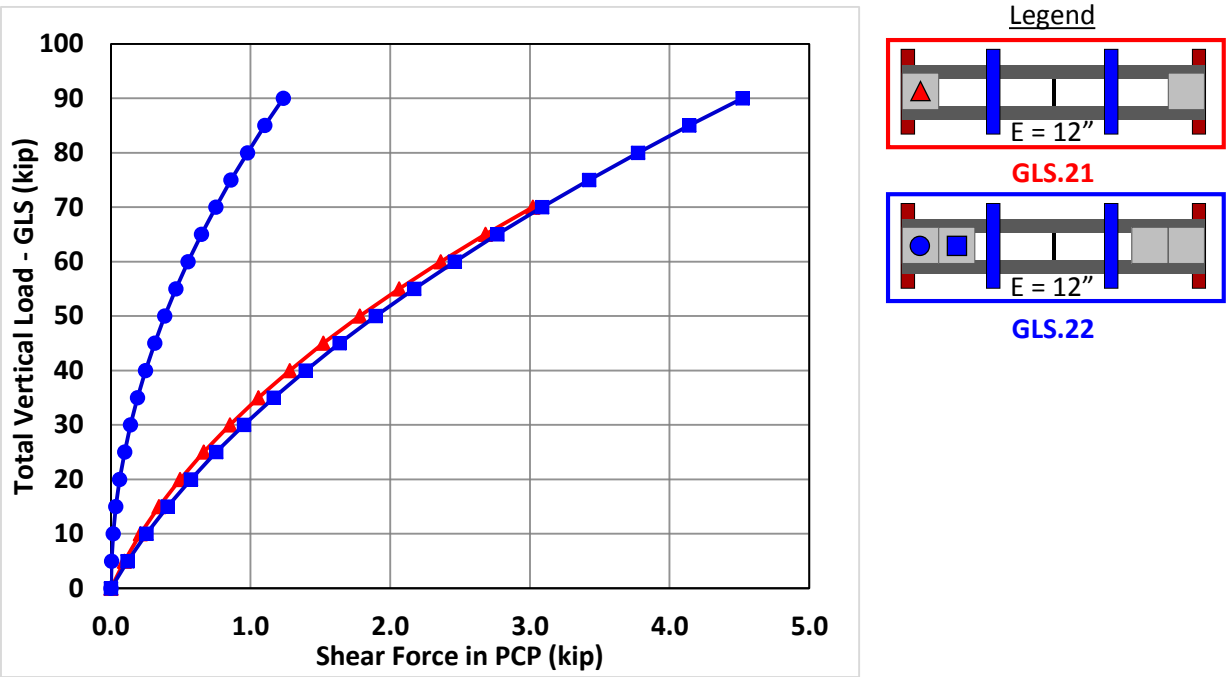

Figure D.71: Estimated Shear in PCP vs. GLS Load (E=12") – with XF

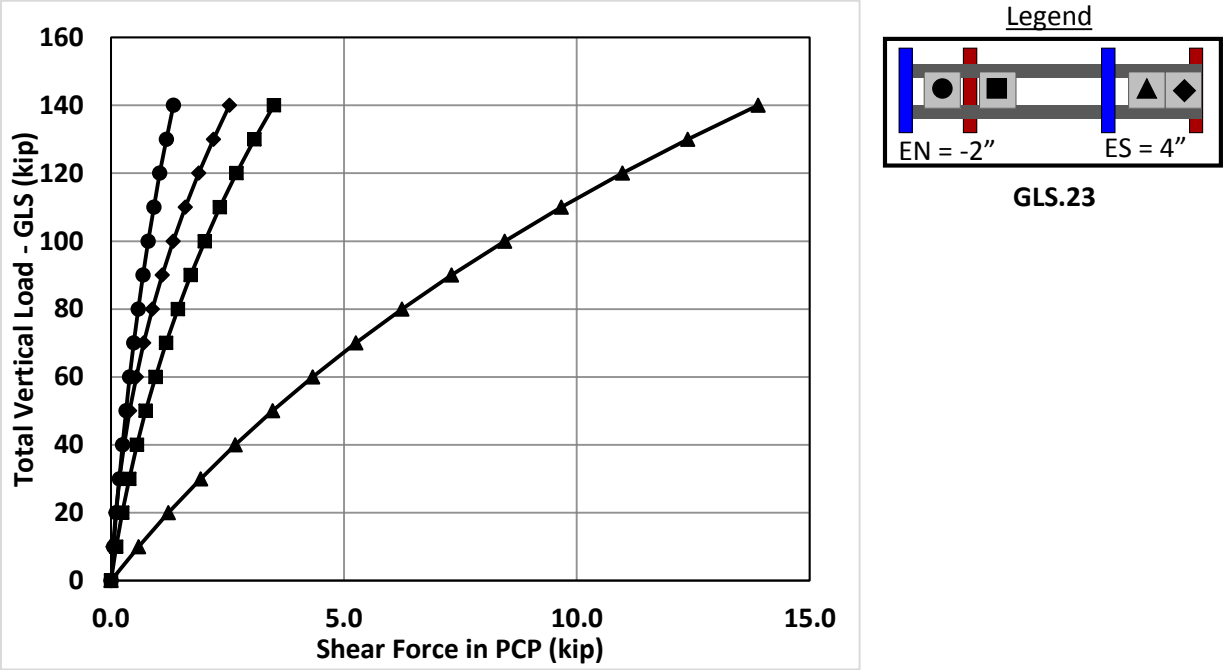

Figure D.72: Estimated Shear in PCP vs. GLS Load (Opposite Eccentricity) - Overhang

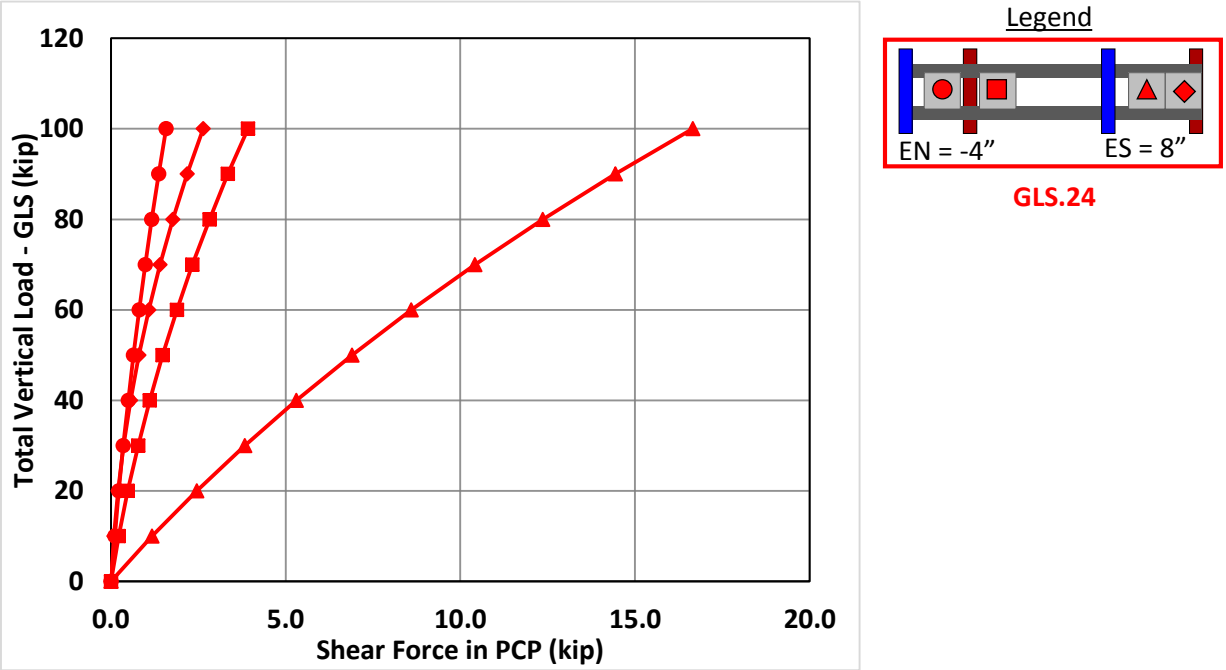

Figure D.73: Estimated Shear in PCP vs. GLS Load (Opposite Eccentricity) - Overhang

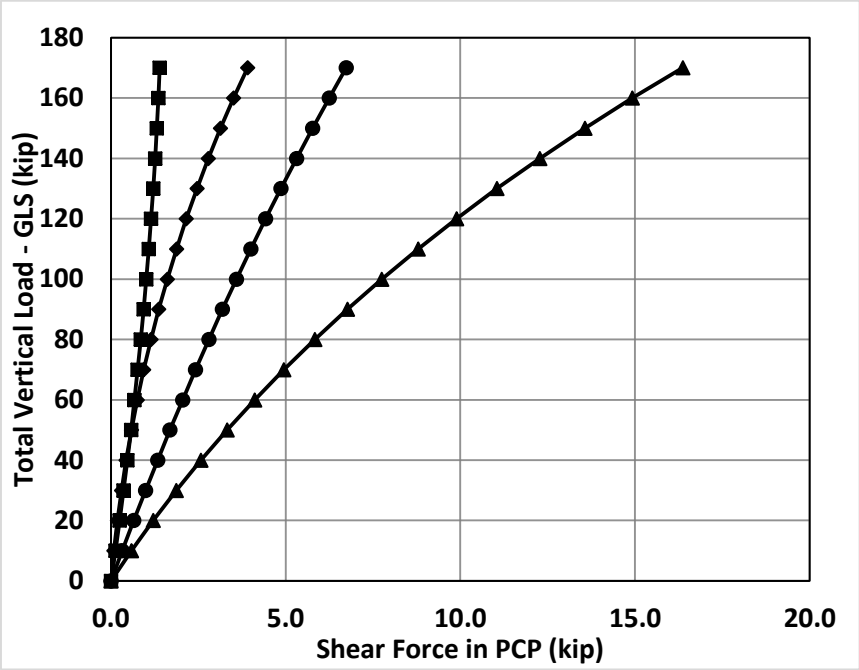

Figure D.74: Estimated Shear in PCP vs. GLS Load (Same Eccentricity) - Overhang

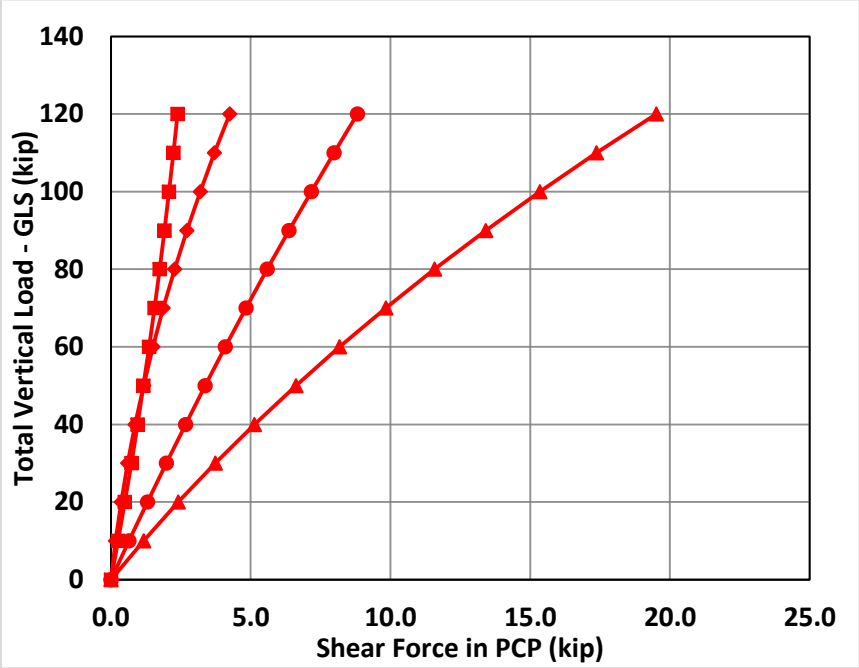

Figure D.75: Estimated Shear in PCP vs. GLS Load (Same Eccentricity) - Overhang

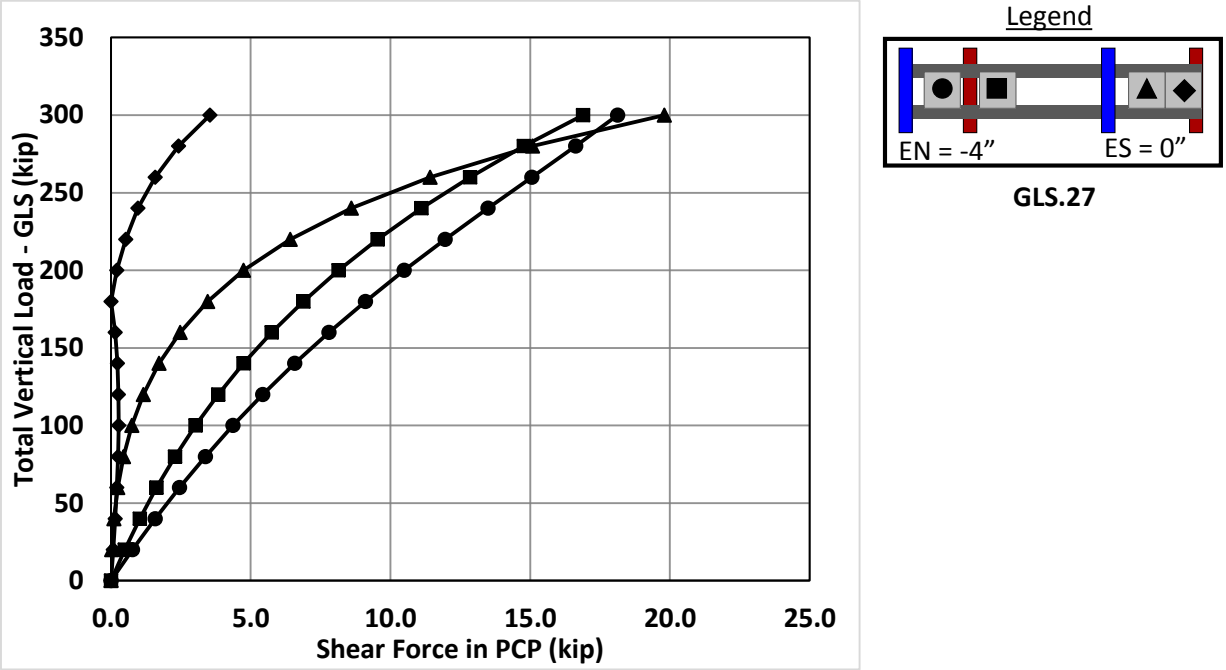

Figure D.76: Estimated Shear in PCP vs. GLS Load (Maximum Load Test) - Overhang

Appendix E. Tub Girder FEA Validation with Experimental Results

E.1 FEA Validation with Experimental Results for Lateral Load Tub Girder Tests

Table E.1: Summary of Lateral Tub Girder Tests

Test Name	Load Loacation	K-Frame Location	Number of Braces
LAT.1	TP	2-Panel	0
LAT.2	TP	2-Panel	2 PCP
LAT.3	TP	2-Panel	4 PCP
LAT.4	TP	2-Panel	2 DIAG
LAT.5	TP	2-Panel	4 DIAG

Key: LAT = Top & Bottom Flange Lateral Load
TP = Third Point Loading, DIA = Diagonal

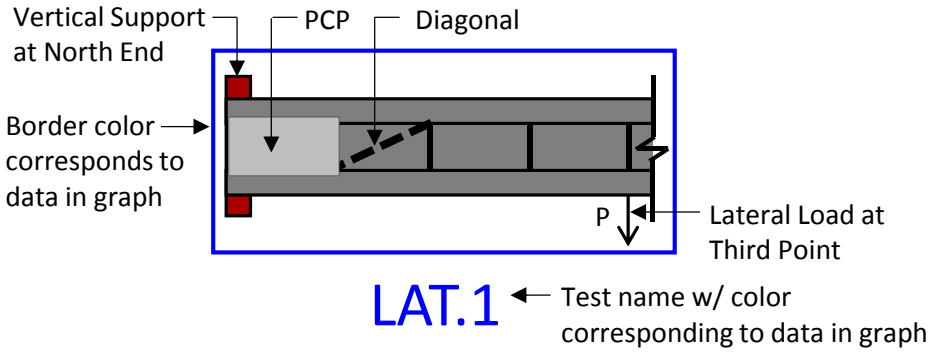

Figure E.1: Nomenclature for Lateral Load Tub Girder Tests

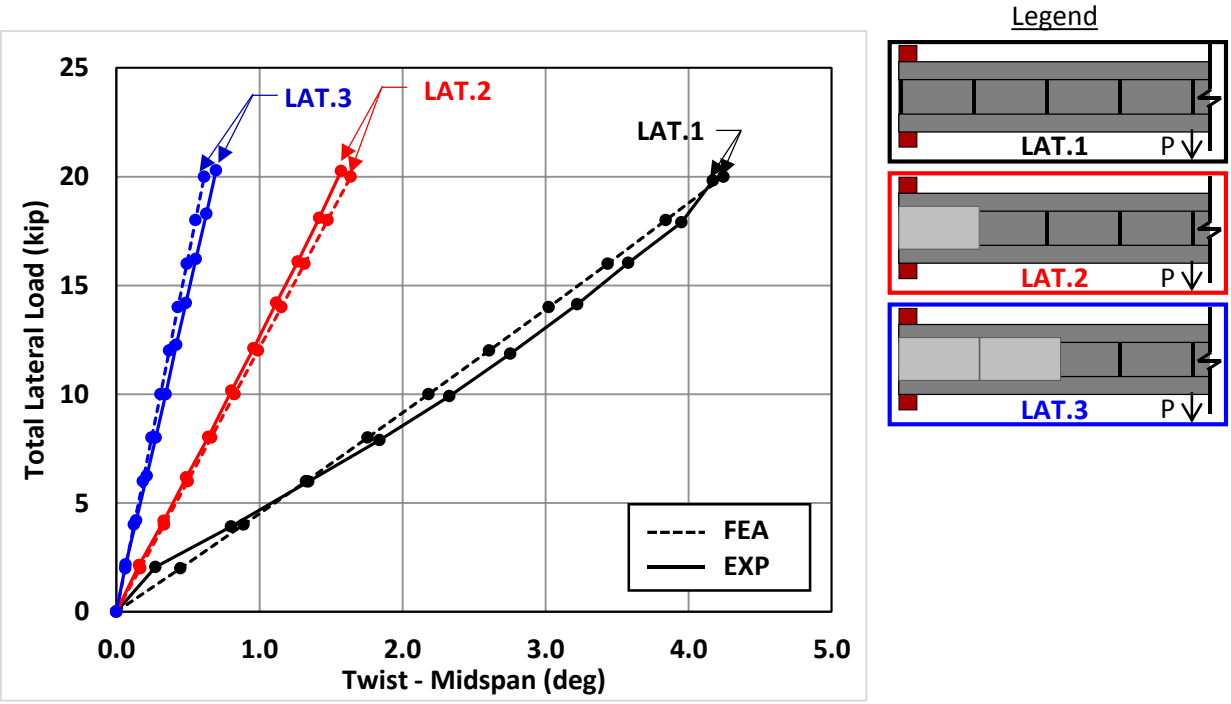

Figure E.2: Twist @ Midspan vs. Lateral Load @ Third Point - PCP

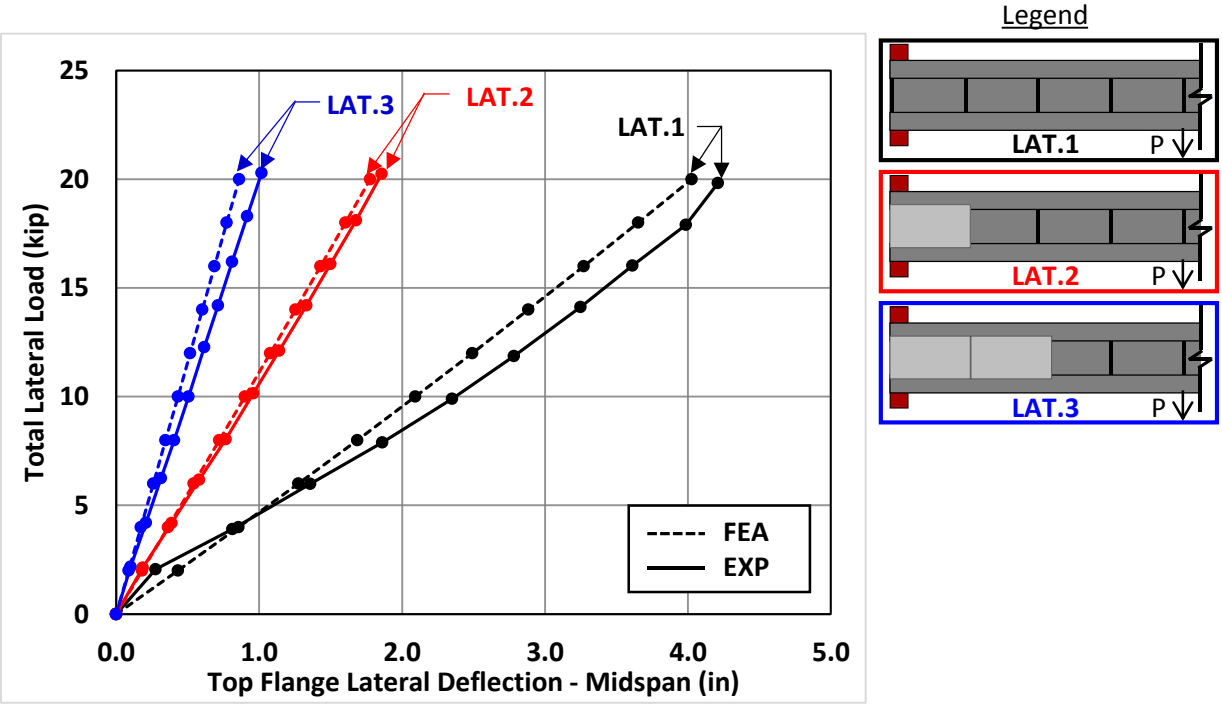

Figure E.3: Lateral Deflection @ Midspan vs. Lateral Load @ Third Point - PCP

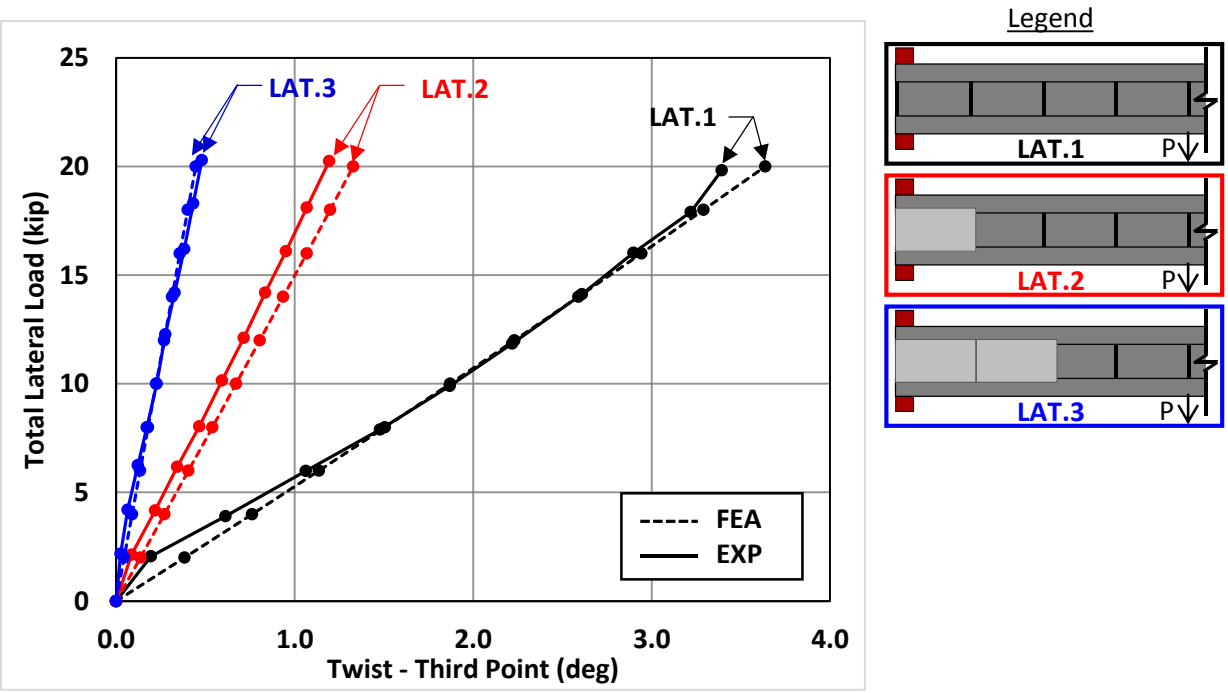

Figure E.4: Twist @ Third Point vs. Lateral Load @ Third Point - PCP

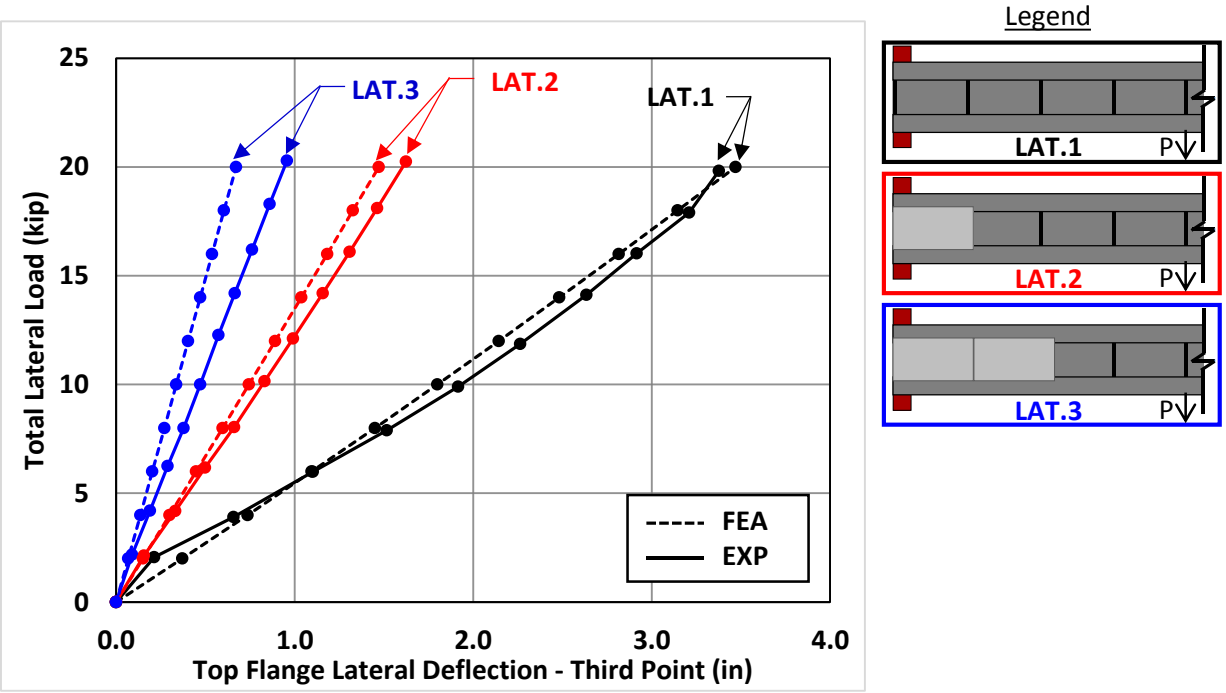

Figure E.5: Lateral Deflection @ Third Point vs. Lateral Load @ Third Point - PCP

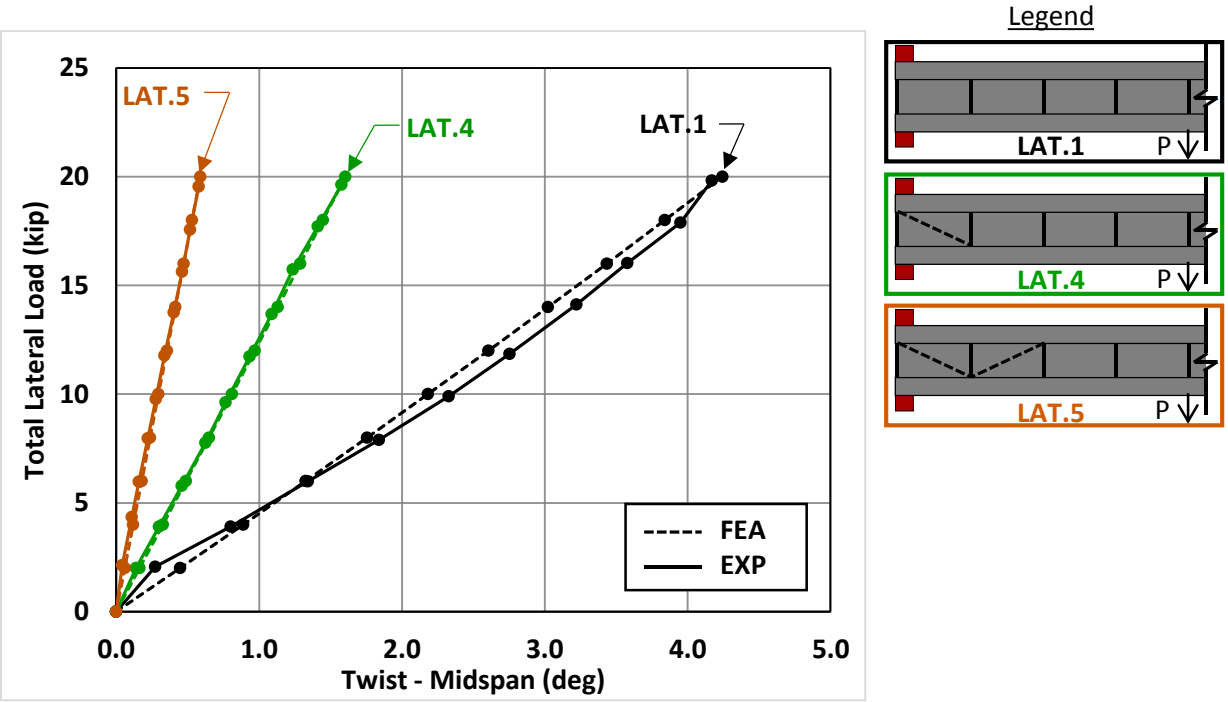

Figure E.6: Twist @ Midspan vs. Lateral Load @ Third Point - DIA

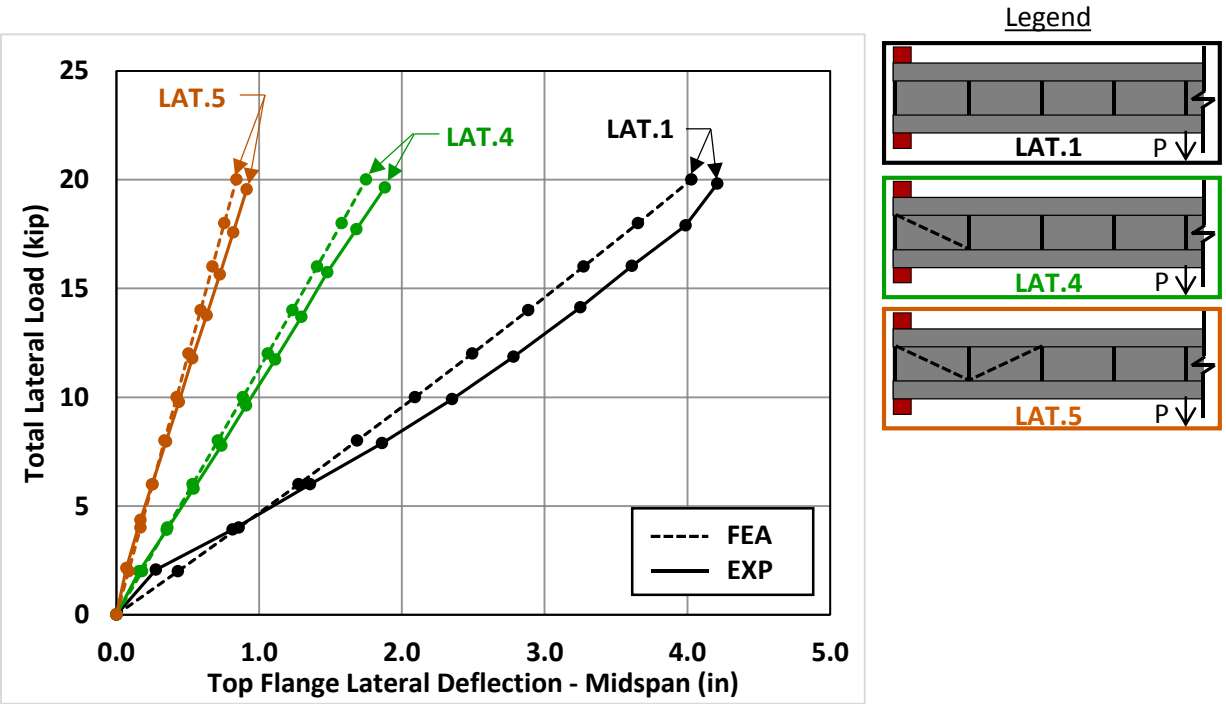

Figure E.7: Lateral Deflection @ Midspan vs. Lateral Load @ Third Point - DIA

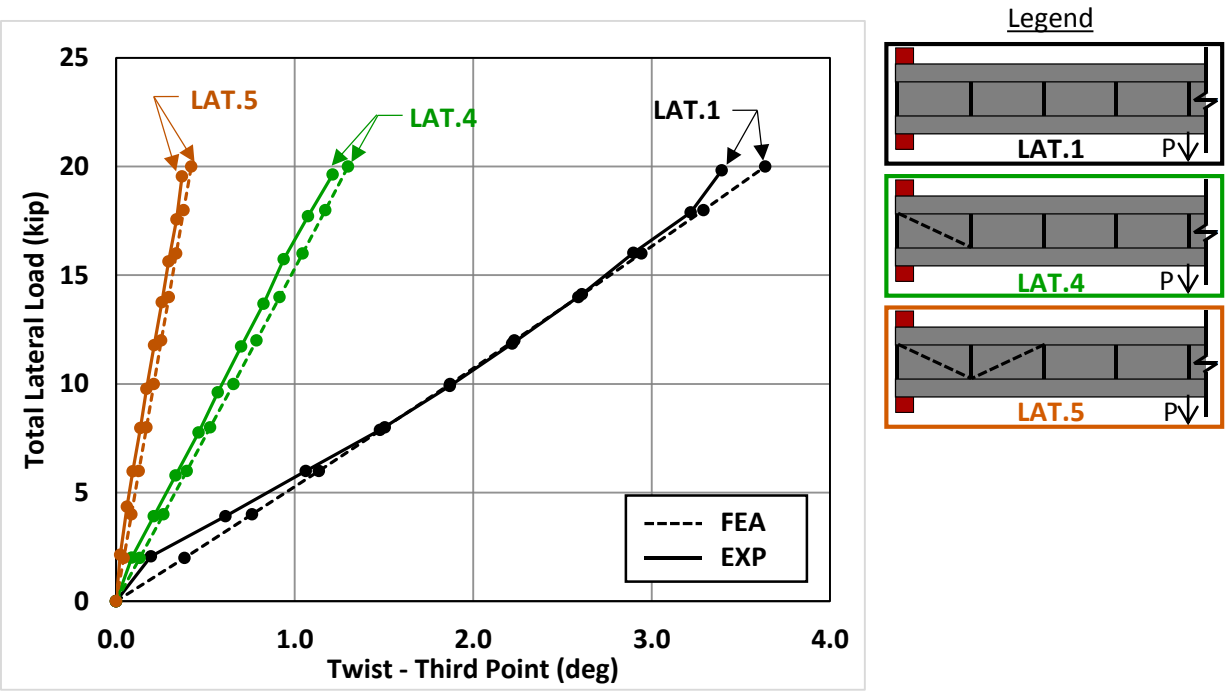

Figure E.8: Twist @ Third Point vs. Lateral Load @ Third Point - DIA

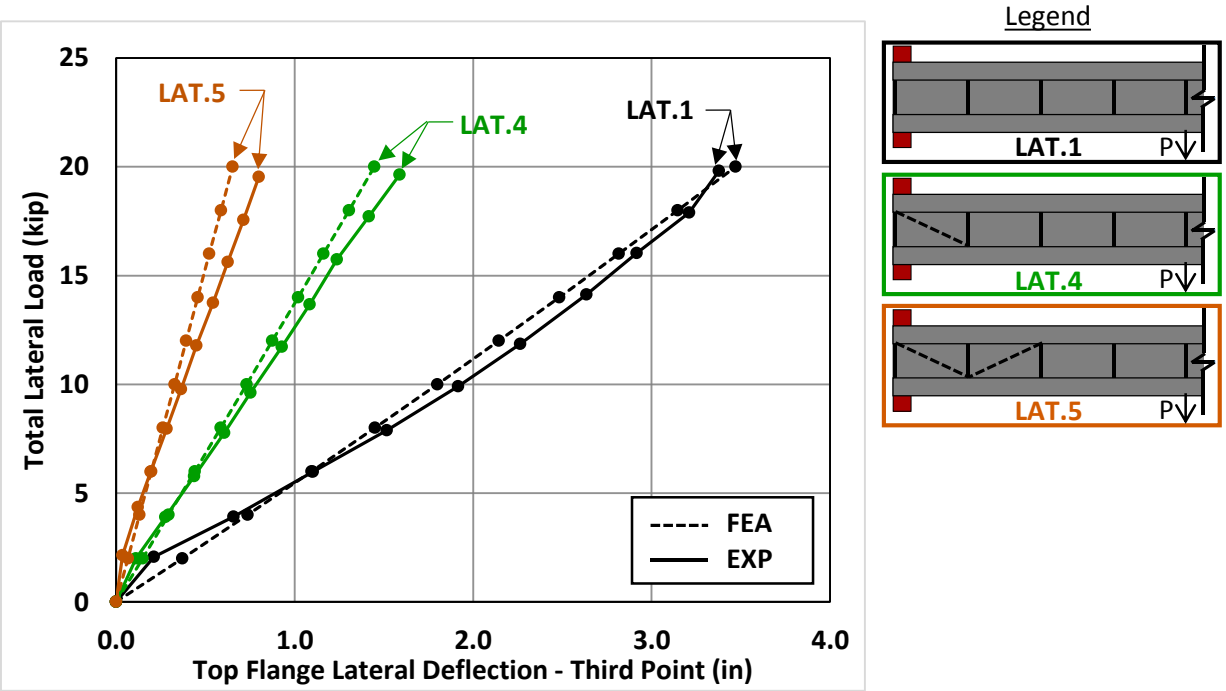

Figure E.9: Lateral Deflection @ Third Point vs. Lateral Load @ Third Point - DIA

E.2 FEA Validation with Experimental Results for Combined Bending and Torsion Simply Supported Tub Girder Tests

Table E.2: Summary of Bending and Torsion Simply Supported Tub Girder Tests

Test Name	Support Condition	Load Eccentricity	K-Frame Location	Number of Braces	Max Total GLS Load
GLS.1	SS	0 & 0	2-Panel	0	84
GLS.2	SS	0 & 0	2-Panel	2 PCP	100
GLS.3	SS	0 & 0	2-Panel	4 PCP	100
GLS.4	SS	0 & 0	2-Panel	2 DIAG	72
GLS.5	SS	0 & 0	2-Panel	4 DIAG	76
GLS.6	SS	8" & 8"	2-Panel	0	52
GLS.7	SS	8" & 8"	2-Panel	2 PCP	100
GLS.8	SS	8" & 8"	2-Panel	4 PCP	100
GLS.9	SS	8" & 8"	2-Panel	2 DIAG	80
GLS.10	SS	8" & 8"	2-Panel	4 DIAG	84
GLS.11	SS	16" & 16"	2-Panel	0	32
GLS.12	SS	16" & 16"	2-Panel	2 PCP	60
GLS.13	SS	16" & 16"	2-Panel	4 PCP	100
GLS.14	SS	16" & 16"	2-Panel	2 DAIG	52
GLS.15	SS	16" & 16"	2-Panel	4 DIAG	80

Key: GLS = Gravity Load Simulator Load, SS = Simply Supported
PCP = Partial Depth Precast Concrete Deck Panel, DIA = Diagonal

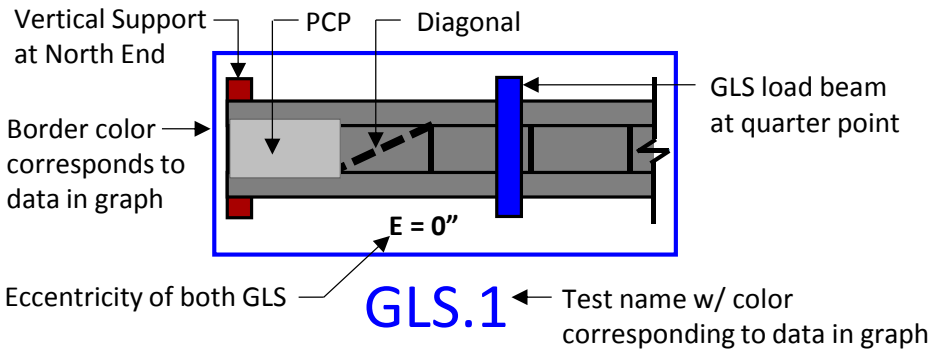

Figure E.10: Nomenclature for GLS Simply Supported Tub Girder Tests

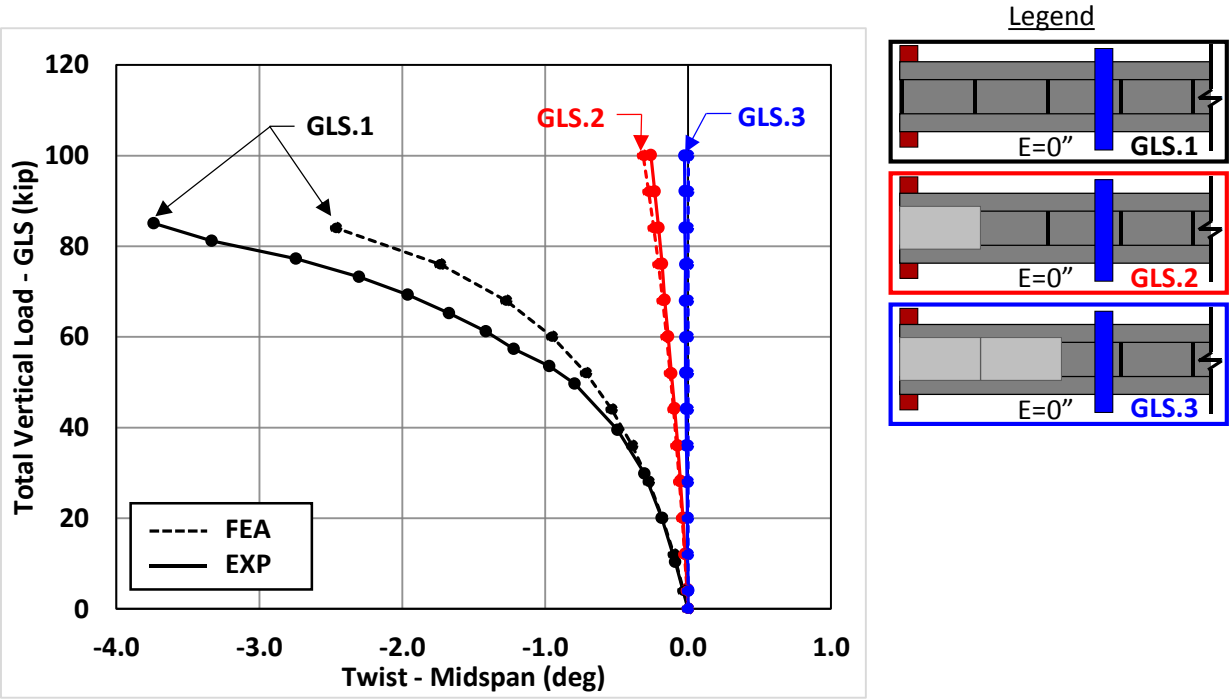

Figure E.11: Twist @ Midspan vs. GLS Load (E=0”) - PCP

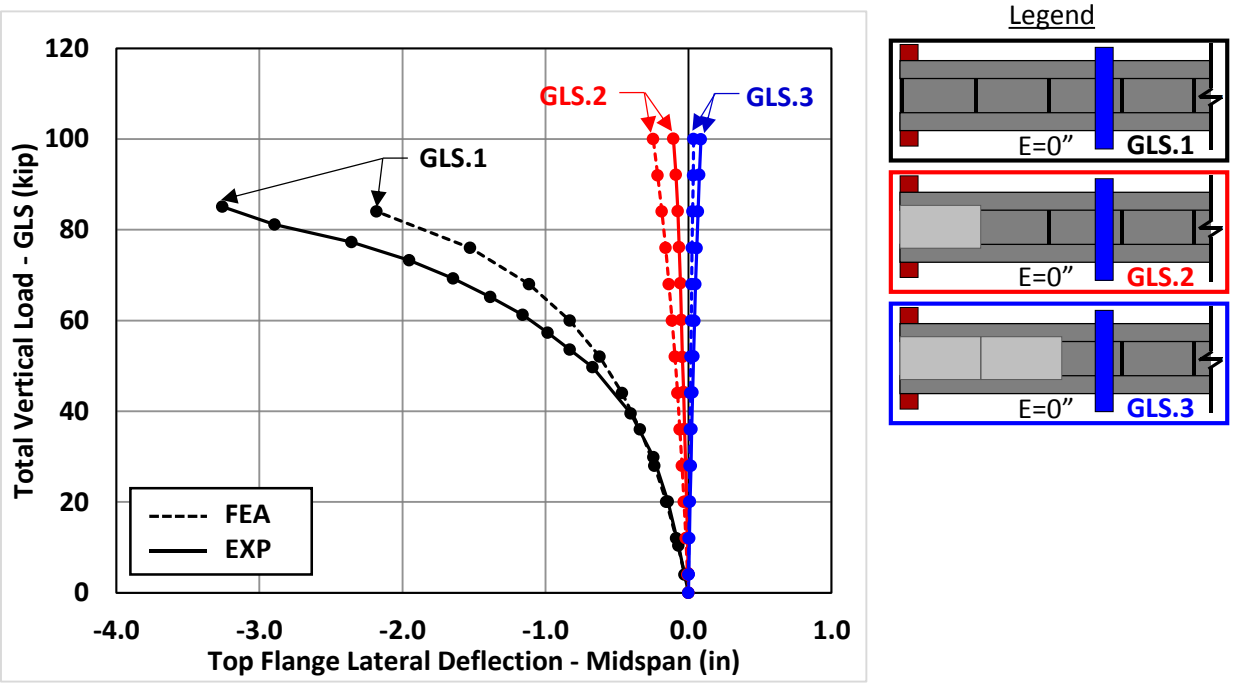

Figure E.12: Lateral Deflection @ Midspan vs. GLS Load (E=0”) - PCP

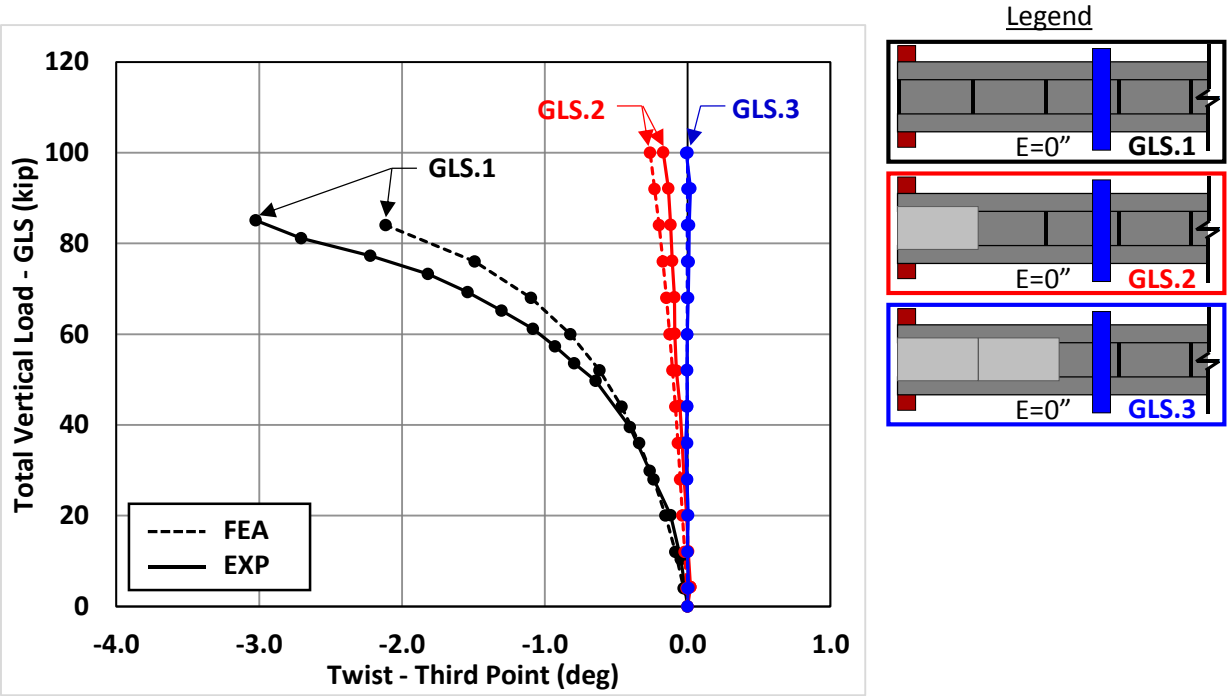

Figure E.13: Twist @ Third Point vs. GLS Load (E=0”) - PCP

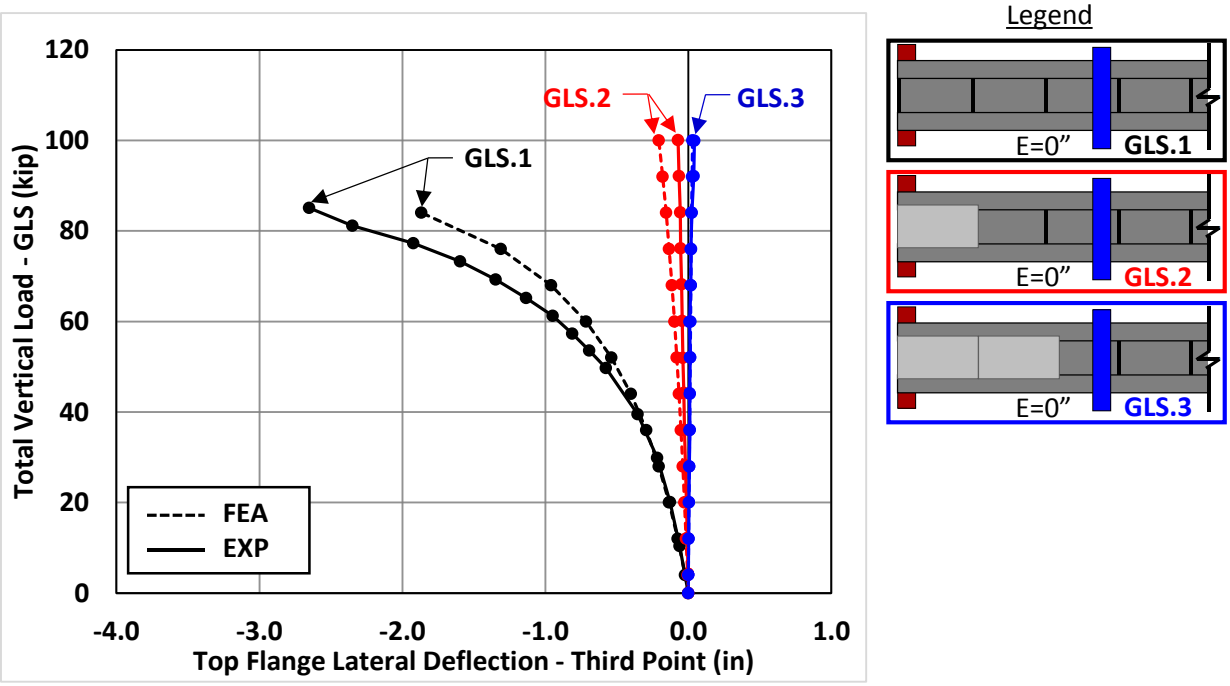

Figure E.14: Lateral Deflection @ Third Point vs. GLS Load (E=0”) - PCP

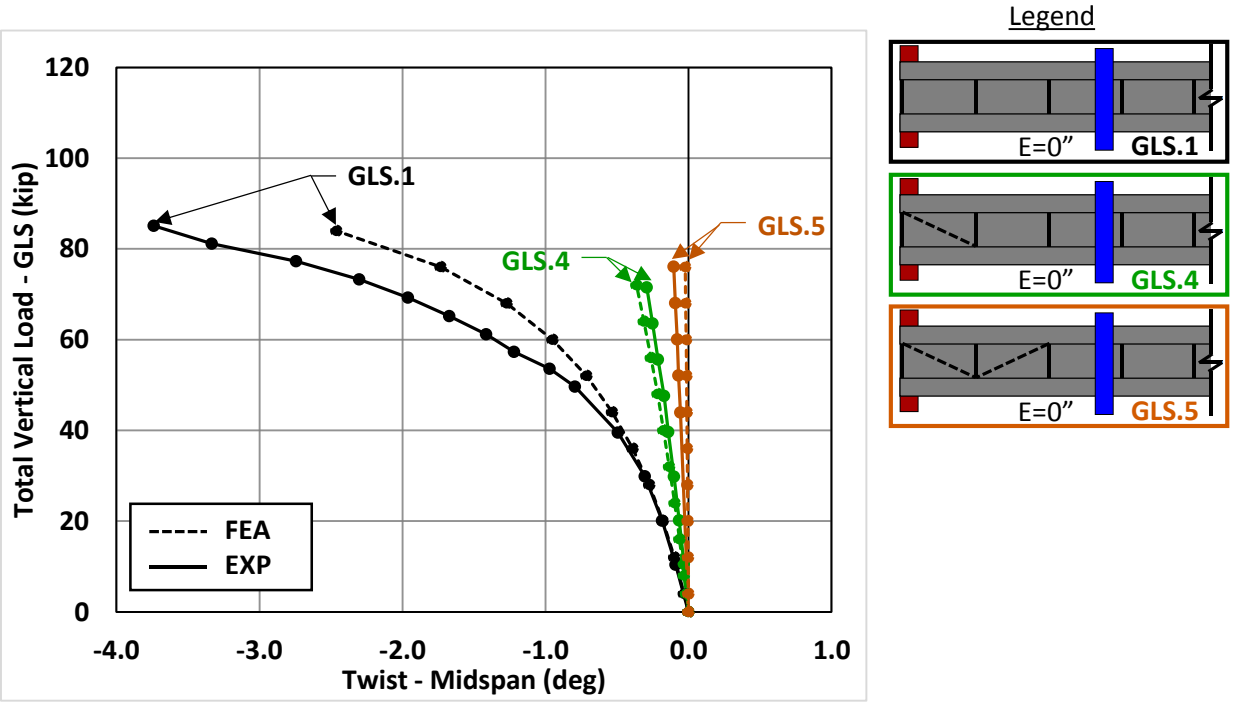

Figure E.15: Twist @ Midspan vs. GLS Load (E=0”) - DIA

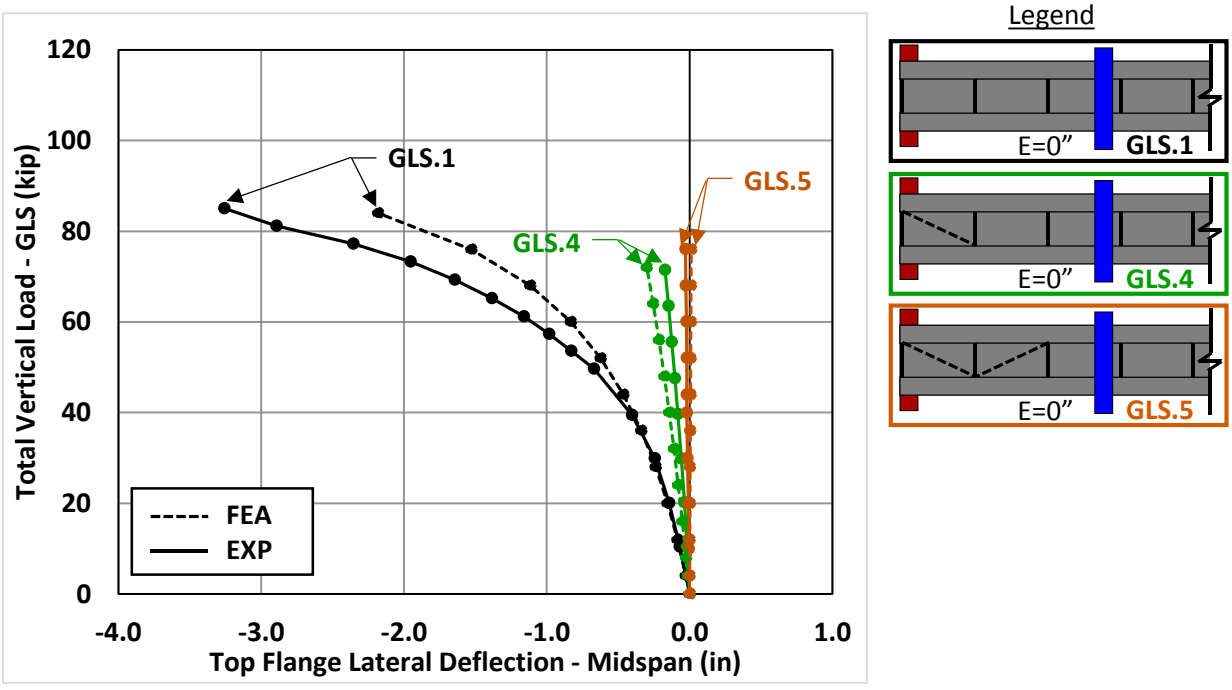

Figure E.16: Lateral Deflection @ Midspan vs. GLS Load (E=0”) – DIA

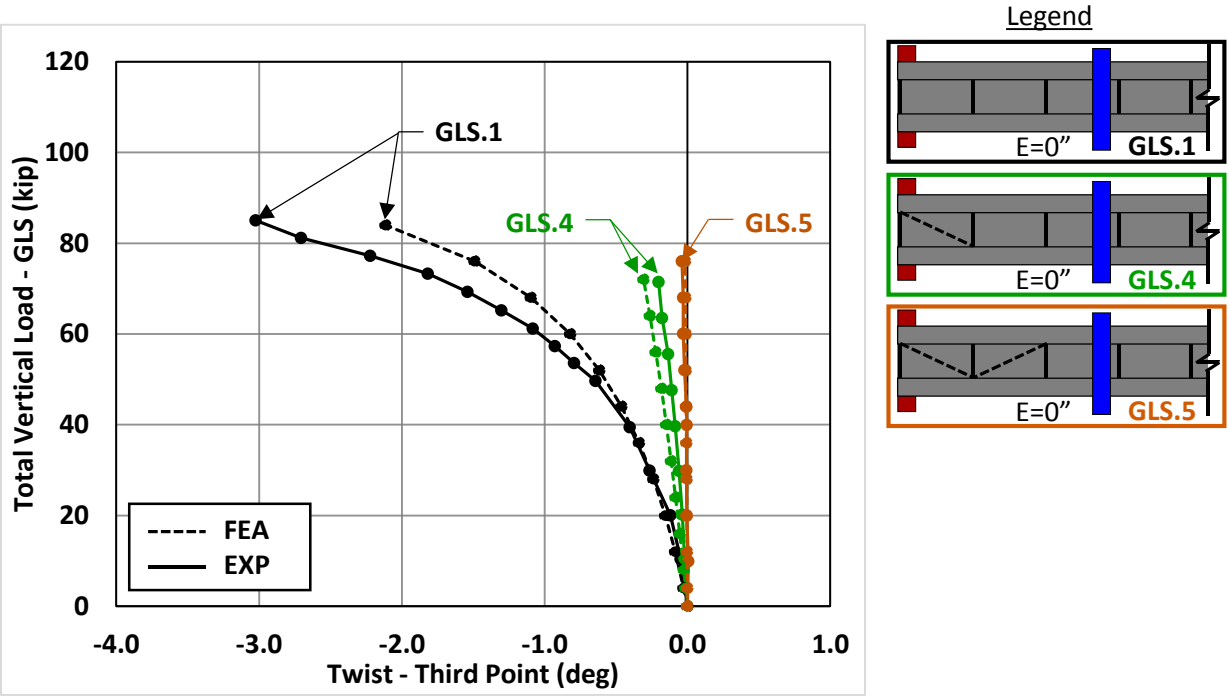

Figure E.17: Twist @ Third Point vs. GLS Load (E=0”) - DIA

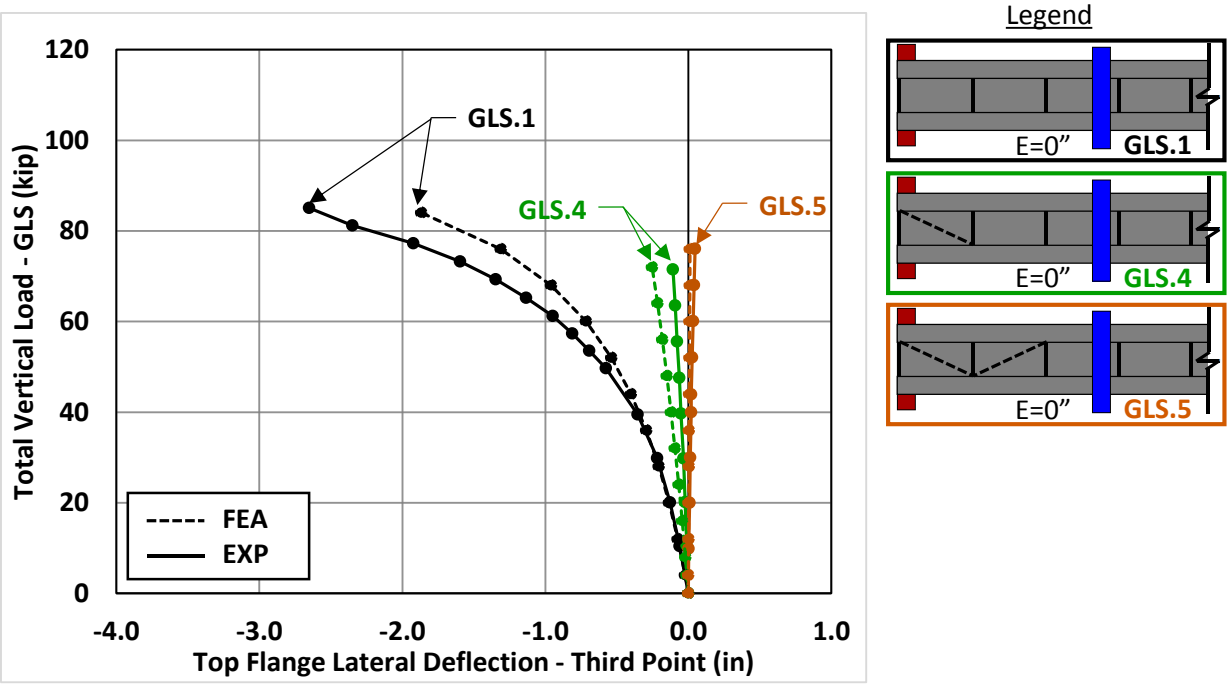

Figure E.18: Lateral Deflection @ Third Point vs. GLS Load (E=0”) - DIA

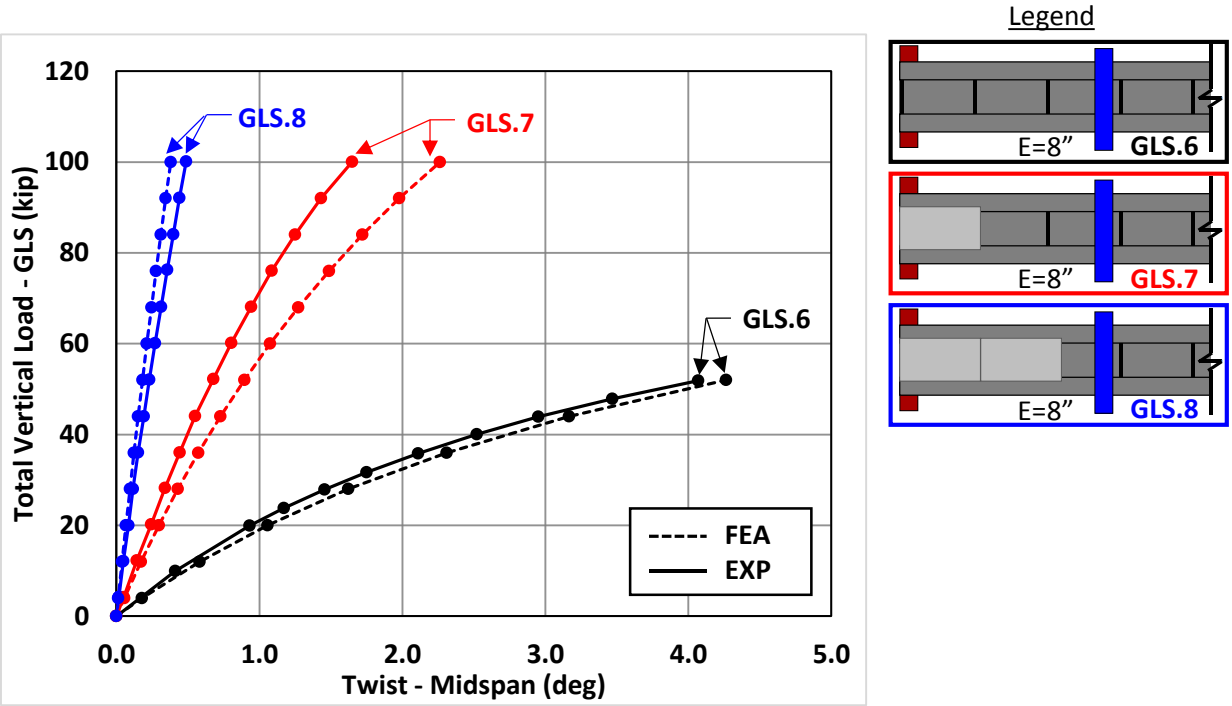

Figure E.19: Twist @ Midspan vs. GLS Load (E=8”) - PCP

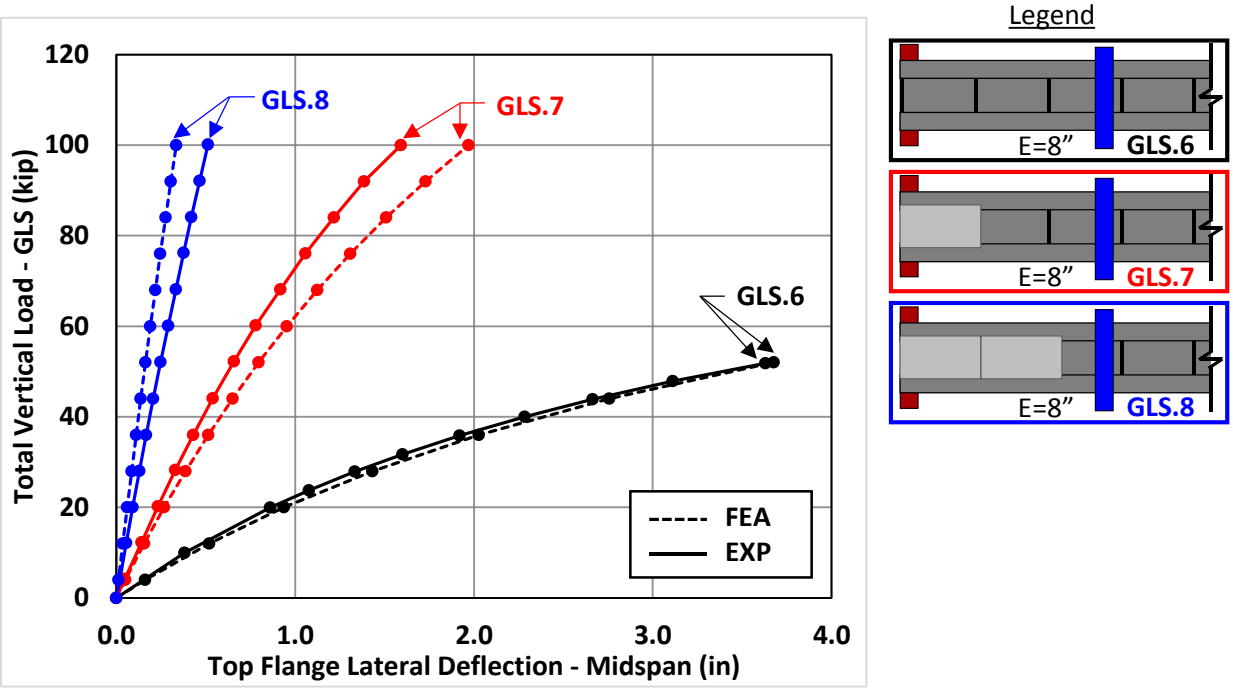

Figure E.20: Lateral Deflection @ Midspan vs. GLS Load (E=8”) - PCP

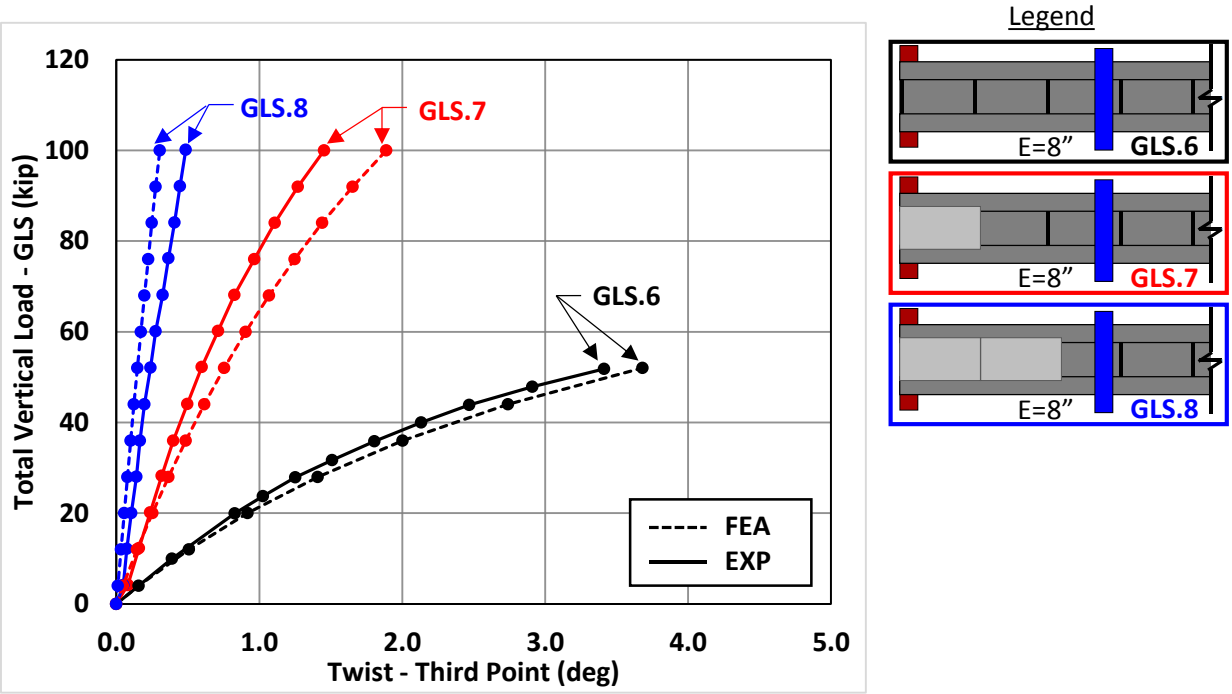

Figure E.21: Twist @ Third Point vs. GLS Load (E=8”) - PCP

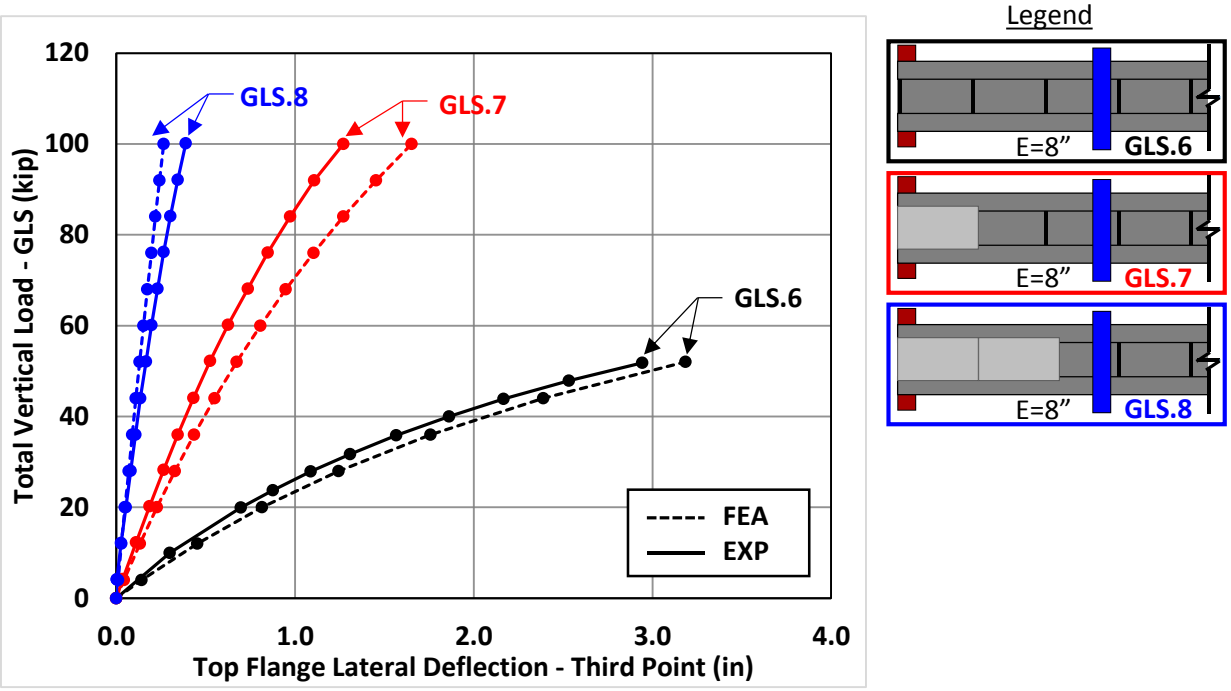

Figure E.22: Lateral Deflection @ Third Point vs. GLS Load (E=8”) – PCP

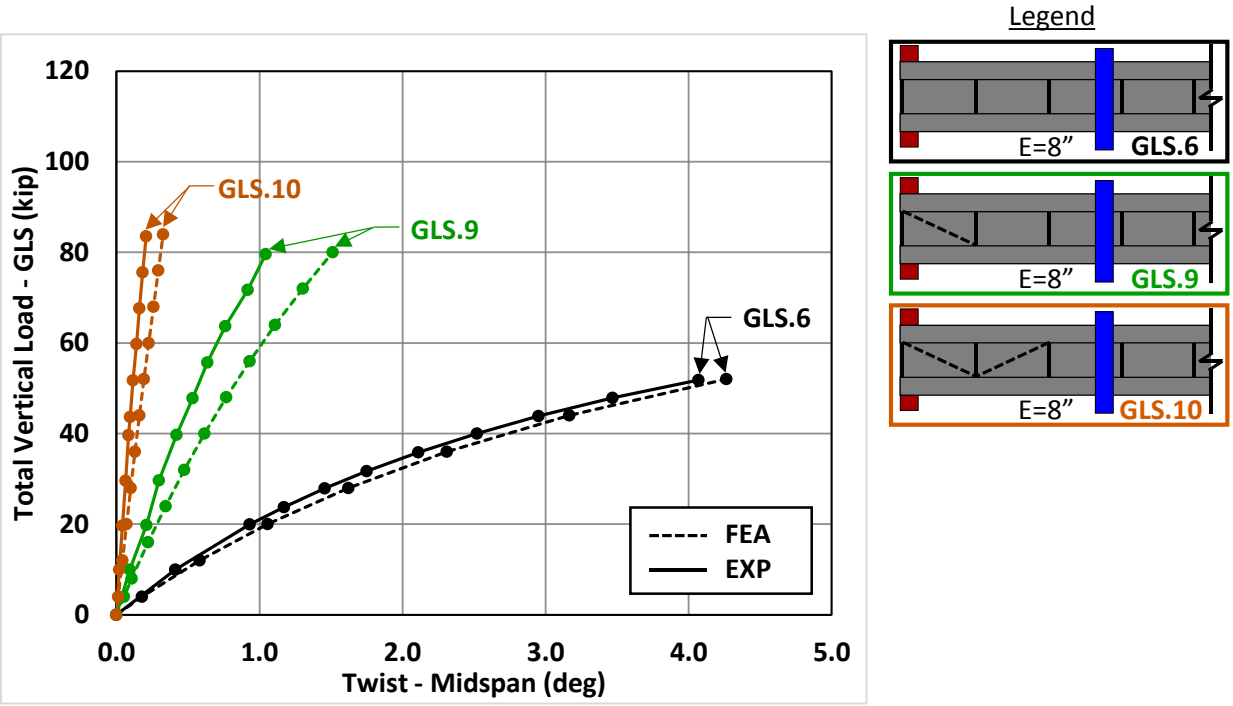

Figure E.23: Twist @ Midspan vs. GLS Load (E=8”) - DIA

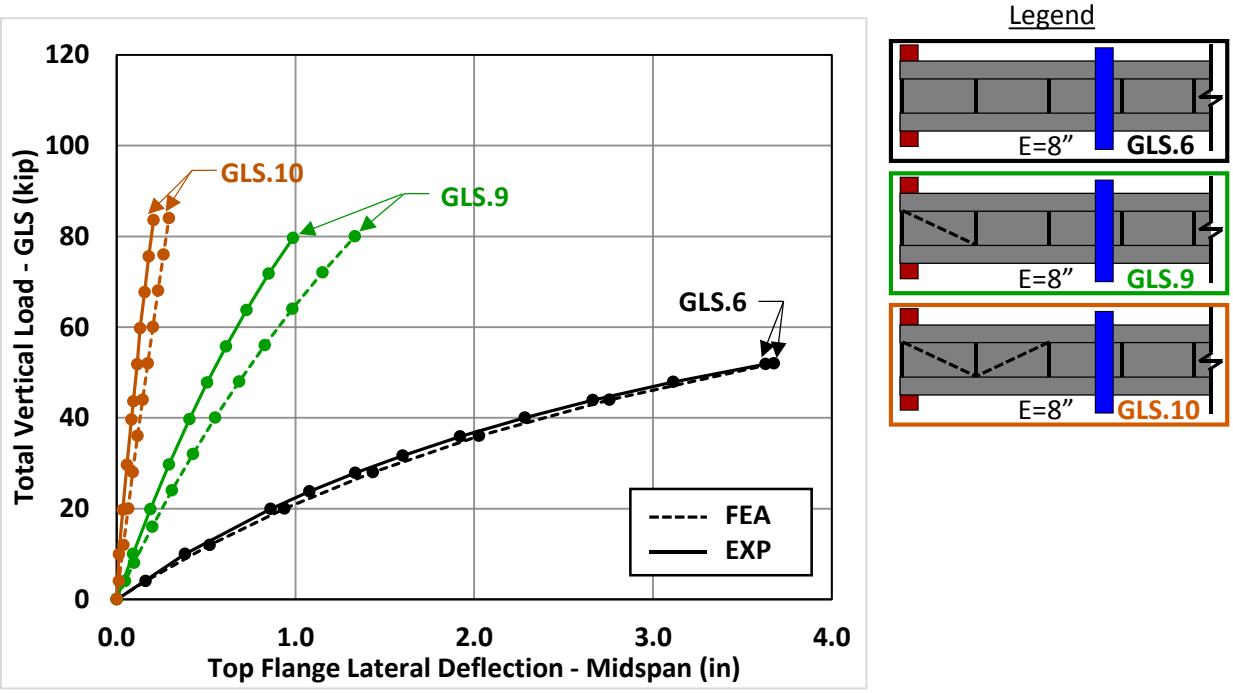

Figure E.24: Lateral Deflection @ Midspan vs. GLS Load (E=8”) - DIA

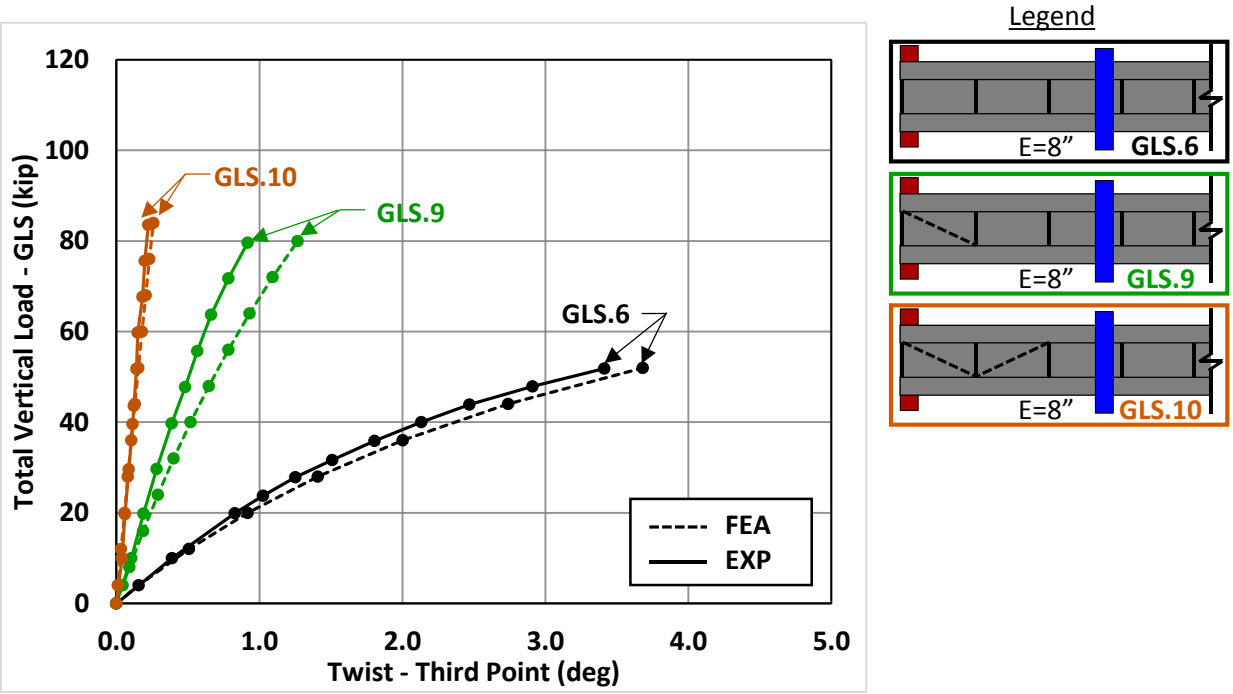

Figure E.25: Twist @ Third Point vs. GLS Load (E=8”) - DIA

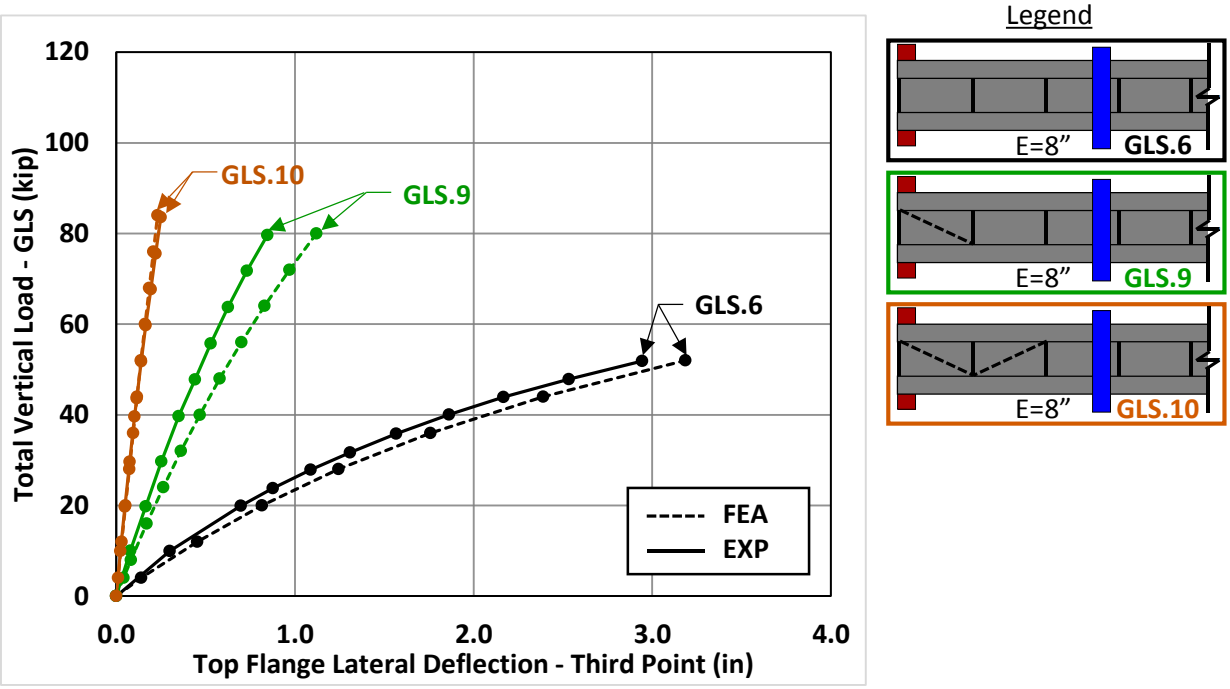

Figure E.26: Lateral Deflection @ Third Point vs. GLS Load (E=8”) - DIA

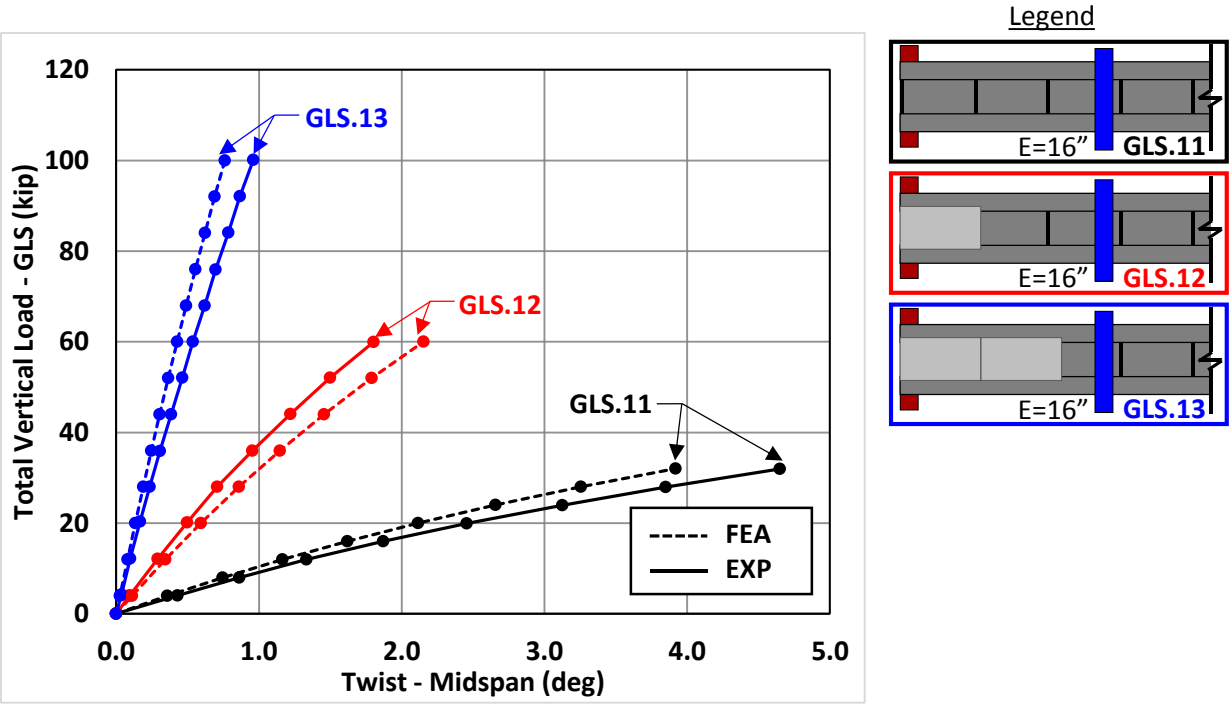

Figure E.27: Twist @ Midspan vs. GLS Load (E=16”) - PCP

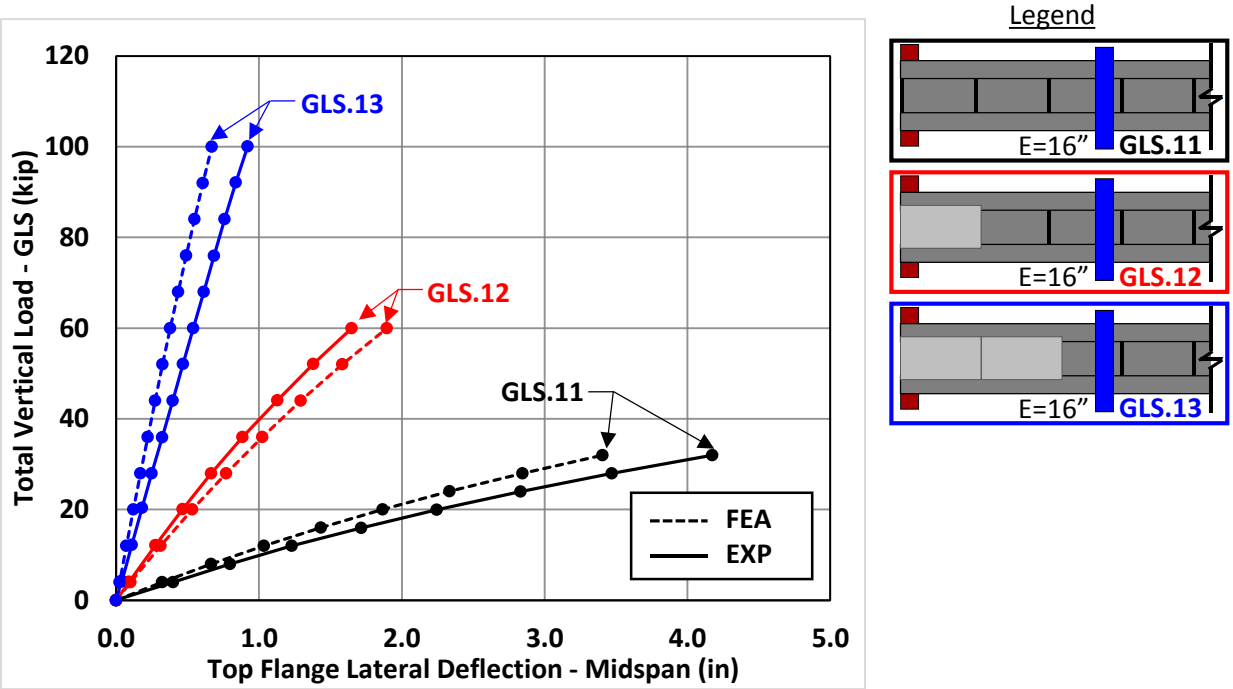

Figure E.28: Lateral Deflection @ Midspan vs. GLS Load (E=16”) - PCP

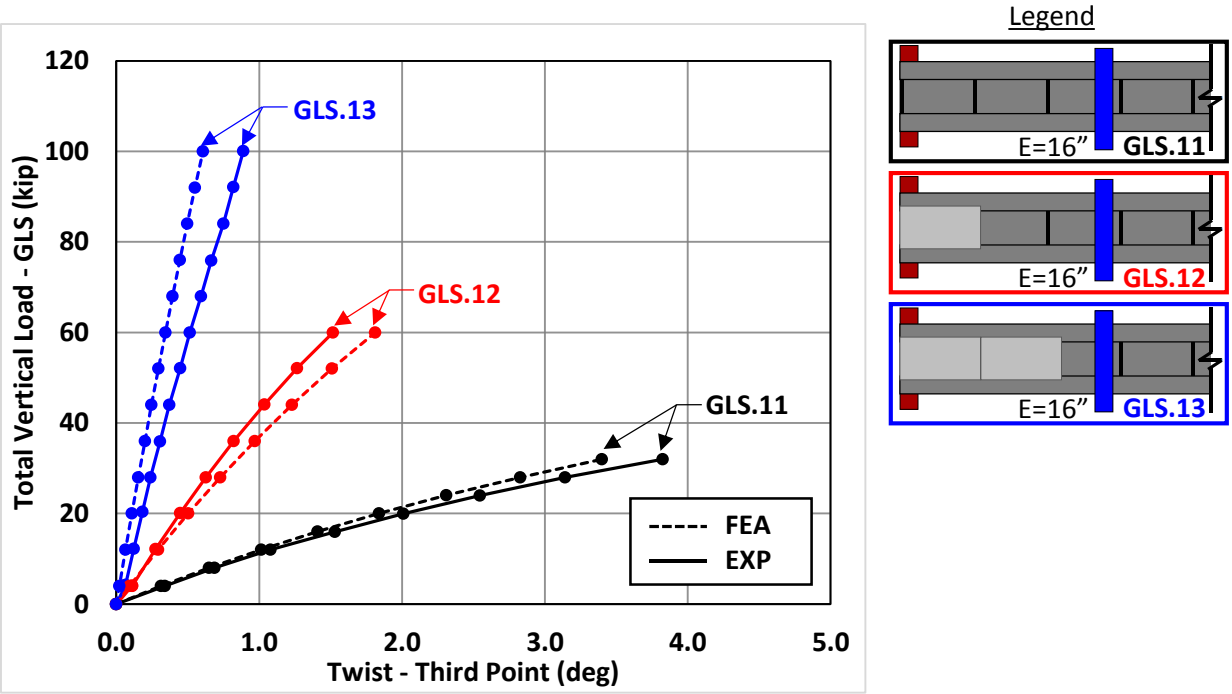

Figure E.29: Twist @ Third Point vs. GLS Load (E=16”) - PCP

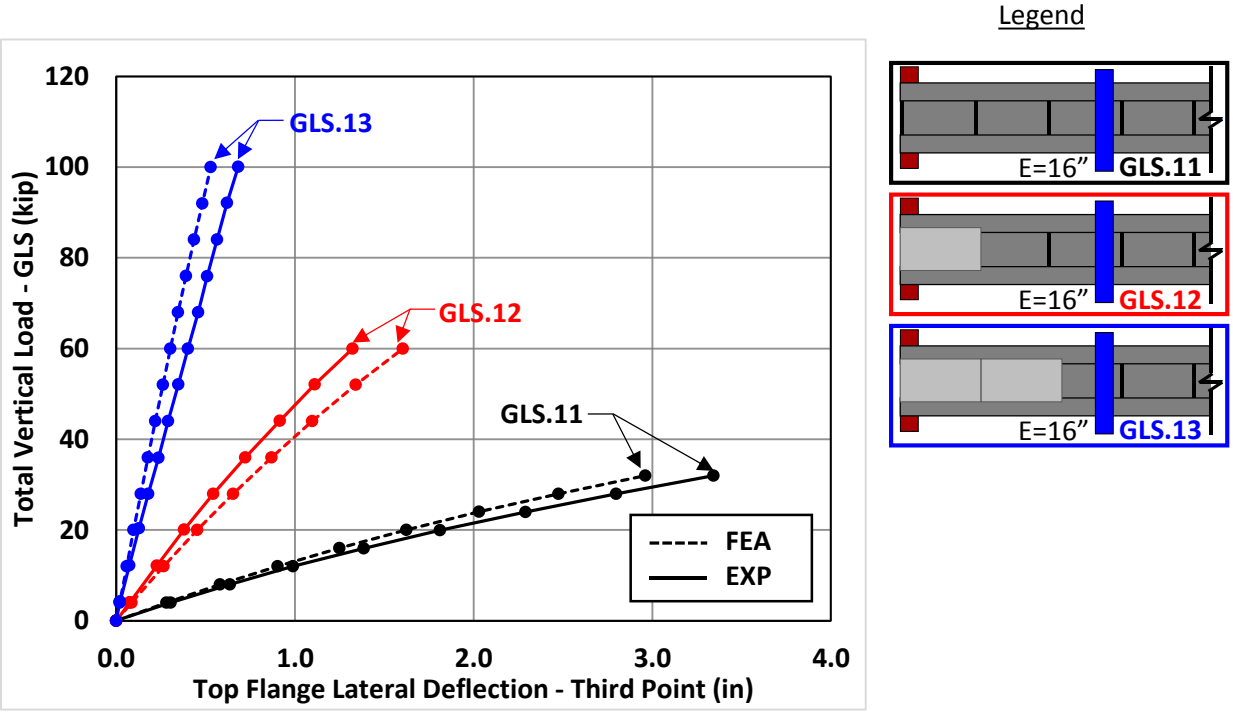

Figure E.30: Lateral Deflection @ Third Point vs. GLS Load (E=16”) – PCP

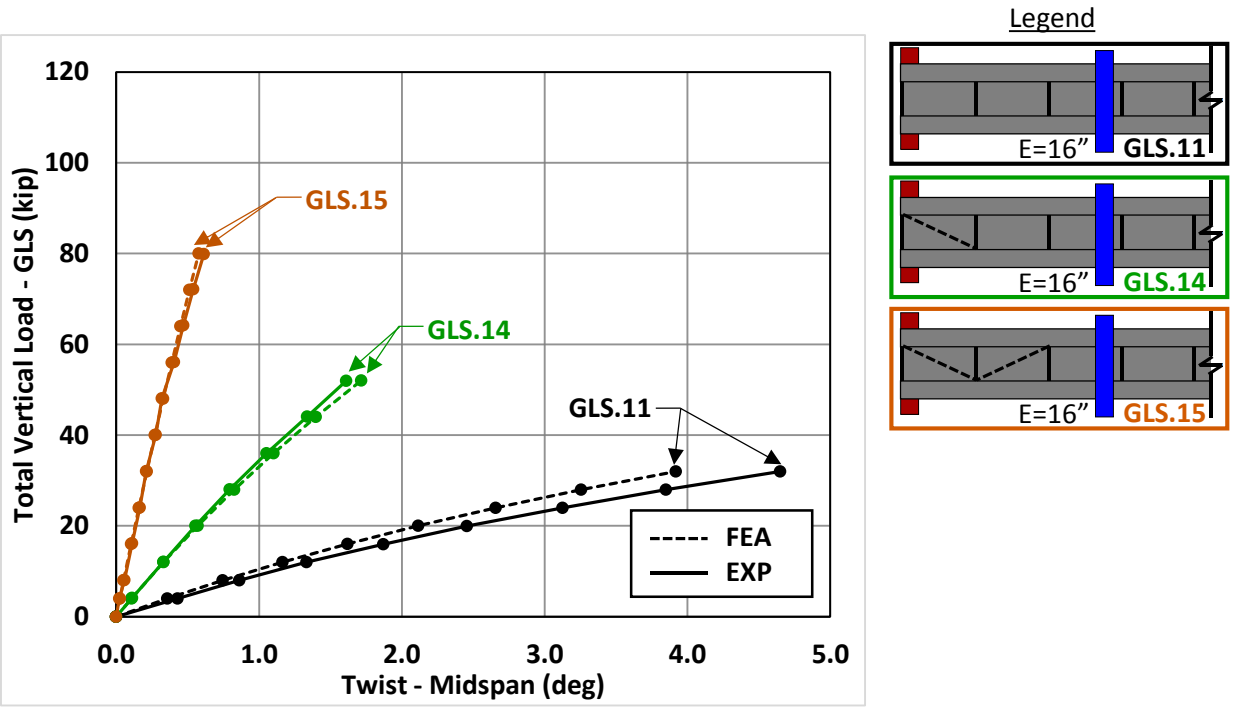

Figure E.31: Twist @ Midspan vs. GLS Load (E=16”) - DIA

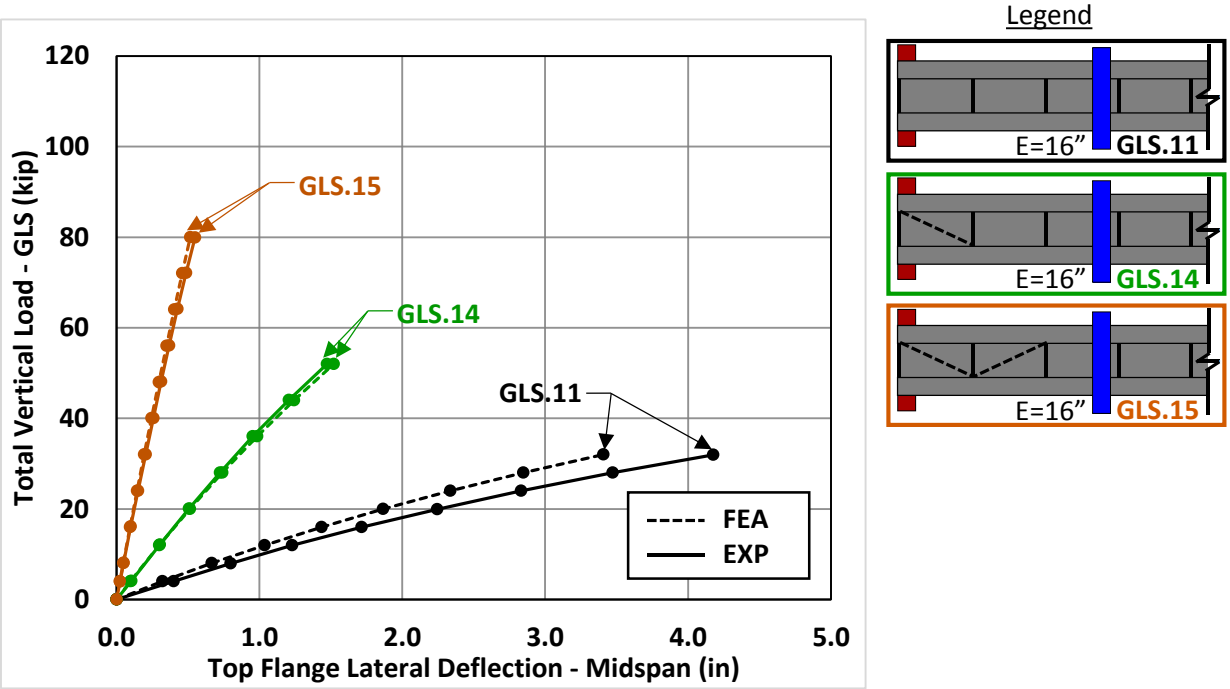

Figure E.32: Lateral Deflection @ Midspan vs. GLS Load (E=16”) - DIA

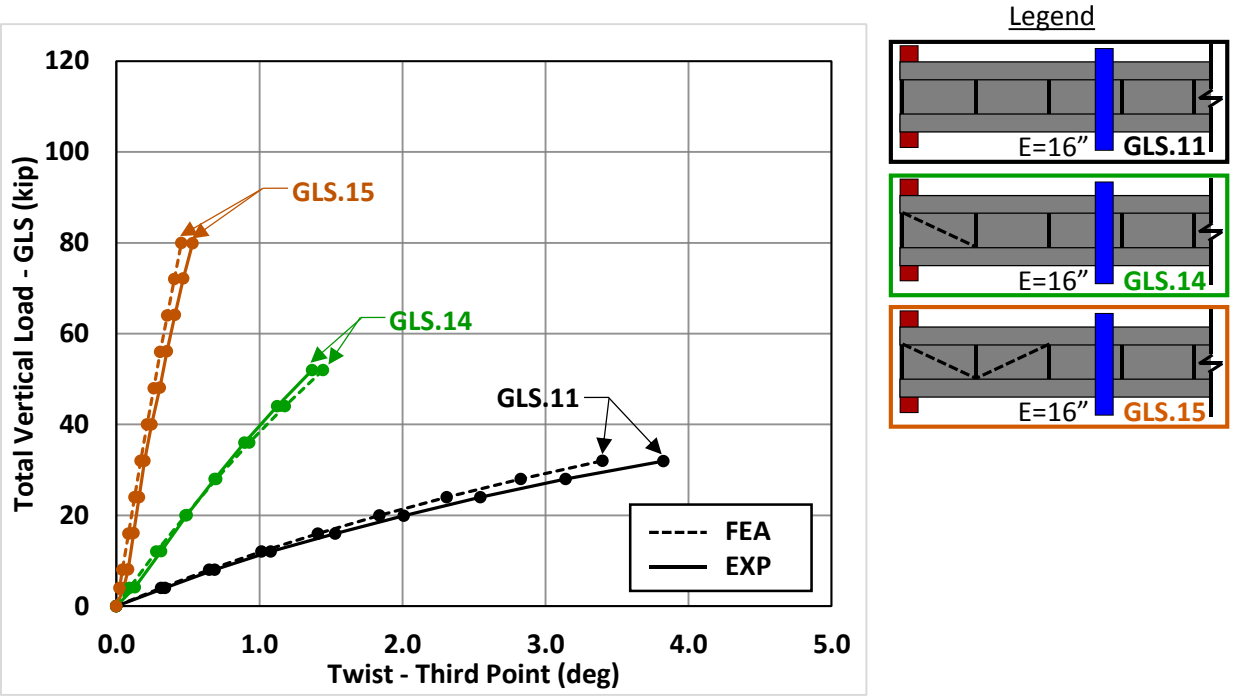

Figure E.33: Twist @ Third Point vs. GLS Load (E=16”) - DIA

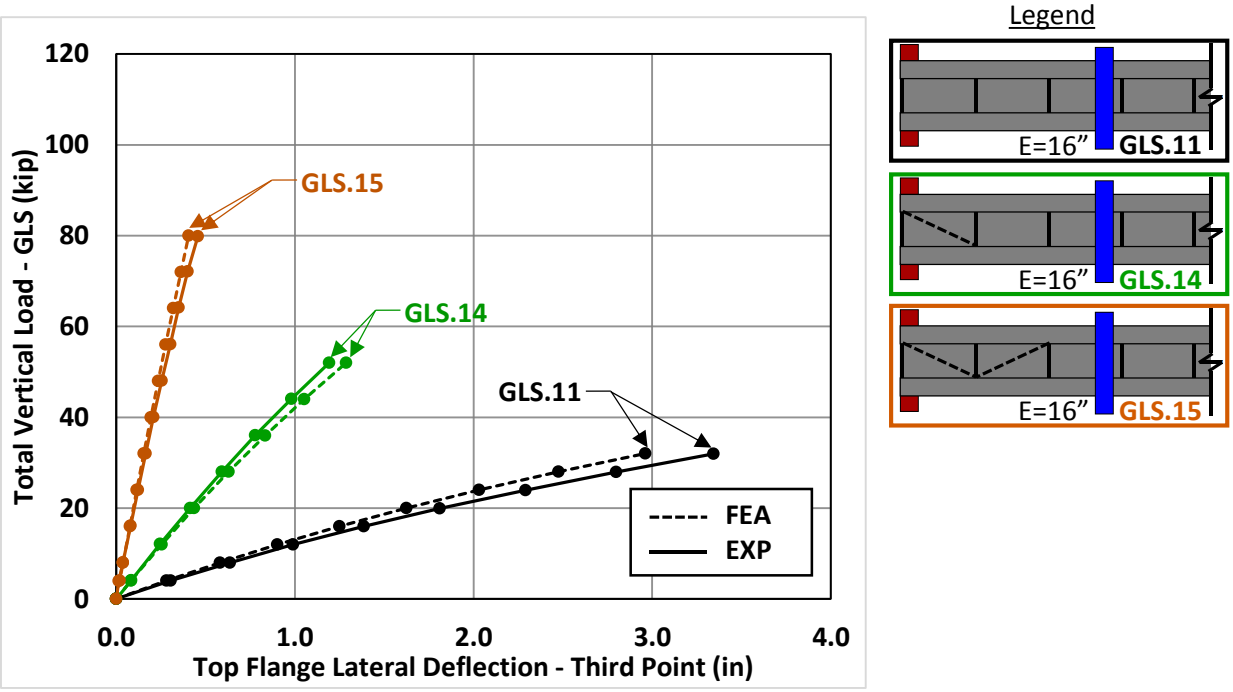

Figure E.34: Lateral Deflection @ Third Point vs. GLS Load (E=16”) - DIA

E.3 FEA Validation with Experimental Results for Combined Bending and Torsion Overhang Tub Girder Tests

Table E.3: Summary of Bending and Torsion Overhang Tub Girder Tests

Test Name	Support Condition	GLS North Eccentricity	GLS South Eccentricity	K-Frame Location	Max Total GLS Load	Max Total GLS Load
GLS.16	OH	-2"	4"	2-Panel	0	200
GLS.17	OH	-2"	4"	2-Panel	3 PCP	200
GLS.18	OH	-2"	4"	2-Panel	3 DIAG	200
GLS.19	OH	-4"	8"	2-Panel	0	200
GLS.20	OH	-4"	8"	2-Panel	3 PCP	200
GLS.21	OH	-4"	8"	2-Panel	3 DIAG	200
GLS.22	OH	-6"	12"	2-Panel	0	200
GLS.23	OH	-6"	12"	2-Panel	3 PCP	300
GLS.24	OH	-6"	12"	2-Panel	3 DIAG	200

Key: GLS = Gravity Load Simulator Load, OH = Overhang Support
PCP = Partial Depth Precast Concrete Deck Panel, DIA = Diagonal

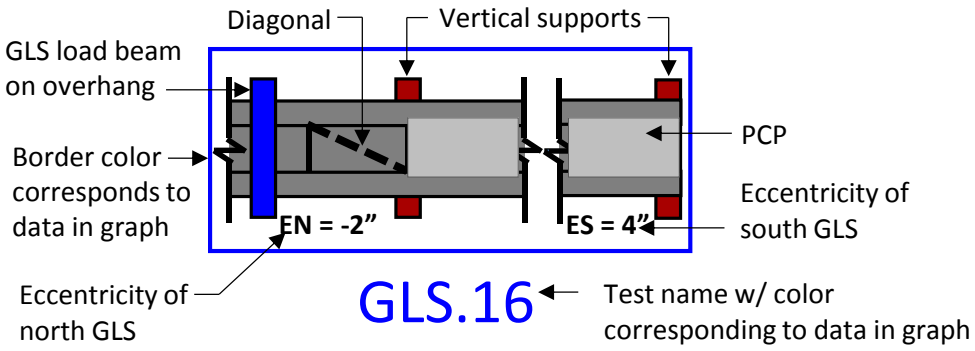

Figure E.35: Nomenclature for GLS Overhang Tub Girder Tests

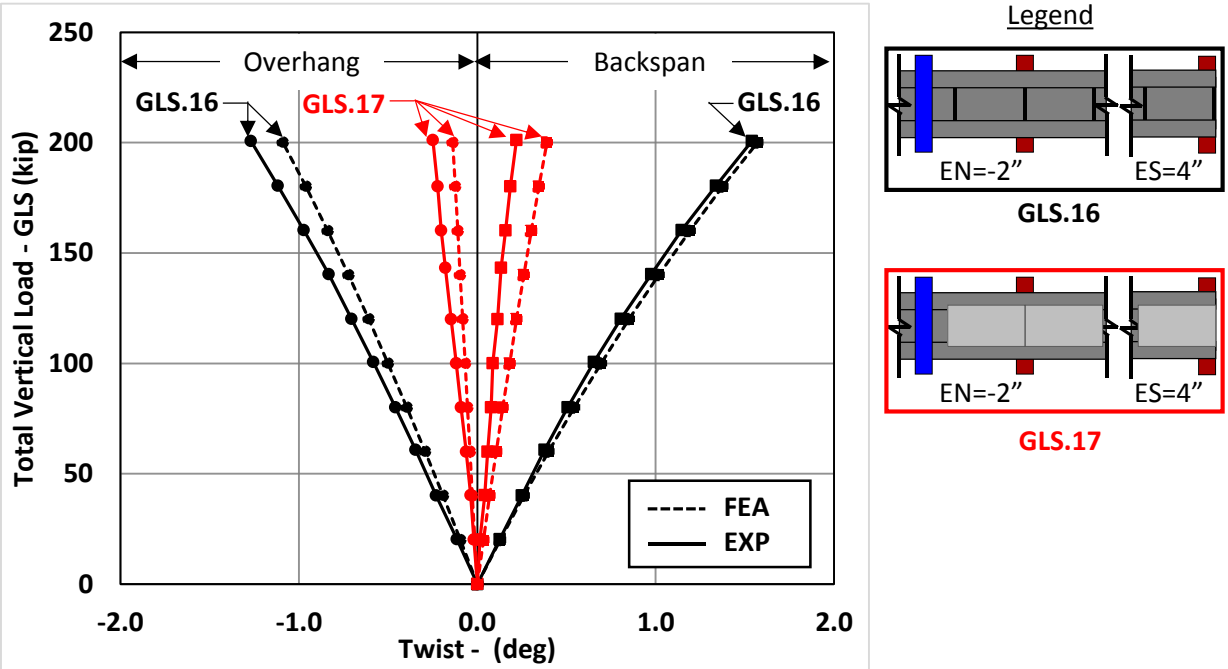

Figure E.36: Twist vs. GLS Load (EN=-2” & ES=4”) - PCP

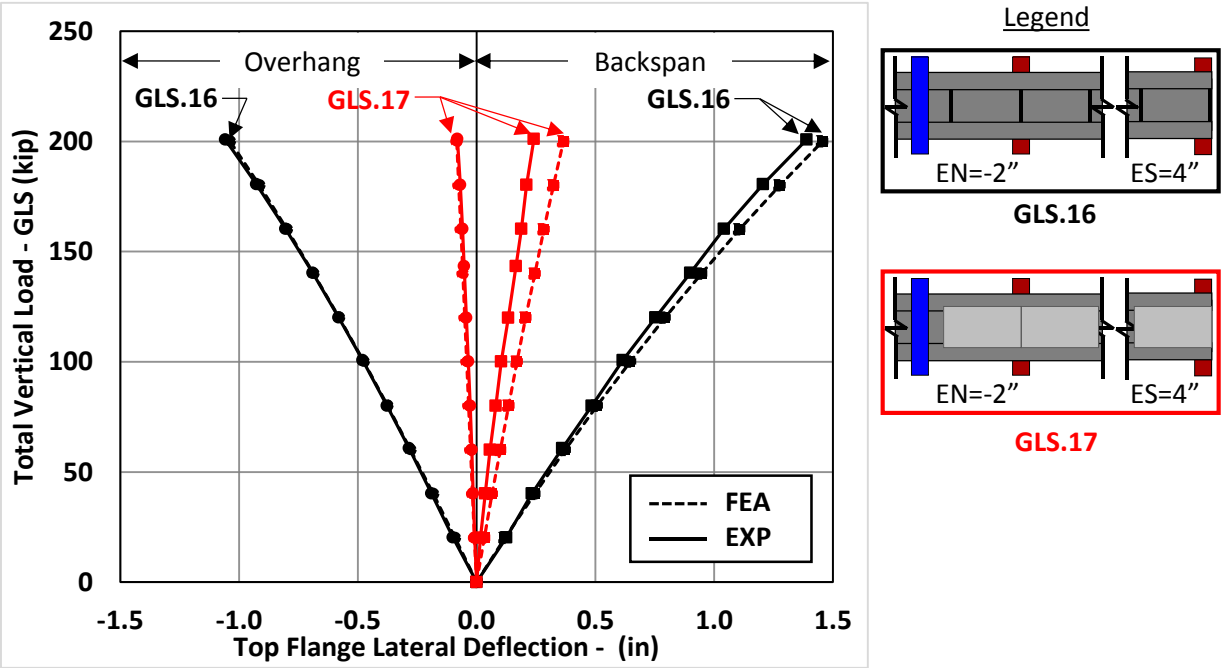

Figure E.37: Lateral Deflection vs. GLS Load (EN=-2” & ES=4”) - PCP

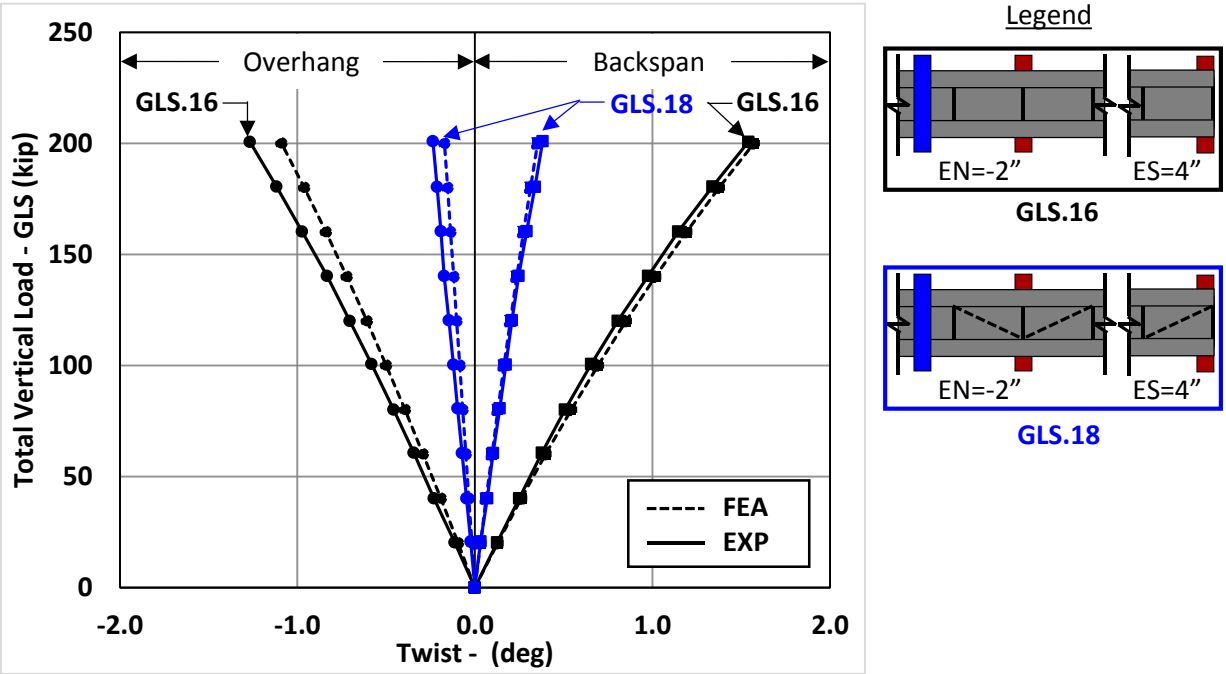

Figure E.38: Twist vs. GLS Load (EN=-2” & ES=4”) - DIA

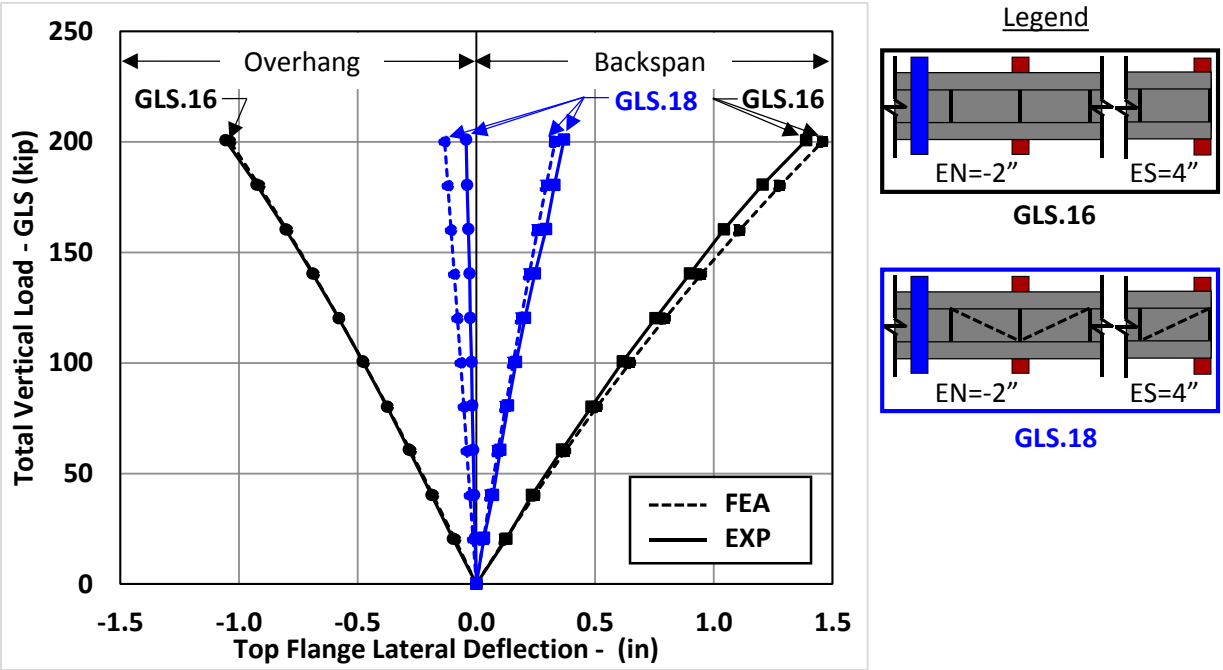

Figure E.39: Lateral Deflection vs. GLS Load (EN=-2” & ES=4”) - DIA

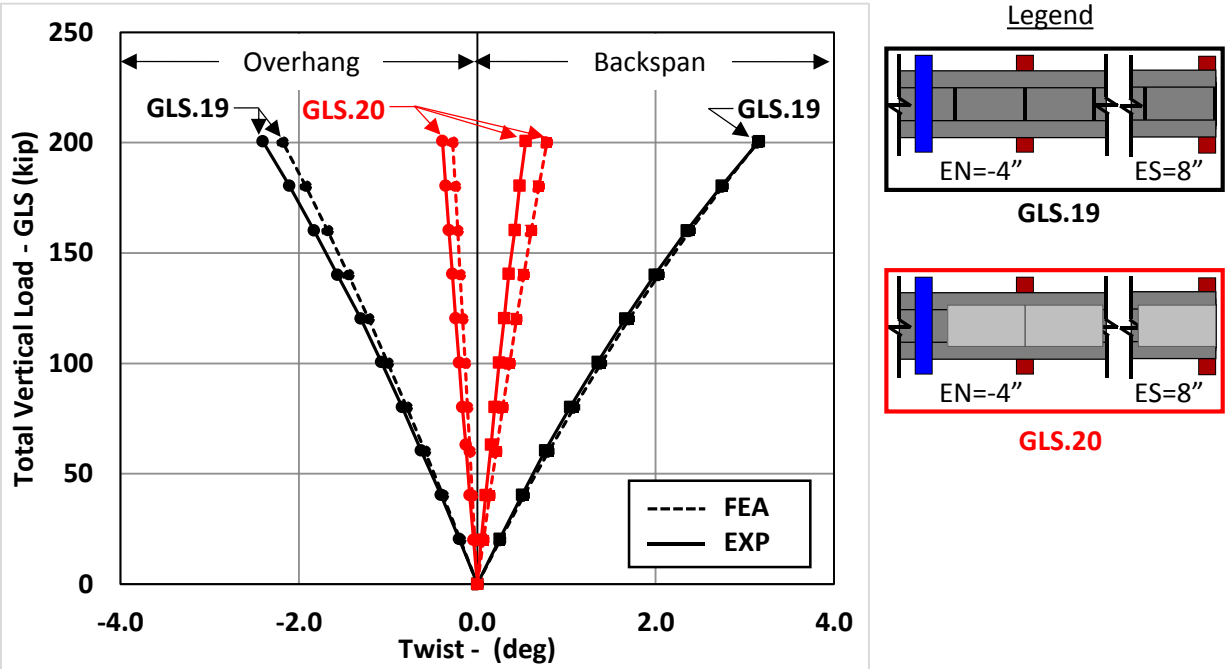

Figure E.40: Twist vs. GLS Load (EN=-4” & ES=8”) - PCP

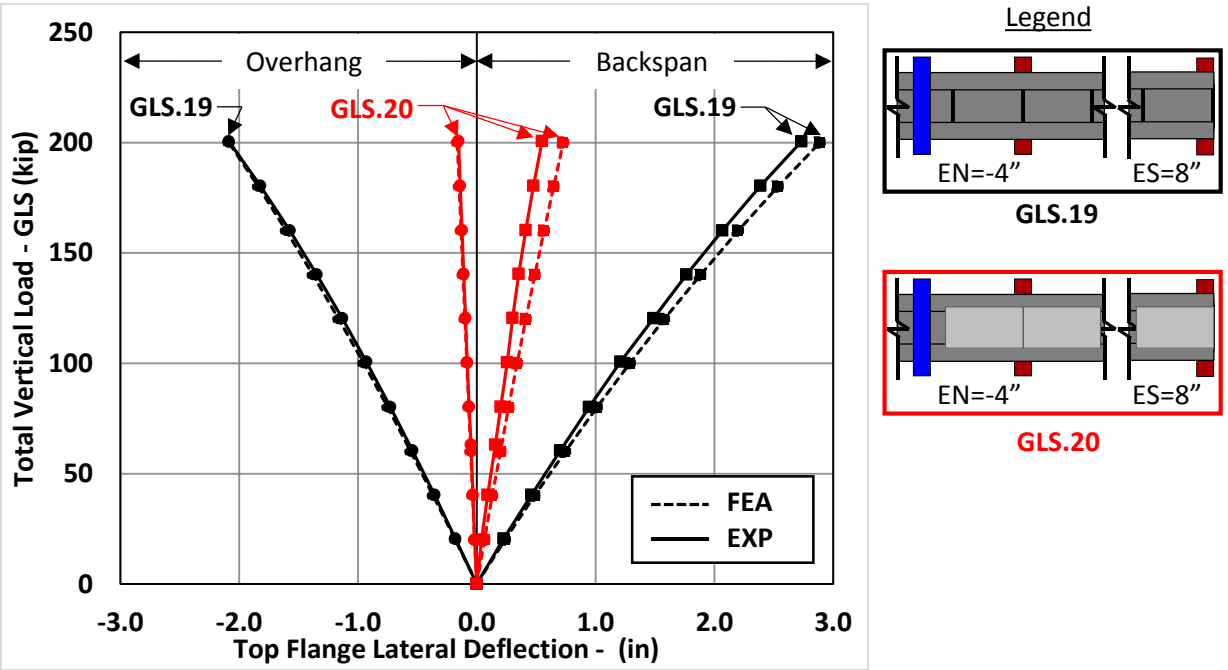

Figure E.41: Lateral Deflection vs. GLS Load (EN=-4” & ES=8”) - PCP

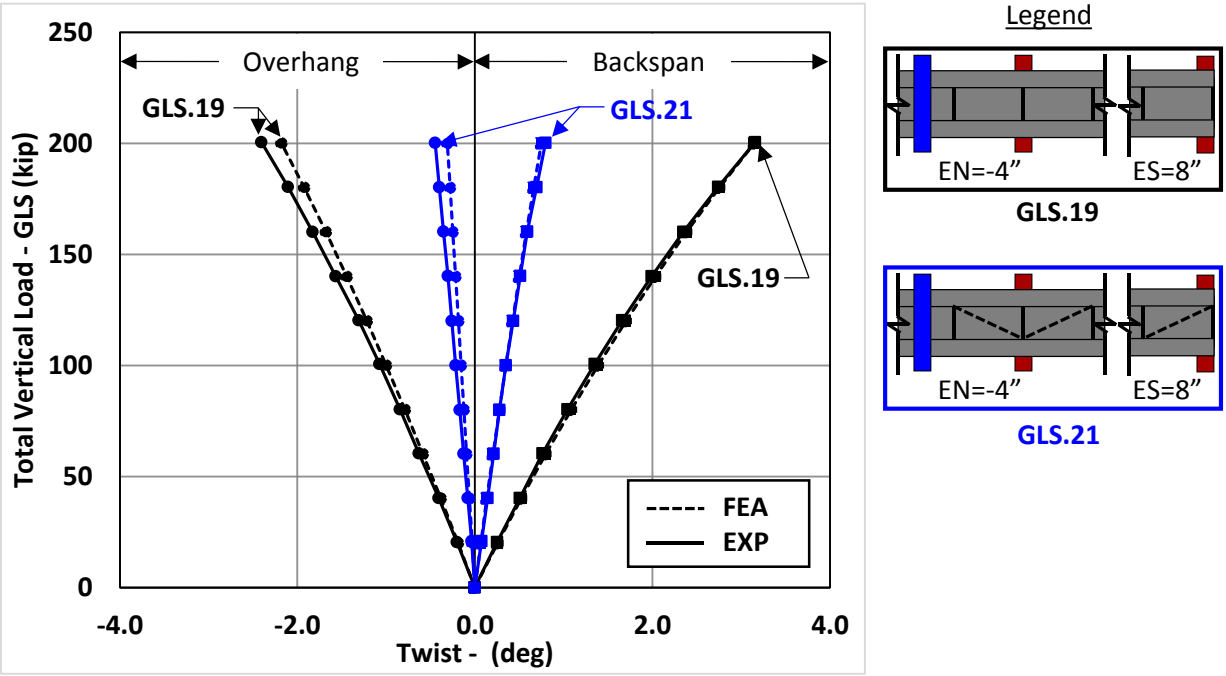

Figure E.42: Twist vs. GLS Load (EN=-4” & ES=8”) - DIA

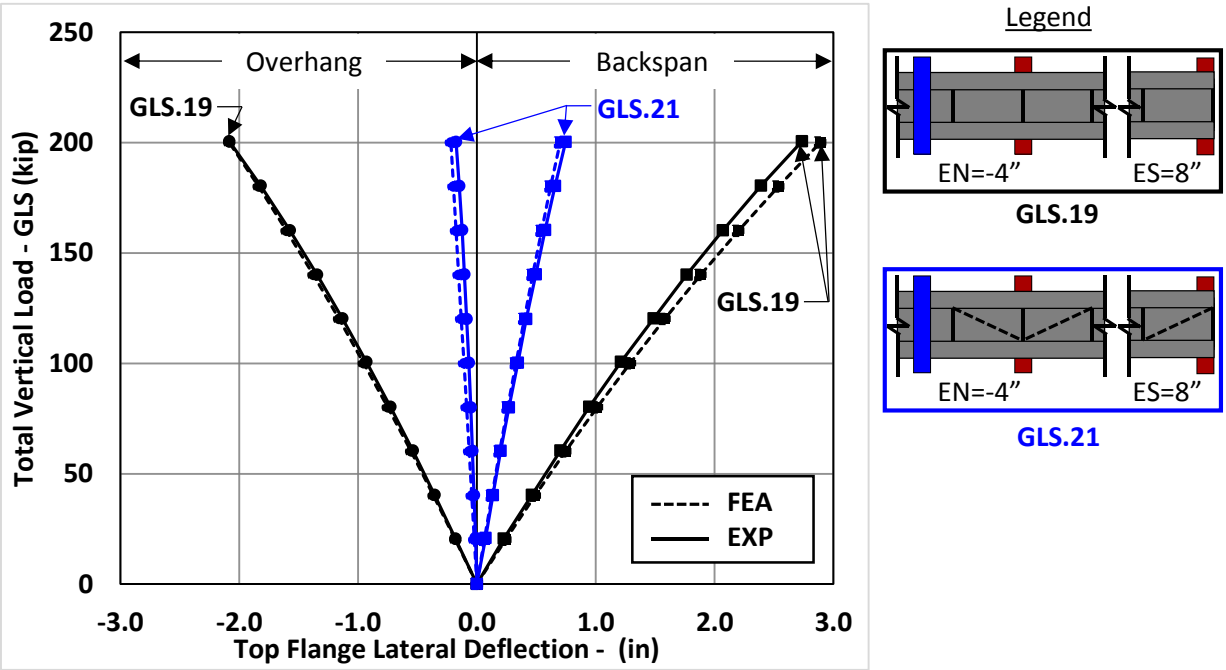

Figure E.43: Lateral Deflection vs. GLS Load (EN=-4” & ES=8”) - DIA

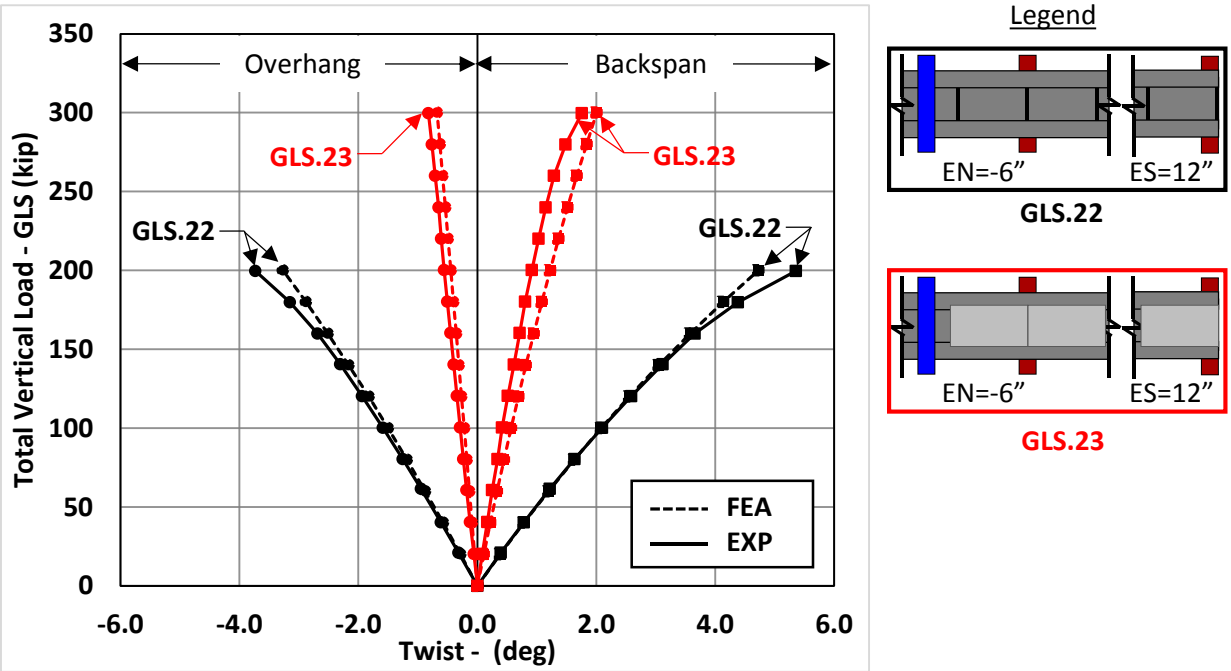

Figure E.44: Twist vs. GLS Load (EN=-6” & ES=12”) - PCP

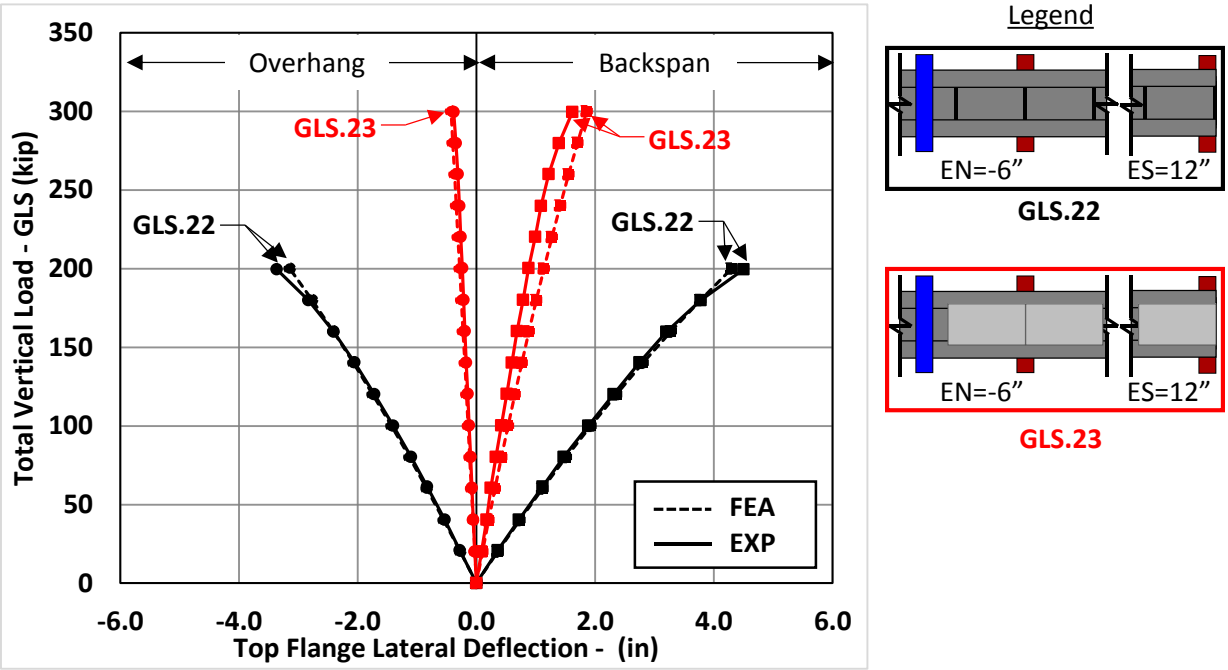

Figure E.45: Lateral Deflection vs. GLS Load (EN=-6” & ES=12”) - PCP

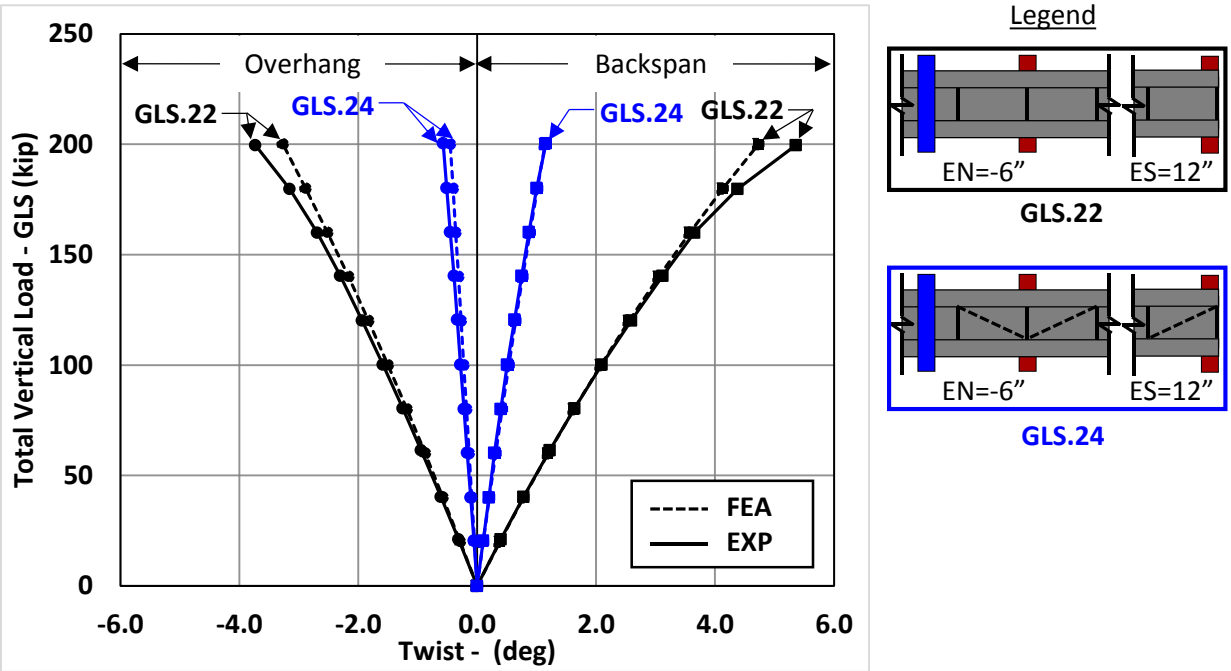

Figure E.46: Twist vs. GLS Load (EN=-6” & ES=12”) - DIA

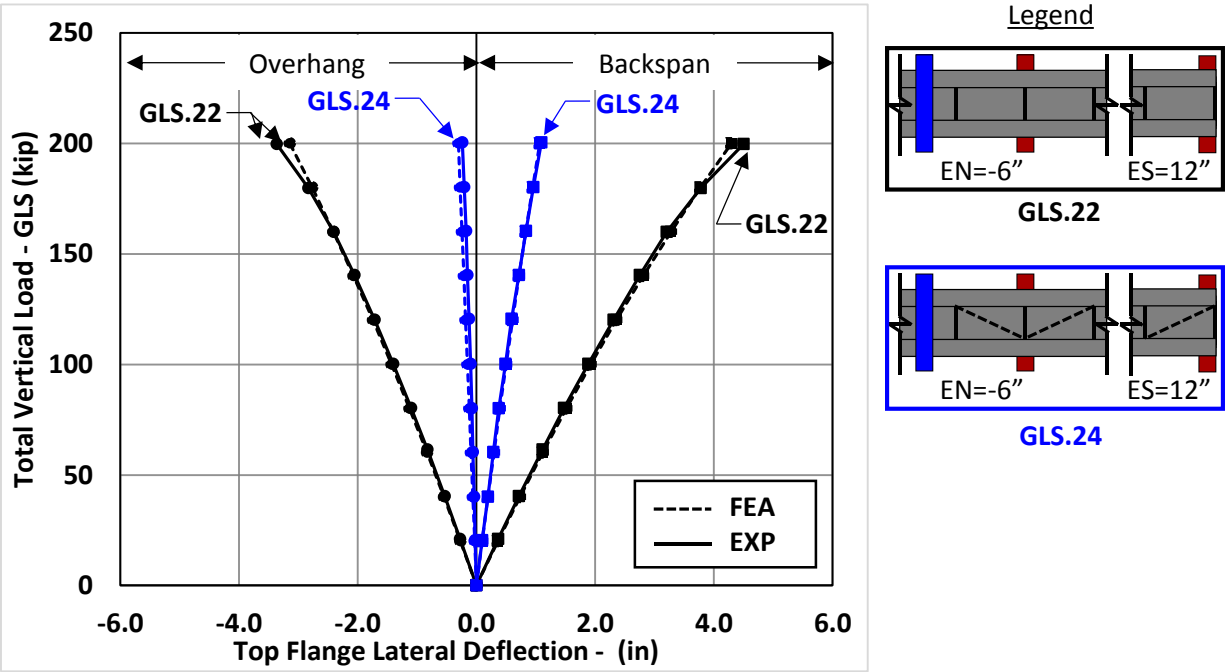

Figure E.47: Lateral Deflection vs. GLS Load (EN=-6” & ES=12”) - DIA

E.4 Estimated PCP Shear Force from Tub Girder FE Models

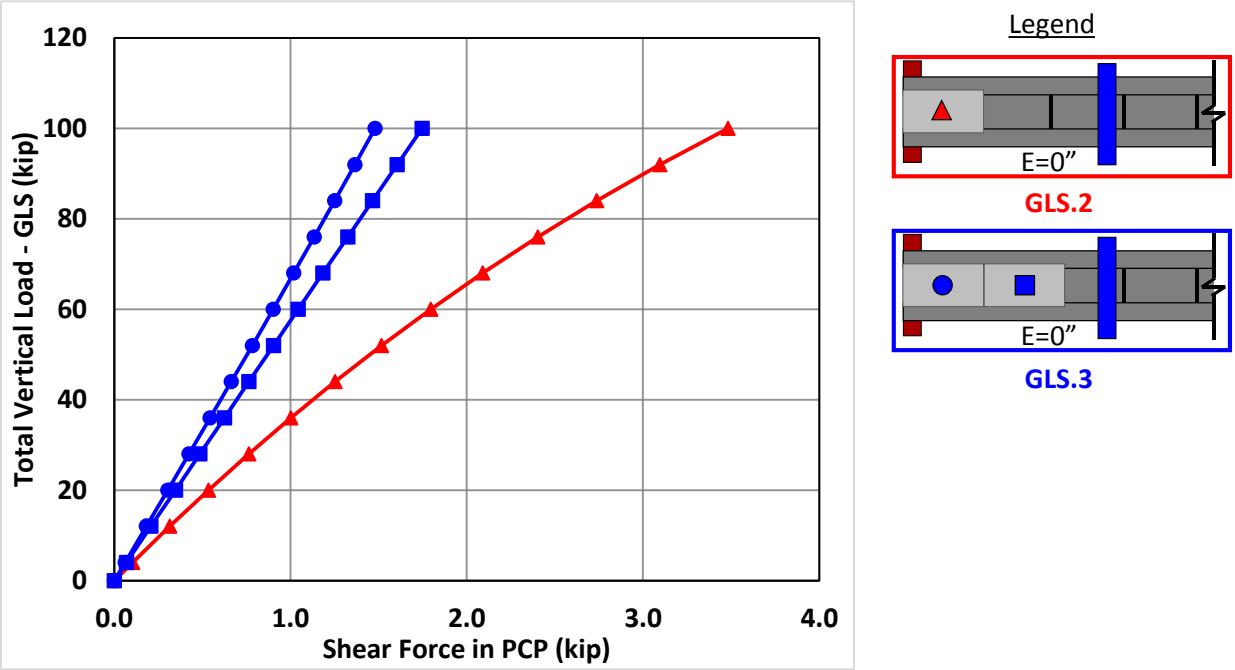

Figure E.48: Estimated Shear in PCP vs. GLS Load (E=0”)

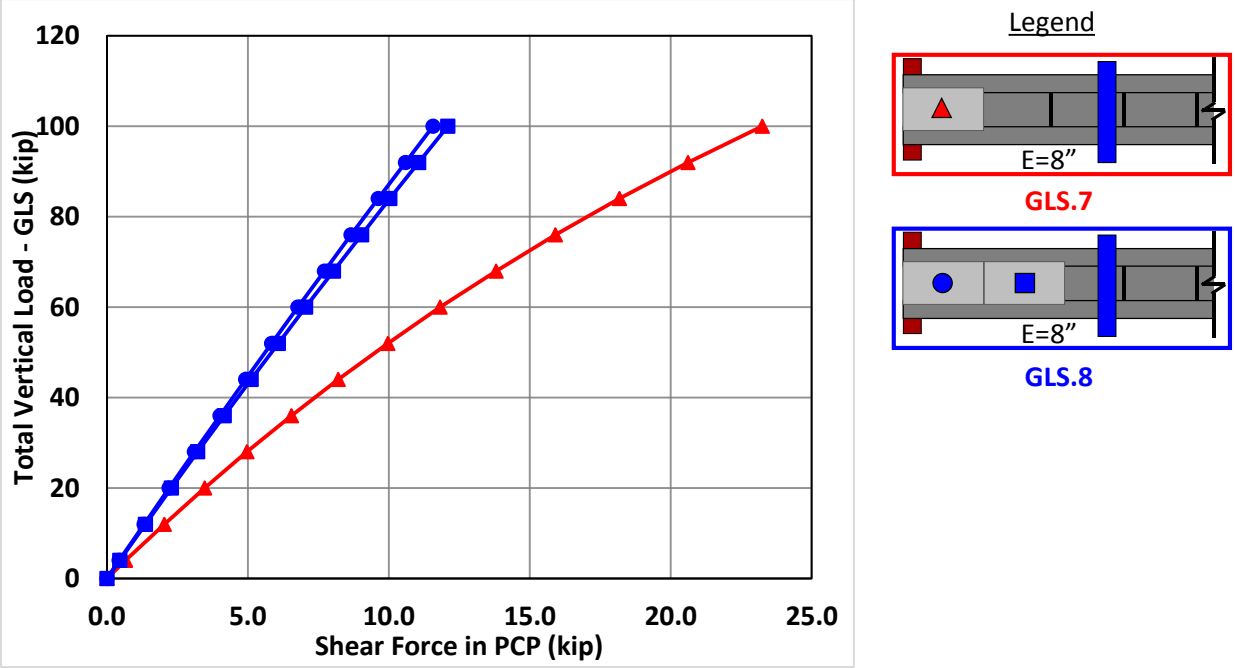

Figure E.49: Estimated Shear Force in PCPs vs. GLS Load (E=8”)

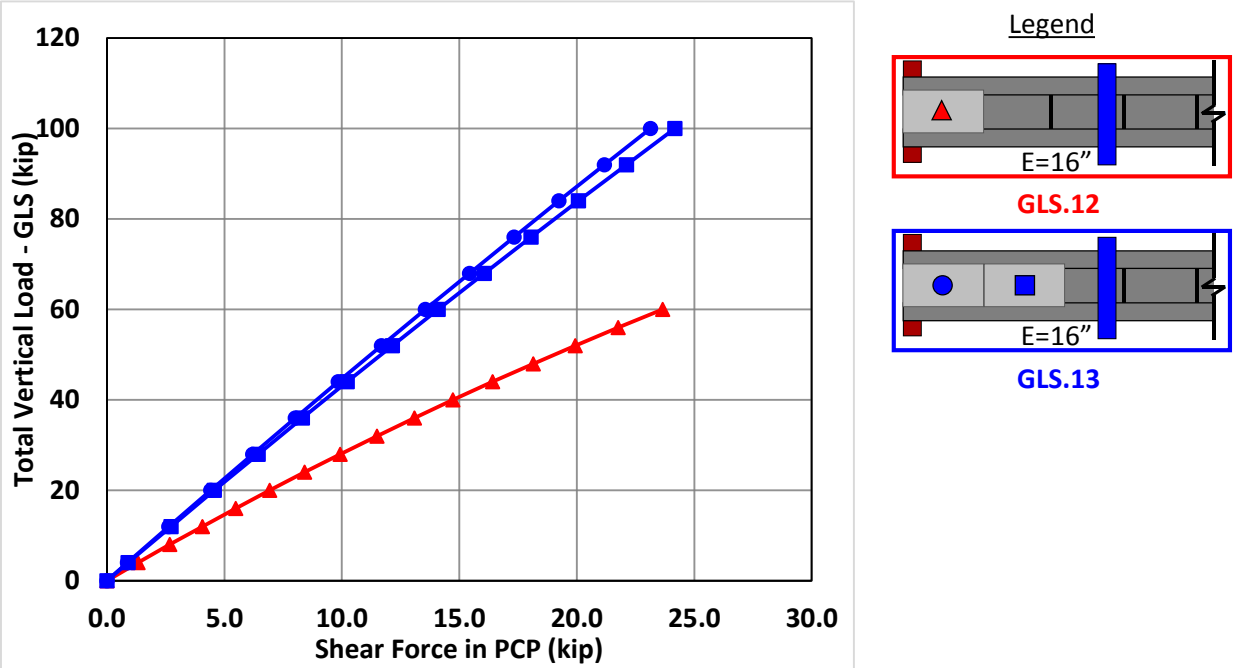

Figure E.50: Estimated Shear Force in PCPs vs. GLS Load (E=16”)

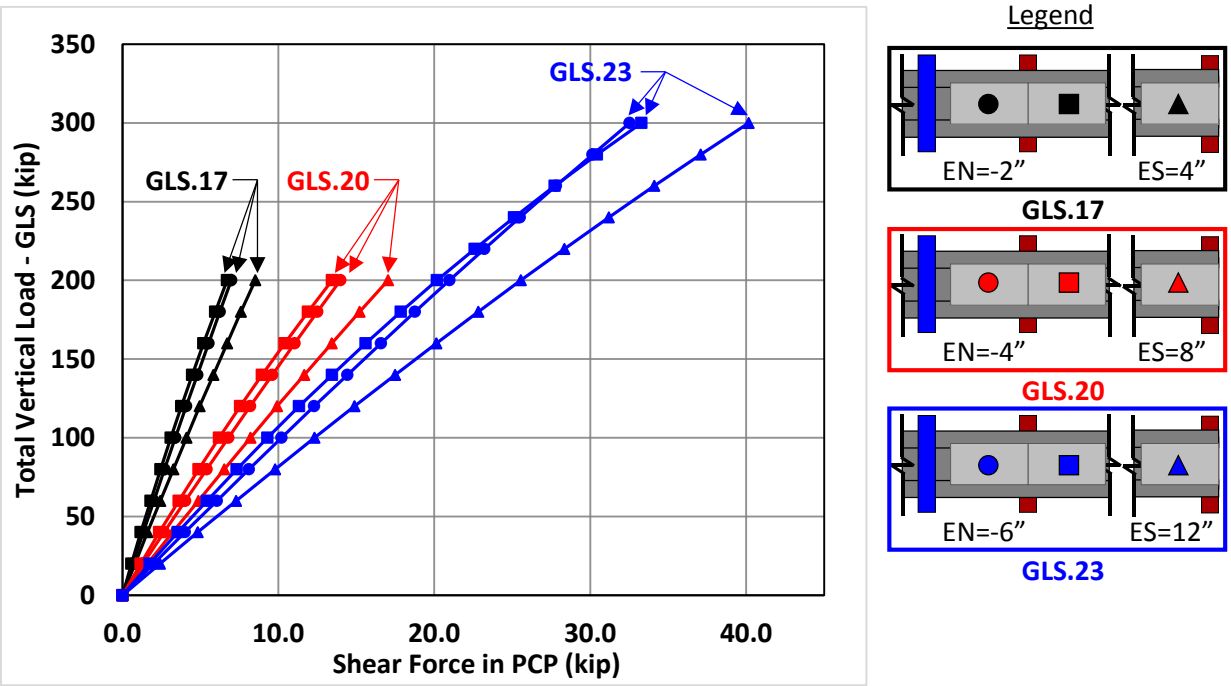

Figure E.51: Estimated Shear Force in PCPs vs. GLS Load – Overhang